Waqar Ahmed · Mark J. Jackson *Editors*

Surgical Tools and Medical Devices

Second Edition

Springer

Surgical Tools and Medical Devices

Waqar Ahmed · Mark J. Jackson
Editors

Surgical Tools and Medical Devices

Second Edition

Springer

Editors
Waqar Ahmed
School of Medicine
University of Central Lancashire
Preston
UK

Mark J. Jackson
Kansas State University
Salina, KS
USA

ISBN 978-3-319-33487-5 ISBN 978-3-319-33489-9 (eBook)
DOI 10.1007/978-3-319-33489-9

Library of Congress Control Number: 2016937516

This Springer imprint is published by the registered company Springer Nature Switzerland AG
The registered company address is: Gewerbestrasse 11, 6330 Cham, Switzerland

Foreword by Sir Harold W. Kroto

The new millennium has seen the birth of a new perspective that conflates research in solid-state physics, biological science as well as materials engineering. The perspective is one that recognizes that future new advances in all these areas will be based on a fundamental understanding of the atomic and molecular infrastructure of materials that has resulted from two centuries of chemistry. Major advances will be achieved when the novel behavior, in particular the quantum mechanical behavior, that nanoscale structures possess, can be controlled and harnessed.

To go with this new perspective the conflated fields have acquired a new name—Nanoscience and Nanotechnology (N&N). The promise of developing functional devices at the molecular and atomic scale is now becoming a reality. However, a massive effort is still needed in order to control the fabrication of such novel nanodevices and nanomachines and exploit processes based on quantum mechanical laws. The next decade should see the emergence of new technologies based on nanosystems with not only improved but hopefully also fundamentally new physico-chemical properties produced at reasonable costs. Experimental and theoretical research should lead to industrial applications yielding important breakthroughs. If universities, independent research centers, government agencies, and innovative industrial organizations invest time and resources imaginatively in this multidisciplinary adventure, a highly synergistic process will ensue in the development of these new technologies.

Nanotechnology is the ability to manipulate atoms and molecules to produce nanostructured materials and functional nanocoatings on biomedical devices and surgical tools. Nanotechnology is likely to have a significant effect on the global economy and on society in this century, and it promises to make breakthroughs in the biological and medical sciences.

This book contains chapters that focus not only on fundamental advances that are taking place but also on important applications, in particular in the biomedical field that promise to revolutionize a wide range of technologies in the 21st century.

The unique properties that emanate from nanoscale structures are immensely varied and in the next decade nanoscience and nanotechnology will give birth to a vast new range of exciting technological applications that promise to help the creation of a sustainable socioeconomic environment.

Prof. Sir Harold W. Kroto, FRS
Nobel Laureate, Chemistry 1996

Preface

Medical devices and surgical tools that contain micro- and nanoscale features allow surgeons to perform clinical procedures with greater precision and safety in addition to monitoring physiological and biomechanical parameters more accurately. While surgeons have started to master the use of nanostructured surgical tools in the operating room, the impact and interaction of nanomaterials and nanostructured coatings has yet to be addressed in a comprehensive manner.

Nobel Laureate Richard Feynman's revolutionary vision on nanotechnology was captured in a paper published in the February 1960 issue of Caltech's journal, '*Engineering and Science*'. In this paper, Feynman speaks about manipulating atoms and constructing products atom-by-atom, and molecule-by-molecule. Feynman describes the scaling down of lathes and drilling machines, and talks about drilling holes, turning, molding, and stamping parts. Even in 1959, Feynman describes the need for micro- and nanofabrication as the basis for creating a microscopic world that would benefit mankind. Nanotechnology encompasses technology performed at nanoscale that has real-world applications. Nanotechnology will have a profound effect on our society that will lead to breakthrough discoveries in materials and manufacturing, medicine, healthcare, the environment, sustainability, energy, biotechnology, and information technology.

President Bill Clinton talked about the exciting promise of nanotechnology in January 2000, and later announced an ambitious National Nanotechnology Initiative (NNI) that was enacted in 2001 with a budget of $497 million to promote nanoscale research that would benefit society. The purpose of this book is to present information and knowledge on the emerging field of surface-engineered biomedical devices and surgical tools. The book is written in the spirit of scientific endeavor outlined by Richard Feynman, who stated that one of the greatest challenges to scientists in the field of miniaturization is the manufacture of objects for medical applications using techniques such as turning, molding, stamping, and drilling. The book presents information on surface-engineered surgical tools and medical devices that looks at the interaction between nanotechnology, nanomaterials, and tools for surgical applications. Chapters of the book describe developments in coatings for

heart valves, stents, hip and knee joints, cardiovascular devices, orthodontic applications, and regenerative materials such as bone substitutes. Also some chapters are dedicated to the performance of surgical tools and dental tools and describe how nanostructured surfaces can be created for the purposes of improving cell adhesion between the medical device and the human body.

The structure of the book is based on the matter provided by many colleagues and has been updated to reflect changes made to the subject area since the first edition published in 2006. The authors wish to thank the contributors of this book for helping construct a source of knowledge and information on surface-engineered medical devices and surgical tools and for granting the editors permission to use such matter.

January 2016

Waqar Ahmed
Mark J. Jackson

Contents

Contributors

W. Ademosu University of Paisley, Scotland, UK

Isma Ahmed School of Pharmacy and Biomedical Sciences, University of Central Lancashire, Preston, UK

Waqar Ahmed School of Medicine, University of Central Lancashire, Preston, UK; Medical Engineering Research Group, University of Central Lancashire, Preston, UK

Mohammed AlHannan School of Pharmacy and Biomedical Sciences, University of Central Lancashire, Preston, UK

Mohamed Albed Alhnan School of Pharmacy and Biomedical Sciences, University of Central Lancashire, Preston, UK

N. Ali University of Aveiro, Aveiro, Portugal; Manchester Metropolitan University, Manchester, UK

Taimur Athar OBC, CSIR-Indian Institute of Chemical Technology, Hyderabad, Andhra Pradesh, India

M. Balazic University of Ljubljana, Ljubljana, Slovenia

D. Bombac University of Ljubljana, Ljubljana, Slovenia

M. Brojan University of Ljubljana, Ljubljana, Slovenia

G. Cabral University of Aveiro, Aveiro, Portugal

R. Caram University of Porto, Porto, Portugal

Charalambos P. Charalambous Department of Trauma and Orthopaedics, Blackpool Victoria Hospital, Blackpool, UK; School of Medicine and Dentistry, University of Central Lancashire, Preston, UK; Faculty of Medical and Human, Institute of Inflammation and Repair Sciences, University of Manchester, Manchester, UK

M.B. da Silva Kansas State University, Salina, Kansas, USA

Abdelbary Elhissi Pharmaceutical Sciences Section, College of Pharmacy, Qatar University, Doha, Qatar

M.H. Fernandes University of Porto, Porto, Portugal

Morris Gordon School of Medicine, University of Central Lancashire, Preston, UK

J. Gracio University of Aveiro, Aveiro, Portugal

D. Hammond School of Medicine, University of Central Lancashire, Preston, UK; Medical Engineering Research Group, University of Central Lancashire, Preston, UK

R. Handy School of Medicine, The University of Utah, Salt Lake City, UT, USA

I.U. Hassan Manchester Metropolitan University, Manchester, UK

Mark J. Jackson Kansas State University, Salina, KS, USA

Aneela Javeed School of Pharmacy and Biomedical Sciences, University of Central Lancashire, Preston, UK

A. Jones Manchester Metropolitan University, Manchester, UK

Iftikhar Khan School of Pharmacy and Biomedical Sciences, University of Central Lancashire, Preston, UK

J. Kopac University of Ljubljana, Ljubljana, Slovenia

F. Kosel University of Ljubljana, Ljubljana, Slovenia

Y. Kousa University of Aveiro, Aveiro, Portugal

Tariq A. Kwaees Department of Trauma and Orthopaedics, Blackpool Victoria Hospital, Blackpool, UK

M. Lafreniere Ohio University, Chillicothe, OH, USA

J.C. Madaleno University of Aveiro, Aveiro, Portugal

C. Maryan Manchester Metropolitan University, Manchester, UK

A.C. Mauricio University of Porto, Porto, Portugal

A. McLean University of Paisley, Scotland, UK

M. McPhillips School of Medicine, University of Central Lancashire, Preston, UK; Medical Engineering Research Group, University of Central Lancashire, Preston, UK

J. Morrell National Security Complex, Oak Ridge, TN, USA

T. Novakov Kansas State University, Salina, Kansas, USA

A.A. Ogwu University of Paisley, Scotland, UK

T. Okpalugo University of Ulster, Newtownabbey, UK

D.A. Phoenix London South Bank University, London, UK

F. Placido University of Paisley, Scotland, UK

C. Rego Manchester Metropolitan University, Manchester, UK

G.M. Robinson Micromachinists Group, Cambridge, MA, USA

J.D. Santos University of Porto, Porto, Portugal

H. Sein Manchester Metropolitan University, Manchester, UK

P. Senarith Medtronic Corporation, Minneapolis, MN, USA

T. Shokufar University of Aveiro, Aveiro, Portugal

N. Sooraj Hussain University of Porto, Porto, Portugal

A. Sousa University of Aveiro, Aveiro, Portugal

Paul M. Sutton Department of Orthopaedics, Northern General Hospital, Sheffield, UK

E. Titus University of Aveiro, Aveiro, Portugal

J. Verran Manchester Metropolitan University, Manchester, UK

R.A.J. Wain School of Medicine, University of Central Lancashire, Preston, UK; Medical Engineering Research Group, University of Central Lancashire, Preston, UK

T.J. Webster Brown University, Providence, RI, USA

M. Whitfield Micromachinists Group, Cambridge, MA, USA

M. Whitt California State Polytechnic, San Luis-Obispo, CA, USA

J.P.M. Whitty School of Engineering, University of Central Lancashire, Preston, UK; Medical Engineering Research Group, University of Central Lancashire, Preston, UK

C. Yao Brown University, Providence, RI, USA

Sakib Yousaf School of Pharmacy and Biomedical Sciences, University of Central Lancashire, Preston, UK

Nomenclature

a-C:H	Hydrogenated amorphous carbon
a-C:H:N	Nitrogen-doped hydrogenated amorphous carbon
a-C:H:Si	Silicon-doped hydrogenated amorphous carbon
AFI	Average fluorescence intensity
AFM	Atomic force microscopy
AIDS	Acquired immune deficiency syndrome
ALP	Alkaline phosphatase activity
BMA	Bone marrow aspirate
BMP	Bone morphogenetic protein
BMU	Basic multicellular unit
BSA	Bovine serum albumin
BSP	Bone sialoprotein
CAM	Cell adhesion molecule
CCD	Charge-coupled device
COL I	Collagen type 1
CPD	Contact potential difference
DAC	Digital-to-analogue converter
DAS	Data acquisition system
DBM	Demineralized bone matrix
DC	Direct current
DCA	Dynamic contact angle
DLC = a-C:H	Diamond-like carbon
DMEM	Dulbecco minimal essential media
DMSO	Dimethylsulphoxide
DSP	Data signal processor
ECM	Extracellular matrix
EDS	Energy dispersive spectroscopy
EDTA	Ethylenediaminetetraacetic acid
EGF	Epithelial growth factor
ELISA	Enzyme linked immuno-sorbent assay
EM	Electrophoretic mobility

FAT	Fixed analyser transmission
FCS	Fetal calf serum
FTIR	Fourier transform infra-red
GPIB	General-purpose interface bus
HeLa	Henrietta Lacks cervical carcinoma cell line (the first in vitro human cell line)
HMDS	Hexamethyldisilaxane
HMEC	Human microvascular endothelial cell
L132	Human embryonic lungs cell line (HeLa-characteristics/contamination)
LASER	Light amplification by stimulated emission of radiation
LED	Light-emitting diode
MCDB	Microvascular endothelial cell growth media
MEM	Minimal essential media
MSM	Metal semiconductor metal sandwich
MTT	3-(4,5-dimethylthiazol-2-yl)-2,5-diphenyl tetrazolium bromide
N1	N-DLC film obtained with nitrogen ions bombardment for 1 h
N1h	N-DLC film obtained with nitrogen ions bombardment for 1.5 h
N2	N-DLC film obtained with nitrogen ions bombardment for 2 h
N2h	N-DLC film obtained with nitrogen ions bombardment for 2.5 h
N-DLC = a-C:H:N	Nitrogen-doped diamond-like carbon
NEAA	Non-essential amino acid
PECVD	Plasma-enhanced chemical vapor deposition
PBS	Phosphate-buffered saline
PPP	Platelet-poor plasma
PRP	Platelet-rich plasma
Ra	Arithmetical mean roughness
RF	Radio frequency
RMS	Root mean square
Sccm	Standard cubic centimeter
SD10	Si-DLC film obtained using TMS flow rate of 10 sccm
SD15	Si-DLC film obtained using TMS flow rate of 15 sccm
SD20	Si-DLC film obtained using TMS flow rate of 20 sccm
SD5	Si-DLC film obtained using TMS flow rate of 5 sccm
SEM	Scanning electron microscope
Si-DLC = a-C H:Si	Silicon-doped diamond-like carbon
SN1	N-DLC film obtained with nitrogen neutrals bombardment for 1 h
SN1h	N-DLC film obtained with nitrogen neutrals bombardment for 1.5 h

SN2	N-DLC film obtained with nitrogen neutrals bombardment for 2 h
SN2h	N-DLC film obtained with nitrogen neutrals bombardment for 2.5 h
SPR	Surface plasmon resonance
SW	Silicon wafer (uncoated)
TCPS	Tissue culture polystyrene
TMS	Tetramethylsilane
T_R	Room temperature
V79	Chinese hamster cell line
WF	Work function
WR	Web reference
XPS	X-ray photoelectron spectroscopy
ZDOI	Zero depth of immersion
σ	Bending strength
θ	Contact angle
λ	Wavelength

Chapter 1
Atomic Scale Machining of Medical Materials

Mark J. Jackson, T. Novakov, M.B. da Silva, R. Handy, G. Robinson, M. Whitfield, J. Morrell and W. Ahmed

Abstract Molecular dynamic simulations of machining at the atomic scale can reveal a significant amount of information regarding the behaviour of machining and grinding processes that cannot be explained easily using classical theory or experimental procedures. This chapter explains how the use of molecular dynamic simulations can be applied to the many problems associated with machining and grinding at the meso-, micro-, and nanoscales. These include: (a) mechanics of nanoscale machining of ferrous and non-ferrous materials; (b) physics of nanoscale grinding of semiconductor materials; (c) effects of simulating a variety of machining parameters in order to minimize subsurface damage; (d) modelling of exit failures experienced during machining such as burr formation and other dynamic instabilities during chip formation; (e) simulation of known defects in microstructures using molecular dynamic simulations, statistical mechanical, and Monte Carlo methods; (f) simulation of machining single crystals of known orientation; (g) extremely high-speed nanometric cutting; (h) tool wear during machining; and (i) the effects of hardness on the wear of tool and workpiece materials. The nature of wear of the material ahead of the machining and grinding process, the variation of machining forces, and the amount of specific energy induced into the workpiece material using molecular dynamic simulations is discussed in this chapter.

M.J. Jackson (✉) · T. Novakov · M.B. da Silva
Kansas State University, Salina, Kansas, USA
e-mail: jacksonmj04@yahoo.com

R. Handy
The University of Utah, Salt Lake City, UT, USA

G. Robinson · M. Whitfield
Micromachinists Group, Cambridge, MA, USA

J. Morrell
National Security Complex, Oak Ridge, TN, USA

W. Ahmed
School of Medicine, University of Central Lancashire, Preston, UK

W. Ahmed and M.J. Jackson (eds.), *Surgical Tools and Medical Devices*,
DOI 10.1007/978-3-319-33489-9_1

1.1 Introduction

Nanotechnology is the creation and utilization of materials, structures, devices, and systems through the control of matter at the nanometre length scale. The essence of nanotechnology is the ability to work at these levels to generate large structures with fundamentally new properties. Although certain applications of nanotechnology, such as giant magnetoresistance (GMR) structures for computer hard disc read head and polymer displays have entered the marketplace, in general nanotechnology is still at a very early stage of development. The barriers between nanotechnology and the marketplace lie in how to reduce the fabrication cost and how to integrate nanoscale assemblies with functional microscale and macro devices. Therefore, reliable mass production of nanostructures is currently one of the most crucial issues in nanotechnology. The commercialization of nanotechnology has to address the underlying necessities of predictability, repeatability, producibility, and productivity in manufacturing at nanometre scale.

Nanometric machining refers to a "top-down" nanofabrication approach. To the authors' knowledge the concept of nanometric machining is more concerned with precision rather than characteristic size of the product. Therefore, nanometric machining is defined as the material removal process in which the dimensional accuracy of a product can be achieved is 100 nm or less. Nanometric machining can be classified into four categories:

- Deterministic mechanical nanometric machining. This method utilizes fixed and controlled cutting tools, which can specify the profiles of 3D components by a well-defined tool surface. The method can remove materials in amounts as small as tens of nanometres. It includes processes such as diamond turning, micro-milling, and nano/micro grinding.
- Loose abrasive nanometric machining. This method uses loose abrasive grits to removal a small amount of material. It consists of polishing, lapping, and honing.
- Non-mechanical nanometric machining comprises processes such as focused ion beam machining, micro-EDM, and excimer laser machining.
- Lithographic method. The method employs masks to specify the shape of the product. 2D shapes are the main outcome; severe limitations occur when 3D products are attempted [19]. Processes include X-ray lithography, LIGA, and electron beam lithography.

The author believes that mechanical nanometric machining has more advantages than other methods since it is capable of machining complex 3D components in a controllable and deterministic way. The machining of complex surface geometries is just one of the future trends in nanometric machining, which is driven by the integration of multiple functions in one product. For instance, the method can be used to machine micro moulds/dies with complex geometric features and high dimensional and form accuracy, and even nanometric surface features. The method is indispensable to manufacturing complex micro and miniature structures,

components, and products in a variety of engineering materials. This chapter focuses on nanometric cutting theory, methods, and its implementation and application perspectives.

1.2 Nanomachining

The scientific study of nanometric machining has been undertaken since the late 1990s. Much attention to the study has been paid especially with the advancement of nanotechnology [26]. The scientific study will result in the formation of the theoretical basis of nanometric machining, which enables the better understanding of nanometric machining physics and the development of controllable techniques to meet the requirements for nanotechnology and nanoscience.

1.2.1 Cutting Force and Energy

In nanomanufacturing, the cutting force and cutting energy are important issues. They are important physical parameters for understanding cutting phenomena as they clearly reflect the chip removal process. From the point of view of atomic structures, cutting forces are the superposition of the interactions of forces between workpiece atoms and cutting tool atoms. Specific energy is an intensive quantity that characterizes the cutting resistance offered by a material [73]. Ikawa et al. [26], and Luo et al. [53] have acquired the cutting forces and cutting energy by molecular dynamics (MD) simulations. Ikawa et al. [26] have carried out experiments to measure the cutting forces in nanometric machining. Figure 1.1 shows the simulation and experimental results in nanometric cutting. Figure 1.1a illustrates the linear relationship that exists between the cutting force per width and depth of cut in both simulations and experiments. The cutting forces per width increase with the increment of the depth of cut.

The difference in the cutting force between simulations and experiment is caused by the different cutting edge radii applied in the simulations. In nanometric machining the cutting edge radius plays an important role since the depth of cut is similar in scale. Under the same depth of cut higher cutting forces are required for a tool with a large cutting edge radius compared with a tool with a small cutting edge radius. The low cutting force per width is obviously the result of fine cutting conditions, which will decrease the vibration of the cutting system and thus improve machining stability and will also result in better surface roughness.

A linear relationship between the specific energy and the depth of cut can also be observed in Fig. 1.1. The figure shows that the specific energy increases with a decreasing of depth of cut, because the effective rake angle is different under different depths of cut. In small depths of cut the effective rake angle will increase with the decreasing of depth of cut. Large rake angles result in an increase in

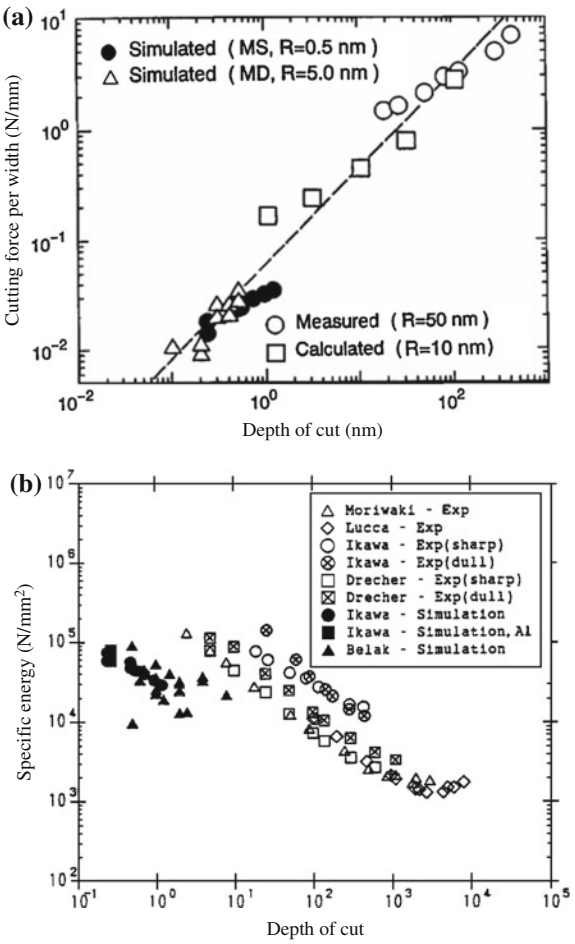

Fig. 1.1 The comparison of results between simulations and experiments: **a** cutting force per width against depth of cut; **b** specific energy against depth of cut [26]

specific cutting energy. This phenomenon is often called the "size effect", which can be clearly explained by material data listed in Table 1.1. According to Table 1.1, in nanometric machining only point defects exist in the machining zone in a crystal. Therefore, the material will need more energy to initiate the formation of an atomic crack or the movement of an atomic dislocation. The decreasing of depth of cut will decrease the chance for the cutting tool to meet point defects in the material and will result in increasing the specific cutting energy.

If the machining unit is reduced to 1 nm, the workpiece material structure at the machining zone may approach atomic perfection; hence more energy will be required to break the atomic bonds. Alternatively, when the machining unit is higher than 0.1 μm, the machining points will fall into the distribution distances of some defects such as dislocations, cracks, and grain boundaries. The pre-existing

Table 1.1 Material properties under different machining conditions [83]

	1 nm–0.1 μm	0.1 μm–10 μm	10 μm–1 mm
Defects/impurities	Point defect	Dislocation/crack	Crack/grain boundary
Chip removal unit	Atomic cluster	Subcrystal	Multi-crystals
Brittle fracture limit	10^4–10^3 J/m^3 Atomic crack	10^3–10^2 J/m^3 Micro crack	10^2–10^1 J/m^3 Brittle crack
Shear failure limit	10^4–10^3 J/m^3 Atomic dislocation	10^3–10^2 J/m^3 Dislocation slip	10^2–10^1 J/m^3 Shear deformation

defects will ease the deformation of workpiece material and result in a comparatively low specific cutting energy.

Nanometric cutting is also characterized by the high ratio of the normal to the tangential component in the cutting force [53, 73], as the depth of cut is very small in nanometric cutting and the workpiece is mainly processed by the cutting edge. The compressive interactions will thus become dominant in the deformation of the workpiece material, which will therefore result in the increase of friction force at the tool–chip interface with a relatively high cutting ratio.

Usually, the cutting force in nanometric machining is very difficult to measure due to its small amplitude compared with the noise generated (mechanical or electronic). A piezoelectric dynamometer, or load cell, is used to measure the cutting forces because of their characteristic high sensitivity and natural frequency. Figure 1.2 shows an experimental force measuring system in micromilling process carried out by Dow et al. [18]. The three-axis load cell, Kistler 9251, is mounted in a specially designed mount on the Y-axis of a Nanoform 600 diamond turning machine. A piece of S-7 steel that has been ground flat on both sides is used as the workpiece and secured through the top of the load cell with a bolt preloaded to

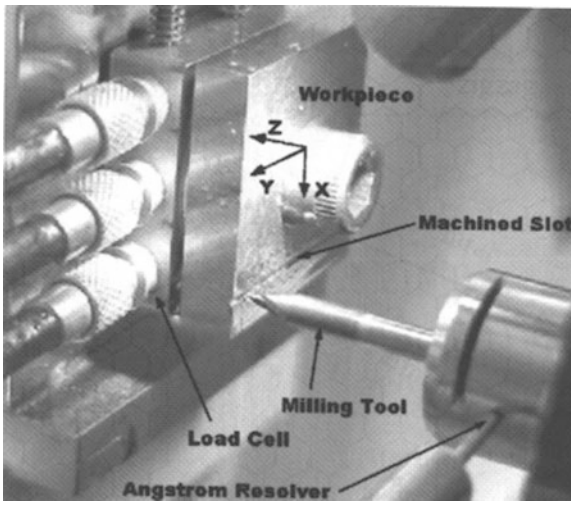

Fig. 1.2 Experimental force measurement system in micromilling process [18]

30 N. The tool was moved in the +Z direction to set the depth of cut and the workpiece was fed in the +y direction to cut the groove.

The milling tool is mounted in a Westwind D1090-01 air bearing turbine spindle capable of speeds up to 60,000 rpm. The spindle is attached to the Z-axis of the Nanoform 600. To determine the rotational speed of the tool and the orientation of each flute, an optical detector (Angstrom resolver) was used to indicate a single rotation of the spindle by reading a tool revolution marker aligned with one flute. The measured 3D cutting forces under depth of cut of 25 μm, feed rate of 18.75 μm/flute, are of the order of several newtons.

1.2.2 Cutting Temperature

In MD simulations, the cutting temperature can be calculated under the assumption that the cutting energy totally transforms into cutting heat and results in increasing the cutting temperature and kinetic energy of system. The lattice vibration is the major form of thermal motion of atoms. Each atom has three degrees of freedom. According to the theorem of equipartition of energy, the average kinetic energy of the system can be expressed as follows:

$$\overline{E_k} = \frac{3}{2} N k_B T = \sum_i \frac{1}{2} m(V_i^2) \tag{1.1}$$

where $\overline{E_k}$ is average kinetic energy in equilibrium state, k_B is Boltzmann's constant, T is absolute temperature, and m_i and V_i are the mass and velocity of an atom, respectively. N is the number of atoms.

The cutting temperature can be calculated using the following equation:

$$T = \frac{2\,\overline{E_k}}{3Nk_B} \tag{1.2}$$

Figure 1.3 shows the variation of cutting temperature on the cutting tool in MD simulation of nanometric cutting of single crystal aluminium [10].

The highest temperature is observed at cutting edge although the temperature at the flank face is also higher than that at the rake face. The temperature distribution suggests that a major source of heat exists at the interface between the cutting edge and the workpiece, and that the heat be conducted from there to the rest of the cutting zone. This is because that most of cutting action takes place at the cutting edge of the tool and the resulting dislocation deformation in the workpiece material will transfer their potential energy into kinetic energy and result in the observed temperature rise. The comparatively high temperature exhibited at the flank face is caused by the friction between the flank face and the workpiece. The released energy due to the elastic recovery of the machined surface also contributes to the

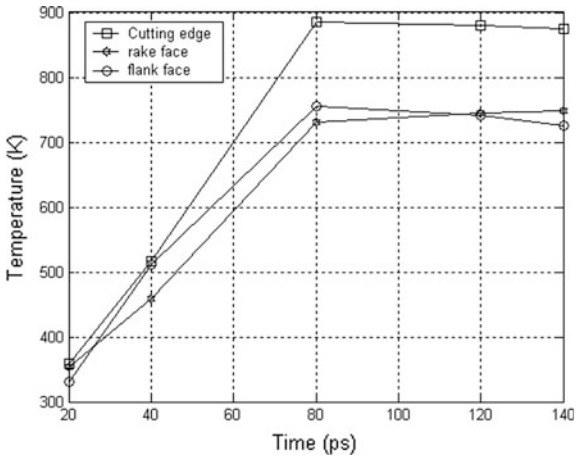

Fig. 1.3 Cutting temperature distribution of cutting tool in nanometric cutting (cutting speed = 20 m/s, depth of cut = 1.5 nm, cutting edge radius = 1.57 nm) [10]

incremental increase in temperature at flank face. Although there is friction between the rake face and the chip, the heat will be taken away from the rake face by the removal of the chip.

Therefore, the temperature at tool rake face is lower than that at the tool cutting edge and tool flank face. The temperature value shows that the cutting temperature in diamond machining is quite low in comparison with that in conventional cutting, due to low cutting energy in addition to high thermal conductivity of diamond and the workpiece material. The cutting temperature is considered to govern the wear of a diamond tool as shown in the MD simulation study by Cheng et al. [9]. In-depth experimental and theoretical studies are needed to find out the quantitative relationship between cutting temperature and tool wear although there is considerable evidence of chemical damage on the surface of diamond in which increases in temperature tends to plays a significant role [9].

1.2.3 Chip Formation and Surface Generation

Chip formation and surface generation can be simulated by MD simulations. Figure 1.4 shows an MD simulation of a nanometric cutting process on single crystal aluminium [10]. From Fig. 1.4a it is shown that after the initial plough of the cutting edge the workpiece atoms are compressed in the cutting zone near to the rake face and the cutting edge. The disturbed crystal lattices of the workpiece and even the initiation of dislocations can be observed in Fig. 1.4b. Figure 1.4c shows the dislocations have piled up to form a chip. The chip is removed with the unit of an atomic cluster as shown in Fig. 1.4d. Lattice disturbed workpiece material is observed on the machined surface.

Based on the visualization of the nanometric machining process, the mechanism of chip formation and surface generation in nanometric cutting can be explained.

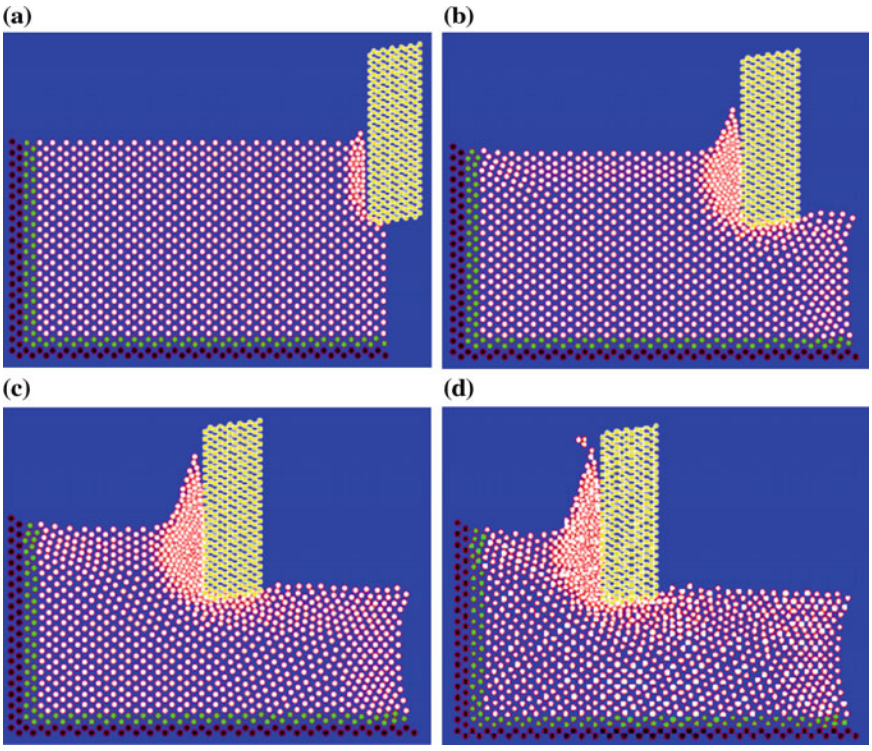

Fig. 1.4 MD simulations of the nanometric machining process (Cutting speed = 20 m/s, depth of cut = 1.4 nm, cutting edge radius = 0.35 nm) [10]

Owing to the ploughing of the cutting edge, the attractive force between the workpiece atoms and the diamond tool atoms becomes repulsive. Because the cohesion energy of diamond atoms is much larger than that of Al atoms, the lattice of the workpiece is compressed. When the strain energy stored in the compressed lattice exceeds a specific level, the atoms begin to rearrange so as to release the strain energy. When the energy is not sufficient to perform the rearrangement, some dislocation activity is generated. Repulsive forces between compressed atoms in the upper layer and the atoms in the lower layer are increasing, so the upper atoms move along the cutting edge, and at the same time the repulsive forces from the tool atoms cause the resistance for the upward chip flow to press the atoms under the cutting line. With the movement of the cutting edge, some dislocations move upward and disappear from the free surface as they approach the surface.

This phenomenon corresponds to the process of chip formation. As a result of the successive generation and disappearance of dislocations, the chip seems to be removed steadily. After the passing of the tool, the pressure at the flank face is released. The layers of atoms move upwards and result in elastic recovery, so that the machined surface is generated.

The conclusion can therefore be drawn that chip removal and machined surface generation are, in nature, dislocation slip motion inside the workpiece material grains. In conventional cutting, dislocations are initiated from the existing defects between the crystal grains, which will ease the movement of dislocations and result in smaller specific cutting forces compared with that in nanometric cutting.

The height of the atoms on the surface creates the observed surface roughness. For this, 2D MD simulation roughness average (R_a) can be used to assess the machined surface roughness. The surface integrity parameters can also be calculated based on the simulation results. For example, the residual stress of the machined surface can be estimated by averaging the forces acting on the atoms in a unit area on the upper layer of the machined surface.

MD simulation has been proved to be a useful tool for the theoretical study of nanometric machining [78]. At present, MD simulation studies on nanometric machining are limited by the computing memory size and speed of the computer. It is therefore difficult to enlarge the dimension of the current MD model on a personal computer. In fact, the machined surface topography is produced as a result of the copy of the tool profile on a workpiece surface that has a specific motion relative to the tool. The degree of the surface roughness is governed by both the controllability of machine tool motions (or relative motion between tool and workpiece) and the transfer characteristics (or the fidelity) of tool profile to the workpiece [26]. A multiscale analysis model, which can fully model the machine tool and cutting tool motion, environmental effects and the tool–workpiece interactions, is needed to predict and control the nanometric machining process in a deterministic manner.

1.2.4 Minimum Undeformed Chip Thickness

Minimum undeformed chip thickness is an important issue in nanometric machining because it relates to the ultimate machining accuracy. In principle, the minimum undeformed chip thickness will be determined by the minimum atomic distance within the workpiece. However, in ultra-precision machining practices it depends on the sharpness of the diamond cutting tool, the capability of the ultra-precision machine tool and the machining environment. Diamond turning experiments of non-ferrous work materials carried out at Lawrence Livermore National Laboratory in the United States of America show the minimum undeformed chip thickness, down to 1 nm, is attainable with a specially prepared fine diamond cutting tool on a very stiff ultra-precision machine tool.

Figure 1.5 illustrates chip formation of single crystal aluminium with the tool cutting edge radius of 1.57 nm [10]. No chip formation is observed when the undeformed chip thickness is 0.25 nm. But the initial stage of chip formation is apparent when the undeformed chip thickness reaches 0.26 nm. In nanometric cutting, as the depth of cut is very small, the chip formation is related to the force conditions on the cutting edge of the tool. Generally, chip formation is mainly a function of tangential cutting force.

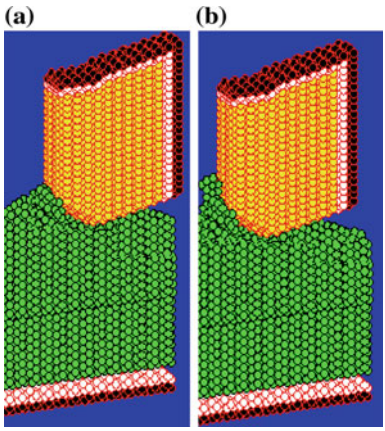

Fig. 1.5 Study of minimum undeformed chip thickness by MD simulation. **a** Undeformed chip thickness = 0.25 nm; **b** Undeformed chip thickness = 0.26 nm [10]

Table 1.2 Minimum undeformed chip thickness against the tool cutting edge radius and cutting forces [10]

Cutting edge radius (nm)	1.57	1.89	2.31	2.51	2.83	3.14
Minimum undeformed chip thickness (nm)	0.26	0.33	0.42	0.52	0.73	0.97
Ratio of minimum undeformed chip thickness to tool cutting edge radius	0.17	0.175	0.191	0.207	0.258	0.309
Ratio of tangential cutting force to normal cutting force	0.92	0.93	0.92	0.92	0.94	0.93

The normal cutting force makes little contribution to the chip formation since it has the tendency to penetrate the atoms of the surface into the bulk of the workpiece. The chip is formed on condition that the tangential cutting force is larger than the normal cutting force. The relationships between minimum undeformed chip thickness, cutting edge radius, and cutting forces are studied by MD simulations. The results are highlighted in Table 1.2 [10]. The data shows that the minimum undeformed chip thickness is about 1/3–1/6 magnitude of the tool cutting edge radius. Chip formation will be initiated when the ratio of tangential cutting force to normal cutting force is larger than 0.92.

1.2.5 Critical Cutting Edge Radius

It is widely accepted that the sharpness of the cutting edge of a diamond cutting tool directly affects the machined surface quality. Previous MD simulations show that the sharper the cutting edge, the smoother the machined surface becomes. But this conclusion is based on zero tool wear. To study the real effects of cutting edge radius, the MD simulations on nanometric cutting of single crystal aluminium are carried out using a tool wear model [78].

Table 1.3 The relationship between cutting edge radius and machined surface quality [10]

	Cutting edge radius (nm)	1.57	1.89	2.31	2.51	2.83	3.14
Depth of cut: 1.5 nm	S_q (nm)	0.89	0.92	0.78	0.86	0.98	1.06
Depth of cut: 2.2 nm	S_q (nm)	0.95	0.91	0.77	0.88	0.96	1.07
Depth of cut: 3.1 nm	S_q (nm)	0.97	0.93	0.79	0.87	0.99	1.08
Mean stress at cutting edge (GPa)		0.91	0.92	−0.24	−0.31	−0.38	−0.44

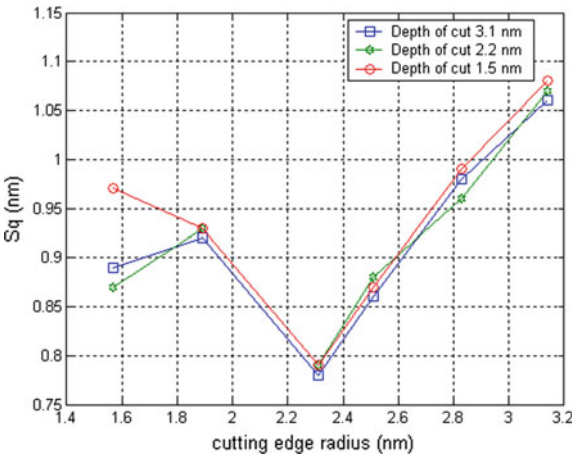

Fig. 1.6 Cutting edge radius against machined surface quality

In the simulations the cutting edge radius of the diamond cutting tool varies from 1.57 to 3.14 nm with depth of cut of 1.5, 2.2, and 3.1 nm. The cutting distance is fixed at 6 nm. The root-mean-square deviation of the machined surface and mean stress on the cutting edge are listed in Table 1.3.

Figure 1.6 shows the visualization of the simulated data, which clearly indicates that surface roughness increases with the decreasing cutting edge radius when the cutting edge radius is smaller than 2.31 nm. The tendency is caused by the rapid tool wear when a cutting tool with small cutting edge radius is used. But when the cutting edge is larger than 2.31 nm, the cutting edge is under compressive stress and no tool wear happens. Therefore, it shows the same tendency that the surface roughness increases with decreasing the tool cutting edge radius as in the previous MD simulations.

The MD simulation results also illustrate that it is not true that the sharper the cutting edge, the better the machined surface quality. The cutting edge will wear and results in the degradation of the machined surface quality if its radius is smaller than the critical value for cutting. But when the cutting edge radius is higher than the critical value, the compressive stress will take place at the tool edge and the tool

condition is more stable. As a result a high-quality machined surface can be achieved. Therefore, there is a critical cutting edge radius for achieving a high-quality machined surface.

For cutting single crystal aluminium, the critical cutting edge radius is 2.31 nm. The MD simulation approach is applicable for acquiring the critical cutting edge radius for nanometric cutting of other materials.

1.2.6 Properties of Workpiece Materials

In nanometric machining the microstructure of the workpiece material will play an important role in affecting the machining accuracy and machined surface quality. For example, when machining polycrystalline materials, the difference in the elastic coefficients at the grain boundary and interior of the grain causes small steps to be formed on the cut surface since the respective elastic "rebound" will vary. The study by Lee and Chueng [46] shows the shear angle varies with the crystallographic orientation of the materials being cut. This will produce a self-excited vibration between cutting tool and workpiece and result in a local variation of surface roughness of a diamond turned surface [14].

A material's destructive behaviour can also be affected by nanometric machining. In nanometric machining of brittle materials it is possible to produce plastically deformed chips if the depth of cut is sufficiently small [14]. It has been shown that a "brittle-to-ductile" transition exists when cutting brittle materials at low load and penetration levels. The transition from ductile-to-brittle fracture has been widely reported and is usually described as the "critical depth of cut", i.e. generally small up to 0.1–0.3 μm. These small depths of cut will result in relatively low material removal rates.

However, it is a cost-effective technique for producing high-quality spherical and non-spherical optical surfaces, with or without the need for lapping and polishing.

The workpiece materials should also have a low affinity with the cutting tool material. If pieces of the workpiece material are deposited onto the tool, this will cause tool wear and will adversely affect the surface in terms of surface roughness

Table 1.4 Diamond turned materials [14]

Semiconductors	Metals	Plastics
Cadmium telluride	Aluminium and alloys	Acrylic
Gallium arsenide	Copper and alloys	Fluoroplastics
Germanium	Electroless nickel	Nylon
Lithium niobate	Gold	Polycarbonate
Silicon	Magnesium	Polymethylmethacrylate
Zinc selenide	Silver	Propylene
Zinc sulphide	Zinc	Styrene

and integrity. Therefore, workpiece materials chosen must possess an acceptable machinability on which nanometric surface finishes can thus be achieved.

Diamond tools are widely used in nanometric machining because of their excellent characteristics. The materials currently turned with diamond tools are listed in Table 1.4. Materials that can be processed using ductile mode grinding with diamond wheels are listed in Table 1.5. Table 1.6 summarizes the comparison of nanometric machining and conventional machining in all major aspects of cutting mechanics and physics. The comparison highlighted in the table is by no means comprehensive, but rather provides a starting point for further study on the physics of nanometric machining.

Table 1.5 Materials that can be processed using ductile mode diamond grinding [14]

Ceramics/intermetallics		Glasses
Aluminium oxide	Titanium aluminide	BK7 or equivalent
Nickel aluminide	Titanium carbide	SF10 or equivalent
Silicon carbide	Tungsten carbide	ULE or equivalent
Silicon nitride	Zirconia	Zerodur or equivalent

Table 1.6 The comparison of nanometric machining with conventional machining [53]

		Nanometric machining	Conventional machining
Fundamental cutting principles		Discrete molecular mechanics/micromechanics	Continuum elastic/plastic/fracture mechanics
Workpiece material		Heterogeneous (presence of microstructure)	Homogeneous (ideal element)
Cutting physics		Atomic cluster or microelement model $\dot{q}_i = \frac{\partial H}{\partial p_i}\ i = 1, 2, \ldots, N$ $p_i = -\frac{\partial H}{\partial q_i}$	Shear plane model (continuous points in material)
		First principal stress $\sigma = \frac{1}{S}\sum_{i=1}^{N_A}\sum_{j=1}^{N_B} f_{ij} - \frac{1}{S}\sum_{i=1}^{N_A}\sum_{j=1}^{N_B} f_{0ij}$ (crystal deformation included)	Cauchy stress principle $\tau_s = \frac{F_s}{A}$ (constant)
Cutting force and energy	Energy consideration	Interatomic potential functional $U(r^N) = \sum_i \sum_{<i} u(rij)$	Shear/friction power $P_s = F_s \cdot V_s$ $P_u = F_u \cdot V_c$
	Specific energy	High	Low
	Cutting force	Interatomic forces $F_I = \sum_{j\neq i}^{N} Fij = \sum_{j\neq i}^{N} -\frac{du(rij)}{drij}$	Plastic deformation/friction $F_c = F(b, d_c, \tau_s, \beta_a, \phi_c, \alpha_r)$

(continued)

Table 1.6 (continued)

		Nanometric machining	Conventional machining
Chip formation	Chip initiation	Inner crystal deformation (point defects or dislocation)	Inter crystal deformation (grain boundary void)
	Deformation and stress	Discontinuous	Continuous
Cutting tool	Cutting edge radius	Significant	Ignored
	Tool wear	Clearance face and cutting edge	Rake face
Surface generation		Elastic recovery	Transfer of tool profile

1.3 Material Requirements for the Medical Industry

Corrosion resistance of titanium (Ti) and its alloys is very good when compared to other materials showing 2.0 V breakdown potential while the value for steel is 0.2 V. Even though Ti alloys belong to the group of materials which do not breakdown passivity in the body, mechanical damage can induce the breakdown (metal-on-metal contact or damage caused with a surgical instrument) and if it does, re-passivation time and oxide growth for the Ti6Al4V alloy is 37–41 and 43.4–45.8 ms, respectively. While for steel it is 35–72000 and 6000–72000 ms, respectively [47]. Biocompatibility is a consequence of the ability of a material to form a protective surface layer of semi or non-conductive oxides that somewhat or completely prevent the flow of ions. The dielectric constant of Ti oxides is similar to that of water which makes the human bone or tissue not recognize the implant as a foreign body [47].

Bioadhesion determines the integration of metallic implants through bone and tissue in-growth. When comparing steel to Ti alloy implants, it has been seen that with steel implants the bone formation was low and there was tissue growing between the metallic implant and the bone which was been deprived of blood and has become granulated and unable to withstand high load bearing capabilities causing loosening of the implant. On the other hand, with Ti implants significant bone formation was observed. The detaching moment of the steel implants was much lower than that of Ti implants. The Ti6Al4V alloy shows that there is a biomechanical as well as a biochemical effect to the growth and formation of a strong bond between implants and bone and tissue showing dependence on both time of exposure as well as surface roughness of the implant [47].

When analyzing the necessary mechanical properties of materials used for implants, it is necessary to achieve adequate Young's modulus, fatigue strength and elongation at fracture. Biofunctionality, which is presented as the ratio of fatigue strength and modulus of elasticity, is superior in Ti alloys when compared with any other materials. Young's modulus of Ti alloys is very close to the value of the bone and the lower it is, the transmission of the functional load is better therefore

stimulating bone growth. However, as Young's modulus is lower by creating a porous layer of the surface, the value of the fatigue strength decreases giving the best results when using plasma sprayed coatings when the difference from the bone is about 10 %. The amount of material that needs to be porous in Ti alloys is around 20 %, which is much less when compared to Cr–Co alloys that requires almost 50 % and still does not achieve the same results. Apart from the amount of porosity, it is necessary for pores to be in the range of 50–100 μm for the in-growth to occur. This can be achieved by spraying or welding cp T onto a Ti alloy [47]. When analyzing the processes available for processing Ti and its alloys, most processes are applicable and the most common ones include casting, forging and machining. The price of Ti alloys is in the range with stainless steel while the rest of the biocompatible materials have a higher cost.

1.3.1 Properties of Titanium Alloys

Ti is considered to be a non-ferrous, light metal that is heavier than any other light metal although it is only half the specific weight of Ni and Fe. Its excellent specific strength and corrosion resistance have made Ti a popular alloy in industries such as aerospace, medical, chemical, etc. The specific strength of Ti alloys is only matched by carbon-reinforced plastics and only at temperatures below 300 °C. The application of these alloys is very attractive at higher temperatures where their strength peaks. However, depending on the alloying elements oxidation can take place starting at temperatures above 500 °C. Ti alloys with added aluminium can withstand higher temperatures and are in the same range with high temperature steels and Ni alloys.

Ti can have two distinct types of crystal structures. At high temperatures, Ti has a stable body-centred-crystal structure (bcc) known as β-Ti while at the transus temperature of 882 °C it undergoes an allotropic modification where β-Ti changes into a hexagonal close packed (hcp) structure, known as α-Ti, which is stable at lower temperatures. The two crystal structures are the reason for the wide range of properties Ti alloys tend to show that influences both plastic deformation and diffusion rate.

Owing to the type of crystal lattice, the α structure has a very limited deformability while this increases for the β phase. This is a consequence of the fact that hcp crystal system has 3 slip systems, while bcc crystal systems have 12 (Fig. 1.8), thus increasing the number of dislocation glide opportunities by a factor of four. Even though the α phase has a packing density of the slip plane of 91 % compared to 83 % for β phase, the energy needed for the activation of the slip planes is higher having as a result favourable plastic deformation in the β phase. Another issue with the α phase is that it has an hcp structure and has only four independent slip planes instead of five necessary for homogeneous plastic deformation making it extremely hard to form.

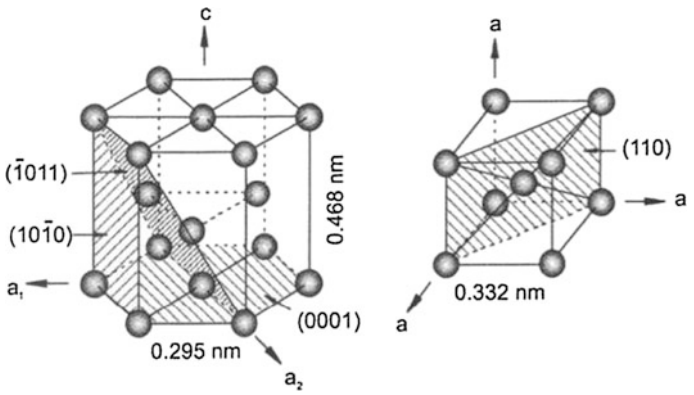

Fig. 1.8 Crystal structure of hcp α and bcc β-phases [47]

1.3.2 Classification of Ti Alloys

Alloying elements play an important role when phase diagrams are analyzed. Alloying elements can extend the α region to higher temperatures, extend the *β* region to lower temperatures or have minimal or no effect on the transus temperature, and are divided into three groups: α stabilizers, *β* stabilizers and neutral alloying elements. Figure 1.9 shows the effect of alloying elements on the phase diagram of Ti alloys.

α stabilizers are responsible for the development of the two-phase region (α + *β*) and are divided further into two distinct categories—*β* isomorphous and *β* eutectic elements shown in Fig. 1.10. The solubility of *β* isomorphous elements such as Mo, V and Ta is higher when compared to the *β* eutectic elements such as Fe, Mn Cr, Co, Ni, Cu, Si, and H which form compounds with titanium. The influence of these alloying elements is on the transus temperature and shape of the phase diagram.

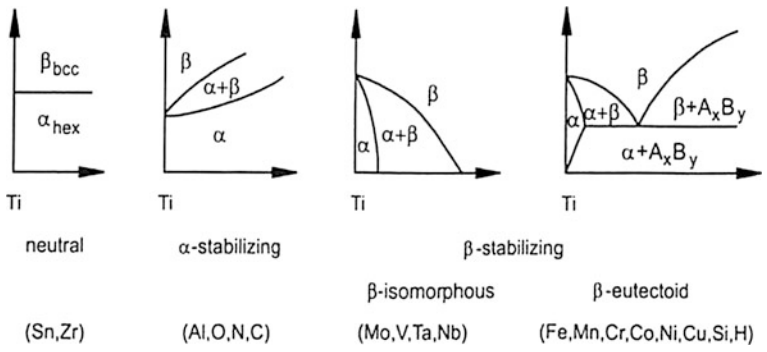

Fig. 1.9 Influence of alloying elements on the phase diagram of Ti alloys [47]

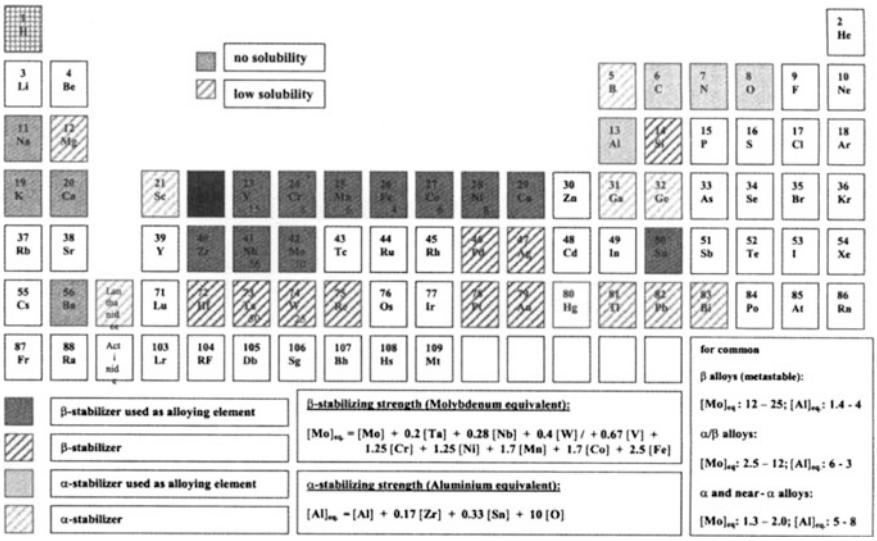

Fig. 1.10 α and β stabilizing elements [47]

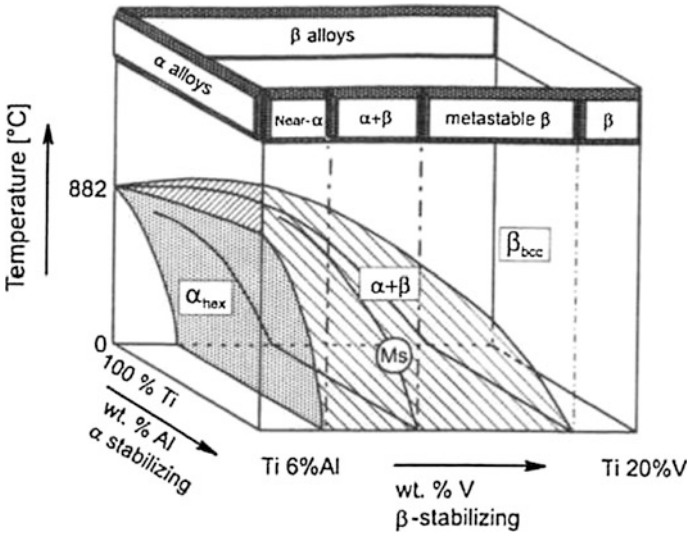

Fig. 1.11 3D phase diagram of Ti alloys [47]

However, their influence on the hardness is indifferent and the neutral elements actually play an important role.

Ti alloys are classified into several types: α, β, near-α, metastable β and $\alpha + \beta$ and are presented in Fig. 1.11. α alloys are considered to be pure Ti and Ti with α-stabilizing elements and/or neutral elements. If these alloys have a small fraction of

β-stabilizing elements then they are considered to be in the group of near α alloys. If the amount of β phase reaches 5–40 % at room temperature, the alloy is considered to be $\alpha + \beta$ phase, which is the most commonly used type of Ti alloys. Metastable β alloys are alloys from the two-phase region in which, due to the amount of β-stabilizing elements, the β phase does not undergo a transformation to martensite upon fast quenching. Finishing up, at the end of the phase diagram alloys with a purely β phase, thus stabilizing and/or neutral elements are usually present [47].

α alloys are used for their corrosion resistance, deformability, high specific strength, toughness and weldability. Grade 1 with its lowest strength and excellent formability is used for deep drawing applications for steel reactors. Grade 2 with somewhat higher strength levels is the most widely used cp Ti alloy, while grade 3 is used only for pressure vessels due to its high strength, and grade 4 is used for fittings and mountings due to the highest value of strength of all alloys. When corrosion resistance is of paramount importance, the addition of Pd developed a new grade, grade 7 that allows greatest corrosion resistance. However, it also makes the alloy very high in price causing alloys such as grade 12 to be used as an alternative. All α alloys can be used for cryogenic applications because they have no ductile-to-brittle transformation.

Near α alloys are used for the high temperature applications due to the excellent creep resistance and high strength coming from α and β phases consecutively. $\alpha + \beta$ alloys are alloys with both the characteristics of α and β regions. The most widely used alloy of all Ti alloys is Ti6Al4V alloy developed by the Illinois institute of Technology. With the great balance of properties and the highest amount of testing that this alloy has undergone due to the interest of the aerospace industry, it has become the most popular Ti alloy in the industry accounting for 50 % of all alloys used. Other $\alpha + \beta$ alloys are also in use for their application due to high strength and toughness and elevated temperature applications.

Metastable β alloys are characterized by extremely high strength levels achieved by hardening, while high toughness can also be retained due to the complex microstructure of the alloy. Owing to the fact that the specific weight of these alloys is low and oxidation and weldability are a problem these alloys still have a limited usage. β alloys are considered to be extremely formable but prone to ductile–brittle transformation making them unsuitable for low temperature applications. Some of the most common alloys in industrial use are: Ti-10V-2Fe-3Al, Ti-15V-3Cr-3Al-3Sn and Ti-3Al-8V-6Cr-4Mo-4Zr.

When preparing the microstructure for metallography cutting the specimen should be conducted with low cutting velocity and feed while using coolant due to the low thermal conductivity of the alloy. Grinding is performed using SiC paper up to 1200 grit size and polishing is done with a synthetic or cotton cloth with diamonds of 6 or 3 grit, while the last polishing phase can be achieved with a synthetic leather cloth with silicon dioxide of fine grit (0.04 μm) or a short fibre velvet cloth with an Al_2O_3 suspension with saturated hydrous oxalic acid can be used. Liquid soap is used for both versions of the final polishing suspensions. Owing to the fact that Ti develops deformation surface layers that show pseudo microstructure etching is done in several steps where final polishing and etching are alternated

approximately three times until the true microstructure is observed. The etchant used is a hydrous solution of 3 ml HF (40 % conc.) + 5 ml HNO_3 (65 % conc.) with 100 ml H_2O.

The observed microstructure transforms from lamellar for cooling from the β region to equiaxial when cooling from the α region. When cooling from the two-phase region, α nucleates at grain boundaries of the β phase. The coarseness of lamellae depends on the cooling rate and is coarsest for the slowest cooling processes. When fast quenching is applied β phase undergoes a martensitic transformation that in contrast to the one in steel shows a moderate influence on the hardness of the alloy. The equiaxial structures are a consequence of recrystallization and require cold working and solution heat treating for acquiring the microstructure.

The amount of α is determined by the solution heat treating temperature and if done close to the β transus temperature results in a bimodal microstructure which is a mix of equiaxial α in the matrix of lamellar $\alpha + \beta$. Equiaxed microstructures have good ductility and fatigue strength and are considered to be desirable for the superplasticity. Lamellar structures have good fracture toughness and are resistant to both creep and fatigue cracks. As expected, because bimodal microstructures have both types of structure, the properties they show are a balance of the equiaxial and lamellar structures. The example of the three types of structures is presented in Fig. 1.12. Depending on the coarseness of the microstructure there will be a difference in the strength of the alloy as well as ductility. Apart from having higher strength and ductility, fine microstructures have a good resistance to crack

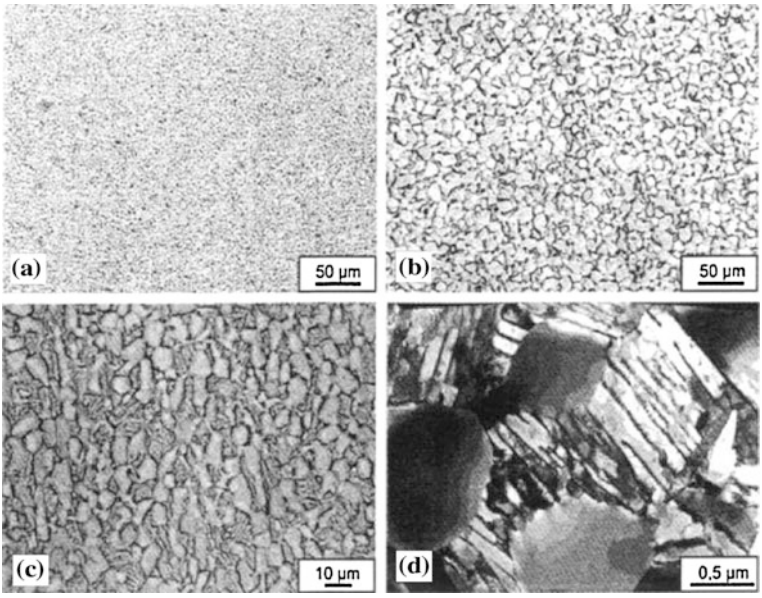

Fig. 1.12 Equiaxed microstructure of TI6Al4V. **a** Fine, **b** coarse, **c** bimodal and **d** bimodal, [47]

nucleation as well. Coarse microstructures are in comparison lower in strength and ductility but show better resistance to creep and fatigue crack propagation.

1.3.3 Medical Applications of Ti Alloys

As mentioned earlier due to the biocompatibility, corrosion resistance, bioadhesion, modulus of elasticity, fatigue strength and ability to be processed easily, Ti alloys have been one of the main types of alloys used for implants, stents, heart valves, fixtures, bone plates, screws, etc. in the biomedical industry. Of all the types of Ti alloys, CpTi, $\alpha + \beta$ and β alloys are used for these purposes with CpTi and Ti6Al4V being the most common ones. For example, CpTi alloys are used for bone plates, especially curved ones, where depending on the required strength grades 1–4 can be used. If higher strength plates are required the alloy can be Ti6Al4V or Ti6Al7Nb; however, these alloys cannot achieve much curvature and are mostly used for straight plates. Ti alloys with high fatigue strength are used for stems of hip joints and are mostly chosen to be of Ti6Al4V. The stems can be both forged and investment cast however, while forged stems have stress relieving as the final step, the microstructure is mill annealed or equiaxial while cast stems will have a fully lamellar microstructure with crack nucleation resistance or a bi-lamellar structure after heat treating giving an even higher crack nucleation resistance than forged parts [54].

1.4 Material Models

Manufacturing processes such as machining and forming introduce large deformations with various stress, strain, and temperature levels creating complex deformation states. Apart from the mentioned parameters, the flow stresses in manufacturing processes are also influenced by strain rate, loading history as well as temperature history. The size effect in micromachining is incorporated in the material models by modelling the material strengthening mechanism. Many models have been developed throughout the years. However, no model has been proven to correctly describe the behaviour of all materials used in the vast number of processes in the manufacturing field while incorporating all the influential parameters. A review of current material models has been presented and the model of choice for the modelling of micromachining of Ti6Al4V alloy has been explored.

1.4.1 Johnson–Cook Model (J–C)

J–C model represents a phenomenological material model most often used in literature for finite element analysis (FEA) and modelling of material behaviour [30]. It is most often used with the aim to show the dependence of the flow stress on strain rate and temperature. The mathematical representation of the J–C model is presented with the following equation [23]:

$$\sigma = (A + B\varepsilon^n)\left[1 + C\ln\frac{\dot{\varepsilon}}{\dot{\varepsilon}_0}\right]\left(1 - T_h^m\right) \tag{1.4}$$

$$T_h = (T - T_{room})/(T_{melt} - T_{room}) \tag{1.5}$$

where ε is the equivalent plastic strain, $\dot{\varepsilon}$ is the strain rate, $\dot{\varepsilon}_0$ is the reference strain rate, and the constants are: A—yield strength, B and n representing strain hardening, and C is the strain rate constant, T_h is the homologous temperature, T_{melt} is the melting temperature, and T_{room} is the room temperature.

There have been several modifications of the J–C model in literature regarding the temperature parameter taking into consideration the effect of temperature before and after the recrystallization temperature has been reached [71], modification with the aim of accounting for the strain softening effect [7], modification using an Arrhenius approach rather than linear dependence of temperature in order to represent adiabatic plasticity [74].

The mathematical formulation of the modified J–C model incorporating the effect of recrystallization temperature is presented as follows [71]:

$$\sigma = (A + B\varepsilon^n)\left[1 + C(\ln\frac{\dot{\varepsilon}}{\dot{\varepsilon}_0})^m\right][1 - (T_h)^m]\frac{(\sigma_f)_{def}}{(\sigma_f)_{rec}} \tag{1.6}$$

σ_{fdef} and σ_{frec} represent flow stress prior to and after recrystallization. The ratio of flow stresses before and after reaching the recrystallization temperature has been introduced in order to account for phase transformations that are triggered by increasing temperature above the recrystallization temperature that would undoubtedly influence the material behaviour.

The mathematical formulation of the modified J–C model incorporating the exponential term to more accurately determine Arrhenius-type dependence for adiabatic plasticity is presented as follows [74]:

$$\tau = [B\gamma^n][1 + C\ln(\dot{\gamma}/\dot{\gamma}_0)]f(\bar{T}) \tag{1.7}$$

$$\bar{T} = T_m - T/T_m \tag{1.8}$$

where, B, n, and C are material constants, $\bar{T}$ is a dimensionless temperature, T_m is the melting temperature T_0 is the reference temperature, and γ_0 is the reference strain rate.

The exponential term that more accurately represents the adiabatic plasticity is presented as follows:

$$f(\bar{T}) = (\tau/\tau_0)_{\gamma,\dot{\gamma}} \tag{1.9}$$

where τ is the shear stress at a given T and τ_0 is the shear stress at a reference temperature.

The mathematical formulation of the modified J–C model incorporating not only the effect of strain rate hardening and thermal softening, but strain softening as well (tanh function), is presented as follows [7]:

$$\sigma = \left(A + B\varepsilon^n\left(\frac{1}{\exp(\varepsilon^a)}\right)\right)\left(1 + C\ln\frac{\dot{\varepsilon}}{\dot{\varepsilon}_0}\right)\left(1 - \left(\frac{T - T_r}{T_m - T_r}\right)^m\right) \left(D + (1 - D)\tanh\left(\frac{1}{(\varepsilon + S)^c}\right)\right) \tag{1.10}$$

$$D = 1 - \left(\frac{T}{T_m}\right)^d$$

$$S = \left(\frac{T}{T_m}\right)^b$$

where A, B, C, a, b, c and d are material constants, σ is the equivalent flow stress, ε is the equivalent plastic strain, $\dot{\varepsilon}$ is the strain rate, $\dot{\varepsilon}_0$ is the reference strain rate, T the workpiece temperature, and T_m and T_r are the material melting and room temperatures, respectively. This model shows a great influence on the chip formation and chip shape because the strain softening effect has an effect on the appearance of shear localization enabling formation of segmented chips. The predictions using this model are not satisfactory when the strain softening level is low.

The J–C model describes the material behaviour relatively well; however, it is a model which does not incorporate the effect of the loading path, strain rate history or temperature history on the overall behaviour. The J–C model uses the determination of constants from experimental data through curve fitting which has no validity if extrapolated beyond the available data, making the model inadequate for application beyond the deformation conditions and microstructures present in the experimental data used. This becomes a serious problem when dealing with machining processes where the deformation is significantly more severe than the deformation achieved in standard tests for material characterization [23].

1.4.2 Mechanical Threshold Model (MTS)

This model has originally been developed by in 1981 [56]. The mathematical representation of this model is shown as [4]:

$$\sigma\left(\varepsilon_p, \dot{\varepsilon}, T\right) = \sigma_a + \left(S_i \sigma_i + S_e \sigma_e\right) \frac{\mu(p, T)}{\mu_0} \tag{1.11}$$

This model is based on the reasoning that the mechanical behaviour of the material is dependent on the change in its microstructure and the dislocation motion. In the model in question σ represents the flow stress, ε_p is the plastic strain, ἑ is the strain rate, σ_a is the athermal component of the mechanical threshold stress, the variable σ_i represents the intrinsic component of the flow stress and is connected to thermally activated dislocation motion, σ_e is the strain-hardening component of the flow stress, and S_i and S_e are temperature and strain rate dependent terms. μ represents the shear modulus which is temperature and pressure dependent (T, p) and μo is the shear modulus at 0 K and ambient pressure.

1.4.3 Power Law Model

The power law is presented in the following mathematical formulation [23]:

$$\sigma = K\varepsilon^n \tag{1.12}$$

As it can be seen from the equation, this is a simple model and it is usually used when describing simple deformation models of materials. The power law model uses fitting of parameters in order to determine material constants K and n and does not account for any temperature or strain rate dependence of flow stress σ.

1.4.4 Zerilli and Armstrong Model

The Zerilli and Armstrong model [95] represents a semi-empirical model based on dislocation mechanics with the aim of incorporating strain hardening and thermal softening effects into the material deformation model. This model actually differentiates between fcc and bcc crystals with the reasoning that the dislocation mechanism characteristics in bcc materials are not affected by temperature and strain rates while fcc crystals are [23].

The mathematical formulation of the Zerilli–Armstrong model for bcc and fcc crystals can be presented as follows [95]:

$$\sigma = \Delta\sigma'_G + C_1 \exp(-C_3 T + C_4 T \ln \dot{\varepsilon}) + C_5 \varepsilon^n + kl^{-1/2} \tag{1.13}$$

$$\sigma = \Delta\sigma'_G + C_2 \varepsilon^{0.5} \exp(-C_3 T + C_4 T \ln \dot{\varepsilon}) + kl^{-1/2} \tag{1.14}$$

where, $\Delta\sigma'_G$ is the additional component of stress that is a result of the influence solute and original dislocation density on yield stress. σ is the yield stress, ε is the strain, έ is the strain rate, k is the microstructural stress intensity, l is the average grain diameter, and C1–C5 are material constants.

The model incorporates the thermal activation necessary in order for the overcoming obstacles for dislocation motion and dislocation interaction in materials [2]. The dislocation mechanisms are considered to be different for different crystal lattices and are considered to be cutting of dislocation forests in fcc and the overcoming of Peierls–Nabarro barriers in bcc metals and therefore the flow stress which incorporates the effect of temperature and strain rate is the function of the yield stress in bcc materials and hardening stress in fcc materials [2].

1.4.5 Japanese Model

An empirical model that is used by some of the Japanese researchers presents the flow stress as a function of reference stress, strain rate and temperature where the reference stress is a measure of deformation history. Even though the deformation history is incorporated, the temperature or strain rate histories are neglected. This increases the error in the modelling because the flow stress is known to be dependent on the strain path [93]. The mathematical formulation of this model can be presented as follows [23]:

$$\bar{\sigma} = A(10^{-3}\dot{\bar{\varepsilon}})^M e^{kT} (10^{-3}\dot{\bar{\varepsilon}})^m \left\{ \int_{T,\dot{\bar{\varepsilon}} \equiv h(\dot{\bar{\varepsilon}})} e^{-kT/N} (10^{-3}\dot{\bar{\varepsilon}})^{-m/N} d\bar{\varepsilon} \right\}^N \tag{1.15}$$

where, A, m, M, N, and k are material constants.

Just like the J–C model and the power law model this is an empirical model that has no viability outside the measured data. The history effect of temperature, strain rate and load path have been neglected and introduce inaccuracy in modelling material deformation.

1.4.6 Bammann, Chiesa, and Johnson Model (BCJ)

BCJ represents an internal state variable plasticity model. The BCJ model takes into consideration temperature sensitivity, strain rate sensitivity and the damage effect by incorporating hardening and recovery into the model by using the deformation path history effect. The model takes into account the rate of change of internal as well as observable state variables including the creep and plasticity through a deviatoric inelastic flow rule represented as a function of the temperature, the kinematic hardening internal state variable, the isotropic hardening internal state variable, and the functions related to yielding with Arrhenius-type temperature function [23]. The mathematical representation is presented as follows:

$$\overset{\circ}{\underline{\sigma}} = \dot{\underline{\sigma}} - \underline{W}^e\underline{\sigma} + \underline{\sigma}\underline{W}^e = \lambda tr(\underline{D}^e)\underline{I} + 2\mu\underline{D}^e \tag{1.16}$$

$$D^e = \underline{D} - \underline{D}^{in} \tag{1.17}$$

$$D^{in} = f(T)\sinh\left[\frac{\|\underline{\sigma} - \underline{\alpha}\| - \{R + Y(T)\}}{V(T)}\right]\frac{\underline{\sigma} - \underline{\alpha}}{\|\underline{\sigma} - \underline{\alpha}\|} \tag{1.18}$$

$$\overset{\circ}{\underline{\alpha}} = \dot{\underline{\alpha}} - W^e\alpha + \alpha W^e = \left\{h(T)\underline{D}^{in} - \left[\sqrt{\frac{2}{3}}r_d(T)\left\|\underline{D}^{in}\right\| + r_s(T)\right]\|\underline{\alpha}\|\underline{\alpha}\right\} \tag{1.19}$$

$$\dot{R} = \left\{H(T)\underline{D}^{in} - \left[\sqrt{\frac{2}{3}}r_d(T)\left\|\underline{D}^{in}\right\| + R_s(T)\right]R^2\right\} \tag{1.20}$$

where $\overset{\circ}{\underline{\sigma}}$ and α are objective rates, $\underline{W}^e$ is the elastic spin, μ and λ are elastic Lame constants, $\underline{D}^e$ is the elastic rate of deformation, $\underline{D}$ is the total rate of deformation, $\underline{D}^{in}$ is the inelastic rate of deformation, f(T) is the strain rate at which yield transition from rate-independent to rate-dependent, h(T) is the anisotropic hardening modulus, H(T) is the isotropic hardening modulus, Rd and rd(T) represent the dynamic recovery, rs(T) and Rs(T) represent diffusion-controlled static or thermal recovery, $\underline{\alpha}$ is the kinematic hardening internal state variable. Even though this model incorporates effects that have been neglected in other models, it has 20 constants that need to be determined for calculations. Even though a nonlinear least square program exists for the determination of these constants, the process is still daunting.

1.4.7 The Applied Model

In order to describe the material behaviour, the material model that will be used in the FEA is a power law model. In order to correctly predict the behaviour, strain hardening, strain rate sensitivity, and thermal softening will be included as well as a damage model as follows [84]:

$$\sigma(\varepsilon^p, \dot{\varepsilon}, T) = g(\varepsilon^p) * \Gamma(\dot{\varepsilon}) * \Theta(T) \tag{1.21}$$

where, $g(\varepsilon^p)$ accounts for strain hardening, $\Gamma(\dot{\varepsilon})$ for strain rate sensitivity and Θ(t) for thermal softening. Strain-hardening function is presented as follows:

$$g(\varepsilon^p) = \sigma_0 \left[1 + \frac{\varepsilon^p}{\varepsilon_0^p}\right]^{\frac{1}{n}} \quad \text{if } \varepsilon^p < \varepsilon_{cut}^p \tag{1.22}$$

$$g(\varepsilon^p) = \sigma_0 \left[1 + \frac{\varepsilon_{cut}^p}{\varepsilon_0^p}\right]^{\frac{1}{n}} \quad \text{if } \varepsilon^p \geq \varepsilon_{cut}^p \tag{1.23}$$

where, σ_0 the initial yield stress, ε^p is the plastic strain, ε_0^p is the reference plastic strain, ε_{cut}^p is the cutoff strain and n is the strain-hardening exponent.

Strain rate sensitivity function is presented as follows:

$$\Gamma(\dot{\varepsilon}) = \left(1 + \frac{\dot{\varepsilon}}{\dot{\varepsilon}_0}\right)^{\frac{1}{m_1}} \quad \text{if } \dot{\varepsilon} \leq \dot{\varepsilon}_t \tag{1.24}$$

$$\Gamma(\dot{\varepsilon}) = \left(1 + \frac{\dot{\varepsilon}}{\dot{\varepsilon}_0}\right)^{\frac{1}{m_2}} \left(1 + \frac{\dot{\varepsilon}_t}{\dot{\varepsilon}_0}\right)^{\left(\frac{1}{m_1} - \frac{1}{m_2}\right)} \quad \text{if } \dot{\varepsilon} > \dot{\varepsilon}_t \tag{1.25}$$

where, $\dot{\varepsilon}$ is the strain rate, $\dot{\varepsilon}_0$ is the reference plastic strain rate, and $\dot{\varepsilon}_t$ is the strain rate of the transition between the high and low strain sensitivity. m_1 and m_2 are the low and high strain rate sensitivity indexes, respectively.

Thermal softening function is presented as follows:

$$\Theta(T) = c_0 + c_1 T + c_2 T^2 + c_3 T^3 + c_4 T^4 + c_5 T^5 \quad \text{if } T < T_{cut} \tag{1.26}$$

$$\Theta(T) = \Theta(T_{cut}) \left(1 - \frac{T - T_{cut}}{T_{melt} - T_{cut}}\right) \quad \text{if } T \geq T_{cut} \tag{1.27}$$

where, c_0–c_5 are the coefficients of the polynomial fit, T is the temperature, Tm is the melting temperature, and T_{cut} is the linear cutoff temperature.

The damage model is presented as follows:

$$D = \sum_i \frac{\Delta \varepsilon_i^p}{\varepsilon_{fi}^p} \tag{1.28}$$

where D is the dimensionless cumulative damage, $\Delta \varepsilon_i^p$ is the instantaneous increment of strain, and ε_{fi}^p is the instantaneous strain to failure.

After elaborating on the existing models from the literature, it is necessary to stress that the effectiveness of a model does not lay in capturing the possible behaviour of each and every material in the sense of correctly developing material parameters, but also on the actual ability to apply a certain model in the sense of the ability to determine material constants and develop FEA. With this in mind, it would be necessary to develop a material model which both correctly describes material behaviour by incorporating not only temperature and strain dependence but also the history effect of temperature, strain rates, and load paths while at the same time keeping the number of necessary material constants as low as possible in order to enable realistic FEA. Until such a model is developed, researchers will continue choosing from the pool of existing models, making the decision based on the material type in question and deformation process that the workpiece of choice is being subjected to.

1.5 Machining of Titanium Alloys for Medical Applications

Even though machining Ti alloys produces forces only slightly higher than those developed when machining steel, the specific metallurgical characteristics of these alloys create difficulties and therefore increase the price. Although hard, it is not impossible to achieve excellent surface finish and good production rates when these alloys are machined; however, it is necessary to take into consideration the very unique characteristics which Ti alloys possess such as low heat conduction, reactivity, low Young's modulus, alloying tendency, surface damage susceptibility, and work-hardening characteristics.

Poor heat conduction of Ti alloys makes the heat linger on the tool cutting edge and tool face effecting tool life. Furthermore, the work-hardening characteristics of the alloy induces the absence of a built-up edge creating localization of heat that in combination with high bearing forces results in rapid tool deterioration. The springback effect in these alloys is high due to the low Young's modulus and consequently the deflections of the workpiece are significant making precision machining hard. Increasing the systems rigidity, using sharp tools, greater tool clearances are one of the ways to reduce this effect. Surface damage in Ti alloys has an effect when they are used in application where fatigue life is important. To

optimize fatigue life it is necessary to maintain sharpness of the tools while machining (mostly grinding) Ti alloys [16].

Main influencing parameters when machining Ti alloys can be considered are as follows:

- Cutting speed
- Feed rate
- Cutting fluid
- Tool sharpness
- Tool–workpiece contact
- Rigidity of the setup.

When setting up the machining parameters for machining Ti alloys, it is necessary to keep the speed low in order to minimize the temperature rise and consequently reduce the influence of heat on the tool tip and edge. Since the tool temperature is affected more by speed and less by feed, then the feed should be kept high while taking into consideration that a work hardened layer is formed after each cut and the consecutive cut needs to be larger than the thickness of this layer. Another influence on the temperature during machining is the amount of cutting fluid used. A generous amount needs to be used to reduce temperatures as well as to clear the work area of chips and reduce cutting forces. The sharpness of the tools used in machining is going to influence the surface finish and if not adequate can cause tearing as well as deflection of the workpiece. The contact of the tool with the workpiece is important because if dwelling of the tool is allowed while tool is in contact with the workpiece it can cause work hardening, smearing, galling, and seizing leading to tool deterioration and eventually breakdown [16].

Most of the efforts made to enhance the machining process of titanium alloys have been focused on decreasing temperature generated at the cutting edge and tool face because it influences tool life and surface characteristics of the workpiece. It has been shown that when machining Ti6Al4V alloys, tool life is increased by decreasing cutting speed and increasing feed. At high cutting speeds, the tool deteriorates rapidly and tool life is dramatically increased by lowering the speed parameter.

The cutting tool material needs to offer abrasion resistance and hot hardness and so far the three most satisfying materials have been proven to be carbide and high speed or highly alloyed steels. Different materials are used for different applications, for example, turning and face milling is mostly done using C2 tungsten carbide grades while HSS tools are used for milling, drilling and tapping of Ti alloys. Productivity is also being influenced by using specific techniques such as specially designed cutters and special cutting techniques [16].

Milling parameter recommendations are given in Tables 1.7, 1.8 and 1.9, for face milling, end milling—slotting, and end milling—peripheral milling, consecutively [16].

The change in cutting speed and/or feed has a significant influence on the chip–tool contact length, chip length, segmentation frequency, segment size, and chip

Table 1.7 Face milling data

Material	Condition	Doc, in	HSS tool			Carbide tool		
			Speed, fpm	Feed in/tooth	Tool material	Speed, fpm	Feed in/tooth	Tool material
Ti6Al4V	Annealed	0.25	40	0.006	M3/T15	130	0.006	C2
Ti6Al4V ELI	Annealed	0.05	50	0.004	M3/T15	170	0.004	C2

thickness therefore presents the two major parameters for process manipulation. Due to this fact, the effect of machining parameters such as cutting speed and feed on chip formation has been a topic of interest for many researchers.

It has been shown [29] that there is a dependence of the contact length on the cutting speed when machining Ti6Al4V alloys where the contact length is considered to be the contact between the chip and the tool rake face when creating a continuous chip. The dependence presented in Fig. 1.13 shows that there is a maximum contact length that is achieved at the transition in the cutting speed from regular to high speed. They attribute this dependence to the effect of "shear banding". The contact length is also shown to be dependent on the undeformed chip thickness, where the increase in the undeformed chip thickness yields an increase in the contact length. It has been stated that the chip compression ratio (ratio of the actual and undeformed hip thickness) is hard to comprehend due to the scattered results and they attribute this to the poor machinability of Ti alloys and shear banding as well.

Chip morphology has been researched [82] showing that the saw-chip formation is present and that the chip length is increased while the width decreased with the increase in cutting speed and feed. The segmentation size increases while the frequency of the segmentation decreases with cutting speed. This has also been determined in further work [13] where it has been shown that the segmentation frequency increases linearly with the increase in cutting speed and decreases with increase in feed, Fig. 1.14.

The chip thickness ratio (ratio of undeformed chip thickness and actual chip thickness) has been shown to increase with the decrease in cutting speed and it decreases with the increase in feed when using low speeds [5]—Fig. 1.15.

The dependence of chip thickness, tool–chip contact length and chip up-curl radius on the tool radius/chip thickness ratio has been presented in Fig. 1.16 [20]. The chip thickness decreases with the increase in the tool radius value as the ratio of the tool radius and undeformed chip thickness is increased. The tool chip contact length follows the same trend as the chip thickness yielding a lower value with the increase of the tool edge radius.

However, the chip thickness is a questionable parameter when Ti alloys are being investigated [36]. The conventional chip thickness ratio for the continuous chip formation models and the parameters such as shear angle which are calculated from the ratio are considered to be incorrect parameters for describing machining

Table 1.8 End milling data—slotting

Material	Condition	Doc, in	High-speed tool (M2)					Carbide tool (C2)				
			Speed, fpm	Cutter diameter, in				Speed, fpm	Cutter diameter, in			
				1/18	3/8	3/4	1–2		1/8	3/8	3/4	1–2
				Feed per tooth					Feed per tooth			
Ti6Al4V	Annealed	0.25	30	–	0.0007	0.003	0.004	75	–	0.0007	0.003	0.005
Ti6Al4V ELI	Annealed	0.125	40	–	0.001	0.003	0.004	100	–	0.0015	0.003	0.005
		0.050	50	0.0005	0.002	0.004	0.005	125	0.0005	0.002	0.005	0.007
		0.015	65	0.0007	0.003	0.005	0.006	165	0.0005	0.003	0.006	0.008

Table 1.9 End milling data—peripheral milling

Material	Condition	Doc, in	High-speed tool (M2)					Carbide tool (C2)				
			Speed, fpm	Cutter diameter, in				Speed, fpm	Cutter diameter, in			
				1/8	3/8	3/4	1–2		1/8	3/8	3/4	1–2
				Feed per tooth					Feed per tooth			
Ti6Al4V	Annealed	0.25	50	–	0.001	0.004	0.005	125	–	0.001	0.004	0.006
Ti6Al4V ELI	Annealed	0.125	60	–	0.0015	0.004	0.005	150	–	0.002	0.004	0.006
		0.050	75	0.0008	0.003	0.005	0.006	190	0.0008	0.003	0.006	0.007
		0.015	90	0.001	0.004	0.006	0.007	225	0.001	0.004	0.007	0.008

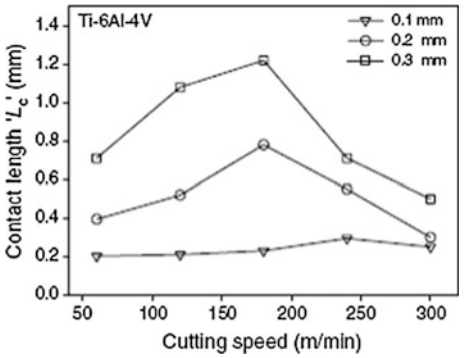

Fig. 1.13 Variation of the contact length with cutting speed for Ti6Al4V [29]

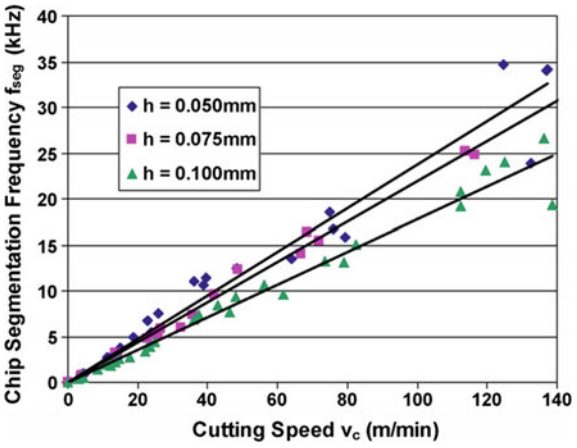

Fig. 1.14 Dependence of chip segmentation frequency on cutting speed [82]

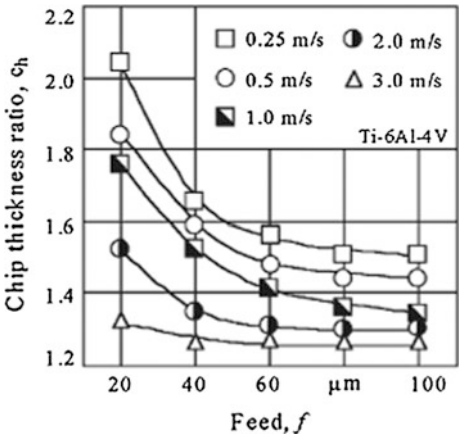

Fig. 1.15 Chip thickness ratio as a function of cutting speed and feed for Ti6Al4V [5]

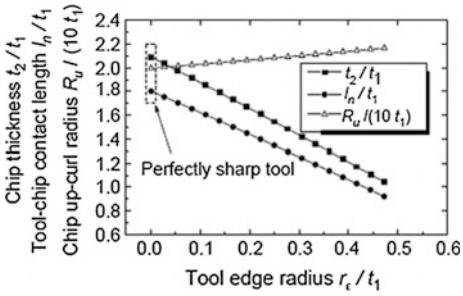

Fig. 1.16 Influence of the tool edge radius [20]

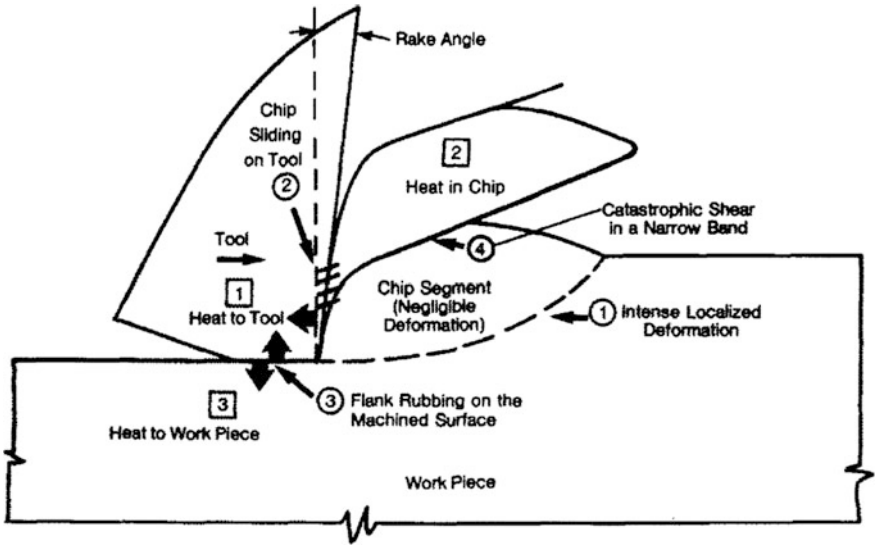

Fig. 1.17 Energy partition when machining Ti alloys [36]

characteristics of Ti alloys [36]. This is because that Ti alloy chips become deformed inconsequentially, and are formed by gradual flattening of a softer half wedge by the tool. Consequently, the chip thickness ratio is close to 1. One of the reasons why the machining of Ti alloys cannot be assessed using a conventional formula is that concentrated shear subjects the chip to large strains creating thick chips with low shear angles and low velocity. Energy partition presented in Fig. 1.17 is also different from steel showing

- Energy into the chip $U_c = R_1 U_s$
- Into the tool $U_t = (1 - R_1)U_s + R_3 U_{ff}$
- Into the workpiece $U_w = (1 - R_3)U_{ff}$

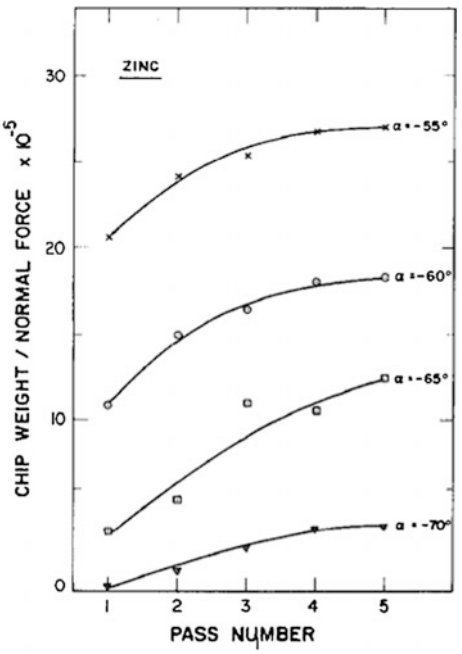

Fig. 1.18 Influence of the rake angle on chip formation [1]

(U_{ff} is the frictional energy per unit volume due to rubbing between the flank and the machined surface and R_3 is the fraction of heat conducted into the tool due to flank friction).

The high temperatures are present when using low values of the depth of undeformed layers due to the rubbing of the flank on the machined surface. When the influence of the rake angle on the chip formation [1] has been investigated, it has been determined that the rake angle has a critical value of −70° when machining zinc, after which there is no chip formation (Fig. 1.18).

This issue has further been addressed [35] where it has been determined that the rake angle at which chip formation ceases is −85°. While elsewhere [68] it has been determined that this value is lower and equals −55°. The mechanism of chip formation when machining Ti6Al4V alloys has been discussed by many researchers and follows two theories. The first theory is the catastrophic thermoplastic shear where thermal softening present in the primary shear zone predominates the strain hardening caused by high strain rates in machining [15, 40, 41, 67, 70]. The second theory is the periodic crack initiation that is considered as a consequence of high stress present during the machining process. This theory is based on the idea that cracks are formed in the primary shear zone and then rewelded through high pressure and heat originating from friction [25, 59, 60, 90]. In the following paper [65] authors show the formation of the chip and its microstructure showing the lack of cracks in Fig. 1.19. The authors have determined that there is no phase

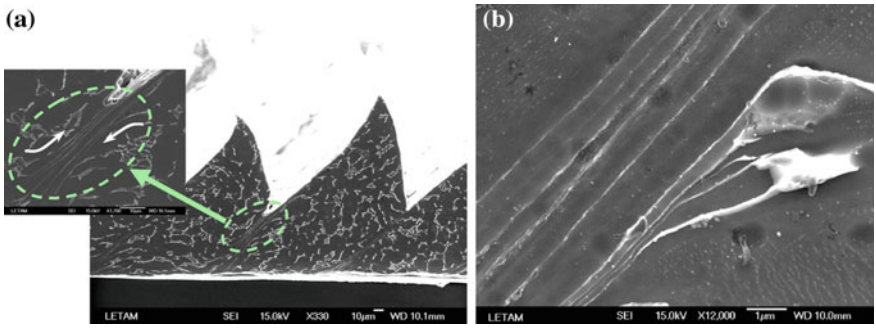

Fig. 1.19 Microstructure of the chips and shear bands in Ti6Al4V [65]

transformation taking place classifying the bands to be deformation shear bands and confirming the catastrophic shear model.

Vyas and Shaw on the other hand confirm the crack initiation presented in Fig. 1.20. They show formation of both gross cracks and micro cracks. Gross cracks continue throughout the chip width while micro cracks seem to be discontinuous. The process is based on the idea that the blocks of material which are between the gross cracks glide out with no plastic deformation; while the material surrounding the micro cracks will undergo adiabatic shear in case when the temperature is high enough which may also result in phase transformations [90]. It is obvious from the fact that both theories are present and confirmed in the literature that the chip formation mechanism is not straightforward and must depend on various parameters. Investigation techniques such as X-ray diffraction, energy dispersive X-ray analysis, scanning electron microscopy, and electron backscattering technique can be found useful in determining the causes of the discussed results. It is yet to be determined why these inconsistencies occur and what influences which one of the theories will be observed in the experimental work. Therefore, this can be considered a field with a vast potential for research.

1.5.1 Micromachining Medical Materials

Development of modern technology has brought with it the necessity of integrating miniature components into the fields of electronics, telecommunications, defense industry, and biomedical devices. For the longest time, the techniques applied have been a product of the development of the electronics industry and have been based on lithography. These processes have been proven to be limited in the materials that can be processed, achievable geometries, lack cost effectiveness in anything but mass production, etc. The need to overcome these shortcomings and manufacture 3D components with intricate geometries and of various materials has increased the interest in machining processes on the microscale. Many non-conventional

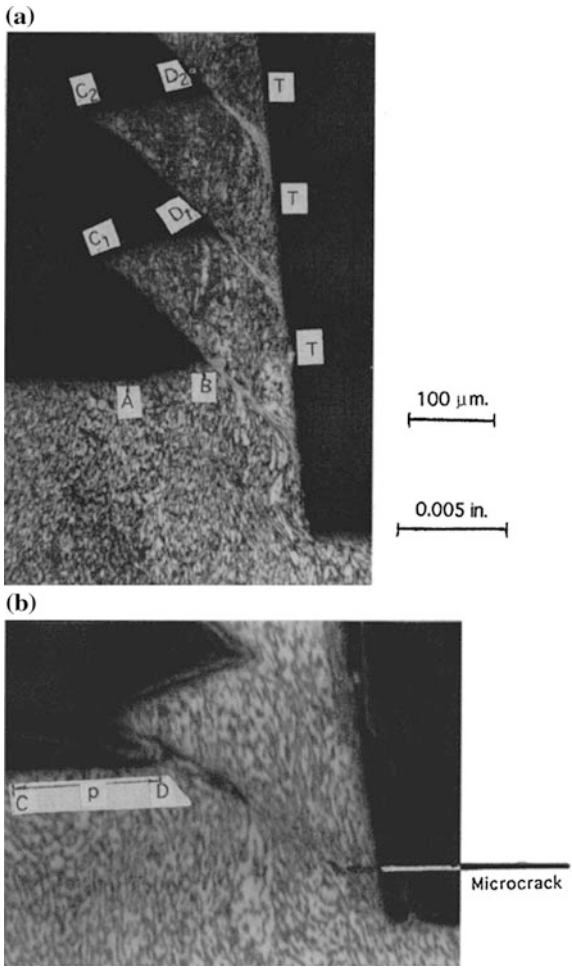

Fig. 1.20 Mechanics of chip formation showing **a** crack formation, **b** micro crack formation in Ti6Al4V [90]

processes have been adopted such as laser machining, focused ion beam machining, and electro discharge machining offering the possibility of creating complex geometries, however, still limited in materials they could be applied to as well as limited in productivity. Due to the inefficiencies of the previously mentioned processes, micromechanical processes have been widely investigated. Micromilling applicability has been confirmed [21, 91, 92] showing the flexibility of the process and the microscale.

1.5.1.1 The Size Effect

When analyzing the micromilling process phenomena it is not possible to describe it by simply scaling down the macromilling process itself. The main and critical

difference between these two scales of the same process is the fact that the assumption of material homogeneity does not stand any more. The assumption that in macromachining the material acts as a homogeneous body is correct because the tool geometry is significantly larger than the microstructural features. On the other hand, when observing micromachining, the tool geometry is now of the same order of magnitude as the microstructural features making it necessary to take the structure of the material into consideration. As it can be seen from current research [92], the more significant effect of the tool geometry on the cutting process on the microscale is simply a consequence of the limitations in the tool manufacturing industry where the fabrication of miniature tools is extremely hard and it also brings with it a decrease in the structural strength of the tool when compared to macro tools. This means that the inability of fabrication of extremely small edge radii on tools used for micromachining yields the comparable size of tool geometry to feed rate values. All this leads to one of the most important phenomena in micromachining which is defined as size effect. Size effect relates to the significant increase in the specific energy as the uncut chip thickness is decreased.

Many researchers have tackled the problem of identifying causes of the phenomena of the size effect [3, 17, 31, 42, 45] and have connected it to the strengthening mechanism of the material through the decreasing number of crystallographic defects in materials microstructure [3], increasing strain rate at the primary shear zone, decreasing of thermal softening, influence of the tool geometry [33, 37, 52, 69], strain rate sensitivity [45], change in temperature and consequently shear plane angle [42], plastic flow under the workpiece surface [61], and gradient plasticity [49]. Some of the widely accepted causes will be addressed in the following text. Owing to the size effect the phases present in a material show an effect on the machining forces and other parameters. This effect has been shown [11, 12] by developing a simulation model for analyzing multiphase materials. The researchers have shown that there is a change in the chip formation mechanism as well as in the cutting force patterns when changing from a single phase to a multiphase material, Fig. 1.21. The material model used for the simulations was the BCJ model accounting for material behaviour under various stresses, strains, temperatures, damage, etc. Material investigated in the study was ductile iron and therefore to account for machining ferrite pearlite and graphite at different points in time due to the size effect they have been modelled as separate homogenous materials.

In literature there has been interest in analyzing machining of ductile iron [88]. In order to capture the actual microstructure of ductile iron consisting of graphite, ferrite, and pearlite, the authors have created a map of microstructural constituents using a grid of points with a probability factor of spheres representing the secondary phases while the tertiary phases were assigned to each grid point. Researchers have shown the effect of the multiphase material on the cutting force magnitude and variation showing that there is a higher frequency variation of forces when micromilling a multiphase material where the microstructure effect accounts for over 35 % of the energy in the force signal. They also show the effect of the spacing of the secondary phase and its size on the frequency and magnitude of the cutting force variation. Another significant difference between milling at the two scales is in

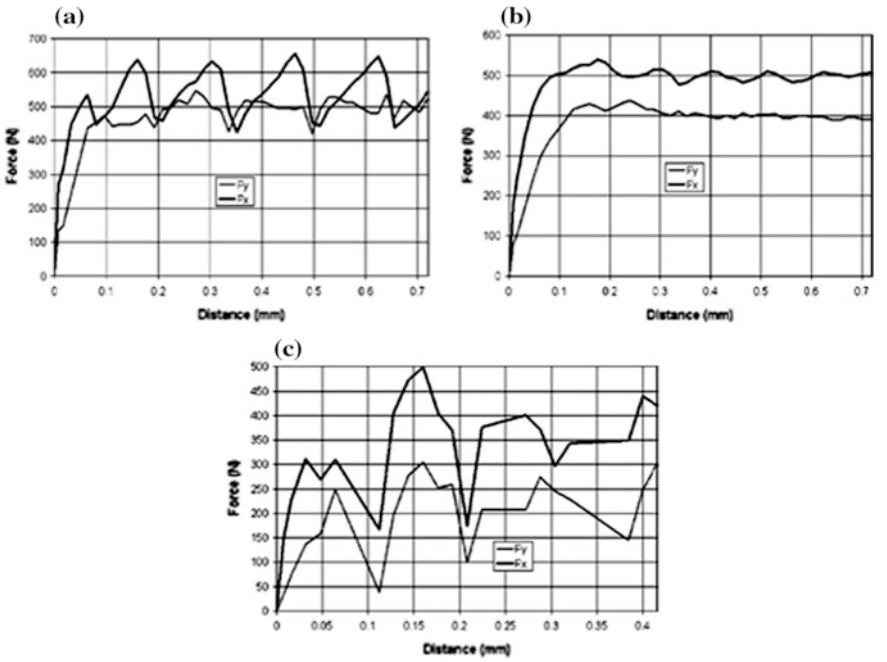

Fig. 1.21 Machining forces from cutting pearlite, ferrite and ductile iron respectively [11]

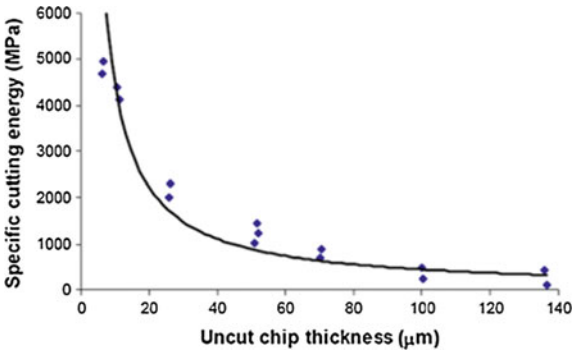

Fig. 1.22 Specific cutting energy versus uncut chip thickness [49]

the function of the dependence of force on the chip thickness. The cutting force increases with the increase in chip thickness when machining on the macroscale; however, when the chip thickness reaches values of the tool edge radius the relationship becomes much more complicated [57]. Many researchers have connected the force function to the chip thickness in their work that will be presented and discussed later in the thesis.

Many researchers have shown the increase in the specific cutting energy with the decrease in the uncut chip thickness [3, 22, 42, 52], Fig. 1.22. The researchers have investigated machining plain carbon steel with ceramic indexable tools.

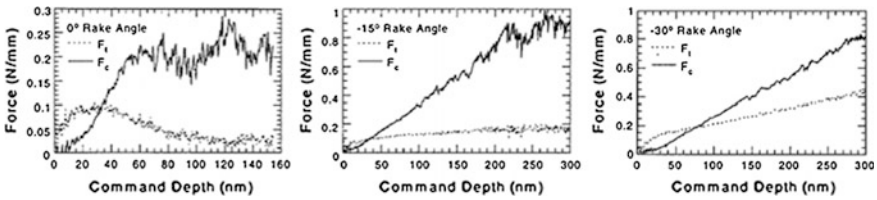

Fig. 1.23 Effect of the depth of cut and rake angle on thrust and cutting forces [51]

It has been accepted in the research community that the machining forces are going to differ if sharp or blunt tools are used in the process. This information has led to research on the topic of the influence of tool geometry on the size effect in machining. It has been concluded by a number of researchers that the size effect is by all means among other things a consequence of tool geometry [33, 37, 52, 69]. Lucca et al. [51] show that when machining germanium the increase in the ratio of thrust force and cutting force is accounted by the decrease in depth of cut and increase in the negative rake angle Fig. 1.23. Tools used in the study were diamond single crystal tools with rake angle of 0°, −15°, −30°, −45°.

It has been stated [52] that when the uncut chip is decreased to the value of the radius of the tool, the effective rake angle has the crucial effect on resulting forces. Due to the decreased uncut chip thickness, the direction of the resulting forces is determined by the effective rake angle in this case and not the nominal rake angle.

Research shows that the thrust and cutting forces increase with the increase in tool edge radius up to a certain value where it becomes independent at higher r [37]. The authors argue that at higher values of radii the rake angle is high and the variation is small; while at low values the variation of the angle is significant enough to cause the dependence. Also, the value of the thrust-to-cutting force ratio increases at low values of the radius while stays more constant at higher values of the radius. It has further been determined that there is an increase in the specific cutting energy when increasing the radius size for tools with small radii but no significant effect if the radius is large to begin with.

The effect of the tool edge geometry on machining has further been investigated showing the increase in force with the decrease in tool edge radius and uncut chip thickness [69], Fig. 1.24. This approach has been taken also by other researchers [8] who claim that the tool edge radius has a significant effect on the material deformation process by expanding and widening the plastic deformation zone and changing the material flow around the tool edge as well as increasing the dissipation of energy because of the higher value of the contact length between the chip and the tool.

In the literature, the size effect has also been attributed to the crystallographic effect [72]. Considering the fact that the tool is extremely small and is approaching the size of the microconstituents in the material, the actual number of defects such as grain boundaries, point defects, etc. is decreasing at the level of machining and the material is considered to be approaching its theoretical strength.

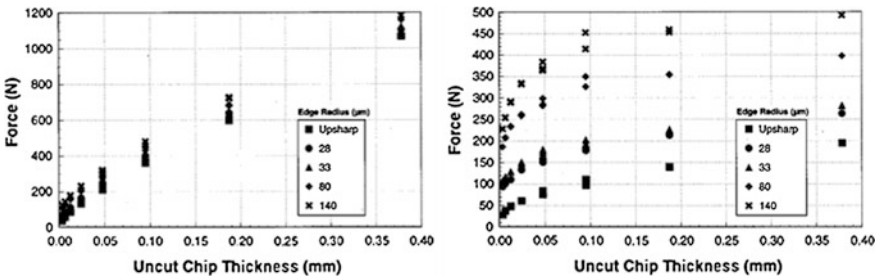

Fig. 1.24 Effect of the tool edge radius and uncut chip thickness on cutting and thrust forces [69]

The strain gradient plasticity model has been used to account for the size effect where the material strength is considered to be a function of both strain and strain gradient rather than just strain as it is considered in regular plasticity theory [31]. The authors state that the size effect can be addressed using the geometry and gradient of the strain field because the density of geometrically necessary dislocations increases in comparison to the density of statistically stored dislocations leading to increase in strength even when the scale of deformation is decreased. They evaluate the strain gradient, density of geometrically necessary dislocations, shear strength, and specific shear energy. Authors show that the length of the shear plane decreases with the decrease in the undeformed chip thickness leading to an increase in the shear strength. This model considers the effect of the strain gradient produced in the primary shear zone only.

The effect of the strain gradient has been explored further [49] and the authors came to the conclusions that it contributes to the size effect even more at low cutting speeds and large uncut chip thicknesses. Also the effect is dominant over temperature effect when machining is done at high cutting speeds and large uncut chip thickness. Strain rate sensitivity [45] has also been used as the reasoning behind the size effect. The authors show that the maximum shear strain rate increases with the decrease in the uncut chip thickness that consequently leads to the increase in the flow stress and therefore explains the increase in specific cutting energy.

The temperature influence on the size effect has been adopted by Kopalinsky and Oxley where the drop in temperature affects the shear plane angle and increases the specific cutting force [42]. The size effect has been accounted for through subsurface plastic flow arguing that the amount of energy is not proportional to the uncut chip thickness and shear angle [61].

It is very easy to conclude from the existing research on the origin of size effect that it is not likely that the size effect is a consequence of only one mechanism. It is highly likely that all the mechanisms have an effect at certain points in time depending on the process parameters and/or materials used.

1.5.1.2 Minimum Chip Thickness

The importance of estimating the minimum chip thickness lies in the fact that it is one of the major limiting factors in achieving accuracy at a microscale because a chip thickness smaller than the critical value results in ploughing and rubbing, therefore increasing the achievable surface roughness significantly. Some authors [32] have used estimation of minimum chip thickness using cutting force periodicity in their work. Their reasoning is based on the fact that the tool edge radius/minimum chip thickness is a function of cutting conditions and workpiece–tool material combination making the actual measurement hard. Therefore, they have based their research on the analysis of the periodicity of cutting forces. They have adopted wavelet analysis, which shows that the global wavelet spectrum achieves a maximum at the most significant period of the data and therefore determines the dominant period of the cutting force signatures.

Gurin [24] has used in his thesis the stability of the cutting process as a measure of the transition from ploughing to cutting showing that the change happens when the stresses due to the normal and tangential forces become equal. A criterion has been developed for determining the transition from interfacial sliding to microcutting [43]:

$$\frac{h}{r} = 0.5\left(1 - \frac{2\tau}{\sigma_T}\right) \tag{1.29}$$

where, h is the depth of indentation (depth of cut), r is the radius of the indenter (cutting edge radius), τ is the shear strength of the adhesive junction, and σ_T is the yield stress of the workpiece material.

Some researchers [44] argue that there is a neutral point on the tool where all the material above it becomes deformed mainly by the rake face creating a chip; while the material below it, which is the surface layer of the machined part, becomes formed by the rake and clearance faces. The obtained relationship is presented as follows:

$$a_{\min} = r(1 - \cos\theta) \tag{1.30}$$

where a_{min} is the minimum chip thickness, r is the cutting edge radius, and θ is the neutral point angle.

Some researchers have further followed the idea of the neutral point and determined that if the undeformed minimum chip thickness is smaller than the critical value, only ploughing will occur; while it is larger, both ploughing and cutting will be present [6]. Analyzing the energy expended in the chip they analytically determined that the critical value of the angle of the natural point is 37.6° and experimentally determined it is between 28° and 33° when machining lead, soft aluminium and mild steel using HSS tools with the addition of 10 % cobalt. It has been determined that the value of the neutral point angle is independent of the cutting edge radius. Further, it has been determined that there will be influence on

the natural point angle from the hardness of the workpiece material, hardness of the tool material, plastic recovery, and friction conditions. Hardness of the material will yield a higher effective edge radius and also higher elastic recovery of the materials; Plastic recovery can be as high as 20 % of the depth of cut for certain materials, which would make it necessary to incorporate into analysis. The friction condition can be various because the process changes from ploughing to cutting while changing along the cutting edge. The authors have shown that if a model developed by other researchers is applied the value of the analytically determined angle is decreased to 30.5°.

The effect of the minimum chip thickness on the surface roughness has experimentally been analyzed [89]. The authors have determined that the value of the minimum chip thickness depends on the material in question and it ranges from 0.2 to 0.35 of the radius from pearlite and ferrite. They have observed that ploughing forces lead to burr formation influencing the surface and subsurface of the workpiece causing potential increase in residual stresses. The relationship between the friction coefficient, tool radius, and minimum chip thickness has been an interesting topic for many researchers [79]. Using analytical methods they have defined the minimum chip thickness as follows:

$$t_m = r\left(1 - \cos\left(\frac{\pi}{4} - \frac{\beta}{2}\right)\right) \tag{1.31}$$

where t_m is the minimum chip thickness, r is the tool edge radius, and β is the friction angle between the tool and uncut workpiece passed under the tool. The researchers have proposed a microcutting model and have confirmed the results by experimental work showing that the increase in the friction coefficient and use of a smaller edge radius result in a smaller minimum chip thickness. One of the important facts that has been acknowledged in this work is that the value of the tangential force in simulations and experiments is not the same because there is piling up of the material in front of the tool which cannot be represented in the simulation.

Fang [20] determined the chip thickness using the chip up-curl radius R, angular velocity ω as well as magnitude of chip velocity V.

$$t = 2\left(\frac{V}{\omega} - R\right) \tag{1.32}$$

By focusing on molecular dynamics simulations for estimating the minimum chip thickness and achievable accuracy it has been shown that this value is material dependent and has a value of 5 % of the cutting edge radius (which had a value of 5–10 nm) when copper and aluminium are machined with diamond [77].

Other researchers have used experimental work to analyze the minimum chip formation when machining aluminium samples using diamond tools showing that the minimum chip thickness reaches a value of 20–40 % of the cutting edge radius when tools with 1–2 μm are used [94]. Instead of using experimental work, some

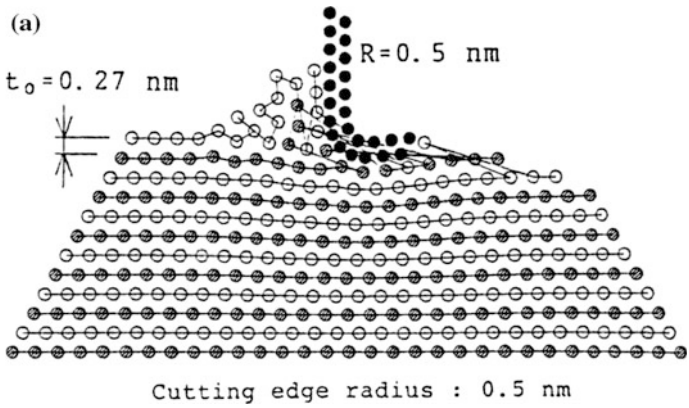

Fig. 1.25 Atomistic simulation of machining copper [27]

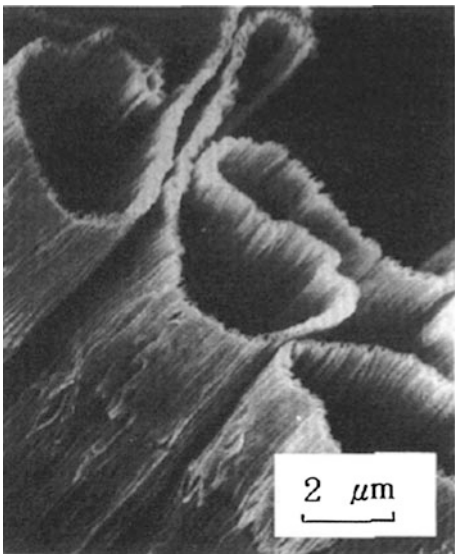

Fig. 1.26 SEM images of the nominal thickness of cut of 1 nm [27]

researchers have focused on the analytical determination of the minimum chip thickness developed on the basis of molecular mechanical theory of friction correlating the values to the workpiece and tool thermo mechanical properties [50].

Ikawa et al. [27] have based their investigations on the atomistic modelling of the machining process, Fig. 1.25. They have determined that with a specially prepared diamond tool a thickness of cut of 1 nm can be achieved experimentally which can be seen in Fig. 1.26. The minimum chip thickness remains an open field for research. The values are obviously material dependent as well as process dependent. There is not only the influence of the tool geometry but also the

influence of the machine tool rigidity and set up on the process. Therefore, calculating the minimum chip thickness for specific operations and specific combination of tool–workpiece materials remains to be tackled.

1.5.1.3 Computational Analysis

Computational analysis has been used in the last several decades and can be divided into approaches representing the Finite Element Methods (FEM) and Molecular Dynamics simulations (MD). In the FEM, the material is represented using the continuum mechanics approach where the chemistry, crystal lattice, grain size, etc. are neglected and the material is considered to be a continuum. The nodes and their number are determined arbitrarily and do not represent features of the material. The mesh parameters are set up in such a way that they only determine the sensitivity during the simulation using a finer mesh when using small feeds or depths of cut in order to capture the fine features. On the other hand, in MD simulations the nodes and the mesh are closely related to the workpiece material in question. The mesh actually represents the crystal lattice of the material while the node distance represents the distance between atoms in the crystal lattice [39]. Further, the interatomic bonding is defined using potential energy functions such as Morse, Lennard-Jones, etc. [39].

When analyzing FEM they can be split into three groups: Lagrangian [76, 80], Eulerian [81] and arbitrary Lagrangian–Eulerian methods [58, 63, 66]. Lagrangian FEM is based on the notion that the mesh is attached to the workpiece and it moves with the material. Owing to the fact that the elements change shape it is often necessary to use remeshing to restore distorted elements and adaptive remeshing is often used. Eulerian FEM involves a workpiece material which flows through the pre-set mesh fixed in space. There is no element distortion in this method; however, the chip formation cannot be modelled and only steady state problems can be analyzed. Owing to the advantages and disadvantages of both methods, a combination of the two called arbitrary Lagrangian–Eulerian approach is more frequently used [85].

The effect of the tool edge radius has been an important one throughout the investigations conducted in the machining field. Analysis has been conducted on the effect of edge roundness on stress and temperature when machining AISI 4340 steel using carbide tools using an arbitrary Lagrangian–Eulerian method [64]. Researchers have simulated material flow around the tool edge without re-meshing or using a chip separation criterion and argue that this way of conducting FEA gives better predictions for machining induced stresses. Others [48] have investigated the effect of the cutting edge radius on forces, chip thickness and tool temperature. Due to the less effective cutting with a large radius tool the resulting cutting forces increase with the increase in the tool edge radius. The chip thickness is influenced somewhat by the increase in the tool edge radius showing slight increasing trend.

A decreasing trend for tool temperature is observed with the increase in tool edge radius and explained by the fact that the high temperature is located at the tip of the

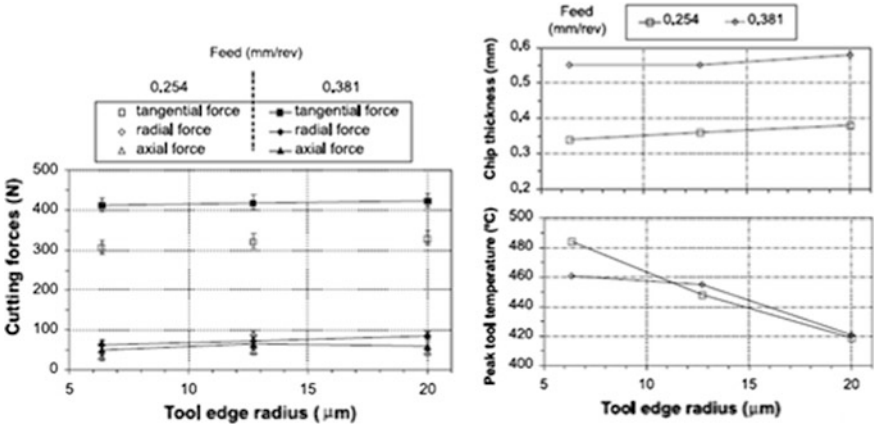

Fig. 1.27 Influence of the tool edge radius on cutting forces, chip thickness and tool temperature [48]

tool resulting at higher values when the tip is sharper. The results of this study can be observed in Fig. 1.27. The mechanism of chip formation and chip morphology has been investigated by a number of authors who compared the simulated results with the experimentally obtained chips in order to understand the chip formation in various materials. An FEA has been presented of both conventional and high-speed machining of Ti6Al4V alloys incorporating the Johnson–Cook material model [86]. The author has investigated the chip formation and morphology and compared it to the experimentally obtained chips. The comparison was satisfactory as shown in Fig. 1.28.

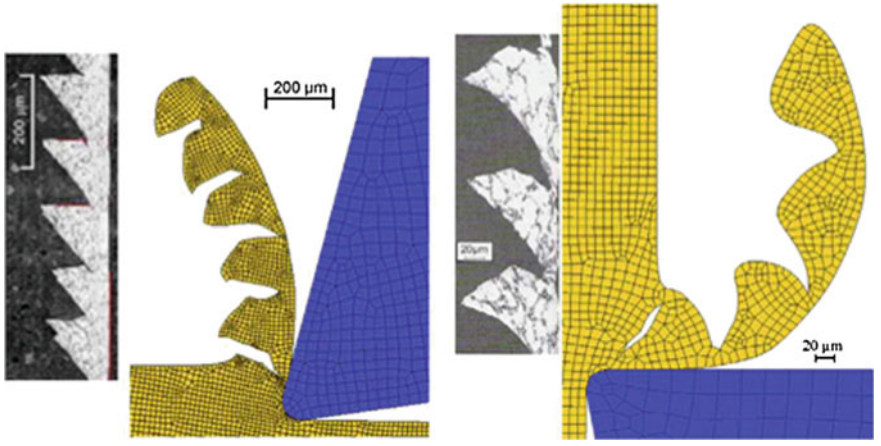

Fig. 1.28 Comparison of the experimentally obtain chips and chips obtained by FEA for conventional and high-speed machining [86]

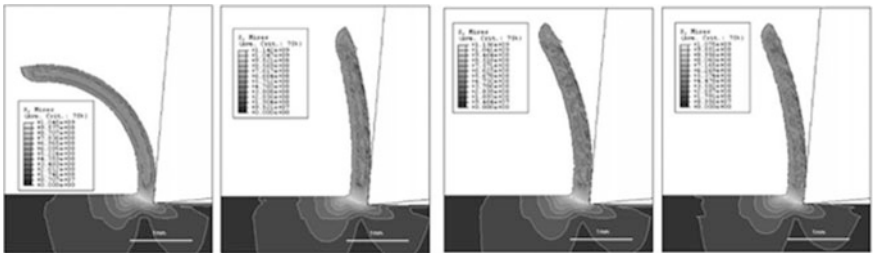

Fig. 1.29 Chips and stress distribution for the Litonski–Batra, power law, Johnson–Cook and Bodner–Partom material models consecutively [75]

Obikawa and Usui have focused their research on implementing a crack growth criterion into finite element modelling to better predict discontinuous chip formation [62]. They have incorporated a fracture strain criterion and obtained results in very close agreement to the experimental findings. The influence of the chosen material model for the FEA has been further investigated [75] and can be seen from Fig. 1.29.

It is easy to see that the choice of the model will make a difference when interpreting the chip morphology results and comparing them with the experimentally obtained shapes. The chip curl radius can be observed to be different for the models applied and is argued that the power law gave the values closest to the actual measured ones. The stress patterns seem to be similar in all cases while on the other hand the actual values are somewhat different depending on the model in question. The temperature distribution is also considered to be the same or similar in all cases. However, even though most parameters behave in a similar manner for all models, residual stresses in the workpiece material differ significantly. Machining simulations have been used to investigate the effect of damage and material softening upon reverse loading in heterogeneous materials. The authors compared their work with experimental data from a reverse loading experiment of ductile iron and obtained good agreement, Fig. 1.30 [11].

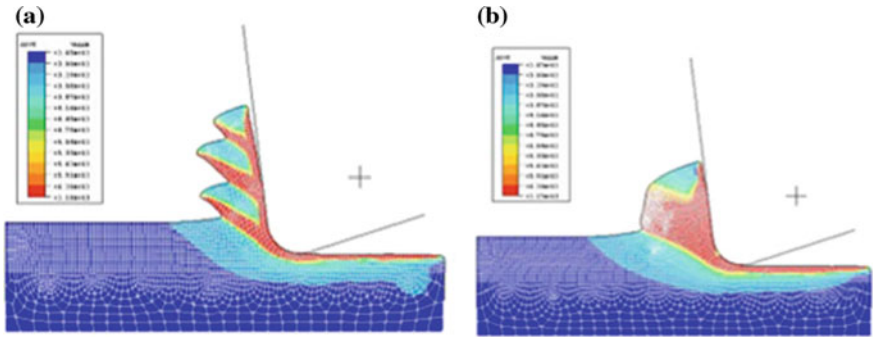

Fig. 1.30 Chip formation when simulating machining with and without the material softening upon reverse loading [11]

Temperature is considered to be another one of the commonly investigated issued using FEA in the process of machining. Usui et al. [87] investigated the tool edge temperature and its effect on the wear characteristics in machining with ceramic tools. The influence of the cutting speed on the temperature generated in the tool has been investigated showing that there is a significant increase in the tool temperature with a higher value registered for the rake compared to flank face of the tool [34]. The fact that the tool temperature increases with the increase in cutting speed was confirmed [87] and it has been shown that the temperatures are close to the melting temperature of the workpiece material. Kim et al. [33] used finite element modelling to determine temperature and stress distributions in micromachining. The researchers chose oxygen-free copper as the workpiece material while the tool was a diamond cutter. It was presented that the highest temperature occurred within the shear plane at it reaches 562 °C even though the depth of cut is only 2 μm. They determined that if the effect of the temperature is ignored the values obtained for the flow stress are doubled when compared to the experimental one resulting in forces considerably higher than those measured. Cao et al. [8] have concluded in their research that the maximum cutting temperature depends greatly on the tool edge radius and it increases with the increase in the radius itself. It has also been noticed that the effect of the radius in not only on the magnitude of the temperature but also on the temperature field distribution as well. As the ultra-precision machining grew in size, tools for modelling these processes became more sophisticated and in the late 1980s molecular dynamic simulations have been introduced to enhance the research in the field. The research was mainly confined to national laboratories because supercomputers are needed for the memory and processing time required to run these simulations. However, only recently several universities have developed computers with which enable conducting simulations of this scale. Figure 1.31 represents the schematic of the MD simulation.

The influence of friction on the process of nanoscale machining and investigation of the chip formation and the morphology by comparing it to the micromachining results is one of the topics covered in the literature [55]. The researchers show the increase in the bond energy leading to increase in chip thickness and contact length as well as increases in cutting forces and the temperature. Figure 1.32 shows that there is a constant increase in the cutting force and this is due to the fact that the simulation did not include any defects such as vacancies, interstitials, dislocations grain boundaries, etc. and it is predicted that with incorporating those features into the simulations, the results would be different.

A number of researchers [26, 28] investigated the effect of the minimum depth of cut and the ratio of minimum depth of cut and edge radius on chip formation as well as subsurface deformation and specific cutting energy in two dimensional cutting of copper with diamond tools. They have concluded that the influence of the cutting edge on the minimum chip thickness was greater than the influence of the type of work piece material. They have determined that the numerical value of the minimum chip thickness is 0.1 of the tool edge radius.

The effect of the edge radius and depth of cut on nanometric machining has been investigated [37]. The authors have investigated the influence on the forces, specific

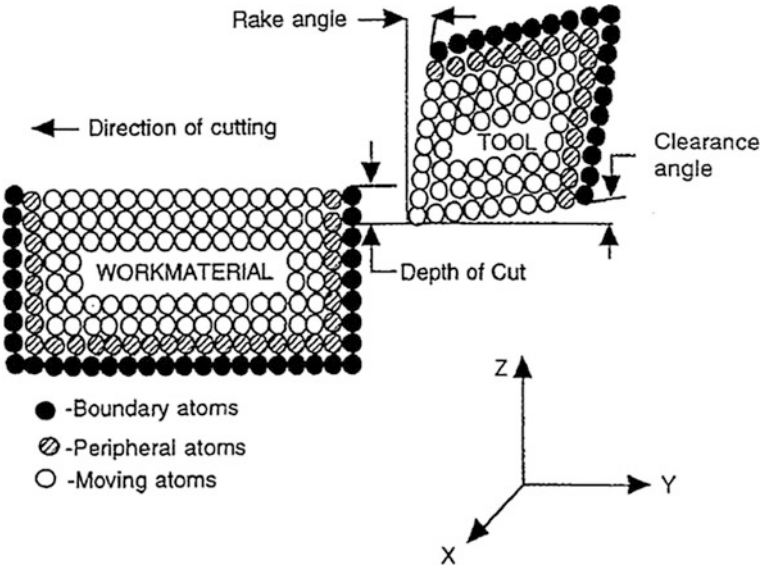

Fig. 1.31 Schematic of the MD simulation [39]

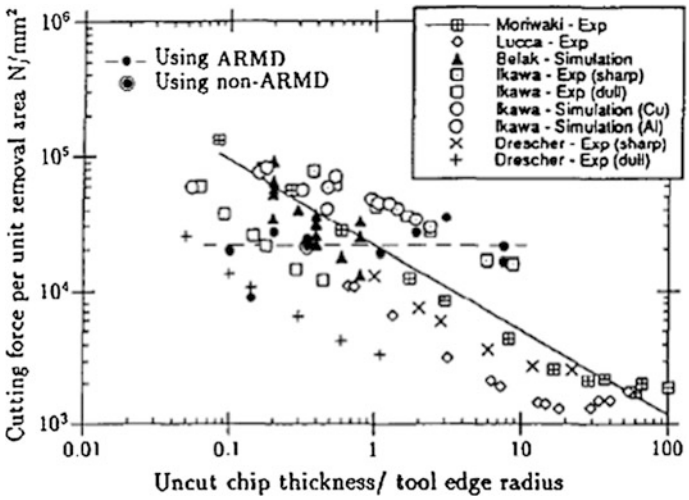

Fig. 1.32 Dependence of the cutting force on the ratio of the chip thickness and tool edge radius [55]

energy as well as subsurface deformation concluding that the depth of cut 33 has a significant influence on the extent of plastic deformation ahead of the tool as well as subsurface deformation. With the increase in the depth of cut to tool radius ratio, chip generation increases increasing cutting forces and decreasing ploughing. The

researchers also conclude that the increase in the tool edge radius yields an increase in the negative rake angle rotating the shear zone towards and into the workpiece material. It has been noted that the increase of forces with the depth of cut is different for the cutting and thrust forces. Cutting force varies linearly while thrust forces have a fast increase at the beginning and saturate at higher depth of cut.

The effect of the rake angle on the cutting and thrust forces has been analyzed by MD simulations [38]. Figure 1.33 shows the results obtained showing that the ratio of the thrust to cutting forces increases from 0.496 to 2.361 when changing the rake angle from 45 to −75 which is also followed by the increase in specific energy from 0.293 to 1.011*E5 N/mm^2. This change has also been determined at non-nanometric circumstances by the author when investigating depths of cut of 10 μm [35]. The ratio of the thrust force to cutting force was seen to increase to around 5 for the rake angle of −85° after which the chip formation seizes and rubbing and side flow start. The investigators have also shown that the depth of cut has an effect on the forces and specific energy independent of the radius/depth of cut ratio. They show that the

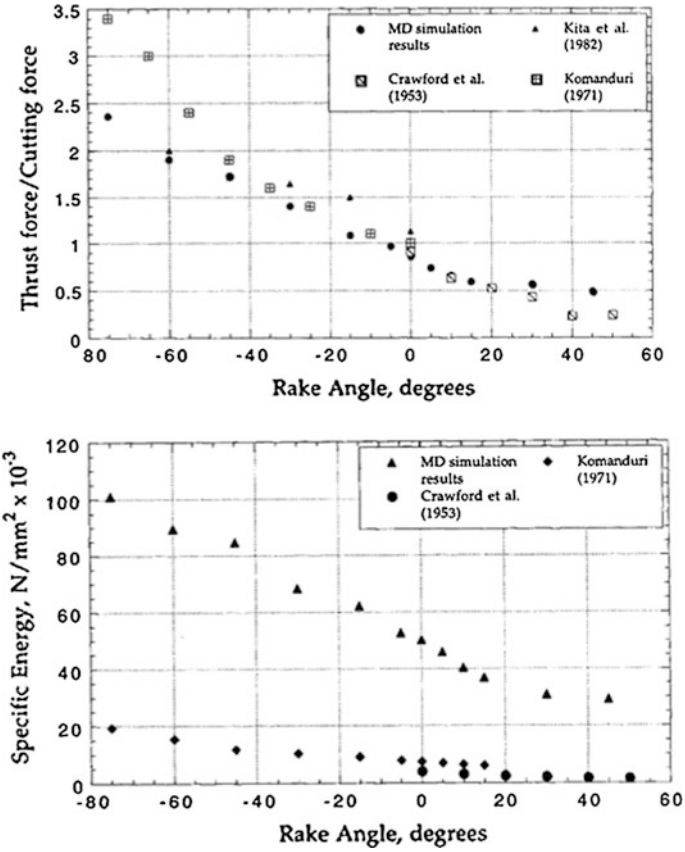

Fig. 1.33 Influence of the rake angle on the force ratio and specific energy [38]

cutting force increases with the cut depth and the specific energy decreases with it. Based on the review presented, it can be concluded that applications of the Lagrangian, Eulerian, Lagrangian–Eulerian as well as MD simulations all have their place in the research community and strongly depend on what the intended research findings are. The FEA models that research chip formation and the influence of the size effect in micromachining are still to be improved in order to obtain better understanding of the process. The MD simulations offer immense insight into the field of nanometric cutting simulating the cutting mechanisms on the atomic level.

1.6 Further Developments

The further developments associated with nanometric machining is concerned with two aspects. The first aspect concerns MD simulations of machining different materials with coated and uncoated cutting tool materials, and the simulation of problems that are commonly encountered in machining such as tool wear during machining, thermal deformation of certain engineering alloys during machining, burr formation during machining, and the modelling of exit failures when the cutting tool has completed its task. The second aspect focuses on developing meso-microscale mechanical machine tools that are in the process of being developed. Here, MD simulations of the machining process will contribute to the design of machine tools dedicated to machining at the nanoscale, and will hopefully illuminate the need for better machine tool design at the meso- and macroscales. There is a growing body of work associated with modelling and machining of medical materials. This chapter shows that there is still plenty of research work to be done in machining of medical materials, especially at the micro- and nanoscales.

Acknowledgements The authors thank Springer and Wiley publishers for allowing the authors permission to re-print and update this chapter that was originally published in, 'Surface Engineered Surgical Tools and Medical Devices', originally published by Springer in 2007 (ISBN 978-0387-27026-5). The authors also wish to thank Springer for allowing the authors to update the chapter with material that was published in 'Machining with Nanomaterials' also published by Springer. *Re-printed with kind permission from Springer Science + Business Media B.V and Wiley Publishers.*

References

1. Abdelmoneim, M. E., & Scrutton, R. F. (1973). Post-machining plastic recovery and the law of abrasive wear. *Wear, 24*, 1–13.
2. Abed, F. H., & Voyiadjis, G. Z. (2005). A consistent modified Zerilli-Armstrong flow stress model for BCC and FCC metals for elevated temperatures. *Acta Mechanica, 175*, 1–18.
3. Backer, W. R., Marshall, E. R., & Shaw, M. C. (1952). The size effect in metal cutting. *Transactions of the ASME, 74*, 61–72.

4. Banerjee, B. (2007). The mechanical threshold stress model for various tempers of AISI 4340 steel. *International Journal of Solids and Structures, 44*(3–4), 834–859.
5. Barry, J., Byrne, G., & Lennon, D. (2000). Observations on chip formation and acoustic emission in machining. *International Journal of Machine Tools and Manufacture, 41*, 1055–1070.
6. Basuray, P. K., Misra, B. K., & Lal, G. K. (1977). Transition from ploughing to rubbing. *Wear, 43*, 341–349.
7. Calamaz, M., Coupard, D., & Girot, F. (2008). A new material model for 2D numerical simulation of serrated chip formation when machining titanium alloy Ti-6Al-4V. *International Journal of Machine Tools and Manufacture, 48*, 275–288.
8. Cao, Z. Y., He, N., & Li, L. (2008). A finite element analysis of micro/meso scale machining considering the cutting edge radius. *Applied Mechanics and Materials, 10–12*, 631–636.
9. Cheng, K., Luo, X., Ward, R., & Holt, R. (2003). Modelling and simulation of the tool wear in nanometric cutting. *Wear, 255*, 1427–1432.
10. Cheng, K., Luo, X., & Jackson, M. J. (2006). In M. J. Jackson (Ed.), *Microfabrication and nanomanufacturing* (pp. 311–338). Florida: Taylor and Francis, CRC Press.
11. Chuzhoy, L., & Devor, R. E. (2003). Machining simulation of ductile iron and its constituents, Part 2: Numerical simulation and experimental validation of machining. *Journal of Manufacturing Science and Engineering, 125*, 192–201.
12. Chuzhoy, L., Devor, R. E., Kapoor, S. G., Beaudoin, A. J., & Bammann, D. J. (2003). Machining simulation of ductile iron and its constituents, Part 1: Estimation of material model parameters and their validation. *Journal of Manufacturing Science and Engineering, 125*, 181–191.
13. Cotterell, M., & Byrne, G. (2008). Dynamics of chip formation during orthogonal cutting of titanium alloy Ti-6Al-4V. *CIRP Annals—Manufacturing Technology, 57*, 93–96.
14. Corbett, J. (2002). Diamond micromachining. In J. McGeough (Ed.), *Micromachining of engineering materials* (pp. 125–146). New York: Marcel Dekker.
15. Davies, M. A., Fick, S. E., & Evans, C. J. (1996). *Dynamic measurement of shear band formation in precision hard turning*. Leuven, Belgium: Katholieke Universiteit.
16. Donachie, M. (2000). *Titanium—A technical guide* (2nd ed.). OH: Materials Park, ASM International.
17. Dornfeld, D., Min, S., & Takeuchi, Y. (2006). Recent advances in mechanical micromaching. *Annals of CIRP, 55*(2), 745–768.
18. Dow, T., Miller, E., & Garrard, K. (2004). Tool force and deflection compensation for small milling tools. *Precision Engineering, 28*(1), 31–45.
19. El-Hofy, H., Khairy, A., Masuzawa, T., & McGeough, J. (2002). Introduction. In J. McGeough (Ed.), *Micromachining of engineering materials*. New York: Marcel Dekker.
20. Fang, N. (2003). Slip-line modeling of machining with a rounded-edge tool—Part II: Analysis of the size effect and the shear strain-rate. *Journal of the Mechanics and Physics of Solids, 51*, 43–762.
21. Friedrich, C., Coane, P., Goettert, J., & Gopinathin, N. (1998). Direct fabrication of deep X-ray lithography masks by micromechanical milling. *Precision Engineering, 22*, 164–173.
22. Furukawa, Y., & Moronuki, N. (1988). Effect of material properties on ultra precision cutting process. *Annals of the CIRP, 37*(1), 113–116.
23. Guo, Y. B., Wen, Q., & Hortemeyer, M. F. (2005). An internal state variable plasticity-based approach to determine dynamic loading history effects on material property in manufacturing processes. *International Journal of Mechanical Sciences, 47*, 1423–1441.
24. Gurin, F. V. (1967). *Mettal cutting using diamond tools with ground cutting edges*. Moscow: MAMI.
25. Hua, J., & Shivpuri, R. (2004). Prediction of chip morphology and segmentation during the machining of titanium alloys. *Journal of Materials Processing Technology, 150*, 124–133.
26. Ikawa, N., Donaldson, R., Komanduri, R., König, W., Mckeown, P. A., Moriwaki, T., et al. (1991). Ultraprecision metal cutting—The past, the present and the future. *Annals of the CIRP, 40*(2), 587–594.

27. Ikawa, N., Shimada, S., & Tanaka, H. (1992). Minimum thickness of cut in micromachining. *Nanotechnology, 3*, 6–9.
28. Ikawa, N., Shimada, S., Tanaka, H., & Ohmori, G. (1991). Atomistic analysis of nanometric chip removal as affected by tool-work interaction in diamond turning. *CIRP Annals, 40*, 551–554.
29. Iqbal, S. A., Mativenga, P. T., & Sheikh, M. A. (2009). A comparative study of the tool-chip contact length in turning of two engineering alloys for a wide range of cutting speeds. *International Journal of Advanced Manufacturing Technology, 42*, 30–40.
30. Johnson, G. R., & Cook, W. H. (1983). A constitutive model and data for metals subjected to large strains, high strain rates and high temperatures. In *Proceedings of the 7th International Symposium on Ballistics, The Hague, The Netherlands*, pp. 541–547.
31. Joshi, S. S., & Melkote, S. N. (2004). An explanation for the size-effect in machining using strain gradient plasticity. *Journal of Manufacturing Science and Engineering, 126*, 679–684.
32. Kim, C.-J., Mayor, J. R., & Ni, J. (2004). A static model of chip formation in microscale milling. *Transactions of the ASME, 126*, 710–718.
33. Kim, K. W., Lee, W. Y., & Sin, H. C. (1999). A finite element analysis of machining with the tool edge considered. *Journal of Material Processing Technology, 86*, 45–55.
34. Kitagawa, T., Kubo, A., & Maekawa, K. (1997). Temperature and wear of cutting tools in high speed machining of Inconel 718 and Ti-6Al-6V-2Sn. *Wear, 202*(2), 515–525.
35. Komanduri, R. (1971). Aspects of machining with negative rake tools simulating grinding. *International Journal of Machine Tool Design and Research, 11*, 223–233.
36. Komanduri, R. (1982). Some clarifications on the mechanics of chip formation when machining titanium alloys. *Wear, 76*, 15–34.
37. Komanduri, R., Chandrasekaran, N., & Raff, L. M. (1998). Effect of tool geometry in nanometric cutting: A molecular dynamics simulation approach. *Wear, 219*, 84–97.
38. Komanduri, R., Chandrasekaran, N., & Raff, L. M. (1999). Some aspects of machining with negative-rake tools simulating grinding: A molecular dynamics simulation approach. *Philosophical Magazine, 79*, 955–968.
39. Komanduri, R., & Rav, L. M. (2001). A review on the molecular dynamics simulation of machining at the atomic scale. *Journal of Process Mechanical Engineering, 215*, 1639–1672.
40. Komanduri, R., & Schroeder, T. A. (1986). On shear instability in machining a nickel-iron base superalloy. *ASME Journal of Engineering for Industry, 108*, 93–100.
41. Komanduri, R., & Von Turkovich, B. F. (1981). New observations on the mechanism of chip formation when machining titanium alloys. *Wear, 69*, 179–188.
42. Kopalinsky, E. M., & Oxley, P. L. B. (1984). *Size effects in metal removal process.* Paper presented at the Institute of physics conference series no. 70. Third conference on mechanical properties at high rates of strain.
43. Kragelsky, I. V., Dobychin, M. N., & Kombalov, V. S. (1982). *Friction and wear, calculations and methods*. New York: Pergamon Press Inc.
44. L'Vov, N. P. (1968). Determining the minimum possible chip thickness. *Machines and Tooling Journal, 40*, 45–46.
45. Larsen-Basse, J., & Oxley, P. L. B. (1973). *Effect of strain-rate sensitivity on scale phenomenon in chip formation.* Paper presented at the 13th International Machine Tool Design and Research Conference, Birmingham.
46. Lee, W., & Cheung, C. (2001). A dynamic surface topography model for the prediction of nano-surface generation in ultra-precision machining. *International Journal of Mechanical Sciences, 43*, 961–991.
47. Leyens, C., & Peters, M. (Eds.). (2003). *Titanium and titaniom alloys fundamentals and applications*. Weinheim: Willey-VCH.
48. Li, R., & Shih, A. J. (2006). Finite element modeling of 3D turning of titanium. *International Journal of Advanced Manufacturing Technology, 29*, 253–261.
49. Liu, K. (2005). Process modeling of micro-cutting including strain gradient effects (PhD, Georgia Institute of Technology, Atlanta).

50. Liu, X., DeVor, R. E., & Kapoor, S. G. (2006). An analytical model for the prediction of minimum chip thickness in micromachining. *Transactions of the ASME, 128*, 474–481.
51. Lucca, D. A., Chou, P., & Hocken, R. J. (1998). Effect of tool edge geometry on the nanometric cutting of Ge. *Annals of CIRP, 47*(1), 475–478.
52. Lucca, D. A., & Seo, Y. W. (1993). Effect of tool edge geometry on energy dissipation in ultraprecision machining. *CIRP Annals, 42*, 83–86.
53. Luo, X., Cheng, K., Guo, X., & Holt, R. (2003). An investigation on the mechanics of nanometric cutting and the development of its test-bed. *International Journal of Production Research, 41*(7), 1449–1465.
54. Lutjering, G., & Williams, J. C. (2003). *Titanium*. Berlin: Springer.
55. Maekawa, K., & Itoh, A. (1995). Friction and tool wear in nano-scale machining-a molecular dynamics approach. *Wear, 188*, 115–122.
56. Mecking, H., & Kocks, U. F. (1981). Kinetics of flow and strain-hardening. *Acta Metallurgica, 29*(11), 1865–1875.
57. Merchant, M. E. (1944). Basic mechanics of the metal-cutting process. *ASME Journal of Applied Mechanics, 12*, 168–175.
58. Movahhedy, M. R., Gadala, M. S., & Altintas, Y. (2000). FE modeling of chip formation in orthogonal metal cutting process: An ALE approach. *Machining Science and Technology, 4*, 15–47.
59. Nakayama, K. (1974). *The Formation of Saw-tooth Chip.* Paper presented at the Proceedings 1st International Conference on Production Engineering, Tokyo, Japan.
60. Nakayama, K., Arai, M., & Kada, T. (1988). Machining characteristics of hard materials. *CIRP Annals, 37*(1), 89–92.
61. Nakayama, K., & Tamura, K. (1968). Size effect in metal-cutting force. *American Society of Mechanical Engineers, 67*, 8.
62. Obikawa, T., & Usui, E. (1996). Computational machining of Ti alloy finite element modeling and few results. *Transactions of the ASME, 118*, 208–215.
63. Olovsson, L., Nilsson, L., & Simonsson, K. (1999). An ALE formulation for the solution of two-dimensional metal cutting problems. *Computers and Structures, 72*, 497–507.
64. Özel, T., & Zeren, E. (2007). Finite element analysis of the influence of edge roundness on the stress and temperature fields induced by high speed machining. *The International Journal of Advanced Manufacturing Technology, 35*(3–4), 255–267.
65. Puerta Velasquez, J. D., Bolle, B., Chevrier, P., Geandier, G., & Tidu, A. (2007). Metallurgical study on chips obtained by high speed machining of a Ti-6 wt.%Al-4 wt.%V alloy. *Materials Science and Engineering A, 452–453*, 469–474.
66. Rakotomalala, R., Joyot, P., & Touratier, M. (1993). Arbitrary Lagrangian-Eulerian thermomechanical finite element model of material cutting. *Communications in Numerical Methods in Engineering, 9*, 975–987.
67. Recht, R. F. (1964). Catastrophic thermoplastic shear. *Transactions of the ASME, 1964*, 189–193.
68. Rubenstein, C., Groszman, F. K., & Koenigsberger, F. (1967). *Force measurements during cutting tests with single point tools simulating action of single abrasive grit.* Paper presented at the International Industrial Diamond Conference.
69. Schimmel, R. J., & Endres, W. J. (2002). Application of an internally consistent material model to determine the effect of tool edge geometry in orthogonal cutting. *Transactions of the ASME, 124*, 536–543.
70. Semiatin, S. L., & Rao, S. B. (1983). Shear localisation during metal cutting. *Material Science and Engineering, 61*, 185–192.
71. Seo, S., Min, O., & Yang, H. (2005). Constitutive equation for Ti-6Al-4V at high temperatures measured using the SHPB technique. *International Journal of Impact Engineering, 31*, 735–754.
72. Shaw, M. C. (2003). The size effect in metal cutting. *Sadhana, 28*(5), 875–896.
73. Shaw, M. C. (2005). *Metal cutting principles*. New York: Oxford University Press.

74. Sheikh-Ahmadn, J. Y., & Bailey, J. A. (1995). A constitutive model for commercially pure titanium. *Journal of Engineering Materials and Technology, 117*, 139–144.
75. Shi, J., & Liu, R. C. (2004). The influence of material models on finite element simulation machining. *Journal of Manufacturing Science and Engineering, 126*, 849–857.
76. Shih, A. J. (1995). Finite element simulation of orthogonal metal cutting. *ASME Journal of Engineering for Industry, 117*, 84–93.
77. Shimada, S., Ikawa, N., Tanaka, H., Ohmori, G., Uchikoshi, J., & Yoshinaga, H. (1993). Feasibility study on ultimate accuracy in microcutting using molecular dynamics simulation. *CIRP Annals, 42*, 91–94.
78. Shimada, S. (2002). Molecular dynamics simulation of the atomic processes in microcutting. In J. McGeough (Ed.), *Micromachining of engineering materials* (pp. 63–84). New York: Marcel Dekker.
79. Son, S. M., Lim, H. S., & Ahn, J. H. (2005). Effects of the friction coefficient on the minimum cutting thickness in micro cutting. *International Journal of Machine Tools and Manufacture, 45*, 529–535.
80. Strenkowski, J. S., & Carroll, J. T. (1985). A finite element model of orthogonal metal cutting. *ASME Journal of Engineering for Industry, 107*, 346–354.
81. Strenkowski, J. S., & Carroll, J. T. (1986). Finite element models of orthogonal cutting with application to single point diamond turning. *International Journal of Mechanical Science, 30*, 899–920.
82. Sun, J., & Guo, Y. B. (2008). A new multi view approach to characterize 3D chip morphology and properties in end milling titanium Ti6Al4V. *International Journal of Machine Tools and Manufacture, 48*, 1486–1494.
83. Taniguchi, N. (1996). *Nanotechnology*. New York: Oxford University Press.
84. ThirdWaveSystems. (1995–2008). Third Wave AdvantEdge™ User's Manual Version 5.2. Minneapolis: ThirdWaveSystems.
85. Trent, E. M., & Wright, P. K. (2000). *Mettal cutting*. Woburn: Butterworth-Heinemann.
86. Umbrello, D. (2008). Finite element simulation of conventional and high speed machining of Ti6Al4V alloy. *Journal of Material Processing Technology, 196*, 79–87.
87. Usui, E., Shirakashi, T., & Kitagawa, T. (1978). Cutting temperature and crater wear of carbide tools. *Journal of Engineering for Industry, 100*(2), 236–243.
88. Vogler, M. P., DeVor, R. E., & Kapoor, S. G. (2001). *Microstructure-level force prediction model for micro-milling of multi-phase materials.* Paper presented at the Proceedings of the ASME Manufacturing Engineering Division, ASME International Mechanical Engineering Congress and Exposition, NY.
89. Vogler, M. P., Devor, R. E., & Kapoor, S. G. (2004). On the modeling and analysis of machining performance in micro-end milling, Part I: Surface generation. *Journal of Manufacturing Science and Engineering, 126*, 685–694.
90. Vyas, A., & Shaw, M. C. (1999). Mechanics of saw-tooth chip formation in metal cutting. *Journal of Manufacturing Science and Engineering, 121*, 163–172.
91. Weck, M., Fischer, S., & Vos, M. (1997). Fabrication of microcomponents using ultraprecision machine tools. *Nanotechnology, 8*, 145–148.
92. Weule, H., Huntrup, V., & Tritschle, H. (2001). Micro-cutting of steel to meet new requirements in miniaturization. *CIRP Annals, 50*, 61–64.
93. Yoshino, M., & Shirakashi, T. (1997). Flow stress equation including effects of strain rate and temperature history. *Journal of mechanical science, 30*(12), 1345–1362.
94. Yuan, Z. J., Zhou, M., & Dong, S. (1996). Effect of diamond tool sharpness on minimum cutting thickness and cutting surface integrity in ultraprecision machining. *Journal of Material Processing Technology, 62*, 327–330.
95. Zerilli, F. J., & Armstrong, R. W. (1986). Dislocation-mechanics-based constitutive relations for material dynamics calculation. *Journal of Applied Physics, 61*(5), 1816–1827.

Chapter 2
Anodization: A Promising Nano Modification Technique of Titanium-Based Implants for Orthopedic Applications

T.J. Webster and C. Yao

Abstract Titanium is protected by a thin titanium oxide layer, which spontaneously forms on its surface when exposed to air or other oxygen-containing environments. This oxide passive layer is typically 2–5 nm thick and is responsible for the well-documented corrosion resistance property of titanium and its alloys. Because of this and their excellent mechanical properties, titanium and its alloys are widely used in orthopedic and dental applications. However, the native TiO_2 layer is not bioactive enough to form a direct bonding with bone, which means the lack of osseointegration to juxtaposed bone might lead to long-term failure after implantation. Specifically, the 10- to 15-year lifetime of current titanium-based orthopedic implants is not as long as expected by many patients. This chapter reviews many of the current research that is being carried out to extend the life of implants by nano modification techniques.

2.1 Introduction

Many attempts have been made to improve the surface properties of titanium-based implants (e.g., topography, chemistry, and surface energy), which directly determine the implant-environment interactions after implantation [1–3]. These surface modification techniques include mechanical methods (e.g., sand-blasting), chemical methods (e.g. acid etching), coatings (e.g., plasma spraying), etc. [4–9]. Through these conventional approaches, a better bonding ability with bone has been achieved due to the creation of a optimum microscale surface roughness, a more favorable surface chemistry, and/or a new morphology preferred by bone-forming cells (or osteoblasts). However, neither these mechanical nor chemical methods

T.J. Webster (✉) · C. Yao
Brown University, Providence, RI, USA
e-mail: Thomas_webster@brown.edu

W. Ahmed and M.J. Jackson (eds.), *Surgical Tools and Medical Devices*,
DOI 10.1007/978-3-319-33489-9_2

have the ability to produce controlled surface topographies. Moreover, these methods have the potential to form surface residuals. Thus, alternative methods to modify titanium surfaces are highly desirable for promoting new bone growth.

Other attempts to improve bone-bonding involves coating titanium-based implants with hydroxyapatite (HA) or other calcium phosphates, which is commonly accomplished by plasma spraying [2]. This is based on the fact that HA and other calcium phosphates are the main inorganic components of bone and they have been shown by many to directly bond to juxtaposed bone [10–13]. Unfortunately, such coatings have long-term failures due to weak adhesion to the metal substrate and dissolution once implanted. Therefore, an alternative method to deposit HA firmly onto titanium surfaces with optimal bioactivity is highly desirable for orthopedic applications.

In this light, a current strategy is to modify titanium-based implants to possess nanometer surface features considering that natural bone is a nanostructured material. It is important to note that type I collagen (organic matrix of bone) is a triple helix 300 nm in length, 0.5 nm in width, and periodicity of 67 nm while HA (inorganic mineral phase of bone) are approximately 20–40 nm long. Besides, HA crystals are uniquely patterned within the collagen network [14]. These indicate that bone cells may be used to an environment in nanoscale rather than microscale. Recently, human osteoblasts were observed to initially adhere to grain boundaries on both nanophase and conventional titanium; greater osteoblast adhesion was found on nanophase titanium that possessed more grain boundaries on the surface [15]. However, the mechanical strength of this nanophase titanium (compacts of nanoparticles) was not high enough for use as a bulk material like titanium alloys through metallurgy techniques. Proper nanometer surface modification methods for current titanium-based implants are, thus, being actively pursued.

An electrochemical method known as anodization or anodic oxidation is a well-established surface modification technique for valve metals to produce protective layers [4]. It has been successfully used as a surface treatment for orthopedic implants in the past few decades and it has some new advances recently. This chapter will present an overview of anodization and discuss processing parameters, microstructure and composition, biological responses of anodized titanium, which are pertinent for orthopedic applications. Finally, this chapter will also discuss mechanisms of enhanced osteoblast functions on anodized titanium that possesses nanometer structures.

2.2 Anodization of Titanium

2.2.1 Basics of Anodization Process

Typical anodization procedures include alkaline cleaning, acid activation, and electrolyte anodizing. Acid activation is performed in a mixture of nitric acid and

hydrofluoric acid (HF) to remove the natural titanium oxide layer and surface contaminants. The electrolyte anodization is carried out in an electrochemical cell, which usually has a three-electrode configuration (titanium anode, platinum cathode, and Ag/AgCl reference electrode). When a constant voltage or current is applied between the anode and cathode, electrode reactions (oxidation and reduction) in combination of field-driven ion diffusion lead to the formation of an oxide layer on the anode surface.

The main chemical reactions specifically for anodizing titanium are listed below (Eq. (2.1)–(2.5) adapted from [4]).

At the Ti/Ti oxide interface:

$$\mathrm{Ti} \Leftrightarrow \mathrm{Ti}^{2+} + 2e^{-} \tag{2.1}$$

At the Ti oxide/electrolyte interface:

$$2\mathrm{H_2O} \Leftrightarrow 2\mathrm{O}^{2-} + 4\mathrm{H}^{+} \tag{2.2}$$

$$2\mathrm{H_2O} \Leftrightarrow \mathrm{O_2} + 4\mathrm{H}^{+} + 4e^{-} \tag{2.3}$$

At both interfaces:

$$\mathrm{Ti}^{2+} + 2\mathrm{O}^{2-} \Leftrightarrow \mathrm{TiO_2} + 2e^{-} \tag{2.4}$$

Because titanium oxides have higher resistivity than the electrolyte and the metallic substrate, the applied voltage will mainly drop over the oxide film on the anode. As long as the electrical field is strong enough to drive the ion conduction through the oxide, the oxide film will keep growing. This explains why the final oxide thickness, d, is almost linearly dependent on the applied voltage, U:

$$d \approx aU \tag{2.5}$$

where a is usually a constant within the range 1.5–3 nm/V [4].

2.2.2 *Influences of Processing Parameters*

The resulting oxide film properties (such as degree of nanometer roughness, morphology, chemistry, etc.) after anodization varies over a wide range according to different process parameters such as applied potential (voltage), current density, electrolyte composition, pH, and temperature. Different acids (phosphoric acid-H_3PO_4, sulfuric acid-H_2SO_4, acetic acid-CH_3COOH, and others), neutral salts, and alkaline solutions are widely used electrolytes for the anodization of titanium. Their detailed electrochemical oxide growth behavior on titanium was studied by Sul et al. [16]. Generally, it was found that among all the electrolytes (including

H_3PO_4, H_2SO_4, CH_3COOH, and NaOH, $Ca(OH)_2$) the anodic oxide thickness in H_2SO_4 was the highest. Importantly, the oxide formation ability in acidic electrolytes exceeded that in hydroxide solutions. Usually, H_3PO_4 and H_2SO_4 were used to produce thick (tens of microns) and microporous oxide layers at high voltages. In contrast, fluoride solutions were found to have the ability of producing biologically inspired nano-tubular structures in the past few years [17–25]. Due to the importance of nanostructures for biological applications as discussed above, this will be discussed in this section.

The anodization process can be done either at constant voltage (potentiostatic) or constant current (galvanostatic). If the applied voltage exceeds the dielectric breakdown limit of the oxide, the oxide will no longer be resistive to prevent further current flow and oxide growth, which will lead to more gas revolution and sparking. This technique is, thus, known as Anodic Spark Deposition (ASD) or Micro-Arc Oxidation (MAO). For example, it has been reported that the breakdown potentials for H_3PO_4 and H_2SO_4 were around 80 and 100 V, respectively [26]. Below the breakdown limit, the anodic oxide film was relatively thin and usually nonporous using non-fluorine electrolytes.

A constant temperature during the anodization process is usually required to maintain a homogeneous field-enhanced dissolution over the entire area. Since increased temperature will accelerate the chemical dissolution rate, the working temperature is often kept relatively low to prevent the oxide from totally dissolving [26].

2.2.3 Creation of Rough Surfaces

The anodization technique was discovered in the early 1930s and was widely studied in the 1960s to enhance titanium implant osseointegration [27]. These studies usually adopted a high voltage anodization (i.e., ASD) of titanium in electrolyte solutions whose ions would be embedded into the oxide coating, resulting in a microporous structure [27–35]. Table 2.1 shows the anodizing parameters of some ASD studies.

The mechanism of the ASD is usually described by the avalanche theory. During anodization, the newly formed oxide layer on the anode is a dielectric barrier to the current flow and it keeps growing until reaching the dielectric breakdown limit. Generally, the anodized layer is not uniform due to the existence of flaws, defects, local stress, and nonuniform oxide thickness. When the applied voltage increases, the potential drop at the weak points exceeds the dielectric limit so that sparking happens. The local temperature at these points can be up to several thousand Kelvin and lead to a local melting process. Thermal stressing of these anodized titanium leads to the multiplication of weak points, i.e., a cascading process, and

Table 2.1 Experimental parameters of some ASD studies

Electrolyte Composition	Molarity	Voltage (current)	Time (s)	Temperature (°C)	Reference
Sulfuric acid	1	125	–	–	Zinger et al. [28]
	0.5, 1, 3	90, 155, 180	–	–	Yang et al. [29]
Acetic acid	1	80	–	RT	Larsson et al. [30]
	0.1	40–80	8–67	17	Sul et al. [16]
Phosphoric acid	2	175	–	25	Zinger et al. [28]
	0.2	200, 300, 350 (70 A/cm^2)	–	20	Zhu et al. [31]
	1	40–80	10–47	17	Sul et al. [16]
Sodium tripolyphosphate	0.15	(210 A/cm^2)	–	–	Chiesa et al. [27]
Sodium hydroxide	5	10–20	–	25	Huang et al. [66]
	0.1	40–80	22–110	17	Sul et al. [16]
Calcium hydroxide	0.1	40–80	13–53	17	Sul et al. [16]
Calcium glycerophosphate and calcium acetate	0.02/0.1	(70 A/cm^2)	1530	4.1–4.5	Chiesa et al. [27]
	0.03/0.15	200, 260, 300 (70 A/cm^2)		20	Zhu et al. [31]
	0.15/0.02	190–600	180	–	Li et al. [32]
	0.02/0.15	(70 A/cm^2)	1800	–	Suh et al. [33]
	0.02/0.15	350	1200	20	Son et al. [34]
β-glycerophosphate and sodium acetate	0.06/0.3	250–350 (50 A/cm^2)	–	–	Fini et al. [35]

RT Room temperature

consequently breakdown of the dielectric. Figure 2.1 shows a schematic diagram of porous titanium oxide formation proposed by Choi et al. [26].

Basically, the anodic film growth is determined by a balance between the oxide film formation rate and the oxide dissolution rate given by the nature of the electrolyte. Meanwhile, the nature of the electrolyte is closely connected with other processing parameters such as electrolyte concentration, applied voltage, current density, pH, etc. The explanations in detail could be found elsewhere [16].

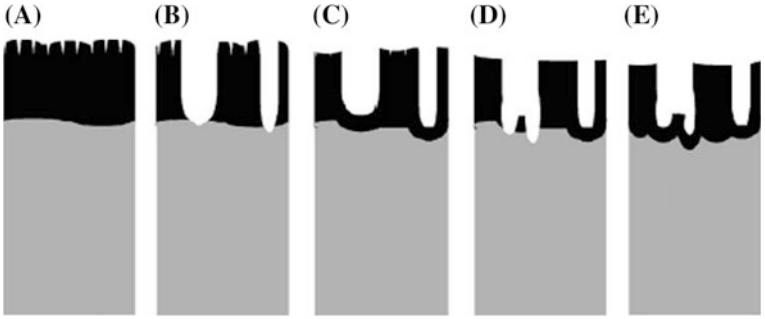

Fig. 2.1 Schematic diagram of porous titanium oxide formation above the breakdown potential: *A* oxide growth to maximal thickness, *B* burst of oxide by the formation of crystallites (pore formation), *C* immediate repassivation of pore tips, *D* burst of repassivated oxide, and *E* dissolution of the formed oxide and second repassivation (adapted from Ref. [26])

2.2.4 Creation of Nano-roughness

While the generation of microstructures through titanium anodization is well-established, current research efforts focus on creating biologically inspired nanometer surface structures. Studies has shown that nanoporous structures can be created by titanium anodization in chromic acid at 10–40 V [36]. Another unique surface morphology obtained through titanium anodization is self-ordered nano-tubular structures [17–25]. For these studies, fluorine electrolyte solutions are used and the applied voltage must be much lower than the dielectric breakdown. Some of the specific anodizing parameters to create titanium nanometer structures are listed in Table 2.2.

The need of fluoride ions to form nanoporous titania structures on a titanium surface under relatively low voltages was first reported by Zwilling et al. [37]. However, the nano-tubular structures were not reported here. In 1999, Grimes and co-workers successfully fabricated self-ordered nanotube arrays after anodizing titanium between 10 and 40 V in dilute (0.5–1.5 wt%) aqueous HF solutions [17]. It was found that the diameters of nanotubes were determined by applied voltage while the final length of tubes were independent of the anodization time.

The tube diameter was approximately 60 nm and tube length was 200 nm at 20 V in 0.5 % HF solution for 20 min (Fig. 2.2). Later, they developed a method to produce tapered, conical-shape titania nanotubes in 0.5 % HF by linearly changing the voltage from 10 to 23 V (Fig. 2.4) [18]. Schmuki and co-workers also observed self-ordered nano-tubular titanium oxide films in HF/H_2SO_4 or CH_3COOH/NH_4F electrolyte solutions [19].

Moreover, the nano-tubular (nano-pore) structure was also achieved in organic electrolytes. Choi et al. used nano-indented titanium for anodization in ethanolic HF and produced a pore lattice with a 500 nm inter-pore distance (Figs. 2.3 and 2.4) [26]. Schmuki's group reported nano-tubular structures using nonaqueous mixtures

Table 2.2 Survey of different fluorine solutions to produce titania nano-tubular structures with different size and thickness

Electrolyte composition (pH)	Voltage (V)	Time (h)	Temperature (°C)	Thickness (nm)	Pore diameter (nm)	Reference
CH_3COOH and 0.5 M HF	10	4	–	60	500 (inter)	Choi et al. [26]
0.5 or 1.5 % HF	10–40	<1	18	250	25–65	Gong et al. [17]
0.5 % HF	10–23	<1	–	300	22–76	Mor et al. [18]
KF and NaF (4.5)	25	20	–	4400	115	Cai et al. [21]
DMSO and CH_3COOH and 4 % HF	20	70	RT	2300	60	Ruan et al. [22]
1 M H_2SO_4 and 0.15 % HF	30	24	–	540	140	Beranek et al. [19]
CH_3COOH and 0.5 % NH_4F	20	1	–	200	30	Tsuchiya et al. [20]
1 M $(NH_4)_2SO4$ and 0.5 % NH_4F	20	–	–	2500	100	Macak et al. [23]
1 M $(NH_4)H_2PO_4$ and 1 M H_3PO_4 and 0.5 % HF	20	40	–	4070	50	Ghicov et al. [24]
0.138 M HF or NaF + 0.5 M H_3PO_4	20	–	24	500	100–120 (outer)	Raja et al. [25]

RT Room temperature

of ethanol and ammonium fluoride without an imprinting treatment [20]. However, in these studies, the depth of titania nanotubes was limited to a few hundred of nanometers. Recently, high-aspect-ratio titania nanotubes up to several micrometers were reported by both Grime's and Schmuki's groups [21–24]. Grime's group reported the formation of 4.4 µm long titania tube arrays by anodizing titanium in NaF or KF of pH 4.5 (Fig. 2.5) [21]. They also reported formation of 2.3 µm thick nano-tubular structures using DMSO/ethanol/HF electrolyte (Fig. 2.6) [22]. Meanwhile, Schmuki's group succeeded in using neutral fluoride solutions to produce nano-tubular structures up to 2.5 µm [23]. They achieved this by controlling the electrochemical parameters to enhance acidification at the bottom of tubes.

Chemical dissolution, field-assisted dissolution, and oxidation are the three main reactions in fluorine electrolyte anodization. Among these, field-enhanced dissolution has been considered as the predominant mechanism of titania tubular structure formation by many researchers [17–24]. The evolution of nanotube

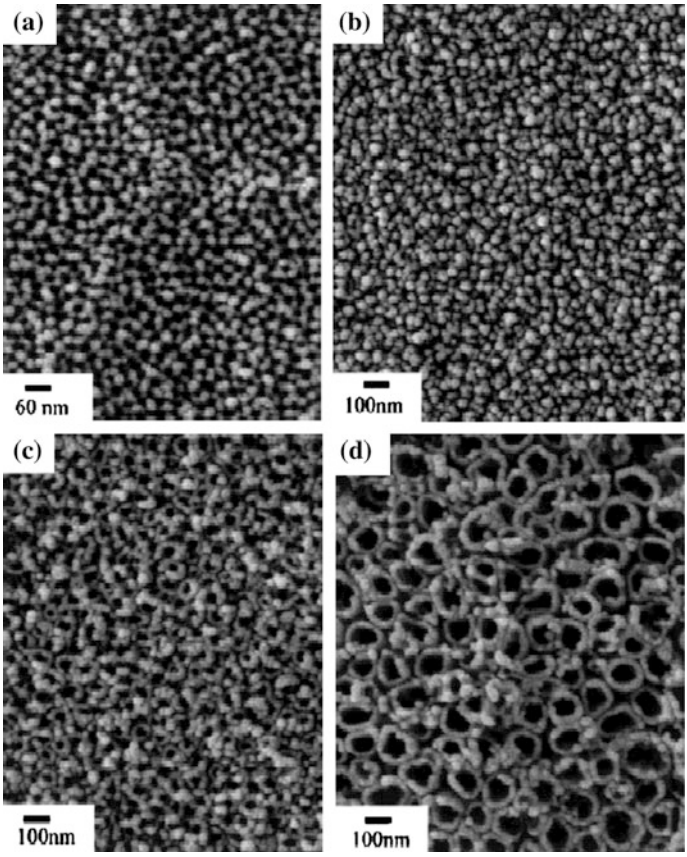

Fig. 2.2 FE-SEM top-view images of porous titanium oxide films anodized in 0.5 wt% HF solution for 20 min under different voltages: **a** 3 V, **b** 5 V, **c** 10 V, and **d** 20 V (adapted from Ref. [17])

structures is shown in Fig. 2.7. Grime and co-workers proposed a mechanism based on a point defect model [18]. Grime proposed that the initial pore formation was due to localized dissolution at weak points and the unanodized metallic portions would exist between the pores. Later, voids were formed in these inter-pore regions by field-enhanced oxidation/dissolution (Fig. 2.8). The growth of voids in equilibrium with the pores would form the final nano-tubular structures. However, it did not explain how voids are created and lead pores to be well-separated, individual tubes. Recently, Raja et al. [25] suggested that the instability of the oxide layer and the self-ordered structures could be explained by the perturbation theory; separation of individual nanotubes of titanium oxide layer from the interconnected nano-pores could be attributed to the repulsion forces of the cation vacancies (Fig. 2.9).

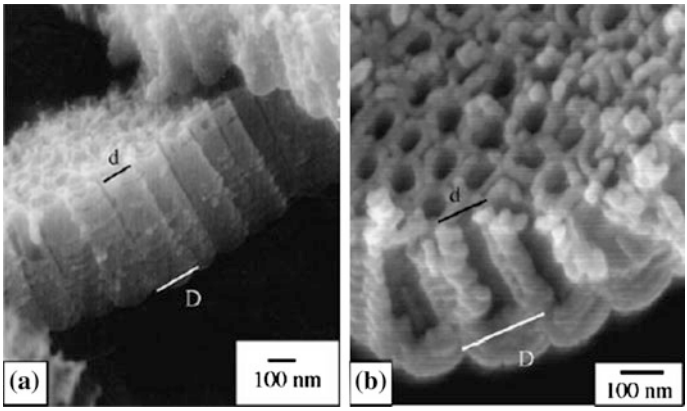

Fig. 2.3 FE-SEM cross-sectional views of the titania nanotubes obtained using a time-varying anodization voltages; *d* denotes diameter of apex and *D* diameter of cone base. **a** Tapered nanotubes obtained using a ramp rate of 0.43 V/min to raise the voltage from 10 to 23 V within 30 min and then holding the voltage at 23 V for 10 min. **b** Tapered nanotubes obtained by initially anodizing the sample at 10 V for 20 min and then increasing the voltage linearly at a rate of 1.0 V/min to 23 V, and finally keeping the voltage at 23 V for 2 min (Ref. [18])

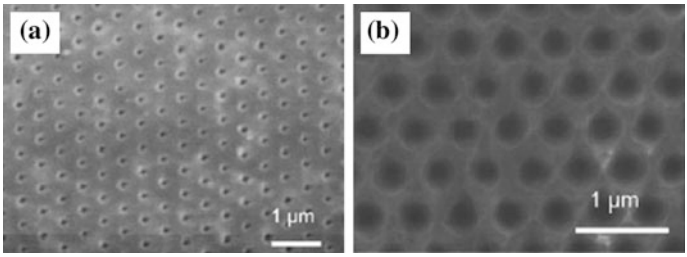

Fig. 2.4 SEM of **a** nano-indented surface of titanium substrate and **b** anodized titanium at 10 V in ethanolic 0.5 M HF for 240 min (adapted from Ref. [26])

2.2.5 Control of Chemical Composition

The ions contained in the electrolyte are usually present in the thick, porous ASD film and the concentration of these elements decreases from the outer layer toward the substrate [31]. For example, phosphorous was found to be embedded in titanium oxide layer after anodization with a H_3PO_4 electrolyte [38]. For electrolytes containing Ca and P, such as calcium glycerophosphate (Ca-GP) and calcium acetate (CA), both Ca and P were contained in the oxide layer with a Ca/P ratio close to HA (1.67) [39]. After an additional hydrothermal treatment (e.g., high pressure streaming), HA crystals were randomly precipitated on the anodic oxide film. These HA crystals were usually columnar or need-like (Fig. 2.10). This could be

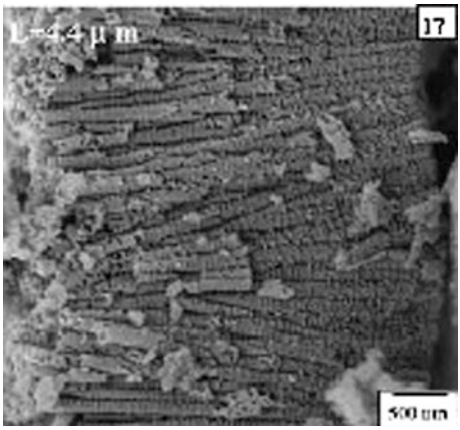

Fig. 2.5 Lateral view of the nanotubes formed in a KF and NaF solution at pH 4.5 under 25 V for 20 h (adapted from Ref. [21])

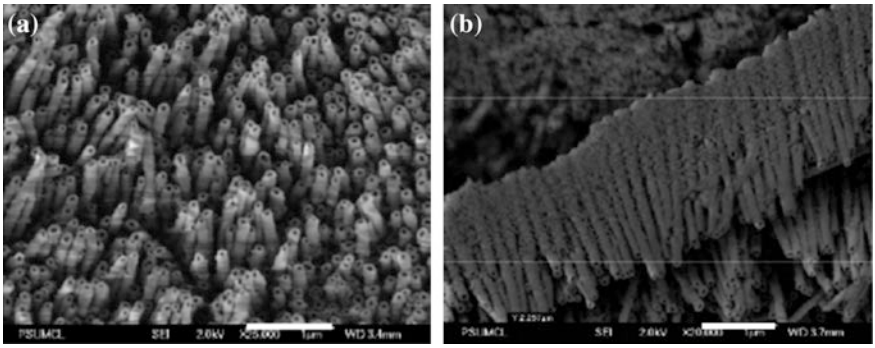

Fig. 2.6 FE-SEM images of titanium foil sample anodized in DMSO and ethanol mixture solution (1:1) containing 4 % HF at 20 V for 70 h. **a** is top-view and **b** is cross-section. Scale bars = 1 μm (adapted and redrawn from Ref. [22])

another way to create HA coatings as opposed to plasma spraying. The advantages of such HA coatings compared to plasma sprayed HA will be discussed in the following sections.

Another approach reported to introduce apatite layers onto the anodized titanium is simply by soaking crystalline titania in simulated body fluid (SBF), because anodized titanium with anatase and rutile titania surfaces were shown to induce apatite formation in vitro. Yang et al. [29] soaked titanium metal in SBF for 6 days after H_2SO_4 anodization and observed uniform apatite formation (Fig. 2.11). One advantage of this method is that the composition and surface morphology of the resulting apatite layer is very close to those in natural bone, but the adhesive strength of such coatings are not clear yet.

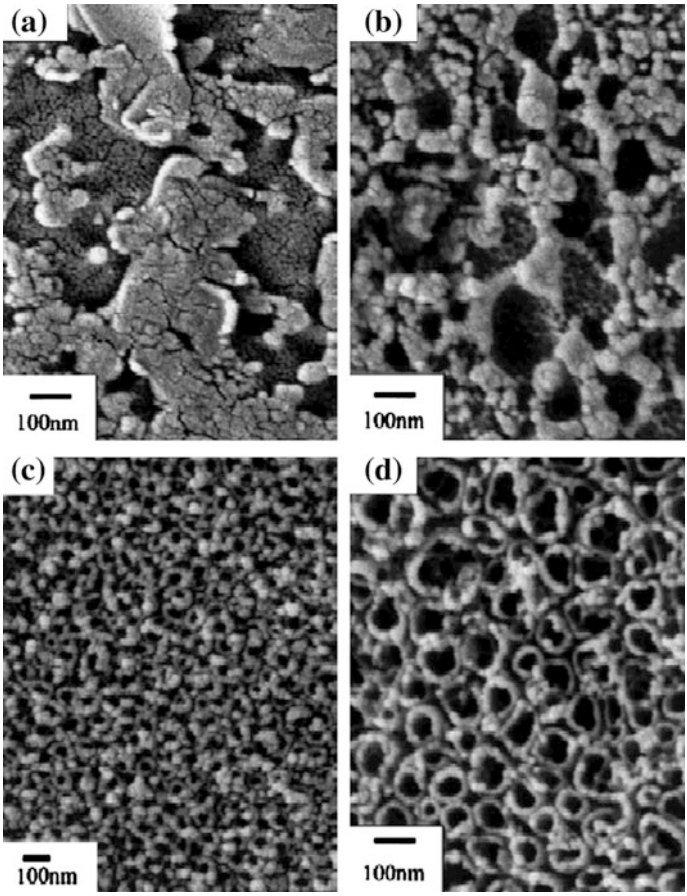

Fig. 2.7 Evolution of nano-tube structures. Porous titanium oxide films anodized in 1.5 % HF at 20 V for **a** 10 s, **b** 30 s, **c** 120 s, and **d** 8 min (adapted from Ref. [17])

Similarly, a two-step procedure was used to produce nanoscale HA for anodized titanium with nano-tubular structures [40]. Specifically, the anodized titanium was treated with NaOH to form nanofibers of bioactive sodium titanate structures on the top edge of the nanotube wall, which was then immersed in a SBF to induce the formation of nanoscale HA (Fig. 2.12). This technique could be useful as well-adherent bioactive nano-HA layers on titanium-based implants are created which simulate the size and shape of natural HA in bone. The advantage of introducing nano-HA onto titanium anodized structures was supported by previous work revealing greater osteoblast functions on nano-HA compared to conventional, or micron grain size, HA [14].

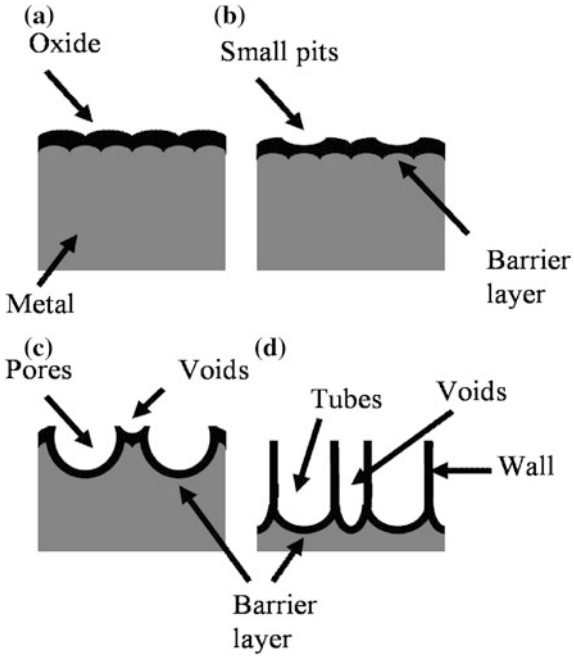

Fig. 2.8 Schematic diagram of the evolution of nano-tube-like structures on the titanium surface during anodization in aqueous HF under constant voltage: **a** oxide formation; **b** pit formation in some concave sites; **c** pore formation and growth under field-enhanced dissolution leading to voids formation; and **d** fully developed tubes (based on the model from Ref. [18] and modified according to experimental observations)

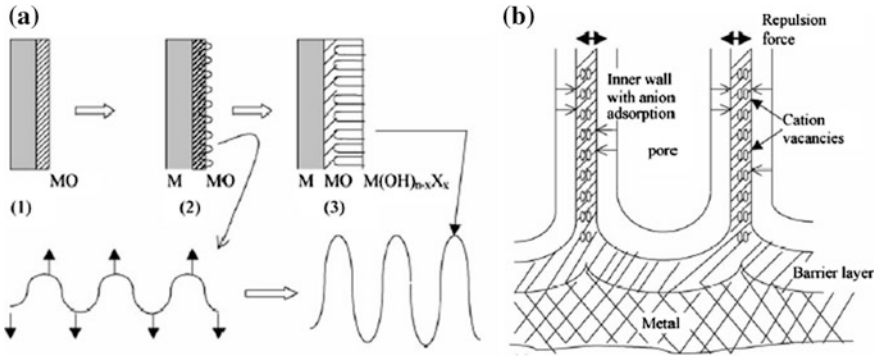

Fig. 2.9 Schematic diagram of **a** pore formation (fluoride addition) during anodization of Ti. The barrier film is intact during porous anodic film formation and substrate metal is not attacked locally. Perturbation of the surface shown in *2* can lead to adsorption of fluorides at the valleys and develop into nano-tubular structure. Higher strain energy density at the valleys drives the mass flow to the lower energy crests; **b** pore separation mechanism. Cation vacancies generated by dissolution of Ti cations are transported radially from the two sides of common wall of the neighbor pores. Charges of similar polarity repel and when electrical neutrality is not maintained this repulsion causes separation of pores into individual nanotubes (adapted and redrawn from Ref. [25])

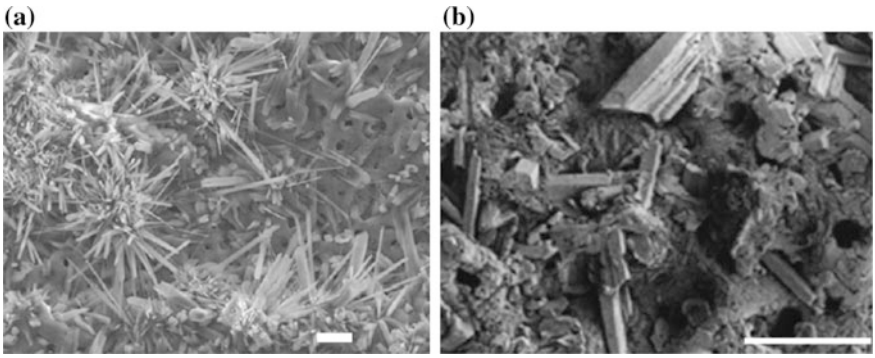

Fig. 2.10 Needle-like or columnar hydroxyapatite crystals deposited on anodized titanium after a hydrothermal treatment. **a** ASD followed by Ishizawa's procedure [43] (adapted and redrawn from reference [27]) and **b** ASD followed by Suh's procedure [33] (adapted and redrawn from Ref. [33]). Scale bars = 10 μm

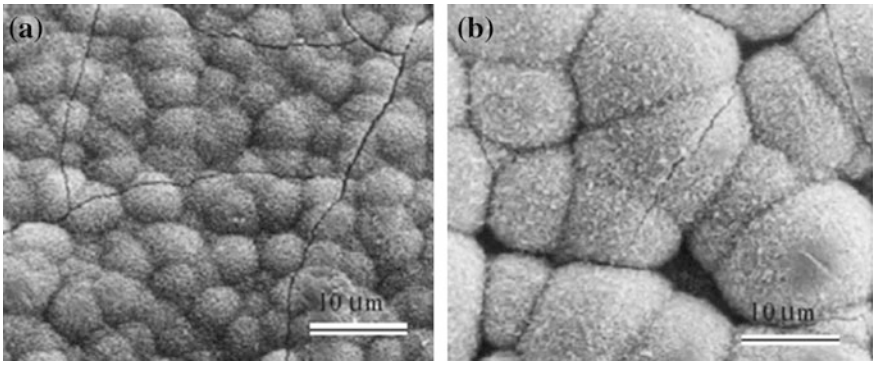

Fig. 2.11 SEM images of titanium metal soaked in SBF for 6 days after they were anodized in 1 M H2SO4 at **a** 155 V and **b** 180 V (adapted and redrawn from Ref. [29])

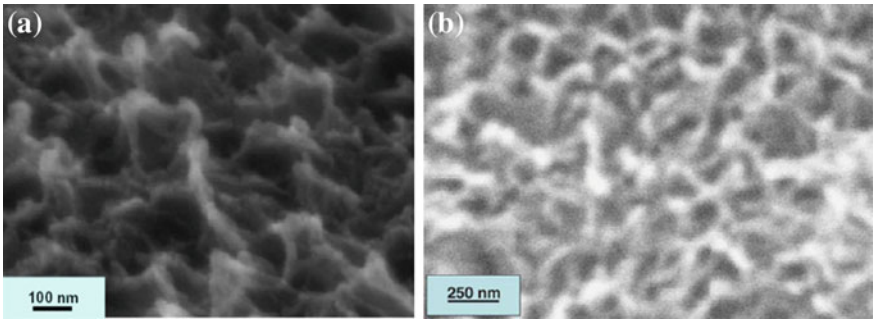

Fig. 2.12 SEM images of **a** nano-inspired sodium titanate nanofibers and **b** nanoscale HA phase (adapted and redrawn from Ref. [40])

2.3 Structure and Properties of Anodized Oxide Film

2.3.1 Structure

The structures and properties of ASD films were widely investigated by Kurze et al. [38]. The typical morphology of the titania layer resulting from ASD is a rough, porous texture with cracks on it (Figs. 2.13 and 2.14). The dimensions of the pores varied from a few hundred nanometers to a few micrometers depending on the processing parameters and are not uniform within the same anodized surface. Moreover, these pores were interconnected and had a layered structure, i.e., they overlapped with each other. The shapes of the pores were mostly round or irregular. The diameter of the pores and the film roughness were reported to increase with greater current densities (Fig. 2.13), [27, 41] applied potential (Fig. 2.14), [29] and electrolyte concentrations [29]. The thickness of oxide film increases with time up to tens of micrometers.

In contrast, the biological-inspired nano-tubular structures were highly ordered. The pore size is determined by the voltage and can be varied from a few tens of nanometers to around 100 nm. The thickness of the tubular-structured oxide was formed to be a few hundred nanometers but has been elongated to a few microns by controlling pH and electrolytes. Generally, the dimensions of nano-tubular structures within one sample are uniform but might be variable due to differences (e.g., surface defects) on a substrate.

2.3.2 Corrosion Resistance and Adhesive Strength

After anodization, thickness of the protective oxide layer increases and it could lead to less ion release in the human body. The oxide barrier layer (the relatively thin,

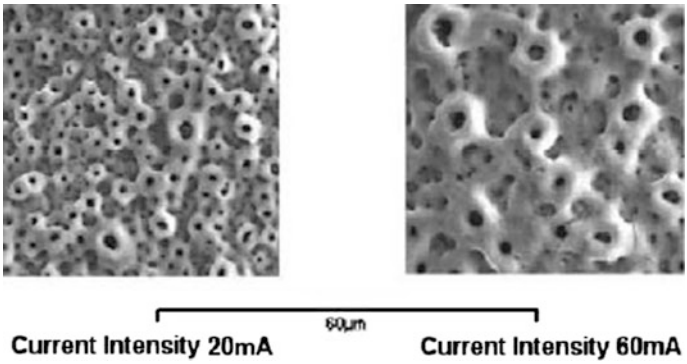

Fig. 2.13 SEM micrographs of an ASD formed film on c.p. grade 2 titanium from an electrolyte containing 0.015 M calcium glycerophosphate and 0.1 M calcium acetate. Increased current density from 20 to 60 mA/cm^2 led to a larger pore size in the ASD porous structure (adapted from Ref. [27])

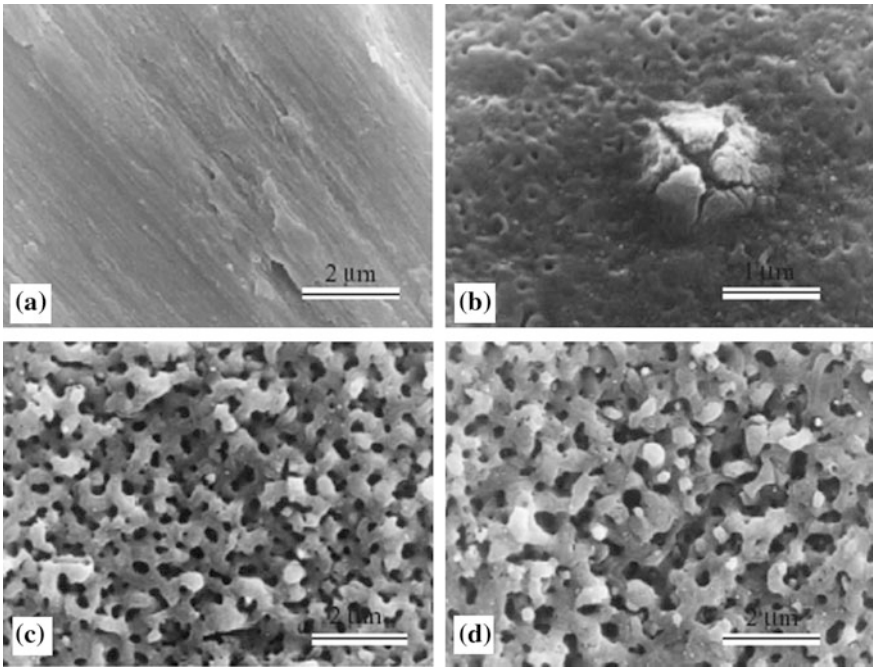

Fig. 2.14 SEM micrographs of ASD formed film on c.p. titanium from an electrolyte containing 1 M H_2SO_4 at voltages of: **a** 0 V, **b** 90 V, **c** 155 V, and **d** 180 V for 1 min. Different voltages from 90 to 155 V led to a larger pore size in the ASD porous structure (adapted from Ref. [29])

nonporous oxide layer under the porous oxide structures) is considered to contribute to the improvement of corrosion resistance. However, it was suggested that the implants' mechanical properties could be impaired with increased spark coating thickness [27].

The interface between the anodic oxide layer and the titanium substrate usually does not show any discontinuity [27]. Besides, the HA crystals on the hydrothermally treated titanium are gradually grown consuming Ca and P in the anodic film. As a result, the interface between the substrate, the anodic film, and the HA film are considerably strong. The adhesive strength between the anodic oxide films and the titanium substrates was reported to be 25 MPa, [42] and the adhesive strength between the oxide/HA coating and the substrate after a hydrothermal treatment was reported to be up to 40 MPa by Ishizawa and Ogino [39, 43] when using less concentrated electrolytes. These values are equivalent or higher than those of plasma sprayed HA onto titanium surfaces, which were reported between 15 and 30 MPa depending on different processing parameters [44, 45]. Moreover, the HA produced from hydrothermal treatment after anodization (AH-HA) seemed to be more stable than plasma sprayed HA (PS-HA). It was reported that the shear strength of PS-HA in SBF decreased from 28.1 to 20.4 MPa after 4 weeks [46]; meanwhile, Ishizawa et al. found that AH-HA retained high durability after

300 days in SBF [39]. So from a mechanical point-of-view, hydrothermally treated anodic titanium would be a better choice than HA plasma sprayed titanium.

2.3.3 Biological Properties of Anodized Titanium

2.3.3.1 In Vitro Studies

Clearly, coating strength, mechanical. and other properties are not the only concern for orthopedic implants. Cytocompatibility leading to promoted bone growth needs to be assessed. Most studies have been reported in vitro bone cell responses to anodized and anodized/hydrothermally treated titanium surface. Fini et al. reported that the adhesion, spreading, proliferation, and differentiation of osteoblast-like cells (HOS-TE85, human osteosarcoma line) were similar on unanodized titanium, titanium anodized enriched with Ca/P, and titanium anodized and hydrothermally treated [35]. An unexpected increase of unattached cells in the latter two substrates was observed. However, the percentage of unattached cells was in the range of 10–20 % which is considered a normal range for cytocompatible materials. On contrast, Rodriguez et al. [47] reported increased osteocalcin production on the anodized and hydrothermally treated titanium surfaces but the highest alkaline phosphate (ALP) activity on control titanium throughout an 8-day study using an osteoblast precursor cell line (ATCC, CRL-1468). Both osteocalcin and ALP are markers of osteoblast differentiation to deposit calcium. They explained that a decrease in ALP activity was in part attributed to the maturation of osteoblast precursor cells and in part attributed to the increased production of mineralized matrix. Also using Ca-GP and CA as an electrolyte, Li et al. reported decreased osteoblastic MG63 cell proliferation when anodization voltage increased above 190 V; however, increased ALP activity of human osteosarcoma cell line was reported with voltages above 300 V [32].

Zhu et al. [31] studied the effects of topography and composition of anodized titanium surfaces on osteoblast (SaOS-2 derived from human osteosarcoma) responses. Their cell experiments showed an absence of cytotoxicity and an increase of cell attachment and proliferation after anodization in an electrolyte composed of Ca-GP and CA. The cells on the surfaces with micropores showed an irregular and polygonal growth and more lamellipodia, while cells on the titanium control showed many thick stress fibers and intense focal contacts. However, they did not find any significant difference for ALP activity. Suh et al. [33] studied the effects of hydrothermally treated anodic films similar to the Zhu formulations and they observed no statistical differences in cell viability using the MTT assay when osteoblasts (ROS 17/2.8, a rat osteosarcoma cell line) were cultured for 4 days on untreated, anodized, and anodized/hydrothermally treated surfaces. In contrast, they found that hydrothermal treatment had an effect on early osteoblast attachment, resulting in a more well-spread shape compared to the cellular rounded shape observed on anodized and control titanium after 6 h (Fig. 2.15).

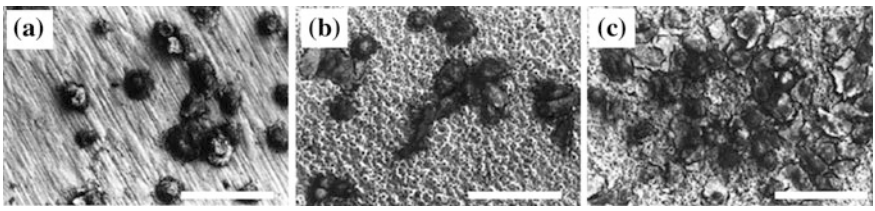

Fig. 2.15 SEM of cells after 6 h culturing on **a** control surface, **b** anodized surface and **c** anodized surface followed by hydrothermal treatment for 4 h. Scale bars = 120 μm (adapted from Ref. [33])

The different observations in the above in vitro studies could be attributed to the use of different anodization parameters and different cell lines. The optimal anodization conditions are still under investigation.

Since the nano-tubular structure is relatively new, few cytocompatibility studies have been completed to examine its potential for use as a novel titanium bone implant surface. However, because of the size and order of the titania tubular structure (which somewhat mimics the natural environment of bone) it is very interesting to determine whether there is any morphological or size advantage of using nano-tubular structures compared to a conventional anodized titanium porous structure for enhancing bone cell functions.

Currently, our research has focused on osteoblast functions on such anodized titanium with nano-tubular titania structures. These structures are similar to those formed by Gong et al. [17]. (0.5 % HF, 20 V, 20 min). After anodization, the tubular structures had increased surface roughness (Fig. 2.16). The inner diameters of the nanotubes were about 70 nm and the depth of them was about 200 nm. To study the effects of nanoroughness and morphology, intermediate samples that possessed a nano-particulate structure and a medium roughness in between the unanodized control and the nano-tubular structure were created (0.5 % HF, 10 V, 20 min) (Fig. 2.16).

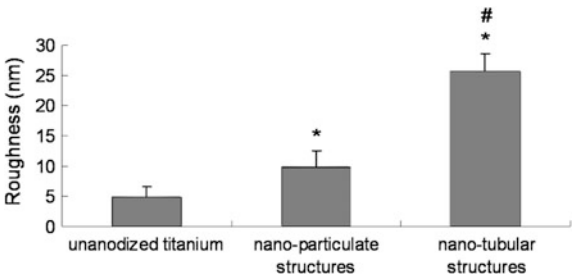

Fig. 2.16 Surface roughness of **a** unanodized titanium, **b** anodized titanium with nano-particulate structures, and **c** anodized titanium with nano-tubular structures. Data = mean ± SEM; n = 3; *p < 0.01 (compared to unanodized titanium) and #p < 0.01 (compared to nano-particulate structure)

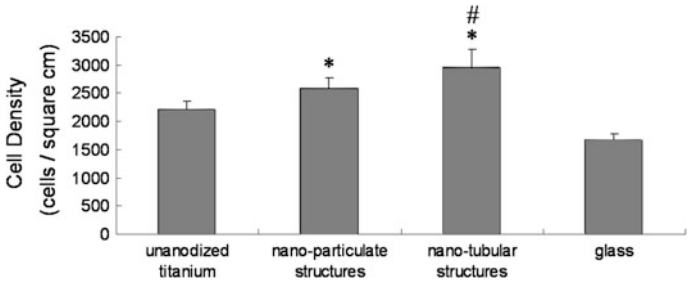

Fig. 2.17 Osteoblast adhesion on unanodized titanium, anodized titanium with nano-particulate structures (10 V, 0.5 % HF, 20 min), anodized titanium with nano-tubular structures (20 V, 0.5 % HF, 20 min), and glass (reference). Values are mean ± SEM; n = 3; *p < 0.1 (compared to unanodized titanium) and #p < 0.1 (compared to anodized titanium with nano-particulate structures)

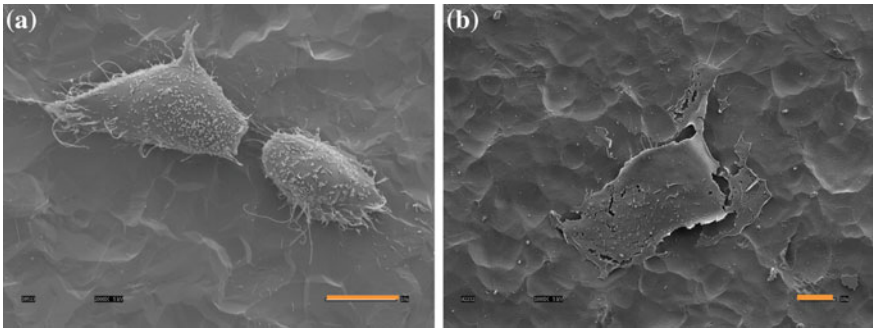

Fig. 2.18 Typical osteoblast morphology on **a** unanodized titanium and **b** anodized titanium surface with nano-tubular structures after 4 h culture. Scale bars = 10 μm

The experiments showed increased osteoblast adhesion after 4 h of culture with greater anodized titanium roughness (Fig. 2.17). The difference in osteoblast morphology was obvious between nano-tubular structures and unanodized titanium. Most cells were well-spread on anodized titanium with nano-tubular structures while they mostly looked round on the control (Fig. 2.18). After 4 weeks of culture, the anodized titanium with nano-tubular structures promoted the highest calcium deposition by osteoblasts among all the samples. These results indicated that the special nano-tubular structures anodized onto the titanium surface may have provided an optimal surface roughness for promoting bone cell function.

2.3.3.2 Mechanisms of Increased Osteoblast Function

Moreover, protein (fibronectin and vitronectin) adsorption on nano-tubular samples has been examined to explore the mechanism of enhanced osteoblast adhesion. Fibronectin and vitronectin are two major proteins that involved in osteoblast

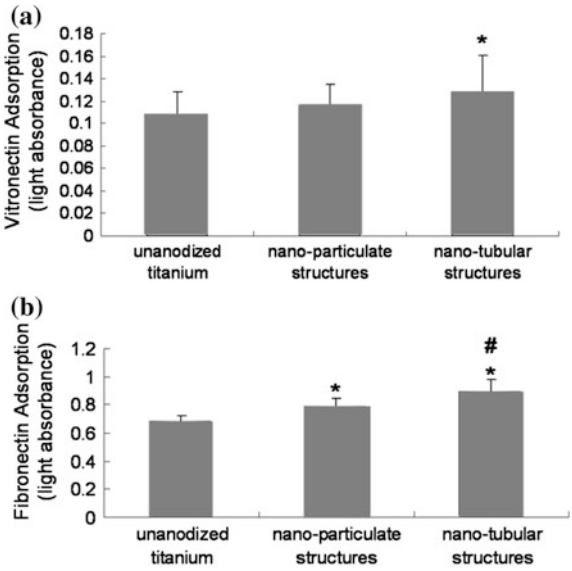

Fig. 2.19 **a** Fibronectin and **b** vitronectin adsorption on unanodized titanium, anodized titanium possessing nano-particulate structures (0.5 % HF, 10 V and 20 min), and anodized titanium possessing nano-tubular structures (0.5 % HF, 20 V and 20 min). Values are mean ± SEM; n = 3; *p < 0.1 (compared to unanodized titanium) and #p < 0.1 (compared to nano-particulate structures)

adhesion [48–50]. Results showed significantly increased both fibronectin (15 %) and vitronectin (18 %) adsorption on nano-tubular structures compared to unanodized titanium samples (Fig. 2.19). Because the cells adhered to the titanium surface via pre-adsorbed proteins, increased fibronectin and vitronectin adsorption on anodized titanium substrates with nano-tubular structures may explain the observed enhanced osteoblast functions.

2.3.3.3 In Vivo Studies

While in vitro assays may generate a quick assessment of cytocompatibility, in vivo studies are necessary to fully evaluate new bone growth. A survey of in vivo investigations of bone tissue reactions to anodized titanium implants is listed in Table 2.3. As with in vitro analysis, the varied oxide properties not only include thickness, but also morphology, chemical composition, crystallinity, and surface roughness.

Some in vivo studies were mainly interested in the effects of thick, porous oxide coating on new bone growth. Less than 200 nm thick oxide film anodized in acetic acid showed no significant difference compared to unanodized samples after implanted into a rabbit 6 weeks [30]. In contrast, a H_3PO_4/H_2SO_4 electrolyte was usually used to form thick anodic films up to tens of microns. Enhanced bone-bonding was found for micron-thick porous anodic oxide films formed in a H_3PO_4/H_2SO_4 electrolyte solution in a rabbit model [51–53].

More importantly, changes of surface chemistry could play a more important role in inducing new bone growth. Several in vivo studies focused on Ca-P enriched anodized titanium with and without hydrothermal treatment [32, 35, 54–57].

Table 2.3 Survey of in vivo investigations of bone tissue reactions to anodized titanium implants

Implant	Treatment	Chemical composition	Oxide thickness (μm)	Oxide/HA morphology (pore size, μm)	Oxide/HA crystallinity	Roughness (μm)	Test	Animal and time (week)	References
cylinder	AO and HT	TiO_2, HA	<10	Porous (1–3)	A + R	ND	Push-out	Rabbits 8	Ishizawa et al. [54]
Screw	E/M and AO	Mainly TiO_2	0.18–0.2	Pores and pits	N	32.3/40.8 nm (rms)	Contact ratio	Rabbits 1, 3, 6	Larsson et al. [30]
Screw	AO	Ti, O, C, P/S	1/10	Porous (1–10)	A + R	1.2 (Sa)	RTQ, RFA	Rabbits 3, 6	Henry et al. [51]
Rod	Ca-P AO w/or w/o HT	Ti, O, Ca/P, HA	5	porous (1–3)/columnar	N/C	1.97 (Ra)	AI	Rats 4, 8	Fini et al. [35]
Screw	Ca-P AO and HT	Ti, O, Ca/P, HA	ND	porous	ND	1.97 (Ra)	AI, push-out strength	Sheep 4, 8, 12	Giavaresi et al. [55, 56]
Screw	Ca-P AO w/or w/o HT	Ti, O, Ca/P, HA	ND	Porous/needle-like	A + R/C	ND	Percent bone contact, RTQ	Rabbits 6,12	Son et al. [57]
Screw	AO	Primary TiO_2	0.2–1	Porous (1.27–2.10)	N, A, A + R	0.96–1.04 (Sa)	RTQ, RFA	Rabbits 6	Sul et al. [52, 53]
Screw	AO	Ti, O, S, P, Ca	1.1–1.3	Porous (<1.5)	A or N	0.82–1.04 (Sa)	RTQ, BMC	Rabbits 6	Sul [59]

Abbreviations: *AO* Anodization, *HT* Hydrothermal treatment, *E* Electropolished, *M* Machined. *C* Crystalline, *N* Noncrystalline, *A* Anatase, *R* Rutile, *RTQ* Removal torque values, *RFA* Resonance frequency analysis, *AI* Affinity index, *BMC* Bone to metal, *ND* Not determined

Ishizawa et al. produced 1–2 μm HA films on anodic oxide layer and compared bone growth on them with unanodized titanium [54]. They found strong bone bonding via push-out tests with anodized titanium after 8 weeks of implantation into rabbits. Following their in vitro work, Fini et al. [35] found the lowest affinity index on anodized titanium while the highest was found on the anodized and hydrothermally treated titanium. The low bone contact on anodized titanium was probably due to the in vivo reduction and degradation of the amorphous titania layer while HA crystals aided bone opposition. Giavaresi et al. [55, 56] also supported the positive role of HA produced from hydrothermal treatment in accelerating bone ingrowth and bone mineralization. Son et al. [57] reported no significant difference for the percent bone contact for all samples but did find significantly increased removal torque strength for anodized implants after 6 weeks of implantation into a rabbit.

The dissolution of AH-HA and PS-HA in vivo was studied by Ishizawa et al. [58]. Basically, the AH-HA was much more durable than PS-HA because of their relatively high crystallinity and their relatively low thickness. Ishizawa et al. also found these two HA had different bone responses [58]. Specifically, new bone thinly spread over the whole AH-HA area while new bone formed from surrounding bones to the PS-HA area. This is probably due to their different degradation properties. One drawback of most of the above studies is that both chemical composition and surface morphology changed after titanium anodization so that it is hard to verify the role of one material property. However, Sul [59] indirectly verified a chemical bonding in vivo by maintaining surface morphology and roughness and changing chemical characteristics (specifically, S, P and Ca enriched implants via anodization).

The removal torque value (RTQ) showed significant differences between Ca-containing anodized titanium implants and unanodized titanium implants as well as S-containing anodized titanium implants and unanodized titanium implants (Fig. 2.20). The bone to metal contact was 186, 232, and 272 % higher in S, P, and Ca implants, respectively, when compared to the control groups. These results

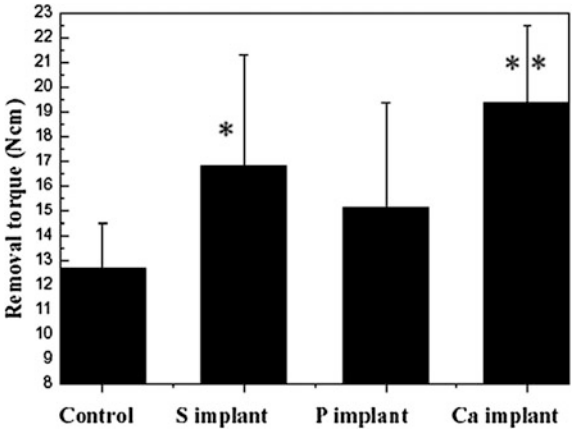

Fig. 2.20 Mean removal torque values after 6 weeks of healing time. *p < 0.05, **p < 0.001 (adapted from Ref. [59])

confirmed that ions incorporated into the titanium oxide layer during anodization could have important roles in enhancing bone juxtaposition.

2.4 Future Directions

As a surface modification method, anodization can lead to desired chemistry and/or topography changes and could be used with other treatments (e.g., hydrothermal) together.

First, anodization provides a controlled way to create nano-roughness or even nano-features. Generally, there are two mechanisms that are responsible for osseointegration of bone: biomechanical interlocking and biological interactions. For biomechanical interlocking, it depends on the roughness, and surface irregularity. Current femoral stems made of titanium alloys are usually macro-textured to provide such surface features for bone to mechanically interlock. For biological interactions, it involves complex systems. Considering roughness in different scales, it is reported that increased micro/submicron-roughness could enhance bone cell function, such as ALP activity [60, 61] while some other studies have revealed the enhanced cell-implant interactions on nanoporous or nanophase materials [14, 15, 62, 63]. Ideally, the future titanium implant should possess roughness in all three scales: macro, micro, and nano. One possible approach to accomplish this is by subjecting implants to techniques like polishing and mechanical grinding that promote micro-roughness, and then to induce nano-tubular structures by a quick anodization process.

Second, micro/nano HA films produced using anodized titanium shows some advantages over conventional ones. Although plasma spray is still widely used for HA coatings on titanium, anodization has a strong role to play to incorporate Ca and P into Ti coatings. For example, anodization has the ability to form uniform and thin HA or calcium phosphate layers on titanium implants of various shapes. Moreover, HA deposited onto the anodized titanium could be nanoscale in dimension. One problem that still needs to be more fully investigated is the bonding strength between apatite crystals and the anodic oxide.

Furthermore, anodization can be used to incorporate drug delivery into titanium-based implants to enhance new bone formation. Porous ASD surfaces could be used as matrices for drug storage and release [64]; similarly, the nano-tubular structures could serve as reservoirs of chemical mediators, such as bone morphogenetic protein-2 (BMP-2) and osteogenic protein-1 (OP-1, BMP-7) [65]. In the future, studies should concentrate on embedding these growth factors into the unique porosity that can be well controlled on titanium for orthopedic applications.

In a word, anodization as a quick and efficient modification method of titanium based implants shows significant promise for enhancing their 10–15-year lifetime.

Acknowledgments The authors would like to thank National Science Foundation Nanoscale Exploratory Research Grant for financial assistance.

References

1. Brunette, D. M, Tengvall, P., Textor, M., & Thomsen, P. (2001). *Titanium in medicine* (p. 171). Berlin: Springer.
2. Shackelford, J. F. (1999). *Bioceramics* (vol. 1, p. 17). Netherlands: Gordon and Breach Science Publishers.
3. Moran, C. G., & Horton, T. C. (2000). *BMJ, 320*, 820.
4. Brunette, D. M., Tengvall, P., Textor, M., & Thomsen, P. (2001). *Titanium in medicine* (p. 232). Berlin: Springer.
5. Larsson, C., Thomsen, P., Aronsson, B. O., Rodahl, M., Lausmaa, J., Kasemo, B., & Ericson, L. E. (1996). *Biomaterials, 17*, 605.
6. Kim, H. M., Miyaji, F., Kokubo, T., & Nakamura, T. (1997). *Journal of Materials Science: Materials in Medicine, 8*, 341.
7. Kokubo, T., Kim, H. M., Kawashita, M., & Nakamura, T. (2004). *Journal of Materials Science: Materials in Medicine, 15*, 899.
8. Sittig, C., Textor, M., Spencer, N. D., Wieland, M., & Vallotton, P. H.: *Journal of Materials Science: Materials in Medicine, 10*, 35.
9. Bordji, K., Jouzeau, J. Y., Mainard, D., Payan, E., Netter, P., Rie, K. T., et al. (1996). *Biomaterials, 17*, 929.
10. Furlong, R., & Osborn, J. F. (2001). *Journal of Bone and Joint Surgery, 73B*, 741.
11. Kim,S.-S., Park, M. S., Jeon, O., Choi, C. Y., & Kim, B.-S. *Biomaterials* (in press).
12. Baker, K. C., Anderson, M. A., Oehlke, S. A., Astashkina, A. I., Haikio, D. C., Drelich, J., et al. *Growth, Materials Science and Engineering: C* (in press).
13. Sato, M., Slamovich, E. B., & Webster, T. J. (2005). *Biomaterials, 26*, 349.
14. Bronzino, J. D. (1995). *Biomedical engineering handbook* (p. 274). Boca Raton: CRC Press.
15. Webster, T. J., & Ejiofor, J. U. (2004). *Biomaterials, 25*, 4731.
16. Sul, Y. T., Johansson, C. B., Jeong, Y., & Albrektsson, T. (2001). *Medical Engineering and Physics, 23*, 329.
17. Gong, D., Grimes, C. A., Varghese, O. K., Hu, W., Singh, R. S., Chen, Z., & Dickey, E. C. (2001). *Journal of Materials Research, 16*, 3331.
18. Mor, G. K., Varghese, O. K., Paulose, M., Mukherjee, N., & Grimesa, C. A. (2003). *Journal of Materials Research, 18*, 2588.
19. Beranek, R., Hildebrand, H., & Schmuki, P. (2003). *Electrochemical and Solid-State Letters, 6*, B12.
20. Tsuchiya, H., Macak, J. M., Taveira, L., Balaur, E., Ghicov, A., Sirotna, K., & Schmuki, P. (2005). *Electrochemistry Communications, 7*, 576.
21. Cai, Q., Paulose, M., Varghese, O. K., & Grimes, C. A. (2005). *Journal of Materials Research, 20*, 230.
22. Ruan, C., Paulose, M., Varghese, O. K., Mor, G. K., & Grimes, C. A. (2005). *The Journal of Physical Chemistry B, 109*, 15754.
23. Macak, J. M., Tsuchiya, H., & Schmuki, P. (2005). *Angewandte Chemie International Edition, 44*, 2100.
24. Ghicov, A., Tsuchiya, H., Macak, J. M., & Schmuki, P. (2005). *Electrochemistry Communications, 7*, 505.
25. Raja, K. S., Misra, M., & Paramguru, K. (2005). *Electrochimica Acta, 51*, 154.
26. Choi, J., Wehrspohn, R. B., Lee, J., & Gosele, U. (2004). *Electrochimica Acta, 49*, 2645.
27. Chiesa, R., Sandrini, E., Santin, M., Rondelli, G., & Cigada, A. (2003). *Journal of Applied Biomaterials and Biomechanics, 1*, 91.
28. Zinger, O., Chauvy, P. F., & Landolt, D. (2003). *Journal of the Electrochemical Society, 150*, 495.
29. Yang, B., Uchida, M., Kim, H.-M., Zhang, X., & Kokubo, T. (2004). *Biomaterials, 25*, 1003.
30. Larsson, C., Thomsen, P., Aronsson, B.-O., Rodahl, M., Lausmaa, J., Kasemo, B., & Ericson, L. E. (1996). *Biomaterials, 17*, 605.

31. Zhu, X., Chen, J., Scheideler, L., Reichl, R., & Geis-Gerstorfer, J. (2004). *Biomaterials, 25*, 4087.
32. Li, L. H., Kong, Y. M., Kim, H. W., Kim, Y. W., Kim, H. E., Heo, S. J., & Koak, J. Y. (2004). *Biomaterials, 25*, 2867.
33. Suh, J. Y., Jang, B. C., Zhu, X., Ong, J. L., & Kim, K. (2003). *Biomaterials, 24*, 347.
34. Son, W. W., Zhu, X., Shin, H. I., Ong, J. L., & Kim, K. H. (2003). *Journal of Biomedical Materials Research Part B: Applied Biomaterials, 66B*, 520.
35. Fini, M., Cigada, A., Rondelli, G., Chiesa, R., Giardino, R., Giavaresi, G., et al. (1999). *Biomaterials, 20*, 1587.
36. Baun, W. L. (1980). *Surface Technology, 11*, 421.
37. Zwilling, V., Darque-Ceretti, E., Boutry-Forveille, A., David, D., Perrin, M. Y., & Aucouturier, M. (1999). *Surface and Interface Analysis, 27*, 629.
38. Kurze, P., Krysmann, W., & Schneider, H. G. (1986). *Crystal Research and Technology, 21*, 1603.
39. Ishizawa, H., & Ogino, M. (1995). *Journal of Biomedical Materials Research, 29*, 1071.
40. Oh, S.-H., Finõnes, R. R., Daraio, C., Chen, L.-H., & Jin, S. (2005). *Biomaterials, 26*, 4938.
41. Delplancke, J. L., & Winand, R. (1973). *Electrochimica Acta, 33*, 1539.
42. Schreckenback, J. P., Marx, G., Schlottig, F., Textor, M., & Spencer, N. D. (1999). Journal of Surface Science. *Materials in Medicine, 10*, 453.
43. Ishizawa, H., & Ogino, M. (1995). *Journal of Biomedical Materials Research, 29*, 65.
44. Lu, Y. P., Zhu, R. F., Li, S. T., Song, Y. J., Li, M. S., & Lei, T. Q. (2003). *Materials Science and Technology, 19*, 260.
45. Yang, Y., & Ong, J. L. (2003). *Journal of Biomedical Materials Research Part A, 64*, 509.
46. Yang, Y. C., Chang, E., & Lee, S. Y. (2003). *Journal of Biomedical Materials Research Part A, 67*, 886.
47. Rodriguez, R., Kim, K., & Ong, J. L. (2003). *Journal of Biomedical Materials Research Part A, 65*, 352.
48. Anselme, K. (2000). *Biomaterials, 21*, 667.
49. Hayman, E. G., Pierschbacher, M. D., Suzuki, S., & Ruoslahti, E. (1985). *Experimental Cell Research, 160*, 245.
50. Thomas, C. H., McFarland, C. D., Jenkins, M. L., Rezania, A., Steel, J. C., & Healy, K. E. (1997). *Journal of Biomedical Materials Research, 37*, 81.
51. Henry, P., Tan, A. E., & Allan, B. P. (2000). *Applied Osseointegration Research, 1*, 15.
52. Sul, Y. T., Johansson, C. B., Jeong, Y., Wennerberg, A., & Albrektsson, T. (2002). *Clinical Oral Implants Research, 13*, 252.
53. Sul, Y. T., Johansson, C. B., Roser, K., & Albrektsson, T. (2002). *Biomaterials, 23*, 1809.
54. Ishizawa, H., Fugino, M., & Ogino, M. (1995). *Journal of Biomedical Materials Research, 29*, 1459.
55. Giavaresi, G., Fini, M., & Cigada, A. (2003). *Biomaterials, 24*, 1583.
56. Giavaresi, G., Fini, M., Cigada, A., Chiesa, R., Rondelli, G., Rimondini, L., et al. (2003). *Journal of Biomedical Materials Research Part A, 67*, 112.
57. Son, W. W., Zhu, X., Shin, H. I., Ong, J. L., & Kim, K. H. (2003). *Journal of Biomedical Materials Research. Part B, Applied Biomaterials, 66B*, 520.
58. Ishizawa, H., Fujino, M., & Ogino, M. (1997). *Journal of Biomedical Materials Research, 35*, 199.
59. Sul, Y. T. (2003). *Biomaterials, 24*, 3893.
60. Feng, B., Wang, J., Yang, B. C., Qu, S. X., & Zhang, X. D. (2003). *Biomaterials, 24*, 4664.
61. Boyan, B. D., Batzer, R., Kiesewetter, K., Lie, Y., Cochran, D. L., Szmuckler-Moncler, S., et al. (1998). *Journal of Biomedical Materials Research, 39*, 77.
62. Karlsson, M., Palsgard, E., Wilshaw, P. R., & Silvio, L. D. (2003). *Biomaterials, 24*, 3039.
63. Webster, T. J., Ergun, C., Doremus, R. H., Siegel, R. W., & Bizios, R. (2001). *Biomaterials, 22*, 1327.

64. Dunn, D. S., Raghaven, S., & Volz, R. G. (1994). *Journal of Applied Biomaterials, 5*, 325.
65. Varkey, M., Gittens, S. A., & Uludag, H. (2004). *Expert Opinion on Drug Delivery, 1*, 19.
66. Huang, H.-H., Pan, S.-J., Lai, Y.-L., Lee, T.-H., Chen, C.-C., & Lu, F.-H. (2004). *Scripta Materialia, 51*, 1017.

Chapter 3
Titanium Dioxide Coatings for Medical Devices

F. Placido, A. McLean, A.A. Ogwu and W. Ademosu

Abstract Titanium dioxide (TiO_2, titania) is a widely abundant and inexpensive material. In bulk form, it is produced as a white powder and it is the most widely used white pigment because of its brightness and very high refractive index ($n = 2.4$). Applications include filler pigment in paints, cosmetics, pharmaceuticals, food products (such as E171, e.g. white lettering on M&Ms) and toothpaste. When deposited as a thin film, its refractive index and colour make it an excellent reflective optical coating for dielectric mirrors. It is also widely used in sun block creams due to its photostability, high refractive index and UV absorption properties. This chapter focuses on describing the type of coatings that are used for medical devices and advances made in this important field of medical research.

3.1 Titanium Dioxide Coatings

TiO_2 is chemically and photochemically stable, non-toxic and insoluble under normal pH conditions. The corrosion resistance of titanium metal is due to the formation of a native oxide passivation layer. TiO_2 occurs in three crystalline forms; brookite, anatase and rutile, the latter two being the more common. Rutile is the thermodynamically stable form. In the crystal lattice of TiO_2, each Ti atom is bonded to six O atoms and each O atom is bonded to three Ti atoms to form a tetragonal crystal lattice. Anatase differs from rutile by the number of common edges of the TiO_6 octahedra i.e. four for anatase and two for rutile. TiO_2 is effectively an insulator at normal temperatures, however, the band gap (3.0 eV for rutile and 3.2 eV for anatase) is such that it will absorb ultra violet light at wavelengths just under 400 nm and it is referred to as a wide-bandgap semiconductor.

TiO_2 powder is prepared on an industrial scale either by the sulphate process or by the vapour phase oxidation of titanium tetrachloride ($TiCl_4$). In the sulphate

F. Placido (✉) · A. McLean · A.A. Ogwu · W. Ademosu
University of Paisley, Scotland, UK
e-mail: frank.placido@uws.ac.uk

W. Ahmed and M.J. Jackson (eds.), *Surgical Tools and Medical Devices*,
DOI 10.1007/978-3-319-33489-9_3

process, the ilmenite ore ($FeTiO_2$) is dissolved in sulphuric acid, iron is removed and the solution is hydrolysed. The hydrated TiO_2 is calcined to remove water. Anatase is the main crystal form produced from this process because sulphate ions, inherently present in the product, stabilise this phase. In vapour phase oxidation (also know as flame hydrolysis) titanium tetrachloride is sprayed into a high temperature flame to produce nanometer-sized particles. The main contaminant is chloride and the phase purity is not good. Powder preparations can be used to make coatings by methods including plasma spray, dip coating and electrophoretic coating. This chapter reports on advances made in this important field of medical research [1–25].

Other methods may be used to produce coatings by the formation of TiO_2 from precursors directly on a substrate surface. If the substrate is Ti metal or alloy, the simplest method of producing a thin film of TiO_2 is to oxidise the surface. This may be achieved by simply leaving the titanium sample in the open atmosphere, where a natural oxide layer will form with time. Alternatively, one may increase the rate of oxidation and control the oxide film thickness by simple thermal treatment in an oxygen atmosphere, exposure to an oxidising solution or atmosphere, or by electrochemical oxidation (anodisation). Methods of producing thin films of TiO_2 on other supporting substrates have been developed including physical, chemical and physicochemical routes. These methods may also be used to coat Ti metal and its alloys.

The main physical route to TiO_2 films is sputter deposition. This involves the formation of a plasma, e.g. argon in a vacuum system. A high electric field is produced between the TiO_2 target and the substrate to be coated. The plasma contains positively charged argon ions, which are accelerated towards the TiO_2. The argon ions impact with a billiard ball effect, dislodging titanium and oxygen atoms, or clusters of TiO_x, with high kinetic energy. These species move out into the plasma and upon collision with the substrate adhere to the surface and form a film of TiO_2. Under optimal conditions, one can achieve a uniform coating of TiO_2 with the desired crystal structure and film thickness. The sputter deposition route lends itself to the coating of a wide range of substrate materials, including polymers, and to different substrate conformations. A disadvantage is the requirement for a vacuum plasma system that can be expensive.

An alternative wet chemical route to TiO_2 thin films is sol gel processing, which has been used in the production of ceramic and glass coatings for many years. For TiO_2 sol gels, the most common precursors are alkoxides, e.g. titanium (IV) propoxide and titanium (IV) butoxide, although inorganic compounds may also be used. Alkoxides are metal organic compounds where the metal is bonded to a hydrocarbon via a bridging oxygen, i.e. the titanium atom replaces the proton in the alcohol. The metal alkoxides are liquid at room temperature and can be produced with high purity. Alkoxides are very reactive with water and the controlled hydrolysis of the alkoxide is followed by a condensation and polymerisation step whereby the titanium hydroxide sol gives up water to form a polymeric TiO_x gel. The sol gel can be coated onto a wide range of substrates using techniques such as dip coating, spin coating, roll coating, etc. In the case of TiO_2 sol gel processing, a

high temperature thermal treatment stage is normally required to yield a crystalline film. High temperature treatment is obviously not applicable for thermolabile materials such as polymers. However, other methods such as hydrothermal annealing have been used to produce crystalline films at much lower temperatures (100–150 °C).

Another commonly employed route to TiO_2 films is chemical vapour deposition (CVD). In this technique, the substrate to be coated is heated and exposed to a volatile metal organic precursor in a carrier gas. Upon contact with the surface, the reactive precursor decomposes to yield an oxide film. Other physicochemical approaches may involve a mixture of techniques, e.g. reactive sputter deposition or plasma enhanced CVD.

Titanium metal and its alloys are important as biomedical and dental implant materials because of their relatively high corrosion resistance and good biocompatibility. The passivating oxide layer is responsible for these properties. However, despite widely reported low rates of corrosion for titanium in vitro, there is evidence to suggest that corrosion rates may be enhanced in vivo, leading to the release of titanium and accumulation in adjacent tissues or transport to other areas of the body [22]. Indeed, the biological environment may be aggressive towards titanium or the native oxide film. Furthermore, oxide film growth and ion incorporation into the film have been noted following implant into humans. Different methods of surface modification have been attempted in order to improve the corrosion resistance and biocompatibility of titanium, titanium alloys and stainless steel. It was reported [23] on the corrosion resistance for biomaterial applications of TiO_2 films deposited on titanium and stainless steel by ion-beam-assisted sputter deposition (IBASD). In that approach, a pure titanium target is sputtered by an argon ion beam, and the sputtered atoms are deposited onto the substrate while a flow of neutral oxygen gas is introduced on the substrate (normal reactive sputter deposition). An additional oxygen ion beam is used as the assisting beam. They reported a two-layer model of the oxide film deposited using this method and that the IBASD films exhibited improved corrosion resistance as compared to a native oxide layer on titanium or stainless steel.

Hemocompatibility is an important parameter for implant materials that come into contact with blood. Almost any medical device introduced into the human body will initially come into contact with blood. Furthermore, thrombogenicity of artificial implant devices such as artificial heart valves is a serious problem as the implant induces blood clotting and patients with such implant devices must be given anticoagulant drugs as ongoing therapy. Surface modification of implant devices is therefore an important approach to improving hemocompatibility. Different materials have been investigated for coating implant devices, e.g. diamond-like carbon, silicon carbide, titanium nitride and aluminium oxide and low temperature isotropic pyrolytic carbon (LTIC). LTIC is widely regarded as the best hemocompatible coating. It has been reported that albumin can passivate a surface, that complement activation can result in the neutrophil recruitment to surfaces, and that fibrinogen initiates the acute inflammatory response. Platelets and inflammatory cells are likely to respond to the layer of adsorbed proteins, not to the material

surface itself. However, the composition of the layer of adsorbed proteins is dependent on the properties of the material. Therefore, the initial reactions that take place on the material surface upon exposure to blood will determine the conditions for subsequent reactions. Nygrean et al. [20] investigated the initial reactions that take place on exposure of TiO_2 surfaces to blood. They compared Ti metal that was passivated in nitric acid to Ti metal which had been passivated by annealing in air at 700 °C. In order to study the initial interactions, they used capillary blood from human donors (without addition of anticoagulants), which was exposed to the surface for only 5 s. Fluorescent immunoassay was used to determine the presence of platelet cells, fibrinogen, $C1_q$ and prothrombin/thrombin. They reported that the serine proteases of the coagulation and complement systems were initiated within 5 s of the blood exposure to the TiO_2 surface. They also found that platelets were adhered to the surface in the initial 5 s' exposure. Both plasma proteins and cells were found at the blood-surface interface after only 5 s and this implied that a complex "biofilm" was formed within a very short contact time. The interaction of plasma proteins will differ for hydrophilic and hydrophobic surfaces. Both annealed and acid-treated samples were macroscopically hydrophilic and there was no significant difference in contact angle, however, there was a significant difference between the levels of prothrombin/thrombin and platelets adhered to the different surfaces. The authors suggest that this may be due to different levels of carbon impurity in the two films. Platelet adhesion to a surface, although probably a prerequisite to activation, does not in itself mean activation.

Huang et al. [13] reported on the hemocompatibility of titanium oxide and tantalum-doped titanium oxide films prepared by plasma immersion ion implantation and deposition (PIIID) and sputtering. The first event to occur following implant's surface contact with blood is the adsorption of a protein layer. If the surface characteristics of the material result in a change in the configuration of the adsorbed protein, e.g. fibrinogen or globulin, it may enhance coagulation and/or platelet activation. Alternatively, adsorption of albumin on the surface with maintenance of the native configuration discourages coagulation. Therefore, a reduction in protein adsorption and denaturation is a key strategy to enhancing anticoagulation properties of surfaces. The anticoagulation nature of a surface depends on multiple characteristics of the material including surface energy, surface charge and surface topography and on the surface effects imposed at different stages of the blood-surface interaction process. Huang et al. [13] reported that their TiO_2 films exhibited lower interface energy compared to LTIC , leading to less fibrinogen adsorption on the TiO_2. Furthermore, changing the structure of the TiO_2 film from amorphous to crystalline, and doping of the films with tantalum also can affect the anticoagulation properties. They postulated that the semiconducting nature of the TiO_2 films is an important contributing factor where *n*-type semiconductor properties helps to prevent protein denaturation on the surface by inhibiting charge transfer from the protein into the TiO_2. Indeed, they found improved behaviour of platelet adhesion on crystalline rutile as compared to amorphous TiO_2 films.

The surfaces of implants used for dental and orthopaedic applications also become coated with a proteinaceous film. The nature of this protein layer depends

on the surface of the implant and may affect the biological response to the implant, including cell attachment. Fibronectin is one of the first extracellular matrix proteins produced by odontoblast and osteoblasts, and therefore, is a useful model to investigate protein surface interactions in vitro. Fibronection is composed of two similar polypeptide chains whose subunits are linked by disulphide bonds and this protein is reported to play a major role in interaction of the implant material and the body. Yang et al. [25] investigated fibronectin adsorption on titanium surfaces and its effect on osteoblast precursor cell attachment. They used Ti metal that was pretreated by wet grinding followed by passivation in 40 % v/v nitric acid (HNO_3) for 30 min. Each sample was sterilised by UV irradiation for at least 24 h, a step that may have had other consequences. X-ray photoelectron spectroscopy analysis confirmed an amorphous oxide layer on the surface of the Ti following the treatment stages. The researchers observed a significant difference in the fibronectin adsorbed after 15 and 180 min exposure to protein containing solution. The amphoteric characteristics of TiO_2 mean that the surface charge changes with pH. The isoelectric point of TiO_2 has been reported to be between pH 4.0 and 6.2, and therefore, at a pH 7.4, the oxide will be mainly anionic (net -ve charge) in character and will electrostatically bind proteins that are cationic (net +ve charge) at pH 7.4. Binding of proteins to surfaces may also involve hydrophobic bonding, the extent of which will be affected by the wettability of the implant surface. TiO_2 surfaces have been reported to have both hydrophilic and hydrophobic components. Therefore, the extent of specific protein attachment to TiO_2 surfaces will be dependent on a complex interplay between hydrophobicity/hydrophilicity and electrostatic interaction. Yang et al. [25] also reported that the pre-adsorption of fibronectin to the TiO_2 surface enhanced the attachment of osteoblast cells as compared to control Ti samples without pre-adsorption of fibronectin. It has been suggested that the presence of fibronectin promotes cell attachment by binding through cell surface receptors and mediating adhesive interactions. Furthermore, adsorption of low concentrations of fibronectin on surfaces causes unfolding of the protein into an inactive conformation, but a high adsorption concentrations unfolding is prevented by steric hindrance due to molecule packing.

More recently, it has been reported that nanostructure control of TiO_2 films can not only improve biocompatibility, but can also improve the bioactivity of the surfaces for bone adhesion. It is hypothesised that tissue–biomaterial interactions occur within 1 nm of the material surface, and therefore the ability to engineer surfaces on the nanometre scale will have major impact on the production of materials with improved biocompatibility and bioactivity.

Due to the increased life expectancy of the population, there has been an enormous increase in the incidence of bone fracture and the need for bone implant surgery. The improvement of implant–bone interface is a real problem. Titanium and its alloys are the most commonly employed metals used in the manufacture of orthopaedic prostheses on account of their excellent mechanical properties, corrosion resistance and biocompatibility. Even so, osseointegration results have not always been satisfactory under altered metabolic bone conditions. Research and development into improvements in osseointegration have focussed on implant

surface properties such as morphology, roughness and chemical composition. All of these factors may affect cell and biochemical responses of host bone and the ability to control these may allow one to promote bone apposition through the acceleration of the chemical bonding between the new bone and the implant surface. For titanium implants, the oxide layer grows slowly on the surface following implant and contributes to the formation of apatite and bone-like tissue. Current passivation methods used in the pre-treatment of titanium prosthesis (machining, ultrasonic cleaning, sterilisation and anodisation) still present limits. For example, low-level contamination with impurities may have a deleterious effect on the osseointegration process, the TiO_2 film thickness is linearly dependent on the anodic potential employed in electrochemical oxidation and the anodically grown oxide may present significant porosity. Giavaresi et al. [10] reported on the osseointegration of a nanostructured titanium oxide coating produced by CVD. The aim of the study was to compare the in vivo (implanted in rabbits) osseointegration of Ti implants coated with TiO_2 CVD thin films with that of Ti-machined implants. They reported that the affinity index (AI: the interface contact between bone and implant as calculated as the length of the bone profile directly opposed to the implant divided by the total length of the bone–implant interface) of the Ti/CVD implants were significantly higher than that of the machined implants. SEM analysis confirmed a high level of osseointegration for the Ti/CVD implants in cortical bone and enhanced osseointegration in cancellous bone, as compared to that observed for the machined implants. They concluded that their histomorphometric, ultra-structural and microhardness findings demonstrated that the nanostructured TiO_2 coating positively affected the osseointegration rate of commercially pure Ti implants in terms of bone mineralization in both cortical and cancellous bone. Further studies were planned on mechanical bonding with bone and bone remodelling around implants.

In 2001 Ramires et al. [23] reported on the influence of titania-hydroxyapatite (TiO_2–HA) composite coatings, obtained via a sol gel route, on in vitro osteoblast behaviour. They found that these materials have no toxic effects (at least in vitro). Cell growth and morphology were similar on TiO_2–HA coatings and TiO_2 coatings. However, alkaline-phosphatase-specific activity and collagen production of osteoblasts cultured on TiO_2–HA coatings were significantly higher than uncoated titanium or polystyrene culture plates. They concluded that the TiO_2–HA coatings were bioactive owing to the presence of hydroxyl groups on the surface that promote calcium and phosphate precipitation and improve interactions with osteoblastic cells.

Other workers have also investigated bone cell proliferation on hybrid TiO_2–HA coatings on Ti implants. For example, Lee et al. [15] produced TiO_2 films by a method known as micro-arc oxidation (MAO) in which a DC pulsed potential is applied to the Ti substrate in an electrochemical cell. In this case, the Ti metal was pre-coated with HA (using e-beam evaporation). The logic behind this approach was to introduce Ca and P into the TiO_2 films to improve osseointegration and cellular activity. The rough, porous TiO_2 films produced by MAO should enhance mechanical interlocking of tissue and implant. A CaP layer is thought to enhance the initial cellular response, due to high osteoconductivity and bioactivity. When

the MAO treatment was carried out at 230 V, the coating surface was observed by SEM to become rough and porous (only isolated areas were affected at lower potentials) and caused the dissolution of the HA layer, however, a large amount of Ca and P were incorporated into the TiO_2 layer and some of the CaP layer remained after MAO treatment. The proliferation of the human osteosarcoma cells was decreased only slightly on the HA surface treated by MAO, similar to Ti surface treated by MAO, and was attributed to the increase in surface roughness. However, there was a marked increase in the alkaline phosphatase activity of the cells on the MAO-treated TiO_2–HA compared to the MAO-treated Ti. They concluded that the use of hybrid coatings obtained by pre-coating of HA on Ti followed by MAO treatment is a possible route to enhanced cell responses for bone implant materials.

Secondary infections are a cause of implant failure, particularly with percutaneous (skin penetrating) implants. However, infections at skin-penetrating titanium implants anchored in the temporal bone can often be cured by local treatment. As mentioned previously, host protein adsorption to the implant material occurs within seconds of implant. Protein adsorption to the surface depends on a number of parameters. Furthermore, microbial adhesion will depend on the nature of the surface and indeed on the nature of the surface-bound proteins. Fibronectin has been proposed to mediate adhesion of staphylococci to implant materials in blood. Staphylococcus epidermidis is a common etiological agent with infections involving polymeric implants, whereas Staphylococcus aureus is the most common etiological agent with infections involving metal implants. Understanding the mechanism of bacterial attachment to surfaces is crucial for enabling the engineering of surfaces for reduced biofilm recruitment and implant failure due to secondary infection. Holgers and Ljungh [12] reported a study into the cell surface characteristics of microbial isolates from human percutaneous titanium implants. They found that no isolates expressed a hydrophobic cell surface, however, isolates from infected implants were less hydrophilic than those from non-inflamed tissue. The degree of hydrophilicity of an implant surface will influence the recruitment of biofilm. This leads to the possible exploitation of other, perhaps more exciting, properties of TiO_2.

The important biocompatible and bioactive properties of TiO_2 have been addressed above. TiO_2 has additional properties which bring added value as a material for use in biomedical applications. In 1972 Japanese researchers, Honda and Fujishima [8], published a paper in Nature reporting the photo-splitting of water using a single crystal of rutile TiO_2 under ultra violet irradiation (Honda and Fujishima [8]). If one could achieve efficient water splitting into hydrogen and oxygen with solar energy, then the world's energy problems might be solved.

Since then, the ability of TiO_2 to absorb UV electromagnetic irradiation and use that energy to drive electrochemical reactions on its surface has been investigated for a wide variety of applications, including water and air treatment and purification [1, 2, 5, 11, 17–19, 24] and "self-cleaning" surfaces [9]. Indeed, Pilkington's are now selling "self cleaning" glass called *Activ*, with a 15-nm layer of TiO_2 on the surface which, under the action of solar UV, can destroy and remove organic contamination. The process has been aptly named photocatalysis, meaning the use

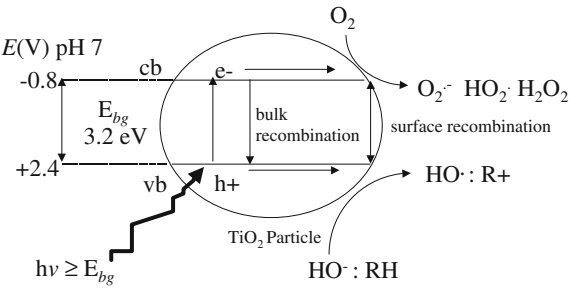

Fig. 3.1 Mechanism of TiO_2 photocatalysis (potentials vs SCE)

of a catalyst to speed up a photochemical reaction. The mechanism of photocatalysis is shown in Fig. 3.1.

TiO_2 is a wide-bandgap semiconductor material. The valence band is filled with electrons and is separated from an empty conduction band by band gap energy (E_{bg}). If illuminated with UV light ($E = h\nu$ where E_{bg} of 3.2 eV is equivalent to 387 nm), a photon is absorbed and an electron is promoted from the valence band to the conduction band leaving a hole in the valence band. These charge carriers can recombine in the bulk, or they can move to the surface of the particle. An electron in the conduction band has a negative electrochemical reduction potential and can reduce an electron acceptor species at the interface, e.g. molecular oxygen producing superoxide radical anion, perhydroxyl radical and hydrogen peroxide. The hole has a very positive electrochemical reduction potential, positive enough to oxidise water or hydroxyl ions to yield hydroxyl radicals. Hydroxyl radicals are powerful and indiscriminate oxidising species. The redox reactions at the surface of the particle lead to the generation of active oxygen species which can attack organic and inorganic species at or near the surface. There are literally thousands of papers in the literature reporting photocatalysis for the destruction of a wide range of organic pollutants, including microorganisms such as viruses, bacteria and fungi, and even tumour cells [1, 7, 9, 14].

The potential for this "self sterilising" property has been identified for use in medical devices. Ohko et al. [21] reported on self-sterilising and self-cleaning of silicone catheters coated with TiO_2 photocatalyst thin films. They described a sol gel method for coating silicone catheters with TiO_2 to produce a photoactive film. The self-cleaning effect was demonstrated using the bleaching of methylene blue dye and the self-sterilising effect was demonstrated by the killing of *Escherichia coli*. The application proposed was that the catheter could be irradiated prior to insertion, thus helping to prevent catheter-related bacterial infection. The authors suggested practical use as an intermittent self-sterilising catheter for neurogenic bladder patients and or for self-sterilising suction tubes for frequent draining of sputa and oral fluid. They also suggested that a dark bactericidal action could be incorporated by surface doping of the TiO_2 with silver.

Another property of TiO_2 that has created a great deal of excitement is the phenomenon of photo-induced superhydrophilicity. UV excitation of the TiO_2 generates electrons and holes. The electrons tend to reduce the Ti(IV) cations to the

Ti(III) state, and the holes oxidise the O_2^- anions. This results in the ejection of oxygen atoms creating oxygen vacancies. Water molecules can then occupy these oxygen vacancies, producing adsorbed OH groups, which tend to make the surface more polar or hydrophilic. After about 30 min or so under a moderate intensity UV source, the contact angle for water approaches zero. It is a combination of this superhydrophilic effect and the photocatalytic effect that is responsible for the 'self-cleaning' nature of these coatings. Even more interesting is that TiO_2 surfaces have been reported to be amphiphilic in nature, i.e. displays both hydrophilic and hydrophobic properties. Fujishima et al. [9] reported light-induced reduction in contact angle for water approaching zero and light-induced reduction in contact angle for glycerol trioleate (a component of vegetable oils) approaching zero.

The wettability of a surface will have an effect on the interactions of the surface with proteins. Therefore, the ability to induce changes in contact angle of the surface would have important implications for implant materials. Liu et al. [16] reported that UV irradiation of TiO_2 coatings prior to immersion in simulated body fluid enhanced the formation of bonelike apatite. They used plasma sprayed nanoparticle TiO_2 to form coatings on the surface of Ti metal. Following coating, one set of samples was irradiated for 24 h using a 125 W medium pressure Hg lamp (main output 365 nm) and a non-irradiated sample set was used as the control. Following four weeks immersion in simulated body fluid, they used energy dispersive x-ray spectroscopy, XRD and FTIR to analyse the surfaces. They found that the samples that had been irradiated with UV prior to immersion had a newly formed layer on the surface that was carbonate-containing hydroxyapatite (bonelike apatite). Without UV irradiation prior to immersion, no new surface precipitates were detected. They reasoned that oxygen vacancies were created and that Ti^{3+} sites were more favourable for the dissociation of water to form an abundance of surface Ti-OH groups. OH groups on ceramic surfaces are suggested to be effective for inducing the formation of an apatite layer. The mechanism is thought to involve the Ti-OH surface groups reacting with hydroxyl ion in the simulated body fluid to produce negatively charged Ti-O^-.

$$\mathrm{Ti-OH + OH^- \rightarrow Ti-O^- + H_2O} \tag{3.1}$$

The Ca^{2+} ions in the solution are electrostatically attracted to the negatively charged surface, followed by reaction with HPO_4^{2-} to form calcium hydrogen phosphate. The CaP continues to grow, also incorporating carbonate anions from solution, and crystallises to form carbonate-containing hydroxyapatite (bonelike apatite). Liu et al. [16] reported that the photo-induced bioactive surface remained for at least one week following UV irradiation.

Cosnier et al. [6] reported the use of nanocrystalline TiO_2 films for use in biomedical sensor applications, i.e. an electrochemical transducer material for the detection of hydrogen peroxide in the presence of oxygen. There is a wide range of oxidase enzymes which play different roles in the body. The best known is glucose oxidase (GOD), which acts to oxidise glucose to gluconic acid and in the process, reduces molecular oxygen to hydrogen peroxide. GOD is commonly employed in

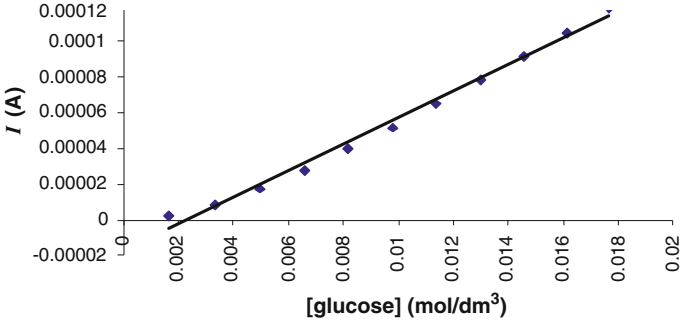

Fig. 3.2 Nanocrystalline TiO_2 electrode's amperometric response to standard additions of glucose. 10 mg GOD was present as free enzyme in 30 cm^3 pH 6 phosphate buffer. The TiO_2 electrode was held at a fixed potential of −0.4 V (SCE) [4]

commercial glucose biosensors in which the electron transfer to the electrode is mediated by a free redox couple. However, the Holy Grail of glucose sensing is to develop an implantable sensor for feedback control of an insulin delivery system (artificial pancreas) and remove the need for routine blood sampling.

Mediated biosensors are not suitable for implant as free mediators will simply diffuse away into the blood stream and immobilised mediators are not as efficient or the mediator may be toxic. An alternative is to use non-mediated electrochemical sensing. TiO_2 has a lower overpotential for the electrochemical reduction of hydrogen peroxide than for the reduction of dissolved oxygen. Therefore, as hydrogen peroxide is a by-product of the action of GOD, a TiO_2 sensor incorporating GOD could be used to detect glucose by the electrochemical reduction of hydrogen peroxide without interference from oxygen reduction. Therefore, there is no requirement for a mediator and TiO_2 is biocompatible. Figure 3.2 shows electrochemical reduction current measured for nanocrystalline TiO_2 electrode as a function of glucose concentration in a solution containing free GOD. The response is linear in the concentration range for glucose found in physiological blood.

3.2 Conclusions

In conclusion, TiO_2 coatings are important for improving the biocompatibility and bioactivity of implant materials. The additional properties of photocatalytic sterilisation and photo-induced superhydrophilicity may bring added value. This remains a vibrant field of research.

References

1. Blake, D. M., & Maness, P. C. (1999). *Separation and Purification Methods, 28*(1), 1–50.
2. Byrne, J. A., Eggins, B. R., Brown, N. M. D., McKinney, B., & Rouse, M. (1998). *Applied Catalysis, B: Environmental, 1998*(17), 25–36.
3. Byrne, J. A., Davidson, A., Dunlop, P. S. M., & Eggins, B. R. (2002). *Journal of Photochemistry and Photobiology A: Chemistry, 148*, 365–374.
4. Byrne, J. A., Hamilton, J. W. J., McMurray, T. A., Dunlop, P. S. M., Jackson, V., Donaldson, A., et al. (2006). *Abstracts of the NSTI Conference*, *Boston*.
5. Coleman, H. M., Routledge, E. J., Sumpter, J. P., Eggins, B. R., & Byrne, J. A. (2004). *Water Research, 38*, 3233–3240.
6. Cosnier, S., Gondran, C., Senillou, A., Gratzel, M., & Vlachopoulos, N. (1997). *Electroanalysis, 9*(18), 1387–1392.
7. Dunlop, P. S. M., Byrne, J. A., Manga, N., & Eggins, B. R. (2002). *Journal of Photochemistry and Photobiology A: Chemistry, 148*, 355–363.
8. Fujishima, A., & Honda, K. (1972). *Nature, 238*, 37–38.
9. Fujishima, A., Rao, T. N., & Tryk, D. A. (2000). *Journal of Photochemistry and Photobiology C: Photochemistry Reviews, 1*, 1–21.
10. Giavaresi, G., Ambrosio, L., Battiston, G. A., Casellato, U., Gerbasi, R., Finia, M., et al. (2004). *Biomaterials, 25*, 5583–5591.
11. Hoffman, M. R., Martin, S. T., Choi, W., & Bahnemann, D. W. (1995). *Chemical Reviews, 95*, 69–96.
12. Holgers, K. M., & Ljungh, A. (1999). *Biomaterials, 20*, 1319–1326.
13. Huang, N., Yang, P., Leng, Y. X., Chen, J. Y., Sun, H., Wang, J., et al. (2003). *Biomaterials, 24*, 2177–2187.
14. Kuhn, K. P., Chaberny, I. F., Massholder, K., Stickler, M., Benz, V. W., Sonntag, H.-G., et al. (2003). *Chemosphere, 53*, 71–77.
15. Lee, S.-H., Kim, H.-W., Lee, E.-J., Li, L.-H., & Kim, H.-E. (2006). *Journal of Biomaterials Applications, 20*, 195–208.
16. Liu, X., Zhao, X., Ding, C., & Chu, P. K. (2006). *Applied Physics Letters, 88*, 13905.
17. McMurray, T. A., Byrne, J. A., Dunlop, P. S. M., Winkelman, J. G. M., Eggins, B. R., & McAdams, E. T. (2004). *Applied Catalysis, A: General, 262*(1), 105–110.
18. McMurray, T. A., Byrne, J. A., Dunlop, P. S. M., & McAdams, E. T. (2005). *Journal of Applied Electrochemistry, 35*, 723–731.
19. Mills, A., & Le Hunte, S. (1997). *Journal of Photochemistry and Photobiology A: Chemistry, 108*, 1–35.
20. Nygren, H., Tengvall, P., & Lundstrom, I. (1997). *Journal of Biomedical Materials Research, 34*, 487–492.
21. Ohko, Y., Utsumi, Y., Niwa, C., Tatsuma, T., Kobayakawa, K., Satoh, Y., et al. (2001). *Journal of Biomedical Materials Research (Applied Biomaterials), 58*, 97–101.
22. Pan, J., Leygraf, C., Thierry, D., & Ektessabi, A. M. (1997). *Journal of Biomedical Materials Research, 35*, 309–318.
23. Ramires, P. A., Romito, A., Cosentino, F., & Milella, E. (2001). *Biomaterials, 22*, 1467–1474.
24. Shani Sekler, M., Levi, Y., Polyak, B., Dunlop, P. S. M., Byrne, J. A., & Marks, R. S., (2004). *Journal of Applied Toxicology, 24*, 395–400.
25. Yang, Y., Glover, R., & Ong, J. L. (2003). *Colloids and Surfaces B: Biointerfaces, 30*, 291–297.

Chapter 4
Effects of Shape and Surface Modification on the Corrosion of Nitinol Alloy Wires Exposed to Saline Solutions

F. Placido, A. McLean, A.A. Ogwu and W. Ademosu

Abstract The corrosion behaviour of Nitinol wire that was chemically etched and mechanically polished was studied in a corrosive 0.9 % saline solution. The electrochemical corrosion tests conducted on the as-received straight and curved wires of nitinol included open circuit potential (OCP) measurement, polarisation resistance and Tafel plots. The chemically etched looped wires exhibited the highest recorded corrosion potential, Ecorr and the lowest values of corrosion current, icorr. The results of the OCP measurements and polarisation resistance, combined with scanning electron microscopy (SEM) indicated the presence of a protective passive corrosion-resistant film on the chemically etched wires. The aim of the current investigation is to study the corrosion and pitting resistance behaviour of nitinol wire with different surface finishes.

4.1 Introduction

One of the most popular shape-memory and super-elastic alloys used for biomedical stents is called Nitinol. It exhibits a number of favourable material properties that makes it well-suited for use as a stent [1]. Its most important properties are the super elasticity and shape memory abilities. Nitinol's ability to be deformed by more than 10 % strain and elastically recover its original shape is described as super elasticity. The material is able to withstand a stress, which induces an elastic deformation, thus causing the material to undergo a phase transformation. Superelasticity results from a stress-induced transformation while shape memory results from a thermal phase transformation. Both of these properties are employed in Nitinol stents [2].

F. Placido · A. McLean · A.A. Ogwu (✉) · W. Ademosu
University of Paisley, Scotland, UK
e-mail: Abraham.ogwu@uws.ac.uk

W. Ahmed and M.J. Jackson (eds.), *Surgical Tools and Medical Devices*,
DOI 10.1007/978-3-319-33489-9_4

Biocompatibility is always an issue whenever implanting a foreign material into the human body [3]. Implanting metals brings its own set of problems, such as corrosion.

When a metal is introduced into the body, a wide variety of processes and interactions with the biological environment can take place. Such processes include metal ion release [4]; oxide formation, either as a passive oxide film [5] or as a particulate oxide; and corresponding reduction reactions that typically involve oxygen reduction but may also include biochemical species such as proteins [6]. These phenomena vary microscopically over the alloy surface and depend on the local environment, local alloy composition and structure as well as local mechanical factors [7].

The aim of the current investigation is to study the corrosion and pitting resistance behaviour of nitinol wire with different surface finishes, i.e. chemical etching and mechanical polishing. The corrosion test was conducted in 0.9 % saline solution at 37 °C by means of electrochemical measurements. OCP, pitting potentials, corrosion potentials and corrosion currents were analysed in each of the materials studied.

4.2 Experimental Methods

The materials under investigation were: Nitinol wire that had been mechanically polished with a diameter of 0.2 mm and nitinol wire that had been chemically etched with a diameter of 0.2 mm provided by Vascutek of Renfrewshire, Scotland, U.K. The material compositions are shown in Table 4.1, from EDX analysis.

The solution used was a commercial NaCl solution, from Parkfields Pharmaceutical limited which contains sodium chloride B.P. 0.9 % w/v in purified water B.P. The experimental arrangement used consists of the electrochemical unit including the VoltaLab 40 (PGZ301) potentiostat that is able to perform conventional electrochemical measurements dedicated to corrosion techniques. The overall system was controlled using a PC-compatible microcomputer with Voltamaster 4 electrochemical software and a basic corrosion cell whose body is made of Pyrex with a double jacketed device allowing thermostatic experiments to be performed (ISO 10993-15).

The experiments were carried out at ±37 °C by circulating the water through the double wall of the cell. The working electrode with a surface area of about 1 cm^2 was inserted into the cell through a rubber sealer. The apparatus and the

Table 4.1 Materials composition: (e) Elemental percentage, (a) Atomic weight percentage

Material	Ni(e)	Ti(e)	Total(e)	Ni(a)	Ti(a)	Total(a)
Mechanical polished	54.4	45.5	100.0	49.5	50.5	100.0
Chemical etched	53.8	46.2	100.0	48.8	51.2	100.0

electrochemical cell conformed to ATM G5-94. The potential of the working electrode was measured against the reference calomel electrode, which contained a porous pin liquid junction and a saturated KCl salt bridge solution from Radiometer analytical. A platinum wire metal electrode was used as the auxiliary counter electrode. The electrolyte was continuously purged with purified nitrogen gas to de-aerate the solution 1 h before OCP and polarisation experiments.

4.2.1 Electrochemical Testing Procedure

OCP and potentiodynamic anodic polarisation measurements were conducted according to ASTM G5 test generated using a potentiostat. The OCP was determined after 22 h for 0.9 % saline solution, the value obtained after stabilisation of the curve being called the rest potential. Potentiodynamic anodic polarisation test was scanned at −1000 to 2500 mV at a scan rate of 0.167 mV/s in order to determine corrosion and breakdown potentials. Current corrosion density (i_{corr}), corrosion potential (E_{corr}) and breakdown potential (E_{bp}) were obtained from polarisation curves using the Tafel slopes.

4.2.2 Experimental Results

Open Circuit Potential (OCP)

OCP is the thermodynamic measurement of how likely the surfaces are to corrode. The more positive an OCP the more stable is the oxide film on the surface and therefore the less reactive the surface. The OCP was measured to determine the stable corrosion potential (E_{corr}) of the nitinol alloy samples, i.e. the values obtained when the potential becomes constant (Fig. 4.1).

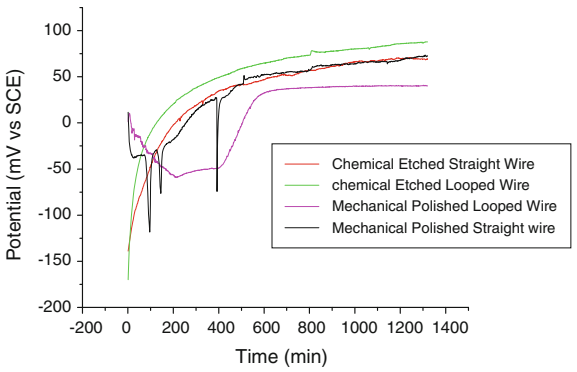

Fig. 4.1 OCP versus time curves for the stable potential determination of nitinol in 0.9 % saline solution

Table 4.2 OCP values after 22 h in 0.9 % saline

Sample	OCP (mV)
Chemical etched	67
Mechanical polished	32
Chemical etched looped	87
Mechanical polished looped	40

The OCP value for chemical etched wire in looped geometry proved to be the most positive value of OCP, the wire progressively becomes more anodic with time, the oxide layer film remains intact and the material stays stable in the passive state, and is therefore the least reactive surface in 0.9 % saline. The mechanically polished wire initially shifted towards more negative values before stabilising in more positive values after 22 h. Table 4.2 shows the OCP value table of the nitinol wires after 22 h.

Tafel Plot

Tafel plots of the different surface treatments, shown in Fig. 4.2, are used to measure the corrosion current i_{corr} which is then used to calculate the corrosion rate. The Tafel plot yields the Tafel constants β_A and β_C which is used with polarisation resistance (R_p) [8, 9] data to calculate corrosion rate as shown in Table 4.3. Results show chemical etched looped sample with the highest corrosion potential and the chemical etched straight wire with the lowest corrosion potential. The results indicate that the chemically etched looped wire is the most stable of the wires, with the highest corrosion potential, a low corrosion current and low corrosion rate as shown in Fig. 4.3.

Potentiodynamic Curves

The potentiodynamic curves are as shown in Fig. 4.4. The potentiodynamic curves indicate the passivation tendencies of the wires in the passive region. Results from

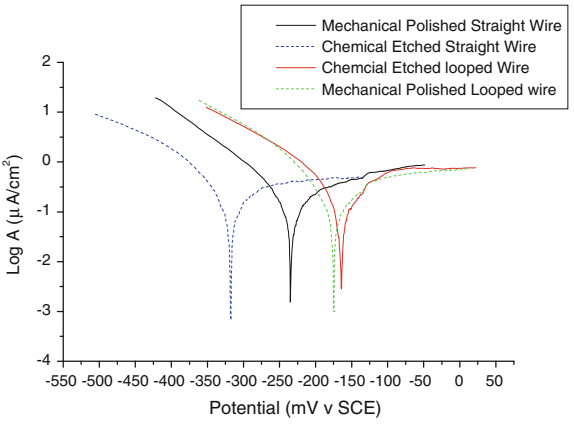

Fig. 4.2 Tafel plot of wires in 0.9 % saline solution

Table 4.3 Tafel parameters for NiTi wires in 0.9 % saline solution

Sample (mV)	E_{corr} (μA/cm^2)	i_{corr} (mV)	β_A (mV)	β_C (mV)	R_p(μm/year)	CR
Chemical etched	−317.8	0.14	68.8	−162.0	0.13	3.74
Mechanical polished	−235.6	0.13	116	−69.6	0.14	3.60
Chemical etched looped	−164	0.18	97.4	−75.5	0.10	4.89
Mechanical polished looped	−175	0.11	72.8	−56.9	0.12	3.07

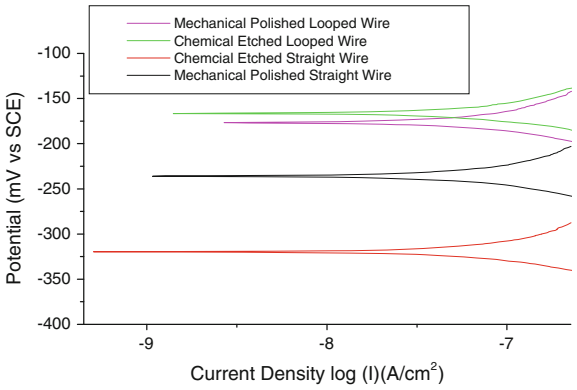

Fig. 4.3 Tafel curve looking at E_{corr} and i_{corr} saline solution

Fig. 4.4 show that the chemically etched looped wire has the largest passivation region, i.e. (−0.78 to +448 mV) [9].

The breakdown potentials (E_{bd}) correspond to the breakdown of the passive surface film, which is identified by the sudden increase in the current flowing in the solution, as shown in Table 4.4.

Figure 4.5 shows the corrosive region of the different wires from the potentiodynamic curve, where there is a sudden increase in the current.

Anodic Polarisation (Localised Pitting Test)

Anodic polarisation behaviour of passive metals examines pitting and crevice corrosion susceptibility. Pitting corrosion occurs when the oxide passive film layer breaks down locally. After local breakdown of the film, an anode forms where the film has broken down whilst the unbroken film acts as the cathode. This then accelerates localised attack and pits develop at the unbroken spots. The "pitting potential" corresponds to the potential at which the current starts to increase on the anodic scan. The "repassivation potential" corresponds to the potential at which the current becomes negligible on the reverse (cathodic) scan. A "repassivation potential" close to the "pitting potential" indicates that the sample is capable of re-protecting itself easily after pitting. Figures 4.6 and 4.7 are graphs of anodic

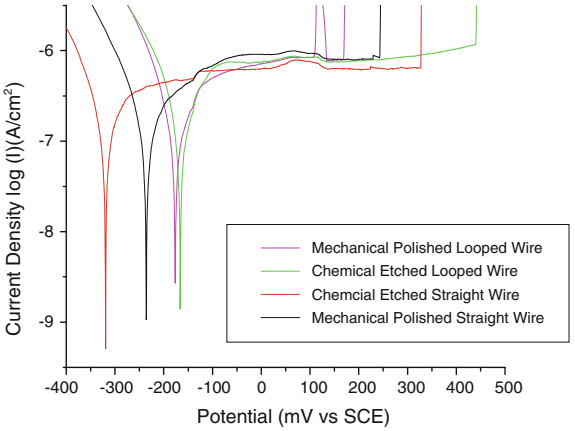

Fig. 4.4 Passivation region of potentiodynamic curve in 0.9 % saline

Table 4.4 Breakdown potential of the nitinol wires in 0.9 % saline

Sample (mV)	E_{corr} (mV)	E_{brk} ($\mu A/cm^2$)	i_{brk}
Chemical etched	−317.8	331	0.66
Mechanical polished	−235.6	248	0.8
Chemical etched looped	−164	445	1.2
Mechanical polished looped	−175	172	0.81

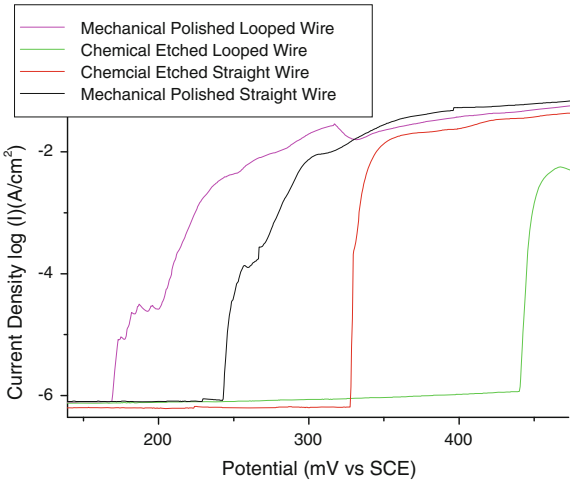

Fig. 4.5 Corrosive region (transpassive region) of the potentiodynamic curve in 0.9 % saline

polarisation. From these curves, it is possible to determine how prone to pitting a metal is in a particular environment.

Anodic polarisation curves reveal the pitting corrosion potential of the chemical etched straight wire at 1415 mV and the chemical etched looped wire at 1451 mV as

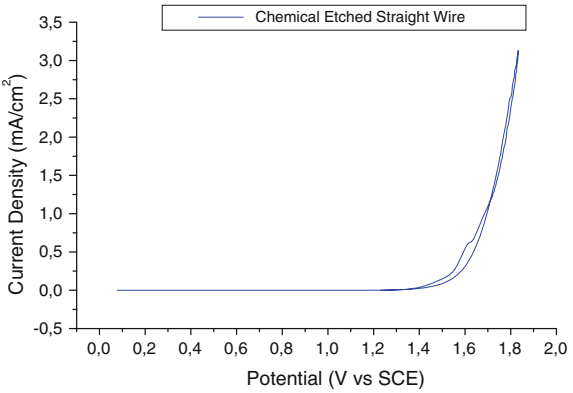

Fig. 4.6 Anodic polarisation of chemical etched straight wire in 0.9 % saline

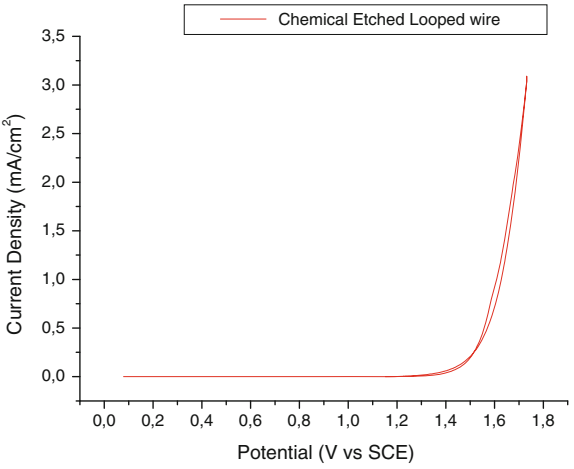

Fig. 4.7 Anodic polarisation of chemically etched looped wire in saline solution

shown in Figs. 4.6 and 4.7 whilst the pitting in the mechanically polished straight wire is at 289 mV and the mechanical polished looped wire is at 233 mV as shown in Figs. 4.8 and 4.9. The protection potential also known as the repassivation potential is the potential at which the current becomes negligible on the reverse scan. For the mechanical polished wire, the repassivation potential is observed at 13.3 mV, whilst the repassivation for the chemical etched wire is observed at 1382 mV. The mechanical polished surfaces undergo early pitting below 300 mV as shown in Figs. 4.8 and 4.9 whilst the chemical etched surfaces remain stable for a while before pitting takes place above 1400 mV as shown in Figs. 4.6 and 4.7. Results also show pitting potential (E_{pitt}) and repassivation potential (E_{rep}) are rather close for the chemically etched surface samples. For the mechanically polished surfaces, the E_{pitt} and E_{rep} potentials are very far apart. Pitting potential and protection potential calculated from the pitting corrosion curves are shown in Table 4.5.

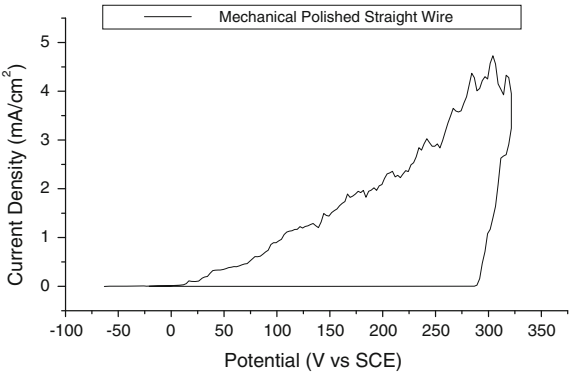

Fig. 4.8 Anodic polarisation of mechanically polished straight wire in 0.9 % saline

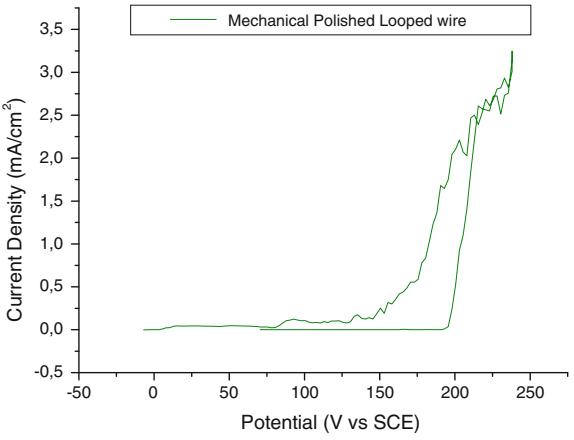

Fig. 4.9 Mechanically polished looped wire in Saline solution

Table 4.5 Pitting potential and repassivation potential of material in 0.9 % saline

Sample (mV)	E_{Pitt} (mV)	E_{rep} (mV)	$E_{Pitt} - E_{rep}$
Chemical etched	1415	1382	33
Mechanical polished	289	13.3	275
Chemical etched looped	1451	1451	42
Mechanical polished looped	233	200	33

A repassivation potential close to the pitting potential indicates that the sample is capable of re-protecting itself easily after pitting.

Surface Studies

SEM images of chemical etched and mechanical polished wires before and after corrosion in 0.9 % saline are as shown in Fig. 4.10a–f.

The SEM images in Fig. 4.10b, c show the chemical etched wire after the pitting test. It is evident that no pitting or corrosion took place. The surface of the wire is

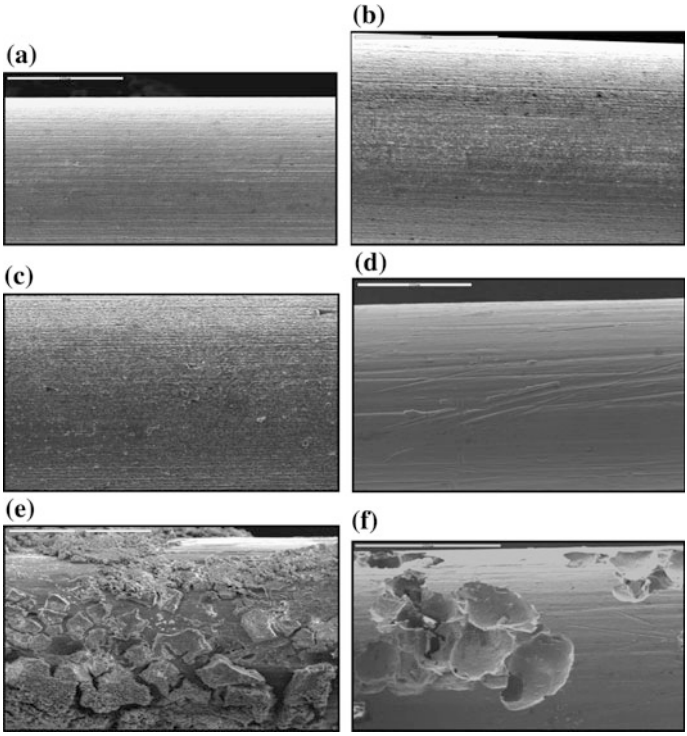

Fig. 4.10 **a** SEM image of chemical etched surface before corrosion (scale bar 100 μm). **b** SEM image of chemically etched straight surface after the potentiodynamic test (Magnification ×500). **c** SEM image of chemically etched looped surface after potentiodynamic test (Magnification ×500). **d** SEM image of mechanically polished wire before corrosion (scale bar 100 μm). **e** SEM image of mechanically polished straight wire after potentiodynamic test (+3500 mV) (scale bar magnification ×500). **f** SEM image of mechanically polished looped wire after potentiodynamic test (+3500 mV) (scale bar magnification ×500)

not as smooth as the as-received wire. There was no significant difference between the looped and the straight geometry. Both pitting and corrosion would seem to have taken place on the surface of the mechanically polished wires in Figs. 4.10e, f. The mechanically polished looped wire in Fig. 4.10f appears to have undergone excessive pitting. In certain areas on the surface, the pits have turned into cracks. Pitting is only observed on certain areas of the surface and other areas have been left untouched. The crumbling effect of the oxide layer on the mechanically polished straight wire can be observed in Fig. 4.10e. Also, it appears that the oxide layer has been broken into smaller parts so that another layer on the mechanical polished wire can be observed. EDX analysis of the chemical etched wire after potentiodynamic test of +3500 mV. Figure 4.11a showed reduced nickel content of less than 10cps on the surface; whilst nickel content of the mechanical polished wire had remained the same at around 70 cps as shown in Fig. 4.11b.

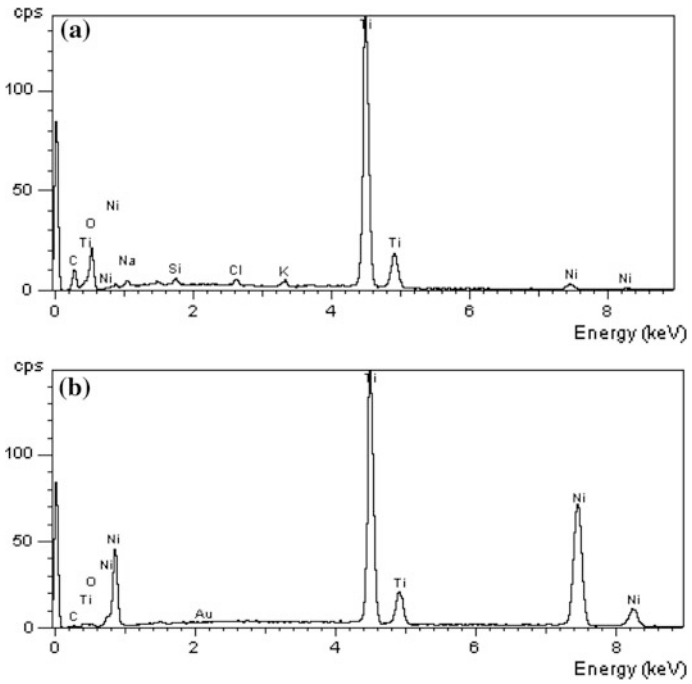

Fig. 4.11 **a** EDX analysis of chemically etched wire PD +3500 mV having very little nickel on its surface. **b** EDX analysis of mechanically polished wire PD +3500 mV

4.3 Summary

The effect of a saline corrosive environment on a typical composition of nitinol alloy used as an implant material in the human body has been investigated. The investigation considered the effect of two surface treatments, namely, mechanical polishing and chemical etching using a proprietary technique, on the resistance of nitinol wires to a corrosive saline environment. It is also considered that the effect of an imposed geometry may change the corrosion conditions, i.e. whether the wires are exposed to the saline solution as straight or looped wires on their resistance to corrosion in a saline environment. It is observed as the most positive open circuit potential (OCP) after 22 h on the chemically etched wire. Tafel plot results also indicated that the chemically etched looped wire had the largest passive region and the repassivation and pitting potentials were found to be quite close to each other for the chemically polished wire. There was a more substantial difference between the repassivation and the pitting potential of the mechanically polished nitinol wires, indicating a higher susceptibility to pitting corrosion. This was confirmed by scanning electron microscopy (SEM) that showed substantial pitting on the mechanically polished wire, whilst the chemically etched wire appears to be almost unaffected by the electrochemical test in saline solution. The proprietary

chemical treatment on the nitinol wire seems to be necessary for corrosion protection in applications where nitinol wire will be exposed to a corrosive saline environment.

Acknowledgments We would like to acknowledge support for this investigation by Mr. Tim Ashton, Vice-president of R&D at Vascutek (Terumo), Scotland.

References

1. Wu, S. K., & Lin, H. C. (2000). Recent development of TiNi-based shape memory alloys in Taiwan. *Materials Chemistry and Physics*, 81–92.
2. Stoeckel, D. P. A., & Duerig, T. (2004). Self-expanding nitinol stent: Material and design considerations. *European Radiology, 14*, 292–301.
3. Williams, D. F. (1981). *Fundamental aspects of biocompatibility*. Boca Raton, Florida: CRC Press.
4. Cisse, O., Savadogo, O., Wu, M., & Yahia, L. H. (2002). Effect of surface treatment of NiTi alloy on its corrosion behavior in Hanks' solution. *Journal of Biomedical Materials Research*, 339–345.
5. O'Brien, B., Carroll, W. M., Kelly, & M. J. (1748). Passivation of nitinol wire for vascular implants—A demonstration of the benefits. *Biomaterials*, 1739–1748.
6. Khan, M. A., Williams, R. L., & Williams, D. F. (1999). The corrosion behaviour of Ti-6Al-4V, Ti-6Al-7Nb and Ti-13Nb-13Zr in protein solution. *Biomaterials*, 631–637.
7. Shabalovskaya, S. A., Anderegg, J., Laab, F., Thiel, P. A., & Rondelli, G. (2003). Surface conditions of nitinol wires, tubing and as-cast alloys: The effect of chemical etching, aging in boiling water and heat treatment. *Journal of Biomedical Materials Research*, 339–345.
8. Ademosu, O., Ogwu, A. A., McLean, J., Corrigan, M., & Placido, F. (2005). Electrochemical corrosion of chemically etched and mechanically polished nitinol wires in Hanks' and saline solution. In *International Conference on Surfaces, Coatings and Nanostructured Materials, nanoSMat2005, Aveiro, Portugal*.
9. Ademosu, O., Ogwu, A. A., Placido, F., McLean, J., & Ashton, T. (2005). Surface characterisation of modified biocompatible nitinol alloy wires exposed to saline and Hanks' physiological solution. In *Institute of Physics (UK) Conference on Novel Applications of Surface Modification, Chester College, UK*.

Chapter 5
Cardiovascular Interventional and Implantable Devices

M. Whitt, P. Senarith, R. Handy and M.J. Jackson

Abstract Cardiovascular interventional and implantable devices must be safe and efficacious, as well as biocompatible. Surface treatment is of importance to the design and function of these devices. Lubricity, wear resistance, thrombogenicity, inflammation, and infections can all be affected significantly by surface treatments. The surfaces of cardiovascular interventional and implantable devices can either be modified with active or passive coating. Devices with active coating such as drug eluting stents (DES) deliver therapeutic agents that can enhance the mechanical function and modulate long-term vascular responses. In some implantable devices such as vascular grafts, endothelial cell growth is desirable. This is achievable with the addition of a coating or a modification to the surface properties of the device. This chapter reviews some of the most commonly used cardiovascular interventional and implantable devices with an overview of the role that surface treatments have in their functionality and safety.

5.1 Introduction

Cardiovascular interventional tools are used in the treatments of coronary arterial diseases, heart failure, and peripheral arterial diseases. These devices are not intended for long-term implantation. There are two main interventional procedures that are performed today: percutaneous transluminal coronary angioplasty (PTCA) and stenting. Both are performed via catheterizations.

M. Whitt
California State Polytechnic, San Luis-Obispo, CA, USA

P. Senarith
Medtronic Corporation, Minneapolis, MN, USA

R. Handy
School of Medicine, The University of Utah, Salt Lake City, Utah, USA

M.J. Jackson (✉)
Kansas State University, Salina, KS, USA
e-mail: jacksonmj04@yahoo.com

W. Ahmed and M.J. Jackson (eds.), *Surgical Tools and Medical Devices*,
DOI 10.1007/978-3-319-33489-9_5

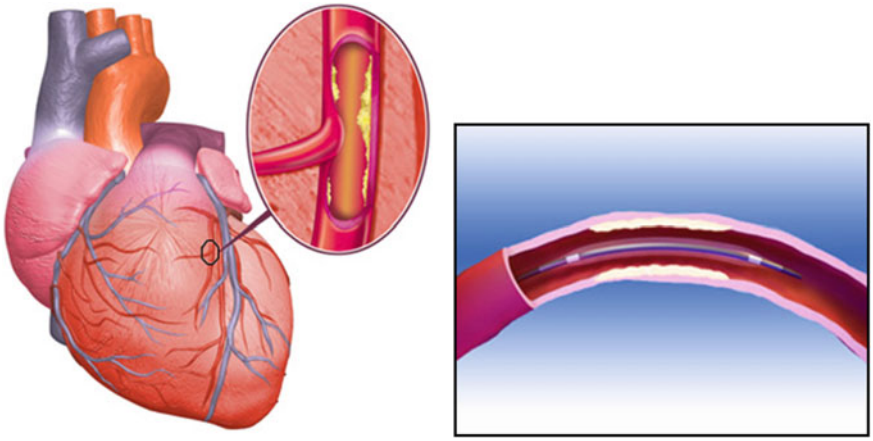

Fig. 5.1 Schematic of percutaneous transluminal coronary Angioplasty (*Courtesy* Medtronic. Inc)

The earliest known cardiac catheterization was performed by Hales in 1711. More recently, Gruntzing and Myler performed the first human coronary angioplasty in May 1977 [1–3]. Currently, 1.2 million Americans undergo cardiac catheterization and over 1.5 million receive a percutaneous coronary intervention such as balloon angioplasty, atherectomy, or stent implantation annually [4].

Percutaneous transluminal coronary angioplasty (PTCA), commonly known as balloon angioplasty, is performed by threading a balloon catheter through the femoral artery, located in the groin, to a trouble spot in an artery of the heart (Fig. 5.1). The balloon is then inflated, compressing the plaque and dilating (widening) the narrowed coronary artery so that blood can flow more easily. This is often accompanied by inserting an expandable metal stent. Stents are wire mesh tubes used to prop open arteries after PTCA.

Cardiovascular interventional devices commonly used include the following:

Guiding catheter—a long, thin, flexible tube that acts as a conduit for injection of contrast. A guiding catheter delivers other devices, i.e., a balloon catheter or a stent delivery catheter into the coronary vasculature. A *guiding catheter* often contains metallic braiding to help provide push-ability and torque-ability [5] (Fig. 5.2).

Guide wire—a long, thin, flexible wire that acts as a railing for delivery of a balloon catheter and stent delivery system. It is typically made from stainless steel or nickel titanium (Fig. 5.3).

Track-ability (the ease of tracking a balloon over the guide wire up to the target lesion) and push-ability (the ability to advance the balloon across the lesion) are more important to the practice of interventional cardiology than any other in vitro measure. However, there are no reliable in vitro methods for measuring these two properties. A variety of lubricious coatings exist for the *guidewires*, which reduce friction, facilitate advancement of interventional devices, and enhance lesion crossing. Examples include hydrophilic coatings, silicone (hydrophobic), and PTFE coating [6].

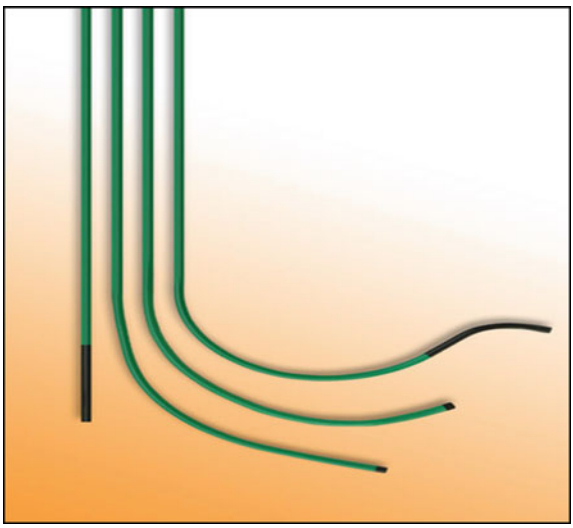

Fig. 5.2 Attain® fixed shape guide catheters (*Courtesy* Medtronic Inc.)

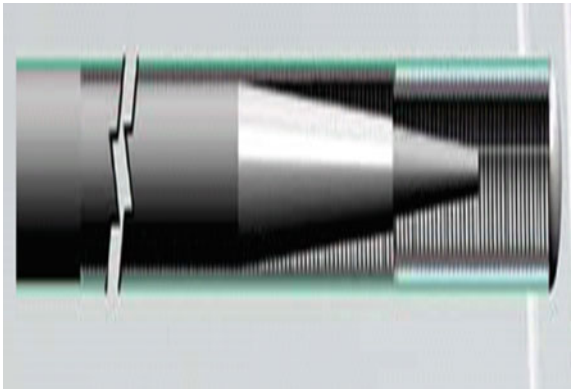

Fig. 5.3 Schematic of guidewire crossection (*Courtesy* Medtronic Inc.)

Hydrophilic coating must be hydrated to be effective. However, this might not be appropriate for all devices. Hydrophobic coatings, such as silicone, when applied to the surface, are not as lubricious as hydrophilic coatings but provide more tactile feedback as the physician manipulates the devices.

5.2 Key Surface Properties for Cardiovascular Interventional Devices

Friction is the primary metric of concern. However, where energy is transmitted from the surface of the devices, for example during ablation, the insulation material property also becomes a concern. Friction generally dissipates energy in the form of

heat. This deficit must be overcome to maintain two objects moving at a constant velocity with respect to one another. The process of wear also accompanies the presence of frictional forces between two surfaces.

Magnitude of friction and wear is generally regulated by modification of the interface between the two surfaces. The various surface treatment methods, solid, liquid, and gas, all provide lubrication. Not only is the coefficient of friction a measurable of importance but also provides insights pertaining to the mechanism of lubrication. The principle lubrication mechanisms are hydrodynamic, elastohydrodynamic, mixed and boundary [7].

In cardiovascular applications, there is usually not sufficient film thickness between two surfaces to provide hydrodynamic lubrication, as the typical distance between the two surfaces is not sufficient. In hydrodynamic lubrication the surfaces are at greater distances from one another. Boundary lubrication represents the opposite situation where the distance between the two surfaces is minimal.

The lubrication mechanism is largely a function of surface property modification. An effective boundary lubricant usually interacts with the surface of the interventional or implantable device. Hydrophilic coatings usually provide effective boundary lubrication of cardiovascular interventional and implantable devices. Elastohydrodynamic lubrication provides a film thickness that is slightly less than that found in hydrodynamic lubrication. In this scenario, pressure waves can cause a deformation in the tissue surface opposite of the interventional or implantable device.

As the distance between the surfaces decreases from elastohydrodynamic lubrication, mixed lubrication occurs. Mixed lubrication has a higher coefficient of friction and wear rate than hydrodynamic lubrication. As a result of the dimensional constraints, most cardiovascular interventional and implantable devices provide lubrication via boundary and mixed lubrication.

The surface properties are modified in an attempt to minimize coefficient of friction. The two primary methods to accomplish this are hydrophobic and hydrophilic coating. Hydrophilic coating is activated by an aqueous environment; where a layer of slippery hydrogel is created on the device surface, reducing the friction force [8–10]. Hydrophilic coating might not be appropriate for all devices such as those that are not constantly hydrated [11]. Hydrophobic coatings such as silicone can also be applied to the surface but it is not as lubricious as a hydrophilic coating. It does, however, provide more tactile feedback to the operating physician.

5.3 Cardiovascular Implantable Devices

Unlike interventional tools, cardiovascular implantable devices remain in the cardiovascular system usually until the device must be removed as a result of functional failure. These failures can be classified as either mechanical or surface property failure. The heart, along with the arterial and venous system, can be

defined as an electromechanical system. Certain implantable devices focus on treatment of electrical aspects while others focus on mechanical aspects.

5.4 Electrical Implantable Devices

The rhythm management of the heart is regulated by two different types of myocardial cells; pacemaker cells and conducting cells. Pacemaker cells, located in the sinoatrial (SA) node and atrioventricular (AV) node are ,respectively located where the superior vena cava and right atrium join in the inferior portion of the interatrial septum [4]. Conducting cells, referred to as the Bundles of His and Purkinje Fibers, serve the function of relaying action potentials from the SA node to the AV node and to all parts of the ventricle.

Devices used by clinicians in the regulation of the rhythm management of the heart include: implantable pulse generators (pacemakers), implantable cardioverter defibrillators (ICD), pacemaker and ICD leads, and implantable loop recorders. These devices are generally implanted in the muscle cavity of the pectoral region (Figs. 5.4, 5.5, 5.6, 5.7 and 5.8).

Pacemakers deliver electrical impulses to the heart via a special conductor called a pacemaker lead (Figs. 5.4 and 5.5). One end of the lead is connected to the pacemaker and the other end of the lead contains a metallic electrode, which is in contact with the heart tissue, stimulating the heart to contract. The lead also carries information from the heart back to the pulse generator, which the physician accesses via a special external programmer [12, 13].

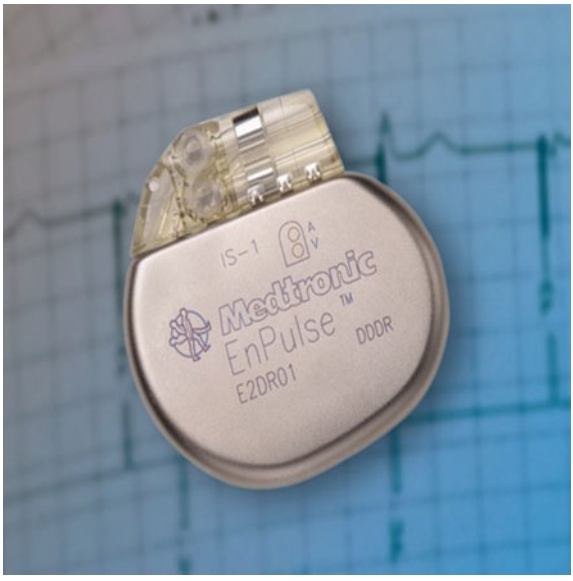

Fig. 5.4 Pacemaker—Enpulse (*Courtesy* Medtronic, Inc.)

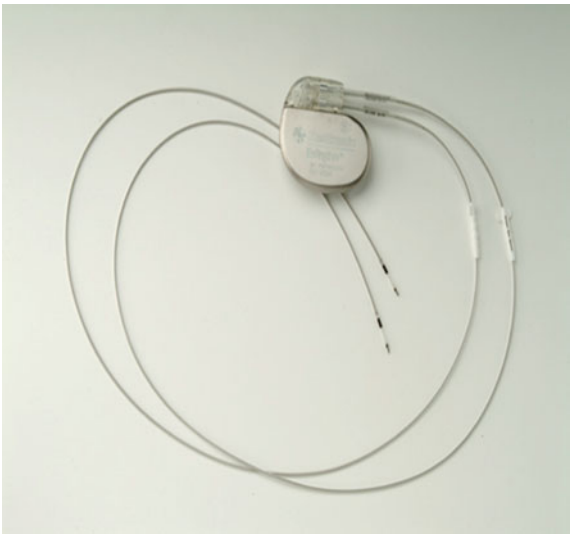

Fig. 5.5 Medtronic EnRhythm pacemaker with leads (*Courtesy* Medtronic, Inc.)

Fig. 5.6 Implantable cardioverter defibrillator (*Courtesy* Medtronic)

The pacemaker case is made of titanium, a metal that is 10 times as strong as steel, but much lighter. Titanium and its alloy are biocompatible. The titanium casing was developed to enclose the battery and circuitry. Epoxy resin with silicone rubber encased the inner components in previous designs.

Titanium casings with special filters help to shield the components and greatly reduce outside electromagnetic interference. Patients with these newly designed pacemakers can now safely use microwave ovens and other appliances and equipment found in the home and office.

A nitride coating can be deposited via sputtering technique onto the surface of the pacemaker metallic electrode on the pacemaker leads to improve the sensing and pacing performances over an electrode with a smooth, unsputtered surface [14].

Fig. 5.7 External programmer (*Courtesy* Medtronic)

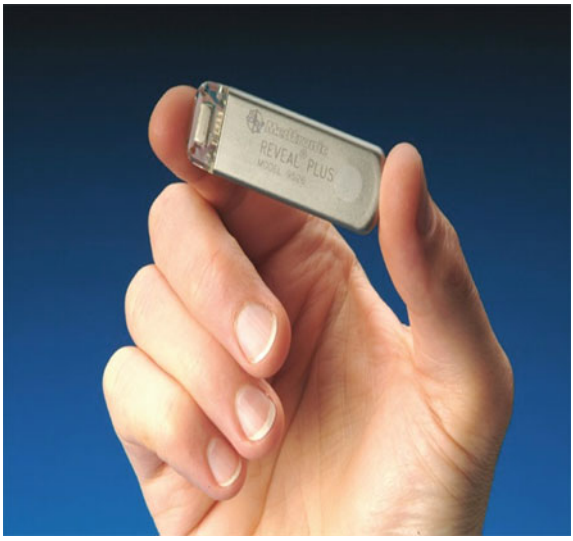

Fig. 5.8 Implantable loop recorder (*Courtesy* Medtronic)

When the heart beats in asynchronous rhythms, the ICD) deliver an electric shock that can "reset" the heart back to its normal rhythm. The standard material construction of the casing is the same as that of the pulse generator. Another implantable electrical device called an implantable loop recorder provides the function of recording an electrocardiogram (ECG) before and after the onset of symptoms (Fig. 5.8).

5.5 Mechanical Implantables

The heart, as a mechanical system, acts as a positive displacement pump to circulate blood through the cardiovascular system. Devices used by clinicians in the treatment of cardiovascular disease include: stents, vascular grafts and stent grafts, and heart valves.

A stent is a wire mesh tube used to prop open an artery during angioplasty (Fig. 5.9). The stent is collapsed to a small diameter and put over a balloon catheter. It is then moved into the area of the blockage. When the balloon is inflated, the stent expands, locks in place and forms a scaffold. This holds the artery open. The stent stays in the artery permanently, holds it open, improves blood flow to the heart muscle and relieves symptoms (i.e., chest pain) [15].

Stents have virtually eliminated many of the complications that used to accompany "plain old balloon angioplasty" (POBA) such as abrupt and unpredictable closure of the vessel, which can result in emergency bypass surgery. The additional structural strength of the stent can also help to keep the artery open while the healing process progresses.

Vascular grafts are classified into two major categories. Large diameter grafts (>10 mm) primarily made up of Dacron (80 %) and PTFE (20 %) are primarily used for aortic and iliac artery reconstruction. The small caliber grafts (<10 mm) are primarily used for coronary artery bypass grafts (CABG), lower-extremity bypass procedures, and hemodialysis access. The patency rates for the synthetic graft material are better for the aortic and iliac artery reconstruction than for when small caliber grafts are used. Saphenous vein grafts and internal mammary grafts both have greater patency rates than the small caliber vascular grafts with the internal mammary artery providing the superior patency rates.

Dacron (polyethylene terphthlate) and PTFE (polytetrafluoroethylene) maintain their tensile strength for years after being implanted. However, other materials such as Nylon (polyamide), Ivalon, and Orlon decrease in tensile strength after months of being implanted. Woven Dacron grafts are nonporous with no stretch while knitted

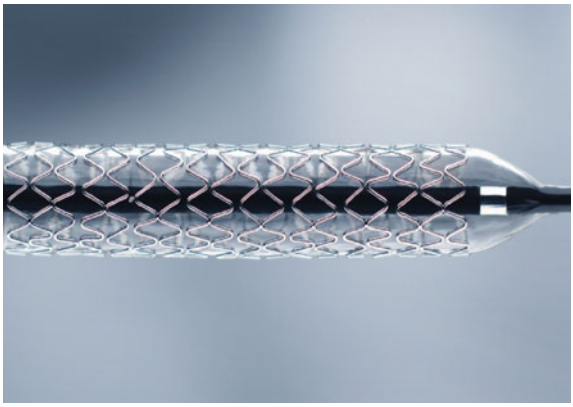

Fig. 5.9 Endeavor drug eluting stent (*Courtesy* Medtronic Inc.)

Dacron grafts have variable stretch and are porous. As previously mentioned, the patency rates for the use of these grafts are better for large vessel grafts [16].

Neointimal hyperplasia, which occurs in the anastomotic area, is the prime reason of failure of small caliber grafts. The low compliance rates leading to compliance mismatch play a role as well. The neointimal hyperplasia could be caused by platelet deposition with local release of platelet-derived growth factor (PDGFP), other growth factor stimulation of smooth muscle cell (SMC) proliferation, monocyte recruitment, complement activation, leukocyte deposition, chronic inflammation, and mechanical stimuli such as stress and shear abnormalities [16]. Additionally, the optimal sizing of a graft is important to provide a wall shear rate that will increase the long-term patency of the synthetic grafts [17].

Other devices within this classification include stent grafts and heart valves. Stent grafts combine the mechanical scaffolding function of stents and conduit function of vascular grafts. Heart valves provide a mechanical replacement for failing bicuspid and tricuspid valves.

These devices primary function is to serve either a structural or dynamic primary function. However, the surface treatment of these devices does have a significant effect on the efficacy of these devices.

5.6 Important Surface Properties for Implantable Cardiovascular Devices

The surface properties of materials are modified to reduce adherence to vascular tissue. This can be accomplished via various treatment methods. However, the surface modification is not always solely for mechanical purposes. The surface modification can also provide therapeutic benefit.

Pyrolitic carbon is used in cardiovascular applications in artificial hearts and prosthetic heart valves. The material has similarities to graphite with covalent bonding present between the graphene sheets. The risk of thrombosis is reduced when using pyrolytic carbon, as blood clots are less likely to form when it is used. However, as a precaution, the patient who receives a prosthetic heart valve must be on an anticoagulant regimen.

In addition to prosthetic heart valves, bioprosthetic heart valves, made from porcine valves or bovine pericardium, can be used to replace the natural valves. The tissue of the valves can be treated to prevent calcification via special processing [18].

TheMosaic® aortic and mitral bioprosthesis, manufactured by Medtronic, uses the AOA method, which has been observed to reduce the buildup of calcium in animal studies. The only stented valve in the U.S. that incorporates this tissue treatment is the Mosaic® bioprosthesis. One likely method of the AOA process function is via the binding of free aldehyde groups of glutaraldehyde to the amino group of AOA molecules. This process, referred to as *capping*, is believed to inhibit

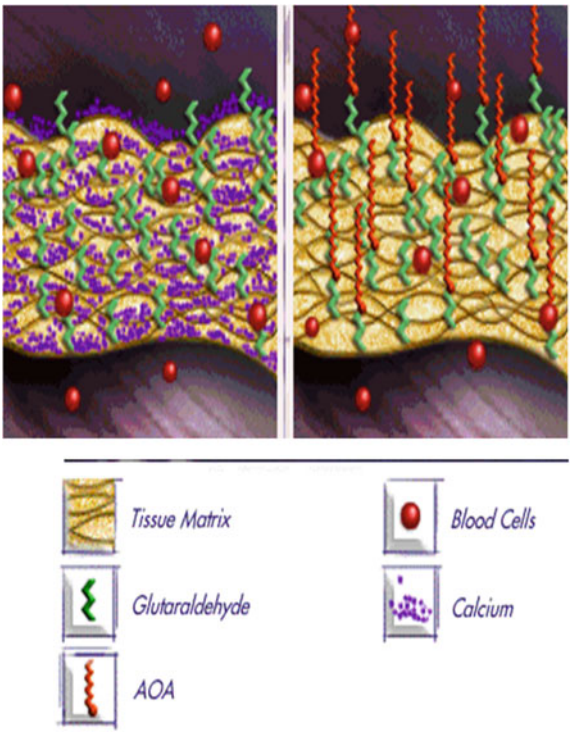

Fig. 5.10 AOA treatment process (*Courtesy* Medtronic)

the mineralization of tissues. Another viable mechanism by which AOA treatment minimizes calcification is slowing down the diffusion of calcium ions though the treated tissues (Fig. 5.10).

The surfaces of stents have evolved to include the delivery of drugs that have proven successful in the reduction of restenosis rates. Restenosis rates have been observed to reduce significantly when the stent surface is coated such that siromilus and paclitaxel are eluted [19]. Biodegradable materials using the mechanism of autologous cell seeding has shown potential. However, the pretreatment of materials increases the opportunity for infection. A biodegradable graft material made up of polylactic-co-glycolic acid as a biodegradable scaffold material compounded with a collagen microsponge has shown positive results. No thrombus formation was observed, while the polylactic-co-glyclolic acid scaffold was almost completely absorbed over a 6-month period [20]. Polyethylene oxide (PEO) has also been used to modify biomaterial surfaces to minimize or prevent protein absorption and cell adhesion.

Minimization of thrombosis is a key to the reduction or restenosis where stents are implanted. To achieve this goal, usually the mechanisms focused on are minimizing coagulation, platelet adhesion, and platelet activation. However, the role of complement activation prior to platelet activation and the role of leukocytes could play a significant role in the minimization of thrombosis as well [21].

Surface oxide formation has also been observed to be a significant factor in determining the degree of thrombosis. However, amorphous oxide film may provide a solution to the thrombosis caused by metal [22].

Several other surface modifications of the stents to reduce restenosis and thrombogenicity by improved biocompatibility have also been evaluated with varying degrees of success: metallic coatings: gold, titanium, copper; phosphorylcholine (PC), a synthetic mimetic outer wall of red blood cells; heparin; silicon carbide; and carbon and fluorinated diamond like carbon (F-DLC) [23–25].

References

1. Blake, D. M., & Maness, P. C. (1999). *Separation and Purification Methods, 28*(1), 1–50.
2. Byrne, J. A., Eggins, B. R., Brown, N. M. D., McKinney, B., & Rouse, M. (1998). *Applied Catalysis, B: Environmental, 1998*(17), 25–36.
3. Byrne, J. A., Davidson, A., Dunlop, P. S. M., & Eggins, B. R. (2002). *Journal of Photochemistry and Photobiology A: Chemistry, 148*, 365–374.
4. Byrne, J. A., Hamilton, J. W. J., McMurray, T. A., Dunlop, P. S. M., Jackson, V., Donaldson, A., et al. (2006). Abstracts of the NSTI conference, Boston.
5. Coleman, H. M., Routledge, E. J., Sumpter, J. P., Eggins, B. R., & Byrne, J. A. (2004). *Water Research, 38*, 3233–3240.
6. Cosnier, S., Gondran, C., Senillou, A., Gratzel, M., & Vlachopoulos, N. (1997). *Electroanalysis, 9*(18), 1387–1392.
7. Dunlop, P. S. M., Byrne, J. A., Manga, N., & Eggins, B. R. (2002). *Journal of Photochemistry and Photobiology A: Chemistry, 148*, 355–363.
8. Fujishima, A., & Honda, K. (1972). *Nature, 238*, 37–38.
9. Fujishima, A., Rao, T. N., & Tryk, D. A. (2000). *Journal of Photochemistry and Photobiology C: Photochemistry Reviews, 1*, 1–21.
10. Giavaresi, G., Ambrosio, L., Battiston, G. A., Casellato, U., Gerbasi, R., Finia, M., et al. (2004). *Biomaterials, 25*, 5583–5591.
11. Hoffman, M. R., Martin, S. T., Choi, W., & Bahnemann, D. W. (1995). *Chemical Reviews, 95*, 69–96.
12. Holgers, K. M., & Ljungh, A. (1999). *Biomaterials, 20*, 1319–1326.
13. Huang, N., Yang, P., Leng, Y. X., Chen, J. Y., Sun, H., Wang, J., et al. (2003). *Biomaterials, 24*, 2177–2187.
14. Kuhn, K. P., Chaberny, I. F., Massholder, K., Stickler, M., Benz, V. W., Sonntag, H.-G., & Erdinger, L. (2003). *Chemosphere, 53*, 71–77.
15. Lee, S.-H., Kim, H.-W., Lee, E.-J., Li, L.-H., & Kim, H.-E. (2006). *Journal of Biomaterials Applications, 20*, 195–208.
16. Liu, X., Zhao, X., Ding, C., & Chu, P. K. (2006). *Applied Physics Letters, 88*, 13905.
17. McMurray, T. A., Byrne, J. A., Dunlop, P. S. M., Winkelman, J. G. M., Eggins, B. R., & McAdams, E. T. (2004). *Applied Catalysis, A: General, 262*(1), 105–110.
18. McMurray, T. A., Byrne, J. A., Dunlop, P. S. M., & McAdams, E. T. (2005). *Journal of Applied Electrochemistry, 35*, 723–731.
19. Mills, A., & Le Hunte, S. (1997). *Journal of Photochemistry and Photobiology A: Chemistry, 108*, 1–35.
20. Nygren, H., Tengvall, P., & Lundstrom, I. (1997). *Journal of Biomedical Materials Research, 34*, 487–492.
21. Ohko, Y., Utsumi, Y., Niwa, C., Tatsuma, T., Kobayakawa, K., Satoh, Y., et al. (2001). *Journal of Biomedical Materials Research (Applied Biomaterials), 58*, 97–101.

22. Pan, J., Leygraf, C., Thierry, D., & Ektessabi, A. M. (1997). *Journal of Biomedical Materials Research, 35*, 309–318.
23. Ramires, P. A., Romito, A., Cosentino, F., & Milella, E. (2001). *Biomaterials, 22*, 1467–1474.
24. Shani Sekler, M., Levi, Y., Polyak, B., Dunlop, P. S. M., Byrne, J. A., & Marks, R. S. (2004). *Journal of Applied Toxicology, 24*, 395–400.
25. Yang, Y., Glover, R., & Ong, J. L. (2003). *Colliods and Surfaces B: Biointerfaces, 30*, 291–297.

Chapter 6
Surface Engineering of Artificial Heart Valves to Using Modified Diamond-Like Coatings

N. Ali, Y. Kousa, J. Gracio, G. Cabral, A. Sousa, T. Shokufar, E. Titus, J.C. Madaleno, W. Ahmed and M.J. Jackson

Abstract There are two types of artificial heart valves, namely, (i) biological valves and (ii) mechanical valves. biological heart valves are made from tissue taken from animals or human cadavers. They are treated with preservatives and sterilized for human implantation. On the other hand, mechanical heart valves are made of man-made materials. The advantage of mechanical valves over biological valves is that they normally last for a comparatively longer lifetime. The biological valves exhibit a shorter lifetime and tend to wear out with time in service. This chapter discusses mechanical heart valves and highlights the underlying problems faced with biomaterials used in the manufacture of such valves.

6.1 Introduction

The history relating to mechanical heart valves will be reviewed, which dates back from 1952. We describe the principal cause of concern facing modern biomaterials used in the manufacture of heart valve components, which is thrombus formation (thrombosis). The hemocompatibility of biomaterials used in human implants will be discussed. Further, we describe the endothelium layer and discuss endothelial cell seeding as a tool for developing a heart valve that overcomes the common problems faced by modern valve materials. Diamond-like carbon (DLC) and its hemocompatibility and/or biological properties have been discussed and reviewed. Finally, we present results of endothelial cell seeding on chromium and silicon modified DLC films. A range of traditional and sophisticated techniques have been

N. Ali · Y. Kousa · J. Gracio · G. Cabral · A. Sousa · T. Shokufar · E. Titus
J.C. Madaleno
University of Aveiro, Aveiro, Portugal

W. Ahmed
School of Medicine, University of Central Lancashire, Preston, UK

M.J. Jackson (✉)
Kansas State University, Salina, KS, USA
e-mail: jacksonmj04@yahoo.com

W. Ahmed and M.J. Jackson (eds.), *Surgical Tools and Medical Devices*,
DOI 10.1007/978-3-319-33489-9_6

used to characterize the physical and biological properties of DLC and modified DLC films for applications in mechanical heart valves.

Heart disease is one of the most common causes of death in the world today, particularly in the western countries. There are various causes of heart disease, related most commonly to diet and exercise. The failure of heart valves accounts for about 25–30 % of heart problems that occur today. Faulty heart valves need to be replaced by artificial ones using sophisticated and sometimes risky surgery. However, once a heart valve has been replaced with an artificial one there should be no need to replace it again and it should last at least as long as the life of the patient. Therefore, any technique that can increase the operating life of heart valves is highly desirable and valuable. Currently, pyrolytic-carbon (PyC) is used for the manufacture of mechanical heart valves. PyC belongs to the family of "turbostratic carbons", which have a similar structure as graphite.

Graphite consists of carbon atoms that are covalently bonded in hexagonal arrays. These arrays are stacked and held together by weak interlayer binding. PyC differs from graphite in that the layers are disordered, thus resulting in wrinkles or distortions within layers. This feature gives PyC improved durability compared to graphite. Although, PyC is widely used for heart valve purposes, it is not the ideal material. In its processed form, PyC is a ceramic-like material and like ceramics, it is subject to brittleness. Therefore, if a crack appears, the material, like glass, has very little resistance to the growth/propagation of the crack and may fail under loads. In addition, its blood compatibility is not ideal for prolonged clinical use. As a result, thrombosis often occurs in patients who must continue to take anti-coagulation drugs on a regular basis [1]. The anti-coagulation therapy can give rise to some serious side effects, such as birth defects. It is therefore extremely urgent that new materials, which have better surface characteristics, blood compatibility, improved wear properties; better availability and higher resistance towards breaking are developed.

6.2 History of Mechanical Heart Valves

Charles Hufnagel [2] was the first person, in 1952, to implant an artificial heart valve, in the form of Lucite tube and methacrylate ball, in the descending aorta of the heart with clamps that facilitated rapid insertion of the valve without arresting the heart. Subsequently, the methacrylate ball was replaced with a hollow nylon ball coated with silicone rubber that was designed to reduce noise. More than 200 Hufnagel valves were implanted in patients with aortic insufficiency and remarkably some of these valves functioned for up to 30 years without any significant wear [3]. Later on Murray [4] employed a similar technique to insert a human homograph in the descending aorta.

Initially flexible polyurethanes and silicon rubber materials were employed for use in heart valve components. The reason for using such materials was that the valves would not only reside in the exact position anatomically but would effectively show mechanical characteristics similar to that of natural heart valves. Valves made from such materials were implanted in humans, in different ways. For example, in some cases, individual leaflet was made from flexible material and in others the entire valve was constructed from elastic materials. However, these elastic valves could not last longer than approx. 2–6 years due to a number of reasons, such as tearing, material fatigue and calcification [5–9].

In 1960, Dwight Harken [3, 10] implanted double cage ball valves in seven patients. Unfortunately, only two of the seven patients survived the surgery. Later the same year, Albert Starr [3, 10] was more fortunate than Dwight Harken, as he implanted prosthetic valve(s), comprising of metal cage and silicon ball, in a number of patients. The success rate increased as the number of survivals was six out of eight patients. These devices though proved durable but continued suffering from several problems like high profile, high rates of thromboembolism (blocking of blood vessel by a blood clot dislodged from its site of origin) and stenotic central position of the ball. Soon after in 1962, Vincent Gott and Ron Daggett [11] addressed two of the problems by introducing a low profile reinforced silicon flap valve that played a significant role in the reduction of central obstruction and the resulting valvular stenois in patients. In 1963, Antolio Cruz [12] devised a heart valve with a free-floating disc tilting on the edge of an orifice ring whose excursion was retained by a cage. Although it had good hemodynamic qualities, it was as stenotic as the ball valves and remained suffering from thromboembolic problems [10]. Wada–Cutter valve [13] was designed which significantly reduced valvular stenosis and was thus first implanted in 1965. This valve enabled the disc to rotate or tilt about an axis slightly offset from the centre opening. With the Wada–Cutter valve, pivot points were fixed so that the stress and wear of the repeated openings was focused on two pivots on the disc. Later in 1974, its production was halted due to excessive wear of the Teflon occluder [10]. Subsequently, Don Shiley and Viking Bjork [3, 10] designed a tilting disk valve known as the Bjork–Shiley valve. This provided the same features, as that of Wada–Cutter valves only with the difference that unlike it, the disk of the Bjork–Shiley valve was not fixed at pivots points [14]. In the original Starr–Edwards, Wada, Shiley prosthetic valves designs, instead of using the metal occluders, polymeric occluders were employed because of their lower density made for more light and more responsive moving parts. Owing to some key characteristics of plastics, plastic occluders were employed in heart valves. The elimination of strain flexure, considered essential for the elastic valves, increased the life of the more rigid plastic parts. But eventually all the polymeric occluders suffered from degenerative failure. Silicone balls would absorb lipids from the blood stream and crack if not cured appropriately [15]; Tefflon was subject to failure through cold flow from repeated stress in a focused location [16]; and Derlin would warp/distort in typical steam sterilization cycles as Derlin absorbs water and changes the configuration of the disc [3, 17].

Gott [3, 10] not just designed the first low profile heart valve but he contributed significantly in the field of biomaterials by performing a series of detailed investigations. Gott's experiments were performed on more than 200 dogs in which he implanted small tubes of different materials in vena cava in order to address thromboembolism through improvement in material selection [18]. The tubes made from polymer and stainless steel materials were used in the construction of heart valves in 1962 and it was found that they uniformly occlude within two hours. Later on it was discovered that an application of a coating made from graphite mixed with Heparin bonded with benzalkonium chloride removed clot formation in five animals for a period of up to two weeks. Lillehei and Nakib Ahmad [10] devised a non-tilting disk valve in 1967 that was entirely made of machined titanium, including the poppet and was called Lillehei–Nakib Toroidal Valve. A special division within a nuclear research company called General Atomics was formed after Gott's publication on the biocompatibility of carbon and working here Dr Jack Bokros [3] developed a new carbon material called Pyrolite (also known as pyrolytic carbon). Eventually, in 1969, after more than six years of development, plastic and metal materials used for heart valves started to become replaced by Pyrolite. Michael DeBakey [19] implanted a valve that was very similar to Starr aortic valve with a hollow pyrolite ball as occluder. Taking advantage of the improved biocompatibility and durability of pyrolytic carbon, translating disk valves like the Beall-Suritool and Cooley Cutter valve were redesigned [20]. Later in 1974, Shiley valve became the most frequently implanted mechanical valve just after when the Derlin disk in the Shiley valve was changed to pyrolytic carbon [21].

The Lillehei-Kaster (LK) [22, 23] tilting disk was introduced in 1970 with a pyrolytic carbon disk and solid titanium orifice and it has a remarkable record of 30 years with only one case reported of structural failure. In 1976, the valve was redesigned by replacing flat disk by a curved disk, which in turn, improved the catastrophic thrombosis [3, 21, 24]. Further improvement was achieved later in 1984 when the orifice was changed from titanium to Pyrolite carbon [3, 25].

Bob Kaster [26] redesigned the LK valve that was introduced seven years ago, by replacing the outflow struts with a single wire running through the centre of the disk. Although the efficiency of this valve was reduced due to the hole through the centre of the disk allowing increased blood leakage through it yet this device maintained the excellent reliability of the original LK design. The only reported structural failure for this design was combated by changing the flat disk to a rounded surface in a D-16 design in order to avoid the observed impacts of disk with the large flat stop when it closes [27]. Basically, this change was implemented in order to reduce haemolysis but this change resulted in three reported cases of disk fracture when combined with Pyrolite disk attached to the extremes of the allowable tolerances.

Today, heart valves employing two leaflets in their design are implanted but the idea of bileaflet valve was documented by John W. Holter in 1958 the time when valves were still being implanted in the descending aorta. In 1963, Vincent Gott and Dr. Ronald Daggett developed a valve called "Gott–Daggett valve", which was a polycarbonate ring containing a disc of Teflon fabric impregnated with silicone

rubber [28]. Then Dr Lillehei implanted an all titanium bileaflet valve in 1968 that was developed by Kalke [29] but the patient died within 48 h so the idea was abandoned. After seven years, the founder of cardiac pacemakers designed a valve very similar to the Kalk Valve (with little modifications) and requested Carbomedics to build it from Pyrolite carbon. This design known as "St Jude Medical heart valve" was the first that was entirely made up of pyrolytic carbon [10, 21] and quickly captured a leading market position. Although this valve had design and material improvement as major factors in its growth but its market acceptance was also pushed up due to strut failure problems in the Shiley valve [30].

The combination of Pyrolyte carbon with a bileaflet valve proved significant but it failed to provide a cure for the patients with prosthetic valves. Soon after five years of the introduction of St Jude's valve, a new valve Baxter–Duromedics [31] entered the market with an improvement in pivot design and with a seating lip that the occluders rest against in the closed position. The seating lip proved effective in reducing the regurgitation but the desired gain in the efficiency was counterbalanced by the loss of orifice area. Further the seating lip enhanced the formation of cavitation bubbles that resulted in significant structural damage and thereby the design was withdrawn after 3 years with only 20,000 valves due to 12 reported cases of structural failure [32].

Sulzer Carbomedics [33] introduced a new bileaflet valve called the Carbomedics Prosthetic Heart Valve (CPHV) in 1986, which improved the pivot design with a titanium stiffening ring to protect the valve. The implant of over 325,000 of these valves in 14 years with no post-operative structural failure demonstrated clearly the effectiveness of titanium stiffening ring. Sorin Biomedics [34] who had been manufacturing tilting disc valves similar to Shiley valves started offering a bileaflet valve as well in 1990. Sorin combined a curved pyrolytic carbon leaflet, similar to Baxter Duromedics design with a titanium orifice. The titanium orifice was basically used both to avoid expense and manufacturing complexities associated with pyrolytic carbon. The Sorin valve was coated with a thin layer of vapour deposited carbon on the titanium. Later Edward Life Sciences [35] obtained the rights of marketing this valve in U.S with little modification in the new sewing ring design with oversized silicon filler but otherwise left the design unchanged. Several independent investigators came up with the conclusion that the carbon layer is subjected to rapid erosion both in vivo and in vitro explaining the limited acceptance of the Sorin bileaflet and Edwards Mira valve [35]. Sorin [36, 37] accepted the need for further studies after knowing that insufficient safety and effectiveness data had been collected for this valve.

In cooperation with the Carbon implants, the Medtronic [21] company began a clinical study and designed Medtronic Parallel Valve to open parallel to the flow of blood with a 90° opening angle rather than the 78°–80° angles used by other manufactures. Pivot in this valve was quite complex, intended to decrease the leakage when the valve was fully closed, and it has been shown to be an important risk factor for valvular thrombosis [38]. Hence it was withdrawn from the market within one year of clinical trials.

Certain employees of Carbon Implants, Inc. formed a spin-out company called as Medical Carbon Research Institute (MCRI) after completing the design of the Medtronic Parallel Valve and developed another valve similar to this. This new valve was called the On-X™ [21] with an elongated orifice, 90° opening angle and 40° closed angle featuring four sizes of carbon orifices labelled 19, 21, 23, and 25 mm. Finally in 1999, Medtronic began another bileaflet valve clinical trail in Europe with an internally developed bileaflet valve called the Medtronic Advantage [34].

Two of the most recent valves are the ATS Open Pivot® bileaflet valve and the On-X® prosthetic valve [39]. ATS open pivot valve (made by ATS Medical, Inc. in 2000) is a mechanical heart valve with two leaflets (flap like structures) in the shape of a circle, each leaflet is half the circle, surrounded by a ring made of polyester fabric. The leaflets are made of carbon.

The On-X® valve (made by Medical Carbon Research Institute, LC in 2001) is a mechanical heart valve with two movable half-discs (bileaflets), contained within a housing surrounded by a man-made fabric-covered ring. The leaflets are made of graphite and tungsten, with a carbon coating.

Mechanical heart valves can be classified into three primary types: (i) ball and cage, (ii) tilting disk, and (iii) bileaflet valves. Table 6.1 shows the types of heart valves used for implantation since 1959. All mechanical heart valves consist of an occluder working as an element to retard the flow of blood and of a mechanism to restrain the motion of the occluder. The occluder functions relatively in response to the pressure across the valve during the cardiac cycle. The occluder opens to permit the blood flow through the valve in case if the upstream pressure is greater than the downstream pressure and closes when the downstream pressure is greater than the upstream pressure to stop the blood flow through the valve. Figure 6.1 shows a typical mechanical heart valve made by Medtronic, USA.

Table 6.1 Summary of the material composition of nine key designs of mechanical valves developed since 1959

Year	Valve name	Type	Poppet	Material
1959	Hfnagel	Ball	Polypropylene	Methacrylate
1964	Starr–Edwards 1000	Ball	Silastic	Stellite
1968	Wada–Cutter	Tilting disc	Teflon	Titanium
1969	Bjork–Shiley	Tilting disc	Derlin	Stellite
1970	Lillehei–Kaster	Tilting disc	Pyrolitic carbon	Titanium
1971	Bjork–Shiley	Tilting disc	Pyrolitic carbon	Stellite
1977	Medtronic–Hall	Tilting disc	Pyrolitic carbon	Titanium
1977	St Jude Medical	Bi-leaflet	Pyrolitic carbon	Pyrolitic C
1991	Jyros	Bi-leaflet	Vitreous carbon	Vitreous C
1999	Medtronic advantage	Bi-leaflet	Pyrolitic carbon	Pyrolitic C

Fig. 6.1 A typical PyC leaflet heart valve (Medtronic)

6.3 Thrombosis

As mentioned earlier, the principal concern with mechanical heart valves is thrombus formation. The process of a blood clot (thrombus) formation inside a blood vessel to stop bleeding is termed as thrombosis. Excessive blood loss is undesirable and physiological feedback systems exist for protection. Therefore, the body has ways of protecting itself in cases when the blood escapes the body. When the human body loses a small amount of blood through a minor wound, the platelets cause the blood to clot in order to stop the bleeding. Because new blood is always being made by hematopoietic stem cells located in bone marrow, the body can replace the lost blood effectively and efficiently. However, when the human body loses a large amount of blood through a major wound, then in such cases blood needs to be replaced through a blood transfusion from other people.

Clotting involves thrombus formation that prevents further blood loss from damaged tissues, blood vessels or organs. Figure 6.2 shows the schematic of the thrombosis process. The first step in the clotting process is the adsorption of blood proteins on the skin surface. There are three types of proteins in human blood: (i) albumin, (ii) fibrinogen and (iii) globulin. Albumin, fibrinogen and globulin are present in the blood in the following percentage (%) ratio: 60:4:35, respectively. Soon after vessel injury occurs, blood clotting is initiated resulting in platelets and tissues to secrete a clotting factor called prothrombin activator. Prothrombin activator and calcium ions catalyse the conversion of prothrombin to thrombin (activated form), which subsequently catalyses the conversion of fibrinogen to fibrin threads. Fibrin threads are sticky and trap more platelets thus further sealing the point of blood leak.

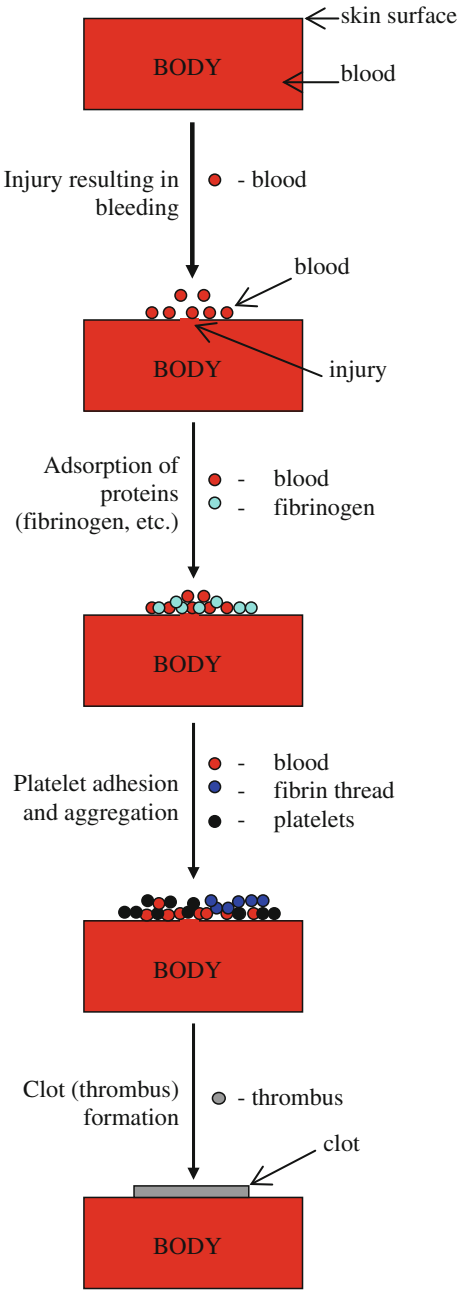

Fig. 6.2 Schematic diagram depicting the thrombosis process in the human body

Platelets are irregularly shaped, colourless bodies that are present in the blood. Their sticky surface enables them, along with other substances, form clots at the blood outlet point(s) to stop bleeding. The mineral calcium, vitamin K and fibrinogen help the platelets form a clot. If blood is lacking these nutrients, it will take longer than normal for the blood to clot. If these nutrients are missing, one could bleed to death. Some clots can be extremely dangerous. A blood clot that forms inside of a blood vessel can be deadly because it blocks the flow of blood, cutting off the supply of oxygen to the body.

There are two pathways that effectively lead to the formation of a blood clot, namely, the intrinsic and extrinsic pathways. Although they are initiated by distinct mechanisms, the two converge on a common pathway that leads to clot formation. The formation of a blood clot in response to an abnormal vessel wall in the absence of tissue injury is the result of the intrinsic pathway. Thrombus formation in response to tissue injury is the result of the extrinsic pathway. Both pathways are complex and involve numerous different proteins termed clotting factors.

There are many circumstances that may lead to thrombosis, however, the principal three situations include: (i) damage to endothelial cells, which line the interior surface of blood vessels; (ii) slow blood flow; and (iii) changes in the composition of blood. There are many ways endothelial cells can be damaged. For example, increased blood pressure (hypertension) is one common cause of endothelial damage. Diseases of blood vessel walls [40] (e.g., atherosclerosis) can damage endothelial cells directly or roughen the endothelial lining producing turbulent blood flow that, in turn, damages endothelial cells. If blood flow becomes abnormally slow, platelets have the opportunity to contact the endothelial lining. Once the platelets are in contact they may stick and initiate the intrinsic blood coagulation pathway. Similarly, other conditions may indirectly initiate blood clotting. For example, certain alterations in red blood cells (e.g., some anemias) can make them stickier than normal resulting in clumping of RBCs (erythrocytes) and reduced blood flow. Similarly, overproduction of RBCs (polycythemia) can cause the blood flow to slow.

6.4 Hemocompatibility

Hemocompatibility can be defined as the implanted material's compatibility with the blood. This definition takes into account the following [41]:

- The activation of the blood coagulation system at the blood-material interface
- The response of the immune system induced after the blood-material contact
- The other tissue responses which appear as consequence of the blood-material contact.

The hemocompatibility of the implant material is closely related to the reactions between the surface of the biomaterial and the inflammatory host response [42].

There are several factors that contribute to this and these may depend on individual patient characteristics, such as general health, age, tissue perfusion, immunological factors, or implant characteristics, such as surface roughness and porosity, chemical reactions at the surface, corrosion properties of the material, and the toxicity of the individual metals present in the alloy [43].

The human body is able to resist against any form of attack from unknown foreign material(s). When a material (foreign body) is implanted in the human body, it comes in direct contact with blood. This contact between the blood and material leads to an inflammatory reaction directed against the material. The following are some of the interactions that can be considered either as good or bad depending on the circumstances [44]:

1. Adsorption of proteins, lipids, or calcium from the blood onto the surface of the device. At a later step, migration of the surface adsorbed material into the bulk may occur.
2. Adhesion of platelets, leukocytes or erythrocytes onto the surface of the device.
3. Formation of "capsules" on the outer surface of the device, or "pseudo-intima" on the inner surface of a device, e.g. for a vascular graft.

The interactions that are generally regarded as undesirable are as follows [45]:

1. Platelet activation and aggregation.
2. Formation of thrombi (blood clot) on the device surface.
3. Transport of thrombotic or other material from the surface of the device to another site via the circulatory system.
4. Injury to cells or tissues adjacent to the device.
5. Injury to circulating blood cells, e.g. Hemolysis (Hemolysis is the breakage of the red blood cell's (RBC's) membrane, causing the release of the hemoglobin and other internal components into the surrounding fluid).
6. Overenthusiastic cell proliferation (increase in cell number by division) on or adjacent to the device resulting in reduced or turbulent blood flow of the blood at the device location.
7. Adsorption of proteins, lipids, or calcium from the blood onto the surface of the device.

The surface of the biomedical device implanted in the body is critically important because it comes into direct contact with the surroundings (i.e., tissues, blood, etc.). It is the response of the host to the material that defines the character of the biomaterial that is used in medical surgery. Surface roughness/smoothness is another important parameter, which can have a noticeable influence on the hemocompatibility of a biomaterial carrying the surface. For example in artificial heart valve applications, a smooth surface is essential as surface roughness causes turbulence in the blood, which leads to the integrity of the red cells being damaged causing bacteria to adhere, and blood coagulation and clots.

A relationship has been proposed between surface charges on materials and protein deposition levels on such surfaces [46]. It has also been stated that the

biocompatibility of materials can be influenced by factors such as hydrophobicity and topography [47, 48]. Reports from Ahluwalia et al. [49] and Bowlin and Rittger [50] based on surface potential measurements using the vibrating Kelvin probe method suggest that positively charged surfaces enhance cell adhesion in comparison to neutral or negatively charged surfaces. The hydrophylic or hydrophobic nature of a surface has also been associated with the extent of cell interactions with the surface [49, 51]. There have also been suggestions in the literature that the electron conduction of materials might have an effect on their biocompatibility. Bruck [52–54] reported, based on his studies on pyrolytic polymers, that intrinsic electronic conduction and semi-conduction may be involved in the extent of hemocompatibility observed in the materials. Bruck [52–54] observed clotting times, six to nine times longer than those observed with non-conducting polymers and also observed little or no platelet aggregation in electro-conducting polymers, when compared to non-conducting control samples.

Boldz and Schaldach [55] and Chen et al. [56] have also reported that there is a relationship between the electronic structure of a surface and it's hemocompatibility. According to these authors [55, 56], the denaturing of fibrinogen at a surface involves an electron transfer from the inactive site of the protein to the surface of the solid, i.e. an oxidation process takes place (a redox reaction). They suggested that fibrinogen decomposes after the electron transfer and transforms into fibrin-monomer and fibrin-peptides, with a cross-linking to form thrombus. Fibrinogen has been reported to have an electronic structure similar to a semiconductor [55] and a band-gap of $\sim$1.8 eV. Boldz and Schaldach [55] have suggested that hemocompatible surfaces will be expected to have a low density of unoccupied states in the energy range of the transfer level with an energy band-gap of greater than 1.8 eV. Their reasoning was that if the charge transfer energy range lies in the band-gap energy range of the artificial surface, the oxidation process involving electron transfer is inhibited. It is well known from the theory of hetero-junctions, that when the band-gap of a semiconductor is contained within the band-gap of another semiconductor (i.e., straddling hetero-junction), electrons and holes need energy (ΔEc and ΔEV) respectively to move from the semiconductor with the small band-gap to the one with the larger band-gap. ΔEc and ΔEV represent the differences of the conduction and valence band edges of the two semiconductors.

6.5 Endothelium and Endothelial Cell Seeding

Endothelium is the layer of thin, flat cells that line the interior surface of blood vessels, forming an interface between circulating blood inside the vessel and rest of the vessel wall. All blood vessels and lymph vessels (a network of vessels throughout the body that drains fluid from tissues and returns it to the bloodstream, managing fluid levels in the body, filtering out bacteria, and housing types of white blood cells) are lined with endothelial cells; the layer being called the *endothelium.*

Under normal circumstances the endothelial surface prevents blood clotting and allows smooth flowing of the blood thus controlling blood pressure [57]. Surface molecules of endothelial cells act as receptors and interaction sites for a whole host of important molecules, especially those that attract or repel WBCs (leucocytes). Leucocyte adhesion molecules are important in inflammation and are normally repelled by endothelium in order to allow the free flow of blood cells over the surface. But in inflammatory states the WBCs are actually attracted to the endothelium by adhesion molecules. In addition, platelets start sticking to the surface and later to each other making a network that end up making a clot [58].

Endothelium is known as "nature's hemocompatible surface", and the performance of any biomaterial's hemocompatibility must be compared with that of the endothelium [59].

A promising and logical approach to reduce thrombogenicity is endothelial cell seeding to synthetic vascular grafts. Endothelial cell function on synthetic grafts can be improved by inserting genes to reduce or inhibit thrombus formation. The graft can be modified to release agents, which inhibit smooth muscle cell growth and promote endothelial cell adhesion and function. For synthetic grafts with diameters less than 6 mm, vascular graft acceptance requires an endothelial monolayer on the graft's luminal surface to reduce thrombosis. Grafts are seeded with endothelial cells prior to insertion in the body in order to encourage the development of a monolayer of endothelial cells. Seeding and implantation must occur rapidly in order to minimize the chance of infection [60]. Otherwise, a confluent endothelial monolayer will not form and a subconfluent layer of endothelium will be exposed to fluid shear stresses, resulting in complications. Endothelial cell adhesion to a synthetic surface involves a defined set of molecular interactions that influence subsequent cell division and/or protein synthesis. Endothelial cell adhesion to vascular grafts involves:

1. attaching and spreading on a rough synthetic surface;
2. maintenance of attachment following exposure to blood flow;
3. normal function.

Experimentally, cell adhesion to foreign biomaterials, such as polymers is influenced by manipulation of the following variables:

1. The surface properties which influence non-specific and specific interactions (e.g., hydrophobicity, surface charge, presence of oxygen and amine groups);
2. The density and affinity of adhesion molecules on the surface;
3. Covalent and non-covalent interactions between the cell and surface molecules;
4. The time of interaction between the cell and the surface;
5. Signalling events within the cell to promote or inhibit cell spreading.

Cell attachment and spreading on artificial surfaces is mediated by bonds formed between cell adhesion proteins at the substrate surface and protein receptors embedded in the cell membrane. The role of adsorbed proteins in cell adhesion has been reviewed elsewhere [61].

6.6 Surface Engineering Artificial Heart Valves

In the following section(s) we focus on biocompatible coatings used to improve the surface characteristics of blood contacting devices, such as mechanical heart valves in order to overcome thrombus formation.

6.6.1 Biological Properties of Diamond-Like Carbon

Diamond like carbon (DLC) is a very promising coating because it is chemically inert, extremely hard, wear resistant and biocompatible [62, 63]. Biological properties of DLC can be altered by alloying [64–67]. DLC, as a biocompatible base material, can be easily alloyed with other biocompatible materials such as titanium or silicon, or toxic materials such as silver, copper and vanadium [68].

In the investigation of hydrogen free DLC, test results show that the higher bonding ratio of sp3/sp2 may contribute to the blood compatibility of DLC. However, as the DLC films doped with nitrogen of certain concentration, even if the bonding ratio of sp3/sp2 is decreased, the behavior of platelet adhesion can be improved significantly [69]. A similar phenomenon has been observed in hydrogen free DLC film doped with argon [70]. As argon atoms are introduced into DLC to a certain content, the bonding ratio Sp3/Sp2 of the DLC films changes from 78/22 to 56/44, and the platelets adhesion behavior of the films is modified significantly. It is also found that above phenomena may be related to changes in surface tension on the films. If DLC films are annealed at the temperature of 600 °C, the DLC films present a p-type characteristic. The blood compatibility becomes deteriorated [71, 72]. The DLC film, which has a more hydrophilic nature, seems to have better blood compatibility than that of the DLC film with more hydrophobic nature [73].

The platelet adhesion is reduced on DLC when compared with Ti surface. Jones et al. [74, 75] showed by In vitro experiments that the DLC surfaces expressed a decreased area coverage of platelets compared to titanium, TiN and TiC. Whereas on the Ti containing surface platelet activation, clotting of platelets and thrombus formation was observed, no such reaction took place on the DLC surface. High albumin to fibrinogen ratio was also observed in DLC as compare to Ti, TiN and Tic coatings which is an indication of the ability of DLC to prevent thrombus formation [75]. Dion et al. [76] also observed higher albumin/fibrinogen ratio in DLC as compare to silicone (a polymer widely used for implants). Cui and Li [77] state from in vitro experiment that DLC and CN films show good tissue- and blood compatibility.

Gutebsohn et al. [78] analysed the intensity of the platelet activation antigens CD62p and CD63 and showed that DLC coating of a stainless steel coronary artery stent resulted in a decrease of these antigens. It indicates a low platelet activation on DLC and, therefore, a low tendency for thrombus formation. In this in vitro experiment, they showed that DLC coating suppressed metal ion release from the

stainless steel stent which may influence negatively the hemocompatibility of the surface. Alanazi et al. [79] conducted an in vitro experiment using a flow chamber and whole human blood, which showed a low percentage of DLC to adhere to the surface. However, the results differed with the deposition conditions used to produce DLC.

Thomson et al. [80] have studied the inflammatory potential of DLC-coated tissue culture plates by measuring the levels of the lysosomal enzymes released from macrophages cells (cells play major role in inflammation and the response to foreign bodies). They showed that no inflammatory response was elicited in vitro. Similarly Fibroblast is another cell used to test biocompatibility. Preliminary result [81] showed no statistically significant differences between fibroblasts grown on in control polystyrene plate and those grown in DLC coating.

Some work has been done showing change in bioreaction on DLC due to alloying [82–88]. A reduced inflammatory reaction was observed on implanted stents when SiO_x was added to DLC [82]. It was noticed that proteins adsorption could be altered as a function of Ti content [85, 87] in the DLC Osteoclasts (osteoclast is a large multinucleated cell that plays an active role in bone resorption) was inhibited by the addition of Ti into DLC [83, 84]. The addition of Ca-O to a DLC film resulted in decreased wetting angle, improved cell morphology and viability of mouse fibroblast cells [88].

6.6.2 Other Biocompatible Coatings

It is worth considering that titanium and its alloys have been used in biomedical implants for many years now and therefore it is sensible to look at the surface treatment of titanium alloys for producing superior surface characteristics, which could be ideal for heart valves. It should be noted that titanium alloys are not brittle like PyC. A large number of research scientists have deposited Ti-based coatings, using energised vapour-assisted deposition methods, and studied their potentials for use in biomedical areas, such as heart valves or stents. Yang et al. [89] deposited Ti-O thin films using plasma immersion ion implantation technique and characterised the anti-coagulant property employing in vivo methods. They found that the Ti-O film coatings exhibited better thrombo-resistant properties than low-temperature isotropic carbon (LTIC), in long-term implantation. Chen et al. [90] deposited TiO coatings doped with Ta, using magnetron sputtering and thermal oxidation procedures, and studied the antithrombogenic and hemocompatibility of $Ti(Ta^{+5})O_2$ thin films. The blood compatibility was measured in vitro using blood clotting and platelet adhesion measurements. The films were found to exhibit attractive blood compatibility exceeding that of LTIC. Leng et al. [91] investigated the biomedical properties of tantalum nitride (TaN) thin films. They demonstrated that the blood compatibility of TaN films was superior to other common biocompatible coatings, such as TiN, Ta and LTIC. Potential heart valve duplex coatings, consisting of layers of Ti-O and Ti-N, have been deposited onto biomedical

Ti-alloy by Leng et al. [92] and their blood compatibility and mechanical properties have been characterised. The TiO layer was designed to improve the blood compatibility, whereas, TiN was deposited to improve the mechanical properties of the TiO/TiN duplex coatings. They found that the duplex coatings displayed (i) better blood compatibility than LTIC; (ii) greater microhardness; and (iii) improved wear resistant than Ti6Al4 V alloys. It has been reported that the TiO coatings display superior blood compatibility to LTIC [93].

6.6.3 *Chromium Modified DLC*

Chromium modified DLC (Cr-DLC) films with varying %Cr content were deposited on 50 mm circular silicon wafers using magnetron sputtering utilising the intensified plasma assisted processing (IPAP) process [94]. Table 6.2 shows the conditions employed to deposit the Cr-DLC samples with varying %Cr contents. The as-deposited Cr-DLC films were nanocomposite and consisted of nano-sized chromium carbide particles embedded in an amorphous DLC matrix.

Figure 6.3 shows the XRD spectrum for a typical Cr-DLC film, with 10 % Cr, in the 2-theta range 15°–115°. It was found from HRTEM studies that the

Table 6.2 Deposition parameters employed in depositing Cr-DLC films using the IPAP process

Sample	Deposition rate (nm/min)	Magnetron current (mA)
Cr(1 %)DLC	6.6	155
Cr(5 %)DLC	7.6	220
Cr(10 %)DLC	15.2	310

Bias voltage: −1000 V; flow rate (sccm): CH_4:Ar 7.4:40; Chamber pressure: 2.66 Pa; Processing time: 2 h; Sputter cleaning: Ar^+ 3.3 Pa, −1500 V, ∼ 20 min

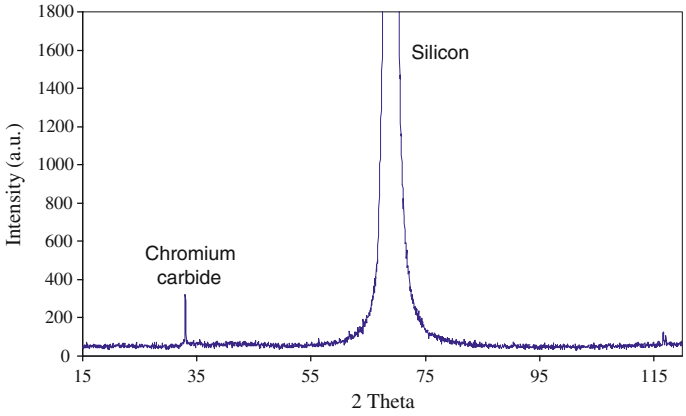

Fig. 6.3 XRD spectrum for sample Cr(10 %)-DLC showing the silicon substrate and chromium carbide peaks

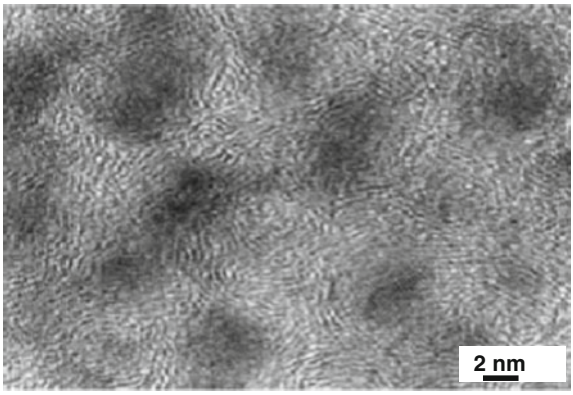

Fig. 6.4 High Resolution TEM micrograph of the 5 %Cr-DLC sample showing the microstructure exhibited by the thin film coating

nano-structured Cr-DLC film consisted of nano-sized (5 nm) chromium carbide particles. The presence of chromium carbide particles was evident from the XRD peak centered at around 33° 2-theta value. The other major intense peak centered at around 68° 2-theta value corresponds to silicon, which was from the silicon wafer substrate material. We found that the Cr-carbide nano-particles were embedded deep into the amorphous DLC matrix and were not present on the DLC surface. This enabled the nano-particles to be protected by the amorphous DLC film.

Figure 6.4 Displays the high-resolution (HRTEM) micrograph representing 5 % Cr-DLC and showing the microstructure exhibited by the same as-deposited film. The micrograph shows the presence of nanoclusters (NCs) around 5 nm in diameter surrounded by a $\sim$2 nm thick amorphous matrix. Electron diffraction showed that the dark contrast NCs correspond to Cr carbide, encapsulated by an amorphous matrix.

The contact angle measurements obtained using the optical method are as shown in Fig. 6.5. Chromium doping leads to a gradual increase in the contact angles as shown in Fig. 6.5. The increase begins to level out with Cr content above 5 % where it begins to reach saturation point. The average contact angles displayed by samples 1 %Cr-, 5 %Cr- and 10 %Cr- DLC samples were calculated to be 80.285°, 97.23° and 99.274°, respectively. Raman spectroscopy was used to characterise the quality of the as-deposited Cr-DLC films with different Cr contents, in terms of diamond carbon-phase purity. The data from the Raman spectroscopy studies, including intensities of D (I_D) and G (I_G) bands, Full width at half maximum (FWHM) of I_D and I_G bands, I_D/I_G ratio and the positioning of the D and G band peaks can all be found in Table 6.3. From the Raman investigations, it was found that the Cr-DLC films displayed the two D and G bands of graphite. The G and D bands are usually assigned to zone centre of phonons of E_{2g} symmetry and K-point phonons of A_{1g} symmetry, respectively. The D band peaks for the three Cr-DLC films were positioned at 1401.6, 1408.4 and 1306.8 cm^{-1}, whereas, the G band peaks were centered at 1538.8, 1540.6 and 1511.8 cm^{-1}. From both D and G bands, 5 %Cr-DLC sample displayed the smallest values for FWHM. The I_D/I_G ratio was the least for 10 % Cr-DLC and the highest out of the three samples for the 5 %Cr-DLC film. This

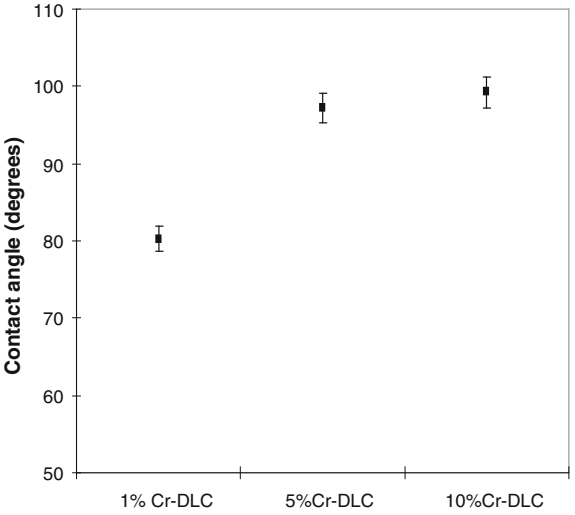

Fig. 6.5 Graph showing the contact angle measurements as obtained using the optical method for the three Cr-DLC samples

Table 6.3 Raman data obtained for the three Cr-DLC samples

Sample	%Cr	I_D (a.u.)	I_G (a.u.)	FWHM (D)	D-peak (cm^{-1})	G-peak (cm^{-1})
CrDLC1	1	21.833	21.043	363.68	1401.6	1538.8
CrDLC2	5	21.628	20.415	361.08	1408.4	1540.6
CrDLC3	10	45.588	49.748	389.90	1306.8	1511.8

The data includes I_D and I_G peak intensities; Full-Width at Half Maximum (FWHM) values for D band; and D and G band intensities

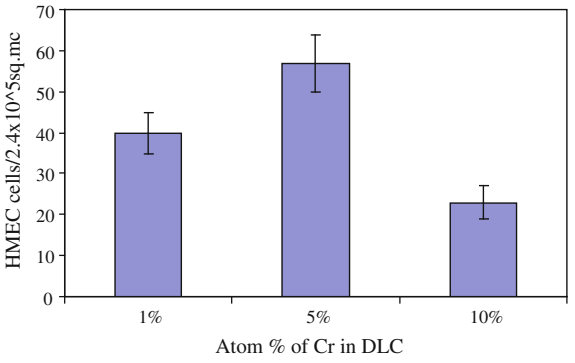

Fig. 6.6 Graph showing the cell count results obtained after seeding the human microvascular endothelial cells onto the Cr-DLC surfaces

suggests that there are more disordered graphitic phases in sample 5 %Cr-DLC and the least similar disorder in 10 %Cr-DLC film.

The results of the cell count analysis shown in Fig. 6.6, give an indication of the influence of Cr content in Cr-DLC films on the adherent cell population of the three samples, 5 %Cr-DLC provided the best conditions for HMV-EC seeding,

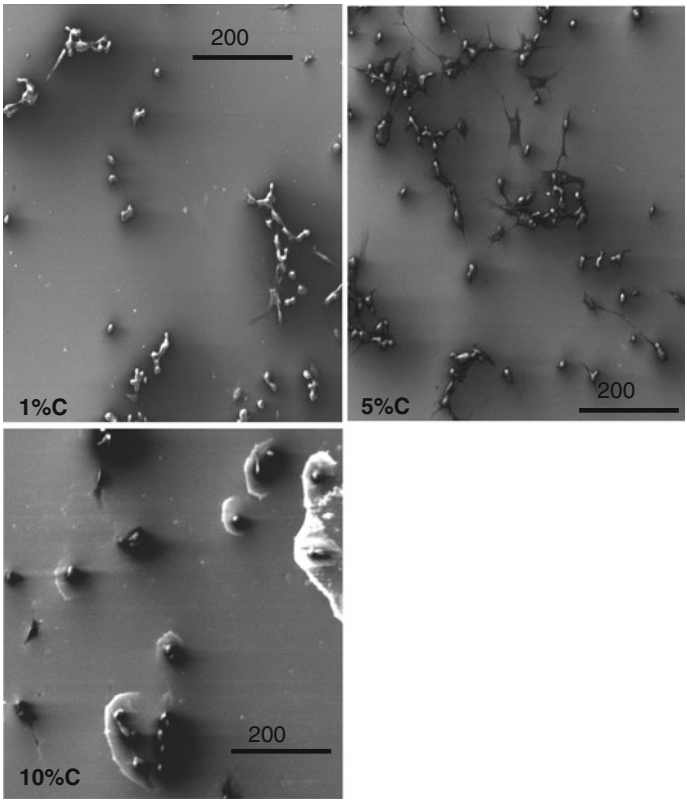

Fig. 6.7 SEM micrographs showing endothelial cell seeding on the three types of Cr-DLC film surfaces

while, 10 %Cr-DLC film resulted in the least population of adherent human endothelial cells onto its surface. It should be noted that sample 1 %Cr-DLC was a better base material for seeding endothelial cells than 10 %Cr-DLC. Figure 6.7 displays the SEM micrographs showing the population of endothelial cell attachment onto 1 %Cr-, 5 %Cr- and 10 %Cr- DLC film surfaces. All three films displayed smooth surface profiles, which is a key requirement in artificial heart valve applications. It was noted that there was a direct correlation between the I_D/I_G ratio and the population of endothelial cells attaching to the three Cr-DLC films with different Cr contents. We noted that from the three Cr-DLC films, the highest value displayed for the I_D/I_G ratio was by 5 %Cr-DLC film, which also gave the highest adherent cell population onto its surface. The lowest I_D/I_G ratio value was for 10 % Cr-DLC, which showed the least, from the three samples investigated in this study, population of cell attachment to its surface after conducting the cell seeding procedures. Furthermore, the density of nano-sized Cr-carbide particles produced during film growth is expected to be the highest in 10 %Cr-DLC and the least in

1 %Cr-DLC sample. This difference in the Cr-carbide content in the three films is sure to influence the surface chemistry of the DLC films.

It was noted that there was a direct correlation between the I_D/I_G ratio and the population of endothelial cells attaching to the three Cr-DLC films with different Cr contents. We noted that from the three Cr-DLC films, the highest value displayed for the I_D/I_G ratio was by 5 %Cr-DLC film, which also gave the highest adherent cell population onto its surface. The lowest I_D/I_G ratio value was for 10 %Cr-DLC, which showed the least, from the three samples investigated in this study, population of cell attachment to its surface after conducting the cell seeding procedures. It is apparent that increased Cr content into the growing DLC films alters the microstructure of the deposited films. Furthermore, the density of nano-sized Cr-carbide particles produced during film growth is expected to be the highest in 10 %Cr-DLC and the least in 1 %Cr-DLC sample. This difference in the Cr-carbide content in the three films is sure to influence the surface chemistry of the DLC films. It was difficult to correlate the water contact angle results with the cell seeding efficiency of the films. However, Grinell [95] reported that wettable (hydrophilic) surfaces tend to be more conducive to cell adhesion than similar hydrophobic surfaces.

6.6.4 Silicon Modified DLC

We investigate to evaluate the potential of a more readily available synthetic silicon modified carbon film (Si-DLC) for thrombo-resistant applications. We study the adhesion and spreading of micro-vascular endothelial cells on the surface of Si-DLC and thermally annealed Si-DLC films. Table 6.4 shows the deposition conditions employed for preparing DLC and Si-DLC film samples.

Table 6.4 Deposition conditions for the DLC and Si-DLC film

Sample	DLC	SD5	SD10	SD15	SD20
DC-volts (V)	400	400	400	400	400
RF-power (W)	~150	~160	~165	~175	~210
Temperature (°C)	ambient	ambient	ambient	ambient	ambient
Pressure (base)/torr	6×10^{-6}	6×10^{-6}	6×10^{-6}	6×10^{-6}	6×10^{-6}
Gas ratio (sccm) Ar: C_2H_2: TMS	10:20:0	10:20:5	10:20:10	10:20:15	10:20:20
Pressure (deposition)/mtorr	$\sim 1.3 \times 10^{-2}$	$\sim 1.9 \times 10^{-2}$	$\sim 2.7 \times 10^{-2}$	$\sim 3.2 \times 10^{-2}$	$\sim 4.5 \times 10^{-2}$
Time (deposition)/min	5	5	5	5	5

The numbers in SD5, SD10, SD15 and SD20 represents the flow rates of TMS in sccm used during deposition

Table 6.5 Raman features of a-C:H and a-C:H:Si thin films

Bias Volts (V)	TMS (sccm)	I_D (a. u)	I_G (a.u)	FWHM (D)	FWHM (G)	I_D/I_G	D-peak (cm^{-1})	G-peak (cm^{-1})
400	5	1231.7	4397.6	211	104.6	0.28	1336.48	1504.99
400	10	1383.2	6396.5	192.8	103.5	0.21	1310.1	1490.07
400	15	2206.7	9687.6	198.8	103.4	0.22	1296.36	1483.18
400	20	1584.4	8423.5	205.5	102.7	0.18	1278.99	1477.16
400	0	1775.9	4501.8	194.8	108.5	0.39	1349.5	1541.96

Raman spectroscopy was used to characterise both the as deposited and the thermally annealed DLC and Si-DLC films. The thermal annealing was conducted at temperatures between 200 and 600 °C under a flowing nitrogen atmosphere for 2 h. The information collected from the Raman spectroscopy investigation included the Raman-peak intensities for the D and G-peaks, that is I_D and I_G peaks, the I_D/I_G ratios and the full-width at half maximum (FWHM) for both peaks as shown in Table 6.5.

The results of the Raman spectroscopy show an increase in the I_D/I_G ratios (Fig. 6.8) with annealing temperature for the DLC and Si-DLC films in agreement with earlier reports in the literature [96]. The increase in I_D/I_G ratio on the annealing of DLC has been associated with the growth of crystallite structures in the DLC thin film. In the DLC films the increase in the I_D/I_G ratio with thermal annealing is linear, but for the Si-DLC films the I_D/I_G ratio increase occurred only at relatively higher annealing temperatures of 300 °C and above. The I_D/I_G ratio also decreases with increasing amount of silicon in the films as shown in Fig. 6.8.

Physical and chemical changes in carbon materials resulting in graphitisation occurs during thermal annealing. Graphitisation is associated with increased sp^2 content, while silicon doping tends to increase the number of sp^3 sites [96]. Silicon does not form π-bonds and it therefore increases the number of sp^3 sites in the Si-DLC films.

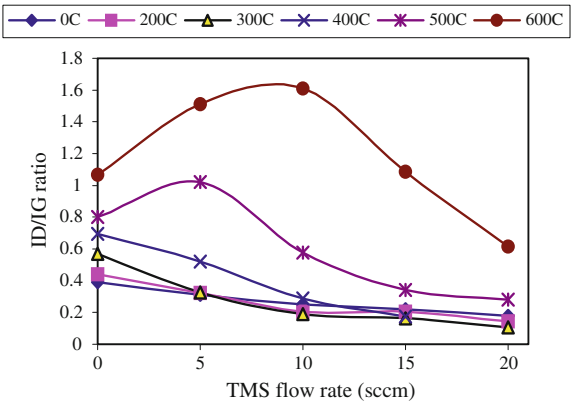

Fig. 6.8 Raman I_D/I_G ratios for the DLC and Si-DLC films both non-annealed and thermally annealed (200–600 °C) under flowing nitrogen for 2 h versus the TMS flow rate during deposition

Table 6.6 XPS chemical analysis and binding energies (B.E) of elements in the as-deposited DLC and Si-DLC thin films

Sample	C (%) (B.E/eV)	Peak (B.E/eV)	O (%) (B.E/eV)	Peak (B.E/eV)	Si (%) (B.E/eV)	Peak (B.E/eV)
DLC/undoped/400 V	89.58	285.11	10.07	532.51	0.36	102.41
DLC(SD5)/400 V	82.83	285.01	12.21	533.31	4.96	101.51
DLC(SD10)/400 V	79.07	285.09	13.32	533.09	7.61	101.29
DLC(SD15)/400 V	76.57	285.10	13.80	533.10	9.63	101.30
DLC(SD20)/400 V	77.09	285.10	12.29	533.10	10.62	101.30

Typical x-ray photoelectron spectroscopy (XPS) chemical analysis for the as deposited and annealed DLC and Si-DLC films are as indicated in Table 6.6. The peak binding energies of the films are consistent with those reported in the literature by Dementjev [97], Grill [98], Constant and Le Normand [99] and Baker and Hammer [100]. There was only a slight change in the values of the binding energies for the silicon-modified films even after annealing to 600 °C. We also observed an increase in sp^3/sp^2 ratios after peak de-convolution.

Typical I–V curves of the metal-semiconductor-metal (MSM) sandwich (Fig. 6.8) shows that the electrical conduction mechanism is not simple ohmic but semi-conducting. We observed that silicon addition to DLC lowers it's resistivity. Thermal annealing of both DLC and Si-DLC leads to a decrease in resistivity (Fig. 6.9), which is likely to be associated with microstructural changes as indicated by the sp^3/sp^2 ratio changes observed for the annealed films by Raman spectroscopy (Fig. 6.10).

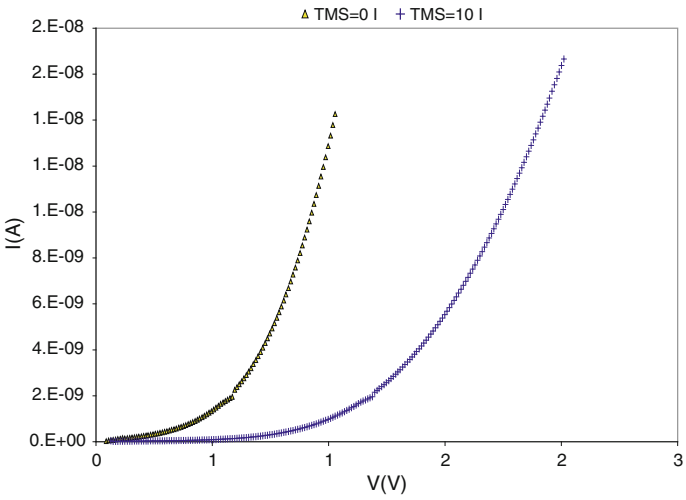

Fig. 6.9 Typical current–voltage (I–V) curves of DLC and Si-DLC (TMS flow rate of 10 sccm)

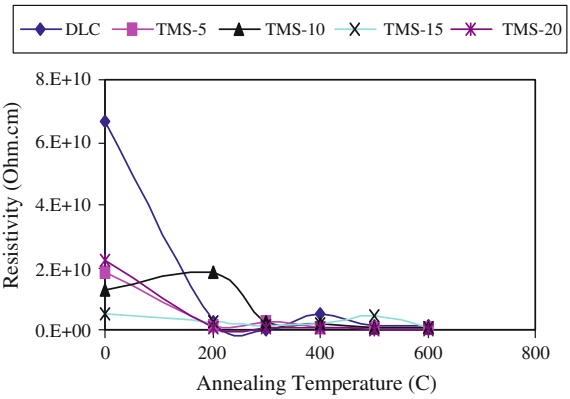

Fig. 6.10 Resistivity versus annealing temperature of DLC and Si-DLC films thermally annealed at 200–600 °C (on *x*-axis 0 indicates room temperature)

When thermal annealing at 600 °C, the conductivity of both DLC and Si-DLC becomes simple Ohmic. This result is consistent with the Raman spectroscopy investigation, which revealed graphitisation at this annealing temperature. The increasing graphitic content of the films at an annealing temperature of 600 °C increases the proportion of de-localised π-bonded electrons and therefore increases the electrical conductivity of the films at this annealing temperature, which results in the ohmic-behaviour.

The contact angle measurement results obtained using the optical method are as shown in Fig. 6.11 and the results of the surface energy measured by the Wilhemy plate technique for films deposited on silicon substrates are as shown in Table 6.6. Silicon doping leads to an increase in the contact angles as shown in Fig. 6.11. Silicon doping also results in a slight reduction of the surface energy values as shown in Table 6.7.

As shown in Fig. 6.12a, there seems to be a little cell adhesion on the non-doped DLC seeded with endothelial cells in comparison to the silicon modified DLC films Fig. 6.12b. The measured contact angle for the non-doped DLC film is 72° (which is lower than those of Si-DLC, Fig. 6.11). The general trend observed in our experiments based on scanning electron microscopy (SEM) and cell counting using

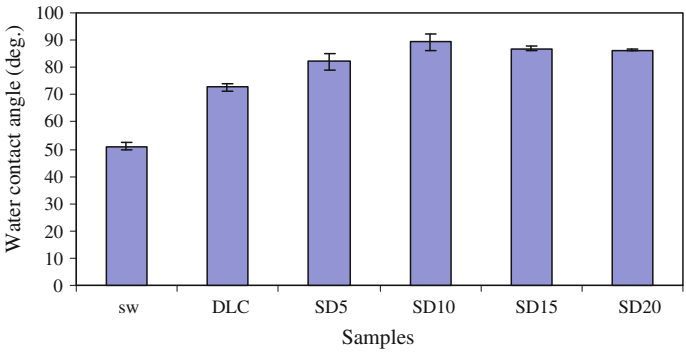

Fig. 6.11 Contact angle in water using direct optical technique

Table 6.7 Surface energy and contact angle measurements for the films deposited on silicon substrates

TMS/ sccm	Bias volt (V)	$\theta_{adv\ water}$ (deg.)	$\theta_{rec\ water}$ (deg.)	γ_P (mN/m)	γ_D (nM/m)	γ_S (mN/m)
(DLC)	400	88.01	55.32	1.17	41.05	42.22
(SD5)	400	82.12	49.27	2.5	41.53	44.03
(SD10)	400	89.54	27.7	1.5	35.73	37.24
(SD15)	400	90.76	41.48	1.24	35.88	37.13

γ_P polar components, γ_D dispersive components, and γ_S total surface energy

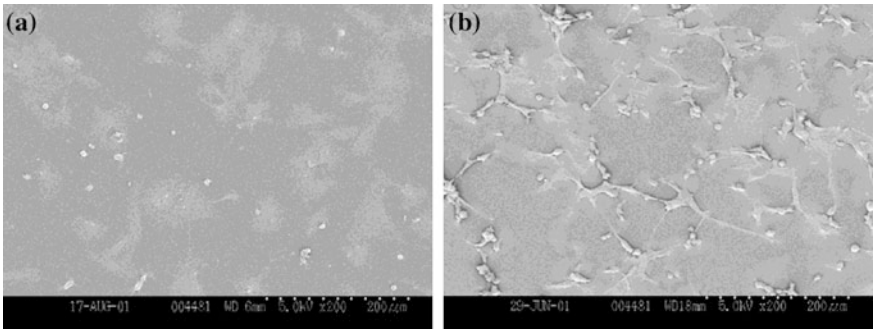

Fig. 6.12 **a** SEM image of DLC seeded with endothelial cells for ~6 h; ×200: **b** Si-DLC (TMS flow rate of 5 sccm) seeded with endothelial cells for ~6 h; ×200

SEM images indicated an increase in cell adhesion with silicon addition in the Si-DLC films. Contrary to earlier reports in the literature by Grinell [101] that wettable (hydrophilic) surfaces tend to be more conducive to cell adhesion, we have observed that more hydrophobic surfaces containing increasing amounts of silicon in the Si-DLC films and increasing contact angle with water, tends to promote human endothelial cell growth and adhesion on the films. The results of the measurements of the surface energy of the DLC and Si-DLC films indicates a substantial contribution to the total surface energy by the dispersive component term, which might play a part in the cell adhesion process.

The contact potential difference (CPD) measures the surface potential difference between the surface of the films and the vibrating reference electrode made of brass (Cu–Zn). The relationship between the work function of the films $\Phi_{(film)}$, the work function of the reference electrode $\Phi_{(brass)}$ and the CPD is given by:

$$\mathrm{CPD} = \Phi_{\mathrm{probe(brass)}} - \Phi_{\mathrm{sample}} = \Phi_{\mathrm{probe(brass)}} - \left[\chi + (\mathrm{E_C} - \mathrm{E_F})_{\mathrm{bulk}}\right] - \Phi_{\mathrm{ss}} \quad (6.1)$$

The changes in the CPD are related to changes in the electron affinity, χ, band bending due to surface states Φ_{ss}, or a shift of the bulk Fermi level $(Ec - E_f)_b$. If χ remains constant, then the changes in the CPD are directly related to the shift of the Fermi level in the bulk material and band bending in the surface states [102–104].

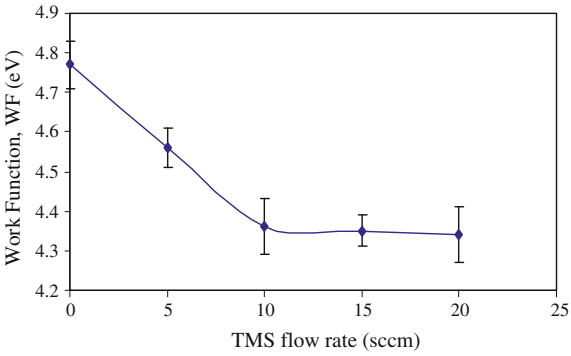

Fig. 6.13 Work function results of DLC and Si-DLC

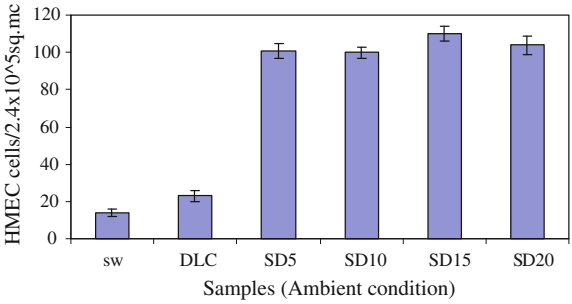

Fig. 6.14 Human micro-vascular endothelial cells (HMEC-1) adhesion on DLC and Si-DLC as obtained (ambient condition, un-annealed samples)

The result of the work-function measurements is as shown in Fig. 6.13. The work function decreased with silicon addition. The decrease in work function values has also been associated with a reduction in the net surface dipole [105]. Bolz and Schaldach [106] have already proposed that the early stages of thrombus formation are preceded by an electron transfer oxidation process, resulting in the transformation of fibrinogen to a fibrin polymer. We observed a substantial increase in the number of adherent endothelial cells in the Si-DLC compared to the DLC films as shown in Fig. 6.14, but further silicon addition did not lead to any substantial change in the number of adherent cells on the Si-DLC film surface. It has been suggested that the cell adhesion process depends on the sign of the charge carried by the adherent cell. Positively charged surfaces will attract cells with a negative charge or dipole and vice versa [106].

The results of the cell count analysis, giving an indication of the adherent cell population against the annealing temperatures are as shown in Figs. 6.15a–c. There is a considerable drop in the population of adherent human endothelial cells for DLC thermally annealed at 600 °C compared to the film annealed at 200 °C as shown in Fig. 6.15a. The Raman spectrum of the film annealed at 600 °C indicates a substantial graphitisation, and this is also the case for the film annealed at 500 °C. Annealing DLC at 500 and 600 °C leads to a substantial graphitisation and our current observation is that this does not appear favourable for human endothelial cell adhesion and growth, although the graphite phase is associated with an

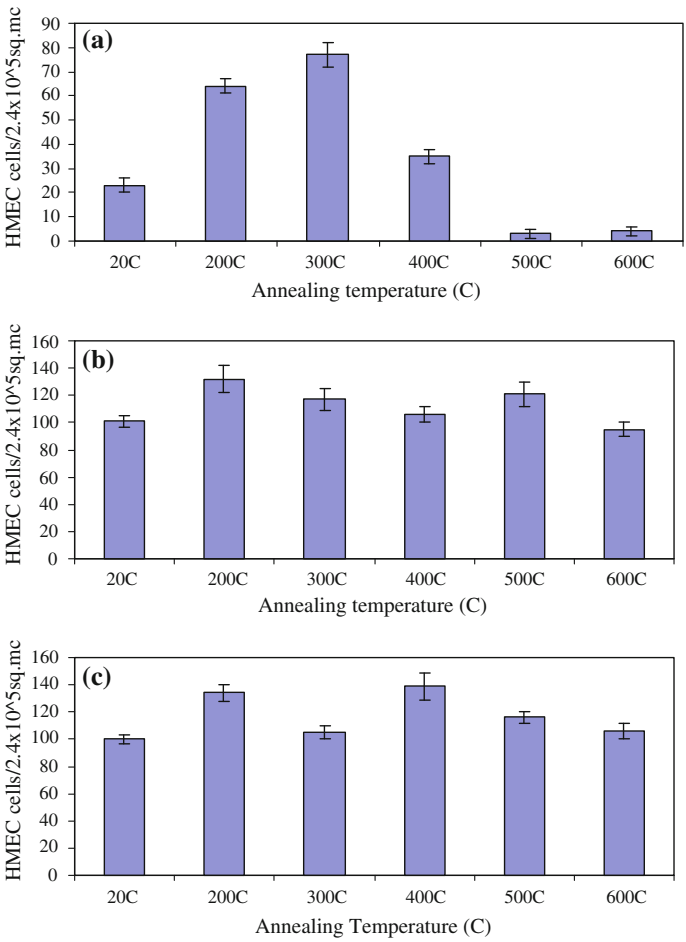

Fig. 6.15 **a** Human endothelial cell adhesion on DLC (as deposited and thermally annealed, 200–600 °C; 20 °C = ambient temperature): **b** Si-DLC (TMS flow rate, 5 sccm, as deposited and thermally annealed, 200–600 °C, 20 °C = ambient temperature); **c** Si-DLC (TMS flow rate, 10 sccm, as deposited and thermally annealed, 200–600 °C, 20 °C = ambient temperature)

improvement in electrical conduction. For the Si-DLC samples annealed between 200 and 600 °C, there was a fairly consistent population of endothelial cells for the 5 and 10 sccm TMS flow rate films as shown in Fig. 6.15b, c. In all the cases investigated for the DLC and Si-DLC films, we observed a direct correlation between electronic conduction in the films and the population of adherent human endothelial cells whenever there was no significant graphitisation detectable by

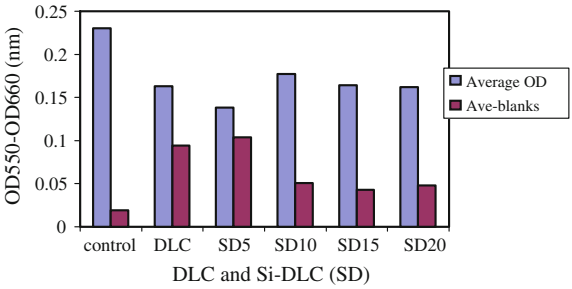

Fig. 6.16 Histogram of MTT-assay of HMEC seeded on 96 well culture plates that were coated with DLC and Si-DLC (TMS flow-rate, 5–20 sccm, SD5-20)

Raman spectroscopy. However, even when electronic conduction was relatively high in the films, graphitisation in such films always led to a substantial reduction in the population of adherent endothelial cells on it's surface. There is a significant statistical difference in endothelial cell count (at 95 % confidence interval level, with $p < 0.05$, paired t-test and Tukey test) between the samples DLC and Si-DLC at ambient temperature.

The results of the MTT-assay shown in the histogram in Fig. 6.16, give the optical density of the active cells in culture after fifty-six (56) h. The averaged-blanks values were subtracted from the total reading in order to take into account the optical density contribution due to the colour of the as-deposited DLC and Si-DLC thin films. This was confirmed by using the reader to read the optical density of the empty culture dishes, both coated and non-coated, and it was observed that there were some readings. The assay detects metabolism in the living cells and the intensity obtained is dependent on the degree of activity of the cells [107]. Further details of the statistical analysis of the MTT assay of HMECs on DLC and Si-DLC films using the ANOVA test has been reported elsewhere by some of the authors of this chapter [108].

6.7 Summary

The contents of the current chapter can be summarised as follows:

- Mechanical heart valves were introduced and the principal concerns relating to such valves were put forward.
- The history of mechanical heart valves has been reviewed dating back from 1952.
- The process of thrombosis has been defined, described and the principals of thrombus formation have been outlined.
- The chapter also discusses the hemocompatibility of biomaterials. Further, we describe the endothelium, its functions and endothelial cell seeding in modern biomaterials engineering.

- The hemocompatibility of DLC films has been reviewed and in particular results of investigations on Cr-DLC and Si-DLC films have been presented and discussed.
- The diamond-like films were deposited containing different levels of Cr and Si contents.
- The contact angle measurements showed that the surface contact angle gradually increased with %Cr content in the films and began to level off at around 10 % Cr content.
- Raman spectroscopy was used to characterise the D and G bands present in all the Cr-DLC films.
- The I_D/I_G ratios were correlated to the population of endothelial cell attachments onto Cr-DLC surfaces. High values of I_D/I_G ratio correlate with better HMC-EC attachment to 5 %Cr-DLC film. This finding suggests that disordered graphitic phases in the DLC film leads to enhancement in the seeding of endothelial cells.
- With silicon modified DLC films, we observed a direct correlation between adherent cell population on the film surfaces and electronic conduction.
- This correlation does not hold when graphitisation, which is detected by Raman spectroscopy, has occurred in the Si-DLC films regardless of their electronic conductivity.
- The micro-structural variation in the films was achieved by varying silicon content and by thermal annealing.
- A direct relationship between increasing contact angle of water (i.e. hydrophobicity) and adherent endothelial cell population was observed. This trend is the opposite of those reported in the literature for other cells, where a hydrophilic interaction was considered necessary for cell attachment on surfaces.
- We suspect that the interaction between endothelial cells and the Si-DLC films could be mediated by dispersive forces.
- Although the work function decreased with increasing silicon addition, and silicon addition lead to an initial increase in the population of adherent endothelial cells on the film surface, further silicon addition did not lead to any substantial changes in the number of adherent endothelial cells on the Si-DLC film surface.
- The cytotoxicity of the endothelial cells on the Si-DLC film was measured by the MTT-assay test and the cells are established to be viable after adhesion to the Si-DLC films.
- The biological response of human microvascular endothelial cells seeded on chromium and silicon modified diamond-like carbon films and on control surfaces was evaluated in terms of initial cell enhancement, growth and cytotoxicity.
- Endothelial cell adhesion and growth was found to be affected by changes in the microstructure of the films induced by chromium/silicon doping and thermal annealing of silicon modified diamond-like carbon films.

- We observed a significant statistical difference in endothelial cell count between DLC and Si-DLC films using the paired t-test.
- MTT-assay tests showed the endothelial cells to be viable when seeded on Si-DLC films before and after thermal treatment based on the ANOVA statistical test.

References

1. Barton, K., Campbell, A., Chinn, J. A., Griffin, C. D., Anderson, D. H., Klein, K., et al. (2001). *Biomedical Engineering Society (BMES) Bulletin, 25*(1), 3.
2. Hufnagel, C. A., & Harvey, W. P. (1953). *Bulletin of Georgetown University Medical Center, 6*, 60–63.
3. Gott, V. L., Alejo, D. E., & Cameron, D. E. (2003). *The Annals of Thoracic Surgery*, *76*, S2230–S2239.
4. Murray, G. (1956). *Angiology, 7*, 466.
5. Braunwald, N. S., Cooper, T., & Morow, A. G. (1960). *Journal of Thoracic and Cardiovascular Surgery, 40*, 1–11.
6. Bahnson, H. T., Spencer, F. C., Busse, E. F. G., & Davis, F. W, Jr. (1960). *Annals of Surgery, 152*, 494.
7. Roe, B. B., Owsley, J. W., & Boudoures, P. C. (1958). *Journal of Thoracic and Cardiovascular Surgery, 36*, 563–570.
8. Roe, B. B. (1969). *Journal of Thoracic and Cardiovascular Surgery, 58*, 59–61.
9. Braunwald, N. S., & Morrow, A. G. (1965). *Journal of Thoracic and Cardiovascular Surgery, 49*, 485–496.
10. DeWall, R. A., Qasim, N., & Carr, L. (2000). *The Annals of Thoracic Surgery*; *69*, 1612–1621.
11. Gott, V. L., Daggett, R. L., Whiffen, J. D., et al. (1964). *Journal of Thoracic and Cardiovascular Surgery, 48*, 713–725.
12. Cruz, A. B., Kaster, R. L., Simmons, R. L., & Lillehei, C. W. (1965). *Surgery, 58*, 995–998.
13. Wada, J., Lomatsu,S., Ikeda, K., et al. (1969). A new hingeless valve. In L. A. Brewer (Eds.), *Prosthetic heart valves* (pp. 304–314). Springfield: Charles C. Thomas.
14. Björk, V. O. (1969). *Journal of Thoracic and Cardiovascular Surgery, 3*, 1–10.
15. Carmen, R., & Mutha, S. C. (1972). *Journal of Biomedical Materials Research, 6*, 327–346.
16. Björk, V. O. (1974). *The surgical treatment of aortic valve disease*. Ingelhelm: C.H. Boehringer Sohn.
17. Messmer, B. J., Rothlin, M., & Senning, A. (1973). *Journal of Thoracic and Cardiovascular Surgery, 65*, 386–390.
18. Gott, V. L., Whiffen, J. D., & Valiathan, S. M. (1968). *Annals of the New York Academy of Sciences, 146*, 21–29.
19. Scott, S. M., Sethi, G. K., Bridgman, A. H., & Takaro, T. (1976). *The Annals of Thoracic Surgery, 21*, 483–486.
20. Beall, A. C., Jr., Morris, G. C., Jr., Noon, G. P., et al. (1973). *The Annals of Thoracic Surgery, 15*, 25–34.
21. Cedars-Sinai Medical center Prosthetic heart valve information, Division of Cardiology: http://www.csmc.edu/pdf/Heart_Valves.pdf
22. Lillehei, C. W., Kaster, R. L., Coleman, M., & Bloch, J. H. (1974). *NY State Journal of Medicine, 74*, 1426–1438.
23. FDA panel meeting for approval of the OmniCarbon®valve, PMA # P830039, 1998.

24. di Summa, M., Poletti, G., Breno, L., et al. (2002). *The Journal of Heart Valve Disease, 11*, 517–523
25. Starek, P. J. K., McLaurin, L. P., Wilcox, B. R., & Murry, G. F. (1976). *THe Annals of Thoracic Surgery, 22*, 362–368.
26. Starek, P. J. K., Beaudet, R. L., & Hall, V. K. (1987). The medtronic-hall valve:development and clinical expe-rience. In F. A. Crawford (Ed.), *Cardiac surgery current heart valve prosthesis* (pp. 223–236). Hanley & Belfus, Philadelphia.
27. *Food and Drug Administration Enforcement Report*, September 7, (1988).
28. Young, W. P., Daggett, R. L., & Gott, V. L. (1969). Long-term follow-up of patients with a hinged leaflet prosthetic heart valve. In L. A. Brewer (Ed.), *Prosthetic heart valves* (pp. 622–632). Springfield, IL: Charles C. Thomas.
29. Kalke, B. R. (1973). *Evaluation of a double-leaflet prosthetic heart valve of a new design for clinical use*. Ph.D. thesis, University of Minnesota.
30. *Lessons of Björk-Shiley Heart Valve Failure*. www.me.utexas.edu/∼uer/heartvalves/shiley.html
31. Klawitter, J. J. (1985). Design and in vitro testing of the duromedics bileaflet valve. In *First International Hemex Symposium on the Duromedics Bileaflet Valves*.
32. Richard, R., Beavan, A., & Strzepa, P. (1994). *Journal of Heart Valve Disease, 3*, S94–S101.
33. Craver, J. (1999) Carbomedics Prosthetic Heart Valve (tm). *European Journal Cardio-Thoracic Surgery, 15*(Suppl. 1) S3–Sll.
34. Prosthetic heart valves: History of mechanical heart valve replacement: *BMES Bulletin, 24*(4).
35. Campbell, A., Baldwin, T., Peterson, G., Bryant, J., & Ryder, K. (1996). *Journal of Heart Valve Disease, 5*, S124–S132.
36. Lung, B., Haghigat, T., Garbaz, E., et al. (1999) Incidence and predictors of prosthetic thrombosis on mitralbileaflet prostheses during the postoperative period. In *Congress of the European Society of Cardiology*, August 1999.
37. Bodnar, E., Arru, P., Butchard, E. G., et al. (1996). Panel discussion. *Journal of Heart Valve Disease, 5*, S148.
38. Gross, J., Shu, M., Dai, F., Ellis, J., & Yoganathan, A. (1996). *Journal of Heart Valve Disease, 5*, 581–590.
39. http://www.accessdata.fda.gov/scripts/cdrh/cfdocs/cfTopic/mda/mda-cardio.cfm?topic=421
40. Spronk, H. M. H., van der Voort, D., & ten Cate, H. (2004). *Thrombosis Journal, 2*, 12. doi:10.1186/1477-9560-2-12
41. William, D. F. (Ed.). *Definitions in biomaterials*. London: Elsevier.
42. Teoh, S. H. (2000). *International Journal of Fatigue, 22*, 825–837.
43. Klinger, A., Steinberg, D., Kohavi, D., & Sela, M. N. (1997). *Journal of Biomedical Materials Research, 36*, 387–392.
44. BMEn 5001-"cardiovascular" *Applications of biomaterials*; November 25, 1998-W. Gleason.
45. http://www.biomed.metu.edu.tr/courses/term_papers/artif-heart-valves_erol.htm
46. Soltys-Robitaille, C. E., Ammon, D. M., Jr., Valint, P. L., Jr., & Grobe III, G. L. (2001). *Biomaterials, 22*, 3257–3260.
47. Pesakova, V., Klezl, Z., Balik, K., & Adam, M. (2000). *Journal of Material Science: Materials in Medicine, 11*(12), 793–798.
48. Bruinsma, G. M., Van der Mei, H. C., & Busscher, H. J. (2001). *Biomaterials, 22* (3217–322), 4.
49. Ahluwalia, A., Basta, G., Chiellini, F., Ricci, D., & Vozzi, G. (2001). *Journal of Material Science: Materials in Medicine, 12*(7), 613–619.
50. Bowlin, G. L., & Rittger, S. E. (1997). *Cell Transplantation, 6*(6), 623–629.
51. Van Wachem, P. B., Schakenraad, J. M., Feijen, J., Beugeling, T., Van Aken, W. G., Blauuw, E. H., et al. (1989). *Biomaterials, 10*, 532–539.
52. Bruck, S. D. (1975). *Polymer, 16*, 25.

53. Bruck, S. D. (1973). *Nature, 243*, 416–417.
54. Bruck, S. D. (1967). *Journal of Polymer Science, C17*, 169–185.
55. Boldz, A., & Schaldach, M. (1990). *Artificial Organs, 14*(4), 260–269.
56. Chen, J. Y., Wang, L. P., Fu, K. Y., Huang, N., Leng, Y., Leng, Y. X., et al. (2002). *Surface & Coatings Technology, 156*, 289–294.
57. http://greenfield.fortunecity.com/rattler/46/endothelium.htm
58. http://teaching.anhb.uwa.edu.au/mb140/MoreAbout/Endothel.htm
59. Gordon, J. L (1986). In J. P., Cazenave, J. A. Davies, M. D. Kazatchkine, & W. G. van Aken (Eds.), *Blood-surface interactions: Biological principles underlying hemocompatibility with artificial materials* (p. 5). London: Elsevier Science Publishers (Biomedical Division).
60. Williams, S. (1994). *Cell Transplantation, 4*, 401–410.
61. Horbett, T. (1994). *Colloids and Surface B: Biointerfaces, 2*, 225–240.
62. Tianen, Veli-Matti. (2001). *Diamond and Related Materials, 10*, 153–160.
63. Grill, A., & Meyerson. (1994). Development and status of diamondlike carbon. In K. E. Spear & J. P Dismukes (Eds.), *Synthetic diamond; emerging CVD science and technology*. New York: Wiley.
64. Schroeder, A., Francz, G., Bruinink, A., Hauert, R., Mayer, J., & Wintermantel, E. (2000). *Biomaterials, 21*(5), 449–456.
65. Hauert, R., Knoblauch-Meyer, L., Francz, G., Schroeder, A., & Wintermantel, E. (1999). *Surface & Coatings Technology, 120–121*, 291–296.
66. Hauert, R., Muller, U., Francz, G., et al. (1997). *Thin Solid Films, 308–309*, 191–194.
67. Dorner-Reisel, A., Schurer, C., Nischan, C., Seidel, O., & Muller, E. (2002). *Thin Solid Films, 420–421*, 263–268.
68. Hauert, R., & Muller, U. (2003). *Diamond and Related Materials, 12*, 171–177.
69. Huang, N., Yang, P., Leng, Y. X., Wang, J., Chen, J. Y., Sun, H., et al. (2004). Surface modification for controlling the blood-materials interface. In *Invited report on 6th Asia Symposium on Biomedical Materials*, *Chengdu, China*. Published in Key Engineering Materials, July 20–23, 2004. http://www.paper.edu.cn/scholar/download.jsp?file=huangnan-6
70. Leng, Y. X., Huang, N., et al. (2003). *Surface Science, 531*, 177.
71. Yang, P., Chen, J. Y., Leng, Y. X., Sun, H., Huang, N., & Chu, P. K. (2003) *7th International Workshop on Plasma Based Ion Implantation, San Antonio, USA*, September 16–20, 2003.
72. Huang, N., Yang, P., Leng, Y. X., Wang, J., Sun, H., Chen, J. Y., et al. (2004). *Surface & Coatings Technology, 186*, 218–226.
73. Yang, P., Kwok, S. C. H., Chu, P. K., Leng, Y. X., Chen, J. Y., Wang, J., et al. (2003). *Nuclear Instruments and Methods in Physics Research. Section B, Beam Interactions with Materials and Atoms, 206*, 721.
74. Jones, M. I., McColl, I. R., Grant, D. M., Parker, K. G., & Parker, T. L. (1999). *Diamond and Related Materials, 8*, 457–462.
75. Jones, M. I., McColl, I. R., Grant, D. M., Parker, K. G., & Parker, T. L. (2000). *Journal of Biomedical Materials Research, 52*(2), 413–421.
76. Dion, I., Roques, X., Baquey, C., Baudet, E., Basse Cathalinat, B., & More, N. (1993). *Bio-Medical Materials and Engineering*, *3y1*, 51–55.
77. Cui, F. Z., & Li, D. J. (2000). *Surface & Coatings Technology, 131*, 481–487.
78. Gutensohn, K., Beythien, C., Bau, J., Fenner, T., Grewe, P., Koester, R., et al. (2000). *Thrombosis Research, 99*, 577–585.
79. Alanazi, A., Nojiri, C., Noguchi, T., Kido, T., Komatsu, Y., Kirakuri, K., et al. (2000). *ASAIO Journal, 46*, 440–443.
80. Thomson, L. A., Law, F. C., Rushton, N., & Franks, J. (1991). *Biomaterials, 12*, 37.
81. Allen, M., Law, F., & Rushton, N. (1994). *Clin. Mater., 17*, 1.
82. De Scheerder, I., Szilard, M., Yanming, H., et al. (2000). *J. Invasive Cardiol., 12*(8), 389–394.
83. Schroeder, A., Francz, G., Bruinink, A., Hauert, R., Mayer, J., & Wintermantel, E. (2000). *Biomaterials, 21*(5), 449–456.

84. Francz, G., Schroeder, A., & Hauert, R. (1999). *Surface and Interface Analysis, 28*, 3.
85. Hauert, R., Knoblauch-Meyer, L., Francz, G., Schroeder, A., & Wintermantel, E. (1999). *Surface & Coatings Technology, 120–121*, 291–296.
86. Hauert, R., Muller, U., Francz, G., et al. (1997). *Thin Solid Films, 308–309*, 191–194.
87. Schroeder, A. (1999). Ph.D. Thesis, Dissertation Nr. 13079, ETH Zurich.
88. Dorner-Reisel, A., Schurer, C., Nischan, C., Seidel, O., & Muller, E. (2002). *Thin Solid Films, 420–421*, 263–268.
89. Yang, P., Huang, N., Leng, Y. X., Chen, J. Y., Sun, H., Wang, J., et al. (2002). *Surface & Coatings Technology, 156*, 284–288.
90. Chen, J. Y., Leng, Y. X., Tian, X. B., Wang, L. P., & Huang, N. (2002). P. K. Chu an P. Yang. *Biomaterials, 23*, 2545–2552.
91. Leng, Y. X., Sun, H., Yang, P., Chen, J. Y., Wang, J., Wan, G. J., et al. (2001). *Thin Solid Films, 398–399*, 471–475.
92. Leng, Y. X., Yang, P., Chen, J. Y., Sun, H., Wang, J., Wang, G. J., et al. (2001). *Surface & Coatings Technology, 138*, 296–300.
93. Li, J. (1993). *Biomaterials, 14*, 229.
94. Adjaottor, A. A., Ma, E., & Meletis, E. I. (1997). *Surface & Coatings Technology, 89*(3), 197–203.
95. Grinnell, F. (1978). *International Review of Cytology, 53*, 65–144.
96. Ogwu, A. A., Lamberton, R. W., Morley, S., Maguire, P., & McLaughlin, J. (1999). *Physica B, 269*, 335–344.
97. Dementjev, A. P., Petukhov, M. N., & Baranov, A. M. (1998). *Diamond and Related Materials, 7*, 1534–1538.
98. Grill, A., Meyerson, B., Patel, V., Reimer, J. A., & Petrich, M. A. (1987). *Journal of Applied Physics, 6*, 2874.
99. Constant, L. (1997). *Le Normand. Diamond and Related Materials, 6*, 664–667.
100. Baker, M. A., & Hammer, P. (1997). *Surface and Interface Analysis, 25*, 629–642.
101. Grinnell, F. (1978). *International Review of Cytology, 53*, 65–144.
102. Magill, D. P., Ogwu A. A., McLaughlin J. A. D., & Maguire P. D. (2001). *Journal of Vaccum Science and Technology A*, *19*(5), 2456–2462.
103. Hadjaj, A., Cabarrocas, R. I., & Equar, B. (1997). *Philosophical Magazine B, 76*, 941.
104. Hadjaj, A., Favre, M., Equer, B., & Cabaroccas, R. I. (1998). *Solar Energy Materials and Solar Cells, 51*, 145–153.
105. Attard, G., & Barnes, C. (1998). *Surfaces* (pp. 64–65). Oxford: Oxford University Press.
106. Boldz, A., & Schaldach, M. (1990). *Artificial Organs, 14*(4), 260–269.
107. Wan, H., Williams, R. L., Doherty, P. J., & Williams, D. F. (1994). *Journal of Materials Science Materials in Medicine, 5*, 441–445.
108. Okpalugo, T. I. T., McKenna, E., Magee, A. C., McLaughlin, J. A., & Brown, N. M. D. (2004). *Journal of Biomedical Materials Research, Part A, 71A*(2), 201–208.

Chapter 7
Diamond Surgical Tools

H. Sein, C. Maryan, A. Jones, J. Verran, N. Ali, I.U. Hassan, C. Rego, W. Ahmed and M.J. Jackson

Abstract Deposition technology has played a major part in the creation of today's scientific devices. Computers, electronic equipment, biomedical implants, cutting tools, optical components, and automotive parts are all based on material structures created by thin film deposition processes. There are many coating processes ranging from the traditional electroplating to the more advanced laser or ion-assisted deposition. However, the choice of deposition technology depends upon many factors including substrates properties, component dimensions and geometry, production requirements, and the exact coating specification needed for the application of interest. For complex geometry components, small feature sizes, good reproducibility, and high product throughput, chemical vapor deposition (CVD) is a highly effective technology. For example, low pressure and plasma-assisted CVD is a well-established technology for semiconductor devices, which has very small feature sizes and complex geometrical arrangements on the surface.

7.1 Introduction

In order to understand both physical vapor deposition (PVD) and chemical vapor deposition (CVD) processes, one has to model them in terms of several steps. These processes can be divided into the following stages:

- **Generation of Vapor Phase Species**

The precursor materials are converted into a convenient form so that transport to the substrates is efficient. Vapor is generated in the reactor. Hot filaments, lasers,

H. Sein · C. Maryan · A. Jones · J. Verran · N. Ali · I.U. Hassan · C. Rego
Manchester Metropolitan University, Manchester, UK

W. Ahmed
School of Medicine, University of Central Lancashire, Preston, UK

M.J. Jackson (✉)
Kansas State University, Salina, KS, USA
e-mail: jacksonmj04@yahoo.com

W. Ahmed and M.J. Jackson (eds.), *Surgical Tools and Medical Devices*,
DOI 10.1007/978-3-319-33489-9_7

microwave, ion beams, electron guns, etc., can be used to activate the source materials, enabling deposition to be carried out.

- **Transport of Source Materials to the Substrate Region**

The vapor species are transported from the source to the substrate with or without collision between the atoms and molecules. During transport, some of the species can be ionized by creating plasma in this space. This is normally carried out in a vacuum system; however, atmospheric CVD systems are also employed.

- **Adsorption of Active Species on the Substrate Surface**

For deposition to take place, the active species must first be adsorbed onto the active sites on the surfaces. Initially, this occurs via physisorption where the species adhere to the surface with weak van der Waals forces and then strong covalent bonds are formed between the species and the surface known as chemisorption.

- **Decomposition Adsorbed Species on the Substrate Surface**

Once the gaseous species are adsorbed onto surface site and the energy of the species is sufficient then decomposition of the precursors can take place resulting in the creation of nucleation center.

- **Nucleation and Film Formation**

The process involves the subsequent formation of the film via nucleation and growth processes. These can be strongly influenced by process parameters resulting in a change in the microstructure, composition, impurities, and residual stress of the films. The final film properties are highly dependent on the microstructural and interfacial characteristics of the deposited coating.

Independent control of these stages is critical and determines the versatility or flexibility of deposition process. For example, PVD process parameters can be independently and precisely monitored and controlled; thus allowing microstructure, properties, and deposition rates to be tailored specifically to the performance requirements of the product. Generally, CVD processes have the advantage of good throwing power enabling complex geometry substrates to be coated, while the deposition rates in PVD processes are much higher than those in CVD processes at lower deposition temperatures.

Although CVD and PVD processes are simple in principle, one must be well versed in vacuum technology, physics, chemistry, material science, mechanical, and electrical engineering as well as in elements of thermodynamics, chemical kinetics, surface mobility, and condensation phenomena in order to obtain a detailed fundamental understanding of these processes. In this chapter, we restrict our attention to the deposition of diamond thin films for use in cutting tools.

Table 7.1 Properties of diamond

Properties	Applications
High wear resistance	Cutting tools
Chemical inertness	Electrochemical sensors
High thermal conductivity	Heat spreaders
Biological inertness	In vitro applications
Semiconducting when doped	Electronic devices
High resistivity (insulator)	Electronic devices
Negative electron affinity	Cold cathode electron sources

7.2 Properties of Diamond

Diamond is an advanced material with an excellent combination of physical and chemical properties. If high-quality diamond films with comparable properties to natural diamond can be formed with low surface roughness, numeral potential applications will emerge in the near future particularly in the emerging field of nanotechnology.

Diamond as a material possesses a remarkable range of physical attributes, which make it a promising material for a large range of applications. Selections of these are given in Table 7.1. However, owing to the cost and availability of large natural diamonds, most of these applications have not been developed to their full potential.

7.3 History of Diamond

7.3.1 Early History of Diamond Synthesis

Diamond is one of the most technologically and scientifically valuable crystalline solids found in nature. Their unique blends of properties are effectively incomparable to any other known material. Sir Isaac Newton was the first to characterize diamond and determine it to be of organic origin while in 1772, the French chemist Antoine L. Lavoisier established that the product of diamond combustion was limited to carbon dioxide.

English chemist Smithson Tennant showed that diamond combustion products were no different than those of coal or graphite and resulted in “bound air.” Later, the discovery of X-rays enabled Sir William Henry Bragg and his son Sir William Lawrence Bragg to determine that carbon allotropes were cubic (diamond), hexagonal (graphite), and amorphous. With this information, early attempts to synthesize diamond began in France in 1832 with C.C. de la Tour and later in England by J.B. Hanney and H. Moisson. The results of their work are disputed to this day.

Synthesis of diamond has attracted widespread attention ever since it was established; that diamond is a crystalline form of carbon. Since diamond is the densest carbon phase, it became immediately plausible that pressure, which produces a smaller volume and therefore a higher density, may convert other forms of carbon into diamond. As understanding of chemical thermodynamics developed throughout the nineteenth and twentieth centuries, the pressure–temperature range of diamond stability was explored. In 1955, these efforts culminated in the development of a high pressure–high temperature (HPHT) process of diamond synthesis with a molten transition metal solvent-catalyst at pressures where diamond is the thermodynamically stable phase [1]. Three major problems can be isolated for emphasizing the difficulty of making diamond in the laboratory. First, there is difficulty in achieving the compact and strongly bonded structure of diamond, which requires extreme pressure. Second, even when such a high pressure has been achieved, a very high temperature is required to make the conversion from other forms of carbon to diamond proceed at a useful rate. Finally, when diamond is thus obtained, it is in the form of very small grains and to achieve large single crystal diamond requires yet another set of constraints. However, less well known has been a parallel effort directed toward the growth of diamond at low pressures where it is metastable. Metastable phases can form from precursors with high chemical potential if the activation barriers to more stable phases are sufficiently high. As the precursors fall in energy, they can be trapped in a metastable configuration. Formation of a metastable phase depends on selecting conditions in which rates of competing processes to undesired products are low [2]. In the case of diamond, achieving the appropriate conditions has taken decades of research [3]. The processes competing with diamond growth are spontaneous graphitization of the diamond surface as well as nucleation and growth of graphitic deposits.

The most successful process for low-pressure growth of diamond has been CVD from energetically activated hydrocarbon/hydrogen gas mixtures. CVD is a process whereby a thin solid film, by definition, is synthesized from the gaseous phase via a chemical reaction. The development of CVD is common with many technologies and has been closely linked to the practical needs of society. The oldest example of a material deposited by CVD is probably that of pyrolytic carbon, since as Ashfold et al. [4] pointed out, some prehistoric art was done on cave walls with soot condensed from the incomplete oxidation of firewood. A similar procedure formed the basis of one of the earliest patents and commercial exploitation of a CVD process, which was issued for the preparation of carbon black as a pigment. The emerging electric lamp industry provided the next major application of CVD with a patent issued for improvements to fragile carbon filaments [4]. Since these improved filaments were far from robust, the future for a pyrolytic carbon CVD industry was limited and a few years later, processes for the deposition of metals to improve the quality of lamp filaments were described [5]. From the turn of the century through to the late 1930s, a variety of techniques appeared for the preparation of refractory metals for a number of applications. It was also during this period that silicon was first deposited by hydrogen reduction of silicon tetrachloride [5] and the use of that material for electronic applications was foreseen by the

development of silicon-based photo cells [6] in 1946 as well as rectifiers [7]. The preparation of high-purity metals, various coatings, and electronic materials has developed significantly in the past 45 years or so, but it is undoubtedly the demand and requirement of the semiconductor and microelectronic industries that have been the main driving force in the development of CVD techniques as well as the greater efforts for understanding the basics of CVD processes. Consequently, a large body of literature and reviews now exist on CVD.

Indeed, it was the CVD from carbon-containing gases that enabled W.G. Eversole, referred to in reference [8], at the Union Carbide Corporation, to be the first to grow diamond successfully at low pressures in 1952, after which conclusive proof and repetition of the experiments took place. In the initial experiments, carbon monoxide was used as a source gas to precipitate diamond on a diamond seed crystal. However, in subsequent experiments, methane and other carbon-containing gases were used as well as a cyclic growth etches procedure to remove co-deposited graphite. In all of his studies, it was necessary to use diamond seeds in order to initiate diamond growth. The deposits were identified as diamond by density measurements, chemical analysis, and diffraction techniques. The synthesis by Eversole preceded the successful diamond synthesis at high pressure by workers at the General Electric Company [1], which was accomplished in 1954. However, the important difference was that Eversole grew diamond on preexisting diamond nuclei whereas the general electric syntheses did not initiate growth on diamond seed crystals. Angus [9], Yarbrough and Messier [10], in the former Soviet Union, began work on low-pressure diamond synthesis in 1956, in which many approaches were taken, which started with the growth of diamond whiskers by a metal-catalyzed vapor–liquid–solid process. Subsequently, epitaxial growth from hydrocarbons and hydrocarbon/hydrogen mixtures was investigated as well as different forms of vapor transport reactions. In addition, theoretical investigations of the relative nucleation rates of diamond and graphite were also performed. Angus and co-workers at Case Western Reserve University concentrated primarily on diamond CVD on diamond seed crystals from hydrocarbons and hydrocarbon/hydrogen mixtures [11, 12]. They grew *p*-type semiconducting diamond from methane/diborane gas mixtures and studied the rates of diamond and graphite growth in methane/hydrogen gas mixtures and ethylene. They were the first to report on the preferential etching of graphite compared to diamond by atomic hydrogen and noted that boron had an unusual catalytic effect on metastable diamond growth.

The role of hydrogen in permitting metastable diamond growth was also recognised by some early workers. The low-energy electron diffraction (LEED) study of Spear [13] and Kamo et al. [14] showed that a {111}-diamond surface saturated with hydrogen gave an unreconstructed (1 × 1) LEED pattern. The unsatisfied dangling bonds normal to the surface are terminated with hydrogen atoms, which maintain the bulk terminated diamond lattice to the outermost surface layer of carbon atoms. When hydrogen is absent, the surface reconstructs into more complex structures. They also showed that carbon atoms are very mobile on the diamond surface at temperatures above 1200 K and stated that these conditions should permit epitaxial growth. Other work [15, 16] suggested that the presence of

hydrogen enhanced diamond growth. Williams et al. [17] and Kobashi et al. [18] as well as Liou et al. [19] showed that addition of hydrogen to the hydrocarbon gas phase suppressed the growth rate of graphite relative to diamond thus resulting in higher diamond yields. Eventually, however, graphitic carbons nucleated on the surface and suppressed further diamond growth. It was then necessary to remove the graphitic deposits preferentially with atomic hydrogen [20] or oxygen [21], and to repeat the sequence. By the mid-1970s, diamond growth at low pressures had been achieved by several groups. The beneficial role of hydrogen was known to some extent and growth rates of 0.1 μm h^{-1} had been achieved. Although the growth rates were too low to be of any commercial importance, the results provided the experimental foundation for much of the work that followed.

7.3.2 Metastable Diamond Growth

Japanese researchers associated with the National Institute for Research in Inorganic Materials (NIRIM) made the first disclosure of methods for rapid diamond growth at low pressures. Research on metastable diamond growth was initiated at NIRIM in 1974. In 1982, they described techniques for synthesizing diamond at rates of several microns per hour from gases decomposed by a hot filament as well as microwave or DC discharges [22–25]. These processes produced individual faceted crystals without the use of a diamond seed crystal. The current worldwide interest in new diamond technology can in fact be directly traced to the NIRIM effort. Although Deryagin, as reported in reference [26], had reported high-rate diamond growth earlier, process details were not disclosed [26]. All the techniques are based on the generation of atomic hydrogen in the vicinity of the growth surface during deposition. Although the CVD of diamond from hydrogen-rich/hydrocarbon-containing gases has been the most successful method of diamond synthesis, numerous other methods have been attempted with varying degrees of success, with ion beam methods being the most successful [27]. In 1971, hard carbon films were first deposited using a beam of carbon ions. As the films had many of the properties of diamond, they were called diamond-like carbon because definitive diffraction identification was not possible. In 1976, Akatsuka et al. [28] formed finely divided polycrystalline diamond (PCD) using a beam of carbon ions with energies between 50 and 100 eV, and subsequently Suzuki et al. [29] grew diamond via ion implantation.

With further research and additional technological progress in improving and devising new methods for synthesis and fabrication, it becomes increasingly likely that new applications will be discovered. In order to be able to take full advantage of the unique characteristics of diamond as a material for the construction of solid-state devices, basic scientific understanding of the various experimental process techniques and in particular the introduction and activation of dopants must be obtained. Attention also needs to be paid to proper design of devices incorporating novel features utilizing concepts and practices established in silicon and

gallium arsenide device technology. The potential of diamond as a material for solid-state devices has been the subject of a few reviews [8, 30–35] that have discussed the electronic material parameters of diamond and the simulated characteristics that can be obtained. Simple devices incorporating diamond have been demonstrated primarily incorporating natural or HPHT diamond. Photodetectors, light-emitting diodes, nuclear radiation detectors, thermistors, varistors, and negative resistance devices in synthetic crystals have been demonstrated. Several groups [36–40] have also demonstrated basic field effect transistor device operation in epitaxial diamond films and boron-doped layers on single crystal diamond substrates. However, for wide application of diamond solid-state devices, high-quality films on more commonly available substrates are essential as well as studies on the device potential of polycrystalline films. So far, only thermistors [41] and Schottky diodes [42] have been produced and characterized in the polycrystalline material. This is due to material problems; in that the polycrystalline nature of the films result in grain boundaries, twins, stacking faults, and other defects, which have restricted exploitation in the electronic industries. To date, there have been no confirmed observations of a means of achieving heteroepitaxy, i.e., single crystal diamond grown on a non-diamond substrate, and therefore no means of achieving diamond devices for practical applications. Indeed, achieving heteroepitaxy stands as the single most prominent technological hurdle for diamond-based electronics. However, CVD synthesis is a very active area that is improving with experience. In the near future, in situ probes may be used to optimize various diamond CVD processes by providing a maximization of the flow of diamond precursors to the surface while simultaneously minimizing the competing deposition of non-diamond carbon forms. The wide variety of means by which diamond is being routinely formed as a film will enhance its deployment and the potential for active electronic exploitation. Indeed, diamond coatings in general are expected to make so large an impact in the future that many people believe that the future age will be known as the diamond age, going chronologically from the Stone Age and Bronze Age, to the Iron Age of the past and the Silicon Age of the present.

7.4 CVD Diamond Technology

The reactor system (comprising the reaction chamber and all associated equipment) for carrying out CVD) processes must provide several basic functions common to all type of systems (Fig. 7.1). It must allow transport of the reactant and diluents gases to the reaction site, provide activation energy to the reactants (heat, radiation, plasma), maintain a specific system pressure and temperature, allow the chemical processes for film deposition to proceed optimally, and remove the by-product gases and vapors. These functions must be implemented with adequate control, maximal effectiveness, and complete safety.

CVD is a crystal growth process used not only for diamond but also for a range of different semiconductor and other crystalline materials such as silicon or gallium

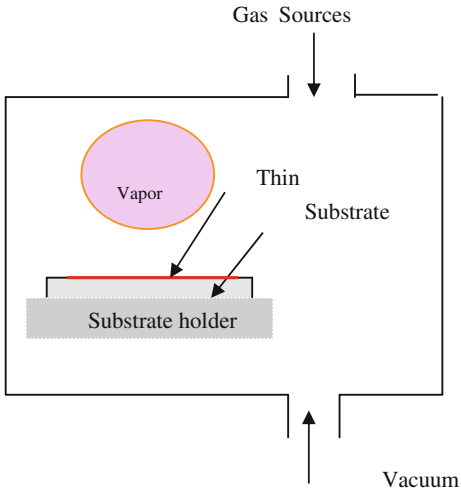

Fig. 7.1 A simple schematic of a vapor deposition process

arsenide. These industrial fields are diverse and range from gas turbines to gas cookers and from coinage to nuclear power plants.

The CVD process relies first on the generation of a species that is produced by the reaction of the element that is to be deposited with another element that results in the substantial increase in the depositing elements' vapor pressure. Second, this volatile species is then passed over or allowed to come into contact with the substrate being coated. This substrate is held at an elevated temperature, typically from 800 to 1150 °C. Finally, the deposition reaction usually occurs in the presence of a reducing atmosphere, such as hydrogen. The film properties can be controlled and modified by varying the problem parameters associated with the substrate, the reactor, and gas composition.

7.5 CVD Diamond Processes

Several different approaches to the deposition of diamond have been investigated and these include the ones described in the following sections.

7.5.1 Plasma-Enhanced CVD

Plasmas generated by various forms of electrical discharges or induction heating have been employed in the growth of diamond. The role of the plasma is to generate atomic hydrogen and to produce the necessary carbon precursors for diamond growth. The efficiencies of the different plasma processes vary from method to

method. Three plasma frequency regimes will be discussed. These are microwave plasma CVD, which typically uses excitation frequencies of 2.45 GHz; Radio-frequency (RF) plasma excitation, which employs frequencies of usually 13.56 MHz; and direct-current (DC) plasmas, which can be run at low electric powers (a "cold" plasma) or at high electric powers (which create an *arc* or a *thermal* plasma).

RF Plasma-Enhanced CVD

Generally, RF power can be applied to create plasma in two electrode configurations, namely, in an inductively coupled or a capacitively coupled parallel plate arrangement. A number of workers have reported the growth of diamond crystals and thin films using inductively coupled RF plasma methods [21–24] as well as capacitively coupled methods [25, 26]. A high power in the discharge leading to greater electron densities was found to be necessary for efficient diamond growth. However, the use of higher power results in physical and chemical sputtering from the reactor walls, leading to contamination of the diamond films [21]. The advantage of RF plasmas is that they can easily be generated over much larger areas than microwave plasmas but the method is not routinely applied for the deposition of diamond films.

DC Plasma-Enhanced CVD

In this method, plasma in a H_2-hydrocarbon mixture is excited by applying a DC bias across two parallel plates, one of which is the substrate [27–29]. DC plasma-enhanced CVD has the advantage of being able to coat large areas as the diamond deposition area is limited by the electrodes and the DC power supply. In addition, the technique has the potential for very high growth rates. However, diamond films produced by DC plasmas were reported to be under high stress and to contain high concentrations of hydrogen as well as impurities resulting from plasma erosion of the electrodes.

Microwave Plasma-Enhanced CVD

Microwave plasma-assisted CVD has been used more extensively than any other method for the growth of diamond films [14–20]. Microwave plasmas are different from other plasmas in that the microwave frequency can oscillate electrons. Collision of electrons with gaseous atoms and molecules generate high ionization fractions. This method of diamond film growth has a number of distinct advantages over the other methods of diamond film growth. Microwave deposition, being an electrodeless process, avoids contamination of the films due to electrode erosion. Furthermore, the microwave discharge at 2.45 GHz, being a higher frequency process than the RF discharges at typically 13.56 MHz, produces a higher plasma density with higher energy electrons, which effectively results in higher concentrations of atomic hydrogen and hydrocarbon radicals leading to efficient diamond growth. In addition, as the plasma is confined to the center of the deposition chamber as a ball, carbon deposition onto the walls of the chamber is prevented.

7.5.2 Hot Filament CVD (HFCVD)

In the early 1970s, it was suggested that the simultaneous production of atomic hydrogen during hydrocarbon pyrolysis may enhance the deposition of diamond. Soviet researchers who generated H by dissociating H_2 using an electric discharge or a hot filament tested this suggestion [8]. It was observed that atomic hydrogen could easily be produced by the passage of H_2 over a refractory metal filament, such as tungsten, heated to temperatures between 2000 and 2500 K. When atomic hydrogen was added to the hydrocarbon, typically with a C/H ratio of ~ 0.01, it was observed that diamond could be deposited while graphite formation was suppressed. The generation of atomic hydrogen during diamond CVD enabled (a) a dramatic increase in the diamond deposition rate to approximately 1 μm h^{-1} and (b) the nucleation and growth of diamond on non-diamond substrates [8–13]. Because of its inherent simplicity and comparatively low operating cost, HFCVD has become very popular in the industry. Table 7.2 outlines typical deposition parameters used in the growth of diamond films by this technique.

A wide variety of refractory materials have been used as filaments including tungsten, tantalum, and rhenium due to their high electron emissivity. Refractory metals, which form carbides (e.g., tungsten and tantalum), typically must carburize their surface before supporting the deposition of diamond films. The process of filament carburization results in the consumption of carbon from the CH_4, and thus a specific incubation time is needed for the nucleation of diamond films. Therefore, this process may affect the early stages of film growth, although it is insignificant over longer periods. Furthermore, the volume expansion due to carbon incorporation leads to cracks along the length of the wire. The development of these cracks is undesirable, as it reduces the lifetime of the filament.

It is believed that thermodynamic near-equilibrium is established in the gas phase at the filament surface. At temperatures around 2300 K, molecular hydrogen dissociates into atomic hydrogen and methane transforms into methyl radicals, acetylene species, and other hydrocarbons stable at these elevated temperatures. Atomic hydrogen and the high-temperature hydrocarbons then diffuse from the filament to the substrate surface. Although the gaseous species generated at the filament are in equilibrium at the filament temperature, the species are at a super equilibrium concentration when they arrive at the much cooler substrate. The reactions that generate these high-temperature species (e.g., C_2H_2), at the surface of the filament or anywhere where there are hydrogen atoms, proceed faster than any

Table 7.2 Typical deposition parameters used in the growth of diamond films by HFCVD

Gas mixture	Total pressure (Torr)	Substrate temperature (K)	Filament temperature (K)
CH_4 (0.5–2.0 %)/H_2	10–50	1000–1400	2200–2500

reactions that decompose these species during the transit time from the filament to the substrate. Consider the equilibrium between methane and acetylene

$$2CH_4 \rightleftarrows C_2H_2 + 3H_2$$

At the filament surface, the reaction is immediately driven to the right, creating acetylene. After acetylene diffuses to the substrate, thermodynamic equilibrium at a substrate temperature of $\sim$1100 K calls for the formation of methane, but the reverse reaction proceeds much slower. Solid carbon precipitates on the substrate in order to reduce the superequilibrium concentration of species such as acetylene in the gas phase. The diamond allotrope of carbon is "stabilized" by a concurrent super equilibrium concentration of atomic hydrogen. This simple explanation emphasizes the importance of reaction kinetics in diamond synthesis by HFCVD.

Advantages of the CVD Process

The process is gas phase in nature, and therefore given a uniform temperature within the coating retort and likewise uniform concentrations of the depositing species the deposition rate will be similar on all surfaces. Therefore, variable- and complex-shaped surfaces, given reasonable access to the coating powders or gases, such as screw threads, blind holes, or channels or recesses, can be coated evenly without build-up on edges.

Disadvantages of the CVD Process

The CVD process is carried out at relatively high temperatures and therefore limitations due to dimensional tolerances are an important consideration. Components that have tight dimensional tolerances will not be amenable to CVD. However, the reduction of distortion during coating can sometimes be controlled by careful stress relieving after rough machining of the component during fabrication.

7.6 Treatment of Substrate

7.6.1 Selection of Substrate Material

Deposition of adherent high-quality diamond films onto substrates such as cemented carbides, stainless steel, and various metal alloys containing transition element has proved to be problematic. In general, the adhesion of the diamond films to the substrates is poor and the nucleation density is very low [43–50]. Mainly, refractory materials such as W (WC-Co), Mo, and Si have been used as substrate materials. Materials that form carbide are found to support diamond growth. However, materials such as Fe and steel possess a high mutual solubility with carbon, and only graphitic deposits or iron carbide result during CVD growth on these materials. For applications in which the substrate needs to remain attached to the CVD diamond film, it is necessary to choose a substrate that has a similar

Table 7.3 Solubility and diffusion rates of carbon atoms in different metals at 900 °C

	α-Fe	γ-Fe	Co	Ni
Solubility of carbon (wt%)	1.3	1.3	0.1	0.2
Carbon diffusion rate (cm/s)	2.35×10^{-6}	1.75×10^{-8}	2.46×10^{-8}	1.4×10^{-8}

thermal expansion coefficient to that of diamond. If this is not done, the stress caused by the different rates of contraction on cooling after deposition will cause the film to delaminate from the substrate. The influence of different metallic substrates on the diamond deposition process has been examined. Interactions between substrate materials and carbon species in the gas phase are found to be particularly important and lead to either carbide formation or carbon dissolution. Carbides are formed in the presence of carbon-containing gases on metals such as molybdenum, tungsten, niobium, hafnium, tantalum, and titanium. The carbide layer formed allows diamond to form on it since the minimum carbon surface concentration required for diamond nucleation cannot be reached on pure metals. As the carbide layer increases in thickness, the carbon transport rate to the substrate decreases until a critical level is reached where diamond is formed [51–57]. Substrates made from metals of the first transition group such as iron, cobalt, and nickel, are characterized by high dissolution and diffusion rates of carbon into those substrates (Table 7.3) [58]. Owing to the absence of a stable carbide layer, the incubation time required to form diamond is higher and depends on substrate thickness. In addition, these metals catalyze the formation of graphitic phases, which is reflected in the graphite-diamond ratio of during the deposition process, yielding a low diamond The importance of this mechanism in relation to diamond deposition decreases from iron to nickel, corresponding to a gradual filling of the 3d-orbital [58]. This effect occurs whenever the metal atoms come into contact with the carbon species, which can take place on the substrate or in the gas phase [59].

7.6.2 *Substrate Pretreatment*

In order for continuous film growth to occur, a sufficient density of crystallites must be formed during the early stages of growth. In general, the substrate must undergo a nucleation enhancing pre-treatment to allow this.

This is particularly true for Si wafer substrates that have been specially polished to be smooth enough for microelectronic applications. Substrates may be pre-treated by a variety of methods including:

- Abrasion with small (∼nm/μm size) hard grits (e.g., diamond, silicon carbide).
- Ultrasonication of samples in slurry of hard grit (e.g., diamond).
- Chemical treatment (acid etching and Murakami agent).
- Bias-enhanced nucleation (BEN) (negative/positive substrate biasing).
- Deposition of hydrocarbon/oil coatings.

The basis for most of these methods is to produce scratches, which provide many sites for nucleation diamond of crystallites. It is also possible that small (~ nm size) flakes of diamond, produced during abrasion with diamond grit, become embedded in the substrate, and that CVD diamond grows on this material [60].

It could be desirable to produce nucleation sites without damage to the underlying substrate. This is particularly important for some applications such as diamond electronics and optical components. One method for encouraging nucleation without damaging the substrate material has been developed: BEN.

(a) *Pretreatment on Mo/Si Substrate*

Prior to pretreatment, Si/Mo substrate are ultrasonically cleaned in acetone for 10 min to remove any unwanted residue on the surface. Abrasion with 1 μm sizes of diamond powder is performed for 5 min. Alternatively, substrate was immersed in diamond solution containing 1–3 μm of diamond particles and water for 1 h in ultrasonic bath. These methods produce scratches on the surface, which create many nucleation sites. The substrates are then washed with acetone in the ultrasonic bath for 10 min. SEM and energy-dispersive X-ray spectroscopy (EDX), characterized abraded surface of substrates.

(b) *Pretreatment on WC-Co Substrate*

The application of diamond coatings on cemented tungsten carbide (WC-Co) tools has attracted much attention in recent years in order to improve cutting performance and tool life. However, deposition of adherent high-quality diamond films onto substrates such as cemented carbides, stainless steel, and various metal alloys containing transition element has proved to be problematic. In general, the adhesion of the diamond films to the substrates is poor and the nucleation density is very low [43–49]. WC-Co tools contain 6 % Co and 94 % WC substrate with grain size 1–3 micron is desirable for diamond coatings.

In order to improve the adhesion between diamond and WC substrates, it is necessary to etch away the surface Co and prepare the surface for subsequent diamond growth. In particular, the cobalt (Co) binder; this provides additional toughness to the tool but is hostile to the diamond adhesion. The adhesion strength to diamond films is relatively poor, and can lead to catastrophic failure of coating in metal cutting [58]. The Co binder can also suppress diamond growth, favoring the formation of non-diamond carbon phases resulting in poor adhesion between the diamond coating and the substrate [61]. Most importantly, it is difficult to deposit adherent diamond onto untreated WC-Co substrates. Figure 7.2a shows sub-micron size Co crystals on diamond films that were deposited on an untreated substrate (without removal of surface Co). EDX spectra showed the trace amount of Co elements on the surface. It also showed poor adhesion of diamond film and shows delaminated film on the surface (Fig. 7.2b).

Poor adhesion can be related to the cobalt binder that is present to increase the toughness of the tool; however, it suppresses diamond nucleation and causes deterioration of diamond film adhesion. To eliminate this problem, it is usual to

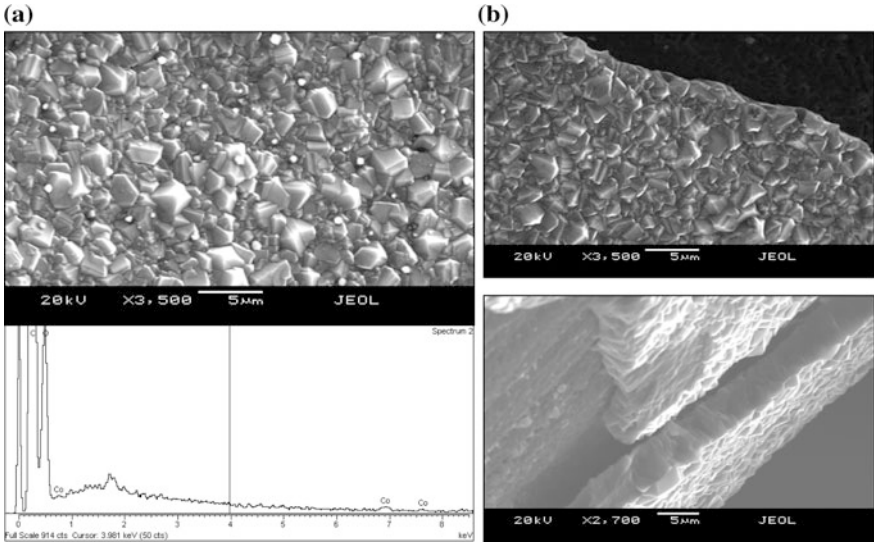

Fig. 7.2 **a** Co trace on diamond film, **b** delaminated diamond film

Table 7.4 WC-Co insert chemical composition

WC grain size (μm)	WC	Co	TaC	Density (g/cm^3)	Hardness (HRA)
WC fine grain 0.5	94.2	5.8	0.2	14.92	93.40
WC coarse grain 6	94.0	6.0		14.95	88.50

pre-treat the WC-Co surface prior to CVD diamond deposition. Various approaches have been used to suppress the influence of Co and to improve adhesion. Therefore, a substrate pre-treatment, for reducing the surface Co concentration and achieving a proper interface roughness, will enhance the surface readily available for coating process [61]. For example, chemical treatment using Murakami agent and acid etching has been used successfully for removal of the Co binder from the substrate surface [62].

The WC-Co substrates (Flat) used were 10 × 10 mm by 3 mm in thickness. The hard metal substrates used were WC-6wt% Co with WC average grain size of 0.5 μm (fine grain) and 6 μm (coarse grain). Table 7.4 shows that the data for substrate, which consist of the chemical composition, density, and hardness of samples, are used for diamond deposition. Figure 7.3a, b show that coarse and fine grain of etched WC-Co insert surface.

The Co cemented tungsten carbide (WC-Co) rotary tools (surgical tools, surgical tools), 20 mm in length including the bur head (WC-Co) and shaft (Fe/Cr) and ~1 mm in diameter, were also used. Prior to pretreatment, both set of substrates are ultrasonically cleaned in acetone for 10 min to remove any loose residues. The following two-step chemical pretreatment procedure is used. A first step etching,

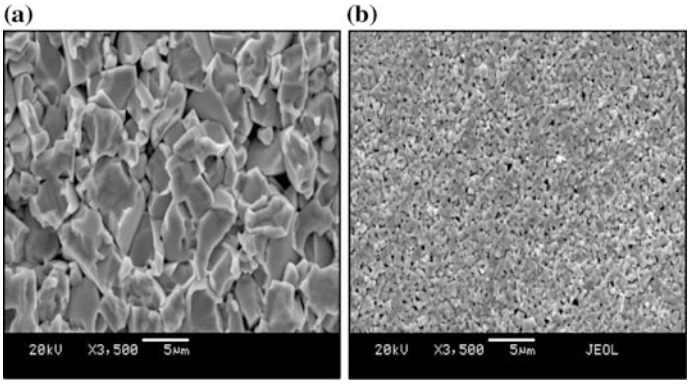

Fig. 7.3 **a** Etched coarse grain; **b** etched fine grain

using Murakami's reagent [10 g $K_3Fe(CN)_6$ + 10 g KOH + 100 ml water] is carried out for 10 min in ultrasonic bath to etch WC substrate, followed by a rinse with distilled water. The second step etching is performed using an acid solution of hydrogen peroxide [3 ml (96 % wt.) H_2SO_4 + 88 ml (30 % w/v) H_2O_2], for 10 s, to remove Co from the surface. The substrates are then washed again with distilled water in an ultrasonic bath. After wet treatment the surgical tool is abraded with synthetic diamond powder (1 μm grain size) for 5 min and followed by ultrasonic treatment with acetone for 20 min. Etched surface of substrates can be characterized by SEM and EDX.

7.7 Modification of HFCVD Process

7.7.1 Modification of Filament Assembly

The filament material and its geometrical arrangement are important factors to consider in order to have improved coatings using the CVD method. Therefore, in order to optimize both the filament wire diameter and the filament assembly/geometry, it is necessary to understand the temperature distributions of the filament. Research by the author indicated that the best thermal distribution and diamond growth uniformity is obtained using tantalum wires of 0.5 mm in diameter. To ensure uniform coating around the cylindrical shape samples (surgical tools or surgical tools), tools were positioned centrally and coaxially within the coils of the filament, the six-spiral (coil) filament was made with 1.5 mm spacing between the coils (Fig. 7.4a, b).

Tantalum wire of 0.5 mm diameter and 12–14 cm length is used as the hot filament. The filament is mounted vertically with the surgical tool held in between the filament coils, as opposed to the horizontal position used in the conventional

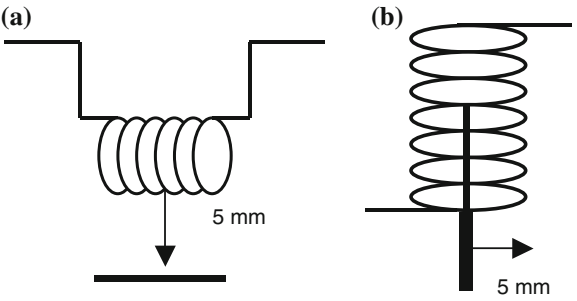

Fig. 7.4 **a** Conventional filament arrangement, **b** modified filament arrangement

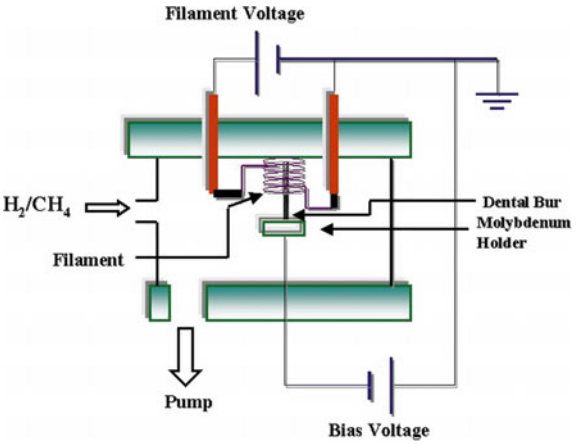

Fig. 7.5 Schematic diagram of HFCVD apparatus

HFCVD system. To ensure uniform coating, the surgical tool is positioned centrally and coaxially within the coils of the filament. A schematic diagram of the modified HFCVD system is presented in Fig. 7.5 and has been designed for surgical tool or wire or surgical tool with similar diameter. The new vertical filament arrangement used in the modified HFCVD system enhances the thermal distribution, ensuring uniform coating, increased growth rates, and higher nucleation densities.

7.7.2 Process Conditions

The CVD reactor is a cylindrical stainless steel chamber measuring 20 cm in diameter and 30 cm in length. Diamond films were deposited onto the cutting edge of the tools at 5 mm distances from the filament. The gas source used during the deposition process is composed of a mixture containing 1 % methane with excess of hydrogen; the volume flow rate for hydrogen is 100 sccm, while the volume flow rate for methane is 1 sccm. The deposition time and pressure in the vacuum chamber were 5–15 h and 20 Torr (2.66 kPa) employed. The substrate temperature

Table 7.5 Process conditions used for diamond film deposition on surgical tools

Process variables	Operating parameters
Tantalum filament diameter (mm)	0.5
Deposition time (h)	5–15
Gas mixture	1 % CH_4 in excess H_2
Gas pressure (Torr)	20 (2.66 kPa)
Substrate temperature (°C)	800–1000
Filament temperature (°C)	1800–2100
Substrate (WC-Co/Mo/Ti) diameter (mm)	Wire/drill/surgical tool (approx. 1 mm)
Distance between filament and substrate (mm)	5
Pre-treatment (Murakami etching and acid etching)	20 min plus 10 s

was measured by a K-type thermocouple mounted on a molybdenum substrate holder. The depositions are carried out between 800 and 1000 °C. The filament temperature is measured using an optical pyrometer and found to be between 1800 and 2100 °C depending upon the filament position. A summary of the process conditions is shown in Table 7.5.

7.8 Nucleation and Growth

The growth of diamond thin films at low pressures, at which diamond is metastable, is one of the most exciting developments in materials science of the past two decades. However, low growth rates and poor quality currently limit applications. Diamond growth is achieved by a variety of processes using very different means of gas activation and transport. Generalized models coupled with experiments show how process variables, such as gas activation temperature, pressure, characteristic diffusion length, and source gas composition, influence diamond growth rates and diamond quality. The modeling is sufficiently general to permit comparison between growth methods. The models indicate that typical processes, e.g., hot filament, microwave, and thermal plasma reactors operate at pressures where concentrations of atomic hydrogen, [H] and methyl radicals, [CH_3] reach maxima. The results strongly suggest that the growth rate maxima with pressure arise from changes in the gas phase concentrations rather than changes in substrate temperature.

The results also suggest that, at 1 atmospheric pressure using only hydrocarbon chemistry, growth rates saturate at gas activation temperatures above 4000 K. Models of defect incorporation indicate that the amount of sp^2, non-diamond material incorporated in the diamond is proportional to [CH_3]/[H] and therefore can be correlated with the controllable process parameters. The unusual and interesting connection between diamond nucleation and growth with the process of the vapor synthesis of diamond is essentially quite simple. Carbon-containing precursor

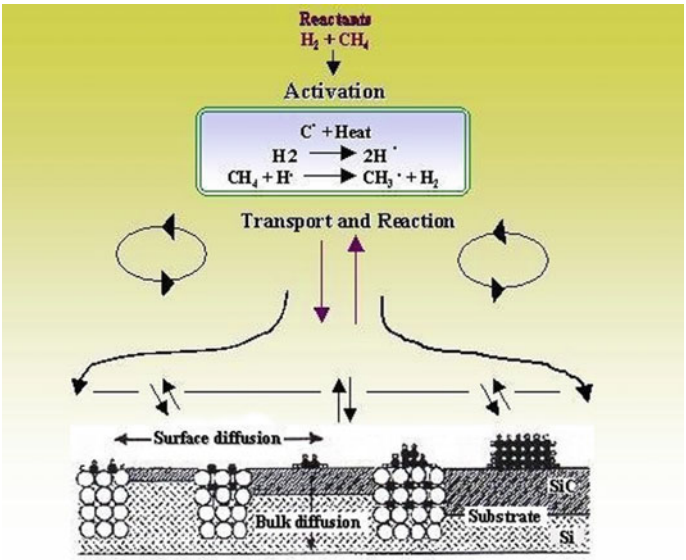

Fig. 7.6 Schematic diagram of diamond nucleation and growth

molecules (like CH_4) are excited and/or dissociated and subsequently condensing via a free dangling bond of the radical in diamond configuration on a surface [63, 64] (Fig. 7.6).

A nucleation pathway occurs through a stepwise process including the formation of extrinsic (pre-treatment) or intrinsic (in situ) nucleation sites, followed by formation of carbon-based precursors. It is believed that nucleation sites could be either grooves of scratching lines or protrusions produced by etching-re-deposition.

The gas activation is done either by hot filaments, microwave, or radio-frequency plasmas. The most crucial parameter in all this process is besides a carbon source the presence of large amounts of atomic hydrogen. The role of atomic hydrogen in the process is

- Creation of active growth sites on the surface
- Creation of reactive growth species in the gas phase
- Etching of non-diamond carbon (like graphite) graphitic, sp^2, precursors will be explored.

7.8.1 Nucleation Stage

Nucleation of diamond is a critical and necessary step in the growth of diamond thin films, because it strongly influences diamond growth, film quality and morphology [65]. Growth of diamond begins when individual carbon atoms nucleate

onto the surface to initiate the beginnings of an sp^3 tetrahedral lattice. There are two types of diamond growth:

Homoepitaxial growth: It is an application of diamond substrates, the template for the required tetrahedral structure is already there, and the diamond lattice is just extended atom-by-atom as deposition proceeds.

Heteroepitaxial growth: It uses the non-diamond substrates, there is no such template for the C atoms to follow, and those C atoms that deposit in non-diamond forms are immediately etched back to the gas phase by reaction with atomic [H].

To deal with the problem of the initial induction period before which diamond starts to grow, the substrate surface often undergoes pre-treatment prior to deposition in order to reduce the induction time for nucleation and to increase the density of nucleation sites. There are two main methods to apply this pre-treatment:

Generally, seeding or manual abrading with diamond powder or immersing in diamond paste containing small crystallites processed in an ultrasonic bath enhances nucleation. The major consideration is the nucleation mechanism of diamond on non-diamond substrates. It has been shown that the pre-abrasion of non-diamond substrates reduces the induction time for nucleation by increasing the density of nucleation sites. The abrasion process can be carried out by mechanically polishing the substrate with abrasive grit, usually diamond power of 0.1–10 μm particle size, although other nucleation methods do exist such as bias-enhanced nucleation which is used in heteroepitaxial growth. The most promising in situ method for diamond nucleation enhancement is substrate biasing. In recent years, more controlled techniques, such as bias-enhanced nucleation and nano-particle seeding, have been used to deposit smoother films [66, 67]. In this method, the substrate is biased negatively during the initial stage of deposition [67]. Before CVD diamond deposition the filament was pre-carburised for 30 min in 3 % methane with excess hydrogen to enhance the formation of tantalum carbide layer on the filament surface in order to reduce the tantalum evaporation during diamond deposition [68].

7.8.2 Bias-Enhanced Nucleation (BEN)

The substrate can be biased both negatively and positively; however, there is much research work and a large volume of literature on negative biasing. Negative substrate biasing is attractive because it can be controlled precisely; it is carried out in situ, gives good homogeneity, and results in improved adhesion. On flat substrates, such as copper and silicon, biasing has been shown to give better adhesion, improved crystallinity and smooth surfaces.

A negative bias voltage up to −300 V has been applied to the substrate relative to the filament. This produced emission currents up to 200 mA. The nucleation times used were between 10 and 30 min. In the activated deposition chamber, CH_4 and H_2 were decomposed into various chemical radical species CH_3, C_2H_2, CH_2, CH, C, and atomic hydrogen H by the hot tantalum filament. The methyl radicals

and atomic hydrogen are known to play important roles in diamond growth. In the biasing process, electrons were emitted from the diamond-coated molybdenum substrate holder and moved to the filament after they gained energy from the electrical field. When the negative bias was applied to the anode, the voltage was gradually increased until a stable emission current was established and a luminous glow discharge was formed near the substrate [69]. The nucleation density of diamond has been calculated from the SEM micrographs. Figure 7.7a, b shows the effects of bias time on the nucleation density at bias voltage of −300 V. As bias time is increased, the nucleation density also increases. The highest nucleation density was calculated to be 0.9×10^{10} cm^{-2} for a bias time of 30 min. At a bias time of 10 min, the nucleation density obtained was 2.7×10^{8} cm^{-2}.

Kim et al. [70] also reported that an increase in the emission current produced higher nucleation densities [71]. Since the bias voltage and emission current are

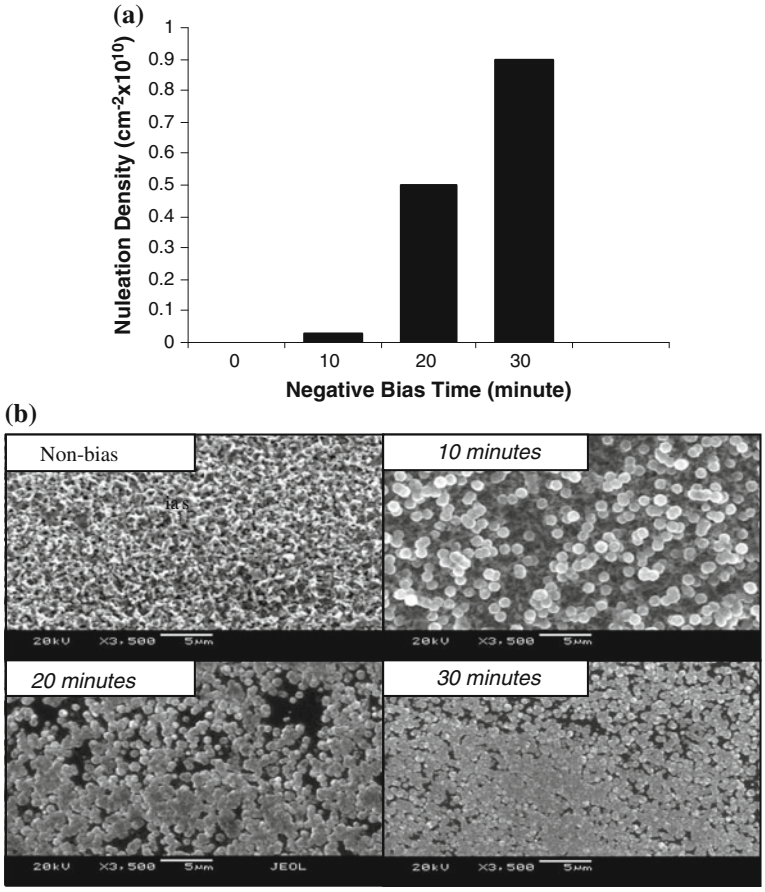

Fig. 7.7 **a** Nucleation density of diamond by BEN; **b** SEM of nucleation density on substrate

related, the enhancement of the nucleation density cannot be attributed to solely ion bombardment or electron emission of the diamond-coated molybdenum substrate holder, but may be a combination of these mechanisms [72]. Results were based on negatively BEN related to the grounded filament. However, it was reported that very low electric biasing current values (μA) were detected for applied substrate biases voltages either positive or negative. Furthermore, when increasing negative biases of up to −200 V resulted in a value of nucleation density similar to that obtained with positively BEN related to the filament. In contrast, an application of negative bias applied to the substrate at −250 V resulted in (10^{10} cm^{-2}) maximum values of nucleation density. The enhancement in the nucleation density can be attributed to the electron current from the filament by increasing the decomposition of H_2 and CH_4. The increase in the nucleation density is expected since negatively biasing the substrate increases the rate of ion bombardment into the surface creating greater numbers and density of nucleation sites. Therefore, the greater the density of nucleation sites the higher the nucleation density. Polo et al. [72] reported that reproducibility of the experiment was poor and that no definite trend in the nucleation density could be found with respect to different bias conditions.

7.8.3 *Influence of Temperature*

Temperature is a major factor in influencing the deposition rate, crystallite size, and controlling the surface roughness. Variation in the average crystallite size of diamond along the length of the substrate (surgical tool) can be attributed to the variation in the substrate temperature. The substrate temperature from the end to the center of the filament is more accentuated for molybdenum wire with a smaller diameter [9]. Figure 7.8 demonstrates the ability of this CVD process to coat 3D-shaped components, illustrating that the process is in the kinetic control regime rather than transport control regime. Most PVD type processes operate at conditions

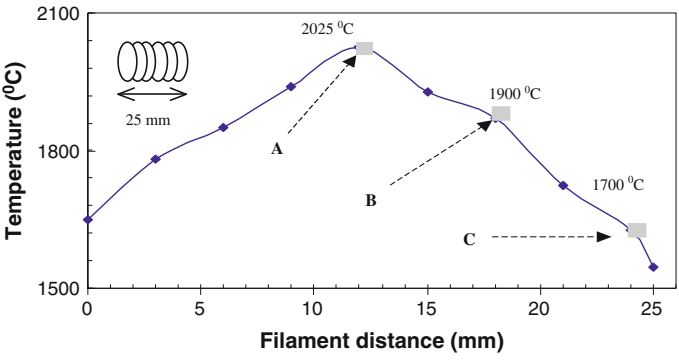

Fig. 7.8 Deposition temperature against filament position

where the rate-determining step of the deposition process is the diffusion of precursor gases to the substrate surface. Generally, this results in poor film uniformity in grooves and at the sharp edges. By operating under kinetic control regime, film uniformity is much enhanced.

Deposition temperature can also influence the diamond film thickness in terms of substrate and filament position. Analysis of temperature distribution along the coiled filament showed that the temperature is highest at the center of the filament with a rapid decrease toward the edges (Fig. 7.8). This suggests that position A is the hottest followed by position B and C on the bur. Generally, higher substrate temperatures increase diamond film growth rate and the crystallite size. At the bottom of the filament coil temperature is lower; therefore, the part of the bur parallel to the coil at this temperature will be coated with the diamond film at a lower growth rate. Therefore, it can be expected that at these regions the film will be thinner. The thermal gradient gives variations in the film thickness and crystal sizes as evident from figure. Generally, with columnar growth, the average crystallite size increases as the films become thicker. The films were thicker and the crystallite size was larger at position A compared to position C.

Analysis of temperature distribution along the coiled filament showed that the temperature is highest at the center of the filament with a rapid decrease toward the edges. The bur substrate and filament temperature have been measured parallel to the positions A, B, and C, respectively (Fig. 7.9). This suggests that position A is

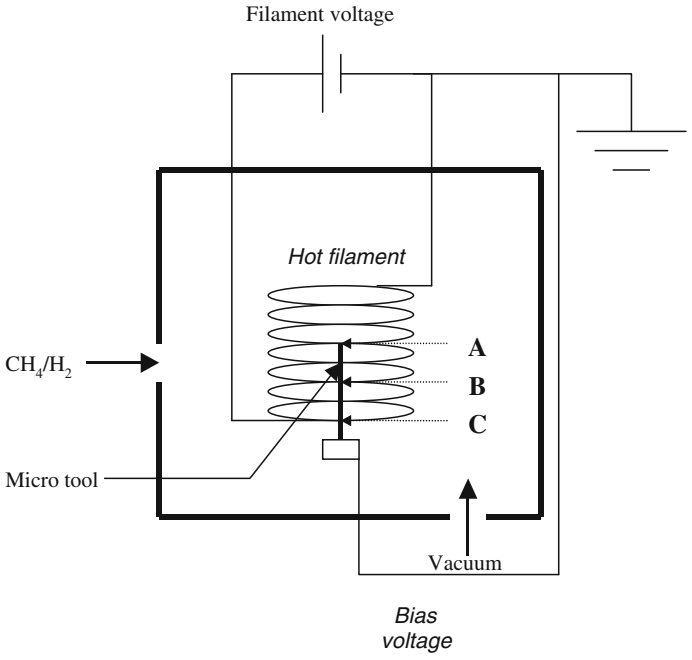

Fig. 7.9 Schematic diagram of a surgical tool assembled with filament

the hottest followed by position B and C on the bur. Variations in the film thickness and crystal sizes are mainly due to thermal gradients at various positions on the bur.

Figure 7.10 indicates that the coated surgical tool was cut in order to study the cross section of the tool. It was found that the coating is thicker at the cutting teeth

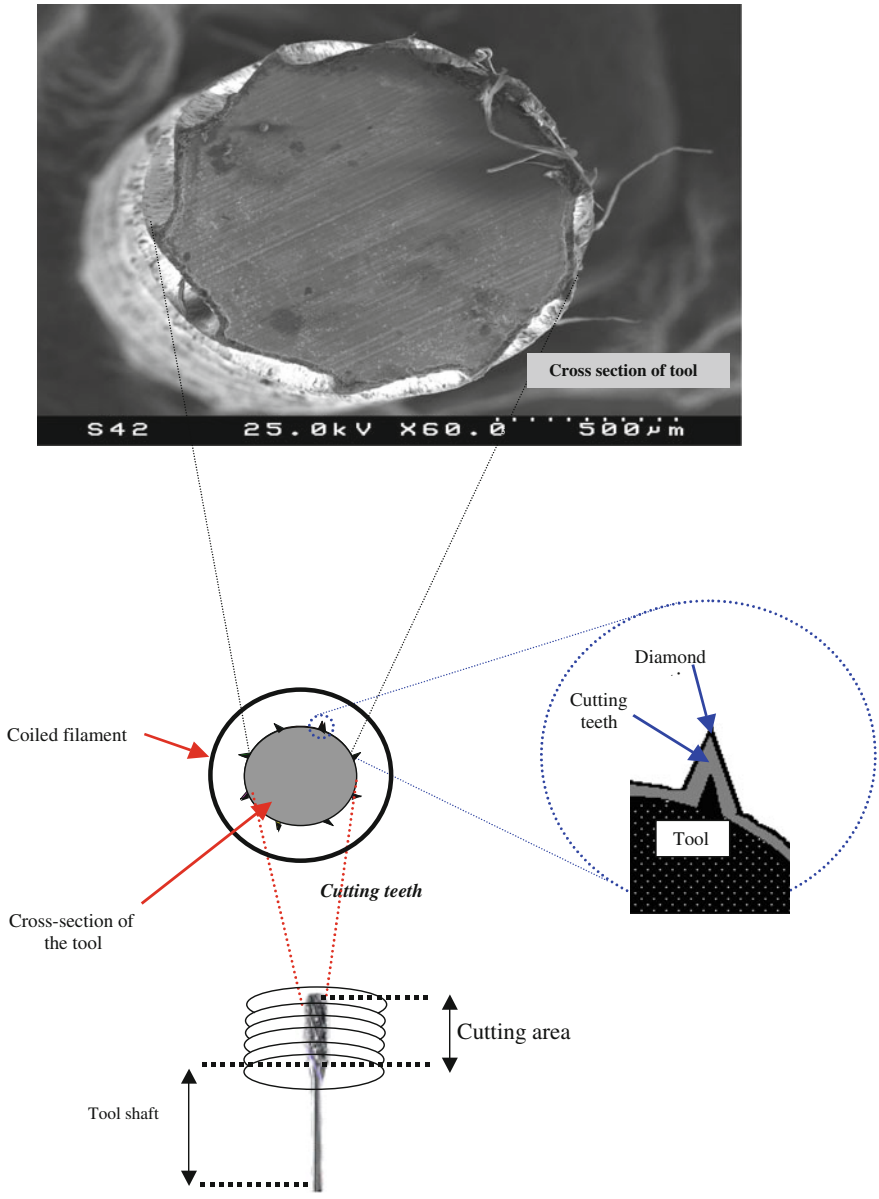

Fig. 7.10 Schematic diagram of surgical tool cutting edges

with average thickness of about 43 μm due to the slightly higher temperature at the bur tip because cutting teeth is closer to the filament coil. At the base of the bur, the heat is carried away faster and therefore it is at a lower temperature giving rise to lower growth rates and hence thinner films, at about 23 μm in thickness. Thicker coating at the tip is expected to give the tool longer life. Further work is required to study the effects of film thickness at the tooth tip and at the base on tool performance and lifetime.

Deposition temperature can also influence the diamond film thickness in terms of substrate and filament position. Analysis of temperature distribution along the coiled filament showed that the temperature is highest at the center of the filament with a rapid decrease toward the edges (Fig. 7.8). This suggests that position A is the hottest followed by position B and C on the bur. Generally, higher substrate temperatures increase diamond film growth rate and the crystallite size. At the bottom of the filament coil temperature is lower; therefore, the part of the bur parallel to the coil at this temperature will be coated with the diamond film at a lower growth rate. Therefore, it can be expected that at these regions the film will be thinner. The thermal gradient gives variations in the film thickness and crystal sizes as evident from figure. Generally, with columnar growth, the average crystallite size increases as the films become thicker. The films were thicker and the crystallite size was larger at position A compared to position C.

Analysis of temperature distribution along the coiled filament showed that the temperature is highest at the center of the filament with a rapid decrease toward the edges. The bur substrate and filament temperature have been measured parallel to the positions A, B, and C, respectively (Fig. 7.9). This suggests that position A is the hottest followed by position B and C on the bur. Variations in the film thickness and crystal sizes are mainly due to thermal gradients at various positions on the bur.

7.9 Deposition on 3D Substrates

7.9.1 Diamond Deposition on Metallic (Molybdenum) Wire

It is difficult to deposit CVD diamond onto cutting tools, which generally have a 3D shape and possess complex geometry and sharp edges, using a single step growth process [73]. The cylindrical shape wire, which has complex geometry, can be used as a model application for deposition of diamond on cutting tools such as surgical tools and surgical tools. The molybdenum (Mo) wires are deposited with CVD diamond by modified vertical filament approach. After deposition time of 5 h, continuous films of 5 μm thick CVD diamond were obtained (Fig. 7.11). The film morphology showed that it has good uniformity and high purity of diamond. The Raman spectroscopy confirmed that sp^3 diamond peak at wave number 1332.6 cm^{-1} as shown on Fig. 7.12.

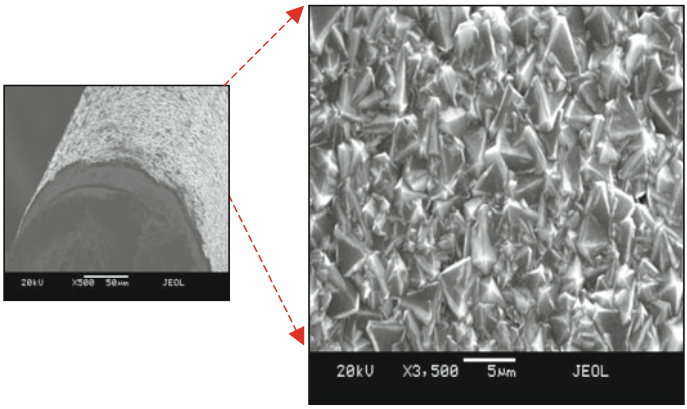

Fig. 7.11 Diamond film on molybdenum

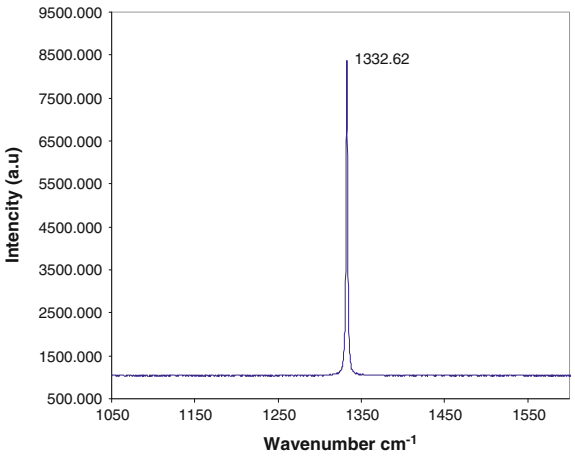

Fig. 7.12 Raman spectra of CVD diamond on molybdenum wire

7.9.2 Deposition on WC-Co Surgical Tool

Deposition of diamond on wires can be readily extended to surgical tools used for machining tool, NEMS, and MEMS devices. The uniform and adherent coating are essential in order to obtain an improved performance. Figure 7.13a shows an SEM micrograph of an uncoated surgical tool. The WC-Co cutting edges are welded onto the steel shaft (Fe–Cr). The cutting tip is 4 mm in length and 0.8 mm in diameter. The surgical tool has six sharp cutting edges, which is clearly visible in Fig. 7.13b.

Figure 7.14 shows the SEM micrographs and the corresponding EDX spectra of the WC-Co surgical tool before and after the chemical etching process. Before

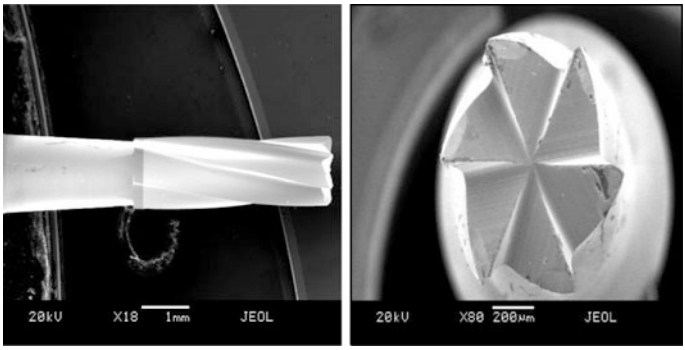

Fig. 7.13 Tip and cutting edge of surgical tool

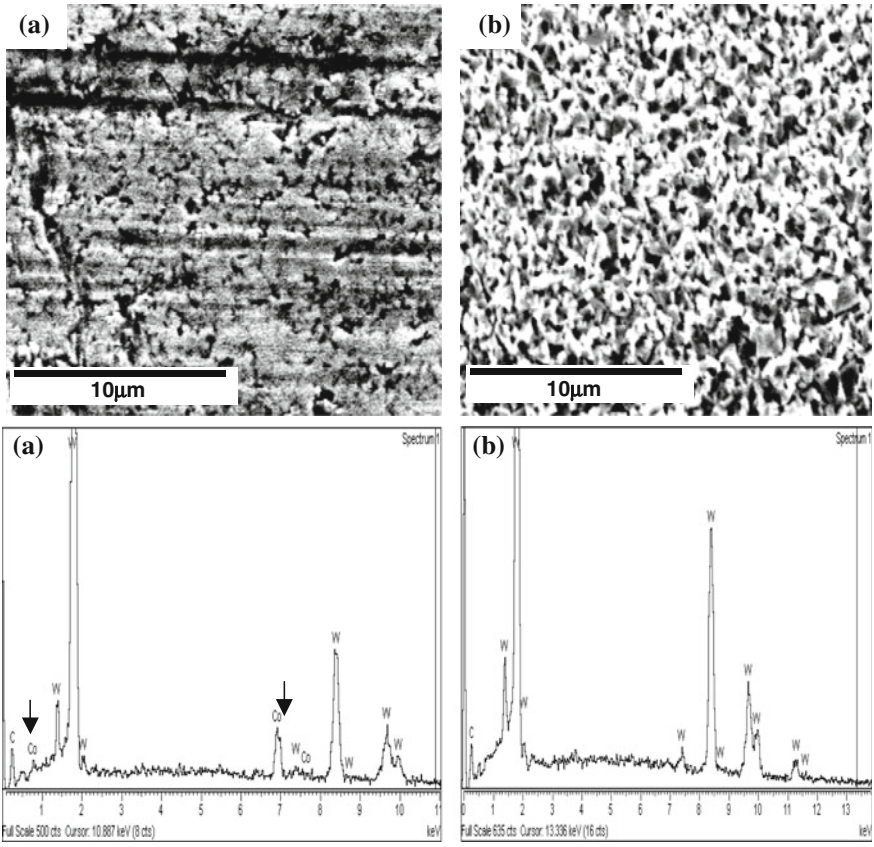

Fig. 7.14 **a** SEM and EDX of WC-Co surgical tool before etching; **b** WC-Co surgical tool after etching

etching, the EDS spectrum (Fig. 7.14a) shows the peaks for cobalt (Co), carbon (C), and tungsten (W). High cobalt content inhibits diamond deposition, resulting generally in graphitic phases, which degrade the coating adhesion. The Co diffuses to the surface regions, preventing effective bonding between the substrate surface and the film coating. To improve the coating adhesion of diamond on WC-Co tools, several approaches can be employed. For example, first, the use of interlayer material such as chromium can act as a barrier against cobalt diffusion during diamond CVD. Second, the cobalt from the tool surface can be etched using either chemical or plasma methods. Third, the cobalt can be converted into stable intermediate interlayer cobalt compounds. These can act as a barrier to cobalt diffusion from the substrate during film growth [74]. Murakami solution followed by H_2SO_4/H_2O_2 etch can be used to chemically remove the cobalt from the bur surface. The EDX spectrum shows that the Co peak has disappeared after etching. This will prove to be beneficial in enhancing the coating adhesion. Comparison of the SEM micrograph in Figs. 7.14a, b shows that the surface topography is significantly altered after etching in Murakami and H_2SO_4/H_2O_2 solutions. The etching process makes the surface much rougher with a significant amount of etch pits, which act as low-energy nucleation sites for diamond crystal growth.

An SEM micrograph of a diamond-coated WC surgical tool is shown in Fig. 7.15. Six cutting edges of the surgical tool tip were coated with a PCD film using the modified vertical HFCVD method. Analysis of the SEM picture shows that the coating uniformly covered the cutting edges as well as the nearby regions in which the placement of the surgical tool within the coils of the filament, ensuring uniform deposition. The diamond crystal structure and morphology are uniform and adherent, as shown in Fig. 7.15a, b. It also shows a close-up view of the diamond-coated region of the surgical tool in Fig. 7.15c.

Typically, the crystallite sizes are of the order 5–8 μm. The visibly adherent diamond coatings on the WC-Co surgical tools consist of mainly (111) faceted diamond crystals. The design of the filament and substrate in the reactor offer the possibility of uniformly coating even larger diameter cylindrical substrates.

Raman analysis was performed in order to evaluate the diamond carbon-phase quality and film stress in the deposited films. The Raman spectrum in Fig. 7.16 shows a single peak at 1335 cm^{-1} for the tip of the diamond-coated surgical tool. The Raman spectrum also gives information about the stress in the diamond coatings. The diamond peak is shifted to a higher wave number of 1335 cm^{-1} than that of natural diamond peak 1332 cm^{-1} indicating that stress, which is compressive in nature, exists in the resultant coatings [74].

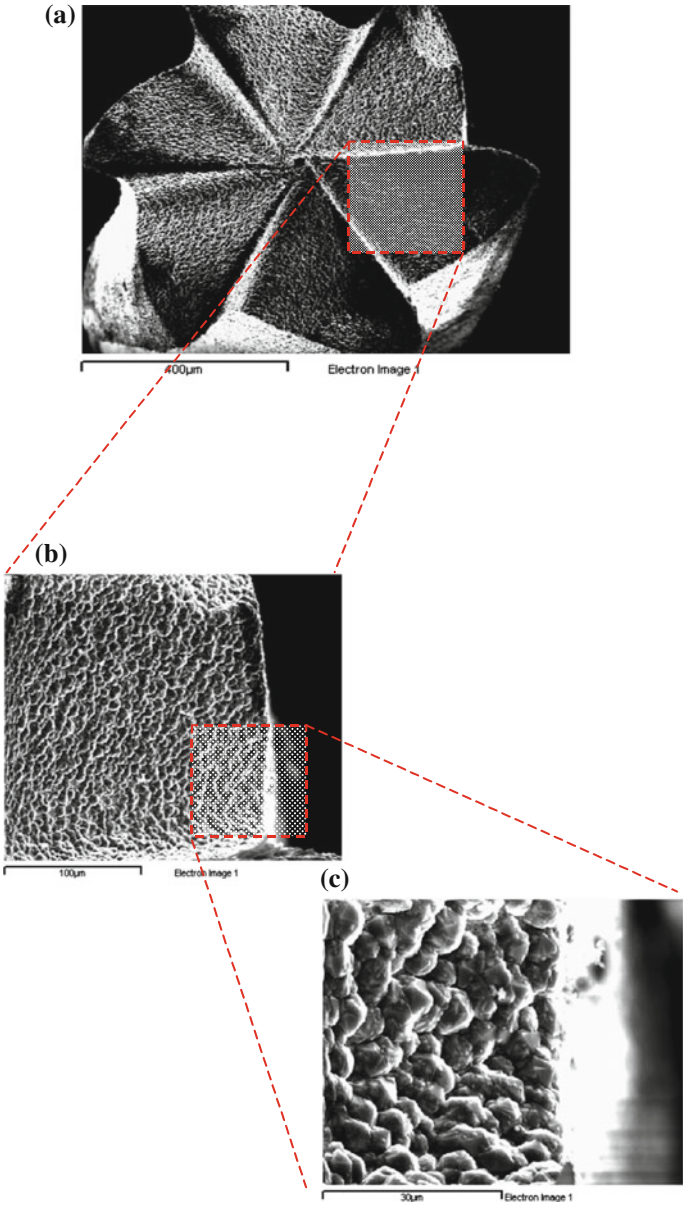

Fig. 7.15 **a** Cutting edge of surgical tool after depositing with CVD diamond; **b** cutting edge of surgical tool uniformly coated with diamond; **c** SEM of surgical tool after coating with diamond

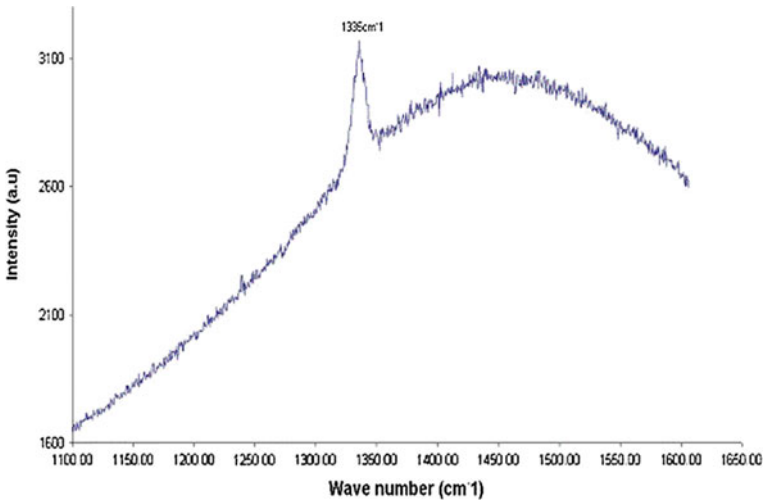

Fig. 7.16 Raman spectra of diamond-coated WC-Co surgical tool

7.9.3 Diamond Deposition on Tungsten Carbide (WC-Co) Surgical Tool

Laboratory grade tungsten carbide (WC-Co) surgical tools are shown in Fig. 7.17a, b (AT23 LR) with fine WC grain sizes (1 μm) 20–30 mm in length and 1.0–1.5 mm in diameter [supplied by Metrodent Ltd, UK] that are used for the CVD diamond deposition process.

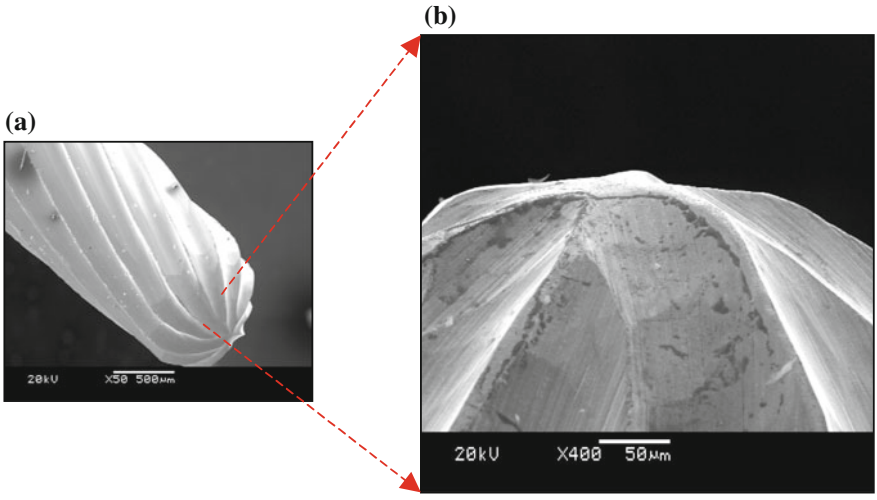

Fig. 7.17 **a** Laboratory used WC-Co surgical tool; **b** laboratory used WC-Co surgical tool before surface treatment

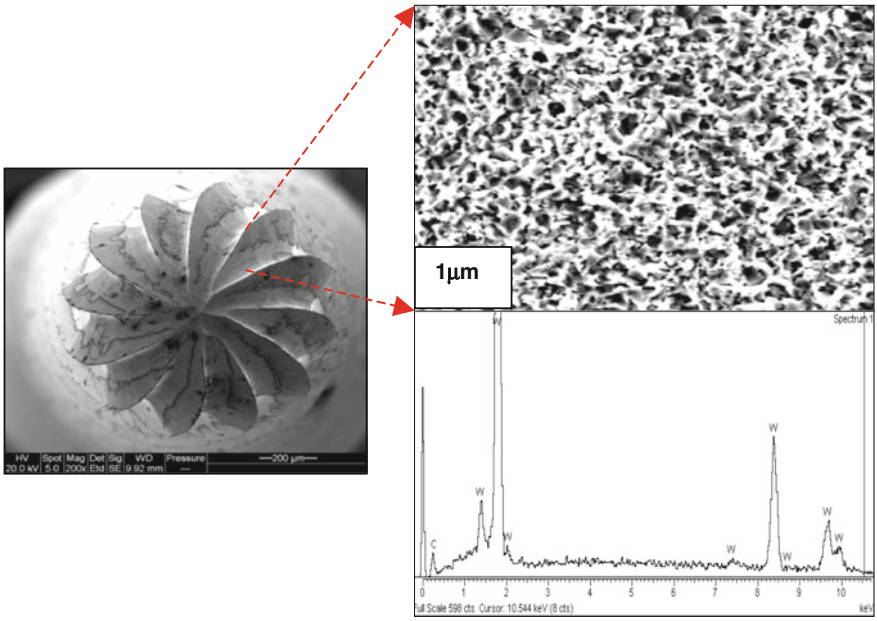

Fig. 7.18 Etched surgical tool surface after chemical treatment

The WC surface has etched away with Murakami solution and surface Co has been removed by acid etching followed by ultrasonically washing in distilled water. The EDX results confirmed that there is no indication of Co left on the surface of the etched surgical (Fig. 7.18). Diamond films have been deposited onto the cutting edge of the tools at a 5 mm distance from the tantalum wire filament.

Surface morphology of predominantly (111) faceted octahedral-shaped diamond films was obtained. The film thickness was measured to be 15–17 µm after diamond deposition for 15 h. Figure 7.19 shows the SEM micrograph of a CVD diamond-coated surgical tool (AT 23LR) at the cutting edge. The film is homogeneous with uniform diamond crystal sizes, typically in the range of 6–10 µm. As expected, the surface morphology is rough making the surgical tools extremely desirable for abrasive applications.

The Raman spectra shown show that at the tip, center, and end of cutting tool single sharps peak at 1336, 1336, and 1337 cm^{-1}, respectively, were observed for different positions (Fig. 7.20). The Raman spectrum also gives an indication about the stress in the diamond coating. The diamond peak is shifted to a higher wave number of magnitude such as 1336, 1337 cm^{-1} than that normally experienced in an unstressed coating where the natural diamond peak occurs at 1332 cm^{-1} thus indicating that the stress is compressive.

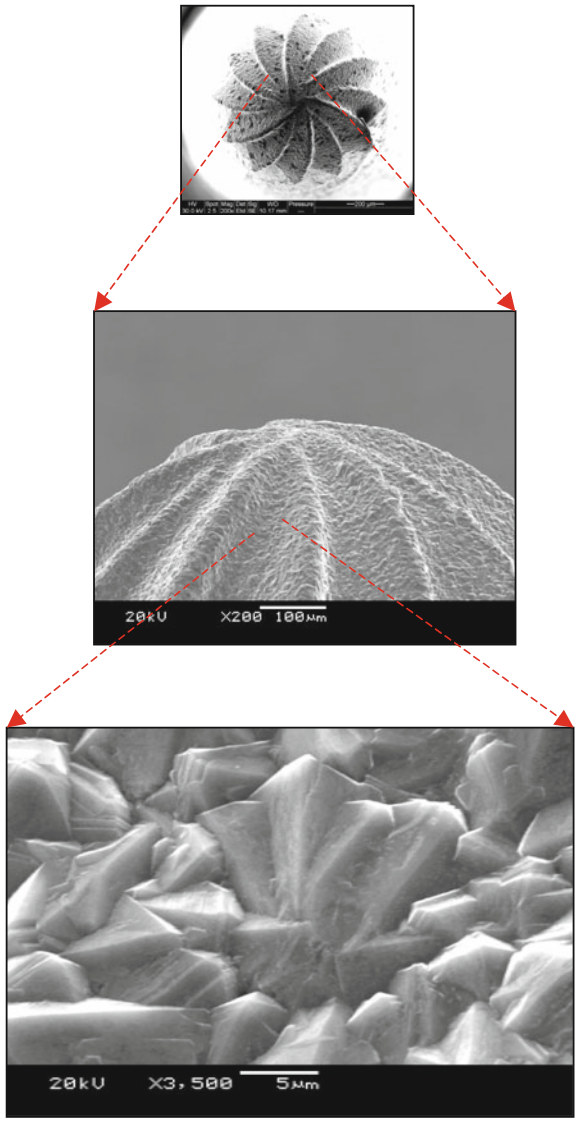

Fig. 7.19 (111) faceted octahedral shape diamond films on a surgical tool

7.10 Wear of Diamond

The quality and economy of industrial production processes are to a great extent determined by the selection and the design of appropriate manufacturing operations. For many machining operations, especially for the technologically relevant processing of metallic materials, machining with geometrically specified cutting edge is applicable. Enhancing the performance of machining operations is therefore an

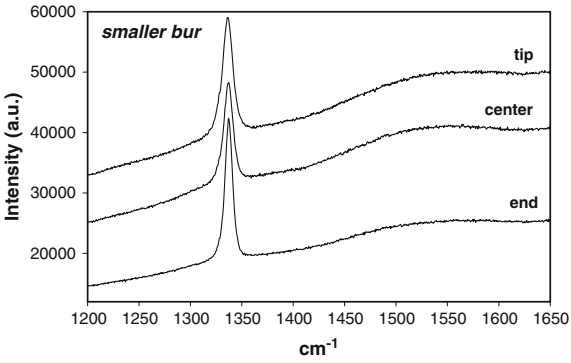

Fig. 7.20 Raman spectra of diamond film on surgical tool

economically important goal; to achieving this, coating technology can contribute in varying ways. The cutting tool is the component that is most stressed, and therefore limits the performance in NEMS and MEMS operations. Thermal and mechanical loading affects the cutting tool edges in a continuous or intermittent way. As a result, in addition to good wear resistance, high thermal stability and high mechanical strength are required for cutting materials. Opposing this objective of an ideal cutting material is the fundamental contradiction of properties hardness, strength at elevated temperature, and wear-resistance on one hand, and bending strength and bending elasticity on the other hand.

Cutting materials for extreme requirements (for example, interrupted cuts or machining of high strength materials) consequently cannot be made from one single material, but may be realized by employing composite materials.

Surface coatings may improve the tribological properties of cutting tools in an ideal way and therefore allow the application of tough or ductile substrate materials, respectively.

The coated surgical tools have been used to machine a number of materials including copper, aluminum, and iron alloys. The coated tools were compared with uncoated surgical tools to distinguish them in terms of their machining behavior. A micro-machining unit was specifically constructed at Purdue University by Professor Mark Jackson for such a purpose with a maximum spindle speed of 500,000 rpm, feed rates of between 5 and 20 μm per revolution, and cutting speeds in the range 100–200 meters per minute [75]. The micro-machining unit is shown in Fig. 7.21. The machining center is constructed using three principal axes each controlled using a D.C motor connected to a Motionmaster^{TM} controller. A laser light source is focused onto the rotating spindle in order to measure the speed of the cutting tool during machining. Post machining analysis was performed using a scanning electron microscope to detect wear on the flanks of the cutting edges.

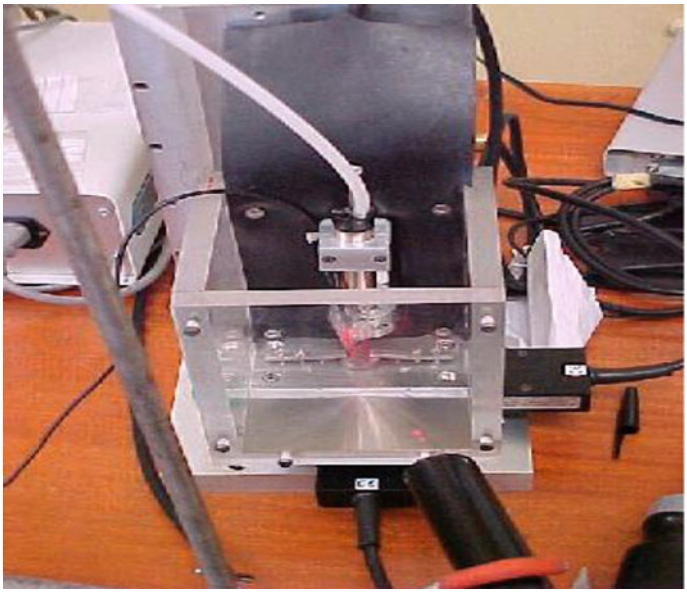

Fig. 7.21 Micro-machining center

7.10.1 Performance of Diamond-Coated Surgical Tool

After machining an aluminum alloy material, very low roughness and chipping of the diamond-coated surgical tool were detected. Figure 7.22 shows a typical machined surface in aluminum alloy. A metal chip created from this machining operation is shown in Fig. 7.23. The chip clearly shows shear fronts separated by lamellae caused by plastic instabilities within the material generated at such high speeds. Diamond-coated tools and uncoated were compared by drilling a series of holes in the aluminum alloy. The wear of each tool was determined by examining the extent of flank wear. Uncoated tools appeared to chip at the flank face, and diamond-coated tools tended to lose individual diamonds at the flank face. Uncoated tools drilled an average of 8000 holes before breakdown occurred, and the diamond-coated tools drilled an average of 24,000 holes [76].

7.10.2 Performance of Diamond-Coated Surgical Tool

In order to examine the cutting performance of the diamond-coated surgical tools machining materials such as borosilicate glass, acrylic teeth, and natural human teeth were used. Machining unit was set up for the laboratory bur (AT23LR supplied by Metrodent, UK), which used to operate at 20,000–30,000 rpm with a feed rate of 0.2–0.5 mm/rev without water-cooling.

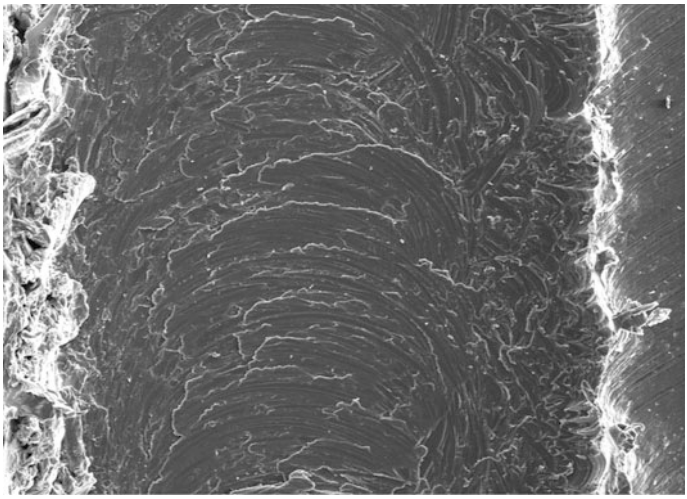

Fig. 7.22 Aluminum alloy material showing a machined track produced by a diamond-coated surgical tool

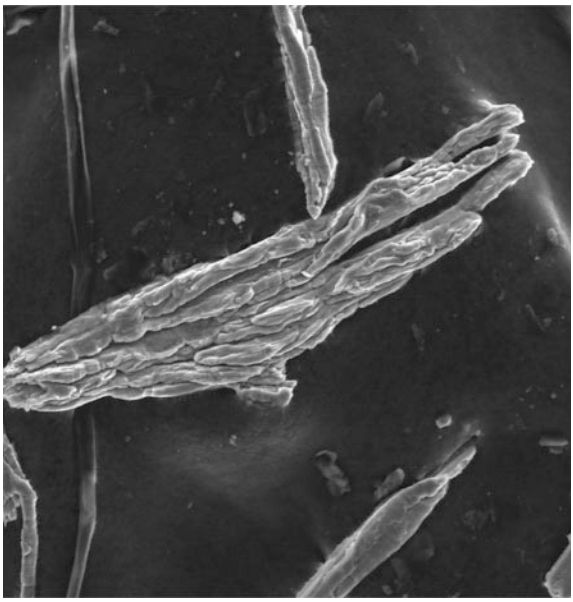

Fig. 7.23 Aluminum alloy chips generated during high-speed micro-machining operations using a diamond-coated surgical tool

The flank wear of the burs were estimated by SEM analysis at selected time interval of 1 and 3 min. Prior to SEM analysis diamond-coated burs were ultrasonically washed with 6 M Sulfuric acid solution to remove any unwanted machining material, which eroded onto surface of CVD diamond-coated bur. For comparison, the commonly used conventional PCD sintered burs with different

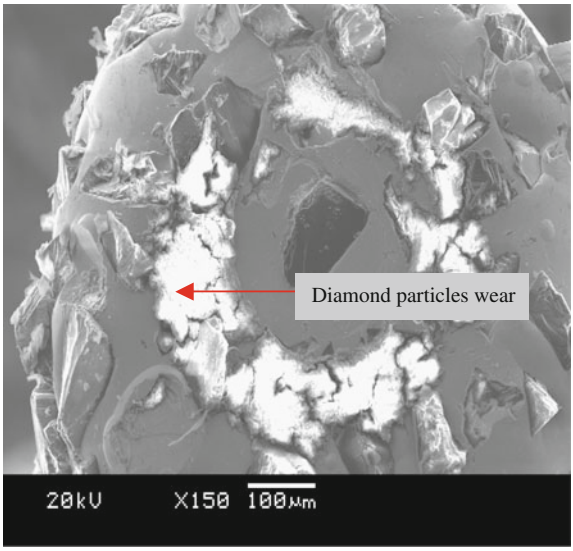

Fig. 7.24 Morphology of sintered diamond surgical tool after machining glass

geometry were also tested on the same machining materials. These burs are made by imbedding synthetic diamond particles into a nickel matrix material to bond the particles at the cutting surfaces.

The morphology of a sintered diamond bur after being tested on borosilicate glass at a cutting speed of 30,000 rpm for 5 min with an interval at every 30 s is shown in Fig. 7.24. It is clearly evident that there is significant removal of diamond particles from the surface of the tool after 500 holes. As expected, there is the deterioration of the abrasive performance of the PCD sintered diamond surgical tools.

SEM images of sintered diamond surgical tool tested on borosilicate glass (Fig. 7.24) and CVD diamond-coated laboratory bur after machining tests on borosilicate glass and acrylic/porcelain teeth, respectively, for 5 min at a cutting speed of 30,000 rpm are shown in Figs. 7.25 and 7.26. After machining, the diamond films are still intact on the pretreated WC substrate and diamond coating displayed good adhesion. There is no indication of diffusive wears after the initial test for 500 holes.

However, it was observed that the machining of materials such as glass pieces is eroded to cutting edge of the diamond surgical tool as adhesive wear (Fig. 7.25). After testing on acrylic teeth, the mechanism of wear probably involves adhesion as well as abrasion. Figure 7.26 shows that inorganic fillers from acrylic teeth adhered to the cutting tool surface in localized areas when a higher rate of abrasion was used [77].

A micrograph of an uncoated WC-Co surgical tool tested on the borosilicate glass using the same machining conditions are shown in Fig. 7.27a, b. The uncoated WC-Co bur displayed flank wear along the cutting edge of the bur. The areas of flank wear were investigated at the cutting edge of the surgical tool. A series of machining experiments have been conducted using uncoated, diamond-coated surgical tools, and sintered diamond burs when machining extracted human tooth, acrylic tooth, and borosilicate glass. The life of the burs in the machining sense was compared by using the amount of flank wear exhibited by

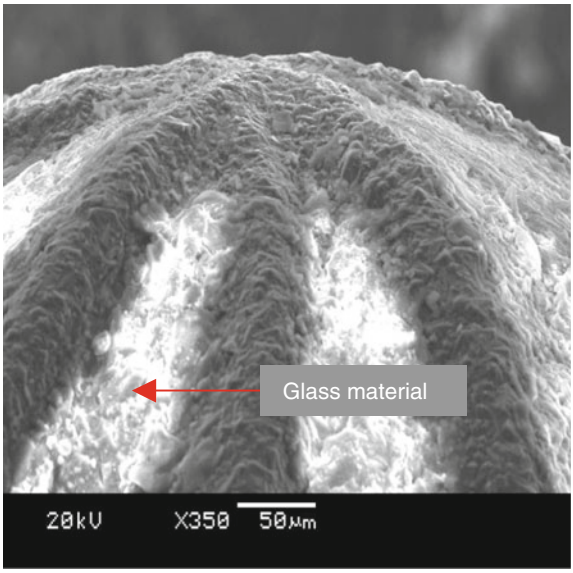

Fig. 7.25 Diamond-coated surgical tool after machining glass

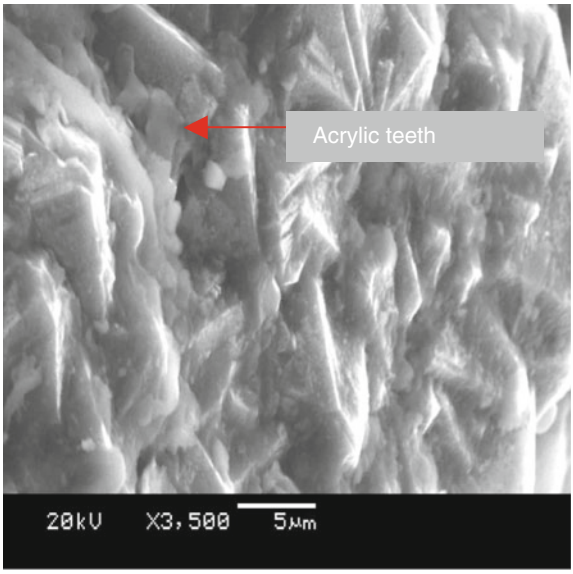

Fig. 7.26 Diamond-coated surgical tool after machining acrylic

each type of surgical tool. The flank wear was measured at time intervals of 2, 3, 4, 5, 6, and 7 min machining duration. Again, the surgical tools were examined using optical and scanning electron microscopic techniques and observed similar trends with burs that were used in drilling experiments.

The measurements of flanks wear for each bur that machined different dental materials are shown in Figs. 7.28, 7.29, and 7.30. It is evident that a longer duty

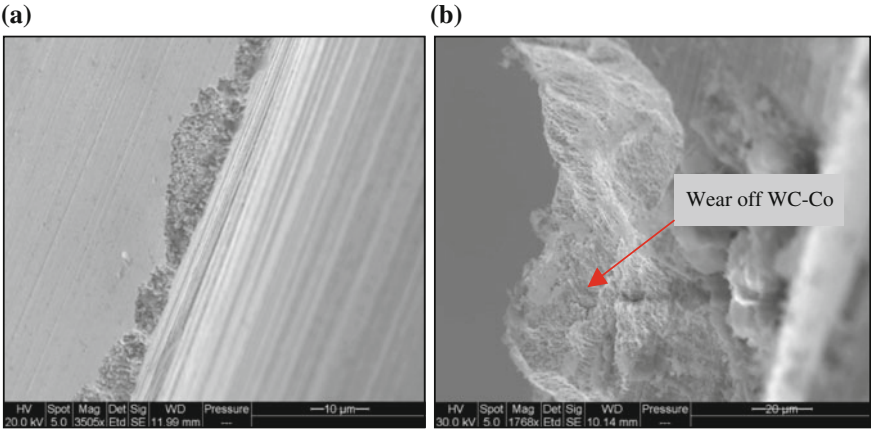

Fig. 7.27 **a** Cutting edge of WC-Co surgical tool after machining glass; **b** close-up view of WC-Co surface of the surgical tool

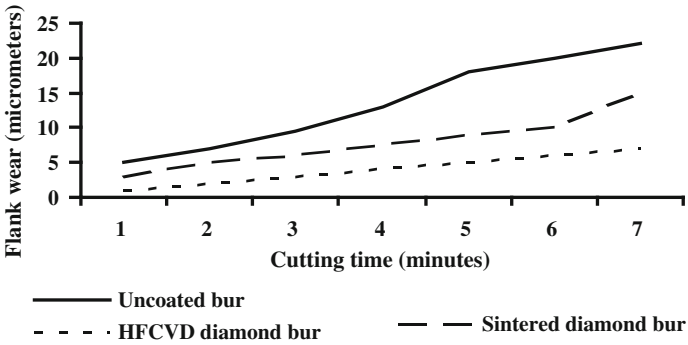

Fig. 7.28 Flank wear of cutting tools when machining borosilicate glass

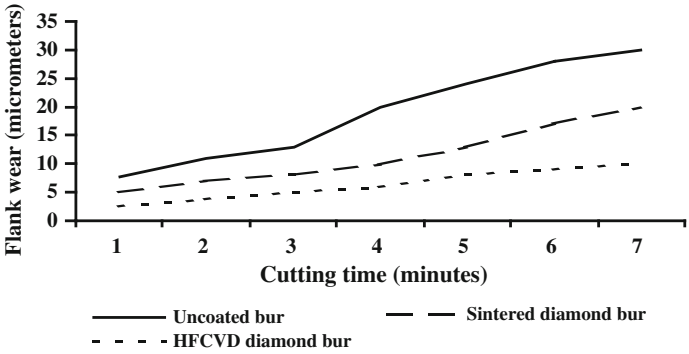

Fig. 7.29 Flank wear of cutting tools when machining acrylic material

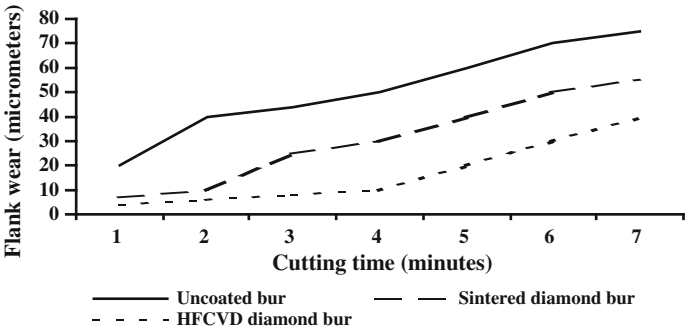

Fig. 7.30 Flank wear of cutting tools when machining dentine/enamel

cycle of machining could cause higher rate of flank wear on the cutting edge of tool. Therefore, the cutting edge of WC-Co surgical tool should have significant thickness of CVD diamond, which will enhance not only quality of cutting but will also prolong the tool life.

7.11 Time-Modulated CVD Diamond

In the conventional HFCVD method, using the relatively short bias voltage pulses in bias-enhanced nucleation in which the CH_4 concentration is increased, the flow of CH_4 during film growth is kept constant. Diamond growth in a CVD vacuum reactor is conventionally performed under constant CH_4 flow, while the excess flow of hydrogen is kept constant throughout the growth process. In developing the new TMCVD process it was considered that diamond deposition using CVD consists of two stages: (1) the diamond nucleation stage and (2) crystal growth stage.

Diamond grains nucleate more efficiently at higher CH_4 concentrations. However, prolonged film growth performed under higher CH_4 concentration leads to the incorporation of non-diamond carbon phases, such as graphitic and amorphous. The TMCVD process combines the attributes of both growth stages. This technique has the potential to replicate the benefits obtained by using pulsed power supplies, which are relatively more expensive to employ.

The key feature of the new process that differentiates it from other conventional CVD processes is that it pulses CH_4, at different concentrations, throughout the growth process, whereas in conventional CVD, the CH_4 concentration is kept constant, for the full growth process. In TMCVD, it is expected that secondary nucleation processes occur during the stages of higher CH_4 concentration pulses. This can effectively result in the formation of a diamond film involving nucleation stage, diamond growth, ad secondary nucleation and the cycle is repeated. The secondary nucleation phase can inhibit further growth of diamond crystallites. The nuclei grow to a critical level and then are inhibited when secondary nuclei form on

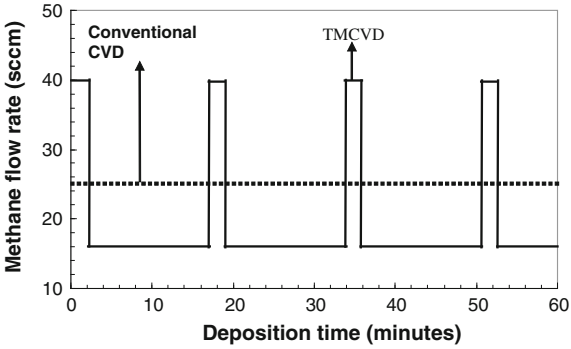

Fig. 7.31 Variations in CH_4 flow rates during film deposition in a typical time-modulated pulse cycle

top of the growing crystals and thus fill up any surface irregularities. This type of film growth can potentially result in the formation of a multilayer type film coating. In such coating systems, the quality and the surface roughness of the film coatings is dependent not on the overall thickness of the film but instead on the thickness of the individual layer of the film coating.

In demonstrating the CH_4 flow regimes, typically employed in conventional diamond CVD and TMCVD processes, Fig. 7.31 shows, as an example, the variations in CH_4 flow rates during film deposition. In the CH_4 pulse cycle employed in Fig. 7.31, the CH_4 flow rate remained constant throughout the conventional CVD process at 25 sccm. It is important to note that the hydrogen flow rate remains constant under both growth modes. CH_4 modulations at 12 and 40 sccm for 15 and 2 min, respectively, were performed during the TMCVD process using the microwave CVD system. Since higher CH_4 content in the vacuum chamber results in the incorporation of non-diamond carbon phases in the film, such as graphitic and amorphous, and degrades the global quality of the deposited film, the higher CH_4 pulse duration was kept relatively short. The final stage of the time-modulated process ends with a lower CH_4 pulse. This implies that hydrogen ions will be present in relatively larger amount in the plasma and these will be responsible for etching the non-diamond phases to produce a good quality film.

Figure 7.32a, b displays the close-up cross-sectional SEM images of diamond films grown using TMCVD and conventional CVD processes. The conventional MCD film displays a columnar growth structure. However, the time-modulated film displayed a somewhat different growth mode. Instead, the cross section consisted of many coarse diamond grains that were closely packed together. A pictorial model of the mechanism for the TMCVD process is depicted in Fig. 7.32c as compared with the conventional CVD process (Fig. 7.32d). Primarily, diamond nucleation occurs first in both the TMCVD and conventional CVD processes. However, in TMCVD, diamond nucleates more rapidly as a result of the high CH_4 pulse at the beginning. The high CH_4 pulse effectively ensures the diamond grains to nucleate quicker to form the first diamond layer. The second stage, in which CH_4 content is reduced to a lower concentration, the diamond crystallites are allowed to grow for a relatively longer period. This step enables the crystals to grow with columnar growth

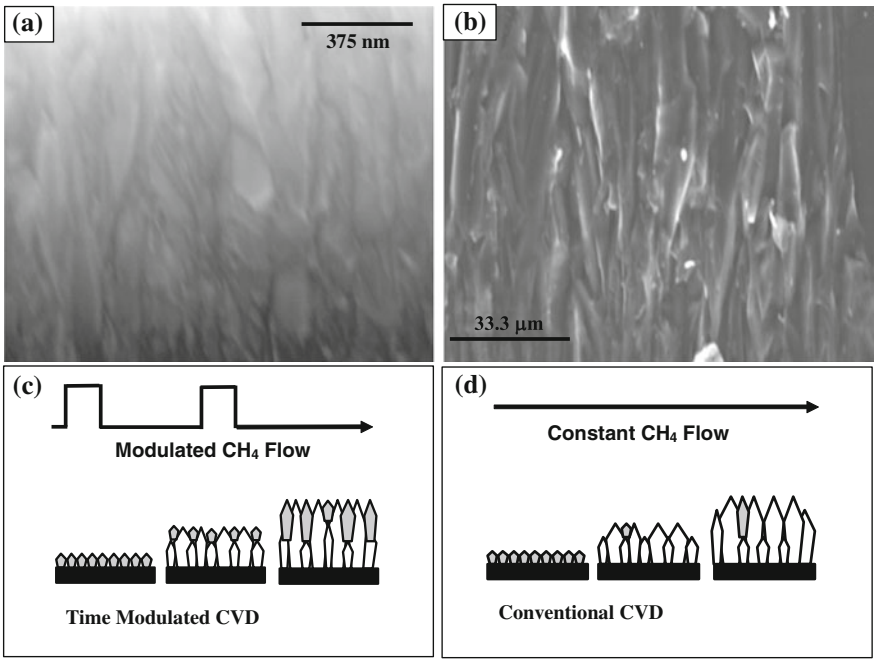

Fig. 7.32 Close-up cross-sectional SEM images of diamond films grown using **a** TMCVD and **b** conventional CVD processes. In addition, the pictorial mechanisms for film growth using TMCVD (**c**) and conventional CVD (**d**) processes are also shown

characteristics. The surface profile of the depositing film becomes rough, as expected. The third stage involves increasing the CH_4 flow back to the higher pulse. This enables further secondary nucleation of NCD to occur in between the existing diamond crystals, where the surface energy is lower. As a comparison, much less secondary nucleation occurs when the CH_4 flow is kept constant throughout the growth process. The distinctive feature of the TMCVD process is that it promotes secondary diamond-particle nucleation to occur on top of the existing grains in order to fill up any surface irregularities. Figure 7.33 displays the SEM micrograph showing secondary nucleation occurring after a high CH_4 pulse. This result justifies the proposition of the mechanism for the TMCVD process, as shown in Fig. 7.32. It can be expected that at high CH_4 bursts, carbon-containing radicals are present in the CVD reactor in greater amount, which favor the growth process by initiating diamond nucleation. The average secondary nucleation crystallite size was in the nanometer range (≤ 100 nm). It is evident that the generation of secondary nano-sized diamond crystallites has lead to the successful filling of the surface irregularities found on the film profile, in between the mainly (111) crystals. Figure 7.34 shows some randomly selected SEM images of as-deposited diamond films deposited using the TMCVD process at different CH_4 pulse duty cycles.

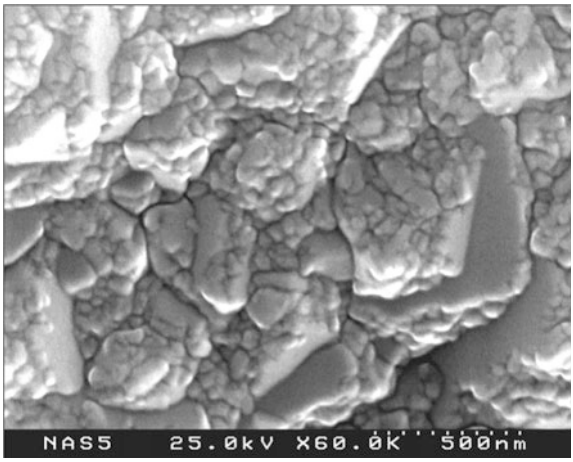

Fig. 7.33 SEM micrograph showing secondary nucleation occurring after a high CH_4 pulse

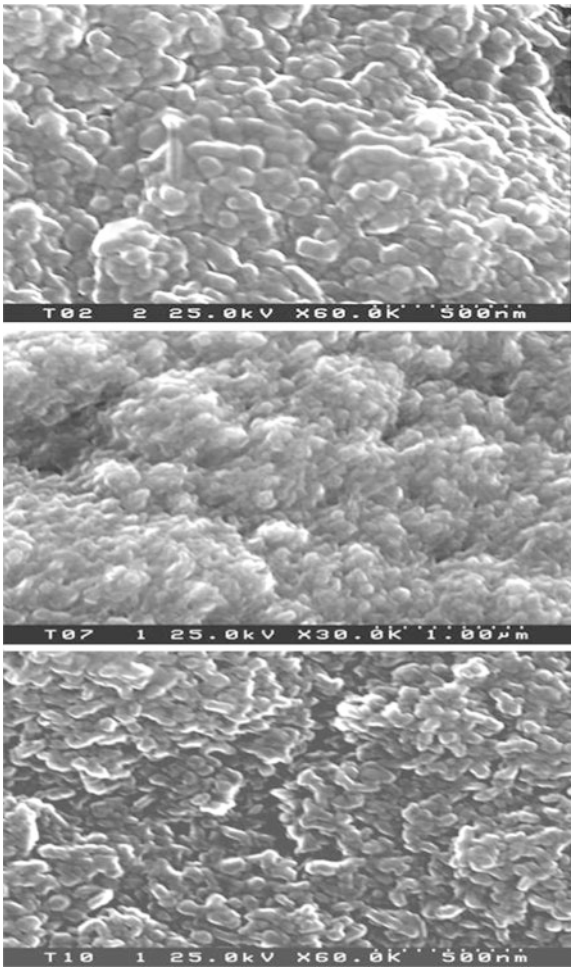

Fig. 7.34 SEM micrographs showing the morphologies of as-deposited diamond films deposited using TMCVD at different CH_4 modulation duty cycles

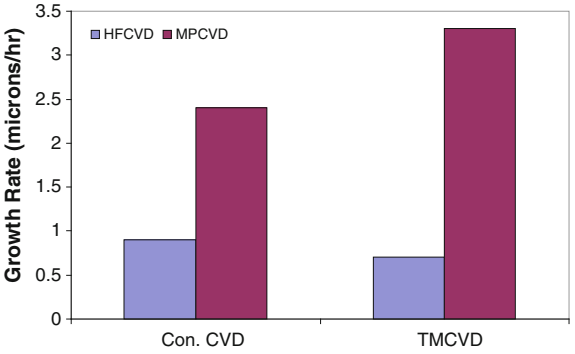

Fig. 7.35 Graph displaying the growth rates of conventional and time-modulated films grown using HFCVD and MPCVD systems

Figure 7.35 shows the graph displaying the growth rates of conventional and time-modulated films grown using HFCVD and microwave plasma CVD (MPCVD) systems. As expected, the MPCVD system gave much higher growth rates under both growth modes, conventional and time modulated, compared to films produced using HFCVD. A growth rate of 0.9 μm/h was obtained using the HFCVD system under constant CH_4 flow. The time-modulated films deposited using HFCVD were grown at a rate of 0.7 μm/h, whereas with the MPCVD system, films grown using constant CH_4 flow were deposited at a rate of 2.4 μm/h and using modulated CH_4 flow the films were grown at a rate of 3.3 μm/h. Although it is known that growth rates increase with CH_4 concentration, in the present case using the HFCVD system, the TMCVD process employs greater CH_4 flow than conventional CVD. Our results show that the growth rate of films deposited using constant CH_4 flow is slightly higher than of similar films grown using timed CH_4 modulations.

However, films grown under both modes, conventional and time modulated, using the MPCVD system produced results that were contrary to those obtained using the HFCVD system. Using the MPCVD system, the trend observed was that the films were deposited at a higher growth rate using the TMCVD process than conventional CVD. The substrate temperature is a key parameter that governs the growth rate in diamond CVD. Since the TMCVD process pulsed CH_4 during film growth, it was necessary to monitor the change in the substrate temperature during the pulse cycles. Figure 7.36 shows the graph relating substrate temperature to CH_4 concentration for both HFCVD and MPCVD systems. For the HFCVD system, it was observed that the substrate temperature decreased with CH_4 concentration. In explaining the observed trend, it needs to be considered that the dissociation of CH_4 by the hot filament absorbs energy (heat) from the filament and is considered as a cooling process. In our case the filament power was kept constant; therefore, less heat can be expected to radiate to the substrate. In addition, only a small percentage of the thermally dissociated CH species reach the substrate and transfer kinetic energy to the substrate.

It is known that the deposition of diamond films increases with substrate temperature. During the high CH_4 pulse in TMCVD, the lower substrate temperature

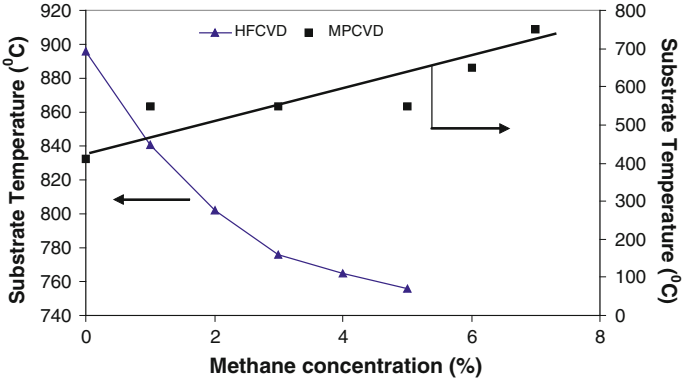

Fig. 7.36 Graph relating substrate temperature to CH_4 concentration for HFCVD and MPCVD systems

may be sufficient to lower the growth rate significantly. Generally, in a MPCVD reactor, the substrate temperature increases with CH_4 concentration, as shown in Fig. 7.36.

As a comparison, H_2 is dissociated more extensively in a MPCVD reactor than in a HFCVD reactor to produce atomic hydrogen. Furthermore, in a MPCVD reactor, the plasma power is much greater, 3400 W, than the plasma power in the HFCVD reactor. In fact, the plasma power used in MPCVD for growing diamond films was approximately 10 times greater than the power used in the HFCVD reactor. Therefore, the dissociation of CH_4 absorbs a lower percentage of the energy/heat from the plasma in a MPCVD compared to the HFCVD reactor. It is also understood that the reaction between atomic hydrogen and CH species at close proximity to the substrate releases heat. Since in a MPCVD reactor there is a greater intensity of atomic H and CH species, there will be a greater number of reactions between atomic H and CH species. This means that more heat will be released in a MPCVD reactor than in a HFCVD reactor because of such reactions.

This effect contributes to the heating of the substrate. In a HFCVD reactor, the hot filament displays much lower ability to dissociate H_2. Since atomic hydrogen is a critical species that plays an important role in producing a good quality diamond film during CVD, the quality of the films grown using HFCVD is generally lower than of similar films grown using MPCVD. In addition, the hydrogen atoms are required for the effective deposition of diamond onto the substrates. As mentioned earlier, atomic H radicals are present in greater concentration in a MPCVD reactor than in a HFCVD reactor, the MPCVD process gives higher growth rates than the HFCVD process. It is also known that by controlling the temperature during the high/low CH_4 pulse cycles, a greater number of secondary diamond grains were generated and the resultant films displayed (1) smoother surfaces and (2) higher growth rates.

7.12 Conclusions

Thin film deposition technologies, particularly CVD and PVD, have become critical for the manufacture of a wide range of industrial and consumer products. Trends in historical developments in the CVD diamond suggest that the technology is highly likely to yield substantial benefits in emerging technological products in fields of nanotechnology, biomedical engineering, NEMS, and MEMS devices. Several methods including plasma CVD, low pressure CVD, and atmospheric pressure CVD have matured into processes that are routinely used in industry. Microwave and hot filament CVD methods are now commonly used to grow diamond and these can be modified to coat uniformly for tools, NEMS, MEMS and biomedical applications. Diamond coatings examined on tools and biomedical tools showed much enhanced performance compared to uncoated tools.

References

1. Spear, K. E., & Dismukes, J. P. (1994). *Synthetic diamond: Emerging CVD science and technology*. New York: The Electrochemical Society, Wiley.
2. Wentorf, R. H. (1965). *Journal of Physical Chemistry, 69*, 3063.
3. Butler, J. E., & Woodin, R. L. (1993). *Philosophical Transactions of the Royal Society of London, A342*, 209.
4. Ashfold, M. N. R., May, P. W., Rego, C. A., & Everitt, N. M. (1994). *Chemical Society Reviews, 23*, 21.
5. Bachmann, P. K., & Messier, R. (1989). *Chemical & Engineering News, 67*, 24.
6. Spear, K. E. (1989). *Journal of American Ceramic Society, 72*, 171.
7. Joffreau, P. O., Haubner, R., & Lux, B. (1988). *Materials Research Society Symposium Proceedings, EA-15*, 15.
8. Spitsyn, B. V., Bouilov, L. L., & Deryagin, B. V. (1981). *Journal of Crystal Growth, 52*, 219.
9. Angus, J. C. (1989). *Proceedings of the Electrochemical Society, 89*, 1.
10. Yarbrough, W. A., & Messier, R. (1996). *Science, 247*, 688.
11. Messier, R., Badzian, A. R., Badzian, T., Spear, K. E., Bachmann, P. K., & Roy, R. (1987). *Thin Solid Films, 153*, 1.
12. Angus, J. C., & Hayman, C. C. (1988). *Science, 241*, 913.
13. Spear, K. E. (1989). *Journal of the American Ceramic Society, 72*, 171.
14. Kamo, M., Sato, U., Matsumoto, S., & Setaka, N. (1983). *Journal of Crystal Growth, 62*, 642.
15. Saito, Y., Matsuda, S., & Nagita, S. (1986). *Journal of Materials Science Letters, 5*, 565.
16. Saito, Y., Sato, K., Tanaka, H., & Miyadera, H. (1989). *Journal of Materials Science, 24*, 293.
17. Williams, B. E., Glass, J. T., Davis, R. F., Kobashi, K. & Horiuchi, T. (1988). *Journal of Vacuum Science Technology A* (*Vacuum, Surface, Films), 6,*1819.
18. Kobashi, K., Nishimura, K., Kawate, Y., & Horiuchi, T. (1988). *Journal of Vacuum Science Technology A* (*Vacuum, Surface, Films), 6*, 1816.
19. Liou, Y., Inspector, A., Weimer, R., & Messier, R. (1989). *Applied Physics Letters, 55*, 631.
20. Zhu, W., Randale, C. A., Badzian, A. R. & Messier, R. (1989). *Journal of Vacuum Science Technology A* (*Vacuum, Surface, Films), 7*, 2315.
21. Matsumoto, S. (1985). *Journal of Materials Science Letters, 4*, 600.
22. Matsumoto, S., Hino, M., & Kobayashi, T. (1987). *Applied Physics Letters, 51*, 737.

23. Vitkayage, D. J., Rudder, R. A., Fountain, G. G. & Markunas, R. J. (1988). *Journal of Vacuum Science & Technology A, 6*, 1812.
24. Meyer, D. E., Ianno, N. J., Woolam, J. A., Swartzlander, A. B., & Nelson, A. J. (1988). *Journal of Materials Research, 3*, 1397.
25. Wood, P., Wydeyen, T., & Tsuji, O. (1988). *Programs and Abstracts of the First International Conference on New Diamond Science and Technology, New Diamond Forum, Tokyo, Japan*.
26. Jackman, R. B., Beckman, J., & Foord, J. S. (1995). *Applied Physics Letters, 66*, 1018.
27. Suzuki, K., Sawabe, A., Yasuda, H., & Inuzuka, T. (1987). *Applied Physics Letters, 50*, 728.
28. Akatsuka, F., Hirose, Y., & Kamaki, K. (1988). *Japanese Journal of Applied Physics, 27*, L1600.
29. Suzuki, K., Sawabe, A., & Inuzuka, T. (1990). *Japanese Journal of Applied Physics, 29*, 153.
30. Niu, C. M., Tsagaropoulos, G., Baglio, J., Dwight, K., & Wold, A. (1991). *Journal of Solid State Chemistry, 91,* 47.
31. Popovici, G., Chao, C. H., Prelas, M. A., Charlson, E. J., & Meese, J. M. (1995). *Journal of Materials Research, 10*, 2011.
32. Chao, C. H., Popovici, G., Charlson, E. J., Charlson, E. M., Meese, J. M., & Prelas, M. A. (1994). *Journal of Crystal Growth, 140*, 454.
33. Postek, M. T., Howard, K. S., Johnson, A. H., & Macmichael, K. L. (1980). *Scanning electron microscopy*.
34. Kobashi, K., Nishimura, K., Kawate, Y., & Horiuchi, T. (1988). *Physical Review B, 38*, 4067.
35. Pickrell, D., Zhu, W., Badzian, A. R., Messier, R., & Newnham, R. E. (1991). *Journal of Materials Research, 6*, 1264.
36. Oatley, C. W. (1972). *Scanning electron microscope*. Cambridge: Cambridge University Press.
37. Tobin, M. C. (1971). *Laser Raman spectroscopy*. New York: Wiley Interscience.
38. Colthup, N. B., Daley, L. H., & Wiberley, S. E. (1975). *Introduction to infrared and raman spectroscopy*. New York: Academic Press.
39. Raman, C. V., & Krishnan, K. S. (1928). *Nature, 121*, 501.
40. Nemanich, R. J., Glass, J. T., Lucovsky, G., & Shroder, R. E. (1988). *Journal of Vacuum Science & Technology A, 6*, 1783.
41. Knight, D. S., & White, W. B. (1989). *Journal of Materials Research, 4*, 385.
42. Solin, S. A., & Ramdas, A. K. (1970). *Physical Review B, 1*, 1687.
43. Leyendecker, T., Lemmer, O., Jurgens, A., Esser, S., & Ebberink, J. (1991). *Surface & Coatings Technology, 48*, 253.
44. Murakawa, M., & Takeuchi, S. (1991). *Surface & Coatings Technology, 49*, 359.
45. Yaskiki, T., Nakamura, T., Fujimori, N., & Nakai, T. (1992). *Surface & Coatings Technology, 52*, 81.
46. Reineck, J., Soderbery, S., Eckholm, P., & Westergren, K. (1993). *Surface & Coatings Technology, 5*, 47.
47. Wang, H. Z., Song, R. H., & Tang, S. P. (1993). *Diamond and Related Materials, 2*, 304.
48. Inspector, A., Bauer, C. E., & Oles, E. J. (1994). *Surface & Coatings Technology, 68*(69), 359.
49. Kanda, K., Takehana, S., Yoshida, S., Watanabe, R., Takano, S., Ando, H., et al. (1995). *Surface & Coatings Technology, 73*, 115.
50. Luz, B. & Haubner, R. (1991). Diamond and Diamond-like films and coatings. In R. E. Clausing, L. L. Horton, J. C. Angus & P. Koidl (Eds.), *NATO-ISI Series B, Physics* (266, 579). NY: Plenum Press.
51. Chen, X., & Narayan, J. (1993). *Journal of Applied Physics, 74*, 1468.
52. Klass, W., Haubner, R., & Lux, B. (1997). *Diamond and Related Materials, 6*, 240.
53. Zhu, W., Yang, P. C., Glass, J. T., & Arezzo, F. (1995). *Journal of Materials Research, 10*, 1455.
54. Lux, B., & Haubner, R. (1996). *Ceramics International, 22*, 347.
55. R. C. Weast (Ed.) (1989–1990). C.R.C. *Handbook of chemistry and physics*. FL: C.R.C. Press.
56. Haubner, R., Lindlbauer, A., & Lux, B. (1993). *Diamond and Related Materials, 2*(1505), 72.

57. Chang, C. P., Flamm, D. L., Ibbotson, D. E., & Mucha, J. A. (1988). *Journal of Applied Physics, 63*, 1744.
58. Gusev, M. B., Babaey, V. G., Khvostov, V. V., Lopez-Ludena, G. M., Yu Brebadze, A., Koyashin, I. Y., et al. (1997). *Diamond and Related Materials, 6*, 89–94.
59. Endler, I., Barsch, K., Leonhardt, A., Scheibe, H. J., Ziegele, H., Fuchs, I., et al. (1999). *Diamond and Related Materials, 8*, 834–839.
60. Kamiya, S., Takahashi, H., Polini, R., & Traversa, E. (2000). *Diamond and Related Materials, 9*, 191–194.
61. Inspector, A., Oles, E. J. & Bauer, C. E. (1997). *International Journal of Refractory Metals and Hard Materials*, *15*, 49.
62. Itoh, H., Osaki, T., Iwahara, H., & Sakamoto, H. (1991). *Journal of Materials Science, 26*, 370.
63. Liu, H. & Dandy, D. S. (1996). *Diamond chemical vapor deposition*. NY: Noyes.
64. Nazare, M. H. & Neves, A. J. (1998). *Properties, growth and application of diamond.*
65. Zhang, G. F., & Buck, V. (2000). *Surface & Coatings Technology, 132*, 256.
66. May, P., Rego, C., Thomas, R., Ashfold, M. N., & Rosser, K. N. (1994). *Diamond and Related Materials, 3*, 810.
67. Gouzman, I., & Hoffmann, A. (1998). *Diamond and Related Materials, 7*, 209.
68. Wang, W., Liao, K., Wang, J., Fang, L., Ding, P., Esteve, J., et al. (1999). *Diamond and Related Materials, 8*, 123.
69. Wang, B. B., Wang, W., & Liao, K. (2001). *Diamond and Related Materials, 10*, 1622.
70. Kim, Y. K., Han, Y. S., & Lee, J. Y. (1998). *Diamond and Related Materials, 7*, 96.
71. Wang, W. L., Liao, K. J., & Gao, G. C. (2000). *Surface & Coatings Technology, 126*, 195.
72. Polo, M. C., Wang, W., Sanshez, G., Andujar, J., & Esteve, J. (1997). *Diamond and Related Materials, 6*, 579.
73. Sein, H., Ahmed, W., Rego, C. A., Jones, A. N., Amar, M., Jackson, M. J., et al. (2003). *Journal of Physics: Condensed Matter, 15*, S2961–S2967.
74. Amirhaghi, S., Reehal, H. S., Plappert, E., Bajic, Z., Wood, R. J. K., & Wheeler, D. W. (1999). *Diamond and Related Materials, 8*, 845–849.
75. Jackson, M. J., Gill, M. D. H., Ahmed, W., & Sein, H. (2003). Proceedings of the Institute of Mechanical Engineers—(Part L). *Journal of Materials, 217*, 77–83.
76. Sein, H., Jackson, M. J., Ahmed, W., & Rego, C. A. (2000). *New Diamond and Frontier Carbon Technology, 12*(6), 1–10.
77. Sein, H., Ahmed, W., Jackson, M. J., Woodwards, R., & Polini, R. (2004). *Thin Solid Films, 447–448*, 455–461.

Chapter 8
Dental Tool Technology

H. Sein, C. Maryan, A. Jones, J. Verran, N. Ali, I.U. Hassan, C. Rego, W. Ahmed and M.J. Jackson

Abstract Dental technology is a discipline of dentistry concerned with the custom manufacture of dental devices to meet the prescription of a dentist. From the earliest times missing teeth have been replaced with dentures or crowns made from a wide variety of materials including gold, human or animal teeth, bone and tusks and wood. Natural teeth were used for dentures, collected from battlefields, hospitals or by grave diggers, these were mounted in carved dentures of walrus or hippopotamus ivory or on gold. By the late eightieth century dentures fused porcelain teeth were introduced, dentures could be carved from blocks of ivory or carved fixed to a gold plate by gold pins. In the mid-ninetieth century the first artificial denture base materials were introduced, vulcanite (or hard rubber) and celluloid, superseded in the 1940s with the introduction of polymethyl methacrylate. During the twentieth century base a wide range of new materials and techniques have been introduced to dentistry, including precision lost wax casting for dental alloys, a wide range of precious metal and base metal alloys and dental ceramics. This chapter focuses on advances in dental tool technology.

8.1 Introduction

Dentures were often made by the dentist who extracted the teeth, or their apprentice, sometimes the dentures were made by craftsmen such as jewellers or silversmiths. As clinical dentistry progressed a mechanical assistant specialising in the making of crowns and dentures developed. Dentistry became regulated form the late ninth century onwards and gradually national legislation restricted the practice

H. Sein · C. Maryan · A. Jones · J. Verran · N. Ali · I.U. Hassan · C. Rego
Manchester Metropolitan University, Manchester, UK

W. Ahmed
School of Medicine, University of Central Lancashire, Preston, UK

M.J. Jackson (✉)
Kansas State University, Salina, KS, USA
e-mail: jacksonmj04@yahoo.com

W. Ahmed and M.J. Jackson (eds.), *Surgical Tools and Medical Devices*,
DOI 10.1007/978-3-319-33489-9_8

to qualified dentists only. In 1921 the Dentists' Act, which restricted clinical practice to qualified dentists, stimulated the British Army to begin training dental mechanics, the first formal courses in dental technology were offered in London in 1936 [1–3]. Initially known as the dental mechanic, the term 'dental technician' was first used in the 1930s. Dental technology qualifications were generally craft based and gradually progressed to more technically and scientifically based programmes of study from the 1970s onwards, the first-degree programmes were approved in a number of universities in the 1990s. This educational basis of dental technology has resulted in few publications in the scientific literature documenting or evaluating materials and techniques and currently a limited research base.

Dental technology has evolved over the last 100 years from the mechanical assistant to a professional discipline, with an estimated global turnover in the billions of dollars it is, however, still largely unregulated in many countries. Emerging markets such as China are providing competitive challenges to dental laboratories in the west, particularly in the USA. Internationally, the levels of regulation vary, across Europe all dental laboratories must be registered with national medical devices agencies. In the UK statutory registration with the General Dental Council is expected to commence in the summer 2006. There are estimated to be up to 250,000 dental technicians across Europe. In the UK there are approximately 2700 dental laboratories and 8–10,000 people working in dental technology. In the USA there are about 12,000 dental laboratories, which employ about 46,000 technicians. About 40 %, of the laboratories, are single-handed. It is estimated that the laboratory industry in the USA is responsible for about $6 billion to $8 billion of productivity annually with growth expected to increase by about 6 % per year for the next several years [4].

Devices are custom-made, largely by hand and require individual machining with small burs. Before the introduction of lost wax casting, metal crowns and components were made using wire or swaged plate and soldered, filed, polished and buffed using hand files and rotary tools that would be found in jewellery making. The rotary tools will have included bowstring drills using hand cut tools. Power drills for clinical dentistry were slow and difficult to work with were developed from spinning wheels, carpenters drills, jewellers' drills and clockwork mechanisms [5, 6]. James Beal Morrison, who patented the dental chair in 1867, patented the foot-treadle drill in 1871 (possibly influenced by the Singer sewing machine introduced in the 1850s) and in 1875 added a flexible shaft [7]. Later developments included electrically powered motors directly powering the drill, or via belts or flexible drives to the drill handpiece. The flexible shaft invented by James Hall Nasmyth (1808–1890) the Scottish engineer is still used by many dental technicians. The handpiece itself was developed to improve reliability, ease of use and the speed of operation. Air-driven turbines running at very high speeds have been tried but the perceived need of dental technicians for sufficient torque when grinding has limited its appeal. Currently the electric micromotor offering speeds of up to 50,000 rpm with high torque are commonly found in most dental laboratories (Fig. 8.1).

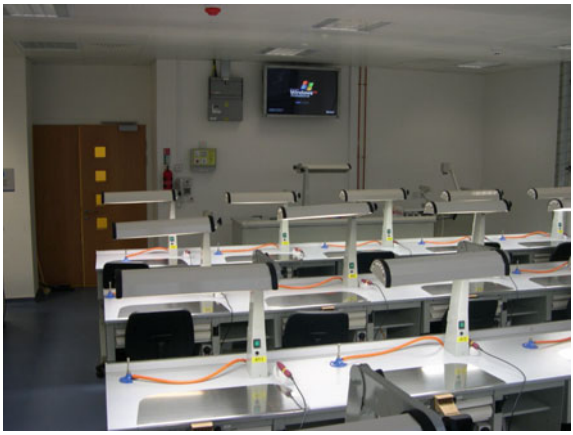

Fig. 8.1 Dental handpieces and drills

8.2 Burs and Abrasive Points

The history of developments in dental burs is limited [8]. The introduction of powered engines stimulated the manufacture and use of dental burs, cutting and grinding tools [6]. Originally hand cut and ground, burs were costly and inconsistent where mass production began in the USA in the 1870s made from carbon steel. The SS White "Revelation Bur" was the first to have a continuous drill edge [9]. Corundum introduced in 1872, which enabled enamel to be worked, was later superseded by silicone carbide (carborundum) stones and discs. Diamond burs were initially produced in the 1890s, and in SS White introduced tungsten carbide (TC) burs to dentistry in 1948 [6]. These burs designed for clinical use will have been used in the dental laboratory for fine work. Most trimming and grinding will have been done using hand files and lathe-mounted wheels.

Almost all devices made in dental laboratories involve the use of a dental laboratory handpiece and burs at some stage. A bur of various abrasive materials, sizes, shapes and cutting characteristics is mounted in a handpiece or on the chuck of a fixed lathe. On a fixed lathe the speed is set and the dental device is held in both hands and manipulated onto the rotating bur altering its position to grind or polish the surfaces. It is commonly used to remove sprues from metal castings, where gross grinding is required. However, some technicians find the use of both hands to secure the dental device whilst grinding beneficial and will undertake all machining on the lathe (Fig. 8.2).

In many laboratories the moveable handpiece is the tool of choice, this may be driven by a flexible drive or by an electric micromotor (Fig. 8.3).

The speed of the handpiece may be fixed by a bench top speed controller, or more normally, a variable speed controller controlled by foot or knee pressure. The speeds vary depending upon the design of the motor but generally range from 0 to 30,000 rpm, however, many machines offer speeds of up to 50,000 rpm. Most machines offer the ability for the operator to set the speed required. They may then

Fig. 8.2 Polishing on the dental lathe

Fig. 8.3 Handpiece and bur being used to grind dental impression tray

operate the motor using a foot or knee controller used either as an on/off switch to the set speed or as a variable speed controller up to the maximum set speed.

When using the handpiece the denture, crown or other device is held in one hand, the handpiece and bur are then brought onto the device varying the position of both hands to enable all surfaces to be trimmed. The pressure used varies during the process, initially for rapid removal of large quantities of material the operator may use heavy pressure and/or high speed. As the device is nearing its required size and shape the operator reduces the pressure and sometimes the speed. The combination of excessive speed and pressure is deprecated in teaching as it generates too much friction which can both damage the tool and the device being trimmed. Acrylic devices can warp and the mechanical properties of metal components can be altered by excessive heat. Pressures in practice together with poor supervision and work-based training can result in misuse of the tools. Complaints of poor performance of burs often relate to use at excessive speed and pressure [10].

The technician uses the drill and bur as a sculptor holding it onto the piece and drawing it along the piece removing the material required. For fine detail such as creating minor texture effects on the surface of a tooth the technician may hold the drill like a pen and gently grind the surface.

The selection of the shape, size and type of bur, cutter or abrasive tool is affected by the material being trimmed, the amount of trimming needed, the nature or form of the trimming being undertaken, the speed of the handpiece or motor and local custom and practice. The range of tool shapes, sizes and materials is very extensive, many of the tools are capable of being used on a wide range of materials and techniques. There are local, regional and national variations in the range of dental rotary tools purchased with no apparent to patterns in usage [10]. Each dental laboratory, or even individual technician in the laboratory, select their own preferences. Large dental laboratories may restrict the choices of tools available to its employees for stock control. In a recent oral survey (unpublished) of 10 laboratories, including three dental schools, each laboratory identified using different burs in the finishing of chromium–cobalt denture frameworks. The bur use varied between lathe and handpiece-mounted tools, course diamond barrels, silicon carbide stones (pink or brown), tungsten carbide burs or mandrel mounted abrasive disks. The costs of diamond or tungsten carbide burs can be 10–20 times the cost of silicon carbide stones, however, the life of the former is greater. One commercial laboratory considered the reduction in production time and longevity as more important that initial cost of the bur. One identified the use of diamond to increase cutting efficiency and reduce friction to avoid overheating of the alloy as the most important [11]. The teaching in schools of dental technology is influenced by available funding, although more expensive burs such as diamond are recommended cost implications on the school or student influence bur selection [11, 12]. The initial pattern of instruction may affect future practice strongly. Responses in the survey from several senior technicians recounted following the instruction they received as an apprentice and had barely changed since as they had adapted their technique to suite the burs they selected. In the teaching of dentists in the USA there is a broad consensus on rotary instrumentation used by dental students with coarser grit burs being used at postgraduate level [13].

8.3 Classification of Dental Burs

The wide range of materials, shapes and cutting surfaces resulted in 20 international standards associated with the manufacture of dental burs these specify aspects of the performance in terms of composition, form, reliability and packaging. BS EN ISO 6360 parts 1, 2, 3, 4, 6, 7 now provides a general numbering system for all types of dental rotary instruments. It was prepared to meet the need for a universal system of

Table 8.1 International standards for dental rotary instruments

BS EN ISO 6360-1:2004	Dentistry. Number coding system for rotary instruments. General characteristics
BS EN ISO 6360-2:2004	Dentistry. Number coding system for rotary instruments. Shapes
BS EN ISO 6360-3:2005	Dentistry. Number coding system for rotary instruments. Specific characteristics of burs and cutters
BS EN ISO 6360-4:2004	Dentistry. Number coding system for rotary instruments. Specific characteristics of diamond instruments
BS EN ISO 6360-6:2004	Dentistry. Number coding system for rotary instruments. Specific characteristics of abrasive instruments
BS 6828-8.1:1987, EN 27787-1:1989, ISO 7787-1:1984	Dental rotary instruments. Cutters. Specification for steel laboratory cutters
BS EN 27787-3:1994, ISO 7787-3:1991	Specification for dental rotary instruments. Cutters. Carbide laboratory cutters for milling machines
BS EN ISO 10323:1996	Dental rotary instruments. Bore diameters for discs and wheels
BS EN ISO 13295:1997	Dental rotary instruments. Mandrels
BS EN ISO 1797-1:1995	Dental rotary instruments. Shanks. Shanks made of metals
BS EN ISO 1797-2:1995	Dental rotary instruments. Shanks. Shanks made of plastic
BS EN ISO 2157:1995	Dental rotary instruments. Nominal diameters and designation code number
BS EN ISO 3823-1:1999	Dental rotary instruments. Burs. Steel and carbide burs
BS EN ISO 3823-2:2003	Dental rotary instruments. Burs. Finishing burs
BS EN ISO 7711-1:1998	Dental rotary instruments. Diamond instruments. Dimensions, requirements, marking and packaging
BS EN ISO 7711-2:1996	Dental rotary instruments. Diamond instruments. Discs
BS EN ISO 7711-3:2004	Dentistry. Diamond rotary instruments. Grit sizes, designation and colour code
BS EN ISO 7786:2001	Dental rotary instruments. Laboratory abrasive instruments
BS EN ISO 7787-2:2001	Dental rotary instruments. Cutters. Carbide laboratory cutters
BS EN ISO 7787-4:2002	Dental rotary instruments. Cutters. Miniature carbide laboratory cutters
BS EN ISO 8325:2004	Dentistry. Test methods for rotary instruments

classification and establishes a comprehensive coding system. They do not, however, specify abrasive/cutting efficiency. The standards are shown in Table 8.1. Although these are current there has been consolidation to create a comprehensive series of standards.

8.4 Coding of Dental Tools

Each item has a 15-digit code, the first 3 numbers identify the materials used in the working part, the next 3 the shank and overall length, the third the shape, the fourth special characteristics, the nominal size of the working part. There are also an optional further 3 numbers for diamond instruments.

The first group is the materials used for the tool, there are 42 materials used for rotary tools of which most are used in the dental laboratory.

8.4.1 Shapes

The shapes are classified in BS EN ISO 6360-2:2004 Dentistry. This standard comprises 5 tables that describe the coding for general shapes and designs of which there are 257 shapes summary information in Table 8.3. In the standard, Table 8.2 describes 70 disk types, Table 8.3 special instruments, Table 8.4 mandrels, and Table 8.5 root canal instruments (these are not used in dental technology).

Table 8.2 Abrasives used in dental technology

Grinding	Polishing
Tungsten carbide	Rubber
Silicon carbide	Natural bristles
Diamond, medium, coarse, very coarse, ultrafine, extra-fine, fine,	Synthetic bristles
Ruby	Brass
High-speed steel	German silver
Normal grade corundum	
High-grade grade corundum, pink	**Buffing**
High-grade grade corundum white	Felt
Tungsten carbide grit	Leather
Titanium	Flannel
Nickel titanium	Muslin
Quartz	Felt cloth
Sapphire	Yarn
Cubic boron nitride	Goat hair
Electrocorundum, red	
Free cutting steel	**Other**
Cold worked steel	Plastic
Spring steel	Quill
Stainless steel	Paper
Stainless spring steel	Gutta percha
	Cuttlefish bone

Table 8.3 Rotary shapes and variants

Basic shape	Example variants
Spherical	With collar, hemispherical
Wheel	End cutting, rim cutting, conical, half circle rim
Cylindrical	Side cut, end and side cut, pointed end, hemispherical end, rounded end, distal end hemispherical proximal end hemispherical, plus others
Conical	Slender, truncated conical, 30 % flatter, side cut only, rounded end
Inverted conical	Side cutting, end cutting, concave collar, rounded conical pointed, others
Bud	Slender, rounded, rounded slender, long, flat end rounded edge
Pear, flame, bullet	
Egg	Long, side cutting
Barrel	
Torpedo	Conical
Lens	

Table 8.4 Summary of coding for toothing burs and cutters

Straight	Right helicoidal
Straight, left cross-cut	Right helicoidal left cross-cut
Straight, sharp cutting angle	Right helicoidal fine left cross-cut
Straight, blunt cutting angle	Right helicoidal, sharp cutting angle left cross-cut
Straight, left cutting	Right helicoidal x-cut, transverse blade at the tip
Straight, left cross-cut	Right helicoidal left cutting
Straight, x-cut	Right helicoidal left cut; right cross-cut
Straight, with grooves	Right helicoidal x-cut
Straight left serpentine cut	Right helicoidal, fine right cross-cut
Left helicoidal	Right helicoidal, right cutting x-cut
Left helicoidal left cross-cut	Right helicoidal, right cutting x-cut right cross-cut
Left helicoidal right cutting	Right helicoidal with grooves
Left cutting x-cut	Right helicoidal, right cutting, 2 cuttings
Left helicoidal right cutting x-cut	Right helicoidal, right and left cutting
Cardia	
Side, finishing bur toothing	
Diamond toothing	
x-cut	

8.4.2 Types of Toothing

Referring to BS EN ISO 6360-3:2005 Dentistry, the number coding system for rotary instruments and specific characteristics of burs and cutters are included in this standard. The standard details the toothing of burs, finishing burs and, very fine, medium, coarse and very coarse cutters. It also includes a Table 8.3 for surgical tools.

Table 8.5 Summary of materials and possible abrasives

Material	Grinding	Polishing	Buffing
Acrylic	• Cold worked steel • High-speed steel • Tungsten carbide • Quartz • Normal grade corundum, white • Silicon carbide • Ruby Sapphire	• Fine sandpaper • Silicone polishers • Goat hair • Natural bristles • Synthetic bristles • Brass wire brushes • German silver wire brushes • Pumice slurry	• Felt • Flannel • Muslin • Felt cloth • Yarn • Whiting • Tripoli
Base metal alloys NiCr, CoCr	• Diamond, coarse or medium • (Fine, ultrafine, extra-fine, very course for fine detail) • Tungsten carbide • Silicon carbide, Pink, brown • Normal grade corundum, pink, white	• Rubber wheels, cylinders, cones • Black • Green	• Synthetic bristles • Felt • Leather • Flannel • Muslin • Felt cloth • Yarn • Chrome oxide
Gold	• Tungsten carbide • Silicon carbide • Normal grade corundum, pink, white • Ruby Sapphire • Cubic boron nitride • Electrocorundum red • High-speed steel • Cold worked steel	• Rubber wheels, cylinders, cones • Black • Green • White • Silicone	• Goat hair • Natural bristles • Synthetic bristles • Leather • Felt • Flannel • Muslin • Felt cloth • Yarn • Tripoli • Rouge
Ceramic	• Diamond, medium fine, • (Ultrafine, extra-fine, coarse, very course) • Silicon carbide green stones	• Diamond paste • Diamond impregnated polishers	

8.4.3 Specific Characteristics of Diamond Instruments

Referring to BS EN ISO 6360-4:2004 Dentistry, the number coding system for rotary instruments and specific characteristics of diamond instruments are included in this standard. The standard describes the additional information that can apply to diamond burs, this is the angle of tapered diamond instruments and the width of diamond-coated discs.

Referring to BS EN ISO 6360-6:2004 Dentistry, the number coding system for rotary instruments and specific characteristics of abrasive instruments, groups

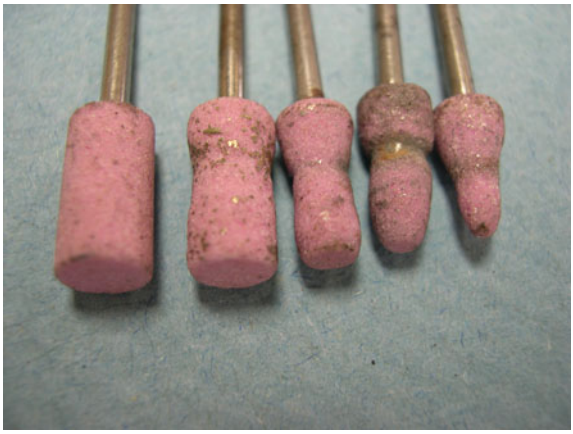

Fig. 8.4 Example of toothing drills

Fig. 8.5 Dental burs

abrasive instruments by the fineness of the grit size: ultrafine, extra-fine, fine, medium, course and very coarse, and within each group it is further subdivided by the hardness of the binding materials very soft, soft, medium, hard, very hard, extra hard. A dental bur will thus be coded as shown in Figs. 8.4 and 8.5.

8.5 Dental Devices

Dental devices may be used for a short term, e.g. removable orthodontic devices, or be in situ for many years, e.g. dental crowns or bridges. All devices are made largely by hand using a variety of equipment and techniques. The techniques are predominantly based on lost wax techniques at some stage in their manufacture whether the devices are made from acrylic, dental alloys or even some ceramics.

Fig. 8.6 Range of devices made by dental technicians

Most newly processed devices normally require trimming, polishing and buffing to make them fit for use in the mouth. As every patient is different, the mouth is a complex three-dimensional structure (Fig. 8.6). The dental technician needs to appreciate the structures and functions of the oral cavity, an understanding of the properties of the materials and their processing and the dexterity and artistic ability to make the device that will fit, function and appear to be natural. The dental handpiece can often be used as a carver to create the lifelike appearance required.

8.6 Dental Laboratory Materials

8.6.1 Gypsum

Gypsum-based products are used for the construction of models or casts of the dental mouth and in refractory investment materials. These may be needed to be ground using dental burs to shape the cast for use, for example to expose the edges of a tooth preparation in the making of a crown. A fine cross-cut of diamond cut tungsten carbide bur is the tool of choice for many technicians for this task. The gypsum used may be modified during its manufacture to increase hardness. Vacuum mixing can enhance its hardness and the surface may be altered by sealants to improve abrasion resistance, with a hardening solution high strength stones the Knoop hardness of a stone was increased to 79 kg/mm^2 [2]. Epoxy resins may also be used for these tasks [2]. Gypsum products will be ground dry under extraction at speeds of under 20,000 rpm due to dust fine burs generate significant amounts of dust, course burs create large particles that can travel in all directions across a laboratory at considerable velocities (Fig. 8.7). Damp gypsum will adhere to the bur and clog the cutting surface.

Fig. 8.7 Dust generated grinding dry plaster cast

8.6.2 Light-Activated Dental Impression Tray Materials

To obtain an accurate cast of a patient's mouth, a clinician will take two impressions. The primary impression is taken using a dental impression material in an impression tray available in a limited range of sizes. The impression is disinfected and then poured in dental plaster upon which a custom-made impression tray can be for the individual patient for greater accuracy. There are many materials for these trays, thermoplastic polymers that are pressure formed onto the cast and then trimmed using dental burs. A common material used is a photopolymerised polymer with high inorganic filler content, up to 76 % [14]. The inorganic filler can be quartz and barium or lithium aluminium silicate glasses, borosilicate glasses, strontium or zinc glasses. These materials are provided as moldable sheet that can be applied to a cast and cured in about 5 min in curing unit using light at about 500 nm [2]. Once cured these materials are trimmed using dental burs. The grinding of these materials creates a very fine dust that many technicians often identified as a nuisance or irritant (Fig. 8.8). Although there is no objective data many dental technicians have reported high wear rates grinding this material. Large tungsten carbide cross-cut burs are the tool of choice for many, some prefer large lathe-mounted abrasive wheels for speed and cost effectiveness.

Fig. 8.8 Grinding of light curing polymer, note method of holding handpiece and dust generated

The particle sizes of some the dust generated is less than 5 μm which is inhalable the particle size varies depending upon the cutting geometry of the bur and the particle size of the filler.

Burs used include ruby abrasives, tungsten carbide and steel burs. The shapes used vary depending upon the form of the tray and the parts that need trimming. Holes are drilled for retention using rose head-shaped burs. There is no published data on wear rates in relation to machining this material, however, many technicians report excessive wear whilst trimming this material as although the matrix of the material will be comparatively soft, the filler content, however, can include quartz (Moh's hardness 7 [14]).

8.6.3 Materials for Dentures

Removable dentures are made on the cast of the oral structures. Teeth are mass-produced in acrylic or porcelain. A trial denture is constructed positioning the teeth into wax that is carved to reproduce the oral tissues. The trial denture is inserted into the mouth to assess the upper and lower jaw relationship, the appearance and tissue support. The wax allows for ease of alteration. When satisfactory the wax trial is returned to the dental laboratory where a mould is made of it embedding it into plaster in a two-part flask, normally metal. The wax is eliminated in boiling water and dental polymers can be inserted either by compression moulding or injection moulding. The polymers are predominantly heat cured or chemically cured polymethyl methacrylate, or alternatively Nylon or other polymers. After curing, the denture is divested from the embedding plaster and trimmed using a dental drill (handpiece) and a range of dental burs. Dentures are polished using pumice slurry with various sizes and shapes of lathe brush or calico mops and buffed to a high lustre using bar compounds of tripoli followed by bar or liquid polishes containing whiting on a wool mop or worn calico mop at high speed.

The grinding of acrylic varies depending upon the type of polymer used or brand. The selection of bur to trim dentures and to prepare them for polishing and buffing is based up the experience of the individual dental technician. The type of bur used, the speed at which it is used and pressure with which it is applied is affected by many factors:

- The skills of the individual, the amount of trimming needed;
- The education and training of the technician;
- The price of the device, this influences the time available and grade of technician undertaking the work;
- The expertise and experience of the dental technician making it; and
- Inexperienced technicians often apply excessive pressure and speed when grinding any device. An acrylic denture can be warped or burnt.

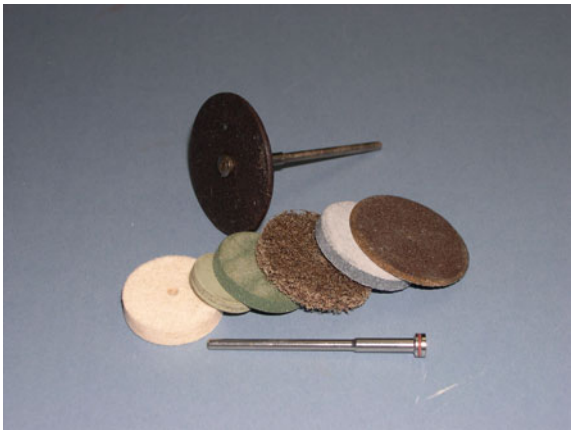

Fig. 8.9 Silicone polishers

The hardness of acrylic resins, Knoop Hardness, 14–17.6 [14], Vickers hardiness 9–23 [15, 16] means that there are a wide variety of burs and stones that can be used. However, excessive speed and pressure must be avoided. Working pressure for laboratory abrasives and tungsten vanadium alloyed tool steel is 1–5 N [17] Tungsten carbide has a recommended pressure of 3.3–7.5 N [17]. The recommended speeds vary depending upon bur material and size of bur.

The burs used for trimming (summarised in Table 8.5) may include:

- Course, medium of fine cut tungsten carbide burs;
- Silicon carbide;
- Ruby abrasives are selected by many for fine grinding of acrylic resin dentures;
- White abrasives; and
- Fine abrading is done using sandpaper of various grit sizes, or abrasive impregnated silicone polishing burs (Fig. 8.9).

Dentures should be trimmed, polished and buffed to a high lustre because surface roughness enhances microbial adhesion and reduces the ability to be cleaned [18–24]. Burs with a threshold surface roughness for bacterial retention of (RA = 0.2 μm) should be used. A number of studies have examined surface finishing techniques [25–29]. The surface lustre produced in the dental laboratory provides the smoothest surface [26–28]. Tungsten carbide burs produce a smoother non-grooved surface than the steel bur on acrylic resins [29].

8.6.4 Metal Components: Crowns, Bridges and Metal Partial Dentures

Metallic crowns, bridges, substructures and partial denture frameworks are made using the lost wax process. Wax forms of either the whole tooth or substructures for

the later addition of aesthetic materials are created on casts and dies of high strength dental stone. These wax forms are attached to a sprue, removed from the die and attached to a casting cone former, they are invested in a refractory investment, and placed in a furnace to eliminate the wax and moisture form the investment. Dental alloys are melted and cast into the mould, after cooling they are divested and sand or bead blasted. They will then be cut from the sprue, trimmed, polished and buffed with a range of disks, burs, stones, rubber tools and buffing mops. Metal partial dentures are made in a similar way but are a more complex shape and using a refractory model of the mouth and use multiple sprues.

The alloys used for metal components include high gold alloys (those containing more than 75 % gold), low gold alloys, palladium silver alloys and base metal alloys. The gold alloys have a Vickers hardness from 90 to 230 depending upon alloy type and brand. Low gold alloys and palladium silver alloys will have a Vickers hardness around 140 [14]. Base metal alloys that may be cobalt chromium, cobalt chromium nickel or nickel chromium have a Vickers hardness number of between 320 and 430. Titanium alloys are increasingly being used due to their lightness, they require specialised casting equipment, their Vickers hardness is about 140 and care is needed when finishing not to overheat the alloy.

The selection of the materials for machining and the shape of the tool the crown will depend upon the alloy used, the stage of finishing, the location of the grinding to the size and type of tooth. For example, for the inside of a lower incisor tooth very fine tools will be needed if any adjustment is needed. For optimum performance the device must be as smooth as possible.

8.6.5 Materials for Partial Denture Frameworks

Cobalt chromium alloys are most commonly used, although these may also be made in gold alloys or titanium. The surface finish required is a high lustre to reduce microbial adhesion, surfaces if rough can also rapidly increase the wear of opposing or abutment teeth. There have been few papers evaluating finishing procedures of cobalt chromium denture frameworks. Aydin [30] determined that the best surface finish was obtained using a systematic approach after sandblasting, hard stone, medium silicone carbide disk, second sandblasting, electropolishing, hard rubber point, felt disk and soft brush with polishing paste, although in the study cutting load was not standardised. Xenodimitropoulou and Radford [31] recommended a 6.5 mm aluminium oxide pink stone as the most efficient and consistent due to low costs and cutting efficiency. The tungsten carbide bur was second, however, it lost 70 % of its cutting efficiency over the duration of the machining. The diamond was the less efficient, the diamond bur showed evidence of plucked out grit, being won flat and with the matrix contaminated by the machined sample. Ponnanna et al. [32] determined the roughness generated by sandblasted and identified a systematic approach to finishing similar to Aydin [30]. The amount of dust generated in the finishing of a cobalt chromium framework for a partially dentate patient using

silicon carbide abrasives and rubber wheels can be up to 2 g, 1 g of cobalt chromium alloy and 1 g of silicon carbide dust [33].

8.6.6 Titanium Alloys

Cast titanium alloys have excellent biocompatibility and are light, which is particularly useful for upper dentures [34, 35]. The mechanical properties are slightly different to Co–Cr alloys and have to be accounted for during design and in manufacture [36, 37]. In finishing titanium castings the hard brittle reaction layers (α-case) on the cast surface must be removed as these layers are reported to reduce the ductility and fatigue resistance of the framework and clasps. [38]. Ohkubo et al. [38] identified that in comparing Ti-6Al-4V with Co–Cr and type iv gold alloys there was little difference in cutting effectiveness using silicon carbide burs finding no correlation between the hardness of the alloy and volume loss. However, the opposite occurred when suing steel fissure burs. Steel burs will blunt, however, SiC stones will present new abrasives particles as they wear off thus maintaining cutting efficiency, although the diameter of the stone will reduce and thus reduce the cutting velocity unless speed of the motor is increased to compensate. Kikuchi et al. [39] compared different alloys compositions of Ti–Cu alloys assessed by their grindability using SiC burs. Hirata et al. [40] comparing the polishing of Ti and Ag–Pd–Cu–Au alloy with five dental abrasives, carborundum points, and silicone polishers found the Ti more difficult to polish and suggested the development of new abrasives for polishing of Ti. In the CAD/CAM milling of titanium devices Hotta et al. [41] identified that tungsten carbide burs displayed chipping at the bur blade and gradual dulling of the tool and an increase in the average surface roughness on the crown. However, they concluded that the tungsten carbide burs could be used to fabricate up to 50 titanium crowns.

8.6.7 Materials for Metal Inlays, Crowns and Bridges

Crowns and bridges are made in a variety of alloys, including noble alloys varying from high gold soft alloys type I (VHN 60-90) [14]—type IV Extra hard (VHN 220), palladium silver alloys, porcelain fused to metal techniques (base metal or noble metal alloys), low gold alloys Ni–Cr and Ti. The selection of bur type and technique will vary depending upon the alloy and local custom and practice, diamond burs, SiC and tungsten carbide the main options. Siegel and Fraunhofer [42] determined that cross-cut diamond burs should be used for base metal alloys and medium grit diamond burs for high noble alloys. Miyawaki et al. [43] identified the tungsten carbide bur generally superior in cutting effectiveness than diamond when using a dental air turbine to grind Ag–Pd–Cu–Au, Ag–Zn–In–Sn, NiCr or Ti alloys.

After grinding base metal crowns are finished using the same tools as for base metal denture frameworks, however, the tools sizes may include many with finer shapes to characterise teeth or trim inside the fitting surface. Noble alloy crowns being softer can use a wider range of polishers. The hard rubber wheels can be too abrasive for soft gold alloys or silver. Silicone polishers with finer abrasives or bristle brushes with polishing pastes are selected for polishing. Buffing is undertaken using wool, chamois or cloth wheels with rouge or proprietary polishing compounds. A high lustre is developed for oral hygiene and on the occlusal surface to reduce wear on the opposing teeth [44–46].

8.6.8 Ceramics

Porcelain has been used for denture teeth since 1790 [14], it has excellent appearance, durability and biocompatibility. Denture teeth are mainly feldspar with about 15 % quartz and 4 % kaolin [14]. Dental crowns may be all ceramic or ceramic fused to metal for additional strength. The material is supplied as ground glass frits and the technician gradually builds up the crown on a removable die in the cast of the patients' mouth. A core of aluminous porcelain is applied on a platinum foil or metal substructure and fired in a vacuum furnace (Fig. 8.10). Incrementally, small amounts of porcelain are then applied using small spatulas or paintbrushes to form the shape of the tooth, this is over built to allow for shrinkage during firing.

The crown is then trimmed and additional porcelain applied as required. The crown is shaped and characterised using rotary tools. The bur of choice for most ceramists appear to be diamond (although there is no published data on this) alternatively silicon carbide abrasives are used. The selection of the shape of the diamond or silicon carbide points used, their grit size, and the speed used varies with local custom and practice (Fig. 8.11). Finally, the crown glazed this can be a natural or a paint on glaze. Dental ceramics have a Vickers hardness of between about 600 and 700 [14].

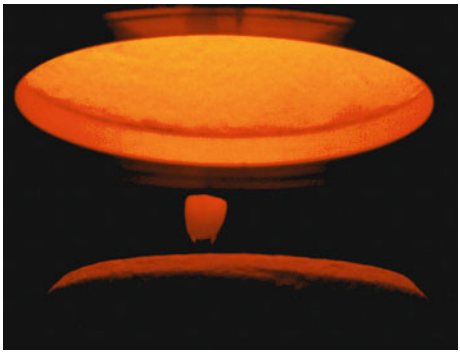

Fig. 8.10 Ceramic crown in furnace

Fig. 8.11 Machining of crown with diamond points

The surface finish of the crown is very important for the dental health of the patient. Rough surfaces increase plaque retention and occlusally can cause considerable damage to the opposing teeth [47–61].

8.6.9 Machinable Ceramic Restorations

In the last 20 years CAD/CAM technology has been introduced in dentistry in some areas replacing lost wax techniques. These systems have been used for the manufacture of inlays, crowns, bridges, substructures and veneers. The tooth, or a cast of the tooth, is scanned with a laser or a probe, the device is milled from tooth coloured ceramics, zirconia or alumina, using computer controlled milling machines. The machines use diamond tools to machine the ceramic. The Cerec system was introduced in the late 1980s [62, 63] a cavity was scanned stereo-photogrammetrically and a precision-fitting restoration milled from a standard ceramic block using a miniature three-axis milling device; driven by a water turbine unit. The CELAY system [64], a copy milling unit, was introduced to the market in 1991. Other systems have been introduced [65–70]. The continual development of more powerful scanners, computing power and software, and improvements in milling technology software milling have increased accuracy [71–83]. Evaluation of enamel wear of these materials has given conflicting results Al-Hiyasat et al.[84] found machinable ceramics were significantly less abrasive yet Ramp et al. [85] and Imai et al. [86] found greater wear. However, the surface roughness of the finished device is an important factor in wear [57].

Yin et al. [87] classified the materials available as machinable dental bioceramics and difficult to machine dental bioceramics. The machinable dental bioceramics had a machinability similar to existing handmade dental ceramics, they could be easily adjusted in the clinic by the use of existing diamond tools. Abrasive damage and edge chipping during finishing procedures can be apparent which can be influenced

by grit sizes and abrasive pressure of the diamond tools and is possibly influenced by the microstructure of the materials.

Difficult to machine dental bioceramics include glass-infiltrated alumina, and surgical grade zirconia. Finishing of these materials has been associated with short tool life, grit microfracture, wear flat, grit pullout and matrix abrasion have all been identified in conventional diamond burs [87, 88]. The small size of dental tools required for internal grinding of devices is the most challenging aspect of machining crowns and bridges [89] as in traditional techniques. The number and shape of diamond particles influences cutting rate and resulting surface roughness of the device [89, 90]. The clinical finish of these materials after adjustment is achieved using diamond pastes [91].

8.7 Dental Cutting Tools

8.7.1 Cutting Efficiency

Evaluation of cutting efficiency of burs has largely related to clinical use [92–97] and the recent developments in CAD/CAM with the few studies applied to dental technology. Diamond burs are manufactured in multiple layers by electrodeposition, sintering, or microbrazing to provide continuous cutting surface as they wear [94]. Cutting efficiency is affected by the substrate being ground and can be affected by clogging (adhesive wear) of the bur as well as wear. Diamond burs and abrasives such as silicon carbide retain cutting efficiency as they wear [43] as the wear exposes new surfaces or particles. Particle size and distribution affect cutting performance [89, 90]. Tungsten carbide was found the most effective with Ag–Pd–Cu–Au alloy, Ag–Zn–In–Sn alloy Ni–Cr alloy and Ti, however, the cutting capability of the carbide bur declined whilst the diamond remained quasi-constant [43]. Xenodimitropoulou and Radford [31] identified the silicon carbide bur as the most effective for grinding Co–Cr alloy in the laboratory but tungsten carbide in the surgery. Siegel and Fraunhofer [42] identified that carbide burs sectioned the base metal alloy significantly faster than the diamond burs but the opposite was observed with noble alloys and medium grit diamond burs should be used. Rimondini et al. [98] identified that small particle diamond burs clogged and observed damage to tungsten burs when grinding titanium and that the most effective were 30 and 15 μm diamonds followed by finer grinding with tungsten carbide burs. Watanabe et al. [99] that when machining cast CP Ti and its alloys, carbide fissure burs possessed a greater machining efficiency than the diamond points. The selection of cutting tool material and the size of the cutting particles or edges is a balance between the speed of removal and the level of finish required. Large particles can remove material quickly but can lead to edge chipping of the substrate, greater surface roughness and poorer mechanical properties. Fine particles are slower, can clog more easily but give a smoother surface. The greater pressure and speed used

the greater the heat and chance of clogging, however, as these tools are all hand controlled individual custom and practice affects selection and performance.

8.7.2 CVD Dental Burs

Cobalt-cemented tungsten carbide burs used in dental technology are subject to edge chipping and wear reducing their performance. The sintered material is ground to create the cutting edges (Figs. 8.12 and 8.13). Examination of the surfaces (Figs. 8.14 and 8.15) shows edge chipping and the dulling of the surface reducing cutting efficiency.

Conventional diamond burs are manufactured embedding the diamonds into place using various techniques. The cutting efficiency of the diamond particles is related to the effectiveness of the method used to bind them to the bur, grit pullout and matrix abrasion have been identified as factors in the wear of dental diamond burs [94]. Chemical vapour deposition of diamond films offer advantages in their uniformity of coating over complex surfaces and the nature of their bonding to the substrate.

In 1996 Haselton et al. [100] published their work on the production of polycrystalline chemical vapour deposition (CVD) diamond from hot filament-assisted technique onto stainless steel dental burs. Further work using molybdenum as a

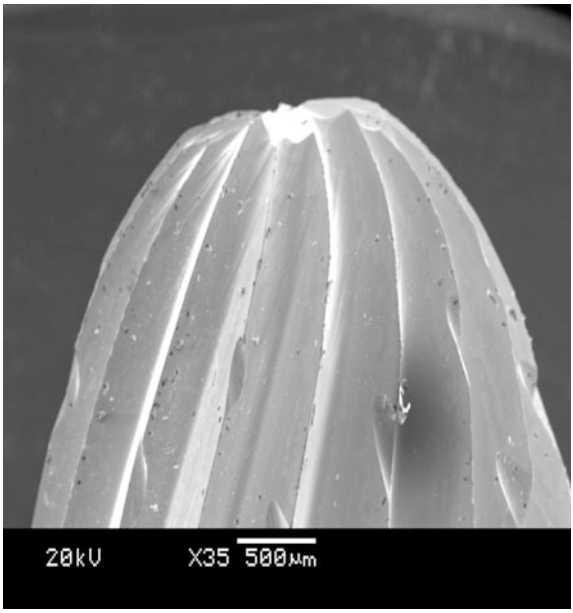

Fig. 8.12 Tungsten carbide bur showing toothing

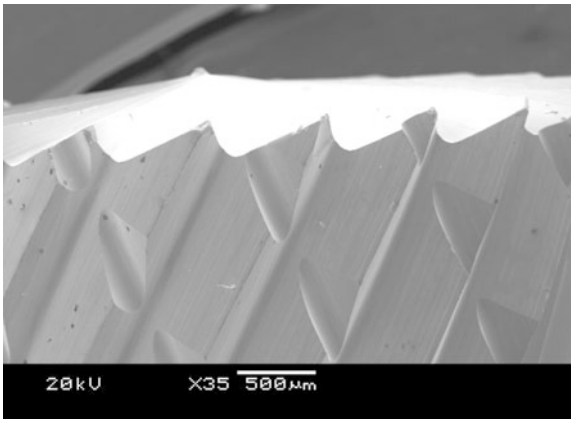

Fig. 8.13 Barrel-shaped tungsten carbide bur

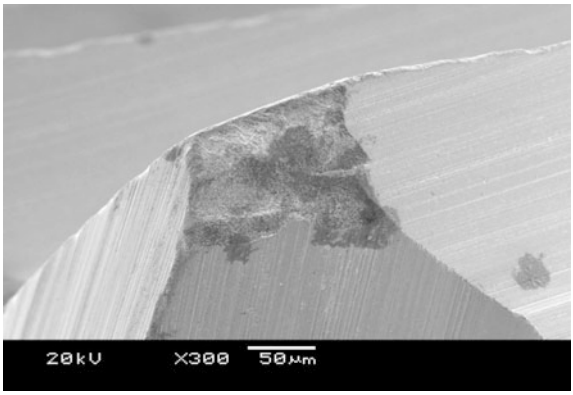

Fig. 8.14 Chip on edge of new tungsten carbide bur

substrate identified better wear characteristics than for a conventional diamond bur [101]. The first report in the dental literature in Borges et al. [102] confirmed greater longevity and identified more efficient cutting ability and the benefit of excluding the risk of metal contamination from the metallic binder used on conventional diamond burs. The unusual combination of housing the Centre for Dental Technology within the Department of Chemistry and Materials Science at Manchester Metropolitan University (MMU) stimulated work on the use of CVD on dental tungsten carbide work. CVD of diamond coatings onto the cemented carbide substrate was poor due to binder materials such as cobalt that can suppress diamond growth [103]. The use of a pre-acid etched substrate surface and a modified HFCVD gave good adhesion [103], further work at MMU developed the CVD techniques for dental burs [104–107].

Studies on the performance of WC–Co CVD diamond-coated burs [108–111] have supported earlier work [102]. Ali et al. [108] identified that the coated WC–Co dental tools remained completely intact after drilling 500 holes into human teeth,

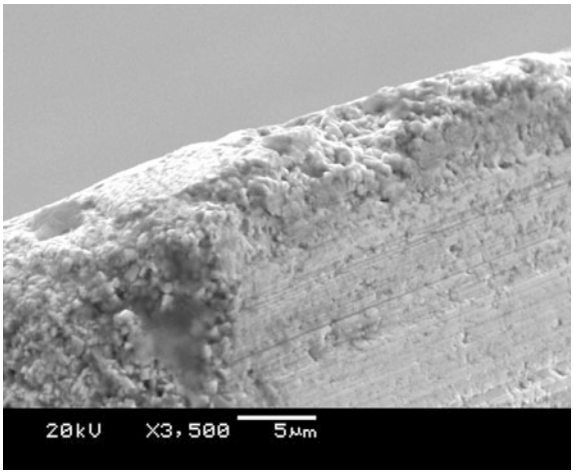

Fig. 8.15 Chip on edge of tungsten carbide bur showing grains and dulling of surface

the conventional bur had lost the majority of its embedded diamond particles. Sein et al. [109] used flank wear to evaluate the wear rates of conventional and CVD diamond-coated burs drilling into a range of substrates. Results show a 300 % improvement with coated burs over conventional burs. Examples of adhesive wear were noted on the bur when grinding acrylic and borosilicate glass. Jackson et al. [110] supported these findings identifying evidence of adhesive and abrasive wear associated with increased rates of abrasion. Polini et al. [111] presented the first quantitative data on the cutting behaviour of uncoated and CVD coated TC burs. They used Co–Cr–Mo dental alloy as the workpiece material grinding at a speed of 20,000 rpm. Some of the uncoated burs failed catastrophically during the tests, the diamond-coated burs exhibited much longer life.

8.7.3 Shanks

The shanks of dental burs may be of the same material as the cutting head or the cutting head will be connected to the head by brazing. The shaft material can be made of metal, e.g. steel or carbide. The type of materials and the treatment given to it is at the discretion of the manufacturer (BS EN ISO 1797-1:1995 Dental rotary instruments. Shanks. Shanks made of metals). The hardness shall be a minimum of 250 HV 5. The shanks are normally 2.35-mm diameter, however, some high-speed laboratory handpieces may require 3.0 mm. If positioned incorrectly in the handpiece or running at excessive speed the shaft may be liable to deformation, Figs. 8.14 and 8.15 there have been occurrences at MMU of the head separating from the shank. The force in these circumstances lead to the bur head embedding the wall across the laboratory. The implications of this are that ideally grinding

occurs in closed chambers, this however is rare practice, then use of bench mounted guards and safety spectacles are normally required.

8.8 Health and Safety

The machining of dental devices exposes dental technicians to several hazards. Impact injuries to the eyes, vibration syndrome and respiratory disease from the dust generated. Eye injuries can be caused by shank failure, abrasive disk failure and debris from the grinding operations. Shields and safety spectacle are required in dental laboratories.

8.8.1 Vibration

The holding of dental handpiece for extended periods with the vibration from the motor itself and the effect of the vibration of the dental bur on the device being ground whilst has been reported to induce vibration syndromes in dental technicians [112–115]. Nakladalova et al. [113] identified damage to both myelinated and unmyelinated fibres in the fingers of subjects exposed to high-frequency vibration. [114] suggested that the usage of high- and low-speed machines may be a cause of vibration syndrome among dental technicians. Mansfield [115] in a study of 120 dental technicians reported paresthesia in the hand fingers (47.4 %) and pain in the joints of upper extremities (elbow 26.6 %, shoulder 10.8 %, wrist 6.6 % and small joints of hand 6.6 %). The EU Physical Agents (Vibration) Directive (2002) came into force 6 July 2005 [116] this requires employers to minimise risk and to address it. Hugonnaud and Lob [117] suggested selection of low vibration handpieces, training in correct usage and recognition of symptoms, health surveillance and periodic reviews. The effect of bur toothing, vibration and its effect has not been investigated, however, increased cutting effectiveness and reduced blunting of tools would benefit. Initial investigations into the performance of CVD coated burs [111] would suggest their benefit in relation to this legislation.

8.8.2 Dust

Since 1967 there have been at least 70 published reports and studies of respiratory conditions associated with dust generated in the making of dental devices [118–129]. The condition dental technicians pneumoconiosis was first specifically described in 1986 by Choudat et al. [124] who described it as complex pneumoconiosis distinct from silicosis, asbestosis, or hard metal disease and that Cr–Co–Mo alloys play a role in its pathogenesis. Since then a number of workers including the Centers for

Disease Control and Prevention in the USA [129] have described a number of respiratory diseases associated with dental laboratory practices including:

- Silicosis (associated with dental ceramics and silica filled polymers);
- Occupational asthma;
- Autoimmune disorders associated with silica;
- Mineral-associated hepatic injury; and
- Sarcoidosis.

8.8.3 Particle Size

The manufacture of dental devices involve numerous techniques and materials and includes significant use of small hand held drills The drills operate at speeds of up to 40,000 rpm. The handpieces hold a range of burs that are used to grind, smooth and polish dental devices. The burs may be made of a range of abrasives including tungsten carbide, silicon carbide (SiC), carborundum (Al_2O_3), rubber, diamond, ruby abrasives or even sandpaper. The materials being ground include precious metal alloys, nickel chromium alloys, cobalt chromium alloys, ceramics, silica/polymer composites, acrylic resins and dental gypsum products. The elements in the dental alloys include, Co, Cr, Cu, Ag, Ni, Sn, Mo.

The dust generated by the processes should be collected by a local dust extractor system. This may be an individual machine or part of a centralised system as in the new development. In use the handpiece and the device being ground are positioned close to the extractor port. The grinding of dental materials generates varying amounts of dust from the materials and the grinding stones. The particle size of these varies depending upon the materials being ground and the grinding tools, Brune and Beltesbrekke identified ranges from 0.6 to 50 μm with a significant proportion below 5 μm that is respirable. This work has been confirmed in a number of undergraduate research projects at MMU. The weight of dust generated in the grinding and polishing of one metal denture base is approximately 1 g. Brune and Beltesbrekke recommended a minimum extraction of 30 l/s (3 m/s) to remove the majority of this dust. Collard et al. reported that a diamond bur created more respirable particles than the carbide bur for each composite tested although this will probably relate to abrasive particle size.

References

1. Ash, Claudius & Sons. (1921). *A centenary memoir 1820–1921*. London: Clowns.
2. Craig, R. G., & Powers, J. M. (2002). *Restorative dental materials* (11th ed.). Maryland Heights: Mosby.
3. Nuffield Report.

4. Christensen, G. J. (2005). Dental laboratory technology in crisis: The challenges facing the industry. *Journal of the American Dental Association, 136*(5), 653–655.
5. Glenner, R. A. (1974). Development of the dental drill. *The Journal of the American Dental Association, 88*, 712–727.
6. Vinksi, I. (1979). Two hundred and fifty years of rotary instruments in dentistry. *British Dental Journal*, *146*(7), 217–223.
7. Ring, M. E., & Hurley, N. (2000). James Beall Morrison: The visionary who revolutionized the practice of dentistry. *The Journal of the American Dental Association, 131*(8), 1161–1167.
8. Siegel, S. C., & von Fraunhofer, J. A. (1998). Dental cutting: The historical development of diamond burs *The Journal of the American Dental Association, 129*(6), 740–745.
9. Crawford, P. R. (1990). The birth of the bur (and how a Canadian changed it all!). *Journal Canadian Dental Association, 56*(2), 123–126.
10. Oral communication, G Needham. Huddersfield, England: Metrodent Ltd.
11. Oral communication, P Gough, Senior Lecturer Dental Technology. Manchester: Manchester Metropolitan University.
12. Oral communication, J Lewis, Senior Lecturer Dental Technology. Cardiff: University of Wales Institute.
13. Siegel, S. C., & von Fraunhofer, J. A. (1999). Dental burs—What bur for which application? A survey of dental schools. *Journal of Prosthodontics, 8*(4), 258–263.
14. O'Brien, W. J. (2003). *Dental materials and their selection*. Chicago: Quintessence.
15. Neppelenbroek, K. H., Pavarina, A. C., Vergani, C. E., & Giampaolo, E. T. (2005). Hardness of heat-polymerized acrylic resins after disinfection and long-term water immersion. *Journal of Prosthetic Dentistry, 93*(2), 171–176.
16. Ilbay, S. G., Guvener, S., & Alkumru, H. N. (1994). Processing dentures using a microwave technique. *Journal of Oral Rehabilitation, 21*(1), 103–109.
17. Dental Laboratory catalogue. Huddersfield: Metrodent Ltd.
18. Verran, J., & Maryan, C. J. (1997). Retention of Candida albicans on acrylic resin and silicone of different surface topography. *Journal of Prosthetic Dentistry, 77*(5), 535–539.
19. Taylor, R., Maryan, C., & Verran, J. (1998). Retention of oral microorganisms on cobalt-chromium alloy and dental acrylic resin with different surface finishes. *Journal of Prosthetic Dentistry, 80*(5), 592–597.
20. Bulad, K., Taylor, R. L., Verran, J., & McCord, J. F. (2004). Colonization and penetration of denture soft lining materials by Candida albicans. *Dental Materials, 20*(2), 167–175.
21. Radford, D. R., Sweet, S. P., Challacombe, S. J., & Walter, J. D. (1998). Adherence of Candida albicans to denture-base materials with different surface finishes. *Journal of Dentistry, 26*(7), 577–583.
22. Morgan, T. D., & Wilson, M. (2001). The effects of surface roughness and type of denture acrylic on biofilm formation by *Streptococcus oralis* in a constant depth film fermentor. *Journal of Applied Microbiology, 91*(1), 47–53.
23. Bollen, C. M., Lambrechts, P., & Quirynen, M. (1997). Comparison of surface roughness of oral hard materials to the threshold surface roughness for bacterial plaque retention: A review of the literature. *Dental Materials, 13*(4), 258–269.
24. Zissis, A. J., Polyzois, G. L., Yannikakis, S. A., & Harrison, A. (2000). Roughness of denture materials: A comparative study. *International Journal of Prosthodontics*, *13*(2), 136–140.
25. Ulusoy, M., Ulusoy, N., & Aydin, A. K. (1986). An evaluation of polishing techniques on surface roughness of acrylic resins. *Journal of Prosthetic Dentistry, 56*(1), 107–112.
26. Radford, D. R., Watson, T. F., Walter, J. D., & Challacombe, S. J. (1997). The effects of surface machining on heat cured acrylic resin and two soft denture base materials: A scanning electron microscope and confocal microscope evaluation. *The Journal of Prosthetic Dentistry, 78*(2), 200–208.
27. Sofou, A., Emmanouil, J., Peutzfeldt, A., & Owall, B. (2001). The effect of different polishing techniques on the surface roughness of acrylic resin materials. *The European Journal of Prosthodontics and Restorative Dentistry*, *9*(3–4), 117–122.

28. Rahal, J. S., Mesquita, M. F., & Henriques, G. E. (2004). Nobilo MA surface roughness of acrylic resins submitted to mechanical and chemical polishing. *Journal of Oral Rehabilitation, 31*(11), 1075–1079.
29. Kuhar, M., & Funduk, N. (2005). Effects of polishing techniques on the surface roughness of acrylic denture base resins. *The Journal of Prosthetic Dentistry, 93*(1), 76–85.
30. Aydin, A. K. (1991). Evaluation of finishing and polishing techniques on surface roughness of chromium-cobalt castings. *Journal of Prosthetic Dentistry, 65*(6), 763–767.
31. Xenodimitropoulou, G., & Radford, D. R. (1998). The machining of cobalt-chromium alloy in partial denture construction. *International Journal of Prosthodontics*, *11*(6), 565–573.
32. Ponnanna, A. A., Joshi, S. M., Bhat, S., & Shetty, P. (2001). Evaluation of the polished surface characteristic of cobalt-chrome castings subsequent to various finishing and polishing techniques. *Indian Society for Dental Research*, *12*(4), 222–228.
33. Pererra, V., & Maryan, C. (2002). *Evaluation of the dust generated finishing and polishing cobalt-chrome castings*. BSc(Honours) dissertation, Manchester Metropolitan University, Manchester.
34. Kononen, M., Rintanen, J., Waltimo, A., & Kempainen, P. (1995). Titanium framework removable partial denture used for patient allergic to other metals: A clinical report and literature review. *Journal of Prosthetic Dentistry, 73*(1), 4–7.
35. Au, A. R., Lechner, S. K., Thomas, C. J., Mori, T., & Chung, P. (2000). Titanium for removable partial dentures (III): 2-year clinical follow-up in an undergraduate programme. *Journal of Oral Rehabilitation, 27*(11), 979–985.
36. Rodrigues, R. C., Ribeiro, R. F., de Mattos, M. G., & Bezzon, O. L. (2002). Comparative study of circumferential clasp retention force for titanium and cobalt-chromium removable partial dentures. *The Journal of Prosthetic Dentistry*, *88*(3), 290–296.
37. Srimaneepong, V., Yoneyama, T., Wakabayashi, N., Kobayashi, E., Hanawa, T. &, Doi, H. (2004). Deformation properties of Ti-6A1-7Nb alloy castings for removable partial denture frameworks. *Dental Materials Journal, 23*(4), 497–503.
38. Ohkubo, C., Watanabe, I., Ford, J. P., Nakajima, H., Hosoi, T., & Okabe, T. (2000). The machinability of cast titanium and Ti–6Al–4V. *Biomaterials*, *21*(4), 421–428.
39. Kikuchi, M., Takada, Y., Kiyosue, S., Yoda, M., Woldu, M., Cai, Z., et al. (2003). Grindability of cast Ti–Cu alloys. *Dental Materials*, *19*(5), 375–381.
40. Hirata, T., Nakamura, T., Takashima, F., Maruyama, T., Taira, M., & Takahashi, J. (2001). Studies on polishing of Ti and Ag–Pd–Cu–Au alloy with five dental abrasives. *Journal of Oral Rehabilitation*, *28*(8), 773–777.
41. Hotta, Y., Miyazaki, T., Fujiwara, T., Tomita, S., Shinya, A., Sugai, Y., et al. (2004). Durability of tungsten carbide burs for the fabrication of titanium crowns using dental CAD/CAM. *Dental Materials Journal*, *23*(2), 190–196.
42. Siegel, S. C., & Fraunhofer, J. A. (1999). Comparison of sectioning rates among carbide and diamond burs using three casting alloys. *Journal of Prosthodontics*, *8*(4), 240–244.
43. Miyawaki, H., Taira, M., Wakasa, K., & Yamaki, M. (1993). Dental high-speed cutting of four cast alloys. *Journal of Oral Rehabilitation, 20*(6), 653–661.
44. Clayton, J., & Green, E. (1970). Roughness of pontic materials and dental plaque. *Journal of Prosthetic Dentistry, 23*, 407–411.
45. Monasky, G. E., & Taylor, D. F. (1971). Studies on the wear of porcelain, enamel and gold. *Journal of Prosthetic Dentistry, 25*, 299–306.
46. Hacker, C. H., Wagner, W. C., & Razzoog, M. E. (1996). An in-vitro investigation of the wear of enamel on porcelain and gold in saliva. *Journal of Prosthetic Dentistry, 75*, 14–17.
47. Newitter, D. A., Schlissel, E., & Wolff, M. S. (1982). An evaluation of adjustment and postadjustment finishing techniques on the surface of porcelain-bonded-to-metal crowns. *Journal of Prosthetic Dentistry, 43*, 388–395.
48. Schlissel, E. R., Newitter, D. A., Renner, R. R., & Gwinnett, A. J. (1980). An evaluation of postadjustment polishing techniques for porcelain denture teeth. *Journal of Prosthetic Dentistry, 43*, 258–265.

49. Smith, G. A., & Wilson, N. H. F. (1981). The surface finish of trimmed porcelain. *British Dental Journal*, *151*, 222–224.
50. Sulik, W. D., & Plekavich, E. J. (1981). Surface finishing of dental porcelain. *Journal of Prosthetic Dentistry, 46*, 217–221.
51. Zalkind, M., Lauer, S., & Stern, N. (1986). Porcelain surface texture after reduction and natural glazing. *Journal of Prosthetic Dentistry, 55*, 30–33.
52. Wiley, M. G. (1989). Effects of porcelain on occluding surface of restored teeth. *Journal of Prosthetic Dentistry, 61*, 133–137.
53. Raimondo, R. L., Richardson, J. T., & Wiedner, B. (1990). Polished versus autoglazed dental porcelain. *Journal of Prosthetic Dentistry, 64*, 553–557.
54. Patterson, C. J. W., McLundie, A. C., Stirrups, D. R., & Taylor, W. G. (1991). Polishing of porcelain by using a refinishing kit. *Journal of Prosthetic Dentistry, 65*, 383–388.
55. Scurria, M. S., & Powers, J. M. (1994). Surface roughness of two polished ceramic materials. *Journal of Prosthetic Dentistry*, *71*, 174–177.
56. Jagger, D. C., & Harrison, A. (1994). An in vitro investigation into the wear effects of unglazed, glazed, and polished porcelain on human enamel. *Journal of Prosthetic Dentistry, 72*(3), 320–323.
57. Jagger, D. C., & Harrison, A. (1995). An in vitro investigation into the wear effects of selected restorative materials on enamel. *Journal of Oral Rehabilitation, 22*(4), 275–281.
58. Ramp, M. H., Suzuki, S., Cox, C. F., Lacefield, W. R., & Koth, D. L. (1997). Evaluation of wear: Enamel opposing three ceramic materials and a gold alloy. *Journal of Prosthetic Dentistry, 77*(5), 523–530.
59. Al-Wahadni, A., & Muir Martin, D. (1998). Glazing and finishing dental porcelain: A literature review. *Journal-Canadian Dental Association*, *64*(8), 580–583.
60. Magne, P., Oh, W. S., Pintado, M. R., & DeLong, R. (1999). Wear of enamel and veneering ceramics after laboratory and chairside finishing procedures. *Journal of Prosthetic Dentistry, 82*(6), 669–679.
61. Clelland, N. L., Agarwala, V., Knobloch, L. A., & Seghi, R. R. (2003). Relative wear of enamel opposing low-fusing dental porcelain. *Journal of Prosthodontics, 12*(3), 168–175.
62. Sirona Dental Systems, CEREC®.
63. Leinfelder, K. F., Isenberg, B. P., & Essig, M. E. (1989). A new method for generating ceramic restorations: A CAD-CAM system. *Journal of the American Dental Association, 118* (6), 703–707.
64. Mikrona. Celay®, http://www.mikrona.com/mikrona_e.html, March 2015.
65. Girrbach Dental GmbH. digiDENT®, www.girrbach.com, March 2015.
66. Nobel Biocare. Procera, http://www.nobelbiocare.com/global/en/Products/Procera/default.htm, March 2006.
67. DCS-Dental AG, Precident®, http://www.dcs-dental.com/eng/cadcam.htm, March 2015.
68. Renishaw plc. http://www.renishaw.com/client/product/UKEnglish/PGP-1306.shtml, March 2015.
69. Concurrent Analysis Corporation., Cicero Dental Systems http://www.caefem.com/dental_crown.htm, March 2015.
70. van der Zel, J. M., Vlaar, S., de Ruiter, W. J., & Davidson, C. (2001). The CICERO system for CAD/CAM fabrication of full-ceramic crowns. *Journal of Prosthetic Dentistry, 85*(3), 261–267.
71. Molin, M., & Karlsson, S. (1993). The fit of gold inlays and three ceramic inlay systems. A clinical and in vitro study. *Acta Odontologica Scandinavica, 51*(4), 201–206.
72. Siervo, S., Bandettini, B., Siervo, P., Falleni, A., & Siervo, R. (1994). The CELAY system: A comparison of the fit of direct and indirect fabrication techniques. *International Journal of Prosthodontics, 7*(5), 434–439.
73. Siervo, S., Pampalone, A., Siervo, P., & Siervo, R. (1994). Where is the gap? Machinable ceramic systems and conventional laboratory restorations at a glance. *Quintessence International, 25*(11), 773–779.

74. Rinke, S., Huls, A., & Jahn, L. (1995). Marginal accuracy and fracture strength of conventional and copy-milled all-ceramic crowns. *International Journal of Prosthodontics, 8* (4), 303–310.
75. Mormann, W. H., & Schug, J. (1997). Grinding precision and accuracy of fit of CEREC 2 CAD-CIM inlays. *Journal of the American Dental Association, 128*(1), 47–53.
76. Sulaiman, F., Chai, J., Jameson, L. M., & Wozniak, W. T. (1997). A comparison of the marginal fit of in-ceram, IPS empress, and Procera crowns. *International Journal of Prosthodontics, 10*(5), 478–484.
77. Sturdevant, J. R., Bayne, S. C., & Heymann, H. O. (1999). Margin gap size of ceramic inlays using second-generation CAD/CAM equipment. *Journal of Esthetic and Restorative Dentistry, 11*(4), 206–214.
78. Boening, K. W., Wolf, B. H., Schmidt, A. E., Kastner, K., & Walter, M. H. (2000). Clinical fit of Procera all ceram crowns. *Journal of Prosthetic Dentistry, 84*(4), 419–424.
79. Molin, M. K., & Karlsson, S. L. (2000). A randomized 5-year clinical evaluation of 3 ceramic inlay systems. *International Journal of Prosthodontics, 13*(3), 194–200.
80. Addi, S., Hedayati-Khams, A., Poya, A., & Sjogren, G. (2002). Interface gap size of manually and CAD/CAM-manufactured ceramic inlays/onlays in vitro. *Journal of Dentistry, 30*(1), 53–58.
81. Yeo, I. S., Yang, J. H., & Lee, J. B. (2003). In vitro marginal fit of three all-ceramic crown systems. *The Journal of Prosthetic Dentistry, 90*(5), 459–464.
82. Tomita, S., Shin-Ya, A., Gomi, H., Matsuda, T., Katagiri, S., Shin-Ya, A., et al. (2005). Machining accuracy of CAD/CAM ceramic crowns fabricated with repeated machining using the same diamond bur. *Dental Materials Journal, 24*(1), 123–133.
83. Reich, S., Wichmann, M., Nkenke, E., & Proeschel, P. (2005). Clinical fit of all-ceramic three-unit fixed partial dentures, generated with three different CAD/CAM systems. *European Journal of Oral Sciences, 113*(2), 174–179.
84. Al-Hiyasat, A. S., Saunders, W. P., Sharkey, S. W., Smith, G. M., & Gilmour, W. H. (1998). Investigation of human enamel wear against four dental ceramics and gold. *Journal of Dentistry*, *26*(5–6), 487–495.
85. Ramp, M. H., Ramp, L. C., & Suzuki, S. (1999). Vertical height loss: An investigation of four restorative materials opposing enamel. *Journal of Prosthodontics, 8*(4), 252–257.
86. Imai, Y., Suzuki, S., & Fukushima, S. (2000). Enamel wear of modified porcelains. *American Journal of Dentistry, 13*(6), 315–323.
87. Yin, L., Song, X. F., Song, Y. L., Huang, T., & Li, J. (in press). An overview of in vitro abrasive finishing & CAD/CAM of bioceramics in restorative dentistry. *International Journal of Machine Tools and Manufacture*.
88. Yin, L., Jahanmir, S., & Ives, L. K. (2003). Abrasive machining of porcelain and zirconia with a dental handpiece. *Wear, 255*(7–12), 975–989.
89. Luthardt, R. G., Holzhuter, M. S., Rudolph, H., Herold, V., & Walter, M. H. (2004). CAD/CAM-machining effects on Y-TZP zirconia. *Dental Materials, 20*(7), 655–662.
90. Yara, A., Ogura, H., Shinya, A., Tomita, S., Miyazaki, T., Sugai, Y., et al. (2005). Durability of diamond burs for the fabrication of ceramic crowns using dental CAD/CAM. *Dental Materials Journal, 24*(1), 134–139.
91. Finger, W. J., & Noack, M. D. (2000). Postadjustment polishing of CAD-CAM ceramic with luminescence diamond gel. *American Journal of Dentistry, 13*(1), 8–12.
92. Wilwerding, T., & Aiello, A. (1990). Comparative efficiency testing 330 carbide dental burs utilizing Macor substrate. *Pediatric Dentistry*, *12*(3), 170–171.
93. Ayad, M. F., Rosenstiel, S. F., & Hassan, M. M. (1996). Surface roughness of dentin after tooth preparation with different rotary instrumentation. *The Journal of Prosthetic Dentistry, 75*(2), 122–128.
94. Siegel, S. C., & von Fraunhofer, J. A. (1996). Assessing the cutting efficiency of dental diamond burs. *Journal of the American Dental Association, 127*(6), 763–772.

95. Nishimura, K., Ikeda, M., Yoshikawa, T., Otsuki, M., & Tagami, J. (2005). Effect of various grit burs on marginal integrity of resin composite restorations. *Journal of Medical and Dental Sciences*, *52*(1), 9–15.
96. Siegel, S. C., & von Fraunhofer, J. A. (2000). Cutting efficiency of three diamond bur grit sizes. *The Journal of the American Dental Association, 131*(12), 1706–1710.
97. Siegel, S. C., & Fraunhofer, J. A. (1999). Dental cutting with diamond burs: Heavy-handed or light-touch? *Journal of Prosthodontics*, *8*(1), 3–9.
98. Rimondini, L., Cicognani Simoncini, F., & Carrassi, A. (2000). Micro-morphometric assessment of titanium plasma-sprayed coating removal using burs for the treatment of peri-implant disease. *Clinical Oral Implants Research*, *11*(2), 129–138.
99. Watanabe, I., Ohkubo, C., Ford, J. P., Atsuta, M., & Okabe, T. (2000). Cutting efficiency of air-turbine burs on cast titanium and dental casting alloys. *Dental Materials, 16*(6), 420–425.
100. Haselton, D. R., Lloyd, P. M., & Johnson, W. T. (2000). A comparison of the effects of two burs on endodontic access in all-ceramic high lucite crowns. *Oral Surgery, Oral Medicine, Oral Pathology, Oral Radiology, and Endodontology, 89*(4), 486–492.
101. Trava-Airoldi, V. J., Corat, E. J., Leite, N. F., do Carmo Nono, M., Ferreira, N. G., & Baranauskas, V. (1996). CVD diamond burrs—Development and applications. *Diamond and Related Materials*, *5*(6–8), 857–860.
102. Borges, C. F., Magne, P., Pfender, E., & Heberlein, J. (1999). Dental diamond burs made with a new technology. *Journal of Prosthetic Dentistry, 82*(1), 73–79.
103. Sein, H., Ahmed, W., & Rego, C. (2002). Application of diamond coatings onto small dental tools. *Diamond and Related Materials*, *11*(3–6), 731–735.
104. Sein, H., Ahmed, W., Jackson, M., Ali, N., & Gracio, J. (2003). Stress distribution in diamond films grown on cemented WC–Co dental burs using modified hot-filament CVD. *Surface and Coatings Technology*, *163–164*, 196–202.
105. Ahmed, W., Sein, H., Ali, N., Gracio, J., & Woodwards, R. (2003). Diamond films grown on cemented WC–Co dental burs using an improved CVD method. *Diamond and Related Materials*, *12*(8), 1300–1306.
106. Sein, H., Ahmed, W., Jackson, M., Polinic, R., Hassan, I., Amara, M., et al. (2004). Enhancing nucleation density and adhesion of polycrystalline diamond films deposited by HFCVD using surface treatments on Co cemented tungsten carbide. *Diamond and Related Materials*, *13*(4–8), 610–615.
107. Ahmed, W., Sein, H., Jackson, M., & Polini, R. (2004). Chemical vapour deposition of diamond films onto tungsten carbide dental burs. *Tribology International, 37*(11–12), 957–964. (Novel Carbons in Tribolgy).
108. Ali, N., Cabral, G., Neto, V. F., Sein, H., Ahmed, W., & Gracio, J. (2003). Surface engineering of WC–Co used in dental tools technology. *Materials Science and Technology*, *19*, 1273–1278.
109. Sein, H., Ahmed, W., Jackson, M., Woodwards, R., & Polini, R. (2004). Performance and characterisation of CVD diamond coated, sintered diamond and WC–Co cutting tools for dental and micromachining applications. *Thin Solid Films, 447–448*, 455–461.
110. Jackson, M. J., Sein, H., & Ahmed, W. (2004). Diamond coated dental bur machining of natural and synthetic dental materials. *Journal of Materials Science: Materials in Medicine, 15*(12), 1323–1331.
111. Polini, R., Allegri, A., Guarino, S., Quadrini, F., Sein, H., & Ahmed, W. (2004). Cutting force and wear evaluation in peripheral milling by CVD diamond dental tools. *Thin Solid Films*, *469–470*, 161–166.
112. Yoshida, H., Nagata, C., Mirbod, S. M., Iwata, H., & Inaba, R. (1991). Analysis of subjective symptoms of upper extremities in dental technicians. *Sangyo Igaku, 33*(1), 17–22.
113. Nakladalova, M., Fialova, J., Korycanova, H., & Nakladal, Z. (1995). State of health in dental technicians with regard to vibration exposure and overload of upper extremities. *Central European Journal of Public Health, 3*(Suppl), 129–131.
114. Directive 2002/44/EC of the European Parliament and of the Council of 25 June 2002 on the minimum health and safety requirements regarding the exposure of workers to the risks

arising from physical agents (vibration) (sixteenth individual Directive within the meaning of Article 16(1)of Directive 89/391/EEC). Official Journal of the European Communities 6.7.2002 L 177/13.
115. Mansfield, N. J. (2005). The European vibration directive–how will it affect the dental profession? *British Dental Journal, 199*(9), 575–577.
116. Jedrzejewski, T., & Ulejska, I. (1967). Air contamination in a dental laboratory as a result of mechanical procedures in the preparation of dental prosthesis. *Protetyka Stomatologiczna, 11*, 65–69.
117. Hugonnaud, C., & Lob, M. (1976). Risks incurred by dental technicians working on metallic prostheses. *Sozial-und Praventivmedizin, 21*(4), 139.
118. Leclerc, P., Fiessinger, J. N., Capron, F., Ameille, J., & Rochemaure, J. (1983). Erasmus syndrome in a dental technician. Importance of the prevention of occupational hazards. *Annales de Medecine Interne (Paris), 134*(7), 653–655.
119. Rom, W. N., Lockey, J. E., Lee, J. S., Kimball, A. C., Bang, K. M., Leaman, H., et al. (1984). Gibbons HL Pneumoconiosis and exposures of dental laboratory technicians. *American Journal of Public Health, 74*(11), 1252–1257.
120. Ichikawa, Y., Kusaka, Y., & Goto, S. (1985). Biological monitoring of cobalt exposure, based on cobalt concentrations in blood and urine. *International Archives of Occupational and Environmental Health, 55*(4), 269–276.
121. Morgenroth, K., Kronenberger, H., Michalke, G., & Schnabel, R. (1985). Morphology and pathogenesis of pneumoconiosis in dental technicians. *Pathology, Research and Practice, 179*(4–5), 528–536.
122. De Vuyst, P., Vande Weyer, R., De, Coster A., Marchandise, F. X., Dumortier, P., Ketelbant, P., et al. (1986). Dental technician's pneumoconiosis. A report of two cases. *American Review of Respiratory Disease, 133*(2), 316–320.
123. Sheikh, M. E., & Guest, R. (1990). Respiratory ill-health in dental laboratory technicians: A comparative study of GP consultation rates. *Journal of the Society of Occupational Medicine*, *40*(2), 68–70.
124. Choudat, D., Triem, S., Weill, B., Vicrey, C., Ameille, J., Brochard, P., et al. (1993). Respiratory symptoms, lung function, and pneumoconiosis among self employed dental technicians. *British Journal of Industrial Medicine, 50*(5), 443–449.
125. Nayebzadeh, A., Dufresne, A., Harvie, S., & Begin, R. (1999). Mineralogy of lung tissue in dental laboratory technicians' pneumoconiosis. *American Industrial Hygiene Association Journal, 60*(3):349–353.
126. Choudat, D. (1994). Occupational lung diseases among dental technicians. *Tubercle and Lung Disease, 75*(2), 99–104.
127. Centers for Disease Control and Prevention (CDC). (2004). Silicosis in dental laboratory technicians—Five states, 1994-2000. *MMWR. Morbidity and Mortality Weekly Report, 53* (9), 195–197.
128. Brune, D., Beltesbrekke, H., & Strand, G. (1980). Dust in dental laboratories. Part II: Measurement of particle size distributions. *Journal of Prosthetic Dentistry, 44*(1), 82–87.
129. Collard, S. M., McDaniel, R. K., & Johnston, D. A. (1989). Particle size and composition of composite dusts. *American Journal of Dentistry, 2*(5), 247–253.

Chapter 9
Nanocrystalline Diamond: Deposition Routes and Clinical Applications

H. Sein, C. Maryan, A. Jones, J. Verran, N. Ali, I.U. Hassan, C. Rego, W. Ahmed and M.J. Jackson

Abstract Diamond is one of the most advanced and most useful engineering materials in use today. The properties of synthetic diamond are very similar to that of single crystal diamond and it is well established that diamond has unique combinations of excellent physical, optical, chemical and biomedical properties. Typically, each application area for diamond requires the optimum properties of the material. The optimisation of diamond properties can only be achieved by operating on the microstructure, since it is almost impossible to alter diamond's molecular structure or its chemical composition. This chapter discusses the use of nanocrystalline diamond for clinical applications.

9.1 Introduction

Diamond is one of the most technologically advanced and potentially the most useful engineering material in existence today. The properties of synthetic diamond are very similar to that of single crystal diamond. Table 9.1 shows some of the key properties of synthetic diamond and single crystal diamond. It is well established that diamond has a unique combination of excellent physical, optical, chemical and biomedical properties [1–3]. Typically, each application area for diamond requires the optimum properties of the material. The optimisation of diamond properties can only be achieved by operating on the microstructure, since it is almost impossible to alter diamond's molecular structure or its chemical composition. It is interesting to note that majority of diamond's properties arises from the fact that carbon atoms, which give diamond its macromolecular structure, are relatively small and light. In

H. Sein · C. Maryan · A. Jones · J. Verran · N. Ali · I.U. Hassan · C. Rego
Manchester Metropolitan University, Manchester, UK

W. Ahmed
School of Medicine, University of Central Lancashire, Preston, UK

M.J. Jackson (✉)
Kansas State University, Salina, KS, USA
e-mail: jacksonmj04@yahoo.com

W. Ahmed and M.J. Jackson (eds.), *Surgical Tools and Medical Devices*,
DOI 10.1007/978-3-319-33489-9_9

Table 9.1 Properties of synthetic diamond and single crystal diamond

Property	Synthetic diamond	Single crystal diamond
Density (g cm^{-3})	2.8–3.51	3.515
Thermal capacity at 27 °C (J mol^{-1} K^{-1})	6.9	6.195
Thermal conductivity at 25 °C (W m^{-1} K^{-1})	2100	2200
Thermal expansion coefficient at 25–200 °C ($\times 10^6$ $°C^{-1}$)	~2.0	0.8–1.2
Band gap (eV)	5.45	5.45
Carrier mobility (cm^2 V^{-1} s^{-1})		
Electron (*n*)	1350–1500	2200
Positive hole (*p*)	480	1600
Electrical resistivity (Ω cm)	10^9–10^{16}	10^{16}
Dielectric constant at 45 MHz to 20 GHz	5.6	5.7
Dielectric strength (V cm^{-1})	10^6	10^6
Saturated electron velocity ($\times 10^7$ cm s^{-1})	2.7	2.7
Young's modulus[a] (GPa)	820–900 at 0–800 °C	910–950
Vickers hardness (GPa)	50–100	57–104
Index of refraction at 10 μm	2.34–2.42	2.40

[a]Young's modulus = 895 $\{1–1.04 \times 10^{-4} (T - 20)\}$, (GPa), where T in °C

addition, when the carbon atoms bond together to form the diamond structure, they form very strong covalent bonds. The C–C bonds and the giant covalent structure give diamond its immense strength and hardness. As a result, diamond is the hardest known material and possesses high wear resistant. Although, diamond has many outstanding properties, in actual fact, it cannot be engineered into many physical configurations required to fully exploit its unique combination of properties.

The development of the chemical vapour deposition (CVD) technique has lead to the ability to deposit diamond in thin film form, i.e. as a coating. This enables the exploitation of more combinations of the extreme properties of diamond for specific applications. Generally, the two well-known and established technologies, in use today, for depositing diamond-based materials are (i) CVD and (ii) physical vapour deposition (PVD). A typical CVD process involves many gaseous phase chemical reactions occurring above a solid surface, which cause film deposition onto that surface, whereas, PVD processes involve the transport of material from the target or source to the substrate surface where the material being transported is influenced by a physical driving mechanism.

However, to date, the most effective and the most successful methodology for depositing diamond-based coatings onto a range of materials is CVD. Although, there are different types of CVD processes, every process requires external energy sources to activate the chemical precursors. Activation can be accomplished in a number of different ways, i.e. thermal, resistive filaments, infrared, ultraviolet, radio

frequency, laser and plasma powers [4–8]. Each individual method of activation has its own particular advantages and disadvantages. A method of activation is selected based on the requirements of a particular application. Subsequent to gas activation, a series of chemical reactions, such as adsorption, desorption, decomposition, reduction, oxidation, hydrolysis and transport occur, which ultimately lead to the growth of a solid film and reaction by-products. It is desirable to have the reaction by-products as stable and volatile. The volatile by-products usually desorb from the substrate and leave the reaction chamber through the pumping system and produce a film free from impurities.

Generally, microcrystalline diamond (MCD) films deposited using conventional CVD processes tend to exhibit high surface roughness mainly due to the columnar growth mode of the non-orientated polycrystalline diamond films. One of the major limitations of the wide scale use of diamond coatings has been the high roughness of the as-grown diamond films. This has prevented its widespread use, especially in microelectronics, optical and biomedical applications. Generally, it is accepted that the mechanical, tribological and biological properties of CVD diamond films depend on the coatings microstructure. For example, it was found that the friction coefficients of the diamond films are proportional to their grain size [9].

In addition, key properties such as wear resistance and hardness, displayed by coatings are highly dependent on the crystallite size and smoothness of the coating surface [10]. Therefore, it is necessary to control film microstructure and roughness. Although, the existing methods currently used to control film microstructure have proven to be useful to some extent, however, the need for newer methods of producing smoother and nanocrystalline diamond (NCD) films are both urgent and timely. This chapter reviews and discusses the deposition routes for NCD formation. Further, it outlines the materials unique properties and potentials for use in biomedical applications and microelectromechanical systems (MEMS).

9.2 Nanocrystalline Diamond

The term *nano* is used to refer to particles with dimensions ≤ 100 nm (nm). Properties, such as electrical, optical, chemical, mechanical, magnetic, biological, etc., of nano-sized particles can be selectively controlled by engineering the size, morphology, and composition of the particles. After developing materials in this near-atomic size range, it becomes possible to combine and exploit the properties of the nanostructured surfaces to create new substances with improved or entirely different properties from their parent materials. For example, nanoparticles can (i) render greater strength and hardness to metals; (ii) give ceramics better ductility and formability; (iii) make it feasible for insulating materials to conduct heat and/or electricity, and (iv) make thin film protective coatings transparent. Nano-sized particles enable the re-engineering of many existing products and designing novel new products/processes that function at unprecedented levels. Furthermore, nano-sized particles offer radical breakthroughs in areas such as materials and

manufacturing; electronics; medicine and healthcare; environment and energy; chemical and pharmaceutical; biotechnology and agriculture; computation and information technology; and national security. In fact, many governments in the western world have increased significantly their annual budgets for innovative nanotechnology research.

Recently, research interest has diverted considerably from conventional MCD films, consisting of an average grain size in the range of several hundred nm to several tens of μm [11–15], to NCD films, having a grain size in the range of 2 nm to a few hundred nm [11–13, 16]. NCD films are known to display some superior properties to conventional MCD coatings. For example, NCD films exhibit smoother surfaces; improved electron emission; less highly orientated grains; better wear resistance; and enhanced optical transmission. Therefore, nano-sized diamond coatings display greater potentials, and increased versatility for use in broader range of applications. As the size of the diamond grains changes from micrometre to nanometre, a factor of a million in volume, new properties start to emerge thus enabling the exploration of newer application areas [17], for example, in X-ray optics, X-ray physics, particle physics, etc. NCD has shown to be cost effective and presents superior performances in the areas of electron field emission [18–24], optical transparency and protective coatings [25–37], tribology [16, 38–45], SAW devices [46] and MEMS [47–49].

9.2.1 Deposition Routes

Many attempts have been made to deposit NCD using a range of different methods and techniques [11, 16, 17, 32, 41, 42, 50–55]. The most common and widely adopted approach in depositing NCD films is by performing deposition at moderately high methane (CH_4) partial pressures and/or lower hydrogen concentrations [56]. Deposition conducted at relatively high CH_4 concentrations favours the deposition of nano-sized diamond particles by inducing high nucleation rates and suppressing the growth of individual crystals. Generally, diamond deposition at CH_4-rich environments deteriorates the crystalline morphology of the depositing film and thus produces a much more disordered film. Typically, the resultant films produced at depositions in hydrogen deficient gas environments vary from the phase: pure NCD to NCD embedded in tetrahedral carbon (*ta*-C) or amorphous carbon (*a*-C) matrix. Michler et al. [57] demonstrated that if in a CH_4/H_2 mixture, the CH_4 content is continuously increased whilst the substrate temperature is kept constant, the morphology of the growing film changes from faceted microcrystals to ball-shaped clusters of nanocrystals to graphitic feather-like morphologies with nano-sized diamond particle inclusions. A number of workers have employed CH_4 concentrations in the range 5–10 % vol., in hydrogen, to produce NCD [27, 42, 58]. Catledge and Vohra [16, 41, 59] reported the synthesis of nanostructured diamond films onto Ti-6AL-4 V materials.

They employed pressures of 95 Torr in a microwave CVD chamber and 5–15 % CH_4 concentration in balanced hydrogen and nitrogen to obtain diamond nanocrystals of the average size 13 nm in a matrix of *ta*-C. Wu et al. [26] prepared NCD of 20–100 nm grain size and surface roughness of approx. 15 nm by using low pressure (5 Torr) and low microwave power (450 W). Zarrabian et al. [28] utilised electron cyclotron resonance plasma to deposit NCD films of 4–30 nm grain size, which were embedded in a DLC matrix. Also, deposition of smooth composite diamond films using hot-filament CVD has been reported [60]. These films consisted of MCD and NCD film layers, and they had dielectric properties similar to conventional MCD films with smooth surfaces, thus making them potentially suitable for MEMS devices.

Konov et al. [61] performed NCD growth using $CH_4/H_2/Ar$ mixtures with a CH_4-content being varied in the range 10–100 % using a dc arc plasma deposition system. The as-deposited NCD films on silicon substrates, seeded with 5 nm diamond particles, consisted of 30–50 nm-sized diamond crystallites. Nistor et al. [62] deposited NCD films from $CH_4/H_2/Ar$ mixtures using d.c. plasma CVD system. Interestingly, Lin et al. [63] studied $CH_4/H_2/Ar$ mixtures in a hot-filament CVD system and reported a change in microstructure from MCD to NCD, with a grain size smaller than 50 nm, at 95.5 % Ar addition. Similarly, it was reported [64] that the surface morphology of the NCD films changed with increasing Ar concentration. The formation of NCD was observed when >90 % Ar was used in the plasma mixture. Amaratunga et al. [65, 66] produced mixed phase films containing diamond crystallites, 10–200 nm in size, which were found embedded in a non-diamond carbon matrix whilst using CH_4/He plasmas. Bi et al. [46] also used $CH_4/H_2/Ar$ mixtures in the ratio 1:4:100 to deposit NCD films specifically for SAW devices.

In addition to using CH_4 as the carbon-containing precursor, fullerene can also be used to prepare NCD coatings [67–70]. Researchers at the Argonne National Laboratory, USA [9, 11, 38, 47, 67, 71–75] successfully employed fullerene molecules (C_{60}) and argon-rich plasmas in a microwave CVD reactor to deposit NCD films. This process takes place in a specially designed microwave discharge chamber filled with a gaseous mixture of 1 % C_{60}, 98 % Ar and 1 % hydrogen. The microwave energy converts the argon (Ar) gas into plasma. The Ar in the plasma collides with the C_{60} molecules and knocks an electron to create a C_{60}^{+} ion. Electrons in the plasma react with the C_{60}^{+} ions to initiate fragmentation, which produces a serious of carbon dimers, C_2. It is these dimers that are believed to be the critical plasma species that initiate the diamond growth process. The NCD films deposited on seeded substrates by this method are composed of 3–15 nm diamond crystallites with up to 1–10 % sp^2 carbon residing at the grain boundaries [11].

Gas dopants, such as nitrogen [21, 22, 76], and oxygen [29–31, 33] have also been used to deposit NCD. Such gas dopants are used to primarily dilute the CH_4 gas source during NCD deposition. The dilution approach alters significantly the nucleation processes occurring during diamond CVD and favours predominantly NCD film growth. Lee et al. [50, 51] proposed a low-temperature process, at low

microwave powers, to deposit NCD at growth rates of up to 2.5 μm/h. This process employs temperatures in the range of 350–500 °C and uses CO/hydrogen mixtures to obtain NCD consisting of 30–40 nm grain size. Recently, Teii et al. [55] formed NCD films consisting of diamond crystallites of 20 nm size at 80 mTorr and 700 °C by inductively coupled plasma employing $CO/CH_4/H_2$ and $O_2/CH_4/H_2$ gas mixtures. A positive bias of 20 V was imposed to the substrate in order to reduce the influence of ion bombardment. The as-deposited films consisted of ball-type grains (100 nm), where each ball-shaped grain was composed of approx. 20 nm NCD.

NCD films can also be deposited using a number of different techniques, including direct-ion beam deposition [77], two-stage growth method [78], dielectrophoresis/spraying coating [18, 20, 79, 80], microwave CVD [81–86], radio-frequency plasma CVD [87], biassed enhanced growth [17, 88–90] and repetitive bias-enhanced nucleation (BEN) [91]. The bias-enhanced growth (BEG) process was developed by Sharda et al. [88] and it was designed to achieve higher diamond nucleation densities, similar to the BEN process. In the BEG process, the BEN stage is extended for the length of the deposition process in a microwave CVD system. The as-deposited films were NCD and these were prepared in 5 % vol. CH_4 in balanced hydrogen whilst the bias current density was controlled in a special arrangement of the microwave CVD system. As a result of the BEG process, a number of other workers also adopted similar biassing techniques to produce NCD films [53, 54, 92–98]. Prawer et al. [99] produced a layer of NCD in fused quartz by the ion implantation technique followed by annealing. This is a unique process, since it does not require any nucleation or any external high pressure, as is the case in the traditional high pressure high temperature (HPHT) technique, to produce diamond. Similarly, Wang et al. [100] produced NCD consisting of grains in the range approx. 2–70 nm by irradiation of graphite.

Recently, Yusa [101] has reported the growth of nano-sized diamond particles from a direct transformation from carbon nanotubes under high pressure. Multiwalled carbon nanotubes were heated in a diamond anvil cell by a CO_2 laser above 17 GPa and at 2500 K. The recovered product consisted of nano-sized octahedral diamond crystallites. Hirari et al. [35, 36] produced NCD by transforming C_{60} fullerene by shock compression and rapid quenching. The resultant transparent NCD platelets consisted of a few nm-sized diamond crystallites. More recently, Gogotski et al. [102] introduced the synthesis of NCD in amalgamation with other types of carbon-forms, e.g. carbon nanotubes, nano-onion rings, amorphous carbon, graphite, etc., onto silicon carbide surfaces. The silicon carbide material is transformed into a number of structures of carbon at ambient pressures after the chlorination processes taking place below 1000 °C. These carbide-derived carbon (CDC) structures are currently been tested for tribological properties as well as their potentials for use in hydrogen gas storage applications.

In industry and in academia, generally, the principal method used for reducing the surface roughness of thin film coatings is by employing mechanical polishing procedures [103]. However, some difficulties arise during polishing the films using standard polishing procedures. As a result, techniques, such as chemical polishing, inert and oxygen ion-beam polishing have been developed to establish smooth

coating surfaces [104–107]. Some researchers have employed pulsed bias procedures during diamond film growth, in order to produce highly orientated films, using different pulse bias duty cycles [108, 109]. However, despite their efforts, greater detailed work is required before the full potentials of pulsed biassing can be realised. An in situ method, which consists of sequential in situ diamond deposition and planarisation in an electron cyclotron resonance plasma system, has been developed to produce smooth diamond films [110]. This method is believed to have the advantage of reducing processing time and costs, as well as maintaining a cleaner process environment. Silva et al. [111] attempted to grow smooth diamond films at lower temperatures by employing a two-step growth process. They proposed to promote non-diamond phase nucleation onto (111) faces. However, no significant progress concerning the smoothness of the film was obtained. Difficulties were encountered in promoting secondary nucleation on a particular facet at low deposition temperatures (approx. 550 °C). Secondary nucleation occurs more favourably on (111) and (100) diamond facets [112, 113]. Instead, they proposed to employ a gold interlayer in between two diamond layers in order to control surface roughness. Chen et al. [19] and Kumar et al. [115] employed a similar 2-step growth process, used by Silva et al. [111], to produce diamond-like-carbon films. These workers employed such processes to control the stress and improve the coating adhesion of the deposited films.

9.2.2 Time Modulated CVD

Although, during the relatively short bias-voltage pulses in bias-enhanced nucleation [116] where the CH_4 concentration is increased, only slightly, in almost all the methods described, the flow of CH_4 during film growth is kept constant. Diamond growth in a CVD vacuum reactor is conventionally performed under constant CH_4 flow, while the excess flow of hydrogen is kept constant throughout the growth process. In developing the new TMCVD process it was considered that diamond deposition using CVD consists of two stages: (i) the diamond nucleation stage and (ii) crystal growth stage. Diamond grains nucleate more efficiently at higher CH_4 concentrations. However, prolonged film growth performed under higher CH_4 concentration leads to the incorporation of non-diamond carbon phases, such as graphitic and amorphous. The TMCVD process combines the attributes of both growth stages. This technique has the potential to replicate the benefits obtained by using pulsed power supplies, which are relatively more expensive to employ. The key feature of the new process that differentiates it from other conventional CVD processes is that it pulses CH_4, at different concentrations, throughout the growth process, whereas, in conventional CVD, the CH_4 concentration is kept constant, for the full growth process. In TMCVD, it is expected that secondary nucleation processes occur during the stages of higher CH_4 concentration pulses. This can effectively result in the formation of a diamond film involving nucleation stage, diamond growth, secondary nucleation and the cycle is repeated. The secondary nucleation

phase can inhibit further growth of diamond crystallites. The nuclei grow to a critical level and then are inhibited when secondary nuclei form on top of the growing crystals and thus fill up any surface irregularities. This type of film growth can potentially result in the formation of a multilayer type film coating. In such coating systems, the quality and the surface roughness of the film coatings are dependant not on the overall thickness of the film but instead on the thickness of the individual layer of the film coating. In demonstrating the CH_4 flow regimes, typically employed in conventional diamond CVD and TMCVD processes, Fig. 9.1 shows, as an example, the variations in CH_4 flow rates during film deposition. In the CH_4 pulse cycle employed in Fig. 9.1, the CH_4 flow rate remained constant throughout the conventional CVD process at 25 sccm. It is important to note that the hydrogen flow rate remains constant under both growth modes. CH_4 modulations at 9 and 40 sccm for 15 and 2 min, respectively, were performed during the TMCVD process using the microwave CVD system. Since higher CH_4 contents in the vacuum chamber results in the incorporation of non-diamond carbon phases in the film, such as graphitic and amorphous, and degrades the global quality of the deposited film, the higher CH_4 pulse duration was kept relatively short. The final stage of the time-modulated process ends with a lower CH_4 pulse. This implies that hydrogen ions will be present in relatively larger amount in the plasma and these will be responsible for etching the non-diamond phases to produce a good quality film.

Figure 9.2a, b displays the close-up cross sectional SEM images of diamond films grown using TMCVD and conventional CVD processes. The conventional MCD film displays a columnar growth structure. However, the time-modulated film displayed a somewhat different growth mode. Instead, the cross section consisted of many coarse diamond grains that were closely packed together. A pictorial model of the mechanism for the TMCVD process is depicted in Fig. 9.2c as compared with the conventional CVD process (Fig. 9.2d).

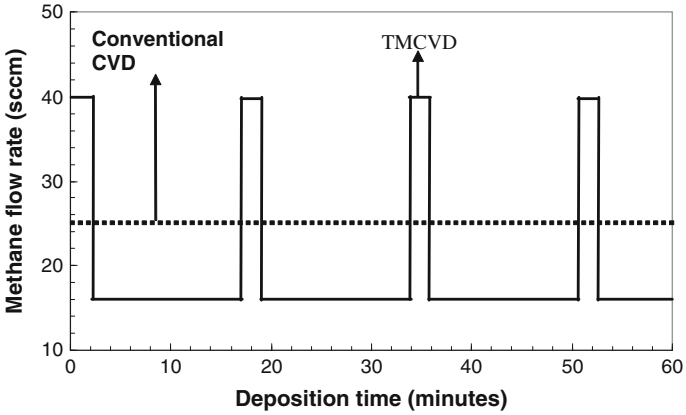

Fig. 9.1 Variations in CH_4 flow rates during film deposition in a typical time-modulated pulse cycle

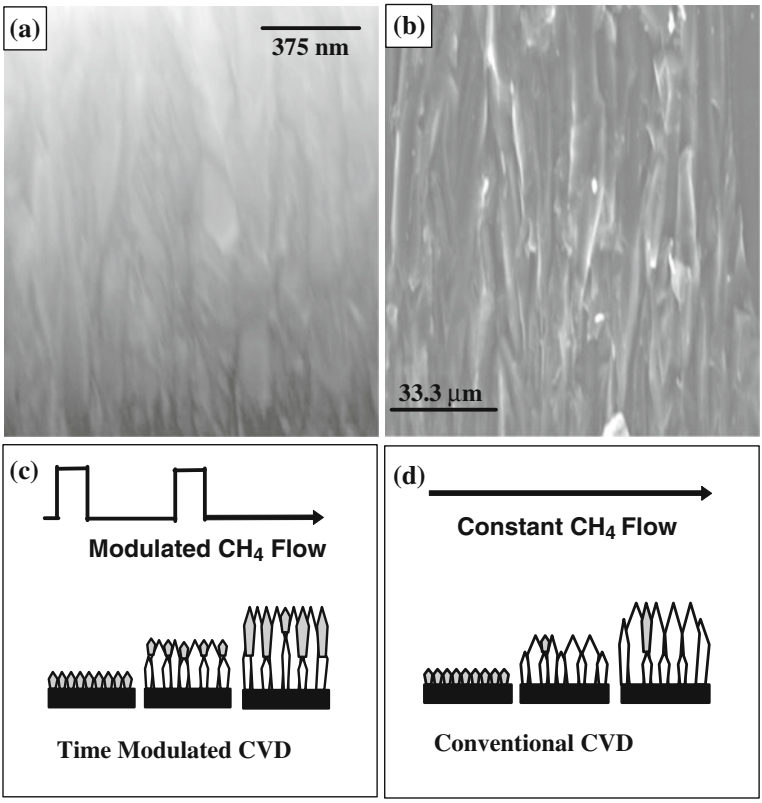

Fig. 9.2 Close-up cross sectional SEM images of diamond films grown using **a** TMCVD and **b** conventional CVD processes. In addition, the pictorial mechanisms for film growth using TMCVD (**c**) and conventional CVD (**d**) processes have also been shown

Primarily, diamond nucleation occurs first in both the TMCVD and conventional CVD processes. However, in TMCVD, diamond nucleates more rapidly as a result of the high CH_4 pulse at the beginning. The high CH_4 pulse effectively ensures the diamond grains to nucleate quicker to form the first diamond layer. The second stage, where CH_4 content is reduced to a lower concentration, the diamond crystallites are allowed to grow for a relatively longer period. This step enables the crystals to grow with columnar growth characteristics. The surface profile of the depositing film becomes rough, as expected. The third stage involves increasing the CH_4 flow back to the higher pulse. This enables further secondary nucleation of NCD to occur in between the existing diamond crystals, where the surface energy is lower. As a comparison, much less secondary nucleation occurs when the CH_4 flow is kept constant throughout the growth process. The distinctive feature of the TMCVD process is that it promotes secondary diamond-particle nucleation to occur on top of the existing grains in order to fill up any surface irregularities.

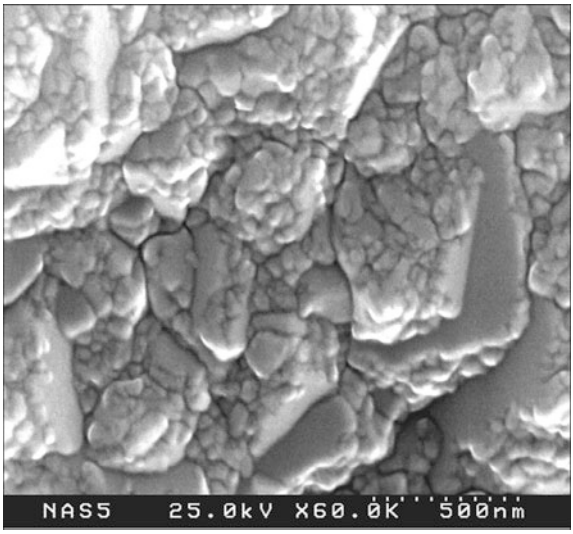

Fig. 9.3 SEM micrograph showing secondary nucleation occurring after a high CH_4 pulse

Figure 9.3 displays the SEM micrograph showing secondary nucleation occurring after a high CH_4 pulse. This result justifies the proposition of the mechanism for the TMCVD process, as shown in Fig. 9.2. It can be expected that at high CH_4 bursts, carbon-containing radicals are present in the CVD reactor in greater amount, which favour the growth process by initiating diamond nucleation. The average secondary nucleation crystallite size was in the nanometer range (≤100 nm).

It is evident that the generation of secondary nano-sized diamond crystallites has lead to the successful filling of the surface irregularities found on the film profile, in between the mainly (111) crystals. Figure 9.4 shows some randomly selected SEM images of as-deposited diamond films deposited using the TMCVD process at different CH_4 pulse duty cycles [117].

Figure 9.5 shows the graph displaying the growth rates of conventional and time modulated films grown using hot-filament CVD (HFCVD) and microwave plasma CVD (MPCVD) systems. As expected, the MPCVD system gave much higher growth rates under both growth modes, conventional and time-modulated, compared to films produced using HFCVD. A growth rate of 0.9 μm/h was obtained using the HFCVD system under constant CH_4 flow. The time-modulated films deposited using HFCVD were grown at a rate of 0.7 μm/h. Whereas, with the MPCVD system, films grown using constant CH_4 flow were deposited at a rate of 2.4 μm/h and using modulated CH_4 flow the films were grown at a rate of 3.3 μm/h. Although, it is known that growth rates increase with CH_4 concentration, in the present case using the HFCVD system, the TMCVD process employs greater CH_4 flow than conventional CVD. Our results show that the growth rate of films deposited using constant CH_4 flow is slightly higher than similar films grown using timed CH_4 modulations.

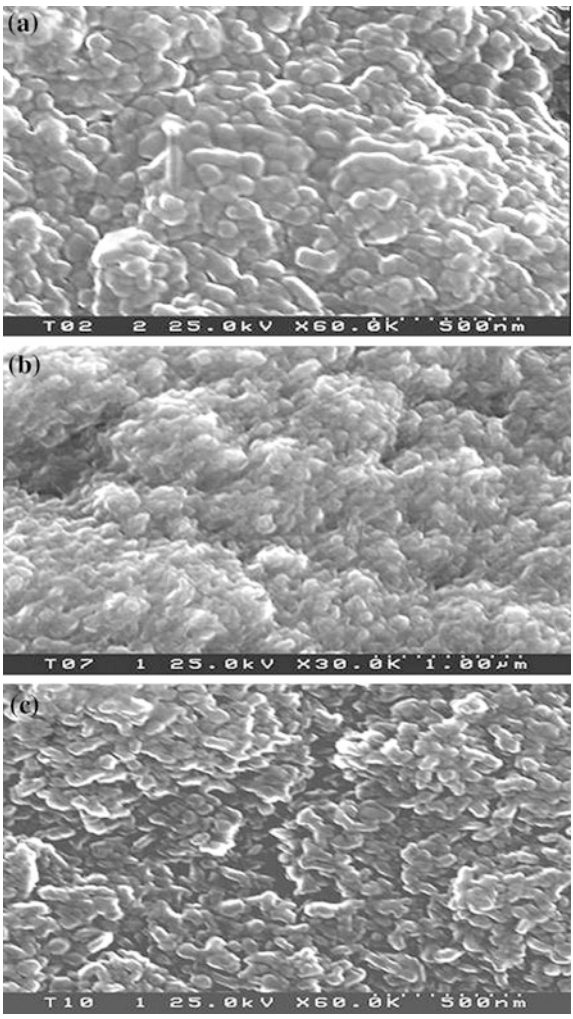

Fig. 9.4 SEM micrographs showing the morphologies of as-deposited diamond films deposited using TMCVD at different CH_4 modulation duty cycles [117]

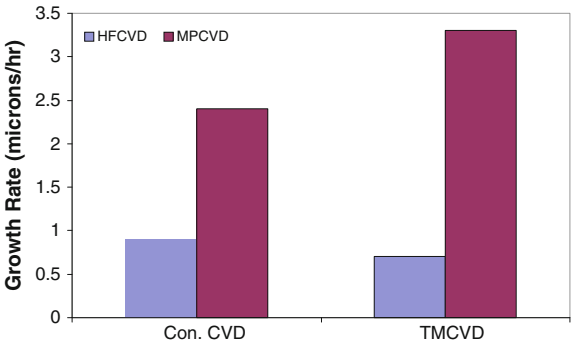

Fig. 9.5 Graph displaying the growth rates of conventional and time-modulated films grown using HFCVD and MPCVD systems

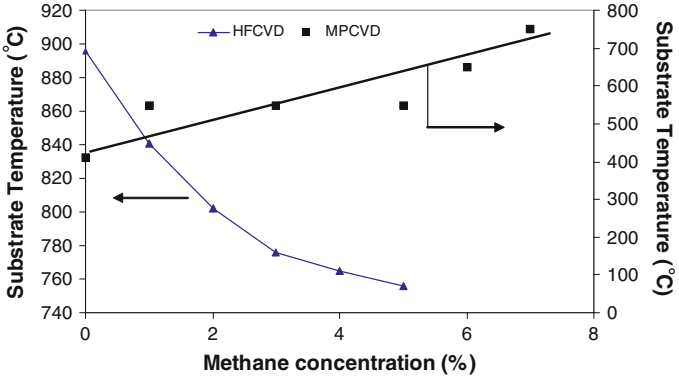

Fig. 9.6 Graph relating substrate temperature to CH_4 concentration for HFCVD and MPCVD systems

However, films grown under both modes, conventional and time modulated, using the MPCVD system produced results that were contrary to those obtained using the HFCVD system. Using the MPCVD system, the trend observed was that the films were deposited at a higher growth rate using the TMCVD process than conventional CVD. The substrate temperature is a key parameter, which governs the growth rate in diamond CVD. Since the TMCVD process pulsed CH_4 during film growth, it was necessary to monitor the change in the substrate temperature during the pulse cycles. Figure 9.6 shows the graph relating substrate temperature to CH_4 concentration for both HFCVD and MPCVD systems.

For the HFCVD system, it was observed that the substrate temperature decreased with CH_4 concentration. In explaining the observed trend, it needs to be considered that the dissociation of CH_4 by the hot filament absorbs energy (heat) from the filament and is considered as a cooling process. In our case the filament power was kept constant, therefore, less heat can be expected to radiate to the substrate. In addition, only a small percentage of the thermally dissociated CH species reach the substrate and transfer kinetic energy to the substrate. It is known that the deposition of diamond films increases with substrate temperature [118].

During the high CH_4 pulse in TMCVD, the lower substrate temperature may be sufficient to lower the growth rate significantly. Generally, in a MPCVD reactor, the substrate temperature increases with CH_4 concentration, as shown in Fig. 9.6 [119]. As a comparison, H_2 is dissociated more extensively in a MPCVD reactor than in a HFCVD reactor to produce atomic hydrogen. Furthermore, in a MPCVD reactor, the plasma power is much greater, 3400 W, than the plasma power in the HFCVD reactor. In fact, the plasma power used in MPCVD for growing diamond films was approximately 10 times greater than the power used in the HFCVD reactor. Therefore, the dissociation of CH_4 only absorbs lower percentage of the energy/heat from the plasma in a MPCVD compared to the HFCVD reactor. It is also understood that the reaction between atomic hydrogen and CH species at close vicinity to the substrate releases heat. Since in a MPCVD reactor there is a greater intensity of

atomic H and CH species, there will be greater number of reactions between atomic H and CH species. This means that more heat will be released in a MPCVD reactor than in a HFCVD reactor due to such reactions.

This effect contributes to the heating of the substrate. In a HFCVD reactor, the hot filament displays much lower ability to dissociate H_2. Since atomic hydrogen is a critical species that plays an important role in producing a good quality diamond film during CVD, the quality of the films grown using HFCVD is generally lower than similar films grown using MPCVD. In addition, the hydrogen atoms are required for the effective deposition of diamond onto the substrates. As mentioned earlier, since atomic H radicals are present in greater concentration in a MPCVD reactor than in a HFCVD reactor, the MPCVD process gives higher growth rates than the HFCVD process. In a separate study, reported elsewhere [120], we found that by controlling the temperature during the high/low CH_4 pulse cycles, a greater number of secondary diamond grains were generated and the resultant films displayed (i) smoother surfaces and (ii) higher growth rates.

9.3 Clinical Applications

Diamond coatings are used in applications such as optical lenses (ophthalmic lenses, aerospace screens), microelectronics (integrated circuits), engineering (piston rings, cylinder liners) and thermal management systems [121]. Although, amorphous diamond-like-carbon (DLC) coatings have been employed for use in hip-joint technology, unfortunately, there is one area where the great benefits of NCD have not been relished—the surface treatment of biomedical implants, such as artificial heart valves and hip prostheses, and dental tools such as burs, hip-joint reamers, orthodontic pliers and tweezers, all of which can benefit in terms of quality, safety and cost from the application of a CVD coating. Since diamond is a biocompatible material, both with human tissues and blood, it can find use in a wider range of biomedical applications. We now focus on four specific applications, namely, mechanical heart valves, dental burs, hip prostheses and MEMS and review the developments made in these key application areas.

9.3.1 Heart Valves

Heart disease is one of the most common causes of death in the world today, particularly in the western countries. There are various causes of heart disease, related most commonly to diet and exercise. The failure of heart valves accounts for about 25–30 % of heart problems that occur today. Faulty heart valves need to be replaced by artificial ones using sophisticated and sometimes risky surgery. However, once a heart valve has been replaced with an artificial one there should be no need to replace it again and it should last at least as long as the life of the patient.

Fig. 9.7 A pyrolitic carbon leaflet heart valve

Therefore, any technique that can increase the operating life of heart valves is highly desirable and valuable. Currently, pyrolytic carbon (PyC) is used for the manufacture of mechanical heart valves. Figure 9.7 shows a typical PyC leaflet heart valve. Although, PyC is widely used for heart valve purposes, it is not the ideal material. In its processed form, PyC is a ceramic-like material and like ceramics, it is subject to brittleness. Therefore, if a crack appears, the material, like glass, has very little resistance to the growth/propagation of the crack and may fail under loads.

In addition, its blood compatibility is not ideal for prolonged clinical use. As a result, thrombosis often occurs in patients who must continue to take anti-coagulation drugs on a regular basis [94]. The anti-coagulation therapy can give rise to some serious side effects, such as birth defects. It is therefore extremely urgent that new materials, which have better surface characteristics, blood compatibility, improved wear properties, better availability and higher resistance towards breaking are developed. In artificial heart valve applications, a principal requirement is that the surface should essentially display a smooth surface, since surface roughness causes turbulence in the blood, which leads to the integrity of the red cells being damaged causing bacteria to adhere, and blood coagulation and clots. A possible method to increase the degree of PyC thrombo-resistance is by alloying the material with silicon [95].

Although, research on the surface engineering of mechanical heart valves has been limited and restricted, a number of researchers have attempted to develop biocompatible coatings, which could potentially be used for artificial heart valve purposes. For example, carbon nitride (CN) thin films have been investigated for biocompatibility and their properties strongly suggest their potentials for use in various surgical implants [96]. Generally, both the bio- and haemo-compatibilities of DLC coatings have been extensively investigated and widely reported in the open literature [97]. Jones et al. [98] deposited DLC coatings, consisting of multilayers of TiC and TiN, onto titanium substrates and characterised the coatings for

haemocompatibility, thrombogenicity and interactions with rabbit blood platelets. It was found that DLC produced no haemolytic effect, platelet activation or tendency towards thrombus formation. Furthermore, the platelet spreading correlated with the surface energy of the coatings. Thomson et al. [99] and Dion et al. [100] have also investigated DLC coatings and characterised their biological properties.

It is worth considering that titanium and its alloys have been used in biomedical implants for many years now and therefore it is sensible to look at the surface treatment of titanium alloys for producing superior surface characteristics, which could be ideal for heart valves. It should be noted that titanium alloys are not brittle like PyC. A large number of research scientists have deposited Ti-based coatings, using energised vapour-assisted deposition methods, and studied their potentials for use in biomedical areas, such as heart valves or stents. Yang et al. [101] deposited Ti–O thin films using plasma immersion ion implantation technique and characterised the anticoagulant property employing in vivo methods. They found that the Ti–O film coatings exhibited better thrombo-resistant properties than low-temperature isotropic carbon (LTIC), in long-term implantation. Chen et al. [102] deposited TiO coatings doped with Ta, using magnetron sputtering and thermal oxidation procedures, and studied the antithrombogenic and haemocompatibility of $Ti(Ta^{+5})O_2$ thin films. The blood compatibility was measured in vitro using blood clotting and platelet adhesion measurements. The films were found to exhibit attractive blood compatibility exceeding that of LTIC. Leng et al. [103] investigated the biomedical properties of tantalum nitride (TaN) thin films. They demonstrated that the blood compatibility of TaN films was superior to other common biocompatible coatings, such as TiN, Ta and LTIC. Potential heart valve duplex coatings, consisting of layers of Ti–O and Ti–N, have been deposited onto biomedical Ti-alloy by Leng et al. [104] and their blood compatibility and mechanical properties have been characterised. The TiO layer was designed to improve the blood compatibility, whereas, TiN was deposited to improve the mechanical properties of the TiO/TiN duplex coatings. They found that the duplex coatings displayed (i) better blood compatibility than LTIC; (ii) greater microhardness; and (iii) improved wear resistant than Ti6Al4 V alloys. It has been reported that the TiO coatings display superior blood compatibility to LTIC [105].

9.3.2 Dental Burs

Dental burs are commonly used on patients as well as in the dental laboratories for removing dental material such as enamel, etc. Conventional dental burs are manufactured by binding hard diamond particles onto the substrate surface using a binder matrix material. Figure 9.8 shows a typical SEM micrograph of a conventional diamond dental bur. Generally, there are certain limitations to dental tools and burs in particular. For example, the particles on some dental tools wear off quite quickly making the tools ineffective after only a short lifetime in operation. In addition, with conventional diamond dental burs, there is the heterogeneity of grain

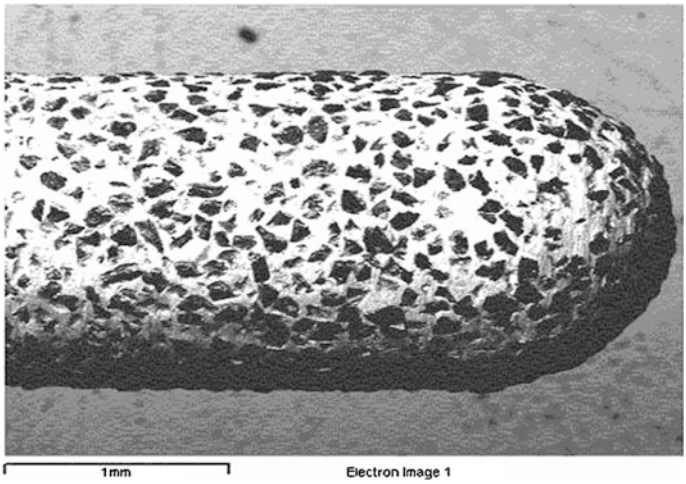

Fig. 9.8 A typical SEM micrograph of a conventional diamond dental bur

shapes and sizes, and the cutting and trimming effectiveness decreases due to repeated sterilisation. Furthermore, there is also the health hazard problem associated with the imbedded diamond particles dislodging from the bur into the patient's mouth. This can result in potential release of Ni^{2+} ions from the metallic binder of the dental burs into the body fluids, which could potentially be toxic to the patient. This aspect not only poses a risk to the respiratory system of the patient, the dentist and the nurse, but also causes contamination of the ceramic during the laboratory manufacturing of dental restorations. There is a growing demand for better quality, long-lasting and more economical dental tools.

Cemented tungsten carbide (WC-Co) is also widely used for manufacturing dental burs. A number of researchers have attempted to grow diamond films onto cemented WC-Co substrates [106–114]. There are limited numbers of researchers who have investigated diamond deposition onto dental burs in any great detail. Borges et al. [115] employed a DC Arc Jet reactor to deposit diamond coatings onto dental burs. Airoldi et al. [116] deposited diamond films onto dental burs using a hot-filament CVD system, where the system configuration was such that two filaments were employed and the dental burs were placed on a rotary substrate holder in between the two filaments. The burs were rotated during film growth in order to obtain uniform film coatings. We have recently modified a conventional hot-filament CVD system to deposit thick diamond coatings onto small tools such as dental burs and micro-drills. The modification was such that the filament was placed vertically in the deposition chamber and the burs are inserted concentrically within the coils of the filament. The readers are encouraged to read some of our papers published on the surface engineering of cemented WC-Co tools [117–120]. However, further work is required before CVD diamond coated dental burs can replace the conventional burs used in dental surgeries.

9.3.3 Hip Prostheses

The increasing life expectancy of the ageing population and the need to surgically treat arthritis in growing numbers of people is placing greater demands on the durability and the expected clinical lifetime of the artificial hip joints. A painful hip can severely hamper a person's ability to live a full active life. The implantation of a hip prosthesis in a patient can eliminate the pain of the damaged hip joint, this being the major benefit of the surgery. It can also reduce disability and renders the patient greater mobility. Over the last 25 years, major advancements in hip replacement have improved the outcome of the hip implantation surgery greatly. Generally, modernised hip prostheses implanted in patients have a clinical success rate of up to approximately 15 years [121]. However, after this period the hip prosthesis begins to fail and thus a revision surgery is necessary. Although the modern hip prosthesis is adequately durable, tiny sized wear particles, in the micrometre and sub-micrometre range, are generated at the articulating surfaces and are released into the surrounding tissues, where they cause inflammation, joint loosening, severe pain and clinical failure [122].

The hip prosthesis is generally constructed of three main components: (i) cup, (ii) spherical head, and (iii) a stem. Suitable materials for hip prosthesis are selected as a compromise, whilst considering tribological issues, corrosion environment, biocompatibility and difficulties encountered in manufacturing. The cups of conventional hip prostheses are typically constructed from ultra-high molecular weight polyethylene material [123]. Unfortunately, this material generates detrimental wear particles. Titanium alloys, such as TiAlV, are commonly used as stems because of their high tensile and fatigue strength, low modulus of elasticity, high corrosion resistance and good biocompatibility [124]. However, blackening of adjacent tissue commonly is observed with titanium alloy implants because of wear particles from bearing surfaces and mechanical instability of stems [125]. Cobalt alloys, such as CoCrMo, are used as stems and spherical heads in hip prostheses. Although, they are less prone to wear and corrosion than titanium alloys, substantial amounts of wear particles are generated in vivo, especially during the initial running in period after surgery [126]. Researchers have attempted to surface engineer conventional hip prostheses in order to overcome the major causes of concern. Methods such as ultrapassivation of titanium [127], nitriding [128], nitrogen ion implantation of titanium alloys [129], titanium nitride [130], PyC [131], silicon nitride [132] and amorphous DLC coatings [133] have been employed. However, most of these methods failed to produce impressive results and acquired only limited market share.

NCD is a natural and trivial choice for use in hip-joint implants. Although, DLC coatings have similar properties to diamond, it is in fact inferior to diamond. Diamond has many superior properties, such as extreme hardness, corrosion resistance, superior wear resistance and good biocompatibility, which make it ideal

for use in artificial hip joints [134]. Furthermore, it is non-irritating material and completely immune to human body fluids. It is highly desirable to transfer these unique properties to the surface of the hip prosthesis. However, before NCD films can succeed in overcoming the constraints facing artificial hip joints, a number of challenges need to be met. For example, it is essential that (i) an ultrasmooth diamond surface is produced; (ii) the strength at the hip/coating interface is sufficient and significant for the application; (iii) and the sp^3/sp^2 ratio in the NCD films is controlled in order to optimise the coating for the application.

9.3.4 Microfluidic Devices

With increasing demand for products associated with the medical, pharmaceutical, and analytical science industries over the past few years, much attention has been paid to the design and manufacture of microfluidic devices. Intensive research has been made on silicon-based microfluidic devices, in particular. Extremely delicate and complex structures such as microflow restrictors, microdroplet spraying nozzles, and micropumps can be manufactured in many industries and research institutes. However, application related issues on device performance such as long-term stability and reliability, biocompatibility, low production costs, and high reproducibility must be considered.

Diamond-like carbon and nanocrystalline diamond coatings possess unique properties such as chemical inertness, biocompatibility, and multifunctionality such as hydrophilicity or hydrophobicity. Deposition of diamond to silicon has been developed for use in such devices. Plasma enhanced CVD processes have been developed to deposit a typical layer thickness of approximately 500 nm with a surface roughness of 1 nm, which can be made hydrophilic or hydrophobic depending on the processing parameters. A layer is deposited on silicon and is immersed in KOH solution for 25 h in order to check for signs of etching. If etching has not taken place then the coating is free from defects. Good conformity of the coating is observed and a cross section of a V-type microchannel is shown in Fig. 9.9. Figure 9.10 shows a microflow restrictor made from silicon with a CVD diamond film deposited to it.

9.3.5 Summary

The significance of NCD in relation to superior film properties, compared to MCD films, for various applications has been put forward. In addition, the different methods employed to deposit NCD films have been reviewed. The current and potential applications of diamond-based films have been briefly described.

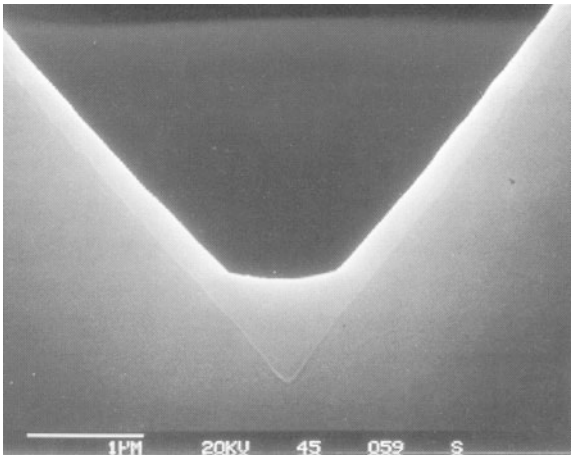

Fig. 9.9 Scanning electron micrograph of a cross section of a V-type microfluidic channel showing diamond coating on top of a silicon substrate. Courtesy of CSEM Switzerland

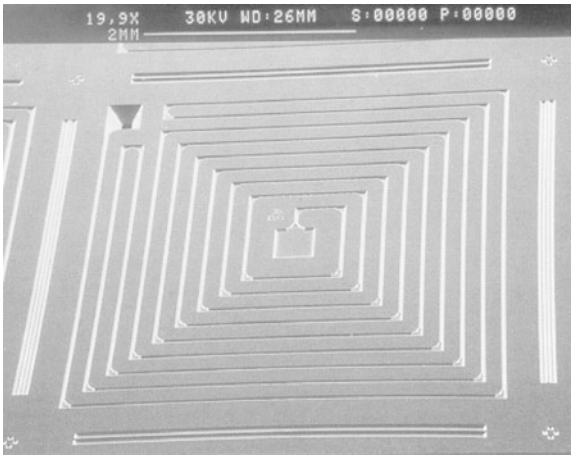

Fig. 9.10 Scanning electron micrograph of a microflow restrictor showing an array of diamond coated V-type channels. Courtesy of CSEM, Switzerland

In particular, the developments and key concerns relating to three specific biomedical applications, namely, artificial heart valves, dental burs and hip prostheses, have been discussed. A new TMCVD process for depositing improved, smoother, MCD and NCD films has been presented. The growth characteristics of films grown using the time-modulated process have been discussed. The growth rate trends observed using the hot-filament and microwave CVD processes have been discussed. As a concluding remark, it must be emphasised that the need for continued research effort in developing nano-sized diamond coatings, to expand the potentials of such coatings for use in newer biomedical applications, remains paramount.

References

1. May, P. W. (2000). *Philosophical Transactions of the Royal Society of London A, 358*, 473.
2. Ashfold, M. N., May, P. W., Rego, C. A., & Everitt, N. M. (1994). *Chemical Society Reviews*, *23*.
3. Ali, N., Ahmed, W., Hassan, I. U., & Rego, C. A. (1998). *Surface Engineering, 14*(4), 292.
4. Ahmed, N. A. G. (1980). *Journal of Physics E: Scientific Instruments, 13*, 295.
5. Mattox, D. M. (1982). In *Proceedings of 4th International Colloquium on Plasma & Sputtering, Nice, France* (p. 187), Paris Societe Fracais du Vide.
6. Mattox, D. M. (1963). *Film deposition using accelerated ions*. Sandia Corporation, Report, SC-DR-28163.
7. Ahmed, W., & Meakin, D. B. (1986). *Journal of Crystal Growth, 79*, 394.
8. Kelly, P. J., Arnell, R. D., & Ahmed, W. (1993). *Materials World, 161*.
9. Fan, Q. H., Pereira, E., Davim, P., Gracio, J., & Tavares, C. J. (2000). *Surface & Coatings Technology, 96*, 111.
10. Ahmed, W., Ackroyd, C. M. J., Ahmed, E., & Sarwar, M. (1991–1998). *Islamabad Journal of Sci*ence*, 11-9*(1–2), 29–34.
11. Gruen, D. M. (1999). *Annual Review of Materials Science, 29*, 211.
12. Zhou, D., Gruen, D. M., Qin, L. C., McCauley, T. G., & Krauss, A. R. (1998). *Journal of Applied Physics, 84*, 1981.
13. Sharda, T., Soga, T., Jimbo, T., & Umeno, M. (2001). *Diamond and Related Materials, 10*, 561.
14. Saito, S., Fujimori, N., Fukunaga, O., Kamo, M., Kobashi, K., & Yoshikawa, M. (1994). *Advances in new diamond science and technology*. Tokyo: MYU.
15. Hirabayashi, K., & Matsumoto, S. (1994). *Journal of Applied Physics, 75*, 1151.
16. Catledge, S. A., & Vohra, Y. K. (1999). *Journal of Applied Physics, 86*, 698.
17. Sharda, T., Umeno, M., Soga, T., & Jimbo, T. (2002). *Applied Physics Letters, 80*, 2880.
18. Zhu, W., Kochanski, G. P., & Jin, S. (1998). *Science, 282*, 1471.
19. Liu, J., Zhirnov, V. V., Mayers, A. F., Wojak, G. J., Choi, W. B., Hren, J. J., et al. (1995). *Journal of Vacuum Science and Technology B, 13*, 422.
20. Gohl, A., Alimova, A. N., Habermann, T., Mescheryakova, A. L., Nau, D., & Müller, G. (1999). *Journal of Vacuum Science and Technology B, 17*, 670.
21. Wu, K., Wang, E. G., Chen, J., & Xu, N. S. (1999). *Journal of Vacuum Science and Technology B, 17*, 1059.
22. Wu, K., Wang, E. G., Cao, Z. X., Wang, Z. L., & Jiang, X. (2000). *Journal of Applied Physics, 88*, 2967.
23. Gu, C., Jiang, X., Jin, Z., & Wang, W. (2001). *Journal of Vacuum Science and Technology B, 19*, 962.
24. Groning, O., Nilsson, L.-O., Groning, P., & Schlapbach, L. (2001). *Solid State Electronics, 45*, 929.
25. Ong, T. P., & Chang, R. P. H. (1989). *Applied Physics Letters, 55*, 2063.
26. Wu, R. L. C., Rai, A. K., Garscadden, A., Lee, P., Desai, H. D., & Miyoshi, K. (1992). *Journal of Applied Physics, 72*, 110.
27. Erz, R., Dotter, W., Jung, D., & Ehrhardt, H. (1993). *Diamond and Related Materials, 2*, 449.
28. Zarrabian, M., Fourches-Coulon, N., Turban, G., Marhic, C., & Lancin, M. (1997). *Applied Physics Letters, 70*, 2535.
29. Bhusari, D. M., Yang, J. R., Wang, T. Y., Lin, S. T., Chen, K. H., & Chen, L. C. (1998). *Solid State Communications, 107*, 301.
30. Chen, K. H., Bhusari, D. M., Yang, J. R., Lin, S. T., Yang, T. Y., & Chen, L. C. (1998). *Thin Solid Films, 332*, 34.
31. Chen, L. C., Wang, T. Y., Yang, J. R., Chen, K. H., Bhusari, D. M., Chang, Y. K., et al. (2000). *Diamond and Related Materials, 9*, 877.

32. Chen, L. C., Kichambare, P. D., Chen, K. H., Wu, J.-J., Yang, J. R., & Lin, S. T. (2001). *Journal of Applied Physics, 89*, 753.
33. Yang, W. B., Lu, F. X., & Cao, Z. X. (2002). *Journal of Applied Physics, 91*, 10068.
34. Sharda, T., Soga, T., & Jimbo, T. (2003). *Journal of Applied Physics, 93*(101), 368.
35. Hirari, H., Kondo, K., Yoshizawa, N., & Shiraishi, M. (1994). *Applied Physics Letters, 64*, 1797.
36. Hirai, H., Kondo, K., Kim, M., Koinuma, H., Kurashima, K., & Bando, Y. (1997). *Applied Physics Letters, 71*, 3016.
37. Davanloo, R., Lee, T. J., Park, H., You, J. H., & Collins, C. B. (1993). *Journal of Materials Research, 8*, 3090.
38. Erdemir, A., Fenske, G. R., Krauss, A. R., Gruen, D. M., McCauley, T. G., & Csencsits, R. T. (1999). *Surface & Coatings Technology, 90–91*, 565.
39. Hogmark, S., Hollman, O., Alahelisten, A., & Hedenqvist, O. (1996). *Wear, 200*, 225.
40. Hollman, P., Wanstrand, O., & Hogmark, S. (1998). *Diamond and Related Materials, 7*, 1471.
41. Catledge, S. A., & Vohra, Y. K. (1998). *Journal of Applied Physics, 84*, 6469.
42. Yoshikawa, H., MoreI, C., & Koga, Y. (2001). *Diamond and Related Materials, 10*, 1588.
43. Davanloo, R., Lee, T. J., Jander, D. R., Park, H., You, J. H., & Co1lins, C. B. (1992). *Journal of Applied Physics*, *71*, 1446.
44. DavanIoo, R., Collins, C. B., & Koivusaari, K. J. (1999). *Journal of Materials Research, 14*, 3474.
45. Toprani, N., Catledge, S. A., Vohra, Y. K., & Thompson, R. (2000). *Journal of Materials Research, 15*, 1052.
46. Bi, B., Huang, W. S., Asmussen, J., & Golding, B. (2002). *Diamond and Related Materials, 11*, 677.
47. Krauss, A. R., Auciello, O., Gruen, D. M., Jayatissa, A., Sumant, A., Tucek, J., et al. (2001). *Diamond and Related Materials, 10*, 1952.
48. Butler, J. E., Hsu, D. S. Y., Houston, B. H., Liu, X., Ignola, J., Feygelson, T., et al. (2002) Paper 6.2. *Presented at the 8th International Conference New Diamond Science and Technology 2002*. The University of Melbourne, Australia. The complete presentation is available online at http://www.conferences.unimelb.edu.au/icndst-8/presenta-tions.htm
49. Sekaric, L., Parpia, J. M., Craighead, H. G., Feygelson, T., Houston, B. H., & Butler, J. E. (2002). *Applied Physics Letters, 81*, 4455.
50. Lee, J., Hong, B., Messier, R., & Collins, R. W. (1996). *Applied Physics Letters, 69*, 1716.
51. Lee, J., Collins, R. W., Messier, R., & Strausser, Y. E. (1997). *Applied Physics Letters, 70*, 1527.
52. Sharda, T., Umeno, M., Soga, T., & Jimbo, T. (2000). *Applied Physics Letters, 77*, 4304.
53. Gu, C. Z., & Jiang, X. (2000). *Journal of Applied Physics, 88*, 1788.
54. Jiang, X., & Jia, C. L. (2002). *Applied Physics Letters, 80*, 2269.
55. Teu, K., Ito, H., Hori, M., Takeo, T., & Goto, T. (2000). *Journal of Applied Physics, 87*, 4572.
56. Bhusari, D. M., Yang, J. R., Wang, T. Y., Chen, K. H., Lin, S. T., & Chen, L. C. (1998). *Journal of Materials Research, 13*(7), 1769–1773.
57. Michler, J., Laufer, S., Seehofer, H., Blank, E., Haubner, R., & Lux, B. (1999). *Proceedings of 10th International Conference on Diamond and Diamond-like Materials, Prague, Czech Republic*, September 9–17, paper 5.231.
58. Heiman, A., Gouzman, I., Christiansen, S. H., Strunk, H. P., Comtet, G., Hellner, L., et al. (2001). *Journal of Applied Physics, 89*, 2622.
59. Jiang, N., Kujime, S., Ota, I., Inaoka, T., Shintani, Y., Makita, H., et al. (2000). *Journal of Crystal Growth, 218*, 265.
60. Xin, H. W., Zhang, Z. M., Ling, X., Xi, Z. L., Shen, H. S., Dai, Y. B., et al. (2002). *Diamond and Related Materials, 11*, 228.
61. Konov, V. L., Smolin, A. A., Ralchenko, V. G., Pimenov, S. M., Obraztsova, E. D., Loubnin, E. N., et al. (1995). *Diamond and Related Materials, 4*, 1073.

62. Nistor, L. C., Landuyt, J. V., Ralchenko, V. G., Obraztsova, E. D., & Smolin, A. A. (1997). *Diamond and Related Materials, 6*, 159.
63. Lin, T., Yu, Y., Wee, T. S., Shen, Z. X., & Loh, K. P. (2000). *Applied Physics Letters, 77*, 2692.
64. Yang, T.-S., Lai, J.-Y., Cheng, C.-L., & Wong, M.-S. (2001). *Diamond and Related Materials, 10*, 2161.
65. Amaratunga, G., Putnis, A., Clay, K., & Milne, W. (1989). *Applied Physics Letters, 55*, 634.
66. Amaratunga, G. A. J., Silva, S. R. P., & McKenzie, D. A. (1991). *Journal of Applied Physics, 70*, 5374.
67. Gruen, D. M., Shengzhong, L., Krauss, A. R., Luo, J., & Pan, X. (1994). *Applied Physics Letters, 64*(9), 1502.
68. Zhou, D., McCauley, T. G., Qin, L. C., Krauss, A. R., & Gruen, D. M. (1998). *Journal of Applied Physics, 83*(1), 540.
69. Gruen, D. M. (1999). *Annual Review of Materials Science, 29*, 211.
70. McCauley, T. M., Gruen, D. M., & Krauss, A. R. (1998). *Applied Physics Letters, 73*(9), 1646.
71. Gruen, D. M., Redfem, P. C., Homer, D. A., Zapol, P., & Curtiss, L. A. (1999). *Journal of Physical Chemistry, 103*, 5459.
72. Gruen, D. M., Pan, X., Krauss, A. R., Liu, S., Luo, J., & Foster, C. M. (1994). *Journal of Vacuum Science and Technology A, 9*, 1491.
73. Zhou, D., Krauss, A. R., Qin, L. C., McCauley, T. G., Gruen, D. M., Corrigan, T. D., & Chang, R. P. H. (1997). *Journal of Applied Physics, 82*, 4546.
74. Zhou, D., McCauley, T. G., Qin, L. C., Krauss, A. R., & Gruen, D. M. (1998). *Journal of Applied Physics, 83*, 540.
75. Bhattacharyya, S., Auciello, O., Birrel, J., Carlisle, J. A., Curtiss, L. A., Goyette, A. N., et al. (2001). *Applied Physics Letters, 79*, 1441.
76. Zhou, D., Krauss, A. R., Qin, L. C., McCauley, T. G., Gruen, D. M., Corrigan, T. D., et al. (1997). *Journal of Applied Physics, 82*(9), 4546.
77. Sun, X. S., Wang, N., Zhang, W. J., Woo, H. K., Han, X. D., Bello, I., et al. (1999). *Journal of Materials Research, 14*(8), 3204.
78. Bhusari, D. M., Yang, J. R., Wang, T. Y., Chen, K. H., Lin, S. T., & Chen, L. C. (1998). *Materials Letters, 36*, 279.
79. Xu, N. S., Chen, J., Feng, Y. T., & Deng, S. Z. (2000). *Journal of Vacuum Science and Technology B, 18*, 1048.
80. Maillard-Schaller, E., Kuettel, O. M., Diederich, L., Schlapbach, L., Zhirnov, V. V., & Belobrov, P. I. (1999). *Diamond and Related Materials, 8*, 805.
81. Yagi, H., Ide, T., Toyota, H., & Mori, Y. (1998). *Journal of Materials Research, 13*(6), 1724.
82. Lee, J., Hong, B., Messier, R., & Collins, R. W. (1996). *Applied Physics Letters, 69*(9), 1716.
83. Xu, T., Yang, S., Lu, J., Xue, Q., Li, J., Guo, W., et al. (2001). *Diamond and Related Materials, 10*, 1441.
84. McGinnis, S. P., Kelly, M. A., Hagstrom, S. B., & Alvis, R. L. (1996). *Journal of Applied Physics, 79*(1), 170.
85. Yoshikawa, H., Morel, C., & Koga, Y. (2001). *Diamond and Related Materials, 10*, 1588.
86. Chen, L. C., Kichambare, P. D., Chen, K. H., Wu, J.-J., Yang, J. R., & Lin, S. T. (2001). *Journal of Applied Physics, 89*(1), 753.
87. Mitura, S., Mitura, A., Niedzielski, P., & Couvrat, P. (1999). *Chaos. Solitons & Fractals, 10* (9), 2165.
88. Sharda, T., Umeno, M., Soga, T., & Jimbo, T. (2000). *Applied Physics Letters, 77*(26), 4304.
89. Sharda, T., Soga, T., Jimbo, T., & Umeno, M. (2000). *Diamond and Related Materials, 9*, 1331.
90. Sharda, T., Soga, T., Jimbo, T., & Umeno, M. (2001). *Diamond and Related Materials, 10*, 1592.
91. Beake, B. D., Hassan, I. U., Rego, C. A., & Ahmed, W. (2000). *Diamond and Related Materials, 9*, 1421.

92. Kundu, S. N., Basu, M., Maity, A. B., Chaudhuri, S., & Pal, A. K. (1997). *Materials Letters, 31*, 303.
93. Zhou, X. T., Li, Q., Meng, F. Y., Bello, L., Lee, C. S., Lee, S. T., et al. (2002). *Applied Physics Letters, 80*, 3307.
94. Groning, O., Kuttel, O. M., Groning, P., & Schlapbach, L. (1999). *Journal of Vacuum Science and Technology B, 17*, 1970.
95. Yang, T. S., Lai, J. Y., Wong, M. S., & Cheng, C. L. (2002). *Journal of Applied Physics*, *92*, 2133.
96. Yang, T. S., Lai, J. Y., Wong, M. S., & Cheng, C. L. (2002). *Journal of Applied Physics, 92*, 499.
97. Zhou, X. T., Li, Q., Meng, R. Y.. Bello, I.. Lee, C. S.. Lee, S. T., et al. (2002). Paper P1.01.11. *Presented at the Eighth International Conference New Diamond Science and Technology*. The University of Melbourne, Australia.
98. Jiang, N., Sugimoto, K., Nishimura, K., Sbintani, Y., & Hiraki, A. (2002). *Journal of Crystal Growth, 242*, 362.
99. Prawer, S., Peng, J. L., Orwa, J. O., McCa11um, J. C., Jamieson, D. N., & Bursill, L. A. (2000). *Physical Review B, 62*, R16360.
100. Wang, Z., Yu, G., Yu, L., Zhu, R., Zhu, D., & Xu, H. (2002). *Journal of Applied Physics, 91*, 3480.
101. Yusa, H. (2002). *Diamond and Related Materials, 11*, 87.
102. Gogotsi, Y., Welz, S., Ersoy, D. A., & McNallan, M. J. (2001). *Nature, 411*, 283.
103. Malshe, A. P., Park, B. S., Brown, W. D., & Naseem, H. A. (1999). *Diamond and Related Materials, 8*, 1198.
104. Tokura, C., Yang, F., & Yoshikawa, M. (1992). *Thin Solid Films, 29*, 49.
105. Zhao, T., Grogan, D. F., Bovard, B. G., & Macleod, H. A. (1992). *Applied Optics, 31*, 1483.
106. Hirata, A., Tokura, H., & Yoshikawa, M. (1992). *Thin Solid Films, 29*, 43.
107. Lee, D. G., & Singh, R. K. (1995). *Beam-solid interactions for materials synthesis and characterization*. In D. E. Luzzi, T. F. Heinz, M. Iwaki, & D. C. Jacobson (Eds.), *Materials Research Society Symposium Proceedings, Pittsburgh, PA* (p. 699).
108. Wolter, S. D., Okuzumi, F., Prater, J. T., & Siter, Z. (2001). *Physical Status Solidi*(a)*, 186*(2), 331.
109. Hassan, I. U., Brewer, N., Rego, C. A., Ahmed, W., Beake, B. D., Ali, N., et al. (2002). In J. Gracio, P. Davim, Q. H. Fan, & N. Ali (Eds.), *Proceedings of New Developments on Tribology: Theoretical Analysis and Application to Industrial Processes* (p. 153). University of Aveiro, Portugal, May 2002. ISBN 972-789-059-8.
110. Gilbert, D. R., Lee, D.-G., & Singh, R. K. (1998). *Journal of Materials Research, 13*(7), 1735.
111. Silva, F., Gicquel, A., Chiron, A., & Achard, J. (2000). *Diamond and Related Materials, 9*, 1965.
112. Gicquel, A., Hassouni, K., & Silva, F. (2000). *Journal of the Electrochemical Society, 14716*, 2218.
113. Zhu, W., Badzian, A. R., & Messier, R. (1990). Diamond Opt. 111, San Diego, California. In: *SPIE* (p. 187). The International Society for Optics Engineering.
114. Chen, C. F., & Hong, T. M. (1993). *Surface & Coatings Technology, 5*, 143.
115. Kumar, S., Dixit, P. N., Sarangi, D., & Bhattacharyya, R. (1999). *Journal of Applied Physics, 85*, 3866.
116. Li, X., Hayashi, Y., & Nishino, S. (1997). *Japanese Journal of Physics, 36*, 5197.
117. Ali, N., Neto, V. F., Sen, M., Misra, D. S., Cabral, G., Ogwu, A. A., et al. (2004). *Thin Solid Films, 469–470*(22), 154.
118. Hayashi, Y., Drawl, W., & Messier, R. (1992). *Japanese Journal of Applied Physics, 31*, L194.
119. Ali, N., Neto, V. F., & Gracio, J. (2003). *Journal of Materials Research, 18*(2), 296–304.
120. Ali, N., Kousar, Y., Fan, Q. H., Neto, V. F., & Gracio, J. (2003). *Journal of Materials Science Letters, 22*, 1039–1042.

121. Field, J. E. (Ed.). (1992). *Properties of natural and synthetic diamond* (p. 667). San Diego, CA: Academic Press.
122. Angus, J. C., & Hayman, C. C. (1988). *Science, 241*, 913.
123. Ahmed, W., Ali, N., Hassan, I. U., & Penlington, R. (1998). *Finishing, 1*, 22.
124. Barton, K., Campbell, A., Chinn, J. A., Griffin, C. D., Anderson, D. H., Klein, K., et al. *Biomedical Engineering Society (BMES) Bulletin, 25*(1), 3.
125. Goodman, S. L., Tweden, K. S., & Albrecht, R. M. (1996). *Journal of Biomedical Materials Research, 32*, 249–258.
126. Cui, F. Z., & Li, D. J. (2000). *Surface & Coatings Technology, 131*, 481–487.
127. McLaughlin, J., Meenan, B., Maguire, P., & Jamieson, N. (1996). *Diamond and Related Materials, 8*, 486–491.
128. Jones, M. I., McColl, I. R., Grant, D. M., Parker, K. G., & Parker, T. L. (1999). *Diamond and Related Materials, 8*, 457–462.
129. Thomson, A., Law, F. G., Rushton, N., & Franks, J. (1991). *Biomaterials, 9*(1), 37.
130. Dion, I., Roquey, C. H., Baudet, E., Basse, B., & More, N. (1993). *BioMedical Materials and Engineering, 3*, 51.
131. Yang, P., Huang, N., Leng, Y. X., Chen, J. Y., Sun, H., Wang, J., et al. (2002). *Surface & Coatings Technology, 156*, 284–288.
132. Chen, J. Y., Leng, Y. X., Tian, X. B., Wang, L. P., Huang, N., Chuan, P. K., et al. (2002). *Biomaterials, 23*, 2545–2552.
133. Leng, Y. X., Sun, H., Yang, P., Chen, J. Y., Wang, J., Wan, G. J., et al. (2001). *Thin Solid Films, 398–399*, 471–475.
134. Leng, Y. X., Yang, P., Chen, J. Y., Sun, H., Wang, J., Wang, G. J., et al. (2001). *Surface & Coatings Technology, 138*, 296–300.

Chapter 10
Medical Device Manufacturing: Environment, Engineering Control and Monitoring

R. Handy, M. Whitt, M. Lafreniere and M.J. Jackson

Abstract The trend toward an aging population in the highly developed countries of the world has the demand for innovative biomedical devices and tools at record levels. The products desired in this market are typically smaller and more portable than their predecessors, and require more sophisticated components and allied manufacturing technologies and automation techniques. In essence, similar to traditional consumer products, biomedical devices such as patient monitors, drug delivery systems, therapeutic devices, and life assisting devices have all decreased in size yet still have market expectations of enhanced performance characteristics and features. This chapter focuses on medical device manufacturing from the environmental, engineering control, and monitoring perspectives.

10.1 Introduction

As a consequence of these market realities, many biomedical device companies have begun modeling their manufacturing environments in a similar fashion to the more traditional industries [1–35]. An example of a modern day portable medical device, an implantable pacemaker, is shown in comparison to its first generation predecessor in Fig. 10.1. A typical biomedical device manufacturing facility starting up today might include the capabilities for fine pitch component placement as a part of a high volume automation line, which is additionally equipped with the necessary advanced testing instrumentation to ensure product quality and assurance.

R. Handy
School of Medicine, The University of Utah, Salt Lake City, UT, USA

M. Whitt
California State Polytechnic, San Luis-Obispo, CA, USA

M. Lafreniere
Ohio University, Chillicothe, OH, USA

M.J. Jackson (✉)
Kansas State University, Salina, KS, USA
e-mail: jacksonmj04@yahoo.com

W. Ahmed and M.J. Jackson (eds.), *Surgical Tools and Medical Devices*,
DOI 10.1007/978-3-319-33489-9_10

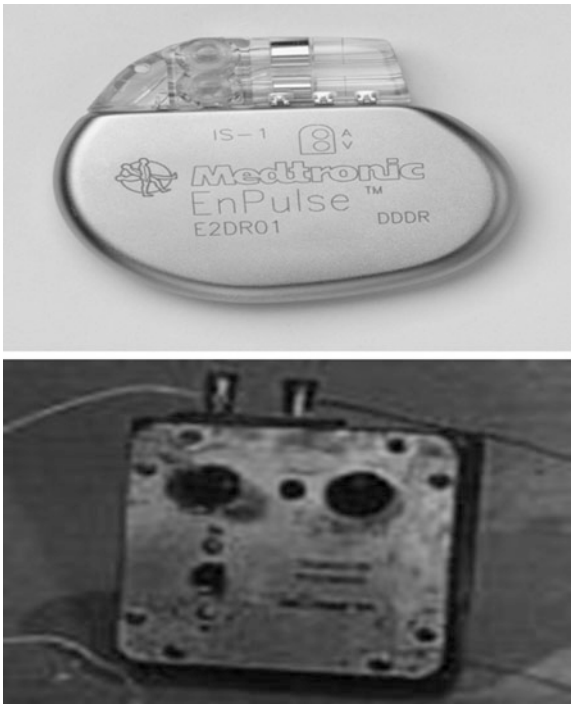

Fig. 10.1 Modern implantable pacemaker (*left*) versus original portable external device (*Permission* Medtronics Canada and Minnesota Technology)

Unfortunately, as similarities increase in manufacturing design, it should also be expected that some of the negative consequences inherent to traditional manufacturing environments should become real issues as well in the biomedical device industry. One major area of concern must be the proper control and monitoring of environmental and worker exposures to potentially harmful chemical, biological, and physical stressors found in increasing concentrations in biomedical device manufacturing.

The purpose of this chapter is to present some of the strategies that could be employed to effectively control and monitor for workplace hazards associated chemical, biological, and physical agents in the biomedical device industry. This chapter begins with a presentation of a comprehensive list of the stressors found in the industry, with an overview of the properties, toxicity/exposure limits, and other pertinent characteristics of each, respectively. This chapter continues with an introduction to the typical environmental and engineering control methods and personal protective equipment (PPE) that should be implemented to help alleviate (or eliminate) the concern for any overexposures to any of these stressors [1–35].

10.2 Stressor Source, Properties, and Characteristics

It is expected that the biomedical device market will significantly grow globally over the next couple of years, with 34.5 % growth rates estimated in the nanoscale market alone through 2007 [1–35]. With the increased production rates brought on by these pressures, it can only be predicted that the use of additional chemical, biological, and physical agents associated with manufacturing these products will also rise substantially. Thus, it can easily be argued that an overall understanding by manufacturing personnel of the capabilities and limitations as well as the potential benefits and detriments of their usage should be imperative. This section attempts to delimit the list to pertinent stressors, with a detailed coverage for each provided on normal source and usage, chemical and physical properties, and toxicity characteristics. A comprehensive list of the stressors provided in this section and deemed the most commonly found in the biomedical device industry, along with source, properties, and toxicity characteristics for each, has been summarized in Table 10.1.

Table 10.1 Common stressors found in biomedical device manufacturing

Stressors	Source	Properties and toxicity characteristics
Ethylene oxide (EtO)	Sterilization	EtO is a colorless, flammable gas at room temperature and pressure with an ether-like odor, which has been linked to leukemia and peritoneal cancer. Acute exposures to >800 parts per million (ppm) can results in severe mucous membrane irritation and edema
Ionizing radiation (IR)	Sterilization, lab instruments	Ionization radiation exposures can be from primarily gamma ray, X-ray, beta particle, alpha particle, and electron beam exposures. Gamma and X-rays are the most penetrating, with beta particles being intermediate and alpha particles depositing energy over only a short traverse
Nonionizing radiation (NIR)	Sterilization, instruments, surface prep, cutting, etc.	The most common nonionizing radiation exposures will be from UV and lasers. UV can cause damage to the skin and eyes while laser energy primarily targets the eyes
Ozone	Welding, sterilization	Ozone is a colorless to blue colored gas at room temperature and pressure, with a very pungent odor. It is nonflammable but a powerful oxidizer that severely irritates the eyes, mucous membranes, and respiratory tract at levels greater than 5 ppm

(continued)

Table 10.1 (continued)

Stressors	Source	Properties and toxicity characteristics
Hydrogen peroxide	Sterilization	Hydrogen peroxide is a noncombustible, colorless liquid with a slightly sharp odor. It is totally miscible in water and a powerful oxidizer with the potential to cause severe damage to the respiratory tract at concentrations greater than 75 ppm
Isopropanol (IPA)	Cleaning, disinfecting	IPA is a colorless liquid with the odor of rubbing alcohol. It is flammable and miscible in water with a vapor pressure of 33 mmHg. At concentrations greater than 4000 ppm, severe dizziness and drowsiness can occur in those exposed
Methanol	Cleaning	Methanol is a colorless, flammable liquid at room temperature and pressure with a characteristic pungent odor. It has a vapor pressure of 96 mmHg and is miscible in water with sever dizziness, drowsiness, and blindness occurring at levels greater than 6000 ppm
Ethanol	Cleaning	Ethanol is a colorless, flammable liquid. It has a vapor pressure of 44 mmHg and totally soluble in water. It can cause severe respiratory and CNS effects at concentrations greater than 1 %
Trichloroethylene (TCE)	Degreasing	TCE is a colorless, combustible liquid with a chloroform-like odor. It has a vapor pressure of 58 mmHg, a specific gravity of 1.46 (sinker), and 0.1 % solubility. At levels >1000 ppm, nausea, convulsions, and death can occur. Skin contact can lead to dermatitis
1,1,1-Trichloroethane	Degreasing	1,1,1-TCA is a colorless, combustible liquid with a mild, chloroform-like odor. It has a vapor pressure of 100 mmHg, a specific gravity of 1.34 (sinker), and 0.4 % solubility. At levels >700 ppm, severe respiratory tract irritation, poor equilibrium, and liver damage can occur. Skin exposures can lead to dermatitis
Acetone	Degreasing, cleaning	Acetone is a colorless, flammable liquid with a mint-like odor. It has a vapor pressure of 180 mmHg, is miscible, and has a specific gravity of 0.79 (floater). High airborne concentrations >5000 ppm can cause CNS depression. Skin exposures can cause dermatitis

(continued)

Table 10.1 (continued)

Stressors	Source	Properties and toxicity characteristics
Perchloroethylene (Perk)	Degreasing	Perk is a colorless, noncombustible liquid with a chloroform-like odor. It is heavier than water, with a low solubility in water (0.02 %) and a low vapor pressure (14 mmHg). Exposures above 150 ppm can cause respiratory problems, dizziness, and liver damage. Exposures have resulted in liver tumors in animals
Hydrofluorocarbons	Degreasing	Hydrofluorocarbons are nonflammable solvents of very low toxicity. They are recyclable and have no effect on the ozone layer. However, emissions do contribute significantly to global warming
Hydrofluoroethers	Degreasing	Same as for hydrofluorocarbons
Perfluorocarbons	Degreasing	Same as for hydrofluorocarbons and hydrofluoroethers
Sulfuric acid	Etching, anodizing	Sulfuric acid is a strong corrosive liquid. It is colorless to dark brown in color, with little odor and an oil-like appearance. The target organs for this miscible, noncombustible liquid include the eyes, skin, and respiratory tract and the IDLH is 15 mg/m^3
Nitric acid	Etching, anodizing	Nitric acid is a noncombustible and colorless, yellow, or red fuming liquid with an acrid, suffocating odor. It is miscible, with a vapor pressure of 48 mmHg. At concentrations >25 ppm, irritation to the eyes, skin, and respiratory tract can occur
Phosphoric acid	Etching, anodizing	Phosphoric acid is a noncombustible, colorless solid with no odor. It is miscible and causes skin burns and dermatitis on contact
Chromic acid	Etching, anodizing	Chromic acid is an odorless, noncombustible red solid, normally used in the flake or powder form. It is a known human carcinogen (septum/lung). Acute reactions include irritation of the respiratory tract and continuous exposures can cause sensitization dermatitis

(continued)

Table 10.1 (continued)

Stressors	Source	Properties and toxicity characteristics
Potassium hydroxide	Etching, anodizing	Potassium hydroxide is a strong corrosive solid (pH > 13.0) with mainly skin and eye contact concerns. It is found as white or yellow lumps, flakes, rods, sticks, or pellets and in aqueous solutions. Inhalation exposures can be a concern if it gets airborne
Sodium Naphthenate	Etching, anodizing	Sodium naphthenate is a corrosive solid with mainly skin and eye contact concerns. It has a low vapor pressure and solubility in water and can be inhaled as an aerosol
Particulate matter	Surface prep, maintenance, welding, general activities, etc.	Particle matter has many sizes, shapes, and origins. It seems that those particles lesser than 2.5 μm have the most detrimental impact on human health. Inhalation of respirable particles can cause severe fibrosis and chronic manifestations such as silicosis
Polymer adhesives	Adhesive application	Exposures to airborne vapors from adhesives can lead to dizziness and headaches in those exposed. Many of the glues dry on contact and can negatively impact the skin and eyes
Heavy metal fumes and oxides	Welding and soldering	Chronic exposures to the various heavy metals can cause severe central nervous system malfunctions. Metal fumes have been linked to metal fume fever, with some metals such as cadmium and nickel classified as probable or known human carcinogens
Fluoropolymers	Surface coatings	Recent studies involving fluoropolymers support a linkage to cancer
Fluorides	Welding and soldering	Significant exposures to fluorides can lead to fluorosis, a severe condition that results in bone and enamel embrittlement
Acetylene	Welding	Acetylene is a very explosive gas that can also be a simple asphyxiant in high enough concentrations
Various aliphatic hydrocarbons	Coatings, adhesives	Dermal exposures to aliphatic hydrocarbons can lead to dermatitis. Hexane is the biggest airborne concern, however, most of those in this chemical group have relatively low toxicity. These are typically very flammable liquids

(continued)

Table 10.1 (continued)

Stressors	Source	Properties and toxicity characteristics
Various aromatic hydrocarbons	Coatings, adhesives	Dermal exposures to aromatic hydrocarbons such as benzene, xylene, and toluene can dry out the skin and cause dermatitis. Benzene is a know carcinogen (blood cancer) and high concentrations can negatively impact the CNS and respiratory tract
Heat stress	Maintenance, some production	Heat stress can be an issue when personal protective equipment is being worn or when various hot working operations are being conducted
Noise	Maintenance, some production areas	Unhealthy levels of noise exposures are typically considered to be in excess of an average of 85 dB for 8 h or more in duration. Hearing protection is mandated at 85 or 90 dB

The major manufacturing processes found in the biomedical industry that are related to this discussion can be generalized to the following categories:

1. Sterilization.
2. Cleaning, etching, and surface preparation.
3. Adhesive application.
4. Coating application.
5. Drilling, grinding, cutting, and other light production machining.
6. Welding and soldering.
7. General maintenance activities.
8. Laboratory research and testing.

10.3 Sterilization

Sterilization activities in the biomedical device industry are required by the European Union (EU) and the United States Federal Department of Agriculture (USFDA) and validation and routine control procedures are outlined in such documents as Association for the Advancement for Medical Instrumentation (AAMI)/International Organization for Standardization (ISO) 11135 for ethylene oxide sterilization and AAMI/ISO 11137 for radiation sterilization. There are literally dozens of ways to sterilize biomedical devices and new techniques are currently being developed and tested in research labs throughout the world. However, the most common methods of sterilization at this time are with ethylene oxide, gamma

rays, and electron beam radiation. The following paragraphs provide an overview of each of these as well as a few of the lesser used techniques (i.e., ozone, vapor phase hydrogen peroxide, plasma, microwave, and steam) and the associated health effects that could be realized if overexposed.

10.3.1 Ethylene Oxide Sterilization

Ethylene oxide (EtO) is widely used as a sterilizing agent in the biomedical device industry, due primarily to its potency in destroying pathogens and material compatibility characteristics. It is estimated that nearly one-half of all medical devices produced are currently sterilized by EtO. EtO kills microbes by alkylation. Alkylation is the process by which EtO takes the place of the hydrogen atoms on molecules needed to sustain life. With enough time and concentration, this proves lethal to all of the microbial life that is present on the device.

Conventional wisdom would lead one to believe that if EtO is toxic to microbes, it would also likely be a human toxin. This is certainly the case. Ethylene oxide is a colorless gas at room temperature, with a flash point of below 0 °F and a flammability range of 3–100 vol.% in air. It has an ether-like odor and is considered a regulatory concern primarily due to its flammability and/or explosivity as well as its acute and chronic human toxicity characteristics. It is classified as a probable human carcinogen (A2), with a United States Occupational Safety and Health Administration (USOSHA) permissible exposure limit (PEL) of 1 ppm averaged over an 8-h shift and 5 ppm as a 15-min excursion.

The EtO sterilization process typically includes five steps: conditioning, sterilization, evacuation, air wash, and aeration. While human exposures to EtO during any of these stages is normally unlikely, there is always a chance of a process system leak or an operator making a deviation from the normal protocol or standard operating procedures. In addition, during setup and changeover periods, there is always a possibility of unsafe airborne exposures to personnel of this highly toxic gas. An illustration showing the precarious safety concerns involving the use of the EtO sterilization process is shown in Fig. 10.2.

10.3.2 Gamma Ray Sterilization

Gamma rays, typically emitted from a source of cobalt-60 (Co-60), are also a common means for sterilizing biomedical devices. In fact, it is estimated that nearly 50 % of all single-use medical supplies (e.g., syringes, catheters, IV sets) have been sterilized by this technique. The gamma radiation emitted by the Co-60 source destroys any residual microbe by attacking the DNA of the molecules.

Fig. 10.2 Illustration of ethylene oxide (EtO) leaking from a sterilization chamber (*Permission* Japanese Advanced Information Center for Safety and Health)

The main advantages using ionizing radiation to sterilize include optimal device penetration, process repeatability, and no product residues. And, from a health and safety standpoint, the typical, properly shielded cobalt-60 source has just enough energy to kill the microorganism of concern, but yet does not have enough energy to impart any harmful radioactivity to the surrounding workers or the environment. While the threat to overexposure to gamma radiation may be minimal to the biomedical device production worker, careful attention must be still taken to minimize the impact of any exposures and to always follow proper as low as reasonably achievable (ALARA) guidelines.

Cobalt-60 is solid substance that has a radioactive half-life of 5.27 years and decays by a beta/gamma scheme. Since it is gamma emitter, external exposures to large sources of this radionuclide can cause severe skin burns, acute radiation syndrome, and death. While careful safeguards have been put into place to prevent any worker exposures to ionizing radiation in the biomedical device industry, accidental emergency releases are always possible. Unlike EtO, the main regulatory responsibility for gamma radiation in the United States is not OSHA or the Environmental Protection Agency (USEPA) but the Nuclear Regulatory Commission (NRC). The acceptable annual dose limit for a nonnuclear energy worker in the U.S. is 1 mSv (100 mrem) dose equivalent while nuclear energy workers are allowed 50 mSv (5 rem) per year, with 100 mSv (10 rem) allowed accumulated exposure over a five-year period. The USOSHA PEL is currently set at 0.1 mg/m^3 for the nonradioactive component.

10.3.3 Electron Beam Radiation Sterilization

Another growing means for sterilization in the biomedical device manufacturing industry is by an electron beam radiation technique. Like gamma ray sterilization, this technique employs a beam of ionizing radiation that alters the DNA of the microorganism it attacks. Commercial electron beam accelerators range in energy from about 3–12 meV (million electron volts) and usually operate at only one energy level. The main advantages to this technique include shorter product exposure times, higher production rates, and less material oxidation.

One key aspect of both gamma ray and electron beam sterilization is the concept of dosimetric release. Dosimetric release is a procedure accepted by the USFDA and detailed in ANSI/AAMI/ISO 11137-1994. Dosimetric release is based upon readings from dosimeters placed on devices during processing. Verification of the minimum and maximum doses applied provides the mechanism for release and shipment. As will be discussed later in the monitoring section of the chapter, radiation dosimeters also provide useful information and control for worker health and safety biomedical device industry as well.

The same dose equivalent standards are used for electron beam sterilization as those in effect for the gamma ray techniques. USOSHA standards for ionizing radiation used in general industry can be found in 29 CFR 1910.1096. The EU regulations for ionizing radiation were set forth in the Council Directive 96/29/EURATOM of 13 May 1996.

10.3.4 Other Sterilization Techniques

While less common than those already addressed, device sterilization methods using ozone gas steam, plasma, vapor phase hydrogen peroxide, and microwave radiation have also been piloted in the laboratory and field settings. While proper safety controls have been normally put into place during circumstances employing one or more of these techniques, there is always a chance of an accidental release or a deviation from normal protocol that could result in an overexposure to either a single individual employee or a group of workers.

Ozone is a toxin that is a significant acute respiratory stressor. The immediately dangerous to life and health (IDLH) guideline for ozone is set a 5 ppm and USOSHA and ACGIH both set the occupational exposure limit for an 8-h shift at 0.1 ppm. In addition, USEPA regulates ozone emission to the environment and considers it to be one of the six National Ambient Air Quality Standards (or criteria pollutants), and the EU sets the ambient air standard for ozone at 0.12 mg/m^3. Hydrogen peroxide vapors are also considered toxic and most be controlled. The target organs for vapor phase hydrogen peroxide would be the eyes, skin, and respiratory tract, with a USOSHA PEL of 1 ppm established. Guidelines for non-ionizing radiation, including microwaves, are provided based upon various

frequency ranges and are delimited in such sources as ACGIH's TLVs for Chemical Substances and BEIs and the ICNIRP's General Approach to Protection Against Non-Ionizing Radiation. Regulations and guidelines for plasma processes are in the current research and findings stage and are not well established for worker health and safety.

10.4 Cleaning, Etching, and Surface Preparation

The effectiveness of the surface cleaning and preparation processes followed both during the manufacturing of the device as well as with the finished product will significantly impact the ultimate reliability and overall quality of the device in the field. For example, it is imperative that electronic medical devices have a clean surface in order to ensure good bonding and coating. In addition, compromised surface preparation can lead to the existence of chemical contaminants that can cause corrosion, and the non-removal of particulate matter may result in an undesirable electrical conductance path and short circuits.

Some of the most common cleaning processes used in biomedical device manufacturing include methanol, ethanol, isopropanol, chlorinated hydrocarbon solvents, fluorinated hydrocarbon solvents, acetone, and deionized water. Common etching or anodizing agents include sulfuric acid, phosphoric acid, chromic acid, sodium naphthenate, and potassium hydroxide. Mechanical surface preparations that many times cause unwanted particle residues and potential airborne contamination include surface and scuff sanding as well as grit blasting. Table 10.2 provides the target organs for each of these potential stressors and the approximate vapor hazard ratio (VHR), based upon the worldwide average occupational exposure limits (OELs), for some of the more commonly used solvents. The VHR, or vapor hazard index (VHI) as it is sometimes called, is found as follows:

$$\text{VHR (or VHI)} = C_{vp}/\text{OEL} \tag{10.1}$$

where C_{vp} = concentration at the saturation vapor pressure in ppm and OEL = occupational exposure limit in ppm.

The VHR provides a convenient means for comparing the potential exposure impact to various solvents. Essentially, the VHR describes by how many times a saturated vapor volume must be diluted by this same volume of air so that the OEL is not exceeded.

10.4.1 Alcohols

There are two types of surface contamination that are produced during the production of biomedical devices: polar and nonpolar. The majority of polar

Table 10.2 Target organs and vapor hazard ratio (VHR) for selected chemical stressors

Chemical stressor	Target organs [25]	Vapor hazard ratio
Isopropanol	Eyes, skin, and respiratory system	100
Methanol	Eyes, skin, respiratory system, and central nervous system (CNS)	700
Ethanol	Eyes, skin, respiratory system, CNS, liver, blood, and reproductive system	75
Trichloroethylene	Eyes, skin, respiratory system, heart, CNS, liver, and kidney	1750
1,1,1 Trichloroethane	Eyes, skin, CNS, cardiovascular system, and liver	800
Perchloroethylene	Eyes, skin, respiratory system, liver, kidneys, and CNS	550
Acetone	Eyes, skin, respiratory system, and CNS	450
Potassium hydroxide	Eyes, skin, and respiratory system	–
Particulates (not otherwise regulation)	Eyes, skin, and respiratory system	–
Sulfuric acid	Eyes, skin, respiratory system, and teeth	–
Phosphoric acid	Eyes, skin, and respiratory system	–
Chromic acid	Blood, respiratory system, liver, kidneys, eyes, and skin	–

contaminants found on biomedical devices during manufacturing include various inorganic compounds, with the source being primarily from flux activators or finger salts. Since alcohol is a polar compound and by taking into consideration the rule that "likes dissolve likes," the alcohols are many times used to remove polar contamination from the surface of biomedical devices. It has been a widely accepted premise that alcohol is the most effective and economical solvent available for removing ionic residues from biomedical devices, and thus, its use has grown concurrently with the increases in market demand over the years.

Employee exposure to airborne concentrations of alcohol can be irritating to the eyes, nose, and respiratory tract, with significant doses having been linked to manifestations of the central nervous system, liver, blood, and reproductive system. Obviously, efforts should be made to limit the exposure of alcohols to the employee's skin due to its solvent nature. Methanol is considered to be more toxic than both ethanol and isopropanol and its use should be limited under most circumstances.

However, as might be expected, methanol is deemed superior to the other two alcohols in the removal of significant ionic surface residues. Typical OELs have been set at 1000 ppm for ethanol, 200 ppm for methanol, and 400 ppm for isopropanol. The alcohols are not currently considered to be either a known or probable human carcinogen by any regulatory authority.

10.4.2 Chlorinated and Fluorinated Hydrocarbons

Chlorinated and fluorinated hydrocarbons are used as nonpolar solvents in the industry. Nonpolar solvents such as methyl chloroform (1,1,1-TCA), trichloroethylene (TCE), and tetrachloroethylene (Perk) have been traditionally used because of their outstanding capabilities of removing oils, greases, rosin flux, etc., during the surface preparation process. However, requirements set forth by occupational and environmental regulatory authorities regarding these highly toxic and flammable compounds had increased the popularity of fluorinated solvents, chlorofluorohydrocarbons (CFCs), and various blends throughout the 1970s and 1980s. Still, with even more recent regulations, biomedical device producers have been dissuaded from using such fluorinated solvents such as trichlorotrifluoroethane. For example, Freon^{TM}, once a widely used industrial fluorochlorohydrocarbon, was identified as a major precursor contaminant that contributed significantly to stratospheric ozone depletion in the atmosphere, and thus, its use has been all but completely eliminated in most modern countries. As a matter of fact, the further production of this CFC in the U.S. was banned completely in 1996.

Today, the majority of biomedical device manufacturers use one or more of the following classes of nonpolar solvents in the production process to remove primarily oils and grease from the devices:

1. Hydrofluorocarbons (HFCs).
2. Hydrofluoroethers (HFEs).
3. Perfluorocarbons (PFCs) or perfluoropolyethers (PFEs).
4. Chlorinated hydrocarbons (e.g., TCE, Perk, 1,1,1-TCA).
5. *trans*-1,2-dichloroethylene.
6. Brominated solvents.
7. Hydrocarbons and oxygenated solvents.

The current trend for cleaning nonpolar compounds from the surface of medical devices appears to be moving away from the traditional chlorinated hydrocarbons and more toward HFCs and HFEs. These compounds are considered relatively benign in toxicity to animals and humans, however, are considered to be significant stressors to the environment, potentially enhancing global warming and greenhouse gas effects with a warming potential as much as five orders of magnitude greater than carbon dioxide gas.

As was mentioned previously, the chlorinated hydrocarbons are very closely scrutinized by both the environmental and occupational regulatory bodies due to both toxicity and flammability detriments. As would be expected, this family of chemicals affects the skin by removing all natural oils and potentially leading to severe dermatitis conditions. They are heavier than water and vapor pressures that range from 14 to 100 mmHg. The relative toxicity of the main three chemicals in the class (TCE, Perk, and 1,1,1-TCA) varies based on the concentration and the extent of the exposure (i.e., acute or chronic).

TCE is a colorless liquid with a chloroform-like odor, with chemical incompatibilities and reactivity to strong caustics and chemically active metals. The USOSHA PEL established for TCE is 100 ppm and has been linked to causing both liver and kidney tumors in animals. Along with the liver and kidneys, the main target organs include the respiratory tract and the central nervous system. The flash point for TCE is 160 °F, which classifies it as a combustible liquid.

Perk is a colorless liquid with a mild, chloroform-like odor and considered to be a strong oxidizer and incompatible with chemically active metals. It has an USOSHA PEL equal to 100 ppm and targets the liver, kidneys, respiratory tract, and central nervous system. Perk has been classified as animal carcinogen by causing liver tumors in test subject. While it is not classified as either a flammable or combustible liquid, it will decompose in the event of a fire to significant concentrations of hydrochloric acid (a corrosive vapor) and phosgene (a highly toxic gas).

Like both TCE and Perk, methyl chloroform (or 1,1,1-TCA) is a colorless liquid with a mild, chloroform-like odor, with incompatibilities to chemically active metals. It will also react with strong oxidizers, caustics, and water. 1,1,1-TCA targets the respiratory tract, skin, central nervous system, and liver but has not been linked to causing cancer in humans or animals. The EU OEL has been established for the stressor at 100 ppm and it is classified as a combustible liquid.

The majority of the HFCs, HFEs, PFCs, and PFEs do not have any occupational exposure established at this time. This is both due to the fact that these chemicals have been determined to be primarily nontoxic as well as their increased usage is a rather recent phenomenon, and thus, have not warranted up to this point much concern to the health and safety community. However, their collective effect on the environment, and particularly, on global warming impacts will undoubtedly be an issue to contend with as emissions are expected to only increase in the future. Figure 10.3 provides an example of a cell washer for in-line process degreasing.

10.4.3 Acids and Alkalis

The primary acids used to surface etch biomedical devices include chromic, phosphoric, nitric, and sulfuric acid. Polymer surfaces are typically etched with a strong oxidizing agent such as chromic acid. The chromic acid provides the means to oxidize the substrate surface, resulting in an optimal surface for further treatments such as adding coatings or adhesives. Chromic, along with sulfuric and phosphoric acid, are many times employed as an etching or anodizing agent for metals such as titanium, stainless steel, and nickel. The surface preparation for fluoropolymers (or materials to be coated with fluoropolymers) is a difficult task. Treatments that have been effectively used in the industry include sodium naphthenate and potassium hydroxide etches as well as flame treatments.

Due to its highly acute and chronic toxicity, airborne and dermal chromic acid exposures to workers in the biomedical device industry must be of an utmost

Fig. 10.3 Vapor degreaser used in biomedical device manufacturing (*Permission* Ramco, Inc.)

concern. Chromic acid has been linked to both human septum and lung cancer and is currently classified as a known human carcinogen. Since it is a strong acid, its corrosive nature can severely affect the respiratory tract as well as the skin of any exposed worker(s). Chromic acid is normally found in a red colored, aqueous solution in industry and is reactive with most readily oxidizable materials. The USOSHA ceiling exposure limit has been established for this chemical at 0.1 mg/m^3.

While the other acids typically used as etching and anodizing agents in biomedical device manufacturing are not considered known human carcinogens, they do exhibit comparable corrosivity. Thus, each of these agents targets the respiratory tract and the skin, with the possibility of severe burns being a reality upon even minimal exposure. The occupational limits established are 1 mg/m^3 for sulfuric, 5 mg/m^3 for nitric, and 1 mg/m^3 for phosphoric. Substance incompatibilities and reactivities include caustics (phosphoric), organic materials, metals, and even water (sulfuric and nitric).

Sodium naphthenate and potassium hydroxide are strong caustic etching agents used effectively on some polymer surfaces. Like their acid counterparts, they are very corrosive materials and target primarily the skin, eyes, and respiratory tract. They are not currently classified as probable human carcinogens and are typically found in industry in an aqueous solution. There is currently no USOSHA PEL or

EU OEL established for either of these agents. However, potassium hydroxide has a recommended TLV ceiling recommended by the ACGIH of 2 mg/m^3. These substances are reactive with acids, water, and metals.

10.4.4 Acetone

Acetone is ubiquitous ketone solution used as a general purpose cleaning solvent in many industries. Its use varies in the biomedical device industry, with toxicity and exposure concerns typically minimal. The established EU OEL for this agent is 500 ppm, with incompatibilities existing between it and acids and oxidizers.

10.4.5 Particulate Matter

Surface preparations such as sanding and blasting can cause the generation of particles and aerosols of various sizes, constituents, and morphology. Not only can their existence potentially compromise the quality and integrity of the completed device, but it can also be troublesome to those workers exposed to potential unhealthy airborne concentrations in their respective breathing zones. Depending primarily on the particle type and shape, there exists a myriad of factors that can be used to help determine the potential for negative impacts on employee health and well-being, both acute and chronic in nature.

Particulate matter is typically classified by aerodynamic diameters in the micron or submicron size ranges. Traditionally, any particles or aerosols of sizes less than 10 μm are considered to be respirable. Particulate matter greater than 10 μm in diameter is considered essentially benign because of the assumption that it will be eventually removed by other body defenses such as nose hair, cilia, and mucus before it reaches the inner respiratory tract. Due primarily to sufficient research on the exponential growth in adverse effects on human health from exposures to particulate matter in the 1–2.5 μm range, the USEPA has recently introduced a new tighter standard for ambient air exposures of this stressor.

Long-term exposures to some types of particulate matter found in the workplace have resulted in various forms of fibroses and pneumoconiosis (“dusty lung”) in otherwise healthy workers. Free silica from chronic exposures to sand has resulted in a chronic condition known as silicosis and exposures to airborne beryllium dust has initiated a manifestation known as berylliosis in those exposed. Recently, concerns have been expressed about the increasing exposures of workers in the biomedical device industry that may come into contact with airborne particles in the nanometer range. The human health effects from exposures to particles in the submicron ranges are not well understood at this time. Currently, USEPA considers

particulate matter as one of the six criteria pollutants and OELs in Spain have been set at 3 mg/m^3 for the respirable fraction. More stringent restrictions have been set for some particulate matter types that have been linked to chronic conditions such as fibrosis and cancer.

10.4.6 Spent Solvents

Whether it is a benign substance like deionized water or a toxic substance such as chromic acid, once the agent has been used in the production process the resulting waste must be dealt with by following local and/or federal guidelines. The USEPA mandates a normal protocol to follow per RCRA and CERCLA provisions for hazardous waste generation and transport based upon the quantity generated. In the U.S., State-run EPA programs handle the management of wastes generated from "cradle to the grave." Depending on the jurisdiction, other countries, territories, provinces, and local governing groups may have different protocols to follow in order to effectively deal with their respective spent surface preparation agents.

10.4.7 The Future of Surface Preparation Techniques

As have been previously discussed, most of the conventional cleaning methods and surface preparations have employed wet chemical techniques. However, the current trend seems to be moving away from chemical treatments and toward such modern techniques as cold plasma, corona discharge, and laser cleaning.

Corona discharge is a process by which high voltage electricity is discharged into an airstream, producing large concentrations of ozone to the oxidize the device surface while plasma cleaning employs an ionized, equally charged oxygen gas stream to chip apart the surface contaminants. Laser cleaning is still yet another recent technology used in the industry. Lasers are, of course, a concentrated form of light energy and are considered nonionizing in nature. The employee exposure concerns of various lasers will be covered in greater detail later on in this section.

Essentially, the health and safety concerns for workers in this environment have been switched from chemical stressors, for the most part, to physical stressors such as electricity, electrical/magnetic fields, and nonionizing radiation. Figure 10.4 provides an example of the plasma cleaning device that might be implemented in the biomedical device industry while Fig. 10.5 shows a laser cleaning method in use.

Fig. 10.4 Plasma cleaning apparatus (*Permission* UCP Processing Ltd.)

Fig. 10.5 Laser cleaning operation (*Permission* Adapt Laser Systems)

10.5 Adhesive Applications

Many of the previously discussed surface preparation techniques were completed in order to effectively and efficiently apply adhesives to various device substrates. While various mechanical fasteners as well as welding, brazing, and soldering techniques can be used to join many biomedical device materials together, there are still other materials, such as thermoplastic and thermosetting polymers, that are considered incompatible to these types of joining processes. Adhesive bonding conditions include:

1. Bonding of dissimilar materials.
2. Joining to promote optimal stress distributions or impact resistance.
3. Joining of very thin materials.
4. Joining of outsourced subassemblies.
5. Bonding for mechanical joint augmentation.

The most common adhesives used in biomedical device manufacturing include urethanes, cyanoacrylates, acrylics, epoxies, and silicones. Collectively, the adhesives primarily attack the skin, eyes, and respiratory tract. While sometimes quite odiferous, their vapor pressures are usually very low and most do not contain ingredients that are carcinogenic. Some of adhesives have components that are recognized as chemical sensitizers, and exothermic polymerization is always a concern if they should ever come into contact with incompatible materials. OELs have not been established specifically for any of these polymer groups but yet exposure standards have been determined for any hazardous ingredients that might be used as a product component.

The commercially available urethanes have a variety of ingredients; however, common to most products will be less than 5 % isocyanates and 5 % naptha. They are not carcinogenic but have been classified as chemical sensitizers, and overexposures can cause severe respiratory tract ailments including pulmonary edema and bronchitis. In case of a fire, urethane-based decomposition products of concern include carbon monoxide, nitrogen oxides, hydrochloric acid, and trace amount of hydrogen cyanide. Cyanoacrylates (or the "superglues") are eye and mucous membrane irritants and tissue bonders. Their vapors are lachrymatory and, if decomposed during a fire, produce a dense, choking smoke. They are incompatible with water, alcohols, and amines, sometimes producing a significant exothermic polymerization event.

The majority of the acrylic adhesive formulations used in biomedical device manufacturing can cause skin dermatitis as well as allergic reactions for those sensitive individuals. At high processing temperatures, it is possible for some employees exposed to acrylic adhesives to exhibit flu-like conditions known as "polymer flu." As for the epoxies, the main health and safety concerns include skin, eye, and respiratory tract irritation and chemical sensitization while silicone formulations being irritants which many times have a major toxic aliphatic or aromatic hydrocarbon component such as n-heptane or xylenes.

10.6 Coating Applications

The most common coatings applied to biomedical devices are urethane-based, fluoropolymers, or polyimide laminates. The techniques with a proven track record for device surface coating vary in sophistication and applicability. Depending on the type of material, as well as product size and configuration, one technique may prove to be more effective than another in ensuring coating quality and repeatability. The required coating thickness is also a major factor in the decision process. In any case, the coating techniques employed have the potential of producing aerosols of varying sizes and shapes of which significant employee exposures could be realized.

Since the majority of the coatings are polymer-based, many of the health and safety concerns with coatings are shared with the common adhesives that were discussed in the previous paragraphs. However, what differs significantly is the potential for toxic aerosols to build up to a significant concentration in the employee breathing zone during the specific coating application.

Like adhesives, there are certainly concerns for employee skin and mucous membrane exposures to the common coatings applied. Additionally, they can be chemical sensitizers and have other toxic ingredients in their formulation. However, what differs substantially between the two involves the potential for exposures to harmful levels of particulate matter and toxic metal pigments that can be inhaled by the associated production worker. Heavy metals linked to human cancer, such as chromium and cadmium, are used to provide color to many industrial coatings. Another major health concern related to biomedical device coating applications involves fluoropolymers such as Teflon®, which is a very common device coating due to its biocompatibility. Recent studies have linked fluoropolymers to increased incidences of cancer and teratogenesis for those exposed to a particular raw material, perfluorooctanoic acid (PFOA), used in its production, yet claims are still very controversial.

10.7 Drilling, Grinding, Cutting, and Machining

Drilling, grinding, and other light machining operations produce fine and course particulate matter, as well as significant concentrations of aerosols from the use of cutting oils and fluids. These particles range from just a few nanometers to well over 10 μm in sizes. Exposures to particles from the near micron range to around 10 μm have resulted in various lung ailments such as bronchitis, emphysema, anthracosis, and silicosis. The kinetics of these particles is pretty well understood and related health effects data is rather complete. However, the effects on human health of particles in the ultrafine particle size region of 100 nm, or less, is not well understood. As a matter of fact, the particles generated in this region behave more like gases than they do particles with regard to motion and kinetics.

While recent efforts have been directed toward removing from manufacturing many oils and cutting fluids with toxic ingredients and replacing them with human and environmentally friendly alternatives, there are still a vast amount of these necessary lubricants available for use in the biomedical industry. While there are an increasing number of aqueous-based fluids becoming commercially available, many of these lubricants are still petroleum-based, with the associated ill effects related to overexposures to aliphatic and aromatic hydrocarbons still a daunting reality.

Traditional cutting techniques also produce particulate matter and aerosols in the micron and submicron ranges. However, advanced techniques, such as laser cutting, have been piloted in the field and gaining popularity.

10.7.1 Laser Cutting

Lasers are used for cutting in many manufacturing industries and the biomedical industry is no exception. Additionally, lasers can be found in welding, sealing, and coating operations as well as in medical micromachinery, lab instrumentation, and in the final device itself. Thus, a discussion on the environmental, health and safety issues regarding its proper use is imperative.

Lasers and laser equipment may be potentially dangerous to eyes and skin of the employee. The relative degree of risk depends on the type of beam, the power frequency, beam divergence, beam intensity, and duration of exposure. The eye is the most susceptible to damage, with retina burns resulting in the possibility of total blindness. Given certain levels and wavelengths of laser radiation, coupled with adequate duration, skin reddening, swelling, blistering, and even charring can occur.

Exposure guidelines are based on the characteristics of the type of laser and are expressed as maximum permissible exposure or MPE. The guidelines most often used involving the safe use of lasers has been published by ANSI, ACGIH, ICNIRP, and IEC [20]. Traditionally, the USFDA has used a laser classification scheme using four roman numbers I, II, IIIa, IIIb, and IV. The Class I laser was considered the most benign and eye safe, whereas the Class IV was the most dangerous for eye and skin exposures. However, the USFDA and ANSI and other industrialized countries are currently in the process of adopting, if they have not already done so, the International Electrotechnical Commission standard, IEC 60825-1. Table 10.3 summarizes the laser classes, with power, duration, and relative hazards provided. It should be pointed out that the “M” designation after the class is for “magnification” while the “R” is for “reduced requirements.”

Table 10.3 Laser classification scheme and characteristics

Laser class (IEC)	Laser class (old US FDA)	Allowable power (W)	Emission duration (s)	Hazard description
1	I	0.39E−60	>10,000	Not a known eye or skin hazard
1M	I	0.39E−60	>10,000	Eye safe with no optical aids
2	II	<1.0E−3	>0.25	Potential eye hazard for chronic viewing
2M	IIIa (low irradiance)	<5.0E−3	>3.8E−4	Potential eye hazard for chronic viewing and may be so with optical aids
3R	IIIa (high irradiance)	<5.0E−3	>3.8E−4	Marginal hazard for intrabeam viewing
3B	IIIb	<5.0E−1	>0.25	Known intrabeam viewing hazard
4	IV	>0.5	NA	Known eye and skin hazard

10.8 Welding and Soldering

Welding and soldering activities can sometimes pose an exposure risk for those not wearing the proper PPE and using adequate ventilation control. The main hazards associated with soldering include skin burns and airborne contaminant exposures, primarily from the solder, soldering flux, and any surface pre- or post-cleaning solutions. The primary welding hazards include exposures of air contaminants from sources such as the base material, welding rod, welding flux, and inerting gases. Potential physical hazards encountered during the process include nonionizing radiation, heat stress, and electricity.

Traditionally, the biggest concern for occupational solderers was the likely exposures to significant concentrations of lead in the air. Lead is an extremely acute and chronic toxin linked to a myriad of potential manifestations. Fortunately, most of the lead-based solder has been removed from manufacturing in the developed countries. However, exposures to the fumes generated from solders even without lead should be kept to a minimum. Many formulations of solder flux provide a substantial potential for unhealthy doses of fluorides. Additionally, normally low vapor pressure cleaners used during the process can become heated and emit higher than normal levels of gases and vapors into the breathing zone of the biomedical manufacturing worker.

Depending on the type of welding and the level of engineering controls implemented, a wide range of contaminant exposures can be realized. Airborne levels of ozone, nitrogen oxides, and fluorides are normally troublesome and heavy metal fumes of varying types and concentrations may also be of paramount concern. Typical metal fumes and oxides include iron, zinc, copper, cadmium, aluminum, magnesium, nickel, chromium, and manganese. The majority of these heavy metals are considered to be chronic toxins, targeting the central nervous system and lungs, and several of these toxins are either known or probable human

carcinogens. Exposures to heavy metal fumes have resulted in a condition known as "metal fume fever."

Workers must be shielded from the nonionizing radiation exposures possible from some welding processes. Harmful, high-frequency ultraviolet radiation has caused a manifestation known as "welder's flash" in some welders and vicinity workers. The symptoms of this condition include visual impairment, the feeling of sand or grit in the eye, and a severe headache with malaise. Additionally, welding should never be conducted near chlorinated cleaning solvents due to the potential of sparks initiating dangerous phosgene gas accumulations. Of course, burns and electrical shock are additional possible physical stressors of which the biomedical device production welder may become exposed.

10.9 General Maintenance Activities

There is a plethora of general maintenance activities possible at each respective biomedical device manufacturing facility, with many of these activities such as welding, drilling, cleaning, etc., having already been covered in the preceding paragraphs. However, the severity and the distinct nature of some of these tasks have merited a separate discussion.

Maintenance activities differ from those in normal production in potentially several ways. For one, the maintenance activities are many times not planned some time in advance before the actual event occurs. This means that exposures to non-expecting workers may be intensified. Second, maintenance activities that create potential environmental stressors are normally completed in a shorter duration, with higher activity levels and robustness. Thus, the potential for exposures is once again enhanced. Finally, maintenance and set-up activities many times lead to process control changes that may, after completion, result in unusual and significant short-term exposures to physical and chemical agents by area production workers.

Machining activities accomplished by maintenance workers sometimes produce noise levels that exceed the occupational limits and heat stress can also be of concern. Increased maintenance activities can produce airborne contaminants such as particulate matter/fibers and noxious gases, vapors, and fumes. Obviously, many the activities of facility maintenance personnel can produce unsafe slip, trips, and falls as well as electrical wiring and pneumatic/hydraulic plumbing concerns for all associated workers.

10.10 Laboratory Research and Testing

The research and quality control laboratories in the biomedical device manufacturing industry provide a rather unique environment for employee exposures. Lab technicians are typically working with a wide range of instruments with a variety of

operational characteristics and potential to exposures from various biological, chemical, and physical stressors. Instruments found in the laboratory environment include, among others, sources such as X-rays, gamma ray, lasers, and some wet chemistry components that could be harmful if not properly controlled.

While concerns involving biological stressors are possible in any of the before mentioned areas or during certain previously discussed activities, the research and quality control laboratories are the places where pilot runs are conducted and final devices are tested for contamination. Experimental procedures might include such activities as biocompatibility testing, with uses of bloods and other body fluids common. Depending on the device, ISO clean room status may be desired at a certain level in the labs as well as on the production floor; thus, various testing for bacteria and fungal contamination may be required. While there are currently no occupational mandates for personal exposure to most biological agents, governmental agencies on the environment and food and drugs have set some standards for microbial contamination.

10.11 Environmental and Engineering Controls

Administrative actions, engineering controls, and PPE are considered as the three main approaches to controlling environmental emissions and employee exposures. The intent of this section is to elucidate the common environmental and engineering controls that could be implemented in the biomedical device manufacturing climate to help protect the employee and the environment. Any of the following implemented individually or in combination are viable engineering control techniques that could work in the biomedical device industry:

1. Substitution.
2. Process controls (continuous or automation).
3. Enclosure/isolation.
4. Process elimination.
5. Process change.
6. Ventilation controls (local exhaust or dilution).

While prevention is not included as one of the above environmental and engineering controls, it should always be the first consideration taken when there is the potential for employee exposure to chemical, biological, and/or physical stressors. In essence, the control assessment should always begin with an evaluation of whether or not the situation that apparently requires control can just be totally prevented instead by some means.

Once the condition that has the potential to adversely impact human health or the environment has been recognized, then a proper controls implementation scheme should be followed. An effective protocol should be systematic and involve a series of steps taken to identify and characterize the hazard, exposure source, worker

involvement, and air movements, as well as identifying all alternatives, with the ultimate goal of implementing and testing/maintaining the best of these alternatives.

10.12 Substitution

Substitution is the process by which a more environmentally friendly substitute is made for a known hazardous substance, process, or piece of equipment. For example, it has been argued that the plasma cleaning process is superior to organic solvent cleaning when it comes to the potential for harmful exposures and negative human health impacts. Another example of substitution in the biomedical device industry might involve the use of lab instruments that employ sensors which work on the principal of nonionizing radiation instead of their predecessors, either gamma or X-ray radiation, which have more damaging characteristics on the cellular or tissue levels.

One must be careful that the substitution made does not result in such an inferior replacement to the original product, process, or equipment that it might compromise the quality and integrity of the final device. An example of this undesirable event might include a process/material change by a company from a nonpolar solvent to the use of a surfactant and water to clean a particular medical device, resulting in ineffective removal of contamination. Economics can also limit the benefits of substitution. For instance, while many biomedical companies have realized successes by substituting automated processes for those that were once somewhat labor intensive, others have failed to accomplish this goal. Quite frequently, this is due to the significant up-front costs associated with automation and the inability of the company to reach any economies of scale because of their size.

10.13 Process Controls

There are times when the current process controls need to be evaluated for their merit. As a general rule, intermittent or batch processes are typically considered to be more hazardous than those that are more continuous in nature. In essence, the automated line takes some of the human component out of the process, and thus, typically also reduces the potential for human exposures. However, as was discussed in the previous subsection, automated processes can have their own set of downfalls and shortcomings.

10.14 Enclosure/Isolation

The use of enclosures and isolation techniques will be found in almost all biomedical device manufacturing facilities. The sophistication of these control alternatives varies widely, with the intent to separate the potentially exposed employee from the hazardous event. A very good example of a type of enclosure being used in the industry is the glovebox setup. These units are found in a myriad of operations to protect the worker from the workpiece and process during applications of various physical, biological, and chemical stressors. For example, a glovebox apparatus might be used in the laboratory of a facility to test a particular medical device's biocompatibility or potential for rapid oxidation when coming in contact with a substance. Another common enclosure used in the industry is the particle and fume hood, typically required to keep microbial and particle concentrations at levels to meet or exceed ISO clean room standards.

The principle of isolation can be by either space or time. The use of walls or complete rooms to separate employees from a potential hazard, of course, is an example of the former. In contrast, conducting a special cleaning operation to remediate facility mold contamination on either the weekend or overnight would be an excellent example of the latter. Table 10.4 provides some examples of potential enclosure or isolation techniques that could be used effectively in biomedical device manufacturing.

Table 10.4 Enclosure/isolation techniques used in biomedical device manufacturing

Type of medical device or process	Enclosure/isolation technique
Co-60 use in teletherapy	Operator kept at safe distance from source and lead shielding from gamma radiation
Irradiator for instrument sterilization	Lead shielding with operator in a secured room
Ethylene oxide use for device sterilization	Specialized containment and time without employee in close proximity
Use of biological agents in the laboratory for testing	Glovebox with proper hazard classification characteristics
Radioactive iodine syringe preparation and assembly	Syringe shields and Plexiglass™ shielding for beta radiation during preparation
Acid etching of the substrate on devices and tools	Special acid enclosure and fume hood use
Controlled storage of chemicals	A regulatory-approved chemical storage cabinet
Automated production line	Clear acrylic safety shields to protect worker from moving parts and potential stressors

10.15 Process Change or Elimination

Sometimes it is possible to change a process to make it less hazardous to the employee. For instance, a surface coating application could be applied through a dipping process rather than one that requires spraying. This change could eliminate the majority of the coating aerosols from ever entering the breathing zone of the worker. Additionally, the dipping process should be considerably more manageable from the aspect of environmental control and regulatory affairs.

It is even possible that a process of concern could be completely eliminated. Given our coating application example, it might be possible to eliminate the coating operation or simply apply a much thinner layer of coating using isolation and an advanced nanotechnology technique. Fortunately, many studies in general industry show that process changes (or eliminations) made in order to increase hazard control have actually resulted in enhanced productivity, as well as an improvement in overall product quality.

10.16 Ventilation Controls

A discussion on environmental and engineering controls would not be complete without a significant effort being put on covering the proper design, development, and implementation of the site ventilation system(s). Without adequate ventilation, there would be, in many cases, no other alternative but to put workers on respirators to eliminate their exposure potential. This is an issue that most companies should try to avoid; mandating respirators for protection complicates production and regulatory matters and adds a significant cost to the company. Fortunately, the use of proper ventilation will eliminate the necessity for respirator use by most biomedical device production workers during their normal work-related activities.

There are two types of ventilation: dilution ventilation and local exhaust ventilation (LEV). Most facilities have both of types of ventilation, with additions and changes to these networks occurring at least periodically, if not frequently. The following paragraphs attempt to elucidate the benefits that can be realized in controlling the production environment with an optimally designed ventilation network.

10.16.1 Dilution Ventilation

Dilution ventilation, also known as general exhaust ventilation, controls the level of airborne stressors by removing the potentially contaminated air and replacing it with fresh dilution air before concentrations reach unhealthy levels. Under certain assumptions and constraints, the resulting equilibrium concentration of any airborne

contamination can be estimated as follows: C = E/Q, where C is the concentration, E is the emission rate, and Q is the ventilation rate.

Traditionally, ventilation experts have used the units of air changes per hour to express dilution ventilation exchange rates, and the notion of an "acceptable concentration" has been used to indicate a safe or comfortable level of exposure. Since a heavy reliance on adjacent sources of outdoor air for dilution exists, it is a must that this fresh air source has less contamination than what is realized on the production floor. Therefore, careful attention must be given to where air intakes are located to minimize the effects from outdoor sources of such ambient air contaminants as ozone, sulfur dioxide, particulate matter, and nitrogen dioxide. Also, during summer and wet months of the year, the dilution air could have significant levels of mold spores that could be brought into the biomedical device manufacturing environment.

Obviously, relying solely upon dilution ventilation to control airborne contaminants in the biomedical device manufacturing can be problematic. It is important to evaluate the potential for various stressor exposures and the relative toxicity of each of these. Inevitably, there will be some operations conducted during the development, testing, and manufacturing of a device that will not allow for engineering control only through dilution ventilation efforts. The use of dilution ventilation independently as a means for environmental and engineering control should be avoided if the following conditions exist:

1. The contaminants realized are highly toxic chemical, biological, or physical stressors.
2. The concentration levels are higher than established action levels or guidelines.
3. The emission rates are variable.
4. There exist only a few, high concentration discharge points for any contaminants.
5. The outdoor air might be suspect for various reasons.
6. The existing HVAC system is not adequate to provide "controllable" dilution air.
7. The worker's breathing zone is in close proximity to the emission point(s).

10.16.2 Local Exhaust Ventilation (LEV)

LEV is many times coupled with effective dilution ventilation to keep airborne contaminant levels down to acceptable concentrations. The LEV commonly employs the use of a properly dimensioned hood, plumbed with the necessary ductwork to a series of mechanical components, with its endpoint being an emissions stack. At a minimum, a properly designed LEV will have an air cleaning device capable of removing the stressor(s) of concern as well as a fan designed to drive the air of the given volume and desired flow rate. Figure 10.6 shows the components of a typical LEV system.

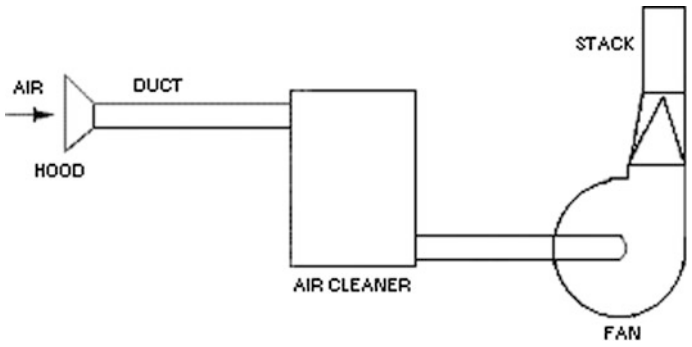

Fig. 10.6 Components of a local exhaust ventilation (LEV) system

The LEV is the primary means for removing gases, vapors, fumes, and particles from the immediate breathing zone of workers in the biomedical device manufacturing industry. It is called "local" exhaust ventilation because the physical location of the system is always in the immediate proximity of the point source emission. In essence, the face of the hood is placed close enough to the workpiece/process to allow for the suction created from the mechanical fan to capture the contaminant and remove it up and out of the associated ductwork. Consequently, it has been written that capturing and removing an airborne stressor, such as an acid etchant vapor or a hydrocarbon solvent vapor, at its source is the principle objective of LEV systems. Typical operations that merit the use of LEVs in the industry include solvent cleaning, acid etching, sterilization, welding, soldering, coating applications, adhesive applications, clean room/laboratory activities, and any other industry-specific operation that produces point source air emissions.

A variation on the traditional LEV, commonly found in the biomedical device industry, is the kind designed specifically to meet international clean room standards for particulate and microbial contamination. In reality, this type of environmental and engineering control is really a combination of both LEV and a form of isolation/enclosure. Unlike the traditional units, the clean room system not only protects the worker from any stressor that may be inside its hood, but also serves the dual purpose of protecting the device/process from any external stressors, which if allowed to be present, could contaminate or corrupt. Many of these types of control devices are of the ductless variety, with installed high efficiency particulate air (HEPA) or ultralow penetration air (ULPA) filters to effectively collect and remove any airborne particles.

The local exhaust hood, in a broad sense, is any suction opening that is intended to draw the contaminant into the control system. Generalized, the three basic types of hoods are capture, enclosing, and canopy. Two important parameters unique to the local exhaust hood are the face velocity and the capture velocity. The face velocity, quite simply, is the air velocity at the hood opening. In contrast, the capture velocity is the air speed at any point in front of the hood (or at the hood opening) required to overcome any opposing air currents and capture the

Table 10.5 Approximate hood capture velocities (adapted from NSC and ACGIH vent manual)

Conditions of contaminant release	Approximate capture velocity in m/s (fpm)	Examples of processes or operations in biomedical device manufacturing
Release with no significant velocity into quiet air	0.25–0.5 (50–100)	Degreasing, cleaning, etching, anodizing, adhesive application
Released with low velocity into moderately quiet air	0.5–1.0 (100–200)	Coating applications, welding, and soldering
Released with considerable velocity or into area of rapid air movement	1.0–2.5 (200–500)	Light surface preparations, some spray coatings, and machining operations
Released with high velocity or into zone of rapid air movement	2.5–10 (500–2000)	Some maintenance operations, grinding, and other heavy machining operations

contaminated air, causing it to flow into the hood. The point in space at which this occurs is called the capture point. Other velocity parameters important to proper hood and LEV design include slot velocity, plenum velocity, duct velocity, and minimum design duct velocity. Table 10.5 provides approximate capture velocities required to properly remove common contaminants found in the biomedical device manufacturing.

Normal capture velocities vary widely in the industry and are based mainly on the spatial characteristics of the LEV system and process interface as well as on the physical and chemical properties of the contaminant(s). Normal face velocities found on hoods in the biomedical device manufacturing industry usually are in the range of 80 feet per minute (fpm)–100 fpm.

After the contaminated air has been captured by the local exhaust hood, the ductwork serves as the carrying conduit on to the other mechanical components of the LEV, and finally, on up the stack and out. The ducts are typically made from sheet metal, with rectangular or circular cross sections of varying dimensions. The mass flow of contaminated air in a duct system is based on the duct velocity and the cross-sectional and can be calculated as follows: $Q = v/A$ where Q is the mass flow, v is the duct velocity, and A is the cross-sectional area. Typically, the economically optimal duct velocity found for systems in the biomedical device industry ranges from 1000 fpm for most cleaning, etching, and adhesive application processes up to around 2000 fpm for some welding or soldering operations. The maximum duct velocity that could possibly be encountered in the industry would be for heavy maintenance and machining operations, where velocities may reach as high as 4000 fpm.

Three critical parameters that require an understanding when calculating and controlling duct velocities include the static pressure, the velocity pressure, and the duct friction losses. The static pressure is the energy source of the system and is created by the fan while the velocity pressure is the pressure creating by the air in flux. It can be said that velocity pressure is what is realized by converting static pressure into air movement within the duct. These important parameters are

typically measured by performing what is known as a pitot traverse. Friction losses (and other losses) must be considered for optimal LEV system design, and values for these losses are based on such characteristics as length, diameter, and configuration. Values for LEV duct friction losses can be found tabulated in various sources including manufacturer specification sheets.

Air cleaners are a necessary component of a properly designed LEV system. Some of the more commonly found types of cleaners commercially available include:

1. Electrostatic precipitators.
2. Simple setting chambers.
3. Wet and dry centrifugal collectors.
4. Venturi scrubbers.
5. Washers.
6. Fabric filters (e.g., HEPA or ULPA).
7. Packed tower or scrubber.
8. Carbon adsorption.
9. Catalytic units.

The type of cleaner chosen for the LEV system must be able to effectively remove the contaminant of concern. Thus, the type of cleaner capable of removing particulate matter at a known efficiency will be more than likely considerably different from one which is effective at removing a vapor or fume. Along with the nature of the contaminant, the other major factors considered when choosing one type over another include airborne concentration, outflow cleanliness, and cost. Air cleaners for removing gases and vapors normally either work on the principle of absorption, adsorption, condensation, or catalytic conversion. For metals fumes, a cloth filter, high efficiency wet collector, or electrostatic precipitator provides the best removal efficiencies. Particles (or dust) of sizes greater than 1 μm can usually be cleaned effectively by such control technologies as cyclones, precipitators, venture scrubbers, settling chambers, settling chambers, and cloth filters. Particles smaller than 1 μm are typically controlled with HEPA or ULPA filter setups. A considerable control challenge is presented by significant concentrations of particles, smoke, of fumes of less than one micron. These stressors show active Brownian movement because of their small size and do not tend to settle out like those particulate contaminants that are greater than 1 μm or so.

The required removal efficiency is an important parameter that needs to be covered on any discussion on air cleaners. Many operations in the device industry require robust collection efficiencies in order to keep the atmosphere at "clean" levels. For example, HEPA and ULPA filters are rated on their ability to remove a certain percentage of particles at a particular diameter. The efficiency and particle sizes specified vary from manufacturer to manufacturer, however, a typical claim for a HEPA filter may be something like '99.99 % removal efficiency of particles 0.3 μm and larger.' Likewise, for a ULPA filter it may claim a '99.997 % removal efficiency of particles greater than 0.1 μm.'

The fan is the mechanical driver of the LEV system and typically is of a centrifugal or axial configuration. The fan is rated based on the required volumetric airflow and static pressure. In addition, specifications for such parameters as voltage, current, revolutions per minute (rpm), outlet velocity, and brake horsepower (BHP) are typically made by the designer, and capacity tables are available from the fan manufacturer to assist in the decision making process. Important criteria that should be taken into consideration in the fan selection process include:

1. The characteristics of the airstream such as contaminant identity and physical state.
2. An evaluation of the physical constraints within its environment.
3. An analysis of the proper drive arrangement and potential configuration.
4. A prediction of the additional noise to be generated by the fan.
5. The dealing with any potential safety concerns posed by its use.
6. An assessment of the requirements for any supplemental accessories.

The exhaust stack is the final component of the complete LEV system, and is simply just an extension of the ventilation system's ductwork above the building rooftop. A properly designed stack will serve two important purposes. First, it should aid in the adequate dispersion of the gas stream stressors well above and beyond the roofline of the facility. Second, the mere existence of the stack in the LEV system causes a reduction in the velocity pressure at the outlet, and therefore, and an overall increase in fan performance. Some rule of thumbs that should be considered for optimal stack design include:

1. The stack should be configured as a straight cylinder to avoid any mechanical losses.
2. The use of rain caps or screens is not recommended.
3. If possible, the location of the stack should be on the highest rooftop.
4. The stack should be kept as far away as possible from any plant air intakes.
5. Stack height increases in lieu of good emission controls should be avoided.
6. Stack height requirements should be increased rather than gas stream exit velocities in order to realize the necessary control.

For those interested in more detailed information on how to design an effective and efficient LEV system for their specific process, a myriad of excellent resources are available for guidance through the design process.

10.17 Personal Protective Equipment and Clothing

A final control option for consideration in biomedical device manufacturing is the use of PPE or personal protective clothing (PPC). However, the paradox lies in the reality that the use of PPE or PPC is many times the easiest contaminant control solution. For example, the device manufacturer might use a dermal barrier device

(e.g., neoprene gloves, barrier cream, etc.) long before ever considering a change of process or materials. Other common examples of PPE and PPC usage in biomedical device manufacturing include ear plugs and muffs for noise protection, cooling vests for heat stress protection, and safety glasses for general eye protection.

The PPE and PPC usage in the industry varies widely and is based upon the type of device being manufactured. A detailed discussion on the various PPE and PPC usage in the various device manufacturing environments is beyond the scope of this chapter and will not be covered in any further detail.

10.18 Control Strategies in Device Manufacturing

The choice of the optimal control strategy to follow depends on a multitude of different factors. Obviously, the type of device being manufactured and the potential stressors associated with its production top this list. However, such additional factors as economics, regulatory requirements, workforce characteristics, and facility design must also be given due attention.

Typically, the best strategy involves the combination of two or more of the discussed control strategies. For example, a barrier or isolation control technique may be used in conjunction with an adequately designed LEV system in order to prevent environmental releases of worker exposures to ethylene oxide during the sterilization process. Another example might be the reliance on dilution ventilation to remove the majority of facility contaminants, with LEVs installed at questionable operations in enclosed areas. Table 10.6 provides the typical strategy (or strategies)

Table 10.6 Control strategies in device manufacturing

Category of stressor(s)	Control strategies
Ionizing radiation (Co-60 or various gamma and beta sources)	Time, distance, shielding, PPE, LEV
Organic degreasing solvents (TCE, 1,1,1-TCA, perchloroethylene)	LEV, dilution ventilation, substitution
Acid etching agents (e.g., sulfuric acid, phosphoric acid, chromic acid)	LEV, PPE
Particles or aerosols from various operations	HEPA or ULPA filtration
Microbial stressors from indoor air quality issues	Dilution ventilation with control over HVAC; HEPA or ULPA
Adhesives and coatings	Process control (i.e., continuous operations over batch), robotic application
Nonionizing radiation (e.g., lasers, microwaves)	PPE, enclosure/isolation
Welding and soldering contaminants (e.g., metal fumes, flux, ozone)	LEV, substitution
Toxic gases and vapors (e.g., EtO, methanol)	Isolation/enclosure, LEV, substitution

Table 10.7 Comparison of clean room international standards

International Standard Organization	Germany VDI 2083	USA 209D	Britain BS 5295	Australia AS 1386	France AFNOR NFX 44-101
3	1	1	C	0.035	–
4	2	10	D	0.35	–
5	3	100	E or F	3.5	4000
6	4	1000	G or H	35	–
7	5	10000	J	350	400000
8	6	100000	K	3500	4000000

followed to control some of the more common stressors found in the biomedical device manufacturing environment.

Control of the clean room environment in biomedical device manufacturing has been realized primarily through the standardization of equipment, facilities, and operational methods. These methods include procedural limits, operational limits, and testing procedures aimed at achieving internationally the desired environmental attributes to minimize microscale contamination. Clean rooms can have localized and enclosed forms of ventilation and contaminant removal or robust area HVAC systems capable of minimizing particle and microbial contamination. A comparison of the current international standards for classifications of clean rooms is given in Table 10.7.

10.19 Monitoring

The use of instruments and techniques to monitor for various hazards common to the device industry is an essential and complementary part of the overall exposure control process. While environmental monitoring will be conducted for various specific reasons, the real impetus behind this activity is to determine the extent of the facility contamination that exists in relationship to the worker and environment. The way that it is performed will normally depend on the actual (or perceived) stressors that are present as well as the existence of any outside pressures, such as regulatory compliance. The overall goal of an effective monitoring program, of course, is to keep the biomedical device employee and the environment free from the potential adverse health impacts from exposures to associated stressors.

While several authors have attempted to segregate or classify the various monitoring techniques and instrumentation in different ways, the simplest strategy for this discussion might be to just break these down into categories by environmental media (i.e., air, water, soil, artifact) and exposure target (i.e., personal or area). For example, if one wants to know the extent of the contamination of a groundwater source from a spill of a tanker filled with chlorinated hydrocarbons, several monitoring wells could be installed with the necessary sensors for

measuring these contaminants in real time. This would be classified as an area (target) monitoring event for groundwater (media) contaminants. Since the scope of this chapter is on the engineering control and monitoring of stressors in the biomedical device manufacturing industry, the majority of the techniques and instruments covered will be for personal exposures to primarily airborne stressors.

Airborne chemical, physical, and biological stressors can be classified as primarily either particles, fumes, vapors, gases, or electromagnetic radiation, with the techniques or instrumentation used dependent upon the particular category. Additionally, monitors for sound pressure energy and heat stress merit adequate coverage due to their potential importance in the industry. The following sections provide an overview of the techniques and instrumentation commonly used in the device industry to monitor for environmental stressors.

10.20 Particle, Fumes, and Aerosol Monitoring

The generation of significant concentrations of particles and dust will occur anywhere there is human activity; obviously, the biomedical device industry is not immune. With such particle-producing activities required in medical device production as surface preparations and coatings, light machining, and welding/soldering, the appropriate particle control and monitoring efforts must be implemented and followed in order to protect employees from the potential harmful effects associated with airborne exposures.

Some of the more commonly used techniques for area particle monitoring involve the use of either laser optics or condensation nuclei counting. In contrast, the current best practice in measuring employee exposures to airborne particulate concentrations is to use a personal sampling device to collect a representative volume of potentially contaminated air, typically conducted over an eight-hour workshift. The monitoring is conducted in compliance to approved analytical methods, with subsequent shipment of the completed samples on to an accredited laboratory for analysis. The metric most often used to determine a relative exposure to microscale particles is the time-weighted mass concentration of each particular aerosol. Table 10.8 provides a summary of particle measurement techniques that are either currently in the developmental stages or have already been implemented in the workplace. This table includes the method, the metric measured, the sensitivity, and the major capabilities and limitations of each.

The first method discussed is a personal sampling device that is size selective. Currently, most analytical methods for particulate matter are based on the collection on a pre-weighed filter of any additional mass sampled at a known airflow rate. This is typically weighed on a laboratory balance and the full production shift (i.e., 8 h) detection limit is approximately 0.02 mg/m^3. Obviously, the use of this technique would present a problem in analysis if the air sample comprised mainly of just particles in the nanoscale range, weighing normally only a fraction of this amount. However, with all of this said, it has still been suggested that a size-selective

Table 10.8 Summary of particle measurement techniques

Method or instrument	Measurement metric	Sensitivity (10^{-9} m)	Major capabilities and limitations
Personal Sampler with accessories (e.g., cyclone, impactor, etc.)	Mass	0.02 mg/m^3	Acceptable for exposure compliance; no size fraction cutoff in nm size
Laser particle Counter and other optics counters	Number concentration	300	Portable and easy to operate; mainly for microscale use
Condensation particle counter (CPC)	Number concentration	10	Portable and easy to operate; not size selective
Scanning mobility particle sizer (SMPS)	Number concentration	3	Excellent sensitivity; not portable or user friendly and cost
Nanometer aerosol size analyzer	Number concentration	3	Excellent sensitivity; not portable and in development stage
MiPac particulate classifier	Number concentration	10	Ease of use; no detection under 10 nm
Electrical low pressure impactor (ELPI)	Number concentration	7	Successful use studies; cost and not portable
Epiphaniometer	Surface area	NA (surface area)	Successful use studies; bulky, complex, and costly
Gas adsorption	Surface area	NA (surface area)	Well understood technology; large samples sizes needed for validity
Scanning electron microscopy (SEM)	Number, size, and morphology	5	Excellent sensitivity and resolution; sophisticated instrumentation
Transmission electron microscopy (TEM)	Number, size, and morphology	1	Excellent sensitivity and resolution; complicated sampling routine
Laser induced plasma system	Composition	3	Outstanding for composition studies; composition information only

personal sampler could be developed with, for instance, a 100 nm cut-off point. This could provide some meaningful accuracy for measuring any coating- or surface preparation-originating aerosols above approximately 50 nm in diameter. Figure 10.7 provides an example of the type of personal air sampler that would be used to monitor for respirable dust. Note that a cyclone is attached in order to collect the respirable fraction of the mass.

The second through seventh methods provided in Table 10.8 are based on the number of particles counted. These methods include laser optical particle counter, condensation nuclei counters, scanning mobility particle sizers (SMPSs), and electrical low pressure impactors. These are primarily real-time counters and range in relative portability, and subsequent applicability, to workplace exposure assessments. Also, several of these methods are still in the developmental stages.

Fig. 10.7 Personal sampler used to monitor for respirable dust (*Permission* SKC, Inc.)

Due to its portability, versatility, and lower detection size limit, laser particle counters have been traditionally used to measure particles down in the low microscale range. However, particles that are less than 300 nm will not be detected by this method. This limits the applicability in the biomedical device manufacturing industry, in particular, the clean room environment, where particles of concern are quite frequently found at an order magnitude smaller. There are more sophisticated optical samplers but these are not currently portable devices, and therefore, would not typically be used in this industry to measure workplace exposures.

The most commonly used instrument capable of measuring ultrafine particles employs condensation particle counting technology. The condensation particle counter (CPC) condenses vapor onto the sampled particles in order to "grow" them to a detectable size range. This type of instrument is usually very portable and easy to operate. The main disadvantage to using this type of instrument is that it is not size selective and only provides the total particle counts above the detection limit, which ranges from 3 to 100 nm on commercially available units. Figure 10.8 shows an example of a typical CPC used to characterize ultrafine particles.

The measurement methods that are currently available, which provide both size-selective information as well as number concentration, are inherently more complicated to use as well as not being very portable or versatile for field exposure assessments. In addition, their higher costs typically eliminate applicability altogether in the workplace. The best instrument examples of these methods are the SMPS and the electrical low pressure impactor (ELPI). Both of these instruments can provide size-selective concentration data of particles all the way down to less than 10 nm in diameter. Examples of both an ELPI and an SMPS are provided in Figs. 10.9 and 10.10.

Fig. 10.8 Condensation particle counter (*Permission* TSI, Inc.)

Fig. 10.9 Electrical low pressure impactor (*Permission* Dekati, Ltd.)

While microscale particles typically do not agglomerate significantly, the majority of nanoscale-sized particles generated do agglomerate to some extent. Therefore, it can be argued that the best way to characterize nanoscale particles is by the measurement of its surface area. The only instrument that has been currently employed to measure surface area is called an epiphaniometer. This instrument uses radioactive tagging to determine the particle's surface area. Again, this instrument

Fig. 10.10 Scanning mobility particle sizer (*Permission* TSI, Inc.)

is very complicated and lacks versatility for field use. Gas adsorption techniques that require rather large sample sizes have also been used infrequently as a bulk method of ascertaining particle surface areas.

Scanning Electron Microscopy (SEM) and Transmission Electron Microscopy (TEM) also provide the means for determining particle and dust characteristics. While these instruments provide the morphology of the particles and excellent resolutions (e.g., TEM = 1 nm; SEM = 5 nm), they are very expensive and usually require an expert technician or specialized training to use effectively. However, recent studies point to the merit of this technique to characterize exposures in the workplace.

Micro- and nanoparticle composition measurements are normally essential components for detailed particle research studies. Not unlike many of the number, size-selective, and surface area techniques previously discussed, most composition techniques are currently in the developmental stages. The laser-induced plasma system and the high temperature nanoparticle measurement systems can detect the composition of nanoscale particles as small as 3 nm.

Each of the portable methods for area monitoring that have been discussed has their own set of merits and limitations. In order to alleviate the negative impact posed by some of these specific limitations, the use of two or more of these techniques in combination may be considered. While the more sophisticated instruments have excellent resolution and many times both concentration and size-selectability, they are primarily limited to research settings due to their complexity, size, and costs. And, for the majority of end users, personal exposure sampling devices, like the one shown in Fig. 10.7, coupled with one clean room portable particle measuring device, will be more than adequate.

10.21 Vapors and Gases

Techniques for monitoring the air for gases and vapors are essentially the same, thus, including them together in a section is appropriate. Both active and passive sampling methods exist to measure concentrations of many of the typical stressors found in device manufacturing such as ethylene oxide, trichloroethylene, phosphoric acid, and isopropanol (IPA). In order to conduct personal exposure monitoring for gases and vapors, an active sampling train such as the one shown in Fig. 10.11 should be used. Once this sampling train is calibrated to a known volumetric flow rate, it can be attached to the worker in order to monitor breathing zone air or placed at a site of concern to conduct an area monitoring event. In each case, the active setup will include a sampling pump, a calibrator, flexible hose, connectors, and some form of sampling media. The sampling media typically will capture the gas or vapor through sorbent action (e.g., adsorption, absorption). Depending on the compliance standard and protocol, a worker will normally be evaluated for his/her exposure for the whole workshift. Like particle exposure monitoring, once the sampling event is completed to accepted protocol, the filter is sent off to an accredited lab for quantification. Normal media material for monitoring airborne contaminants includes activated charcoal, silica gel, or a series of organic polymers.

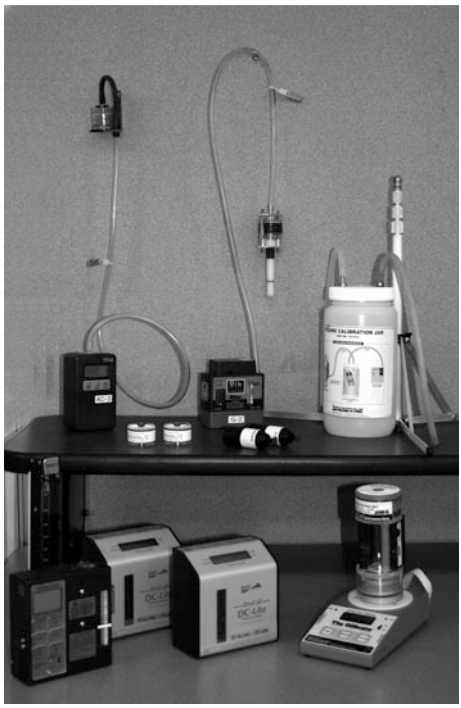

Fig. 10.11 Personal exposure air sampling equipment

There are now also passive methods for monitoring workplace and environmental exposures to some gases and vapors. For example, ethylene oxide, the common sterilizer, has a fully validated passive method of monitoring. The passive monitors are typically worn as badges or dosimeters. After the monitoring event duration is complete and in similar fashion to both loaded filters and absorbent media samples, the dosimeter or badge is packaged up and sent off to an accredited lab for subsequent analysis. While lab quantification is still the usual means of analysis for compliance testing, there is a current impetus to test and approve direct-reading techniques for monitoring workplace exposures. Before a company considers conducting a comprehensive personal exposure assessment, it is recommended that an evaluation using direct-reading instruments and/or colorimetric techniques be performed to screen the potentially contaminated areas and develop a concentration profile of the facility.

There are several techniques for conducting this "snapshot" monitoring scheme, with normally a significant payoff realized by the company due to the useful information obtained. These instruments work on such principles as X-ray fluorescence, ionization potential, and chemical luminescence. These techniques vary on their relative accuracies and resolution and either provide qualitative, quantitative, or both qualitative and quantitative data to the end user. Due to their significance and usefulness, the following paragraphs elucidate the principles and operational characteristics of these instruments and techniques with respect to the common gases and vapors found in biomedical device manufacturing.

10.21.1 Detector (Colorimetric) Tubes

The use of detector tubes to provide a concentration profile in the workplace is common due primarily to economics. These tubes are available for a wide variety of organic and inorganic vapors as well as for common gases found in industry and in the environmental field. A monitoring event can be conducted with one or even several colorimetric tubes for a fraction of the cost of some of the available survey instruments calibrated to measure the same stressor. Typically, ten tubes are included in a package with easy instructions on how to use them effectively in the field. The principle of operation involves a colorimetric reaction between the sorbent material in the tubes and the gas or vapor being monitored. While this technique is an excellent means of determining whether or not a contaminant exists in appreciable concentrations, it cannot be used for compliance purposes for employee exposures. The tube has other colorimetric chemical interferences and a normal concentration accuracy of only about 60–70 %. However, this technique provides an inexpensive means for detecting several common airborne contaminants in the biomedical industry. Colorimetric tubes are considered to be both a qualitative and pseudoquantitative in nature. The list of contaminants identified and partially quantified includes methanol, isopropanol, ethanol, trichloroethylene, methyl chloroform, perchloroethylene, sulfuric acid, and phosphoric acid, to name a few.

For those just getting into the characterization phase of the worker exposure assessment program, the use of colorimetric tubes make the most sense initially. Additional instrumentation can be acquired subsequently, if needed, as the level of survey and assessment procedure becomes more sophisticated. Figure 10.12 provides an example of a detector tube used to measure methanol concentrations. Figure 10.13 (top, right) shows the latest generation of colorimetric detection device.

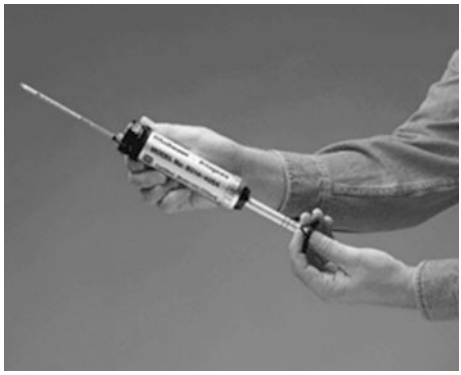

Fig. 10.12 Colorimetric tubes for field surveys (*Permission* TerraUniversal)

Fig. 10.13 Examples of field portable air monitoring instrumentation

10.21.2 Photoionization Detectors (PIDs)

The photoionization detector, or PID, is another common means for detecting organic vapors and gases in the workplace. The PID works on the principle that vapors and gases will ionize if a sufficient source of energy (e.g., UV radiation from a lamp) is allowed to come into intimate contact with them in a chamber. The PIDs have a range of ionization energy potentials, with 9.5, 10.2, and 11.7 eV being the most common. The different energies are a means for differentiating between two or more contaminants coexisting in a particular airspace. However, the instrument does not have the ability to determine the different contaminants by any direct means. Thus, it is considered to be quantitative but not qualitative in nature. The ionization potential of common device industry stressors include the values of 10.56 eV for EtO, 10.10 eV for IPA, and 9.45 eV for TCE [25]. An example of a common PID is given in Fig. 10.13 (top, left).

The biomedical device manufacturing professional might use this instrument if a known chemical hazard is possibly present at unsafe levels. As long as there are no other significant concentrations of different gases or vapors, which ionize at or under the ionization energy output of the device, a calibrated device should provide an accurate (e.g., within ±2 ppm or 10 % of the reading) representation of the concentration existing at any point in time. Of course, this assumes that the known gas being evaluated ionizes at or under the lamps ionization energy. The normal resolution of a commercially available PID is 0.1 ppm. Common industry contaminants that can be characterized by a PID include the various sterilizers, cleaning solvents, coatings, and adhesives.

10.21.3 Flame Ionization Detectors (FIDs)

The flame ionization detector, or FID, is another means for detecting primarily organic vapors and also works on the principle of ionization potential. However, in contrast to the PID, the FID energy source is a hydrogen gas-initiated flame. Because of the hot flame, this instrument is capable of a wider range of ionization potentials. For this reason, it is used many times in conjunction with a PID out in the environmental field where substantial concentrations of methane gas, with an ionization potential of 12.98 eV, may exist. Essentially, the two instruments are used in conjunction to identify both the methane concentration of the air as well as the concentration of organic vapors that exist. In essence, the trained user can differentiate the concentrations by subtracting the PID concentration (i.e., parts per million of organic vapors other than methane only) concentration from the FID output (i.e., parts per million of both organic vapors and methane) to get the total methane. Due to its use of an explosive gas as the energy source and complicated operational characteristics, this instrument is used mainly in the environmental field and would unlikely ever be considered for use in the biomedical device industry.

Figure 10.13 (bottom, right) shows an example of a flame ionization detector coupled with a gas chromatograph column. Figure 10.13 (top, middle) also shows a combination PID/FID instrument for field surveys.

10.21.4 Electrochemical Sensor Monitors

Electrochemical sensor monitors are available from the original one gas monitor all the way up to the present day, five-sensor model. Typically, these monitors measure percent oxygen, percent lower explosive limit, hydrogen sulfide concentration, carbon monoxide concentration, and an end user gas concentration of choice. However, any of the sensors can be interchanged and the programming functions allow for customizing to the application. A common electrochemical multigas monitor to be used in the biomedical device industry might include sensors for ethylene oxide, % oxygen, hydrogen peroxide, ozone, and carbon monoxide. This device is considered to be both qualitative and quantitative, with accuracies of approximately ±5 % and resolutions of 0.1 ppm. Figure 10.13 (bottom, left) provides an example of a multigas monitor.

10.21.5 Infrared Spectrophotometers

Portable infrared spectrophotometers are also available to measure airborne organic and inorganic contaminants. These are sensitive instruments with a series of mirrors that direct significant wavelengths within the unit. These are bulkier instruments that cost several times the amount of a PID, and thus, are currently in limited use in the biomedical device industry. However, this may change in the near future due to decreases in size and pricing, coupled with the instrument's inherent capability of providing relatively accurate qualitative and quantitative concentration measurements for many of the common airborne contaminants found in the industry.

10.21.6 Gas Chromatographs (GCs)

While gas chromatographs (GCs) have been used for years as lab bench top instruments to identify and quantify many organic compounds, the technology has only been portable for the last couple of decades. Like the infrared spectrophotometers, the inherent cost and complexity of operating these units have limited their usage in the field. Still, with only a few known contaminants and an experienced operator, this instrument provides a viable option to monitor many of the airborne contaminants found in the device industry. Figure 10.13 (bottom, right) provides an example of a commercially available GC unit, couple with a FID.

Fig. 10.14 Portable XRF being used in the field to characterize heavy metals (*Permission* Niton)

10.21.7 X-ray Fluorescence (XRFs)

Portable X-ray fluorescence instruments provide an alternative for measuring heavy metals in the environment. The units are very portable and use a radioactive gamma-emitting source to produce the characteristic X-rays for each heavy metal of concern. While being relatively costly, they have the added benefit of being approved for usage on an airborne lead compliance method, with additional methods targeting the measurement of other heavy metals currently in the validation stage. This unit would be used to monitor concentrations of heavy metals during such operations as welding or machining. An example of a typical portable XRF is provided in Fig. 10.14.

10.22 Ionizing Radiation

The main types of ionizing radiation found in the biomedical device industry include gamma ray, X-ray, beta particle, alpha particle, and electron beam. The worker's occupational exposure to the various forms of ionizing radiation is typically monitored by the use of personal dosimeters and portable survey meters. Some of the most common operations for sterilizing medical devices employ the use of radioactive sources. In addition, radioactive tracers are many times used during the research phase of the device development, with sources also included as integral components in some the lab instrumentation.

Worker exposure could be monitored during the workshift by personal dosimeters, such as a thermoluminescent dosimeter (TLD). This is simply worn for the time period and then removed and analyzed by a qualified technician. Additionally, there are other active and passive dosimeters designed specifically to measure the dose of certain types of ionizing radiation to which an individual may be exposed. Another means for determining worker exposure is by performing a

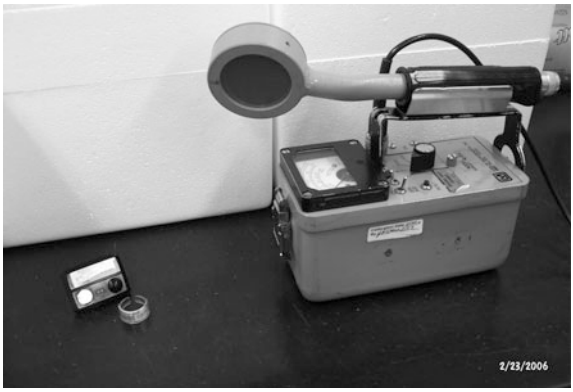

Fig. 10.15 Radiation dosimeter (*left*) and Geiger-Mueller counter for radioactivity surveys

bioassay after the event. A detailed discussion on these various dosimeters and their appropriate uses is beyond the scope of this chapter.

As for the survey-type instruments, the type of detector will be chosen based on whether or not the source of radiation is gamma/X-ray, beta, alpha, or electron beam. Normally, a Geiger-Mueller survey meter will be the instrument of choice, with various added capabilities such as data logging and programmability. Both a common radiation dosimeter and a Geiger-Mueller counter, with associated detector, are shown in Fig. 10.15.

10.23 Nonionizing Radiation

The major forms of nonionizing radiation that a worker may be exposed to in this industry include, but are not limited to, laser, ultraviolet, microwave, and infrared. The majority of nonionizing radiation monitors provide an output on the magnitude of both the electric and magnetic fields associated with their operations. Other important parameters that must be ascertained include the frequency, wavelength, duration of both signal and exposure, and power of the source. These are determined by various instruments and techniques and are not outputs from just a single monitor. Figure 10.16 shows a monitor capable of measuring the associated fields produced by a particular nonionizing source.

10.24 Noise and Heat Stress

Personal exposures to noise are monitored by noise dosimeters. They are typically attached to the worker and allowed to collect the data for the entire workshift. The value is then integrated over the duration and then compared to the acceptable time-weighted average for the time frame. To determine area noise levels or

Fig. 10.16 Monitor for measuring electromagnetic radiation (*Permission* Gentec-EO)

environmental noise, an instrument known as a sound level meter (SLM) is typically used to log the data. This instrument provides a means for determining a noise profile for a whole facility. Once the problem areas are identified, personal exposure monitoring is conducted for those potentially overexposed. Figure 10.17 provides examples of both typical noise dosimeters (middle) as well as a common type of SLM (right).

Heat stress monitoring is normally conducted using a wet bulb globe temperature apparatus. This instrument provides a combination measure of the effects of dry air temperature, radiant heat transfer, and humidity. While there is no universal standard for heat stress, there are guidelines that normally involve work–rest regimens and different work rates. While the use of this monitor in the biomedical device manufacturing environment would be atypical, there still could be conditions necessitating its use (e.g., laborious maintenance activities). A portable heat stress monitor is also shown in Fig. 10.17 (left).

10.25 Microbial Environmental Monitoring

Significant concentrations of contaminants originating from biological origin are often found in the device industry. In particular, there is a major concern to limit the amount of microbial activity in the facility air (and on surfaces) due to the nature of

Fig. 10.17 Monitors for heat stress (*left*), noise dosimetry (*center*), and sound level measurement (*Permission* Quest Technologies, Inc.)

the product. Biomedical device manufacturers use microbial environmental monitoring programs to evaluate the effectiveness of facility-wide cleaning and disinfection procedures as well as to assess the overall microbial cleanliness of their manufacturing environment. The ultimate goal must be to minimize the bioburden on the biomedical device being manufactured. If allowed to exist, undesirable bioburden spikes on the finished product can cause a reduction in the sterility assurance level for the device.

Fig. 10.18 Viable contaminant monitoring apparatus with agar plates

In order to manage and control the indoor environment with respect to biological stressors, usually it is necessary to get a baseline of contamination through an approved microbial environmental monitoring procedure. This procedure normally includes a sampling train made up of a calibrator, vacuum pump, Anderson impactor (or comparable), and necessary tubing and accessories. The sample media is usually an agar plate prepared with the proper substrate of microbial subsistence. Figure 10.18 gives an example of a typical biological stressor monitoring apparatus.

The available monitors, like the one shown in Fig. 10.18, typically work on the principle of collecting a known volume of air at a certain flow rate and then, in much the same fashion as for chemical samples, the sampling media is shipped off to an accredited lab for subsequent analysis. The monitoring duration varies based on the collection procedure and objective for monitoring, but typically is less than 20 min per location. Since personal exposure standards are essentially nonexistent at this time from most biological contaminants, area monitoring is the only type currently conducted in the majority of cases.

10.26 Clean Room Monitoring Requirements

In the majority of biomedical device manufacturing settings, there will exist at least one condition or operation that requires a mandated clean room environment. Therefore, it is appropriate to discuss the monitoring requirements in order to meet compliance standards as a separate topic altogether in this section. Current international regulations require the monitoring of particulate matter and biological agents as a part of good manufacturing practice. The following paragraphs provide an overview of details surrounding proper clean room monitoring.

Table 10.9 provides the airborne classification used by the EU as the guide to good manufacturing practice (EU 2003). Grade A and B correspond to a class 100 (USFDA) or ISO 5 clean room while Grade C corresponds to a class 10000 or ISO 7 clean room and a Grade D corresponds to a class 100000 or ISO 8 clean room. The particle monitoring requirements can either be completed manually or automatically, and typically measurements of the critical sizes (i.e., 0.5 and 5.0 μm) are taken with a laser-based detector with an isokinetic sampling probe. Normal flow rates and sampling duration at each monitoring location are 1.0 cubic feet per minute and 20 min, respectively; however, this rate and duration will vary on case-to-case basis. For clean rooms of ISO 5 and lower, the mandatory testing time interval to demonstrate compliance to particle limit standards is every 6 months, with those greater than ISO 5 required to be tested every 12 months. Air pressure differentials and airflow velocity is also required at 12-month intervals. Portable devices which measure both air velocity and pressure are commercially available and normally used to quantify these parameters. The number of monitoring locations per site varies based on class level and regulatory authority, respectively.

There are also limits to the microbial contamination that exists in a clean room environment. Thus, the monitoring of the clean room air for total microbes is essential to attain and maintain compliance. Figure 10.18 provides an excellent example of the monitoring setup typically used to collect the colony forming units (cpu) for each air sample. Additionally, there are cpu sampling requirements for settle plates, contact plates, and gloves. The EU GMP for recommended limits at each grade level for microbial contamination for all four of these is shown in Table 10.10.

Table 10.9 Airborne particle classification in the EU guide to good manufacturing practice (maximum number of particles permitted per cubic meter)

Grade	$\geq$0.5 μm (at rest)	$\geq$5.0 μm (at rest)	$\geq$0.5 μm (in operation)	$\geq$5.0 μm
A	3500	0	3500	0
B	3500	0	350,000	2000
C	350,000	2000	3,500,000	20,000
D	3,500,000	20,000	Not defined	Not defined

Table 10.10 Airborne microbial classification in the EU guide to good manufacturing practice

Grade	Air sample cfu/m^3	Settle plates 90 mm diameter cfu/m^3	Contact plates 55 mm diameter cfu/m^3	Glove print (5 fingers) cfu/glove
A	<1	<1	<1	<1
B	10	5	5	5
C	100	50	25	–
D	200	100	50	–

10.27 Monitor Selection in Device Manufacturing

The choice of the best monitor for the application is based on such factors as the type and physical state of the stressor, environmental media contaminated, concentration of the contaminant, goal of the monitoring effort, and overall economics. If the monitoring event is just to provide an area characterization of the extent of contamination, many of the direct-reading instruments and techniques may suffice. However, if the goal is to show environmental or occupational regulatory compliance, then personal monitoring techniques, with subsequent accredited lab testing and analysis, is the correct choice. Table 10.11 pairs up some of the more common industry stressors with the instrument or technique normally used to

Table 10.11 Common stressor and instruments/techniques normally used to characterize

Chemical, physical, or biological stressor	Instrument or technique
Cleaning and disinfecting alcohols (e.g., methanol, isopropanol, ethanol, etc.)	PID, detector tubes (area or snapshot/screening) Sampling pump with silica gel media (personal or area)
Chlorinated hydrocarbons for cleaning and degreasing (e.g., TCE, Perk, etc.)	PID, detector tubes (area or snapshot/screening) Sampling pump with activated charcoal media (personal or area)
Ethylene oxide from sterilization	Electrochemical sensors (area or snapshot/screening) Sampling pump with activated charcoal media or passive badge (personal or area)
Ozone from sterilization, welding activities, and air cleaners	Electrochemical sensors, detectors tubes (area or snapshot/screening) Sampling pump with coated glass filter media (personal or area)
Hydrogen peroxide from disinfecting and sterilization	Electrochemical sensors, detector tubes (area or snapshot/screening) Sampling pump with impinger (personal or area)
Heavy metals from welding and machining operations	X-ray fluorescence (area, snapshot/screening, or personal) Sampling pump with 0.8 μm mixed cellulose filter media (personal)

(continued)

Table 10.11 (continued)

Chemical, physical, or biological stressor	Instrument or technique
Particulate matter and dust from a myriad of sources	Laser counters, condensation nuclei counters (area or snapshot/screening) Sampling pump with cyclone and filter media (personal)
Acids and alkalis used for etching and anodizing	Detector tubes, IR spec (area or snapshot/screening) Sampling pump with activated charcoal media (personal)
Gamma radiation from sterilization and instrument-specific sources	Geiger-Mueller survey meter with gamma detector (area and survey) TLD, film badge, or other dosimeter (personal)
Fungal and bacterial species from indoor air quality problems	Impactor with high volume sampling pump and agar plate (area and survey)
Noise from plant and maintenance activities	Sound level meter (area and survey) Dosimeter (personal)

identify and/or quantify each. The second column of Table 10.11 also identifies whether or not the instrument or technique is typically used for area, snapshot/screening, or personal monitoring events.

10.28 Summary

The effective monitoring and control of chemical, biological, and physical stressors in the biomedical device manufacturing environment is imperative. This chapter began with an overview of the sources, properties, and characteristics of some of the more common contaminants found in the industry. Once these stressors were identified and characterized, examples of some of the more typical techniques implemented for controlling their presence in the workplace and the potential risk of exposures associated with each were discussed. The chapter concluded with a synopsis of the potential monitoring techniques and instruments that may be used as a means to qualify and quantify the extent of contamination and potential employee exposures to the hazardous stressors inherent to biomedical device manufacturing.

Acknowledgments The authors thank Springer and Wiley publishers for allowing the authors permission to reprint and update this chapter that was originally published in, 'Surface Engineered Surgical Tools and Medical Devices,' originally published by Springer in 2007 (ISBN 978-0387-27026-5). *Reprinted with kind permission from Springer Science+Business Media B.V and Wiley Publishers.*

References

1. American Conference of Governmental Industrial Hygienists. (2005). *Threshold limit values for chemical substances and biological exposure indices*. Cincinnati: ACGIH.
2. American Conference of Governmental Industrial Hygienists. (2001). *Air sampling instruments* (9th ed.). Cincinnati, OH: ACGIH.
3. American Conference of Governmental Industrial Hygienists. (1995). *Industrial ventilation: A manual of recommended practice* (22nd ed.). Cincinnati: ACGIH.
4. Burgess, W. A., et al. (1989). *Ventilation for control of the work environment*. New York: Wiley.
5. Burton, D. J. (2003). General methods for the control of airborne hazards. In *The occupational environment: Its evaluation, control, and management* (2nd ed.) (S.R. DiNardi). Fairfax, VA: AIHA.
6. Conviser, S. (2000). *The future of ethylene oxide sterilization*. Infection control today. http://infectioncontroltoday.com/articles/061feat.html. Accessed December 2015.
7. Environmental Science and Technology Online. (2005). *It's in the microwave popcorn, not the Teflon® pan, Science News report November 16th.* Accessed December 2015.
8. European Agency for Safety and Health at Work. (2006). *Indicative occupational exposure limit values.* http://europa.eu.int/comm/employment_social/health_safety/docs/oels_en.pdf. Accessed December 2015.
9. European Environmental Agency. http://www.eea.eu.int. Accessed December 2015.
10. European Union. (1996). Council directive 96/29/EURATOM. *Official Journal, L159*, 0001–0114 (June 29, 1996).
11. European Commission Guide to Good Manufacturing Practice Revision to Annex 1. (2003). *Manufacture of sterile medicinal products*. http://pharmacos.eudra.org. Accessed December 2015.
12. Gaggeler, H. W., et al. (1989). The epiphaniometer, a new device for continuous aerosol monitoring. *Journal of Aerosol Science, 20*(6), 557–564.
13. George, D. K., et al. (2003). An introduction to the design of local exhaust ventilation systems. In *The occupational environment: Its evaluation, control, and management* (2nd ed.) (S.R. DiNardi). Fairfax, VA: AIHA.
14. Institute of Occupational Medicine for Health & Safety Executive. (2014). (Research Report 274). http://www.hse.gov.uk/research/rrpdf/rr274.pdf. Accessed December 2015.
15. International Commission on Non-Ionizing Radiation Protection. (2002). General approach to protection against non-ionizing radiation. *Health Physics, 82*(4), 540–548.
16. International Organization for Standardization. http://www.iso.org. Accessed December 2015.
17. International Organization for Standardization. (2000). *Cleanrooms and associated controlled environments-part 2: Specifications for testing and monitoring to prove continued compliance with ISO 14644-1, ISO 14644-2:2000.* Geneva: ISO.
18. International Organization for Standardization. (1999). *Cleanrooms and associated controlled environments-part 1: Classification of air cleanliness, ISO 14644-1:1999*. Geneva: ISO.
19. Heinsohn, R. J. (1991). *Industrial ventilation: Engineering principles*. New York: Wiley-Interscience.
20. Hitchock, A., et al. (2003). Nonionizing radiation. In S.R. DiNardi (Ed.), *The occupational environment: Its evaluation, control, and management* (2nd ed.). Fairfax, VA: AIHA.
21. Kittleson, D. B. (1998). Engines and nanoparticles: A review. *Journal of Aerosol Science, 29* (6), 575–578.
22. Maslansky, C. J., & Maslansky, S. P. (1993). *Air monitoring instrumentation*. New York: Van Nostrand Reinhold.
23. Maynard, A. D. (2004). Examining elemental surface enrichment in ultrafine aerosol particles using analytical scanning transmission electron microscopy. *Aerosol Science and Technology, 38*(4), 365–381.

24. National Institute of Safety and Hygiene at Work. http://www.mtas.eu/insht/en/principal/insht_en.htm. Accessed December 2015.
25. National Institute of Occupational Safety and Health. (2005). *Pocket guide to chemical hazards*. Washington, DC: US Dept. of Health and Human Resources.
26. Nickerson, R., & Sheu, M. (2000). Plasma cleaning of medical devices. Critical Cleaning in Precision Manufacturing.
27. Reitz, V. (2004). Sterilization for beginners. *Medical Design Magazine—06/2004*. http://www.medicaldesign.com/articles/ID/12003. Accessed December 2015.
28. Ritter, G. W. (2000). Using adhesives effectively in medical devices. *Medical Device and Diagnostic Industry Magazine*. http://www.devicelink.com. Accessed December 2015.
29. Salditt, P. (2004). Trends in medical device design and manufacturing. *Journal of SMT, 17*(3), 19–24.
30. SKC, Inc. (2004). *Comprehensive catalog and sampling guide*. Eighty Four, PA: SKC Inc.
31. Soule, R. D. (1991). Industrial hygiene engineering controls. In G. D. Clayton & F. E. (Eds.), *Patty's industrial hygiene and toxicology* (4th ed.). New York: Wiley.
32. The InfoShop. (2003). *Biomedical applications of nanoscale devices*. The InfoShop report September 12th. Accessed December 2015.
33. US Environmental Protection Agency. http://www.epa.gov. Accessed December 2015.
34. US Occupational Safety and Health Administration. http://www.osha.gov. Accessed December 2015.
35. Virginia Commonwealth University. Dr. Daren Chen's faculty webpage, http://mechanical-and-nuclear.egr.vcu.edu/faculty/chen/. Accessed December 2015.

Chapter 11
Biomaterial–Cell Tissue Interactions in Surface Engineered Carbon-Based Biomedical Implants and Devices

N. Ali, Y. Kousa, J. Gracio, G. Cabral, A. Sousa, T. Shokufar, E. Titus, J.C. Madaleno, W. Ahmed and M.J. Jackson

Abstract Implantable prosthesis and medical devices are subjected to several interacting forces whenever they come in contact with the physiologic systems (blood, immune, musculoskeletal, nervous, digestive, respiratory, reproductive and urinary) and organs of the human body. These interactions include the effects of core body temperature (and/or variable temperatures in the oral cavity), the body physiologic fluids containing several ions and biomolecules, proteins and cells of various progeny and functions. This chapter focuses on cell tissue–implant interactions and how carbon-based implants are being developed for next-generation implantable devices.

11.1 Introduction to Surface Engineered Carbon-Based Materials

Pathological diseases of the arteries and the heart that cause life-threatening blood flow restrictions, for example can be treated either by open heart surgery intervention, by implantation of intracoronary stents and/or by use of artificial devices like artificial heart valves in heart valve pathologies. However, in spite of considerable advances in improving the mechanical properties of stents, advances in

N. Ali · Y. Kousa · J. Gracio · G. Cabral · A. Sousa · T. Shokufar · E. Titus · J.C. Madaleno
University of Aveiro, Aveiro, Portugal

W. Ahmed
School of Medicine, University of Central Lancashire, Preston, UK

M.J. Jackson (✉)
Kansas State University, Salina, KS, USA
e-mail: jacksonmj04@yahoo.com

W. Ahmed and M.J. Jackson (eds.), *Surgical Tools and Medical Devices*,
DOI 10.1007/978-3-319-33489-9_11

implants techniques, and advances in antithrombosis therapy, the use of stents and heart valves are still complicated by substantial cases of thrombotic occlusions/stenosis and restenosis [1–4] due to platelet activation resulting from the release of metallic particles/ions (in metallic stents), shear forces and blood contacting of the metallic surface [5–8]. Likewise, thromboembolism (valve thrombosis and systemic embolism) remains as the major draw back in the management of implanted mechanical heart valve prostheses [9, 10]. Patients with these implanted prostheses are faced with life-threatening bleeding problems because they are kept under life-long anticoagulant therapies in order to reduce the risk of thromboembolism. Platelet aggregation in these prostheses is the key factor in thrombus formation and dissemination as emboli which can be life threatening, if not promptly managed. In order to reduce the risk of platelet aggregation/thromboembolism and complications following the life-long course(s) of anticoagulants, the biomaterials need to be improved in order to achieve better biocompatibility/hemocompatibility [11–13].

Apart from thrombosis, other problems associated with the failure of medical implants and devices that need to be overcome are problems of mechanical failure, wear, tear and/or fatigue; the problem of chemical degradation, corrosion and oxidative degeneration; the problem of calcification and the problem of excessive immune response and/or infection as triggered by these biomaterial implants. Metallic implants may have good fatigue life and may be cheap (stainless steel for example) but they can release metallic ions and wear debris into the surrounding tissues leading to osteolysis, loosening and/or failure of the implants. All these problems encountered with implanted prostheses and medical devices could be solved with carbon thin film surface coating modifications using appropriate, durable and biocompatible biomaterial.

The passive nature of carbon in tissues has been known since ancient times. Charcoal and lampblack were used for ornamental and official tattoos by many. Other forms of carbon have been studied for possible use for biomedical applications stimulated primarily by Gott's original studies [14]: artificial graphite, vitreous or glassy carbons, carbon fibres, pyrolytic carbons, composites, and vacuum vapour-deposited carbon coatings [15]. The fundamental nature of these carbon materials and their interactions with the living tissues needs to be explored therefore. Likewise, pyrolytic carbon-coated heart valve leaflets have been successfully applied as artificial clinical heart valves [16]. Pyrolytic carbon has the major advantage of being resistant to thrombus formation, which was the biggest limitation to the earlier generation of stainless steel artificial heart valves. There was always a need to use anticoagulant drugs by patients who had the earlier stainless steel heart valves to prevent clot formation on the stainless steel, but this had the potential to suppress the beneficial effect of the natural blood clotting mechanism in patients. Pyrolytic carbon is an artificial material made of carbon microcrystals with a high-density turbostatic structure, originally engineered for use in nuclear reactors and may not be readily available for large-scale use. When pyrolytic carbon is alloyed with silicon, it shows excellent thromboresistance [16]. Pyrolytic carbon

has also been used as a coating on different types of implant prostheses, such as dental implants, percutaneous devices and tendon tracheal replacements. This chapter tends to report the state of the art in the potential of a more readily available synthetic carbon-based thin film coatings (DLC and its doped hybrids) for thromboresistant applications and various biomedical applications as stated below.

Surface coating modification is essential because it is now known that the outermost layer of a biomaterial (few nanometre scale range) is most crucial in its interfacial interaction in vivo. Baier et al. [17] have shown that exposure of an organic-free surface to fresh flowing blood for as little as 5 s leads to its complete coating by a very uniform, tenaciously adherent proteinaceous thin film. The biomaterial's outer surface dictates the configuration of this attached protein film that in turn plays an important role in determining the fate of the biomaterial in the host via a series of cascade interactions. Thus intensive research has been focused on DLC over the last few decades due to the ability of forming ultrathin films of DLC and due to the promising characteristics of DLC-like attractive tribological, electrical, chemical and optical properties. The issue of biocompatibility and hemocompatibility of DLC when used as implants and medical devices will no doubt be expected to stem from possibly favourable tissue–biomaterial surface and interactions. Generally, two main pathways could be feasible, in an effort to create a biocompatible material: creating a material with surfaces that are bioactive (like the host tissue) that can actively support the body's control mechanisms; and/or creating materials that are 'inert or passive' to the body's control mechanism in order to avoid triggering an adverse reaction (though there being nothing exactly like absolute inertness in a hostile physiological environment [18]). Moreover, it is impossible to exaggerate though, that among a large number of events occurring during the process of blood coagulation (including perhaps thrombus formation and possible thromboembolism) and decoagulation, the physicochemical adsorption is virtually the main reaction that can be readily regulated unless a bioactive material is used [19]. Thus the present chapter reports on researches into the use of DLC thin films (and its doped hybrids) as an approach to modify the physicochemical properties of biomaterials and to create a material that may be 'passive' and/or 'bioactive' in the tissue.

The endothelial lining has been reported to be the best non-thrombogenic surface [20, 21]. According to Herring et al. [22, 23] various methods including improvement of physicochemical properties, pretreatment with proteins and incorporation of negative charges have been proposed in order to reduce the surface thrombogenicity of vascular prostheses. Pesakova et al. [24, 25] have also stated that the biocompatibility of materials can be influenced by factors such as surface charge, hydrophobicity and topography. It has been reported by Ahluwalia et al. [26, 27] based on surface potential measurements using the vibrating Kelvin probe method, that positively charged surfaces enhance cell adhesion in comparison to neutral or negatively charged surfaces. The hydrophyllic or hydrophobic nature of a surface has also been associated with extent of cell interactions with the surface [26, 28]. Altankov and Groth [28] have reported that wettable (hydrophilic)

surfaces tend to be more conducive for cell adhesion. Grinnell [29] also reported observing cell adhesion to occur preferentially to water wettable surfaces. Van Wachem et al. [30, 31] carried out investigation of in vitro interaction of human endothelial cells (HEC) with polymers of different wettabilities in culture, and reported observing optimal adhesion of cells with moderately wettable polymers. The biocompatibility and hemocompatibility of Diamond-Like Carbon (DLC) films has been investigated in the literature [32–40]. Jones et al. [33] deposited DLC coatings prepared by PECVD on titanium substrates and tested them for hemocompatibility, thrombogenicity and interactions with rabbit blood platelets, and reported that the DLC coatings produced no haemolytic effect, platelet activation or tendency towards thrombus formation and that platelet spreading correlated with the surface energy of the coatings. Cytotoxicity tests have also been carried out on DLC coatings by [41–43] amongst others, and they all reported observing no negative effects by DLC coatings on the viability of cells which showed normal metabolic activities like cell adhesion and spreading. Mouse fibroblasts grown on DLC coatings for 7 days showed no significant release of lactate dehydrogenase [44], an enzyme that catalyses lactate oxidation, often released into the blood when tissue is damaged, compared to control cells, indicating no loss of cell integrity. It has also been reported by Allen et al. [45, 46] that mouse macrophages, human fibroblasts and human osteoblast-like cells grown on DLC coatings on various substrates exhibited normal cellular growth and morphology, with no in vitro cytotoxicity.

Szent-Gyorgyi [47, 48] suggested that proteins may have an electronic structure similar to that of semiconductors. Eley et al. [49] reported semiconductivity in certain proteins. This was later corroborated by works from others like that of Postow and Rosenberg [50]. Bruck in 1973 suggested that intrinsic semiconduction and electronic conduction may be involved in blood compatibility of polymeric systems [51–54], instead of mere ionic interaction, after the compatibility of the blood with surfaces has been associated chiefly with ionic charges, based on the observation that endothelial wall, platelets, and plasma proteins carry net ionic charges in normal physiologic conditions. Bruck [51, 52] observed clotting times six to nine times longer than those observed with non-conducting polymers and also observed little or no platelet aggregation in electroconducting polymers, when compared to non-conducting control samples based on his study with pyrolytic polymers. Bruck concluded that ‘it is possible that electroconduction and semi-conduction is involved in the interaction of surfaces with plasma proteins in the activation of the Hageman factor and the platelets by an unknown mechanism’ [53].

Since changes in surface energy [27], surface charge conditions [26] and electronic conduction [52] have all been suggested to have an effect on the biocompatibility and hemocompatibility of materials, the present investigation is directed to understanding the effect of the above-identified factors in DLC biomaterials on especially the human microvascular endothelial cell compatibility, the platelet interaction (thrombus formation) and the cytotoxicity of various cell lines

(eg. retinal pericytes, V79, L132, etc). These factors were changed by modifying the DLC films by doping with Si, N, for example which is known to alter the surface energy, surface charge condition and electronic conduction in DLC films. This investigation has the final aim of assisting with furthering the understanding of the underlying physics of material interactions in a biological environment, and the potential to develop Si-DLC as a more readily available alternative to pyrolytic carbon and to discover and exploit the fundamental role of the electrical property and the surface energy of DLC biomaterial, so as to use it as a key to turn the potential biocompatibility and hemocompatibility of DLC into any desirable (particular) biomedical application. Surface topography is another important factor in biomaterial–cell tissue interaction. Surface engineered and patterned surfaces are now commonly created and used model for studying biomaterials–cell tissue interaction. This philosophy is based on the spatial distribution/extension of cellular appendages (cell spreading) and cell–cell/cell–material interactions based on this communication channels as one of the cell signalling modalities. Cell–cell interactions and cell–material interactions are thought to be physicochemical and electrochemical.

The physicochemical surface properties of the outermost interface of bacteria, for example and other particles as well as phagocytic cells, can essentially be of only two kinds: (a) interfacial tension and (b) electrical surface potential [55]. When a foreign surface, solid, liquid or gas, is brought into contact with the body tissue fluid/protein solution, a certain amount of the dissolved protein will be adsorbed to the surface. This process is consistent with the Gibbs theory of surface energy and may be described by the adsorption isotherm of Freudlich or Langmuir. The amount of protein adsorbed and the characteristics of the protein monolayer depend mainly on the nature of the foreign surface and the structure and the concentration of the proteins in solution [56]. The protein needs to first approach a distance to the foreign surface that will allow interaction between the molecular forces associated with the foreign surface and the protein—this is governed by diffusion. Then the characteristics of the foreign surface determine the nature of bonds or the type of changes that takes place in the configuration of the protein and the biologic molecule present.

In this chapter the biocompatibility and hemocompatibility of carbon-based thin film materials is reviewed and categorised based on certain models already existing as well as models being proposed by the author, under specific interaction with various proteins and cells due to possible differences in particular cell behaviour, and also taking into consideration whether the cells used for the test is human or animal cells and if the test is in vitro, ex vivo and or in vivo. These tests can equally be categorised under direct cell–biomaterial interactions to estimate the number of cells adherent (cell adhesion and/or cell aggregation for platelets), cell characteristics on the surfaces (cell spreading for example) and assays to determine the level of enzymes from the intracellular compartment. It is to be noted that some cells that actually exist in the blood when used for toxicity test or examined for cellular proliferation on the biomaterial are actually a test of biocompatibility rather than

hemocompatibility, although almost all hemocompatibility tests may equally be used to assess degree of biocompatibility, biocompatibility tests may not be used to assess hemocompatibility.

11.2 Potential Biomedical Applications of DLC

Very well adherent and appropriate DLC coating could be chemically inert and impermeable to liquids. They could therefore protect biological implants against corrosion as well as serve as diffusion barriers. DLC films are considered for use as coatings of metallic as well as polymeric biocomponents to improve their compatibility with body fluids [57–59]. The potential biomedical applications of DLC and modified DLC include protection of surgical prostheses of various kinds: intracoronary stents [60, 61]; prosthetic heart valves [9, 10, 42, 62, 63]. The new prosthetic heart valve designed by FII Company and Pr. Baudet is composed of a Ti6Al4V titanium alloy coated with DLC [42]. When artificial heart organ polymers used for making heart organs are compared to DLC-coated polymers, these polymers seem to show higher complement activation compared to DLC counterpart (Polycarbonate substrates coated with DLC, PC-DLC compared with Tecoflex, polyurethane) [64]. DLC and modified DLC can be used in blood contacting devices, e.g. rotary blood pump [65]. DLC is now being investigated for anti-Prion protective coating on surgical instruments and as well as anti-MRSA bug in hospital utensils where appropriate due to its known hydrophobic and low surface energy properties.

DLC is equally being investigated as a template/model surface for DNA writing and immobilisation for biochemical sensor applications. Specific biomolecules could be easily immobilised on the DLC. Surface immobilisation of DNA was reported to have several advantages: (1) Minimising the amount of DNA needed to achieve a desired effect and enhancing effective concentration vector; (2) Preventing DNA/vector aggregation; (3) reducing toxicity and degradation of delivered particles and (4) Delivering DNA to specific cellular sites [66]. DLC-Ag-Pt nanocomposites were reported to exhibit significant antimicrobial efficacy against staphylococcus bacteria, and to exhibit low corrosion rates at the open-circuit potentials in a PBS electrolyte [67].

In orthopaedics DLC can be used for coating orthopaedic pins [57] and coating of hip implants (e.g. femoral heads) [68–70]. DLC can reduce the wear of the polyethylene cup by a factor of 10–600 when used on metal implants to form a DLC-on-DLC sliding surface. The wear (and the amount of particles causing a foreign body reaction) is 10^5–10^6 lower compared to metal on metal pairs. The corrosion of a DLC-coated metal implant can be 100000 times lower than in an uncoated one. DLC can diminish the bone cement wear by a factor of 500, which can improve the bone cement to implant bonding [69–71].

In urological dialysis (hemodialysis), DLC-coated microporous polycarbonate and DLC-coated dialysis membranes show that DLC imparted an enhanced enzyme electrode performance [72, 73]. DLC has also been reported to do well in both

organ [74] and cell culture [75] when compared to the materials conventionally used for this purpose. DLC can be used as active barrier against attack by microorganisms and against biodeterioration of advanced technological devices operating in closed spaces of satellites, aircrafts and submarines, for examples [76] and as good protectors against environmental pollutants and atmospheric wastes [77]. In addition nanocrystallite copper-modified DLC has been reported to have a fungicidal effect [78].

11.3 Definitions and General Aspects of Biocompatibility

Biocompatibility can be defined as 'the ability of a material to perform with an appropriate host response in a specific application' [18]. Four components of biocompatibility have been identified:

1. The initial events that take place at the interface, mainly including the adsorption of constituents of tissue fluids onto the material surface [79];
2. Changes in the material as a result of its presence in the tissues, usually described under the headings of corrosion or degradation [80];
3. The effects that the material has on the tissue, the local host response [81];
4. The sequelae of the interfacial reaction that are seen systematically or at some remote sites [82].

Possible tests useful for evaluation of biocompatibility are listed below:

Level I:

- Initial Screening and Quality Control of Polymers
- Agar overlay response of materials
- Agar overlay response of materials extracts
- Inhibition of cell growth by water extracts of materials
- Intradermal irritation test for materials extract and leachable components.

Level II:

- Initial Evaluation of Novel Biomaterial
- Tissue culture test on materials
- Tissue culture test on materials extracts
- Cell growth in contact with test materials
- Hemolytic activity test
- Intramuscular implantation of material
- Test of osmotic fragility of erythrocytes
- In vitro mutagenicity test
- Test of material extracts by perfusion of isolated rabbit heart.

11.3.1 Specie Differences

1. The dog model is relatively inexpensive and convenient, but may lack relevance to humans;
2. The baboon model is relatively expensive and unavailable, but is relevant to humans and
3. Similarity of platelet function, the concentration and activity of clotting factors, and the hematocrit should be the primary determinants for deciding which species are most relevant to humans.

11.3.2 Cell Specificity

It is important to note that different cells perform different functions and thus their interactions with same biomaterial may differ. Specific biomaterial–cellular interaction can be compared with that of another cell line if the cell type, origin and function are very similar.

11.4 Blood

The blood is a fluid connective tissue with a matrix called plasma. The plasma proteins are in solution unlike the other connective tissues that occur in insoluble forms like fibres, thus the proteins in solution in the plasma make the plasma slightly denser than water. The blood is composed of plasma (46–63 %) and formed elements (37–54 %). The plasma is composed of water (92 %), plasma proteins (7 %) and other solutes (1 %). The formed elements of blood are composed of red blood cells 99.9 %, and the remaining 0.1 % platelets and white blood cells. The water 'dissolves' and transports organic and inorganic molecules, formed elements and heat from one part of the body to the other. The plasma proteins are composed of albumins (60 %), globulins (35 %, transports ions, hormones, lipids; immune function), fibrinogen (4 %) and regulatory proteins (<1 %: enzymes, proenzymes, hormones). Other solutes of blood are composed of electrolytes (major ones are Na^+, K^+, Ca^{2+}, Mg^{2+}, Cl^-, HCO_3^-, HPO_4^{2-}, SO_4^{2-}), organic nutrients (lipids: fatty acids, cholesterol, glycerides; carbohydrates mainly glucose; and amino acids) and organic wastes (eg., urea, uric acid, creatinine, bilirubin, ammonium ions). Albumin is the major contributor to osmotic pressure of plasma and transport lipids and steroid hormones. Fibrinogen is an essential component of blood clotting system that can be converted to insoluble fibrin [83].

11.4.1 Definitions and General Aspects of Hemocompatibility

The European Society for Biomaterials Consensus Conference following the considerations of the Macromolecule Division of the International Union of Pure and Applied Chemistry (IUPAC) thought that definition of blood compatibility should take into account the following [81]:

- The activation of the blood coagulation system at the blood–material interface;
- The response of the immune system induced after the blood–material contact;
- Other tissue responses which appear as consequences of the blood–material contact.

At the conference they proposed to define four properties characteristic of the biomaterial's blood compatibility:

- Thrombogenicity
- Antithrombogenicity
- Complement activation ability
- Complement inhibition ability.

The understanding of the process of coagulation occurring during injury to the blood vessel wall like a cut may give some background idea of the events that may apply to the blood–material interaction. The process of haemostasis, the cessation of bleeding and establishment of a framework for tissue repair consists of three phases: the vascular phase, the platelet phase and the coagulation phase, all of which occurring in a chain reaction. The vascular and platelet phases occur within a few seconds after the injury, but the coagulation phase does not start until 30 s or more after the vessel wall has been damaged. When the blood vessel wall is cut in an injury, for example contraction of the vessel's smooth muscle is triggered locally (vascular spasm) and this decreases the diameter of the vessel wall. This vascular spasm and constriction helps to stop the loss of blood and lasts for about 30 min—a period known as the vascular phase. During this phase also changes occur in the local vessel endothelium: the endothelial cells contract and expose the underlying basement membrane to the blood stream; the endothelial cells begin releasing chemical factors and local hormones (e.g. ADP, tissue factor, prostacyclin, endothelins); and then the endothelial cell membranes become 'sticky'. Platelets now begin to attach to the sticky endothelial surfaces, to the basement membrane, and to the exposed collagen fibres. This attachment marks the start of the platelet phase of the haemostasis—platelet adhesion, activation, platelet aggregation and the formation of a platelet plug. Platelet aggregation begins within 15 s after an injury occurs. As the platelets arrive at the injury site, they become activated, change shape, become spherical and develop cytoplasmic processes that extend towards adjacent platelets. The platelets begin releasing ADP (stimulates platelet

aggregation and further secretion from the platelets), thromboxane A2 and serotonin which stimulate vascular spasm, clotting factors, PDGF (platelet-derived growth factor, a peptide that promotes vessel repair) and calcium ions (required for platelet aggregation and by several steps in clotting process). The platelet phase proceeds rapidly, because the ADP, thromboxane and calcium ions that each arriving platelet releases stimulate further platelet aggregation. Finally, the blood coagulation occurring during the coagulation phase involves a complex sequence of steps that leads to the conversion of circulating fibrinogen into the insoluble protein fibrin which forms a growing network that covers the surface of the platelet plug [83]. Listed below are various hypotheses proposed for blood–biomaterial interactions by several authors.

The interfacial blood–biomaterial interactions: some 'conventional wisdom' and some 'unresolved hypotheses' **are** adapted partly from [84–86]:

11.4.2 General Hypothesis

The overall process of in vivo thrombogenesis, thromboembolization and subsequent endothelialisation on a foreign surface is dominated by surface properties rather than hemodynamics (or by hemodynamics rather than by surface properties).

11.4.3 Material

1. A material with a critical surface tension of about 25 dyn/cm will have a low thrombogenic potential.
2. A small negative surface charge lowers material thrombogenicity.
3. High water content materials have a low thrombogenic potential due to the lowered free energy of the hydrated interface.
4. High water content materials may continually expose a fresh foreign interface, leading to a high thrombogenic potential; however, they also tend to exhibit low thromboadherance due to their low interfacial free energy.
5. H-bonding group in a surface lead to strong interactions with biological species and therefore endow a surface with a high thrombogenic potential.
6. A surface with a high apolar/polar ratio is desirable for low thrombogenic potential.
7. Thrombus is nucleated in regions of the surface where a specific spatial distribution of specific chemical (electrostatic) groups is present.
8. Flexible (as opposed to stiff) polymer chain ends and loops in the material interface lower the thrombogenic potential of the foreign surface.

11.4.4 Material and Hemodynamics

1. Thrombi will always be generated at surface imperfections due to flow disturbances, surface compositional differences and/or trapped gas bubbles.
2. Smooth surfaces in arterial flow conditions may release thromboemboli before they grow too large to be dangerous (corollary: high shear rates can detach thromboemboli before they have grown too large).
3. Certain rough and textured surfaces may form and retain fibrin, thrombus, leading to a 'passivated' surface.

11.4.5 Hemodynamics

1. Thrombi will always be generated in regions of low flow or flow separation.
2. Low shear rates can lead to regional accumulation of activated protein coagulation factors and subsequent thrombogenesis on a nearby surface.
3. High shear rates can be destructive to blood cells (e.g. shear rates can initiate platelet activation and lead to thrombogenesis).
4. In a tubular flow field, the platelets tend to accumulate preferentially near the wall and the red cells near the central core (Corollary: the red cells enhance the rate of collision of platelets with the wall).

11.4.6 Erythrocytes and Leucocytes

1. The role of leucocytes in thrombogenesis may be related to their ability to recognise a particular biomaterial surface as 'foreign' after certain proteins and/or platelets have adhered to that surface.
2. Red blood cells may play only a minor role in the thrombogenic process.

11.4.7 Blood Cells and Protein Surface Tensions

Surface tensions of cells and proteins can be measured by a variety of techniques.

Surface tension of cells and proteins are relatively high, they tend to be hydrophilic in their natural state [87].

11.4.8 Heparinised Surfaces and Drugs

1. The natural endothelium is non-thrombogenic because endothelial cells produce the powerful antiplatelet aggregation agent prostacyclin (PGI_2).
2. There may be synergistic interaction between specific drug therapies and specific biomaterials such that reduced drug regimens may be indicated in combination with the use of specific biomaterials in devices or implants.
3. Heparinised surfaces must leach heparin to be non-thrombogenic. (General corollary: 'immobilised' antithrombogenic drugs are ineffective unless they leach into the flowing blood.)
4. Heparinised surfaces that bind antithrombin III do not need to leach heparin to be non-thrombogenic.

11.4.9 Calcification

1. Calcification may be initiated at points of high mechanical strain in a foreign material (such as blood pump diaphragm).
2. Calcification in foreign materials is a biological process; γ-carboxy glutamic acid is a necessary amino acid in one key protein involved in this process.

11.4.10 Surface Charges

1. Under normal conditions, the blood vessel wall and blood cells are negatively charged (potentials across the blood vessel wall were measured using Ag–AgCl reference electrodes: under normal conditions the inner electrode was negative with respect to the outer electrode) [88].
2. Injury to the blood vessel wall reduces the magnitude of the negative charge density and very often even causes a reversal in the sign of the surface charge (injury is generally accompanied by thrombus formation) [89].
3. 3. A decrease in pH reduces the negative charge density of the blood vessel wall and of blood cells. The isoelectric point occurs at pH $\sim$4.7 (The pH of the electrolyte has a significant effect on the surface charge of the blood vessel walls. At pH $\sim$4.7 the blood vessel wall has zero surface charge and below this pH the blood vessel wall is positively charged) [90].
4. Antithrombogenic drugs increase the magnitude of the negative charge density, whereas thrombogenic drugs have the opposite effect and in many cases even reverse its signs (electrophoresis measurements conducted on RBC and WBC in

the presence and absence of antithrombogenic and coagulant drugs show similar actions of these drugs on both blood cells and blood vessel wall) [91].

5. Positively charged prosthetic materials are thrombogenic whereas negatively charged surfaces tend to be non-thrombogenic—the higher and the more uniform the negative charge density, the better is the chance of the material being non-thrombogenic (tubes of various metals were implanted in the canine thoracic aorta or the canine thoracic inferior vena cava—metals which have negative standard electrode potential tended to function longer in dogs than those which registered positive potential; with insulator materials using streaming potential to determine surface charge characteristics and using untreated, chemically treated and electrically treated Teflon tubes, the more negative the surface the more useful the material) [92].

11.5 Cell Culture/Seeding Peculiar to Each Cell

11.5.1 Human Microvascular Endothelial Cells (HMEC-1)

Human Microvascular Endothelial Cells (HMEC-1) were recovered from the molecular biology departmental bank of the University of Ulster. Cell cultures were maintained in MCDB-131 supplement with L-glutamine (200 mM), 10 % foetal Calf Serum (FCS), epidermal growth factor (EGF) (10 ng/ml) and Penicillin (20 IU/ml), streptomycin (20 µg/ml). Cells were grown as mono layers in tissue culture flasks at 37 °C under 5 % CO_2/95 % air. Proteins are removed with two washings of phosphate-buffered saline (PBS: 8.2 g/l NaCl, 3.1 g/l Na_2HPO_4. $12H_2O$, 0.2 g/l $NaH_2PO_4.2H_2O$; pH 7.4). Harvesting of cells for subculturing or testing was performed with a trypsin solution (0.05 % trypsin/0.02 % EDTA), shortly afterwards, the trypsin was inactivated with the culture media and by centrifugation supernatants were separated from the cells. Cells were used when cells were about to confluent under exponential growth phase. The samples were sterilised with 70 % ethanol before they are taken into the hood and given sufficient time to dry inside the hood for the experiment and afterwards rinsed with PBS or distilled water. Every normal culturing sterility precaution was taken throughout the experiment. Approximately, 4.0×10^5 cells/ml were seeded on top of the silicon wafers (placed inside the Petri dishes) of the a-C:H samples. About 5.5×10^5 cells/ml were seeded into the rest of the samples, and about 1×10^3 cells/ml were seeded into the wells of 96 well culture plates that were coated with a-C:H and Si-DLC. The uncoated samples were used as control. For the MTT assay some control wells were also created and marked blank by the computer program. The MTT assay was carried on for about 56 h, some of the test using silicon wafer substrates were carried on for up to about 36 h, and the rest for 6 h (length of time indicated as the case may be).

11.5.2 Human Platelets

Whole blood was taken from normal healthy individuals into a standard tube with anticoagulant (3.8 % sodium citrate). Centrifugation at 1200 rpm for 5 min to get PRP (platelet rich plasma) and at 3000 rpm for 10 min to get PPP (Platelet poor plasma) was done as soon as possible. The platelet number in the PRP was diluted with PPP to $\sim 1 \times 10^8$ cells/ml by mixing PRP with PPP. The samples were sterilised with 70 % ethanol before they were taken into the hood and given sufficient time to dry inside the hood. Every normal culturing sterility precaution was taken throughout the experiment. About 1×10^8 cells/ml were seeded on top of the a-C:H and Si-DLC samples placed inside the Petri dish. Incubation was done at 37 °C under 5 %CO_2/95 % air for the 15, 30 and 75 min. Afterwards proteins were removed with two washings of phosphate buffered saline (PBS) before the fixation. The cells on the silicon wafer substrates were fixed with 2.5 % glutaraldehyde in 0.1 M phosphate solution, followed by 1 % osmium tetraoxide in 0.1 M phosphate solution. The samples were dried with increasing concentrations of ethanol successively and finally with hexamethyldisiloxane (HMDS).

11.5.3 Pericytes Cell Line

The cells are normal bovine retinal pericytes isolated from the eye at the University of Ulster biomedical science department (see appendix for procedure). The cells used for the test was of passage number 4 (not to exceed passage number 6 in this particular cell line). The media used for cell culturing was made up with DMEM (500 ml), FCS (100 ml), fungizone (5 ml) and Pen/Strept (2 ml). Cells were grown as mono layers in tissue culture flasks at 37 °C under 5 % CO_2/95 % air. Proteins are removed with two washings of phosphate buffered saline (PBS: 8.2 g/l NaCl, 3.1 g/l $Na_2HPO_4.12H_2O$, 0.2 g/l $NaH_2PO_4.2H_2O$; pH 7.4). Harvesting of cells for subculturing or testing was performed with a trypsin solution (0.05 % trypsin/0.02 % EDTA), shortly afterwards, the trypsin was inactivated with the culture media and by centrifugation supernatants were separated from the cells. Cells were used when cells were about to confluent under exponential growth phase. About 1–2 $\times 10^3$ cells/ml were seeded into various 96 well plates (coated with a-C:H, or Si-DLC, or uncoated control TCPS) for MTT assay. The samples were sterilised with 70 % ethanol before they are taken into the hood and given sufficient time to dry inside the hood for the experiment. Every normal culturing sterility precaution was taken throughout the experiment.

11.5.4 Human Embryonic Lung, L132 Cell Lines

The cell line originally purchased from ATCC (CCL-5), is epithelial and normal but with Hela characteristics. The passage number is important so the passage number (P33) of the cells used for the test was under the normal passage number. The culture media was composed of MEM (500 ml, with L-glutamine), FCS (50 ml), sodium pyruvate (5 ml), Penicillin/streptomycin (5 ml) and non-essential amino acids, NEAA (5 ml). Cells were grown as mono layers in tissue culture flasks at 37 °C under 5 % CO_2/95 % air. Proteins are removed with two washings of phosphate buffered saline (PBS: 8.2 g/l NaCl, 3.1 g/l $Na_2HPO_4.12H_2O$, 0.2 g/l $NaH_2PO_4.2H_2O$; pH 7.4). Harvesting of cells for subculturing or testing was performed with a trypsin solution (0.05 % trypsin/0.02 % EDTA), shortly afterwards, the trypsin was inactivated with the culture media and by centrifugation supernatants were separated from the cells. Cells were used when cells were about to confluent under exponential growth phase. The samples were sterilised with 70 % ethanol before they are taken into the hood and given sufficient time to dry inside the hood for the experiment, and afterwards rinsed with PBS or distilled water. Every normal culturing sterility precaution was taken throughout the experiment. About 12×10^3 cells/ml were seeded into various 96 well plates (coated with a-C:H, or Si-DLC, or uncoated control TCPS) for MTT assay.

11.5.5 V79 Cell Lines

The Chinese hamster fibroblast like normal cell line (V79) was originally bought from ATCC (V79-4; CCL-93). The culture media was composed of DMEM (500 ml), FCS (50 ml), Penicillin/streptomycin (5 ml), NEAA (5 ml) and sodium pyruvate (5 ml). Cells were grown as mono layers in tissue culture flasks at 37 °C under 5 % CO_2/95 % air. Proteins are removed with two washings of phosphate buffered saline (PBS: 8.2 g/l NaCl, 3.1 g/l $Na_2HPO_4.12H_2O$, 0.2 g/l $NaH_2PO_4.2H_2O$; pH 7.4). Harvesting of cells for subculturing or testing was performed with a trypsin solution (0.05 % trypsin/0.02 % EDTA), shortly afterwards, the trypsin was inactivated with the culture media and by centrifugation supernatants were separated from the cells. Cells were used when cells were about to confluent under exponential growth phase. About $1–2 \times 10^3$ cells/ml were seeded into various 96 well plates (coated with a-C:H, or Si-DLC, or uncoated control TCPS) for MTT assay. The samples were sterilised with 70 % ethanol before they are taken into the hood and given sufficient time to dry inside the hood for the experiment. Every normal culturing sterility precaution was taken throughout the experiment.

11.6 Statistics and Counting of Cells

11.6.1 Cell Fixation and Drying

The cells on the silicon wafer samples were fixed with 2.5 % Glutaraldehyde in 0.1 M phosphate solution for 5 min, followed by 1 % Osmium Tetraoxide in 0.1 M phosphate solution for 5 min. The samples were successively dried with increasing concentrations of ethanol and finally with hexamethyldisiloxane (HMDS).

11.6.2 Gold–Platinum Coating for Charging Compensation

The samples in silicon wafer substrates were coated with a conducting material (gold–platinum), after cell fixation and drying, to about 30 nm thickness, using Polaron E5000 SEM coating unit, in order to reduce charging and obtain a better contrast during scanning electron microscope (SEM) imaging.

11.6.3 SEM Imaging of Cells

A low-vacuum SEM Hitachi S-3200 N was used for the observation of the cells interaction with the Si-DLC (a-C:H:Si) films on silicon substrates. The conditions for SEM imaging were high secondary electron (HSE), aperture 3 (#3), 0°-tilt, scan-4, 5.0 kV, and $\times$200 magnification.

11.7 Stereological Investigations

The cells number counting over an area of 600 μm $\times$ 400 μm on the SEM image of various samples were performed using the UTHSCSA, ImageTool program developed in the department of dental diagnostic science at the University of Texas Health Science Center, San Antonio, by Wilcox et al. [93].

11.7.1 Stereological Investigation and Statistical Analysis (Endothelial and Other Cells)

Human microvascular endothelial cells (HMEC-1) were obtained from the molecular biology department of the University of Ulster at Jordanstown, Northern Ireland. Cell cultures were maintained in MCDB-131 supplement with L-glutamine

(200 mM), 10 % foetal calf serum (FCS), EGF (10 ng/ml) and Penicillin (20 I. U/ml), streptomycin (20 μg/ml). Cells were grown as monolayers in tissue culture flasks at 37 °C under 5 %CO_2/95 % air. Proteins were removed with two washings of PBS. Harvesting of cells for subculturing or tests was performed with a trypsin solution. Shortly afterwards, the trypsin was inactivated with the culture media and by centrifugation supernatants were separated from the cells. Cells were used when they were about to confluent and under exponential growth phase. The samples were sterilised with 70 % ethanol before they were taken into the hood and given sufficient time to dry inside the hood (and afterwards rinsed with PBS or distilled water). Every normal culturing sterility precaution was taken throughout the experiment. Approximately, 4×10^5cells/ml were seeded on top of the DLC and Si-DLC samples placed inside the petri dishes, and about 1×10^3cells/ml were seeded into the wells of 96 well culture plates that were coated with DLC and Si-DLC.

The uncoated samples were used as control. For the MTT assay some control wells were also created and marked blank. The cells for the MTT assay were seeded for a total of about 56 h. The cells on the silicon wafer substrates were fixed with 2.5 % glutaraldehyde in 0.1 M phosphate solution for 5 min, followed by 1 % osmium tetraoxide in 0.1 M phosphate solution for 5 min. The samples were dried with increasing concentrations of ethanol successively and finally with HMDS.

11.7.2 Stereological Investigations and Statistical Analysis (Platelets)

The cell number counting over an area of 600 μm × 400 μm on the SEM image of various samples was performed using the ImageTool program [93]. In order to cover a statistically reasonable large area of the tested film area, several ×200 (higher magnifications cover only very small sample area) images of the SEM were acquired (the SEM stage with the mounted samples was moved ≥ 2 mm in both *X* and *Y* directions before SEM was acquired in order to avoid scanning same area twice) for counting the number of platelet aggregates. This is because platelets are numerous ($\sim$300,000 cells/μl) and the average size of platelets is very small ($\sim$2 μm). In estimating the number of adherent platelets, high magnification (×1500) is used to enable visibility of platelet-full morphology and counting. However, at such high magnifications, the sample areas covered by the SEM scan become so small that the estimation of the number of adherent platelets may become subjective if several images were not taken at different spots for each sample and the analysis of these painstakingly recorded and averaged. The effect of silicon doping on the mean of the number of platelet aggregates counted on the films examined was tested using a two-tailed heteroscedastic *t*-test to compare group means for the undoped and silicon-doped films that had an unequal variance in the number of platelet aggregates counted. Statistical significance was defined as a *p*-value of <0.05.

11.8 Photo-Fluorescent Imaging of Cells/Tissues

In photo-fluorescent imaging, fluorophores (fluorescent compounds: eg fluoroscein, rhodamine, luminol) are incorporated to the cell/tissue to be examined in order to label the sample. Fluorophores naturally absorb light at one wavelength and emit at a longer wavelength following some energy transitions. A fluorophore on absorbing a photon has its outer shell of electron excited from a ground to an excited energy level, this energy can be released as a thermal radiation (with the electron returning to the ground state) or part of this energy can be transferred to the molecular environment (e.g. cell/tissue) with the remainder photon energy emitted (photon with less energy and longer wavelength). This absorption and emission of photons creates contrasts which can be utilised in the imaging process to image structures at a molecular level in either live or fixed cells/tissues. The temperature and the micro-molecular environment do affect the fluorescent process, making different molecules of the same fluorophore to release different amounts of energy and creating a range of emission spectrum. These days, the molecular structure of the fluorescent material can be modified to target specific regions or molecules within a cell or tissue in order to study the entity of interest. Thus the chosen photo-fluorescent molecule can be used to label specific proteins and/or transfect (genetically alter) cells in order to insert, for example a fluorescent peptide called green fluorescent protein (GFP) in the native protein of the cell.

11.8.1 Typical Sample Preparation for Photo-Fluorescent Microscopy

Place samples in 6 well plate in triplicate and seed with 1×10^5 cells (3 ml media) and incubate at 37 °C and 5 % CO_2 for 24 h. Fix cells using a solution of 4 % paraformaldehyde and 2 % sucrose in PBS for 20 min; bovine serum albumin (BSA) in PBS and then permeabilise using buffered 0.5 % Triton X-100 (0.5 % Triton supplemented with 20 mM Hepes buffer, 300 mM sucrose, 50 mM NaCl and 3 mM $MgCl_2$) by chilling to 0 °C for 5 min. Wash samples again with 1 % BSA/PBS. Add TRITC-conjugated phalloidin solution at a concentration of 10 μg/ml, in 1 % BSA/PBS, for 20 min at room temperature. Then remove the phalloidin, wash samples and mounte on microscope slides with glycerol. Observe samples with, for example a Confocal laser scanning microscope (CLSM). Finally, analyse cell shape factor and cell spreading area from the micrographs. The software calculates the shape factor using the formula 4π (area/perimeter)^2 which gives a value between zero and one, a value of one being a perfect circle.

11.9 Biocompatibility and Hemocompatibility Models

Several models for assessing biocompatibility and haemocompatibility of materials in vitro exist (Fig. 11.1). These models are used in an attempt to find a platform for explaining what actually goes on at the material-biointerfaces. Interestingly, all these are influenced by electron and ionic exchanges at these interfaces. The balance (ratio) of non-adhesive to adhesive proteins, for example say albumin–fibrinogen ratio is thought to depict how these models tend to overlap and therefore all together may be important in interpreting material-biointerfacial interactions.

11.9.1 Proteins-Adhesive and Non-adhesive Proteins

This model is based on adhesive verses non-adhesive protein interactions on surfaces, and/or Vroman effect of protein adsorption, where proteins and the adhesion molecules compete for specific binding sites. It is now known that proteins either present in serum or secreted by the cells play a key role in the adhesion and spreading of the cells on the substrate biomaterial. The existing hypotheses are as follows [84–86]:

1. Protein adsorption comprises the initial interaction of a foreign material with blood (only the outermost $\sim$1 nm range of the surface is involved in the interfacial interaction). Exposure of an organic-free surface to fresh flowing

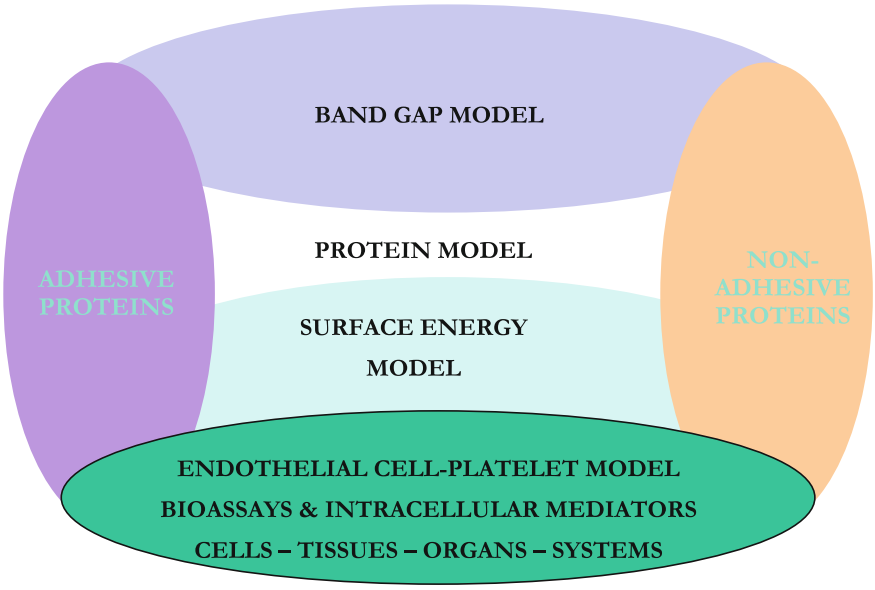

Fig. 11.1 Overlapping models for assessing material-biointeractions

blood for as little as 5 s, leads to its' complete coating by a very uniform, tenaciously adherent proteinaceous film. Thus the focus of attention has shifted from the substrate as the inducers of thrombogenicity, to the substrate as the dictators of a special configuration of adsorbed protein molecules that will favour or inhibit the subsequent events, including activation of the clotting mechanism and adhesion of platelets [94, 95].

2. The composition and organisation of the initial protein layer are determined by the surface properties of the material.
3. The composition and organisation of the initial protein layer mediates subsequent platelet interactions in vivo, and may also determine long-term effects.
4. In vitro protein adsorption studies are relevant to in vivo behaviour in humans.
5. The heat evolved on adsorption of proteins can lead to their denaturation on the surface; the magnitude of the heat evolved may be determined by the surface composition.
6. Hydrophobic surfaces will tend to adsorb protein more 'strongly' than hydrophilic surfaces, leading to greater denaturation of proteins on the hydrophobic surfaces.
7. Fibrinogen dominates the initial protein layer on most foreign materials and fibrinogen adsorption leads to high thrombogenic potential for that surface.
8. A layer of adsorbed albumin reduces in vitro platelet adhesion; materials that preferentially adsorb albumin will be antithrombogenic in vivo.
9. Certain other specific proteins may also adsorb and have a significant influence on subsequent events (e.g. CIG, or fibronectin, VWF, complement factors, high molecular weight kininogen, lipoproteins, etc.)
10. The various carbohydrate components of adsorbed glycoproteins may play an important role in the recognition of the biomaterial as foreign and in the subsequent events leading to thrombus deposition.

11.9.2 Surface Energy Model

Materials surface energy (and/or contact angle) is known to influence protein and cellular interactions on these surfaces. The actual interaction superseding depends on the properties of the surface and/or the biomolecule(s) arriving on the surface. Some of the existing hypothesis is stated above (Sect. 11.4), for example: 'a material with a critical surface tension of about 25 dyn/cm will have a low thrombogenic potential'. It is important to know that that the contact angle based of single liquid cannot give a good or accurate indication of the material's surface chemistry. There is need to use more than one liquid for measuring the contact angle, essentially a polar liquid on one hand and a dispersive liquid on the other. Surface energy of the material can be calculated from the contact angles values obtained using more than one liquid if the appropriate equations are applied. The calculated surface energy can equally be resolved into the surface energy components (by the use of appropriate equation/method, e.g. DLVO (Derjaguin–Landau–Verwey–Overbeek), Owens–Wendt, Van Oss–Chaudhry–Good): the Lifshitz-van

der Waals dispersive, the polar and the acid–base components. Equally the hydrophobic and the hydrophilic forces can be assigned. It may be possible to relate the biocompatibility of various materials to the appropriate surface energy components (and/or the total surface energy), the hydrophobic or hydrophilic energies and to determine the major contributing component in the biocompatibility behaviour.

11.9.3 Band Gap Model

Both materials' surfaces and the interacting biomolecules have got some electronic properties and more so when the two different interacting surfaces come into close ranges/contact. The band gap of the biomaterial under investigation can be related to that of the interacting biomolecule or protein. It is possible to predict the biomaterial–biomolecule interactions based on the distribution of electrons (or density of states, DOS), or contact potential difference (CPD), work function (WF) and/or band gap. The complexity and dynamic nature of these interactions have to be taken into account. If some electrons move from their occupied valence band level in the biomolecule to the free state of the biomaterials surface, it is expected that the biomolecules morphology could change or denature. This is only possible where the energy gap at the biomaterial–biomolecule interface allows a charge transfer. Chen et al. [96] studied the hemocompatibility of $Ti(Ta^{+5})O_2$ and reported an improved biocompatibility based on the band gap of $Ti(Ta^{+5})O_2$ being 3.2 eV compared to 1.8 eV of fibrinogen arriving on the surface. Thus because the band gap of fibrinogen is within that of $Ti(Ta^{+5})O_2$, it is not possible to affect electron transfer from the protein to the materials surface, and less amount of fibrinogen become adherent on the surface, which subsequently led to less adherent platelets.

11.9.4 Surface Topography, Roughness and Patterning

Surface topography, roughness and patterning have been implicated in altering protein adhesion and conformational changes. Studies creating various patterns on surfaces have indicated the implication of having various features of shape, size and depth dimensions on the surfaces to the degree of information gained on cellular and developmental biology [97]. It is almost impossible to change surface pattern without changing the chemical, physical and biological interactions. The author is of the opinion that this parameter is important in understanding the processes of developmental biology rather than directing dictation biocompatibility interactions. The experimental data presented in this chapter by the author is based on using samples with same and similar ultrasmooth surfaces having a non-statistically different surface topography, roughness and patterns.

11.9.5 Endothelial-Platelet Model

The seeding of bovine thoracic endothelial cells on cellulose surfaces with increasing hydrophobicity resulted in increased endothelial cell adhesion and proliferation and decreased migration [98]. Investigation on endothelial-specific cell adhesion to peptide sequences on different extra cellular matrix (ECM) molecules grafted on to various surfaces reveal that the arg-glu-asp-val (REDV) sequence from fibronectin was selective for the adhesion of endothelial cells but not fibroblasts, smooth muscle cells, or activated platelets where other sequences like arg-gly-asp (RGD), tyr-ile-ser-gly-arg (YISGR) or pro-asp-ser-gly-arg (PDSGR) were implicated [99]. The material–microvascular endothelial cellular interaction could be related inversely to those of platelets (in vitro and in vivo) since increased platelets aggregation/adhesion on a material could be associated with increased potential of a material to induce clotting [36], whilst increased endothelial–material adhesion could be associated on the other hand with an increased potential of a material not to induce clotting [40] (Fig. 11.2). Further detail of this model is implied in the discussions below [35, 36, 39, 40].

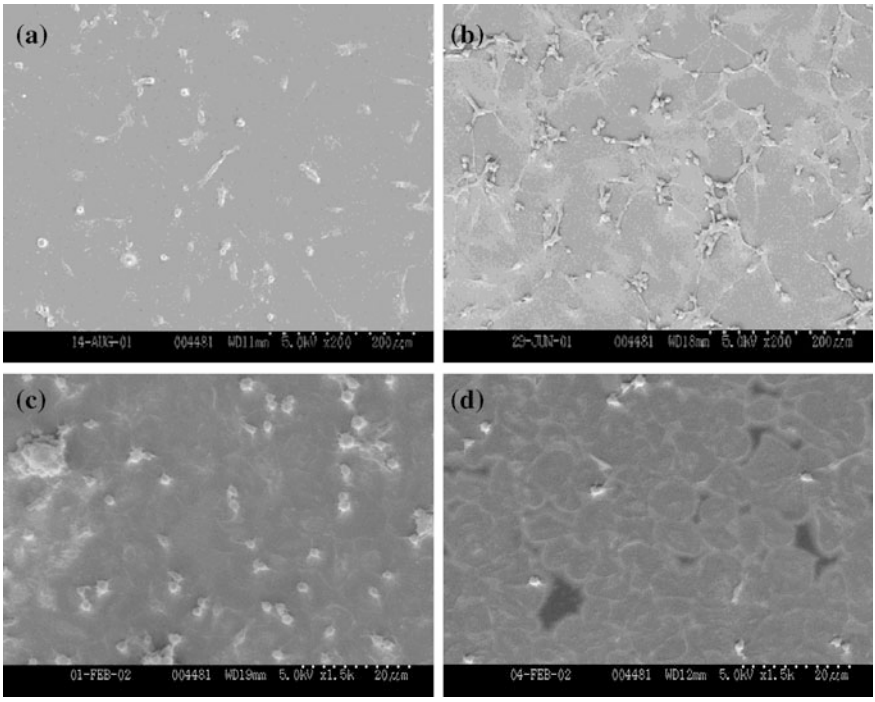

Fig. 11.2 Endothelial-Platelet model: **a** endothelial cells on DLC, **b** endothelial cells on Si-DLC, **c** platelets on DLC and **d** platelets on Si-DLC thin films

11.10 Carbon-Based Materials Interaction with Selected Proteins and Cells

When a cell is coming in contact with a biomaterial the degree of interaction can generally be taken as adsorption, contact, attachment and or spreading [29]. For activated platelets five stages of spreading can be described according to the increasing degree of activation [100]:

1. Round or discoid with no pseudopodia;
2. Dendritic, early pseudopodial with no flattening;
3. Spread-dendritic, intermediate pseudopodial with one or more flattened pseudopodia, but with no spreading of the cell body;
4. Spreading, late pseudopodial with the cell body beginning to spread;
5. Fully spread morphology, the cell is well spread with no distinct pseudopodia.

11.11 DLC Interactions with Fibroblasts In Vitro

The body's connective tissues can be classified as proper connective tissue (subdivided into loose and dense connective tissue proper), fluid connective tissues (subdivided into blood and lymph) and supporting connective tissues (subdivided into the cartilage and the bone). Fibroblasts are the most abundant permanent residents of the connective tissue proper and are the only cells always present in it. Fibroblasts secrete hyaluronans (a polysaccharide derivative) and proteins, both of which interact in the extracellular fluid to form proteoglycans that make ground substances viscous. They also secrete protein subunits that interact to form large extracellular fibres which could create loose/open framework or densely packed framework.

11.11.1 Human Fibroblasts

Dowling et al. [101] carried out a cell adhesion test on a DLC (obtained by saddle beam deposition) partially coated 2.8 cm diameter stainless steel disc using human fibroblast cell line and reported a very good cell adhesion and good spreading of the cells on the coated as well as the non-coated surfaces of the disc [101].

Allen et al. [102] tested DLC-coated polysterene (coating obtained by the low temperature dual ion beam technique using a saddle field source) and control uncoated polysterene tissue culture plates with primary cultured human synovial fibroblast (HSFs) and reported that there was no statistically significant difference in the cell growth on both samples [102]. The LDH assay of the fibroblasts also indicate that DLC has not caused any significant level of cell toxicity when compared to the uncoated samples [102].

Mouse fibroblasts

Hauert et al. [103] examined the interaction of mouse fibroblast (3T3 cell line) with a-C:H:Si (0.2–22.5 at.% silicon addition) obtained with PACVD system and reported that the cells proliferated well on the coated culture dishes, that no influence like any toxic effect was observed from the Si–C bonds present on the surface to the growth and proliferation of the cells after 2 days of incubation [103]. Hauert et al. [103] concluded that the toxic effect described by Allen et al. [104] is caused by bulk Si-C not present in the a-C:H:Si thin film.

McColl et al. [105] and **Parker et al**. [106, 107] studied the interaction of DLC with 3T3-1 mouse fibroblasts in vitro. The 3T3-1 cell viability in inserts Millicell-PCF membrane with DLC coating and without coating were determined in their study by Trypan Blue dye exclusion and reported that the cells grew well in both control membrane inserts and DLC-coated sample hich implies that DLC is not cytotoxic to the growing 3T3-1 cells.

Thomson et al. [108] following exposure of mouse fibroblast (C3H10T1/2 cell line) to DLC-coated 24 well culture plate obtained by saddle field source (using acetylene, butane or propane source gas) over a period of 7 days, reported that there was no significant difference in release of lactate dehyrogenase (LDH) in any of the coated samples and the uncoated control sample. Also their photomicrographic morphological examination confirmed that there was no cellular damage in the coated samples when compared to the uncoated control samples [108].

Murine fibroblast

Dowling et al. [101] did a cytotoxicity study using murine fibroblast to examine DLC-coated alloy, titanium alloy and a plastic sample using SEM after 6-, 24- and 48-h incubation period. According to Dowling et al. [101] there was good cell morphology, adhesion, density and spreading observed on both the DLC-coated alloy and on the plastic, but the tinanium alloy surface exhibited many cell death, thus the DLC coating acts as a barrier between the titanium alloy and the murine fibroblast cell line and demonstrates a low level of cytotoxicity.

11.11.2 DLC Interaction with Osteoblasts In Vitro

Osteoblasts are the bone forming cells and have major role in mineralisation leading to osseointegration of a prosthesis.

Allen et al. [109] investigated the effect of DLC coatings (obtained by fast atom bombardment from a hexane precursor) deposited on polystyrene 24-well tissue culture plates on two osteoblast-like cell lines cultured on the uncoated and DLC-coated plates for periods of up to 72 h and by measuring the production of three osteoblast-specific marker proteins: alkaline phosphatase, osteocalcin and type I collagen. According to Allen et al. [109] there was no evidence that the presence

of the DLC coating had any adverse effect on any of these measured parameters which are indicative of metabolic processes in these osteoblast-like musculoskeletal system cells.

Schroeder et al. [110] evaluated a new surface coating for bone-related implants by combining the hardness and inertness of a-C:H (DLC, obtained by a combination of radio frequency plasma and DC magnetron sputtering deposition techniques) films with the biological acceptance of titanium. They incorporated different amounts of titanium (7–24 atm.%) into a-C:H films by a combined radio frequency (RF) and magnetron sputtering set-up. Their X-ray photoelectron spectroscopy (XPS) of air-exposed a-C:H/titanium.
(a-C:H/Ti) films revealed that the films were composed of TiO_2 and TiC embedded in and connected to an a-C:H matrix. They performed cell culture tests using primary adult rat bone marrow cell cultures (BMC) to determine effects on cell number and on osteoblast and osteoclast differentiation. According to Schroeder et al. [110] addition of titanium to the carbon matrix, leads to cellular reactions such as increased proliferation and reduced osteoclast-like cell activity, while these reactions were not seen on pure a-C:H films and on glass control samples, thus they concluded that a-C:H/Ti could be a valuable coating for bone implants, by supporting bone cell proliferation while reducing osteoclast-like cell activation.

Du et al. [74] reported based on their study of interaction between osteoblasts (isolated from 4-day-old Wistar rats) and DLC as well as CN (carbon nitride) thin films (obtained by IBAD technique), that the osteoblasts attach, spread and proliferate on both DLC and CN sample surfaces without apparent impairment on the cell physiology [74].

Allen et al. [102] have also reported that DLC interact well with human 'osteoblast-like' cell line SaOS-2. When they compared the growth of human osteoblasts in both the DLC-coated and non-coated polysterene plates, they found out that there was similar level of growth observed in both samples, and the osteoblasts adhered well to the DLC samples and produced extensive filopodia when viewed under the SEM. The LDH assay of the osteoblast-like cells also indicated that DLC has not caused any significant level of cell lysis/toxicity when compared to the uncoated samples [102].

11.11.3 DLC Interaction Kidney Cells In Vitro

Human embryonic kidney (HEK-293) cells

Lu et al. [111] observed the interaction of DLC (obtained by ion beam assisted deposition) with HEK-293 cells using a haemocytometer for cell counting and Trypan Blue dye exclusion for assessing HEK-293 cell viability in DLC-coated P-35 dishes. According to Lu et al. [111] HEK-293 cells grew well, there was no delay attachment to the DLC-coated dishes compared to the control and that both

the cells growing in the DLC-coated and the control dishes had cell viability of 60 % at the first day of incubation which increased to >90 % at the second day of incubation.

Baby hamster kidney cells

Evans et al. [112] examined the interaction of DLC obtained using saddle field source and baby hamster kidney cells and reported good cell adhesion on the coated surfaces indicating good cell compatibility.

11.11.4 Mutagenicity Evaluation of DLC

Dowling et al. [101] performed a mutagenicity test (Ames test) on DLC coatings on stainless steel samples coated on both sides and uncoated samples using five strains of *Salmonella typhimurium* bacteria (TA-98, TA-100, TA-1535, TA-1537, TA-102) with and without metabolic activation in accordance with the method originally reported by Ames et al. [113]. According to Dowling et al. [101] both the DLC and the stainless steel samples were not mutagenic as they induced no significant increase in the number of revertants of the five strains of *Salmonella typhimurium* tested.

11.11.5 DLC Interaction with Specific Cells (Hemocompatibility)

Bruck [114] has pointed to the importance of specie-related haematological differences of experimental animals in the proper assessment of biomaterials for human use. He pointed out that 'the terms "biocompatibility" and "hemocompatibility" are often used inaccurately to denote the performance of biomaterials based on single or few in vitro tests; these tests frequently ignoring considerations of hemorheological parameters, damages to the reticuloendothelial system, and haematological species-related differences' [114]. DLC, deposited on stainless steel and titanium alloys used for components of artificial heart valves has been found to be biologically and mechanically capable of improving their performance [115]. Devlin et al. [116] has shown improvement of carbon/carbon composite prosthesis by DLC coating [116].

11.11.6 DLC Interaction with Endothelial Cells

Endothelium is nature's haemocompatible surface, and the performance of any biomaterial designed to be haemocompatible must be compared with that of the

endothelium [117]. Endothelial hemocompatibility can be considered under three areas: the interaction between the endothelium and circulating cells (mainly platelets and leucocytes—close interactions between erythrocytes and endothelium are rare); the modulation of coagulation and fibrinolysis by endothelium; and other activities that affect the circulating blood or the vascular wall. Under normal circumstances, platelets do not interact with the endothelial cells—that is platelet adhesion to the vessel wall and the formation of platelet aggregates do not normally take place except when required for haemostasis. Hence, the surface of endothelial cells does not promote platelet attachment [117]. The formation of platelet aggregates in close proximity to the endothelium is also rendered difficult by prostacyclin (PGI2), a powerful inhibitor of platelet aggregation secreted by the endothelial cells. Prostacyclin can be secreted by endothelial cells in culture as well as by isolated vascular tissue [118]. The vascular endothelium is now known to be a dynamic regulator of haemostasis and thrombosis with the endothelial cells playing multiple and active (rather than passive) roles in haemostasis and thrombosis [119, 120]. Many of the functions of the endothelial cells appear to be antithrombotic in nature. Several of the 'natural anticoagulant mechanisms', including the heparin–antithrombin mechanism, the protein C-thrombomodulin mechanism, and the tissue plasminogin activator mechanism, are endothelial-associated. Among the proteins on the endothelial surface is antithrombin III [121] which catalyses the inactivation of thrombin by heparin. Endothelial cells also have heparan sulphate and dermatan sulphate (glycosaminoglycans) on their surfaces [122] which are known to have anticoagulant activity. On the other hand, the endothelial cells also appear to be capable of active prothrombotic behaviour in some extreme conditions of anticoagulation, because endothelial cells synthesise adhesive cofactors such as von Willibrand factor [123], fibronectin and thrombospondin [124]. Endothelial cells are now known to play crucial roles in a large number of physiological and pathological processes [125–134]. Most of these physiopathologic events take place at the microvasculature (capillary beds) which constitutes the vast majority of the human vascular compartment. Thus it becomes vital to conduct hemocompatibility studies using microvascular endothelial cells. This is also vital because not all endothelial cells are alike. Endothelial cells derived from the microvascular structures of specific tissues differ significantly from large-vessel endothelial cells [135–140]. The study of human microvascular endothelial cells has been limited due to the fact that these cells are difficult to isolate in pure culture, are fastidious in their in vitro growth requirements, and have very short life span undergoing senescence at passages 8–10. Ades et al. [141] overcame these problems by the transfection and immortalization of human dermal microvascular endothelial cells (HMEC). These cells termed CDC/EU.HMEC-1 (HMEC-1) do retain the characteristics of ordinary endothelial cells (HMEC) and could be passaged up to 95 times, grow to densities 3–7 times higher than ordinary HMEC and require much less stringent growth medium [141]. HMEC-1 is just like ordinary endothelial cells and exhibits typical cobblestone (or polyhedral) morphology when grown in a monolayer culture.

Van Wachem et al. [142] reported that in their investigation of in vitro interaction of HEC and polymers with different wettabilities in culture, optimal adhesion

of HEC generally occurred onto moderately wettable polymers. Within a series of cellulose type of polymers, the cell adhesion increased with increasing contact angle of the polymer surfaces [142]. Moderately wettable polymers may exhibit a serum and/or cellular protein adsorption pattern that is favourable for growth of HEC [142]. Van Wachem et al. [143] reported that moderately wettable tissue culture poly(ethylene terephthalate) (TCPETP), contact angle of 44° as measured by captive bubble technique, is a better surface for adhesion and proliferation of HEC than hydrophobic poly(ethylene terephthalate) (PETP), contact angle of 65° suggesting that vascular prostheses with a TCPETP-like surface will perform better in vivo than prostheses made of PETP.

11.11.7 Nitrogen-Doped DLC Interaction with Endothelial Cells

This section reports the initial response of atomic nitrogen-doped diamond-like carbon (DLC) to endothelial cells in vitro. The introduction of nitrogen atoms/molecules to the diamond-like carbon structures leads to atomic structural changes favourable to the thriving of human microvascular endothelial cells, thus the bioresponse of ordinary diamond-like carbon could be improved with atomic nitrogen doping. Whilst the semiconductivity and stress-relieving properties of nitrogen in DLC are thought to play a part, the increase in the non-bonded N atoms and N_2 molecules in the atomic-doped species (with the exclusion of the charged species) seems to contribute to the improved bioresponse [39, 40]. The bioresponse is associated with a lower WF and slightly higher water contact angle in the atomic-doped films, where the heavy charged particles are excluded, as confirmed by SIMS analysis. The films used in the study were synthesised by RF PECVD technique followed by post-deposition doping with nitrogen, and afterwards the films were characterised by XPS, Raman spectroscopy, SIMS and Kelvin probe. The water contact angles were measured, and the counts of the adherent cells on the samples were carried out. This study is relevant to improving biocompatibility of surgical implants and prostheses.

The results in Fig. 11.3 show the water contact angle of uncoated, DLC-coated, N-DLC-coated as well as 'SN'-DLC-coated samples. The water contact angle increased with DLC coating when compared with uncoated sample. However, the contact angle value for the N-doped film is slightly lower than that of DLC whereas the values for the doping where the sweep plate (to remove ions) were employed is higher. The adherent endothelial cells are shown in Fig. 11.4. The number of adherent cells seems to be highest for the doped films (where the sweep plates were employed), followed by the doped films including the ionic species, DLC and finally, uncoated sample. This shows that the trend in the endothelial behaviour seems not to be directly related to the degree of hydrophobicity. These preliminary results seem to suggest therefore that hydrophobic films, with additional properties like decreased compressive stress, increased atomic networks and decreased

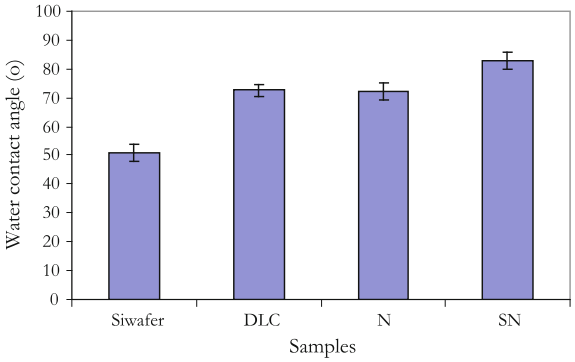

Fig. 11.3 Water contact angle of control silicon wafer, DLC and N-doped DLC obtained by the water drop optical technique

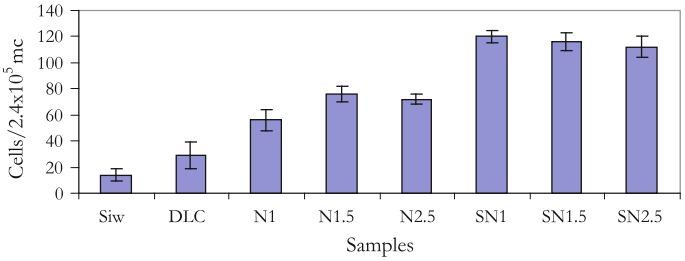

Fig. 11.4 HMEC attachment per 2.4 × 10^5 μ^2 of a-C:H:N (SN1-2.5 h—with use of sweep plate to remove ions, and N-films doped with ions included), a-C:H (DLC) thin films and bare silicon wafer (Siw) control samples

graphitic clusters as well as semiconductivity [36] may be favourable to human microvascular endothelial cellular attachment and proliferation. Other researchers have reported surface properties expressed in terms of hydrophobicity to be the key factor dictating the type and conformation of adsorbed proteins and therefore the cell adhesion. The seeding of bovine thoracic endothelial cells on cellulose surfaces with increasing hydrophobicity resulted in increased endothelial cell adhesion and proliferation and decreased migration [98]. Investigation on endothelial-specific cell adhesion to peptide sequences on different ECM molecules grafted on to various surfaces reveal that the arg-glu-asp-val (REDV) sequence from fibronectin was selective for the adhesion of endothelial cells but not fibroblasts, smooth muscle cells or activated platelets where other sequences like arg-gly-asp (RGD), tyr-ile-ser-gly-arg (YISGR) or pro-asp-ser-gly-arg (PDSGR) were implicated [99]. The material–microvascular endothelial cellular interaction could therefore be related inversely to those of platelets (in vitro and in vivo) since increased platelets aggregation/adhesion on a material could be associated with increased potential of a material to induce clotting [36], whilst increased endothelial–material adhesion

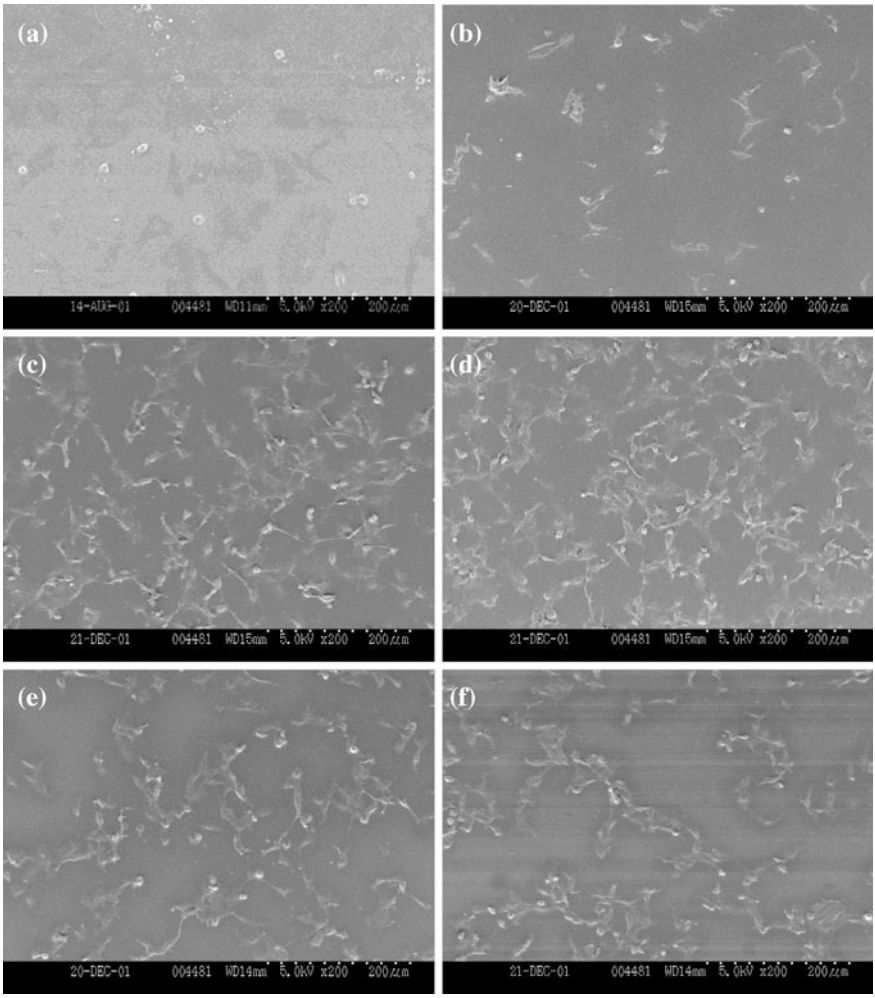

Fig. 11.5 SEM micrographs of endothelial cells attached to a-C:H:N thin films, ×200; **a** Uncoated substrate, **b** DLC-coated substrate, **c** sample 'SN1' (1 h exposure to atomic nitrogen), **d** sample 'SN2.5', atomic species for 2.5 h; **e** 'N1' (1 h, atomic and charged species) and **f** 'N2.5' (2.5 h, atomic and charged species)

could be associated on the other hand with an increased potential of a material not to induce clotting. Figures 11.4 and 11.5 compares directly the cell adhesion results obtained with both types of nitrogen species used for the doping over the duration of ∼1–2.5 h. The doping changes with time seem to be insignificant (1 h compared with 2.5 h). This is not surprising as only a small amount of impurities are usually required to effect a change in the microstructure, and the doping effects seem peak after some time. It seems that the films obtained with the use of sweep plates (to remove ions) encouraged more endothelial growth and proliferation compared

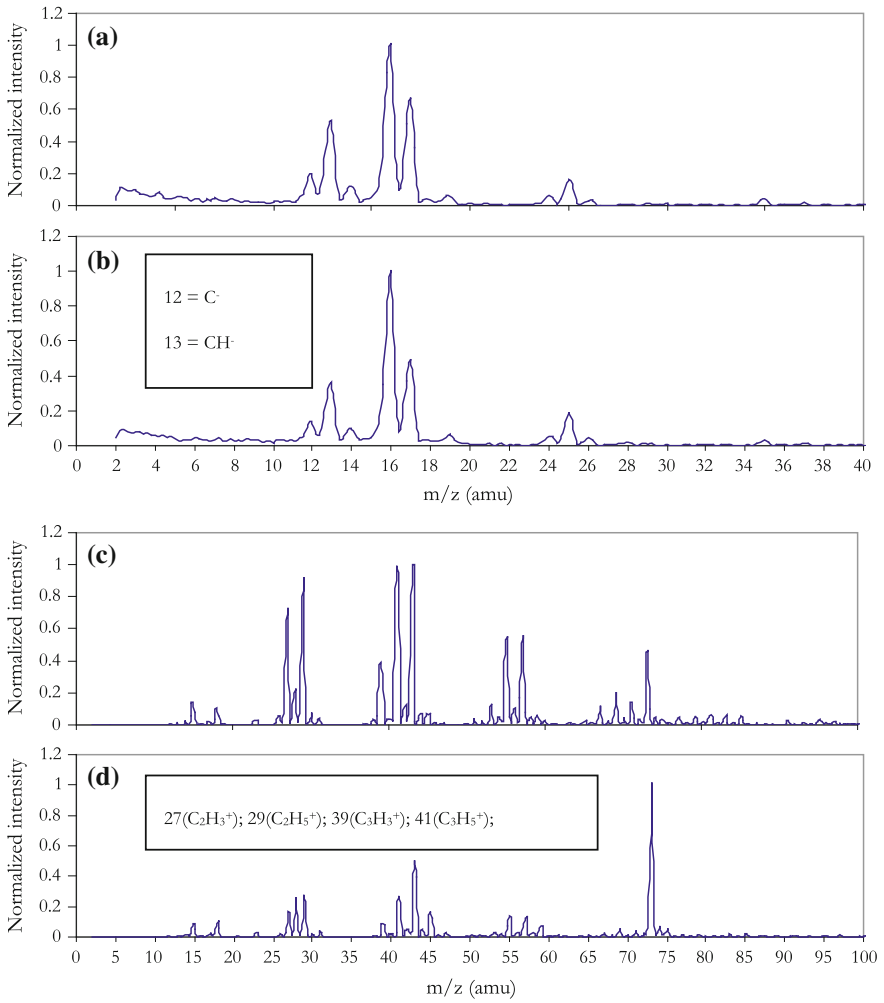

Fig. 11.6 SIMS analysis of nitrogen-doped DLC thin films: negative ions **a** 'N', **b** 'SN'; positive ions, **c** 'N', **d** 'SN'

to its counterpart. This is thought to be due to some changes in the films microstructure and chemical bonding as revealed by XPS and SIMS techniques.

The results of the atomic chemical bonding inferred from the XPS peak assignment suggest an increased atom percentage of the non-bonded N atoms (Peak at 399.6 eV) and N_2 molecules (Peak at 401.1 eV) in the films where the sweep plates were used to remove the ions. The non-bonded N atoms in these films are up to five times ($\times 5$) higher when compared to their counterparts [39].

The SIMS analysis of the films is shown in Fig. 11.6, and is displayed as normalised intensity of mass to charge ratios of various ions detected. The negative

ion scans for both the 'N' and 'SN' type films are very similar. These ions are of low m/z ratio (<25 amu), Fig. 11.6a, b. However, the relative/normalised intensity of the positive ions seems to be different, and the detected ions include heavier particles of higher m/z ratio (Fig. 11.6b, c). The relative intensity of the heavier particles of higher m/z ratio (>25 < 73 amu) seems to be higher in the 'N' type films. The heavier ions associated with higher plasma energies may be important during processing in increasing the films density, and establishing the integrity of the film's surface barrier to gas/moisture percolation, as the peak at 73 [$H_3O(H_2O)_3^+$] seems to be smaller in the 'N' type films (Both films were subjected to deionised water drops that were dried up afterwards, before SIMS analysis). The pattern of the SIMS depth profile with time is shown in Fig. 11.7. The positive ions depth profile was performed to probe for m/z corresponding to 14 (N^+, CH_2^+), 28 (N_2^+, $CHNH^+$, CO^+), and 30 (CH_3NH^+); and the negative ions depth profile for m/z corresponding to 14 (N^-, CH_2^-), 26 (CN^-) and 38 (C_2N^-). The depth profile result shows that the non-bonded N_2 (28 amu) species are relatively more intense and steadily distributed in the 'SN' type films (Fig. 11.7b), compared to its counterpart.

The structural vibration information gained by the Raman spectroscopy shows a slight difference. The Raman D and G peak positions shifted slightly to a higher energy as a result of the inclusion of the ionic species [39]. This may be indicative of an increased sp^3/sp^2 fraction in the film, also suggested by the XPS results [39].

The relative WF of the films as measured by the Kelvin probe technique shows that the relative work functions change from higher values ('N') films to lower values ('SN') films {Au–Au:250 mV, Au–N_2:200 mV, Au–SN2.5:100 mV, Au–SN1:75 mV}, Fig. 11.8. Kaukonen et al. [144] suggested based on their density function theoretical (DFT) calculation that a single N atom substitution at sp^3 or sp^2 site in a-C subsurface layers increases the total density of states (TDOS) below the energy gap resulting in Fermi energy (E_f) level moving down and the WF increasing. Whereas substitution on the sp^1 and sp^2 rings in the outer surface leads to TDOS increase near the conduction band edge with the Fermi level moving up and the WF decreasing. This decrease in the WF is thought to be dependent on the new states formed above the E_f following N substitution and a redistribution of the surface charges resulting in changes in the surface dipoles. Based on this interpretation it seems that N substitution in this study is dominant at the sp^1, sp^2 rings in the outer surface for 'SN' type N-doped films, that is, the 'SN' atomic species substitute preferentially at the sp^1 and sp^2 rings compared to the ionic N species. Nitrogen doping of a-C is known to increase the sp^2/sp^3 ratio and density function theoretical (DFT) calculations [144] suggest that N atoms positioned at an sp^3 site decrease their coordination number with resulting sp^2 N (or N with a non-planar threefold coordination). It therefore seems logical that N atoms positioned at sp^1 or sp^2 sites could increase the coordination number with resulting sp^2 N or sp^3 N, respectively. The Raman and XPS analysis suggest that both sp^3 C and sp^2 C are higher in the 'N' films, with the I_D/I_G ratios being equally higher. Thus its seems that in the 'N' type films where higher energy of the impinging N species are concerned, the more substitutions occur at the sp^3 sites, and thus decreasing the coordination number with resulting sp^2 N. On the other hand, it seems that

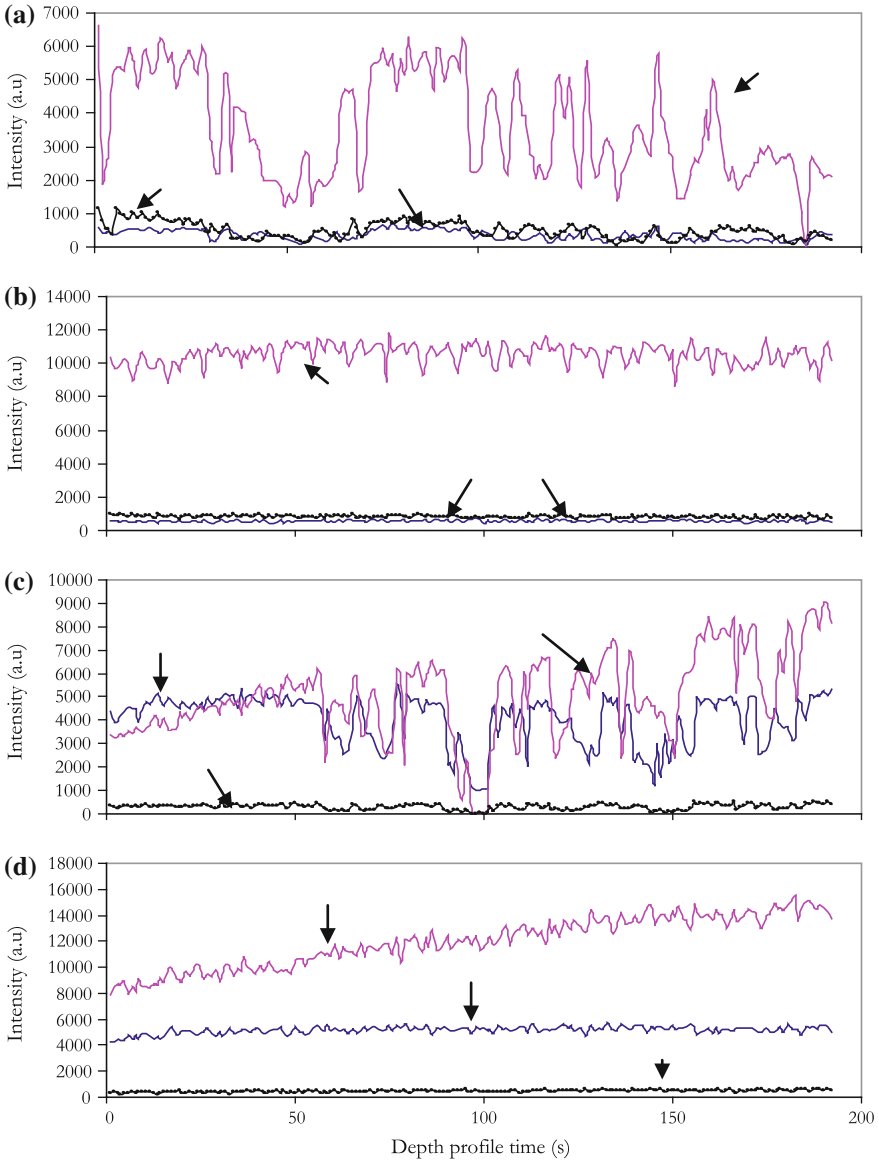

Fig. 11.7 SIMS depth profiling of some positive and negative ions: **a** + ions sample 'N', **b** + ions of sample 'SN'; **c** negative ions of sample 'N' and **d** sample 'SN'

relatively less substitution occurs in the 'SN' films. It is therefore not surprising that nitrogen incorporation into DLC as in the 'N' type species reduces the contact angle (increases the surface energy), whereas the N-neutral specie ('SN') doping increased the contact angle (slightly) in this study (Fig. 11.3).

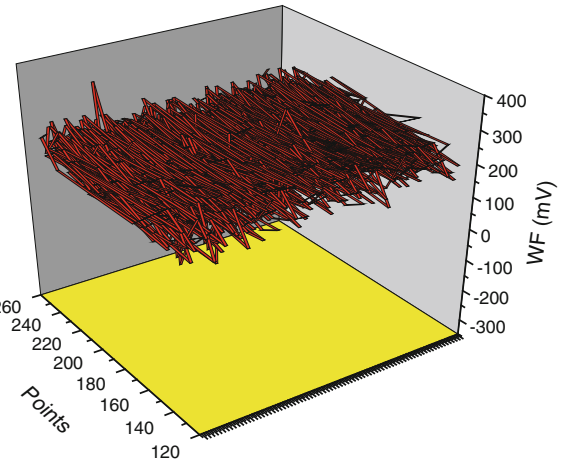

Fig. 11.8 The work function ('N2' film) over a scan area of 60 × 30 μm to 80 × 30 μm as determined by Scanning Kelvin Probe

Typical SEM imaging of the adherent cells on the film surfaces is shown in Fig. 11.5. Figure 11.5a, b shows the endothelial cell attachment on bare (uncoated) substrate and DLC-coated substrate, respectively. The worst bioresponse occurs on the bare substrate (Fig. 11.5a), followed by DLC coatings (Fig. 11.5b) and the best response is seen on the nitrogen-doped counterparts. However, it can be seen from the SEM images that there are better endothelial cell adhesion and proliferation on the 'SN' films (Fig. 11.5c, d) compared to 'N' films (Fig. 11.5e, f). Statistical analysis at 95 % confidence interval with 2-tailed paired sample analysis shows that there is a significant difference between uncoated samples and DLC-coated samples, between DLC and either 'N' or 'SN' type films, as well as between 'N' type and 'SN' type films.

Nitrogen-doped DLC thin films and their interaction with microvascular endothelial cells were examined. The nitrogen-doped DLC seems to have a better bioresponse compared to the undoped DLC thin films even though some of the N-doped films (where the ions were not excluded) have lower contact angle (more hydrophilic). Amongst the nitrogen-doped films, the films synthesised with the exclusion of ions seem to improve the bioresponse compared to its counterpart. The non-bonded N atoms in these films are higher and the contact angles obtained are also higher. Biocompatibility is therefore not simply related to hydrophobicity but may also relate to other materials micro and atomic structural changes induced by atomic nitrogen, like semiconductivity and films stress relieve.

11.11.8 DLC Interaction with Platelets

Platelets are small, granulated bodies 2–4 μm in diameter. They are round to spindle-shaped cytoplasmic fragments containing enzymes and prenzymes but no nucleus. There are about 300,000/μl of platelets in the circulating blood and they

normally have a half-life of about 4 days. The membranes of platelets contain receptors for collagen, vessel wall von Willebrand factor (vWF), and fibrinogen. When a blood vessel wall is severed, platelet adhere to the exposed collagen, laminin and vWF in the wall via intergrins. This process of platelet adhesion, unlike platelet aggregation does not require platelet metabolic activity [145]. However, binding of platelets to collagen initiates platelet activation (this can also be induced by ADP or thrombin). The activated platelets change shape, put out pseudopodia, discharge their granules which attract other platelets to stick to other platelets, a process known as platelet aggregation. The cytoplasm of platelets contains actin, myosin, glycogen, lysosomes and two kinds of granules (dense granules and α-granules) which may be released after platelets are activated. The dense granules contain non-protein substances (includes serotonin, ADP and other adenine nucleotides) that are secreted in response to platelet activation and the α-granules contain secreted proteins other than hydrolases in lysosomes which includes clotting factors and platelet-derived growth factor (PDGF). Released platelet granules generate inflammatory response to injury, the white blood cells (leucocytes) are attracted by selectins and bind to integrins on endothelial cells leading to their extravasation through the blood vessel walls [145].

Platelet adhesion hypothesis:

1. Platelets adhesion on a foreign surface is a necessary precursor to platelet aggregation on that surface.
2. High platelet adhesion on a foreign surface is bad.
3. In vitro platelet adhesion is related directly to in vivo thrombus formation and embolisation on foreign surfaces.
4. Platelets adhere with different strengths on different sites.
5. Platelet adhesion and release reactions at foreign interfaces occur when specific platelet membrane receptor sites ‘recognise’ specific groups on the foreign surface (corollary: platelet adhesion is not a random process).
6. Some platelet release factors (e.g. serotonin and ADP from dense granules) enhance platelet aggregation on foreign surfaces, while the roles of others (platelet factor IV with its heparin neutralising activity, HNA, and β-thomboglobulin from α-granules) remain to be clarified.

Chen et al. [146] varied acetylene to argon flow ratios in the DLC obtained with plasma immersion ion implantation deposition technique in their study. According to Chen et al., the blood compatibility of DLC depends on the sp^3 to sp^2 ratio rather than absolute sp^3 or sp^2 content and that the blood compatibility becomes worse with larger sp^3 to sp^2 ratio [146].

Krishnan et al. [147] did a quantitative analysis of I-125 radio-labelled platelet to examine platelet adhesion (using radiscintigraphy techniques) on titanium and DLC-coated titanium and have shown that DLC-coated titanium exhibited a lower platelet adhesion compared to uncoated titanium [147].

Cui and Li [75] also studied platelet interaction with DLC-coated PMMA intraoccular lens and uncoated PMMA intraoccular lens (IOLs). Their result shows that DLC-coated PMMA-IOLs had a lower platelet adhesion compared to the uncoated sample [75].

Gutensohn et al. [148] studied the interaction of stents coated on both inner and outer surfaces with DLC (obtained by plasma-induced cold deposition technique) and human platelets. In their study they used DLC to achieve a uniform protective coating to reduce the release of metal ion, platelet activation and thrombogenicity. Flow cytometric analyses revealed significantly higher increase of mean channel fluorescence intensity for the platelet activation-dependent antigens CD62p and CD63 in non-coated stents compared to DLC-coated stents ($p < 0.05$). Patients undergoing coronary angioplasty and stenting procedures are known to be at higher risk for reocclusion and restenosis of vessel when plate express increased numbers of activation-dependent antigens [2, 3]. Of all the antigens they analysed that P-selectin (GMP-140) seems to play a key role and appears to be most closely associated with an increase in thrombotic risk [2, 3]. Using atomic adsorption spectrophotometry and inductively coupled plasma mass spectrometry analyses they have shown that there was a significant release of metallic ion in the non-coated stents compared to DLC-coated stents. As a consequence of reduced metal ion release due to DLC coating platelet activation was significantly lower in DLC-coated stents compared to the non-coated stents under otherwise identical experimental conditions [148].

Alanazi et al. [64, 65] evaluated the interaction of polycarbonate-coated DLC (obtained with CVD under varied deposition conditions), segmented polyurethane (SPU, usually used for fabrication of medical devices including artificial heart) and an amphiphilic block copolymer composed of 2-hydroxyethylmethacrylate (HEMA) and styrene (St) (HEMA/St; an excellent non-thrombogenic polymer was used as a negative control) with platelets in whole human blood. They used the parallel plate flow chamber and epifluorescent video microscopy (EVM) using whole human blood containing Mepacrine-labelled platelets perfuse at a wall shear rate of 100 s^{-1} at 1 min intervals for a period of 20 min. In their assessment of the optical penetration of their EVM system and the activation/adhesion of platelets, they concluded that the activation of platelets on PC-DLC compared with the other biomaterials was minimal, the surface roughness before and after the coating applied to blood contacting devices is insignificant (16–23 nm), the contact angle is improved after DLC coating, the contact angle and chemical composition are independent of film thickness, defects of DLC films can be caused by elevated substrate, and blood compatibility depends on deposition conditions [64, 65].

Jones et al. [33] studied interaction between rabbit platelets and components of a Ti-TiN-TiC-DLC multilayer system. They adopted an interlayer approach in order to achieve adequate adhesion between DLC coatings deposited by plasma-assisted CVD and titanium substrate. The substrate, interlayers and DLC were assessed for haemocompatibility and thrombogenicity using a dynamic blood method and interactions with rabbit blood platelets, respectively. The adhesion, activation and morphology of the platelets were determined by stereological techniques using

SEM. The coatings produced no significant haemolytic effect compared to the medical grade polysterene control. In contrast to the DLC coating, all of the interlayers showed a slight tendency towards thrombus formation during the later stages of the incubation [33].

Dion et al. [42] evaluated the in vitro platelet retention of the new prosthetic heart valve that has been designed by FII Company and Pr. Baudet which is composed of Ti6Al4V titanium alloy coated with DLC (obtained by chemical vapour deposition technique). The retention/adhesion of platelets was evaluated by analysing radioactivity on the exposed wall of test or control tubes through which a blood cell suspension containing ^{111}In-labelled platelets had circulated. Their results show that on DLC/Ti6Al4V platelets adhere twice the amount that they do on the reference material (a silicone medical grade elastomer, the behaviour of which in contact with blood is the same as that observed with the NIH recommended polydimethyl siloxane) [42].

Okpalugo et al. [36, 40]
The human blood platelets interaction with a-C:H:Si films has revealed a relation between the microstructure of a-C:H:Si and its level of platelets aggregation. An increase in contact angle (or lowering of surface energy) of a-C:H and a moderate increase in the intrinsic electron conduction (semiconduction)/decrease in WF may lead to decreased platelets aggregation implying an increase in clotting time (decreased rate of clotting), high surface energy (low contact angle), non-conduction (insulating films), and graphitisation seems to lead to an increase in platelet aggregation implying a decrease in clotting time and an increase in the rate of blood clotting. Thus the hemocompatibility and biocompatibility of a-C:H and a-C:H:Si seems to be dependent on its electrical properties as well as the surface energy and the microstructure of the thin film biomaterials.

Silicon-doped films show a much lower level of platelet aggregation [36]. This seems to correlate with the lowering of surface energy, CPD/WF, resistivity and degree/rate of graphitisation due to silicon doping. Bruck [52–54] observed clotting times six to nine times longer than those observed with non-conducting polymers and also observed little or no platelet aggregation on electroconducting polymers, when compared to non-conducting control samples. In this study, thermal annealing of a-C:H below 400 °C led to excellent performance similar to that observed in a-C:H:Si. This is attributed to the increased electroconduction without graphitisation at the lower annealing temperature of a-C:H (Fig. 4.2.1-4). Chen et al. [96] varied acetylene to argon flow ratios during the deposition of a-C:H obtained by plasma immersion ion implantation. According to Chen et al. [96], the blood compatibility of a-C:H depends on the sp^3 to sp^2 ratio rather than absolute sp^3 or sp^2 content and that the blood compatibility becomes worse with larger sp^3 to sp^2 ratio. The results of the surface roughness as obtained with the AFM have shown that all the films analysed have smooth surfaces [40].

The results of the Raman spectroscopy show an increase in the I_D/I_G ratios [34–40] with annealing temperature for the a-C:H films in agreement with earlier reports in the literature [149, 150] and also for the a-C:H:Si thin films. The increase

in I_D/I_G ratio on the annealing of a-C:H has been associated with the growth of crystallites structure in the a-C:H thin film. In the a-C:H films the increase in the I_D/I_G ratio with thermal annealing seems to be linear whereas in a-C:H:Si the increase occurred only at relatively higher annealing temperatures above 300 °C. The I_D/I_G ratio decreases with increasing amount of silicon in the films [34–40].

Physical and chemical changes in carbon materials resulting in graphitisation may occur during thermal annealing of carbon materials. Graphitisation occurred at higher annealing temperatures greater than 400 °C [34–40] as revealed by the bimodal shoulders. Silicon doping seems to lower the degree of graphitisation [34–40]. Graphitisation is associated with increased sp^2 content, while silicon doping seems to increase the sp^3 sites. Shoulder peaks associated with annealing and graphitisation appeared on a-C:H and lightly doped a-C:H:Si (TMS = 5 sccm) at 400–600 °C [34–40]. A much higher annealing temperature is required to give a shoulder on films with higher amounts of silicon. Silicon does not form π-bond and it therefore increases the amount of sp^3 bonds in the film.

Typical XPS chemical analysis for the as deposited and thermally annealed a-C:H and a-C:H:Si films are as indicated [34–40]. The peak binding energies of the films are consistent with those reported in the literature by Dementjev [151, 152], Grill [153], Miyake [154] and Baker and Hammer [155]. There was only a slight change in the values of the binding energies for the silicon-modified films even after annealing to 600 °C. Also in agreement with Demichelis et al. [156] there was an increase in sp^3/sp^2 ratios after peak deconvolution. Silicon does not form π-bonds, thus silicon doping of a-C:H films would be associated with increase in sp^3 bonds and delayed graphitisation observed in a-C:H:Si films annealed between 200 and 600 °C, which is associated with decreased platelet aggregation observed in these a-C:H:Si films. The contact angle measurement results obtained using the optical method and the surface energy measured (and calculated) by the Wilhemy plate technique of films deposited on silicon substrates reveal that silicon doping leads to an increase in the contact angle and a lowering of the surface energy which could be associated with decreased platelet aggregation [36, 40].

The histograms below shows the summary of the result of the platelet aggregation on the a-C:H and Si-a-C:H thin films (as deposited and thermally annealed films) seeded with platelets for 15 min (Fig. 11.9) and 30 min (Fig. 11.10),

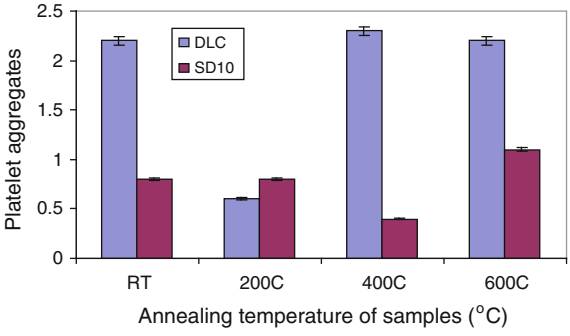

Fig. 11.9 Averaged human platelets aggregates/2.4 × 10^5 μ^2 on a-C:H and a-C:H:Si (as obtained and thermally annealed) samples (seeded for 15 min)

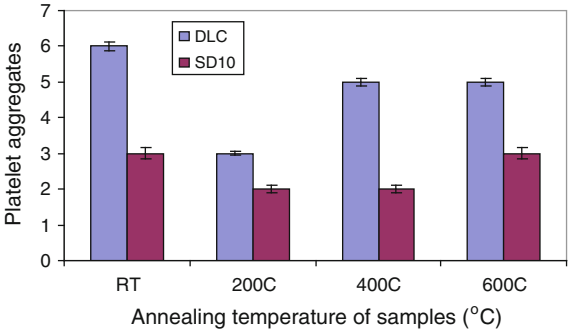

Fig. 11.10 Averaged human platelet aggregates/2.4 × 10^5 μ^2 on a-C:H and a-C:H:Si (as obtained and thermally annealed) samples (seeded for 30 min). RT = Room temperature

respectively. Figure 11.11 shows the SEM image of platelet seeding for 75 min on as deposited DLC and silicon-doped DLC thin films.

The electrical properties of the a-C:H and a-C:H:Si samples as well as the CPDs/WF have shown a correlation with the microstructure of the films as revealed by the Raman spectroscopy and XPS investigation, and the platelet aggregation on the films (Figs. 11.12, 11.13). Typical I–V curves of the metal–semiconductor–metal (MSM) sandwich show that the electrical conduction mechanism is not simple ohmic but semiconducting. The resistivity curve of the as deposited shows that silicon addition to a-C:H lowers the resistivity.

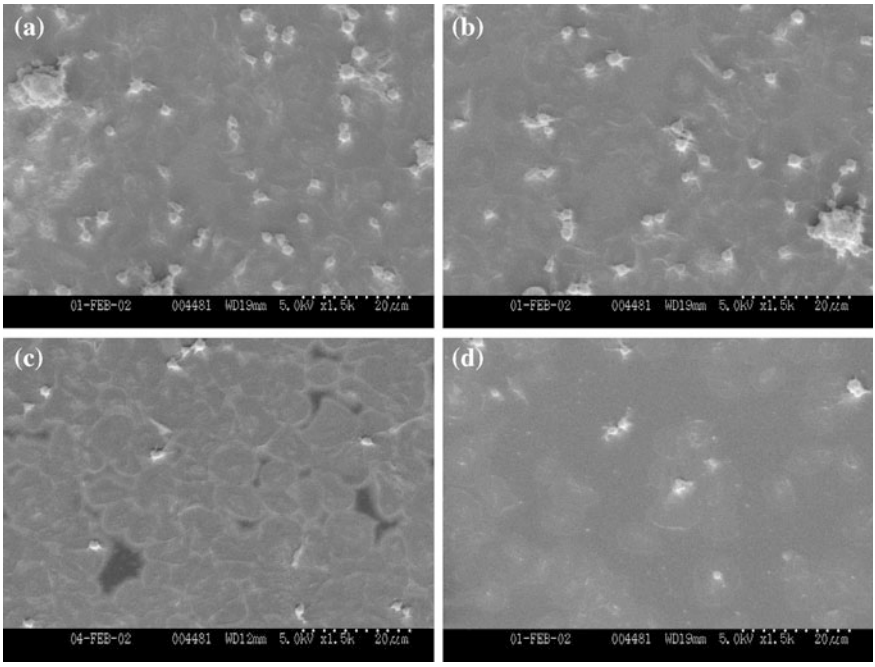

Fig. 11.11 SEM images of platelets seeded for 75 min on as obtained a-C:H (**a**, **b**), SD10 (**c**) and SD5 (**d**); ×1500

Thermal annealing of both a-C:H and a-C:H:Si leads to a decrease in the resistivity (Fig. 11.12, 11.13) which is likely to be associated with microstructural changes monitored by Raman spectroscopy as indicated by the sp^3/sp^2 ratios. At 600 °C of annealing temperature, the conductivity in both a-C:H and a-C:H:Si becomes simple ohmic [38, 40]. This result is consistent with the Raman spectroscopy investigation, which revealed graphitisation at this annealing temperature. Though decreased resistivity and decreased WF resulted in less platelet aggregates, graphitisation leads to increased number of platelet aggregates in the film [35, 36, 38].

The increasing graphitic content of the films at an annealing temperature of 600 °C increases the proportion of delocalised π-bonded electrons and therefore increases the electrical conductivity of the films as well, which hence result in the ohmic behaviour. The CPD and the WF of a-C:H thin films decreased with increasing amount of silicon doping and with increasing annealing temperatures as

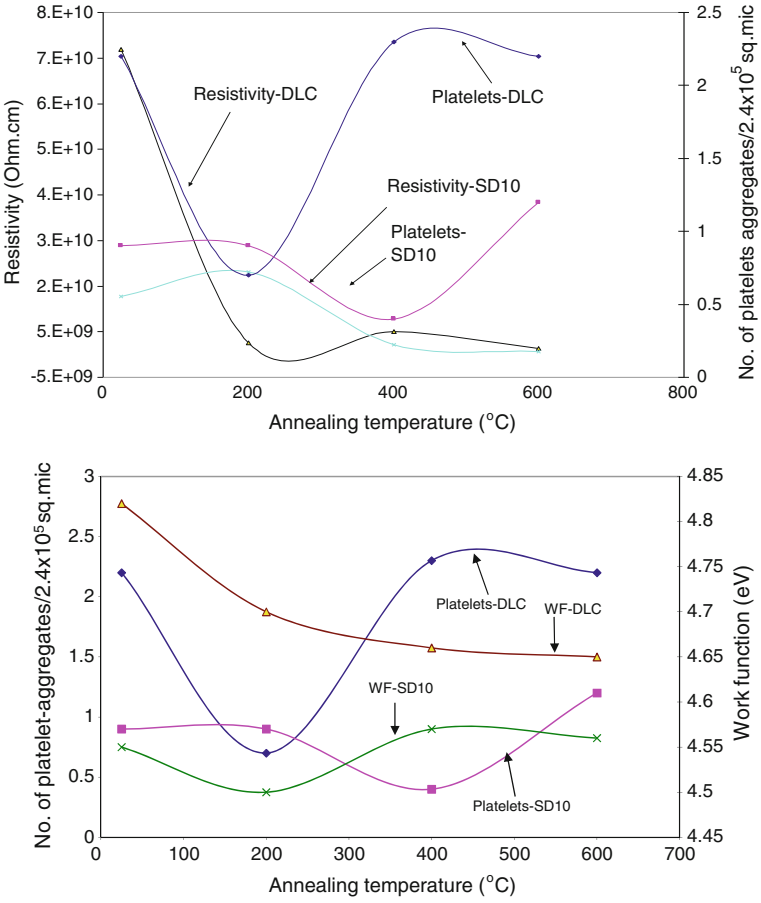

Fig. 11.12 Number of platelets aggregation (Seeded for 15 min) per 2.4×10^5 μ^2 as a function of resistivity and work function of a-C:H (DLC) and a-C:H:Si (SD10) thin films

shown in Figs. 11.12, 11.13. These electrical properties are related to the observed changes in the platelet aggregation on the a-C:H and a-C:H:Si thin films (Figs. 11.12, 11.13).

11.11.9 DLC Interaction with Blood Cells not Involved in the Clotting Process

Going strictly by the definition of hemocompatibility, apart from endothelial cells and platelets that are directly involved in the process of thrombosis and antithrombosis, the other blood cells though present in the blood can only be used to assess biocompatibility instead of hemocompatibility since they are not directly involved in thrombus formation and or prevention of thrombus formation. Thus the interaction of DLC with the other blood cells like neutrophils, lymphocytes, monocytes, erythrocytes (RBC), etc., can only give an indication of biocompatibility and not really 'hemocompatibility'.

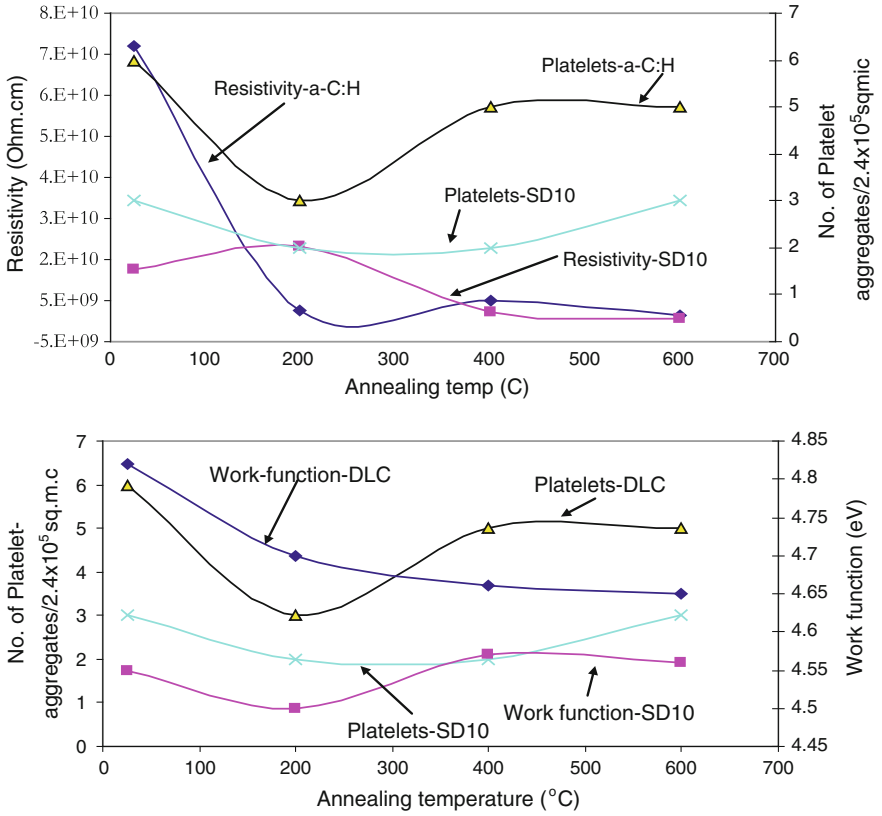

Fig. 11.13 Number of platelets aggregation (Seeded for 30 min) per 2.4 × 10^5 μ^2 as a function of resistivity and work function of a-C:H (DLC) and a-C:H:Si (SD10) thin films

11.11.10 DLC Interaction with Erythrocytes (Red Blood Cells, RBC)

Higson et al. [72, 73] examined the biocompatibility and substrate diffusion-limiting properties for a range of DLC (obtained from a saddle field source) coated porous polycarbonate membrane (nominal pore size of 0.01 μm) and hemodialysis membranes in whole blood. According to Higson et al. [72, 73] after 30 min exposure to unstirred whole blood, the uncoated polycarbonate did show red blood cells (and possibly other blood cells) adherent to the membrane surface, while in the DLC-coated membranes there was much reduced surface adherence of red blood cells and proteins, though some deposition of amorphous materials occurred. They also found that glucose sensors employing DLC-coated outer covering membranes were found to have suffered smaller losses of response following exposure to whole blood [72, 73].

Dion et al. [42] also evaluated the in vitro RBC retention of the new prosthetic heart valve that has been designed by FII Company and Pr. Baudet which is composed of Ti6Al4V titanium alloy coated with DLC (obtained by chemical vapour deposition technique). The retention/adhesion of RBC was evaluated by analysing radioactivity on the exposed wall of test or control tubes through which a blood cell suspension containing ^{99m}Tc-labelled red blood cells had circulated. According to Dion et al., the red cell retention, which may be due to either poor rinsing or morphological irregularities, leads to greater platelet retention; that mechanical entrapment accounted for only 0.07 % of red cell retention for silicone and 0.08 % for DLC/Ti6Al4V [42].

11.11.11 DLC Interaction with Human Haematopoietic Myeloblasts In Vitro

The haematopoietic myeloblasts are young blast cells derived from the progenitor cells in the bone marrow responsible for the generation of new white blood cells-granulocytes (neutophils, basophils and eosinophils).

ML-1 cells

ML-1 human haematopoietic myeloblasts were used in the study of **Lu et al**. [111] for assessing the biocompatibility of DLC. Using the hemacytometer for cell counting and Trypan Blue dye exclusion for determining cell viability, Lu et al. [111] found out that ML-1 cells cultured in DLC-coated P-35 dishes proliferated very well when compared to ML-1 cells growing in the uncoated control dishes and there was no sign to indicate cellular differentiation occurring among the ML-1 cells growing on the DLC-coating dishes [111].

11.11.12 DLC Interactions with Granulocytes (Neutrophils or Basophils or Eosinophils) In Vitro

Granulocytes are white blood cells containing granules (granules can either be acidic, basic or neutral thereby giving rise to different types of granulocytes, neutrophils, basophils and eosinophils, see Table 11.1), that are also responsible for combating infections. Neutrophils and eosinophils are also called microphages.

Neutrophils (polymorphonuclear leucocytes or PMNs, polymorphs)

Neutrophils are the most abundant white blood cells numbering an average of 4150 cells/μl (50–70 % of total number of white blood cells). They are round cells with a lobed nucleus (usually 2–5 lobes) that may resemble a string of beads and cytoplasm containing large pale inclusions, their granules being neutral and difficult to stain with either acidic or basic dyes. Their function is phagocytic, engulfing pathogens or debris in tissues and releasing cytotoxic enzymes and chemicals (lysosomal enzymes and bactericidal compounds). They measure about 12 μm in diameter and are the first of the WBCs to arrive at an injury site. High neutrophil adhesion produces negative effect on tissue biocompatibility.

Li et al. [157] reported based on their study of neutral granulocytes/neutrophils () interaction with DLC (obtained by ion beam assisted deposition, IBAD technique) coated polymethylmethacrylate (PMMA) intraoccular lens (IOLs), that DLC-coated PMMA-IOLs exhibit a lower neutophils adhesion compared to the uncoated PMMA-IOLs [157].

Eosinophils (acidophils)

Eosinophils are another type of granulocytes with cytoplasms that contain large granules that generally stain bright red with a red dye eosin, and can also stain with other acid dyes, hence also known as acidophils. The size of eosinophils is similar to that of neutrophils (∼12 μm). Eosinophils have bilobed nucleus and make up ∼2–4 % of the white blood cell population. They are phagocytic and engulf

Table 11.1 Operating conditions for SVTA RF plasma source for atomic nitrogen post-deposition doping of a-C:H thin films

Operating conditions	SVTA RF plasma source	PECVD
Power (W)	500	140
Reflected power (W)	25	5
Sweep plate voltage (V)	100–120	–
Bias voltage (V)	–	400
Deposition temperature (°C)	<100	25
Source temperature (°C)	300	–
Pressure (torr)	0.3	$\sim 7 \times 10^{-3}$
Atomic flux (atoms/s)	0.8×10^{18}	–
Exposure time (h)	1–2.5	∼0.1

antibody coated or marked foreign substances. Their primary mode of attack is the exocytosis of toxic compounds, including nitric oxide and cytotoxic enzymes, onto the surface of their targets. They are attracted to site of injury and so the increase in their number may indicate inflammation, allergy, etc.

Basophils

These are another type of granulocytes with numerous granules that stain darkly with basic dyes. They measure 8–10 μm in diameter and make up only about 1 % of the white blood cells. Basophils migrate to injury sites and cross the capillary endothelium to accumulate in the damage tissue where they discharge their granules which contain histamine (dilate blood vessels) and heparin (prevents clotting). They enhance local inflammation at the sites of injury and other chemicals that they release attract eosinophils and other basophils in the area of injury.

11.11.13 DLC Interaction with Monocytes (Macrophages) In Vitro

The monocytes also fall into the white blood cell category primarily produced in the bone marrow. The monocytes are 'agranular leucocytes' (agranulocytes), that is they lack abundant, deeply stained granules, though they also contain vesicles and lysosomes which are much smaller compared to those of the granulocytes [145]. They are very large cells ($\sim$15 μm in diameter, nearly about 2$\times$ the diameter of red blood cells) with kidney bean-shaped nucleus and abundant pale cytoplasm. They constitute about 2–8 % of the population of the circulating white blood cells. Monocytes move from the flowing blood to the tissues after 1–2 days. When monocytes enter the tissue they become to be known as macrophages and are responsible for fighting foreign bodies or pathogen and debris by engulfing and inactivating and digesting them in a process known as phagocytosis. They are aggressive phagocytes, often attempting to engulf as large or larger than their size. When activated they release chemicals that attract and stimulate neutrophils, monocytes and other phagocytic cells, as well as fibroblasts to the region of injury. The fibroblasts then begin producing scar tissues which walls off the injured area.

Linder et al. [158] studied the adhesion, cytoarchitecture and activation of primary human monocytes and their differentiated derivatives, macrophages, on DLC (obtained by radio frequency PACVD using methane/helium mixture: 1.5 vol.%/98.5 vol.%) coated glass coverslips using immunofluorescence technique. According to Linder et al. [158] the adhesion of primary monocytes to a DLC-coated coverslip is slightly, but not significantly, enhanced in comparison to uncoated coverslips, while the actin and microtubule cytoskeletons of mature macrophages show a normal development. The activation status of macrophages, as judged by polarisation of the cell body, was not affected by growth on a diamond-like carbon surface, thus DLC

shows good indications for biocompatibility to blood monocytes in vitro. It is therefore unlikely that contact with a DLC-coated surface in the human body could cause the cells to elicit inflammatory reaction [158].

Allen et al. [102] reported that DLC-coated polysterene (coating obtained by the low temperature dual ion beam technique using a saddle field source) culture plates produced good macrophage (murine macrophage cell line, IC-21) cell proliferation with a statistically significant faster growth rate (observed at the 48 and 72 h time points) when compared to the uncoated polysterene, and with no evidence of cytoplasmic vacuolation, membrane damage or excessive macrophage cell death [102]. Their LDH assay also indicates that there was no significant increase in LDH release from cells grown on DLC-coated surfaces as compared with cells grown on control surfaces, thus DLC has not caused any significant level of cell toxicity when compared to the uncoated samples [102].

Thomson et al. [108] by measuring the level of lysosomal enzymes *N*-acetyl-D-glucosaminidase released (enzyme is usually released as part of inflammatory reaction) in cell culture medium by macrophages (mouse peritoneal macrophage) after the cells interacted with DLC, reported that there was no significant difference in the amount of enzyme detected in the DLC-coated samples (using saddle field source and different source gases: acetylene, butane or propane) compared with the uncoated control tissue culture sample (24 well tissue culture plates) [108]. This implies that DLC is not cytotoxic and may not have elicited an inflammatory reaction. This was also corroborated by their lactate dehydrogenase, LDH assay which indicated that there was no statistically significant different level of LDH detected on the DLC-coated samples when compared to the non-coated samples.

11.11.14 DLC Interaction with Lymphocytes

The lymphocytes are also ‘agranular leucocytes’ (agranulocytes) lacking abundant and deeply stained granules. In a blood smear they are seen as a thin hallow of cytoplasm around a relatively large nucleus. In diameter they are slightly larger than the RBCs. Lymphocytes account 20–30 % of the WBC population of blood. Some lymphocytes are in circulation (small percentage) while others are in various tissues, organs and lymphatic system. Three classes of lymphocytes exist in the circulating blood, the T cells (responsible for cell-mediated immunity), the B cells (responsible for humoral immunity) and the NK cells (natural killer cells responsible for immune surveillance, are important in preventing cancer, sometimes known as large granular lymphocytes).

Plasma proteins and cell adhesion proteins/molecules (CAM)

Plasma, the fluid portion of the blood is a remarkable solution containing an immense number of ions, inorganic molecules, and organic molecules that are in transit to transport substances to various parts of the body. The plasma proteins

consist of albumin, globulin and fibrinogen fractions. Cells are attached to the basal lamina and to each other via the cell adhesion molecules (CAM) which are adhesion proteins. Many of these proteins pass through the cell membranes of the cells and are anchored to the cytoskeleton. Many CAMs have been characterised biochemically, and their functions are being investigated. Some of the CAMs bind to like molecules on other cells (homophilic binding) and the others to other molecules (heterophilic binding). Many CAMs bind to laminins, a family of large cross-shaped molecules with multiple receptor domains in the extracellular matrix. Nomenclature of CAM is still chaotic due partly of rapid growth in the field and also due to extensive use of acronyms in modern biology, however four broad families of CAM are known. The CAM categories are (1) the 'integrins' which are heterodimers that bind to various receptors; (2) the adhesion molecules of the 'IgG superfamily' of immunoglobulins, some of which bind to their molecules and some binding homophilically; (3) the 'cadherins', Ca^{2+}-dependent molecules that mediate cell-to-cell adhesion by homophilic reactions and (4) 'selectins', which have lectin-like domains that bind carbohydrates [145]. Goodman et al. [159] reported that since shape change responses of in vitro column-purified platelets to several polymeric biomaterials are very similar to those of circulating non-anticoagulated platelets and because column separation significantly reduces the protein content [160] of in vitro platelets, it appears that differences in platelet spreading on various materials are not entirely dependent on the preferential adsorption of plasma proteins from blood. They also observed that in vitro shape changes on Formvar and glass are the same in the presence and the absence of protein-containing buffer. Also cell spreading is similar in the presence and the absence of serum proteins [159, 161, 162]. A 'shine-through' hypothesis has been proposed to explain this biomaterial–protein–cellular interaction [163]. Additionally, fibroblasts and platelets appear to remove or move (sweep aside) adsorbed proteins [164–167], it is therefore conceivable that platelets alter adsorbed albumin layer(s) and adhere directly or via particular adhesion proteins on platelets surface to the material surface, if this occurs it would be expected that platelets would exhibit little differences in spreading on uncoated and albumin-coated surfaces, regardless of the thickness of an albumin layer. It has also been observed that initially adsorbed proteins tend to be more denatured than subsequent layers [168], and that the initial layer also appears to be more important in determining thrombotic responses [169]. Park et al., 1985 have also shown that platelet deposition in ex vivo circulation is determined by the first layer of adsorbed proteins and not subsequent layers, suggesting that platelets remove secondarily adsorbed layers of proteins. Another hypothesis is that platelets may not make direct contact with the substrate but are nonetheless influenced by surface character through an intervening layer of proteins, which is itself influenced by the surface. Different orientations or conformations of adsorbed proteins, as determined by the substrate, would then influence the behaviour of adherent platelets and other cells [159]. How these proteins may interact with DLC and DLC-like materials is yet to be explored.

Non-adhesive proteins: Albumin, Transferrin, like proteins

Albumin and tranferin like proteins with non-adhesive functions tend to decrease subsequent thromboembolic events [159, 170].

Dion et al. [42] have examined ^{131}I-labelled albumin plasma protein adhesion on DLC-coated Ti6Al4V and silicone elastomer and reported that DLC can adhere more albumin than the medical grade elastomer.

Adheisve proteins: Fibrinogen, Fibronectin, VWF and CAM

In general these plasma proteins with adhesive functions tend to increase thrombosis [159, 171]. Adhesive proteins and likely increased expression of CAM, e.g. ICAM-1, VCAM-1, ELAM-1, E-selectin, GMP-140 (P-selectins) and other molecules/ligands from the immunoglobulin and selectin superfamily have been shown to be important in cascade reactions like the platelet–leucocyte and leucocyte–endothelial cell adhesion and activation reactions [172–174]. When expressed on the cell surface the NH_2-terminal lectin-like domains of the selectins bind with their counter-receptors (specific carbohydrate ligands on white blood cells and platelets).

Dion et al. [42] have also examined ^{125}I-labelled fibrinogen plasma protein adhesion on DLC-coated Ti6Al4V and silicone elastomer and reported that DLC can adhere slightly more fibrinogen than the silicone elastomer.

Non-adhesive/Adhesive protein ratios: Albumin/Fibrinogen ratios

It has been shown that platelet adhesion depends on the albumin/fibrinogen ratio: the higher the albumin/fibrinogen ratio the lower the number of adhering platelets and hence less risk of platelet aggregation and less risk of thromboembolism. The albumin/fibrinogen ratio for DLC is 1.24 and 0.76 for silicone elastomer [42]. According to Dion et al. [42] these two ratios allow us to consider that platelet adhesion would be weaker on DLC than on silicone elastomer but, infact the opposite occurred, which they thought could be explained by the large dispersion of results in percentage of platelet retained due to the device concept itself they added [42].

Cui and Li [75] also studied the adhesion of plasma proteins on DLC-coated, CN-coated PMMA, and uncoated PMMA using radioactive targed proteins. They reported the albumin/fibrinogen ratio of 1.008 for DLC, 0.49 for CN and 0.39 for PMMA [75].

11.12 Endothelial Preseeding on Biomaterials for Tissue Engineering

Preliminary study on the platelet interaction with a-C:H:Si and a-C:H thin film samples preseeded with endothelial cells in vitro is reported in this section to corroborate the reported results in the other sections where a-C:H:Si and a-C:H

were interacting with endothelial cells and platelets separately. These joint interactions were investigated in order to confirm the reports in the literature on the opposing but complementary interactions of endothelial cells and platelets in blood coagulation/thrombus formation regulation in the body. The role of microvascular endothelial cell in preventing platelet aggregation and acting as a simple model in haemocompatibility assessment is hereby affirmed. This investigation also tries to demonstrate that since these interactions do not occur either separately or in sequence but, at about the same time, the microstructural finish of the biomaterial before implantation becomes crucial therefore in determining the fate of the biomaterial in vivo.

11.12.1 Endothelial Cell–Platelet Interactions on a-C:H and a-C:H:Si Thin Films

Human microvascular endothelial cells were seeded on a-C:H and a-C:H:Si thin films for about 6 h, washed with PBS twice, followed finally by seeding of human platelets for 30 min. This section of the study acts as an adjunct to the reports already presented in this chapter.

In the above micrograph (Fig. 11.14), there seems to be no platelet aggregation present on the as obtained a-C:H. Instead there seems to be endothelial cell activation, and or aggregation in response to potential platelet attachment and or aggregation. Also there seems to be some changes in the morphology of the endothelial cells. However, the exact relation of this change in morphology in the presence of platelets is not known to the author. That is whether the endothelial cells engulf the platelets and or by its secretions wall off platelets where ever they seem to appear is not really understood by the author. The other possibility could be that the endothelial cell do not allow the platelets to adhere at all, such that they could all be washed off by the PBS washing (to remove proteins) before samples were prepared for imaging.

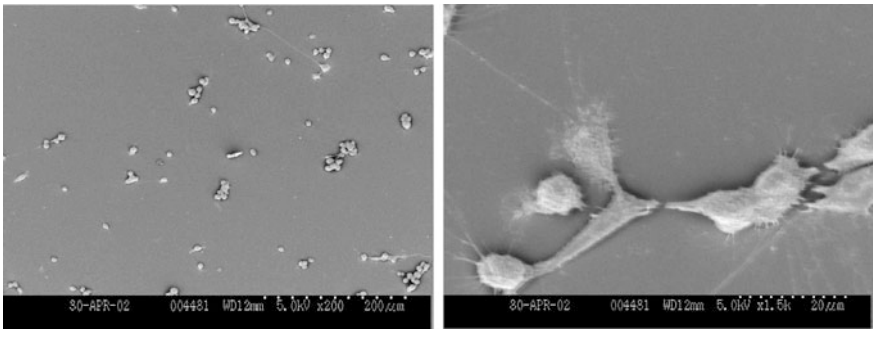

Fig. 11.14 Endothelial cell seeded on as obtained a-C:H for 6 h and followed by platelets seeding for 30 min; ×200 (*left*), ×1500 (*right*)

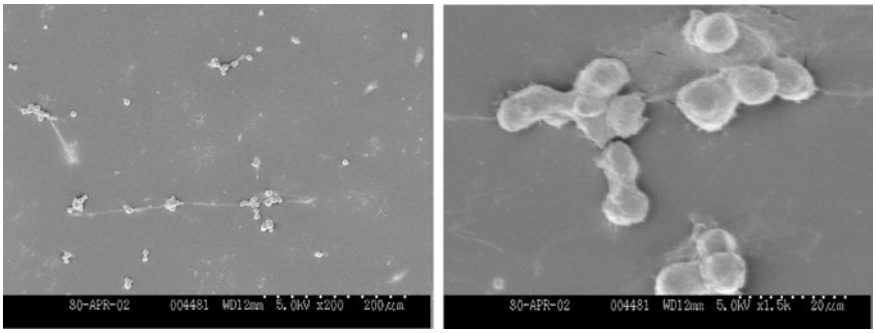

Fig. 11.15 Endothelial cell seeded on as obtained a-C:H:Si (SD10) for 6 h and followed by platelets seeding for 30 min; ×200 (*left*), ×1500 (*right*)

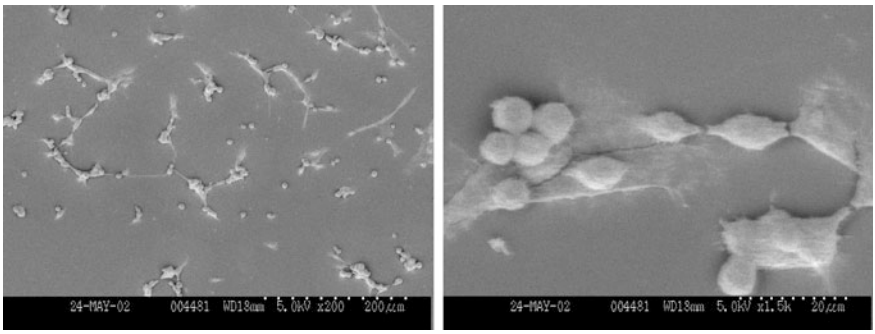

Fig. 11.16 Endothelial cell seeded on a-C:H (thermally annealed at 200 °C) for 6 h and followed by platelets seeding for 30 min; ×200 (*top*), ×1500 (*bottom*)

Under normal circumstances, platelets do not interact with the endothelial cells—that is platelet adhesion to the vessel wall and the formation of platelet aggregates do not normally take place except when required for haemostasis. Hence, the surface of endothelial cells does not promote platelet attachment [117]. The formation of platelet aggregates in close proximity to the endothelium is also rendered difficult by prostacyclin (PGI2), a powerful inhibitor of platelet aggregation secreted by the endothelial cells. Prostacyclin can be secreted by endothelial cells in culture as well as by isolated vascular tissue [118]. The vascular endothelium is now known to be a dynamic regulator of haemostasis and thrombosis with the endothelial cells playing multiple and active (rather than passive) roles in haemostasis and thrombosis [119, 120].

Figures 11.15, 11.16 and 11.17 show both the doped (Silicon, SD10) and non-doped DLC films, as deposited and thermally annealed (at low temperature, <400 °C) preseeded with endothelial cells (6 h) and then seeded with platelets. At both low (×200) and high magnifications (×1.5 K) the features seen are neither that of platelet aggregation nor individual platelet adhesion (Figs. 11.15, 11.16 and 11.17).

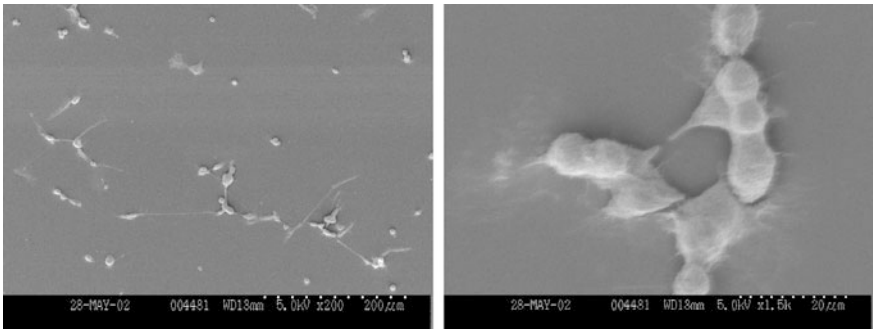

Fig. 11.17 Endothelial cell seeded on a-C:H:Si (SD10, thermally annealed at 200 °C) for 6 h and followed by platelets seeding for 30 min; ×200 (*left*), ×1500 (*right*)

Many of the functions of the endothelial cells appear to be antithrombotic in nature. Several of the 'natural anticoagulant mechanisms', including the heparin–antithrombin mechanism, the protein C-thrombomodulin mechanism, and the tissue plasminogin activator mechanism, are endothelial-associated. Among the proteins on the endothelial surface is antithrombin III [121] which catalyses the inactivation of thrombin by heparin. Endothelial cells also have heparan sulphate and dermatan sulphate (glycosaminoglycans) on their surfaces [122] which are known to have anticoagulant activity.

In this micrograph (Fig. 11.18) a bit strange star-shaped features that seemingly engulfing platelet aggregates are seen in this 400 °C thermally annealed a-C:H. These could possibly be endothelial cell(s) in 'extreme activation'. Based on the results from previous chapters, fewer endothelial cells combating with more platelet aggregations are expected in this supposedly graphitized film. This could possibly lead to extreme endothelial cell activation and extreme flattening/spreading of the few endothelial cells expected to be interacting with platelet aggregations.

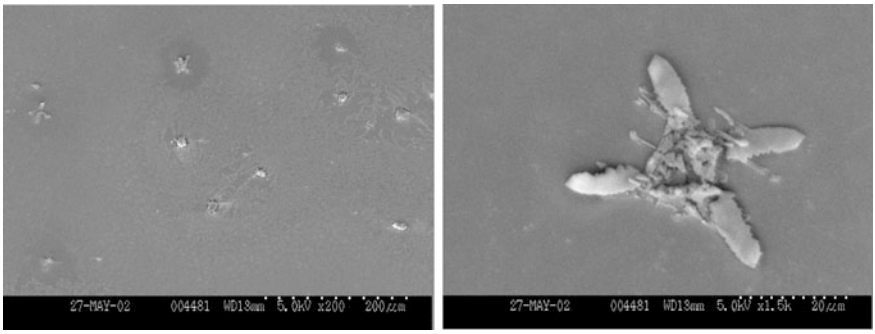

Fig. 11.18 Endothelial cell seeded on a-C:H (thermally annealed at 400 °C) for 6 h and followed by platelets seeding for 30 min; ×200 (*left*), ×1500 (*right*)

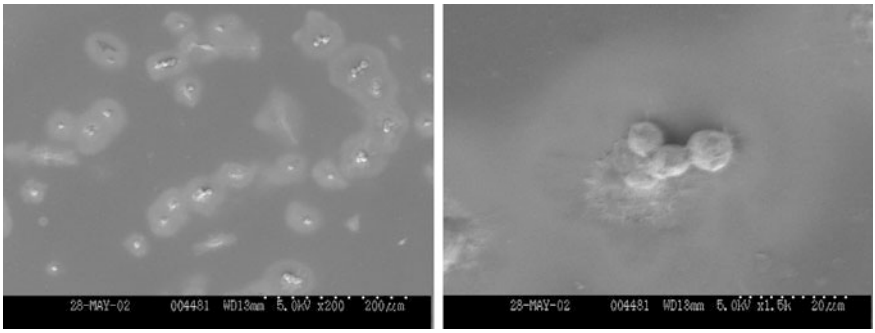

Fig. 11.19 Endothelial cell seeded on a-C:H:Si (SD10, thermally annealed at 400 °C) for 6 h and followed by platelets seeding for 30 min; ×200 (*left*), ×1500 (*right*)

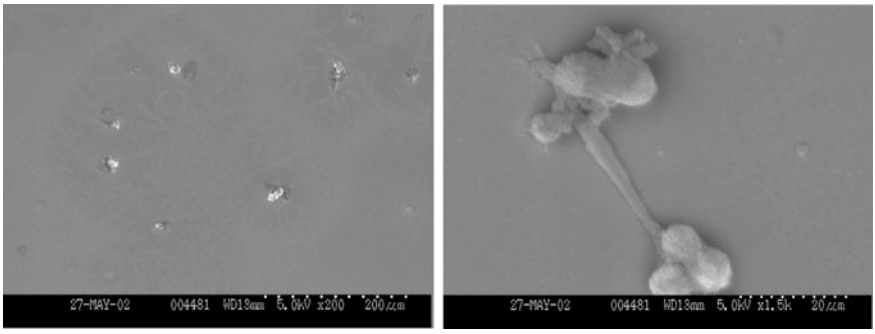

Fig. 11.20 Endothelial cell seeded on a-C:H (thermally annealed at 600 °C) for 6 h and followed by platelets seeding for 30 min; ×200 (*left*), ×1500 (*right*)

The clump seen above (Fig. 11.19) seems to be a platelet aggregate walled off by endothelial cell or endothelial secretions. No individual platelet or platelet aggregates are identifiable.

In this micrograph (Fig. 11.20) is seen also 'endothelial aggregates' and star-shaped endothelial cells in 'extreme activation'. This film is also expected to be graphitized.

The top left micrograph (Fig. 11.21) seems to show some platelet aggregates surrounded by a halo of what could be endothelial secretion. This preliminary study seems to show that in the presence of endothelial cells, platelet aggregation could be almost impossible. Therefore, any biomaterial with good surface properties suitable for endothelial cell adhesion could be confirmed as haemocompatible biomaterial until proven otherwise.

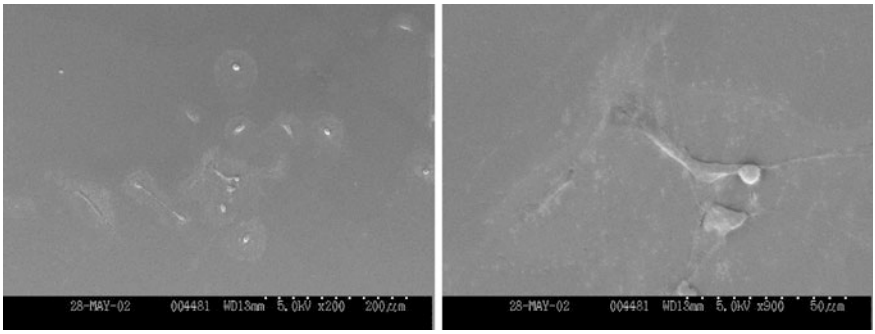

Fig. 11.21 Endothelial cell seeded on a-C:H:Si (SD10, thermally annealed at 600 °C) for 6 h and followed by seeding with platelets for 30 min

11.13 Bioassays and Assessment of Intracellular Activities

Bioassays are generally adopted biochemical protocols for assessing intracellular activities such as free ions concentration, radicals or even membrane potentials. These bioassays are based on the assumption that biomaterial–cellular interactions occurring over a reasonable length of time at the cell–biomaterials interfaces are able to triggers some intracellular event/processes via the cell mediators. Cell viability, cell proliferation, cell morphology and cytotoxicity are commonly determined and some live cell functions such as gene expression, apoptosis, level of protein phosphorylation, chemotaxis, endocytosis, cell secretions, cell transduction or production of cell signalling molecules such as nitric oxide or flux of Ca^{2+} and expression of CAM can be determined by some bioassays. The effect of the biomaterials surface features on first overlying protein biofilms and the morphological changes induced on these proteins result in some cellular events. Various bioassays exist and involve in most cases the use of various biochemical agents and reagents to assess some of the expressed biochemical mediators and/or enzymes (proteins). The results of the bioassays depend on the cell function being investigated and may be detected by microscopy, microplate (e.g. ELISA) readers and flow cytometry. There is some challenge in using bioassay to detect early biomaterial–cellular interactions occurring at the cell–material interface. Assessment of cell proliferation can be achieved by various bioassays: (a) the detection of proliferation associated antigens by immunohistochemical techniques, e.g. Ki-67 antigen [175], proliferating cell nuclear antigen, PCNA; (b) quantification of DNA synthesis by measuring tritiated thymidine, ^{3}H-thymidine or bromodeoxyuridine, BrdU uptake; (c) measurement of changes in total DNA content with DNA specific dyes (e.g. Hoechst 33258); (d) determination of intracellular metabolic activity or reduction state by Tetrazolium salts (MTT, XTT, MTS), or Alamar Blue reduction; (e) Determination of the optical absorbance of Neutral Red stained cells. Cell viability can be assessed by various methods: (a) Trypan Blue exclusion and Propidium iodide exclusion as these are excluded from the viable cells; (b) CFDA

staining, Crystal violet inclusion and Neutral red staining of viable cells; (c) Quantification of cell-mediated cytotoxicity by measurement of the LDH (lactate dehydrogenase) activity, measurement of the release of ^{51}Cr or Europium Titriplex V from labelled cells; (d) Alamar Blue reduction.

11.13.1 MTT Assay

MTT (3-(4,5-dimethylthiazol-2-yl)-2,5-diphenyl tetrazolium bromide; Sigma) was dissolved in PBS at 5 mg/ml concentration and filter sterilised inside the hood to remove a small amount of insoluble residues usually present in some batches of MTT. About 5 h before the end of the incubation period, 20 µl of MTT solution was added to each well including the blank wells (wells with added media, but no cells added). The plates were then transferred back to the incubator (37 °C) for 5 h. After the incubation period, the media were gently removed from all the wells with a syringe and 200 µl of DMSO were added to each of the wells (DMSO was handled in the dark, because it is unstable in the light). The plates were returned to the incubator for 5 min in order to dissolve air bubbles. These samples were then transferred to the Titertek+plus MS2 Microelisa reader and the optical density was read using a test wavelength of 550 nm and a reference wavelength of 660 nm. The plates were read within 1 hour of adding DMSO.

11.13.1.1 The Interaction of a-C:H and a-C:H:Si Thin Films with Bovine Retinal Pericytes

Another carefully selected cell in this study is the pericytes which are cells supporting the blood vessel walls. The bovine pericytes used in this study is from the eye compartment (retinal) which is a special compartment of the body. The pericytes and the other cells (human embryonic lung cells, L132, and Chinese hamster-V79 cell lines) used in this study were essentially used to examine the possible cytotoxicity/biocompatibility of the a-C:H:Si thin film biomaterial. The results (Fig. 11.22) show that when pericytes are seeded on 96-well plates coated with a-C:H and a-C:H:Si, the cells viability in these coated wells are comparable (and/or generally slightly better) to those in the non-coated TCPS (control) wells [37]. This is in agreement with reports in the literature using some other cell lines [74, 75]. a-C:H has also been reported to do well in both organ [74] and cell culture [75] when compared to the materials conventionally used for this purpose. It should be noted however that the MTT assay of different cell line could be different due to the origin, nature, function and rate of proliferation/metabolic activation state of the cells in culture. Growing pericytes on the surfaces of these as deposited thin films coated on silicon wafers are shown below, a-C:H (Fig. 11.23) and SD10 (Fig. 11.24).

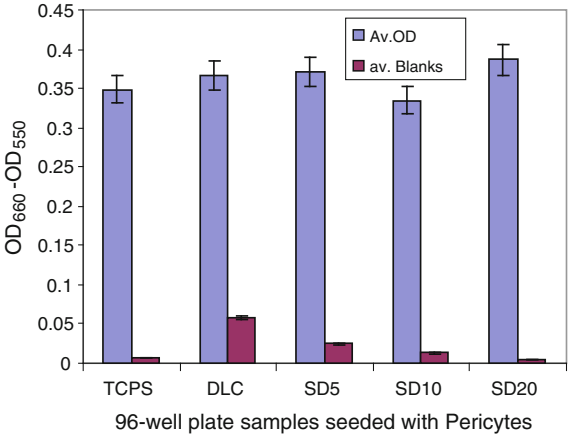

Fig. 11.22 MTT assay of pericytes seeded on standard tissue culture 96-well plates coated with a-C:H and a-C:H:Si (SD5-20), TCPS = control (uncoated) [37]

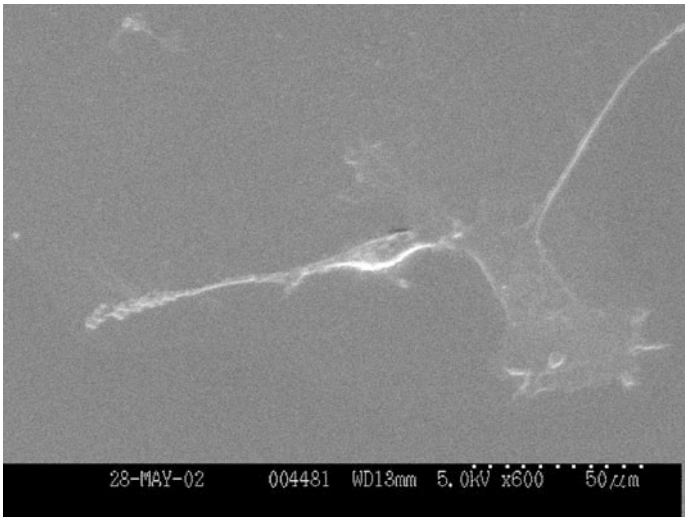

Fig. 11.23 Pericytes growing on the as deposited a-C:H after seeding for >12 h [37]

Pericytes are intimately associated with the vasculature and appear to be present in most tissues. They are generally considered to be restricted to the microvessels (arterioles, venules and capillaries where there are no smooth muscles) [176]. Pericytes embrace capillary, and their nuclei bulge outward rather than inward like endothelial nuclei. Pericytes are thought to contribute to endothelial cell proliferation, via selective inhibition of endothelial cell growth and lack of pericytes has lead to endothelial hyperplasia and abnormal vascular morphogenesis in the brain [177]. They exhibit small, oval cell body with multiple processes extending for

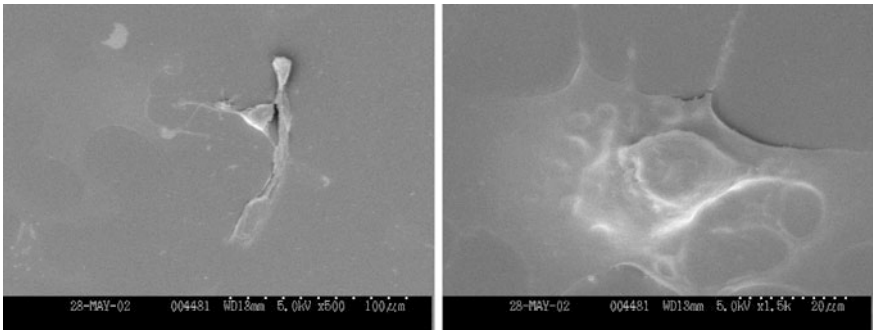

Fig. 11.24 Pericytes growing on the as deposited a-C:H:Si (SD10) after seeding for >12 h

some distances along the vessel axis and these primary processes then give rise to orthogonal secondary branches which encircle the vascular wall. They function as macrophages and have multiple suggested functions. Pericytes have a close physical association with the endothelium. Gap junction communication between pericyte and endothelial cells, as well as at endothelial–endothelial junctions, has been shown in vitro.

This SEM image (Fig. 11.24) shows that bovine retinal pericytes grow well in silicon-modified a-C:H thin films. On the whole these results show that bovine retinal pericytes grow well in both coated and uncoated TCPS tissue culture wells, thus the a-C:H and a-C:H:Si coatings are not toxic to these cells. Thus a-C:H and a-C:H:Si thin films could possibly function well in the eye compartment as materials for medical/optical prostheses. However, this study requires further investigation possibly with human pericytes and possibly to assess the differential cell attachment in relation to microstructural changes like the electrical properties, graphitisation and so on.

11.13.1.2 The Interaction of a-C:H and a-C:H:Si Thin Films with L132 Cell Line

The L132 cell line (human embryonic lung cells) originally purchased from ATCC (CCL-5), is epithelial and normal but with Hela characteristics. This cell line has Hela contamination and thus proliferates in a very rapid rate characteristic of Hela tumour cells. The results of MTT assay of L132 cell lines on 96-well TCPS plates coated with a-C:H and a-C:H:Si (Fig. 11.25) show that L132 cell lines proliferate well on both the uncoated TCPS (control) and the a-C:H, a-C:H:Si coated wells.

In this SEM images (Fig. 11.26), the L132 cell lines are seen growing on silicon wafer but, the morphology of these cells is not as good as those of the coated samples (Figs. 11.27, 11.28, 11.29 and 11.30), indicating possibly less proliferation in these samples. This could be attributed to high surface energy of this uncoated silicon wafer substrate.

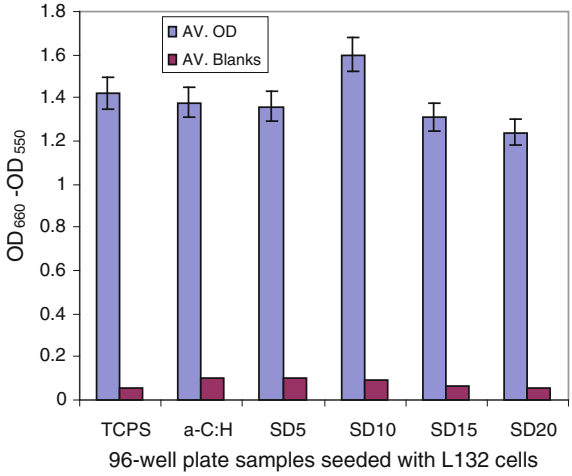

Fig. 11.25 MTT assay of L132 cells seeded on standard tissue culture 96-well plates coated with a-C:H and a-C:H:Si (SD5-20), TCPS = control

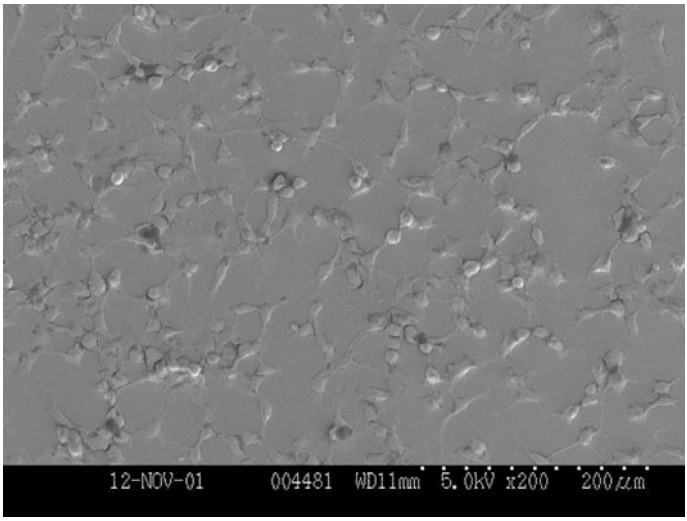

Fig. 11.26 SEM image of L132 cell lines seeded on uncoated silicon wafer samples

The L132 cell lines proliferate well on a-C:H samples as shown in Fig. 11.27. The morphology of these cells is clearly defined indicating a good proliferation in this sample.

Again the L132 cells are seen proliferating very well in this a-C:H:Si sample (Fig. 11.28). The morphology and spreading of these cells are better in this sample compared to the uncoated substrate. Compared to the a-C:H samples the morphology and spreading seem to be slightly better in these silicon-doped samples.

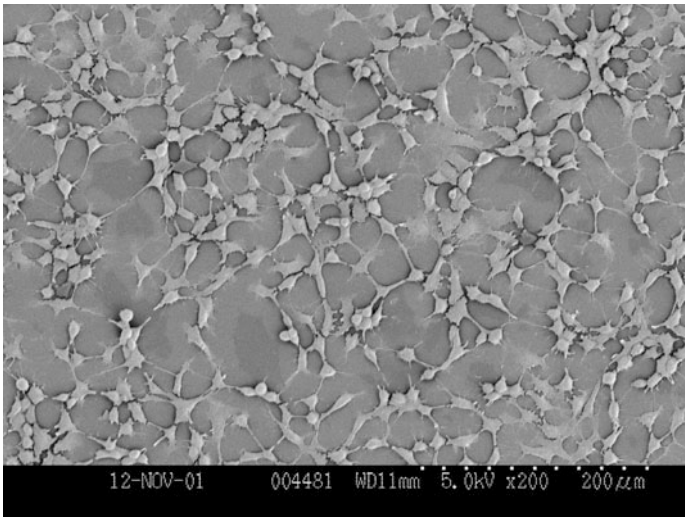

Fig. 11.27 SEM image of L132 cell lines seeded on as deposited a-C:H sample

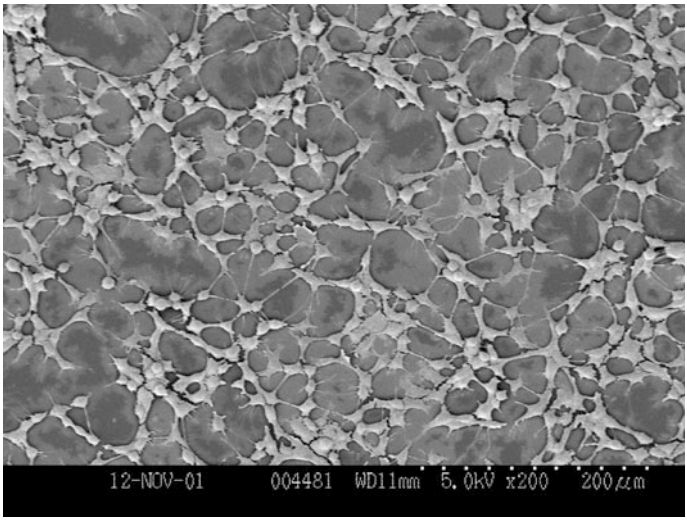

Fig. 11.28 SEM image of L132 cell lines seeded on as obtained a-C:H:Si (SD10) sample

In a-C:H (Fig. 11.29) and a-C:H:Si (Fig. 11.30) films thermally annealed at 400 °C the L132 cells are seen proliferating fairly well. Though the onset of graphitisation is expected at this temperature in the a-C:H film thermally annealed at 400 °C, the proliferation of L132 cells on these samples does not seem to reflect this. This could be attributed to the nature of this Hela-contaminated cell line. These cell lines are contaminated with Hela cells (high proliferation/cancerous) and are

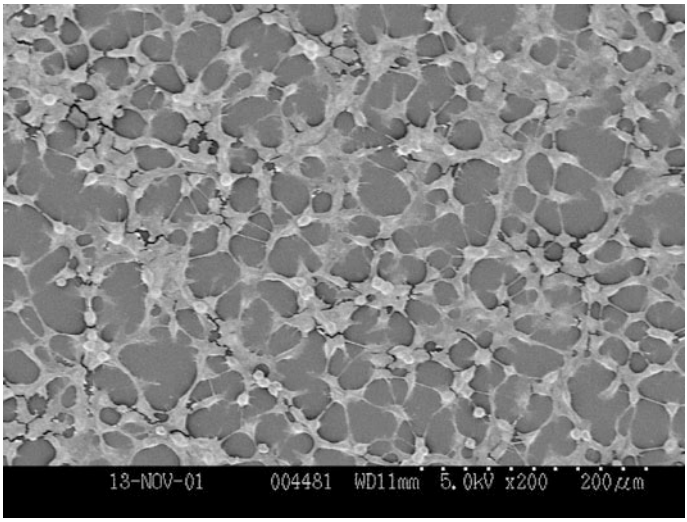

Fig. 11.29 SEM image of L132 cell lines seeded on a-C:H (thermally annealed at 400 °C)

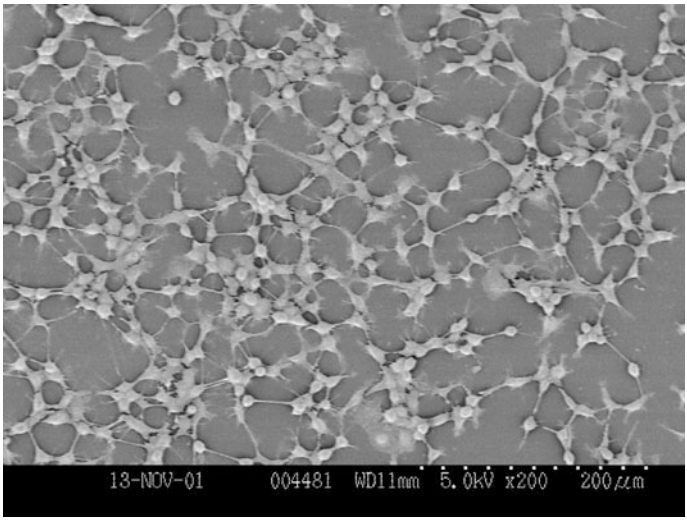

Fig. 11.30 SEM image of L132 cell lines seeded on a-C:H:Si (SD5, thermally annealed at 400 °C)

suitable for investigating cellular toxicity but may not be sensitive enough for assessing differential cell proliferation on closely varied sample surface properties due to this contamination on the original cell line.

However, thermal annealing at higher temperature 600 °C, thought to produce high graphitic films which does show a poor proliferating/spreading L 132 cell lines (Fig. 11.31). This a-C:H sample thermally annealed at 600 °C shows the L132 cells

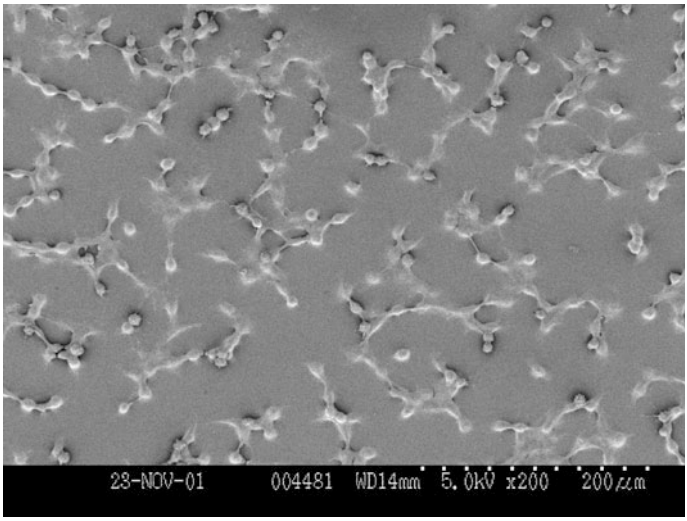

Fig. 11.31 SEM image of L132 cell lines seeded on a-C:H (thermally annealed at 600 °C)

growing on the sample but with poorly defined morphological features similar to that observed on the uncoated sample (Fig. 11.26). This poorly defined morphology could be attributable to graphitisation in this film. Thus low contact angle (high surface energy) and graphitisation may lead to impaired L132 cell spreading and morphology.

11.13.1.3 The Interaction of a-C:H and a-C:H:Si Thin Films with V79 Cell Line

Figure 11.32 shows the MTT assay of Chinese Hamster cell line (V79) on uncoated TCPS (control), a-C:H and a-C:H:Si coated 96-well plate standard tissue culture plates. The cells proliferate well on the coated and uncoated control plates, but generally the cells seem to proliferate slightly better on the coated samples. This could be attributed to the change in surface energy in these as obtained thin film coatings. This result also agrees with reports in the literature using some other cell lines [74, 75], a-C:H has been reported to do well in both organ [74] and cell culture [75] when compared to the materials conventionally used for this purpose.

In summary, it could therefore be inferred from this section that endothelial cells prevent platelet adhesion and aggregation. The a-C:H and a-C:H:Si thin films are not toxic to the bovine retinal pericytes, the L132 (human embryonic lung) cell line and the Chinese hamster (V79) cell lines. Based on these MTT assay results it seems that these cells seem to proliferate slightly better in the a-C:H and a-C:H:Si coated wells compared to uncoated TCPS conventionally used for cell culture.

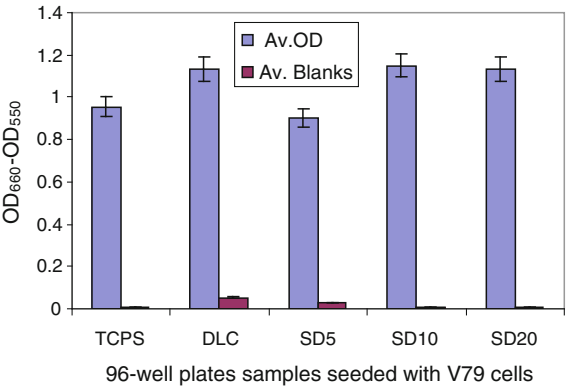

Fig. 11.32 MTT assay of V79 cells (Chinese hamster) seeded on standard tissue culture 96-well plates (*TCPS*) coated with a-C:H and a-C:H:Si (*SD*)

11.13.2 Other Bioassays Techniques

Alamar Blue Assay

The Alamar Blue dye contains a fluorometric/colorimetric growth indicator which detects metabolic activity in the cell. Cell growth causes a chemical reduction of the medium; this causes the Redox indicator to change from an oxidised, non-fluorescent blue colour, to a reduced, fluorescent red colour. The indicator has been shown to be minimally toxic to living cells and produces a clear, stable, distinct colour change. When the assay is completed the Alamar Blue dye can be removed and the cells can be used for further experiments.

See samples with 1×10^5 cells per well in a 6 well plate with 3 ml of the RPMI medium. Incubate cells in standard incubator (37 °C and 5 % CO_2). Perform test at chosen/different day/time points. Prepare 1:20 dilution of the stock solution of Alamar Blue dye by adding 1 ml of Alamar Blue and 19 ml of Hank's Balanced Salt Solution (HBSS). Wash cells twice with HBSS and add the Alamar Blue dye to each well in 2.5 ml volumes. Incubate at 37 °C and 5 % CO_2 for 90 min. Following incubation, volumes of 100 µl were taken from each well in duplicate and added to a black 96 well plate. Read the fluorescence on a fluorescence reader at excitation 530 nm and emission 590 nm.

DNA Assay

The DNA content of cell suspensions can be measured using the binding of bis-benzamide to DNA. Prepare a stock solution of (bis-benzamide) 33258 by the addition of 1 mg of the dye to 1 ml deionised water, covered in foil and stored at 4 °C. Prepare a 1:50 dilution of the 1 mg/ml bis-benzamide with TNE buffer, to give a working solution of 20 µg/ml. Lyse cells to release DNA, using a freeze thaw method by freezing at −80 °C and allowed to thaw; repeat procedure three times. Add sample volumes of 50–50 µl of TNE buffer and 100 µl of bis-benzamide 33258. Read plate on the plate reader at excitation wavelength of

360 nm and an emission wavelength of 460 nm. Determined values against a calf thymus DNA standard curve and displayed as µg/ml.

Hydrogen Peroxide Production: Dichlorofluorescein Diacetate Assay

The dichlorofluorescein diacetate assay was employed to measure the amount of H_2O_2 peroxide production from cells, e.g. monocytes following growth on materials. The generation of reactive oxygen intermediates, such as H_2O_2, is usually increased in inflammatory, injury and repair processes.

Prepare a 1 mM stock solution of dichlorofluorocein diacetate by the addition of 4.87 mg of dichlorofluorocein diacetate (DCFH-DA) to 10 ml of ethanol. Suspend monocytes in Hanks balanced salt solution without phenol red. Seed samples with 5×10^5 cells in a 6 well plate, with 2 ml of Hanks balanced salt solution. Incubated for 3–4 h in a standard incubator (37 °C and 5 % CO_2). As a positive control, 1 µg/ml PMA [178] should be added to cells to give a final concentration of 50 ng/ml. After incubation, add 10.2 µl of 1000 µM DCFH-DA to each well and incubated for 1 h at 37 °C and 5 % CO_2. After incubation, transfer 100 µl to a 96 well plate. Read plate on a fluorescence plate reader at an excitation wavelength of 485 nm and an emission wavelength of 528 nm.

11.14 In Vivo Studies of Carbon-Based Materials: Cell–Tissue Interactions In Situ

11.14.1 In Vivo Studies on the Biocompatibility and Hemocompatibility of DLC

Allen et al. [109] implanted DLC-coated cobalt-chromium cylinders in the intramuscular locations in rats and in transcortical sites in sheep and their histological analysis of specimens retrieved 90 days after surgery showed that the DLC-coated specimens were well tolerated in both sites [109].

Fournier et al. [179] has shown from their clinical and angiographic data that the ***hydrogenated silicon carbide coating*** of the Tenax coronary stent may indeed play a beneficial role in patient outcome, and should therefore be evaluated by prospective clinical trials. They implanted the prostheses (231 Tenax stents) in 206 patients (62 ± 5 years) in the patients left anterior descending (51 %) and right coronary arteries (36 %). Their results show that revascularization was complete in 70 %, elective in 80 %, and the implantation was direct in 25 % of the cases and that the procedure was successful in all the lesions, reducing stenosis from 62 ± 16 to 16 ± 10 % and increasing the minimal luminal diameter from 0.81 ± 0.40 to 2.61 ± 0.59 mm. Also the TIMI flow was reduced in 30 %, but normalised after the stent in all but one case. They also reported that the incidence of cardiac events was minimal: 1 acute thrombosis (0.5 %) resolved by a new angioplasty and 1 non-Q myocardial infarction (0.5 %) and finally at the 6-month clinical follow-up 10 % of the patients presented complaints of angina greater than class II [179].

De Scheerder et al. [180] investigated the in vivo biointeraction with one particular class of modified DLC coatings: diamond-like nanocomposite coatings (DLN or Dylyn, Bekaert, Kortrijk, Belgium). Either coated or non-coated stents were randomly implanted in two coronary arteries of 20 pigs so that each group contained 13 stented arteries. Pigs underwent a control angiogram at 6 weeks and were then sacrificed. They performed a quantitative coronary analysis before, immediately after stent implantation, and at 6 weeks using the semi-automated Polytron 1000 system (Siemens, Erlangen, Germany). They also performed a morphometry using a computerised morphometric program and their angiographic analysis showed similar baseline selected arteries and post-stenting diameters. At 6-week follow-up, they discovered no significant difference in minimal stent diameter and their histopathological investigation revealed a similar injury score in the three groups. According to De Scheerder et al. [180] inflammatory reactions were significantly increased in the DLN–DLC coating group, thrombus formation was significantly decreased in both coated stent groups and neointimal hyperplasia was decreased in both coated stent groups; however, the difference with the non-coated stents was not statistically significant; and also area stenosis was lower in the DLN-coated stent group than in the control group (41 ± 17 % vs. 54 ± 15 %; $p = 0.06$). in their conclusion they indicated that the diamond-like nanocomposite stent coatings are compatible, resulting in decreased thrombogenicity and decreased neointimal hyperplasia and covering this coating with another DLC film resulted in an increased inflammatory reaction and no additional advantage is compared to the single-layer diamond-like nanocomposite coating [180].

Tran et al. [181] reviewed the mechanical heart valves' (MHV) thrombogenicity and pointed out that the application of surface modification technology to reduce the incidence of thrombus formation on MHV is a novel undertaking requiring the collaboration within the bioengineering and cardiothoracic surgery fields. From reviewing results of recent and past investigations, and their own preliminary study with DLC coating and plasma or glow discharge treatment (GDT) of MHV, they identified and discussed several potentially beneficial effects that may reduce the extent of valve-related thrombogenesis by surface modification: DLC and GDT may affect the surfaces of MHV in many ways, including cleaning of organic and inorganic debris, generating reactive and functional groups on the surface layers without affecting their bulk properties, and making the surfaces more adherent to endothelial cells and albumin and less adherent to platelets; therefore these different effects of surface modification, separately or in combination, may transform the surfaces of MHV to be more thromboresistant in the vascular system [181].

Dowling et al. [69] implanted two DLC-coated and uncoated stainless steel cylinders into both cortical bone (femur) and muscle (femoral quadriceps) sites of six adult (>40 kg) sheeps, for a period of 4 weeks (three sheep) and the rest for 12 weeks. According to Dowling et al. [69] after explantation of the implants and the pathological/histological examination of the implanted cylinders, no macroscopic adverse effect was observed on both the bone and the muscles of the used sheep.

Yang et al. [9, 10] examined in vivo interactions of dics coated with TiN, DLC (deposited on SS316L disc using PVD) and or Pyrolytic carbon (PyC) films, implanted into the descending aorta of anaesthesized sheep (6 animals) for 2 h. They evaluated the three different samples simultaneously in each animal. After explantation they examined the thombus-free area on the disc with close-up photography and planimetry, and the test surfaces with SEM. Yang et al. [9, 10] found out that there were many leucocytes adherent, activated and spread onto PyC and DLC, but on TiN it was the erythrocytes that were mainly adherent [9, 10].

Patients using implanted prostheses are faced with life-threatening bleeding problems because they are kept under life-long anticoagulant therapies in order to reduce the risk of thromboembolism. In order to reduce the risk of platelet aggregation/thromboembolism and complications following the life-long course(s) of anticoagulants, the biomaterials need to be improved in order to achieve better haemocompatibility. Platelet aggregation in the surfaces of these prostheses is the key factor in thrombus formation. The platelets is known to play a crucial role in blood clotting/thrombus formation which is indicative of the ability of a foreign body to trigger off clot formation and or thrombosis which may impair free flow of blood and result in some damaging effect on the internal body organs.

11.14.2 Summary

In this chapter, the role of microstructure, electrical properties and surface energy of amorphous hydrogenated carbon (a-C:H) and silicon-modified a-C:H (a-C:H:Si) in relation to their biocompatibility/haemocompatibility interactions with human microvascular endothelial cells and human platelets have been investigated in full. Preliminary investigations on nitrogen modified films (a-C:H:N) and a-C:H, a-C:H:Si interactions with other cell lines have been carried out. The findings are summarised as follows:

Microstructure

- The microstructure was tailored by the films deposition parameters, silicon and nitrogen doping and thermal annealing.
- Surface roughness: a-C:H, a-C:H:Si and a-C:H:N are ultrasmooth thin films that can be used to improve the surface features necessary for improved biocompatibility in biomedical implants and devices made with conventionally rougher metals or polymers for example. Silicon incorporation seems to slightly increase the surface roughness. Thermal annealing also seems to increase slightly the surface roughness.
- Intrinsic Compressive stress: stress reduction in the film seems to be important in improving biocompatibility. Stress reduction was achieved by thermal annealing of the films. Silicon incorporation also seems to reduce the intrinsic stress in the film. Lowered intrinsic stress is associated with decreased surface energy.

- Graphitisation: excessive graphitisation seems to impair biocompatibility. Graphitisation occurs at annealing temperature greater than 400 °C in a-C:H thin films and may occur as well in a-C:H:Si film at a higher annealing temperatures of ~600 °C. Silicon seems to lower the rate and degree of graphitisation in a-C:H and thereby improving hemocompatibility.
- The sp^2/sp^3 ratio and the sp^2 cluster size in the sp^3 matrix and not the absolute sp^2 or sp^3 content play a role in hamocompatibility.
- Silicon doping of a-C:H thin films decreases the I_D/I_G ratio and on annealing the I_D/I_G ratio starts to increase above 300 °C of annealing temperature.

Electrical properties

- Conductivity/resistivity: silicon incorporation lowers the resistivity (Fig. 11.33) of a-C:H thin film from 6.7×10^{10} Ω cm (a-C:H) to 5.4×10^9 Ω cm (a-C:H:Si) and thereby increased the conductivity. Increased conductivity (without graphitisation) is associated with an improved haemocompatibility (Fig. 14.1). Resistivity behaviour is electric field dependent, and for high amount of silicon, the resistivity first increases and then later decreases as the field increases (≥ 1.5–1.8×10^4 V/cm).
- Work Function: Lower work functions in the examined films seem to improve biocompatibility. Silicon doping and nitrogen doping seem to lower the WF. Silicon doping lowers the WF from 4.77 eV (a-C:H) to 4.56–4.34 eV (a-C:H:Si), a reduction of 0.21–0.43 eV. Silicon atomic percentage concentration of up to ~7.61 % (TMS = 10 sccm) led to a rapid jump in decrease of WF.
- Band gap: Optical band gap was determined by ellipsometry technique. Silicon addition seems to increase the optical band gap energy. The optical gap values depend on the type of transition assumed and the model used for the calculation.

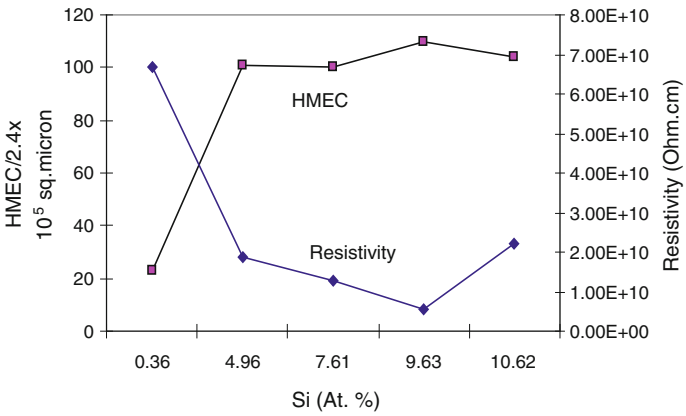

Fig. 11.33 HMEC adhesion related to resistivity as a function of percentage atomic concentration of silicon in a-C:H thin films

- The author suggests that the density of states (DOS) and charge carriers could play a greater role compared to the optical band gap energy. Moderate amount of silicon (≤ 10 at.%) seems to increase the DOS in the sp^2 cluster region even though silicon does not form π-bond. There is however the need to establish the exact DOS distribution, at the extended states, at the mobility edge, the band tail or the defect states in the valence and conduction band within the band structure; and for the band gap determination there is need to ascertain the degree (percentage) of different electrons in (assumed different) transitions (Fig. 11.34).

Surface energy/contact angle

- Contact angle: a higher contact angle seems to improve hemocompatibility. Silicon incorporation increases the contact angle (by up to $\sim 17°$) while nitrogen incorporation decreases it (Fig. 11.35).

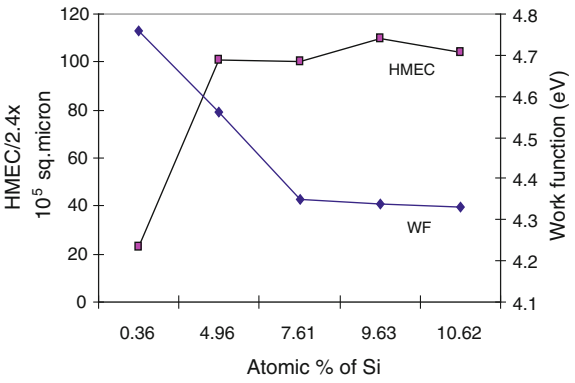

Fig. 11.34 HMEC adhesion related to the work function of a-C:H thin films as a function of percentage atomic concentration of silicon in the a-C:H thin films

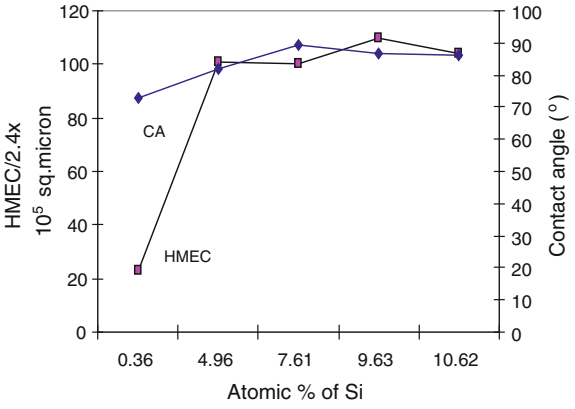

Fig. 11.35 HMEC adhesion related to the water contact angle of a-C:H films as a function of percentage atomic concentration of silicon in a-C:H thin films

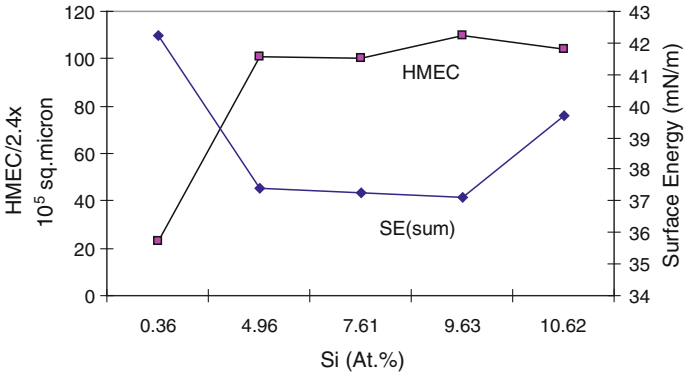

Fig. 11.36 HMEC adhesion related to the surface energy (sum) of a-C:H films as a function of percentage atomic concentration of silicon in a-C:H thin films

- Surface energy: About 99 % of the surface energy components of a-C:H:Si and a-C:H are dispersive and seem to be responsible for the biocompatibility of these thin films. Silicon addition decreased the surface energy by ~5–10 mN/m (Fig. 11.36).

Cellular interactions

- Cellular origin-specie differences: Human cells are relevant to biocompatibility studies for biomedical use in man and seem to be much more sensitive than cells from other species that may not be relevant to man.
- Cell specificity/function/sensitivity: Human cells should be carefully chosen from tissue of interest for biocompatibility studies in relation to those tissues for specific application in the particular tissue, organ and or system. Endothelial cells and platelets seem to be the most suitable cells in the blood compatibility studies.
- The results of these investigations have shown that microstructural changes in the films, especially the electrical conductivity, work functional changes, the contact angle/surface energy and the degree of graphitisation in these films play a key role in especially the haemocompatibility of these thin films. These physical changes are easily detected when these thin films interact with microvascular endothelial cells and human platelets in vitro. However, with other cell lines which may not be human and which may not play crucial roles like the endothelial cells and platelets, these changes may not easily be detected. Nevertheless these other cells may be good enough in investigations to say whether or not a material is just cytotoxic.
- MTT assay reveals that a-C:H and a-C:H:Si are generally not toxic to the cells, and may in some cases even encourage better cell proliferation when compared to tissue culture polystyrene (TCPS) conventionally used for cell culture.

Film adhesion in biological fluids

- Si-DLC-coated stainless steel substrates were also immersed in various biological fluids (Saliva, PBS and FCS) similar to human body fluids incubated at body temperature. The adhesion properties of the films were tested using both the four-point bend test and the pull tensile substrate plastic straining techniques. With the use of SEM the crack initiation strain and the saturation crack spacing were determined. Statistical analysis of the data using two-parameter Weibull, lognormal probability density function models as well as Gamma function suggests long-term reliability and good adhesion of Si-DLC to stainless steel and metallic substrates if used in biomedical implants and devices in continuous contact with body fluids.

Silicon doping of a-C:H lowers the WF, the resistivity, the surface energy of the films and the rate and degree of graphitisation in the films. Silicon doping also

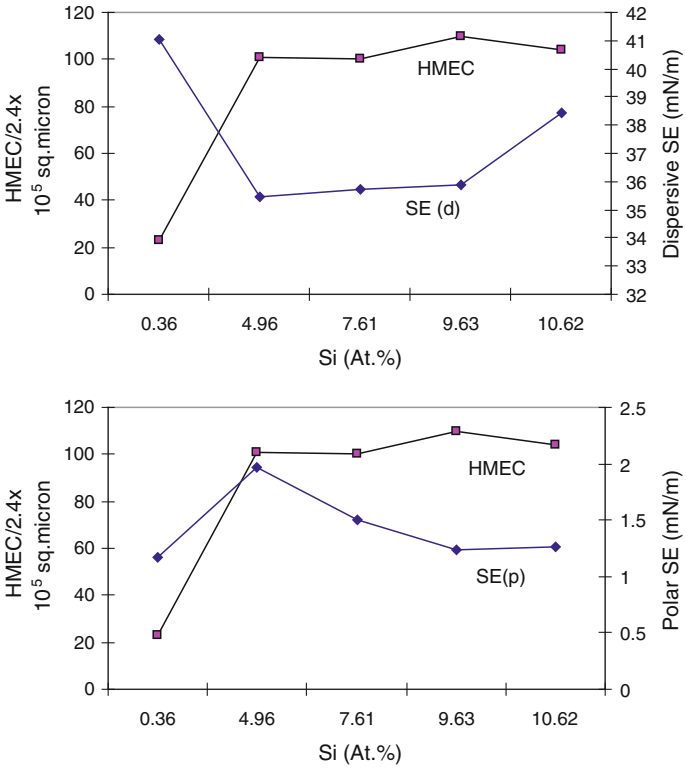

Fig. 11.37 HMEC adhesion related to the surface energy (dispersive and polar components) of a-C:H films as a function of percentage atomic concentration of silicon in a-C:H thin films

improves the adhesion of a-C:H thin films to its substrates. The a-C:H:Si thin films and conducting a-C:H thin films with less internal stress and less degree of graphitisation are good haemocompatible materials suitable for biomedical applications as in heart valve prostheses, stents, etc (Fig. 11.37).

Generally, a-C:H and a-C:H:Si are non-toxic to cells in vitro. Also a-C:H:Si coated stainless steel on immersion and incubation inside biological fluids have shown good shear strength and are therefore suitable for use for biomedical applications.

11.15 Ongoing and Future Investigations

- ^{13}C-NMR and the X-ray excited Auger electron spectroscopy studies of a-C:H:Si.
- Determination of exact amorphous–crystal structure, bond angles, bond angle disorders, number of and or distributions of dangling bonds, and dislocations in the films.
- Density of States (DOS) determination in a-C:H, a-C:H:Si, a-C:H:N and a-C:H:Me.
- Determination of the effective band gaps of the a-C:H:Si -Protein-Cellular system and to relate the interactions with the DOS and/or the band gap.
- The reported results and discussions termed 'preliminary investigations' are under further investigation.
- The interaction of a-C:H and a-C:H:Si with proteins with adhesive and non-adhesive functions needs to be investigated in order to see the exact role of these proteins in biocompatibility and haemocompatibility. The role and the mechanism interaction of CAM should be investigated. Surface Plasmon Resonance (SPR) technique is envisaged to be useful in monitoring these interacting proteins in situ.
- The effects of a-C:H, a-C:H:Si and a-C:H:N optical properties on cellular growth and interaction in situ.
- Optical techniques to monitor the underside of cells, the mechanism of cell attachment, cell proliferation and density of distribution over the attached surfaces of a-C:H, a-C:H:Si and a-C:H:N coated transparent/glass substrates. By measuring the refractive indices of the glass, the medium (protein layer without cells), the cells and how the refractive index changes, the cell density and the cell cytoskeleton and how they change when the cell attaches to the surface can be monitored (Fig. 11.38).

The relative intensity, R, of the reflected light at the interfaces of the glass and cell is given by

$$\mathrm{R} = \left(\frac{r_g - r_c}{r_g + r_c}\right)^2 \tag{1}$$

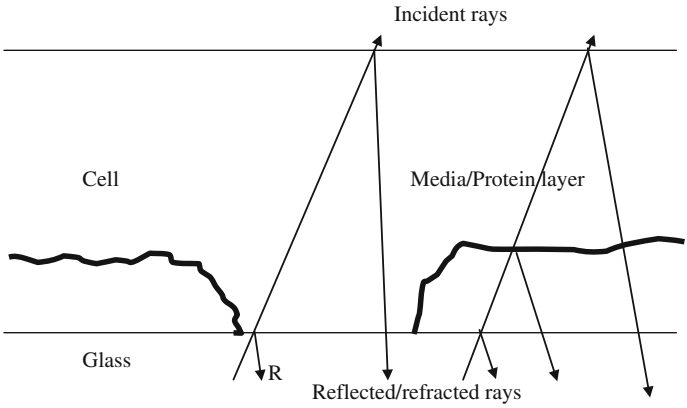

Fig. 11.38 Illustration of principles of optical method of cell characterization [182]

$$r_c = r_g \times \frac{1-\sqrt{R}}{1+\sqrt{R}}$$

where r_c = Refactive index of cell; r_g = refractive index of glass.

In this case, the refractive index of a-C:H, a-C:H:Si (SD) or a-C:H:N thin film coating has to be substituted in the above equation:

$$\mathrm{R} = \left(\frac{r_{SD}-r_c}{r_{SD}+r_c}\right)^2 \tag{2}$$

$$r_c = r_{SD} \times \frac{1-\sqrt{R}}{1+\sqrt{R}}$$

The cytoplasmic content of the cells follows the distribution of the cellular attachments on the substrates/samples. Therefore, regions of focal or more condensed cellular attachment imply heavy density of cytoplasm and a relatively higher refractive index. The cellular microfilaments and cytoskeleton are condensed in the region of attachment, thereby allowing less amount of light to pass through and thus a higher refraction occurring. Well spread cells on the other hand have more widely distributed cytoplasmic content since the volume of the cytoplasm is relatively the same (the larger the area, the lesser the thickness for the same volume of material inclusion). However, there has to be an assumption that the same thickness of protein interlayer exists between every cell and the substrate at the points of cell attachment, and at regions where there is no attached cells but just layer of protein/culture media. For further reading refer to [183, 184].

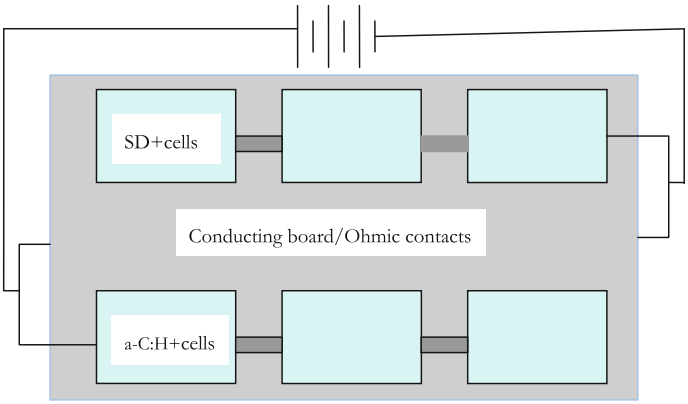

Fig. 11.39 Schematics of the layout for applying electric field on the coatings with seeded cells in culture

- Further investigation on the role of surface charges is needed. By applying a small electric field (not to affect the cells) through the film while the cells are growing in culture will help to redistribute the charges (11.39).
- Similarly, impedance spectroscopy can be used to monitor the cell growth and distribution on the a-C:H, a-C:H:Si and a-C:H:N thin film coatings in situ.
- For a-C:H, a-C:H:Si and a-C:H:N to find their way into routine use as biomedical prostheses, they need to be tested in vivo with animals with close physiological relation with the humans, e.g. the baboons.
- Extensive clinical trials of a-C:H, a-C:H:Si and a-C:H:N coated implant.

References

1. Bittl, J. A. (1996). Advances in coronary angioplasty. *New England Journal of Medicine, 335*, 1290–1302.
2. Gawaz, M., Neumann, F. J., Ott, I., May, A., & Schomig, A. (1996). *Circulation, 94*, 279–285.
3. Inoue, T., Sakai, Y., Fujito, T., Hoshi, K., Hayashi, T., Takayanagi, K., et al. (1996). *Circulation, 94*, 1518–1523.
4. Lahann, J., Klee, D., Thelen, H., Bienert, H., Vorwerk, D., & Hocker, H. (1999). *Journal of Materials Science: Materials in Medicine, 10*, 443–448.
5. Haycox, C. L., & Ratner, B. D. (1993). *Journal of Biomedical Materials Research, 27*, 1181–1193.
6. Courtney, J. M., Lamba, N. M. K., Sundaram, S., & Forbes, C. D. (1994). *Biomaterials, 15*, 737–744.
7. Klein, C. L., Nieder, P., Wagner, M., Kohler, H., Bittinger, F., Kirkpatrick, C. J., et al. (1994). *Journal of Pathophysiology, 5*, 798–807.
8. Gutensohn, K., Beythien, C., Koester, R., Bau, J., Fenner, T., Grewe, et al. (2000) *Infusionstherapie und Transfusionmedizin, 27*(4), 200–206.

9. Yang, Y. (1996). S. F Franzen, C.L Olin. *Cells and Materials, 6*(4), 339–354.
10. Yang, Y., Franzen, S. F., & Olin, C. L. (1996). *The Journal of Heart Valve Disease, 5*, 532–537.
11. Bittl, J. A. (1996). Subacute stent occlusion: Thrombus horribilis. *JACC, 28*, 368–370.
12. Mark, K., Belli, G., Ellis, S., & Moliterno, D. (1996). *Journal of the American College of Cardiology, 27*, 494–503.
13. Colombo, A., Hall, P., Nakamura, S., Almagor, Y., Maiello, L., Martini, G., et al. (1995). *Circulation, 91*, 1676–1688.
14. Gott, V. L., Koepke, D. E., Daggett, R. L., Zarnstorff, W., & Young, W. P. (1961). The coating of intravascular plastic prostheses with colloidal graphite. *Surgery, 50*, 382–389.
15. Haubold, A. (1977). *Annals of the New York Academy of Sciences, 283*, 383.
16. Goodman, S. L., Tweden, K. S., & Albrecht, R. M. (1996). Platelet interaction with pyrolytic carbon heart-valve leaflets. *Journal of Biomedical Materials Research, 32*, 249–258.
17. Baier, R. E. (1972). *The Bulletin of the New York Academy of Medicine, 48*, 273.
18. Williams, D. F. (1989). *Journal of Biomedical Engineering, 11*, 185.
19. Salzman, E. (Ed.). (1981). *Interaction of blood with natural and artificial surfaces*. New York: Marcel Dekker.
20. Gordon, J. L. (1986). In J. P. Cazenave, J. A. Davies, M. D. Kazatchkine, & W.G. van Aken (Eds.), *Blood-surface interactions: Biological principles underlying hemocompatibility with artificial materials* (p. 5). Amsterdam: Elsevier Science Publishers (Biomedical Division).
21. Cenni, E., Arciola, C. R., Ciapetti, G., Granchi, D., Savarino, L., Stea, S., et al. (1995). *Biomaterials, 16*, 973–976.
22. Herring, M. B., Gardner, A. & Gloves, J. A. (1978). *Surgery, 84*, 498.
23. Remy, M., Bordenave, L., Bareille, R., Rouais, F., Baquey, C., Gorodkov, A., et al. (1994). *Journal of Materials Science Materials in Medicine, 5*, 808.
24. Pesakova, V., Klezl, Z., Balik, K., & Adam, M. (2000). *Journal of Material Science: Materials in Medicine, 11*, p797.
25. Hallab, N. J., Bundy, K. J., O'Connor, K., Clark, R., & Moses, R. L. (1995) *Journal of Long-Term Effects of Medical Implants, 5*, 209.
26. Ahluwalia, A., Basta, G., Chiellini, F., Ricci, D., & Vozzi, G. (2001). *Journal of Material Science: Materials in Medicine, 12*, 613–619.
27. Bowlin, G. L., & Rittger, S. E. (1997). *Cell Transplantation, 6*, 623.
28. Altankov, G., & Grott, T. (1997). *Journal of Biomaterials Science, Polymer Edition, 8*, 299.
29. Grinnell, F. (1978). *International Review of Cytology, 53*, p65.
30. Van Wachem, P. B., Schakenraad, J. M., Feijen, J., Beugeling, T., van Aken, W. G., Blaauw, E. H., et al. (1989). *Biomaterials, 10*, 532–539.
31. Van Wachem, P. B., Beugeling, T., Feijen, J., Bantjes, A., Detmers, J. P., & van Aken, W. G. (1985). *Biomaterials, 6*, 403–408.
32. McLaughlin, J., Meenan, B., Maguire, P., & Jamieson, N. (1996). Properties of diamond like carbon thin film coatings on stainless steel medical guidewires. *Diamond and Related Materials, 8*, 486–491.
33. Jones, M. I., McColl, I. R., Grant, D. M., Parker, K. G., & Parker, T. L. (1999). Hemocompatibility of DLC and TiC-TiN interlayers in titanium. *Diamond and Related Materials, 8*, 457–462.
34. Okpalugo, T. I. T., Ogwu, A. A., Maguire, P., & McLaughlin, J. A. D. (2001). Technology and health care. *International Journal of Health Care Engineering, 9*(1–2), 80–82.
35. Okpalugo, T. I. T., Ogwu, A. A., Maguire, P. D., McLaughlin, J. A., & Hirst, D. G. (2004). In-vitro blood compatibility of a-C:H: Si and a-C: H thin films. *Diamond and Related Materials, 13*(4–8), 1088–1092.
36. Okpalugo, T. I. T., Ogwu, A. A., Maguire, P. D., & McLaughlin, J. A. (2004). Platelet adhesion on silicon modified hydrogenated amorphous carbon films. *Biomaterials, 25*(3), 239–245.
37. Okpalugo, T. I. T., McKenna, E., Magee, A. C., McLaughlin, J. A., & Brown, N. M. D. (2004). The MTT assays of bovine retinal pericytes and human microvascular endothelial

cells on DLC and Si-DLC-coated TCPS. *Journal of Biomedical Materials Research, Part A, 71A*(2), 201–208.
38. Okpalugo, T. I. T., Maguire, P. D., Ogwu, A. A., & McLaughlin, J. A. (2004). The effect of silicon doping and thermal annealing on the electrical and structural properties of hydrogenated amorphous carbon thin films. *Diamond and Related Materials, 13*(4–8), 1549–1552.
39. Okpalugo, T. I. T., Ogwu, A. A., Maguire, P. D., McLaughlin, J. A., & McCullough, R. W. (2006). Human micro-vascular endothelial cellular interaction with atomic N-doped compared to Si-doped DLC. *Journal of Biomedical Materials Research Part B: Applied Biomaterials, 78B*(2), 222–229.
40. Okpalugo, T. I. T. (2002). The hemocompatibility of ultra-smooth silicon and nitrogen doped hydrogenated amorphous carbon thin films—The role of the microstructure, electrical properties, and surface energy (G2c., Ph.D., Ulster, 53-4066). (BL: DXN062999).
41. Parker, T. L., Parker, K. L., McColl, I. R., Grant, D. M., & Wood, J. V. (1993). *Diamond and Related Materials, 93*, 118.
42. Dion, I., Roques, X., Baquey, C., Baudet, E., Basse Cathalinat, B., & More, N. (1999). *Biomedical Materials and Engineering, 3*, 51–55 (spring).
43. O'Leary, A., Bowling, D. P., Donnelly, K., O'Brien, T. P., Kelly, T. C., Weill, N., et al. (1995). *Key Engineering Materials, 99–100*, 301–308.
44. Freitas, R. A., IMM report number 12. http://www.imm.org/reports/rep012.html
45. Allen, M., Law, F. C., & Rushton, N. (1994). *Clinical Materials, 17*, p1–p10.
46. Allen, M. J., Myer, B. J., Law, F. C., & Rushton, N. (1995). *Transaction of Orthopaedic Research Society, 20*, 489.
47. Szent-Gyorgyi, A. (1957). *Bioenergetics*. New York: Academic Press.
48. Szent-Gyorgyi, A. (1946). *Nature, 157*, 875.
49. Eley, D. D., Parfitt, G. D., Perry, M. J., & Taysum, D. H. (1953). *Transactions of the Faraday Society, 49*, 79.
50. Postow, E., & Rosenberg, B. (1970). *Bioenergetics, 1*, 467.
51. Bruck, S. D. (1965). *Polymer, 6*, 319.
52. Bruck, S. D. (1967). *Journal of Polymer Science Part C, 17*, 169.
53. Bruck, S. D. (1973). Intrinsic semiconduction, electronic conduction of polymers and blood compatibility. *Nature, 243*, 416–417.
54. Bruck, S. D. (1975). The role of electrical conduction of macromolecules in certain biomedical problems. *Polymer, 16*, 25.
55. Van Oss, C. J. (1978). Phagocytosis as a surface phenomenon. *Annual Review of Microbiology, 32*, 19–39.
56. Kochwa, S., Litwak, R. S., Rosenfield, R. E., & Leonard, E. F. (1977). *Annals of New York Academy of Sciences, 283*, 37.
57. Lettington, A. H. (1991). Applications of diamond films and related materials. In Y. Tzeng, et al (Ed.), Materials *science monographs* (Vol. 73, p. 703). New York: Elsevier.
58. Evans, A. C., Franks, J., & Revell, P. J. (1991). *Surface and Coatings Technology, 47*, 662–667.
59. Grill, A. (1999). *Diamond and Related Materials, 8*, 428.
60. Gutensohn, K., Beythien, C., Bau, J., Fenner, T., Grewe, P., Koester, R., et al. (2000). *Thrombosis Research, 99*, 577–585.
61. Gutensohn, K., Beythien, C., Koester, R., Bau, J., Fenner, T., Grewe, P., et al. (2000). *Infusionstherapie und Transfusionmedizin, 27*(4), 200–206.
62. Zheng, C., Ran, J., Yin, G., & Lei, W. (1991). In Y. Tzeng, et al (Ed.), *Applications of diamond films and related materials, materials science monographs* (Vol. 73, p. 711). New York: Elsevier.
63. Jones, M. I., McColl, I. R., Grant, D. M., Parker, K. G., & Parker, T. L. (2000). *Journal of Biomedical Materials Research, 52*(2), 413–421.
64. Alanazi, A., Nojiri, C., Noguchi, T., et al. (2000). *ASAIO Journal, 46*(4), 440–443.

65. Alanazi, A., Nojiri, C., Noguchi, T., Ohgoe, Y., Matsuda, T., Hirakuri, K., et al. (2000). *Artificial Organs, 24*(8), 624–627.
66. Bangali, Z., & Shea, L. D. (2005). *MRS Bulletin, 30*(9), 659.
67. Morrison, M. L., Buchanan, R. A., Liaw, P. K., Berry, C. J., Brigmon, R. L., Riester, L., et al. (2006). Electrochemical and antimicrobial properties of diamond like carbon-metal composite films. *Diamond and Related Materials, 15*(1), 138–146.
68. Maizza, G., Saracco, G., & Abe, Y. (1999). Advances in science and technology. In Vincenzini, P. (Eds.), *9th Cimetec-World Forum on New Materials, Faenza* (pp. 75–82).
69. Dowling, D. P., Kola, P. V., Donnelly, K., Kelly, T. C., Brumitt, K., Lloyd, L., et al. (1997). *Diamond and Related Materials, 6*, 390–393.
70. Tiainen, V. M. (2001). *Diamond and Related Materials, 10*, 153–160.
71. Butter, R. S., & Lettington, A. H. (1995). DLC for biomedical applications (reviews). *Journal of Chemical Vapor Deposition, 3*, 182–192.
72. Higson, S. P. J., & Vadgama, P. M. (1995). *Analytica Chemica Acta, 300*, 77–83.
73. Higson, S. P. J., & Vadgama, P. M. (1995). *Biosensors and Bioelectronics, 10*(5), VIII.
74. Du, C., Su, X. W., Cui, F. Z., & Zhu, X. D. (1998). *Biomaterials, 19*, 651–658.
75. Cui, F. Z., & Li, D. J. (2000). *Surface Coatings Technology, 131*, 481–487.
76. Ivanov-Omskii, V. I., Panina, L. K., & Yastrebov, S. G. (2000). *Carbon, 38*, 495–499.
77. Dyuzhev, G. A., Ivanov-Omskii, V. I., Kuznetsova, E. K., Rumyantsev, V. D., et al (1996). *Journal of Molecular Materials, 8*, 103–106.
78. Ivanov-Omskii, V. I., Tolmatchev, A. V., & Yastrebov, S. G. (1996). *Philosophical Magazine Part B, 73*(4), 715–722.
79. Andrade, J. D. (Ed.). (1988). *Surface and interfacial aspect of biomedical polymers. Protein Adsorption* (Vol. 2). New York: Plenum.
80. William, D. F. (1985). Physiological and microbiological corrosion CRC Crit (review). *Biocompatibility, 1*, 1–30.
81. William, D. F. (Ed.) (1987). *Definitions in biomaterials*. Amsterdam: Elsevier.
82. William, D. F. (1981). *Systemic aspects of biocompatibility* (Vol. 1–2). Boca Raton: CRC Press.
83. Martini, F. C. (2001). *Fundamentals of anatomy and physiology* (5th ed.). New Jersey, USA: Prentice Hall.
84. Hoffman, A. S. (1982). *Advances in Chemistry Series, 199*, 3.
85. Vroman, L. (1977). *Annals of the New York Academy of Science, 283*, 65 (L. Vroman & E. F. Leonard (Eds.)).
86. National Heart, Lung, and Blood Institute (NHBLI), (1980). *Clinical Guidelines for Biocompatibility*. Washington D.C. USA.
87. Neumann, A. W., Absolom, D. R., Francis, D. W., Omenyi, S. N., Spelt, J. K., Policova, Z., et al. (1983). *Annals of the New York Academy of Sciences, 416*, 276.
88. Srinivasan, S., & Sawyer, P. N. (1970). *Journal of Colloid and Interface Science, 32*(3), 456.
89. Sawyer, P. N., & Pate, J. W. (1953). *American Journal of Physiology, 175*, 113.
90. Sawyer, P. N., & Srinavasan, S. (1967). *American Journal of Physiology, 114*, 42.
91. Srinivasan, S., & Sawyer, P. N. (1969). *JAAMI, 3*, 116.
92. Martin, J. G., Afshar, A., Kaplitt, M. J., Chopra, P. S., Srinivasan, S., & Sawyer, P. N. (1968). Implantation studies with some non-metallic prostheses. *Transaction of American Society for Artificial Internal Organ, 14*, 78.
93. Wilcox, C. D., Dove, S. B. McDavid, W. D., & Greer, D. B., Imagetool. http://ddsdx.uthscsa.edu/dig/itdesc
94. Baier, R. E. (1972). *The Bulletin of the New York Academy of Medicine, 48*, 273.
95. Baier, R. E., Loeb, G. I., & Wallace, G. T. (1971). *Federation Proceedings, 30*, 1523–1538.
96. Chen, J. Y., Leng, Y. X., Tian, X. B., Wang, L. P., Huang, N., Chu, P. K., et al. (2002). Antithrombogenic investigation of surface energy and optical bandgap and hemocompatibility mechanism of Ti (Ta + 5)O_2 thin films. *Biomaterials, 23*, 2545.
97. Curtis, A. (2004). Tutorial on the biology of nanotopography. *IEEE Transactions on Nanobioscience, 3*(4), 293–295.

98. Matsuda, T., & Kurumatani, H. (1990). Surface induced in vitro angiogenesis: Surface property is a determinant of angio-genesis. *ASAIO Transactions, 36*, M565–M568.
99. Hubbell, J. A., Massia, S. P., & Drumheller, P. D. (1992). Surface-grafted cell-binding peptides in tissue engineering of vascular graft. *Annals of the New York Academy of Sciences, 665*, 253–258.
100. Goodman, S. L., Lelah, M. D., Lambrecht, L. K., Cooper, S. L., & Albrecht, R. M. (1984). *Scanning Electron Microscopy, 1*, 279.
101. Dowling, D. P., Kola, P. V., Donnelly, K., Kelly, T. C., Brumitt, K., Lloyd, L., et al. (1997). *Diamond and Related Materials, 6*, 390–393.
102. Allen, M., Law, F. C., & Rushton, N. (1994). *Clinical Materials, 17*, p1–p10.
103. Hauert, R., Muller, U., Francz, G., Birchler, F., Schroeder, A., Mayer, J., et al. (1997). *Thin Solid Films, 308–309*, 191–194.
104. Allen, M., Butter, R., Chandra, L., Lettington, A., & Rushton, N. (1995). *Biomedical Materials and Engineering, 5*(3), 151–159.
105. McColl, I. R., Grant, D. M., Green, S. M., et al. (1993). *Diamond and Related Materials, 3*, 83.
106. Parker, T. L., Parker, K. L., McColl, I. R., Grant, D. M., & Wood, J. V. (1993). *Diamond and Related Materials, 93*, 118.
107. Parker, T. L., Parker, K. L., McColl, I. R., Grant, D. M., & Wood, J. V. (1994). *Diamond and Related Materials, 3*, 1120–1123.
108. Thomson, L. A., Law, F. C., Rushton, N., & Franks, J. (1991). *Biomaterials, 12*, 37–40.
109. Allen, M., Myer, B., & Rushton, N. J. (2001). *Journal of Biomedical Materials Research, 58* (3), 319–328.
110. Schroeder, A., Francz, G., Bruinink, A., Hauert, R., Mayer, J., & Wintermantel, E. (2000). *Biomaterials, 21*, 449–456.
111. Lu, L., Jones, M. W., & Wu, R. L. C. (1993). *Biomedical Materials and Engineering, 3*, 223.
112. Evans, A. C., Franks, J., & Revell, P. J. (1991). *Surface and Coatings Technology, 47*, 662–667.
113. Ames, B. N., McCann, J., & Yamasaki, E. (1975). *Mutation Research, 31*, 347–367.
114. Bruck, S. D. (1977). *Biomaterials, Medical Devices, and Artificial Organs, 5*(1).
115. McHargue, C. J. (1991). In: Y. Tzeng et al. (Eds.), *Application of diamond films and related materials, materials science monographs* (p. 113). New York: Elsevier.
116. Devlin, D., et al. (1997). In: B. Simons (Ed.), *Proceedings of the ASME International Mechanical Engineering Congress and Exposition* (p. 265), Fairfield, NJ, USA: Bioengineering Division.
117. Gordon, J. L. (1986). In J. P. Cazenave, J. A. Davies, M. D. Kazatchkine, van Aken, W. G. (Eds.), *Blood-surface interactions: Biological principles underlying hemocompatibility with artificial materials* (p. 5). Amsterdam: Elsevier Science Publishers (Biomedical Division).
118. Moncada, S., & Vane, J. R. (1982). The role of prostaglandins in platelet-vessel wall interactions. In H. L. Nossel & H. J. Vogel (Eds.), *Pathobiology of endothelial cells* (pp. 253–285). New York: Academic Press.
119. Gimbrone, M. A., Jr. (1986). In M. A. Gimbrone Jr. (Ed.), *Vascular endothelium in hemostasis and thrombosis* (pp.1–13). Edinburgh: Churchill Livingstone.
120. Gimbrone, M. A, Jr. (1987). *Annals of New York Acad. Sci., 516*, 5–11.
121. Chan, T. K., & Chan, V. (1981). Antithrombin III, the major modulator of intravascular coagulation is synthesised by human endothelial cells. *Thrombosis and Haemostasis, 46* (1981), 504–506.
122. Busch, C., Ljungman, C., Heldin, C.-M., Waskson, E., & Obrink, B. (1979). Surface properties of cultured endothelial cells. *Haemostasis, 8*(1979), 142–148.
123. Jaffe, E. A. (1982). Synthesis of factor VIII by endothelial cells. *Annals of New York Academy of Sciences, 401*(1982), 163–170.
124. Mosher, D. F., Doyle, M. J., & Jaffe, E. A. (1982). Secretion and synthesis of thrombospondin by cultured human endothelial cells. *Journal of Cell Biology, 93*(1982), 343.
125. Folkman, J., & Haudenschild, C. (1980). Angiogenesis in vitro. *Nature, 288*, 551–556.

126. Tonnesen, M. G., Smedly, L. A., & Henson, P. M. (1984). *The Journal of Clinical Investigation, 74*, 1581–1592.
127. Kubota, Y., Kleinman, H. K., Martin, G. R., & Lawley, T. J. (1988). *Journal of Cell Biology, 107*, 1589–1598.
128. Pauli, B., & Lee, C. (1988). *Laboratory Investigation, 58*, 379–387.
129. Picker, L. J., Nakache, M., & Butcher, E. C. (1989). Monoclonal antibodies to human lymphocyte homing receptors define a novel class of adhesion molecules on diverse cell types. *Journal of Cell Biology, 109*(2), 927–937.
130. Pober, J. (1988). *American Journal of Pathology, 133*, 426–433.
131. Berg, E. L., Goldstein, L. A., Jutila, M. A., Nakache, M., Picker, L. J., Streeter, P. R., et al. (1989). *Immunological Reviews, 108*, 1–18.
132. Rice, G. E., & Bevilacqua, M. P. (1989). *Science, 246*, 1303–1306.
133. Springer, T. (1990). *Nature, 346*, 425–433.
134. Hynes, R. (1992). *Cell, 69*, 11–25.
135. Folkman, J., Haudenschild, C., & Zetter, B. R. (1979). *Proceedings of the National Academy of Sciences of the United States of America, 76*, 5217.
136. Keegan, A., Hill, C., Kumar, S., Phillips, P., Schof, A., & Weiss, J. (1982). *Journal of Cell Science, 55*, 261.
137. Charo, I., Karasek, M. A., Davison, P. M., & Goldstein, I. M. (1984). *Journal of Clinical Investigation, 74*, 914.
138. Gerritsen, M. E. (1987). *Biochemical Pharmacology, 36*, 2701–2711.
139. Fujimoto, T., & Singer, S. J. (1988). *Journal of Histochemistry and Cytochemistry, 36*, 1309–1317.
140. Kubota, Y., Kleinman, H. K., Martin, G. R., & Lawley, T. J. (1988). *Journal of Cell Biology, 107*, 1589.
141. Ades, E. W., Candal, F., Swerlick, J., George, R. A., Summers Susan, V. G., Bosse, D. C., et al. (1992). *Journal of Investigative Dermatology, 99*, 683–690.
142. Van Wachem, P. B., Beugeling, T., Feijen, J., Bantjes, A., Detmers, J. P., & van Aken, W. G. (1985). *Biomaterials, 6*, 403–408.
143. Van Wachem, P. B., Schakenraad, J. M., Feijen, J., Beugeling, T., van Aken, W. G., Blaauw, E. H., et al. (1989). *Biomaterials, 10*, 532–539.
144. Kaukonen, M., Nieminen, R. M., Poykko, S., & Settsonen, A. (1999). Nitrogen doping of amorphous carbon surfaces. *Physical Review Letters, 83*(25), 5346–5349.
145. Ganong, W. F. (1995). *Ganong's review of medical physiology* (17th ed.). New York: Appleton & Lang.
146. Chen, J. Y., Wang, L. P., Fu, K. Y., Huang, N., Leng, Y., Leng, Y. X., et al. (2002). *Surface and Coatings Technology, 156*, 289–294.
147. Krishnan, L. K., Varghese, N., Muraleedharan, C.V., Bhuvaneshwar, G.S., Derangere, F., Sampeur, Y., et al. (2002). *Biomolecular Engineering, 1–3*.
148. Gutensohn, K., Beythien, C., Bau, J., Fenner, T., Grewe, P., Koester, R., et al. (2000). *Thrombosis Research, 99*, 577–585.
149. Ogwu, A. A., Lamberton, R. W., McLaughlin, J. A., & Maguire, P. D. (1999). *Journal of Physics Part D. Applied Physics, 32*, 981.
150. Jiu, J. T., Wang, H., Cao, C. B., & Zhu, H. S. (1999). *Journal Materials Science, 34*, 5205–5209.
151. Dementjev, A. P., Petukhov, M. N., & Baranov, A. M. (1998). *Diamond and Related Materials, 7*, 1534–1538.
152. Dementjev, A. P., & Petukhov, M. N. (1997). *Diamond and Related Materials, 6*, 486.
153. Grill, A., Meyerson, B., Patel, V., Reimer, J. A., & Petrich, M. A. (1987). *Journal of Applied Physics, 61*, 2874.
154. Miyake, S., Kaneko, R., Kikuya, Y., & Sugimoto, I. (1991). *Transactions of the ASME Journal of Tribology, 113*, 384.
155. Baker, M. A., & Hammer, P. (1997). *Surface and Interface Analysis, 25*, 629–642.

156. Demichelis, F., Pirri, C. F., & Tagliaferro, A. (1992). *Materials Science and Engineering B, 11*, 313–316.
157. Li, D. J., Cui, F. Z., Gu, H. Q., & Adhesion, J. (1999). *Sci. Technol., 13*, 169.
158. Linder, S., Pinkowski, W., & Aepfelbacher, M. (2002). *Biomaterials, 23*, 767–773.
159. Goodman, S. L., Cooper, S. L., & Albrecht, R. M. (1991). *Journal of Biomaterials Science, Polymer Edition, 2*(2), 147–159.
160. Tangen, D., Berman, H. J., & Marfey, P. (1971). *Thrombosis et Diathesis Haemorrhagica, 25*, 268.
161. Schakenraad, J. M., Busscher, H. J., Wildevuur, C. R. H., & Arends, J. (1988). *Cell Biophysics, 13*, 75.
162. Goodman, S. L., Cooper, S. L., & Albrecht, R. M. (1985). In Y. Nose, C. Kjellstrand, & P. Ivanovich (Eds.) *Progress in artificial organs* (pp. 1050–1055). Cleveland, OH: ISAO Press.
163. Schakenraad, J. M., Busscher, H. J., Wildevuur, C. R. H., & Arends, J. (1986). *Journal of Biomedical Materials Research, 20*, 773.
164. Grinnell, F. (1987). *Annals of the New York Academy of Sciences, 516*, 280.
165. Grinnell, F. (1986). *Journal of Cell Biology, 103*, 2697.
166. Feuerstein, I. A. (1987). *Annals of the New York Academy of Sciences, 516*, 484
167. Park, K., & Park, H. (1989). *Scanning Microscopy, 3*(Suppl), 137.
168. Pitt, W. G., Spiegelberg, S. H., & Cooper, S. L. (1987). *Transactions of the Society for Biomaterials, 10*, 59.
169. Park, K., Mosher, D. F., & Cooper, S. L. (1985). *Journal of Biomedical Materials Research, 20*, 589.
170. Brash, J. L. (1985). *Macromolecular Chemistry, 9*(Suppl), 69.
171. Lambrecht, L. K., Young, B. R., Stafford, R. E., Park, K., Albrecht, R. M., Mosher, D. F., et al. (1986). *Thrombosis Research, 41*, 99.
172. Wildner, O., Lipkow, T., & Knop, J. (1992). Increased expression of ICAM-1, E-selectin and V-CAM-1 by cultured endothelial cells upon exposure to haptens. *Experimental Dermatology, 1*, 191.
173. Klein, C. L., Nieder, P., Wagner, M., Kohler, H., Bittinger, F., Kirkpatrick, C. J., et al. (1994). *Journal of Pathophysiology, 5*, 798–807.
174. Albelda, S., Smith, C., & Ward, P. (1994). Adhesion molecules and inflammatory injury. *FASEB Journal, 8*, 504–512.
175. Gerdes, J., Schwab, U., Lemke, H., & Stein, H. (1983). Production of a mouse monoclonal antibody reactive with a human nuclear antigen associated with cell proliferation. *International Journal of Cancer, 31*(1), 13–20.
176. Thomas, W. E. (1999). *Brain Research Reviews, 31*(1), 42–57.
177. http://users.ahsc.arizona.edu/davis/bbbpericytes.htm
178. Chen, X., & Zuckerman, S. T. (2005). Weiyuan John Kao. Intracellular protein phosphorylation in adherent U937 monocytes mediated by various culture conditions and fibronectin-derived surface ligands. *Biomaterials, 26*(8), 873–882.
179. Fournier, J. A., Calabuig, J., Merchán, A., Augé, J. M., Melgares, R., Colman, T., et al. (2001). *Revista Espanola de Cardiologia, 54*(5), 567–572.
180. De Scheerder, I., Szilard, M., Yanming, H., Ping, X. B., Verbeken, E., Neerinck, D., et al. (2000). *The Journal of Invasive Cardiology, 12*(8), 389–394.
181. Tran, H. S., Puc, M. M., Hewitt, C. W., Soll, D. B., Marra, S. W., Simonetti, V. A., et al. (1999). *Journal of Investigative Surgery: The Official Journal of the Academy of Surgical Research, 12*(3), 133–140.
182. http://www.tiem.utk.edu/~gross/bioed/webmodules/cellattach.htm
183. Izzard, C. S., & Lochner, L. R. (1976). Cell-to-substrate contacts in living fibroblasts: An interference reflection study with an evaluation of the technique. *Journal of Cell Science, 21*, 129.
184. Bereiter-Hahn, J., Fox, C. H., & Thorell, B. (1979). Quantitative reflection contrast microscopy of living cells. *Journal of Cell Biology, 82*, 767–779.

Chapter 12
Applications of Carbon Nanotubes in Bio-Nanotechnology

T. Okpalugo, W. Ahmed and M. J. Jackson

Abstract Patients are seeking for better health care, while healthcare providers and insurance companies are calling for cost-effective diagnosis and treatments. The biomedical industry thus faces the challenge of developing devices and materials that offer benefits to both patients and healthcare industry. The combination of biology and nanotechnology is expected to revolutionize biomedical research by exploiting novel phenomena and properties of materials present at nanometer length scale. This will lead to the creation of functional materials, devices, and systems through control of matter on the nanometer meter scale and the direct application of nanomaterials to biological targets.

12.1 Introduction

Nanomaterials existed in nature, long before mankind was able to identify forms at the nanoscale level [1–5]. Today, nanomaterials have been designed for a variety of biomedical and biotechnological applications, including biosensors, enzyme encapsulation, neuronal growth, drug delivery, and bone growth [6–10]. The advances in bio-nanotechnology is based on the introduction of novel nanomaterials which can result in revolutionary new structures and devices using extremely biological sophisticated tools to precisely position molecules and assemble hier-

The original version of this chapter was revised: Erroneously added author name has been removed. The correction to this chapter is available at https://doi.org/10.1007/978-3-319-33489-9_24

T. Okpalugo
University of Ulster, Newtownabbey, UK

W. Ahmed
School of Medicine, University of Central Lancashire, Preston, UK

M. J. Jackson (✉)
Kansas State University, Salina, Kansas, USA
e-mail: jacksonmj04@yahoo.com

W. Ahmed and M.J. Jackson (eds.), *Surgical Tools and Medical Devices*,
DOI 10.1007/978-3-319-33489-9_12

archal structures and devices. The application of the principles of biology to nanotechnology provides a valuable route for further miniaturization and performance improvement of artificial devices. The feasibility of the bottom-up approach that is based on molecular recognition and self-assembly properties of biomolecules has already been proved in many inorganic–organic hybrid systems and devices [11]. Nanodevices with bio-recognition properties provide tools at a scale, which offers a tremendous opportunity to study biochemical processes and to manipulate living cells at the single molecule level. The synergetic future of nano- and bio-technologies holds great promise for further advancement in tissue engineering, prostheses, pharmacogenomics, surgery, and general medicine.

In this chapter, we discuss about various aspects of carbon nanotubes that have been successfully applied to bio-nanotechnology. We focus particularly on biological applications of carbon nanotubes, and take a comprehensive look at the advances in this fast-moving and exciting research field. We review the results on modifications of carbon nanotubes, and highlight some of the recent achievements in the fabrication and evaluation of carbon nanotube-based biological devices and implants.

12.2 Bio-Nanomaterials

Many nanomaterials have novel chemical and biological properties and most of them are not naturally occurring [12]. Carbon nanotubes (CNTs) are in the top list of artificial bio-nanomaterials [13–17], which has won enormous popularity in nanotechnology for its unique properties and applications. CNTs have highly desirable physicochemical properties for use in commercial, environmental and medical sectors. The inclusion of CNTs to improve the quality and performance of many widely used products, as well as potentially in medicine, will dramatically affect occupational and public exposure to CNT-based bio-nanomaterials in the near future.

Even since the discovery of carbon nanotubes, researchers have been exploring their potential in bioapplications [18]. One focal point has been the development of nanoscale biosensor [19] and drug delivery systems [20] based on carbon nanotubes, which has been driven by the experimental evidence that biological species such as proteins and enzymes can be immobilized either in the hollow cavity or on the surface of carbon nanotubes [21]. Recently, hopes have been raised for the use of carbon nanotubes as superior biosensor materials in light of the successful fabrication of various electroanalytical nanotube devices, especially those modified by biological molecules [22]. These prototype devices, sometimes prepared as ordered arrays or single-nanotube transistors, have shown efficient electrical communications and promising sensitivities required for such applications as antigen recognition, [23] enzyme-catalyzed reactions [24] and DNA hybridizations [25]. The CNT/hydroxyapatite composite coated [26] bio-implants has also received much attention recently, for the surface modification of implant materials to promote interaction with living bone tissues owing to its similar chemical composition and crystal structure as natural apatite in the human skeleton.

12.3 Carbon Nanotubes

12.3.1 Introduction

The discovery of carbon nanotubes [27] in 1991 has stimulated significant scientific interest and research leading to rapid progress in the field. Since their discovery, enormous researches have been focused on the problems of synthesizing nanotubes, on their physical properties and on possible applications in nanoelectronics [28–32], catalysis [33, 34, 35] and other fields including bioapplications [36–42]. The highly impressive structural, mechanical, and electronic properties such as small size and mass, high strength, higher electrical, and thermal conductivity, etc., are some of the fascinating properties of this remarkable material that are ideal for various potential applications.

12.3.2 Synthesis

Carbon nanotubes can be manufactured using a variety of methods that include (Fig. 12.1): (i) Laser ablation [43] uses a high-power laser to vaporize a graphite source loaded with a metal catalyst (Fig. 12.1a). The carbon in the graphite reforms as predominantly single-wall nanotubes on the metal catalyst particles. (ii) Arc discharge [44] involves an electrical discharge from a carbon-based electrode in a suitable atmosphere to produce both single and multiwall tubes of high quality but in low quantities (Fig. 12.1b). (iii) Chemical vapor deposition (CVD) [45], where a hydrocarbon feedstock is reacted with a suitable metal-based catalyst in a reaction chamber to grow CNTs (Fig. 12.1c) is subsequently removed from the substrate and catalyst by a simple acid wash.

The laser vaporization method is widely used for the production of single-walled (SW) CNTs. The laser is suitable for materials with a high boiling temperature, such as carbon, as the energy density of lasers is much higher than that of other vaporization devices. The basic principle of this method is as follows: a CO_2 laser beam is introduced onto the target (carbon composite doped with catalytic metals) located in the center of a quartz tube furnace; the target is vaporized in a high temperature argon atmosphere and SWCNTs are formed; and the SWCNTs produced are conveyed by the gas to a special collector. The method has several advantages, such as the high quality of the diameter and controlled growth of the SWCNTs. The change of the furnace temperature, catalytic metals, and flow rate directly affect the SWCNT diameter [46].

Large scale synthesis of Multiwalled (MW) CNTs by arc discharge was reported [47] in a helium, argon, and methane atmosphere. It was found that methane is the best gas for the synthesis of MWCNTs. This is due to the thermal decomposition of

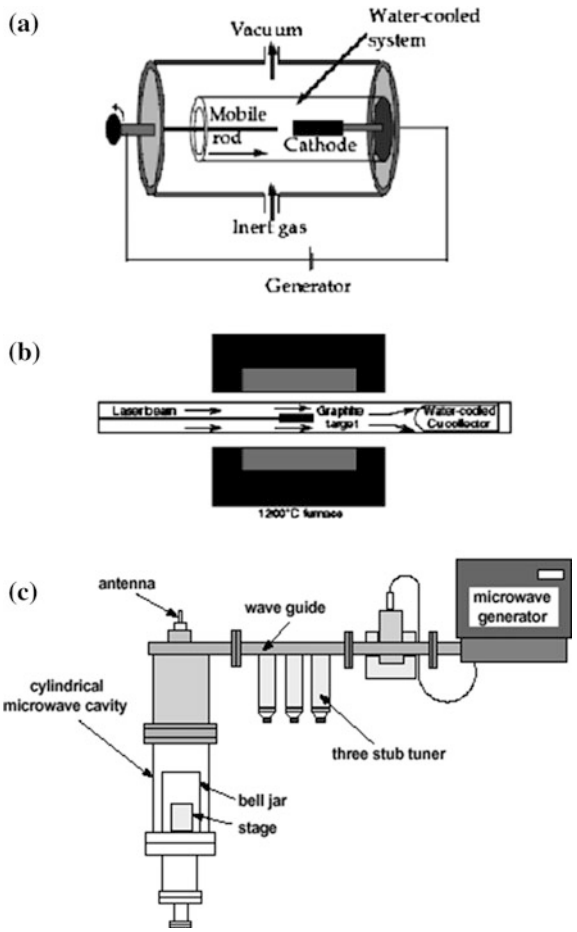

Fig. 12.1 Methods of manufacture for carbon nanotubes: **a** laser ablation; **b** arc discharge; and **c** microwave chemical vapor deposition

methane producing hydrogen that achieves higher temperature and activity compared to inert gasses, such as Helium or Argon. The hydrogen is also found to be an effective factor in the synthesis of MWCNTs [48–50]. The drawback of arc discharge method is purification of CNTs. Removal of non-nanotube carbon and metal catalyst material in as-grown CNTs is much more expensive than production itself.

The first two methods, arc discharge and laser furnace, also have the drawback that they do not allow control of the location and the alignment of the synthesized CNTs. CVD is suggested as an alternate method which uses hydrocarbon vapor (e.g., methane) that is thermally decomposed in the presence of a metal catalyst and CNTs are deposited directly on desired substrate.

12.3.3 Structure and Properties

A CNT can be regarded as one gigantic carbon molecule obtained by folding graphite planes into a cylinder (Fig. 12.2) whose diameter is measured in nanometers and whose length can reach macroscopic dimensions [51].

This linear structure determines the extremely high mechanical strength of CNT [52] whereas their electrical conductivity depends strongly on the diameter and the helicity that is the angle between the most highly packed chains of atoms and the axis of the cylinder [53].

Two types of CNTs exist: (i) whose walls contain a single layer of carbon atoms, SWCNTs [54] and (ii) nanotubes with walls consisting of several concentric cylindrical graphite layers, MWCNTs [55] as illustrated in Fig. 12.3. The hexagonal lattice structure of CNTs gives rise to three types of SWCNTs and their

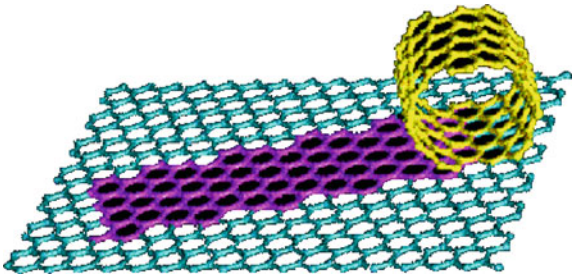

Fig. 12.2 Folding of graphite sheets to form a carbon nanotube

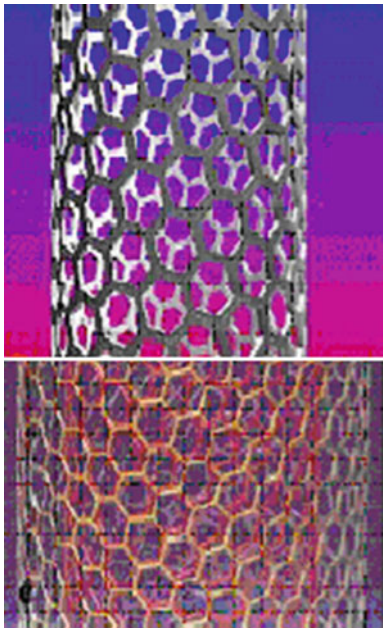

Fig. 12.3 Nanotubes with walls consisting of several concentric cylindrical graphite layers known as multiwalled carbon nanotubes (MWCNTs)

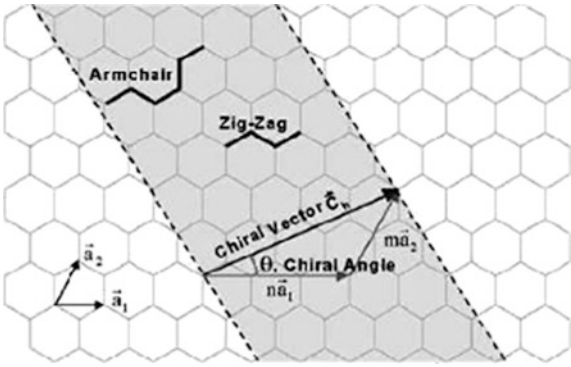

Fig. 12.4 Unit cell of a carbon nanotube

diameter varies between 0.4 and 2 nm. Based on the unit cell of a CNT (Fig. 12.4), it is possible to identify armchair nanotubes, formed when n = m and the chiral angle is 30; zig-zag nanotubes, formed when either n or m are zero and the chiral angle is 0; and chiral tubes, with chiral angles intermediate between 0 and 30. SWNTs are either metallic or semiconducting depending on their diameter and helicity. All armchair nanotubes are metallic, while zig-zag and chiral nanotubes can be metallic or semiconducting.

12.3.4 Applications

There is a wealth of potential applications for CNTs [56–59] due to their extraordinary properties [60–63]. They are probably the best electron field-emitter possible. They are polymers of pure carbon and can be reacted and manipulated using the tremendously rich chemistry of carbon. This provides opportunity to modify the structure and to optimize solubility and dispersion. Very significantly, CNTs are molecularly perfect, which means that they are free of property-degrading flaws in the nanotube structure. These extraordinary characteristics give CNTs potential in numerous applications including electronic, mechanical, chemical, thermal, and biological applications. The electrical properties of single wall carbon nanotubes are highly sensitive to surface charge transfer and changes in the surrounding environment as the walls of nanotubes constitute a monolayer of atomic arrangement. Due to their surface sensitivity, surface charge mechanisms can cause covalent/noncovalent interactions and van der Waals forces to induce sufficient change in their electronic properties and local density of states. The diversity of available chemistries and easiness of modification makes CNTs viable candidates for biological applications. The biological assembly of CNTs can be attained by their manipulation, dispersion, and separation.

12.3.4.1 CNTs as Biosensors

The first application of CNTs for biosensors was proposed in 1996 by Britto et al. [64]. Later, the study by Star et al. on SWNTs have shown to exhibit a significant change in response to the presence of small biomolecules and proteins [65]. The adsorption of cytochrome c, a redox catalyst in the respiratory chain of mitochondria, has been detected in situ using a SWCNT device [66]. Biotin-modified SWCNTs have been used to electronically detect biotin-streptavidin binding [65]. It has been demonstrated that the binding of streptavidin to biotin-functionalized SWCNTs results in a reduced conductance of the carbon nanotubes. Although the mechanism of chemical sensing exhibited by SWNTs has not been unequivocally identified, it seems probable that the resistance changes experienced by these devices originate from the doping of the carbon nanotubes as a result of charge transfer processes that are associated with interactions between the SWCNTs and the analyte. Nevertheless, the interpretation of the electrical responses in thin film devices is complicated by the nature of carbon nanotube networks that are a mixture of bundled semiconducting and metallic SWCNTs.

In some cases the conductance change originates from electronic effects occurring at the metal-nanotube contacts during adsorption. Despite having the absence of a definitive understanding of the sensing mechanism, remarkable achievements in electrical biosensing have been reported [67, 68]. Covalent coupling of the alkaline phosphatase (ALP) enzyme to CNTs has lead to the highest sensitivity (detection limit of 1 pg L^{-1}) reported thus far for electrical detection of DNA. This CNT-ALP-linked assay can be modified for antigen detection by using specific antibody–antigen recognition. Thus, it could provide a fast and simple solution for molecular diagnosis in pathologies where molecular markers exist, such as DNA or protein [69].

Demand for the reliable monitoring of blood glucose has stimulated further research on the development of biosensors based on CNTs. The voltametric behavior of oxidized SWCNTs with physically adsorbed glucose oxidase has been investigated [70]. The magnitude of the catalytic response to the addition of D-glucose was tenfold greater than that observed with a glassy carbon electrode. Further improvements in sensitivity and temporal resolution were made by using glucose oxidase-functionalized individual SWCNTs in a (field emission transistor) FET configuration which allowed for the measurement of enzymatic activity at the level of a single molecule.

Enzyme immobilization is central to bioreactor and biosensor technologies. The current immobilization methods include covalent binding and physical adsorption of enzymes on high surface area materials (carbon silica and polymers). The first step in enzyme immobilization on CNTs is to create active sites on their stable walls. The immobilization of antibodies on the sensor platform to convert a nonelectrical, physical or chemical, quantity into an electrical signal is the key for the control and the improvement of the performance of such a biosensor. Several immobilization methods have been reported for the improvement of the antibody–antigen binding to increase detection sensitivity or for covalent binding of antibody or protein on solid

surface [71]. Huang et al. studied the antibody immobilization on the surfaces of various oxidation processed nanodiamond and carbon nanotubes [72].

Electron transfer in biological systems is one of the leading areas of biochemical and biophysical sciences, and has received more and more attention [73–80]. The direct electron transfer of enzymes with electrodes can be applied to the study of enzyme-catalyzed reactions in biological systems and the development of an electrochemical basis for the investigation of the structure of enzymes, mechanisms of redox transformations of enzyme molecules and metabolic processes involving redox transformations. Enzyme-modified electrodes provide a basis for constructing biosensors, biomedical devices, and enzymatic bioreactors. If an enzyme immobilized on an electrode surface is capable of direct electron transfer and keeping its bioactivity, it can be used in biosensors without the addition of mediators or promoters onto the electrode surface or into the solution. Unfortunately, it is difficult for an enzyme to carry out a direct electrochemical reaction due to several factors. For example, enzymes would be adsorbed on the electrode surface, resulting in the denaturation, and loss of their electrochemical activities and bioactivities. In addition, usually, the larger three-dimensional structure of enzymes and the resulting inaccessibility of the redox centers have made it generally difficult to obtain direct electron transfer between enzymes and electrode surfaces, so that promoters and mediators are needed to obtain their electrochemical responses. Therefore, suitable electrode materials and immobilization methods of enzymes onto the electrode surface are important for obtaining their direct electrochemical reaction and keeping their bioactivities.

For the immobilization and/or modification of cells, there are mainly two types of interface interactions being used between a substrate and cells; one is chemical modification of substrate surface to have high affinity to cells, and the other is attaching biomolecules on substrate to recognize the cells [81]. Since the pioneering work of Decher [82], there has been great interest in using the layer-by-layer immobilization of polyelectrolytes for the development of biosensors [83].

Since carbon nanotubes show good electric conductivity, they have been used to modify electrodes, and catalyze various biomolecules electrochemically [84]. Direct electrochemistry of redox proteins may provide a model for the study of electron transport of enzymes in biological system [85] and establish a foundation for fabricating a new generation of electrochemical biosensors without using mediators [86]. The CNT has been demonstrated as biochemically compatible, electrically conductive nanoscale interface between redox enzymes and macro-scale electrodes [87]. CNTs are capable of maintaining the functional properties of redox enzymes while linking biomolecules into nanoelectronic platforms. Wang et al. [88] have developed biosensors of exceptional sensitivity by exploiting the efficiency and specificity inherent in redox proteins. The direct electron transfer of redox enzymes to an electrode surface of CNT has been reported by Guiseppi-Elie also [89]. A relatively new approach to realize direct electrochemistry of proteins is to incorporate proteins into films modified on surface of solid electrodes [90]. Li et al. [91] reported direct electrochemistry of cytochrome c (Cyt c) in SWCNT films cast on glassy carbon (GC) electrodes.

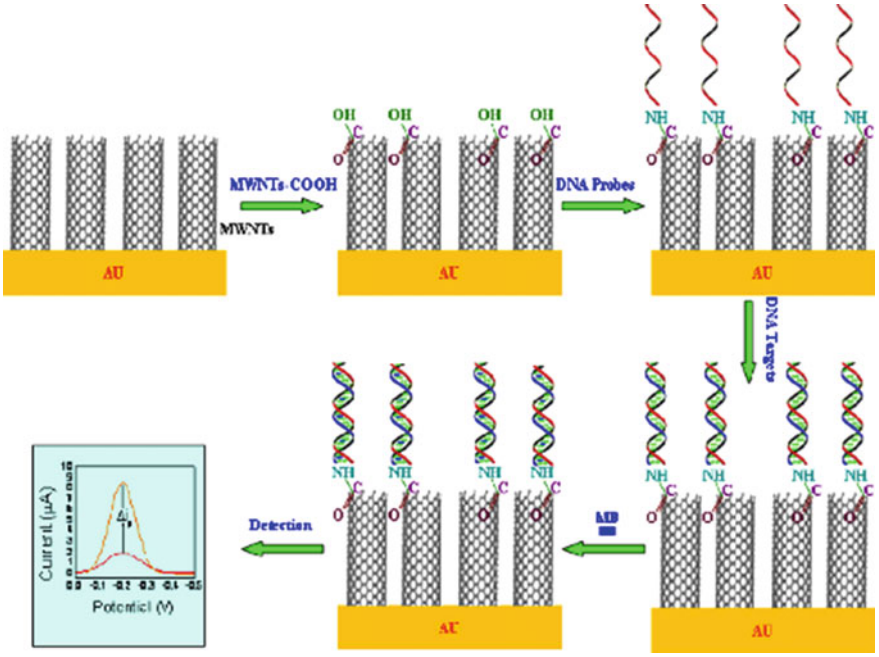

Fig. 12.5 Schematic diagram of self-assembly of DNA probes to MWCNTs

Several other important investigations have also been directed to the attachment of natural proteins and DNA immobilization onto MWCNT to construct biosensors. Davis et al. [92] have reported the high surface area possessing multiply acidic sites that may make an offer of special opportunities for the immobilization of enzymes. MWNTs can be activated in acid oxidation conditions due to the residues such as –COOH, –COH, and –OH introduced on the surface of MWNTs [93, 94]. The schematic of self-assembly of DNA probes onto MWCNTs described by them are illustrated in Fig. 12.5. Azamian et al. [95] have described that BSA can be covalently attached to SWNTs and MWNTs by way of diimide-activated amidation under ambient conditions, while the majority of the protein in the nanotube–BSA conjugates remain bioactive. CNTs have been used as modified electrodes to catalyze the electrochemical reaction of some biomolecules, such as dopamine, β-nicotinamide adenine dinucleotide (NADH), cytochrome *c*, etc., [96].

Wang and Musameh [97] have shown that the catalytic activities of the immobilized β—lactamase I on or in carbon nanotubes had no drastic conformational change. The carbon nanotubes appeared to act as a host in its ability to encapsulate protein molecules within an environment, which offered some protection. Wu et al. [98] also reported the application of carbon nanotubes as an electrode material. Redox proteins such as cytochrome *c* and azurin were immobilized on and within carbon nanotubes and gave reproducible, well-behaved voltammetric responses. The performance of carbon nanotubes paste electrode

(CNTs-PE) prepared by dispersion of multiwall carbon nanotubes (MWCNTs) within mineral oil is also reported [99]. The resulting electrode showed excellent electrocatalytic activity toward ascorbic acid, uric acid, and dopamine.

Rubianes and Rivas [100] observed direct cyclic voltammograms (CV) of myoglobin (Mb) and other proteins at MWCNT-modified.

GC electrodes, in which they dipped the MWCNT electrodes into Mb solution and Mb was absorbed into MWCNT films. A reversible CV peak pair of catalase in SWCNT films cast on gold (Au) electrodes and used the films to electrochemically catalyze reduction of hydrogen peroxide was also observed by them. Zhao et al. [101] coated a mixture of hemoglobin (Hb), glucose oxidase (GO_X), or horseradish peroxidase (HRP) solution with carbon nanotube dispersions onto GC electrodes. After drying, the films demonstrated good direct electrochemistry of Hb, GO_X, or HRP in blank buffers. Cai et al. [102] covalently attached Mb or HRP onto the ends of vertically oriented SWCNT forest arrays assembled on pyrolytic graphite (PG) electrodes. Quasi-reversible heme Fe(III)/Fe(II) CV response of Mb or HRP at this electrode was observed. There have also been suggestions of using nanodiamond [103] as the signal transducer for glucose sensing enzyme due to the biocompatibility and chemical robustness of these systems.

12.3.4.2 Processibility

A major drawback of CNTs particularly relevant to biological applications is their complete insolubility in all types of solvents. However, CNTs have been found to exhibit a certain degree of chemical reactivity towards many reagents, thus leading to increased solubility and processability. An aqueous medium is highly essential in order to study CNTs in the presence of live cells and therefore the solubilization of CNTs in aqueous solutions is the focus of biological research. Several strategies have been developed to introduce carbon nanotubes into solvent systems, including dispersion and suspension under special experimental conditions and the chemical modification and functionalization. The well-dispersed and solubilized carbon nanotubes make it possible to characterize and study the carbon nanotubes by using solution-based techniques, to realize some of the unique properties of the nanotubes, and to carry out further chemical transformations. The recent bloom of chemical modification and functionalization methods has made it possible to solubilize and disperse carbon nanotubes in water, thus opening the path for their facile manipulation and processing in physiological environments. Equally important is the recent experimental demonstration that biological and bioactive species such as proteins, carbohydrates, and nucleic acids can be conjugated with carbon nanotubes. These nanotube bioconjugates will play a significant role in the research effort toward bioapplications of carbon nanotubes.

Chemical functionalization of CNTs has been shown to impart solubility in a variety of solvents, to modify their electronic properties and to cause significant debundling. The chemical reactivity of CNTs arises from the curvature-induced strain due to misalignment of the π-orbitals of adjacent conjugated carbon atoms.

The induced strain is higher at the carbon atoms that comprise the CNT caps because they are curved in two-dimensions, and therefore the caps are more reactive than the sidewalls. Hence, treatment in strong oxidizing agents such as HNO_3 or H_2SO_4 preferentially disrupts the aromatic ring structure at the caps of CNTs and introduces carboxylic acid groups that undergo further chemical reactions. Thus, SWNT–COOH are produced by refluxing arc discharge produced SWCNTs in HNO_3 or H_2SO_4. Numerous amidation and esterification reactions of acid functionalised SWCNTs have been reported [104]. In addition to the chemistry that occurs at the oxidized open ends of SWCNTs, it is also possible to react the side wall carbon atoms with highly reactive reagents, such as carbenes, fluorine, aryl radicals, and azome-thineylides. Furthermore, the surface chemistry developed for SWCNTs has been applied to MWCNTs in specific cases. End [105] and/or sidewall [106] functionalization, use of surfactants with sonication [107], polymer wrapping of nanotubes [108], and protonation by superacids [109] have been reported. Although acid treatment methods for CNT functionalisation are quite successful, they often indicate cutting the CNTs into smaller pieces (sonication and/or functionalization), thus partly losing the high aspect ratio of SWCNTs. Riggs et al., have shown, it is possible to solubilize carbon nanotubes in aqueous solutions by covalently attaching water soluble linear polymers [110]. By applying the preceding functionalization scheme, poly-m-aminobenzene sulphonic acid (PABS), has been covalently linked to SWCNTs to form a water soluble nanotube-graft copolymer [111], which could be used for future biological applications.

Titus et al. reported the effective functionalisation of CNT using a novel surfactant and its performance of dispersion of CNT in Poly Vinyl Alcohol (PVA) medium [112]. The as-grown CNTs synthesized using microwave plasma (MP) CVD method was in bundle form (Fig. 12.6) and bundles were dispersed effectively in nanodisperse surfactant by ultrasonication (Fig. 12.7). The surfactant functionalisation promoted further unbundling of CNT in PVA medium. Titus et al. have also reported the attachment of COOH group onto CNT in nonaqueous

Fig. 12.6 As-grown CNTs in bundle form synthesized using the microwave plasma (MP) CVD method

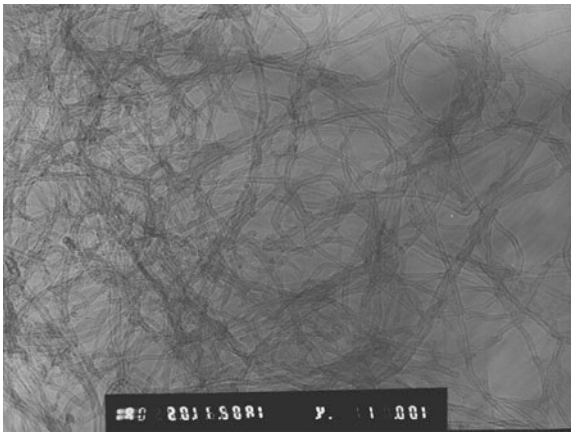

Fig. 12.7 Bundles of CNTs dispersed effectively using a nanodisperse surfactant by ultrasonication

medium by metal CVD process [113]. The advantage of this method is the formation of high population density of carboxyl groups along the walls of CNT compared to the aqueous method. A carboxylic acid groups forms an overall electrophylic surface that can minimizes hydrophobic adsorption of biological molecules like protein. In addition, the wall thickness (20–30 Å) of high-curvature MWCNT, is dimensionally compatible with typical dimensions of proteins (e.g., GO_x, 60 Å × 52 Å × 77 Å). This presumably reduces potential nonspecific binding regions, minimizing surface denaturation effects [114].

Biological functionalization of CNTs have come to be of significant interest also due to the possibility of developing sensitive and ultra-fast detection systems that can be addressed using electronic or optical techniques [115]. Most often, biological sensing techniques depend on optical signals derived from the analytes in use, thus involving a series of steps for preparation, varying reagents to differentiate components, and a relatively large sample size. Although these techniques are relatively sensitive, they result in complex data analysis involving unnecessary time consumption and expensive examination techniques. Miniaturizing processes in biological sensing could result in lowering sample size, time and expenses related to detection and sensing. CNTs functionalized with biological assays could be the key to novel nano-biosensing techniques. Several issues are important regarding functionalization of biomaterials on solid-state nanomaterials such as biocompatibility, specificity to the target biomolecule, extent of functionalization, interface effects and the corresponding sensor performance.

12.3.4.3 Fabrication

One of the key focuses of biosensor research is the need to fabricate bio-electrodes which exhibit high selectivity, high sensitivity and long-term stable response to bioanalytes. Researchers have demonstrated that CNTs have a high electrocatalytic effect, a fast electron transfer rate, and a large working surface area [116]. CNTs

have been used for preparing biosensors employing different strategies: by dispersing them in acidic solutions [117], *N*,*N*-dimethylformamide [118], Nafion [119] and chitosan [120] among others; by incorporating in composites matrices using different binders like Teflon [121], bromoform [122], mineral oil [123] and inks [124]; by immobilizing on pyrolitic graphite electrodes [125]. Wang et al. [126] have demonstrated the ability of the perfluorosulfonated polymer Nafion to disperse single wall (SWCNTs) and multiwall (MWCNTs) carbon nanotubes. They reported a dramatic decrease in the overvoltage for hydrogen peroxide oxidation and reduction as well as highly selective glucose quantification after immobilization of glucose oxidase (GOx) by cross-linking with glutaraldehyde.

Various chemical sensors and biosensors based on CNTs have been developed to detect some important species that are related to human health, such as glucose, NADH, ascorbic acid, and cytochrome C [127]. Significant research and development efforts have been devoted to producing CNT-based glucose chemical and biosensors for in vitro or in vivo applications because of the importance of monitoring blood glucose for the treatment and control of diabetes [128–131]. The measurement principle of CNT-based electrochemical glucose sensors relies on the direct measurement of the oxidation current of glucose on the CNT surface [132] or the immobilization of glucose oxidase on the CNT surface to detect the redox current produced by the enzymatic product H_2O_2 [133]. Lim et al. [134] reported nonenzymatic glucose detection using a well-aligned multiwall CNT electrode in an alkaline medium. The oxidation overvoltage of the glucose on CNT electrodes was reduced 400 mV compared to that on a glassy carbon electrode. The direct oxidation of glucose on the CNT surface avoids the use of glucose oxidase and over comes the problem of the sensors' life and stability; however, the interference from other electroactive species, such as uric acid and ascorbic acid, still exists. Most of the CNT-based electrochemical glucose biosensors are based on glucose oxidase (GO_x), which catalyzes the oxidation of glucose to gluconolactone

$$\text{Glucose} + O_2 \xrightarrow{GO_x} \text{Gluconolactone} + H_2O_2$$

The quantification of glucose can be achieved via electro- catalytic redox detection of the enzymatic product H_2O_2 on the CNT transducer at reduced oxidation or reduction overvoltage. Here, CNTs play multiple roles: (1) a substrate to immobilize GO_x, (2) electrocatalytic oxidation or reduction of H_2O_2 at the CNT surface to reduce overvoltage and avoid interference from other coexisting electroactive species, and (3) an enhanced signal because of its fast electron transfer and large working surface area.

The approaches, such as covalent binding [135], direct adsorption [136], and entrapment [137] has also been widely used to construct GO_x/CNT biosensors. A drawback to physical adsorption and entrapment is that the distribution of enzyme molecules is not uniform, is sometimes unstable, and tends to leach with time. Covalent binding of GO_x on the functionalized CNT needs a relatively longer reaction time. The ideal immobilization method should employ mild chemical

conditions and a short immobilization time to allow for large quantities of enzyme to be immobilized, provide a large surface area for enzyme—substrate contact within a small total volume, minimize barriers to mass transport of substrate and product, and provide a chemically and mechanically robust system.

12.3.4.4 Carbon Nanotubes for Neuronal Growth

Neurons are electrically excitable cells that on network formation serve as conduits for information transfer. A vast amount of information is transferred through the cells in the spinal cord via synaptic and gap junctions in an electroionic fashion mediated by neurotransmitters. The growth of neurites and formation of synapses during development and regeneration is controlled by a highly specialized motile structural specialization at the tip of the neurite called the growth cone. Carbon nanotubes (CNT) are strong, flexible and conduct electrical current. They are biocompatible and nonbiodegradable. They can be functionalized with different biomolecules like neuron growth factors and adhesion agents. These properties are useful in the formation of neuron hybrids [138]. These capabilities of carbon nanotubes make them potentially successful candidates to form scaffolds to guide neurite outgrowth.

Xuan Zhang et al., established the ability of the growth cone to grasp onto carbon nanotube matrices functionalized with neuron growth factors [139]. The need, however, is the ability to guide the formation of neuronal networks and establishment of synaptic connections essential for signal transmission leading to regeneration. Their latest research shows the ability of forming highly directed neural networks in vitro over patterned nanotube substrates (Fig. 12.8). Nanotubes not only function as scaffolds for the neurons, but the patterned boundary serves as markers for directing the growth and network formation. A number of patterns of vertically aligned multiwalled carbon nanotube (MWNT) substrates are used to determine the geometry and NT length most suitable for scaffolding purposes. Surface characterization is performed using scanning electron microscopy. The

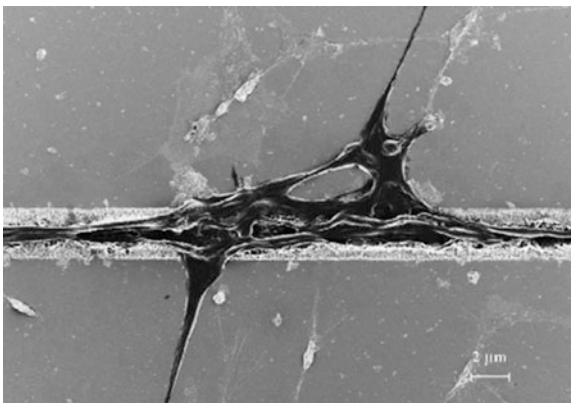

Fig. 12.8 Highly directed neural networks in vitro over a patterned nanotube substrate

interaction between the neuron membrane and the CNT scaffold is also visually analyzed to obtain an insight into network formation in in vitro conditions. This is an essential prerequisite in forming three-dimensional scaffolds.

The growth of cells and neurons on carbon nanotube films also have been reported [140]. The two-dimensional network of aligned nanotube arrays are proposed to be a good substrate for the cell growth. Hu et al. [141], demonstrated the growth of cultured hippocampal neurons on MWCNTs deposited on polyethyleneimine-coated coverslips. SEM was used to identify the morphological changes of neuron growth brought about by the presence of the MWCNTs. The neuronal bodies were found to adhere to the surface of the MWCNTs with their neurites extending through the bed of CNTs and elaborating into many small branches (Fig. 12.9). Neurons remained alive on the nanotubes for at least 11 days, and it was shown that the physisorption of 4-hydroxynonenal on the MWNTs enhanced both neurite outgrowth and branching.

12.3.4.5 Drug Delivery by CNTs

The diversity of available chemistries and cell-penetrating structures makes CNTs viable candidates as carriers for the delivery of drugs, DNA, proteins and other molecular probes into mammalian cells [142]. An important issue in intracellular drug delivery is the poor permeability of the plasma membrane to many drugs. Thus, various carriers, including polyethylene glycol, peptides and lipids, have been developed to facilitate the cellular entry of drugs. One of the prerequisites for such a task is therefore the ability of the carrier to bind to biologically relevant molecules [143].

The feasibility of using SWCNTs for intracellular drug delivery has been demonstrated [144]. Water soluble SWCNTs were functionalized with a fluorescent probe, FITC, to allow tracking of SWCNTs. When murine and human fibroblast cell lines were exposed to SWCNT-FITC, the nanotubes could be shown to accumulate within the cells. Similarly, SWCNTs, covalently functionalized with biotin and reacted with streptavidin, were internalized within human promyelocytic leukemia (H60) cells, human T cells, Chinese hamster ovary (CHO) and 3T3 fibroblast cell lines.

While the mechanism of the CNT cell entry remains undelined, these experiments suggest the viability of CNTs as carriers for delivering relatively large molecules to mammalian cells.

MWCNTs are also demonstrated in drug delivery. Balavoine et al., reported the interactions between MWCNTs and proteins and revealed the self-organization of streptavidin molecules and the growth of its helical crystals on the CNT surface [145]. Similarly, DNA molecules may be adsorbed on MWCNTs, and small protein molecules, such as cytochrome c and -Lactase I, can be inserted within the interior cavity of open CNT. CNTs have also been used to deliver proteins and peptides inside a cell [146] by the direct covalent bonds between a CNT and biomolecules

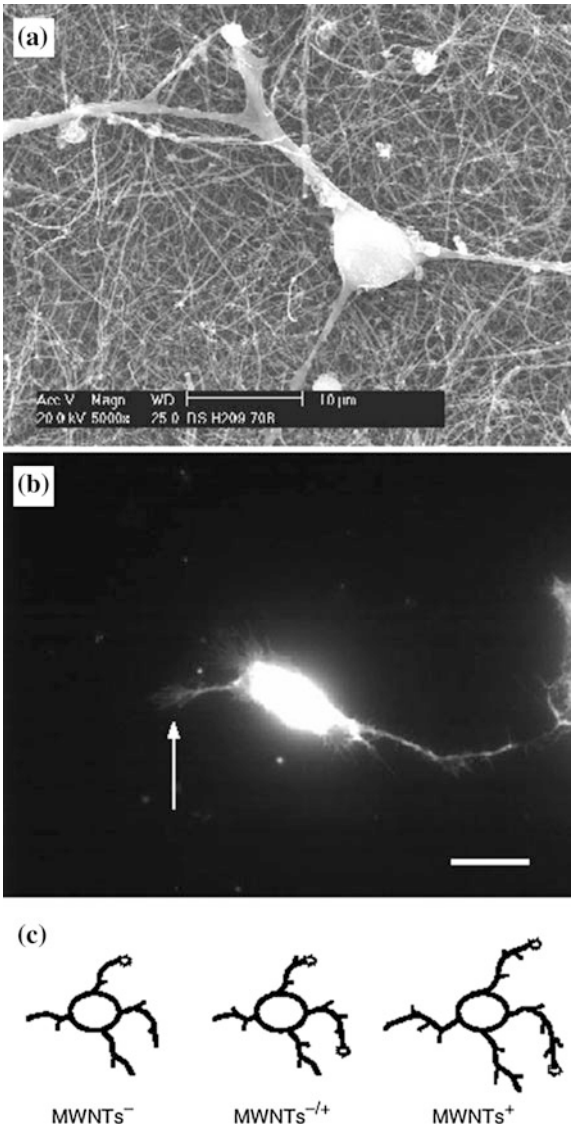

Fig. 12.9 **a** Neuronal bodies found to adhere to the surface of the MWCNTs with their neurites extending through the bed of CNTs **b**; and **c** elaborating into many small branches

formed by attaching functional groups via acidic treatments [147]. As an alternative to the binding of molecules to the outside of the CNTs, it would also be convenient to fill the interior cavity of tubes, whose open ends might be capped to generate a nanopill containing a drug for delivery to the cell. Towards that end, a template method has been used to synthesize nano test tubes, which are CNTs with one end closed and the other open. Such an approach might be construed as a first step toward the development of a nanopill, in which the substance to be delivered is introduced into the interior of the nanotube and then bottled by resealing the open end.

12.3.4.6 Biomedical Implant Applications of CNT

The primary issues in materials science of new bone biomaterials are mechanical properties and biocompatibility. Although mechanical properties of biomaterials have been well characterized, the term bio- compatibility is only a qualitative description of how the body tissues interact with the biomaterial within some expectations of certain implantation purpose and site. Materials scientists have investigated metals, ceramics, polymers, and composites as biomaterials. The general criteria for materials selection for bone implant materials are:

- It is highly biocompatible and does not cause an inflammatory or toxic response beyond an acceptable tolerable level.
- It has appropriate mechanical properties, closest to bone.
- Manufacturing and processing methods are economically viable.

The hip joint consists of two complementary articular surfaces separated by articular cartilage and the synovial fluid that has a pH between 7.29 and 7.45. Excessive wear of the interfaces due to degenerative disease (such as osteoarthritis) or injury requires a replacement of the entire hip joint. Historically, a total hip replacement the articulation of a human hip is simulated with the use of two components, a cup type and a long femoral type element [148], K.S. Katti, Colloids and surfaces. A typical hip implant fabricated from titanium is shown in Fig. 12.10.

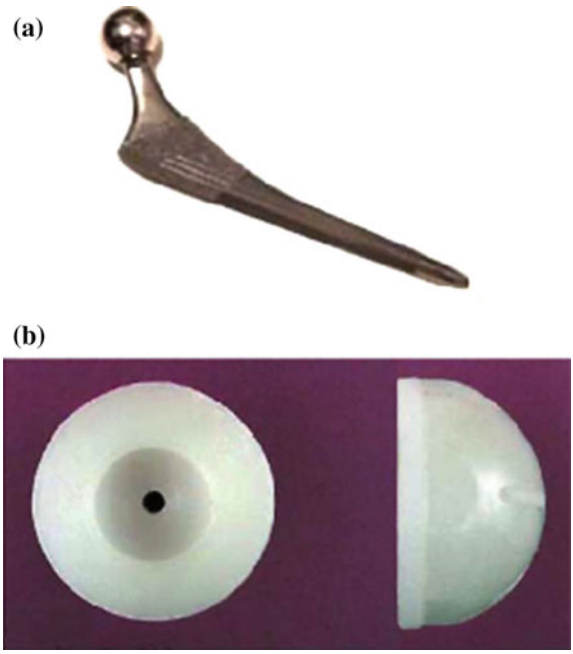

Fig. 12.10 Artificial hip implant fabricated from titanium alloy: **a** artificial hip implant; and **b** femoral head manufactured from UHMWPE

The head of the femoral element fits inside the cup to enable the articulation of the human joint. These two parts of the hip implant have been made using a variety of materials such as metals, ceramics, polymers and composites. Typically polymeric materials alone tend to be too weak to be suitable for meeting the requirement of stress deformation responses in the THR components. Metals typically have good mechanical properties but show poor biocompatibility, cause stress shielding and release of dangerous metal ions causing eventual failure and removal of implant. Ceramics generally have good biocompatibility but poor fracture toughness and tend to be brittle. A hip implant therefore should be such that it exhibits an identical response to loading as real bone and is also biocompatible with existing tissue. The average load on a hip joint is estimated to be up to three times body weight and the peak load during other strenuous activities such as jumping can be as high as 10 times body weight. In addition hip bones are subjected to cyclic loading as high as 10^{6} cycles in 1 year [148]. The compatibility issue involves surface compatibility, mechanical compatibility and also osteocompatibility. These materials are also classified as bioactive (illicit a favorable response from tissue and bond well), bioinert and biodegradable. The commercial metallic total hip replacement (THR) implants are five to six times stiffer than bone and result in significant problems associated with stress shielding. Titanium (Ti) alloys in the femoral elements of the THR have shown improvement in wear properties [149]. The regenerative and remodeling processes in bone are directly triggered by loading, i.e., bone subjected to loading or stress regenerates and bone not subjected to loading results in atrophy. Thus, the effect of a much stiffer bone implant is to reduce the loading on bone resulting in the phenomenon called as stress shielding. The key problems associated with the use of these metallic femoral stems are thus release of dangerous particles from wear debris, detrimental effect on the bone remodeling process due to stress shielding and also loosening of the implant-tissue interface. It has been shown that the degree of stress shielding is directly related to the difference in stiffness of bone and implant material [150]. Ti alloys are favorable materials for orthopedic implants due to their good mechanical properties. However, Ti does not bond directly to bone resulting in loosening of the implant. Undesirable movements at the implant-tissue interface results in failure cracks of the implant.

One approach to improving implant lifetime is to coat the metal surface with a bioactive material that can promote the formation and adhesion of hydroxyapatite, the inorganic component of natural bone [151]. The application of bioactive coatings to Ti-based alloys enhance the adhesion of Ti-based implants to the existing bone, resulting in significantly better implant lifetimes than can be achieved with materials in use today. Typically, several silicate glasses are used as bioactive coatings [152]. Some ceramic coatings are known to be bioactive and have also been tested on Ti implants. As compared to metals, ceramics often cause reduced osteolysis and are regarded as favorable materials for joints or joint surface materials. Several ceramics due to their ease of processing and forming and superior mechanical properties were investigated as bone substitute materials [153].

Conventional ceramics such as alumina were evaluated due to their excellent properties of high strength, good biocompatibility, and stability in physiological environments [154]. Alumina, because of the ability to be polished to a high surface finish and its excellent wear resistance, is often used for wear surfaces in joint replacement prostheses. Femoral heads for hip replacements and wear plates in knee replacements have been fabricated using alumina. In year 2003, the United States Food and Drug Administration (FDA) has approved alumina ceramic-on-ceramic articulated hips for marketing in the United States of America. Other ceramic materials have also been investigated for potential applications in orthopedics. Considerable research has focused on zirconia and yttria ceramics that are characterized by fine-grained microstructures. These ceramics are known as tetragonal zirconia polycrystals (TZP). TZP in the body have been limited by the low strength and low fracture toughness of the synthetic phosphates. Alumina and titanium dioxide have been used as nanoceramics separately or in nanocomposites with polymers such as polylactic acid or polymethlyl methacrylate. The nanoceramic formulations promote selectively enhanced functions of osteoblasts (bone-forming cells). These functions include cell adhesion, proliferation, and deposition of calcium-containing minerals, an indication of new bone formation in a laboratory setting. Despite of many advantages, the lack of chemical bonding between sintered alumina and tissue, however limited its applications as a potential bone substitute to a certain extent. The other problems arise when attempting to coat metals with ceramics are: the thermal expansion coefficients of the ceramic and metal are usually different, and as a result, large thermal stresses are generated during processing. These stresses lead to cracks at the interface and compromise coating adhesion. In addition, chemical reactions between the ceramic and metal can weaken the metal in the vicinity of the interface, reducing the strength of the coated system.

Calcium hydroxyapatite [$Ca_{10}(PO_4)_6(OH)_2$] is the principal calcium phosphate commonly used for biomedical implant applications. However, the high brittleness and poor strength of sintered hydroxyapatite (HA) restricts its clinical applications under load-bearing conditions and therefore coating of HA on metal implants is an alternate option. The excellent biocompatibility and osteointegration are the key characteristics of existing bioceramic hydroxyapatite coatings. Synthetic HA elicits a direct chemical response at the interface and forms a very tight bond to tissue [155]. Attempts have been made to form high strength consolidated HA bodies [156]. However, its poor mechanical properties such as low strength and limited fatigue resistance restrict its applications. Bending strength as high as 90 MPa has been achieved by colloidal processing of HA [157].

The first priority for the development of a better coating is therefore improvement of the interfaces (metal-coating and coating-bone interfaces) so that the coating binds well with both metal and bone. Thermal stresses, chemical reactions between coating and metal, and biocompatibility are the key issues to be considered. Although HA coverings are able to enhance bone ingrowth and reduce early loosening of hip and knee prostheses, the optimum coating quality and surface texture are still a matter open to debate. Moreover the significance of coating

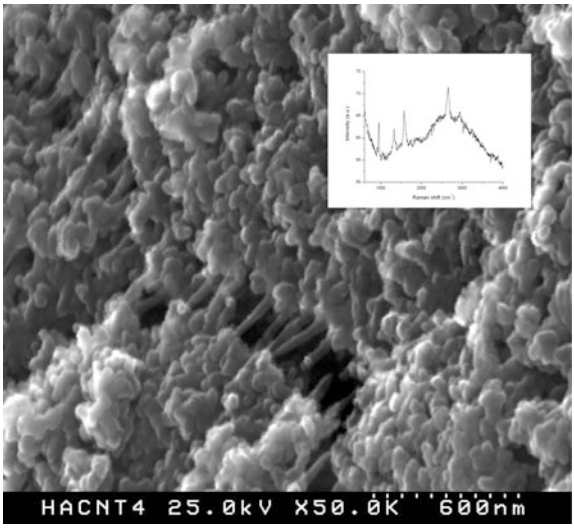

Fig. 12.11 SEM image of uniform distribution of CNT in HA matrix. The uniform distribution of CNT in HA matrix was confirmed using Raman analysis (*inset*)

resorption is controversial. It has been suggested that resorption disintegrates the coating and reduces the bonding strength between the implant and bone, and the strength of coating implant interface, which might lead to implant loosening, coating delamination and acceleration of third body wear process.

The extremely light weight, extra strong and nano sized carbon nanotubes (CNTs) are highly recommended as an additional ingredient for the synthesis of HA coating. Carbon materials are known to be inert to cells and tissues because of their pure carbon composition. Some recent investigations indicated that carbon nanotubes may have promising potentials in biomedical applications both at molecular and cellular levels [158]. Functionalisation of CNTs are important in HA/CNT coating since chemical reactions can take place at functionalised sites on CNT in a colloidal state and it play a potential role in its uniform dispersion in composite media. Titus et al. achieved, uniform dispersion of CNT into HA matrix by ultrasonication and other novel methods. Figure 12.11 shows the SEM image of uniform distribution of CNT in HA matrix. The uniform distribution of CNT in HA matrix also was confirmed using Raman analysis (inset of Fig. 12.11).

12.4 Analysis

The determination of structure function relationships in biological macromolecules is central to elucidating biochemical pathways, and thereby designing new drugs and understanding their mode of action. Structural biology has played and will continue to play a key role in these endeavors because biomolecule function is closely tied to three-dimensional structures. The workhorse tools of structural

biology, X-ray diffraction, electron diffraction, and NMR can almost routinely be used to determine atomic resolution structure of single biomolecule. Continued advances in these methods are pushing the limits of the size and complexity of systems that can be characterized [159], although in the future, expanded needs for biomolecular structure analysis are expected in several areas, including: (i) increased throughput to characterize new gene products discovered by genomic DNA sequencing [160], (ii) routine analysis of multimeric protein, protein and protein-nucleic acid structures involved in, for example, signaling and gene regulation; and (iii) elucidation of dynamic processes in these multimeric systems. It is unlikely that the conventional structural tools will meet all of these needs, both because of the increased difficulty of crystallizing large signaling and regulatory protein complexes, which will limit diffraction methods, and the challenges of using solution NMR for large biomolecular systems [161]. Future progress in understanding complex processes in biological systems will therefore clearly require additional, perhaps revolutionary techniques for structural analysis.

AFM [162] is one technique with the potential to probe both structure and dynamics of large macromolecular systems, since it permits direct visualization of individual biological structures in vitro [163]. The potential for AFM to impact structural biology has been suggested by beautiful images of, for example, two-dimensional arrays of proteins with 'sub-molecular resolution' [164], although such captivating data are not without limitations. These shortcomings, which if overcome could dramatically extend the applicability of AFM to structural biology, can be understood by reviewing the key features of an AFM (Fig. 12.12).

Common to all AFMs are an integrated cantilever-tip assembly, a detector to measure cantilever displacement as the sample is scanned, and electronics to acquire and display images. The basic features of AFM and methods of imaging have been reviewed recently [165]. Central to reproducible high-resolution characterization of biological macromolecules with AFM especially new systems not crystallographically characterized is the size and shape of the probe tips used for imaging.

An ideal AFM probe tip should have (i) a subnanometer radius, (ii) a zero degree cone angle, (iii) mechanical and chemical robustness and, (iv) the potential for molecularly precise modification of the tip end. Moreover, it should be possible to prepare such tips reproducibly with the same features, such that the resolution and other imaging characteristics are predictable, as is the case in diffraction experiments.

The first demonstration of nanotube probes used mechanical mounting of bundles of MWCNTs onto standard AFM tips [166]. AFM studies with mechanically mounted MWCNT probes yielded only modest improvements in resolution on amyloid fibrils, protofibrils, and gold nanocluster standards with respect to standard Si tips [167]. In contrast, probes fabricated from etched SWCNT bundles, which occasionally have just a few SWCNTs protruding from the end, demonstrated up to fivefold better resolution than conventional probes on inorganic nanostructures and DNA [168]. While these results indicated the potential for SWCNTs to enhance AFM resolution, tip radii were still 10 times larger than what would be obtained

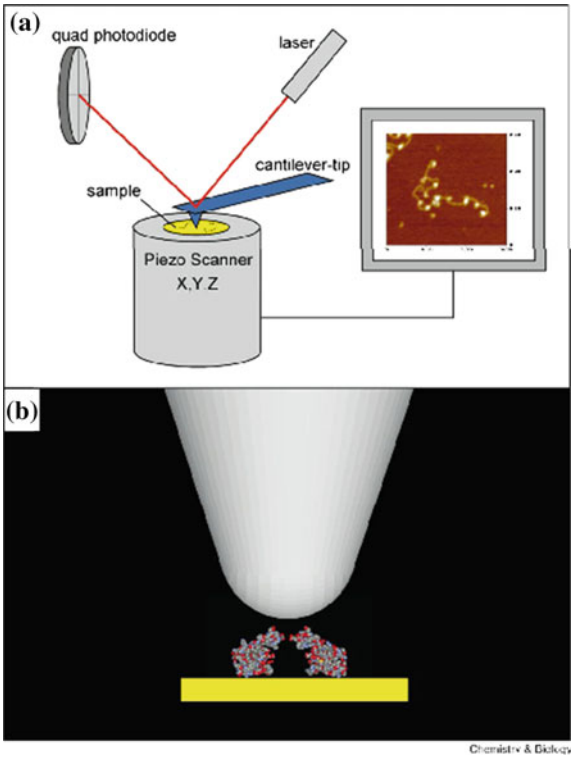

Fig. 12.12 Schematic diagram of the atomic force microscope

with a single 0.25 nm radius nanotube [169]. Moreover, the conceptual simplicity of mechanical nanotube tip fabrication is hampered by its difficulty in scale-up and by its intrinsic selectivity towards thicker nanotube bundles. Mechanical nanotube tip assembly in a scanning electron microscope (SEM) [170] allows assembly of somewhat smaller 10 nm diameter tips, but this method is even slower than mounting in an optical microscope. Thus, a different approach is needed for reproducible and scalable fabrication of ultrahigh resolution nanotube tips. All of the problems associated with manual assembly can be solved by directly growing nanotubes on AFM tips using metal-catalyzed chemical vapor deposition (CVD). By carefully manipulating CVD reaction conditions and the catalyst, one can selectively produce SWCNTs [171] with radii as small as 0.35 nm [172]. Since carbon nanotube probes can provide enhanced imaging in diverse areas, they are particularly suited to the field of biology. The use of SWCNT probes will therefore improve the imaging resolution of small proteins, such as antibodies in DNA analysis. The widespread availability of nanosurgery involves the manipulation of single cells or cell structures. The advantage of CNT AFM probes is that they can be easily functionalized, and the range of chemical groups that can be added specifically to the tip of a CNT make them an ideal high resolution probe for mapping chemical domains by using chemical force microscopy. Thus probes can

be developed to sense polarity, pH and many other chemical characteristics of the sample by adding different residues to the CNT, as shown by studies using CNT AFM tips patterned with terminal carboxylic groups in which it was possible to chemically map the substrate by using tapping mode AFM (Fig. 12.13). Figure 12.14 shows the oriented isolated CNTs grown directly on copper substrate by CVD method [Gil Cabral et al.]. The orientation and size of the CNTs were controlled by maintaining growth conditions.

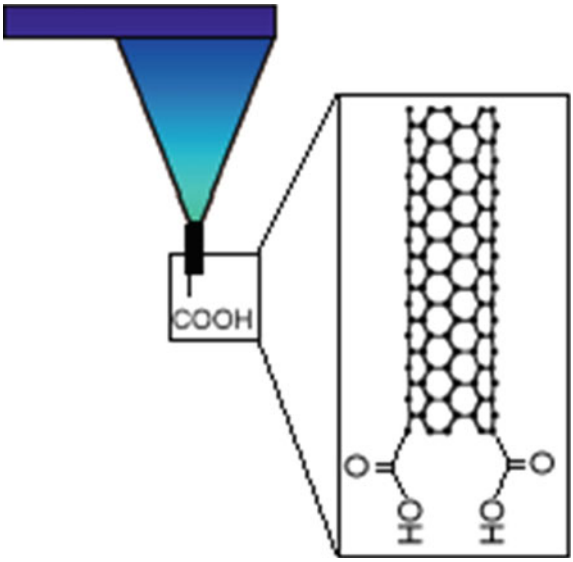

Fig. 12.13 AFM probes are developed to sense polarity, pH and many other chemical characteristics of the sample by adding different residues to the CNT. It is possible to chemically map the substrate by using tappingmode AFM

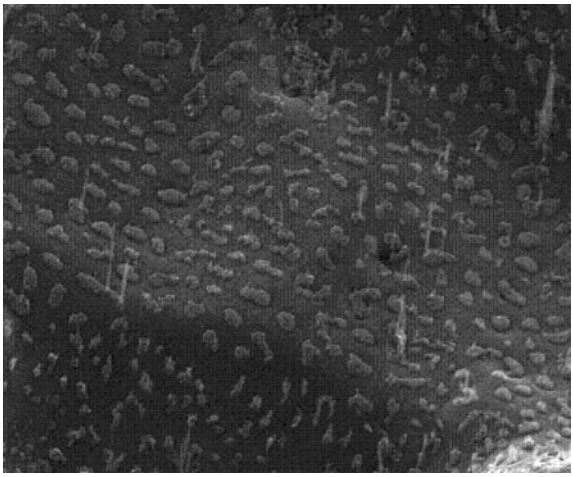

Fig. 12.14 Oriented isolated CNTs grown directly on a copper substrate by the CVD method. Maintaining strict growth conditions controls the orientation and size of the CNTs

12.5 Toxicity of Carbon Nanotubes

Toxicity is one of the important issues regarding the use of CNTs in biology and medicine [173]. Currently, CNTs are under investigation in various laboratories, and therefore, the widespread commercialization and exposure of the general populace to this material must occur only after adequate testing. Detailed toxicological studies are required in this regard, and few of the reported studies have shown negative effects on human health. For example, the exposure of cultured human skin cells to SWCNTs caused oxidative stress and loss of cell viability, indicating that dermal exposure may lead to skin conditions. This is perhaps to be expected, since graphite and carbon materials have been associated with increased dermatitis and keratosis. Additional studies have investigated the pulmonary toxicity of SWCNTs, and it was shown that exposure to SWCNTs lead to the development of granulomas in rodents. Since these studies used very high concentrations of SWCNTs, which were directly exposed to skin and instilled into the lungs of the animals, further testing is required to establish their toxicity. Also the toxicity is expected to be less in functionalized CNTs and CNT composites.

12.6 Conclusions

The multidisciplinary field of Bio-nanotechnology holds the promise of delivering the technological breakthrough and is moving very fast from concept to reality. The flexibility to modify or adapt bio-nanotechnology to meet the needs of pathologic conditions either for therapeutic applications or as a diagnostic tool is the important characteristic of the technology.

The CNTs represent one of the most promising materials for application in bio-nanotechnology due to their amazing electronic and mechanical properties. CNTs provide a new generation of biocompatible nanomaterials for sensors and probes, implants, electrochemical devices, reinforcements in composites, and nanometer-sized electronics that could revolutionize the world. It provides a wide range of new technologies for developing customized solutions that optimize the delivery of pharmaceutical products. It involves the creation and use of materials and devices at the atomic and molecular level. The scope of nanomaterial is vast and the potential for breakthroughs is enormous and is being pursued on multiple fronts.

References

1. Xiao, Y., et al. (2003). *Science, 299*, 1877.
2. Elghanian, R., et al. (1997). *Science, 277*, 1078.
3. Averitt, R. D., et al. (1997). *Physical Review Letters, 78*, 4217.
4. Clapp, A. R., et al. (2004). *Journal of the American Chemical Society, 126*, 301.

5. Wang, S., et al. (2002). *Nano Letters, 2*, 817.
6. Chan, W. C. W., & Nei, S. (1998). *Science, 281*, 2016.
7. Cao, Y. W. C., Jin, R. C., & Mirkin, C. A. (2002). *Science, 297*, 1536.
8. Hartgerink, J. D., Beniash, E., & Stupp, S. I. (2001). *Science, 294*, 1684.
9. Koltover, I., Salditt, T., Radler, J. O., & Sa, C. R. (1998). *Science, 281*, 78.
10. Ulrich, K. E., Cannizzaro, S. M., Langer, R. S., & Shakesheff, K. M. (1999). *Chemical Reviews, 99*, 3181.
11. Fandrich, M., Fletcher, M. A., & Dobson, C. M. (2001). *Nature, 410*, 165.
12. Seeman, N. C., & Belcher, A. M. (2002). *Proceedings of the National Academy of Sciences of the United States of America, 99*, 6451.
13. Ravindran, S., Chaudhary, S., Colburn, B., Ozkan, M., & Ozkan, C. S. (2003). *Nano Letters, 3*, 447.
14. Haremza, J. M., Hahn, M. A., Krauss, T. D., Chen, S., & Calcines, J. (2002). *Nano Letters, 2*, 1253.
15. Hazani, M., Naaman, R., Hennrich, F., & Kappes, M. M. (2003). *Nano Letters, 3*, 153.
16. Dwyer, C., Guthold, M., Falvo, M., & Washburn, S. (2002). *Nanotechnology, 13*, 601.
17. Ellis, A. V., Vijayamohanan, K., Goswami, R., Chakrapani, N., Ramanathan, L. S., Ajayan, P. M., & Ramanath, G. (2003). *Nano Letters, 3*, 279.
18. Wilkinson, J. M. (2003). *Medical Device Technologies, 14*, 29.
19. Shim, M., Kam, N. W. S., Chen, R. J., Li, Y., & Dai, H. (2002). *Nano Letters, 2*, 285.
20. Pantarotto, D., Briand, J.-P., Prato, M., & Bianco, A. (2004). *Chemical Communications, 16*.
21. Kam, N. W. S., Jessop, T. C., Wender, P. A., & Dai, H. (2004). *Journal of the American Chemical Society, 126*, 6850.
22. Gooding, J. J., Wibowo, R., Liu, J., Yang, W., Losic, D., Orbons, S., et al. (2003). *Journal of the American Chemical Society, 125*, 9006.
23. Wang, J., Liu, G., & Jan, M. R. (2004). *Journal of the American Chemical Society, 126*, 3010.
24. Wang, J., Li, M., Shi, Z., Li, N., & Gu, Z. (2002). *Electroanalysis, 14*, 225.
25. Wang, J., Kawde, A. N., & Jan, M. R. (2004). *Biosensors and Bioelectronics, 20*, 995.
26. Chen, Y., Zhang, Y. Q., Zhang, T. H., Gan, C. H., Zheng, C. Y., & Yu, G. (2006). *Carbon, 44*, 37.
27. Iijima, S. (1991). *Nature, 354*, 56.
28. Thess, A., et al. (1996). *Science, 273*, 483.
29. Tans, S. J., et al. (1997). *Nature, 386*, 474.
30. Joachim, C., & Gimzewski, J. K. (1997). *Chemical Physics Letters, 265*, 353.
31. Tomanek, D., & Enbody, R. J. (Eds.). (2000). *Science and application of nanotubes*. New York: Kluwer Academic/Plenum Publishers.
32. Fischer, J. E., et al. (1997). *Physical Review B, 55*, R4921.
33. Lee, R. S., Kim, H. J., Fischer, J. E., Thess, A., & Smalley, R. E. (1997). *Nature, 388*, 255.
34. Claye, A. S., Fischer, J. E., Huffman, C. B., Rinzler, A. G., & Smalley, R. E. (2000). *Journal of the Electrochemical Society, 147*, 2845.
35. Gavalas, V. G., Andrews, R., Bhattacharyya, D., & Bachas, L. G. (2001). *Nano Letters, 1*, 719.
36. Garjonyte, R., & Malinauskas, A. (2001). *Biosensor & Bioelectronics, 15*, 445.
37. Rubianes, M. D., & Rivas, G. A. (2003). *Electrochemistry Communications, 5*, 689.
38. Wang, J., Kawde, A. N., & Jan, M. R. (2004). *Biosensors & Bioelectronics, 20*, 995.
39. Ye, J. S., Liu, X., Cui, H. F., Zhang, W. D., Sheu, F. S., & Lim, T. M. (2005). *Electrochemistry Communications, 7*, 249.
40. Shim, M., Kam, N. W. S., Chen, R. J., Li, Y., & Dai, H. (2002). *Nano Letters, 2*, 285.
41. Huang, W., Taylor, S., Fu, K., Lin, Y., Zhang, D., Hanks, T. W., et al. (2002). *Nano Letters, 2*, 311.
42. Sotiropoulou, S., Gavalas, V., Vamvakaki, V., & Chaniotakis, N. A. (2003). *Biosensors & Bioelectronics, 18*, 211.

43. Biro, L. P., Horvath, Z. E., Szlamas, L., Kertesz, K., Weber, F., Juhasz, G., et al. (2003). *Chemical Physics Letters, 399*, 402.
44. Journet, C., & Bernier, P. (1998). *Applied Physics A, 1*, 9.
45. Zhang, Y. (2001). *Applied Physics Letters, 79*, 3155.
46. Chiang, M., Liu, K., Lai, T., Tsai, C., Cheng, H., & Lin, I. (2001). *Journal of Vacuum Science and Technology B, 19*, 1034.
47. Biro, L. P., Horvath, Z. E., Szlamas, L., Kertesz, K., Weber, F., Juhasz, G., et al. (2003). *Chemical Physics Letters, 399*, 402.
48. Park, D., Kim, Y. H., & Lee, J. K. (2003). *Carbon, 41*, 1025.
49. Qin, L. C., Zhou, D., Krauss, A. R., & Gruen, D. M. (1998). *Applied Physics Letters, 72*, 3437.
50. Meyyappan, M., Delzeit, L., Cassell, A., & Hash, D. (2003). *Plasma Sources Science and Technology, 12*, 205.
51. Dai, H. (2002). *Surface Sci, 500*, 218.
52. Popov, V. (2004). *Materials Science and Engineering R Reports, 43*.
53. Dresselhaus, M., Dresselhaus, G., & Saito, R. (1995). *Carbon, 33*, 883.
54. Liang, W. Z., Chen, G. H., Li, Z., & Tang, Z. K. (2002). *Applied Physics Letters, 80*, 3415.
55. Ajayan, P. M. (1999). *Chemical Reviews, 99*, 1787.
56. Baughman, R. H., Zakhidov, A. A., & Heer, W. A. (2002). *Science, 297*, 787.
57. Thostenson, E. T., Ren, Z., & Chou, T. W. (2001). *Composites Science and Technology, 61*, 1899.
58. Lupo, F., Kamalakaran, R., Scheu, C., Grobert, N., & Ruhle, M. (2004). *Carbon, 42*, 1995.
59. Mintmire, J. W., Dunlap, B. I., & White, C. T. (1992). *Physical Review Letters, 68*, 631.
60. Hamada, N., Sawada, S. I., & Oshiyama, A. (1992). *Physical Review Letters, 68*, 1579.
61. Saito, R., Fujita, M., Dresselhaus, G., & Dresselhaus, M. S. (1992). *Applied Physics Letters, 60*, 2204.
62. Kataura, H., Kumazawa, Y., Maniwa, Y., Umezu, I., Suzuki, S., Ohtsuka, Y., & Achiba, Y. (1999). *Synthetic Metals, 103*, 2555.
63. Chen, J., Hamon, M. A., Hu, H., Chen, Y., Rao, A. M., Eklund, P. C., & Haddon, R. C. (1998). *Science, 282*, 95.
64. Britto, P. J., Santhanam, K. S. V., & Ajayan, P. M. (1996). *Bioelectrochemistry and Bioenergetics, 41*, 121.
65. Star, A., Gabriel, J.-C. P., Bradley, K., & Gruner, G. (2003). *Nano Letters, 3*, 459.
66. Boussaad, S., Tao, N., Zhang, R., Hopson, T., & Nagahara, L. A. (2003). *Chemical Communications, 1502*.
67. Besteman, K., Lee, J. O., Wiertz, F. G., Heering, H. A., & Dekker, C. (2003). *Nano Letters, 3*, 727.
68. Chen, R, J., Bangsaruntip, S., Drouvalakis, K. A., Kam, N. W. S., Shim, M., Li, Y., et al. (2003). *Proceedings of National Academy of Sciences U.S.A, 100*, 4984.
69. Wang, J., Liu, G., & Jan, M. R. (2004). *Journal of the American Chemical Society, 126*, 3010.
70. Azamian, B. R., Davis, J. J., Coleman, K. S., Bagshaw, C. B., & Green, M. L. H. (2002). *Journal of the American Chemical Society, 124*, 2664.
71. Pathirana, S. T., Barbaree, J., Chin, B. A., Hartell, M. G., Neely, W. C., & Vodyanoy, V. (2000). *Biosensors & Bioelectronics, 15*, 135.
72. Huang, T. S., Tzeng, Y., Liu, Y. K., Chen, Y. C., Walker, K. R., Guntupalli, R., & Liu, C. (2004). *Diamond and Related Materials, 13*, 1098.
73. Bandyopadhyaya, R., Nativ-Roth, E., Regev, O., & Yerushalmi-Rozen, R. (2002). *Nano Letters, 2*, 25.
74. Bodanszky, M., & Bodanszky, A. (1994). *Journal of the American Chemical Society, 126*, 12750.

75. Bourdillon, C., Demaille, C., Gueris, J., Moirourx, J., & Saveant, J. M. (1993). *Journal of the American Chemical Society, 115*, 12264.
76. Cai, C., & Chen, J. (2004). *Analytical Biochemistry, 332*, 75.
77. Gooding, J. J., Wibowo, R., Liu, J., Yang, W., Losic, D., Orbons, S., et al. (2003). *Journal of the American Chemical Society, 125*, 9006.
78. Guiseppi-Elie, A., Lei, C., & Baughman, R. H. (2002). *Nanotechnology, 13*, 559.
79. Hecht, H. J., Kalisz, H. M., Hendle, J., Schmid, R. D., & Shomburg, (1993). *Journal of Molecular Biology, 229*, 153.
80. Li, J., Ng, H. T., Cassell, A., Fan, W., Chen, H., Ye, Q., et al. (2003). *Nanoletters, 3*, 597.
81. Domynguez, E., Rincon, O., & Narvaez, A. (2004). *Analytical Chemistry, 76*, 3132.
82. Decher, G. (1997). *Science, 277*, 1232.
83. Narvaez, A., Suarez, I., Popescu, I., Katakis, I., & Domynguez, E. (2004). *Biosensors & Bioelectronics, 15*, 43.
84. Musameh, M., Wang, J., Merkoci, A., & Lin, Y. (2002). *Electrochemistry Communications, 4*, 743.
85. Dryhurst, G., Kadish, K. M., Scheller, F., & Rennerberg, R. (1982). *Biological electro-chemistry*. New York: Academic Press.
86. Gorton, L., Lindgren, A., Larsson, T., Munteanu, F. D., Ruzgas, T., & Gazaryan, I. (1999). *Analytica Chimica Acta, 400*, 91.
87. Hu, N. (2001). *Pure and Applied Chemistry, 73*, 1979.
88. Wang, J., Li, M., Shi, Z., Li, N., & Gu, Z. (2002). *Analytical Chemistry, 74*, 1993.
89. Guiseppi-Elie, A., Lei, C., & Baughman, R. H. (2002). *Nanotechnology, 13*, 559.
90. Cai, C., & Chen, J. (2004). *Analytical Biochemistry, 332*, 75.
91. Li, M., Wang, J., Shi, Z., Li, N., & Gu, Z. (2002). *Analytical Chemistry, 74*, 1993.
92. Davis, J. J., Coles, R. J., & Hill, H. A. O. (1997). *Journal of Electroanalytical Chemistry, 440*, 279.
93. Wang, S. G., Wang, R., Sellin, P. J., & Zhang, Q. (2004). *Biochemical and Biophysical Research Communications, 325*, 1433.
94. Tsang, S. C., Davis, J. J., Green, M. L. H., Hill, H. A. O., Leung, Y. C., & Sadler, P. J. (1995). *Journal of the Chemical Society, Chemical Communications, 1803*.
95. Azamian, B. R., Davis, J. J., Coleman, K. S., Bagshaw, C. B., & Green, M. L. H. (2002). *Journal of the American Chemical Society, 124*, 664.
96. Shim, M., Kam, N. W. S., Chen, R. J., Li, Y., & Dai, H. (2002). *Nano Letters, 2*, 285.
97. Wang, J., & Musameh, M. (2003). *Analytical Chemistry, 75*, 2075.
98. Wu, Z., Chen, Z., Du, X., Logan, J. M., Sippel, J., Nikolou, M., et al. (1998). *Inorg Chemica Acta, 27*, 261.
99. Maria, D. R., & Gustavo, A. R. (2003). *Electrochemistry Communications, 5*, 689.
100. Rubianes, M., & Rivas, G. (2003). *Electrochemistry Communications, 5*, 689.
101. Zhao, G., Zhang, L., Wei, X., & Yang, Z. (2003). *Electrochemistry Communications, 5*, 825.
102. Cai, C., Chen, J., & Lu, T. (2004). *Science in China, Series B: Chemistry, Life Sciences, & Earth Sciences, 47*, 113.
103. Yu, X., Chattopadhyay, D., Galeska, I., Papadimitrakopoulos, F., & Rus-ling, J. F. (2003). *Electrochemistry Communications, 5*, 408.
104. Chan, W. C. W., & Nei, S. (1998). Quantum dot bioconjugates for ultra- sensitive nonisotopic detection. *Science, 281*, 2016.
105. Hamon, M. A., Chen, J., Hu, H., Chen, Y., Itkis, M. E., Rao, A. M., et al. (1999). *Advanced Materials, 11*, 834.
106. Strano, M. S., Dyke, C. A., Usrey, M. L., Barone, P. W., Allen, M. J., Shan, H., et al. (2003). *Science, 301*, 1519.
107. Koshio, A., Yudasaka, M., Zhang, M., & Iijima, S. (2001). *Nano Letters, 1*, 361.
108. Hiura, H., Ebbesen, T. W., & Tanigaki, K. (1995). *Advanced Materials, 7*, 275.

109. Wang, J. X., Li, M. X., Shi, Z. J., Li, N. Q., & Gu, Z. N. (2001). *Electrochimica Acta, 47*, 651.
110. Lin, Y., Taylor, S., Li, H. P., Fernando, K. A. S., Qu, L. W., Wang, W., et al. (2004). *Journal of Materials Chemistry, 14*, 527.
111. Riggs, J. E., Guo, Z.-X., Carroll, D. L., & Sun, Y. P. (2000). *Journal of the American Chemical Society, 122*, 5879.
112. Zhao, B., Hu, H., & Haddon, R. C. (2004). *Advanced Functional Materials, 14*, 71.
113. Titus, E., Ali, N., Cabral, G., Ramesh Babu, P., & Gracio, J. (2006) *Journal of Materials Engineering and Performance, 2*.
114. Sotiropoulou, S., & Chainiotakis, N. A. (2003). *Analytical and Bioanalytical Chemistry, 375*, 103.
115. Xu, J. M. (2003). Nanotube electronics: non-CMOS routes. *Proceedings of the IEEE, Special Issue on Nanoelectronics and Giga-scale Systems, 91*, 1819–1829.
116. Fu, K., Huang, W., Lin, Y., Zhang, D., Hanks, T. W., Rao, A. M., & Sun, Y.-P. (2002). *Nanotechnology, 2*, 457.
117. Yao, D., Cao, H., Wen, S., Liu, D., Bai, Y., & Zheng, W. (2005). *Bioelectrochemistry, 68*, 131.
118. Musameh, M., Wang, J., Merkoci, A., & Lin, Y. (2002). *Electrochemistry Communications, 4*, 743.
119. Wang, J., Li, M., Shi, Z., Li, N., & Gu, Z. (2002). *Analytical Chemistry, 74*, 1993.
120. Gong, K., Dong, Y., Xiong, S., Chen, Y., & Mao, L. (2004). *Biosensors and Bioelectronics, 20*, 253.
121. Zhang, M., Smith, A., & Gorski, W. (2004). *Analytical Chemistry, 76*, 5045.
122. Wang, J., & Musameh, M. (2003). *Analytical Chemistry, 75*, 2075.
123. Davis, J., Coles, R., & Hill, H. (1997). *Electroanalytical Chemistry, 440*, 279.
124. Rubianes, M., & Rivas, G. (2003). *Electrochemistry Communications, 5*, 689.
125. Wang, J. (2004). Musameh. *Analyst, 129*, 1.
126. Guo, M., Chen, J., Liu, D., Nie, L., & Yao, S. (2004). *Bioelectrochemistry, 29*, 29.
127. Wang, J., Musameh, M., & Lin, Y. (2003). *Journal of the American Chemical Society, 125*, 2408.
128. Wang, Z., Liu, J., Liang, Q., Wang, Y., & Luo, G. (2002). *Analyst, 127*, 653.
129. Joshi, P., Merchant, S. A., Wang, Y., & Schmidtke, D. (2005). *Analytical Chemistry, 77*, 3183.
130. Lin, Y., Lu, F., Tu, Y., & Ren, Z. (2004). *Nano Letters, 4*, 191.
131. Guan, W., Li, Y., Chen, Y., Zhang, X., & Hu, G. (2005). *Biosensors & Bioelectronics, 21*, 508.
132. Tang, H., Chen, J., Yao, S., Nie, L., Deng, G., & Kuang, Y. (2004). *Analytical Biochemistry, 331*, 89.
133. Gao, M., Dai, L., & Wallace, G. (2003). *Synthetic Metals, 137*, 1393.
134. Lim, S., Wei, J., Lin, J., Li, Q., & KuaYou, J. (2005). *Biosensors & Bioelectronics, 20*, 2341.
135. Ye, J., Wen, Y., Zhang, W., Gan, L., Xu, G., & Sheu, F. (2004). *Electrochemistry Communications, 6*, 66.
136. Yang, M., Yang, Y., Liu, Y., Shen, G., & Yu, R. (2006). *Biosensors & Bioelectronics, 27*, 246.
137. Joshi, P., Merchant, S. A., Wang, Y., & Schmidtke, D. (2005). *Analytical Chemistry, 77*, 3183.
138. Sun, H., & Hu, N. (2005). *Analyst, 130*, 76.
139. Mattson, M. P., Haddon, R. C., & Rao, A. M. (2000). *Journal of Molecular Medicine, 14*, 175.

140. Zhang, X., Prasad, S., Niyogi, S., Morgan, A., Ozkan, M., & Ozkan, C. S. (2005). *Sensors and Actuators B, 106*, 843.
141. Hu, H., Ni, Y., Montana, V., Haddon, R. C., & Parpura, V. (2004). *Nanoletters, 4*(3), 507.
142. Bekyarova, E., Ni, Y., Malarkey, E. B., Montana, V., McWilliams, J. L., Haddon, R. C., & Parpura, V. (2005). *Journal of Biomedical Nanotechnology, 1*, 17.
143. Kam, N. W. S., Jessop, T. C., Wender, P. A., & Dai, H. (2004). *Journal of the American Chemical Society, 126*, 6850.
144. Balavoine, F., Schultz, P., Richard, C., Mallouh, V., Ebbesen, T. W., & Mioskowski, C. (1999). *Angewandte Chemie Int Ed, 38*, 1912.
145. Pantarotto, D., Briand, J.-P., Prato, M., & Bianco, A. (2004). *Chemical Communications, 16*.
146. Balavoine, F., Schultz, P., Richard, C., Mallouh, V., Ebbesen, T. W., & Mioskowski, C. (1999). *Angewandte Chemie Int Ed, 38*, 1912.
147. Guo, Z., Sadler, P. J., & Tsang, S. C. (1998). *Advanced Materials, 10*, 701.
148. Recum, V. (Ed.). (1999). *Handbook of biomaterials evaluation, scientific, technical and clinical testing of implant materials* (2nd ed., p. 915). PA: Taylor and Francis.
149. Black, J. (1992). *Biological performance of materials: Fundamentals of biocompatibility*. New York: Marcel Deckker.
150. Christel, P., Meunier, A., & Lee, A. J. C. (Eds.). (1997). *Biological and biomechanical performance of biomaterials* (p. 81). Amsterdam, The Netherlands: Elsevier.
151. Khor, K. A., Fu, L., Lim, V. J. P., & Cheang, P. (2000). The effects of ZrO_2 on the phase compositions of plasma sprayed HA/YSZ composite coatings. *Materials Science and Engineering A, 276*, 160.
152. Van Blitterswijk, C. A., Grote, J. J., Kuijpers, W., Daems, W. T., & de Groot, K. A. (1986). *Biomaterials, 7*, 553.
153. Tancred, D. C., McCormack, B. A. O., & Carr, A. J. (1998). *Biomaterials, 19*, 1735.
154. Wang, M., Deb, S., Tanner, K., & Bonfield, W. (1996). In *Proceedings of the 7th European Conference on Composite Materials, London*, 455.
155. Hulbert, S. F., & Hench, L. L. (1987). In P. Vineenzini (Ed.), *High technology ceramics* (Vol. 3). Amsterdam: Elsevier.
156. Bagambisa, F. B., Joos, U., & Schilli, W. (1993). *Journal of Biomedical Research, 27*, 1047.
157. Rodriguez-Lorenzo, L. M., Valler-Regi, M., & Ferreira, J. M. F. (2001). *Biomaterials, 22*, 583.
158. Yasuda, H. Y., Mahara, S., Umakoshi, Y., Imatazo, S., & Ebisu, S. (2001). *Bio-materials, 21*, 2045.
159. Lupo, F., Kamalakaran, R., Scheu, C., Grobert, N., & Uhle, M. R. (2004). *Carbon, 42*, 1995.
160. Siegal, G., van Duynhoven, J., & Baldus, M. (1999). *Chemistry & Biology, 3*, 530.
161. Kim, S. H. (1998). *Nature Structural Biology, 5*, 643.
162. Wuthrich, K. (2000). *Nature Structural Biology, 7*, 188.
163. Bustamante, C., Rivetti, C., & Keller, D. J. (1997). *Current Opinion in Structural Biology, 7*, 709.
164. Hansma, H. G. & Pietrasanta, L. I. (1998). *Current Opinion in Chemical Biology, 2*, 579.
165. Woolley, A. T., Cheung, C. L., Hafner, J. H., & Lieber, C. M. (2000). *Chemistry & Biology, 7*, R193–R204.
166. Kasas, S., Thomson, N. H., Smith, B. L., Hansma, P. K., Miklossy, J., & Hansma, H. G. (1998). *International Journal of Imaging Systems and Technology, 8*, 151.
167. Dai, H., Hafner, J. H., Rinzler, A. G., Colbert, D. T., & Smalley, R. E. (1996). *Nature, 384*, 147.
168. Wong, S. S., Harper, J. D., Lansbury, P. T, Jr, & Lieber, C. M. (1998). *Journal of the American Chemical Society, 120*, 603.
169. Wong, S. S., Woolley, A. T., Odom, T. W., Huang, J.-L., Kim, P., Ve- zenov, D. V., & Lieber, C. V. (1998). *Applied Physics Letters, 73*, 3465.

170. Sun, L. F., Xie, S. S., Liu, W., Zhou, W. Y., Liu, Z. Q., Tang, D. S., et al. (2003). *Nature, 403*, 384.
171. Nishijima, H., Kamo, S., Akita, S., Nakayama, Y., Hohmura, K. I., Yoshimura, S. H., & Takeyasu, K. (1999). *Applied Physics Letters, 74*, 4061.
172. Hafner, J. H., Bronikowski, M. J., Azamian, B. R., Nikolaev, P., Rinzler, A. G., Colbert, D. T., et al. (1998). *Chemical Physics Letters, 296*, 195.
173. Nikolaev, P., Bronikowski, M. J., Bradley, R. K., Rohmund, F., Colbert, D. T., Smith, K. A., & Smalley, R. E. (1999). *Chemical Physics Letters, 313*, 91.

Chapter 13
Bonelike® Graft for Regenerative Bone Applications

M.H. Fernandes, R. Caram, N. Sooraj Hussain, A.C. Mauricio and J.D. Santos

Abstract Bone is a complex mineralized living tissue exhibiting the property of marked rigidity and strength whilst maintaining some degree of elasticity. In general, there are two types of bones in the skeleton, namely, the flat bones, i.e. skull bones, scapula, mandible, ilium, and the long bones, i.e. tibia, femur and humerus. In principle, bone serves the following three main functions in human bodies: (i) acts as a mechanical support; (ii) is the site of muscle attachment for locomotion, protective, for vital organs and bone marrow; and (iii) to assist metabolism, it acts as a reserve of ions for the entire organism, especially calcium and phosphate. This chapter describes the mechanics of bone and a newly developed material that mimics bone for applications in regenerative medicine.

13.1 Introduction

13.1.1 Bone Physiology

Bone consists of metabolically active cells that are integrated into a mineralized extracellular matrix. The cellular components consist of osteogenic precursor cells, osteoblasts, osteoclasts, osteocytes, bone-lining cells and the hematopoietic elements of bone marrow. The matrix, essentially collagen type I (about 90 %), non-collagenous proteins and proteoglycans, is calcified with the deposition of highly substituted hydroxyapatite.

During a lifetime, bone mass is continuously involved in the remodelling process, which is responsible for the renewal of the skeleton, necessary for the maintenance of bone tissue integrity and mineral homeostasis. Bone remodelling involves the coordination of activities of cells from two distinct lineages, the osteoblasts and the osteoclasts, which form and resorb the mineralized tissue.

Bone exists in two main forms, woven bone and lamellar bone. Woven bone is a primitive and immature bone that is formed during bone development, fracture

M.H. Fernandes · R. Caram · N. Sooraj Hussain (✉) · A.C. Mauricio · J.D. Santos
University of Porto, Porto, Portugal

W. Ahmed and M.J. Jackson (eds.), *Surgical Tools and Medical Devices*,
DOI 10.1007/978-3-319-33489-9_13

healing, tumours and metabolic diseases. It forms very rapidly and is characterized by a random organization of the collagen fibers, irregularly shaped vascular spaces and calcification occurring as irregularly distributed patches. Woven bone is gradually replaced by organized lamellar bone, which is the form that constitutes most of the mature skeleton. In lamellar bone, the collagen fibers form highly organized sheets in which successive layers of fibers are oriented perpendicular to each other with little interfibrillar space, and calcification occurs in an orderly manner. Lamellar bone may be formed as cortical and trabecular bone. The external parts of the bones are formed by a thick and dense layer of calcified tissue—the cortical bone, in which 80–90 % of the volume is calcified. The internal space of the bones is filled with a network of thin calcified trabeculae—the trabecular bone, with 15–25 % of the volume being calcified. The cortical bone fulfils mainly mechanical and protective functions and the trabecular bone, which is filled with bone marrow, is mainly involved in metabolic functions.

Osteoblast and Bone Formation

Cells of the osteoblast lineage originate from multipotent mesenchymal stem cells, adjacent to all bone surfaces. Osteoblastic differentiation proceeds along an osteogenic pathway progressing from osteoprogenitors, preosteoblasts to fully mature osteoblasts and then, to lining cells or osteocytes. This process is controlled by a cascade of events that involves a combination of genetic programming and gene regulation by various hormones, cytokines, growth factors and other soluble factors [1].

The osteoblasts are cuboidal or slightly elongated cells that are located at the bone surfaces undergoing remodelling. Their primary function is to lay down the extracellular matrix and regulate its mineralization. The osteoblast is highly anchorage dependent and is a typical protein-producing cell having an extremely well-developed rough endoplasmatic reticulum and a large circular Golgy complex. Teams of 100–400 osteoblasts per bone-forming site produce a highly organized organic extracellular matrix called the osteoid. The lifespan of an osteoblast is around one month, during which it lays down 0.5–1.5 m^3 osteoid per day [2]. Eventually, some osteoblasts may become "trapped" in the newly formed matrix, thus they are converted into osteocytes, whereas, others remain on the bone surface as bone-lining cells or undergo apoptosis. The osteoid is a complex mixture of a variety of proteins secreted in a certain and specific order. It includes type I collagen (about 90 %) and a number of other matrix proteins, i.e. osteocalcin (bone GLA protein), osteopontin, osteonectin, bone sialoprotein and fibronectin, proteoglycans, carbohydrates and lipids. The initial mineralization of the osteoid typically occurs within a few days of secretion but is completed over the course of several months [2]. Matrix vesicles, lipid bilaminar organelles which bud from the osteoblasts, appear to be the initiators of this process. These structures contain phosphatases (which hydrolyse organic phosphates providing high local levels of phosphate ions, i.e. alkaline phosphatase, ALP), phospholipids and calcium ions. At a point of supersaturation, mineral deposition begins. As the matrix vesicles disintegrate, the mineral is exposed to the matrix, where the mineralization proceeds in a

self-perpetuating manner [2]. The inorganic content of bone consists primarily of calcium phosphate and calcium carbonate, with small quantities of magnesium, fluoride and sodium. Bone mineral is referred as hydroxyapatite [$Ca_{10}(PO_4)_6(OH)_2$], a plate-like crystal 20–80 nm in length and 2–5 nm thick. It is four times smaller than naturally occurring apatites and less perfect in structure, being more reactive and soluble which facilitates chemical turnover [3].

Osteoclast and Bone Resorption

The osteoclast is the bone cell responsible for bone resorption. Osteoclasts originate from hematopoietic stem cells that undergo proliferation and differentiate into preosteoclasts and osteoclasts. Osteoclasts are found in contact with a calcified bone surface and within lacunae, which is the result of its own resorptive activity. Usually, there are only one or two osteoclasts per resorptive site. They are highly migratory, multinucleated and polarized cells that present abundance of Golgy complexes, mitochondria and transport vesicles loaded with lysosomal enzymes. The most prominent feature of the osteoclast is the existence of deep foldings of the plasma membrane in the area facing the bone matrix, the ruffled border that is surrounded by a ring of contractile proteins (actin, vinculin and talin) serving to attach the cell to the bone surface and sealing off the resorbing compartment (the sealing zone). Protons and lytic enzymes are secreted across the ruffled border to the resorbing compartment. The low pH (between 2 and 4) allows the dissolution of the mineral, exposing the organic matrix. Subsequently, a variety of enzymes (including tartrate-resistant acid phosphatase, TRAP), at low pH, degrades the matrix components. The resultant residues are either internalized or transported by transcytosis and released at the basolateral membrane. An activated osteoclast is able to resorb 200,000 m^3/day, an average amount of bone formed by seven to ten generations of osteoblasts with an average lifespan of 15–20 days [2].

Cellular Organization Within the Extracellular Matrix—The Osteocyte

Osteocytes are the most differentiated cells of the osteoblast lineage and may persist in bone matrix for prolonged time periods. They are derived from the osteoblasts but are different in morphology and function i.e. smaller in size, with less cell organelles such as ribosomes and endoplasmatic reticula and an increased nucleus to cytoplasm ratio. Osteocytes are the most abundant cells in bone (about 90 %, 25,000 cells/mm^3) and are found embedded deep within the mineralized matrix in small lacunae. They present an extensive network of cellular processes that are enclosed within fine tubules (canaliculi) permeating the entire bone matrix.

The structural design of the osteocytes in the bone matrix allows for a tremendous cell–bone surface contact area, an extensive communication network between neighbouring osteocytes, cells lining the bone surface and blood vessels and, also, diffusion of solutes and gases (via the canaliculi). This structure has the characteristics of a three-dimensional sensor and communication system in bone. Osteocytes have a critical role in the maintenance of bone mass, with an important function in the local response of bone to stress, mechanical deformation and fluid flow [1].

Bone Re-modelling

Living bone is continually undergoing remodelling and the turnover rate is around 10 % a year in adult bone. Remodelling is required to replace dead or damaged tissue and to give bone the capacity to adapt to changes in loading and to respond to nutritional and/or metabolic changes. It is an orderly sequence of events achieved by the concerted actions of different bone cells—the basic multicellular unit (BMU) [4]. It includes four different phases—activation, resorption, reversal and formation—the ARRF sequence, which takes about 3–6 months for completion.

The process begins with activation of bone-lining cells, to uncover bone surface locally allowing for osteoclast adhesion. In the resorption phase, which lasts from one to two weeks, the osteoclasts degrade the mineralized matrix with the formation of resorption lacunae. Subsequently, in the reverse phase, believed to be critical for the coupling between bone resorption and bone formation, a heterogeneous population of mononuclear cells appears in the resorption lacunae and secretes a cement line substance. The formation phase, performed by the osteoblasts, includes the production of a highly organized collagenous matrix and its mineralization; these events continue to occur until the cavity becomes filled, i.e. taking up to several months. Complete refilling of the resorption lacunae is of great importance in maintaining the constant level of bone mass.

Regulation of bone remodelling is a complex process with several regulatory pathways operating and acting on the generation and activity of differentiated bone cells, namely circulating hormones, local growth factors and mechanical stress. Hormones, which are produced and secreted by endocrine glands at different locations in the body, enter the systemic circulation and reach the bone microenvironment, thus affecting local cells either directly or indirectly by inducing them to produce growth factors, peptide mediators with autocrine/paracrine effects. The regulation of bone remodelling at the molecular level remains to be inadequately understood. Specific factors are believed to regulate each step in the remodelling process and to integrate the development of osteoblasts and osteoclasts and their activities, as well as modulate control that is exerted through the endocrine system [1].

Bone Healing Process

A wound represents an anatomical or functional interruption in the continuity of a tissue that is accompanied by cellular damage and death. Every injury initiates a series of coordinated events directed towards restoring the injured tissue to as near normal as possible—the healing process, which can be accomplished by regeneration or repair.

Bone healing can be considered as regeneration rather than repair because it restores the tissue to its original physical, mechanical and functional properties. Healing is regulated by a complex interplay of systemic and local factors and occurs in three distinct but overlapping stages: the early inflammatory stage, the repair stage and the late remodelling stage [5, 6].

The initial biological response to a disruption in the continuity of bone is bleeding from ruptured vessels. A hematoma develops within the injury site during the first few hours and days and is accompanied by a typical inflammatory response. The hypoxic tissue environment stimulates the migration of inflammatory cells and fibroblasts to the injured zone, and the initial hematoma is replaced by granulation tissue. Ingrowth of vascular tissue favours the migration of mesenchymal stem cells, which contributes to the establishment of the repair stage. Fibroblasts begin to lay down a stroma that helps supporting vascular ingrowth, while cells of the osteoblastic lineage secrete osteoid, which is subsequently mineralized (formation of a callus around the repair site). This early immature bone consists of arrays of collagen fibers and randomly oriented spicules of bone (woven bone). Bone healing is completed during the remodelling phase in which various cellular molecular and functional regulators modify woven bone to organized lamellar bone, restoring the original shape, structure and mechanical strength. Remodelling occurs slowly over months to years, and is strongly influenced by local mechanical stress placed in the bone.

The process of bone graft incorporation is similar to the bone healing process that occurs in fractured long bones [6]. The most critical period is the first one to two weeks in which inflammation and revascularization occur. Incorporation and remodelling of a bone graft requires that the precursor bone cells have vascular access to the graft to differentiate into osteoblasts and osteoclasts. Bone grafts are also strongly influenced by local mechanical forces during the remodelling phase. Mechanical demands modulate the density, geometry, thickness and trabecular orientation of bone, allowing to optimize the structural strength of the graft [6].

13.1.2 Regenerative Graft Procedures

Regenerative graft procedure refers to technologies that repair or replace any defective, diseased tissues or organs by trauma, ageing, etc. Bone grafting is commonly used in the reconstruction of surgical procedures to swift a de novo bone formation in vivo with the aim of providing a rigid structure and supports other parts, in which the host bone can regenerate and heal in a proper way at particular defined time periods [7]. There are generally four types of bone grafts, namely autograft, allograft, xenograft and synthetic graft that have been widely used in regenerative surgery [8].

Autografts are those where the bone to be grafted is from another site in or on the body of the same individual. It is immunologically safe and thus limiting rejection concerns. The harvest of the autograft implies an extra and invasive surgical procedure coupled with the post-operative pain. Another disadvantage is the limited quantity of bone available for harvesting. Allografts are taken from human donors such as organ, tissues or cells donated from genetically distinct individual of the same specie. The use of this graft can solve some of the drawbacks related with autologous bone grafting since the second surgical procedure is eliminated and the

quantity of tissue is available in large amounts. However, the risk of post-operative infection and disease transmission, etc. are higher than with autograft. Xenografts are harvested from animals to human. The animal bone, most commonly bovine (cow) is specially processed to make it biocompatible and sterile. It acts like filler, which in time, the body will replace with natural bone. Synthetic graft substitutes have been developed to provide an alternative to autografts and allografts [7–11].

Synthetic bone graft substitutes offer many advantages compared to autografts including a lower probability of rejection or risk of morbidity, patient pain and recovery time. Hence, synthetic substances are gaining growing interest for use as bone graft materials. For successful bone grafting, there are three basic criteria namely, osteogenesis, osteoinduction and osteoconduction [8]. Osteogenesis is the process to produce a direct bone formation by transplanted living cells (osteoblasts and osteoblast precursors). To date, the only material that displays true osteogenic properties is autograft. Osteoinducion is the process, which stimulates new bone production in bone-forming cells [7]. Blood-borne proteins, peptides, growth factors and a specific group of named cytokines provide this stimulation. Osteoconduction is the process, which provides a structural framework and environment that supports the migration, attachment and growth of osteoblasts and osteopregeneitor cells into the graft. Autografts, allografts, many of mineral bone graft substitutes such as hydroxyapatite (HA) and bioactive glass provide this property.

Hence, osteoconductive materials, such as synthetic calcium phosphate ceramics are of special interest for bone repair because of the occurrence of biological apatites in normal calcified tissues, e.g. enamel, dentine and bone. Therefore, calcium phosphates act as motivators because they are the main inorganic constituents of hard tissues in the body. They are generally used in dense, granular or porous form as well as coatings of metal prostheses and implants or in the form of composites. The benefits of synthetic grafts include availability, sterility, cost-effectiveness and reduced morbidity. However, the selection of grafting procedure to use is purely dependent on the nature and complication of the bone defects as well as the choice of available bone grafts.

Ideally, synthetic bone graft substitutes should be biocompatible, show minimal fibrotic reaction, undergo remodelling and support ossification. HA, $Ca_{10}(PO_4)_6(OH)_2$ is one of the most biocompatible material used today and has been used as bone graft for a long time. HA implant materials are osteoconductive, however they are very slow resorbable materials. Hence, different approaches have been used to overcome this hindrance. For example, HA can be modified or combined with other materials to improve its functionality and enable faster resorption. Tricalcium phosphate, $Ca_3(PO_4)_2$, in their allotropic forms β and α-TCP has higher solubility and resorption rate than HA. Hence due to their relative solubility, TCP is generally used in circumstances where structural support is less important.

Glass-based materials are considered as a surface reactive ceramics. These types of materials when implanted undergo surface dissolution and release ions into the surrounding environment with consequent change of pH environment. The

Table 13.1 List of the most commercially available synthetic graft material on the market

Name of the product	Characteristics	Company
Hydroxyapatite (HA)		
Ceros 80	Dense polycrystalline HA	Straumann Ltd, UK
Biocoral	Natural mineral skeletons of Scleractinian corals	Inotebm, France
Pro Osteon	Coralline macroporous HA	Interpore Int., USA
Osteograft	Crystalline HA	CeraMed, USA
Calcitite	Dense crystalline HA	Calcitek, USA
Tricalcium Phosphates (TCP)		
Chronos/Ceros 82	Tricalcium phosphate	Mathys Suisse
Biosorb	Tricalcium phosphate	SBM S.A., Lourdes
Vitoss	Ultraporous TCP	Orthovita, USA
Cerasorb	Tricalcium phosphate	Curasan AG, Germany
Bioactive glasses		
Bioglass®	Bioactive glass	Novabone, USA
Ceravital	Group of glasses and glass ceramics of various compositions	E. Pfeil and H. Bromer, Germany
Biogran	Bioactive glass	Orthovita, USA

composition of the glasses controls surface reactivity and some are known to closely adhere to the surrounding living bone tissues.

In Table 13.1 are listed some of the most widely used and commercially available synthetic bone graft materials. These materials are available in different forms such as blocks, granules, cements, gels and strip products. The block and granule types are the most commercialized on the market [11]. Blocks are normally used in situations of trauma, interbody spinal fusion and non-unions; they stay in one place without migrating and can be shaped to fit the defect. Granules are generally used for posterior/lateral spinal fusion, filling cystic voids as well as for hip and knee revisions. Among other indications, cement is used for the augmentation of pedicle screw fixation, whereas gels can be used percutaneously and injected into closed fractures. Strips are less commonly used, but could be utilized in acetabular reconstructions [11].

According to the statistical and published data on bone graft substitutes, it is estimated that 500,000–600,000 bone grafting procedures are performed annually in the United States. Approximately half of these surgeries involve spinal arthrodesis whereas 35–40 % are used for general orthopaedic applications [7, 12]. In Europe, the number of grafting procedures was reported to be 287,300 in the year 2000, with a predicted increase to 479,079 in the year 2005 [11, 13]. Synthetic bone graft substitutes currently represent only 10 % of the bone graft market, but their share is increasing day-by-day as experience and confidence accumulated [12].

Today, tissue-engineering methods are being increasingly used to optimize actual surgical treatments and to develop new treatment methods. The objectives are accelerated towards the healing of bone or soft-tissue defects. The properties of the carrier play an important role in the effect of biological modulators. On one hand, they act as a delivery system for the morphogenic factors and on the other hand they have to provide a stable matrix for cell adhesion and growth. Recent approaches which are being implemented include (a) platelet-rich (PRP) harvested from the patient's blood, (b) genetically engineered growth factors (BMP's), (c) autogenous cells enriched millions of times in the laboratory and (d) autogenous bone marrow (transplants), already containing cells and growth factors [14].

13.2 Synthetic Bone Graft Material—Bonelike®

13.2.1 Bonelike® Development and Preparation

Bone graft substitutes have been developed to provide an alternative to autografts and allografts. Nowadays, it is possible to prepare synthetic bone substitutes that have very similar composition to the mineral osseous tissue. This is important aspect to increase the regeneration of bone, since bone graft should promote an ideal microenvironment where it is possible for cellular adhesion, differentiation and mitoses to occur. Some of these biomaterials have the ability of being re-absorbable in a time-controlled way, in order to permit the correct process of natural reconstruction of involved bone tissue. Therefore, in order to design a scaffold that supports bone formation while gradually being replaced by bone, an optimum balance between the more stable phase like HA and the more soluble phases like TCPs' must be essentially required.

J.D. Santos and co-authors developed [15–18] glass reinforced HA (GR-HA) composites with the incorporation of a $CaO–P_2O_5$-based glass in the HA matrix. This patented material has been recently registered and marketed as Bonelike®. This bone graft displays two distinctive advantageous characteristics: (a) enhanced bioactivity, by reproducing the inorganic phase of HA in bone which contains several ionic substitution which modulates its biological behaviour, (b) improved mechanical properties using $CaO–P_2O_5$-based glasses that act as liquid phase sintering process of HA which reduces porosity and grain size [19]. Due to the chemical composition, Bonelike® induces bone formation through specific activation of the bone cells with controlled release of ions such as F^-, Mg^{2+}, Na^+ etc. from its surface to the surrounding medium, which can be schematically described and as shown in Fig. 13.1.

The preparation of Bonelike® can be briefly described as follows: $CaO–P_2O_5$-based glasses are prepared from reagent grade chemical using conventional glass making techniques, which are then crushed to fine particles and mixed to phase pure

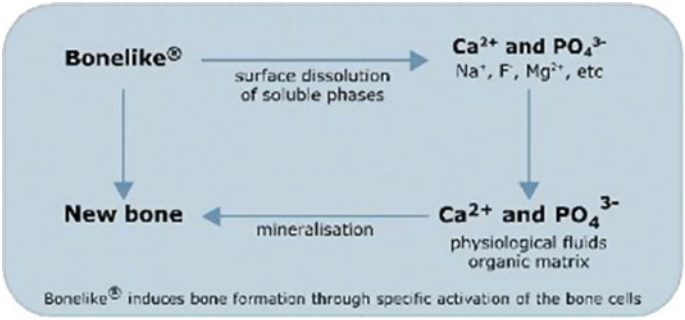

Fig. 13.1 Bone regeneration mechanism of Bonelike®

HA powder. Usual sintering temperature for HA in the range of 1200–1350 °C the glass melts, and diffuses into the HA structure, leading to several ionic substitutions in the lattice [20].

13.2.2 Physico-Chemical Characterisation

The first step in a complex series of biophysical/biochemical processes related to the interaction of an implanted material with a host biological tissue consists of the spontaneous formation of a proteinaceous layer absorbed onto the implanted materials. Therefore, surface properties are critical in biomaterial biocompatibility and must be considered as in their selection for medical applications, together with bulk property characteristics [21–24]. Chemical composition, hydrophobicity and electrical surface charge are well known parameters that influence the complex process of protein adsorption onto biomaterials, and their subsequent influence on the attachment and spreading of cells that ultimately determine the success or failure of the implant during service [25].

Phase transformations and interstitial and/or substitution of trace elements during the liquid phase sintering process of Bonelike® were examined by X-ray diffraction and FTIR analyses [16, 26].

The characterisation of Bonelike® using FTIR shows that carbonate ions CO_3^{-2} that are present in the samples at 1200 °C (Fig. 13.2a), as indicated by bands in the region of 880 cm^{-1}, systematically decreases until at 1350 °C (Fig. 13.2b), the bands are almost indistinguishable. Furthermore, there is a significant loss in the hydroxyl groups OH^-, denoted by the band at 3570 cm^{-1}. The bands at 880 cm^{-1} have been assigned to ν_2 vibrational mode [27].

XRD analysis showed that, depending on the glass amount and the glass composition, as well as the sintering temperatures, the microstructure of Bonelike® was composed of the HA matrix, and α- and β-TCP secondary phases (Fig. 13.3).

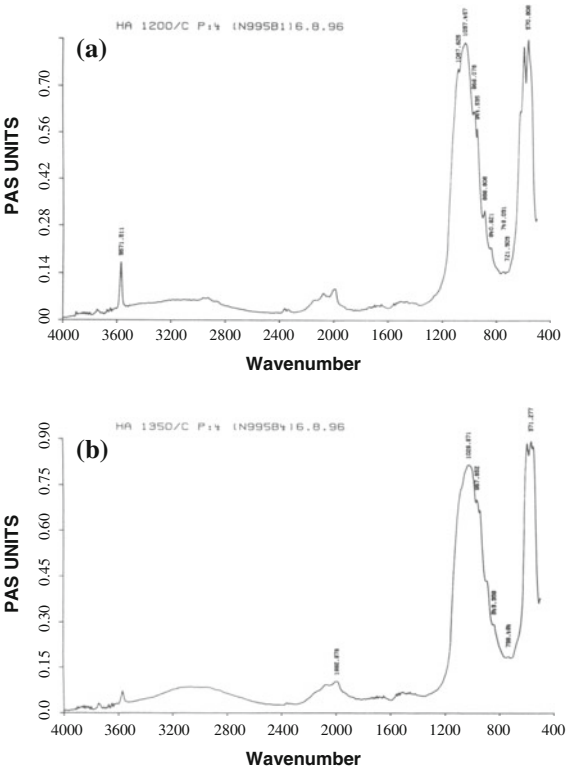

Fig. 13.2 FTIR spectra for Bonelike® with 4 wt% glass addition sintered. **a** at 1200 °C and **b** at 1350 °C

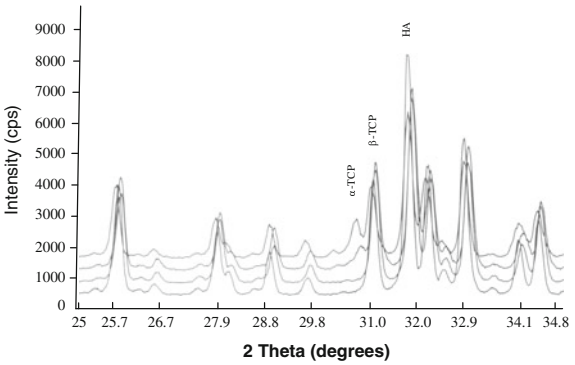

Fig. 13.3 Overlaid traces of XRD data sets from 1200 °C (bottom) to 1350 °C (top) for Bonelike® containing 4 wt% glass

The HA is decomposed by the presence of a reactive glass, which enters into the HA structure and causes the OH^- groups to be driven out and also alters the Ca: P ratio. However, the β-TCP formed in the presence of high amount of glass is likely to contain more residual ions from the glass and thus it becomes unstable, and therefore α-TCP is formed.

The glasses can give rise to formation of between approximately 30 and 60 % TCP. At high temperatures, the β-TCP inverts to α-TCP without further decomposition of the residual HA. For example, the Mg^{2+} containing glasses induced the α-TCP phase formation in the structure of Bonelike® and retarded the α-TCP into β-TCP transformation at higher temperatures [16, 28–30]. The chemical composition of the glasses also induces modifications in the lattice parameters of the crystallographic phases present in the microstructure of the composites [16].

The mechanism and the extent of any ion substitutions and/or interstitial in the calcium phosphate phases lattice depends on the size and content of the ion as well as on the temperature of the liquid phase sintering process [19].

XRD studies highlighted the effect glass had on the crystallographic structure of the main phases of Bonelike® [16, 26]. It was proposed that the larger addition of glass gives a larger number of ions present, and it is these ions that enter into phase structures and may become interstitial ions. Wettability and zeta potential studies have been performed to characterize the hydrophobicity and surface charge of Bonelike® [31]. Despite the glass composition used and with the glass amount addition between 2.5 and 4.0 wt%, zeta potential values in between pure phase HA and α-TCP values were observed, i.e. between −28.7 mV and −18.1 mV. This intermediate behaviour was also observed regarding the wettability studies performed by static contact angle measurements using water. The presence of the secondary phases namely α-TCP, influenced surface charge and hydrophobicity of the Bonelike®, and therefore indirectly affects cell—biomaterial interactions [31].

13.2.3 Mechanical Characterisation

Mechanical properties of bioactive ceramic materials that are known to form a direct bond with natural bone have been extensively studied to improve their reliability when used in medical applications [32, 33]. To assess the mechanical behaviour of Bonelike®, namely the bending strength, elastic properties and fracture toughness, a concentric ring-on-ring testing, an impulse excitation method and Vickers indentation technique, respectively, have been performed. The Duckworth–Knudsen model was also applied to determine the dependence of bending strength as well as Young's and shear modulus on microstructural parameters of Bonelike®.

Bending Strength

Flexural bending strength (σ) of Bonelike® (Glass reinforced HA composites) was found [34] to be about two or three times higher than that of HA, as seen in Fig. 13.4. The level of reinforcement obtained is exemplified in Fig. 13.5 where, using Weibull statistics analysis, failure probability is plotted versus bending strength for HA and Bonelike® sintered at 1350 °C.

The strength of both HA and Bonelike® seems to be strongly dependent on porosity and tended to increase with densification, following the expected pattern

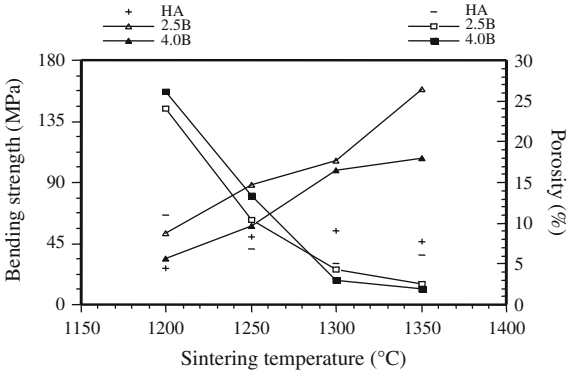

Fig. 13.4 Flexural bending strength (MPa) and Porosity (%) versus sintering temperature (°C) for HA and Bonelike®

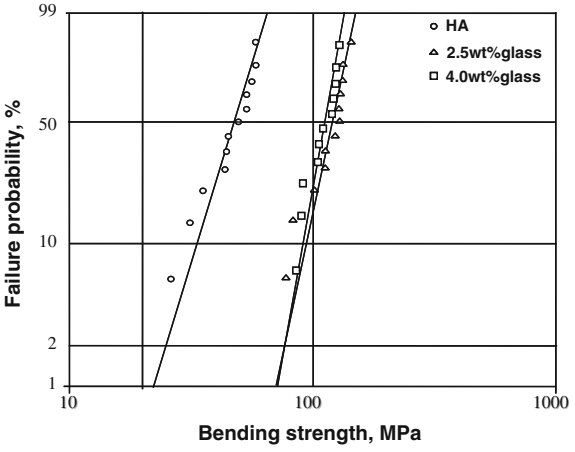

Fig. 13.5 Weibull distribution function (failure probability vs. flexural bending strength) for HA and Bonelike®

for the sintering process (Fig. 13.4). However, for the Bonelike®, the secondary phases (β- and α-TCP) present in the microstructure and these phases strongly influence the mechanical behaviour of the material.

The Duckworth–Knudsen exponential model is widely used to characterize the mechanical behaviour of ceramic matrix composites [35] and using the rule of mixture it was possible to estimate the zero porosity rupture modulus for each phase (HA, β and α-TCP) and the porosity correction factor, b. Zero porosity rupture modulus for HA, β-TCP and α-TCP were estimated as being 83.1, 179.9 and 233.5 MPa, respectively, and the strength versus porosity equation of Bonelike® was obtained using the relationship:

$$\sigma = (83.1X_{HA} + 179.9X_{\beta} + 233.5X_{\alpha})\, e^{-4.02P} \quad (1)$$

Elastic Properties

The elastic properties such as dynamic Young's modulus (E) and shear modulus (G) of Bonelike® have been determined using an impulse excitation method [18] of vibration according to ASTM C 1256-96 using the following equation:

$$E = 0.9465\left\{mf_f^2/\ b\right\}\left\{l^3/t^3\right\}T_1 \quad (2)$$

where E is the Young's modulus (Pa), *m* the mass of the bar (g), *b* the width of the bar (mm), *l* the length of the bar (mm), *t* the thickness of the bar (mm), f_f the fundamental resonant frequency of bar in flexure (H_z) and T_1 the correction factor for fundamental flexural mode.

For the shear modulus (G) determination, the following equation was used:

$$G = \left\{4lmf_t^2/\ bt\right\}\left\{b\ /1 + A\right\} \quad (3)$$

where *G* is the dynamics shear modulus (Pa), f_t the fundamental resonant frequency of bar in torsion (Hz), *A* the empirical correction factor.

The Young's and shear moduli were experimentally determined and the results were correlated with respect to porosity and the presence of secondary β- and α-TCP phases in the microstructure of Bonelike® using the Duckworth–Knudsen model. Zero porosity values determined for E and G were as follows:

E_0 = 120 GPa and G_0 = 41.8 GPa for HA, and E_0 = 64.1 GPa and G_0 = 27.4 GPa for β-TCP and the obtained general equations were

$$E = (120.0\ X_{HA} + 64.1X_\beta + 188.6\ X_\alpha)\ e^{-4.04P} \quad (4)$$

$$G = (41.8\ X_{HA} + 27.4\ X_\beta + 91.3\ X_\alpha)\ e^{-4.11P} \quad (5)$$

Fracture toughness

Fracture toughness (K_{IC}) of Bonelike® graft has been assessed using an indentation technique and results calculated according to Laugier and Evans' equations [17]. A 3 N load was applied for 10 s using a pyramid-shaped diamond indenter. Each specimen was indented 15 times and at least three samples were used to check for reproducibility of results. Statistical analysis was performed using Student's *t-test.* The highest value was obtained for Bonelike® K_{1C} = 1.45 ± 0.25 % MPa $m^{1/2}$ compared to 0.70 ± 0.09 % MPa $m^{1/2}$ for HA. However, the fracture toughness of Bonelike® strongly depended on the chemical composition and the percentage of the added glass and on the sintering temperature [17].

The combination of crack bridging, crack deflection and transformation—toughness mechanism were used to explain the enhanced fracture toughness of Bonelike® when compared to HA [17, 36].

13.2.4 Biological Evaluation

Biological evaluation is of great importance in assessing the potential benefit of implantable materials for human applications. Biocompatibility testing is concerned with "biosafety" and "the ability to perform with appropriate host response in a specific application". In vitro and in vivo studies form an integral part of biological testing for potential implant materials.

13.2.4.1 In Vitro Studies

As a result of time, effort, cost, increasing restriction and lack of precise basic data derived from animal experimentation, in vitro testing has become a major tool for evaluating the basal and specific cytocompatibility of new and modified materials for biomedical applications. In vitro procedures are the basic starting point whereby biological responses to materials are determined initially, as required by a number of standardization agencies [37].

The biological performance of Bonelike® composite scaffolds was assessed using human bone osteoblastic cell cultures, namely the osteosarcoma cell line MG63 and osteogenic-induced bone marrow cells. The cell response was evaluated by a direct assay, i.e. culturing the cells on the material's surface, and also using an indirect assay, with the cultures being performed in the presence of Bonelike® extracts. The major advantage of the direct assay is that it closely mimics physiological conditions by establishing a concentration gradient of chemicals, which diffuse away from the cells, as it would occur in intact tissues in situ. Also, in studying such direct cell-surface interactions, the surface charge, surface topography and surface free energy play a fundamental part in cell adhesion, spreading, growth and, ultimately, function of the cell [37, 38]. On the other hand, the indirect method, in which test materials are first "extracted" by immersion in a physiological solution, which is subsequently added to the target cells, has the advantage of being able to examine whether substances are "leached" from the test materials and exert a deleterious, or induce a beneficial effect [37, 38].

Osteoblastic cell cultures were maintained for appropriate time periods and culture conditions, depending on the culture system used [39–41]. Cell behaviour was assessed in terms of attachment and spreading, morphology, cell viability/proliferation and functional activity regarding the expression of key extracellular matrix antigens and, in the case of human bone marrow cells, the ability to form a cell-mediated mineralized matrix. Bonelike® composites were prepared in several compositions in order to incorporate in its microstructure, ions commonly found in human bone tissue. Table 13.2 shows the compositions selected for in vitro testing. HA was always used as the control material.

Biocompatibility of composites A, B and C was assessed by monitoring their effects on the proliferation and function of osteoblast-like MG63 cells. Flow cytometry technique was used to evaluate cell-cycle progression, cell size and

Table 13.2 Bonelike® compositions subject to in vitro testing

Bonelike®	Glass (in % mol)					Glass added to HA (wt%)
	P_2O_5	CaO	MgO	Na_2O	CaF_2	
A	50	16.5	33.5	–	–	2.5
B	50	16.5	33.5	–	–	4.0
C	75	15.0	–	–	10	4.0
D	45	28	–	27	–	2.5
E	65	15	–	10	10	4.0

granularity and expression of collagen type I, fibronectin and osteocalcin. In addition, cultures were observed by scanning electron microscopy (SEM). Evaluation of DNA synthesis and content was also performed regarding composites B and C. Data showed that MG63 cells growing on the surface of the three composites presented a normal morphology, a high growth rate and were able to express collagen type I, fibronectin and osteocalcin, proteins known to have major roles in connective tissue integrity, adhesion and bone structure and differentiation [42]. In addition, cells cultured on the plastic surface in the presence of the extracts of composites B and C did not show any significant deleterious effect on cell morphology and function, and data yielded information similar to that observed in the direct testing assay [40].

Bonelike® samples with the compositions D and E (Table 13.2) were evaluated regarding the proliferation/differentiation response of human bone marrow osteoblastic cells, using a direct assay. Bone marrow cells (first subculture) were plated on the surface of the composites and the colonized materials were incubated for 35 days in an osteogenic-inducing medium.

SEM observation of Bonelike® samples incubated in the absence of cells (Fig. 13.6) showed significant surface modifications resulting from the dissolution of resorbable phases, with the formation of different size microcavities that became progressively larger with the incubation time; simultaneously, deposition of an apatite layer was also observed.

Biochemical evaluation of seeded samples of Bonelike® showed that bone marrow cells presented a high proliferation rate and produced significant levels of alkaline phosphatase (ALP). HA had a slightly lower biological profile regarding these parameters (Fig. 13.7).

Cells growing on the material surface adapted successfully to the surface irregularities and were able to grow towards the forming cavities. Cell-mediated matrix mineralization began to occur during the third week, as evident by the presence of abundant globular mineralized structures incorporated into a network of fibers in 28-day cultures (Figs. 13.8 and 13.9). It is noteworthy that with composite E, the formation of the mineralized matrix was especially associated with the surface cavities resulting from the dissolution of resorbable phases. High magnification SEM micrographs showed exuberant cell-mediated mineralization inside

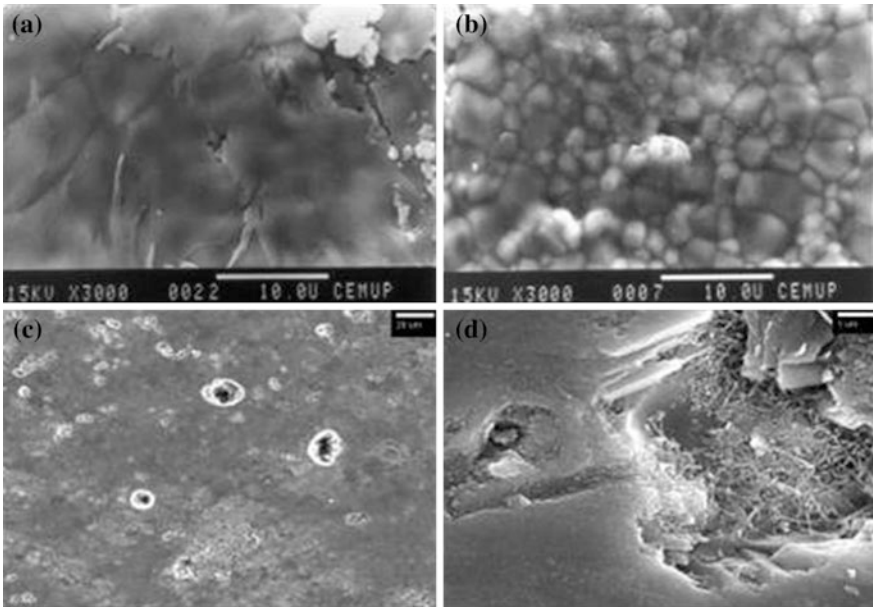

Fig. 13.6 SEM micrographs of the dissolution/deposition reactions on the surface of Bonelike® after incubation with culture medium. Composite D: "as-received" condition (**a**); 21 days incubation (**b**); Composite E: 21 days incubation: **c** Bar, 20 μm; **b** Bar, 1 μm

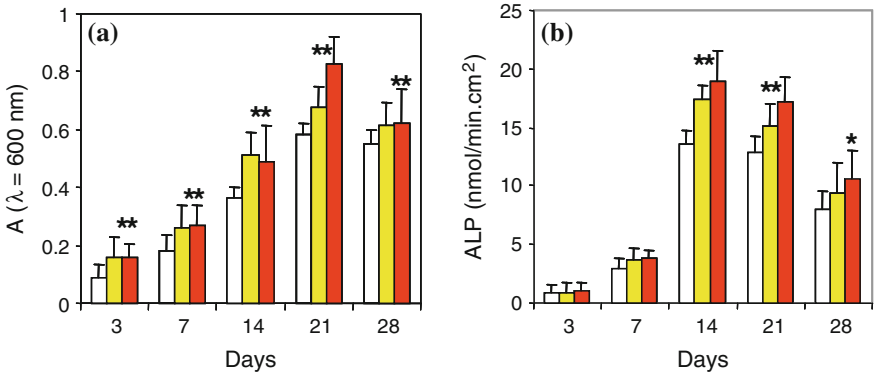

Fig. 13.7 Cell viability/proliferation (**a**, MTT assay) and ALP activity (**b**) of human bone marrow osteoblastic cells cultured on the surface of composites D (*Yellow column*) and E (*Red column*). HA (*White column*) presented a slightly lower biological profile

these cavities (Fig. 13.9). In general, HA presented a slightly lower biological profile, reflected by a delayed and relatively poor matrix mineralization (Fig. 13.8).

Results regarding the response of human bone marrow osteoblastic cells to Bonelike® with the compositions D and E (Table 13.2) showed, in general, that, in

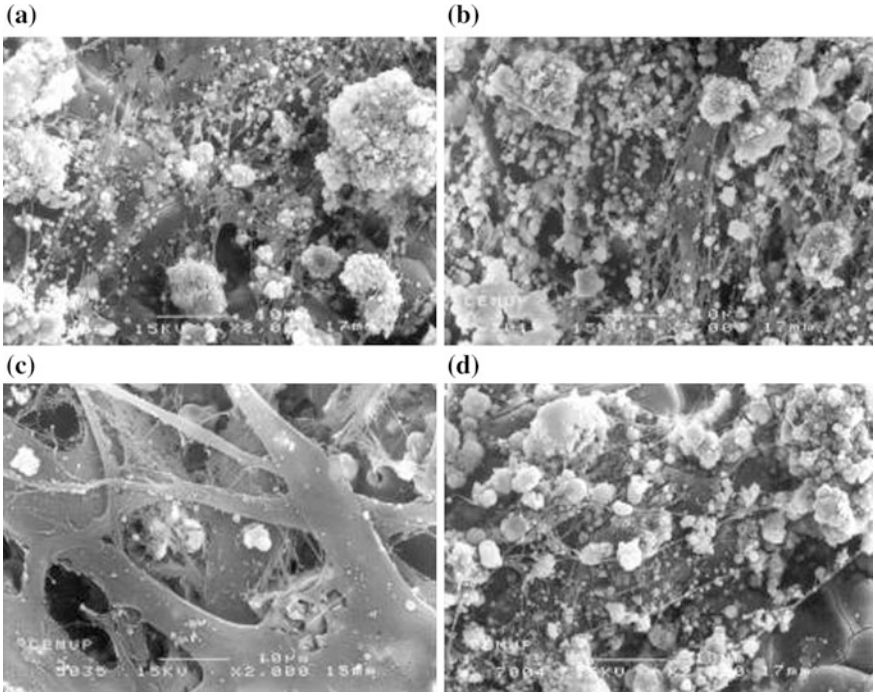

Fig. 13.8 SEM micrographs showing composite D, cultured with human bone marrow osteoblastic cells at days 21 (**a**) and 28 (**b**). For comparison, results regarding the cell response to HA at the same time points are also shown: **c** 21 days; **d** 28 days. Bonelike® presented an earlier onset of matrix mineralization

comparison with HA, the composites had a positive effect regarding cell proliferation, synthesis of ALP and formation of a mineralised matrix. The improved biological performance of Bonelike® is most probably related with its chemical composition.

This biomaterial is composed of an HA matrix with bioresorbable α- and β-tricalcium phosphate phases, which are more soluble than single HA and liberate Ca and P ionic species to the local environment. Surface reactions occurring as a result of ongoing dissolution/deposition events appeared to induce osteoblastic growth and differentiation. In addition, the presence of fluoride ions in the composite E may also have a positive contribution, as this ion is known to have a potent influence on cell proliferation [43].

13.2.4.2 In Vivo Experimentation

The in vivo animal testing of Bonelike® were performed in rabbits and sheep models and all procedures carried out with the approval of the National veterinary

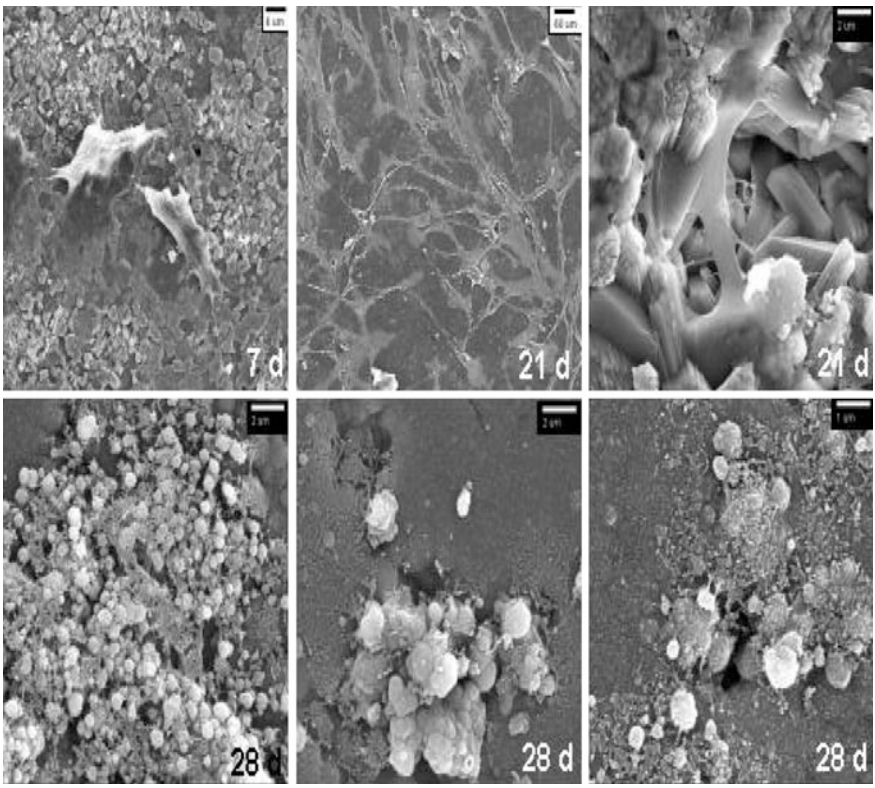

Fig. 13.9 SEM micrographs showing composite E, cultured with human bone marrow osteoblastic cells for 7 days (Bar: 6 μm), 21 days (Bar: 60 and 2 μm) and 28 days (Bar: 2, 2 and 1 μm). Matrix mineralization occurred preferentially in the surface cavities resulting from dissolution of the resorbable phases

authorities and local Ethic Commission, and in accordance with the European Communities Council Directive 86/609/EEC [44, 45]. For several medical applications of bone regeneration, the use of a vehicle to carry the bone graft is considered as being a very relevant issue. In fact, this association not only facilitates the medical application of the bone graft but also will open-up new areas of application in medicine, namely those related to: (i) minimal invasive surgery and (ii) the possibility of associating therapeutic molecules that have crucial function in bone regeneration [46, 47].

Rabbit and Sheep Testing

For the in vivo testing of Bonelike® associated to several vehicles, healthy skeletally mature male New Zealand White rabbits [46, 47] and adult Merino sheep were used as experimental models. For surgery, rabbits and sheep were placed prone under sterile conditions and under deep anaesthesia a longitudinal incision

was made on the lateral surface exposing the femur. In each femur, several holes were drilled through the cortex and into medulla using a micro-burr continuously flushed with a saline solution (NaCl 0.9 %, Braun) to minimize thermal damage and to remove any residual bone [46, 47] (Fig. 13.10). Several vehicles have been tried in association with Bonelike®, such as Floseal®, Normal Gel 0.9 % NaCl® and chitosan-derived gel that were mixed with Bonelike®granules and implanted into the holes. These vehicles were associated with two types of therapeutic molecules, raloxifene hydrochloride and bone morphogenic proteins (BMPs).

FloSeal® is easily used and it can be extruded from a syringe and applied topically to the bleeding area. This haemostatic agent has the ability to acquire irregular shapes fitting the wounded site [48, 49].

When the FloSeal® is in contact with blood, the collagen particles are hydrated and swell. The thrombin present converts the patient fibrinogen into a fibrin polymer, originating a clot around the granules [48, 49]. Normal Gel 0.9 % NaCl® (Moneylycke, Portugal) is a polymeric vehicle [46] and the chitosan-derived materials are known for their biocompatibility and bioactivity [50].

The raloxifene hydrochloride is a known selective estrogen receptor modulator (SERM) and acts as an estrogen agonist on bone and liver, also to increase bone mineral density [51–53], being used for prevention of osteoporosis in post-menopausal women [51]. Raloxifene hydrochloride also inhibits in vitro mammalian osteoclast differentiation and bone resorption in the presence of interleukin-6 (IL-6) [51–53]. The demonstration that recombinant BMPs have the potential to induce bone formation suggests that this may have enormous therapeutic potential in the management of numerous clinical conditions in which there is a requirement for new bone formation [54]. A number of studies have demonstrated that BMP-2, -3, -4 and -7 can up-regulate features of the mature osteoblast phenotype, including ALP activity, collagen synthesis, and osteocalcin expression [54].

Through sequential X-ray images, it was possible to follow the healing process every week in both species. X-ray analysis of rabbit femurs revealed increased osteointegration and defect healing for both particle size ranges of implanted Bonelike® associated to both vehicles, Normal Gel 0.9 % NaCl® and FloSeal® [46, 47]. During the healing period, rabbits and sheep easily recovered and no rejection symptoms were observed in the implantation site for all implanted samples.

Rabbits and sheep were sacrificed 12 and 16 weeks after implantation, respectively, and the retrieved samples analyzed by SEM and Solo Chrome R/Haematoxylin-Eosin stained for histological studies. SEM characterization of unstained slices was performed to quantify the contact percentage of new bone formed with implanted granules and assess the in vivo degradation process. The interface layer implanted material/new bone formed was evaluated by SEM-EDX (energy dispersion X-ray microanalyser) [46, 47]. Both SEM and histological analyses confirmed the osteointegration of Bonelike® granules and the new bone formation, with almost complete regeneration of the bone defect [46, 47]. Bonelike® associated with Floseal® and raloxifene hydrochloride showed that new bone was rapidly apposed on implanted granules after 12 weeks of implantation in

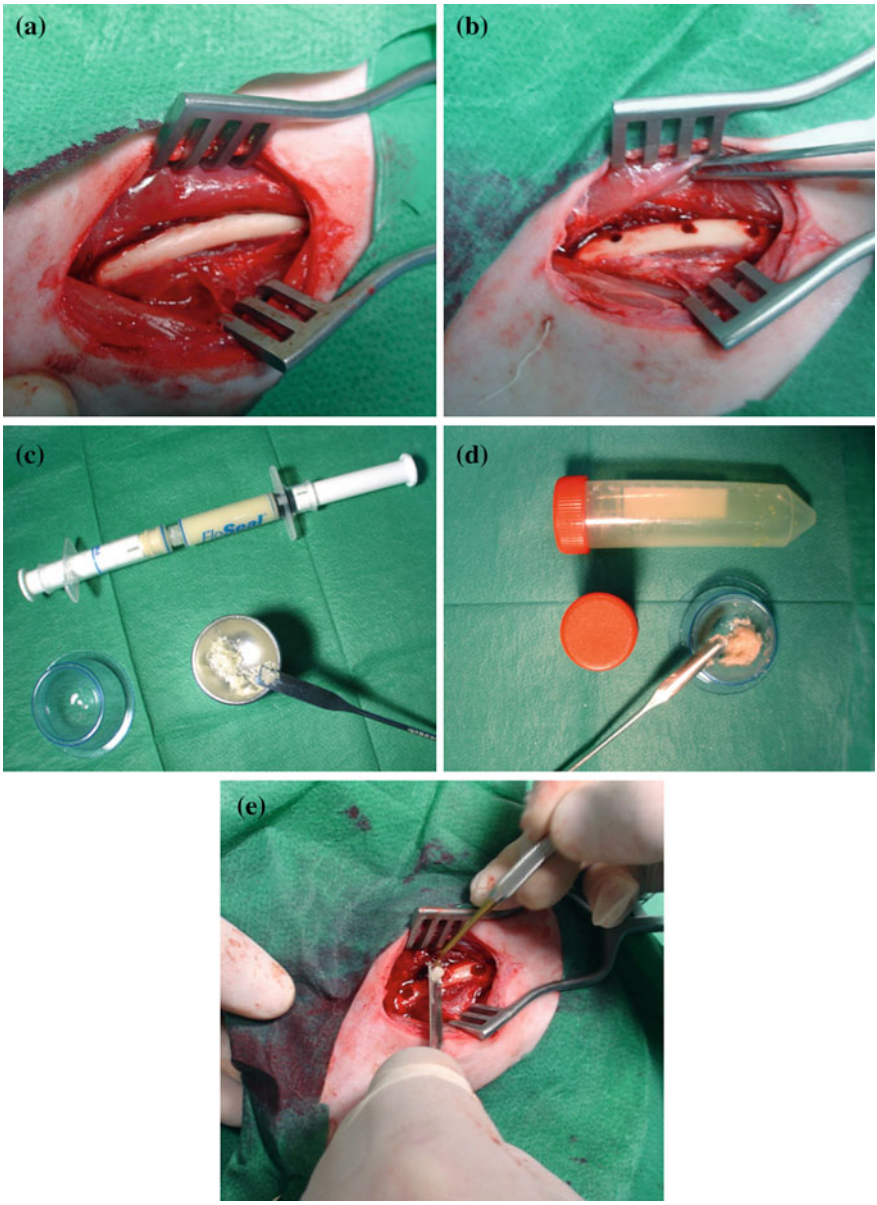

Fig. 13.10 Surgical procedures: **a** exposed rabbit femur; **b** rabbit femur showing 3 holes of 3 mm diameter; **c** mixture of Floseal® and Bonelike® granules; **d** mixture of Bonelike® granules with raloxifene hydrochloride and **e** implantation of Floseal®, Bonelike® granules and raloxifene hydrochloride in the bone defects

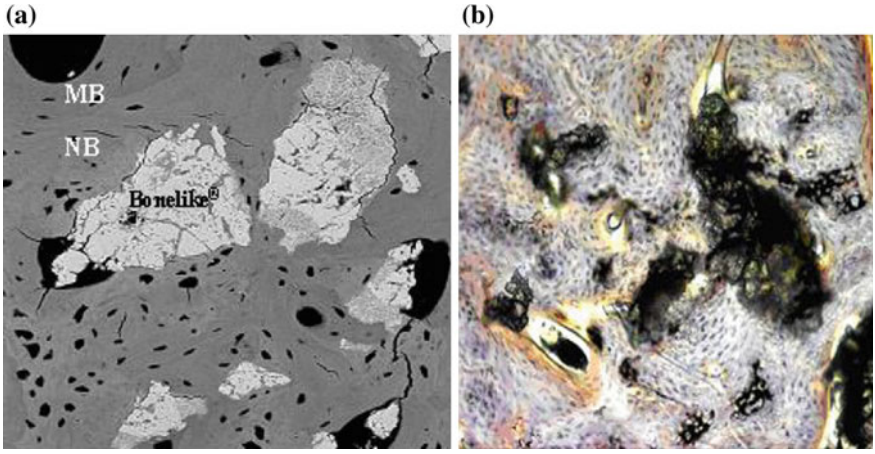

Fig. 13.11 **a** Scanning electron microscopic image (200×); **b** Solo Chrome R staining images of the experimental samples (20×) showing Bonelike® granules involved in the de novo mature bone tissue, (*NB* New Bone, *MB* Matured Bone, and *OC* Osteocytes)

rabbits. Bonelike® granules are completely surrounded by de novo mature bone (Fig. 13.11) and in the SEM image (Fig. 13.11a) it is possible to observe the complete osteointegration of the Bonelike® granules with bone tissue formed among them with the presence of new osteon. Additionally, an extensive surface dissolution of Bonelike® granules could be observed [46, 47]. No evidence of osteoclasts activity seems to have taken place which may be explained by the presence of raloxifene hydrochloride that is known to inhibit osteoclast activity [51–53] and BMPs, known to up-regulate osteoblast functions [54]. Similar results were observed on the histological slices in Fig. 13.11b where the granules were completely surrounded by new bone (fibroreticular) with vascular structures and cement lines indicating active bone regeneration. Several blood channels without signs of inflammation throughout the osteoid matrix have been observed and no inflammatory cells and fibrous tissue have been found. The presence of blood vessels was due to active angiogenesis process that is an extreme important process for bone regeneration [47]. SEM and histology analysis of the ovine model also revealed the high bioactivity of the Bonelike®/chitosane-derived matrix. Through histological analysis, it was possible to see some chitosane-derived matrix after 4 months. Although, it appears in an extensive dissolution features and the granules were surrounded by new bone formation with some degree of maturity.

In conclusion, the Bonelike® graft associated to Floseal®, Normal Gel® or chitosan-derived matrix seemed to serve as an excellent scaffold for bone regeneration [46, 47]. In addition, the association of Bonelike® to a resorbable vehicle can act as a controlled release system to osteoinductive molecules and therefore enhances the osteointegration of Bonelike® graft. It is also much more easy to handle and can be considered as an injectable osteoconductive synthetic bone graft substitute [46, 47].

Push-out Testing

Push-out testing was performed [55] in a rabbit model for characterizing bone/Bonelike® bonding, and the shear force needed to detach the implanted material was measured. For this testing, a longitudinal incision was made on the anterior surface, extending from about 10 mm below the knee joint for a distance of 25 mm. 4.0 mm diameter holes were drilled through cortex and into medulla and then cylindrical specimens of 4.0 mm in diameter and 20 mm in length were press-fitted into the holes. This study was performed using periods of implantation time up to 16 weeks.

Back-scattering SEM image showed that the place where failure occurred for implanted samples during push-out testing depended upon the implantation period. Figure 13.12 shows the back-scattering image of the interface between Bonelike® and bone, after 16 weeks implantation. Breakage occurred essentially through the implant body after such a long implantation period, which indicates a strong implant /new bone bonding as well as maturity of newly formed bone around implant. On the other hand, breakage occurred at the bone/implant interface at early stages after implantation such as 2 and 4 weeks showing that a weak bone-bonding strength was established, due to the lack of time for a complete bone formation around Bonelike® and to its immaturity.

Results of push-out testing showed bonding between Bonelike® and new bone, ranging from 130 to 145 N after 2 weeks of implantation, similar to the values achieved for pure phase HA. After the longest implantation period, 16 weeks, the Bonelike® prepared with 4.0 wt% of $CaO–P_2O_5$-based glass showed a higher bonding force of 606 ± 45 N compared to 459 ± 30 N for sintered pure phase HA.

The enhanced biological response of Bonelike® is a consequence of the synergistic effect of the presence of secondary phases, β- and α-TCP phases, and the local release of ions to the surrounded biological medium.

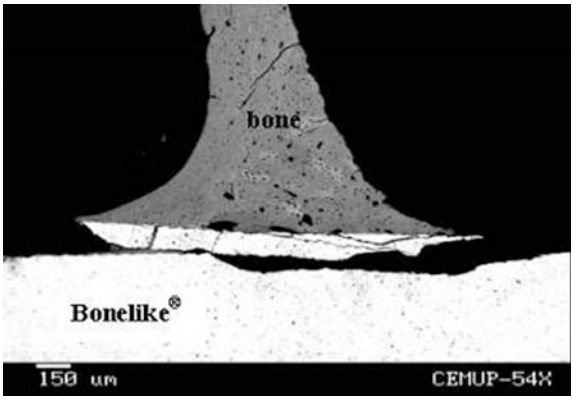

Fig. 13.12 Back-scattering image of interface between Bonelike® material and bone, after 16 weeks implantation

13.2.5 Medical Applications

Bonelike® graft has been successfully applied in several areas of regenerative surgery namely in oral and maxillofacial surgery, implantology and orthopaedics [56–60]. In oral surgery, Bonelike® has been used for the regeneration of bone defects after cyst removal and retained tooth extraction in maxillofacial surgery for bone maxilla and mandible reconstruction, in implantology for bone augmentation around implants, ridge augmentation for later implantation and sinus floor elevation, in periodontology furcation and intraosseous defects, and in orthopaedic for the regeneration of bone defects caused by trauma, ageing and for the correction of valgus knee using open wedge high tibial osteotomies (HTO).

13.2.5.1 Oral and Maxillofacial Surgery

In oral and maxillofacial surgery [58], Bonelike® has been used to regenerate bone defects after cyst removal in 11 patients, aged between 24 and 53 years with a mean age of 36 years, consisting of five men and six women. Most cysts of the oral and facial regions under treatment were located within the jaws as an intrabony lesion with a median mandibular cyst, and referred to as a non-odontogenic cyst in the midline aspect of mandible. Sometimes, resection of a large segment of the jaw was necessary to insure complete removal of the lesion. Thereby, the pathological "tissue destruction" process and its suitable surgical removing led to a significant bone loss. The size of the cavities varied from 3 cm diameter in the minor lesion up to 12 cm of the bigger diameter of the widest cyst. After the cyst was completely removed, the remaining bone cavities were firmly packed with Bonelike® granules mixed with blood and crushed bone remnants compound in an attempt to completely fill bony cavities and "to sculpt" the cortical bone contour.

According to the standard follow-up protocols, radiological examinations were performed and Bonelike®/bone retrieved samples have been analyzed histologically using non-decalcified sections obtained perpendicular to bone length axis. Radiographic examination and histological results clearly demonstrated an extensive new bone formation apposed on Bonelike®granules with a significant degree of maturation.

An example of the complete clinical application of the Bonelike® graft is shown in Fig. 13.13. A gingival and periosteal tissue covering the entire maxillary cystic lesion can be observed in Fig. 13.13a along with an operative image of maxillary cystic's lesion in Fig. 13.13b. Post-operative radiological analysis shows excellent granules adaptation to the host cavity without material dislocation accompanied by local bone defect regeneration after 3 months (Fig. 13.13c) and after 12 months a complete restoration of the local biofunctionality was achieved (Fig. 13.13d).

These clinical applications in maxillary bone defects indicated perfect bonding between newly formed bone and Bonelike®granules, along with partially surface

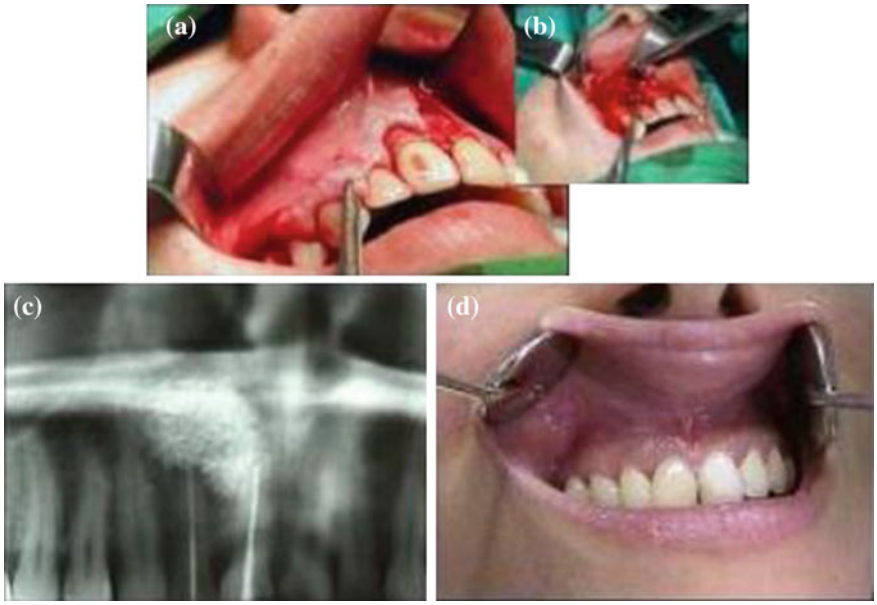

Fig. 13.13 **a** A gingival and periosteal tissue covering the entire maxillary cystic lesion. **b** Operative image of maxillary cystic lesion. **c** Post-operative radiograph shows the excellent Bonelike®granules adaptation to the bone cavity without any sings of material dislocation after 3 months, and **d** Complete restoration of the bone defect and biofunctionality may be seen 12 months after implantation

biodegradation. This quick and effective osteoconductive response from Bonelike® reduced the time required to reconstruct the bone defected area of patients.

13.2.5.2 Orthopaedics

In orthopaedics applications [60], Bonelike® granules ranging from 500 to 1000 μm were implanted in the cortical bone of 11 patients undergoing osteotomy in the lateral aspect of the tibia to assess the behaviour. The patients' mean age was 59 years (ranging 48–70 years), eight women and three men, all suffering form medical compartment ostoarthritis of the knee. At surgery, a 1 × 1 × 1 cm cortical defect was created 3 cm distal to the entry point of the screws, in line with the long axis of tibia. An implanted Bonelike® graft sample was retrieved for histological and SEM analyses during removal of the metallic prosthesis after implantation times of 6, 9 and 12 months.

Based on quantitative histomorphometric studies from approximately 43 assessed slices for the three different implantation periods, the bone implant contact average value varied from 67 ± 10 to 84 ± 5 % through the healing period analyzed. The high levels of the percentage bone-to-graft contact demonstrated the

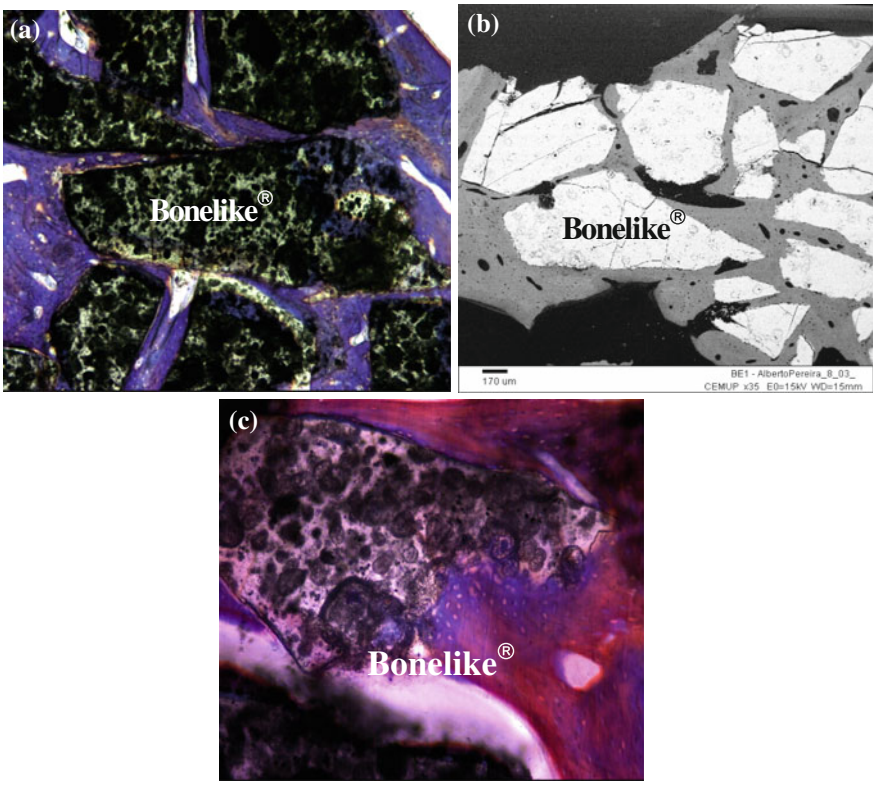

Fig. 13.14 Histological and SEM images showing implantation of Bonelike®granules and new bone formation after 9 months (**a**, **b**). Surface resorption of Bonelike®granules observed by histology after 6 months implantation (**c**), which indicates that this novel bone graft shows controlled biodegradation in vivo

osteoconductive capacity of Bonelike® in humans and extensive mature bone formation around the implanted granules as shown in Fig. 13.14a–c. Bonelike® granules bioresorption was observed which resulted from the presence of β- and α-TCP phases in its structure, as shown in Fig. 13.14c. This phenomenon may allow the full regeneration of bone defect area at longer implantations period with complete bioresorption of Bonelike®.

13.3 Summary

Bonelike® represents a new concept for synthetic bone grafts manufacturing and has the ability of mimicking the inorganic chemical composition and structure of natural bone tissues thus enabling enhanced osteointegration. With the increasing

demand of synthetic grafts from the market due to their advantages compared to autografts and allografts, the application of Bonelike® in regenerative surgery is therefore expected to increase for the benefit of the vast number of patients.

References

1. Hughes, F. J., Turner, W., Belibasakis, G., & Martuscelli, G. (2006). Effects of growth factors and cytokines on osteoblastic differentiation. *Periodontology, 2000*(41), 48.
2. Sommerfeldt, D. W., & Rubin, C. T. (2001). Biology of bone and how it orchestrates the form and function of the skeleton. *European Spine Journal, 10*, S86–S95.
3. Weiner, S., & Traub, W. (1992). Bone structure: from angstroms to microns. *FASEB Journal, 6*, 879.
4. Parfitt, A. M. (1990). Pharmacological manipulation of bone remodelling and calcium homeostasis. In. A. J. Kanis (Ed.), *Calcium metabolism* (pp. 1–27). Basel: Karger.
5. Hollinger, J., & Wong, M. E. K. (1996). The integrated process of hard tissue regeneration with special emphasis on fracture healing. *Oral Surgery, Oral Medicine, Oral Pathology, Oral Radiology and Endodontics, 82*, 594.
6. Kalfas, I. H. (2001). Principles of bone healing. *Neurosurgical Focus, 10*, 1.
7. Doron, I. I., & Amy, L. L. (2003). Bone graft substitutes. *Operative Techniques in Plastic and Reconstructive Surgery, 9*(4), 151.
8. Giannoudis, P. V., Dinopoulos, H., & Tsiridis, E. (2005). Bone substitutes: An update. *Injury: International Journal of the Care of the Injured, 365*, 520.
9. Mary, E. A. R., & Raymond, A. Y. (1998). Bone replacement grafts—The bone substitutes. *Dental Clinics of North America, 42*(3), 491.
10. Cato, T. (2003). In C. T. Laurencin (Ed.), *Laurencin and Yusuf Khan: Bone grafts and bone graft substitutes: A brief history* (p. 3). USA: ASTM International.
11. Wright, S. (1999). Commentary the bone-graft market in Europe. In Datamonitor plc. (Ed.), *Emerging technologies in orthopedics I: Bone graft substitutes. Bone growth stimulators and bone growth factors* (p. 591).
12. Boden, S. D. (2003). Osteoinduction bone graft substitutes: Burden of proof. *American Academy of Orthopaedic Surgeons Bulletin, 51*(1), 42.
13. Anon. (2003, April 9). Synthetic bone graft to be tested in revision hip surgery. *News Letter.* London, UK: ApaTech Limited.
14. Attawia, M., Kadiyala, S., Fitzgerald, K., Kraus, K., & Bruder, S. P. (2003). In C. T. Laurencin (Ed.), *Cell-based approaches for one graft substitutes* (p. 126). USA: ASTM International.
15. Santos, J. D., Hastings, G. W., & Knowles, J. C. (1999). *Sintered hydroxyapatite compositions and method for the preparation thereof*. European Patent WO 0068164.
16. Lopes, M. A., Santos, J. D., Monteiro, F. J., & Knowles, J. C. (1998). Glass reinforced hydroxyapatite: a comprehensive study of the effect of glass composition on the crystallography of the composite. *Journal of Biomedical Materials Research, 39*, 244.
17. Lopes, M. A., Monteiro, F. J., & Santos, J. D. (1999). Glass-reinforced hydroxyapatite composites: Fracture toughness and hardness dependence on microstructural characteristics. *Biomaterials, 20*, 2085.
18. Lopes, M. A., Silva, R. F., Monteiro, F. J., & Santos, J. D. (2000). Microstructural dependence of Young's and shear moduli of P_2O_5 glass reinforced hydroxyapatite for biomedical applications. *Biomaterials, 21*, 749.
19. Santos, J. D., Reis, R. L., Monteiro, F. J., Knowles, J. C., & Hastings, G. W. (1995). Liquid phase sintering of hydroxyapatite by phosphate and silicate glass additions structure and properties of the composites. *Journal of Materials Science: Materials in Medicine, 6*, 348.

20. Santos, J. D., Silva, P. L., Knowles, J. C., Talal, S., & Monteiro, F. J. (1996). Reinforcement of hydroxyapatite by adding P_2O_5–CaO glasses with Na_2O, K_2O and MgO. *Journal of Materials Science: Materials in Medicine, 7*, 187.
21. Davies, J. E. (1988). The importance and measurement of surface charge species in cell behaviour at the biomaterial interface. In B. D. Ratner (Ed.), *Surface characterization of biomaterials* (pp. 219–234). New York: Elsevier.
22. Ratner, B. D. (1987). Biomaterial surfaces. *Journal of Biomedical Materials Research, 21*, 59.
23. Manson, S. R., Harker, L. A., Ratner, B. D., & Hoffman, A. S. (1980). In vivo evaluation of artificial surfaces with a non human primate model of arterial thrombosis. *Journal of Laboratory and Clinical Medicine, 95*, 289.
24. Grinnell, F., Milamand, M., & Srere, P. A. (1972). Studies on cell adhesion. *Archives of Biochemistry and Biophysics, 153*, 193.
25. Chang, S. K., Hum, O. S., Moscarello, M. A., Neumann, A. W., Zing, W., Leutheusser, M. J., & Ruegsegger, B. (1997). Platelet adhesion to solid surfaces: The effect of plasma proteins and substrate wettability. *Medical Progress Through Technology, 5*, 57.
26. Lopes, M. A., Knowles, J. C., & Santos, J. D. (2000). Structural insights of glass reinforced hydroxyapatite composites by Rietveld refinement. *Biomaterials, 21*, 1905.
27. Rehman, I., & Bonfield, W. (1995). 'Structural characterisation of natural and synthetic bioceramics by photo acoustic-FTIR spectroscopy'. In J. Wilson, L. L. Hench, & D. Greenspan (Eds.), *bioceramics* (Vol. 8, pp. 163–168). Oxford: Butterworth-Heinmann Ltd.
28. Okazaki, M., & Sato, M. (1990). Computer graphics of hydroxyapatite and β-tricalcium phosphate. *Biomaterials, 11*, 573.
29. Bigi, A., Falini, G., Foresti, E., Gazzano, M., Ripamonti, A., & Roveri, N. (1996). Rietveld structure refinements of calcium hydroxyapatite containing magnesium. *Acta Crystallographica Section B: Structural Science, B52*, B87.
30. Kotani, S., Fijita, Y., Kitsugi, T., Nakamura, T., Yamamuro, T., Ohtsuki, C., & Kokubo, T. (1991). Bone bonding mechanism of β-tricalcium phosphate. *Journal of Biomedical Materials Research, 25*, 1303.
31. Lopes, M. A., Monteiro, F. J., Santos, J. D., Serro, A. P., & Saramago, B. (1999). Hydrophobicity, surface tension, and zeta potential measurements of glass-reinforced hydroxyapatite composites. *Journal of Biomedical Materials Research, 45*, 370.
32. Santos, J. D., Knowles, J. C., Reis, R. L., Monteiro, F. J., & Hastings, G. W. (1994). Microstructural characterization of glass reinforced hydroxyapatite composites. *Biomaterials, 15*(1), 5.
33. Yamamuro, Y., Hench, L. L., & Wilson, J. (1990). *CRC Handbook of bioactive ceramics*. Boca Raton: CRC Press.
34. Lopes, M. A., Monteiro, F. J., & Santos, J. D. (1999). Glass reinforced hydroxyapatite composites: Secondary phase proportions and densification effects assessing biocompability. *Journal of Biomedical Materials Research (Biomaterial Applications), 48*, 734.
35. Rice, R. W. (1977). Microstructure dependence of mechanical behaviour. In R. K. MacCrone (Ed.), *Treatise on materials science and technology* (Vol. 11, pp. 200–382). New York: Academic Press.
36. Hauberm, R. A., & Anderson, R. M. (1991). Engineering properties of glass–matrix composites. In *Ceramics and glasses, engineered materials handbook* (pp. 858–869). USA: ASM Publication.
37. Kirkpatrick, C. J. (1992). A critical view of current and proposed methodologies for biocompatibility testing: cytotoxic in vitro. *Regulatory Affairs, 4*, 13.
38. Hanson, S., Lalor, P. A., Niemi, S. M., Ratner, B. D., et al. (1996). Testing biomaterials. In: B. D. Ratner & A. S. Hoffman (Eds.), *Biomaterials science. An introduction to materials in medicine* (p. 215). Basel: Karger.
39. Lopes, M. A., Knowles, J. C., Kuru, L., Santos, J. D., Monteiro, F. J., & Olsen, I. (1998). Flow cytometry for assessing biocompatibily. *Journal of Biomedical Materials Research, 41*, 649.

40. Lopes, M. A., Knowles, J. C., Santos, J. D., Monteiro, F. J., & Olsen, I. (2000). Direct and indirect effects of P_2O_5-glass reinforced hydroxiapatite on the growth and function of osteoblast-like cells. *Biomaterials, 21*, 1165.
41. Costa, M. A., Gutierres, M., Almeida, R., Lopes, M. A., Santos, J. D., & Fernandes, M. H. (2004). In vitro mineralisation of human bone marrow cells cultured on Bonelike®. *Key Engineering Materials, 254–256*, 821.
42. Frank, O., Heim, M., Jakob, M., Barbero, A., Schafer, D., Bendik, I., et al. (2000). Real-time quantitative RT-PCR analysis of human bone marrow stromal cells during osteogenic differentiation in vitro. *Journal of Cellular Biochemistry, 85*, 737.
43. Marie, P. J., de Vernejoul, M. A., & Lomri, A. (1992). Stimulation of bone formation in osteoporosis patients treated with fluoride associated with increased DNA synthesis by osteoblastic cells in vitro. *Journal of Bone and Mineral Research, 7*, 103.
44. Council of Europe. (1986). *Convention for the protection of vertebrata animals used for experimental and other scientific purposes (ET 123)*. Council of Europe: Strasbourg.
45. European Commission. (1986). Directive for the protection of vertebrate animals used for experimental and other scientific purposes (86/609/EEC). *Official Journal of the European Commission, L 358*, 1.
46. Lobato, J. V., Sooraj Hussain, N., Botelho, C. M., Rodrigues, J. M., Luis, A. L., Mauricio, A. C., et al. (2005). Assessment of the potential of Bonelike® graft for bone regeneration by using an animal model. *Key Engineering Materials, 284–286*, 877.
47. Lobato, J. V., Sooraj Hussain, N., Botelho, C. M., Mauricio, A. C., Afonso, A., Ali, N., et al. (2006). Assessment of Bonelike® graft with a resorbable matrix using an animal model. *Thin Solid Films, 515*, 642.
48. User, H. M., & Nadler, R. B. (2003). Applications of FloSeal in nephron-sparing surgery. *Urology, 62*(2), 342.
49. Weaver, F. A., Hood, D. B., Zatina, M., Messina, L., & Badduke, B. (2002). Gelatin-thrombin-based hemostatic sealant for intraoperative bleeding in vascular surgery. *Annals of Vascular Surgery, 16*, 286.
50. Dodane, V., & Vilivalam, V. (1998). Pharmaceutical applications of chitosan. *Pharmaceutical Science & Technology Today, 1*, 246.
51. Ettinger, B., Genant, H. K., & Cann, C. E. (1985). Long-term estrogen replacement therapy prevents bone loss and fractures. *Annals of Internal Medicine, 102*, 319.
52. Bryant, H., Glasebrook, A. L., Yang, N. N., & Sato, M. (1999). An estrogen receptor basis for raloxifene action in bone. *Journal of Steroid Biochemistry and Molecular Biology, 69*, 37.
53. Delmas, P. D., Bjarnason, N. H., Mitlak, B. H., Ravoux, A. C., Shah, A. S., Huster, W. J., et al. (1997). Effects of raloxifene on bone mineral density, serum cholesterol concentrations, and uterine endometrium in postmenopausal women. *New England Journal of Medicine, 337*, 1641.
54. Reddi, A. H., & Cunningham, N. S. (1993). Initiation and promotion of bone differentiation by bone morphogenic proteins. *Journal of Bone and Mineral Research, 8*(2), S499.
55. Lopes, M. A., Santos, J. D., Monteiro, F. J., Osaka, A., & Ohtsuki, C. (2001). Push-out testing and histological evaluation of glass reinforced hydroxyapatite composites implanted in the tibia of rabbits. *Journal of Biomedical Materials Research, 54*, 463.
56. Duarte, F., Santos, J. D., & Afonso, A. (2004). Medical applications of Bonelike in maxillofacial surgery. *Materials Science Forum, 455–456*, 370.
57. Costa, M. A., Gutierres, M., Almeida, L., Lopes, M. A., Santos, J. D., & Fernandes, M. H. (2004). In vitro mineralisation of human bonemarrow cells cultured on bonelike®. *Key Engineering Materials, 254–256*, 821.
58. Sousa, R. C., Lobato, J. V., Sooraj Hussain, N., Lopes, M. A., Mauricio, A. C., & Santos, J. D. (2006). Bone regeneration in maxillofacial surgery using novel Bonelike® synthetic bone graft: Radiological and histological analyses. *British Journal of Oral and Maxillofacial Surgery* (submitted).

59. Gutierres, M., Sooraj Hussain, N., Afonso, A., Almeida, L., Cabral, A. T., Lopes, M. A., et al. (2005). Biological behaviour of bonelike® graft Implanted in the tibia of humans. *Key Engineering Materials, 284–286*, 1041.
60. Gutierres, M., Sooraj Hussain, N., Lopes, M. A., Afonso, A., Cabral, A. T., Almeida, L., et al. (2006). Histological and scanning electron microscopy analyses of bone/implant interface using the novel Bonelike® synthetic bone graft. *Journal of Orthopaedic Research, 24*, 953.

Chapter 14
Machining Cancellous Bone Prior to Prosthetic Implantation

M.J. Jackson, M. Whitfield, G.M. Robinson, R. Handy and W. Ahmed

Abstract The chapter describes the machining of compact and cancellous bone using a micromachining tool with a specially adapted spindle and the associated mechanics of chip formation. The chapter focuses on the design of the high-speed spindle, the structure of cancellous and compact bone, the theory of machining, chip curl modeling, the development of a biomachining center, and associated experimental results. The chapter concludes by stating that high-speed machining of compact and cancellous bone to prevent necrosis of the bone is possible.

14.1 Introduction

The design of a high-speed spindle for machining bone is no easy task. The major components of a high-speed air turbine spindle are bearings, rotor, stator, and spindle shaft. To drive a high-speed spindle a motor, or compressor, is integrated with the spindle shaft. Bearings provide stability at high speeds to prevent chatter and poor surface finish and to permit accurate cutting tool paths. The speed of the spindle depends on the rotational speed of the rotor. The spindle shaft, rotor, and bearings must be held in a housing. High-pressure compressed air enters into the housing of the spindle from the compressor through a pneumatic connector. The compressed air enters the housing through the shaft and rotates the rotor of the spindle. The microcutting tool, which is attached to the center of the rotor, rotates

M.J. Jackson (✉)
Kansas State University, Salina, Kansas, USA
e-mail: jacksonmj04@yahoo.com

M. Whitfield · G.M. Robinson
Micromachinists Group, Cambridge, MA, USA

R. Handy
The University of Utah, Salt Lake City, UT, USA

W. Ahmed
School of Medicine, University of Central Lancashire, Preston, UK

W. Ahmed and M.J. Jackson (eds.), *Surgical Tools and Medical Devices*,
DOI 10.1007/978-3-319-33489-9_14

with the speed of the rotor and cuts the workpiece more quickly than conventional spindles. The rotor is supported by an air bearing, which provides stability to the rotor and also transmits the necessary torque.

In high-speed machining with high-speed spindles (HSS), the pressure variation on the rotor surface is of vital importance. The pressure coefficient is defined as the difference between the highest and lowest pressure on the rotor surface, normalized by the imposed inlet pressure. Pressure coefficient determines pressure variation exerted by high-speed compressed air on the rotor and for the optimum design of the rotor, the pressure coefficient should be as low as possible as the large values of pressure coefficient indicate high-pressure variations, which could cause the severe imbalance of the load and deformation of the rotor and this generates failure of the rotor. Various designs of rotor for different rotational speeds are proposed and fluid analysis of rotors has been carried out with a computational fluid dynamics (CFD) software package called FLUENT. Pressure coefficients of rotors were calculated and compared for different designs of rotor to determine the optimum design of the rotor.

14.2 Analysis of Fluid Flow

14.2.1 Assumptions

The following assumptions were considered for the numerical solution of HSS using CFD:

- HSS rotor rotational speed depends on the pressure of the compressed air entering from the compressor. The numerical simulation was carried out by a considering decoupled system, i.e., for a given inlet pressure (60 psi), the rotating speed of the rotor was assumed as a constant value such as half-million rpm, i.e., the current study deals only with the fluid problem, not the fluid/structure problem.
- Steady-state simulation was assumed for all numerical simulations.

14.2.2 CFD Geometry Model

The bearing component of the HSS was omitted in the CFD model. The outer diameter of the rotor is 0.3 in (7.6 mm), inner diameter of the rotor is 0.092 in (2.34 mm), the height along the z-direction is 0.1445 in (3.6 mm) and the angle between the rotor blades is 90°. A cylindrical housing with a diameter of 0.31 in (7.8 mm) was modeled around the rotor with a height of 0.1735 in (4.4 mm) so that the rotor could rotate freely inside the housing. The spindle is driven by compressed

air. Three inlets, with a diameter of 0.055 in (1.4 mm), that make an angle of 120° with each other, were created around the housing. The inlets were created at an angle of 45°. An outlet for the air was created at the center of the housing.

14.2.3 Fluid Model

Air was considered as an ideal gas. The flow in HSS is turbulent. The turbulence is described by k-ε turbulent model, in which k is the turbulence kinetic energy and ε is the turbulence eddy dissipation. The total energy heat transfer model considered as kinetic energy effects are important in the model.

Applied Boundary Conditions

The following boundary conditions were applied to the model:

- Static pressure of 60 psi at the inlets;
- Static pressure of 0 (zero) at the outlet;
- A no-slip (moving) wall boundary condition on the rotor. A constant angular speed of the rotor was specified;
- A no-slip (stationary) wall boundary condition on the housing and inlet surfaces.

Governing Equations

The governing equations of three-dimensional fluid flow were represented as

Continuity Equation:

$$\frac{\partial(\rho U_i)}{\partial X_i} = 0 \tag{14.1}$$

Momentum Equation:

$$\frac{\partial(\rho U_i U_j)}{\partial x_j} = -\frac{\partial P}{\partial x_i} + \frac{\partial}{\partial x_j}\left(\mu_{eff}\frac{\partial U_i}{\partial x_j} + \mu_{eff}\frac{\partial U_j}{\partial x_i}\right) \tag{14.2}$$

where repeated indices imply summation from 1 to 3, ρ is density, U_i are the cartesian velocity components, P is pressure, X_i are the coordinate axes, and μ_{eff} is the effective viscosity, which is defined as

$$\mu_{eff} = \mu + \mu_t;\ \mu_t = C_\mu \rho \frac{k^2}{\varepsilon} \tag{14.3}$$

where μ_t is the eddy viscosity, C_μ is a constant and is equal to 0.09, k is the turbulence kinetic energy, and ε is the turbulence eddy dissipation. The turbulence model is given by

$$\frac{\partial \rho k}{\partial t} + \frac{\partial}{\partial x_j}(\rho U_j k) - \frac{\partial}{\partial x_j}\left(\frac{\mu_{eff}}{\sigma_k}\frac{\partial k}{\partial x_j}\right) = \mu_t \frac{\partial U_i}{\partial x_j}\left(\frac{\partial U_i}{\partial x_j} + \frac{\partial U_j}{\partial x_i}\right) - \frac{2}{3}\frac{\partial U_j}{\partial x_j}\left(\mu_t \frac{\partial U_j}{\partial x_j} + \rho k\right) - \rho\varepsilon \tag{14.4}$$

And,

$$\begin{aligned}&\frac{\partial \rho \varepsilon}{\partial t} + \frac{\partial}{\partial x_j}(\rho U_j \varepsilon) - \frac{\partial}{\partial x_j}\left(\frac{\mu_{eff}}{\sigma_\varepsilon}\frac{\partial \varepsilon}{\partial x_j}\right)\\ &= \frac{\varepsilon}{k}\left(C_{\varepsilon 1}\left(\mu_t \frac{\partial U_i}{\partial x_j}\left(\frac{\partial U_i}{\partial x_j} + \frac{\partial U_j}{\partial x_i}\right) - \frac{2}{3}\frac{\partial U_j}{\partial x_j}\left(\mu_t \frac{\partial U_j}{\partial x_j} + \rho k\right)\right) - C_{\varepsilon 2}\rho\varepsilon\right)\end{aligned} \tag{14.5}$$

where σ_k and σ_ε are k-ε turbulence model constants and are equal to 1.0 and 1.3, respectively, and $C_{\varepsilon 1}$ and $C_{\varepsilon 2}$ are equal to 1.45 and 1.92, respectively

Energy Equation:

$$\frac{\partial(\rho U_j h_{tot})}{\partial X_j} = \frac{\partial(\lambda \frac{\partial T}{\partial X_j})}{\partial X_j} + S_E \tag{14.6}$$

where h_{tot} is defined as the specific total enthalpy, which for the general case of variable properties is given in terms of the specific static enthalpy, h, by

$$h_{tot} = h + \frac{1}{2}U^2;\ h = h(p, T) \tag{14.7}$$

And S_E is the source term, which represents the work done by the viscous and pressure forces. The equation of state for an ideal gas is given as

$$p = \rho RT \tag{14.8}$$

where T is the temperature of the fluid and R is the gas constant.

Pressure Coefficient

The parameter "pressure coefficient" was defined to determine the pressure variation on the rotor,

$$\text{Pressure coefficient} = \frac{P_{max} - P_{min}}{P_{inlet}} \tag{14.9}$$

where P_{max} = Maximum pressure exerted by air on the rotor, P_{min} = Minimum pressure exerted by air on the rotor, and P_{inlet} = Air pressure at the inlet. Maximum pressure and minimum pressure exerted by air can be obtained by FLUENT. Inlet pressure was used to nondimensionalize the value of the pressure coefficient.

14.3 Experimental Results and Discussion

Flow topology and pressure variation of rotor geometries such as rotor with 90° blade angle, rotor with inlets, inclined at 45° to the z-axis of the rotor, and two-stage rotor are described and pressure coefficient values for all geometries are calculated. The optimum design of the high-speed spindle is identified based on the magnitude of the pressure coefficient.

14.3.1 Numerical Results

Numerical simulations of the spindle geometries were carried out using FLUENT. Air was the ideal gas with an inlet pressure of 60 psi and an outlet pressure of zero, and the rotor was considered to be at no-slip conditions at the wall with specific rotational speeds such as half-million rpm, one million rpm, etc. The total number of control volumes for the numerical grid was approximately between 437,000 and 532,000 based on the geometry of the rotor, and the number of iterations for numerical simulations was 200. The maximum continuity loops are advantageous for achieving convergence especially for high-speed flows and the value of maximum continuity loops was specified as 2 for numerical simulations of all geometries under consideration. The governing equations such as continuity equation, momentum equation, energy equation, and equation of state were solved by FLUENT to provide the pressure distribution on the rotor. The pressure values were obtained using FLUENT and the pressure coefficient values were calculated using Eq. (14.9).

Initially, numerical simulations of rotor geometries such as the basic geometry of the rotor, rotor with fillets, rotor with 70° blade angle, and the rotor with 90° blade angle were carried out for different rotational speeds of the rotor such as half-million rpm, one million rpm, two million rpm, and five million rpm. The number of control volumes considered for the numerical simulation of basic geometry of the rotor was 437,273; for the numerical simulation of rotor with filets it was 439,092; for the numerical simulation of rotor with 70° blade angle it was 488,786 and for the numerical simulation of rotor with 90° blade angle it was 520,324. The residual target for the convergence criterion was specified as 1e−6 and the maximum number of iterations considered for convergence control was 200 for the described geometries. The values of the nondimensional pressure coefficients obtained form the numerical simulations are shown in Table 14.1.

From Table 14.1 it is observed that for a particular geometry as the rotating speed of the rotor increases, the pressure coefficient value increases because of the variation of pressure values on the surface of the rotor. Figure 14.1 shows the variation of pressure coefficient for the specified geometries with the rotational speeds of the rotor. From Table 14.1 it can be said that the pressure coefficient values of rotor with 90° blade angle are less than those of the other geometries of the rotor for the rotational speeds of half-million, one million, and two million rpm

Table 14.1 Pressure coefficient values for rotor geometries such as the basic geometry of the rotor, a rotor with fillets, a rotor with 70° blade angle, and a rotor with 90° blade angle for different rotational speeds

Rotational speed (rpm)	Basic geometry of rotor	Rotor with fillets	Rotor with 70° blade angle	Rotor with 90° blade angle
Half-million	0.11	0.10	0.09	0.07
One million	0.18	0.20	0.16	0.11
Two million	0.45	0.46	0.40	0.42
Five million	1.28	1.18	1.15	1.19

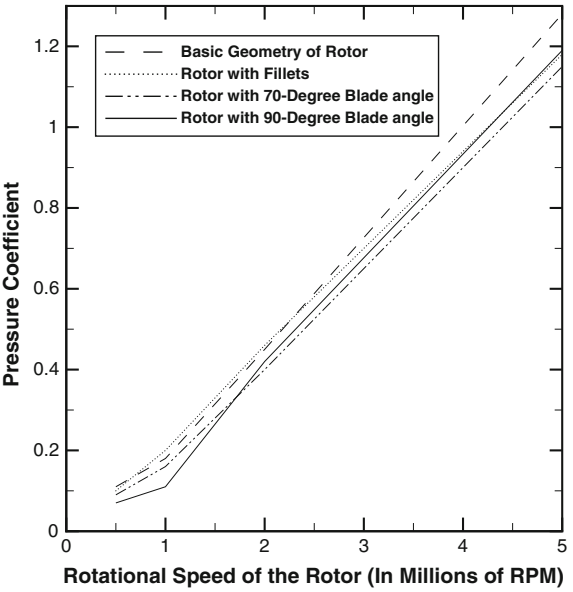

Fig. 14.1 Variation of pressure coefficient with rotating speed of the rotor for different geometries of the rotor such as basic geometry of the rotor, rotor with fillets, rotor with 70° blade angle and rotor with 90° blade angle. Reproduced with permission. Copyright retained by Inderscience Publishers

of the rotor which is in the typical range of micromachining operations. For two million and five million rpm rotational speed of rotor, the rotor with a 70° blade angle possessed pressure coefficient values that were less when compared to other geometries of the rotor. The geometry of the rotor with 90° blade angle was considered to be the optimum design compared to other geometries of the rotor for the rotational speeds that are in the typical range of micromachining conditions. Modifications in the spindle geometry were conducted by changing the number of blades of the rotor, changing the angle of the inlets, and by changing the number of inlets and outlets for the fluid. Numerical simulations of the rotor with 12 blades, rotor with 3 inlets inclined at an angle of 30°, rotor with three inlets inclined at an angle of 45°, and rotor with three inlets, and three outlets were carried out. The number of control volumes associated with the numerical simulations of the rotor with 12 blades was 467,311; with that of rotor with three inlets inclined at an angle of 30° it was 513,116; with that of rotor with three inlets inclined at an angle of 45°

it was 532,447, and with that of rotor with three inlets and three outlets it was 509,288. The residual target for satisfying the convergence criterion was specified as 1e−6 and the maximum number of iterations specified for convergence control was 200. The pressure coefficient values obtained for these geometries for different rotational speeds of the rotor are shown in Table 14.2.

Figure 14.2 shows the variation of pressure coefficient values for rotor with 12 blades, rotor with inlets, inclined at an angle of 30°, rotor with inlets, inclined at an angle of 45°, and rotor with three inlets and three outlets for different rotating speeds of the rotor. From Fig. 14.2 it could be said that as the rotating speed of the rotor increases, pressure coefficient increases and the pressure coefficient values are almost the same for all geometries with the increase in rotational speed similar to the previous case.

From Table 14.2 it can be concluded that for both half-million rpm and one million rpm rotating speed of rotor, rotor with three inlets inclined at an angle of 45°

Table 14.2 Pressure coefficient values for rotor geometries of a rotor with 12 blades, a rotor with three inlets inclined at an angle of 30°, a rotor with three inlets inclined at an angle of 45°, and a rotor with three inlets and three outlets

Rotational speed (rpm)	Rotor with 12 blades	Rotor with three inclined inlets at 30°	Rotor with three inclined inlets at 45°	Rotor with three inlets and three outlets
Half-million	0.09	0.10	0.08	0.36
One million	0.15	0.15	0.10	0.48
Two million	0.39	0.41	0.40	0.44
Five million	1.07	1.14	1.12	1.15

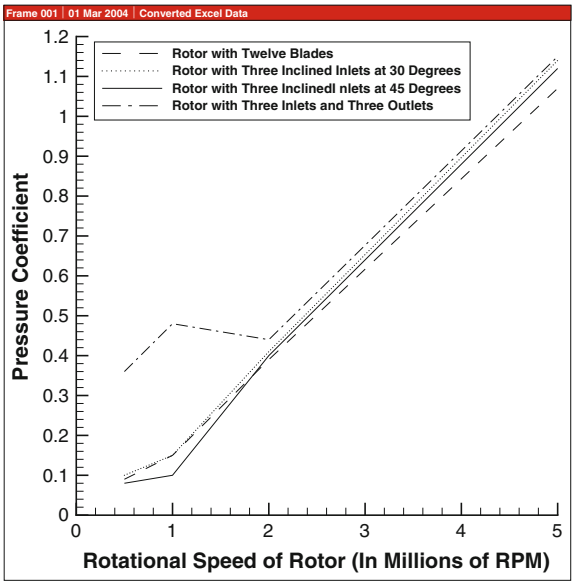

Fig. 14.2 Variation of pressure coefficient with rotating speed of the rotor for different geometries of the rotor such as rotor with twelve blades, rotor with three inlets inclined at an angle of 30°, rotor with three inlets inclined at an angle of 45°, and rotor with three inlets and three outlets. Reproduced with permission. Copyright retained by Inderscience Publishers

is the optimum design compared to the other geometries of the rotor considered after modifying the rotor geometry and for two million and five million rpm rotational speed of the rotor, the rotor with 12 blades is the optimum design of rotor for HSS compared to the other geometries of the rotor. Rotor geometries considered for numerical simulations of HSS were the two-stage rotor and its modified geometry. The values of pressure coefficients obtained for different rotational speeds of these rotors are given in Table 14.3. The number of control volumes associated with the numerical simulations of two-stage rotor and its modified geometry were 522,046 and 521,614, respectively. The maximum number of iterations considered for convergence control was 200 and the residual target for convergence criteria was specified as 1e−6 for the geometries. From the table, it could be observed that the pressure coefficient values obtained for the numerical simulations of two-stage rotor and its modified geometry are very high compared to other geometries of rotor for half-million, one million, and two million rpm rotational speeds. The pressure coefficient was found to be almost the same with other geometries of the rotor for five million rpm. Figure 14.3 shows the variation of pressure coefficient with the rotational speed of rotor for two-stage rotor and its modified geometry.

Table 14.3 Pressure coefficient values for rotor geometries two-stage rotor and its modified geometry

Geometry	Half-million	One million	Two million	Five million
Two-stage rotor	1.17	1.19	1.20	1.46
Modified geometry of two-stage rotor	1.21	1.26	1.35	1.65

Reproduced with permission. Copyright retained by Inderscience Publishers

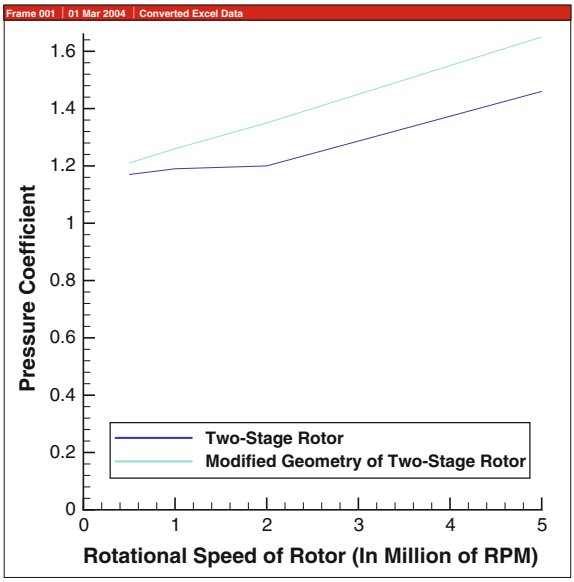

Fig. 14.3 Variation of pressure coefficient with rotational speed for two- stage rotor and its modified geometry. Reproduced with permission. Copyright retained by Inderscience Publishers

From all the geometries discussed above, it can be concluded that for half-million rpm rotational speed of the rotor, rotor with 90° blade angle is the optimum geometry for rotor and for one million rpm rotating speed of the rotor, rotor with three inlets inclined at an angle of 45° is the optimum design compared to other geometries of the rotor. For two million and five million rpm rotational speed of the rotor, rotor with 12 blades is the optimum design of rotor for high-speed spindle compared to the other geometries of the rotor.

14.3.2 Flow Topology and Pressure Variations

Flow topology and pressure variation of rotor geometries such as rotors with 90° blade angle, rotors with three inlets inclined at an angle of 45°, and two-stage rotors are described.

14.3.2.1 Rotor with 90° Blade Angle

Flow topology and pressure variation of this geometry will be explained as the pressure coefficient of this geometry was found to be lower than for the other geometries of rotors. The rotational speed of the rotor was specified as one million (1,000,000) rpm.

Flow topology: Fig. 14.4 shows the flow pattern in rotor with 90° blade angle. Air enters into the housing from three inlets with a pressure of 60 psi and exists from outlet at a pressure of zero. The three inlets are normal to the surface of the housing and the outlet is at the center of the housing. Air entering from the inlets impinges on the rotor surfaces and flows inside of housing. At the hollow part of the rotor, the fluid is swirled and at the outlet the velocity increases due to the sudden contraction of the surface area at the outlet.

Pressure Variation: Fig. 14.5 describes the pressure variation on the surfaces of the rotor. From the figure it can be observed that the regions of the rotor, where the fluid impinges directly are having maximum pressure due to the stagnation of the fluid compared to the other regions of the rotor. At the stagnation point, the total kinetic energy of the fluid is converted into pressure energy; so the maximum pressure occurs at the stagnation point of the fluid. The pressure coefficient on the rotor can be determined from the Eq. 14.9 by substituting the values of maximum and minimum pressure on the rotor as shown in Fig. 14.5 and inlet pressure (60 psi).

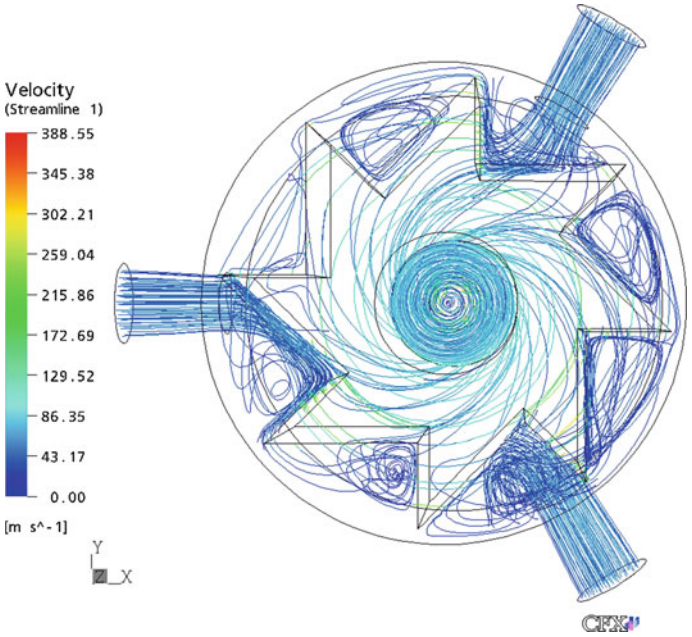

Fig. 14.4 Streamlines describing the flow pattern for rotor with 90° blade angle at one million rpm rotational speed of rotor. Reproduced with permission. Copyright retained by Inderscience Publishers

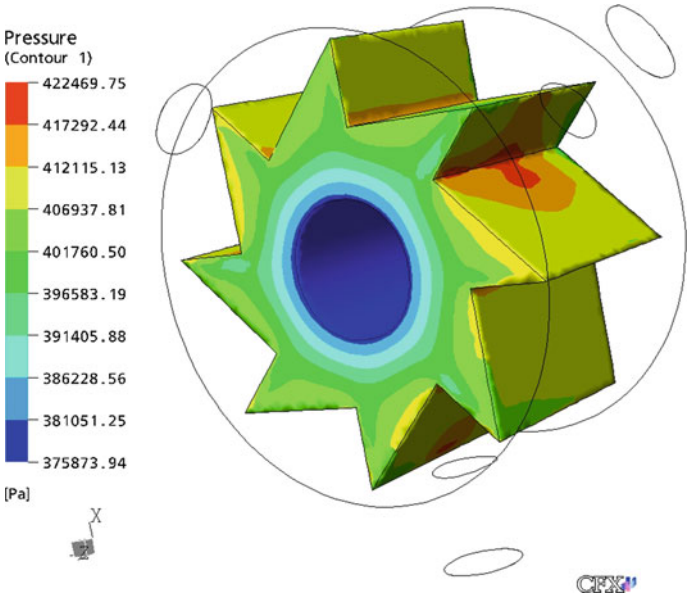

Fig. 14.5 Static pressure distribution on the rotor with 90° blade angle at one million rpm rotational speed of rotor. Reproduced with permission. Copyright retained by Inderscience Publishers

14.3.2.2 Rotor with Three Inlets Inclined at 45°

Flow topology and pressure variation on the rotor with three inlets, inclined at an angle of 45° with z-axis is described. The rotational speed of the rotor was specified as half-million (500,000) rpm.

Flow Pattern:

Flow pattern in the geometry can be seen in the Fig. 14.6. Air is entering into the housing from three inlets with a pressure of 60 psi and exists from outlet at a pressure of zero. Fluid entering from three inlets impinges on the rotor blades directly, unlike the previous case (Fig. 14.4), where flow from the inlets is not impinging directly on the rotor blades, but impinging in between the rotor blades. Figure 14.6 clearly shows the impingement of the fluid on the rotor blades. At the hollow part of the rotor, the fluid is swirled and at the outlet the velocity increases due to the sudden contraction of the surface area at the outlet. This forms a vortex flow at the outlet.

Pressure Variation

Figure 14.7 shows the pressure variation of the rotor, along with housing, outlet, and three inlets on a plane parallel to the X–Y plane, at a distance of 0.08675 in from the center, in the z-direction. From the figure it could be seen that the regions of the rotor where the fluid flow directly impinges are having maximum pressure due to stagnation of the fluid when compared to other regions. At the outlet, which

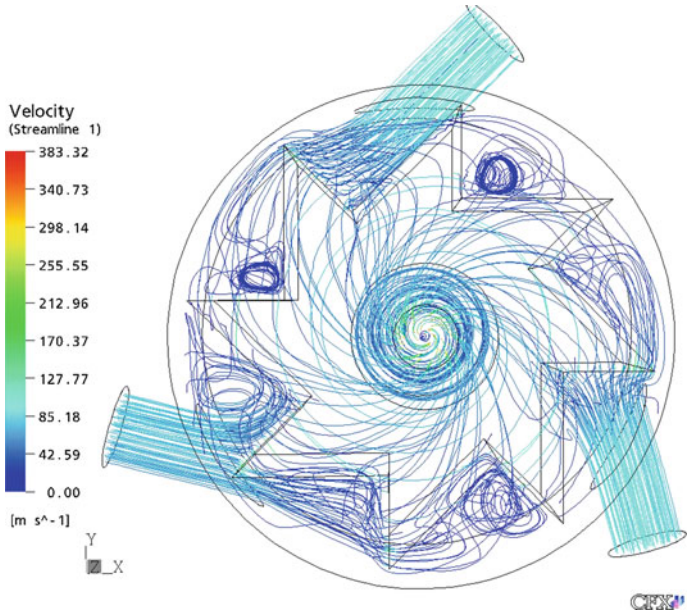

Fig. 14.6 Stream lines describing the flow pattern for rotor with three inclined inlets at an angle of 45° for half-million rpm rotational speed. Reproduced with permission. Copyright retained by Inderscience Publishers

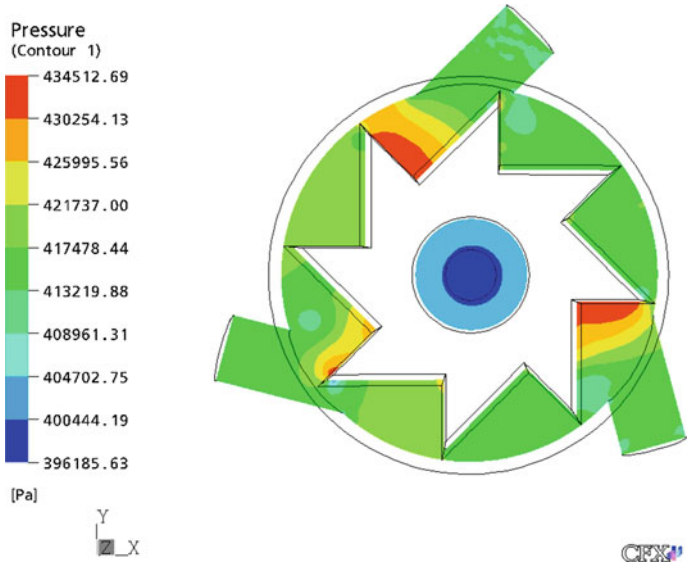

Fig. 14.7 Static pressure variation on the spindle parallel to the X–Y plane for half-million rpm rotational speed. Reproduced with permission. Copyright retained by Inderscience Publishers

is at the center of the housing pressure is found to be minimum. Figure 14.8 shows the three-dimensional view of the pressure variation on the rotor surfaces. The legend shows the pressure values at different surfaces of the rotor.

14.3.2.3 Two-Stage Rotor

Flow topology and pressure variation of two-stage rotor is described.

Flow Topology

The inlet static pressure was considered to be 60 psi and outlet static pressure as zero. Rotor's rotational speed was specified as two million rpm (2,000,000). Flow topology is illustrated in Fig. 14.9. Air entering from the upper part of the housing (through inlets 1 and 2) is diverted by rotor blades. One part slides through the upper part of the housing and exits to the atmosphere through outlets 3 and 4, and the other flows over the rotor blade into the housing and exits to the atmosphere through the outlets 1 and 2. Fluid entering from the lower part of the housing (through inlets 3 and 4) is bifurcated and most of the fluid builds a recirculation zone in the lower part of the housing and exits to the atmosphere through outlets 1 and 2, and the other part flows into the housing and exits to the atmosphere through outlets 3 and 4. From Figs. 14.4, 14.6 and 14.9, it could be observed that the maximum values of velocity of fluid are different, as the rotational speeds of the rotor are different. For rotors with high rotational speed, the maximum velocity is high compared to other rotors.

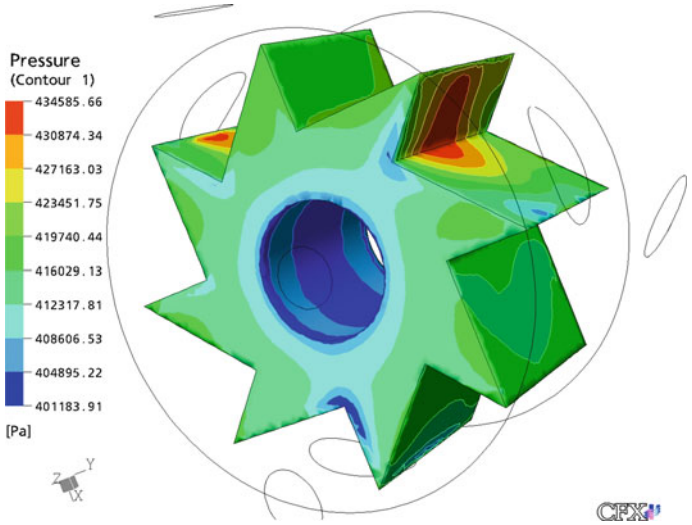

Fig. 14.8 Static pressure distribution on the rotor with three inclined inlets at an angle of 45° for half-million rpm rotational speed of rotor. Reproduced with permission. Copyright retained by Inderscience Publishers

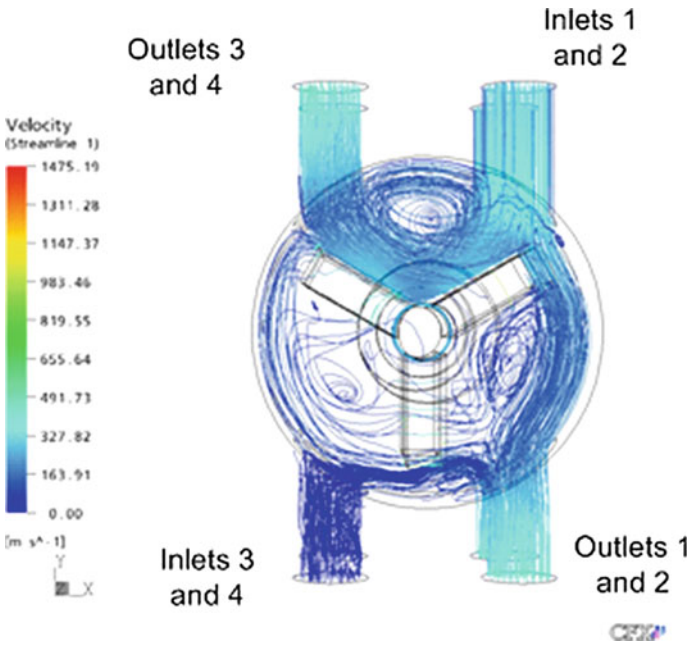

Fig. 14.9 Stream lines describing the flow pattern of two-stage rotor for two million rpm rotational speed of rotor. Reproduced with permission. Copyright retained by Inderscience Publishers

Pressure Variation

In Fig. 14.10, static pressure distribution of spindle geometry obtained from the numerical simulation of rotor is shown parallel to the X–Y plane at a distance of 3 mm from one side of the rotor (and at a distance of 11 mm from the other side of the rotor) in the z-direction. Air entering from the lower part of the housing impinges directly on the rotor blade surface and the total kinetic energy of the fluid gets converted into the pressure energy due to the stagnation of the fluid. Therefore, the maximum pressure is observed in the vicinity of the leading edge of the rotor blades, which bifurcate the inlet stream entering from the lower part of the housing. Figure 14.11 shows the static pressure distribution on the rotor. The pressure distribution was found to be symmetric on the blades of the rotor.

14.3.3 Mach Number

Mach number plays an important role for high-speed flows. Mach number on the surfaces of the rotor was found using FLUENT. For all the geometries of the rotor at the rotational speeds of half-million rpm, one million, and two million rpm, the

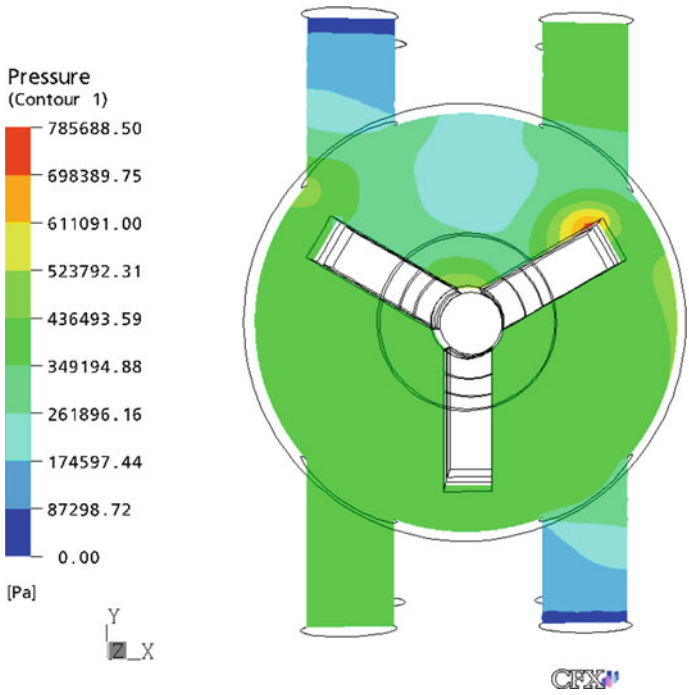

Fig. 14.10 Static pressure contours parallel to X–Y plane for two million rpm rotational speed of rotor. Reproduced with permission. Copyright retained by Inderscience Publishers

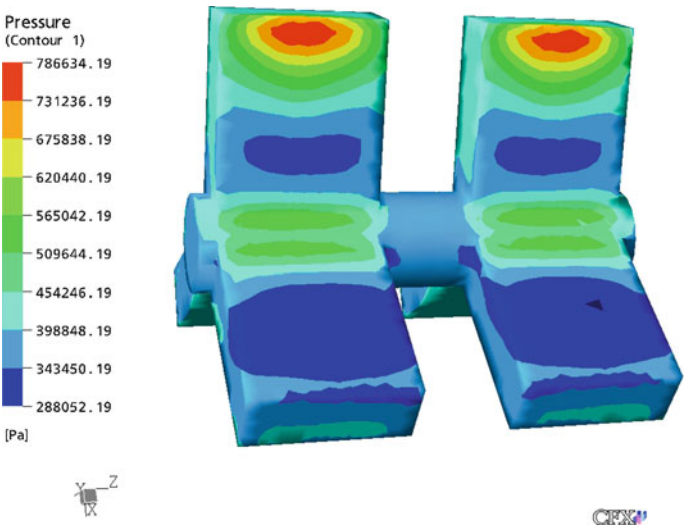

Fig. 14.11 Static pressure distribution on the two-stage rotor for two million rpm rotational speed of rotor. Reproduced with permission. Copyright retained by Inderscience Publishers

Mach number is within the subsonic regime, with only a few spots exceeding a Mach number of 1. For rotating speeds below two million, the subsonic assumption is well justified. However, for higher rpm, the transonic and supersonic flow regimes need to be taken into consideration.

Using Fluent: Mach number on the surfaces of the rotor was determined using CFD software. FLUENT needs the user to specify the flow as subsonic, or supersonic flow as input. Fluent does not require that specification before the calculation. The regime of the flow (subsonic, transonic, or supersonic) comes as part of the solution. The geometry of the rotor with three inlets, inclined at 45° with three inlets and a housing was created and the mesh was created. Volume elements considered for the mesh were approximately 600,000. The ideal gas, air, was considered as the fluid and the k-epsilon turbulence method was used for modeling turbulent flow. An inlet boundary condition, with a pressure of 60 psi was considered at three inlets. At the outlet, outlet boundary condition with a pressure of zero was considered. The rotor was defined as a moving wall with no-slip boundary condition, with an angular speed of two million rpm along its axis. For the remaining surfaces of the geometry, a default no-slip stationary wall boundary condition was applied.

For this compressible flow, a coupled implicit scheme was considered for the solution. The maximum number of iterations for the convergence control for the solver was specified as 4500 and the target residual for the convergence criterion was specified as 1e−6. The governing equations such as continuity, momentum, energy equations, and equation of state were solved by FLUENT and the Mach number at various zones was determined. Figure 14.12 shows the variation of Mach

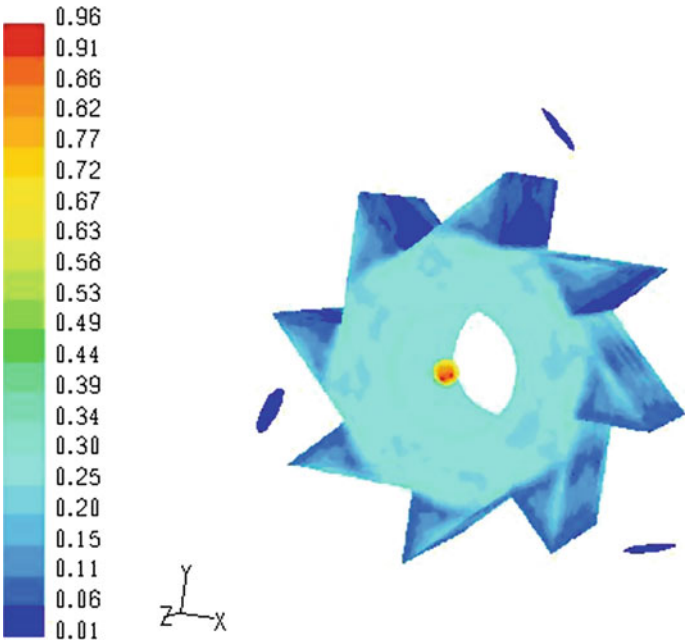

Fig. 14.12 Mach number contours for rotor with three inlets, inclined at an angle of 45° for two million rpm rotational speed of rotor. Reproduced with permission. Copyright retained by Inderscience Publishers

number at three inlets, outlet, and on the rotor surface for the rotational speed of the rotor of two million rpm. From the figure it can be observed that the maximum value of Mach number is 0.96 and the minimum value is 0.01. At the inlets and on the surfaces of the rotor, the Mach number is significantly less than 1 and at the outlet, the value is 0.96. From the results it can be said that only at the outlet, the flow is transonic, as the velocity of the flow is maximum at the outlet because of zero pressure condition. At the inlets and on the rotor surfaces, the flow is found to be subsonic.

An experimental high-speed spindle has been manufactured and is shown in Fig. 14.13. Further experiments are planned that will measure the velocity of the rotor shown in Fig. 14.13 at various inlet air pressures.

The experimental spindle has been modeled using FLUENT to determine the pressures and velocities. The schematic of the spindle is shown in Fig. 14.14.

The grid for this geometry is shown in Fig. 14.15. The grid has been generated in GAMBIT. The grid is made of total 2200 points and triangular mesh elements. The grid is clustered near the tip clearance and near the hub. The inlet to the domain is based on the stagnation pressure and temperature inlet BC while at the outlet the back-pressure of suction is applied. The fluid domain is divided into two parts: static fluid and rotating fluid. The static fluid is the fluid portion in the straight ducts of the inlet and outlet where the fluid is not rotating. The rotating fluid is the fluid

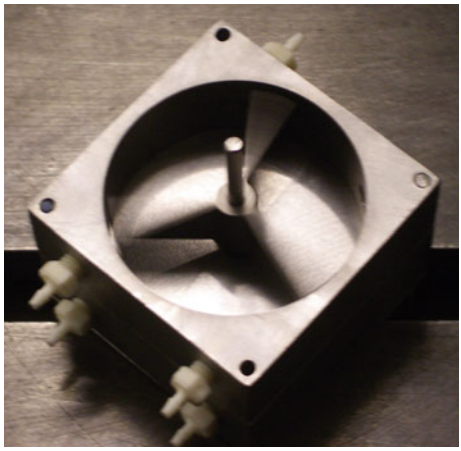

Fig. 14.13 Construction of the prototype three-blade rotor. Reproduced with permission. Copyright retained by Inderscience Publishers

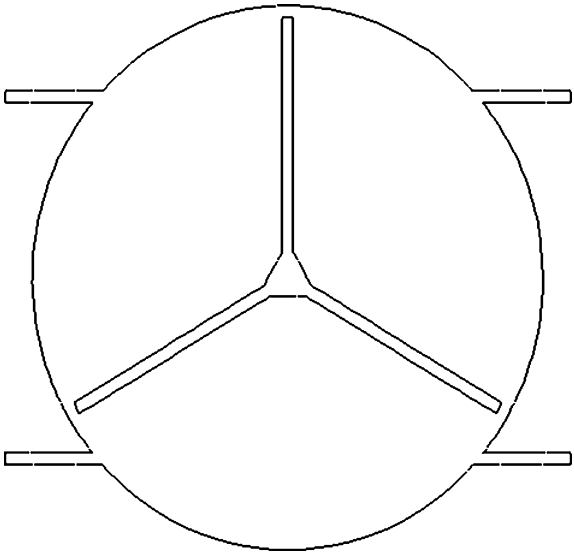

Fig. 14.14 Schematic of the rotor. Reproduced with permission. Copyright retained by Inderscience Publishers

surrounding the blades and enclosed in the casing. The angular rotation of half a million rpm is to be applied to the rotating fluid which is explained later.

The residual plot of the rotor is seen in Fig. 14.16, which shows that the solution has not converged. Further analysis is required to produce fully converged results.

The static pressure contours are shown in Fig. 14.17 for the experimental rotor.

The x- and y-velocity contours are shown in Fig. 14.18, while Fig. 14.19 shows the total pressure exerted with accompanying flow lines.

The magnitude of velocities and pressure are too high and thus indicates us to reevaluate our boundary conditions used in the problem. Additional computations can be done with a much denser grid to capture the unsteady dynamics of the

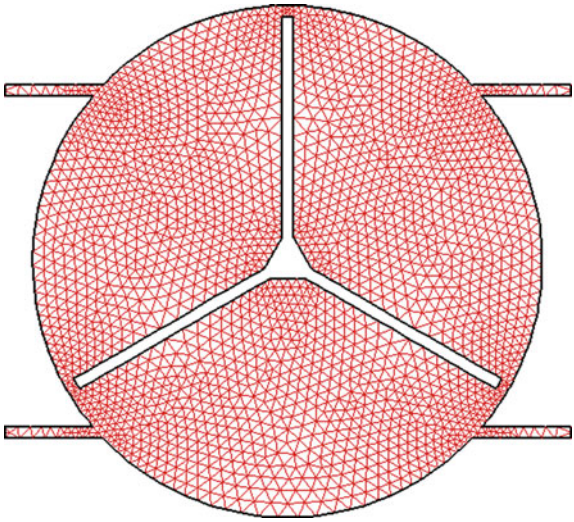

Fig. 14.15 Mesh of the experimental rotor. Reproduced with permission. Copyright retained by Inderscience Publishers

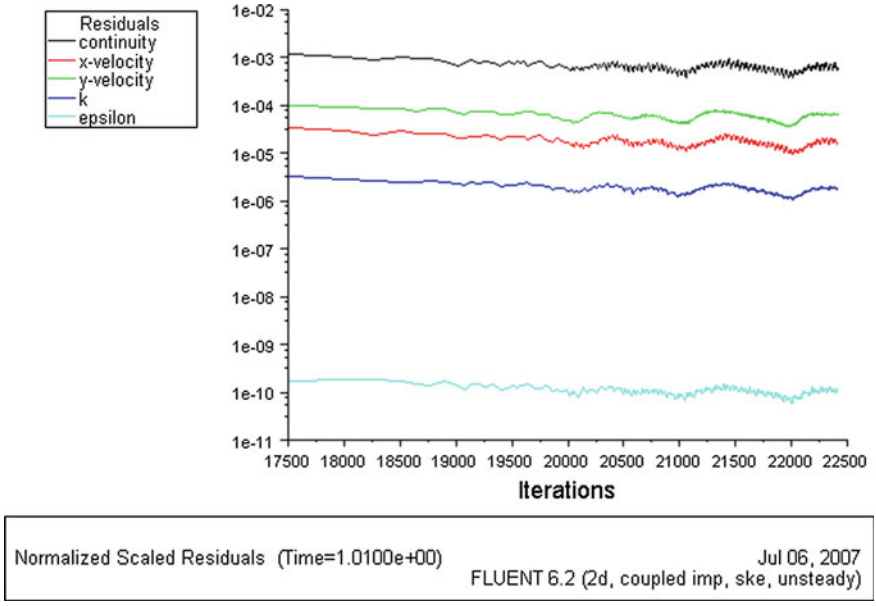

Fig. 14.16 The residual plot of the CFD analysis of the experimental rotor. Reproduced with permission. Copyright retained by Inderscience Publishers

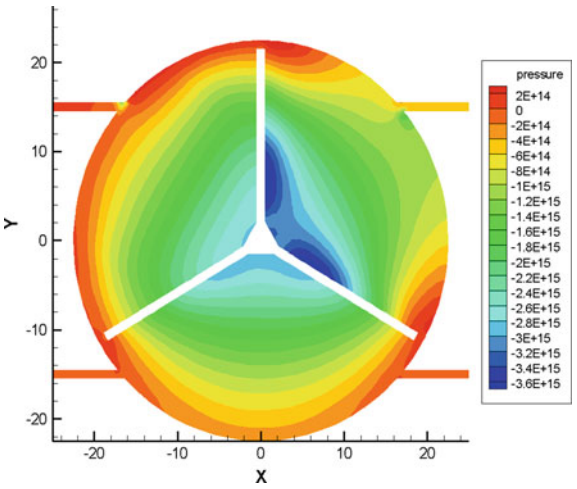

Fig. 14.17 Static pressure contours of the experimental rotors. Reproduced with permission. Copyright retained by Inderscience Publishers

problem. Flow topology and pressure variation of different geometries has been described. Pressure coefficient values of all geometries were given and the variation of pressure coefficient value with the rotating speed of rotor was presented. It can be observed that changes in inlet, outlet, and rotor geometries affect the pressure coefficient significantly.

14.4 Machining of Bone

The structure of cancellous bone (i.e., bone with a relative density less than 0.7) is made up of an elaborate sandwich of compact dense bone on the outer shell and a core of porous, cellular material. This configuration minimizes the weight of the bone over a fairly large load-bearing area. As patients become older, weight loss can result in fractures that can be alleviated by using implants at an earlier age. However, the cancellous bone that is replaced is thought to be a primary cause of osteoarthritis in older patients and so implants must match the bone it replaces. When replacing cancellous bone, the area to be removed must be replaced with great care so that the replacement can attach itself to the bone that is still in the body. It is known that nanostructured hard tissue such as bone allows the surfaces of implants to attach themselves to the bone a lot quicker than existing surface profiles. This is because living cells have an affinity to nanostructured features. In this chapter, we describe a machining technique that easily removes bone without destroying the natural features of the bone so that implants can attach themselves to the bone on the nanoscale.

One technique that shows much promise in machining bone is ultra-high-speed milling; this technique has been shown to produce micro- and nanoscale structures in the same way as a conventional machine tool produces macroscale features. A special requirement of machining at such small scales is the need to increase the

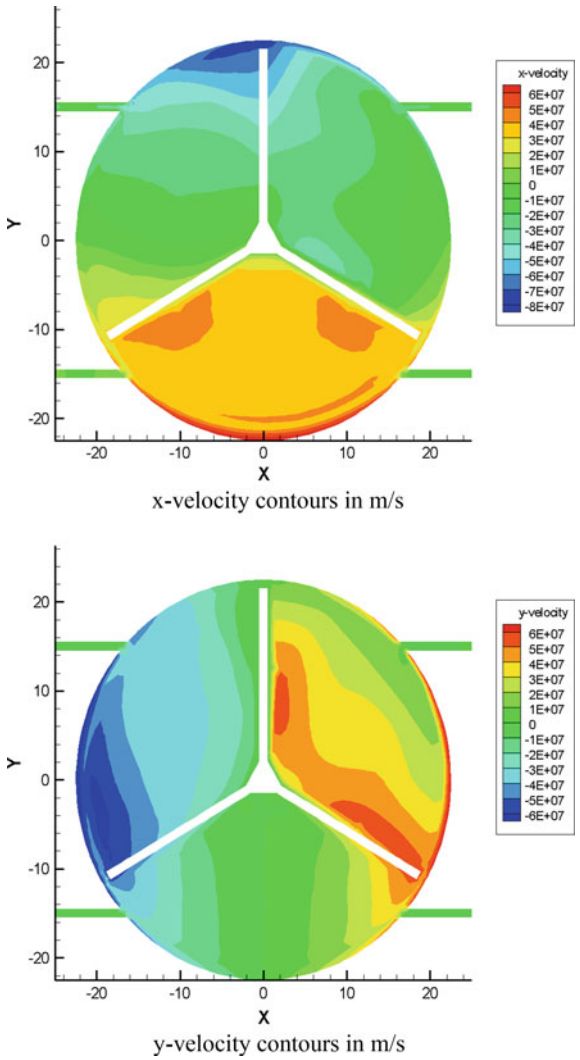

Fig. 14.18 Velocity contours for the experimental rotor. Reproduced with permission. Copyright retained by Inderscience Publishers

rotational speed of the cutting tool. The cutting speed of the cutting tool is given by the following equation:

$$V = r\omega \tag{14.10}$$

where V is the cutting velocity (m/s), r is the cutting tool radius (m), and ω is the rotational speed in (radians/s). From this relationship it can be seen that as the cutter diameter reduces in size to create micro- and nanoscale features, the rotational speed must dramatically increase to compensate for the loss of cutting speed at the

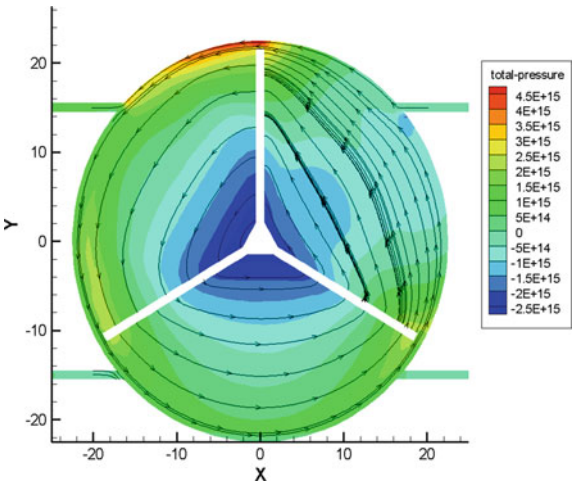

Fig. 14.19 Total pressure in Pa with accompanying flow streamlines for the experimental rotor. Reproduced with permission. Copyright retained by Inderscience Publishers

micro- and nanoscale. At the present time, the fastest spindle commercially available rotates around 360,000 rpm under load conditions.

Research is currently being undertaken to improve the performance of these spindles where the initial aim is to reach 1,000,000 rpm [1]. Strain rates induced at these high speeds cause chip formation mechanisms to be significantly different than at low speeds. Additionally, it is now possible to experiment at the extreme limits of the fundamental principles of machining at ultra high speed and at the micro- and nanoscales using the conventional theories of machining. This chapter discusses the use of these theories at the microscale and at high strain rates and discusses the development of a model of initial chip formation during high strain rate deformation at the microscale.

14.5 Structure of Cancellous Bone

At the lower extremities of density, cancellous bone appears to be a complex set of open pores. As density increases the rods of hard tissue spread and flatten, they become plate-like and finally fuse to form the dense outlying structure at the surface of the bone. Cancellous bone grows in response to an applied stress. Trabeculae develop along the principal stress directions in the loaded bone. These ideas have been measured in vivo of the strains exerted in the cortex of the calcaneus of sheep. The exhibition of directional and anisotropic properties yields special attention from a machining viewpoint. Also, the nature of the microstructure may well exaggerate the wear of very small cutting tools. At the microscale, the

cancellous bone is a composite of a fibrous, organic matrix of proteins mainly collagen, filled with inorganic calcium compounds such as crystalline hydroxyapatite, $Ca_{10}(PO_4)_6(OH)_2$, and amorphous calcium phosphate, $CaPO_3$. These compounds provide the bone with its stiffness. The compositions of compact and cancellous bone are almost the same, i.e., 35 % organic matrix, 45 % calcium compounds, and the remainder water.

14.6 Theory of Micromachining

Following the development of equations proposed by Shaw [2], these expressions will be applied to a 6 flute end milling cutter with a shank of diameter 1.59 mm, cutting diameter 700 μm, rotated at a speed of 250,000 rpm or 26180 rad/s. The rake angle was $\alpha = 7°$, clearance angle $\theta = 10°$, and the shear plane angle $\varphi = 24°$. The material cut was cancellous bovine femur, and the horizontal force F_h was calculated using the equation assuming that the mass of the tool is concentrated at radius, r;

$$F_h = mr\omega^2 \tag{14.11}$$

where m is the tool mass (kg) and r is the tool radius (m). Coefficients of friction between different materials have been investigated by Bowden and Tabor [3]. They also describe the methods used for the determination of the coefficient of friction. Using the method of the inclined plane, the coefficient of friction of cancellous bovine femur on tungsten carbide and steel is in the range $\mu = 0.5–0.6$ under lubricating conditions, i.e., sliding on a plane coated with a saline solution. Using the following equation,

$$\beta = \tan^{-1}\mu \tag{14.12}$$

The friction angle β can then be determined under these conditions. It was found to be 30.96°. This is in excellent agreement with Merchant and Zlatin's nomograph [2]. The vertical force F_V can be found using the relationship

$$F_v = \frac{\mu F_h - F_h Tan\,\alpha}{1 + \mu Tan\,\alpha} \tag{14.13}$$

This was found to be 5.25N. Again, referring to the Merchant and Zlatin's [2] nomograph for the coefficient of friction, the value of F_h can be independently predicted to be 5.33N. The force tangential to the tool plane F is found to be

$$F = F_h Sin\alpha + F_v Cos\alpha \tag{14.14}$$

F was determined as 6.66N. The force normal to the tool plane N is provided using the equation

$$N = F_h Cos\alpha - F_v Sin\alpha \tag{14.15}$$

where N was found to be 11.1N. The force perpendicular to the shear plane F_s can now be determined by,

$$F_s = F_h Cos\phi - F_v Sin\phi \tag{14.16}$$

And was estimated to be 8.76N. The force normal to the shear plane N_s is given by the equation

$$N_s = F_v Cos\phi + F_h Sin\phi \tag{14.17}$$

where N_s is 9.61N. Now the frictional force F_f is

$$F_f = F_v Cos\,\alpha + F_h Sin\alpha \tag{14.18}$$

F_f is approximately 6.66N. It is possible to check this value with Merchant and Zlatin's [2] nomograph for frictional force. However, the values for F_h and F_v are so small the extreme limits of the nomograph are being tested so it is difficult to give an accurate value for F_f; it is certain this value is below 10N which is in close agreement with the calculated answer. The shear stress τ is found using the following quotient:

$$\tau = \frac{F_s}{A_s} \tag{14.19}$$

which has a value of 1.8 GN/m^2. The direct stress ρ is found by applying the relationship,

$$\sigma = \frac{N_s}{A_s} \tag{14.20}$$

σ is found to be 1.95 GN/m^2. The chip thickness ratio, r, is given by

$$r = \frac{t}{t_c} \tag{14.21}$$

where t is the undeformed chip thickness (or depth of cut) and t_c is the measured chip thickness. The machining of bone was conducted at such a small scale that it was difficult to measure t. Therefore, r was calculated using the equation

$$r = \frac{\tan\phi}{\cos\alpha + \sin\alpha\,\tan\phi} \tag{14.22}$$

which yields r = 0.425 and therefore t = 4.25 μm. This is in excellent agreement with Merchant and Zlatin's [2] nomograph for shear angles and the calculation can be made in confidence. Shear strain γ is found from

$$\gamma = \frac{Cos\,\alpha}{Sin\phi Cos(\phi - \alpha)} \tag{14.23}$$

γ was found to be 2.55, this can be independently verified from Merchant and Zlatin's nomograph [2] for shear strain which yields a value of 2.51. The cutting velocity V is found using

$$V = T_{td}\omega \tag{14.24}$$

where V is 9.1 m/s. The chip velocity is found from applying the following equation:

$$V_c = \frac{Sin\phi}{Cos(\phi - \alpha)} \tag{14.25}$$

where V_c is equal to 3.9 m/s, this can also be found from

$$V_c = rV \tag{14.26}$$

The two results are in agreement with each other. The shear velocity V_s is given by

$$V_s = \frac{VCos\alpha}{Cos(\phi - \alpha)} \tag{14.27}$$

where r V_s is calculated to be 9.5 m/s. V_s can also be found from

$$V_s = \gamma VSin\phi \tag{14.28}$$

Again, the two results are in agreement with each other. The strain rate $\dot{\gamma}$ is given by

$$\dot{\gamma} = \frac{VCos\alpha}{\Delta yCos(\phi - \alpha)} \tag{14.29}$$

where Δy is the shear plane spacing and $\dot{\gamma}$ is found to be 8333 s^{-1}. The feed rate is 1 mm/min under experimental conditions and the feed per tooth δ is given by

$$\delta = \frac{F_r}{N\omega} \tag{14.30}$$

where N is the number of teeth. Therefore, Δ is 6.66 μm and the scallop height is found by using the following:

$$h = \frac{\delta}{\left(\frac{4T_{td}}{\delta}\right) + \left(\frac{8N}{\pi}\right)} \tag{14.31}$$

Therefore, h is calculated to be 1.59×10^{-11} m under the experimental conditions of machining.

14.7 Initial Chip Curl Modeling

Chip curvature is a highly significant parameter in machining operations from which a continuous chip is produced. In this chapter, observations are made on the initial chip curl in the simplified case of orthogonal cutting at the micro- and nanoscales. The cutting process may be modeled using a simple primary shear plane and a frictional sliding of the chip along the rake face. When the region of chip and tool interaction at the rake face is treated as a secondary shear zone and the shear zones are analyzed by means of slip-line field theory, it is predicted that the chip will curl. Thus, chip curvature may be interpreted as the consequence of secondary shear. Tight chip curl is usually associated with conditions of good rake face lubrication [4]. At the beginning of the cut, a transient tight curl is often observed, the chip radius increasing as the contact area on the rake face grows to an equilibrium value. Thus it might be suggested that the tight curl is an integral part of the primary deformation.

The process of continuous chip formation is not uniquely defined by the boundary conditions in the steady state and that the radius of the curl may depend on the build-up of deformation at the beginning of the cut [4]. A treatment of primary chip formation at the microscale is presented, which considers chip curl as a series of heterogeneous elements in continuous chip formation at the microscale. The free surface of the chip always displays "lamellae," which are parallel to the cutting edge. The chip is usually considered to form by a regular series of discrete shear events giving a straight chip made up of small parallel segments. However, no account is taken of the bone material that moves pass the tool between shear events. The following observations follow on from Doyle, Horne, and Tabor's [4] analysis of primary chip formation.

Figure 14.20 shows the instabilities during chip formation that gives rise to primary chip curl. The shaded range of Fig. 14.20b is the consequence of a built-up edge that very quickly becomes part of the segmented chips shown in Fig. 14.20d. This "material" provides the means to curl the chip and as a consequence of this event, the following model is presented. Previous treatments of chip curl analysis [5] have focused on chip formation with a perfectly stiff cutting tool. However, during the machining of bone it is observed that the cutting tool bends as it cuts [6].

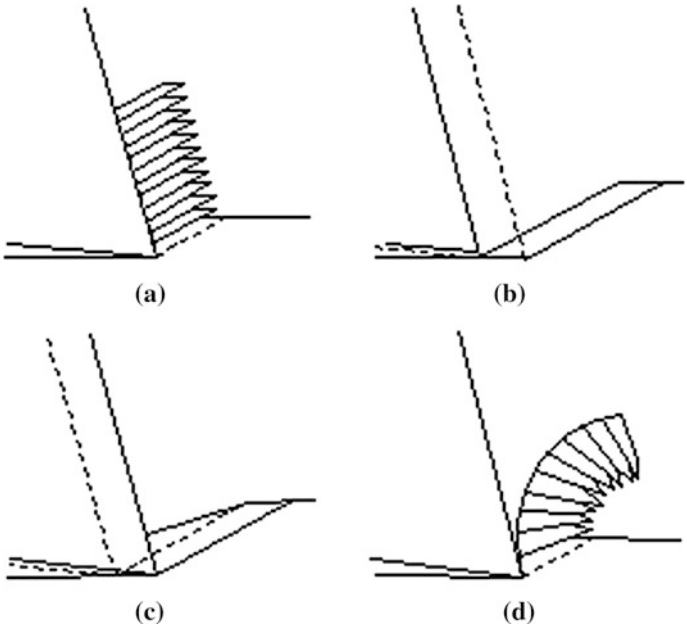

Fig. 14.20 Instability during the formation of a chip during micromachining: **a** segmented, continuous chip; **b** chip forming instability due to built-up edge; **c** movement of a built-up edge to form a chip; **d** serrated, continuous chip curl

This means that primary chip curl models must account for deflection of the cutting tool by bending during an orthogonal machining operation. Computational approaches to modeling chip formation at the micro- and nanoscales have been attempted in recent years by a number of researchers [7–10], who have used a molecular dynamics simulation approach using stiff cutting tools.

The generation of a transient built-up edge ahead of the cutting tool between the shearing events in a bulging-type of motion generates the shape of the segment of the metal chip. This is shown in Fig. 14.20c, with the built-up edge forming the "shaded triangle" above the shear plane. If it is assumed that the built-up edge does not "escape" under the tool edge, then the areas of the shaded triangles in Fig. 14.20b, c will be equal. The chip moves away from the rake force in a manner shown in Fig. 14.20d. The radius of chip curl can be calculated by assuming that the built-up edge in transient and that the element of the "bulged" material contains a small angle relative to the tool and workpiece. This angle will inevitably change during the bending action of the cutting tool. With reference to Fig. 14.21, if we assume that the cutting tool moves from point A to point D then the shear plane AC rotates to position HC as the build-up edge from triangle ABD is pushed into the segment of the chip. At point D, the shear along DF begins and the segment DHCF is completed. HC and DF meet at R, the center of the circle of the chip segment.

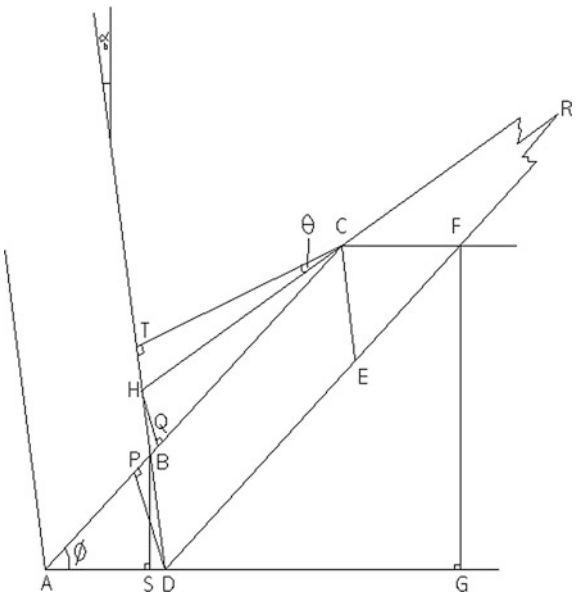

Fig. 14.21 Schematic diagram of the geometry of the primary chip that forms a curled chip

Since the angle HRD is small, RD may be referred to as the radius of the chip. The clearance angle is θ.

Triangles ABD and HBC are equal in area and the depth of the cut FG is equal to d. The spacing between the segments, i.e., the lamellae, is CE, which is equal to BD which in turn is equal to s. The chip thickness between lamellae, TC, is equal to t, while the rake angle SBD is equal to α. The cutting tool bends when machining at the microscale, which reduces the effective rake angle to α_b. We know that the chip radius r can be taken as RD, while the shear angle subtended is BÂD, or ϕ. The calculation of the chip radius is provided by the following analysis:

$$\mathrm{DP} = s.\cos(\phi - \alpha_b) \tag{14.31}$$

$$\mathrm{AB} = \frac{B.S}{\sin\,\phi} \tag{14.32}$$

where

$$\mathrm{BS} = s.\cos\alpha_b \tag{14.33}$$

Thus,

$$\mathrm{DF} = \mathrm{AC} = \frac{d}{\sin\,\phi} \tag{14.34}$$

And,

$$\mathrm{AB} = \frac{s.\cos\alpha_b}{\sin\ \phi} \tag{14.35}$$

Now,

$$\mathrm{BC} = \mathrm{AC} - \mathrm{AB} = \frac{d}{\sin\ \phi} - \frac{s.\cos\alpha_b}{\sin\ \phi} \tag{14.36}$$

Therefore,

$$\mathrm{BC} = \frac{(d - s.\cos\alpha_b)}{\sin\ \phi} \tag{14.37}$$

The areas of ΔABD and ΔHBC are equal, such that,

$$\mathrm{AB.DP} = \mathrm{HQ.BC} \tag{14.38}$$

Hence,

$$HQ = \frac{DP.AB}{BC} = \frac{s.\cos\alpha_b.s.\cos(\phi - \alpha_b).\sin\phi}{\sin\phi.(d - s.\cos\alpha_b)} \tag{14.39}$$

And thus,

$$HQ = \frac{s^2.\cos\alpha_b.\cos(\phi - \alpha_b)}{(d - s.\cos\alpha_b)} \tag{14.40}$$

Also,

$$BH = \frac{HQ}{\cos(\phi - \alpha_b)} = \frac{s^2.\cos\alpha_b}{(d - s.\cos\alpha_b)} \tag{14.41}$$

And,

$$DH = BH + BD = s + \frac{s^2.\cos\alpha_b}{(d - s.\cos\alpha_b)} \tag{14.42}$$

Such that,

$$DH = \frac{s.d}{(d - s.\cos\alpha_b)} \tag{14.43}$$

Hence,

$$CH = \frac{TC}{\cos\theta} = \frac{t}{\cos\theta} \tag{14.44}$$

Therefore,

$$\sin H\hat{R}D = \sin H\hat{C}B = \frac{HQ}{HC} = \frac{s^2.\cos\alpha_b.\cos(\phi - \alpha_b).\cos\theta}{t.(d - s.\cos\alpha_b)} \tag{14.45}$$

And,

$$\sin D\hat{H}R = \sin T\hat{H}C = \cos\theta \tag{14.46}$$

In triangle HRD,

$$\frac{RD}{\sin D\hat{H}R} = \frac{DH}{\sin H\hat{R}D} \tag{14.47}$$

Therefore,

$$RD = r = DH.\frac{\sin D\hat{H}R}{\sin H\hat{R}D} = \frac{s.d}{(d - s.\cos\alpha_b)}.\frac{\cos\theta.t.(d - s.\cos\alpha_b)}{s^2.\cos\alpha_b.\cos(\phi - \alpha_b).\cos\theta} \tag{14.48}$$

Thus,

$$r = \frac{d.t}{s.\cos\alpha_b.\cos(\phi - \alpha_b)} \tag{14.49}$$

If the width of the lamellae, s, is small compared to the chip thickness, then for continuous machining with a single shear plane,

$$\frac{d}{t} = \frac{\sin\phi}{\cos(\phi - \alpha_b)} \tag{14.50}$$

Hence

$$\frac{t}{\cos(\phi - \alpha_b)} = \frac{d}{\sin\phi} \tag{14.51}$$

And so,

$$r = \frac{d^2}{s.\cos\alpha_b.\sin\phi} \tag{14.52}$$

Equation 14.52 predicts a positive chip radius at negative rake angles. The approximations considered in this model are appropriate when one considers that the model assumes that a secondary shear plane exists.

14.8 Experimental

14.8.1 Micromachining Apparatus

The machining of bovine femur was performed using a modified machining center. The biomachining center was constructed to incorporate a high-speed air turbine spindle rated to operate at 360,000 rpm under no-load conditions. When operating at relatively deep depths of cut, the speed of the spindle decreases to approximately 250,000 rpm. The table of the machine tool was configured to move in x–y–z coordinates by attaching a cross-slide powered by a DC motor, in all the three principal axes. Each motor was controlled by a Motionmaster™ controller with a resolution as low as 500 nm. The cutting tools used were coated with diamond. The biomachining center is shown in Fig. 14.22.

The bovine femur samples were machined at various depths of cut at high speed and were machined in an aqueous saline solution. The cutting tools were inspected at the end of all machining experiments using an Environmental Scanning Electron Microscope. The measured spindle speed was 250,000 rpm during the machining experiments. The depth of the cut ranged between 50 and 100 μm for all machining

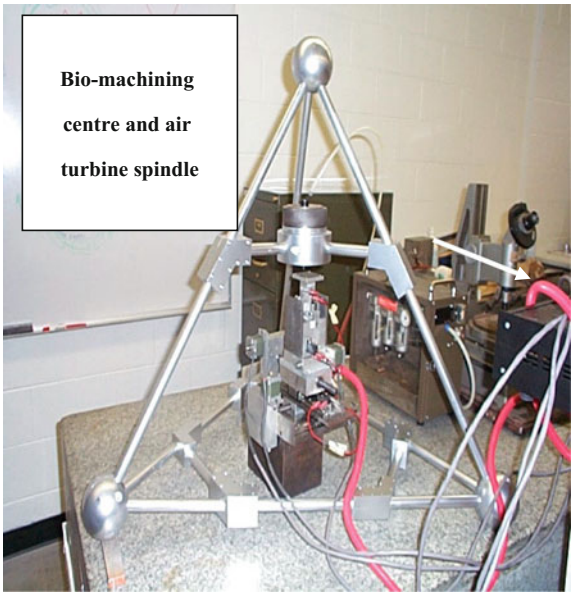

Fig. 14.22 Biomachining center equipped with a high-speed air turbine spindle for rotating coated micromilling tools

experiments. The machining feed rate was conducted at 5 mm/s (0.3 m/min). The microscale cutting tool used was 700 μm in diameter (microscale) and was associated with a cutting speed of 117 m/min and a machining feed rate of 0.3 m/min. The results of the experimental procedures are shown in Table 14.4.

The machined chips were examined in an environmental scanning electron microscope where the lamellar spacing on each chip was determined. Transient chip curl was measured at the first 90° of tight chip curl. The curl radii was then compared with the calculated value derived using the idealized model, taking into account the degree of bending of the cutting tool.

14.8.2 Observations of Bone Chips

There are significant differences in the size and shape of chips when machined at medium and high speeds. This is especially so for biological materials such as cancellous bone. Figure 14.23 shows a collection of chips machined from bovine femur. It is seen in Fig. 14.23 that many of the particles are in fact chunks of material rather than nicely formed chips. It is possible that the chunks were

Table 14.4 Experimental data comparing initial chip curl during biomachining and initial chip curl predicted by the model. The depth of cut was 100 μm

Rake angle after bending (°)	Shear plane angle (°)	Mean lamellar spacing (μm)	Observed chip curl (mm)	Calculated chip curl (mm)
22	37	0.98	17.55	18.01
15	25	1.55	14.42	14.65
8	18	1.9	16.55	17.1
3	12	2.95	15.82	16.22

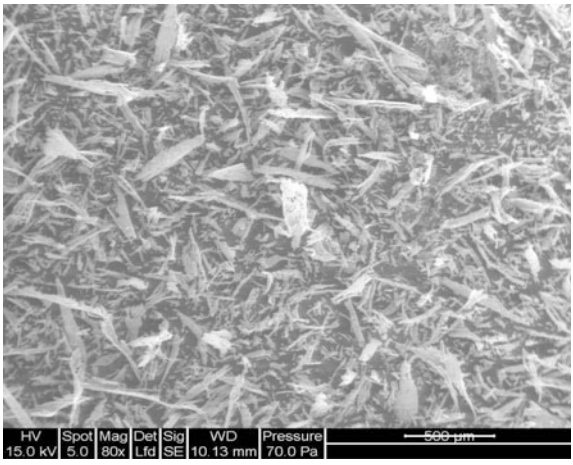

Fig. 14.23 Characteristic chip shapes cutting bovine femur at high speeds

formerly parts of larger chips that have since broken down and that chip thickness values should be recalculated based on the larger chip size. It can also be seen that the chips in Fig. 14.24 are more consistent in terms of length, width, and depth. Their lamellar spacing is also regular in period, which would indicate that cutting conditions at high speed are stable. Single chip formations are shown in Fig. 14.25. While the width observed is similar to that for low-speed cutting, the chip length of high-speed chips is much shorter than low-speed chips. This could be because at low speed the chip has a greater time in contact with the bone thereby removing more material, which is reflected in the increased chip length.

One of the major differences observed between low- and high-speed biomachining of bone is in the spacing of the lamellae. In low-speed cutting, the chip spacing varies by a significant amount.

However, at high cutting speeds the spacing is regular in period. At high speeds, this process is accelerated to an extremely high level as the strain rate calculations

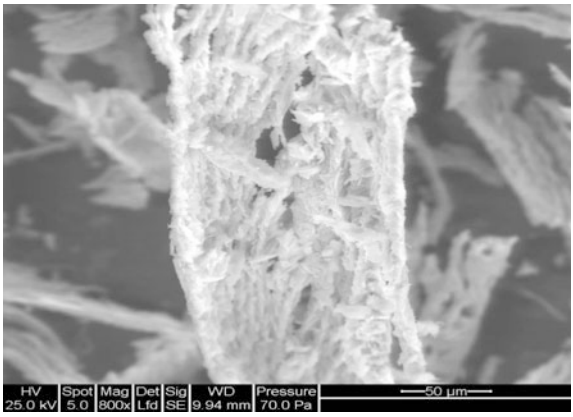

Fig. 14.24 Individual chip formation at high speed

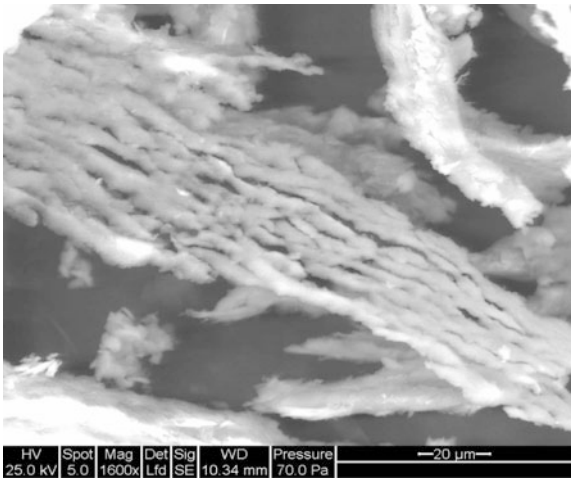

Fig. 14.25 Lamellae spacing of bovine femur at high speed

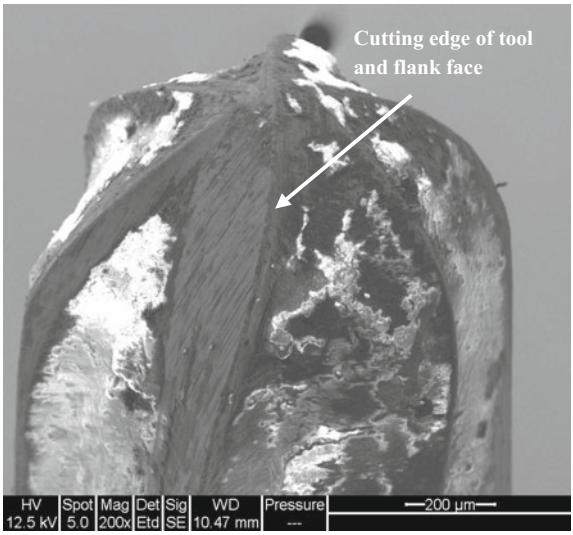

Fig. 14.26 Magnified image of the cutting tool showing cutting edges and adhered bone material

have shown. In fact, experiments show that chip types are similar in other materials such as metals. Figure 14.26 shows a magnified image of a coated cutting tool. The clearance faces of the flutes of the cutting tool show adherent bone chips with finely striated lamellae, as noted on the left-hand side of the tool. Figure 14.27 shows a magnified image of a coated cutting tool detailing the cutting edge and its relationship to the adherent film of bovine femur showing fine striations of lamellae generated at high strain rates.

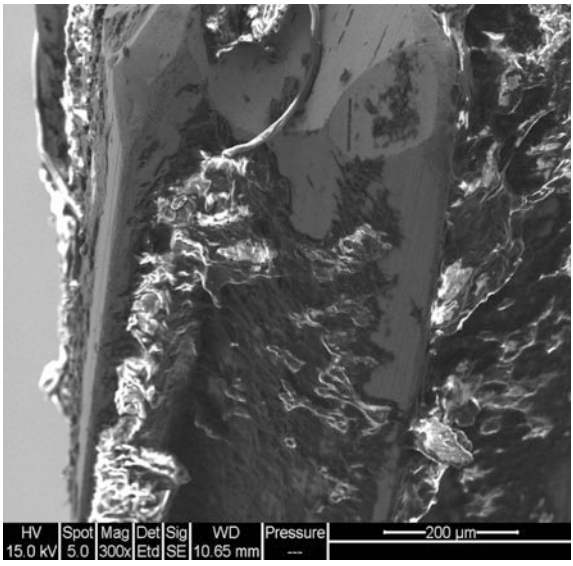

Fig. 14.27 View of cutting edges and adherent bovine femur chip showing fine striations of lamellae

14.8.3 Biomachining Results

The results of machining bovine femur at the microscale are compared to the model described for primary chip curl during the primary stages of chip formation. It should be noted that all results presented in Table 14.4 are for bones machined in an aqueous saline environment. Table 14.4 shows the results for biomachining using a variety of rake angles. It should be noted that bending of the cutting tool produces a less-acute rake angle when machining takes place. However, the shear plane angle is increased and larger chips are produced.

14.9 Discussion

It can be seen from the above analysis that despite the extremely high strain rates imposed due to high-speed cutting, macroscale equations can be applied accurately and produce impressive results. The most significant differences, however, appear in the following categories: strain rate, scallop height, and chip type. Many of the forces are of a similar order of magnitude offering no significant difference between macro-low-speed and micro-high-speed machining. This is important during tool design as small tools must absorb the same impact forces as larger tools do during impact. However, when considering the strain rate it can be seen that during micro-high-speed machining, the strain rate is 8333 s^{-1} compared to the macro-low-speed case of 667 s^{-1}, a 12.5 times increase which relates directly to a 12.5 increase in speed from 20,000 to 250,000 rpm. The increase in strain rate is directly related to the increase in cutting speed; this is expected as the cutter is imparting the strain and therefore a rate of strain to the material. The lamellae spacing Δy in Eq. 14.20 has a significant effect on the strain rate; comparing the macro- and microscale chips it is found that lamellae are ten times more closely packed in the high-speed chips than the low-speed chips.

The purpose of machining is to create surfaces that are useful; hence, surface quality should be an important consideration of milling, a measure of this is scallop height. An improvement is seen in the micro-high-speed case with a scallop height of 1.58×10^{-11} m compared to 8.9×10^{-9} m for macro slow speeds. Although both values seem insignificant, it must be remembered that at the micro- and nanoscales postprocess finishing is inappropriate; therefore, created structures must be produced to specification without further processing. Additionally, owing to the aspect ratio, small imperfections become serious defects at small scales. From the calculations it can be seen that there is an improvement in the scallop height, which is not the improvement required when considering the scale order of magnitude has changed by a factor of four. This is because the current spindle speeds reached are not high enough for effective machining; if this speed is increased to 1,000,000 rpm, then the orders of magnitude are increased further still.

The experimental results and observations provide an interesting view of machining bone at the microscale. When one considers the approximations made in the derivation of the chip curl model, the experimentally measured results compare well with the calculated chip curl. This indicates that cutting tool bending contributes significantly to initial chip curl prior to any significant frictional interactions on the rake face of the cutting tool. The proposed model describes the initial stages of chip curl quite well. If the description of chip curl is accurate, then continuous chip formation at the microscale needs to be reinvestigated. If one considers the movement of the cutting tool (Fig. 14.2), from point A towards point D, we expect the shear plane to oscillate between AC and HC depending on the amount of energy required to move the built-up edge into the segment of the subsequent chip. The cycle begins again when the accumulated material is deposited on to the edge of the cutting tool and then on to the subsequent segment of the chip produced during machining.

14.10 Conclusions

The equations of metal cutting can be applied in the high-speed microscale environment. The nomographs of Merchant and Zlatin [2] can be applied confirming that future calculations can be compared to these well-constructed charts. High strain rates change the mechanism of chip formation thereby altering the shape of the chip. Also, high strain rates appear to provide less dependence on material properties in determining chip formation and shape.

A model of chip curl at the microscale has been developed and agrees well with experimental data. It appears that the bending of the cutting tool contributes significantly to the primary chip prior to significant frictional interactions on the rake face of the cutting tool. It is shown that the primary chip curl is initiated by the amount of material deposited onto the cutting tool that manifests itself as a wedge angle that controls the amount of material pushed into the base of the segment of the chip between the oscillations of the primary shear plane. Further studies on chip formation at the atomic scale are needed to develop nanomanufacturing processing methods for biological materials such as the bone. The future development of this technique lies in the ability to rotate cutting tools at extremely high spindle speeds.

Acknowledgments The authors thank Springer and Wiley publishers for allowing the authors permission to reprint and update this chapter that was originally published in, "Surface Engineered Surgical Tools and Medical Devices," originally published by Springer in 2007 (ISBN 978-0387-27026-5). *Re-printed with kind permission from Springer Science + Business Media B. V and Wiley Publishers.* The authors are grateful to Inderscience for allowing the authors to reproduce the material published in the International Journal of Nano and Biomaterials, 2009, Volume 2, Number 6, p. 505. Inderscience retains the copyright of the material used in this chapter. The authors thank their graduate students for contributing to this chapter by helping to formulate the numerical models.

References

1. Kanjarkar, K. C., Cui, J., Jackson, M. J., Hyde, L. J., & Robinson G. M. (2004, May). Optimum design and analysis of high-speed spindles for nanomachining applications using computational fluid dynamics approach. *Applied Mathematical Modeling* (submitted).
2. Shaw, M. C. (1996). *Metal cutting principles* (pp. 18–46). UK: Oxford Science Publications—Series on advanced manufacturing, Clarendon Press.
3. Bowden, F. P., & Tabor, D. (2001). *The friction and lubrication of solids* (pp. 73–75, 83–85). UK: Oxford Science Publications, Clarendon Press, University of Oxford.
4. Doyle, E. D., Horne, J. G., & Tabor, D. (1979). Frictional interactions between chip and rake face in continuous chip formation. *Proceedings of the Royal Society of London,* A366, 173–183.
5. Jawahir, I. S., & Zhang, J. P. (1995). An analysis of chip formation, chip curl and development, and chip breaking in orthogonal machining. *Transactions of the North America Manufacturing Research Institute—Society of Manufacturing Engineering, 23*, 109–114.
6. Kim, C. J., Bono, M., & Ni, J. (2002). Experimental analysis of chip formation in micro-milling. *Transactions of the North America Manufacturing Research Institute—Society of Manufacturing Engineering*, *30*, 247–254.
7. Komanduri, R., Chandrasekaran, N., & Raff, L. M. (2001). Molecular dynamics simulation of the nanometric cutting of silicon. *Philosophical Magazine, B81*, 1989–2019.
8. Luo, X., Cheng, K., Guo, X., & Holt, R. (2003). An investigation into the mechanics of nanometric cutting and the development of its test bed. *International Journal of Production Research, 41*, 1449–1465.
9. Ahmed, W., & Jackson, M. J. (2015). *Emerging nanotechnologies for manufacturing* (2nd ed.). Elsevier, London: Micro and Nanotechnology Series. ISBN 978-0-323-28990-0.
10. Davim, J. P., & Jackson, M. J. (2009). *Nano and Micromachining*. London: ISTE-Wiley Publishers. ISBN 978-1848-211032.

Chapter 15
Titanium and Titanium Alloy Applications in Medicine

M.J. Jackson, J. Kopac, M. Balazic, D. Bombac, M. Brojan and F. Kosel

Abstract Titanium is a transition metal. It is present in several minerals including rutile and ilmenite, which are well dispersed over the Earth's crust. Even though titanium is as strong as some steels, its density is only half of that of steel. Titanium is broadly used in a number of fields, including aerospace, power generation, automotive, chemical and petrochemical, sporting goods, dental and medical industries. The large variety of applications is due to its desirable properties, mainly the relative high strength combined with low density and enhanced corrosion resistance. This chapter discusses the applications of titanium and its alloys in the medical field.

15.1 Metallurgical Aspects

15.1.1 Introduction

Among the metallic materials, titanium and its alloys are considered the most suitable materials in medical applications because they satisfy the property requirements better than any other competing materials, such as stainless steels, Cr–Co alloys, commercially pure (CP) Nb and CP Ta [1–6]. In terms of biomedical applications, the properties of interest are biocompatibility, corrosion behavior, mechanical behavior, ability to be processed, and availability [7–9].

Titanium may be considered as being a relatively new engineering material. It was discovered much later than the other commonly used metals, its commercial application started in the late 1940s, mainly as structural material. Its usage as implant material began in the 1960s [10]. Despite the fact that titanium exhibits superior corrosion resistance and tissue acceptance when compared with stainless

M.J. Jackson (✉)
Kansas State University, Salina, KS, USA
e-mail: jacksonmj04@yahoo.com

J. Kopac · M. Balazic · D. Bombac · M. Brojan · F. Kosel
University of Ljubljana, Ljubljana, Slovenia

W. Ahmed and M.J. Jackson (eds.), *Surgical Tools and Medical Devices*,
DOI 10.1007/978-3-319-33489-9_15

steels and Cr–Co-based alloys, its mechanical properties and tribological behavior restrain its use as biomaterial in some cases. This is particularly true when high mechanical strength is necessary, like in hard tissue replacement or under intensive wear use [11]. To overcome such restrictions, CP titanium was substituted by titanium alloys, particularly, the classic grade 5, i.e., Ti-6Al-4V alloy. The Ti-6Al-4V α + β-type alloy, the most worldwide utilized titanium alloy, was initially developed for aerospace applications [12, 13]. Although this type of alloy is considered a good material for surgically implanted parts, recent studies have found that vanadium may react with the tissue of the human body [2]. In addition, aluminum may be related with neurological disorders and Alzheimer's disease [2]. To overcome the potential vanadium toxicity, two new vanadium-free α + β-type alloys were developed in the 1980s. Vanadium, a β-stabilizer element, was replaced by niobium and iron, leading to Ti-6Al-7Nb and Ti-5Al-2.5Fe (α + β)-type alloys [4, 6, 14]. While both alloys show mechanical and metallurgical behavior comparable to those of Ti-6Al-4V, a disadvantage is that they all contain aluminum in their compositions.

In recent years, several studies have shown that the elastic behavior of α + β-type alloys is not fully suitable for orthopedic applications [15–18]. A number of studies suggest that unsatisfactory load transfer from the implant device to the neighboring bone may result in its degradation [9]. Also, numerical analyses of hip implants using finite element method indicate that the use of biomaterials with elastic behavior similar to cortical bones improves the distribution of stress around the implanted bone [19]. While the elastic modulus of a cortical bone is close to 18 GPa [7], the modulus of Ti-6Al-4V alloy is 110 GPa [7]. In such a case, the high elastic modulus of the implant material may lead to bone resorption and possible unsuccessful implantation procedure. The elastic behavior mismatch between the implant and the adjacent bone is named the 'stress shielding effect' [19].

Since CP titanium and some specific α + β-type titanium alloys do not completely meet the demands of medical applications, especially concerning mechanical behavior and toxicity to human body, a new class of alloys has been investigated for biomedical applications in the past decade, the β-type alloys. After proper heat treatments, these types of alloys may exhibit low elastic modulus, very good corrosion resistance, suitable mechanical properties after proper heat treatments, and good biocompatible behavior, as they may be obtained by adding biocompatible alloying elements like Nb, Ta, and Zr to titanium [20–24].

15.1.2 Basic Aspects of Titanium Metallurgy

The microstructure diversity of titanium alloys is a result of an allotropic phenomenon. Titanium undergoes an allotropic transformation at 882 °C. Below this temperature, it exhibits a hexagonal close-packed (HCP) crystal structure, known as α-phase, while at higher temperature it has a body-centered cubic (BCC) structure, β-phase. The latter remains stable up to the melting point at 1670 °C [5]. As

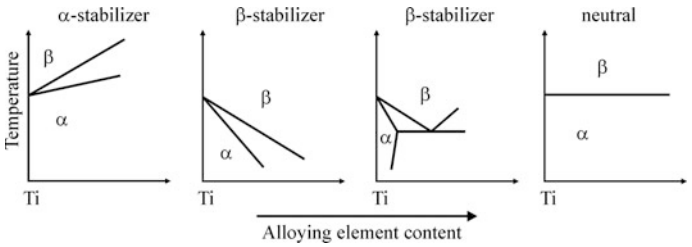

Fig. 15.1 Schematic representation of types of phase diagram between titanium and its alloying elements [5, 25]

titanium is a transition metal, with an incomplete d-shell, it may form solid solutions with a number of elements and hence, α- and β-phase equilibrium temperature may be modified by allowing titanium with interstitial and substitutional elements.

Titanium alloying elements fall into three class: α-stabilizers, β-stabilizers, and neutral. While elements defined as α-stabilizers lead to an increase in the allotropic transformation temperature, other elements, described as β-stabilizers provoke a decrease in such a temperature [25]. When a eutectoid transformation takes place, this β-stabilizer is termed eutectoid β-stabilizer, otherwise, it is called isomorphous β-stabilizer. If no significant change in the allotropic transformation temperature is observed, the alloying element is defined as neutral element. Figure 15.1 shows a schematic representation of types of phase diagram between titanium and its alloys elements [5, 25].

As a result, titanium alloys with an enormous diversity of compositions are possible. Among α-stabilizer elements are the metals of IIIA and IVA groups (Al and Ga) and the interstitials C, N, and O. On the contrary, β-stabilizer elements include the transition elements (V, Ta, Nb, Mo, Mg, Cu, Cr, and Fe) and the noble metals.

Addition of α- and β-stabilizer elements to titanium gives rise to a field in the corresponding phase diagram where both α- and β-phase may coexist. Titanium alloys exhibit a variety of properties, which are connected to chemical composition and metallurgical processing [26–28]. According to the nature of their microstructure, titanium alloys may be divided as either α-alloys, β-alloys, and α + β-alloys [29]. Beta alloys may be further classified into near β and metastable β-alloys.

Alpha titanium alloys are especially formed by CP titanium and alloys with α-stabilizer elements, which present only α-phase at room temperature. Such alloys show high creep resistance and are thus suitable for high temperature service. Since no metastable phase remains after cooling from high temperature, no major modification in terms of microstructure and mechanical properties are possible using heat treatments. Finally, as α-phase is not subjected to ductile–brittle transition, these alloys are proper for very low temperature applications. Regarding mechanical and metallurgical properties, α-alloys present a reasonable level of mechanical strength, high elastic modulus, good fracture toughness, and low plastic deformation, which is due to the HCP crystal structure.

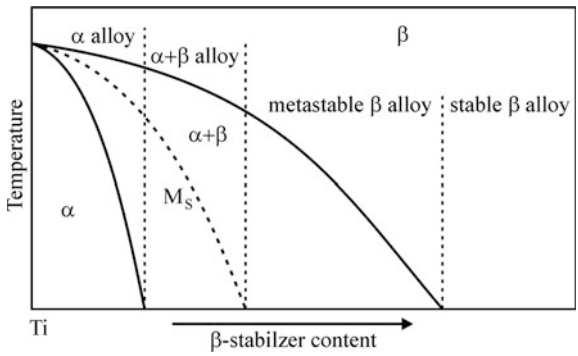

Fig. 15.2 Partial phase diagram of titanium and a β-stabilizer element [5, 6]

Beta titanium alloys are obtained when a high amount of β-stabilizer elements are added to titanium, which decreases the temperature of the allotropic transformation (α/β transition) of titanium [30]. If the β-stabilizer content is high enough to reduce the martensitic start temperature (M_S) to temperatures below the room temperature, nucleation and growth of α-phase will be very restricted, and hence, metastable β is retained at room temperature under rapid cooling, as depicted in Fig. 15.2. This type of titanium alloy may be hardened using heat treatment procedures [31]. In some cases, depending upon composition and heat treatment parameters, precipitation of ω-phase is possible. However, ω-phase may cause embrittlement of a titanium alloy and, in general its precipitation must be avoided [32]. β-titanium alloys are very brittle at cryogenic temperatures and are not meant to be applied at high temperatures, as they show low creep resistance.

Finally, α + β-*alloys* include alloys with enough α- and β-stabilizers to expand the α + β field to room temperature [5, 25]. The (α and β) phase combination allows one to obtain an optimum balance of properties. The characteristics of both α- and β-phases may be tailored by applying proper heat treatments and thermo-mechanical processing. A significant assortment of microstructures may be obtained when compared to α-type alloys. The Ti-6Al-4V alloy is an example of α + β-type alloy. Due to its large availability, very good workability, and enhanced mechanical behavior at low temperatures, such an alloy is the most common composition among the titanium alloys and based on these characteristics it is still largely applied as a biomaterial, mainly in orthopedic implant devices. Figure 15.3 depicts the microstructures of β and α + β-titanium alloys.

As in the case of iron (steels), allotropic transformation is the main reason for the enormous variety of microstructure in titanium alloys. Titanium alloy microstructures are formed by stable and metastable phases [33, 34]. In general, for limited β-stabilizer content and depending on cooling conditions, titanium alloys show only α- and β-phases.

However, if the thermodynamic equilibrium is not reached, metastable phases may be retained at room temperature, mainly, martensitic and ω-phases. According to several authors [35–37], titanium alloys with β-stabilizer elements such as Mo, Nb, Ta, and V, may form two types of martensitic structures. If the β-stabilizer

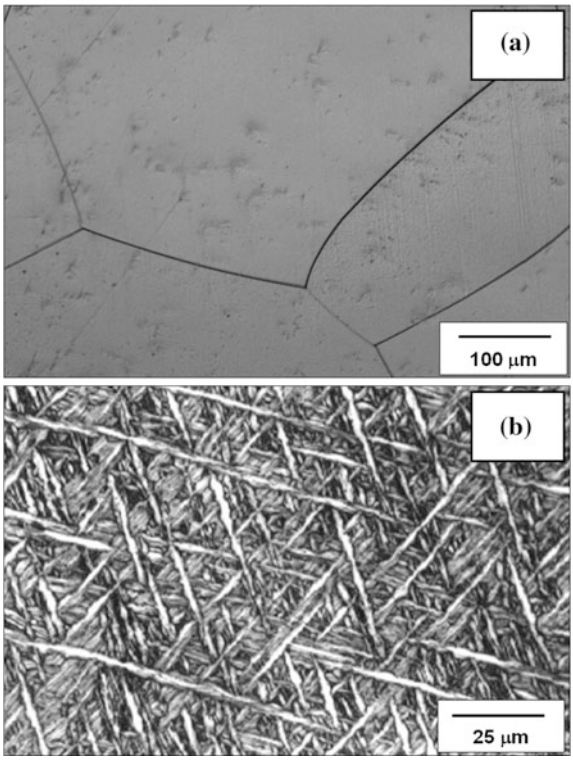

Fig. 15.3 Microstructures of **a** β Ti-35Nb (wt%) and **b** α + β Ti-6Al-7Nb (wt%) alloys cooled in air

content is considered low, rapid cooling leads to formation of hexagonal martensite, termed α′. When this content is high α′ martensite undergoes a distortion, loses its symmetry, and is substituted by orthorhombic martensite, defined as α″ [37].

When titanium alloys with β-stabilizer elements are submitted to rapid cooling from high temperature, the β-phase may transform either in martensitic structures or eventually, in metastable ω-phase [35]. Figure 15.4 presents a microstructure of the Ti-25Nb (wt%) after cooling in water and in air showing α″ and ω formation.

Precipitation of ω-phase occurs only in a limited range of the alloy element and may arise during the quenching from high temperature (β-phase), forming a thermal ω-phase. However, ω-phase may also form after aging of a rapid by quenched structure at medium temperatures, resulting in isothermal ω-phase, as indicated in Fig. 15.5.

15.1.3 Mechanical Behavior

Concerning mechanical behavior, biomedical titanium alloys applied as biomaterial mainly in hard tissue replacement, must exhibit a low elastic modulus combined

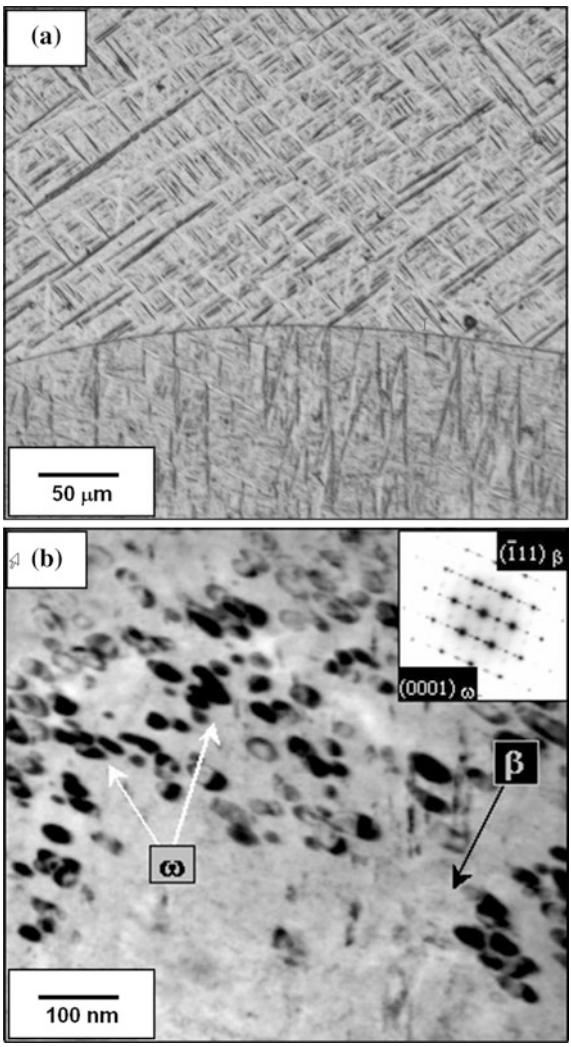

Fig. 15.4 Microstructure of the Ti-25Nb (wt%) alloy: **a** water cooled sample showing martensitic structure (MO analysis) and **b** air cooled sample showing ω phase dispersed in β matrix and respective SADP showing ω and β phases microstructure (TEM analysis)

with enhanced strength, good fatigue resistance, and good workability. Mechanical behavior of titanium alloys is directly related to composition and mainly, thermo-mechanical processing. Some mechanical properties of selected titanium-based materials applied as biomaterials are shown in Table 15.1 [38].

Mechanical strength may be increased by adding alloying elements, which may lead to solid-solution strengthening or even, precipitation of second phases. Also, using aging processes, metastable structures obtained by rapid quenching from β field may give rise to fine precipitates, which considerably increases mechanical strength.

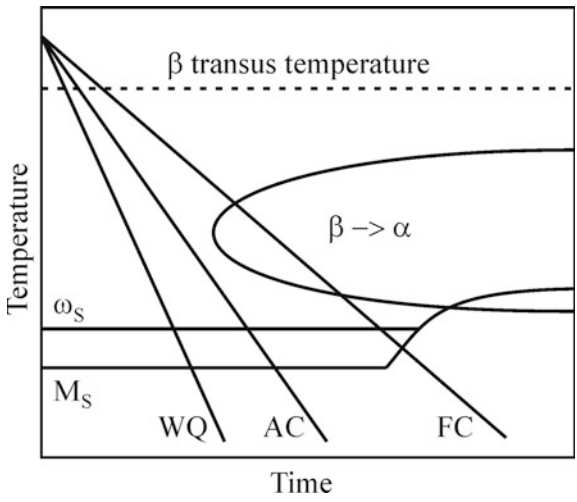

Fig. 15.5 A schematic TTT diagram for β phase transformation in titanium alloys with β-stabilizer elements [35]

Table 15.1 Selected Ti-based materials developed for medical applications [38]

Material	Tensile strength (MPa)	Yield strength (MPa)	Elongation (%)	Elastic modulus (GPa)
α type				
Pure Ti grade 1	240	170	24	102.7
Pure Ti grade 2	345	275	20	102.7
Pure Ti grade 3	450	380	18	103.4
Pure Ti grade 4	550	485	15	104.1
α + β type				
Ti-6Al-4V	895–930	825–869	6–10	110–114
Ti-6Al-4V ELI	860–965	795–875	10–15	101–110
Ti-6Al-7Nb	900–1050	880–950	8.1–15	114
Ti-5Al-2.5Fe	1020	895	15	112
β type				
Ti-13Nb-13Zr	973–1037	836–908	10–16	79–84
Ti-12Mo-6Zr-2Fe	1060–1100	1000–1060	18–22	74–85
Ti-15Mo	874	544	21	78
Ti-15Mo-5Zr-3Al	852–1100	838–1060	18–25	80
Ti-15Mo-2.8Nb-0.2Si	979–999	945–987	16–18	83
Ti-35.3Nb-5.1Ta-7.1Zr	596.7	547.1	19	55
Ti-29Nb-13Ta-4.6Zr	911	864	13.2	80

Titanium alloys present a high strength-to-weight ratio, which is higher than with most of steels. While CP titanium has yield strength between 170 (grade 1) and 485 MPa (grade 4), titanium alloys may present values higher than 1500 MPa [25].

The elastic modulus or Young modulus corresponds to the stiffness of a material and is associated to the way inter-atomic forces vary with distance between atoms in the crystal structure. A comparison between both crystal structures of titanium has led to the conclusion that HCP structure presents higher values of elastic modulus than the BCC structure. Hence, addition of β-stabilizer elements allows β-phase stabilization and hence, low elastic modulus alloys. While CP titanium shows elastic modulus values close to 105 GPa, Ti-6Al-4V-type α + β alloy presents values between 101 and 110 GPa, type-β titanium alloys may present values as low as 55 GPa [38]. When compared with common alloys used as biomaterials, such 316 L stainless steel (190 GPa) and Co–Cr alloys (210–253), low elastic modulus titanium alloys display a more compatible elastic behavior to that of the human bone [39]. In general, as the elastic modulus decreases, so does the mechanical strength and vice versa.

Analysis of slip systems in different crystal structures reveals that plastic deformation is easier in BCC crystal structure than in HCP structure. It explains the enhanced ductility of β-phase when compared to α-phase. In a HCP structure, the number of slip systems is only three, while this number increases to 12 in the case of BCC structure. In addition, the ease of plastic deformation facility is directly connected to the minimum slip distance, $b_{\min}$ [25], which is given by the inter-atomic distance divided by the respective lattice parameter. Since, HCP structure exhibits a higher slip distance than BCC structure, it is possible to conclude that the atomic planes slip or the plastic deformation is easier in BCC structure than HCP. Hence, β-type alloys present the best formability among the titanium alloys.

15.1.4 Corrosion Behavior

Corrosion resistance is one of the main properties of a metallic material applied in the human body environment and the success of an implant depends on the careful examination of this phenomenon. The performance of an implant is directly related to its ability in functioning in the aggressive body fluids. In general, these fluids consist of a series of acids and certain amount of NaCl. In normal conditions, its pH is 7, however, it may be altered due to immune system response, like in the case of an infection or inflammation. In an event of a corrosion process, the implant component may lose its integrity, leading to a failure. In addition, release of corrosion products may lead to undesirable biological reactions. Certainly, this will depend on the nature of chemical reactions on the implant surface in view of the fact that corrosion is essentially a chemical process.

Titanium shows an excellent corrosion resistance, which is directly related to the formation of a stable and protective oxide layer, essentially TiO_2. The reactivity of titanium can be measured by its standard electrode potential (standard electromotive force (EMF) series), which is −1.63 V [5]. Such a value indicates that titanium has a high chemical reactivity and is easily oxidized, giving rise to a very adherent and

thin oxide layer on the titanium surface. This oxide layer passivates the titanium, which results in a protection against further corrosion process as long as this layer is maintained. Actually, formation of passivation films on titanium does not mean cessation of corrosion processes. It means that the corrosion rate will be significantly reduced. Therefore, titanium is corrosion resistant in oxidizing environments but not resistant in reducing medium [5].

In general, anodic polarization testing is an efficient method of analyzing corrosion behavior of metallic material in a corrosive environment. Figure 15.6 depicts

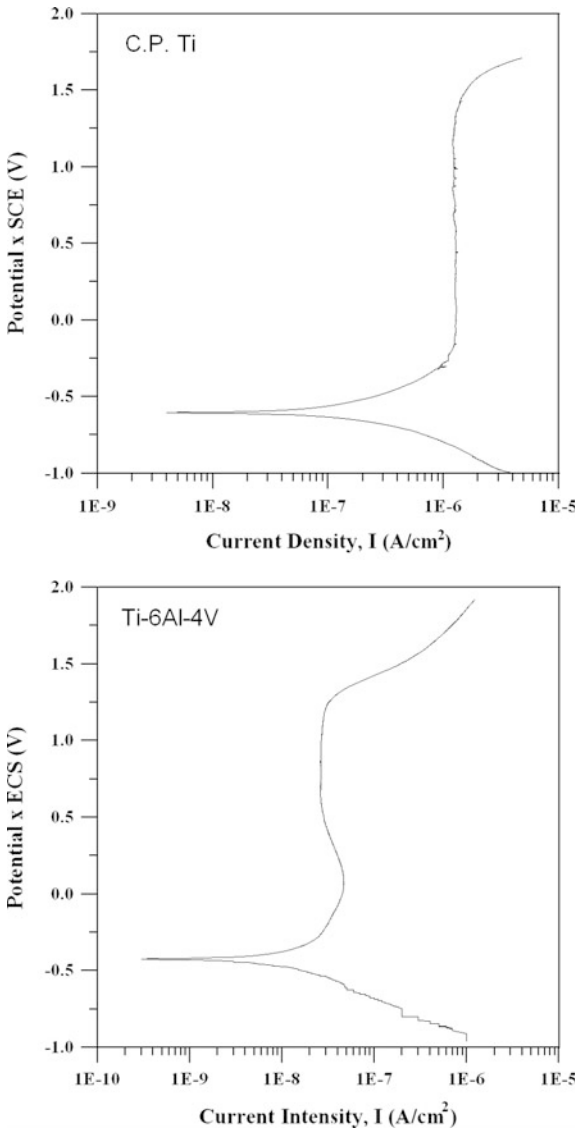

Fig. 15.6 Polarization curves for CP titanium and Ti-6Al-4V alloy (Scan rate of 0.1 mV s^{-1})

the anodic polarization curve for CP titanium and Ti-6Al-4V alloys, showing the electric current intensity versus potential (versus saturated calomel electrode (SCE)), obtained with 5 g/l NaCl, pH 4 solution as an electrolytic medium at 310 K. The potential was scanned at 0.1 mV s^{-1} [11].

The anodic portion of the polarization curve allows one to evaluate the corrosion behavior of a metallic material in an electrolytic medium. Evaluation is obtained by determining the range of potentials in which passivation films are stable, and also by finding the current intensity of passivation. As usual, polarization tests started at a negative potential of −1.0 V versus SCE, reaching more positive values. In such a process, the initial sector of the anodic polarization curve refers to the beginning of a corrosion phenomenon, where the metallic material reacts with the supporting electrolyte, leading to active corrosion.

The following segment is related to the formation of an oxide passivation film, when the electric current stabilization takes place. As the potential increases, the current intensity also increases and eventually, the rupture of passivation film occurs. At this point, the protective layer loses its efficiency causing pitting corrosion. However, this hypothesis is not confirmed during the reverse scanning of potential. Polarization curves obtained during forward and backward scans of potential are superimposed and no pitting potential is observed, which allows one to conclude that both materials show outstanding resistance to corrosion.

15.2 Principal Requirements of Medical Implants

15.2.1 Introduction

Medical implants are products that have to satisfy the functionality demands defined by the working environment-human body. They could be used in almost every organ of the human body. Ideally, they should have biomechanical properties comparable to those of autogenous tissues without any adverse effects. The principal requirements of all medical implants are corrosion resistance, biocompatibility, bioadhesion, biofunctionality, processability, and availability. To fulfill these requirements most of the tests are directed into the study extracts from the material, offering screens for genotoxicity, carcinogenicity, reproductive toxicity, cytotoxicity, irritation, sensitivity, and sterilization agent residues [40]. The consequences of corrosion are the disintegration of the implant material per se, which weakens the implant, and the harmful effect of corrosion on the surrounding tissues and organs is produced.

Medical implants are regulated and classified in order to ensure safety and effectiveness to the patient. One of the main goals of implant research and development is to predict long-term, in vivo performance of implants. Lack of useful computer-modeling data about in vivo performance characteristics makes the evaluation of synergistic contributions of materials, design features, and therapeutic drug regimens difficult. The present trends in modern implant surgery are

networking various skilled and gifted specialists such as trauma specialists, orthopedists, mechanical engineers, pharmacists, and others in order to get better results in research, development and implementation into practice.

15.2.2 Metallic Biomaterials

The first metal alloy developed specifically for the human body environment was the 'vanadium steel' that was used to manufacture bone fracture plates (Sherman plates) and screws. Most metals that are used to make alloys for manufacturing implants such as iron (Fe), chromium (Cr), cobalt (Co), nickel (Ni), titanium (Ti), tantalum (Ta), niobium (Nb), molybdenum (Mo), and tungsten (W), can only be tolerated by the body in minute amounts. Sometimes these metallic elements, in naturally occurring forms, are essential in red blood cell functions (Fe) or synthesis of a vitamin B_{12} (Co), etc. but cannot be tolerated in large amounts in the body [41].

Metallic biomaterials can be divided into four subgroups: stainless steels, the cobalt-based alloys, titanium metals, and miscellaneous others (including tantalum, gold, dental amalgams, and other special metals). They are very effective in binding the fractured bone, do not corrode, and do not release harmful toxins when exposed to body fluids and therefore can be left inside the body for a long period of time. Their disadvantage is a much larger hardness and stiffness compared to the bone and possibility of interfering with the regrowth of the bone.

15.2.3 The Surface-Tissue Interaction

Good corrosion resistance of titanium depends upon the formation of a solid oxide layer (TiO_2) to a depth of 10 nm. After the implant is inserted, it immediately reacts with body liquids that consist of water molecules, dissolved ions, and proteins as shown in Fig. 15.7.

Geometry, roughness, and other characteristics of the implant surface also importantly influence the surface-tissue interaction, which is considered to be dynamic. Due to these phenomena, over time new stages of biochemical formations

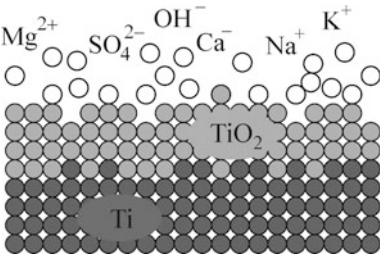

Fig. 15.7 Interaction between titanium and body liquids [129]

can be developed. In the first few seconds, after the contact has been made, there is only water, dissolved ions, and free biomolecules in the closest proximity of the surface, but no cells. The composition of the body liquid changes continuously as inflammatory and healing processes continue to proceed, causing changes in the composition of the adsorbed layer of biomolecules on the implant surface until it is balanced. Cells and tissues eventually contact the surface and, depending on the nature of the adsorbed layer, they respond in specific ways that may further modify the adsorbed biomolecules [42].

Surface roughness also plays an important role in osteointegration. Osteoblast cells are more likely to get attached to rough-sand blasted surfaces, meaning lower cell numbers on the rougher surfaces, decreased rate of cellular proliferation, and increased matrix production compared to smooth surface. Experiments made by Feighan [43] showed that an average roughness increased from 0.5 to 5.9 μm also increase the interfacial shear strength from 0.48 to 3.5 MPa.

15.2.4 Machining of Titanium Alloys

Titanium alloys are among the most widely used and promising materials for medical implants. Selection of titanium alloy for implementation is determined by a combination of the most desirable characteristics including immunity to corrosion, biocompatibility, shear strength, density, and osteointegration [3]. The excellent chemical and corrosion resistance of titanium is to a large extent due to the chemical stability of its solid oxide surface layer to a depth of 10 nm [44]. Under in vivo conditions, the titanium oxide (TiO_2) is the only stable reaction product whose surface acts as catalyst for a number of chemical reactions. However, micromotion at the cement-prosthesis and cement-bone are inevitable and consequently, titanium oxide and titanium alloy particles are released in the cemented joint prosthesis. Sometimes this wear debris accumulates as periprosthetic fluid collections and triggers giant cell response around the implants [45]. TiO_2 film, such as the ones anodically formed in aqueous electrolytes, consists mainly of anatase and is an n-type semiconductor with low electronic charge conductivity and a high resistance to anodic current [46].

Processes of machining titanium alloys involve conventional machining operations (turning, face milling, high-speed cutting (HSC), milling, drilling), forming operations (cold and hot forming; hydroforming, forging) and alternative machining operations (laser cutting, waterjet cutting, direct metal laser sintering). Machining operations of titanium alloys are considered to be difficult, due to its relatively high tensile strength, low ductile yield, 50 % lower modulus of elasticity (104 GPa) and approximately 80 % lower thermal conductivity than that of steel [47]. The lower modulus of elasticity may cause greater ‘spring back’ and deflection effect of the workpiece. Therefore, more rigid setups and greater clearances for tools are required. In the tool contact zones high pressures and temperatures occur (the tool-to-workpiece interface). The amount of heat removed by laminar chips is only

approximately 25 %, the rest is removed via the tool. Due to this phenomenon titanium alloys can be machined at comparatively low cutting speeds. At higher temperatures caused by friction the titanium becomes more chemically reactive and there is a tendency for titanium to » weld « to tool bits during machining operations. Over-heating of the surface can result in interstitial pickup of oxygen and nitrogen, which will produce a hard and brittle alpha case. Carbides with high WC–Co content (K-grades) and high-speed steels with high cobalt content are suitable for use as cutting materials in titanium machining operations [47]. Turning operations of titanium alloys should have cutting depths as large as possible, cutting speeds V_C from 12 to 80 m/min and approximately 50 % lower when high-speed steel (HSS) tools are used. The heat generated should be removed via large volumes of cooling lubricant. Chlorinated cutting fluids are not recommended because titanium can be susceptible to stress corrosion failures in the presence of chlorine. Any type of hot working or forging operation should be carried out below 925 °C due to the high level of titanium reactivity at high temperature.

Some medical implants are produced modularly, using different materials and processing techniques. For example, the femoral stem as part of the hip endoprosthesis is produced in a combination of casting, forging, and milling. The final machining operation is performed on CNC machine using CAD-CAM principle.

Good alternatives to conventional machining techniques are alternative techniques such as waterjet cutting, sintering, or direct metal laser sintering. The latter is a rapid prototyping technique enabling prompt modeling of metal parts with high bulk density on the basis of individual three-dimensional data, including computer tomography models of anatomical structures. The concept of layer by layer building rather than removing waste material to achieve the desired geometry of a component opens up endless possibilities of alternative manufacture of medical devices and is more environment friendly.

Even though machining Ti alloys produces forces only slightly higher than those developed when machining steel, the specific metallurgical characteristics of these alloys create difficulties and therefore increase the price. Although hard, it is not impossible to achieve excellent surface finish and good production rates when these alloys are machined, however, it is necessary to take into consideration the very unique characteristics which Ti alloys posses such as low heat conduction, reactivity, low Young's modulus, alloying tendency, surface damage susceptibility, and work hardening characteristics. The following review of machining titanium and its alloys are shown in greater detail in reference [48].

Poor heat conduction of Ti alloys makes the heat linger on the tool cutting edge and tool face effecting tool life. Furthermore the work hardening characteristics of the alloy induces the absence of a built-up edge creating localization of heat that in combination with high bearing forces results in rapid tool deterioration. The spring back effect in these alloys is high due to the low Young's modulus and consequently the deflections of the workpiece are significant making precision machining hard. Increasing the systems rigidity, using sharp tools, greater tool clearances are one of the ways to reduce this effect. Surface damage in Ti alloys has an effect when they are used in application where fatigue life is important. In the aim of optimizing

fatigue life it is necessary to maintain sharpness of the tools while machining (mostly grinding) titanium alloys. Main influencing parameters when machining Ti alloys to be considered are as follows:

- Cutting speed
- Feed rate
- Cutting fluid
- Tool sharpness
- Tool–workpiece contact
- Rigidity of the setup.

When setting up the machining parameters for machining Ti alloys, it is necessary to keep the speed low in order to minimize the temperature rise and consequently reduce the influence of heat on the tool tip and edge. Since the tool temperature is affected more by speed and less by feed, than the feed should be kept high while taking into consideration that a work hardened layer is formed after each cut and the consecutive cut needs to be larger than the thickness of this layer. Another influence on the temperature during machining is the amount of cutting fluid used. A generous amount needs to be used to reduce temperatures as well as to clear the work area of chips and reduce cutting forces. The sharpness of the tools used in machining is going to influence the surface finish and if not adequate can cause tearing as well as deflection of the workpiece. The contact of the tool with the workpiece is important due to the fact that if dwelling of the tool is allowed while tool is in contact with the workpiece it can cause work hardening, smearing, galling, and seizing leading to tool deterioration and eventually breakdown. Most of the efforts made to enhance the machining process of titanium alloys have been focused on decreasing temperature generated at the cutting edge and tool face due to the fact that it influences tool life and surface characteristics of the workpiece. It has been shown that when machining Ti6Al4V alloys, tool life is increased by decreasing cutting speed and increasing feed. At high cutting speeds, the tool deteriorates rapidly and tool life is dramatically increased by lowering the speed parameter [49].

The cutting tool material needs to offer abrasion resistance and hot hardness and so far the three most satisfying materials have been proven to be carbide and high speed or highly alloyed steels. Different materials are used for different applications, for example, turning and face milling is mostly done using C2 tungsten carbide grades while HSS tools are used for milling, drilling, and tapping of Ti alloys. Productivity is also being influenced using specific techniques such as specially designed cutters and special cutting techniques [49].

Milling parameter recommendations are given in Tables 15.2, 15.3, and 15.4, for face milling, end milling–slotting, and end milling–peripheral milling, consecutively. The change in cutting speed and/or feed has a significant influence on the chip–tool contact length, chip length, segmentation frequency, segment size, and chip thickness therefore presents the two major parameters for process manipulation. Owing to this fact, the effect of machining parameters such as cutting speed and feed on chip formation has been a topic of interest for many researchers [49].

Table 15.2 Face milling data [49]

Material	Condition	Doc, in	HSS tool			Carbide tool		
			Speed, fpm	Feed in/tooth	Tool material	Speed, fpm	Feed in/tooth	Tool material
Ti6Al4V	Annealed	0.25	40	0.006	M3/T15	130	0.006	C2
Ti6Al4V ELI	Annealed	0.05	50	0.004	M3/T15	170	0.004	C2

It has been shown that there is a dependence of the contact length on the cutting speed when machining Ti6Al4V alloys where the contact length is considered to be the contact between the chip and the tool rake face when creating a continuous chip [50]. The dependence presented in Fig. 15.8 shows that there is a maximum contact length that is achieved at the transition in the cutting speed from regular to high speed. They attribute this dependence to the effect of "shear banding." The contact length is also shown to be dependent on the undeformed chip thickness, where the increase in the undeformed chip thickness yields an increase in the contact length. It has been stated that the chip compression ratio (ratio of the actual and undeformed hip thickness) is hard to comprehend due to the scattered results and they attribute this to the poor machinability of Ti alloys and shear banding as well.

Chip morphology has been researched [51] showing that the saw-chip formation is present and that the chip length is increased while the width decreased with the increase in cutting speed and feed. The segmentation size increases while the frequency of the segmentation decreases with cutting speed. This has also been determined in further work [52], where it has been shown that the segmentation frequency increases linearly with the increase in cutting speed and decreases with increase in feed (Fig. 15.9).

The chip thickness ratio (ratio of undeformed chip thickness and actual chip thickness) has been shown to increase with the decrease in cutting speed and it decreases with the increase in feed when using low speeds (Fig. 15.10) [53].

The dependence of chip thickness, tool–chip contact length and chip up-curl radius on the tool radius/chip thickness ratio has been presented in Fig. 15.11 [54]. The chip thickness decreases with the increase in the tool radius value as the ratio of the tool radius and undeformed chip thickness is increased. The tool–chip contact length follows the same trend as the chip thickness yielding a lower value with the increase of the tool edge radius.

However, the chip thickness is a questionable parameter when Ti alloys are being investigated [55]. The conventional chip thickness ratio for the continuous chip formation models and the parameters such as shear angle which are calculated from the ratio are considered to be incorrect parameters for describing machining characteristics of Ti alloys [55]. This is due to the fact that Ti alloy chips become deformed inconsequentially, and are formed by gradual flattening of a softer half wedge by the tool. Consequently, the chip thickness ratio is close to unity. This is one of the reasons that when machining Ti alloys, the shear angle cannot be assessed using a conventional formula as it can when machining steel where

Table 15.3 End milling data—slotting [49]

Material	Condition	Doc, in	High-speed tool (M2)					Carbide tool (C2)				
			Speed, fpm	Cutter diameter, in				Speed, fpm	Cutter diameter, in			
				1/18	3/8	3/4	1–2		1/8	3/8	3/4	1–2
				Feed per tooth					Feed per tooth			
Ti6Al4V	Annealed	0.25	30	–	0.0007	0.003	0.004	75	–	0.0007	0.003	0.005
Ti6Al4V ELI	Annealed	0.125	40	–	0.001	0.003	0.004	100	–	0.0015	0.003	0.005
		0.050	50	0.0005	0.002	0.004	0.005	125	0.0005	0.002	0.005	0.007
		0.015	65	0.0007	0.003	0.005	0.006	165	0.0005	0.003	0.006	0.008

Table 15.4 End milling data—peripheral milling [49]

Material	Condition	Doc, in	High-speed tool (M2)					Carbide tool (C2)				
			Speed, fpm	Cutter diameter, in				Speed, fpm	Cutter diameter, in			
				1/8	3/8	3/4	1–2		1/8	3/8	3/4	1–2
				Feed per tooth					Feed per tooth			
Ti6Al4V	Annealed	0.25	50	–	0.001	0.004	0.005	125	–	0.001	0.004	0.006
Ti6Al4V ELI	Annealed	0.125	60	–	0.0015	0.004	0.005	150	–	0.002	0.004	0.006
		0.050	75	0.0008	0.003	0.005	0.006	190	0.0008	0.003	0.006	0.007
		0.015	90	0.001	0.004	0.006	0.007	225	0.001	0.004	0.007	0.008

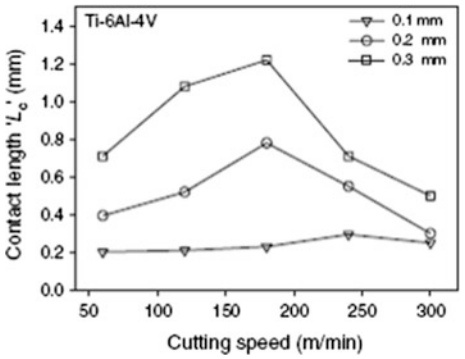

Fig. 15.8 Variation of the contact length with cutting speed for Ti6Al4V [50]

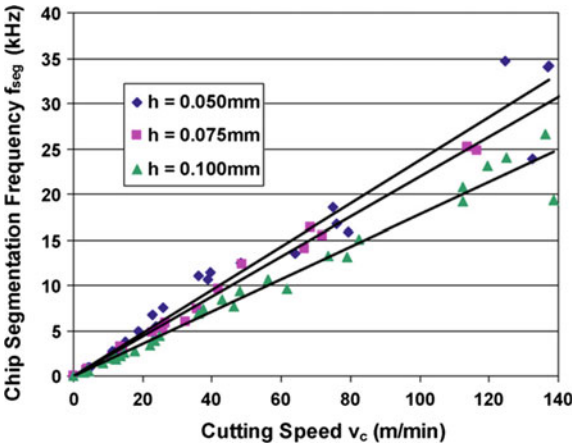

Fig. 15.9 Dependence of chip segmentation frequency on cutting speed [51]

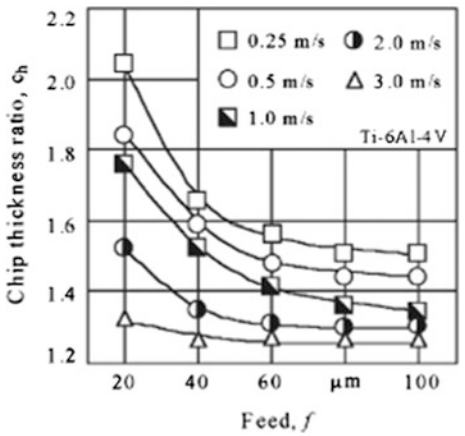

Fig. 15.10 Chip thickness ratio as a function of cutting speed and feed for Ti6Al4V [53]

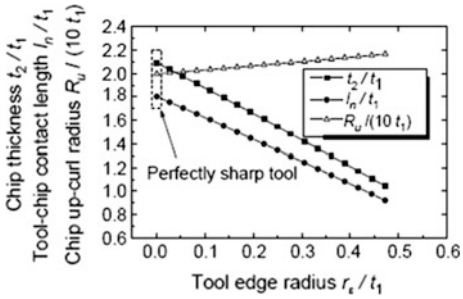

Fig. 15.11 Influence of the tool edge radius [54]

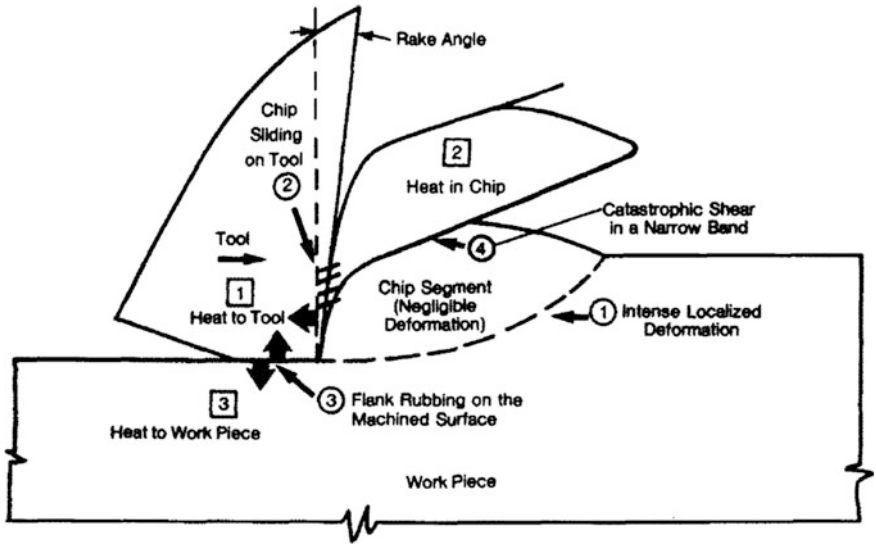

Fig. 15.12 Energy partition when machining Ti alloys [55]

concentrated shear subjects the chip to large strain creating thick chips with low shear angles and low velocity. Energy partition presented in Fig. 15.12 is also different from steel showing:

- Energy into the chip $U_c = R_1 U_s$
- Into the tool $U_t = (1 - R_1)U_s + R_3 U_{ff}$
- Into the workpiece $U_w = (1 - R_3)U_{ff}$.

(U_{ff} is the frictional energy per unit volume due to rubbing between the flank and the machined surface and R_3 is the fraction of heat conducted into the tool due to flank friction).

The high temperatures are present when using low values of the depth of undeformed layers due to the rubbing of the flank on the machined surface. When

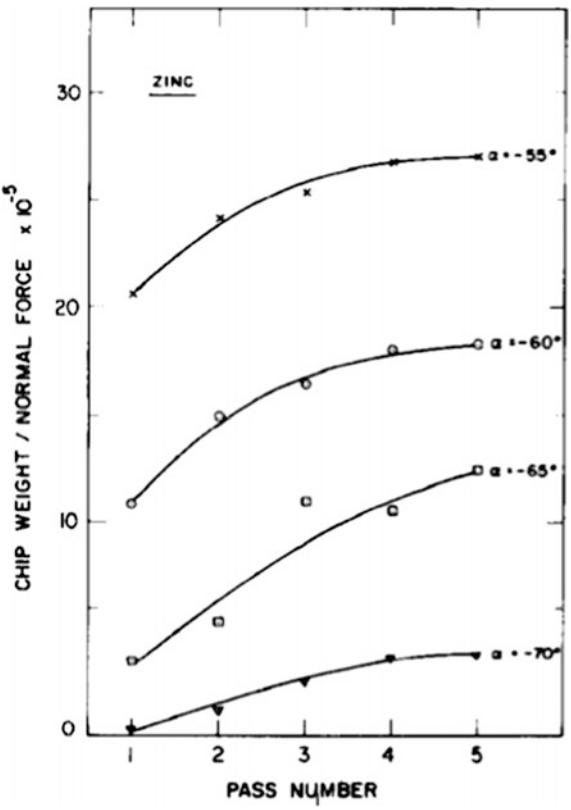

Fig. 15.13 Influence of the rake angle on chip formation [56]

the influence of the rake angle on the chip formation [56] has been investigated, it has been determined that the rake angle has a critical value of −70° when machining zinc, after which there is no chip formation (Fig. 15.13).

This issue has further been addressed [57] where it has been determined that the rake angle at which chip formation seizes is −85°. While elsewhere [58] it has been determined that this value is lower and equals −55°. The mechanism of chip formation when machining Ti6Al4V alloys has been discussed by many researchers and follows two theories. The first theory is the catastrophic thermoplastic shear where thermal softening present in the primary shear zone predominates the strain hardening caused by high strain rates in machining. The second theory is the periodic crack initiation that is considered as a consequence of high stress present during the machining process. This theory is based on the idea that cracks are formed in the primary shear zone and then rewelded through high pressure and heat originating from friction. In the following paper [59], the authors show the formation of the chip and its microstructure showing the lack of cracks in Fig. 15.14. The authors have determined that there is no phase transformation taking place classifying the bands to be deformation shear bands and confirming the catastrophic shear model.

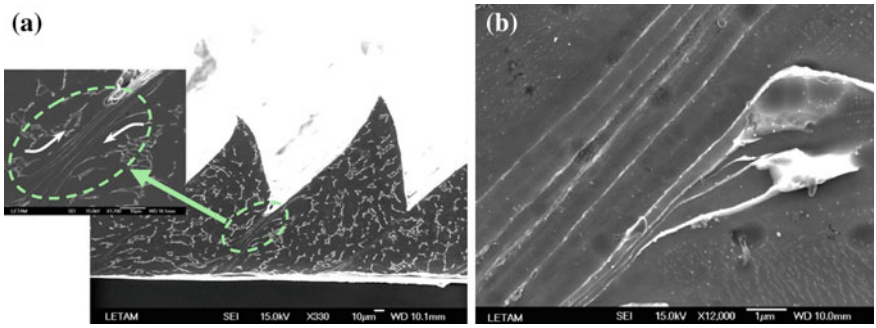

Fig. 15.14 Microstructure of the chips and shear bands in Ti6Al4V [59]

Vyas and Shaw on the other hand confirm the crack initiation presented in Fig. 15.15. They show formation of both gross cracks and micro cracks. Gross cracks continue throughout the chip width while micro cracks seem to be discontinuous. The process is based on the idea that the blocks of material which are between the gross cracks glide out with no plastic deformation while the material surrounding the micro cracks will undergo adiabatic shear in case that the temperature is high enough which may also result in phase transformations [60]. It is obvious from the fact that both theories are present and confirmed in the literature that the chip formation mechanism is not straightforward and must depend on various parameters. Investigation techniques such as X-ray diffraction, energy dispersive X-ray analysis, scanning electron microscopy, electron backscattering technique can be found useful in determining the causes of the discussed results. It is yet to be determined why these inconsistencies occur and what influences which one of the theories will be observed in the experimental work. Therefore, this can be considered a field with a vast potential for research.

15.2.5 Surface Treatments and Coatings

Mechanical methods for surface treatment can be divided into methods involving removal of surface material by cutting (machining of the surface), abrasive action (grinding and polishing) and those where the treated material surface is deformed by particle blasting. Chemical methods are based mainly on chemical reactions occurring at the interface between titanium and a solution (solvent cleaning, wet chemical etching, passivation treatments, and other chemical surface treatments such as hydrogen peroxide treatment). Electrochemical surface methods are based on different chemical reactions occurring at an electrically energized surface (electrode) placed in an electrolyte (electropolishing and anodic oxidation or anodizing).

Improving the method for both wear and corrosion resistance of titanium implant surfaces in cases where the protection by natural surface oxide films is insufficient

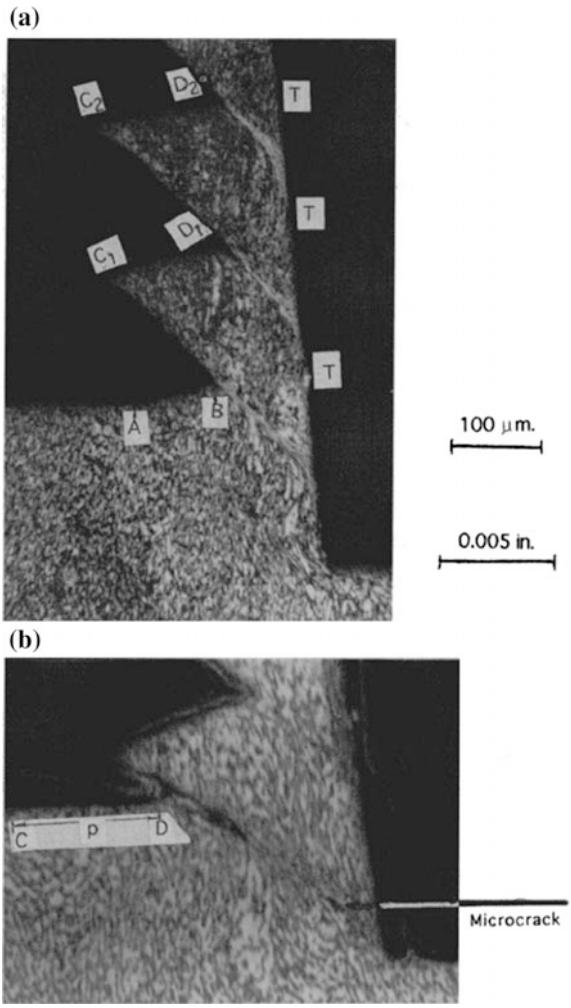

Fig. 15.15 Mechanics of chip formation showing **a** crack formation, **b** micro crack formation in Ti6Al4V [60]

can be done through the deposition of thin films. These coatings should have a sufficiently high adherence to the substrate throughout the range of conditions to which the implant is exposed in service. They must tolerate the stress and strain variations that any particular part of the implant normally impose on the coating. The coating process must not damage the substrate and must not induce failure in the substrate or introduce impurities on the surface, which may change interface properties [46]. Coatings should be wear resistant, barrier layers preventive of substrate metal ion release, to low-friction haemocompatible, non-thrombogenic surfaces [46]. Such surface modification could be done by various processes such as precipitations from the chemical vapor phase, sol–gel coatings, chemical vapor deposition (CVD), or physical vapor deposition (PVD). The properties of PVD coatings are good thickness, roughness, hardness, strength, and adhesion as well as

structure, morphology, stoichiometry, and internal stresses. PVD processes include evaporation, sputtering, ion plating, and ion implantation. They are carried out in vacuum, at backpressures of less than 1 Pa [46]. Speaking of the CVD methods, they involve the reaction of volatile components at the substrate surface to form a solid product. Typical CVD coatings are depositions of TiN, TiC, and TiC_xN_{1-x}. The early coatings were deposited onto hard metal tools such as WC–Co. Good coating uniformity is an advantage of the CVD method, lower operating temperatures of PVD method that can be combined in the plasma-assisted CVD process. Biomaterial produced by low temperature CVD and PVD is diamond-like carbon (DLC). DLC coatings can address the main biomechanical problems with the implants currently used, e.g., friction, corrosion, and biocompatibility [61].

The concept of bioactive coatings uses a principle of enabling an interfacial chemical bond between the implant and the bone tissue due to a specific biological response [62]. Surface modifications should provide distinct properties of interaction with cell molecules, which promote the adaptation or in-growth of cells or tissue onto the surface of fixation elements of a medical implant or prevent cell interaction with the implant surface.

Suitable bioactive surface modifications are comparable to those known from the stoichiometrically passivated titanium surface, in terms of high mechanical stability against shearing forces, long-term chemical stability, and corrosion resistance in a biocompatible manner. One of the most popular bioactive coatings is hydroxyapatite (HA), which is similar to the mineral phase of natural hard tissue, i.e., about 70 % of the mineral fraction of a bone has a HA-like structure. HA can also be regarded as non-resorbable in a physiological environment, as long as it remains crystalline and is of high purity. It is the most stable calcium phosphate phase in aqueous solutions [63]. It has weaker mechanical properties and low resistance to fatigue failure. Surface treatments techniques for HA are plasma spraying (vacuum plasma spraying-VPS) electrophoretic deposition of HA and micro-arc oxidation.

15.2.6 Applications in Practice

Different types of fracture repair mechanisms are known in medical practice. Incomplete fractures such as cracks, which only allow micromotion between the fracture fragments, heal with a small amount of fracture-line callus, known as primary healing. In contrast, complete fractures that are unstable, and therefore generate macromotion, heal with a voluminous callus stemming from the sides of the bone, known as secondary healing. The treatments can be nonsurgical or surgical. Nonsurgical treatments are immobilization with plaster or resin casting and bracing with a plastic apparatus. The surgical treatments of bone fractures (osteosynthesis) are divided into external fracture fixation, which does not require opening the fracture site, or internal fracture fixation, which requires opening the fracture. With external fracture fixation, the bone fragments are held in alignment by pins placed through the skin onto the skeleton, structurally supported by external

bars. With internal fracture fixation, the bone fragments are held by wires, screws, plates, and/or intramedullary devices [64].

Surgical wires are used to reattach large fragments of bone. They are also used to provide additional stability in long-oblique or spiral fractures of long bones which have already been stabilized by other means. Straight wires are called Steinmann pins. In the case of a pin diameter less than 2.38 mm, they are named Kirschner wires. They are widely used primarily to hold fragments of bones together provisionally or permanently and to guide large screws during insertion. *Screws* are the most widely used devices for fixation of bone fragments, Fig. 15.16a. There are two types of bone screws cortical bone screws, which have small threads, and cancellous screws, which have large threads to get more thread-to-bone contact. They may have either V or buttress threads. According to their ability to penetrate the cortical screws are subclassified further, into self-tapping and nonself-tapping. The self-tapping screws have cutting flutes that thread the pilot drill-hole during insertion. In contrast, the nonself-tapping screws require a tapped pilot drill-hole for insertion. The bone immediately adjacent to the screw often undergoes necrosis initially, but if the screw is firmly fixed when the bone revascularizes, permanent secure fixation may be achieved [65]. This is particularly true for titanium alloy screws or screws with a roughened thread surface, with which bone growth results in an increase in removal torque [65]. *Plates* are available in a wide variety of shapes and are intended to facilitate fixation of bone fragments, Fig. 15.16b. They range from the very rigid, intended to produce primary bone healing, to the relatively flexible, intended to facilitate physiological loading of bone. The rigidity and strength of a plate in bending depends on the cross-sectional thickness and material properties of which it is made. Consequently, the weakest region in the plate is the screw hole, especially if the screw hole is left empty, due to a reduction of the cross-sectional area in this region. The effect of the material on the rigidity of the plate is defined by the elastic modulus of the material for bending, and by the shear modulus for twisting [66]. Thus, given the same

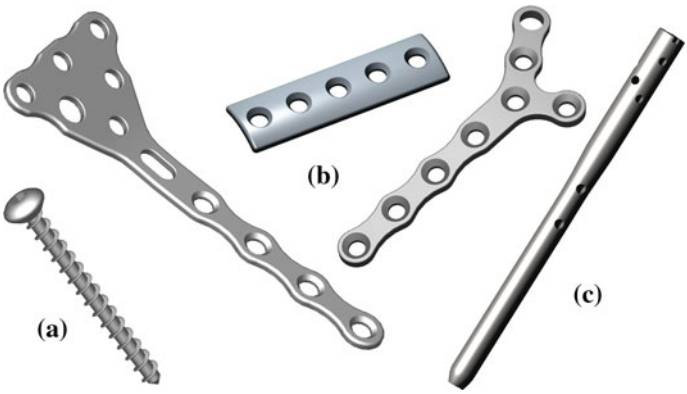

Fig. 15.16 Titanium trauma medical implants

dimensions, a titanium alloy plate will be less rigid than a stainless steel plate, since the elastic modulus of each alloy is 110 and 200 GPa, respectively. *Intramedullary devices (IM nails or rods)* are used as internal struts to stabilize long bone fractures, Fig. 15.16c. IM nails are also used for fixation of femoral neck or intertrochanteric bone fractures; however, this application requires the addition of long screws. A whole range of designs are available, going from solid to cylindrical, with shapes such as cloverleaf, diamond, and slotted cylinders. Compared to plates, IM nails are better positioned to resist multidirectional bending than a plate or an external fixator, since they are located in the center of the bone. However, their torsional resistance is less than that of the plate [66].

The design of an implant for joint replacement should be based on the kinematics and dynamic load transfer characteristic of the joint. The material properties, shape, and methods used for fixation of the implant to the patient determines the load transfer characteristics. This is one of the most important elements that determines long-term survival of the implant, since bone responds to changes in load transfer with a remodeling process, known as Wolff's law. Overloading the implant-bone interface or shielding it from load transfer may result in bone resorption and subsequent loosening of the implant [67]. *The endoprosthesis for total hip replacement* consists of a femoral component and an acetabular component, Fig. 15.16b. The femoral stem is divided into head, neck, and shaft. The femoral stem is made of Ti alloy or Co–Cr alloy and is fixed into a reamed medullary canal by cementation or press fitting. The femoral head is made of Co–Cr alloy, aluminum, or zirconium. Although Ti alloy heads function well under clean articulating conditions, they have fallen into disuse because of their low wear resistance to third bodies, e.g., bone or cement particles. The acetabular component is generally made of ultra-high molecular weight polyethylene (UHMWPE). *The prosthesis for total knee joint replacement* consists of femoral, tibial, and/or patellar components, Fig. 15.17a. Compared to the hip joint, the knee joint has a more complicated geometry and movement mechanics, and it is not intrinsically stable.

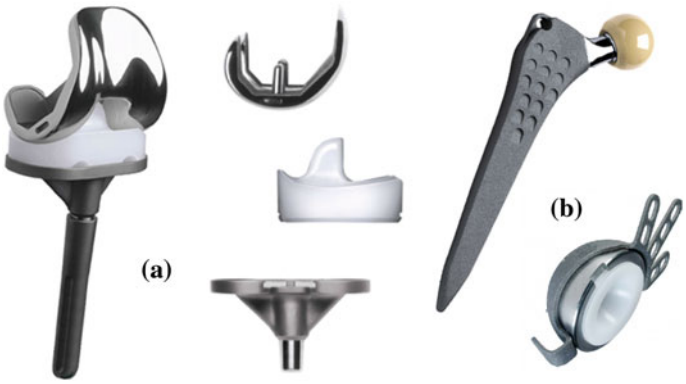

Fig. 15.17 Titanium orthopedics medical devices [130]

In a normal knee, the center of movement is controlled by the geometry of the ligaments. As the knee moves, the ligaments rotate on their bony attachments and the center of movement also moves. The eccentric movement of the knee helps distribute the load throughout the entire joint surface [68]. Total knee replacements can be implanted with or without cement, the latter relying on porous coating for fixation. The femoral components are typically made of Co–Cr alloy and the monolithic tibial components are made of UHMWPE. In modular components, the tibial polyethylene component assembles onto a titanium alloy tibial tray. The patellar component is made of UHMWPE, and a titanium alloy back is added to components designed for uncemented use.

For maxillofacial osteosynthesis in *the cranio-facial and mandibular areas titanium plate and screw systems* are preferred. In order to make them pliable, many of the plates are made from CP titanium sheet that is in the soft-recrystallized condition. The corresponding screws are either made from CP titanium or alloy and can be as small as 1 mm in diameter [69].

15.3 Shape Memory Alloys

15.3.1 Introduction

Smart materials have been given a lot of attention mainly for their innovative use in practical applications. One example of such materials is also the family of shape memory alloys (SMA) which are arguably the first well known and used smart material. Shape memory alloys possess a unique property according to which, after being deformed at one temperature, they can recover to their original shape upon being heated to a higher temperature. The effect was first discussed in the 1930s by Ölander [70] and Greninger and Mooradian [71]. The basic phenomenon of the shape memory effect was widely reported a decade later by Russian metallurgist G. Kurdjumov and also by Chang and Read [72]. However, presentation of this property to the wider public came only after the development of the nickel–titanium alloy (nitinol) by Buehler and Wang [73]. Since then, research activity in this field has been intense, and a number of alloys have been investigated, including Ag–Cd, Au–Cd, Cu–Zn, Cu–Zn–Al, Cu–Al–Ni, Cu–Sn, Cu–Au–Zn, Ni–Al, Ti–Ni, Ti–Ni–Cu, Ni–Ti–Nb, Ti–Pd–Ni, In–Ti, In–Cd and others. Crystallography of shape memory alloys have been studied for the past four decades. Only a fraction of the available literature is listed here [74–83]. Because these materials are relatively new, some of the engineering aspects of the material are still not well understood. Many of the typical engineering descriptors, such as Young's modulus and yield strength, do not apply to shape memory alloys since they are very strongly temperature dependent. On the other hand, a new set of descriptors must be introduced, such as stress rate and amnesia. That is why numerous constitutive models have been proposed over the past 25 years to predict thermomechanical behavior [84–97].

15.3.1.1 Thermomechanical Behavior

These materials have been shown to exhibit extremely large, recoverable strains (on the order of 10 %), and it is these properties as functions of temperature and stress that allow SMAs to be utilized in many exciting and innovative applications. From a macroscopic point of view, the mechanical behavior of SMAs can be separated into two categories: the *shape memory effect* (SME), where large residual (apparently plastic) strain can be fully recovered upon raising the temperature after loading and unloading cycle; and the *pseudoelasticity* or *superelasticity*, where a very large (apparently plastic) strain is fully recovered after loading and unloading at constant temperature. Both effects are results of a martensite phase transformation. In a stress-free state, an SMA material at high temperatures exists in the parent phase (usually a body-centered cubic crystal structure, also referred as the austenite phase). Upon decreasing the material temperature, the crystal structure undergoes a self-accommodating crystal transformation into martensite phase (usually a face-centered cubic structure). The phase change in the unstressed formation of martensite from austenite is referred to as 'self-accommodating' due to the formation of multiple martensitic variants and twins that prohibits the incurrence of a transformation strain. The martensite variants, evenly distributed throughout material, are all crystallographically equivalent, differing only by habit plane. The process of self-accomodation by twinning allows an SMA material to exhibit large reversible strains with stress. However, the process of self-accomodation in ordinary materials like stainless steel does not take place by twinning but via a mechanism called slip. Since slip is a permanent or unreversible process, the shape memory effect cannot occur in these materials. The difference between the twinning and slip process is shown in Fig. 15.18.

In the stress-free state, an SMA material has four transition temperatures, designated as M_f, M_S, A_S, A_f, i.e., Martensite Finish, Martensite Start, Austenite Start, and Austenite Finish, respectively. In the case of 'Type I' materials, temperatures are arranged in the following manner: $M_f < M_S < A_S < A_f$. A change of temperature within the range $M_S < T < A_S$ induces no phase changes and both phases can coexist within $M_f < T < A_f$. With these four transformation temperatures and the concepts of self-accommodation, the shape memory effect can be adequately explained. As an example let us consider a martensite formed from the parent phase

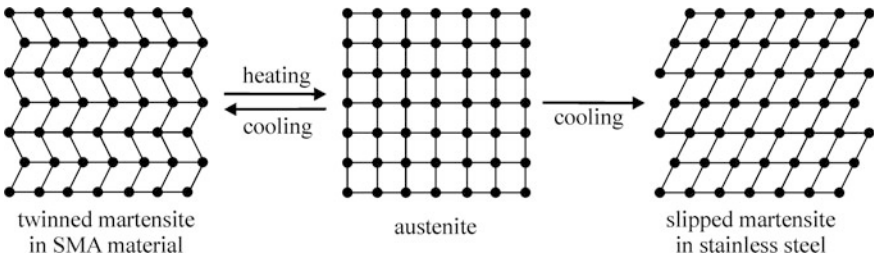

Fig. 15.18 Martensite transformation in shape memory alloys and steels

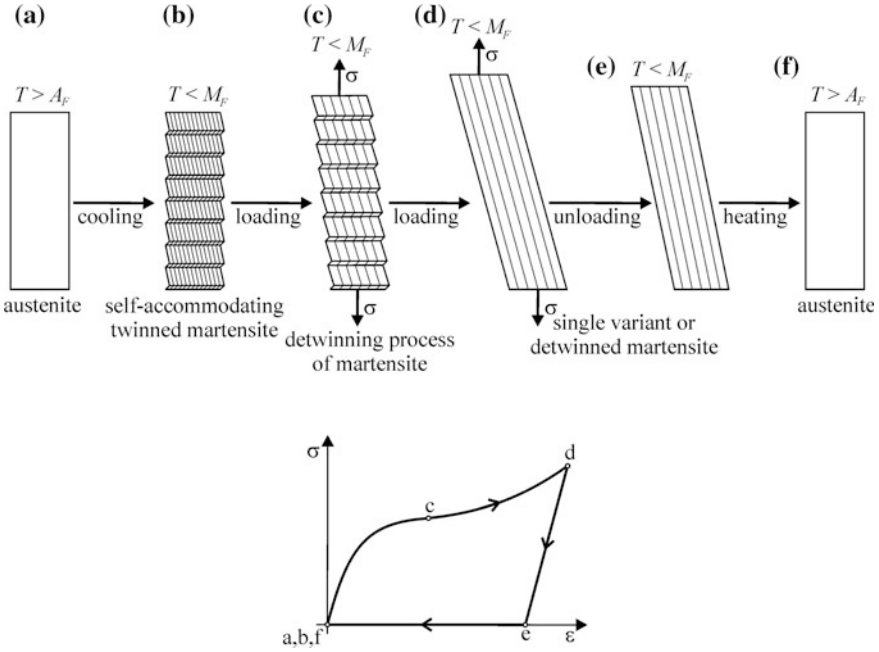

Fig. 15.19 Shape memory effect

(Fig. 15.19a) cooled under stress-free conditions through M_S and M_f. This material has multiple variants and twins present (Fig. 15.19b), all crystallographically equivalent but with different orientation (different habit plane indices). When a load applied to this material reaches a certain critical stress, the pairs of martensite twins begin 'de-twinning' to the stress-preferred twins (Fig. 15.19c). It means that the multiple martensite variants begin to convert to a single variant determined by alignment of the habit planes with the direction of loading (Fig. 15.19d). During this process of reorientation, the stress rises very slightly in comparison to the strain. As the single variant of martensite is thermodynamically stable at $T < A_S$, upon unloading there is no conversion to multiple variants and only a small elastic strain is recovered, leaving the material with a large residual strain (Fig. 15.19e). The de-twinned martensite material can recover the entire residual strain by simply heating above A_f; the material then transforms to the parent phase, which has no variants, and recovers to its original size and shape (Fig. 15.19f), thus creating the shape memory effect.

The pseudoelastic effect can be explained, if an SMA material is considered to be entirely in the parent phase (with $T > A_f$), Fig. 15.20a. When stress is applied to this material, there is a critical stress at which the crystal phase transformation from austenite to martensite can be induced, Fig. 15.20b. Due to the presence of stress during the transformation, specific martensite variants will be formed preferentially and at the end of transformation, the stress-induced martensite will consist of a

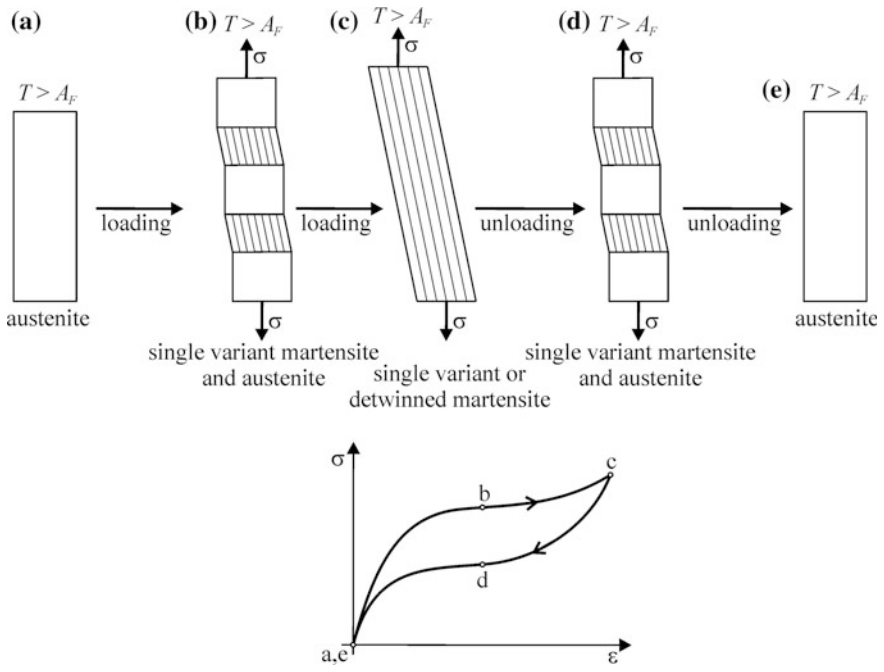

Fig. 15.20 Pseudoelasticity or superelasticity

single variant of detwinned martensite, Fig. 15.20c. During unloading, a reverse transformation to austenite occurs because of the instability of martensite at $T > A_f$ in the absence of stress, Fig. 15.20e. This recovery of high strain values upon unloading yields a characteristic hysteresis loop, diagram in Fig. 15.20, which is known as pseudoelasticity or superelasticity.

Many of the possible medical applications of SMA materials in the 1980s were attempting to use the thermally activated memory effect. However, temperature regions tolerated by the human body are very limited. Small compositional changes around the 50–50 % of Ti–Ni ratio can make dramatic changes in the operating characteristics of the alloy. Therefore, very precise control of phase transition temperatures is required. On the other hand, pseudoelasticity is ideally suited to medical applications since the temperature region of optimum effect can easily be located to encompass ambient temperature through body temperature.

15.3.2 Biocompatibility

It is important to understand the direct effects of an individual component of the alloy since it can dissolve in the body due to corrosion and it may cause local and systemic toxicity, carcinogenic effects, and immune response. The cytotoxicity of

elementary nickel and titanium has been widely researched, especially in the case of nickel, which is a toxic agent and allergen [98–100]. Nickel is known to have toxic effects on soft tissue structures at high concentrations and also appears to be harmful to bone structures, but substantially less than cobalt or vanadium, which are also routinely used in implant alloys. Experiments with toxic metal salts in cell cultures have shown decreasing toxicity in the following order: Co > V > Ni > Cr > Ti > Fe [101]. The dietary exposure to nickel is 160–600 mg/day. Fortunately most of it is eliminated in the feces, urine, and sweat. Pure nickel implanted intramuscularly or inside bone has been found to cause severe local tissue irritation and necrosis and high carcinogenic and toxic potencies. Due to corrosion of medical implants, a small amount of these metal ions is also released into distant organs. Toxic poisoning is later caused by the accumulation, processing and subsequent reaction of the host to the corrosion of the Ni-containing implant. Nickel is also one of the structural components of the metalloproteins and can enter the cell via various mechanisms. Most common Ni^{2+} ions can enter the cell utilizing the divalent cation receptor or via the support with Mg^{2+}, which are both present in the plasma membrane. Nickel particles in cells can be phagocytosed, which is enhanced by their crystalline nature, negative surface energy, appropriate particle size (2–4 μm), and low solubility. Other nickel compounds formed in the body are most likely to be NiCl and NiO, and fortunately there is only a small chance that the most toxic and carcinogenic compounds like Ni_3S_2, are to be formed. Nickel in soluble form, such as Ni^{2+} ions, enters through receptors or ion channels and binds to cytoplasmic proteins and does not accumulate in the cell nucleus at concentrations high enough to cause genetic consequences. These soluble Ni^{2+} ions and are rapidly cleaned from the body. However, the insoluble nickel particles containing phagocytotic vesicles fuse with lysosomes, followed by a decrease of phagocytic intravesicular pH, which releases Ni^{2+} ions from nickel containing carrier molecules. The formation of oxygen radicals, DNA damage, and thereby inactivation of tumor suppressor genes is contributed by that.

On the other hand, titanium is recognized to be one of the most biocompatible materials due to the ability to form a stable titanium oxide layer on its surface. In an optimal situation, it is capable of excellent osteointegration with the bone and it is able to form a calcium phosphate-rich layer on its surface, Fig. 15.21, very similar

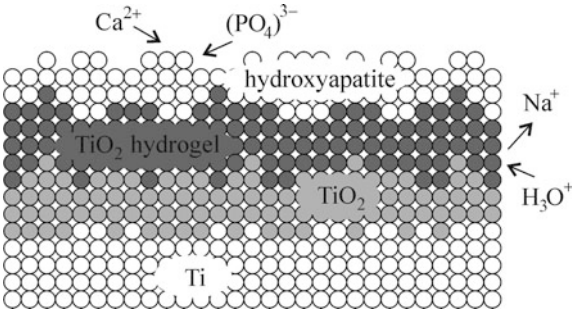

Fig. 15.21 Formation of hydroxyapatite layer on titanium oxide film [131]

to hidroxyapatite which also prevents corrosion. Another advantageous property is that in case of damaging the protective layer the titanium oxides and Ca-P layer regenerate.

The properties and biocompatibility of nitinol have their own characteristics which are different from those of nickel or titanium alone. In vitro NiTi biocompatibility studies on the effects of cellular tolerance and its cytotoxicity have been performed on various cell culture models [102, 103]. Human monocytes and microvascular endothelial cells were exposed to pure nickel, pure titanium, stainless steel, and nitinol. Nitinol has been shown to release higher concentrations of Ni^{2+} ions in human fibroblast and osteoblast cultures, which did not affect cell growth [104–106]. Metal ion release study also revealed very low concentrations of nickel and titanium that were released from nitinol. Researchers therefore concluded that nitinol is not genotoxic.

For in vivo biocompatibility studies of nitinol effect, different experiments have been done on animals. Several in vivo nitinol biocompatibility studies that were done in the past decade disclosed no allergic reactions, no traces of alloy constituents in the surrounding tissue and no corrosion of implants. Studies of rat tibiae response to NiTi, compared with Ti-6Al-4V and stainless steel, showed that the number and area of bone contacts was low around NiTi implants, but the thickness of contact was equal to that of other implants. Normal new bone formation was seen in rats after 26 weeks after implantation. Good biocompatibility results of NiTi are attributed to the fact that implants are covered by a titanium oxide layer, where only small traces of nickel are being exposed.

15.3.2.1 Corrosion Behavior

The body is a complicated electrochemical system that constitutes an aggressive corrosion environment for implants which are surrounded by bodily fluids of an aerated solution containing 0.9 % NaCl, with minor amounts of other salts and organic compounds, serum ions, proteins, and cells which all may modify the local corrosion effect. High acidity of certain bodily fluids is especially hostile for metallic implants. Acidity can increase locally in the area adjacent to an implant due to inflammatory response of surrounding tissues mediating hydrogen peroxide and reactive oxygen and nitrogen compounds. The local pH changes for infected tissues or near haematoma are relatively small, however, these changes can alter biological processes and thereby the chemistry around the implant. It is known that small point corrosion or pitting prevails on surfaces of metallic implants. Another important feature is roughness of the surface which increases the reacting area of the implant and thereby adds to total amount of corrosion. Therefore, surface finishing is a major factor in improving corrosion resistance and consequently biocompatibility of medical devices [107, 108].

Corrosion resistance of SMA has also been studied in vivo on animals. Plates and stents have been implanted in dogs and sheeps for several months. Corrosion has been examined under microscope and pitting was established as predominant

after the implants were removed. Thus surface treatments and coatings were introduced. The improvement of corrosion resistance was considerable, since pitting decreased in some cases from 100 μm to only 10 μm in diameter.

15.3.3 Surface of Implant

The human response to implanted materials is a property closely related to the implant surface conditions. The major problems associated with the implants currently used are inadequate implant-tissue interface properties. Parameters that characterize surface property are chemical composition, crystallinity and heterogeneity, roughness and wettability or surface free energy that is a parameter important for cell adhesion. Each parameter is of great importance to biological response of the tissue. Another problem is implant sterilization that can remarkably modify desired parameters. Steam and dry sterilization are nowadays replaced by more advanced techniques such as hydrogen peroxide plasma, ethylene oxide, and electron and γ-ray irradiation.

The surface of NiTi SMA has revealed a tendency towards preferential oxidation of titanium. This behavior is in agreement with the fact that the free enthalpy of formation of titanium oxides is negative and exceeds in absolute value the enthalpy of formation of nickel oxides by at least two to three times. The result of oxidation is an oxide layer of a thickness between 2 and 20 nm, which consists mainly of titanium oxides TiO_2, smaller amounts of elemental nickel Ni^{2+}, and low concentrations of nickel oxides NiO. The surface chemistry and the amount of Ni may vary over a wide range, depending on the preparation method. The ratio of Ti/Ni on polished surface is around 5.5, while boiled or autoclaved items in water show decreased concentration of Ni on the surface and the Ti/Ni ratio increases up to 23–33 [109]. Different in vitro studies have shown how the physical, chemical and biocompatible properties of the implant surface can be improved [110–114].

15.3.3.1 Surface Improvements

Some of the most important techniques for improving the properties of Ni–Ti alloy surfaces are: (1) *Surface modification using energy sources and chemical vapors* such as hydroxyapatite, laser and plasma treatment, ion implantation, TiN and TiCN chemical vapor deposits. Hydroxyapatite coatings result in the best known biocompatibility and reveal a tendency to dissolution due to its relative miscibility with body fluids. Ion implantation and laser treatments usually result in surface amorphization that improves corrosion resistance, but the obtained amorphous surface layers are often not uniform. Laser surface melting leads to an increased oxide layer, decrease of Ni dissolution and improvement of the cytocompatibility up to classical Ti level. There is also a possibility that laser melted surfaces may be enriched in nickel, and become harder than bulk and swell. TiN and TiCN coatings are known to improve corrosion

resistance but large deformations caused by the shape memory effect may cause cracking of the coating. Therefore, for plates and staples a plasma-polymerized tetrafluoroethylene has been introduced; (2) *Development of bioactive surfaces* is another approach to improve biocompatibility of the SMA. Human plasma fibronectin covalently immobilized to NiTi surface improved the attachment of cells while corrosion rates were reduced drastically. Studies showed NiTi surface improved with this method caused a development of Ca-P layers, which in fact eliminate the need for hydroxyapatite coatings [111, 115]; (3) *Electrochemical processing for oxidation in air/oxygen* is a most common way of metal surface treatment. The technique combines electrochemical processes and oxidation in various media. Growth of native passive films that are highly adhesive and do not crack or break due to dynamic properties of SMA is promoted with this method. Oxide films obtained in air have different colors, thickness, and adhesive properties, with TiO_2 as a predominant oxide type; (4) *Oxidation of SMA medical devices in water and steam* is also one of the surface improvement techniques. Implants are preliminary chemically etched and boiled in water. The result is a surface with a very low Ni concentration, while etching removes surface material that was exposed to processing procedures and acquired various surface defects and heterogeneity. It also selectively removes nickel and oxidizes titanium. Surfaces obtained after oxidation in steam show better properties than those oxidized in water; and (5) *Electrochemical techniques* are commonly used to passivate NiTi surfaces. Surface passivation using electropolishing is often considered as a treatment of first choice just because this technique is used for surface conditioning of stainless steel, Co–Cr alloys, etc. However, the universal techniques developed for surface passivation of various alloys used for medical purposes are not necessary efficient for NiTi.

It should also be noted that the implant surface coatings are not always beneficial. The major problem of titanium-based alloys is that the formation of TiO_2, according to the chemical equation $Ti + 2H_2O \rightarrow TiO_2 + 4H^+ + 4e^-$, reduces the pH level at the titanium/coating interface. This means that if the coating is composed of hydroxyapatite, it can dissolve, which gradually leads to detachment of the coating.

15.3.4 Medical Applications

The trends in modern medicine are to use less invasive surgery methods that are performed through small, leak tight portals into the body called trocars. Medical devices made from SMAs use a different physical approach and can pull together, dilate, constrict, push apart and have made difficult or problematic tasks in surgery quite feasible. Therefore unique properties of SMAs are utilized in a wide range of medical applications. Some of the devices used in various medical applications are listed below.

Stents are most rapidly growing cardiovascular SMA cylindrical mesh tubes that are inserted into blood vessels to maintain the inner diameter of a blood vessel. The

product has been developed in response to limitations of balloon angioplasty, which resulted in repeated blockages of the vessel in the same area. Ni–Ti alloys have also become the material of choice for superelastic *self-expanding* (*SE*) *stents* that are used for a treatment of the superficial femoral artery disease (Fig. 15.22a). The SE nitinol stents are produced in the open state mainly with laser cut tubing and later compressed and inserted into the catheter. They can also be produced from wire and laser welded or coiled striped etched sheet. Before the compression stage, the surface of the stent is electrochemically polished and passivated to prescribed quality. Deployment of the SE stent is made with the catheter. During the operation procedure, when the catheter is in the correct position in the vessel, the SE stent is pushed out and then it expands against the inner diameter of the vessel due to a rise in temperature (thermally triggered device). This opens the iliac artery to aid in the normal flow of blood. The delivery catheter is then removed, leaving the stent within the patient's artery. Recent research has shown that implantation of a self-expanding stent provides better outcomes, for the time being, than balloon angioplasty [116–118]. *The Simon Inferior Vena Cava* (*IVC*) *filter* was the first SMA cardiovascular device. It is used for blood vessel interruption for preventing pulmonary embolism via placement in the vena cava. The Simon filter is filtering clots that travel inside bloodstream [119]. The device is made of SMA wire curved similarly to an umbrella that traps the clots that are better dissolved in time by the bloodstream. For insertion, the device is exploiting the shape memory effect, i.e., the original form in the martensitic state is deformed and mounted into a catheter. When the device is released, the body's heat causes the filter to return to its predetermined shape. *The Septal Occlusion System* is indicated for use in patients with complex ventricular septal defects (VSD) of significant size to warrant closures that are considered to be at high risk for standard transatrial or transarterial surgical closure based on anatomical conditions and/or based on overall medical condition. The system consists of two primary components; a permanent implant, which is constructed of an SMA wire framework to which polyester fabric is attached, and a coaxial polyurethane catheter designed specifically to facilitate attachment, loading, delivery and deployment to the defect [120]. The implant is placed by advancing the delivery catheter through blood vessels to the site of the defect inside the heart. The implant remains in the heart and the delivery catheter is removed. Instruments for minimally invasive surgery used in endoscopic surgery could not be feasible without implementation of SMA materials. The most representative instruments such as *guidewires*, *dilatators* and *retrieval baskets* exploit good kink resistance of SMAs [121]. *Open-heart stabilizers* are instruments similar to a steerable joint endoscopic camera. In order to perform bypass operations on the open-heart stabilizers are used to prevent regional heart movements while performing surgery. Another employment of the unique properties of SMAs such as constant force and superelasticity in heart surgery is a *tissue spreader* used to spread fatty tissue of the heart (Fig. 15.22b).

In general, conventional orthopedic implants by far exceed any other SMA implant in weight or volume. They are used as fracture fixation devices, which may or may not be removed and as joint replacement devices. Bone and nitinol have similar

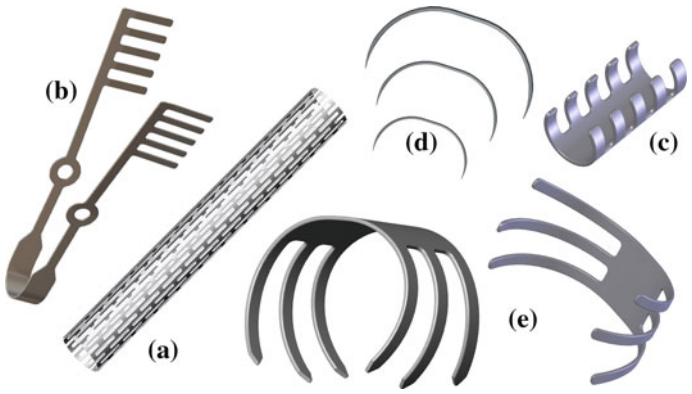

Fig. 15.22 Examples of nitinol medical devices

stress–strain characteristics, which makes nitinol a perfect material for production of bone fixation plates, nails, and other trauma implants [122]. In traditional trauma surgery bone plates and nails fixated with screws are used for fixation of broken bones. Shape memory fixators are one step forward applying a necessary constant force to faster fracture healing. *The SMA embracing fixator*consists of a body and sawtooth arms [123]. It embraces the bone about 2/3 of the circumference (Fig. 15.22c). The free ends of the arms that exceed the semi-circle are bent more medially to match the requirement fixation of a long tubular body whose cross section is not a regular circle. The applied axial compression stress is beneficial for enhancing healing and reducing segmental osteoporosis caused by a stress shielding effect. Its martensitic transformation temperature is 4–7 °C and shape recovery temperature is around the body's normal temperature, 37 °C. Similar to the embracing fixator is the so called *Swan-Like Memory-Compressive Connector* (*SMC*) for treatment of fracture and nonunion of upper limb diaphysis. The working principle of the device is similar with one important improvement. The SMC trauma implant is able to put constant axial stress to a fractured bone [124]. For fixation of tibial and femoral fractures nails fixated with screws are normally used. New *SMA inter-locking intramedullary nails* have many advantages compared to traditional ones. For example, when cooled SMA inter-locking nails are inserted into a cavity, guiding nails are extracted and body heat causes bending of nails into a preset shape applying constant pressure in the axial direction of the fractured bone [125]. The SMA effect is also used in surgical fixators made from wire. Certain devices that have been developed to fix vertebra in spine fractures are similar to an ordinary staple. *Staple shaped compression medical devices* are also used for internal bone fixation [126]. The compression staple is one of most simple and broadly used SMA devices in medicine (Fig. 15.22d). Since its introduction in 1981, over a thousand patients have been all successfully treated using this device. *The SMA Patellar Concentrator* was designed to treat patellar fractures (Fig. 15.22e). The device exerts continuous compression for the fixation of patella fracture. The shape of patellar concentrator consists of two basic patellae claws,

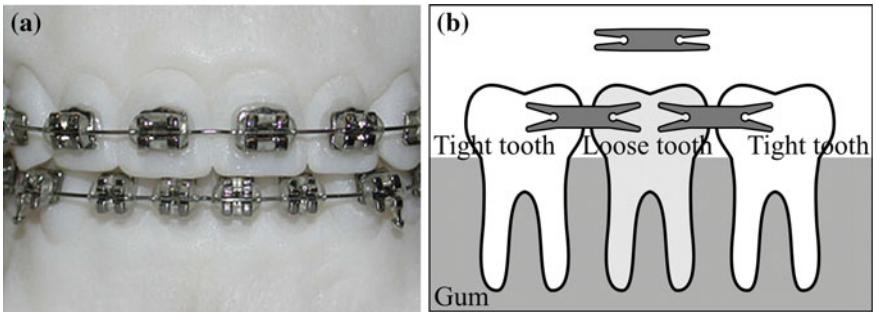

Fig. 15.23 Dental applications of nitinol

conjunctive waist, and three apex patellae claws. The thickness of the device may vary between 1.8 and 2.2 mm depending on different sizes of the concentrator. In clinical surgery, the claws are unfolded and put over fractured patella. Exposed to body temperature, the device tends to recover to its original state resulting in a recovery compressive force [127].

Dentists are using devices made from SMA for different purposes. NiTi-based SMA material performs exceptionally at high strains in strain-controlled environments, such as exemplified with *dental drills* for root canal procedures. The advantage of these drills is that they can be bent to rather large strains and still accommodate the high cyclic rotations [120]. Superelastic SMA wires have found wide use as orthodontic wires as well, Fig. 15.23a. *NiTi orthodontic archwire* was first produced in batches and clinically used in China in the beginning of 1980s [128]. Due to its unique property—superelasticity—the wire exerts gentle and retentive force to teeth, which is superior to stainless steel wire. Shape memory bracelets do not require as frequent visits to the dentist as the classical ones because of their ability to self adjust. The therapeutic period is therefore cut down by 50 %.

Lately a special *fixator for mounting bridgework* has been developed, Fig. 15.23b. A small piece of SMA metal is notch on both sides and placed between teeth and bridgework. As the temperature rises the notched area of metal is expanded on both sides causing a permanent hold of bridgework. The tooth fixator can also be used to prevent a loose tooth from falling out.

15.4 Conclusions

The use of titanium alloys as biomaterials has been growing due to their reduced elastic modulus, superior biocompatibility, high strength-to-weight ratio and enhanced corrosion resistance when compared to more conventional stainless steel and Co–Cr alloys. Ti-6Al-4V (and Ti-6Al-4V ELI), the most common titanium alloy is still the most extensively used titanium alloy for medical applications.

However, V and Al have been found to be toxic to the human body. In this context, β titanium alloys have been studied and developed and due to their high strength, biocompatible behavior, low elastic modulus, superior corrosion resistance, and good formability, they are likely to replace the classic α + β-type Ti-6Al-4V for medical applications in the near future.

SMA implants and medical devices have been successful because they offer a possibility of performing less invasive surgeries. Nitinol wires in medical instruments are more kink resistant and have smaller diameters compared to stainless steel 316L or polymer devices. Research to develop composite materials, containing SMA that will prove cost efficient and porous SMAs that will enable the transport of body fluids from the outside to inside of the bone is currently underway.

Acknowledgments The authors thank Springer and Wiley publishers for allowing the authors permission to reprint and update this chapter that was originally published in, 'Surface Engineered Surgical Tools and Medical Devices,' originally published by Springer in 2007 (ISBN 978-0387-27026-5). The authors also wish to thank Springer for allowing the authors to update the chapter with material that was published in 'Machining with Nanomaterials' also published by Springer. *Reprinted with kind permission from Springer Science + Business Media B.V and Wiley Publishers.*

References

1. Sibum, H. (2003). Titanium and titanium alloys—from raw material to semi-finished products. *Advanced Engineering Materials, 5*(6), 393.
2. Wang, K. (1996). The use of titanium for medical applications in the USA. *Materials Science and Engineering A, 213*, 134.
3. Rack, H. J., & Qazi, J. I. (2006). Titanium alloys for biomedical applications. *Materials Science and Engineering C, 26*, 1269.
4. Niinomi, M. (2002). Recent metallic materials for biomedical applications. *Metallurgical and Materials Transactions, 33A*, 477.
5. Lütjering, G., & Williams, J. C. (2003). *Titanium*. Berlin: Springer-Verlag.
6. Long, M., & Rack, H. J. (1998). Titanium alloys in total joint replacement—a materials science perspective. *Biomaterials, 19*, 1621.
7. Katti, K. S. (2004). Biomaterials in total joint replacement. *Colloids and Surfaces B: Biointerfaces, 39*, 133.
8. Disegi, J. A. (2000). Titanium alloys for fracture fixation implants, Injury. *International Journal of the Care of the Injured, 31* (200) S-D14.
9. He, G., & Hagiwara, M. (2006). Ti alloy design strategy for biomedical applications. *Materials Science and Engineering C, 26*, 14.
10. Bannon, B. P., & Mild, E. E. (1983). Titanium alloys for biomaterial application: An overview, titanium alloys in surgical implants. In H. A. Luckey & F. Kubli, Jr (Eds.), *American Society for Testing and materials* (pp. 7–15). Pennsylvania: ASTM STP 796.
11. Oliveira, V., Chaves, R. R., Bertazzoli, R., & Caram, R. (1998). Preparation and characterization of Ti-Al-Nb orthopedic implants. *Brazilian Journal of Chemical Engineering, 17*, 326.
12. Boyer, R. R. (1996). Ana overview on the use of titanium in the aerospace industry. *Materials Science and Engineering A, 213*, 103.

13. Ferrero, J. G. (2005). Candidate materials for high-strength fastener applications in both the aerospace and automotive industries. *Journal of Materials Engineering and Performance, 14*, 691.
14. Semlitsch, M., Staub, F., & Weber, H. (1985). Titanium-aluminum-niobium alloy, development for biocompatible, high-strength surgical implants. *Biomedizinische Technik, 30*, 334.
15. Vail, T. P., Glisson, R. R., Koukoubis, T. D., & Guilak, F. (1998). The effect of hip stem material modulus on surface strain in human femora. *Journal of Biomechanics, 31*, 619.
16. Niinomi, M., Akahori, T., Takeuchi, T., Katsura, S., Fukui, H., & Toda, H. (2005). Mechanical properties and cyto-toxicity of new beta type titanium alloy with low melting points for dental applications. *Materials Science and Engineering C, 25*, 417.
17. Kikuchi, M., Takahashi, M., & Okuno, O. (2006). Elastic moduli of cast Ti-Au, Ti-Ag, and Ti-Cu alloys. *Dental Materials, 22*, 641.
18. Kim, H. S., Kim, W.-Y., & Lim, S.-H. (2006). Microstructure and elastic modulus of Ti-Nb-Si ternary alloys for biomedical applications. *Scripta Materialia*, *54*, 887–891.
19. Gross, S., & Abel, E. W. (2001). A finite element analysis of hollow stemmed hip prostheses as a means of reducing stress shielding of the femur. *Journal of Biomechanics, 34*, 995.
20. Hao, Y. L., Niinomi, M., Kuroda, D., Fukunaga, K., Zhou, Y. L., & Yang, R. (2003). Aging response of the Young's modulus and mechanical properties of Ti-29Nb-13Ta-4.6Zr. *Metallurgical and Materials Transactions, 34A*, 1007–1012.
21. Hao, Y. L., Niinomi, M., Kuroda, D., Fukunaga, K., Zhou, Y. L., Yang, R., et al. (2002). Young's modulus and mechanical properties of Ti-29Nb-13Ta-4.6Zr in relation to α'' martensite. *Metallurgical and Materials Transactions, 33A*, 3137–3144.
22. Gunawarman, B., Niinomi, M., Akahori, T., Souma, T., Ikeda, M., & Toda, H. (2005). Mechanical properties and microstructures of low cost β titanium alloys for healthcare applications. *Materials Science and Engineering C, 25*, 304.
23. Sakaguchi, N., Niinomi, M., Akahori, T., Takeda, J., & Toda, H. (2005). Relationship between tensile deformation behavior and microstructure in Ti-Nb-Ta-Zr. *Materials Science and Engineering C, 25*, 363.
24. Kuroda, D., Niinomi, M., Morinaga, M., Kato, Y., & Yashiro, T. (1998). Design and mechanical properties of new β type titanium alloys for implant materials. *Materials Science and Engineering A, 243*, 244.
25. Peters, M., Hemptenmacher, H., Kumpfert, J., & Leyens, C. (2003). In C. Leyens & M. Peters (Eds.), *Titanium and Titanium Alloys* (pp. 1–57). New York: Wiley-VCH.
26. Ari-Gur, P., & Semiatin, S. L. (1998). Evolution of microstructure, macrotexture and microtexture during hot rolling og Ti-6Al-4V. *Materials Science and Engineering A, 257*, 118.
27. Lütjering, G. (1999). Property optimization through microstructural control in titanium and aluminum alloys. *Materials Science and Engineering A, 263*, 117.
28. Prasad, Y. V. R. K., & Seshacharyulu, T. (1998). Processing maps for hot working of titanium alloys. *Materials Science and Engineering A, 243*, 82.
29. Freese, H. L., Volas, M. G., & Wood, J. R. in: D. M. Brunette, P. Tengvall, M. Textor & P. Thomsen (Eds.), *Titanium in medicine* (pp. 25–51). New York: Springer.
30. Froes, F. H., & Bomberger, H. B. (1985). The beta titanium alloys. *Journal of Metals, 37*, 28.
31. Karasevskaya, O. P., Ivasishin, O. M., Semiatin, S. L., & Matviychuk, Y. V. (2003). Deformation behavior of beta-titanium alloys. *Materials Science and Engineering A, 354*, 121.
32. Lin, D. J., Chern, J. H., & Ju, C. P. (2002). Effect of omega phase on deformation behavior of Ti-7.5Mo-xFe alloys. *Materials Chemistry and Physics, 76*, 191.
33. Moffat, D. L., & Larbalestier, D. C. (1988). The competition between the alpha and omega phases in aged Ti-Nb alloys. *Metallurgical Transactions, 19A*, 1687.
34. Flower, H. M., Henry, S. D., & West, D. R. F. (1974). The $\beta\alpha \leftrightarrows \alpha\beta$ transformation in dilute Ti-Mo alloys. *Journal of Materials Science, 9*, 57.

35. Tang, X., Ahmed, T., & Rack, H. J. (2000). Phase transformations in Ti-Nb-Ta and Ti-Nb-Ta-Zr alloys. *Journal of Materials Science, 35*, 1805.
36. Dobromyslov, A. V., & Elkin, V. A. (2003). Martensitic transformation and metastable b-phase in binary titanium alloys with d-metals of 4–6 periods. *Materials Science and Engineering A, 354*, 121.
37. Dobromyslov, A. V., & Elkin, V. A. (2006). The orthorhombic α″-phase in binary titanium base alloys with d-metals of V–VIII groups. *Materials Science and Engineering A, 438*, 324–326 (in press).
38. Niinomi, M. (1998). Mechanical properties of biomedical titanium alloys. *Materials Science and Engineering A, 243*, 231.
39. Brunski, J. B. (2004). In B. D. Ratner, A. S. Hoffman, F. J. Schoen, & J. E. Lemons (Eds.), *Biomaterials science—an introduction to materials in medicine* (pp. 137–153). San Diego: Elsevier Academic Press.
40. Wataria, F., Yokoyamaa, A., Omorib, M., Hiraic, T., Kondoa, H., Uoa, M., & Kawasakia, T. (2004). Biocompatibility of materials and development to functionally graded implant for bio-medical application. *Composites Science and Technology, 64*, 893–908.
41. Black, J. (1992). *Biological performance of materials* (2nd ed.). New York: M. Dekker Inc.
42. Park, J. B., & Kim, J. B. (2000). Metallic biomaterials, chapter 37. In J. D. Bronzino & B. Raton (eds.), *The biomedical engineering handbook*, (2nd ed.). Boca Raton: CRC Press LLC.
43. Feighan, J. E., Goldberg, V. M., Davy, D., Parr, J. A., & Stevenson, S. (1995). The influence of surfaceblasting on the incorporation of titanium-alloy implants in a rabbit intramedullary model. *The Journal of Bone & Joint Surgery. American Volume, 77A*, 1380–1395.
44. Tengvall, P., & Lundstrom, I. (1992). Physico-chemical considerations of titanium as a biomaterial. *Clinical Materials, 9*, 115–134.
45. Henrich, V. E., & Cox, P. A. (1994). *The surface science of metal oxides*. Cambridge: Cambridge University Press.
46. Thull, R., & Grant, D. (2001). Physical and chemical vapor deposition and plasma-assisted techniques for coating titanium. In D. M. Brunette, P. Tengvall, M. Textor & P. Thomsen (Eds.), *Titanium in medicine* (pp. 284–335). Berlin Heidelberg: Springer-Verlang.
47. Klocke, F. (2001). *Manufacturing technology I*. Aachen: WZL-RWTH.
48. Jackson, M. J., & Morrell, J. S. (Eds.). (2015). *Machining with Nanomaterials* (2nd ed.). New York and Heidelberg: Springer.
49. Donachie, M. (2000). *Titanium—a technical guide* (2nd ed.). Materials Park, OH: ASM International.
50. Iqbal, S. A., Mativenga, P. T., & Sheikh, M. A. (2009). A comparative study of the tool-chip contact length in turning of two engineering alloys for a wide range of cutting speeds. *International Journal of Advanced Manufacturing Technology, 42*, 30–40.
51. Sun, J., & Guo, Y. B. (2008). A new multi view approach to characterize 3D chip morphology and properties in end milling titanium Ti6Al4V. *International Journal of Machine Tools and Manufacture, 48*, 1486–1494.
52. Cotterell, M., & Byrne, G. (2008). Dynamics of chip formation during orthogonal cutting of titanium alloy Ti-6Al-4V. *CIRP Annals - Manufacturing Technology, 57*, 93–96.
53. Barry, J., Byrne, G., & Lennon, D. (2000). Observations on chip formation and acoustic emission in machining. *International Journal of Machine Tools and Manufacture, 41*, 1055–1070.
54. Fang, N. (2003). Slip-line modeling of machining with a rounded-edge tool—Part II: Analysisof the size efect and the shear strain-rate. *Journal of the Mechanics and Physics of Solids, 51*, 43–762.
55. Komanduri, R. (1982). Some clarifications on the mechanics of chip formation when machining titanium alloys. *Wear, 76*, 15–34.
56. Abdelmoneim, M. E., & Scrutton, R. F. (1973). Post-machining plastic recovery and the law of abrasive wear. *Wear, 24*, 1–13.

57. Komanduri, R. (1971). Aspects of machining with negative rake tools simulating grinding. *International Journal of Design and Research MTDR, 11*, 223–233.
58. Rubenstein, C., Groszman, F. K., & Koenigsberger, F. (1967). *Force measurements during cutting tests with single point tools simulating action of single abrasive grit*. Paper presented at the International Industrial Diamond Conference.
59. Puerta Velasquez, J. D., Bolle, B., Chevrier, P., Geandier, G., & Tidu, A. (2007). Metallurgical study on chips obtained by high speed machining of a Ti-6 wt.%Al-4 wt.%V alloy. *Materials Science and Engineering A, 452–453*, 469–474.
60. Vyas, A., & Shaw, M. C. (1999). Mechanics of Saw-Tooth Chip Formation in Metal Cutting. *Journal of Manufacturing Science and Engineering, 121*, 163–172.
61. Morshed, M. M., McNamara, B. P., Cameron, D. C., & Hashmi, M. S. J. (2003). Stress and adhesion in DLC coatings on 316L stainless steel deposited by a neutral beam source. *Journal of Materials Processing Technology, 143*, 922–926.
62. Hench, L. L., Splittr, R. J., Allen, W. C., & Greenlec, T. K. (1971). Bonding mechanisms at the interface of ceramic prosthetic materials. *Journal of Biomedical Materials Research, 2*, 117–141.
63. de Groot, K., Klein, C. P. A. T., Wolke, J. G. C., & de Blieck-Hogervorst, J. M. A. (1990). *Plasma-sprayed coatings of calcium phosphate, CRC handbook of bioactive ceramics* (Vol. 2, pp. 133–142). Boston: CRC Press.
64. Hulth, A. (1989). Current concepts of fracture healing. *Clinical Orthopaedics and Related Research*, 249–265.
65. Hutzschenreuter, P., & Brümmer, H. (1980). Screw design and stability. In H. Uhthoff (Ed.), *Current concepts of Internal Fixation* (pp. 244–250). Berlin: Springer-Verlag.
66. Cochran, G. V. B. (1982). Biomechanics of orthopaedic structures. In *Primer in orthopaedic biomechanics* (pp. 143–215). New York: Churchill Livingstone.
67. Sarmiento, A., Ebramzadeh, E., & Gogan, W. J. (1990). Cup containment and orientation in cemented total hip arthroplasties. *Journal of Bone & Joint Surgery, 72B*(6), 996.
68. Burstein, A. H., & Wright, T. H. (1993). Biomechanics. In J. Insall, R Windsor & W. Scott (Eds.), *Surgery of the knee* (2nd ed., Vol. 7) (pp. 43–62). New York: Churchill Livingstone.
69. Perren, M. S., Pohler, O. E. M., & Schneider, E. (2001). Titanium as implant material for osteosynthesis applications. In D. M. Brunette, P. Tengvall, M. Textor & P. Thomsen (Eds.), *Titanium in medicine* (pp. 772–823). Berlin Heidelberg: Springer-Verlang.
70. Olander, A. (1932). An electrochemical investigation of solid cadmium-gold alloys. *Journal of the American Chemical Society, 54*, 3819–3833.
71. Greninger, A. B., & Mooradian, V. G. (1938). Strain transformation in metastable beta copper-zinc and beta copper-tin alloys. *AIME, 128*, 337–368.
72. Chang, L. C., & Read, T. A. (1951). Plastic deformation and diffusionless phase changes in metals-the gold-cadmium beta phase. *Transaction of the American Institute of Mining and Metallurgical Engineers, 191*(1), 47–52.
73. Buehler, W. J., & Wang, F. E. (1967). A summary of recent research on the Nitinol alloys and their potential application in ocean engineering. *Journal of Ocean Engineering, 1*, 105–108.
74. Wayman, C. M. (1964). *Introduction to the crystallography of martensitic transformations*. UK: The Macmillan Company.
75. Otsuka, K., & Wayman, C. M. (1998). *Shape memory materials*. Cambridge: Cambridge University Press.
76. Wechsler, M. S., Liberman, D. S., & Read, T. A. (1953). On the theory of the formation of martensite. *Transaction of the AIME, 197*, 1503–1515.
77. Bowles, J. S., & Mackenzie, J. K. (1954). The crystallography of martensite transformations I. *Acta Metallurgica, 2*, 129–137.
78. Saburi, T., & Wayman, C. M. (1979). Crystallographic similarities in shape memory martensites. *Acta Metallurgica, 27*(6), 979–995.

79. Adachi, K., Perkins, J., & Wayman, C. M. (1986). Type II twins in self-accommodating martensite plate variants in a Cu-Zn-Al shape memory alloy. *Acta Metallurgica, 34*(12), 2471–2485.
80. James, R. D., & Hane, K. F. (2000). Martensitic transformations and shape-memory materials. *Acta Materialia, 48*(1), 197–222.
81. Krishnan, Madangopal. (1998). The self accommodating martensitic microstructure of Ni-Ti shape memory alloys. *Acta Materialia, 46*(4), 1439–1457.
82. Inamura, T., Kinoshita, Y., Kim, J. I., Kim, H. Y., Hosoda, H., Wakashima, K., et al. (2006). Effect of {0 0 1} < 1 1 0 > texture on superelastic strain of Ti-Nb-Al biomedical shape memory alloys. *Materials Science and Engineering A, 438*, 865–869 (In Press).
83. Bhattacharya, K. (2003). *Microstructure of martensite: Why it forms and how it gives rise to the shape-memory effect, Oxford series on materials modelling* (1st ed.). Oxford: Oxford University Press.
84. Stalmans, R., Delaey, L., & Van Humbeeck, J. (1997). Generation of recovery stresses: Thermodynamic modelling and experimental verification. *Le Journal de Physique IV, 7*, 47–52.
85. Barsch, G. R., & Krumhansl, J. A. (1984). Twin boundaries in ferroelastic media without interface dislocations. *Physical Review Letters, 53*(11), 1069–1072.
86. Falk, F. (1980). Model free energy, mechanics, and thermodynamics of shape memory alloys. *Acta Metallurgica, 28*, 1773–1780.
87. Maugin, G. A., & Cadet, S. (1991). Existence of solitary waves in martensitic alloys. *International Journal of Engineering Science, 29*(2), 243–258.
88. Brinson, L. C., & Lammering, R. (1993). Finite element analysis of the behavior of shape memory alloys and their applications. *International Journal of Solids and Structures, 30*(23), 3261–3280.
89. Ivshin, Y., & Pence, T. J. (1993). A thermomechanical model for a one variant shape memory material. *Journal of Intelligent Material Systems and Structures, 5*(7), 455–473.
90. Liang, C., & Rogers, C. A. (1990). One-dimensional thermomechanical constitutive relations for shape memory materials. *Journal of Intelligent Material Systems and Structures, 1*(2), 207–234.
91. Boyd, J. G., & Lagoudas, D. C. (1994). Thermomechanical response of shape memory composites. *Journal of Intelligent Material Systems and Structures, 5*, 333–346.
92. Tanaka, K. (1986). A thermomechanical sketch of shape memory effect: One-dimensional tensile behavior. *Res Mechanica, 18*, 251–263.
93. Brinson, L. C. (1993). One-dimensional constitutive behavior of shape memory alloys: Thermomechanical derivation with non-constant material functions and redefined martensite internal variable. *Journal of Intelligent Material Systems and Structures, 4*, 229–242.
94. Lubliner, J., & Auricchio, F. (1996). Generalized plasticity and shape-memory alloys. *International Journal of Solids and Structures, 33*(7), 991–1003.
95. Panoskaltsis, V. P., Bahuguna, S., & Soldatos, D. (2004). On the thermomechanical modeling of shape memory alloys. *International Journal of Non-Linear Mechanics, 39*(5), 709–722.
96. Sun, Q. P., & Hwang, K. C. (1994). Micromechanics constitutive description of thermoelastic martensitic transformations. *Advances in Applied Mechanics, 31*, 249–298.
97. Kosel, F., & Videnic, T. (2007). Generalized plasticity and uniaxial constrained recovery in shape memory alloys. *Mechanics of Advanced Materials and Structures, 14*(1), 3–12.
98. Denkhaus, E., & Salnikow, K. (2002). Nickel essentiality, toxicity, and carcinogenicity. *Critical Reviews in Oncology/Hematology, 42*, 35–56.
99. Nieboer, E., Tom, R. T., & Sanford, W. E. (1988). Nickel metabolism in man and animals. In H. Sigel (Ed.), *Nickel and its role in biology: Metal ions in biological systems* (Vol. 23, pp. 91–121). New York: Marcel Dekker.
100. Fletcher, G. G., Rossetto, F. E., Turnbull, J. D., & Nieboer, E. (1994). Toxicity, uptake, and mutagenicity of particulate and soluble nickel compounds. *Environmental Health Perspectives*, *102*(Suppl 3), 69–79.

101. Yamamoto, A., Honma, R., & Sumita, M. (1998). Cytotoxicity evaluation of 43 metal salts using murine fibroblasts and osteoblastic cells. *Journal of Biomedical Materials Research, 39*, 331–340.
102. Shih, C., Lin, S., Chung, K., Chen, Y., Su, Y., Lai, S., et al. (2000). The cytotoxicity of corrosion products of Nitinol stent wires on cultured smooth muscle cells. *Journal of Biomedical Material Research, 52*, 395–403.
103. Wever, D. J., Veldhuizen, A. G., Sanders, M. M., Schakenraad, J. M., & Horn, J. R. (1997). Cytotoxic, allergic and genotoxic activity of a nickel-titanium alloy. *Biomaterials, 18*, 1115–1120.
104. Wataha, I. C., Lockwood, P. E., Marek, M., & Ghazi, M. (1999). Ability of Ni-containing biomedical alloys to activate monocytes and endothelial cells in vitro. *Journal of Biomedical Materials Research, 45*, 251–257.
105. Ryhänen, J., Niemi, E., Serlo, W., Niemelä, E., Sandvik, P., Pernu, H., et al. (1997). Biocompatibility of nickel-titanium shape memory metal and its corrosion behavior in human cell cultures. *Journal of Biomedical Materials Research, 35*, 451–457.
106. Wirth, C., Comte, V., Lagneau, C., Exbrayat, P., Lissac, M., Jaffrezic-Renault, N., et al. (2005). Nitinol surface roughness modulates in vitro cell response: A comparison between fibroblasts and osteoblasts. *Materials Science and Engineering C, 25*, 51–60.
107. Trepanier, C., Leung, T., Tabrizian, M., Yahia, L. H., Bienvenu, J., Tanguay, J., et al. (1999). Preliminary investigation of the effect of surface treatment on biological response to shape memory NiTi stents. *Journal of Biomedical Materials Research, 48*, 165–171.
108. Shabalovskaya, S. A. (2002). Surface, corrosion and biocompatibility aspects of Nitinol as an implant material. *Bio-Medical Materials and Engineering, 12*, 69–109.
109. Shabalovskaya, S. A. (1996). On the nature of the biocompatibility and on medical applications of NiTi shape memory and superelastic alloys. *BioMedical Materials and Engineering, 6*, 267–289.
110. Frauchiger, V. M., Schlottig, F., Gasser, B., & Textor, M. (2004). Anodic plasma-chemical treatment of CP titanium surfaces for biomedical applications. *Biomaterials, 25*, 593–606.
111. Lu, X., Zhao, Z., & Leng, Y. (2006). Biomimetic calcium phosphate coatings on nitric-acid-treated titanium surfaces. *Materials Science and Engineering: C, 27*(4), 700–708 (in Press).
112. Park, J., Kim, D. J., Kim, Y. K., Lee, K. H., Lee, K. H., Lee, H., et al. (2003). Improvement of the biocompatibility and mechanical properties of surgical tools with TiN coating by PACVD. *Thin Solid Films, 435*(1–2), 102–107.
113. Shevchenko, N., Pham, M. T., & Maitz, M. F. (2004). Studies of surface modified NiTi alloy. *Applied Surface Science, 235*, 126–131.
114. Endo, K. (1995). Chemical modification of metallic implant surfaces with biofunctional proteins (Part 1). Molecular structure and biological activity of a modified NiTi alloy surface. *Dental Materials Journal, 14*, 185–198.
115. Liu, F., Wang, F., Shimizu, T., Igarashi, K., & Zhao, L. (2006). Hydroxyapatite formation on oxide films containing Ca and P by hydrothermal treatment. *Ceramics International, 32*(5), 527–531.
116. Schillinger, M., Sabeti, S., & Loewe, C. (2006). Balloon angioplasty versus implantation of nitinol stents in the superficial femoral artery. *Journal of Vascular Surgery, 44*(3), 684.
117. Rapp, B. (2004). Nitinol for stents. *Materials Today, 7*(5), 13.
118. Tyagi, S., Singh, S., Mukhopadhyay, S., & Kaul, U. A. (2003). Self- and balloon-expandable stent implantation for severe native coarctation of aorta in adults. *American Heart Journal, 146*(5), 920–928.
119. Simon, M., Kaplow, R., Salzman, E., & Freiman, D. (1977). A vena cava filter using thermal shape memory alloy experimental aspects. *Radiology, 125*, 87–94.
120. Duerig, T., Pelton, A., & Stöckel, D. (1999). An overview of nitinol medical applications. *Materials Science and Engineering, A273–275*, 149–160.

121. Fischer, H., Vogel, B., Grünhagen, A., Brhel, K. P., & Kaiser, M. (2002). Applications of shape-memory alloys in medical instruments. *Materials Science Forum, V, 394–395*, 9–16.
122. Pelton, A. R., Stöckel, D., & Duerig, T. W. (2000). Medical uses of nitinol. *Materials Science Forum, 327–328*, 63–70.
123. Dai, K., Wu, X., & Zu, X. (2002). An investigation of the selective stress-shielding effect of shape-memory sawtooth-arm embracing fixator. *Materials Science Forum, 394–395*, 17–24.
124. Zhang, C., Xu, S., Wang, J., Yu, B., & Zhang, Q. (2002). Design and clinical applications of swan-like memory-compressive connector for upper-limb diaphysis. *Materials Science Forum, 394–395*, 33–36.
125. Da, G., Wang, T., Liu, Y., & Wang, C. (2002). Surgical treatment of tibial and femoral factures with TiNi Shape-memory alloy interlocking intramedullary nails. *Materials Science Forum, 394–395*, 37–40.
126. Song, C., Frank, T. G., Campbell, P. A., & Cuschieri, A. (2002). Thermal modelling of shape—memory alloy fixator for minimal-access surgery. *Materials Science Forum, 394–395*, 53–56.
127. Xu, S., Zhang, C., Li, S., Su, J., & Wang, J. (2002). Three-dimensional finite element analysis of nitinol patellar concentrator. *Materials Science Forum, 394–395*, 45–48.
128. Chu, Y., Dai, K., Zhu, M., & Mi, X. (2000). Medical application of NiTi shape memory alloy in China. *Materials Science Forum, 327–328*, 55–62.
129. Kokubo, T., Kim, H. M., & Kawashita, M. (2003). Novel bioactive materials with different mechanical properties. *Biomaterials, 24*(13), 2161–2175.
130. Lima-L to SpA, Medical Systems, Via Nazionale 52, 33030 Villanova di San Daniele del Friuli (Udine), Italy. http://www.lima.it/english/medical_syst.html
131. Combes, C., Rey, C., & Freche, M. (1998). XPS and IR study of dicalcium phosphate dihydrate nucleation on titanium surfaces. *Colloids and Surfaces B: Biointerfaces, 11*(1–2), 15–27.

Chapter 16
Nanocoatings for Medical Devices

Waqar Ahmed, Mohammed AlHannan, Sakib Yusuf and Mark J. Jackson

Abstract Recent developments integrating nanotechnology with electronics and computing are producing a large number of medical devices for health care. In this chapter, we focus on the advances made in the use of coatings to enhance functionality of dental implants, stents, hip prosthesis, and miscellaneous devices. Despite numerous publications the potential for using coatings in the healthcare industry is enormous and yet relatively untapped.

16.1 What Is a Medical Device?

A strong focus has always been placed upon the role of Active Pharmaceutical Ingredients (API's) in the treatment of medical complaints. The formulation of these API's into drug delivery systems to achieve localised delivery, reduce first-pass metabolism and side effects, has as a consequence also received much attention. However, it is evident that without the aid of medical devices many API's or formulations would not nearly be as effective. This said, the question arises, what may be classed as a medical device? Devices such as inhalers, nebulizers, injections and even implants are but some of the common examples which spring to mind. However, the EU Directive for the registration of medical devices defines a medical device as

> Any instrument, apparatus, appliance, material or other article, whether used alone or in combination, together with any accessories or software for its proper functioning, intended by the manufacturer to be used for human beings in the:

W. Ahmed (✉)
School of Medicine, University of Central Lancashire, Preston, UK
e-mail: wahmed4@uclan.ac.uk

M. AlHannan · S. Yusuf
School of Pharmacy and Biomedical Sciences, University of Central Lancashire, Preston, UK

M.J. Jackson
Kansas State University, Salina, Kansas, USA
e-mail: jacksonmj04@yahoo.com

W. Ahmed and M.J. Jackson (eds.), *Surgical Tools and Medical Devices*,
DOI 10.1007/978-3-319-33489-9_16

- Diagnosis, prevention, monitoring, treatment or alleviation of disease, injury or handicap,
- Investigation, replacement or modification of the anatomy or of a physiological process, or
- Control of conception,

and which does not achieve its principal intended action in or on the human body by pharmacological, immunological or metabolic means, but which may be assisted in its function by such means [14].

The range of possible devices in use today which come under this definition is vast to say the least. It is therefore no surprise that in the USA alone the medical devices industry was set to reach a value of 133 billion dollars by 2016 [66]. As a result, alongside developments in fields such as drug discovery and delivery, there is also innovation within the field of medical devices with many novel devices being approved by the Food and Drug Administration (FDA) each year. However, whilst predominant attention is focused on the development of wholly novel devices, i.e. completely new and innovate; enhancement of existing devices is an avenue where research is also focused.

16.2 Coating

The coating of materials to protect or enhance their functionality is certainly not a new concept; very early coatings were used in the decoration of statues and jewels using gold and silver metals [28]. Subsequent common examples of widely used coatings have been the application of protective coatings to metal substrates for many years in order to prevent corrosion, a cause of energy and material loss [70]. Further examples include the application of protective coatings to pharmaceutical grade tablets in order to protect and modify the release of API's [40, 56].

Whilst protection and enhancement of material properties through coating is a widely established field within itself; the introduction of the field of nanotechnology, termed the revolution of the twenty-first century [34] has resulted in a surge of developments in the coatings industry. The National Science and Technology Council [13] defined nanotechnology as

The understanding and control of matter at dimensions between approximately 1 and 100 nm, where unique phenomena enable novel applications.

Typically there are two broadly defined approaches which form the basis of nanotechnology, i.e. the bottom-up and top-down approach, which are used in the fabrication of nanostructures. The bottom-up approach involved the fabrication of nanostructures from a molecular or even atomic level. These nanostructures may then be used in the manufacture of micro or macro structures. Contrastingly, the top-down approach entails the breakdown of micro or macro structures to form nanostructures [58].

These nanostructures examined within nanotechnology may by themselves be functional, i.e. their incorporation into a given material may exhibit a given set of enhanced properties. However, the usage of these nanostructures to form coatings is

something which the health industry has given little precedence to, apart from in recent years. Coatings produced from nanostructures or from material a nanometre thickness have been accurately defined as nanocoatings. These have been deemed to elicit significant benefits and unique properties when compared to their micro or macro counterparts including superhydrophobicity [37], improved resistive properties [62], enhanced mechanical strength and many more [48].

16.3 Nanocoating of Medical Devices

Medical applications of nanocoatings are rapidly diversifying. Coating orthopaedic and dental implants improves what is known as *osseointegration*. The term refers to the structural and functional connection between organised living bone and the surface of the implanted substrate [39]. Though this is a complexly mediated process, it is not the only area where nanocoatings are beneficial in the field of biomedicine. Recently, the coating of cells and stents has achieved focus, demonstrating enhanced compatibility of nanocoated stents with vascular tissue and cell preservation on implantation. Moreover, with increasing trends in antibiotic resistant, there is a strong focus upon bactericidal coatings which reduce the incidence of infections following implantation procedures. This said, the following section examines some of the developments in the dental industry in terms of coating of medical devices.

16.3.1 Dental Applications

Dental implants and prosthetics alone account for a substantial proportion of the dental industry. It is therefore of no surprise that researchers focus heavily on this avenue. In contrast to other industries, dental industry nanocoatings do not perpetually involve the deposition of thin nanolayers onto a substrate. Often they can refer to the incorporation of nanostructured materials or particles into coatings on contact surfaces. For instance, a recent piece of work examined the usage of nanostructured hydroxyapatite (HA) as a filler material for root canal. HA (a commonly used material in coating implants to aid cell proliferation) particles sized at approximately 26 nm were incorporated into root canal sealer at variable ratios. At high concentrations, there was little difference in film thickness (implying they would meet ISO standards for root canal sealers). The observed improvements suggested that nanostructured HA could be used to formulate more stable tooth material interfaces [12].

Zirconia-based dental restorations are heavily dependent on the adhesive bond strength exhibited on cores in clinical applications. The usage of nanostructured alumina coatings on dental cement has been investigated in terms of exhibited bond

strength. The applications of such coatings were shown to improve resin strength two- to fourfold [29].

While HA has been commonly used as a coating material of implants, calcium phosphate has also been investigated as a potential alternative. Research has compared the degree of osseointegration (the direct bone deposition onto implant surfaces [33]) of dental calcium-phosphate-nanocoated implants with varied surface roughness. Although the effect of surface roughness of the nanocoating on osseointegration was the focus of this research, nanocoatings of calcium phosphate were shown to be successful in terms of osseointegration as well as theorised to have a direct effect on bone apposition across the implant surface [8].

With respect to the health sciences, nanocoatings have been used extensively in implants often improving their overall biocompatibility with tissues, resulting in greater degrees of integration than non-nanocoated implants. To this end, the dental industry has seen explosive interest surrounding nanocoatings and perceived potential benefits which may come with it. Whilst nanotechnology impaction in terms of coating is the focal point of this article, it is by far the only aspect in which nanotechnology has influenced the dental technology industry. Aside from nanocoatings, dental nanotechnology has been particularly fruitful in the manipulation of resin materials for example: Nanofilled composite resin materials have been theorised to offer outstanding wear resistance, strength and unparalleled aesthetics pertaining to characteristics such as their remarkable polishability and luster retention [41].

In 2012, the UK dental industry's net worth was estimated to be in excess of 5.7 billion pounds by report published by the Office of Fair Trading (OFT) [65]. Dental implants (Fig. 16.1) and prosthetics alone account for a substantial proportion of this industry. It is therefore of no surprise why researchers focus so heavily upon this avenue seeking out new ventures for improvement. In parallel,

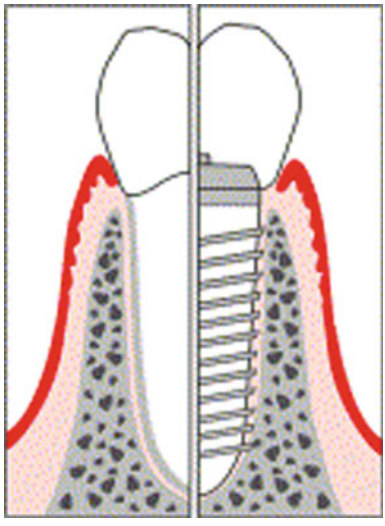

Fig. 16.1 Diagrammatic representation of a dental implant [50]

alternative industries have uncovered and capitalised on ultra-thin coatings, nanocoatings with enhanced properties as discussed in the aforementioned text. Improved substrate protection and importantly in the coating of implants, improved acceptance, adherence and strength are a handful of benefits which may be translated into the dental industry. It is therefore of no surprise why there remains considerable interest surrounding this area.

Unlike many other industries, in the dental industry nanocoatings are not necessarily created through the deposition of material of a nanometre thickness onto the desired product. More often than not, they refer to nanocoatings formulated through the inclusion of nanostructured materials into the coating material, theoretically imbibing the coating with qualities of the nanostructure. For instance, a recent piece of work examined the usage of nanostructured Hydroxyapatite (HA) as a filler material for root canal. Hydroxyapatite (a material commonly used in coating implants aid cell proliferation) particles sized at approximately 26 nm were incorporated into root canal sealer at varied ratios. As is well documented, root canal sealers preferably should biologically inert, but bioactive with respect to human body tissues and finally possess a good degree of radiopacity. As synthetic HA is compositionally the same as natural HA found in teeth, it was theorised that the inclusion of synthetic HA nanoparticles would provide a greater degree of biomimetic mineralization (i.e. mimicking of the natural mineralization process) in the surrounding tissue. Thus, the incorporation of nano HA particles was seen as promising approach to improve the sealing ability of such fillers. The study under discussion aimed to investigate the potential negative impact of HA nanoparticle inclusion in methylacrylate-based root canal sealers, analysing properties such as; the film thickness produced by the sealer and viscosity as well as radiopacity (opacitity exhibited on exposure to radiation). The results indicated that even at high concentrations there was little difference in film thickness however positively, radiopacity was increased. The observed improvements suggested a strong possibility that nanostructured hydroxyapatite could be used to formulate more stable tooth material interfaces [12].

The in vivo stability of HA nanoparticle coatings on titanium implants has also been investigated as previous studies had indicated a positive effect on bone healing surrounding implants when nanostructured surfaces were utilised. Wennerberg et al. [71] examined titanium implants coated with radioactively labelled nanoparticles using rats as model animals to perform the implantation upon. The desired aim was to establish the potential negative effects such as nanocoating instability. At set intervals, the localization of the nanocoatings constituent particles were monitored showing that whilst accumulation of the nanoparticles in a number of the body's organs was found, these were deemed to be unlikely to exert any negative effect on body organs due its rapid excretion [71].

Nanocoatings have been further demonstrated to be influential on osseointegration of dental implants. In 2014, Walkenhorst described a bio-nanocoating

which has been shown to notably improve the adhesion of osteoblasts to dental implants [69]. The applied nanocoating was demonstrated to adhere strongly to the substrate, but also maintained molecular flexibility. The concluding remarks posed that the coating would reduce the incidence of peri-implantitis (lesions around osseointegrated implants) and additional complications associated with lack of tissue adhesion to the implant. The effects of the nanocoating are illustrated in a rabbit model which may be observed in (Fig. 16.2) where a greater degree of osseointegration may be observed in the nanocoated implants at 6 weeks.

As is perhaps well known, aesthetic restorations in dentistry conceivably is the main driving force behind many of the new developments. Zirconia-based dental restorations (Fig. 16.3) are heavily dependent on the adhesive bond strength exhibited on cores in clinical applications. Usage of nanostructured alumina coatings on dental cement has been investigated in terms of bond strength exhibited. Applications of such coatings were shown to improve resin strength two- to fourfold significantly improving the bond strength compared to comparable methods [69].

Moving away from biocompatibility of implants and bonding strength, bacterial cell proliferation and subsequent infection following dental and orthopaedic implantation are very real issues, often only being solvable by removing the infected implant. Prevention of bacterial adhesion to the implant remains the focus of much research to prevent infection, surface modification being one of the

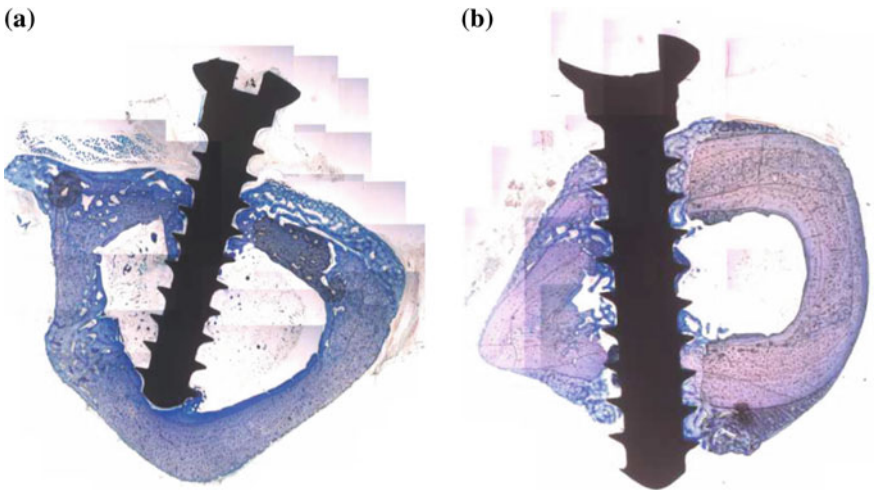

Fig. 16.2 Osseointegration of dental imant in rabbit bone without nancoating (**a**) and with nanocoating (**b**) at six weeks

Fig. 16.3 Zirconia based implant [50]

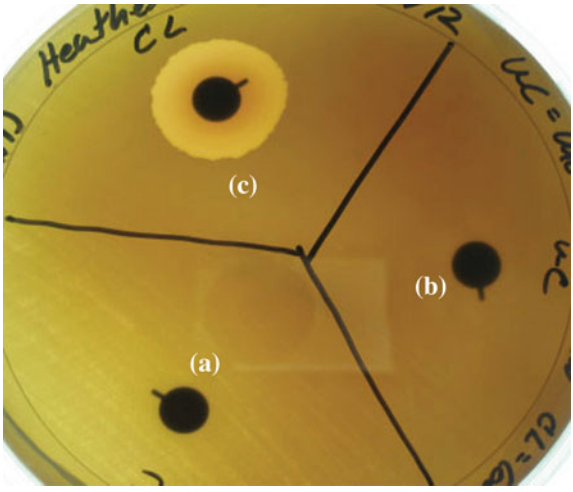

Fig. 16.4 Zone of inhibition tests show that cefazolin incorporated in polypeptide multilayer nanocoatings can inhibit *S. aureus* growth. Three different types of stainless steel discs were used: **a** disc without coating, **b** disc coated with a polypeptide multilayer nanocoating, **c** disc coated with a polypeptide multilayer nanocoating and incorporated with cefazolin

strategies adopted. For example, a recent study showed how multilayer nanocoatings of synthetic polypeptides which were negatively charged and impregnated with Cefazolin could prevent post-operative infection following implantation [31]. On examination of Fig. 16.4, it can be noted that only where the nanocoating was impregnated with the cephalosporin antibiotic was a zone of inhibition shown, i.e. an area of no bacterial proliferation.

Whilst much of dental nanocoating is directed upon the coating of implants, orthodontics is perhaps an area where nanocoating has been utilised successfully for a number of years. Orthodontic teeth movement, performed by sliding archwire-bracket systems were documented to be influenced by a high level of friction force developed at the wire-bracket border. The disproportionate force generated was believed to cause unwanted teeth movement as well increasing chances of tooth resorption. Reduction in friction generated by wires was deemed to be the logical approach to resolve the problem. The coating of the orthodontic wires with in organic fullerene tungsten disulphide nanoparticles was described first by Prof. Reshef Tenne in 1992. Though these layers formed by these particles were weakly held together by van der Waals forces, they provided excellent lubricity markedly improving friction and wear properties under various contact conditions, additionally resulting a remarkable reduction in the degree of force required to move the coated wire along the bracket [49].

The element fluoride is strongly correlated with a decline in the incidence and the degree of severity in dental carries. Dental restorations are a viable method of delivering fluoride directly to the intended tooth component; this gives a controlled release of the formulation containing fluoride or as a by-product of setting reactions. Glass ionomer cement, known for its ease of use, fluoride release properties and pleasing aesthetic properties has been investigated as a restoration material. With glass ionomer cement, fluoride is able to be release into the oral environment without compromising the structural integrity. Moreover, the actual material is known to be inhibitory on cariogenic microorganisms as well maintaining decreased solubility of the tooth.

Though glass ionomer has demonstrated suitable properties as a dental restorative material, poor mechanical properties and sensitivity to initial desiccation and moisture are prominent issues which have negated its use within clinical settings. Surface coatings particularly those containing nanofillers (in this case a product known as G-coat plus (Fig. 16.5), used for improving wear resistance and smoothness) have also been instrumental in controlling the release rate of fluoride ions from glass ionomer cement which is used in the treatment of dental carries. The uniform dispersion of nanofillers applied to glass ionomer restorations were found to enhance wear resistance and provide protection against acid allowing for the steady release of fluoride from the restoration [64].

The usage of zirconia as an implant material has seen much popularity owing to its good biocompatibility and mechanical properties [3]. Surface stability of zirconia however remains problematic with no sustainable chemical or mechanical bond forming to it. To remedy this, nanostructured alumina coatings have been trialled showing improvements in bonding. However, till recently, the effects of inevitable clinical contamination due to saliva and blood was not investigated. Zhang et al. [73] in vitro work examined exactly this clinical contamination over an extended period of time. The nanostructured surfaces were found to perform partially well under the contamination conditions and subsequent cleaning. Those contaminated with saliva were easily restored using phosphoric acid retaining much of the resin bond strength. Contrastingly, the resin bond strength of the implant

Fig. 16.5 Nanofilled protective coating available on the market [1]

material following exposure to silicone disclosing material was rendered irrevocable and resin bond strength could not be restored [73].

Biocompatibility of metal implants remains an issue which receives much focus, owing to problems associated with corrosion upon implantation into biological environments. Niobium has been investigated as a potential material to remedy issues surrounding biocompatibility [47]. Research conducted by Ramirez et al. [47] investigated the potential niobium-based films in improving the stability and life of stainless steel dental implants. Upon comparison to Ti_6Al_4V films.

Whilst the dental industry has made many significant developments in terms of devices in the preceding decades. Specifically, materials such as silicone have become a popular choice of material used in denture soft liners and sections obturators (prosthetic devices used to close defects of the hard/soft palate) due to their low density, flexibility and hypoallergenic properties [15]. However, biomaterials used orally are quick to become colonised by microflora due their abundance in the oral cavity and as a consequence of the ideal environmental, i.e. high level moisture, warmth and nutrition-rich conditions [23]. A common infection includes denture stomatitis which is associated with fungal infestation of denture soft lining and obturator materials, which are often silicones [21]. A recent study conducted by Garner et al. [21] demonstrated the ability of nanoparticles containing chlorhexidine (an antibacterial) to act as an anti-fungal coating against *Candida albicans* for dental silicones [21]. Coatings applied to silicones exhibited substantial anti-fungal

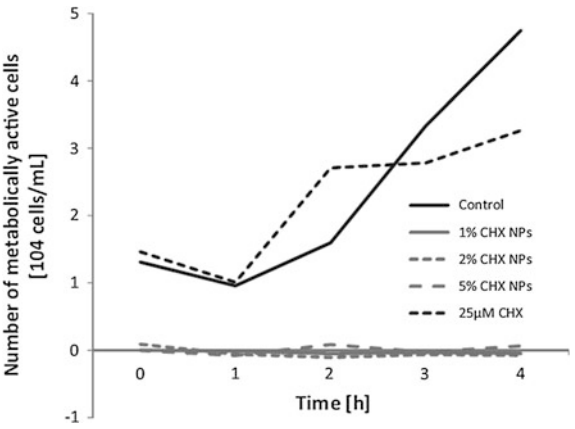

Fig. 16.6 *Candida albicans* expressed as 104 metabolically active cells per mL growth medium, as a function of exposure time to chlorhexidine hexametaphosphate nanoparticles, 25 mM aqueous chlorhexidine or no treatment (control) [21]

activity retarding growth significantly when compared to an aqueous solution of chlorhexidine and a control (Fig. 16.6).

As many dental implants are metal-based (i.e. titanium or titanium-based), prevention of corrosion (which results in the release metal ions into the surrounding tissue) via application of coatings is also an area of research interest. A recent investigation by Gazia et al. [22] examined material such as aluminium nitride and silicon dioxide for their anti-corrosive properties when applied to titanium implants [22]. When exposed to a biological environment using Hanks salt solution, whilst the aluminium nitride nanocoatings exhibited superiority in terms of reducing localised corrosion silicon dioxide nanocoating showed superior overall corrosion resistance with no dissolution of the coating occurring. The inferiority shown by the silicon dioxide coating in terms of preventing localised corrosion was attributed to poor homogeneity of the applied coating. Overall, the ability of both coatings to offer substantial anti-corrosive properties provides foundation for the development of novel dental implants.

A material which has shown much promise in recent years as a coating material is bioactive glass, owing to its ability to form strong bonds with living tissue in a relatively short space of time. Recent research by Popa et al. [45] demonstrated the benefits of coating dental titanium implants in bioactive glass for implantation in sections of pig mandibular bone which showed concordance with human dental implantology technique; in addition to testing their biocompatibility with human stem cells [45]. Implantation in mandibular bone (Fig. 16.7) demonstrated the durability of the bioactive glass coating; moreover, upon exposure to human stem cells, bioactive glass exhibited strong cellular adhesion without influencing differentiation of the cells, suggesting promise for enhancing implant integration.

Applications discussed in this section have ranged from nanocoatings which directly come in contact with dental surfaces through to nanocoatings upon dental equipment which are used in dental procedures. As may be derived from the aforementioned content, the applications of such nanocoatings have either elicited enhancement of the overall function of the coated substrate, or provided some level

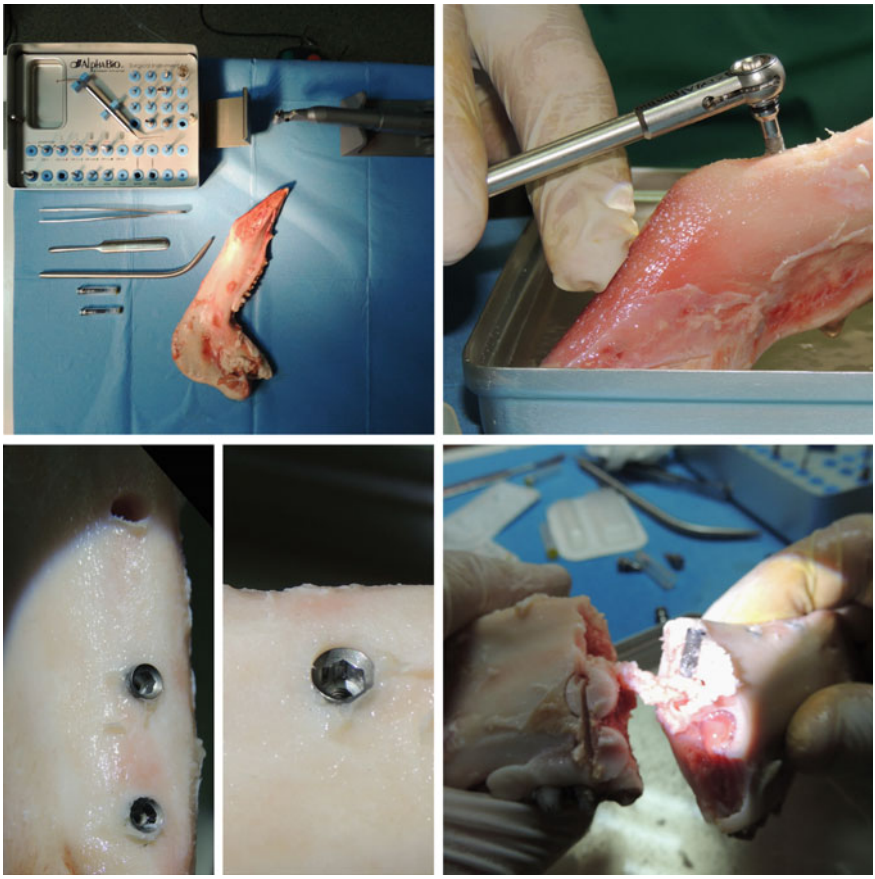

Fig. 16.7 Representative images acquired during the implantation-extraction procedure of the Alpha-Bios DFI dental screws biofunctionalized by RF-MS with bioglass coatings

of novel functionality. Though this section has focused primarily on the benefits of nanocoating as an avenue of nanotechnology in dentistry, the applications of nanotechnology within dental industry are many and multifarious, moving far beyond simple nanocoatings.

16.3.2 Applications in Implants

As an implant material, titanium has demonstrated wide-spread popularity in the fields of dentistry and orthopaedics owing to the high degree of biocompatibility exhibited by the material as well unique material properties and low cost [30]. Unfortunately, biomedical device associated infections (BAI) are commonly responsible for reduced healing rate and repeated surgeries [2, 35, 57].

As a consequence, methods of preventing infection have been widely explored. One such method entails the application of silver nanoparticles upon implant surfaces, in a bid to reduce BAI's.

The implantation of structures or devices within the body is fraught with difficulties such as infection and inflammatory and immune responses. As the surface of implants is the first point of contact with cells, the modification of this surface is the logical area to initiate research. HA, a bone mineral, is often used in bone implants to facilitate osseointegration and its application in nanocoatings. Although the nanoscale is ideal for manipulation of matter, inherent material properties will dictate to an extent the functionality of a coating and will limit the extent to which they may be modified. However, more coating techniques are being developed to improve surface bioactivity and biocompatibility such as LBL assembly or sol–gel methods. These coating methods can be produced at a thickness of as little as several nanometers, thus opening up future possibilities for substrate choice [16].

A study examining ovariectomized rats' bone formation illustrated the extent of difference that coating thickness could make in coating functionality. Thick HA coatings applied by traditional coating methods such as plasma spraying are associated with poor adhesion to the metallic substrate. On application of nano HA coatings, numerous biological benefits were identified such as an increase of bone apposition onto implant surface, stronger attachment to the HA coating and substrate boundary, enhancement of bone growth, as well as inhibition of metallic ion release from the substrate. The smaller the particles, the higher the subsequent dissolution of the coating, suggesting higher release rates of calcium (which is favourable in bond formation of the implant and bone in rats). This substantiated previous findings of better bone integration and bonding strength when HA nanocoatings were implemented [7].

In addition to bone implants, nanocoatings have been successfully implemented for artificial corneas made from inert polymeric materials. The lack of biocompatibility exhibited from these materials is known to result in poor fixation of implants at target sites; nanocoatings of HA were proposed as a way to overcome this. Such improvements were brought about by introducing a porous fringe around the edge of the membrane to allow for cells to adhere and grow. These were then coated with a bioactive material, HA nanoparticles, which is also known to effect corneal cell growth. When tested with cell cultures, enhanced corneal cell growth was elicited [38].

Nanoparticles of HA are known to buffer implant degradation when implanted. While improving properties of nanoparticles may be challenging, a novel way to achieve this is by the ultra-thin coating of nanoparticles. The improved mechanical properties offered by nanosized HA when these are combined with polymers in the form of composites are negated due to weak binding of the polymer to the particles. To overcome this, a nanocoating of nanoparticles using a degradable polymer was implemented. Mechanical strength of the polymer composite and its cytocompatibility was significantly improved using ultra-thin degradable coatings when compared to uncoated and non-degradable controls [43].

A unique nanostructure which has been used in drug delivery is that of CNTs. These have also seen a rise in interest in terms of biomedical and alternative applications. Carbon as an element was previously shown to be free from adverse effects on cells when used as coating material [48]. However CNTs have been shown to influence cellular function owing to the scale at which they act, the nanoscale. CNTs adhere well to cells, suggesting potential applications such as scaffolding; moreover, they have been shown to selectively adhere to surfaces [36]. Furthermore, CNTs have been used to reinforce composite coatings, showing promise for load-bearing orthopaedic implants such as hip, knee and shoulder joints. Cellular adherences to material coated in CNTs have been further investigated by Hirata et al. [26]. Polylactic acid, a highly desirable material for tissue engineering, suffers from known problems of cell adhesion to the surface. Coating polylactic acid sheets using CNTs was shown to improve the surface wettability and cell adhesion by comparison with traditional methods such as plasma treatment, and in chemical attachment. The major identified benefits from using CNTs as a nanocoating were a reduction in the requirement for machinery and convenience [26].

As discussed earlier, the incidence of post-operative infection remains a major issue, often with dire consequences following implantation. Titanium implants are widely used clinically but also suffer from this issue. Therefore, surfaces with antibacterial coatings are extremely desirable. Research has demonstrated that incorporation of silver nanoparticles into titanium nanotubes enable such effects. Zhao et al. [74] showed adequate activity against planktonic bacteria within several days and preventing their subsequent growth for up to 30 days.

Cell adhesion and proliferation are the two main initial steps of osseointegration prior to cell differentiation. The scale at which the coating material is applied is extremely important. Many studies investigating cell adhesion and proliferation have looked at these properties on a microscale as opposed to a nanoscale. However, in a recent study apple pectins were used as a coating material for titanium implant surfaces. Interestingly, whereas previous studies showed improved cell adhesion and proliferation on rougher surfaces, this research showed greater cell adhesion and proliferation on the smoother modified nanocoatings. Gurzawska et al. proposed that this improved adhesion could be an effect of the better interaction between the cells and the side chains on the pectin [24].

This is not the only example where nanocoatings have come into contact with biological systems. Working at the nanoscale has allowed for interaction at a cellular level. Nanodiamond monolayers (nanostructured diamond deposited as a monolayer onto a substrate surface) have been used as a platform for neural growth. Four different materials—glass, polycrystalline diamond, nanocrystalline diamond and silicone—were coated with monolayers of monodispersed nanodiamonds, resulting in good similarity to the protein-coated materials regarding neuronal cell attachment. When compared to those on protein-coated substrates, neurons were able to grow in direct contact with the nanodiamond-coated material and could be easily maintained in culture for a prolonged period. Nanodiamonds thus demonstrated superior biocompatibility. Moreover, nanodiamond layering has been deemed a potentially viable and valuable technique for implants [63].

Microstructured surfaces made from biodegradable polyesters have been proven to be inhospitable for the growth of vascular cells. In contrast, nanostructured surfaces have been shown to provide hospitable conditions for soft tissue cells such as gingival fibroblasts. Poly (ε-caprolactone) (PCL), a polymer which has been used in biomedical applications, is known to interact poorly with biospecialized cells [9]. Chitosan, an amino polysaccharide containing groups acting as bioactive factors, was modified to promote cell growth and multiplication. A recent study investigated the effect of surface nanoscale roughness of films with and without chitosan on cell proliferation. When applied with different levels of surface nano roughness to PCL molds, the highly nanorough chitosan-coated PCL surfaces promoted cell proliferation.

A recent piece of research by Braic et al. [4] highlighted the potential of complex carbonitride coatings as protective films for orthopaedic implants. The research specifically focused upon (Zr, Ti) CN coatings which were deposited onto Si (silicon) and $TiAl_4V$ alloy substrates. When compared in terms of corrosion resistance the coated substrate showed a distinct advantage over the $TiAl_4V$ alloy alone; moreover cell viability studies demonstrated that whilst the coated surfaces were severely hydrophobic (indicated by high contact angle values) up to 90.5 % cell viability was observed when coated substrates were exposed to osterosarcoma cells [4].

Transcutaneous implants are less well known implants which essentially include: catheters, dental implants, external hearing aid devices and many more including amputation prostheses [44]. Prevention of bacterial proliferation and promoting superior healing are two major challenges associated with implants. Recent research conducted by Calliess et al. [5] demonstrated that select polymers such as hexyl bromide treated 4-vinylpyridine were not only able to prevent microbial proliferation but also reduced scar tissue formation when implants were implanted in mice [5].

Finding man-made materials holding properties which are renascent of biological properties is also an interesting avenue of research. Chen et al. [6] highlighted research conducted by Verne et al. [67] and Vitale-Brovarone et al. [68]; when discussing the use of glass and glass–ceramic scaffolds as bioactive trabecular-like coatings upon prosthetic implants (Fig. 16.8), in order to enhance osseointegration [6]. Findings were indicative that glass-derived scaffolds as a trabecular coating would induce biological fixation of prosthetic elements to bone. Interestingly, whilst the design proposed a spherical join as in the hip, testing was conducted upon two-dimensional (2D) flat surface samples.

The usage of stainless steel in implant materials is well established in the medical field; owing to mechanical strength exhibited by the material as well as general cost-effectiveness in terms of use. Surface corrosion of the material however, also remains a prominent issue [10] resulting in the potential release of metal ions from the material surface [25]. Cieślik et al. [10] demonstrated that through application of poly-paraxylylene/Parylene poymeric coatings upon stainless steel surface smoothness increased dramatically, as observable from Scanning Electron Microscopy (SEM) images following scratch tests on coated and uncoated surfaces (Fig. 16.9). Moreover, not only did metal ion release from stainless steel surface

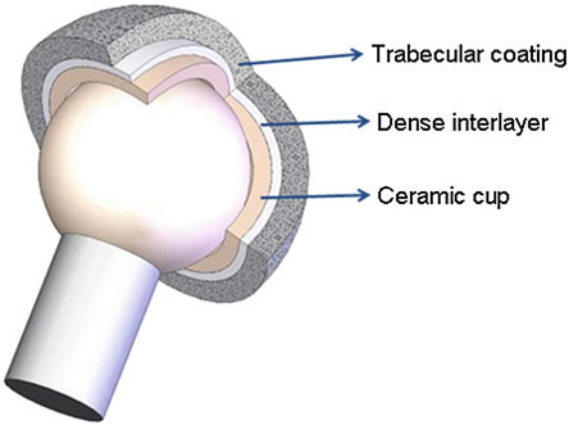

Fig. 16.8 Schematic representation of the acetabular cup as revealed in Verne et al. [67] patent and as imaged by Vitale-Brovarone et al. [68]

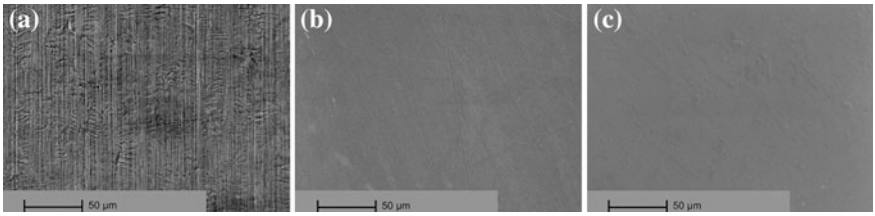

Fig. 16.9 SEM images of stainless steel surface **a** uncoated, **b** coated with parylene N and **c** parylene C [10]

reduce threefold when exploded to simulated bodily fluids; but also superior mechanical and protective properties when applied as a micro coating.

The usage of hydroxyapatite in implants aiming to improve osseointegration is well documented as discussed in the aforementioned sections. A novel application of this material is impregnation with silver nanoparticles. Recent research conducted by Ciobanu et al. [11] demonstrated that hydroxyapatite coatings featuring silver nanoparticles showed up to 94.3 % antimicrobial efficiency when compared the uncoated substrate alone [11].

The usage of silver in preventing bacterial proliferation is not exclusive to the aforementioned research. A study conducted by Fordham et al. [17] investigated the use of silver as a thin film coating for biomedical implants [17]. Whilst it was established that silver possessed antimicrobial activity (Fig. 16.10), the inability of the material to create a zone of inhibition when exposed to *Escherichia coli* and *Staphylococcus aureus* was suggestive that the material alone was insufficient to be classed as a bactericide; but may be used as an additive measure to prevent bacterial adhesion or colonisation upon implants.

Fig. 16.10 A direct comparison of bacterial growth in samples with (*left tube*) and without (*right tube*) a silver coating. Cloudiness of the liquid in the right tube is indicative of bacterial growth whereas the tube on the left contains a clear amber solution indicating absence of growth [17]

Whilst silver is commonly recognised for its antibacterial properties, it is not the only metal which has been incorporated as particles within coatings. Alternative means of preventing bacterial proliferation following implantation of joint implants have included the impregnation of hydroxyapatite film with magnetite (a commonly occurring oxide of Iron) [19]. When exposed to *E. coli* bacteria these coatings were able to significantly reduce bacterial adhesion on the film surface. When compared to a control film of hydroxyapatite it was found that in the presence of an external magnetic field the ability of the coating to prevent bacterial adhesion to the film surface was amplified, though this effect was noted more substantially for films free from magnetite (Fig. 16.11).

Whilst the application or addition of silver nanoparticles applied to implant surfaces has been established as a potentially viable technique to reduced bacterial proliferation and subsequent rejection of implants, maintaining regular cell function is also a concern expressed by researchers in the field of medical devices [30].

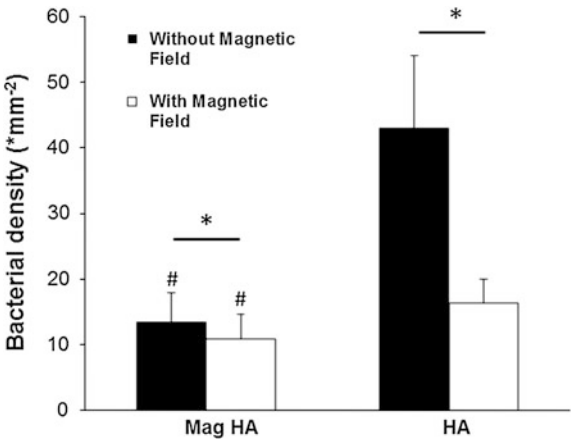

Fig. 16.11 Adhesion of *E. coli* to magnetic and non-magnetic hydroxyapatite films at 4 h from seeding [19]

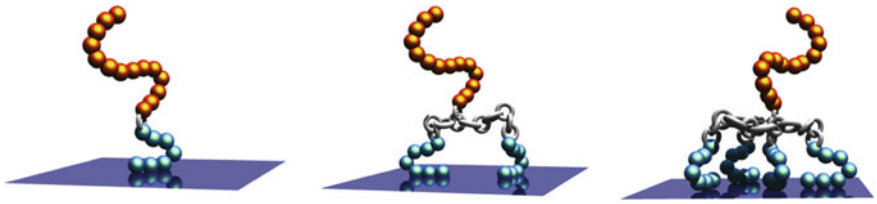

Fig. 16.12 Bacteriophobic coatings with one or more TBPs (in *blue*), a peptide linkage (in *silver*) and a PEG region (in *gold*)

An investigation conducted by Jia et al. [30] yielded the development of a silver nanoparticle coating which offered protection of the coated substrate from corrosion whilst offering sustained release of silver nanoparticles for up to 28 days. Additionally, following subcutaneous implantation, the coated substrates elicited a low inflammatory response when compared directly to the control sample.

The impregnation of implant coatings with molecules or particles which offer antibacterial activity has been a commonly employed strategy in preventing bacterial proliferation and subsequent implant rejection. However, as protein adsorption onto implant surfaces is a precursor for bacterial proliferation [72], a logical point of interception is the prevention of this process. This said, a recent piece of research conducted by Khoo et al. [35] showed that through coating of titanium implant using various PEGylated titanium-binding peptides (TBPs) (Fig. 16.12); *S. aureus* attachment and subsequent bacterial biofilm formation (which are notably difficult to eradicate) could be prevented [35].

16.3.3 Progression in Stents

Vascular stents are important medical devices in the treatment of a number of circulatory disorders and have been extensively used by cardiac surgeons for a number of years. They are, however, associated with a number of problems pertaining to the body's ability to accept their presence. Coatings have provided a method of countering this. Endothelialization of vascular stents, which are used to widen blood vessels often following a cardiac event, is a prominent area of research. Coating of cardiovascular stents is an area within biomedicine that has gained from the benefits of nanocoating. The ideal requirements of stent coatings are numerous, such as antithromobogenicity, anticalcification, superior mechanical properties, and much more, all of which nanocoatings may provide [60].

Improper growth of tissue in stents necessitates secondary procedures and causes problems such as thrombosis following cessation of antiplatelet therapy [61]. Focusing on problems associated with endothelial cell adherence to stents, Tang et al.'s research utilised plasma nanocoatings of 50 nm thickness applied to different types of intravascular stents. On analysis, it could be seen that the plasma-coated

stents in comparison to bare stents demonstrated significantly higher cell adherence, indicating that plasma coating of stents may be a viable option to improve endothelialization.

Endothelialization of stents is highly important due to low adherence of the cell surface and reduced chances of renostenosis and thromboembolic complications [54]. Research [54, 56] has further highlighted potential complications using NiTi-based stents, which had the potential to induce allergic reactions or toxicity. Functional nanocoatings containing vascular endothelial growth factor have been utilised to improve endothelial cell growth on the surface of NiTi cardiovascular stents. Specifically, a nanocoating of Al_2O_3 significantly led to a 16-fold reduction in the release rate of Ni from the stent.

Moreover, research into tissue regeneration, specifically stent re-endothelialization, demonstrated the benefits of nanocoatings based on poly (3,4-ethylenedioxythiophene) (PEDOT) possessing biocompatibility with cells. The study highlighted how thick polymer coatings were responsible for inciting inflammatory responses as well as localised higher endothelium sensitivity. In addition, the poor uniformity in these thick coatings was thought to contribute to potential thrombosis. The usage of PEDOT nanocoatings showed a good compatibility with the endothelial cells, where the thinness of the films as well as the low surface roughness contributed to the compatibility of the coatings [32].

The high importance of nanocoatings in the preservation and successful implantation of vascular stents is clear, but the ability to coat smaller substrates on a cellular level is significantly more intriguing.

In the mid 1980s 316 stainless steel coronary artery stents were introduced in the treatment of artery occlusion [42, 52, 53]. These are bare stents, with no coating applied to improve acceptance or prevent infection. With circa 1.4 million stent implantations worldwide, a 20–40 % rate of in-stent restenosis (i.e. the abnormal narrowing of arteries or valves following corrective surgery) is troubling.

Since their introduction in the mid-1980s, 316L stainless steel coronary artery stents have been a valuable asset in treating occluded arteries. 1–4 Each year, nearly 1.4 million stents are implanted worldwide. 5, 6 Unfortunately, in-stent restenosis occurs within 20–40 % of stent recipients. 7 Restenosis occurs due to inflammation of the tissues in contact with the stent. Smooth muscle cells, which are normally present within the vasculature, proliferate extensively and thus eventually closing the stented vessel. Such closure requires invasive corrective action that could ultimately result in arterial bypass.

Coronary stents with drug eluting coatings to prevent restenosis are a commonly investigated strategy in improving stent implantation outcomes. A novel type of coating recently investigated, employs the use of genes and cationic liposomes as an alternative to drug eluting stents in prevent restenosis [20]. Using a combination of in vitro and in vivo (using rabbit iliac artery) studies it was found that maximum transfection (gene delivery) of cells was achieved by 28 days with persistent gene expression for up 42 days observed following implantation of stents. The prolonged action of the coatings indicates gene eluting stents as a viable option in the prevention of complications associated with stent implantation.

Coating of coronary stents used during balloon angioplasty to scaffold problem arteries is also an avenue which has seen significant attention in recent years. [18]. PPAA (Plasma polymerized allylamine) was recently investigated as a nanocoating material applied by a low pressure plasma reactor upon stainless steel stents in a bid to reduce restenosis (recurrence of stenosis i.e. narrowing of the arteries) rates, by reducing corrosion. Results showed that coatings were homogeneous and resistant to plastic deformation (an indicator of the stent resistance to the deployment process), with no metallic compounds detectable following deformation; indicating sufficient adhesion to the substrates surface. Whilst good mechanical and adhesion properties were exhibited by the PPAA coatings, upon contact with distilled water coatings demonstrated defects such as delamination (attributed to solubilisation of the coating polymer).

16.3.4 Miscellaneous

Silicone hydrogels may be described as polymers which are comprised of silicon–oxygen bonds; these have been studied substantially in the field of medical devices due to their enhanced biocompatibility and high permeability to oxygen [27]. However, hydrogels are susceptible to biofouling (accumulation of proteins, cells in addition to bacterial contamination on the surface) due to their surface hydrophobicity [46]. Research conducted by [27] showed that application of zinc nanoparticles (with incorporated polyethylene glycol) onto the surface of silicon hydrogels were able to reduce protein accumulation on the hydrogel surface by up to 50 %. Importantly, when exposed to two separate types of bacteria, the zinc nanoparticle coated hydrogels exhibited significant retardation of bacterial growth which was time dependant (i.e. increasing with time) (Fig. 16.13).

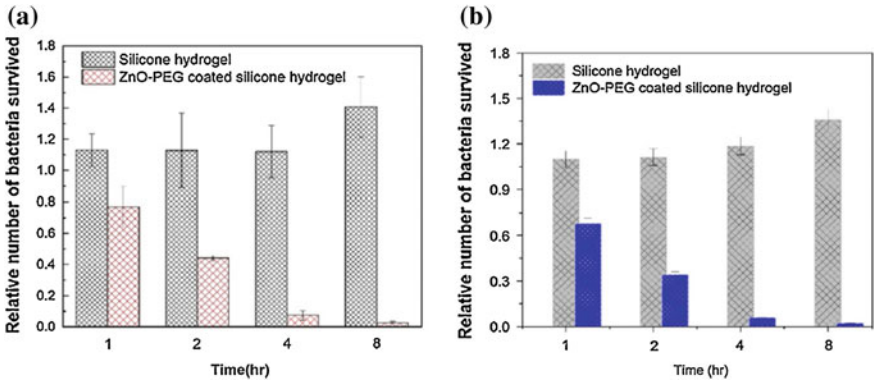

Fig. 16.13 Antibacterial efficacy of silicon hydrogel alone and with zinc oxide nanoparticles with polyethylene glycol coatings when exposed to **a** *Escherichia coli* and **b** *Staphylococcus aureus*

Kapton® HN is a general purpose polyimide film which is known for its chemical resistance, thermal and mechanical properties, making it a desirable material for catheters [51]. As has been discussed in the preceding sections silver has been identified as a material which demonstrate bactericidal activity. Recent research conducted b [55] demonstrated the potential of sputtered silver nanolayers upon polyimide films, with particular emphasis upon post deposition conditions (i.e. annealing) [55]. Whilst the sputtered silver alone exhibited significant antibacterial activity when compared to the control, this effect was substantially amplified following annealing of the silver nanocoatings (Fig. 16.14). This effect was attributed to structural transformations in the metal layer which increased the surface area of the metal coating. It was further established that as the surface area of the individual islands which formed the silver coating increased the resultant antibacterial effect was also greater. This research highlighted the importance of processing and post processing conditions, showing that a material activity could be enhanced by appropriate conditioning.

Additional research which has focused on enhancing or prolonging the efficacy of silver coatings was conducted by Taheri et al. [59]. Silver nanoparticles were surface modified with a monolayer of 2-mercaptosuccinic acid which is known to facilitate immobilisation of nanoparticles to the surface of solid substrates In addition to reducing the rate of oxidation of silver nanoparticles which in turn extended the lifetime of the coatings; coatings were found to exhibit significant

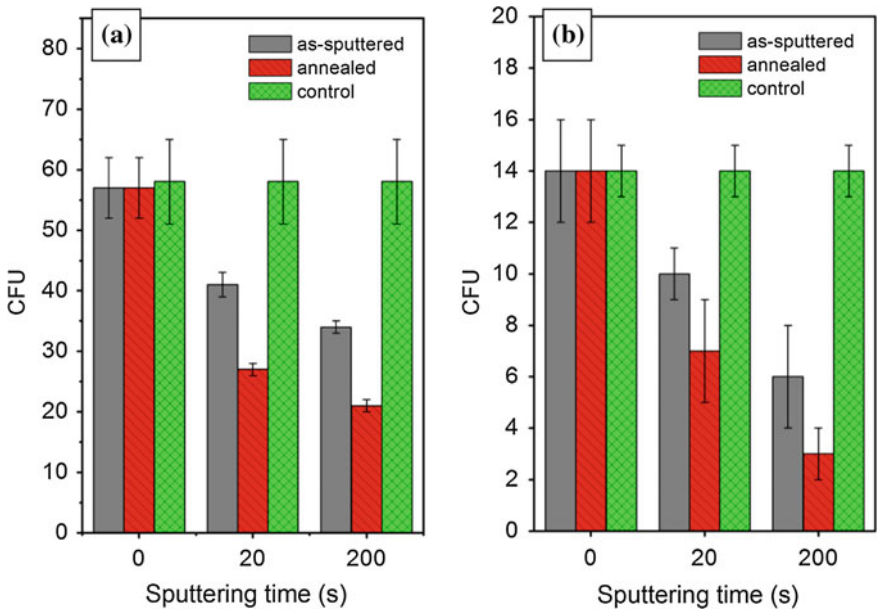

Fig. 16.14 CFU dependency for *S. epidermidis* (**a**) and *E. coli* (**b**) upon deposition to pristine, silver coated PI, silver coated PI following annealing, taken from Siegel et al. [55]

antibacterial efficacy against three separate bacterial including: *Staphylococcus epidermidis*, *S. aureus* and Pseudomonas. Pleasingly, further studies with human fibroblast cell found the coatings to exhibit no cytotoxicity in vitro. Moreover, immunity studies using macrophages showed that the coatings did not notably affect the level of pro-inflammatory cytokines or the ability to adhere of the cells. Much like the research conducted by Siegel et al. [55] the research concluded that the silver coating were ideal for deposition upon medical devices such as catheters, implants and even wound dressings.

16.4 Conclusions

It is clear that coating of medical devices is an ever expanding avenue with many interesting current developments. This chapter has highlighted many recent pieces of research which have been conducted in this area. As can be noted, there is a heavy shift in focus to preventing bacterial proliferation upon medical device surfaces which may have an innumerate of deleterious effects which may lead to life threatening conditions. Not only are new materials and methods of application discovered and unveiled each year, but a significant body of research shows that the potential of many pre-existing materials remains untapped, with many researchers demonstrating that there are still many potential applications and potential of enhancing of current coating materials.

References

1. America, G. (2014). *G-Coat Plus*™. Available online at http://www.gcamerica.com/products/operatory/G-Coat_Plus/index.php. Accessed on February 20, 2014 (AD 1902).
2. Berglundh, T., Persson, L., & Klinge, B. (2002). A systematic review of the incidence of biological and technical complications in implant dentistry reported in prospective longitudinal studies of at least 5 years. *Journal of Clinical Periodontology, 29*, 197–212.
3. Blatz, M. B. (2002). Long-term clinical success of all-ceramic posterior restorations. *Quintessence International, 33*, 415–426.
4. Braic, V., Braic, M., Balaceanu, M., Vladescu, A., Zoita, C. N., Titorencu, I., et al. (2011). (Zr, Ti)CN coatings as potential candidates for biomedical applications. *Surface and Coatings Technology, 206*, 604–609.
5. Calliess, T., Bartsch, I., Haupt, M., Reebmann, M., Schwarze, M., Stiesch, M., et al. (2016). In vivo comparative study of tissue reaction to bare and antimicrobial polymer coated transcutaneous implants. *Materials Science and Engineering C, 61*, 712–719.
6. Chen, Q., Baino, F., Pugno, N. M., & Vitale-Brovarone, C. (2013). Bonding strength of glass-ceramic trabecular-like coatings to ceramic substrates for prosthetic applications. *Materials Science and Engineering C, 33*, 1530–1538.
7. Cheng, Z., Guo, C., Dong, W., He, F. M., Zhao, S. F., & Yang, G. L. (2012). Effect of thin nano-hydroxyapatite coating on implant osseointegration in ovariectomized rats. *Oral Surgery, Oral Medicine, Oral Pathology and Oral Radiology, 113*, e48–e53.

8. Choi, J. Y., Jung, U. W., Kim, C. S., Jung, S. M., Lee, I. S., & Choi, S. H. (2013). Influence of nanocoated calcium phosphate on two different types of implant surfaces in different bone environment: An animal study. *Clinical Oral Implants Research, 24*, 1018–1022.
9. Chung, T. W., Wang, S. S., Wang, Y. Z., Hsieh, C. H., & Fu, E. (2009). Enhancing growth and proliferation of human gingival fibroblasts on chitosan grafted poly (epsilon-caprolactone) films is influenced by nano-roughness chitosan surfaces. *Journal of Materials Science. Materials in Medicine, 20*, 397–404.
10. Cieślik, M., Kot, M., Reczyński, W., Engvall, K., Rakowski, W., & Kotarba, A. (2012). Parylene coatings on stainless steel 316L surface for medical applications—Mechanical and protective properties. *Materials Science and Engineering C, 32*, 31–35.
11. Ciobanu, G., Ilisei, S., & Luca, C. (2014). Hydroxyapatite-silver nanoparticles coatings on porous polyurethane scaffold. *Materials Science and Engineering C, 35*, 36–42.
12. Collares, F. M., Leitune, V. C., Rostirolla, F. V., Trommer, R. M., Bergmann, C. P., & Samuel, S. M. (2012). Nanostructured hydroxyapatite as filler for methacrylate-based root canal sealers. *International Endodontic Journal, 45*, 63–67.
13. Council, N. S. A. T. (2014). *National nanotechnology initiative strategic plan*. Available online at http://www.nano.gov/sites/default/files/pub_resource/2014_nni_strategic_plan.pdf. Accessed on January 11, 2016.
14. Council, T. E. P. A. O. T. (2007). Directive 2007/47/EC. *Official Journal of the European Union*.
15. Depprich, R. A., Handschel, J. G., Meyer, U., & Meissner, G. (2008). Comparison of prevalence of microorganisms on titanium and silicone/polymethyl methacrylate obturators used for rehabilitation of maxillary defects. *The Journal of Prosthetic Dentistry, 99*, 400–405.
16. Engel, E., Michiardi, A., Navarro, M., Lacroix, D., & Planell, J. A. (2008). Nanotechnology in regenerative medicine: The materials side. *Trends in Biotechnology, 26*, 39–47.
17. Fordham, W. R., Redmond, S., Westerland, A., Cortes, E. G., Walker, C., Gallagher, C., et al. (2014). Silver as a bactericidal coating for biomedical implants. *Surface and Coatings Technology, 253*, 52–57.
18. Gallino, E., Massey, S., Tatoulian, M., & Mantovani, D. (2010). Plasma polymerized allylamine films deposited on 316L stainless steel for cardiovascular stent coatings. *Surface and Coatings Technology, 205*, 2461–2468.
19. Gambardella, A., Bianchi, M., Kaciulis, S., Mezzi, A., Brucale, M., Cavallini, M., et al. (2016). Magnetic hydroxyapatite coatings as a new tool in medicine: A scanning probe investigation. *Materials Science and Engineering: C*.
20. Ganly, S., Hynes, S. O., Sharif, F., Aied, A., Barron, V., McCullagh, K., et al. (2013). Liposomal surface coatings of metal stents for efficient non-viral gene delivery to the injured vasculature. *Journal of Controlled Release, 167*, 109–119.
21. Garner, S. J., Nobbs, A. H., McNally, L. M., & Barbour, M. E. (2015). An antifungal coating for dental silicones composed of chlorhexidine nanoparticles. *Journal of Dentistry, 43*, 362–372.
22. Gazia, R., Mandracci, P., Mussano, F., & Carossa, S. (2011). AlNx and a-SiOx coatings with corrosion resistance properties for dental implants. *Surface and Coatings Technology, 206*, 1109–1115.
23. Glass, R. T., Bullard, J. W., Hadley, C. S., Mix, E. W., & Conrad, R. S. (2001). Partial spectrum of microorganisms found in dentures and possible disease implications. *Journal of the American Osteopathic Association, 101*, 92–94.
24. Gurzawska, K., Svava, R., Syberg, S., Yihua, Y., Haugshoj, K. B., Damager, I., et al. (2012). Effect of nanocoating with rhamnogalacturonan-I on surface properties and osteoblasts response. *Journal of Biomedical Materials Research Part A, 100*, 654–664.
25. Herting, G., Odnevall Wallinder, I., & Leygraf, C. (2006). Factors that influence the release of metals from stainless steels exposed to physiological media. *Corrosion Science, 48*, 2120–2132.

26. Hirata, E., Akasaka, T., Uo, M., Takita, H., Watari, F., & Yokoyama, T. (2012). Carbon nanotube-coating accelerated cell adhesion and proliferation on poly (L-lactide). *Applied Surface Science, 262*, 24–27.
27. Huang, G., Chen, Y., & Zhang, J. (2016). Nanocomposited coatings produced by laser-assisted process to prevent silicone hydogels from protein fouling and bacterial contamination. *Applied Surface Science, Part A*, *360*, 383–388.
28. Ingo, G. M., Guida, G., Angelini, E., Di, C. G., Mezzi, A., & Padeletti, G. (2013). Ancient mercury-based plating methods: Combined use of surface analytical techniques for the study of manufacturing process and degradation phenomena. *Accounts of chemical research, 46*.
29. Jevnikar, P., Golobic, M., Kocjan, A., & Kosmac, T. (2012). The effect of nano-structured alumina coating on the bond strength of resin-modified glass ionomer cements to zirconia ceramics. *Journal of the European Ceramic Society, 32*, 2641–2645.
30. Jia, Z., Xiu, P., Li, M., Xu, X., Shi, Y., Cheng, Y., et al. (2016). Bioinspired anchoring AgNPs onto micro-nanoporous TiO2 orthopedic coatings: Trap-killing of bacteria, surface-regulated osteoblast functions and host responses. *Biomaterials, 75*, 203–222.
31. Jiang, B., & Li, B. (2009). Polypeptide nanocoatings for preventing dental and orthopaedic device-associated infection: pH-induced antibiotic capture, release, and antibiotic efficacy. *Journal of Biomedical Materials Research. Part B, Applied Biomaterials, 88*, 332–338.
32. Karagkiozaki, V., Karagiannidis, P. G., Gioti, M., Kavatzikidou, P., Georgiou, D., Georgaraki, E., et al. (2013). Bioelectronics meets nanomedicine for cardiovascular implants: PEDOT-based nanocoatings for tissue regeneration. *Biochimica et Biophysica Acta (BBA)-General Subjects.*
33. Khan, S. N., Ramachandran, M., Kumar, S. S., Krishan, I., & Undaram, R. (2012). Osseointegration and more—A review of literature. *Indian Journal of Dentistry, 3*, 72–76.
34. Khan, W. S., & Asmatulu, R. (2013). Chapter 1—Nanotechnology emerging trends, markets, and concerns. In R. Asmatulu (Ed.), *Nanotechnology safety*. Amsterdam: Elsevier.
35. Khoo, X., O'Toole, G. A., Nair, S. A., Snyder, B. D., Kenan, D. J., & Grinstaff, M. W. (2010). Staphylococcus aureus resistance on titanium coated with multivalent PEGylated-peptides. *Biomaterials, 31*, 9285–9292.
36. Li, X., Liu, X., Huang, J., Fan, Y., & Cui, F. (2011). Biomedical of investigation of CNT based coatings. *Surface and Coatings Technology, 206*, 759–766.
37. Lin, J., Fei, T., & Zhang, J. (2013). Highly transparent superhydrophobic organic-inorganic nanocoating from the aggregation of silica nanoparticles. *Colloids and Surfaces A: Physiochemical and Engineering Aspects, 421*, 51–62.
38. Lin, R., Mao, X., Yu, Q., & Tan, B. (2007). Preparation of bioactive nano-hydroxyapatite coating for artificial cornea. In *Current Applied Physics,* 3*rd China–Korea Symposium on Biomaterials and Nano-Bio Technology.* Elsevier.
39. Mavrogenis, A. F., Dimitriou, R., Parvizi, J., & Babis, G. C. (2009). Biology of implant osseointegration. *Journal of Musculoskeletal and Neuronal Interactions, 9*, 61–71.
40. McConnell, E. L., Fadda, H. M., & Basit, A. W. (2008). Gut instincts: Explorations in intestinal physiology and drug delivery. *International Journal of Pharmaceutics, 364*, 213–226.
41. Mota, E. G., & Subramani, K. (2012). Chapter 4—Nanotechnology in operative dentistry: A perspective approach of history, mechanical behavior, and clinical application. In K. Subramani & W. Ahmed (Eds.), *Emerging nanotechnologies in dentistry micro and nano technologies.* Boston: William Andrew Publishing.
42. Nakamura, S., Colombo, A., Gaglione, A., Almagor, Y., Goldberg, S. L., Maiello, L., et al. (1994). Intracoronary ultrasound observations during stent implantation. *Circulation, 89*, 2026–2034.
43. Nichols, H. L., Zhang, N., Zhang, J., Shi, D., Bhaduri, S., & Wen, X. (2007). Coating nanothickness degradable films on nanocrystalline hydroxyapatite particles to improve the bonding strength between nanohydroxyapatite and degradable polymer matrix. *Journal of Biomedical Materials Research Part A, 82*, 373–382.

44. Pendegrass, C. J., Gordon, D., Middleton, C. A., Sun, S. N., & Blunn, G. W. (2008). Sealing the skin barrier around transcutaneous implants: in vitro study of keratinocyte proliferation and adhesion in response to surface modifications of titanium alloy. *Journal of Bone and Joint Surgery. British Volume, 90*, 114–121.
45. Popa, A. C., Stan, G. E., Enculescu, M., Tanase, C., Tulyaganov, D. U., & Ferreira, J. M. F. (2015). Superior biofunctionality of dental implant fixtures uniformly coated with durable bioglass films by magnetron sputtering. *Journal of the Mechanical Behavior of Biomedical Materials, 51*, 313–327.
46. Pozuelo, J., Compañ, V., González-Méijome, J. M., González, M., & Mollá, S. (2014). Oxygen and ionic transport in hydrogel and silicone-hydrogel contact lens materials: An experimental and theoretical study. *Journal of Membrane Science, 452*, 62–72.
47. Ramirez, G., Rodil, S. E., Arzate, H., Muhl, S., & Olaya, J. J. (2010). Niobium based coatings for dental implants. *Applied Surface Science, 257*, 2555–2559.
48. Ranjbar, Z., & Rastegar, S. (2010). Nano mechanical properties of an automotive clear-coats containing nano silica particles with different surface chemistries. *Progress in Organic Coatings, 72*, 40–43.
49. Redlich, M., & Tenne, R. (2013). Chapter 13—Nanoparticle coating of orthodontic appliances for friction reduction. In K. Subramani, W. Ahmed & J. K. Hartsfield (Eds.), *Nanobiomaterials in clinical dentistry.* William Andrew Publishing.
50. Reinhardt, B., & Beikler, T. (2014). Chapter 4—Dental implants. In J. Z. Shen & T. KOSMA-Ì (Eds.) *Advanced ceramics for dentistry.* Oxford: Butterworth-Heinemann.
51. Richardson, R. R., Miller, J. A., & Reichert, W. M. (1993). Polyimides as biomaterials: Preliminary biocompatibility testing. *Biomaterials, 14*, 627–635.
52. Schatz, R. A., Baim, D. S., Leon, M., Ellis, S. G., Goldberg, S., Hirshfeld, J. W., et al. (1991). Clinical experience with the Palmaz-Schatz coronary stent. Initial results of a multicenter study. *Circulation, 83*, 148–161.
53. Schatz, R. A., Palmaz, J. C., Tio, F. O., Garcia, F., Garcia, O., & Reuter, S. R. (1987). Balloon-expandable intracoronary stents in the adult dog. *Circulation, 76*, 450–457.
54. Shen, W., Cai, K., Yang, Z., Yan, Y., Yang, W., & Liu, P. (2012). Improved endothelialization of NiTi alloy by VEGF functionalized nanocoating. *Colloids and Surfaces B: Biointerfaces, 94*, 347–353.
55. Siegel, J., Polívková, M., Staszek, M., Kolářová, K., Rimpelová, S., & Švorčík, V. (2015). Nanostructured silver coatings on polyimide and their antibacterial response. *Materials Letters, 145*, 87–90.
56. Siepmann, F., Wahle, C., Leclercq, B., Carlin, B., & Siepmann, J. (2008). pH-sensitive film coatings: towards a better understanding and facilitated optimization. *European Journal of Pharmaceutics and Biopharmaceutics, 68*, 2–10.
57. Simonis, P., Dufour, T., & Tenenbaum, H. (2010). Long-term implant survival and success: a 10–16-year follow-up of non-submerged dental implants. *Clinical Oral Implants Research, 21*, 772–777.
58. Subramani, K., & Ahmed, W. (2011). Nanotechnology and the Future of Dentistry. In *Emerging nanotechnolgies in dentistry.* Elsevier.
59. Taheri, S., Cavallaro, A., Christo, S. N., Smith, L. E., Majewski, P., & Barton, M. (2014). Substrate independent silver nanoparticle based antibacterial coatings. *Biomaterials, 35*, 4601–4609.
60. Tan, A., Alavijeh, M. S., & Seifalian, A. M. (2012). Next generation stent coatings: convergence of biotechnology and nanotechnology. *Trends Biotechnology, 30*, 406–409.
61. Tang, C. J., Wang, G. X., Shen, Y., Wan, L. J., Xiao, Zhang, Q., et al. (2009). A Study on surface endothelialization of plasma coated intravascular stents. *Surface and Coatings Technology, 204*, 1487–1492.
62. Taylor, S. R., & Sieradzki, K. (2003). The development of a multi-functional aerospace coating: considerations in the use of nano-dimensioned materials. *Progress in Organic Coatings, 47*, 173.

63. Thalhammer, A., Edgington, R. J., Cingolani, L. A., Schoepfer, R., & Jackman, R. B. (2010). The use of nanodiamond monolayer coatings to promote the formation of functional neuronal networks. *Biomaterials, 31*, 2097–2104.
64. Tiwari, S., & Nandlal, B. (2013). Effect of nano-filled surface coating agent on fluoride release from conventional glass ionomer cement: an in vitro trial. *Journal of Indian Society of Pedodontics and Preventive Dentistry, 31*, 91–95.
65. Trading, O. O. F. (2012). Dentistry an OFT market study.
66. USA, S. (2015). *The Medical Device Industry in the United States*. Available online at http://selectusa.commerce.gov/industry-snapshots/medical-device-industry-united-states.html. Accessed on January 08, 2013 (2016).
67. Verne, E., Vitale-Brovarone, C., Robiglio, L., & Baino, F. (2008). *Single-piece ceramic prosthesis elements*.
68. Vitale-Brovarone, C., Baino, F., Tallia, F., Gervasio, C., & Verné, E. (2012). Bioactive glass-derived trabecular coating: a smart solution for enhancing osteointegration of prosthetic elements. *Journal of Materials Science Materials in Medicine, 23*, 2369–2380.
69. Walkenhorst, J. (2014). *BioNanoImplant: Optimized Osseointegration with bio-nanocoating*. Available online at http://www.technologieallianz.de/webtemp/1902_TO_BioNanoImplec39c602.pdf
70. Wang, D., & Bierwagen, G. P. (2009). Sol-Gel coatings on metals for corrosion protection. *Progress in Organic Coatings, 64*, 327–338.
71. Wennerberg, A., Jimbo, R., Allard, S., Skarnemark, G., & Andersson, M. (2011). In vivo stability of hydroxyapatite nanoparticles coated on titanium implant surfaces. *International Journal of Oral and Maxillofacial Implants, 26*, 1161–1166.
72. Williams, D. F. (2008). On the mechanisms of biocompatibility. *Biomaterials, 29*, 2941–2953.
73. Zhang, S., Kocjan, A., Lehmann, F., Kosmac, T., & Kern, M. (2010). Influence of contamination on resin bond strength to nano-structured alumina-coated zirconia ceramic. *European Journal of Oral Sciences, 118*, 396–403.
74. Zhao, L., Wang, H., Huo, K., Cui, L., Zhang, W., Ni, H., et al. (2011). Antibacterial nano-structured titania coating incorporated with silver nanoparticles. *Biomaterials, 32*, 5706–5716.

Chapter 17
Microvascular Anastomoses: Suture and Non-suture Methods

R.A.J. Wain, D. Hammond, M. McPhillips, J.P.M. Whitty and W. Ahmed

Abstract A plethora of methods have been proposed for coapting microvessels, with the mainstay being hand-suturing under an operating microscope. A broad range of hand-sutured techniques have been described and these are still evolving today. Alongside this, non-suture methods of microvascular anastomosis have gained popularity over recent years with numerous intra- and extravascular approaches being proposed. This section addresses the development of microsurgical suture technique for microvascular anastomosis, and continues to present the array of non-suture methods currently proposed as alternatives to standard suturing.

17.1 Microvascular Anastomoses

A microsurgical procedure is defined as one which would be otherwise impossible without the aid of magnification. Whilst the joining, or anastomosis, of blood vessels had been performed in the late nineteenth century, it was not until the mid-twentieth century that the operating microscope was introduced for repair of small blood vessels. Since this time, a wide range of methods have been proposed for coapting microvessels, and these are still evolving today. This section addresses the development of microsurgical suture technique for microvascular anastomosis, and continues to present the array of non-suture methods currently proposed as alternatives to standard suturing.

R.A.J. Wain (✉) · D. Hammond · M. McPhillips · J.P.M. Whitty · W. Ahmed (✉)
School of Medicine, University of Central Lancashire, Preston, UK
e-mail: richwain@doctors.org.uk

W. Ahmed
e-mail: wahmed4@uclan.ac.uk

W. Ahmed and M.J. Jackson (eds.), *Surgical Tools and Medical Devices*,
DOI 10.1007/978-3-319-33489-9_17

17.2 Background of Microvascular Anastomoses

The first end-to-end arterial anastomosis was reported in 1889 [1], joining carotid arteries of sheep with fine silk thread and curved needles. Standardising the technique and gaining consistent success was the natural progression, as demonstrated by development of the triangulation technique (Fig. 17.1) by Carrel [2], work which would later secure him the Nobel Prize in Medicine and Physiology (1912). Despite this, vascular anastomoses were not performed for reconstruction or in repair of traumatic injuries for another 50 years, with the procedure remaining largely experimental till the end of World War II [3].

The first reported microvascular anastomosis was performed by Jacobson and Suarez in 1960 [5], achieving 100 % patency rates in vessels as small as 1.4 mm diameter. The key to success here was introduction of the operating microscope, which was first popularised by otolaryngology and ophthalmology several years previously, and of course development of finer instruments and sutures.

Microsurgical techniques became more widely practised over the next decade first with successful replantations of upper limbs [6] and then digits [7] being performed. By the early 1970s, free-tissue transfer was reported in a variety of specialist centres [8–10]. Since then, both surgical techniques and instrumentation have been refined to permit reconstructive options for the whole body and, most recently, allotransplantation of complex anatomical units has been achieved [11].

Whilst reliable results are now seen routinely with free-tissue transfer in the majority of centres, there is ongoing debate as to the best method of performing a vascular anastomosis. Characteristics of the ideal technique would be: (1) simple to perform and teach, (2) quick, i.e. minimises tissue ischaemia time, (3) avoids vessel wall trauma and (4) provides best short- and long-term patency rates [12]. As well as these qualities, it is vital that the principles of sound microsurgical practice are adhered to, in particular choice of a good quality vessel, tension-free repair, suture line eversion and direct intima–intima contact [12–14].

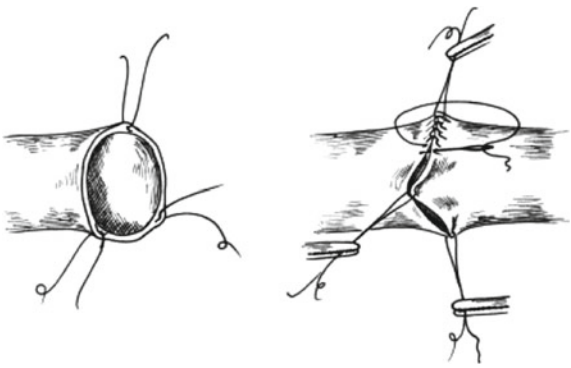

Fig. 17.1 Carrel's triangulation technique [2] (from [4])

17.3 Sutured Anastomoses

It remains conventional that the majority of microvascular anastomoses are performed using hand-sutured techniques, although use of the microvascular anastomotic coupler is widely accepted for venous anastomoses [15]. Since the 1960s, the interrupted (individual) suture method has been regarded as the gold standard [16, 17] for microvascular anastomosis. Whilst many suturing techniques are practised, a recent systematic review found no statistical difference in patency rates between them, provided the principles of microsurgical practice are followed [12].

17.3.1 Suture Properties

The number, type and material properties of the sutures are important considerations for success. Too few sutures will inevitably lead to leaking with subsequent haematoma formation, and too many can damage endothelial cells causing activation of the clotting cascade [18], and indeed weakening the anastomosis [19]. In addition, a recent computational study has demonstrated that closely positioned sutures causes high shear strain rates (SSR) at the vessel wall which itself can induce thrombus formation via activation of platelets [20].

Whilst both non-absorbable and absorbable sutures have been used for microvascular anastomoses, most surgeons favour a non-absorbable material such as polypropylene or nylon. The combination of an inert monofilament material and a sharp-tipped, round-bodied, curved and smoothly swaged needle permits accurate placement with minimal vessel trauma.

17.3.2 Suture Techniques

A wide range of suture techniques are available to the surgeon to coapt microvessels. These vary from the conventional interrupted suture method to complex horizontal mattress sutures (Fig. 17.2) which involve modifying the vessel ends. Other methods include continuous, locking continuous, continuous horizontal, interrupted horizontal, sleeve, interrupted spiral and posterior-wall first [12, 18]. Despite being faster to perform, the continuous methods have been criticised for their potential to purse-string, thereby narrowing the lumen and predisposing to thrombosis [16, 17]. Experimental models have demonstrated that this is not necessarily the case [21] and, as previously mentioned, a recent systematic review has found that a careful, precise microsurgical technique is the only determinant in achieving consistent, successful long-term results [12].

Fig. 17.2 Simple interrupted (*left*) and horizontal mattress (*right*) suture techniques [18]

17.4 Non-suture Anastomoses

Whilst advances in magnification, instruments and materials have resulted in reliable successful microvascular anastomoses, simply suturing involves a degree of vessel handling and therefore potential for intimal damage. In addition, the suture material itself, either polypropylene or nylon, remains within the vascular lumen. These factors, amongst others, contribute to a failure rate of sutured anastomoses of approximately 2–6 % [22–24], usually secondary to thrombus formation. Even for the experienced microsurgeon, microvascular anastomosis remains challenging and time consuming. Alternative methods to the conventional hand-sutured techniques have therefore been sought over the last half century, with some devices now being routinely used in clinical practice [15, 25–27]. Broadly speaking, these non-suture techniques can be divided into clips/staples, adhesives, laser-assisted anastomoses, stents, magnets, gels and ring-pin devices [4, 28].

17.4.1 Clips/Staples

The first use of clips to coapt blood vessels was in 1953 by Bikfalvi and Dubecz [29]. Several evolutions of this procedure took place over subsequent years with much work being carried out by Kirsch et al. [30]. His group modified previous devices to produce a series of non-penetrating clips which could be individually placed around an anastomosis. This work ultimately led to the development of the commercially available vessel closure system (VCS)[1] which is currently used in clinical practice. This system requires the positioning of a series of stay sutures and eversion of the vessel ends using a specialised instrument. The non-penetrating clips are then placed between the sutures which are then removed (Fig. 17.3). There have been multiple studies demonstrating the efficacy of this technique with equivalent patency rates to that of sutured and coupled anastomoses [26, 27, 31–33].

[1]AutoSuture, United States Surgical Corporation, Norwalk, Connecticut, USA.

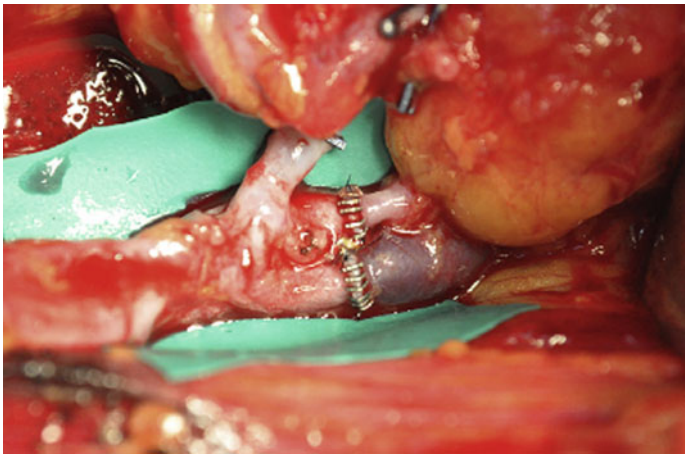

Fig. 17.3 Vessel closure system (VCS) arterial and venous anastomoses [26]

Another clip system has been developed for vascular anastomosis called the U-Clip.[2] This differs from the VCS as the clips are penetrating, in the same way as sutures would pierce the vessel wall. The advantage over a sutured anastomosis is there is no need to tie microsurgical knots; hence, the procedure is notably quicker. It does however mean that, unlike the VCS, there is foreign material within the vessel lumen. This system is not as widely used as the VCS, but does have a small body of evidence to support its use clinically [34–36].

17.4.2 Adhesives

There has been an upward trend in the use of glues and adhesives within surgery over recent years for a wide range of applications [37]. Broadly adhesives can be divided into two categories: 'cyanoacrylates' and thrombin-based 'fibrin-glues'. The fibrin-based glues contain components mimicking the final steps of blood coagulation [4] and are often used as an adjunct to a sutured anastomosis with the aim of reducing the number of sutures needed and anastomotic time, as demonstrated by Cho et al. cohort study [38]. There has been one large clinical study examining the use of fibrin glues for anastomoses in breast reconstruction patients with no reported increase in anastomotic failure [39]. Nevertheless, given the constituent of the glue itself, many surgeons are concerned about using a substance which could induce clotting in their microvascular anastomosis [40].

Cyanoacrylate-based glues were first used experimentally for vascular anastomosis in the 1960s [41]; however, within a relatively short space of time, several

[2]Medtronic, Inc.; Minneapolis, MN, USA.

problems with this method were identified. Green et al. [42] experiments demonstrated an early foreign body response with giant cell formation and later extreme thinning of the vessel wall. For these reasons, amongst others including the high heat expelled during polymerisation [4], cyanoacrylates have not been routinely used for microvascular anastomoses. It is important to note, however, that some of the newer generation cyanoacrylates do not exhibit the same tissue reaction seen in these studies, and indeed, actually show *less* foreign body response than a sutured anastomosis [43, 44].

17.4.3 Laser-Assisted Microvascular Anastomosis (LAMA)

Initial experimental attempts at coapting vessels using heat energy were carried out in the 1960s [45]; however, this method did not prove particularly effective, and there are no studies demonstrating its use clinically [4]. Lasers, on the other hand, have shown to produce some promising results in a number of studies [46–49]. One of the longest standing groups to utilise LAMA is that of Leclère who reported use of a 1.9-micron diode laser to perform welded anastomoses [50], typically requiring four sutures each. LAMA can therefore be viewed as a 'suture-reducing' technique rather than a 'non-suture' method. Fifty eight anastomoses were performed using LAMA and reported only one (1.7 %) failure as a 'rupture' possibly due to it being carried out in an irradiated field. Leclère has since reported a review of 30-years experience with the LAMA technique [49] and has stated that this method can be performed more quickly than conventional anastomosis, and the surgically induced vessel damage is limited. Whilst this method is largely confined to experimental findings and small clinical studies, further technical innovation will likely lead to its greater use in theatre over the coming years.

Although not classified as a laser-assisted method, the use of visible light has also been reported as an anastomotic technique [51]. Photochemical tissue bonding (PTB) combines photoactive dyes with visible light to create fluid-tight seals between tissue surfaces without causing collateral thermal damage. This study was carried out experimentally and found equal (80 %) patency rates between sutured and PTB anastomoses. One may argue that the sutured anastomosis group in this study had a higher than expected failure rate, given these are usually quoted at 2–6 % [22–24] rather than the 20 % experienced here, thereby over-emphasising the effectiveness of PTB anastomoses.

17.4.4 Stents

Whilst intravascular stents have been used since the late nineteenth century in one form or another, possibly the first microvascular anastomosis performed using a stent was in 1979 by Yamagata et al. [52]. This study compared three types of

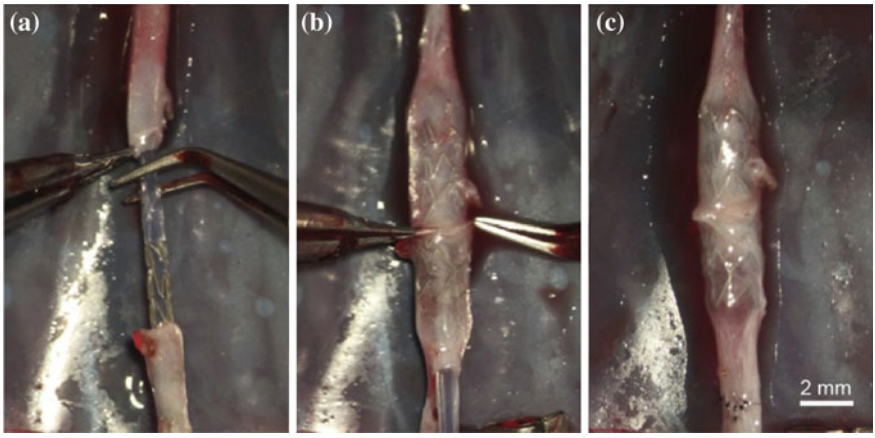

Fig. 17.4 Stainless steel intravascular stent insertion procedure [56]

soluble tube stent made of polyvinyl alcohol (PVA) used to anastomose carotid arteries in rats, along with the topical application of cyanoacrylate glue. Their bilayered stents demonstrated patency from 92 to 98 % for a maximum of six months. Further experimental studies have been carried out using absorbable stents in 0.35 mm vessels, again with the adjunct of adhesive, which showed immediate and short-term patency rates better than those associated with suture technique [53]. The work of Mikaelsson and Arnbjörnsson [54] used intravascular cylindrical stents to anastomose rat aortas, without the aid of adhesives, showing all to be patent and healed at 25 days. More recently existing metallic cardiac stents have been used to perform microanastomoses in a proof-of-concept study [55] with promising initial outcomes. This stent, however, relies on a balloon to expand it to the correct size, and hence necessary puncture of the vessel wall at a site distant from the anastomosis, which may not be ideal in many plastic surgical applications, e.g. free-tissue transfer. A similar study was carried out by Bauer et al. [56] using stainless steel stents in nine rat aorta anastomoses (Fig. 17.4). They reported one vessel tear, one complete thrombus occlusion and four anastomoses requiring additional sealant, e.g. with fibrin glue. These studies clearly demonstrate technical difficulties with expandable stenting and as such this remains purely experimental for the purposes of microvascular anastomoses.

17.4.5 Magnets

The approximation of vessel ends using magnets was preliminarily reported as early as 1978 by Obora et al. [57], with a full scientific paper published two years later by the same group [58]. This method involved passing the vessel ends through a hollow magnet and securing the everted edges on pins. The magnets then provided

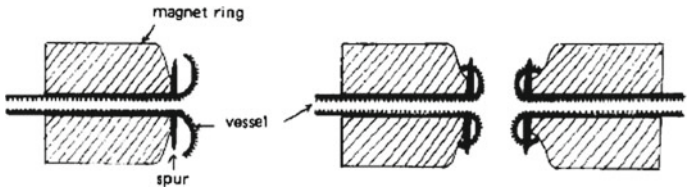

Fig. 17.5 Magnet ring anastomosis [58]

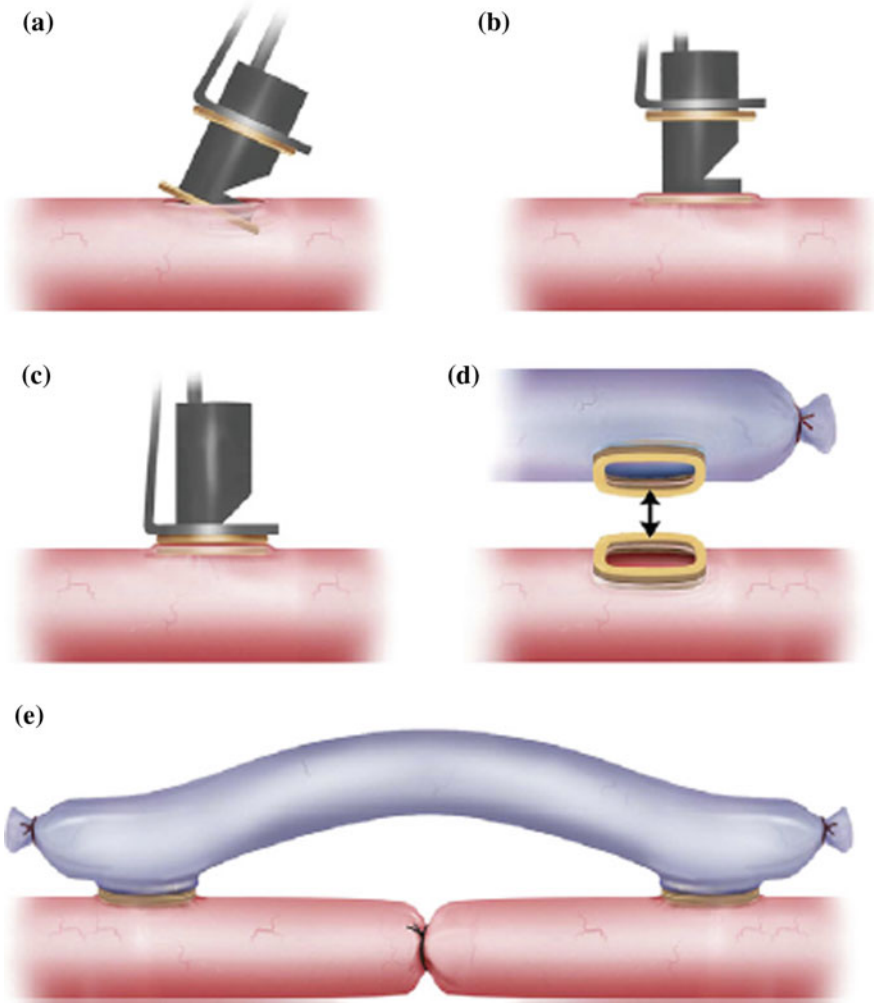

Fig. 17.6 Magnetic anastomosis for vein grafts [59]

the necessary force to coapt the two vessel lumens (Fig. 17.5). Results reported by this group demonstrated 90 % patency rates in vessels with a maximum diameter of 1 mm, with an average time for anastomosis of 8.0 min. Despite these apparently encouraging results, magnetic microvascular anastomosis has not become routine practice. Since then there have been isolated studies documenting the use of magnets for anastomoses in vein grafts [59] (Fig. 17.6), and also for non-suture anastomosis in a dog model using magnetised ring-pins [60].

17.4.6 Gels

Gels for microvascular anastomoses are principally used to produce a temporary 'bung' in the vessel ends with two purposes, first to negate the use of vascular clamps, and second to keep the vessel end open in order to facilitate the desired method of anastomosis. The gels themselves are composed of a range of substances which dissolve with exposure to high [43, 44] or low [61, 62] temperatures. The gel does not form the anastomosis properly; rather it assists with suture placement or application of an adhesive. Use of the commercially available LeGoo[3] has been well documented in cardiac surgery since 2010, and was used for microvascular anastomoses in rats by Manchio et al. [62] prior to this. However, it was only recently reported clinically in free-tissue transfer by Giessler et al. [61]. In this situation, the gel was used to facilitate a sutured anastomosis (Fig. 17.7) and subsequently was dissolved using topically applied cold saline. They reported no anastomotic failures and suggested that the gel was an attractive alternative to micro-clamps, especially for atherosclerotic arteries and confined anastomosis sites [61].

A uniquely formulated poloaxamer gel was used in the study by Chang et al. [43] to enable an adhesive-based anastomosis using cyanoacrylate glue with no sutures (Fig. 17.8). The gel was subsequently dissolved using a heat source applied externally. Qassemyar and Michel [44] used the commercially available LeGoo gel to perform an almost identical procedure; however, LeGoo does not require addition of an external heat source to dissolve, and as such is an overall simpler procedure. Both groups described approximately equal patency rates and significantly quicker anastomoses time when compared to their sutured controls. Whilst the LeGoo gel has been approved for clinical use, the unique poloaxamer gel from Chang et al. [43] remains experimental at this time. An important addition to this is that both groups found significantly less foreign body reaction in the cyanoacrylate anastomoses than the sutured ones. This is likely to be due to the specific newer generation of cyanoacrylates used compared to the original studies carried out in the 1980s [42].

[3]Pluromed Inc., Woburn, MA, USA, www.pluromed.com.

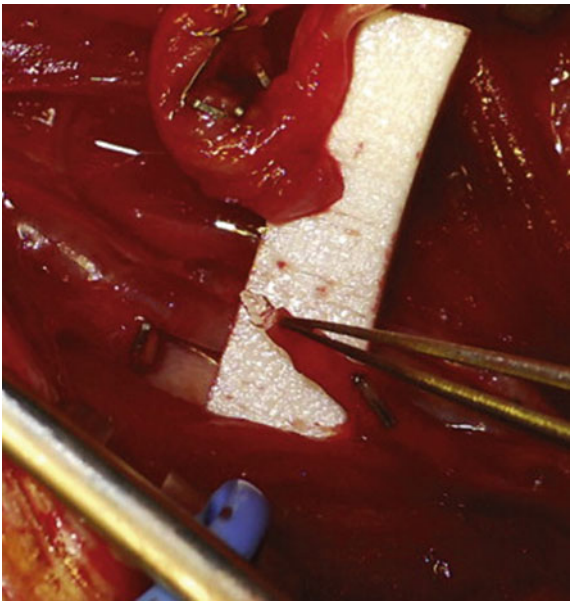

Fig. 17.7 Use of LeGoo gel for microvascular anastomosis in free-tissue transfer [61]

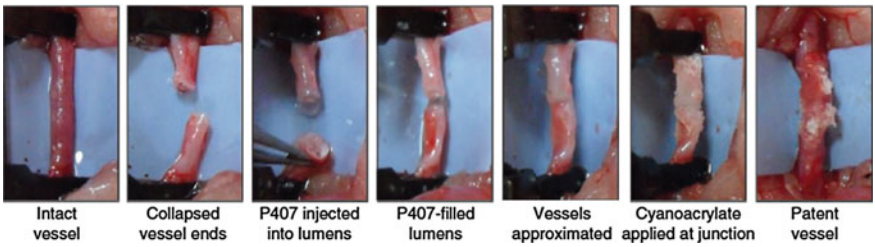

Fig. 17.8 Poloaxamer gel anastomosis with cyanoacrylate glue [43]

17.4.7 Bioabsorbable Pin Device

A further experimental method for microvascular anastomosis is that described by Ueda et al. [63]. This consists of an extra-lumenal cuff with hooks onto which the vessel wall is placed. It is composed of a bioabsorbable polymer and relies on one end of the vessel being reflected back over the cuff and onto the pins, whilst the other end then slips over the first, akin to an invaginating technique (Fig. 17.9). A suture is then placed around the outside of the vessel to secure the hooked walls in place. The experimental data suggest favourable patency rates and no significant impact of the bioabsorbable agent itself. Whilst these results are promising, they are purely experimental at this stage.

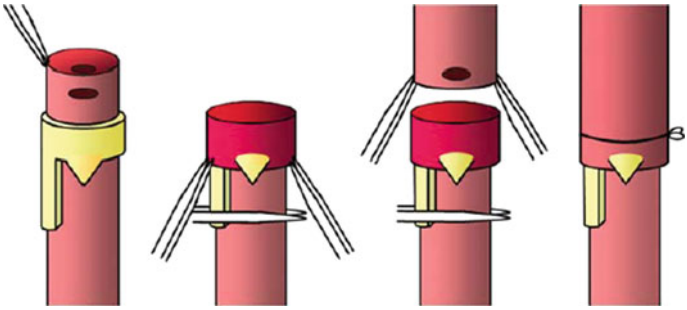

Fig. 17.9 Bioabsorbable pin device [63]

17.4.8 Ring-Pin Devices

The most popularly used ring-pin device is an evolution of the original design by Nakayama et al. in 1962 [64] (Fig. 17.10), although Payr had devised a strikingly similar device (Fig. 17.11) in 1900 furnished from magnesium [65]. In 1976 Ostrup [66] studied the Nakayama rings and found that anastomoses were performed in one

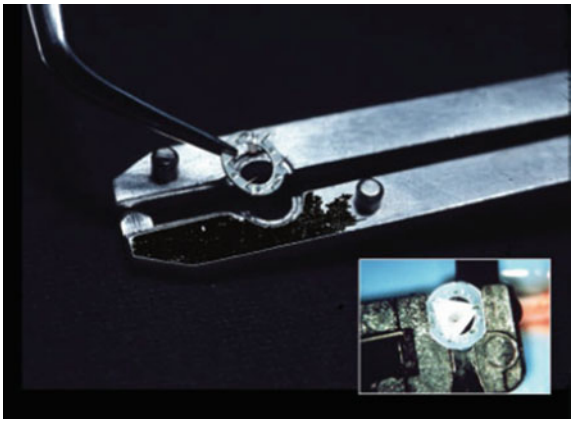

Fig. 17.10 Ring-pin coupling device developed by Nakayama et al. [64] (from [4])

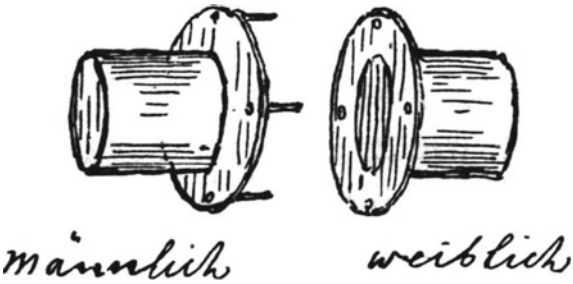

Fig. 17.11 Ring-pin coupling device as depicted by Payr (Fig. 17.7 from [65])

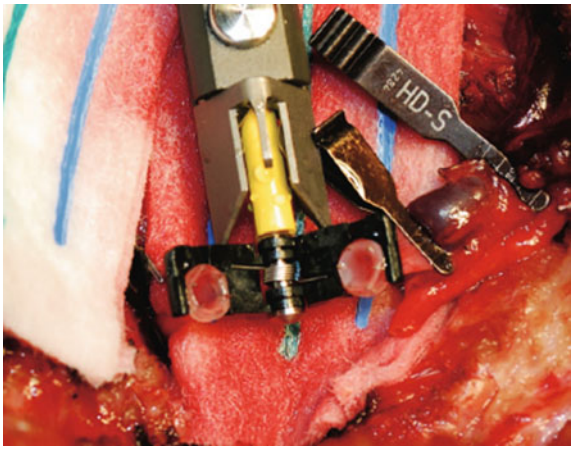

Fig. 17.12 Unilink microvascular coupler as described by Ostrup and Berggren [67] (from [15])

third of the time of a hand-held sutured anastomosis. He later developed an evolution of the Nakayama rings [67] which consisted of polyethylene rings and interlocking stainless steel pins (Fig. 17.12), whilst working alongside Unilink.[4] Each vessel end is passed through the polyethylene ring and reflected back over the steel pins. The two rings are then pressed together until the pins interlock. This device was suitable for coapting vessels as small as 0.8 mm and has since become the commercially available GEM Microvascular Anastomotic Coupling (MAC) System produced by Synovis[5] used in many microsurgical centres today. A large number of studies have been published demonstrating faster and simpler anastomoses, with similar, if not better, patency rates of coupled anastomoses when compared to the standard hand-sutured method [15, 33, 68–70].

Whilst the MAC System was not specifically designed for arteries, some groups have successfully performed microarterial anastomoses using this system [71–73], albeit with varying degrees of success. The more variable patency rates and technical difficulties associated with arterial coupling prevent it from becoming routine practice in many centres. Thicker and less-pliable arterial walls are most commonly implicated as the reasons for this as these characteristics make placement of the wall onto the pins challenging, often necessitating the use of a smaller diameter coupler.

More recently, another anastomotic ring-pin style coupler has been developed [74]. The Vascular Coupling Device (VCD) is similar in appearance to the MAC system; however, it has a series of hinged wings onto which the pins are fixed at an angle of 45° (Fig. 17.13). This simplifies the mounting of the vessel wall onto the pins themselves at which point the wings are closed to fully open the lumen and evert the vessel walls. The accompanying tools used to apply the device appear to

[4]3M Healthcare, 3M Center, St. Paul, MN 55144-1000, USA.

[5]Synovis Micro Companies Alliance Inc., 439 Industrial Lane, Birmingham, AL 35211, USA.

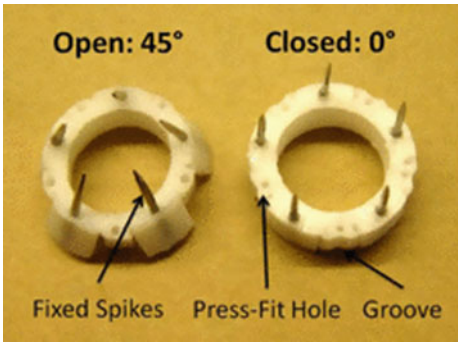

Fig. 17.13 Vascular coupling device (VCD) [74]

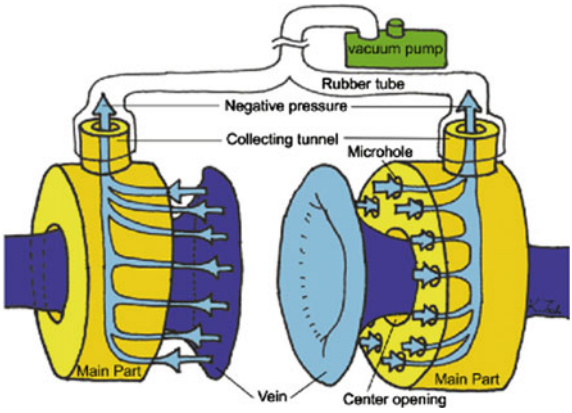

Fig. 17.14 Vacuum-assisted microvascular anastocoupler (VaMAC) [75]

offer greater manoeuvrability compared to the existing MAC System; however, the VCD is still in the developmental stages and is not in clinical use.

Though not strictly a ring-pin device, the vacuum-assisted microvascular anastocoupler (VaMAC) [75] has been developed as an alternative to the MAC system. It consists of two rings with micro-holes connected to a negative pressure system (Fig. 17.14). The vessel ends are then passed through the rings and held in place, everted by suction alone until the plastic rings are pressed together. The rings are then secured using sutures through holes in their periphery. The perceived advantages of this technology over the MAC, or in fact the VCD, is the avoidance of penetrating the vessel wall with pins, and the semi-automatic manner in which the vacuum locates the vessel wall onto the ring. As with the VCD, this technology is currently experimental only, but has shown promising initial results.

Fig. 17.15 Use of robotics in microvascular anastomoses [76]

17.5 Summary

The evidence in favour of both the MAC device and the VCS has reached level 2b as outlined by the Oxford Centre for Evidence-Based Medicine (CEBM) [4]. This signifies that benefits have been demonstrated for both techniques via well-constructed, cohort-controlled studies. Apart from the aforementioned study in breast reconstruction [38], there is very little evidence to endorse the use of laser-assisted anastomoses, adhesives, stents or gels in microvascular anastomoses.

Although not discussed here in detail, one of the next steps in advancing technology in practice is toward the integration of robotics into microsurgery, as has been the case for many other facets of surgery. There have been a select few studies demonstrating their use for microvascular anastomosis [76–78] (Fig. 17.15) with apparent good degrees of success. This will undoubtedly be one of the directions microsurgery is sure to adopt in the coming years.

References

1. Jassinowsky, A. (1889). Die Arteriennhat: Eine experimentelle Studie. *Inaugural Dissertation Dorpat*, 1–103.
2. Carrel, A. (1902). La technique operatoire des anastomoses vasculaires et la transplantation des visceres. *Lyon Medical, 98*, 859–864.
3. Rickard, R. F., & Hudson, D. A. (2014). A history of vascular and microvascular surgery. *Annals of Plastic Surgery, 73*(4), 465–472.
4. Zeebregts, C. J., Heijmen, R. H., van den Dungen, J. J., & van Schilfgaarde, R. (2003). Non-suture methods of vascular anastomosis. *British Journal of Surgery, 90*(3), 261–271.
5. Jacobson, J. H, I. I., & Suarez, E. L. (1960). Microsurgery in anastomosis of small vessels. *Surgical Forum, 11*, 243–245.
6. Malt, R. A., & McKhann, C. F. (1964). Replantation of severed arms. *JAMA: The Journal of the American Medical Association, 189*(10), 716–722.

7. Komatsu, S., & Tamai, S. (1968). Successful replantation of a completely cut-off thumb. *Plastic and Reconstructive Surgery, 42*(4), 374–377.
8. McLean, D. H., & Buncke, H. J, Jr. (1972). Autotransplant of omentum to a large scalp defect, with microsurgical revascularization. *Plastic and Reconstructive Surgery, 49*(3), 268–274.
9. Daniel, R. K., & Taylor, G. I. (1973). Distant transfer of an island flap by microvascular anastomoses. A clinical technique. *Plastic and Reconstructive Surgery, 52*(2), 111–117.
10. O'Brien, B. M., MacLeod, A. M., Hayhurst, J. W., & Morrison, W. A. (1973). Successful transfer of a large island flap from the groin to the foot by microvascular anastomoses. *Plastic and Reconstructive Surgery, 52*(3), 271–278.
11. Petruzzo, P., Testelin, S., Kanitakis, J., Badet, L., Lengelé, B., Girbon, J.-P., et al. (2012). First human face transplantation: 5 years outcomes. *Transplantation*, *93*(2), 236–240.
12. Alghoul, M. S., Gordon, C. R., Yetman, R., Buncke, G. M., Siemionow, M., Afifi, A. M., et al. (2011). From simple interrupted to complex spiral: A systematic review of various suture techniques for microvascular anastomoses. *Microsurgery*, *31*(1), 72–80.
13. Acland, R. D. (1988). *Practice manual for microvascular surgery* (2nd revised ed.). Mosby.
14. Shurey, S., & Green, C. (2011). *Basic microsurgical techniques: A laboratory manual*. Middlesex, UK: Surgical Research Department, NPIMR, Northwick Park Hospital.
15. Jandali, S., Wu, L. C., Vega, S. J., Kovach, S. J., & Serletti, J. M. (2010). 1000 consecutive venous anastomoses using the microvascular anastomotic coupler in breast reconstruction. *Plastic and Reconstructive Surgery*, *125*(3), 792–798.
16. Cobbett, J. (1967). Small vessel anastomosis. A comparison of suture techniques. *British Journal of Plastic Surgery, 20*(1), 16–20.
17. Jenkins, J. D. (1967). Repair of small vessels. *The British Journal of Surgery, 54*(6), 558–560.
18. Siemionow, M. (2015). *Plastic and reconstructive surgery: Experimental models and research designs*. Springer.
19. Colen, L. B., Gonzales, F. P., & Buncke, H. J. (1979). The relationship between the number of sutures and the strength of microvascular anastomoses. *Plastic and Reconstructive Surgery, 64* (3), 325–329.
20. Wain, R. A. J., Whitty, J. P. M., Hammond, D., McPhillips, M., & Ahmed, W. (2015). Microarterial anastomoses: A parameterised computational study examining the effect of suture position on intravascular blood flow. *Microvascular Research, 105*, 141–148.
21. Little, J. R., & Salerno, T. A. (1978). Continuous suturing for microvascular anastomosis. Technical note. *Journal of Neurosurgery, 48*(6), 1042–1045.
22. Disa, J. J., Cordeiro, P. G., & Hidalgo, D. A. (1999). Efficacy of conventional monitoring techniques in free tissue transfer: An 11-year experience in 750 consecutive cases. *Plastic and Reconstructive Surgery, 104*(1), 97–101.
23. Bui, D. T., Cordeiro, P. G., Hu, Q.-Y., Disa, J. J., Pusic, A., & Mehrara, B. J. (2007). Free flap reexploration: Indications, treatment, and outcomes in 1193 free flaps. *Plastic and Reconstructive Surgery*, *119*(7), 2092–2100.
24. Kroll, S. S., Schusterman, M. A., Reece, G. P., Miller, M. J., Evans, G. R., Robb, G. L., et al. (1996). Choice of flap and incidence of free flap success. *Plastic and Reconstructive Surgery, 98*(3), 459–463.
25. Ardehali, B., Morritt, A. N., & Jain, A. (2014). Systematic review: Anastomotic microvascular device. *Journal of Plastic, Reconstructive and Aesthetic Surgery: JPRAS, 67*(6), 752–755.
26. Reddy, C., Pennington, D., & Stern, H. (2012). Microvascular anastomosis using the vascular closure device in free flap reconstructive surgery: A 13-year experience. *Journal of Plastic, Reconstructive and Aesthetic Surgery: JPRAS, 65*(2), 195–200.
27. Zeebregts, C., Acosta, R., Bölander, L., van Schilfgaarde, R., & Jakobsson, O. (2002). Clinical experience with non-penetrating vascular clips in free-flap reconstructions. *British Journal of Plastic Surgery, 55*(2), 105–110.
28. Pratt, G. F., Rozen, W. M., Westwood, A., Hancock, A., Chubb, D., Ashton, M. W., et al. (2012). Technology-assisted and sutureless microvascular anastomoses: Evidence for current techniques. *Microsurgery*, *32*(1), 68–76.

29. Bikfalvi, A., & Dubecz, S. (1953). Observations in animal experiments with mechanised vessel suture. *Journal International De Chirurgie, 13*(5), 481–496.
30. Kirsch, W. M., Zhu, Y. H., Hardesty, R. A., & Chapolini, R. (1992). A new method for microvascular anastomosis: Report of experimental and clinical research. *The American Surgeon, 58*(12), 722–727.
31. Zeebregts, C. J., Kirsch, W. M., van den Dungen, J. J., Zhu, Y. H., & van Schilfgaarde, R. (2004). Five years' world experience with nonpenetrating clips for vascular anastomoses. *American Journal of Surgery, 187*(6), 751–760.
32. Cope, C., Lee, K., Stern, H., & Pennington, D. (2000). Use of the vascular closure staple clip applier for microvascular anastomosis in free-flap surgery. *Plastic and Reconstructive Surgery, 106*(1), 107–110.
33. Rozen, W. M., Whitaker, I. S., & Acosta, R. (2010). Venous coupler for free-flap anastomosis: Outcomes of 1,000 cases. *Anticancer Research, 30*(4), 1293–1294.
34. Taylor, J., Katz, R., & Singh, N. (2006). Use of the U-clip for microvascular anastomosis. *Microsurgery, 26*(8), 550–551.
35. Baynosa, R. C., Stutman, R., Mahabir, R. C., Zamboni, W. A., & Khiabani, K. T. (2008). Use of a novel penetrating, sutureless anastomotic device in arterial microvascular anastomoses. *Journal of Reconstructive Microsurgery, 24*(1), 39–42.
36. Maher, J. L., Roehl, K. R., & Mahabir, R. C. (2012). A prospective evaluation of U-clips for arterial microvascular anastomoses. *Journal of Reconstructive Microsurgery, 28*(8), 543–548.
37. Lee, M. G. M., & Jones, D. (2005). Applications of fibrin sealant in surgery. *Surgical Innovation*, *12*(3), 203–213.
38. Cho, A. B., Wei, T. H., Torres, L. R., Júnior, R. M., Rugiero, G. M., & Aita, M. A. (2009). Fibrin glue application in microvascular anastomosis: Comparative study of two free flaps series. *Microsurgery*, *29*(1), 24–28.
39. Andree, C., Munder, B. I. J., Behrendt, P., Hellmann, S., Audretsch, W., Voigt, M., et al. (2008). Improved safety of autologous breast reconstruction surgery by stabilisation of microsurgical vessel anastomoses using fibrin sealant in 349 free DIEP or fascia-muscle-sparing (fms)-TRAM flaps: A two-centre study. *Breast (Edinburgh, Scotland)*, *17*(5), 492–498.
40. Marek, C. A., Amiss, L. R., Morgan, R. F., Spotnitz, W. D., & Drake, D. B. (1998). Acute thrombogenic effects of fibrin sealant on microvascular anastomoses in a rat model. *Annals of Plastic Surgery, 41*(4), 415–419.
41. Gottlob, R., & Blümel, G. (1968). Anastomoses of small arteries and veins by means of bushings and adhesive. *The Journal of Cardiovascular Surgery, 9*(4), 337–341.
42. Green, A. R., Milling, M. A., & Green, A. R. (1986). Butylcyanoacrylate adhesives in microvascular surgery: An experimental pilot study. *Journal of Reconstructive Microsurgery, 2*(2), 103–105.
43. Chang, E. I., Galvez, M. G., Glotzbach, J. P., Hamou, C. D., El-ftesi, S., Rappleye, C. T., et al. (2011). Vascular anastomosis using controlled phase transitions in poloxamer gels. *Nature Medicine*, *17*(9), 1147–1152.
44. Qassemyar, Q., & Michel, G. (2015). A new method of sutureless microvascular anastomoses using a thermosensitive poloxamer and cyanoacrylate: An experimental study. *Microsurgery, 35*(4), 315–319.
45. Sigel, B., & Acevedo, F. J. (1962). Vein anastomosis by electrocoaptive union. *Surgical Forum, 13*, 233–235.
46. Puca, A., Esposito, G., Albanese, A., Maira, G., Rossi, F., & Pini, R. (2009). Minimally occlusive laser vascular anastomosis (MOLVA): Experimental study. *Acta Neurochirurgica*, *151*(4), 363–368; discussion 368.
47. Wolf-de Jonge, I. C. D. Y. M., Beek, J. F., & Balm, R. (2004). 25 years of laser assisted vascular anastomosis (LAVA): What have we learned? *European Journal of Vascular and Endovascular Surgery: The Official Journal of the European Society for Vascular Surgery*, *27* (5):466–476.

48. Lorincz, B. B., Kálmán, E., & Gerlinger, I. (2007). KTP-532 laser-assisted microvascular anastomosis (experimental animal study). *European archives of Oto-Rhino-Laryngology: Official Journal of the European Federation of Oto-Rhino-Laryngological Societies (EUFOS): Affiliated with the German Society for Oto-Rhino-Laryngology—Head and Neck Surgery, 264* (7), 823–828.
49. Leclère, F. M., Duquennoy-Martinot, V., Schoofs, M., Buys, B., & Mordon, S. (2011). Thirty years of laser-assisted microvascular anastomosis (LAMA): What are the clinical perspectives? *Neuro-Chirurgie, 57*(1), 1–8.
50. Leclère, F. M. P., Schoofs, M., Buys, B., & Mordon, S. R. (2010). Outcomes after 1.9-μm diode laser-assisted anastomosis in reconstructive microsurgery: Results in 27 patients. *Plastic and Reconstructive Surgery*, *125*(4), 1167–1175.
51. O'Neill, A. C., Winograd, J. M., Zeballos, J. L., Johnson, T. S., Randolph, M. A., Bujold, K. E., et al. (2007). Microvascular anastomosis using a photochemical tissue bonding technique. *Lasers in Surgery and Medicine*, *39*(9), 716–722.
52. Yamagata, S., Handa, H., Taki, W., Yonekawa, Y., Ikada, Y., & Iwata, H. (1979). Experimental nonsuture microvascular anastomosis using a soluble PVA tube and plastic adhesive. *Journal of Microsurgery, 1*(3), 208–215.
53. Moskovitz, M. J., Bass, L., Zhang, L., & Siebert, J. W. (1994). Microvascular anastomoses utilizing new intravascular stents. *Annals of Plastic Surgery, 32*(6), 612–618.
54. Mikaelsson, C., & Arnbjörnsson, E. (1996). Nonsuture end-to-end microvascular anastomosis using intravascular stents. *Annales Chirurgiae Et Gynaecologiae, 85*(1), 36–39.
55. Prabhu, I. S., & Homer-Vanniasinkam, S. (2013). A proof-of-principle study on animals for a new method of anastomosing vessels using intraluminal stents. *Journal of Cranio-Maxillo-Facial Surgery: Official Publication of the European Association for Cranio-Maxillo-Facial Surgery*, *41*(4), 327–330.
56. Bauer, F., Fichter, A. M., Loeffelbein, D. J., Wolff, K.-D., Schütz, K., & Mücke, T. (2015). Microvascular anastomosis using modified micro-stents: A pilot in vivo study. *Journal of Cranio-Maxillofacial Surgery, 43*(2), 204–207.
57. Obora, Y., Tamaki, N., & Matsumoto, S. (1978). Nonsuture microvascular anastomosis using magnet rings: Preliminary report. *Surgical Neurology, 9*(2), 117–120.
58. Obora, Y., Tamaki, N., & Matsumoto, S. (1980). Nonsuture microvascular anastomosis using magnet rings. *Neurologia Medico-Chirurgica, 20*(5), 497–505.
59. Heitmann, C., Khan, F. N., Erdmann, D., Olbrich, K. C., Sharkawy, A. A., & Klitzman, B. (2007). Vein graft anastomoses with magnets. *Journal of Plastic, Reconstructive and Aesthetic Surgery: JPRAS*, *60*(12), 1296–1301.
60. Liu, S.-Q., Lei, P., Cao, Z.-P., Lv, Y., Li, J.-H., & Cui, X.-H. (2012). Nonsuture anastomosis of arteries and veins using the magnetic pinned-ring device: A histologic and scanning electron microscopic study. *Annals of Vascular Surgery, 26*(7), 985–995.
61. Giessler, G. A., Fischborn, G. T., & Schmidt, A. B. (2012). Clampless anastomosis with an intraluminal thermosensitive gel: First application in reconstructive microsurgery and literature review. *Journal of Plastic, Reconstructive and Aesthetic Surgery, 65*(1), 100–105.
62. Manchio, J. V., Litchfield, C. R., Zeheb, R., & Bryan, D. J. (2009). Evaluation of a novel reverse thermosensitive polymer for use in microvascular surgery. *Journal of Reconstructive Microsurgery*, *25*(1), 69–76.
63. Ueda, K., Mukai, T., Ichinose, S., Koyama, Y., & Takakuda, K. (2010). Bioabsorbable device for small-caliber vessel anastomosis. *Microsurgery, 30*(6), 494–501.
64. Nakayama, K., et al. (1962). A simple new method for small vessel anastomoses (free autograft of the sigmoid included). *Surgery, 52*, 918–931.
65. Payr, E. (1900). Beiträge zur Technik der Blutgefäss und Nervennaht nebst Mittheilungen über die Verwendung eines resorbirbaren Metalles in der Chirurgie. *Langenbecks Arch Klin Chir*, *62*, 67–93.
66. Ostrup, L. T. (1976). Anastomosis of small veins with suture or Nakayama's apparatus. A comparative study. *Scandinavian Journal of Plastic and Reconstructive Surgery, 10*(1), 9–17.

67. Ostrup, L. T., & Berggren, A. (1986). The UNILINK instrument system for fast and safe microvascular anastomosis. *Annals of Plastic Surgery, 17*(6), 521–525.
68. Ahn, C. Y., Shaw, W. W., Berns, S., & Markowitz, B. L. (1994). Clinical experience with the 3m microvascular coupling anastomotic device in 100 free-tissue transfers. *Plastic and Reconstructive Surgery, 93*(7), 1481–1484.
69. Cope, C. (2001). Technique and clinical experience of the Unilink/3m(R) microvascular anastomotic coupling device in free flap surgery. *Internet Journal of Plastic Surgery*, *1*, 1.
70. Yap, L. H., Constantinides, J., & Butler, C. E. (2006). Venous thrombosis in coupled versus sutured microvascular anastomoses. *Annals of Plastic Surgery*, *57*(6), 666–669.
71. Ross, D. A., Chow, J. Y., Shin, J., Restifo, R., Joe, J. K., Sasaki, C. T., et al. (2005). Arterial coupling for microvascular free tissue transfer in head and neck reconstruction. *Archives of Otolaryngology–Head and Neck Surgery*, *131*(10), 891–895.
72. Chernichenko, N., Ross, D. A., Shin, J., Chow, J. Y., Sasaki, C. T., & Ariyan, S. (2008). Arterial coupling for microvascular free tissue transfer. *Otolaryngology–Head and Neck Surgery: Official Journal of American Academy of Otolaryngology—Head and Neck Surgery*, *138*(5), 614–618.
73. Jason Spector, J. A., Draper, L. B., Levine, J. P., & Ahn, C. Y. (2006). Routine use of microvascular coupling device for arterial anastomosis in breast reconstruction. *Annals of Plastic Surgery*, *56*(4), 365–368.
74. Gehrke, C., Li, H., Sant, H., Gale, B., & Agarwal, J. (2014). Design, fabrication and testing of a novel vascular coupling device. *Biomedical Microdevices, 16*(1), 173–180.
75. Tachi, K., Furukawa, K. S., Koshima, I., & Ushida, T. (2011). New microvascular anastomotic ring-coupling device using negative pressure. *Journal of Plastic, Reconstructive and Aesthetic Surgery, 64*(9), 1187–1193.
76. Katz, R. D., Rosson, G. D., Taylor, J. A., & Singh, N. K. (2005). Robotics in microsurgery: Use of a surgical robot to perform a free flap in a pig. *Microsurgery, 25*(7), 566–569.
77. Taleb, C., Nectoux, E., & Liverneaux, P. (2009). Limb replantation with two robots: A feasibility study in a pig model. *Microsurgery, 29*(3), 232–235.
78. Saleh, D. B., Syed, M., Kulendren, D., Ramakrishnan, V., & Liverneaux, P. A. (2015). Plastic and reconstructive robotic microsurgery—A review of current practices. *Annales de Chirurgie Plastique Esthétique, 60*(4), 305–312.

Chapter 18
Delivery of Anticancer Molecules Using Carbon Nanotubes

Isma Ahmed, Aneela Javeed, Waqar Ahmed, D.A. Phoenix, Abdelbary Elhissi and Mark J. Jackson

Abstract Since their discovery in 1991, carbon nanotubes (CNTs) have emerged as material structures with numerous potential applications with a number of products already in the market place. An exciting application, which is emerging, is the use of carbon nanotubes for drug delivery. In this chapter, we focus on the functionalization, mechanism of cellular update, and using carbon nanotubes for delivery of anticancer drugs.

18.1 Introduction

Carbon nanotubes (CNTs) were discovered by Iijima [1] in 1991 and are described as long, thin tubes of carbon which have a diameter of approximately 1–3 nm and can extend in length to the micrometres range. The unique physical, electronic, thermal and mechanical properties of CNTs make them extremely useful in many

I. Ahmed · A. Javeed
School of Pharmacy and Biomedical Sciences, University of Central Lancashire, Preston, UK

W. Ahmed
School of Medicine, University of Central Lancashire, Preston, UK
e-mail: wahmed@uclan.ac.uk

D.A. Phoenix
London South Bank University, London 103 Borough Road, London SE1 0AA, UK

A. Elhissi (✉)
Pharmaceutical Sciences Section, College of Pharmacy, Qatar University, P.O. Box 2713, Doha, Qatar
e-mail: aelhissi@gmail.com; aelhissi@qu.edu.qa

M.J. Jackson
Kansas State University, Salina, Kansas, USA
e-mail: jacksonmj04@yahoo.com

W. Ahmed and M.J. Jackson (eds.), *Surgical Tools and Medical Devices*,
DOI 10.1007/978-3-319-33489-9_18

Table 18.1 Typical properties of CNTs [2]

Property	SWNT[a]	DWNT[b]	MWNT[c]
Tensile strength (GPa)	50–500	23–63	10–60
Elastic modulus (TPa)	~1	–	0.3–1
Elongation at break (%)	5.8	28	–
Density (g/cm3)	1.3–1.5	1.5	1.8–2.0
Electrical conductivity (S/m)	~106		
Thermal stability	>700 °C (in air)		
Typical diameter (nm)	1	~5	~20
Specific surface area (m2/g)	10–20		

[a]SWNT denotes single-walled nanotube
[b]DWNT denotes double-walled nanotube
[c]MWNT denotes multi-walled nanotube

applications including engineering, environmental sciences and biomedicine. CNTs are also remarkably strong, being 100 times as strong as steel whilst only weighing one sixth its weight. CNTs have a wide range of applications; they can conduct electricity and be used as a tool of analysis for fundamental sciences. The wide spectrum of uses of CNTs, being attributed to their exceptional mechanical, thermal and electronic properties is further elucidated in Table 18.1 [2]. The use of CNTs can have various advantages including the extensive use for improving the properties of polymeric composites. Therefore, a great increase of the use of CNTs in polymer composites has been observed from early stages of CNTs discovery [3, 4] showing improvements in the tensile strength, electrical conductivity, solvent resistance and thermal conductivity.

There are two main types of CNTs:

- Single-walled nanotubes (SWNTs)
  SWNTs consist of a single graphite sheet wrapped to form a cylindrical tube. SWNTs can be metallic or semiconducting depending on the direction of the sheet of graphite lining the nanotube. The nanotube type is defined by a pair of integers for example, n = m is of the armchair variety, n = 0 or m = 0 denotes a zigzag nanotube and any other n, m variety is chiral. SWNTs are very strong with an exceptionally high tensile strength. However, SWNTs are currently only made on a small scale because of their high cost. It costs about $750/g for a high purity sample and about $60/g for a sample containing a large proportion of impurities [5].
- Multi-walled nanotubes (MWNTs)
  MWNTs have similar electronic properties to SWNTs, but are rather made of many walls. If a CNT is made from two walls, it can be referred to as double-walled nanotube (DWNT). Electronic transport occurs quickly in metallic SWNTs and MWNTs due to the nearly one-dimensional structure of both nanotubes. Transport occurs over long nanotube lengths allowing them to carry high currents. The measured room temperature thermal conductivity of an individual MWNT is greater than that of natural diamond and graphite [5].

18.2 Functionalisation of Carbon Nanotubes

As stated by Sahooa et al. [2], CNTs are very difficult to disperse and align in a polymer matrix because they tend to agglomerate due to Van der Waals forces; therefore it is a challenge to obtain individual CNTs in a polymer matrix. To overcome this problem, functionalisation of CNTs is performed by addition of a functional group onto the CNT surfaces. This improves the stability of the CNTs and their ability to disperse in aqueous phase. There are various methods of functionalisation of CNTs, i.e. defect, non-covalent and covalent functionalisation [6].

- Defect functionalisation
  Defect functionalisation involves the use of oxidative methods to remove metal particles and amorphous carbon from the raw materials to purify the CNTs. The resulting SWNTs contain oxidised carbon atoms in a –COOH group, which are then broken down into short tubes with a length of about 100–300 nm [2]. However, a drawback of this method is that the defective sites created on the surface of the CNTs are few, and therefore cannot promote exceptional dispersion properties [2].
- Non-covalent functionalisation
  This method is of particular importance as it improves stability and processability whilst not compromising the physical properties of CNTs as reported by Sahooa et al. [2]. Surfactants, biomacromolecules or wrapping with polymers is mainly involved with this type of functionalisation. Surfactants are used to transform CNTs to aqueous phase for example anionic surfactants, i.e. sodium dodecylsulphate (SDS) and sodium dodecylbenzene sulphonate (NaDDBS). However, the extent of interaction is based on the structure of the surfactants, as SDS has much weaker interactions with CNTs [2]. This will again give an opportunity for further research, as the discovery of surfactants with higher levels of interaction with the graphite sheet of the CNT will be very useful for further functionalisation. As Sahooa et al. [2] elucidated, the benzene ring on the NaDDBS facilitated the good interaction between the surfactant and CNT, therefore this gives a good background for further research to perhaps discover more functional groups which may also have a high interaction propensity with CNT structures. Non-surfactant mediated immobilisation of protein and DNA onto CNTs has also been investigated, this method allows CNTs to be better solubilised in aqueous or organic solvents due to the much better coverage of functional groups [7].
- Covalent functionalisation
  Covalent functionalisation can be achieved by the addition of functional groups onto the side walls of CNTs or by modifying carboxylic acid groups on the CNT [2]. This method can improve solubility and dispersion in polymers and solvents. As reported by Sahooa et al. [2] SWNTs were fluorinated at their side walls by

passing elemental fluorine at different temperatures and these showed improved solubility in isopropanol and dimethyl formamide. This could help in new drug treatment if this primary idea could be used for other drug applications.

18.3 Rationale Behind Using Carbon Nanotubes in Delivery of Anticancer Drugs

Functionalised CNTs have shown the ability to enter mammalian cells [8]. Therefore CNTs are established as delivery vehicles for small drug molecules such as anticancer drugs [9].

CNTs use as anticancer agents is mainly due to its characteristics, i.e. size and surface characteristics. For drug delivery of anticancer agents, specific targeting of the drug is extremely important; hence the size of drug carrier must to be small enough to escape uptake by macrophages of the liver and spleen, and be large enough to retard rapid leakage into blood capillaries [10]. The surface characteristics of CNTs describe the functionalisation of CNTs; this is imperative as without doing so CNTs are completely insoluble, which is of concern regarding toxicity of drugs [10]. This knowledge of functionalisation of CNTs for use in anticancer agents can be further manipulated and researched, as this may give potential for more drug applications with less drug toxicity and better tumour targeting.

18.4 Mechanism of Cellular Uptake of Carbon Nanotubes

There are three defined mechanisms of cellular uptake of carbon nanotubes as stated by Raffa et al. [11]; these are phagocytosis, diffusion and endocytosis. Therapeutic agents face a difficulty when attempting to cross biological membranes. Cellular uptake of CNTs may take place via diffusion depending on the extent of polarity of the CNTs, as non polar molecules may easily pass through diffusion. During the uptake of CNTs several cellular processes are avoided, such as translocation of the therapeutic agent to its target, and release of the therapeutic agent into the cytoplasm. These processes are avoided due to the structure of CNTs, the therapeutic agent is wrapped in the CNT therefore it is sheltered from the biological environment. This therefore controls the delivery of the intracellular drug delivery, which is possibly due to the fact that the drug is internalised in the CNT and is not exposed to the compounds physical properties [11].

Cellular drug delivery of CNTs may also occur via endocytosis, which can be phagocytosis, pinocytosis or receptor mediated endocytosis. Pinocytosis can occur in most cell types and involves the ingestion of sub-micron material and substances in water. For the ingestion of larger particles, phagocytosis occurs, only very few types of cells can perform phagocytosis and it occurs for particles of up to 10 μm in

diameter. There are two types of receptor mediated endocytosis, clathrin and caveolin coated. Clathrin mediated, creates a membrane indentation of about 50 nm in size [12]. Cross-linking of receptors to ligands attached to CNTs occurs, which results in the formation of an endosome which travels through the membrane. Additionally, as reported by Jiang et al. [13], it may be advantageous to selectively target nanoparticles rather than expressing those receptors to different cellular types. An example of this is the attachment of many herceptin molecules on the surface of nanoparticles, this encouraged the cross-linking of receptors which are over expressed on breast cancer cells, i.e. ErbB2 [13].

Studies conducted by Shi Kam and Dai [14] suggested that the uptake mechanism of CNTs involves clathrin-dependant uptake. Shi Kam and Dai [14] assessed the uptake of CNTs by comparing two methods; caveolae-mediated and clathrin dependent endocytosis. To first define that the uptake of CNTs is via active transport and therefore does require ATP, they did this by cooling the CNTs and reacting them with an inhibitor that inhibits the production of ATP. This resulted in no cellular uptake of CNTs, therefore they concluded that uptake occurred via an energy-dependent endocytosis [14]. Caveolae are lipid-based indentations. This type of endocytosis is where molecules from the medium enter the indentations forming a bubble which then travels into the interior of the cell.

Clathrin dependent endocytosis involves clathrin molecules forming a tripod shaped cavity in which the medium forms a bubble which enters the interior cell. The researchers inhibited the formation of Caveolae by disrupting lipid distribution, however, this did not prevent the uptake of CNTs. However when the same was done with the clathrin molecules, this did stop the absorption of the CNTs. This therefore shows that clathrin-dependant endocytosis is in fact the cellular uptake mechanism for CNTs. However there is opposing findings which suggest that cellular uptake of CNTs occurs via a non-endocytic pathway. It is hard to define which method of uptake a drug will undergo when it is administered. There is a possibility that the drug is taken up by all three types, or just one type of uptake mechanism.

Paclitaxel is a current treatment of many cancers, however, it is not only poorly soluble in water, but also has a short blood circulation time when given parenterally. Most Paclitaxel formulations contain Cremophor E, which solubilises the drug, however this solvent system has toxic effects. Therefore current research into anticancer treatment looks into alternative drug delivery systems, such as nano-vesicles and nanoparticles.

Liu et al. [15] conducted a study which highlighted carbon nanotube as a drug delivery system for Paclitaxel in mice injected with breast cancer cells. The drug-laden nanotubes were administered to the mice every six days following recognition that the tumour had grown to a specific size. Other groups of mice in the same study were given Paclitaxel in the following forms:

- Taxol
- Pegylated Paclitaxel (PEG-PTX)
- Pegylated Paclitaxel associated with distearoylphosphatidylethanolamine (DSPE-PEG-PTX)

- Plain single-walled carbon nanotubes (Plain SWNT)
- Single-walled carbon nanotubes associated with Paclitaxel (SWNT-PTX)
- Untreated

It was found from this investigation that tumours treated with SWNT-PTX were reduced in size by more than half when compared with the next most effective tumour suppressing treatment, Taxol (Fig. 18.1). This study correlates with the findings of Dai [16] who suggested that carbon nanotubes accumulated in the spleen and the liver; however they were cleared from the body without causing any lasting organ damage.

In spite of the positive findings, it is important to consider that unlike many other nanoparticles, carbon nanotube safety has not yet been fully established. Although this particular study suggests no toxicity when the carbon nanotubes were used as a control, other research such as that conducted by Van Tassel and Goldman [17] reports asbestos like side effects are a possibility.

The tumour suppression mechanism of carbon nanotubes was investigated by Liu et al. [15] via a TUNEL assay looking into the levels of apoptosis in the tumours of mice receiving different treatments. The highest apoptosis level was observed in taxol associated with carbon nanotube treated tumours. This particular study noted only a 20 % cell proliferation of active cells when compared to untreated and taxol treated tumours. Taxol treated tumours also appeared to show similar levels of active cells in the G1, G2 and S phases of the cell cycle in comparison to untreated tumours in mice. The control used in this experiment was plain SWNT without PTX, which showed no tumour suppressing effect. From these findings, it can be concluded that when Paclitaxel was taken up by a cell via carbon nanotubes and the treatment efficacy is increased in comparison to that without carbon nanotubes. This might be attributed to the inhibition of cancer cell proliferation and induced apoptosis.

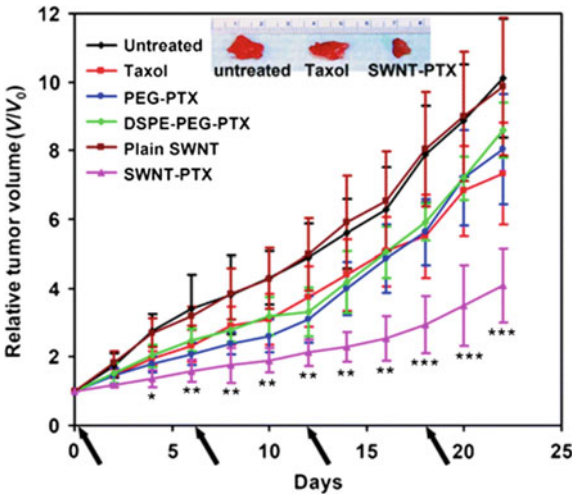

Fig. 18.1 An illustration on how carbon nanotubes associated with Paclitaxel can have the lowest relative tumour volume, it is clear that SWNT-PTX suppress tumour growth most effectively compared with the other formulations investigated [15]

18.5 Use of Folate Derivatives and Other Targeting Moieties

Chemotherapy traditionally relies on the principle that cytotoxic agents are more likely to target and kill rapidly proliferating cancer cells. However, in actual fact this leads to systemic toxicity and undesirable side effects such as kidney, liver and bone marrow toxicity as well as the typical hair loss observed in many cancer patients undergoing chemotherapy, due to the fact that traditional cytotoxic agents had very little specificity against cancer cells. Current research conducted within the last three decades looks at the morphological and physiological differences between normal tissues and cancerous tissues [18].

The problem with most anticancer drugs is the short blood circulation time, which usually results in reduced of the anticancer drug by the tumour tissue. According to Dhar et al. [19] agents containing a folic acid derivative specifically targets tumour cells enriched with folate-receptors. Dhar et al. [19] conducted a study in which they prepared broad spectrums of malignant tumours that over express the folate receptor, which allows for the selective delivery of agents to tumour cells.

Cancer cells are rapidly dividing in nature and as a result they require the rapid formation of new blood vessels. Jaracz et al. [18] have described the enhanced permeability and retention (EPR) effect, which explains changes in the tumour vasculature, and clarifies its defects. When a malignant tumour develops, it results in both the ability of large molecules to enter the tumour extravascular space and the inability of these molecules to leave the tumour because the lymphatic drainage system is undeveloped. Physiologically, cancer cells have an enhanced metabolic rate resulting in hypotoxicity. As a direct result anaerobic metabolism predominating, lactate production is increased and consequently the pH of cancer cells becomes lower [20]. This principle explains the reason that certain conjugates have been designed to release cytotoxic agents at acidic pH.

Rapidly dividing tumour cells also require numerous vitamins and minerals, which provide another reason for the overexpression of many tumour specific receptors. The understanding of this mechanism has been the central point of a lot of ongoing research into tumour targeting by exploiting the overexpression of these receptors. Several tumour targeting drug conjugates have been identified as efficient cancer chemotherapy agents, since they bear cancer recognition moieties. These advances can be divided into certain groups which include [21]:

- Folic acid
- Hyaluronic acid
- Monoclonal antibodies
- Oligopeptides
- Polyunsaturated fatty acids

Several limitations exist in anticancer technology despite profound developments in chemotherapy; cancer still appears to be a leading cause of death, being

the second most common cause of death in the US [19]. Current chemotherapy must look at tumour specific treatment aiming to reduce toxicity to normal cells and increasing selectivity towards cancer cells.

Having considered the current research, still there appears to be several problems that hinder the possibility of an effective anticancer agent. Most importantly, the fact that folic acid (FR) receptors are expressed in the lungs, thyroid gland and other parts of the body although limited in comparison to tumour cells [22]. This still allows for the conjugate to be taken up by these body parts causing undesirable side effects. Current research appears to be limited to one particular tumour targeting moiety; further research needs to address the possibility of active anticancer agents with more than one moiety, for instance folic acid and certain hormones, according to receptor composition in the target tumour cells. Research needs to be conducted into targeting tumours according to composition of receptors, since research suggests that other receptors are also elevated in certain tumours. It may also be interesting to address the possibility of carbon nanotubes and their uses in imaging with a view to target the tumour. Carbon nanotubes may be capable of being multifunctional if administered as a labelled radioactive drug, there is the possibility to observe how extensively it has been taken up, which could allow for the same carbon nanotube with the same targeting moieties to be used again with the active drug. The exact uptake of the drug may then be quantified. Furthermore the multiple covalent functionalisation on tips of carbon nanotubes may allow them to carry numerous cytotoxic drugs. Simultaneously, cytotoxic drugs with the addition of other compounds which may allow the reduction of systemic side effects, or an enhancement of treatment efficiency.

The most effective anticancer agent would need to look at what receptors are expressed in the tumour that is being targeted, record receptor densities and formulate conjugates with the relevant anticancer targeting moieties.

18.6 Pegylated Taxol Carbon Nanotube Formulations

A study conducted by Nie et al. [23] suggested that coating carbon nanotubes with the molecule polyethylene glycol (PEG) allowed the attachment of the anticancer drug Paclitaxel to each of the three branches of the PEG molecule. PEGylation of the carbon nanotubes also allows the duration of action of the drug molecules to be increased. The branched PEG molecule remains stable in the bloodstream for a relatively long time, which gives the carbon nanotubes more time to locate and treat a tumour before excretion from the body [24]. PEGylation describes the covalent conjugation of a biological molecule, such as a carbon nanotube to the nontoxic and non-immunogenic polymer polyethylene glycol (PEG). The rationale behind the use of PEGylation includes changes in the chemical and physical properties of drugs. Current research such as that conducted by Nie et al. [23] describes how PEGylation of carbon nanotubes results in increased tumour suppression in mice.

PEG as a polymer has specific characteristics that make it very attractive in the field of pharmaceutics [25]:

- High water solubility—will not precipitate in the blood.
- High mobility in solution—branched molecule.
- Lack of immunogenicity and toxicity—prevents opsonisation of the attached molecule.
- Biocompatibility and biodegradability.

Nie et al. [23] functionalised double-walled carbon nanotubes with two PEG azides, both azido terminated monomethylether and diazido terminated PEG. The aqueous solubility of the regulated double-walled nanotubes was largely increased for both PEG—azides. From this particular article, however, an interesting point came to light. The aqueous solubility for both molecules was 0.36 and 0.37 mg/ml even though one had a molecular weight of 800 and the other 750 g/mole. This may be important when looking at ways to reduce the drug molecules.

A key problem is long term toxicity and side effects. Despite their potential benefits, it is still important to bear in mind the past introductions of chemicals such as asbestos, benzene and thalidomide, amongst others. It is important to establish a clinically effective yet safe and nontoxic delivery system without causing long term health consequences. For these to be eliminated and further pharmaceutical development in correlation with cytotoxic drugs it seems systematic data is required on the long term effects, since carbon nanotubes are a relatively new developing drug delivery approach. Maybe the effects over time need to be mentioned before clinically optical levels can be implemented as therapeutic agents.

Carbon nanotubes have been reported to exhibit pathogenetically similar to asbestos in the lung [17]. Over the years, it may be the case that after clinical trials they show no toxicity, however, as this avenue has not yet been fully explored; it poses risks for preparation, functionalisation and inhalation of carbon nanotubes. PEG molecules are highly biocompatible [23] which means that their application is a real possibility in clinical and therapeutic fields relating to cancer and carbon nanotubes. From a drug molecule design perspective the advantages of carbon nanotubes may also be hindered by the fact that by the addition of both PEG molecules and other tumour targeting moieties, the resulting molecule may have a very different confirmation and size, which has implications on the pharmacokinetics of the drug molecule.

References

1. Iijima, S. (1991). Helical microtubules of graphitic carbon. *Letters to Nature, 354*, 56–58.
2. Sahooa, N. G., Ranab, S., Chob, J. W., Lia, L., & Chana, S. H. (2010). Polymer nanocomposites based on functionalized carbon nanotubes. *Progress in Polymer Science, 35*, 837–867.
3. Ajayan, P. M., Stephan, O., Colliex, C., & Trauth, D. (1994). Aligned carbon nanotube arrays formed by cutting a polymer resin-nanotube composite. *Science, 265*, 1212–1214.

4. Coleman, J. N., Khan, U., Blau, W. J., & Gun'ko, Y. K. (2006). Small but strong: A review of the mechanical properties of carbon nanotubes—polymer composites. *Carbon, 44*, 1624–1652.
5. Valentin, N. P. (2004). Carbon nanotubes: Properties and application. *Materials Science and Engineering, 43*, 61–102.
6. Plank, N. O. V., & Cheung, R. (2004). Functionalisation of carbon nanotubes for molecular electronics. *Microelectronic Engineering, 73*, 578–582.
7. Star, A., Stoddart, J. F., Steuerman, D., Diehl, M., Boukai, A., Wong, E., et al. (2001). Preparation and properties of polymer-wrapped single-walled carbon nanotubes. *Angewandte Chemie International, 40*, 1721–1725.
8. Bianco, A., Kostarelos, K., & Prato, M. (2005). Application of carbon nanotubes in drug delivery. *Current Opinion in Chemical Biology, 9*, 674–679.
9. Elhissi, A. M., Ahmed, W., Ul Hassan, I., Dhanak, V. R., & D'Emanuele, A. (2012). Carbon nanotubes in cancer therapy and drug delivery. *Journal of Drug Delivery*, *2012*. Article ID 837327.
10. Cho, K., Wang, X., Nie, S., Chen, Z., & Shin, D. M. (2008). Therapeutic nanoparticles for drug delivery in cancer. *Clinical Cancer Research, 5*, 1310–1316.
11. Raffa, V., Ciofani, G., Vittorio, O., Riggio, C., & Cuschieri, A. (2010). Physicochemical properties affecting cellular uptake of carbon nanotubes. *Nanomedicine, 1*, 89–97.
12. Faraji, H. A., & Wipf, P. (2009). Nanoparticles in cellular drug delivery. *Bioorganic & Medicinal Chemistry, 17*, 2950–2962.
13. Jiang, W., Kim, B. Y. S., Rutka, J. T., & Chan, W. C. W. (2008). Nanoparticles-mediated cellular response is size-dependent. *Nature Nanotechnology, 3*, 145–150.
14. Shi Kam, N. W., & Dai, H. (2005). Carbon nanotubes as intracellular protein transporters: Generality and biological functionality. *Journal of the American Chemical Society, 127*, 6021–6026.
15. Liu, Z., Chen, K., Davis, C., Sherlock, S., Qizhen, C., Chen, X., et al. (2008). Drug delivery with carbon nanotubes for in vivo cancer treatment. *Cancer Research, 68*, 6652–6658.
16. Dai, H. (2002). Carbon nanotubes: Synthesis, integration, and properties. *Accounts of Chemical Research, 35*, 1035–1044.
17. Van Tassel, K., & Goldman, R. (2010). Manufacturing the wings of icarus: FDA regulation of nanotechnology used in products for human consumption including food, dietary supplements, cosmetics and sunscreens. *Journal of Law, Technology and Policy, 32*, 2140–2183.
18. Jaracz, S., Chen, J., Kuznetsova, V. L., & Ojima, I. (2005). Recent advances in tumour targeting anticancer drug conjugates. *Bioorganic & Medicinal Chemistry, 13*, 5043–5054.
19. Dhar, S., Liu, Z., Thomale, J., Dai, H., & Lippard, J. S. (2008). Targeted single-wall carbon nanotube-mediated Pt (IV) prodrug delivery using folate as a homing device. *Journal of American Chemical Society, 130*, 11467–11476.
20. Low, P. S., & Antony, A. C. (2004). Folate receptor targeted drugs for cancer and inflammatory disease. *Advanced Drug Delivery Review, 56*, 1057–1238.
21. Shim, M., Kam, W. S. N., Chen, J. R., Li, Y., & Dai, H. (2002). Functionalization of carbon nanotubes for biocompatibility and biomolecular recognition. *Nanoletters, 2*, 285–288.
22. Antony, A. C. (1996). Folate receptors. *Annual Review of Nutrition, 16*, 501–521.
23. Nie, H., Wei, G., Yuan, Y., Dou, Z., Zujin, S., Liu, Z., et al. (2010). PEGylation of double-walled carbon nanotubes for increasing their solubility in water. *Nanoresearch, 3*, 103–109.
24. Prencipe, G., Tabakman, M. S., Welsher, K., Liu, Z., Goodwin, P. A., Zhang, L., et al. (2009). PEG branched polymer for functionalization of nanomaterials with ultralong blood circulation. *Journal of American Chemical Society, 131*, 4787–4793.
25. Veronese, F. M., & Mero, A. (2008). The impact of PEGylation on biological therapies. *Biodrugs, 22*, 315–329.

Chapter 19
Design Characteristics of Inhaler Devices Used for Pulmonary Delivery of Medical Aerosols

Iftikhar Khan, Sakib Yousaf, Mohamed Albed Alhnan, Waqar Ahmed, Abdelbary Elhissi and Mark J. Jackson

Abstract For the treatment of respiratory diseases, it is vital to deliver therapeutic doses of drugs to specific regions in the tracheobronchial tree (TBT) of the lung with maximal efficiency and minimal wastage of medication. Since the nineteenth century, many devices have been designed to deliver drugs but the modern era started from 1956 with the introduction of the first metered dose inhaler. These devices can generate aerosols with uniform size distribution, resulting in high deposition in the deep lung which has high surface area (100 m^2). Devices that have been commonly used for pulmonary drug delivery are pressurized metered dose inhalers (pMDIs), dry powder inhalers (DPIs) and nebulizers. This review introduces and evaluates the applications of devices used in inhalation therapy and the influence of design characteristics on the delivery of medical aerosols.

19.1 Introduction

Pulmonary delivery is a non-invasive route that was historically used for inhalation therapy to treat cough by smoking the leaves of *Atropa belladonna* 4000 years ago [26]. Tobacco mixed with stramonium powder was used in the nineteenth and twentieth

I. Khan · S. Yousaf · M.A. Alhnan
School of Pharmacy and Biomedical Sciences, University of Central Lancashire, Preston PR1 2HE, Preston, UK

W. Ahmed
School of Medicine, University of Central Lancashire, Preston, UK
e-mail: wahmed@uclan.ac.uk

A. Elhissi (✉)
Pharmaceutical Sciences Section, College of Pharmacy, Qatar University, P.O. Box 2713, Doha, Qatar
e-mail: aelhissi@qu.edu.qa

M.J. Jackson
Kansas State University, Salina, Kansas, USA
e-mail: jacksonmj04@yahoo.com

W. Ahmed and M.J. Jackson (eds.), *Surgical Tools and Medical Devices*,
DOI 10.1007/978-3-319-33489-9_19

centuries as cigarettes that can be smoked for the treatment of asthma [35]. However, since then revolutionary developments in the field of inhalation drug therapy have taken place. In particular, there have been significant advances in inhalation devices. Pulmonary delivery devices are essentially of three types: pressurized metered dose inhalers (pMDIs), dry powder inhalers (DPIs) and nebulizers [5, 66]. The classification is based on the physical state of the formulation and their delivery as aerosols to the lung. However, every class is further divided on the basis of design of the device and composition of the formulation [66]. DPIs and pMDIs are unlike nebulizers because in nebulizer, the drug is dissolved or dispersed in an aqueous solution. Nebulizers are made mostly for patients who require a prolonged drug delivery [8, 66]. By contrast, DPIs and pMDIs are used two to four times daily to deliver the drug in small doses.

19.2 Types of Devices

19.2.1 Pressurized Metered Dose Inhalers (PMDIs)

The modern techniques of aerosol delivery started in 1956, when Dr. George Maison a Riker company president was told by his asthmatic daughter Susie (13 years old) that her bulb atomizer leaks and that it was like her mother's hair spray [8, 56]. He worked with two other researchers (Charles Thiel and Irving Porush) and made the first pMDI [49, 67]. After this model, they began to use new technology and techniques to develop innovative models which would enhance the delivery through inhalation [26]. pMDIs are also called "puffers" and most commonly used for pulmonary disorders such as asthma and chronic obstructive pulmonary disease (COPD) [15].

As shown in Fig. 19.1, pMDI is composed of a disposable canister (containing formulation), a metering valve and an actuator [28]. The canister is usually made of aluminium or stainless steel and contains a mixture of constituents: drug (approx. 1 %) and propellant (>80 %) in addition to surfactants, preservatives and other excipients [28, 56]. The pMDI is also designed to be light and robust to maintain a high interior pressure of 3–5 atmospheres. The device normally accommodates about 15–30 ml of formulation [16, 42].

Effectiveness and function of pMDIs depend upon the metering valve that delivers the drug as aerosolized dose in a volume of 25–100 μl per actuation [28, 42]. The propellant seal must be properly tight to maintain the high pressure in order to keep the propellant in liquid form, hence the drug remains solubilized or dispersed [31]. One smart approach to manufacture pMDI formulations potentially with controlled release properties of the drug in the lung is achieved by the inclusion of phospholipid as one of the formulation excipients [21]. Chlorofluorocarbons (CFCs) are propellants that were used in the old pMDI formulations; however, they have been banned because of their depletive effect on the ozone layer [69]. Therefore, alternative propellants such as hydrofluoroalkanes (HFAs; e.g. Propellant 134a) have been introduced [8, 35, 56]. HFAs are chemically stable, non-inflammable and

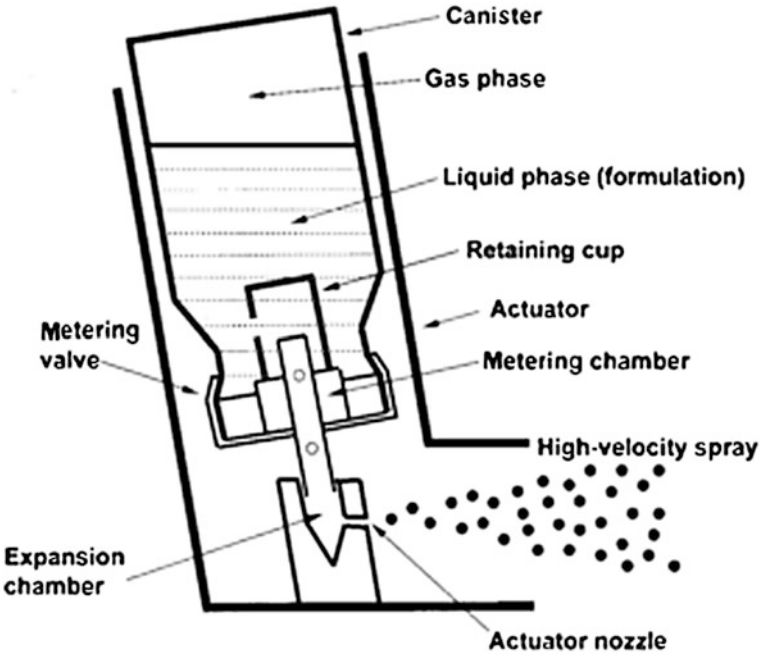

Fig. 19.1 A schematic presentation of pMDI [42]

non-toxic [15] but are not good solvents as CFCs for phospholipids [5]. The actuator consists of a nozzle, body and mouthpiece that are enclosed in a cover for protection. The mouthpiece is the part where the patient inhales the drug, while the nozzle controls the particle size distribution of the emitted aerosol particles [42, 59].

pMDIs are not free from disadvantages. For instance, the extended use of pMDIs may cause irregular drug delivery or a "tailing-off" effect. The other key limitation is when pMDIs are used incorrectly, possibly leading to inconsistent dosing [23, 56]. pMDIs are the most generally used device; however, proper coordination between inhalation and actuation is essential to obtain the optimum effect [54]. In addition, pMDIs might be unsuitable for use by young children [50–52], owing to their inability to coordinate their inhalation with the device actuation. Delivery of therapeutic agents to the peripheral airways can be achieved by pMDIs if the particle size is between 0.5 and 4.5 μm; because, larger particles are likely to deposit in the upper regions of the tracheobronchial tree (TBT) [56].

19.2.2 Dry Powder Inhalers (DPIs)

DPI formulations typically consist of micronized drug particles loaded onto larger carrier particles (e.g. lactose with particle size >50 μm). Inhalation causes the drug

particles to liberate from the carrier and deposit in the central and lower regions of the TBT. Controlled release applications of DPIs involve the delivery of dried powders of liposomes or niosomes prepared by freeze-drying [57] or spray-drying [25]. DPI formulations are delivered to the targeted area of TBT for prophylaxis or treatment applications [7]. A prime advantage of DPI formulations is their freedom from propellants and the ability to deliver relatively larger drug doses [14, 40]. The drug is also more stable when it is present in the dry form [7] but the micronized drug particles have high cohesive properties which may cause them to aggregate [35]; this can be reduced by using higher proportions of the carrier [28]. A DPI device consists of a dry powder and a metering system (Fig. 19.2). Actuation in this case is performed via inhalation by the patient and may cause the drug particles to pass through the mouthpiece to reach the respiratory system of the patient in the forms of aerosols [15]. The large particles are retained by the upper respiratory tract and cleared by the mucoescalator system [66]. The drug after administration should reach the target region of the respiratory system; thus, it is important that the powdered formulation has good flowability, small aerodynamic size and narrow size distribution [7].

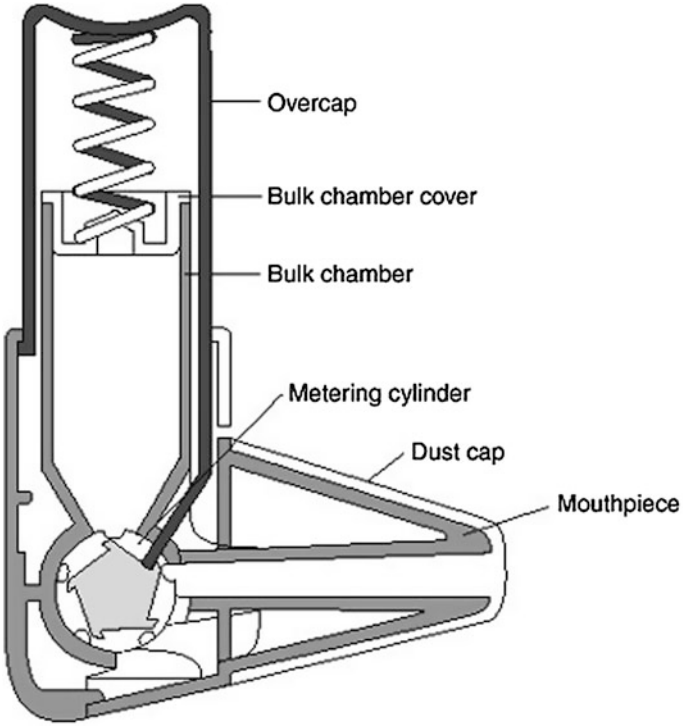

Fig. 19.2 A schematic presentation of a dry powder inhaler (DPI) device [32]

Particle properties play a key role in DPI formulations; for instance, increasing the porosity of the particles decreases the density of formulation, enhancing the chance of particle deposition in the deep lung. Moreover, preparation of small geometric particle size enhances the performance of the dry powder by lowering the aerodynamic particle diameter. The interaction of particles can be reduced by decreasing the internal forces between the particles [7].

DPIs are conventionally prepared by crystallization of the drug followed by micronization via milling. There are some factors that need to be controlled such as particle size and size distribution of the drug and carrier, shape of the carrier particles and drug particle porosity and crystallinity [7, 66]. There are different types of DPI devices such as Spinhaler®, Rotahaler®, Diskhaler® and Turbuhaler® [8, 51]. However, there are several limitations associated with the use of DPI formulations such as the possible particle deposition in the upper respiratory tract [8] and the need for powerful inspiration by the patient through the mouthpiece of the device. Children and old people cannot apply high negative pressure during inhalation [15]. Also, the powder itself might be affected by the environmental humidity, resulting in particle aggregation [51].

19.2.3 Nebulizers

The administration of small aerosol droplets via nebulization has been established for decades [12]. Nebulizers are devices that deliver a continuous and comparatively large volumes of drug solutions or dispersions to the lung in the form of aerosol [9, 17, 37] for prophylaxis or treatment purposes; for instance, for protection against or treatment of asthma and COPD. Nebulizers can be more efficient than pMDIs and DPIs. Unlike pMDIs and DPIs, nebulizers may not require multiple dosing, or particular modes of inhalation [30]. Also, inhalation via nebulizers is more convenient for children and elderly patients [63] as patients need minimum effort and coordination for inhalation [54].

One of the major benefits of a nebulizer is its ability to deliver high drug concentrations to the respiratory tract [30]. However, the effectiveness of nebulizers depends upon factors such as aerosol particle size, formulation surface tension, nebulizer design and patient inhalation pattern. Extensive research has been conducted on the delivery of drugs in controlled release formulations by using nanocarrier systems such as liposomes, niosomes and dendrimers. Studies have reported that small particle size (1–5 μm) of liposomes or niosomes are likely to reach the deep lung [38]. Small drug particles dispersed in the nebulizer solution have better ability to be incorporated into the nebulized droplets; hence, it is highly desirable to use fine drug dispersions if suspensions. Laser diffraction is used to measure the size of the aerosol droplets produced from liposome dispersions [5]. Nebulizers are of three types according to their mechanism of operation; these are: air-jet, ultrasonic and vibrating-mesh nebulizers [19].

19.2.3.1 Air-Jet Nebulizer

Air-jet nebulizer is a T-shaped inhalation device which consists of a mouthpiece (Fig. 19.3) [70], a medication plastic bottle and a compressor which converts the liquid medication into fine small droplets by forcing compressed gas/air through the nebulizer [33, 58]. The flow rate of the compressed gas/air may influence the size of the droplets produced [1]. The mouthpiece is connected to the plastic bottle which contains the drug formulation, and the compressed gas is supplied through a plastic tube to the "venturi" nozzle of the plastic bottle of the nebulizer [24, 45, 47]. The "venturi" nozzle is a small orifice having a diameter of 0.3–0.7 mm [40].

Air-jet nebulizers have two designs of nozzles (Fig. 19.4): the internal mixing design in which compressed gas and drug solution interact before leaving the "venturi", while in external mixing design both compressed gas and solution interact after being emitted from the nozzle [6, 30].

Within the medication bottle, as a result of supplying the compressed gas, the pressure decreases on top of the medical fluid. The liquid formulation is pulled upwards (Fig. 19.5) to form ligaments [18, 27, 35, 40], resulting in formation of droplets due to the liquid's surface tension [17]. The diameter of these droplets (primary aerosol) is 15–500 μm [10]. As shown in Fig. 19.5, the droplets impact on the baffle of the nebulizer and break up into smaller droplets (secondary aerosol) [8] that are suitable for inhalation while the larger droplets are deflected for further atomization within the nebulizer [28, 45, 58]. In addition, the droplet diameter is dependent upon the efficiency of the baffle system [5]. The output is different from one nebulizer to another and the aerosol properties are dependent on the baffles, the "venturi" orifice of the nebulizer, and the pressure of the compressed gas [43, 47].

Nebulizers are convenient devices for aerosol delivery in infants, children and elderly patients as it requires no specific skills or strong inspiration for the aerosols

Fig. 19.3 An air-jet nebulizer consisting of a medication bottle, T-shaped mouthpiece and a plastic tube responsible for delivering the compressed gas from a gas cylinder or an electrically operated compressor (http://medsupplies101.com/product_details.php?id=471797018&merchant_id=9973)

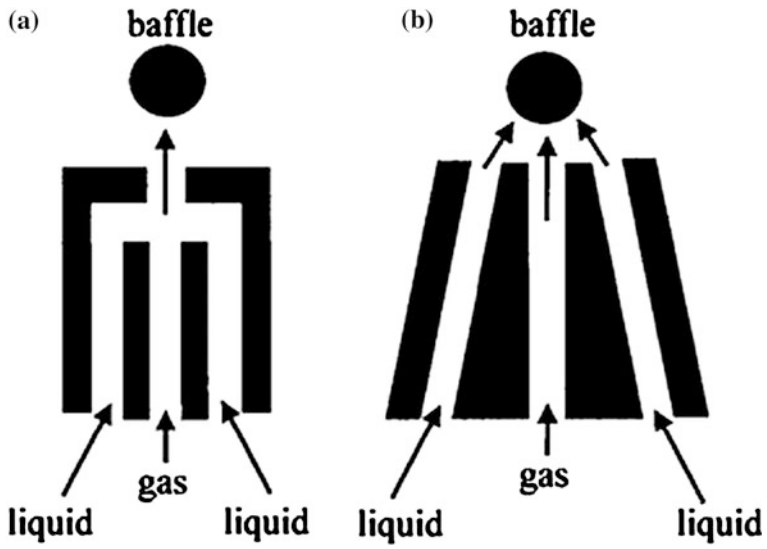

Fig. 19.4 The design of an internal (**a**) and an external (**b**) mixing nebulizer [30]

to be delivered to the respiratory airways [47, 55]. For aerosolization of novel drug delivery systems (e.g. liposomes), the vesicle size of liposomes may be reduced upon fragmentation within the jet nebulizer; this is a manifestation of liposome instability during nebulization [5, 46, 65]. The physical damage of liposomes is reduced when liposome vesicles to be nebulized are smaller.

For Jet nebulization of liposomes, aerosol droplet size is dependent on the concentration of phospholipid and the independent bilayer composition and size of liposome [5]. Moreover, the construction and design of the jet nebulizer affect the aerosol performance in terms of nebulization time and droplet size [39, 71]. Formulations with high viscosity and low surface tension produce smaller droplet size, and high viscosity of the formulation may prolong the time needed to complete

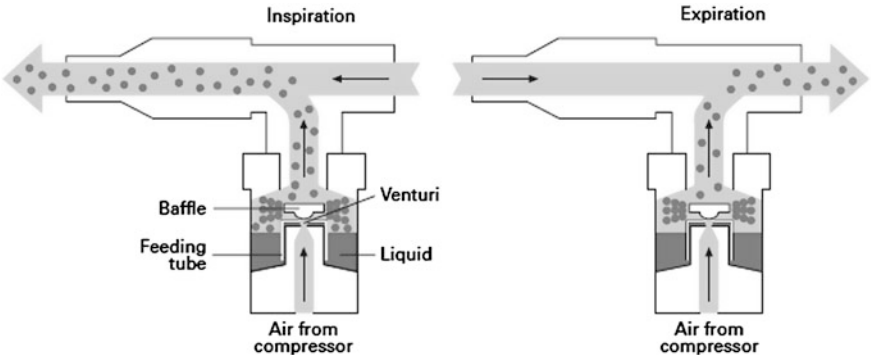

Fig. 19.5 This diagram represents the working principle of a conventional air-jet nebulizer [47]

the nebulization [40]. A decrease in temperature of nebulizer fluid by ~10 °C was observed within the first 3 min of nebulization, followed by a slight decrease in temperature for further 7 min [4]. Conventional nebulizers are bulky and require electricity to operate their air compressors, resulting in poor portability. In addition, many nebulizers produce continuous aerosols during inhalation and exhalation, causing significant drug losses in the surrounding environment [70]. Another drawback is the high residual (dead) volume left in the nebulizer reservoir [28, 29]. This, however, can be decreased by increasing the diluent volume and gas flow rate. Conventional nebulizers may cause as high as 50 % waste of the drug as residual volume [47]. This was the reason behind the need for development of new nebulizer designs to give more effective nebulization with less drug wastage [30, 47]. These designs are presented by the open-vent nebulizers, breath-assisted/enhanced open-vent nebulizers and breath-actuated nebulizers.

(a) **Open-Vent Nebulizers**

Open-Vent nebulizers operate in a similar mechanism to that of conventional jet nebulizers where a compressed gas produces a negative pressure on top of the medical fluid, causing droplets to form upon impaction with the baffles. However, in the open-vent model, a small open vent (Fig. 19.6) is designed in the chamber for additional air flow to push the smaller droplets for inhalation by the patient, shortening the nebulization time and potentially enhancing deposition in the lower respiratory airways [3]. However, it is not confirmed whether additional air flow would reduce the size of aerosol droplets [47].

Unfortunately, young children with slow inspiration may not be able to anticipate the high flow of an open-vent nebulizer and this can lead to wastage of the aerosol. To overcome the loss of aerosol, an intermittent nebulizer (e.g. Pari LL) (Fig. 19.7) was introduced containing a special button to control the nebulization. This technique requires the patient to have good coordination in order to get the required nebulized dose within the right time frame [47].

(b) **Breath-Assisted/Enhanced Open-Vent Nebulizer**

Breath-assisted/enhanced open-vent nebulizers (Fig. 19.8) have similar operation principle to open-vent nebulizers. However, during inspiration, smaller droplets are pushed by the extra air flow to the patient whilst during expiration a valve located nearby the mouthpiece opens and closes the open vent on the top of the nebulizer [3]. The aerosol loss is almost the same to conventional nebulizer because the aerosol generation is continuous. However, nebulization time is shorter than that of conventional jet nebulizers but longer than that of open-vent devices [47, 68]. An example of this design is the Pari LC Plus nebulizer shown in Fig. 19.8.

19.2.3.2 Ultrasonic Nebulizers

Ultrasonic nebulizer (Fig. 19.9) has a special mechanism of creating energy via the generation of ultrasonic sound waves using piezoelectric crystals [22, 34, 36, 55].

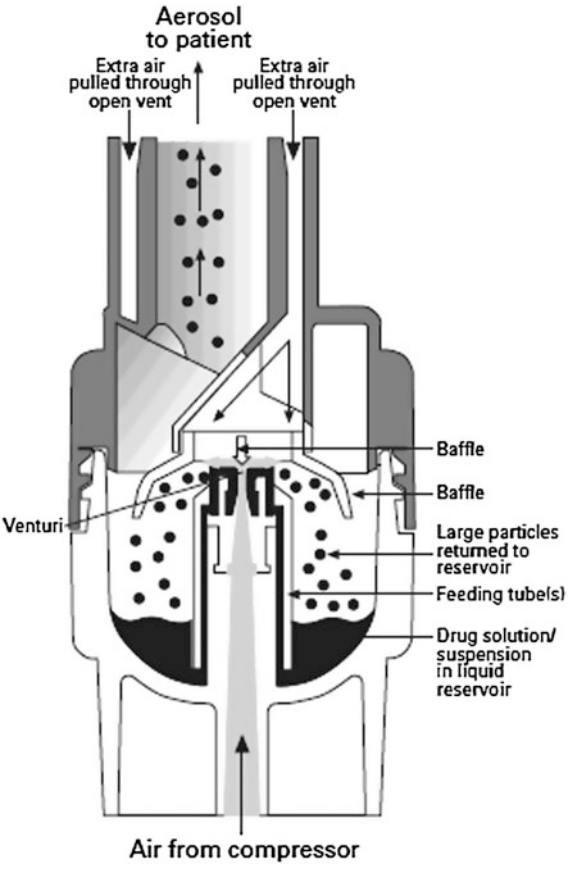

Fig. 19.6 A schematic presentation of an open-vent nebulizer [47]

This results in the production of high-frequency vibrations of 1–3 MHz in the medical solution, converting it into a fountain that may detach aerosol droplets [8, 24, 35, 41]. The higher the frequency of vibration, the smaller the aerosol droplet generated by the nebulizer [1]. Larger droplets are formed at the apex of the fountain, while smaller droplets are detached from the bottom. Large droplets are deflected by the baffles and recycled for further fragmentation into smaller droplets. Modern ultrasonic nebulizers have a speed-controlled fan in situ within the device to help driving the aerosol towards the mouthpiece for inhalation by the patient [47]. Portability of modern ultrasonic nebulizers is better than that of old designs, in terms of both weight and size of the device; this is achieved by the battery operation of the new devices.

Generally, two mechanisms have been proposed for aerosol production by ultrasonic nebulizers [2]. First, is the capillary wave mechanism and the other is the cavitation bubble formation (Fig. 19.10) [5, 63]. In the first mechanism, a high level of vibration frequency creates a capillary jet. Liquid crests form and break with continuous formation of small droplets [63]. Capillary wave theory is favoured by

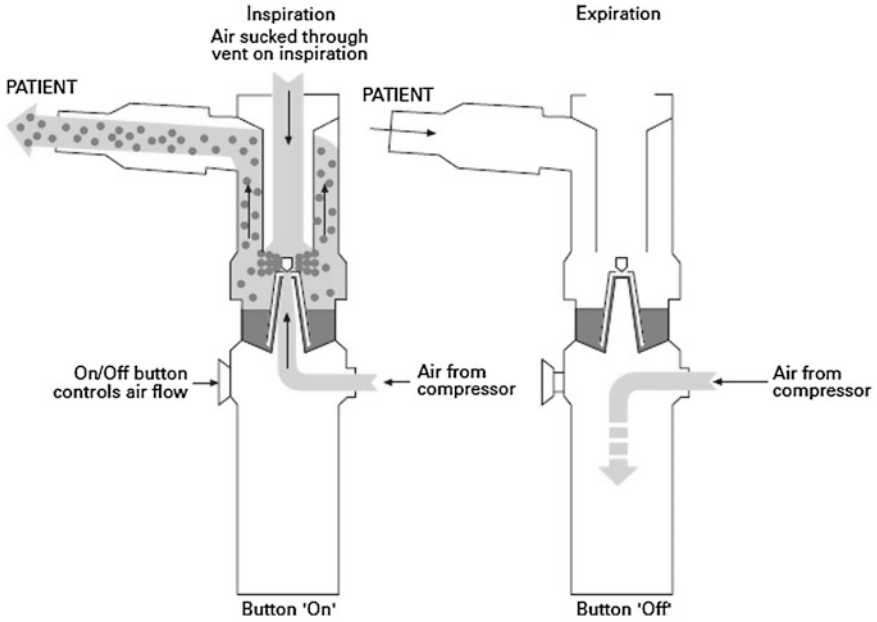

Fig. 19.7 The diagram illustrate the operation of dosimetric nebulizer (Pari LL) [47]

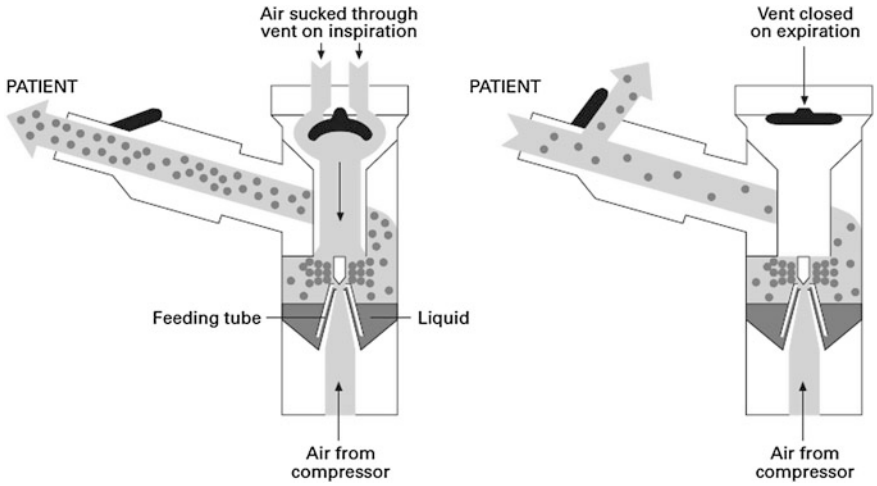

Fig. 19.8 A schematic presentation of the Pari LC Plus breath-enhanced nebulizer [47]

the strong correlation between capillary wavelength and mean droplet size [2]. In the cavitation bubble formation, a low-frequency energy produced by the piezoelectric crystal is used to create bubbles inside the formulation. These bubbles burst

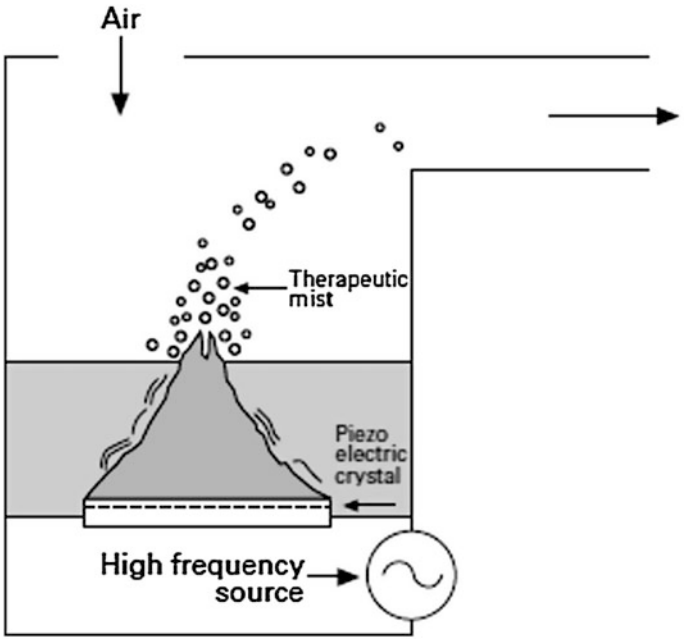

Fig. 19.9 The design of an ultrasonic nebulizer representing the vibration of the fluid to release the aerosols from the fountain of liquid generated as a result of a high vibrating frequency piezoelectric crystal [47]

on the surface as their internal pressure becomes equal to their external pressure, resulting in the formation of small droplets for inhalation (Fig. 19.10) [63].

Ultrasonic nebulizers generate aerosols with very high polydispersity. This problem can be overcome by employing an electro-formed static mesh having optimum aperture size to produce droplets with controlled size and narrow size distribution. The BESPAK Piezo Electric Actuator shown in Fig. 19.11 produces droplets of adjustable size depending on the size of the apertures employed in the ultrasonic device [63].

Both the type of nebulizer and the physiochemical properties of formulation affect nebulization performance. Viscosity of the formulation affects the droplet size. It has been previously reported that the increase in viscosity causes the formation of larger droplets and may reduce the nebulization output. Suspensions usually have relatively low nebulization efficiency when ultrasonic nebulizers are used [48, 72]. Ultrasonic nebulizers have high residual volume (i.e. lower fluid output), and aerosol droplet size is larger compared to jet nebulizers [62].

Ultrasonic nebulizers usually heat liquid during aerosol generation [13, 55, 61], resulting in temperature elevation by around 20 °C within the first 6 min of operation [53]. Reports have indicated possible degradation of heat-sensitive drugs during ultrasonic nebulization [45]. However, looking at the positive side, generation of heat may enhance the solubility of poorly water-soluble drugs during liquid

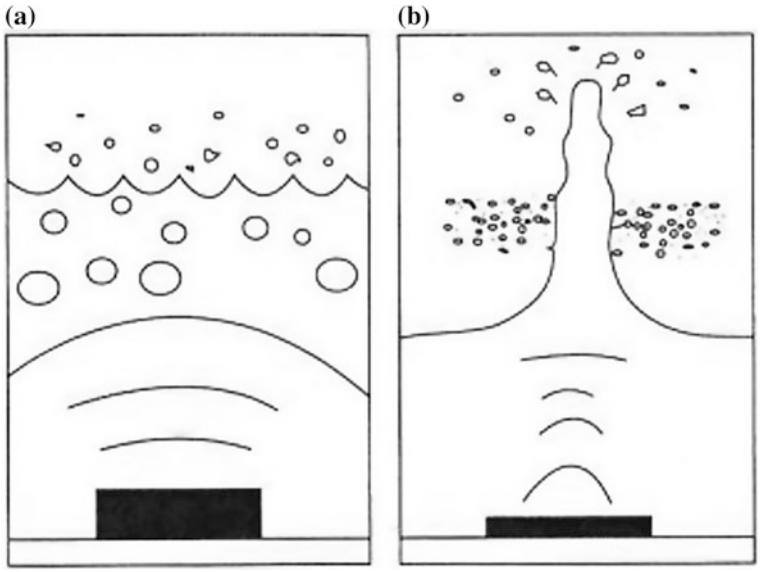

Fig. 19.10 A schematic presentation of **a** cavitational bubble formation mechanism and **b** capillary wave formation mechanism [64]

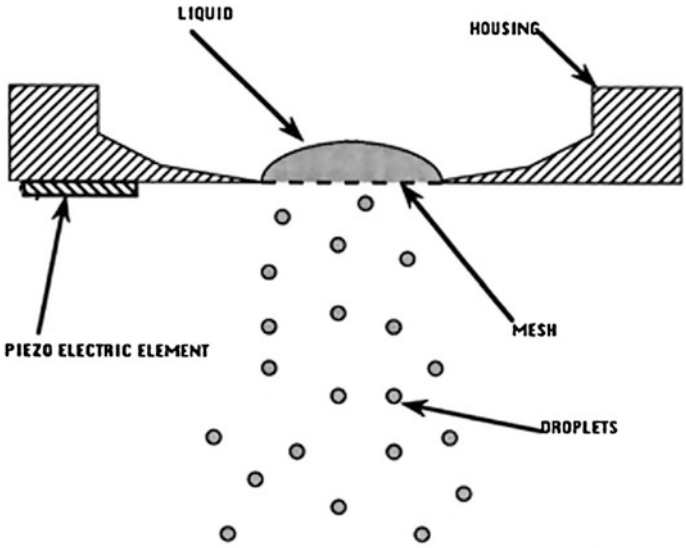

Fig. 19.11 Bespak Piezoelectric actuator employing a static mesh to control the polydispersity of the aerosol droplets [63]

atomization within the nebulizer [60]. Also, the elevation in temperature may enhance the nebulization efficiency by decreasing the droplet size as a result of reducing the formulation viscosity [63]. Delicate structures such as liposomes might be negatively affected by ultrasonic nebulization. For instance, liposomes have been shown to undergo aggregation or fusion after being degraded and fragmented as a result of heat elevation during ultrasonic nebulization [36]. In addition, ultrasonic nebulizers may not be appropriate for delivering large respirable volume of liposomes compared to air-jet and vibrating-mesh nebulizers [17].

19.2.3.3 Vibrating-Mesh Nebulizers

Vibrating mesh nebulizer consists of a plate having micro-sized tapered holes which vibrates in order to produce slow moving small aerosol droplets [18, 70] with minimal residual volumes at the end of nebulization [11]. There are two types of mesh nebulizers: passively vibrating-mesh and actively vibrating-mesh nebulizers [44].

(a) **Passively vibrating-mesh nebulizers**

An example of passively vibrating-mesh nebulizers is the Omron MicroAir NE-U22 device employs a piezoelectric crystal that produces high-energy vibrations [11]. The vibrations are transmitted via a transducer horn to a perforated plate, inducing "passive" vibrations of the plate to extrude the medical fluid through the plate apertures and produce small aerosol droplets [18, 41]. Nebulization devices like Omron NE-U03 and Omron MicroAir NE-U22 (Fig. 19.12) employ this mechanism of operation [20, 24, 70].

(b) **Actively vibration-mesh nebulizers**

An example of the actively vibrating mesh nebulizers is the Aeroneb Pro nebulizer. This nebulizer produces aerosols by employing a "micropump" technology that supplies direct electrical current to the mesh plate. The mesh consists of dome-shaped apertures containing around 1000 micro-sized apertures [24] surrounded by a piezoceramic vibrational element. The medication fluid is placed above the mesh plate and the power supply causes the mesh to move up and down by a few micrometres to generate slow moving aerosol droplets [11, 28]. Aeroneb Go and Aeroneb Pro are two nebulizers utilizing the same principle of operation. However, in general, Aeroneb Pro nebulizer (Fig. 19.13) is recommended for patients on mechanical ventilation and is attached to the aspiratory limb of the ventilator circuit to produce a constant nebulization [70]. Additionally, Aeroneb pro and jet nebulizer both demonstrated significantly higher aerosol output and fine particle fraction of electrolyte (i.e. halides) solutions, but the nebulization properties are highly affected by the concentration of halide solutions [41].

As an alternative to the "micropump" technology, TouchSpray technology can generate inhalable aerosols. The novel vibrating-mesh (electronic) nebulizer e-Flow (Pari, GmbH, Germany) has a TouchSpray atomizing head which incorporates a

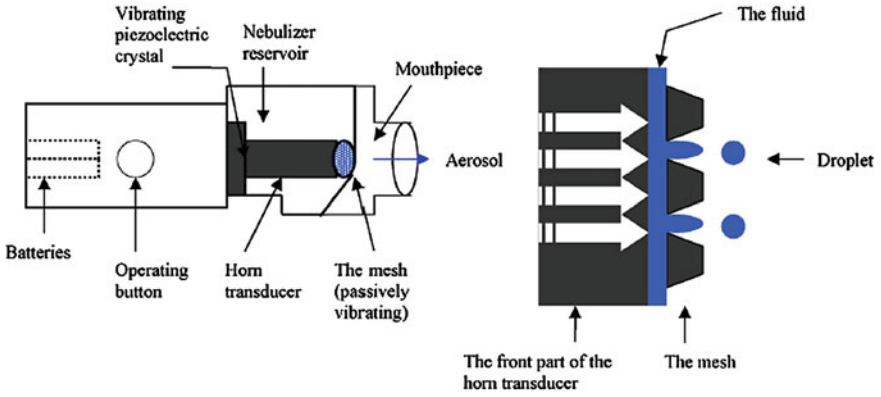

Fig. 19.12 A schematic presentation of Omron MicroAir NE-U22 nebulizer, where it illustrates the transfer of vibrations to the mesh through the horn transducer to move the mesh up and down to produce the droplets [24]

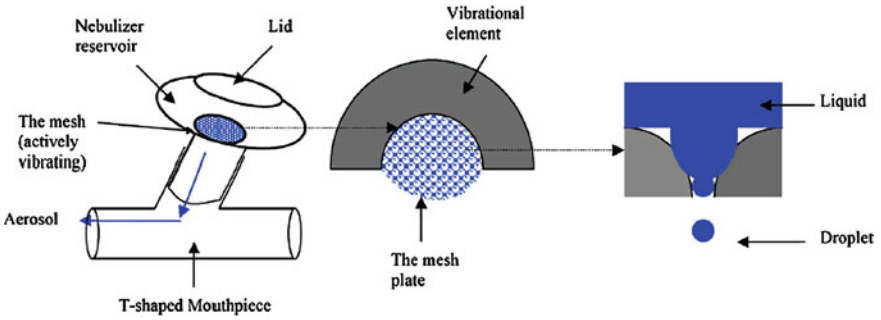

Fig. 19.13 Diagrammatic presentation of Aeroneb Pro nebulizer showing the mouthpiece, the mesh and the formation of droplet [24]

piezoelectric actuator and a perforated membrane consisting of a circular, wafer-thin metal plate with micrometre-size tapered holes (Fig. 19.14) [28]. The piezoelectric actuator is driven by an electronic circuit in order to vibrate the membrane against the medication fluid. Small jets of fluid are formed and passed through the perforated membrane in order to form droplets of controlled size and low velocity [11]. The nebulized droplets of a steroid suspension have been reported to be smaller and more uniform using the e-Flow nebulizer compared to droplets generated from the Pari LC Plus/Proneb Turbo air-jet system. The fill volume capacity of this nebulizer is 4 ml and it has been shown to be effective for nebulization of solutions, suspensions, proteins and surfactants. Moreover, relatively viscous formulations might be successfully atomized into aerosol droplets when using this nebulizer [70].

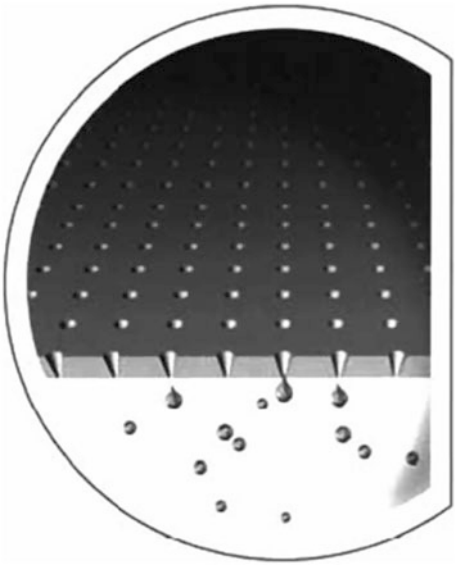

Fig. 19.14 An image showing conical holes and aerosol droplets formation of Pari eFlow [70]

19.3 Conclusions

Pulmonary delivery may be achieved by using three main types of devices: pMDIs, DPIs and medical nebulizers. This review has focused on nebulizers as they are able to deliver large volumes of aerosols using simple solutions or suspensions. As a drug delivery device, nebulizers possess several advantages; these include enhanced lung deposition, delivery of large volumes of drug solution as well as the elimination of coordination being a deciding factor in the extent of drug delivery. The three major types of nebulizers discussed and evaluated in this review have their own individual benefits and pitfalls. For usage in secondary care, it is generally agreed that jet nebulizers provide the most rapid drug delivery making them ideal for this setting. Ultrasonic nebulizers suffer notably from increased polydispersity of the droplets negating their use. In terms of high patient convenience, it is evident that vibrating-mesh nebulizers possess the edge, being wholly portable and easy to use. On the basis of the reviewed content, it is clear that nebulizers are an integral device in the prophylaxis and treatment of respiratory disorders.

References

1. Arzhavitina, A., & Steckel, H. (2010). Surface active drugs significantly alter the drug output rate from medical nebulizers. *International Journal of Pharmaceutics, 384*, 128–136.
2. Avvaru, B., Patil, M. N., Gogate, P. R., & Pandit, A. B. (2006). Ultrasonic atomization: Effect of liquid phase properties. *Ultrasonics, 44*, 146–158.

3. Barry, P. W., & O'Callaghan, C. (1999). An in vitro analysis of the output of salbutamol from different nebulizers. *European Respiratory Journal, 13*, 1164–1169.
4. Beck-Broichsitter, M., Kleimann, P., Schmehl, T., Betz, T., Bakowsky, U., Kissel, T., et al. (2012). Impact of lyoprotectants for the stabilization of biodegradable nanoparticles on the performance of air-jet, ultrasonic, and vibrating-mesh nebulizers. *European Journal of Pharmaceutics and Biopharmaceutics*, *82*, 272–280.
5. Bridges, P. A., & Taylor, K. M. G. (1998). Nebulisers for the generation of liposomal aerosols. *International Journal of Pharmaceutics, 173*, 117–125.
6. Bridges, P. A. (2000). An investigation of some of the factors influencing the jet nebulisation of liposomes. *International Journal of Pharmaceutics, 204*, 69–79.
7. Chougule, M. B., Padhi, B. K., Jinturkar, K. A., & Misra, A. (2007). Development of dry powder inhalers. *Recent Patents on Drug Delivery & Formulation, 1*, 11–21.
8. Clark, A. R. (1995). Medical aerosol inhalers: Past, present, and future. *Aerosol Science and Technology, 22*, 374–391.
9. Colacone, A., Wolkove, N., Stern, E., Afilalo, M., Rosenthal, T. M., & Kreisman, H. (1990). Continuous nebulization of albuterol (salbutamol) in acute asthma. *Chest, 97*, 693–697.
10. Dennis, J. H., Stenton, S. C., Beach, J. R., Avery, A. J., Walters, E. H., & Hendrick, D. J. (1990). Jet and ultrasonic nebuliser output: Use of a new method for direct measurement of aerosol output. *Thorax, 45*, 728–732.
11. Dhand, R. (2002). Nebulizers that use a vibrating mesh or plate with multiple apertures to generate aerosol. *Respiratory Care, 47*, 1406–1416 (discussion 1416–1418).
12. Dhand, R. (2003). *New nebuliser technology—Aerosol generation by using a vibrating mesh or plate with multiple apertures*. University of Missouri Hospital and Clinics, for Omeron Healthcare, Inc.
13. Dhand, R. (2008). Aerosol delivery during mechanical ventilation: From basic techniques to new devices journal of aerosol medicine and pulmonary. *Drug Delivery, 21*, 45–60.
14. Dolovich, M. (1999). New propellant-free technologies under investigation. *Journal of Aerosol Medicine, 12*(Suppl 1), S9–s17.
15. Dolovich, M., & Dhand, R. (2011). Aerosol drug delivery: Developments in device design and clinical use? Authors' reply. *The Lancet, 378*, 1032–1045.
16. Dunbar, C. A., Watkins, A. P., & Miller, J. F. (1997). An experimental investigation of the spray issued from a pMDI using laser diagnostic techniques. *Journal of Aerosol Medicine, 10*, 351–368.
17. Elhissi, A., & Taylor, K. M. G. (2005). Delivery of liposomes generated from pro liposomes using air-jet, ultrasonic and vibrating-mesh nebulisers. *Journal of Drug Delivery Science and Technology, 15*, 261–265.
18. Elhissi, A., Hidayat, K., Phoenix, D. A., Mwesigwa, E., Crean, S., Ahmed, W., et al. (2013). Air-jet and vibrating-mesh nebulization of niosomes generated using a particulate-based proniosome technology. *International Journal of Pharmaceutics, 444*, 193–199.
19. Elhissi, A. M. A., & Ahmed, W. (2011). Chapter 1: Advances in design and technology of devices manufactured for drug delivery applications. In M. Jackson & J. P. Davim (Eds.), *Medical device manufacturing*. USA: Nova Publisher.
20. Elhissi, A. M. A., Faizi, M., Naji, W. F., Gill, H. S., & Taylor, K. M. G. (2007). Physical stability and aerosol properties of liposomes delivered using an air-jet nebulizer and a novel micropump device with large mesh apertures. *International Journal of Pharmaceutics, 334*, 62–70.
21. Farr, S. J., Kellaway, I. W., & Carman-Meakin, B. (1987). Assessing the potential of aerosol-generated liposomes from pressurised pack formulations. *Journal of Controlled Release, 5*, 119–127.
22. Flament, M. P., Leterme, P., & Gayot, A. T. (2001). Study of the technological parameters of ultrasonic nebulisation. *Drug Development and Industrial Phamacy, 27*, 643–649.
23. Ganderton, D. (1999). Targeted delivery of inhaled drugs: Current challenges and future goals. *Journal of Aerosol Medicine, 12*(Suppl 1), S3–S8.

24. Ghazanfari, T., Elhissi, A. M., Ding, Z., & Taylor, K. M. (2007). The influence of fluid physicochemical properties on vibrating-mesh nebulization. *International Journal of Pharmaceutics, 339*, 103–111.
25. Goldbach, P., Brochart, H., & Stamm, A. (1993). Spray-drying of liposomes for a pulmonary administration. II. Retention of encapsulated materials. *Drug Development and Industrial Pharmacy, 19*, 2623–2636.
26. Grossman, J. (1994). The evolution of inhaler technology. *Journal of Asthma, 31*, 55–64.
27. Hamilton, R. D., & Guz, A. (1991). Jet and ultrasonic nebuliser output: Use of a new method for direct measurement of aerosol output. *Thorax, 46*, 151–152.
28. Hess, D., MacIntyre, N., & Mishoe, S. (2011). *Respiratory care: Principles and practice*. Burlington, MA.: Jones & Bartlett Learning.
29. Hess, D., Fisher, D., Williams, P., Pooler, S., & Kacmarek, R. M. (1996). Medication nebulizer performance. Effects of diluent volume, nebulizer flow, and nebulizer brand. *Chest, 110*, 498–505.
30. Hess, R. D. (2000). Nebulizers: Principles and performance. *Respiratory care, 45*, 609–622.
31. Hugh, D. C. S. (2003). The influence of formulation variables on the performance of alternative propellant-driven metered dose inhalers. *Advanced Drug Delivery Reviews, 55*, 807–828.
32. Juntunen-Backman, K., Kajosaari, M., Laurikainen, K., Malinen, A., Kaila, M., Mustala, L., et al. (2002). Comparison of easyhaler metered-dose, dry powder inhaler and a pressurised metered-dose inhaler plus spacer in the treatment of asthma in children. *Clinical Drug Investigation, 22*, 827–839.
33. Kendrick, A. H., Smith, E. C., & Wilson, R. S. (1997). Selecting and using nebuliser equipment. *Thorax, 52*(Suppl 2), S92–S101.
34. Khatri, L., Taylor, K. M., Craig, D. Q., & Palin, K. (2001). An assessment of jet and ultrasonic nebulisers for the delivery of lactate dehydrogenase solutions. *International Journal of Pharmaceutics, 227*, 121–131.
35. Labiris, N. R., & Dolovich, M. B. (2003). Pulmonary drug delivery. Part II: The role of inhalant delivery devices and drug formulations in therapeutic effectiveness of aerosolized medications. *British Journal of Clinical Pharmacology, 56*, 600–612.
36. Leung, K. K. M., Bridges, P. A., & Taylor, K. M. G. (1996). The stability of liposomes to ultrasonic nebulisation. *International Journal of Pharmaceutics, 145*, 95–102.
37. Lin, C.-Y., Meng, H.-C., & Fu, C. (2011). An ultrasonic aerosol therapy nebulizer using electroformed palladium–nickel alloy nozzle plates. *Sensors and Actuators A: Physical, 169*, 187–193.
38. Máiz Carro, L., & Wagner, S. C. (2011). Beneficios de la terapia nebulizada: conceptos básicos. *Archivos de BronconeumologíaSupplement, 47*(Supplement 6), 2–7.
39. McCallion, O. N. M., Taylor, K. M. G., Thomas, M., & Taylor, A. J. (1995). Nebulization of fluids of different physicochemical properties with air-jet and ultrasonic nebulizers. *Pharmaceutical Research, 12*, 1682–1688.
40. McCallion, O. N. M., Taylor, K. M. G., Bridges, P. A., Thomas, M., & Taylor, A. J. (1996). Jet nebulisers for pulmonary drug delivery. *International Journal of Pharmaceutics, 130*, 1–11.
41. Najlah, M., Vali, A., Taylor, M., Arafat, BT., Ahmed, W., Phoenix, DA., et al. (2013). A study of the effects of sodium halides on the performance of air-jet and vibrating-mesh nebulizers. *International Journal of Pharmaceutics*, *456*, 520.
42. Newman, S. P. (2005). Principles of metered-dose inhaler design. *Respiratory Care, 50*, 1177–1190.
43. Newman, S. P., & Clarke, S. W. (1983). Therapeutic aerosols 1-physical and practical considerations. *Thorax, 38*, 881–886.
44. Newman, S. P., & Gee-Turner, A. (2005). The Omron microair vibrating mesh technology nebuliser, a 21st century approach to inhalation therapy. *Journal of Applied Therapeutic Research, 5*, 29–33.

45. Niven, R. W., & Brain, J. D. (1994). Some functional aspects of air-jet nebulizers. *International Journal of Pharmaceutics, 104*, 73–85.
46. Niven, R. W., Speer, M., & Schreier, H. (1991). Nebulization of liposomes. II. The effects of size and modeling of solute release profiles. *Pharmaceutical Research, 8*, 217–221.
47. O'Callaghan, C., & Barry, P. W. (1997). The science of nebulised drug delivery. *Thorax, 52* (Suppl 2), S31–S44.
48. O'Riordan, T. G. (2002). Formulations and nebulizer performance. *Respiratory Care, 47*, 1305–1312 (discussion 1312-1313).
49. Oliveira, R. F., Teixeira, S., Silva, L. F., Teixeira, J. C., & Antunes, H. (2010). *Study of a pressurized metered-dose inhaler spray parameters in fluent*. London: World Congress on Engineering.
50. Pedersen, S. (1987). Inhaler use in children with asthma. *Danish Medical Bulletin, 34*, 234–249.
51. Pedersen, S. (1996). Inhalers and nebulizers: Which to choose and why. *Respiratory Medicine, 90*, 69–77.
52. Pedersen, S., Frost, L., & Arnfred, T. (1986). Errors in inhalation technique and efficiency in inhaler use in asthmatic children. *Allergy, 41*, 118–124.
53. Phipps, P. R., & Gonda, I. (1990). Droplets produced by medical nebulizers. Some factors affecting their size and solute concentration. *CHEST Journal, 97*, 1327–1332.
54. Ramlal, S. K., Visser, F. J., Hop, W. C. J., Dekhuijzen, P. N. R., & Heijdra, Y. F. (2013). The effect of bronchodilators administered via aerochamber or a nebulizer on inspiratory lung function parameters. *Respiratory Medicine, 107*, 1393–1399.
55. Rau, J. L. (2002). Design principles of liquid nebulization devices currently in use. *Respiratory Care, 47*, 1257–1275 (discussion 1275–1278).
56. Rubin, B. K., & Fink, J. B. (2005). Optimizing aerosol delivery by pressurized metered-dose inhalers. *Respiratory Care, 50*, 1191–1200.
57. Schreier, H., & Bouwstra, J. (1994). Liposomes and niosomes as topical drug carriers: Dermal and transdermal drug delivery. *Journal of Controlled Release, 30*, 1–15.
58. Smye, S., & Jollie, M. (1992). A simple mathematical description of jet nebuliser performance. *Journal of Aerosol Science, 01*, 221–224.
59. Smyth, H., Hickey, A. J., Brace, G., Barbour, T., Gallion, J., & Grove, J. (2006). Spray pattern analysis for metered dose inhalers I: Orifice size, particle size, and droplet motion correlations. *Drug Development and Industrial Pharmacy, 32*, 1033–1041.
60. Steckel, H., & Eskandar, F. (2003). Factors affecting aerosol performance during nebulization with jet and ultrasonic nebulizers. *European Journal of Pharmaceutical Sciences, 19*, 443–455.
61. Takanami, C., & Goto, Y. (1990). Physical properties of antibiotic aerosols produced by jet and ultrasonic nebulizers. *Journal of Aerosol Medicine, 3*, 45–52.
62. Taylor, K. M. G., & Hoare, C. (1993). Ultrasonic nebulisation of pentamidine isethionate. *International Journal of Pharmaceutics, 98*, 45–49.
63. Taylor, K. M. G., & McCallion, O. N. M. (1997). Ultrasonic nebulisers for pulmonary drug delivery. *International Journal of Pharmaceutics, 153*, 93–104.
64. Taylor, K. M. G., & McCallion, O. N. M. (2002). Ultrasonic nebulizers. In J. Swarbrick & J. C. Boylan (Eds.), *Encyclopaedia of pharmaceutical technology* (pp. 2840–2847). New York: Marcel Dekker.
65. Taylor, K. M. G., Taylor, G., Kellaway, I. W., & Stevens, J. (1990). The stability of liposomes to nebulisation. *International Journal of Pharmaceutics, 58*, 57–61.
66. Telko, M. J., & Hickey, A. J. (2005). Dry powder inhaler formulation. *Respiratory Care, 50*, 1209–1227.
67. Terzano, C. (2001). Pressurized metered dose inhalers and add-on devices. *Pulmonary Pharmacology & Therapeutics, 14*, 351–366.
68. Vecellio, L., Abdelrahim, M. E., Montharu, J., Galle, J., Diot, P., & Dubus, J.-C. (2011). Disposable versus reusable jet nebulizers for cystic fibrosis treatment with tobramycin. *Journal of Cystic Fibrosis, 10*, 86–92.

69. Vervaet, C., & Byron, P. R. (1999). Drug-surfactant-propellant interactions in HFA-formulations. *International Journal of Pharmaceutics, 186*, 13–30.
70. Waldrep, J. C., & Dhand, R. (2008). Advanced nebulizer designs employing vibrating mesh/aperture plate technologies for aerosol generation. *Current Drug Delivery, 5*, 114–119.
71. Waldrep, J. C., Keyhani, K., Black, M., & Knight, V. (1994). Operating characteristics of 18 different continuous-flow jet nebulizers with beclomethasone dipropionate liposome aerosol. *Chest, 105*, 106–110.
72. Yoshiyama, Y., Seki, K., Mino, K., Yazaki, T., Kanke, M., Arai, M., et al. (2003). Nebulization property and utility of a newly designed mesh nebulizer. *Oto-Rhino-Laryngology Tokyo*, *46*, 41–44.

Chapter 20
Surface Modification of Interference Screws Used in Anterior Cruciate Ligament Reconstruction Surgery

Charalambos P. Charalambous, Tariq A. Kwaees and Paul M. Sutton

Abstract In anterior cruciate ligament reconstruction surgery the graft is often secured to the tibial and femoral bone tunnels using interference screws. Surface modification of such interference screws may be used to help promote graft-bone integration and reduce the risk of infection. This could allow faster post-surgical rehabilitation, earlier return to sports, and improved long term clinical outcomes. This chapter reviews surface modification techniques that have already been tried in anterior cruciate ligament reconstruction interference screws, but also reviews surface modification techniques that have been applied to other orthopaedic implants and which could potentially be extrapolated to cruciate ligament reconstruction surgery.

The anterior cruciate ligament (ACL) is one of the main ligaments giving stability to the knee. It passes from the posteromedial aspect of the lateral femoral condyle to insert onto the tibia. It consists of an antero-medial and an antero-lateral band. The ACL provides stability in limiting anterior translation of the tibia onto the femur as well as rotational stability.

ACL ruptures are common, with an estimated incidence rate of 37 per 100,000 person-years [1]. They occur as a result of contact as well as noncontact injuries, with the latter accounting up to 60 % of cases [2]. Of nine sports studied by Joseph et al. in USA, female soccer and male football had the largest number of ACL

C.P. Charalambous (✉) · T.A. Kwaees
Department of Trauma and Orthopaedics, Blackpool Victoria Hospital, Whinney Heys Road, Blackpool FY3 8NR, UK
e-mail: bcharalambos@hotmail.com

C.P. Charalambous
School of Medicine and Dentistry, University of Central Lancashire, Preston, UK

C.P. Charalambous
Faculty of Medical and Human, Institute of Inflammation and Repair Sciences, University of Manchester, Manchester, UK

P.M. Sutton
Department of Orthopaedics, Northern General Hospital, Sheffield, UK

W. Ahmed and M.J. Jackson (eds.), *Surgical Tools and Medical Devices*,
DOI 10.1007/978-3-319-33489-9_20

injuries and the highest competition-related ACL injury rate [3]. In their study athletes were up to seven times more likely to have an ACL injury whilst in competition than in practice.

Some of the patient characteristics that may increase the risk of ACL rupture include female sex [4], a narrow femoral inter-condylar notch [5, 6], greater posterior inferior medial tibial plateau slope [7, 8], joint hypermobility with increased knee extension [9, 10], increased ilio-tibial band flexibility [11], high body mass index [12], poor core stability and poor core proprioception [13, 14]. Knee positioning and biomechanics during landing from a jump or during cutting and pivoting manoeuvres also appear to influence the risk of ACL rupture (a higher rupture risk is reported in athletes who perform these manoeuvers with decreased knee and hip flexion, increased knee abduction, a shorter stance time, increased hip internal rotation and tibia external rotation) [15, 16].

In the acute phase, ACL ruptures typically causes significant pain, limitation of movement and swelling that occurs due to the intra-articular inflammation and bleeding. In the long term the injury can also confer substantial disability as a result of residual knee instability [17, 18]. A considerable proportion of patients sustaining an ACL rupture may regain functional knee stability by compensating for the effect of the ruptured ligament, by muscle strengthening and proprioception training of their knee [17]. Equally, a substantial proportion of such patients (one to two thirds) will continue to experience residual instability that either limits their day-to-day activity or the ability to participate in sports. In these patients, ACL reconstruction may be performed to try and improve knee stability [19, 20]. In the Joseph et al. study of ACL injuries in athletes in the USA, 76.6 % of all ACL injuries needed surgery [3].

ACL reconstruction is a surgical procedure to replace the torn ligament with a natural or artificial graft. Grafts from the same individual (autograft) are most commonly utilised, however, occasionally cadaveric grafts or synthetic grafts are employed. The use of autograft hamstring tendon grafts, bone patellar tendon bone and quadriceps tendon grafts is well described. In a recent international survey of orthopaedic surgeons 63 % reported using a hamstring tendon graft and 26 % a one patellar tendon bone graft [21].

In ACL reconstruction the graft is secured to the tibia and the femur in a position aiming to replicate the attachments of the torn ACL ligament. Traditional ACL reconstruction techniques aim to reproduce the antero-medial band of the native ACL, but more recently developed techniques aim to reproduce both the larger antero-medial and posterolateral bands [22–25]. In ACL reconstruction, bone tunnels are created in the femur and tibia into which the graft is inserted and fixed. Over time biological fixation and graft integration occurs making the initial mechanical fixation redundant. Several techniques have been described for securing the graft into these bone tunnels. These can be divided into four types [26–31]:

1. Direct extra-cortical fixation (staples)
2. Indirect extra-cortical fixation (femoral or tibial buttons)

3. Semi-anatomical fixation (transfixation systems)
4. Anatomical fixation (interference screws).

The aim of these fixation techniques is to hold the graft in place until permanent stability is achieved through bone to graft healing and osseo-integration of the graft [32].

This chapter focuses on surface modification of interference screws as such screws are one of the most popular methods of graft fixation (Fig. 20.1) [33, 34]. Interference screw fixation involves the insertion of a screw alongside the graft in a bone tunnel (Fig. 20.2). The screw compresses the graft against the bone tunnel wall holding the graft in place.

Interference screws may be metal or non-metal. Non-metal screws may be made of bio-absorbable or non-absorbable material. Both titanium and stainless steel interference screws are available [34]. Disadvantages of metal screws include the potential to damage the graft during screw insertion because of the materials

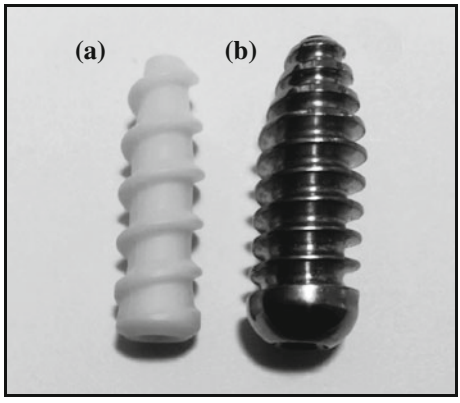

Fig. 20.1 Examples if interference screws used for ACL reconstruction. **a** Non-metallic (MILAGRO Advanced, DePuy UK). **b** Metallic (RCI screw, Smith and Nephew, USA)

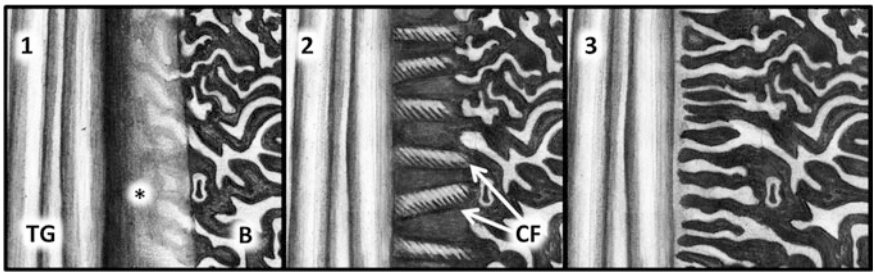

Fig. 20.2 Graft to bone healing. *1* Initial phase demonstrating fibro-vascular interface (*star*) between tendon graft (TG) and bone (B). *2* Collagen fibres (CF) link the tendon graft to bone. *3* Obliteration of the fibro-vascular interface by bone

hardness, and interference with post-operative MRI imaging of the knee due to the creation of artefacts [35, 36]. In addition, if revision ACL reconstruction surgery were to be performed, the presence of metal interference screws may complicate surgery, as they may have to be removed leaving residual bone void that may require filling with bone graft before proceeding with new graft insertion. In contrast, bio-absorbable screws may provide strong fixation until the graft incorporates and then be replaced by bone. This can allow easier revision surgery, as new tunnels can be simply drilled through, without the need of hardware removal and bone grafting.

Several types of bio-absorbable screws have been developed and include [26, 37–40]:

1. Bio-absorbable Polymers—(Poly-l-lactide acid (PLLA), poly-lactic-co-glycolic acid (PLGA), poly-L/D-lactide (PLDLA), poly-D,L-lactide-co-glycolide (PDLG)).
2. Bio-composites—a polymer (such as PLLA, PLGA, PLDLA, PDLG) combined with a ceramic (such as β-Tricalcium phosphate (β-TCP), Hydroxyapatite (HA), Calcium carbonate, Biphasic Calcium phosphate).

The first commercially available bio-absorbable screws made of PLLA followed by PDLG. Degradation of bio-absorbable polymers was described in 5 stages including hydration, depolymerisation, loss of mass, absorption and elimination [41]. However, clinical studies show that the true in vivo absorption and osseo-integration rate of these materials happens very slowly if at all [42]. There was also concern with PLLA about possible inflammatory reactions related to the material's crystallinity. In an attempt to enhance osteo-conductivity and osseo-integration, bio-composite screws were developed which combined a bio-absorbable polymer with a bio-ceramic. The bio-ceramics used are normal bone calcium components such as calcium carbonate and calcium phosphate (β-TCP, HA). The calcium components allow the formation of strong bonds with the surrounding bone, providing a scaffold for osteocyte invasion and new bone formation. The ceramic component therefore facilitates osseo-integration, both on the surface and from within the implant [42, 43]. In addition bio-composite screws may lead to fewer inflammatory reactions due to neutralisation of the acidity produced by the degradation products of polymers.

A review of approximately 13,000 ACL reconstructions on the Swedish national knee ligament register reported a 1.6 % incidence of revision surgery at a 2-year follow up [44]. Patients with metal interference screw fixation of a semitendinosus tendon autograft on the tibia had a significantly reduced risk of early revision surgery. A systematic review of overlapping meta-analyses comparing metal versus bio-absorbable screws in ACL reconstruction, reported that although clinical and functional outcomes were similar with both types of screws, prolonged knee effusion, femoral tunnel widening (in line with other studies [45, 46]) and screw breakage were more commonly observed when bio-absorbable screws were employed [30].

It is considered that following graft insertion and tunnel fixation with an interference screw the following process occur:

1. Ligamentisation of the intra-articular part of the graft—this involves ischemic necrosis of the graft, acute inflammation followed by revascularization, host fibroblast invasion and proliferation and ultimately new collagen formation and remodelling [47].
2. Graft to bone healing in the tibial and femoral bone tunnels—tunnel reaming and interference screw insertion is believed to cause bone necrosis due to physical trauma, heat generation and the release of local inflammatory mediators. Necrotic bone may then be removed by osteoclast activation and production of matrix metalloproteinases. At the same time graft to bone healing is initiated. Graft to bone healing in the bone tunnels is mainly indirect healing and occurs in several stages, as demonstrated by histological animal studies [48, 49]:

    - A layer of granulation tissue, consisting of connective tissue, rich in cellular and vascular components, forms in the interface between graft and bone. This acts as an interzone between the two. The bone margins of the tunnel show osteoid formation and bone remodelling with osteoblastic and osteoclastic activity.
    - Maturation of the interzone with reduction in cellularity and with development of collagen fibres passing perpendicularly between the graft and bone.
    - The fibrous inter-zone is replaced by the ingrowth of bone trabeculae (Fig. 20.2).

Rodeo et al. evaluated tendon bone tunnel healing in a canine model [48]. They reported that collagen fibres connecting tendon and bone were seen at 4 weeks and were fully established by 12 weeks. Prior to 12 weeks, pull out testing caused separation of the graft from the bone but after 12 weeks interstitial graft failure was more likely to be observed suggesting that graft to bone healing was complete by this stage. Grana et al. evaluated semitendinosus tendon to bone tunnel healing in rabbits [49]. They observed collagen fibres connecting the graft to bone by 3 weeks post fixation. In accord with this they reported that in specimens tested at less than 2 weeks after ACL reconstruction, the graft pulled out of the tunnel, whereas by 3 weeks graft failure occurred within the intra-articular portion. Pinczewski et al. evaluated tissue at the graft-bone interface in 2 patients having revision ACL reconstruction for early failure (due to graft substance rupture), and suggested that graft to bone integration occurs between 6 and 15 weeks after surgery [50].

ACL reconstruction surgery is a commonly performed procedure and the frequency of this is rising. The incidence of ACL reconstruction in the USA rose from an estimated 86,687 (95 % CI, 94,993–164,679; 32.9 per 100,000 person-years) in 1994 to 129,836 (95 % CI, 94,993–164,679; 43.5 per 100,000 person-years) in 2006 [51]. It is a costly procedure with an estimated mean cost in 2013 of about $2040 [52]. ACL reconstruction is a demanding and challenging surgery with a relatively high rate of intra-operative as well as post-operative complications

[53–55]. Poor bone integration of the graft as well as post-operative infection are important complications which can lead to failure of ACL reconstruction or compromise its long term functional outcomes.

Surface modification of interference screws used in graft to bone fixation of ACL reconstructions may be used to help to promote graft-bone integration and reduce the infection risk. These possibilities are discussed considering surface modification techniques that have already been tried to ACL reconstruction interference screws but also reviewing surface modification techniques applied to other orthopaedic implants and which could potentially be extrapolated to ACL reconstruction surgery.

20.1 Poor Graft-Bone Integration

During ACL reconstruction using hamstring tendons and interference screw fixation, the graft is pulled into the tibia and femoral tunnels and one interference screw is inserted into each tunnel. The interference screw compresses the graft against the tunnel bony wall (Fig. 20.3). The aim of interference screw fixation is to hold the graft in place, to prevent partial or complete slippage of the graft out of the tunnel into the knee joint. A partial slip would cause loss of graft tension and the potential for ongoing instability and complete slippage of the graft would result in failure of the surgical reconstruction. This initial fixation by the interference screw is

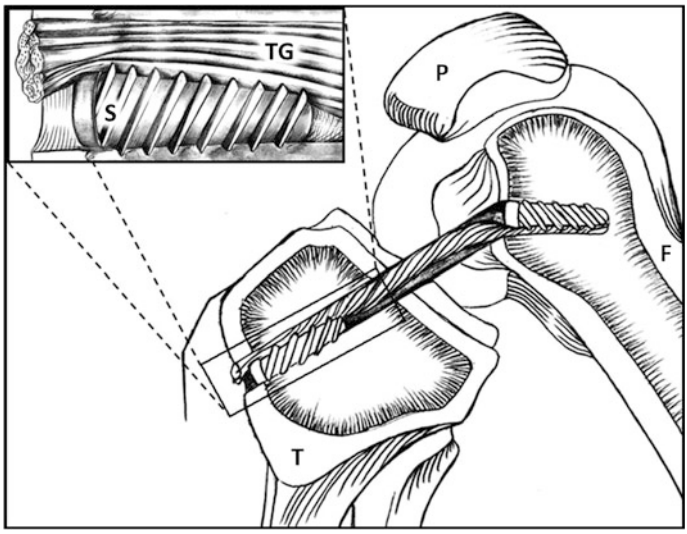

Fig. 20.3 Illustration of ACL reconstruction demonstrating screw placement. Femur *F*, patella *P*, interference screw *S*, tibia *T*, tendon graft *TG*

temporary but is essential until the graft heals permanently onto bone. Initial fixation stability achieved with interference screws is influenced by screw diameter [56], length [57], bone porosity and screw to tunnel diversion [58]. The tibial attachment is usually the weak link in ACL reconstruction surgery, due to the poor bone density (relative to the femur). This maybe further compounded by relative immobility of the knee and resultant disuse osteopenia. Initial fixation stability is important to allow early mobilisation and rehabilitation of the operated knee. Rehabilitation may have to be delayed in patients in whom secure fixation cannot be achieved due to poor bone stock. This may delay the milestones of functional recovery following ACL reconstruction.

Graft to bone healing and osseo-integration of both the graft and fixation device is important in providing permanent graft stability. Hence, a fast and thorough healing process may minimise the risk of graft slippage, allowing early and more aggressive rehabilitation. Tunnel widening is a phenomenon observed following ACL reconstruction, it is an expansion of the volume of the bone tunnels occurring between 6 weeks and 6 months after ACL reconstruction surgery [46]. Tunnel widening is more common following extra-cortical graft fixation but has also been reported using interference screw fixation with both metal and bio-absorbable screws [45, 59]. The clinical significance of tunnel widening is controversial, but there is evidence to suggest that it may increase graft laxity. Cohen et al. showed that patients with tunnel widening were more likely to have increased tibial translation on Lachman testing compared to those without tunnel widening [58]. Tunnel widening may lead to migration of the graft in the antero-posterior plane and loss of graft tension. Tunnel widening makes revision ACL reconstruction more challenging, as wider tunnels or bone voids need to be thoroughly bone grafted. The pathogenesis of tunnel widening is uncertain with several mechanisms including; excessive graft motion within the bone tunnel, large tunnel relative to the graft diameter, oversized bio-absorbable interference screws, inflammatory reactions due to screw breakdown, early aggressive rehabilitation, ingress of synovial fluid between the graft and tunnel interface has also been implicated [60–63]. The mechanism of this is that synovial fluid cytokines have been shown to activate osteoclasts which may lead to bone resorption; thus reduction of the interface gaps between graft to bone or bone to screw may reduce the risk of tunnel widening as may early graft to bone healing.

Surface modification of interference screws could promote this graft to bone healing and osseo-integration. Such modifications could include

1. Coating surfaces with factors that are locally released to promote osseo-integration or inhibit implant related bone necrosis and osteolysis. Such coatings may also attract bone forming cells, without being released in the surrounding tissues [64].
2. Modification of surface topography to attract bone forming cells [65].

Several factors have been shown to promote graft to bone healing and could be considered for screw coating. These include

1. Growth factors—transforming growth factor β(TGFβ), epithelial growth factor (EGF), platelet derived growth factor (PDGF), insulin-like growth factor (IGF) [66–68], granulocyte colony stimulating factor (G-CLF) [69], human bone morphogenic protein-2 and 7 (BMP-2 and 7) [70–72].
2. Biomaterials–calcium ceramics with composition similar to bone–β-TCP, HA, calcium carbonate, biphasic calcium phosphate [43, 73].
3. Osteoclast and MMP inhibitors—alpha-2-macroglobulin, osteoprotegerin, bisphosphonates [74–76].

Coating of screws, metal or non-metal, with these factors could potentially promote graft-bone healing and could improve osseo-integration. Extensive work has been performed to assess the effects of coating orthopaedic screws that are used internally for fracture fixation or other bone stabilisation. Most of these studies evaluated the effect of coating screws with calcium based biomaterials [77, 78], collagen [79, 80] or bisphosphonates [81, 82] and demonstrate that these materials can successfully augment local bone formation and healing [82]. There is evidence to suggest that these coatings can also be applied to the graft to bone healing process and promote osseo-integration.

Lu et al. examined whether bio-absorbable interference screws coated with a hydroxyapatite-based mineral layer designed to release an engineered peptide growth factor (link-BMP-2) would improve tendon to bone healing compared with uncoated screws [83]. They studied 14 sheep randomised to receive a link-BMP-2 coated or uncoated screw. Over 80 % of the initially bound link-BMP-2 was shown in vitro to be released within 6 weeks and histological analysis showed that the tendons fixed with the link-BMP-2 coated screws had better tendon to bone healing compared to those with uncoated screws. The authors also reported that mesenchymal cells were present at the screw tendon interface in the coated but not in the uncoated group. The study conclusion was that link-BMP-2 can be successfully bound to a mineral coated interference screw surfaces and subsequently released from the screw in a sustained manner improving tendon to bone healing.

Surface topography, roughness, wettability and electrical charge can influence implant-host interaction and osseo-integration [84–88]. Rough surfaces can facilitate cellular adherence and facilitate bone formation [85, 87, 89, 90]. Altering the surface roughness of an implant from conventional micron-size features to nanometer size features can further enhance osteoblast adhesion and calcium deposition whilst inhibiting fibroblast's functions [86, 90, 91]. Surgical implants often have micro-rough surfaces prepared by grit-blasting and acid-etching. However, proteins and cells interact with implant surfaces in the nanometer range. Hence surface modifications to provide nanostructures may aid osseo-integration for both coated and uncoated surfaces.

Salou et al. compared the osseo-integration of machined standard alumina grit-blasted and acid-etched (MICRO) implants in rabbit femurs with that of nanostructured (NANO) implants [92]. They reported that the MICRO surface showed typical random cavities (average roughness 1.5 μm), whilst the NANO

surface showed a regular array of titanium oxide nanotubes (7 ± 11 nm diameter, 160 nm thick). The resistance to pull of these implants 4 weeks after implantation was higher for the NANO than the other groups. Furthermore histological examination showed direct apposition of bone onto the NANO surface. Bone-to-implant contact and bone growth values were also higher for the NANO surface. Based on these findings the authors concluded that nanostructured surfaces may improve the osseo-integration of titanium implants and could be a valuable alternative to conventional surface preparation techniques.

In a similar study Lin et al. evaluated different surface structures of titanium implants on osseo-integration [89]. They developed three types of structures of TiO_2 coating on Ti implants including nanotube structure, nanosponge-like structure and nano/micro nest-like structure. The in vivo osseo-integration of the coated Ti screws inserted into the knees of rabbits was evaluated histologically. They found that the nano/micro nest-like and nanotube surface structured provided better osseo-integration as compared to untreated screws or screws with a nano sponge-like structure. Similarly, screw removal torque force was higher in those with nano/micro nest-like and nanotube surface structure.

In a recent systematic review Goldman et al. evaluated studies that examined the influence of various nanostructure surface modifications of titanium implants upon osteoblast proliferation [93]. In most of the articles they reviewed nanostructured surfaces enhanced osteoblast proliferation compared to microstructured or smooth surfaces. With regards to nanocomposite materials incorporated onto implants' surface, niobium (Nb_2O_5) doped TiO_2 nanoplate structures promoted cell adhesion and proliferation. Strontium doped hydroxyapatite with nm grain morphology was shown to accelerate osteoblast cell proliferation [94, 95]. The evidence suggests that nanosurface modification of interference screws could offer new directions in facilitating local bone growth and potentially speeding graft osseo-integration.

Infection following ACL reconstruction is uncommon, it may be superficial and of relatively minor consequence or deep and cause significant morbidity. Deep infections may be a septic arthritis which is within the joint and involves the intra-articular part of the graft, osteomyelitis involving the bone tunnels where graft to bone fixation occurs, or a combination of both. Septic arthritis has a reported incidence of approximately 0.4 [96, 97] to 0.6 % [98] following ACL reconstruction.

Deep infection is a serious complication following ACL reconstruction, as it can lead to graft failure, articular cartilage destruction, joint stiffness and seconder osteoarthritis. There is evidence to suggest that hamstring autografts are associated with higher infection rates than bone patellar tendon bone autografts and allogenic grafts; a registry with over 10,000 reconstructions reported that the risk of infection with hamstring autografts was about three times higher than that of bone patellar tendon bone grafts [99].

Treatment when treating deep infections after ACL surgery aims to eradicate the infection whilst preserving the ACL graft. However, evidence suggests that in up to 14 % of patients both graft and interference screw removal along with bone tunnel

debridement, maybe necessary to help eliminate infection [100]. This is usually the case in the presence of osteomyelitis and infection of the fixation implant. Once infection is established on orthopaedic implants a biofilm layer forms which protects the microorganisms from antibiotic treatment and infection eradication typically requires implant removal [101–103].

A substantial proportion of implant related infections are caused by *Staphylococci*, particularly *Staphylococcus aureus* and coagulase negative *Staphylococci* [104]. Bacterial contamination of implant surfaces may occur at the time of surgery when implant and surgical site are exposed to the environment at a time distant from surgery due to transient release of bacteria known as bacteraemia. This can occur due to infection elsewhere or even during simple activities of daily living such as brushing teeth. Bacteria have the ability to remain dormant on an implant surface for a prolonged period until local conditions (host immune activity, poor surrounding tissue environment) allows them to multiply, leading to infection.

Adhesion of bacteria to the surface of an implant is an important step in the pathogenesis of infection and occurs via special cell wall receptors called adhesions. Bacterial adhesions is thought to consist of two stages [105, 106]:

1. Physical phase of attachment to the surface which is reversible.
2. Molecular and cellular phase. This is irreversible, with a firmer adhesion of bacteria to the surface.

Bacterial adhesion is influenced by several factors including [102, 103, 107–110]:

1. Length of exposure to bacteria.
2. Bacterial characteristics such as contamination load, hydrophobicity, surface change.
3. Host factors such as serum or tissue proteins—fibrinogen and fibronectin promotes adhesion and albumin inhibits adhesion.
4. Environmental conditions—blood flow rates (there is lower bacterial adhesion at higher flow and hence higher shear rates), local pH has an influence and polysaccharide production is optimum at around pH 7 for most bacteria, local temperature.
5. Implant characteristics such as surface geometry affects bacterial adhesion. There are increased adherence rates to rough surfaces which may protect bacteria against sheer forces.

Once adhered, bacteria settle on the surface, further multiplying and colonising the surface. Adhered bacteria can secret a layer of exopolymers (mainly polysaccharides) know as slime, which surrounds and protects bacteria from antibiotics and other host defence mechanisms (Fig. 20.4) [107]. *Staphylococcus epidermidis* is particularly adept at producing such a layer. The bacteria along with the extracellular layer are knows as biofilm. Slime can act as a filter allowing in nutrients to pass through, but protecting from potentially harmful agents such as antibiotics, and may favour local anaerobic conditions aiding bacterial survival.

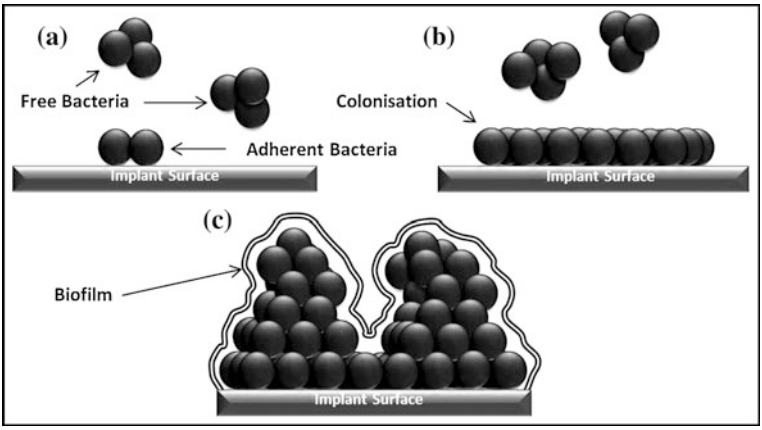

Fig. 20.4 Infection and colonisation of an implant's surface. **a** Initial bacterial adherence. **b** Proliferation and colonisation. **c** Mature biofilm formation, resistant to antibiotics and host defences. This stage is irreversible

Surface modification of interference screws may make implants more resistant to infection by disrupting the processes of adhesion, colonisation and biofilm formation, or by killing bacteria. Several techniques of surface modification have been explored as shown in Table 20.1. Some aim at creating a passive barrier to the initial bacteria surface adhesion, but most aim at actively killing bacteria.

Table 20.1 Methods used to prevent bacterial infection and colonisation of an implanted prosthesis

Anti-adhesion barriers
Nano-patterned Surfaces [130–133]
Super-hydrophobic surfaces [114, 134, 135]
Hydrogels [136–139]
Non-adhesive polymers [140–143]
Albumin [118]
Bactericidal approach
Antibiotic coating and covalent linking [116, 144–147]
Biotic antimicrobial peptides [112, 148–152]
Biotic Chitosan derivatives [153–156]
Lytic bacteriophages [157]
Cytokines [158]
Positively charged polymers [113]
Silver nanoparticles [159–165]
Copper ion [124, 125]
Zinc ion [126, 127]
Titanium dioxide [166–168]
Selenium ion [128, 129, 169]

It is of particular note that surface modifications aimed at to promoting osseo-integration (such as coating with calcium based bio-ceramics), may also protect against infection. Gristina et al. put forwards the concept of a "race for the surface" according to which host cells and bacteria compete as to which will colonise first the implant surface [111]. According to this theory, when host cells are successful in colonising the surface first, the probability of bacterial adherence is very low, and vice versa.

Material surface characteristics can influence bacterial adherence and include surface charge [108, 112, 113], hydrophobicity [109, 114], surface roughness [88, 115], and nanoscale topography [84, 116]. It is believed that surface modification of implants to provide hydrophilic, smooth surfaces could help reduce bacteria adhesion. Metals have high surface energy and are negatively charged and hydrophilic; polymers have lower surface energy, are less charged and are hydrophobic. Bacteria may adhere differently to materials with different hydrophobicities. Surface roughness may promote bacterial adhesion by providing a greater surface area for contact and binding. Increased surface smoothness could prevent bacterial colonisation. Protein coating of implant surfaces may also reduce adhesion Charville et al. reported that implant surface treatment with bovine serum albumin caused a decrease in surface hydrophobicity and reduced bacterial adhesion for each of three bacteria species tested [117]. Albumin applied to material surfaces has been shown to inhibit bacterial adhesion to polymer, ceramic and metal surfaces [118]. In contrast, fibronectin [119, 120] and fibrinogen [117, 121] seem to promote bacteria adhesion such as of *Staphylococcus* and *S. epidermidis*.

Puckett et al. examined in vitro the adhesion of *S. aureus*, *S. epidermidis*, and *Pseudomonas aeruginosa* on conventional Ti, nanorough Ti, and nanotubular and nanotextured Ti produced by two different anodization processes [122]. They reported that compared to conventional (nano-smooth) Ti, the nanorough Ti decreased the adherence of all bacteria species. They concluded that certain nanometer sized Ti topographies may be useful for reducing bacteria adhesion while promoting bone tissue formation.

Controlling the topography and hydrophobic properties of material surfaces may be a way to influence bacterial interaction with the surfaces and must be taken into account when developing anti-infective biomaterials. Although such surface modifications maybe of value in orthopaedic surfaces that are not required for mechanical or biological fixation, when employed in interference screws it is important such modifications do not counteract local bone stimulation and osseo-integration.

Bacteria killing may be achieved through surface modifications such as coatings that allow contact killing, local release of antibiotics and other agents that disrupt bacterial processes (such as respiratory and metabolic pathways, cell membrane integrity and bacterial genome). Surfaces coatings that aim at killing bacteria may be in the form of:

1. Antibiotics
2. Organic agents such as anti-bacterial peptides and cytokines

3. Metals
4. Non-metal elements for example selenium.

Antibiotic coating of implant surfaces (either directly or via antibiotic carriers) can allow bacterial elimination. However, this is only effective against those bacteria which are sensitive to the coated antibiotic, therefore broad spectrum antibiotics are needed if this approach is to be successfully used in infection prophylaxis. Antibiotic-resistant bacteria, such as methicillin-resistant *S. aureus* (MRSA) may not be responsive to routine antibiotic coatings. Up to 40 % of *S. aureus* strains in hospitals maybe MRSA [123]. In an attempt to counteract such antibiotic limitations, non-drug anti-bacterial peptide agents have been used. These may have a broader spectrum of anti-bacterial action and be less prone to the development of bacterial resistance. These agents may exert a direct anti-bacterial activity or act by boosting local host defence pathways.

Specific nano-scale metal coatings may exert a bactericidal effect. Silver has been extensively investigated, and its ions are effective in interfering with cell metabolism, disrupting bacterial membrane permeability, inactivating vital proteins and leading to reactive oxygen species formation. Copper [124, 125] and zinc [126, 127] have also been shown to be effective anti-bacterial agents.

Selenium is a trace element in both animal and human organisms and has shown promise as a method of reducing bacterial attachment on prosthetic implants. Tran and Webster demonstrated that Selenium coated polymeric surfaces exposed to bacterial contamination had significantly lower *S. aureus* densities compared to uncoated surfaces [128]. In a further study, Holinka et al. assessed the effect of selenium coating titanium discs on bacterial adhesion and osteoblast growth [129]. They showed that adherence of *S. aureus* and *S. epidermidis* was significantly reduced in selenium coated titanium discs, without any inhibitory effect on the osteoblast cell growth.

Despite advances in our understanding of the processes of graft osseo-integration and the pathogenesis of infection allied to manufacturing advances that allow surface modification of fixation devices such as interference screws, several challenges remain. Understanding local pharmacokinetics including elution rates and longevity is essential before laboratory observations are translated into clinical practise. Minimising cytotoxicity to local host tissues and local inflammatory reactions is also essential. The majority of evidence on the beneficial effects of surface modifications comes from in vitro or in vivo animal studies, with clinical evaluation in humans largely still waited. Additionally, in coating the surfaces of interference screws, the effects of this on the physical properties, such as sharpness must be thoroughly understood [55]. This is important, as sharp screw threads may lead to graft laceration and fixation compromise during screw insertion [35, 36]. A standardised system describing the laceration properties of interference screws could help guide surgeons in screw choice. With assessment of new surface coatings, clinical studies must evaluate the potential unwanted effects of surface coatings. For example, disruption of surface coatings and intra-articular migration of coating fragments could cause third body wear, intra-articular damage and synovial inflammation.

In conclusion, surface modification of interference screws used in ACL reconstruction surgery is an exciting, advancing area. In the future surface modification of interference screws may act to improve the biology of graft healing, promote resistance to infection, aid faster rehabilitation and improve the functional outcomes of ACL reconstruction surgery. Collaboration between orthopaedic surgeons, scientists and implant manufacturers is needed to allow the translation of basic science into improved patient clinical outcomes.

References

1. Gianotti, S. M., Marshall, S. W., Hume, P. A., & Bunt, L. (2009). Incidence of anterior cruciate ligament injury and other knee ligament injuries: A national population-based study. *Journal of Science and Medicine in Sport, 12*(6), 622–627.
2. Siegel, L., Vandenakker-Albanese, C., & Siegel, D. (2012). Anterior cruciate ligament injuries: Anatomy, physiology, biomechanics, and management. *Clinical Journal of Sport Medicine, 22*(4), 349–355.
3. Joseph, A. M., Collins, C. L., Henke, N. M., Yard, E. E., Fields, S. K., & Comstock, R. D. (2013). A multisport epidemiologic comparison of anterior cruciate ligament injuries in high school athletics. *Journal of Athletic Training, 48*(6), 810–817.
4. Mihata, L. C., Beutler, A. I., & Boden, B. P. (2006). Comparing the incidence of anterior cruciate ligament injury in collegiate lacrosse, soccer, and basketball players: Implications for anterior cruciate ligament mechanism and prevention. *American Journal of Sports Medicine, 34*(6), 899–904.
5. Shelbourne, K. D., Davis, T. J., & Klootwyk, T. E. (1998). The relationship between intercondylar notch width of the femur and the incidence of anterior cruciate ligament tears: A prospective study. *American Journal of Sports Medicine, 26*(3), 402–408.
6. Souryal, T. O., & Freeman, T. R. (1993). Intercondylar notch size and anterior cruciate ligament injuries in athletes: A prospective study. *American Journal of Sports Medicine, 21*(4), 535–539.
7. Wordeman, S. C., Quatman, C. E., Kaeding, C. C., & Hewett, T. E. (2012). In vivo evidence for tibial plateau slope as a risk factor for anterior cruciate ligament injury: A systematic review and meta-analysis. *American Journal of Sports Medicine, 40*(7), 1673–1681.
8. Hashemi, J., Chandrashekar, N., Gill, B., et al. (2008). The geometry of the tibial plateau and its influence on the biomechanics of the tibiofemoral joint. *Journal of Bone and Joint Surgery. American Volume, 90*(12), 2724–2734.
9. Ramesh, R., Von Arx, O., Azzopardi, T., & Schranz, P. J. (2005). The risk of anterior cruciate ligament rupture with generalised joint laxity. *Journal of Bone and Joint Surgery. British Volume, 87*(6), 800–803.
10. Vaishya, R., & Hasija, R. (2013). Joint hypermobility and anterior cruciate ligament injury. *Journal of Orthopaedic Surgery, 21*(2), 182–184.
11. Kramer, L. C., Denegar, C. R., Buckley, W. E., & Hertel, J. (2007). Factors associated with anterior cruciate ligament injury: History in female athletes. *Journal of Sports Medicine and Physical Fitness, 47*(4), 446–454.
12. Evans, K. N., Kilcoyne, K. G., Dickens, J. F., et al. (2012). Predisposing risk factors for non-contact ACL injuries in military subjects. *Knee Surgery, Sports Traumatology, Arthroscopy, 20*(8), 1554–1559.
13. Zazulak, B. T., Hewett, T. E., Reeves, N. P., Goldberg, B., & Cholewicki, J. (2007). Deficits in neuromuscular control of the trunk predict knee injury risk: A prospective biomechanical-epidemiologic study. *American Journal of Sports Medicine, 35*(7), 1123–1130.

14. Smith, H. C., Vacek, P., Johnson, R. J., et al. (2012). Risk factors for anterior cruciate ligament injury: A review of the literature—part 1: Neuromuscular and anatomic risk. *Sports Health, 4*(1), 69–78.
15. Hewett, T. E., Ford, K. R., Hoogenboom, B. J., & Myer, G. D. (2010). Understanding and preventing ACL injuries: Current biomechanical and epidemiologic considerations—Update 2010. *North American Journal of Sports Physical Therapy, 5*(4), 234–251.
16. Alentorn-Geli, E., Myer, G. D., Silvers, H. J., et al. (2009). Prevention of non-contact anterior cruciate ligament injuries in soccer players. Part 1: Mechanisms of injury and underlying risk factors. *Knee Surgery, Sports Traumatology, Arthroscopy, 17*(7), 705–729.
17. Eastlack, M. E., Axe, M. J., & Snyder-Mackler, L. (1999). Laxity, instability, and functional outcome after ACL injury: Copers versus noncopers. *Medicine and Science in Sports and Exercise, 31*(2), 210–215.
18. Hurd, W. J., & Snyder-Mackler, L. (2007). Knee instability after acute ACL rupture affects movement patterns during the mid-stance phase of gait. *Journal of Orthopaedic Research, 25*(10), 1369–1377.
19. Grindem, H., Eitzen, I., Engebretsen, L., Snyder-Mackler, L., & Risberg, M. A. (2014). Nonsurgical or surgical treatment of ACL injuries: Knee function, sports participation, and knee reinjury: The delaware-oslo ACL cohort study. *Journal of Bone and Joint Surgery. American Volume, 96*(15), 1233–1241.
20. Andersson, C., Odensten, M., & Gillquist, J. (1991). Knee function after surgical or nonsurgical treatment of acute rupture of the anterior cruciate ligament: A randomized study with a long-term follow-up period. *Clinical Orthopaedics and Related Research*, *264*, 255–263.
21. Chechik, O., Amar, E., Khashan, M., Lador, R., Eyal, G., & Gold, A. (2013). An international survey on anterior cruciate ligament reconstruction practices. *International Orthopaedics, 37*(2), 201–206.
22. Suomalainen, P., Kannus, P., & Jarvela, T. (2013). Double-bundle anterior cruciate ligament reconstruction: A review of literature. *International Orthopaedics, 37*(2), 227–232.
23. Jarvela, T., & Jarvela, S. (2013). Double-bundle versus single-bundle anterior cruciate ligament reconstruction. *Clinics in Sports Medicine, 32*(1), 81–91.
24. Li, Y. L., Ning, G. Z., Wu, Q., et al. (2014). Single-bundle or double-bundle for anterior cruciate ligament reconstruction: A meta-analysis. *The Knee, 21*(1), 28–37.
25. van Eck, C. F., Schreiber, V. M., Mejia, H. A., et al. (2010). "Anatomic" anterior cruciate ligament reconstruction: A systematic review of surgical techniques and reporting of surgical data. *Arthroscopy, 26*(Suppl 9), S2–S12.
26. Hapa, O., & Barber, F. A. (2009). ACL fixation devices. *Sports Medicine and Arthroscopy Review, 17*(4), 217–223.
27. Saccomanni, B. (2011). Graft fixation alternatives in anterior cruciate ligament reconstruction. *Musculoskeletal Surgery, 95*(3), 183–191.
28. Martin, S. D., Martin, T. L., & Brown, C. H. (2002). Anterior cruciate ligament graft fixation. *Orthopedic Clinics of North America, 33*(4), 685–696.
29. Lee, Y. H., Siebold, R., & Paessler, H. H. (2014). Implant-free ACL reconstruction: A review. *Archives of Orthopaedic and Trauma Surgery, 134*(3), 395–404.
30. Mascarenhas, R., Saltzman, B. M., Sayegh, E. T., et al. (2015). Bioabsorbable versus metallic interference screws in anterior cruciate ligament reconstruction: A systematic review of overlapping meta-analyses. *Arthroscopy, 31*(3), 561–568.
31. Gulman, B., Mollaian, S., & Tomak, Y. (1999). Femoral fixation of patellar tendon grafts using the bone-block locking technique in ACL reconstruction. A biomechanical study. *Bulletin/Hospital for Joint Diseases, 58*(2), 71–75.
32. Deehan, D. J., & Cawston, T. E. (2005). The biology of integration of the anterior cruciate ligament. *Journal of Bone and Joint Surgery. British Volume, 87*(7), 889–895.
33. McGuire, D. A., Barber, F. A., Elrod, B. F., & Paulos, L. E. (1999). Bioabsorbable interference screws for graft fixation in anterior cruciate ligament reconstruction. *Arthroscopy, 15*(5), 463–473.

34. Duquin, T. R., Wind, W. M., Fineberg, M. S., Smolinski, R. J., & Buyea, C. M. (2009). Current trends in anterior cruciate ligament reconstruction. *The Journal of Knee Surgery, 22*(1), 7–12.
35. Moisala, A. S., Jarvela, T., Paakkala, A., Paakkala, T., Kannus, P., & Jarvinen, M. (2008). Comparison of the bioabsorbable and metal screw fixation after ACL reconstruction with a hamstring autograft in MRI and clinical outcome: A prospective randomized study. *Knee Surgery, Sports Traumatology, Arthroscopy, 16*(12), 1080–1086.
36. Brand, J. C, Jr, Nyland, J., Caborn, D. N., & Johnson, D. L. (2005). Soft-tissue interference fixation: Bioabsorbable screw versus metal screw. *Arthroscopy, 21*(8), 911–916.
37. Zantop, T., Weimann, A., Schmidtko, R., Herbort, M., Raschke, M. J., & Petersen, W. (2006). Graft laceration and pullout strength of soft-tissue anterior cruciate ligament reconstruction: In vitro study comparing titanium, poly-d, l-lactide, and poly-d, l-lactide-tricalcium phosphate screws. *Arthroscopy, 22*(11), 1204–1210.
38. Pereira, H., Correlo, V. M., Silva-Correia, J., Oliveira, J. M., Reis, R. L., & Espregueira-Mendes, J. (2013). Migration of "bioabsorbable" screws in ACL repair. How much do we know? A systematic review. *Knee Surgery, Sports Traumatology, Arthroscopy, 21*(4), 986–994.
39. Johnston, M., Morse, A., Arrington, J., Pliner, M., & Gasser, S. (2011). Resorption and remodeling of hydroxyapatite-poly-L-lactic acid composite anterior cruciate ligament interference screws. *Arthroscopy, 27*(12), 1671–1678.
40. Suchenski, M., McCarthy, M. B., Chowaniec, D., et al. (2010). Material properties and composition of soft-tissue fixation. *Arthroscopy, 26*(6), 821–831.
41. Radford, M. J., Noakes, J., Read, J., & Wood, D. G. (2005). The natural history of a bioabsorbable interference screw used for anterior cruciate ligament reconstruction with a 4-strand hamstring technique. *Arthroscopy, 21*(6), 707–710.
42. Mavrogenis, A. F., Dimitriou, R., Parvizi, J., & Babis, G. C. (2009). Biology of implant osseointegration. *Journal of Musculoskeletal and Neuronal Interactions, 9*(2), 61–71.
43. Bernstein, A., Tecklenburg, K., Sudkamp, P., & Mayr, H. O. (2012). Adhesion and proliferation of human osteoblast-like cells on different biodegradable implant materials used for graft fixation in ACL-reconstruction. *Archives of Orthopaedic and Trauma Surgery, 132*(11), 1637–1645.
44. Andernord, D., Bjornsson, H., Petzold, M., et al. (2014). Surgical predictors of early revision surgery after anterior cruciate ligament reconstruction: Results from the swedish national knee ligament register on 13,102 patients. *American Journal of Sports Medicine, 42*(7), 1574–1582.
45. Iorio, R., Di Sanzo, V., Vadala, A., et al. (2013). ACL reconstruction with hamstrings: How different technique and fixation devices influence bone tunnel enlargement. *European Review for Medical and Pharmacological Sciences, 17*(21), 2956–2961.
46. Leonardi, A. B., Duarte A, Jr, & Severino, N. R. (2014). Bone tunnel enlargement on anterior cruciate ligament reconstruction. *Acta Ortopedica Brasileira, 22*(5), 240–244.
47. Claes, S., Verdonk, P., Forsyth, R., & Bellemans, J. (2011). The, "ligamentization" process in anterior cruciate ligament reconstruction: What happens to the human graft? A systematic review of the literature. *American Journal of Sports Medicine, 39*(11), 2476–2483.
48. Rodeo, S. A., Arnoczky, S. P., Torzilli, P. A., Hidaka, C., & Warren, R. F. (1993). Tendon-healing in a bone tunnel. A biomechanical and histological study in the dog. *Journal of Bone and Joint Surgery. American Volume, 75*(12), 1795–1803.
49. Grana, W. A., Egle, D. M., Mahnken, R., & Goodhart, C. W. (1994). An analysis of autograft fixation after anterior cruciate ligament reconstruction in a rabbit model. *American Journal of Sports Medicine, 22*(3), 344–351.
50. Pinczewski, L. A., Clingeleffer, A. J., Otto, D. D., Bonar, S. F., & Corry, I. S. (1997). Integration of hamstring tendon graft with bone in reconstruction of the anterior cruciate ligament. *Arthroscopy, 13*(5), 641–643.

51. Mall, N. A., Chalmers, P. N., Moric, M., et al. (2014). Incidence and trends of anterior cruciate ligament reconstruction in the united states. *American Journal of Sports Medicine, 42*(10), 2363–2370.
52. Archibald-Seiffer, N., Jacobs, J. C, Jr, Saad, C., Jevsevar, D. S., & Shea, K. G. (2015). Review of anterior cruciate ligament reconstruction cost variance within a regional health care system. *American Journal of Sports Medicine, 43*(6), 1408–1412.
53. Fay, C. M. (2011). Complications associated with use of anterior cruciate ligament fixation devices. *American Journal of Orthopedics (Belle Mead, NJ), 40*(6), 305–310.
54. Phelan, D. T., Cohen, A. B., & Fithian, D. C. (2006). Complications of anterior cruciate ligament reconstruction. *Instructional Course Lectures, 55*, 465–474.
55. Charalambous, C. P., Alvi, F., & Sutton, P. M. (2015). Management of intraoperative complications in arthroscopic primary anterior cruciate ligament reconstruction. *The Journal of Knee Surgery, 28*(2), 165–174.
56. Namkoong, S., Heywood, C. S., Bravman, J. T., Ieyasa, K., Kummer, F. J., & Meislin, R. J. (2006). The effect of interference screw diameter on soft tissue graft fixation. *Bulletin/Hospital for Joint Diseases, 63*(3–4), 153–155.
57. Harvey, A. R., Thomas, N. P., & Amis, A. A. (2003). The effect of screw length and position on fixation of four-stranded hamstring grafts for anterior cruciate ligament reconstruction. *The Knee, 10*(1), 97–102.
58. Cohen, S. B., Pandarinath, R., O'Hagan, T., et al. (2015). Results of ACL reconstruction with tibial retroscrew fixation: Comparison of clinical outcomes and tibial tunnel widening. *The Physician and Sportsmedicine, 43*(2), 138–142.
59. Lind, M., Feller, J., & Webster, K. E. (2009). Tibial bone tunnel widening is reduced by polylactate/hydroxyapatite interference screws compared to metal screws after ACL reconstruction with hamstring grafts. *The Knee, 16*(6), 447–451.
60. Hantes, M. E., Mastrokalos, D. S., Yu, J., & Paessler, H. H. (2004). The effect of early motion on tibial tunnel widening after anterior cruciate ligament replacement using hamstring tendon grafts. *Arthroscopy, 20*(6), 572–580.
61. Yu, J. K., & Paessler, H. H. (2005). Relationship between tunnel widening and different rehabilitation procedures after anterior cruciate ligament reconstruction with quadrupled hamstring tendons. *Chinese Medical Journal (English), 118*(4), 320–326.
62. Siebold, R., Kiss, Z. S., & Morris, H. G. (2008). Effect of compaction drilling during ACL reconstruction with hamstrings on postoperative tunnel widening. *Archives of Orthopaedic and Trauma Surgery, 128*(5), 461–468.
63. Hoher, J., Moller, H. D., & Fu, F. H. (1998). Bone tunnel enlargement after anterior cruciate ligament reconstruction: Fact or fiction? *Knee Surgery, Sports Traumatology, Arthroscopy, 6*(4), 231–240.
64. Goodman, S. B., Yao, Z., Keeney, M., & Yang, F. (2013). The future of biologic coatings for orthopaedic implants. *Biomaterials, 34*(13), 3174–3183.
65. Streicher, R. M., Schmidt, M., & Fiorito, S. (2007). Nanosurfaces and nanostructures for artificial orthopedic implants. *Nanomedicine (London), 2*(6), 861–874.
66. Molloy, T., Wang, Y., & Murrell, G. (2003). The roles of growth factors in tendon and ligament healing. *Sports Medicine, 33*(5), 381–394.
67. Sciore, P., Boykiw, R., & Hart, D. A. (1998). Semiquantitative reverse transcription-polymerase chain reaction analysis of mRNA for growth factors and growth factor receptors from normal and healing rabbit medial collateral ligament tissue. *Journal of Orthopaedic Research, 16*(4), 429–437.
68. Wolfman, N. M., Hattersley, G., Cox, K., et al. (1997). Ectopic induction of tendon and ligament in rats by growth and differentiation factors 5, 6, and 7, members of the TGF-beta gene family. *Journal of Clinical Investigation, 100*(2), 321–330.
69. Sasaki, K., Kuroda, R., Ishida, K., et al. (2008). Enhancement of tendon-bone osteointegration of anterior cruciate ligament graft using granulocyte colony-stimulating factor. *American Journal of Sports Medicine, 36*(8), 1519–1527.

70. Hashimoto, Y., Yoshida, G., Toyoda, H., & Takaoka, K. (2007). Generation of tendon-to-bone interface "enthesis" with use of recombinant BMP-2 in a rabbit model. *Journal of Orthopaedic Research, 25*(11), 1415–1424.
71. Hunziker, E. B., Enggist, L., Kuffer, A., Buser, D., & Liu, Y. (2012). Osseointegration: The slow delivery of BMP-2 enhances osteoinductivity. *Bone, 51*(1), 98–106.
72. Mihelic, R., Pecina, M., Jelic, M., et al. (2004). Bone morphogenetic protein-7 (osteogenic protein-1) promotes tendon graft integration in anterior cruciate ligament reconstruction in sheep. *American Journal of Sports Medicine, 32*(7), 1619–1625.
73. Mayr, H. O., Dietrich, M., Fraedrich, F., et al. (2009). Microporous pure beta-tricalcium phosphate implants for press-fit fixation of anterior cruciate ligament grafts: Strength and healing in a sheep model. *Arthroscopy, 25*(9), 996–1005.
74. Demirag, B., Sarisozen, B., Ozer, O., Kaplan, T., & Ozturk, C. (2005). Enhancement of tendon-bone healing of anterior cruciate ligament grafts by blockage of matrix metalloproteinases. *Journal of Bone and Joint Surgery. American Volume, 87*(11), 2401–2410.
75. Bedi, A., Kovacevic, D., Hettrich, C., et al. (2010). The effect of matrix metalloproteinase inhibition on tendon-to-bone healing in a rotator cuff repair model. *Journal of Shoulder and Elbow Surgery, 19*(3), 384–391.
76. Rodeo, S. A., Kawamura, S., Ma, C. B., et al. (2007). The effect of osteoclastic activity on tendon-to-bone healing: An experimental study in rabbits. *Journal of Bone and Joint Surgery. American Volume, 89*(10), 2250–2259.
77. Sul, Y. T., Johansson, C. B., & Albrektsson, T. (2002). Oxidized titanium screws coated with calcium ions and their performance in rabbit bone. *International Journal of Oral and Maxillofacial Implants, 17*(5), 625–634.
78. Mutsuzaki, H., Ito, A., Sakane, M., et al. (2007). Calcium phosphate coating formed in infusion fluid mixture to enhance fixation strength of titanium screws. *Journal of Materials Science. Materials in Medicine, 18*(9), 1799–1808.
79. Rammelt, S., Heck, C., Bernhardt, R., et al. (2007). In vivo effects of coating loaded and unloaded ti implants with collagen, chondroitin sulfate, and hydroxyapatite in the sheep tibia. *Journal of Orthopaedic Research, 25*(8), 1052–1061.
80. Sartori, M., Giavaresi, G., Parrilli, A., et al. (2015). Collagen type I coating stimulates bone regeneration and osteointegration of titanium implants in the osteopenic rat. *International Orthopaedics, 39*(10), 2041–2052.
81. Wermelin, K., Suska, F., Tengvall, P., Thomsen, P., & Aspenberg, P. (2008). Stainless steel screws coated with bisphosphonates gave stronger fixation and more surrounding bone. Histomorphometry in rats. *Bone, 42*(2), 365–371.
82. Wermelin, K., Tengvall, P., & Aspenberg, P. (2007). Surface-bound bisphosphonates enhance screw fixation in rats—Increasing effect up to 8 weeks after insertion. *Acta Orthopaedica, 78*(3), 385–392.
83. Lu, Y., Markel, M. D., Nemke, B., Lee, J. S., Graf, B. K., & Murphy, W. L. (2009). Influence of hydroxyapatite-coated and growth factor-releasing interference screws on tendon-bone healing in an ovine model. *Arthroscopy*, *25*(12), 1427–1434.
84. Rieger, E., Dupret-Bories, A., Salou, L., et al. (2015). Controlled implant/soft tissue interaction by nanoscale surface modifications of 3D porous titanium implants. *Nanoscale, 7*(21), 9908–9918.
85. Bahl, S., Shreyas, P., Trishul, M. A., Suwas, S., & Chatterjee, K. (2015). Enhancing the mechanical and biological performance of a metallic biomaterial for orthopedic applications through changes in the surface oxide layer by nanocrystalline surface modification. *Nanoscale, 7*(17), 7704–7716.
86. Webster, T. J., & Ejiofor, J. U. (2004). Increased osteoblast adhesion on nanophase metals: Ti, Ti6Al4 V, and CoCrMo. *Biomaterials, 25*(19), 4731–4739.
87. Price, R. L., Ellison, K., Haberstroh, K. M., & Webster, T. J. (2004). Nanometer surface roughness increases select osteoblast adhesion on carbon nanofiber compacts. *Journal of Biomedical Materials Research Part A, 70*(1), 129–138.

88. Katainen, J., Paajanen, M., Ahtola, E., Pore, V., & Lahtinen, J. (2006). Adhesion as an interplay between particle size and surface roughness. *Journal of Colloid and Interface Science, 304*(2), 524–529.
89. Lin, L., Wang, H., Ni, M., et al. (2014). Enhanced osteointegration of medical titanium implant with surface modifications in micro/nanoscale structures. *Journal of Orthopaedic Translation., 2*, 35–42.
90. Miyauchi, T., Yamada, M., Yamamoto, A., et al. (2010). The enhanced characteristics of osteoblast adhesion to photofunctionalized nanoscale TiO2 layers on biomaterials surfaces. *Biomaterials, 31*(14), 3827–3839.
91. Biggs, M. J., Richards, R. G., Gadegaard, N., Wilkinson, C. D., & Dalby, M. J. (2007). The effects of nanoscale pits on primary human osteoblast adhesion formation and cellular spreading. *Journal of Materials Science. Materials in Medicine, 18*(2), 399–404.
92. Salou, L., Hoornaert, A., Louarn, G., & Layrolle, P. (2015). Enhanced osseointegration of titanium implants with nanostructured surfaces: An experimental study in rabbits. *Acta Biomaterialia, 11*, 494–502.
93. Goldman, M., Juodzbalys, G., & Vilkinis, V. (2014). Titanium surfaces with nanostructures influence on osteoblasts proliferation: A systematic review. *Journal of Oral & Maxillofacial Research, 5*(3), e1.
94. Zhao, X., Wang, G., Zheng, H., et al. (2013). Delicate refinement of surface nanotopography by adjusting TiO2 coating chemical composition for enhanced interfacial biocompatibility. *ACS Applied Materials & Interfaces, 5*(16), 8203–8209.
95. Roy, M., Bandyopadhyay, A., & Bose, S. (2011). Induction plasma sprayed sr and mg doped nano hydroxyapatite coatings on ti for bone implant. *Journal of Biomedical Materials Research. Part B, Applied Biomaterials, 99*(2), 258–265.
96. Warren, D. K., Nickel, K. B., Wallace, A. E., Mines, D., Fraser, V. J., & Olsen, M. A. (2014). Can additional information be obtained from claims data to support surgical site infection diagnosis codes? *Infection Control and Hospital Epidemiology, 35*(Suppl 3), S124–S132.
97. Scully, W. F., Fisher, S. G., Parada, S. A., & Arrington, E. D. (2013). Septic arthritis following anterior cruciate ligament reconstruction: A comprehensive review of the literature. *Journal of Surgical Orthopaedic Advances, 22*(2), 127–133.
98. Wang, C., Lee, Y. H., & Siebold, R. (2014). Recommendations for the management of septic arthritis after ACL reconstruction. *Knee Surgery, Sports Traumatology, Arthroscopy, 22*(9), 2136–2144.
99. Maletis, G. B., Inacio, M. C., Reynolds, S., Desmond, J. L., Maletis, M. M., & Funahashi, T. T. (2013). Incidence of postoperative anterior cruciate ligament reconstruction infections: Graft choice makes a difference. *American Journal of Sports Medicine, 41*(8), 1780–1785.
100. Burks, R. T., Friederichs, M. G., Fink, B., Luker, M. G., West, H. S., & Greis, P. E. (2003). Treatment of postoperative anterior cruciate ligament infections with graft removal and early reimplantation. *American Journal of Sports Medicine, 31*(3), 414–418.
101. Toms, A. D., Davidson, D., Masri, B. A., & Duncan, C. P. (2006). The management of peri-prosthetic infection in total joint arthroplasty. *Journal of Bone and Joint Surgery. British Volume, 88*(2), 149–155.
102. Teughels, W., Van Assche, N., Sliepen, I., & Quirynen, M. (2006). Effect of material characteristics and/or surface topography on biofilm development. *Clinical Oral Implants Research, 17*(Suppl 2), 68–81.
103. Cerca, N., Martins, S., Pier, G. B., Oliveira, R., & Azeredo, J. (2005). The relationship between inhibition of bacterial adhesion to a solid surface by sub-MICs of antibiotics and subsequent development of a biofilm. *Research in Microbiology, 156*(5–6), 650–655.
104. Brause, B. D. (1989). Prosthetic joint infections. *Current Opinion in Rheumatology, 1*(2), 194–198.
105. Costerton, J. W., Stewart, P. S., & Greenberg, E. P. (1999). Bacterial biofilms: A common cause of persistent infections. *Science, 284*(5418), 1318–1322.

106. Stoodley, P., Ehrlich, G. D., Sedghizadeh, P. P., et al. (2011). Orthopaedic biofilm infections. *Current Orthopaedic Practice, 22*(6), 558–563.
107. Gallo, J., Holinka, M., & Moucha, C. S. (2014). Antibacterial surface treatment for orthopaedic implants. *International Journal of Molecular Sciences, 15*(8), 13849–13880.
108. An, Y. H., & Friedman, R. J. (1998). Concise review of mechanisms of bacterial adhesion to biomaterial surfaces. *Journal of Biomedical Materials Research, 43*(3), 338–348.
109. Katsikogianni, M., & Missirlis, Y. F. (2004). Concise review of mechanisms of bacterial adhesion to biomaterials and of techniques used in estimating bacteria-material interactions. *European Cells & Materials, 8*, 37–57.
110. Galliani, S., Viot, M., Cremieux, A., & Van der Auwera, P. (1994). Early adhesion of bacteremic strains of *Staphylococcus epidermidis* to polystyrene: Influence of hydrophobicity, slime production, plasma, albumin, fibrinogen, and fibronectin. *Journal of Laboratory and Clinical Medicine, 123*(5), 685–692.
111. Gristina, A. G., Naylor, P., & Myrvik, Q. (1988). Infections from biomaterials and implants: A race for the surface. *Medical Progress Through Technology, 14*(3–4), 205–224.
112. Bouchet, A. M., Iannucci, N. B., Pastrian, M. B., et al. (2014). Biological activity of antibacterial peptides matches synergism between electrostatic and non electrostatic forces. *Colloids and Surfaces B: Biointerfaces, 114*, 363–371.
113. Gottenbos, B., van der Mei, H. C., Klatter, F., et al. (2003). Positively charged biomaterials exert antimicrobial effects on gram-negative bacilli in rats. *Biomaterials, 24*(16), 2707–2710.
114. Poncin-Epaillard, F., Herry, J. M., Marmey, P., Legeay, G., Debarnot, D., & Bellon-Fontaine, M. N. (2013). Elaboration of highly hydrophobic polymeric surface–a potential strategy to reduce the adhesion of pathogenic bacteria? *Materials Science & Engineering. C, Materials for Biological Applications, 33*(3), 1152–1161.
115. Scheuerman, T. R., Camper, A. K., & Hamilton, M. A. (1998). Effects of substratum topography on bacterial adhesion. *Journal of Colloid and Interface Science, 208*(1), 23–33.
116. Antoci, V, Jr, Adams, C. S., Parvizi, J., Ducheyne, P., Shapiro, I. M., & Hickok, N. J. (2007). Covalently attached vancomycin provides a nanoscale antibacterial surface. *Clinical Orthopaedics and Related Research, 461*, 81–87.
117. Charville, G. W., Hetrick, E. M., Geer, C. B., & Schoenfisch, M. H. (2008). Reduced bacterial adhesion to fibrinogen-coated substrates via nitric oxide release. *Biomaterials, 29* (30), 4039–4044.
118. An, Y. H., Stuart, G. W., McDowell, S. J., McDaniel, S. E., Kang, Q., & Friedman, R. J. (1996). Prevention of bacterial adherence to implant surfaces with a crosslinked albumin coating in vitro. *Journal of Orthopaedic Research, 14*(5), 846–849.
119. Williams, R. J., Henderson, B., Sharp, L. J., & Nair, S. P. (2002). Identification of a fibronectin-binding protein from *Staphylococcus epidermidis*. *Infection and Immunity, 70*(12), 6805–6810.
120. Francois, P., Letourneur, D., Lew, D. P., Jozefonwicz, J., & Vaudaux, P. (1999). Inhibition by heparin and derivatized dextrans of *Staphylococcus epidermidis* adhesion to in vitro fibronectin-coated or explanted polymer surfaces. *Journal of Biomaterials Science, Polymer Edition, 10*(12), 1207–1221.
121. Arciola, C. R., Campoccia, D., Gamberini, S., Donati, M. E., & Montanaro, L. (2004). Presence of fibrinogen-binding adhesin gene in *Staphylococcus epidermidis* isolates from central venous catheters-associated and orthopaedic implant-associated infections. *Biomaterials, 25*(19), 4825–4829.
122. Puckett, S. D., Taylor, E., Raimondo, T., & Webster, T. J. (2010). The relationship between the nanostructure of titanium surfaces and bacterial attachment. *Biomaterials, 31*(4), 706–713.
123. Parvez, N., Jinadatha, C., Fader, R., et al. (2010). Universal MRSA nasal surveillance: Characterization of outcomes at a tertiary care center and implications for infection control. *Southern Medical Journal, 103*(11), 1084–1091.

124. Hoene, A., Prinz, C., Walschus, U., et al. (2013). In vivo evaluation of copper release and acute local tissue reactions after implantation of copper-coated titanium implants in rats. *Biomedical Materials, 8*(3), 035009-6041/8/3/035009.
125. Hans, M., Erbe, A., Mathews, S., Chen, Y., Solioz, M., & Mucklich, F. (2013). Role of copper oxides in contact killing of bacteria. *Langmuir, 29*(52), 16160–16166.
126. Elizabeth, E., Baranwal, G., Krishnan, A. G., Menon, D., & Nair, M. (2014). ZnO nanoparticle incorporated nanostructured metallic titanium for increased mesenchymal stem cell response and antibacterial activity. *Nanotechnology*, *25*(11), 115101-4484/25/11/115101.
127. Hu, H., Zhang, W., Qiao, Y., Jiang, X., Liu, X., & Ding, C. (2012). Antibacterial activity and increased bone marrow stem cell functions of Zn-incorporated TiO2 coatings on titanium. *Acta Biomaterialia, 8*(2), 904–915.
128. Tran, P. A., & Webster, T. J. (2011). Selenium nanoparticles inhibit *Staphylococcus aureus* growth. *International Journal of Nanomedicine, 6*, 1553–1558.
129. Holinka, J., Pilz. M., Kubista, B., Presterl, E., & Windhager, R. (2013). Effects of selenium coating of orthopaedic implant surfaces on bacterial adherence and osteoblastic cell growth. *Bone & Joint Journal, 95-B*(5), 678–682.
130. Singh, A. V., Vyas, V., Patil, R., et al. (2011). Quantitative characterization of the influence of the nanoscale morphology of nanostructured surfaces on bacterial adhesion and biofilm formation. *PLoS ONE, 6*(9), e25029.
131. Shida, T., Koseki, H., Yoda, I., Horiuchi, H., Sakoda, H., & Osaki, M. (2013). Adherence ability of *Staphylococcus epidermidis* on prosthetic biomaterials: An in vitro study. *International Journal of Nanomedicine, 8*, 3955–3961.
132. Ivanova, E. P., Truong, V. K., Wang, J. Y., et al. (2010). Impact of nanoscale roughness of titanium thin film surfaces on bacterial retention. *Langmuir, 26*(3), 1973–1982.
133. Truong, V. K., Lapovok, R., Estrin, Y. S., et al. (2010). The influence of nano-scale surface roughness on bacterial adhesion to ultrafine-grained titanium. *Biomaterials, 31*(13), 3674–3683.
134. Zhu, H., Guo, Z., & Liu, W. (2014). Adhesion behaviors on superhydrophobic surfaces. *Chemical Communications (Cambridge, England), 50*(30), 3900–3913.
135. Stallard, C. P., McDonnell, K. A., Onayemi, O. D., O'Gara, J. P., & Dowling, D. P. (2012). Evaluation of protein adsorption on atmospheric plasma deposited coatings exhibiting superhydrophilic to superhydrophobic properties. *Biointerphases, 7*(1–4), 31-012-0031-0.
136. Pandit, V., Zuidema, J. M., Venuto, K. N., et al. (2013). Evaluation of multifunctional polysaccharide hydrogels with varying stiffness for bone tissue engineering. *Tissue Engineering Part A, 19*(21–22), 2452–2463.
137. Zhao, C., Li, X., Li, L., Cheng, G., Gong, X., & Zheng, J. (2013). Dual functionality of antimicrobial and antifouling of poly(N-hydroxyethylacrylamide)/salicylate hydrogels. *Langmuir, 29*(5), 1517–1524.
138. Drago, L., Boot, W., Dimas, K., et al. (2014). Does implant coating with antibacterial-loaded hydrogel reduce bacterial colonization and biofilm formation in vitro? *Clinical Orthopaedics and Related Research, 472*(11), 3311–3323.
139. Zan, X., Kozlov, M., McCarthy, T. J., & Su, Z. (2010). Covalently attached, silver-doped poly(vinyl alcohol) hydrogel films on poly(l-lactic acid). *Biomacromolecules, 11*(4), 1082–1088.
140. Bernthal, N. M., Stavrakis, A. I., Billi, F., et al. (2010). A mouse model of post-arthroplasty *Staphylococcus aureus* joint infection to evaluate in vivo the efficacy of antimicrobial implant coatings. *PLoS ONE, 5*(9), e12580.
141. Follmann, H. D., Martins, A. F., Gerola, A. P., et al. (2012). Antiadhesive and antibacterial multilayer films via layer-by-layer assembly of TMC/heparin complexes. *Biomacromolecules, 13*(11), 3711–3722.
142. Neoh, K. G., & Kang, E. T. (2011). Combating bacterial colonization on metals via polymer coatings: Relevance to marine and medical applications. *ACS Applied Materials & Interfaces, 3*(8), 2808–2819.

143. Muszanska, A. K., Rochford, E. T., Gruszka, A., et al. (2014). Antiadhesive polymer brush coating functionalized with antimicrobial and RGD peptides to reduce biofilm formation and enhance tissue integration. *Biomacromolecules, 15*(6), 2019–2026.
144. Hickok, N. J., & Shapiro, I. M. (2012). Immobilized antibiotics to prevent orthopaedic implant infections. *Advanced Drug Delivery Reviews, 64*(12), 1165–1176.
145. Walter, M. S., Frank, M. J., Satue, M., et al. (2014). Bioactive implant surface with electrochemically bound doxycycline promotes bone formation markers in vitro and in vivo. *Dental Materials, 30*(2), 200–214.
146. Antoci, V, Jr, King, S. B., Jose, B., et al. (2007). Vancomycin covalently bonded to titanium alloy prevents bacterial colonization. *Journal of Orthopaedic Research, 25*(7), 858–866.
147. Chennell, P., Feschet-Chassot, E., Devers, T., Awitor, K. O., Descamps, S., & Sautou, V. (2013). In vitro evaluation of TiO2 nanotubes as cefuroxime carriers on orthopaedic implants for the prevention of periprosthetic joint infections. *International Journal of Pharmaceutics, 455*(1–2), 298–305.
148. Rapsch, K., Bier, F. F., Tadros, M., & von Nickisch-Rosenegk, M. (2014). Identification of antimicrobial peptides and immobilization strategy suitable for a covalent surface coating with biocompatible properties. *Bioconjugate Chemistry, 25*(2), 308–319.
149. Costa, F., Carvalho, I. F., Montelaro, R. C., Gomes, P., & Martins, M. C. (2011). Covalent immobilization of antimicrobial peptides (AMPs) onto biomaterial surfaces. *Acta Biomaterialia, 7*(4), 1431–1440.
150. Zheng, D., Neoh, K. G., Shi, Z., & Kang, E. T. (2013). Assessment of stability of surface anchors for antibacterial coatings and immobilized growth factors on titanium. *Journal of Colloid and Interface Science, 406*, 238–246.
151. Lopez-Leban, F., Kiran, M. D., Wolcott, R., & Balaban, N. (2010). Molecular mechanisms of RIP, an effective inhibitor of chronic infections. *International Journal of Artificial Organs, 33*(9), 582–589.
152. Chen, F., Gao, Y., Chen, X., Yu, Z., & Li, X. (2013). Quorum quenching enzymes and their application in degrading signal molecules to block quorum sensing-dependent infection. *International Journal of Molecular Sciences, 14*(9), 17477–17500.
153. Norowski, P. A., Courtney, H. S., Babu, J., Haggard, W. O., & Bumgardner, J. D. (2011). Chitosan coatings deliver antimicrobials from titanium implants: A preliminary study. *Implant Dentistry, 20*(1), 56–67.
154. Chen, X. N., Gu, Y. X., Lee, J. H., Lee, W. Y., & Wang, H. J. (2012). Multifunctional surfaces with biomimetic nanofibres and drug-eluting micro-patterns for infection control and bone tissue formation. *European Cells & Materials, 24*, 237–248.
155. Renoud, P., Toury, B., Benayoun, S., Attik, G., & Grosgogeat, B. (2012). Functionalization of titanium with chitosan via silanation: Evaluation of biological and mechanical performances. *PLoS ONE, 7*(7), e39367.
156. Tan, H., Ma, R., Lin, C., Liu, Z., & Tang, T. (2013). Quaternized chitosan as an antimicrobial agent: Antimicrobial activity, mechanism of action and biomedical applications in orthopedics. *International Journal of Molecular Sciences, 14*(1), 1854–1869.
157. Yilmaz, C., Colak, M., Yilmaz, B. C., Ersoz, G., Kutateladze, M., & Gozlugol, M. (2013). Bacteriophage therapy in implant-related infections: An experimental study. *Journal of Bone and Joint Surgery. American Volume, 95*(2), 117–125.
158. Li, B., & McKeague, A. L. (2011). Emerging ideas: Interleukin-12 nanocoatings prevent open fracture-associated infections. *Clinical Orthopaedics and Related Research, 469*(11), 3262–3265.
159. Cheng, H., Li, Y., Huo, K., Gao, B., & Xiong, W. (2014). Long-lasting in vivo and in vitro antibacterial ability of nanostructured titania coating incorporated with silver nanoparticles. *Journal of Biomedical Materials Research Part A, 102*(10), 3488–3499.
160. Gao, A., Hang, R., Huang, X., et al. (2014). The effects of titania nanotubes with embedded silver oxide nanoparticles on bacteria and osteoblasts. *Biomaterials, 35*(13), 4223–4235.

161. Mei, S., Wang, H., Wang, W., et al. (2014). Antibacterial effects and biocompatibility of titanium surfaces with graded silver incorporation in titania nanotubes. *Biomaterials, 35*(14), 4255–4265.
162. Dong, W., Zhu, Y., Zhang, J., et al. (2013). Investigation on the antibacterial micro-porous titanium with silver nano-particles. *Journal of Nanoscience and Nanotechnology, 13*(10), 6782–6786.
163. Panacek, A., Balzerova, A., Prucek, R., et al. (2013). Preparation, characterization and antimicrobial efficiency of ag/PDDA-diatomite nanocomposite. *Colloids and Surfaces B: Biointerfaces, 110*, 191–198.
164. Knetsch, M. L. W., & Koole, L. H. (2011). New strategies in the development of antimicrobial coatings: The example of increasing usage of silver and silver nanoparticles. *Polymers, 3*, 340–366.
165. Kvitek, L., Panacek, A., Soukupova, J., et al. (2008). Effect of surfactants and polymers on stability and antibacterial activity of silver nanoparticles (NPs). *The Journal of Physical Chemistry C, 112*, 5825–5834.
166. Koseki, H., Asahara, T., Shida, T., et al. (2013). Clinical and histomorphometrical study on titanium dioxide-coated external fixation pins. *International Journal of Nanomedicine, 8*, 593–599.
167. Haenle, M., Fritsche, A., Zietz, C., et al. (2011). An extended spectrum bactericidal titanium dioxide (TiO2) coating for metallic implants: In vitro effectiveness against MRSA and mechanical properties. *Journal of Materials Science. Materials in Medicine, 22*(2), 381–387.
168. Yue, C., Kuijer, R., Kaper, H. J., van der Mei, H. C., & Busscher, H. J. (2014). Simultaneous interaction of bacteria and tissue cells with photocatalytically activated, anodized titanium surfaces. *Biomaterials, 35*(9), 2580–2587.
169. Rodriguez-Valencia, C., Lopez-Alvarez, M., Cochon-Cores, B., Pereiro, I., Serra, J., & Gonzalez, P. (2013). Novel selenium-doped hydroxyapatite coatings for biomedical applications. *Journal of Biomedical Materials Research Part A, 101*(3), 853–861.

Chapter 21
Biomechanics of the Mandible and Current Evidence Base for Treatment of the Fractured Mandible

D. Hammond, J. Whitty, R. Wain, M. McPhillips and W. Ahmed

Abstract For the treatment of fractured mandibles the structure, biomechanics, mechanical forces involves and healing mechanism needs to be taken into consideration and these are described in this chapter. It also highlights a real case study of a male patient describing the diagnosis, treatment plan, surgery, the post operative plan and a review of the case to elucidate the lessons that can be applied to future approaches to the treatment of fractures.

21.1 Structure of the Mandible

The mandible or lower jaw is the largest and strongest bone of the face, and it articulates with the skull at the temporomandibular joint.

The mandible consists of a horseshoe-shaped body and a pair of rami. The body of the mandible meets the ramus on each side at the angle of the mandible.

The body of the mandible, on its external surface in the midline, has a faint ridge indicating the line of fusion of the two halves during development at the mental symphysis. The mental foramen can be seen below the second premolar tooth; it transmits the terminal branches of the inferior alveolar nerve and vessels.

On the medial surface of the body of the mandible in the median plane are seen the mental spines; these give origin to the genioglossus muscles above and the geniohyoid muscles below. The mylohyoid line can be seen as an oblique ridge that runs backward and laterally from the area of the mental spines to an area below and behind the third molar tooth. The submandibular fossa, for the superficial part of the

D. Hammond (✉) · R. Wain · M. McPhillips · W. Ahmed
School of Medicine, University of Central Lancashire,
Preston, UK
e-mail: douglashammond1976@gmail.com

J. Whitty
School of Engineering, University of Central Lancashire,
Preston, UK

W. Ahmed and M.J. Jackson (eds.), *Surgical Tools and Medical Devices*,
DOI 10.1007/978-3-319-33489-9_21

submandibular salivary gland, lies below the posterior part of the mylohyoid line. The sublingual fossa, for the sublingual gland, lies above the anterior part of the mylohyoid line.

The upper border of the body of the mandible is called the alveolar part; in the adult, it contains 16 sockets for the roots of the teeth.

The lower border of the body of the mandible is called the base. It is in these fossae that the anterior bellies of the digastric muscles are attached.

The ramus of the mandible is vertically placed and has an anterior coronoid process and a posterior condyloid process, or head; the two processes are separated by the mandibular notch.

On the lateral surface of the ramus are markings for the attachment of the masseter muscle. On the medial surface is the mandibular foramen for the inferior alveolar nerve and vessels. In front of the foramen is a projection of bone, called the lingula, for the attachment of the sphenomandibular ligament. The foramen leads into the mandibular canal, which opens on the lateral surface of the body of the mandible at the mental foramen. The incisive canal is a continuation forward of the mandibular canal beyond the mental foramen and below the incisor teeth.

The coronoid process receives on its medial surface the attachment of the temporalis muscle. Below the condyloid process, or head, is a short neck.

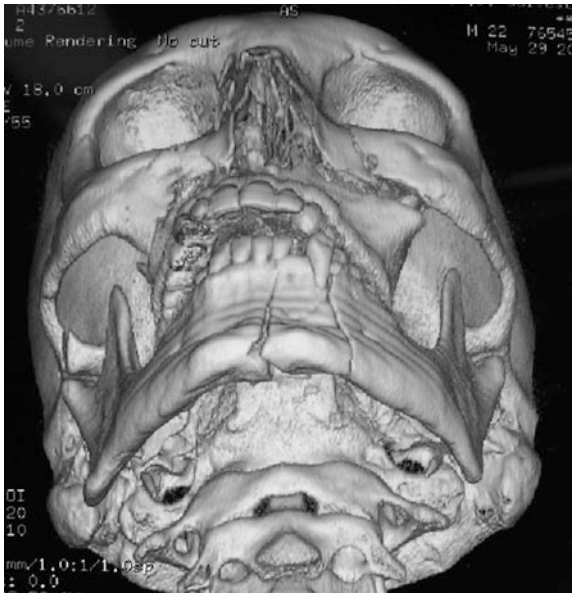

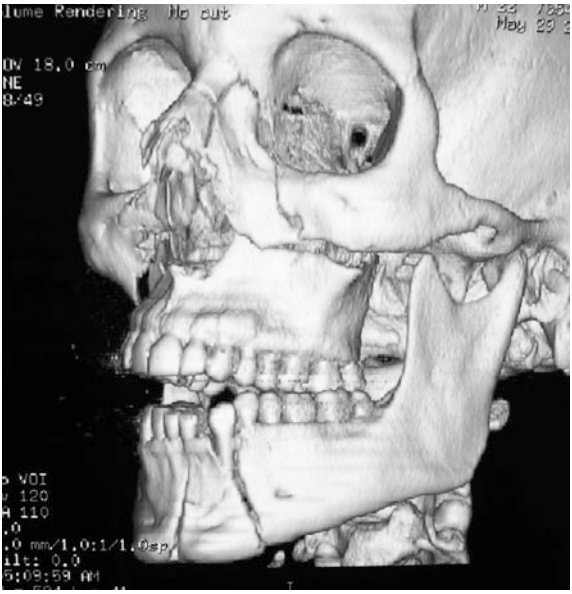

The structure of the mandible is determined by its material properties and by its mechanical role. The midfacial bones consist of thin laminae that provide an increased surface area to bone volume ratio compared to the mandible. Therefore, the midfacial bones heal better because the blood vessels are closer than those in the mandible.

Bone constantly undergoes remodelling and resorption. Different cells have different actions within the bone as a whole. Osteoblasts produce osteoid, which is the organic matrix of bone, which is the precursor of mineralised bone. Osteoid can be produced at a rate of 1 μm per day. It then matures for 10 days before it calcifies.

The microscopic structure of osteoid is different in woven bone and lamellar bone. In lamellar bone the collagen is arranged in parallel bundles, whereas in woven bone the collagen is randomly orientated. Woven bone mineralises immediately, and in fracture healing woven bone is transformed into lamellar bone.

Osteoclasts have the opposing action to osteoblasts. They have the ability to resorb 50–100 μm of bone per day.

Osteons are cylindrical vascular tunnel formed by haversian canals. They contain pluripotent precursor cells and endosteum known as the cutting cone. The bone removed by the cutting cone is replaced by osteobalst rich tissue, known as the closing cone. This enables the formation of concentric layers of lamellar bone which surround the haversian canal.

21.2 Biomechanics and Anatomical Considerations of the Bony Mandible

During mastication the mandible is subjected to forces produced by the muscles of mastication and by reactionary forces applied to the temporomandibular joints and the teeth. Various aspects of these forces and their mutual relationships have been studied thoroughly [3–6]. In the majority of studies, the mandible has been treated as a rigid non-deformable structure. However, as a result of external loading, stresses and strains are produced in the mandible. The range and distribution of these stresses and strains depend on the nature of the external loading and on the material properties and geometry of the mandible, including the amount and distribution of bone tissue. An understanding of the biomechanics of the mandible is important for several reasons. It may give us an insight into the factors that determine mandibular bone structure, since loading conditions are thought to play an important role in the modelling and remodelling of bone [7]. In addition, clinical situations, e.g. tooth loss, orthodontic treatment, dental implants, or reconstructive surgery, will alter the loading of the mandible. This in turn might affect the architecture of the mandibular bone.

Arendts and Sigolotto [8] suggest that the cortical bone of the mandible is anisotropic. It is stiffer in the longitudinal direction than it is in the bucco-lingual and supero-inferior direction. The average elastic moduli in both the bucco-lingual and supero-inferior directions is 40–70 % of those in the longitudinal direction. The elastic moduli of the bucco-lingual and supero-inferior directions is similar. Therefore, the cortical bone of the mandible can be considered to be isotropic in the transverse direction, with a higher elastic modulus in the longitudinal direction, and a lower elastic modulus in all transverse directions. The strength of the mandible is also greater in the longitudinal direction than in transverse directions.

Mean yield compressive stress values are [9]:

- Longitudinal Direction 200 MPa.
- Supero-Inferior Direction 110 MPa.
- Bucco-Lingual Direction 100 MPa.

Strain values at the yield points were [9]:

- Longitudinal Direction 1.55 %.
- Supero-Inferior Direction 2.05 %.
- Bucco-Lingual Direction 2.25 %.

The fact that the mandible is stiffer and stronger in the longitudinal direction may be due to the orientation of the osteons, collagen fibres and hydroxyapatite crystals which mainly lie in a longitudinal direction [10]. The larger longitudinal stiffness and strength indicate that the mandible is most resistant to sagittal bending movements. The shear moduli, indicate that the mandible is most resistant to shear in a plane constructed of the longitudinal and supero-inferior axes [11], whereas the least resistance to shear is found in a plane constructed of the bucco-lingual and supero-inferior axes.

The elastic moduli and yield strengths show regional variations up to a factor of 1.5 between minimum and maximum values [8, 9, 11], their data does not point to systematic differences between regions of the mandible. This is in contrast to Dechow [12], who found that the stiffest region of the mandible to be at the lower border directly inferior to the root of the canine. The reason that this should be so is that this region has the highest resistance to torsion, and is the region where the torsional stresses are suspected to change during function.

Schwartz–Dabney and Dechow showed that the direction of maximum stiffness was near parallel to the occlusal plane within the body of the mandible [13]. On the buccal ramus, the direction of maximum stiffness was more vertically oriented. Several sites in the mandible did not show a consistent direction of maximum stiffness among specimens, although all specimens exhibited significant orthotropy. Mandibular cortical thickness varied significantly ($P < 0.001$) between sites, and decreased from 3.7 mm (SD = 0.9) anteriorly to 1.4 mm posteriorly (SD = 0.1). The cortical plate was also significantly thicker ($P < 0.003$) on the buccal side than on the lingual side. Bone was 50–100 % stiffer in the longitudinal direction than in the supero-inferior or bucco-lingual directions. The results suggest that material properties and directional variations have an important impact on mandibular mechanics. The accuracy of stresses calculated from strains and average material properties varies regionally, depending on variations in the direction of maximum stiffness and anisotropy. Limited evidence suggests that the orientations and anisotropies of cortical elastic properties correspond with features of cortical bone microstructure, although the relationship with functional stresses and strains is not clear.

21.3 Mono-Cortical Fixation

By using smaller plates with mono-cortical screws, the forces maintaining the stability of the treated fracture segments should be at least in excess of the critical load characteristics for the fracture fragment displacement forces. Clinically the relevant parameters for in vitro force application can be deduced from both the non-operated healthy individual and also the post-operative population.

The occlusal forces produced in the immediate post-operative phase in patients, who have had mandibular angle fractures fixed with miniplates are much less than those recorded in both the later healing phase and in healthy patients who have not had any surgery [14].

Patients who have had miniplate fixation for fractures of the angle of the mandible were studied to compare their maximal occlusal forces with known norms [15]. These patients were shown to have 31 % of their expected maximal occlusal force at 1 week, and 58 % at 6 weeks post-surgery. The reason for this is that pain is the limiting factor in the initial stages of healing.

In the healthy patient knowledge of the masticatory stresses exerted on the mandible is fundamental, because these stresses determine the rational design and

positioning of osteosynthesis plates and their mechanical characteristics. The activity of the muscles of mastication can be divided into:

(a) Temporalis forces.
(b) Masseter forces.
(c) Reactive biting forces.

These forces vary from patient to patient. By means of strain gauges connected to a Wheatstone bridge, maximal biting forces can be measured [16].

The following values were obtained:

- Incisor region 290 N.
- Canine region 300 N.
- Premolar region 480 N.
- Molar region 660 N.

The interaction of these forces varies from patient to patient, and as such in each case there is a differing amount of fracture displacement which needs to be overcome by treatment. The external forces produced by the muscles of mastication results in these forces being produced. Physiologically coordinated muscle action produces forces of tension at the upper border of the mandible and compressive forces at the lower border of the mandible [17]. Additionally, Sustrac [18] demonstrated that torsional forces occur anterior to the canines.

Every mandibular fracture which occurs causes distraction at the alveolar crest region, accentuated by the degree of trauma and by contraction of the muscles of the floor of the mouth, which may lead to displacement of the fragments. The compressive force at the lower border of the mandible is a force which is both a dynamic and a physiological force and is always exerted on the fracture fragments [16]. This compressive force is due to the muscular tone which increases during mastication. When the fracture is adequately reduced, and fixation is adequately provided then this dynamic compression equals exactly the physiological strains exerted on an intact mandible [1].

The momentums of tension, compression and torsion have been established to using a mathematical model of the mandible using the formula:

$E = F \times L/d$

- E = State of constraints.
- F = Masticatory forces.
- L = Distance from chin to fracture line.
- d = Distance from plate to lower border of mandible.

In any method of fixation of a fractured bone, friction forces controlling shearing and torsion stresses are an important factor of stability. These forces between fracture surfaces exist due to interdigitation of fracture fragments and are enhanced by compressive forces. It was Champy's opinion [16, 17] that in these cases double plate fixation is required. However, these principles are not followed today at the angle of the mandible.

If Champy's principles are followed then a fixation which is stable, elastic and dynamic will be produced.

Fixation is stable when:

(a) No movement is visible between the fragments.
(b) After precise reduction of the fracture it provides the compressive forces with a solid support at the basilar border and ensures interdigitation and frictional forces between the contacting fracture surfaces.
(c) It neutralises harmful distraction forces.
(d) It allows some early return to function but not complete loading.

Fixation needs to have an element of elasticity, as rigid immobilisation of the fractured bone can disrupt bone repair, as it inhibits the inflammatory phase of bone healing [18]. Elasticity is important as micro motion between the fracture surfaces enhances the healing process [19].

Fixation needs also to be dynamic because of the adequate elasticity of the plate, masticatory activity creates compression strains at the lower border of the mandible. The interdigitation between fracture surfaces creates friction, enhancing the stability of the mechanical fixation. This compression is dynamic and physiological. It leads to a perfect contact between bone surfaces due to the adequate elasticity of the plate and, at the same time, to a stimulus for bone healing. The value of micro motion is 0.5 μm. The dimension of a mandibular osteon is 60 μm. It is generally accepted that motion smaller than that of an osteon is insignificant to the healing process. If this mobility is abolished by complete rigid fixation then the inflammatory process of bone repair is shortened, which leads to impaired repair. For completeness, Cornell [20] states that appropriate stimulus and blood supply are crucial to osteosynthesis. Controlled motion at a micromechanical level appears to optimise the physiological conditions which facilitate fracture healing.

21.3.1 Rationale for Fixation

Michelet [21] produced a mono-cortical fixation system, which was initially used for the fixation of mid-face fractures. However, Champy [22] used this successfully for the fixation of mandibular fractures. The use of mono-cortical screws are required to prevent injury to the dentition and also to the inferior alveolar nerve. Champy [22] delineates ideal lines of osteosynthesis for the fixation of mandibular fractures. He mentions three different zones.

1. A neutral zone. This is located immediately subapical to the dentition in the lateral portion of the mandible. In this region a single plate is required for adequate fixation.
2. A two-level zone. This is between the mental foramina. In this region, two plates are required to resist the tensional and torsional forces.
3. The angle of the mandible. Fixation can be adequately achieved either cranially, or buccally to the external oblique ridge with a single plate.

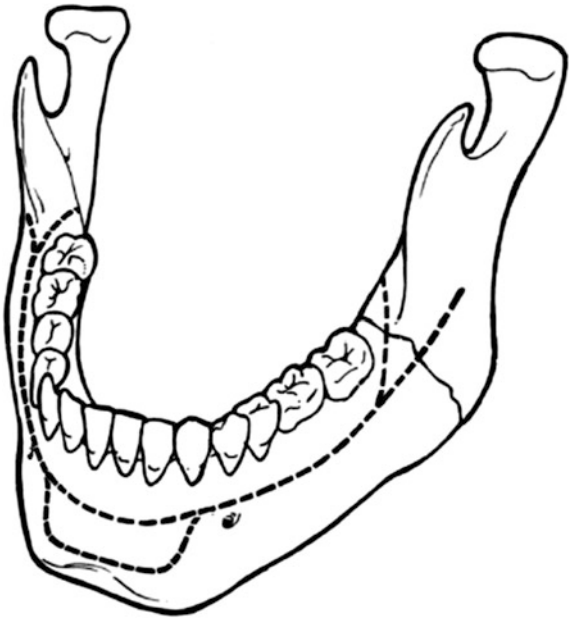

The treatment of fractures of the angle of the mandible is controversial, as there have been few prospective, randomised controlled trials [23]. Even when these studies are published the exclusion criteria are not well defined and, especially in regard to the vertically or horizontally favourable, or unfavourable nature of fractures. The in vitro experimentation regarding mono-cortical fixation of mandibular fractures should reveal clinical evidence justifying plating patterns, however it does not.

Any plating to the lateral aspect of the ascending ramus or to the angle of the mandible, demands a stab incision for a trans-cutaneous screwdriver trochar and subsequent perpendicular screw placement. This procedure is associated with possible complications such as scarring, trigeminal and facial nerve damage, bleeding and an added level of difficulty is required to remove the plates if required in the future. However, currently the popular conventional screw application in most mono-cortical plating systems is perpendicular to the plate, and using a trans-cutaneous trochar is the best method of being able to place the screw perpendicular to the plate. By using a trans-cutaneous trochar, this increases operative time and hence has a cost implication [24].

With the advent of superior border miniplates via an intraoral approaches within the United Kingdom the trans-cutaneous approach to place miniplates, the extra oral approach is used less frequently when treating mandibular angle fractures.

Champy [22] suggested that a single 2 mm thick four hole spaced plate with four mono- cortical non compression screws (normally of 6 mm length) is adequate for the fixation of a mandibular angle fracture when placed either cranial or buccal to the external oblique ridge. In spite of this there are advocates of bi-plating in bi-planar fashion [25–27] (one plate on the superior border and one plate on the

lateral aspect of the mandible), and also of bi-plating in a mono-planar fashion (superior and inferior on the buccal aspect of the mandible). This is a contentious issue, and there is debate as to the biomechanical stability of each method and the amount of either lingual or lower border gaping post fixation, and whether it is relevant [28].

21.3.2 How the Fracture Heals

There are two types of fracture healing, one is direct healing and the other is indirect healing.

In direct healing, the close apposition of the fracture segments provides mechanical stability. Because of this, the osteons of the fracture ends are in direct contact. This allows transverse bridging of the haversian system with no callus formation.

Indirect healing occurs via the pluripotent cells located within the cortical and cancellous bone periosteum and surrounding soft tissue. Indirect bone healing occurs because of instability of the fracture, caused by resorption of the fracture ends and callus formation.

In maxillofacial surgery, we are aiming for direct bone healing, which should be produced after anatomical reduction of the fracture and appropriate stable fixation. It was first discovered radiographically, and featured a lack of callus formation, and disappearance of the fracture lines. It has been shown that with regards to the mandible, interfragmentary compression is not required to produce direct bone healing [29].

Schenk and Willenegger [30] described both contact and gap healing as two different types of direct bone healing.

Contact healing of bone occurs after stable anatomical positioning, with perfect interfragmentary contact and without the possibility of vascular or cellular ingrowth. Cutting cones are able to cross the fracture from one fragment to the other by remodelling of the Haversian Canal. This remodelling is the main way in which the internal architecture of the compact bone is restored. Contact healing generally only takes place immediately beneath the miniplate.

Gap Healing takes place in stable gaps with a width greater than the 200 μm diameter of an osteon. In Gap Healing there is in growth of vessels and mesenchymal cells after surgery. Osteoblasts then deposit osteoid on the fragment ends. Lamellar bone is formed within these gaps primarily, and this is usually complete within 6 weeks. Between 6 and 10 weeks, the transversely orientated bone lamellae are replaced by axially orientated osteons. This process is commonly known as haversian remodelling. After 10 weeks the fracture is replaced by cortical bone.

Gap healing mainly occurs lingually to the miniplate, and plays a major role in bone healing, as gaps are more prevalent than contact areas. However the contact areas are essential for stabilisation of the fracture, and protect the gaps against deformation.

21.4 Case History

A 25-year-old male was brought to the Accident and Emergency Department after an alleged assault. A witness said that he had been allegedly hit once, and had been knocked unconscious. The patient had no recollection of a time period of greater than 1 hour previous to his alleged assault. He also had a Glasgow Coma Score of 11 on arrival in the Emergency Department. He was complaining of pain in his mandibular region, and had obvious deviation of his mandible.

He had drunk ten to fifteen units of alcohol, and a witness stated that he had been allegedly assaulted with a single blow. He was knocked unconscious and remained unconscious for around a minute. He was triple immobilised and brought to the Emergency Department.

The patient was fit and healthy, had no medical problems, no previous admissions or surgery. He took no regular medication and had no drug allergies.

As the patient was triple immobilised and given that he met two of the NICE guidelines for requiring an urgent CT scan to rule out a brain injury, we had little input initially. Fortunately his CT scan showed that he had sustained no radiologically significant injury to his brain. Unfortunately, however, despite requesting the CT scan to include his mandible, this was not done. His Cervical Spine was clinically cleared by the Accident and Emergency team. His Glasgow Coma Score returned to fifteen, and his clinical observations were normal. After the secondary survey, no other injuries were found other than the fractured mandible.

On examination he had a full thickness laceration of his lower lip. He had obvious ecchymosis to his chin and neck. His mandible was visibly displaced, and he had an obvious anterior open bite. His Temporomandibular Joints were non tender.

An Orthopantomogram (Fig. 21.1) and a PA mandible (Fig. 21.2) radiograph were taken. These demonstrated fractures of the mandible bilaterally through the mental region.

Fig. 21.1 Orthopantomogram pre-op

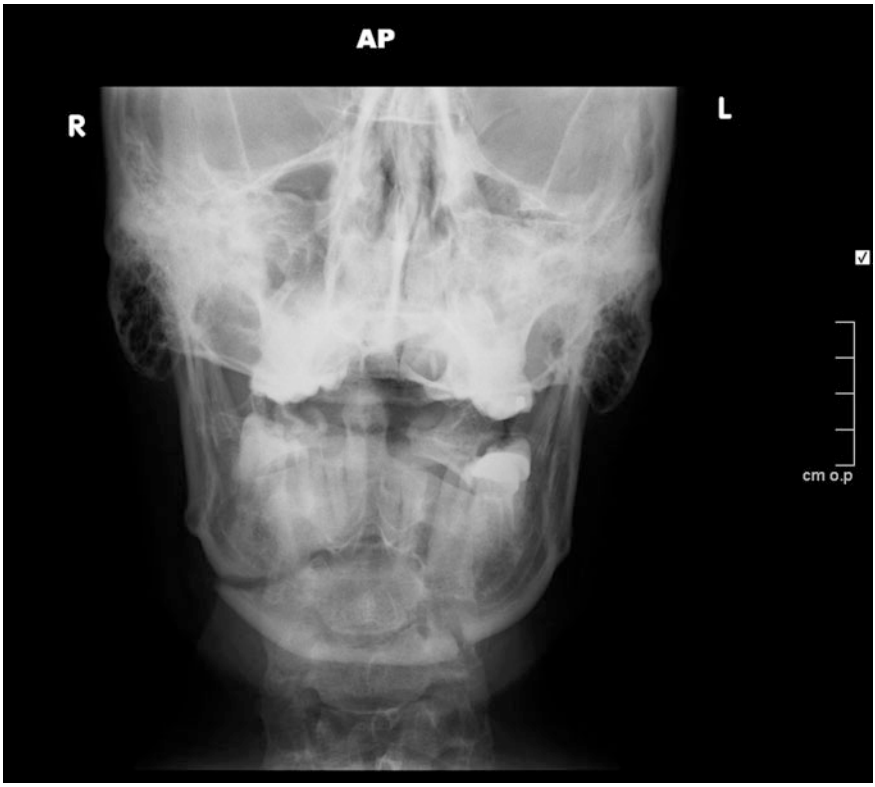

Fig. 21.2 PA mandible of Dr. B.S.

21.4.1 Diagnoses

1. Bilateral Fractured Mandible with butterfly fragment.
2. Buccal luxation of 31, 32.
3. Lip Laceration.
4. Post traumatic Concussion.

21.4.2 Treatment

a) Treatment of Post Traumatic Concussion

The patient was assessed for Neurological Observations for 24 h, as he had a significant concussive episode. This would mean delaying his surgery for his fractured mandible by 24 h.

b) Treatment of Buccal Luxation of 31, 32 and Lip Laceration

- Infiltration from 35 to 45 and lip laceration with 10 ml 2 % Lignocaine with 1:80,000.
- Manipulation of 31, 32 into normal anatomical position.
- Placement of a bridle wire from 43 to 33.
- Lip was debrided, and closed with 3/0 vicryl.
- Skin was closed with 5/0 Prolene.

Tetanus status was verbally checked. He was immediately started on 1.2 g Augmentin Intravenously TDS, and appropriate analgesia.

21.4.3 Treatment Plan

- Open Reduction Internal Fixation of bilateral mandibular fractures with mini-plates and Intermaxillary fixation via an intraoral approach.

21.4.4 Surgery

- Standard preparation and Draping of the patient.
- 10 ml 2 % Lignocaine with 1:80,000 adrenaline infiltrated from 36 to 46.
- 10 mm Intermaxillary Fixation screws were placed in the maxilla symmetrically.
- A buccal incision was made from 33 to 43 onto bone.
- Dissection was undertaken to identify the mental nerves and protect them whilst the incision was extended from 36 to 46.
- The fractures were reduced and an Erich arch bar was placed from 37 to 47. This was held with 0.45 mm wires.
- The Erich Arch bar and the Intermaxillary fixation screws were held in the correct occlusion with 0.50 mm wires.
- The left side was plated initially. The superior we placed a 2.0 mm four hole non spaced plate and this was held with 4 $\times$ 6 mm screws.
- The inferior plate was a initially the same plate, however it did not provide adequate fixation, so a 2.4 mm four hole spaced plate and 4 $\times$ 8 mm screws.
- On the right hand side there was a butterfly fragment present which made reduction difficult. To enable there to be at least 2 screws distal to the fracture, 2 screws medial to the fracture and 2 screws in the butterfly fragment, an 8 hole 2.0 mm non spaced plate was used. 7 $\times$ 6 mm screws were placed, and the unused hole was on the fracture line.
- Superiorly we placed a 2.0 mm four hole non spaced plate and this was held with 4 $\times$ 6 mm screws.
- The incision was closed with 3/0 vicryl and the 0.50 mm wire Intermaxillary Fixation was released and the occlusion was checked. The occlusion was found to be correct.

21.4.5 Post-Operative Plan

- 2 Further doses of Intravenous Antibiotics leading into Augmentin 625 mg tds 5/7.
- Analgesia as required.
- To place elastic bands to guide occlusion prior to discharge.
- Removal of sutures at 5 days.
- Review 1 week.

21.4.6 Review Appointments

The patient was discharged and reviewed post operatively without complication.

21.5 Discussion

This case is interesting as the patient had two different methods of Intermaxillary Fixation [31] (Figs. 21.3 and 21.4). This was used in conjunction with Open Reduction and Internal Fixation to produce stable fixation of difficult fractures. It raises questions regarding what is the most efficacious mode of Intermaxillary Fixation.

Intermaxillary fixation is a procedure which has been used traditionally as a sole treatment as a Closed procedure, or in conjunction with Open Reduction and Internal Fixation. However in the present era of miniplates, both the patient and surgeon prefer open reduction, reducing the duration of hospitalisation with minimal discomfort to the patient and early return to the work.

Conventional types of Intermaxillary Fixation include tooth mounted devices such as arch bars, dental and interdental wiring, metallic and non-metallic splints. However,

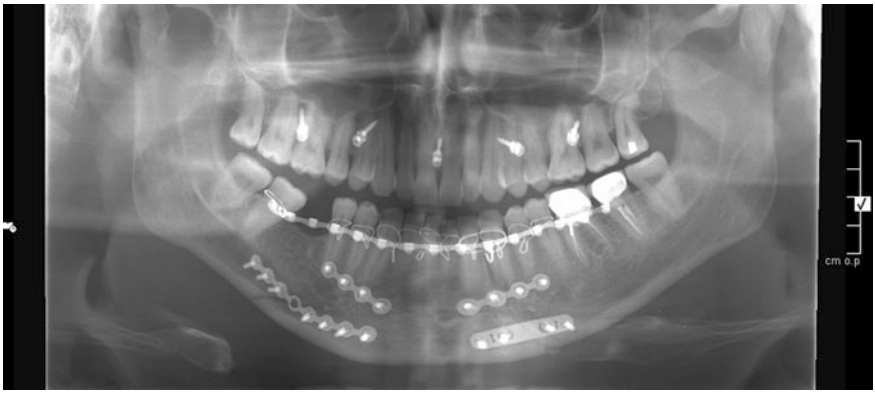

Fig. 21.3 Post operative orthopantomogram

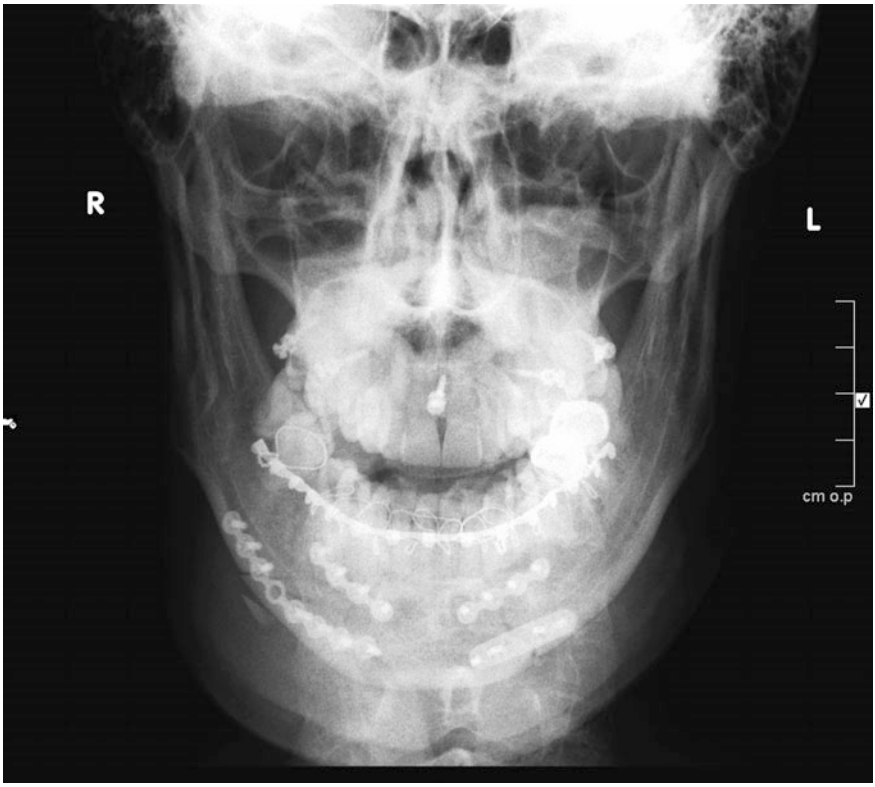

Fig. 21.4 Post operative PA mandible

tooth borne devices are always associated with problems like poor oral hygiene, periodontal health, extrusion of teeth, loss of tooth vitality, traumatic ulceration of the buccal mucosa and the risk of a sharps injury to the surgeon. Placing conventional Intermaxillary Fixation is time consuming. It is also not suitable to place wire based Intermaxillary Fixation in patients with multiple missing teeth, grossly carious teeth, crown and bridge work, extensively restored and periodontally involved teeth.

The use of Intermaxillary Screws is not without complications [32]. The most common complications include screws loosening (6.5 %) and root fracture/ iatrogenic damage to teeth (4 %). Fracture of the screws has also been reported [33]. Soft tissue coverage of screws occurred in 5 % of all cases [34].

One of the major advantages in the usage of Intermaxillary Fixation Screws is the reduced operative time. The time taken to place Intermaxillary Fixation Screws is between 5.7 and 10 min [35, 36], whereas the time taken to place Erich Arch Bars is between 25 and 100 min.

To negate the issues of damage to adjacent teeth Key [37] stated that the angulation of roots should be assessed radiographically. He recommended

placement of self-tapping screws between the canine and the first premolar region at the mucogingival junction.

The literature supports both the use of Traditional Intermaxillary Fixation as well as the use of Intermaxillary screws to aid fixation. The Traditional Intermaxillary fixation techniques take longer to apply, have a smaller set and rate of complications, however there are some contraindications to its usage. Intermaxillary screws are easier and faster to apply and remove. However, they fail more frequently and lead to more frequent damage of existing dentition. There is no definitive answer over which is the gold standard for treatment [38].

21.6 Final Word from the Expert

The Cochrane Review of Mandibular Fractures states 'This review illustrates that there is currently inadequate evidence to support the effectiveness of a single approach in the management of mandibular fractures without condylar involvement'. This necessitates the ability to be adaptable and coherent in different methods of fixation, and be able to use of different methods of fixation in a single case.

The increase in research into biomechanics is leading to development of further scientific evidence in the field of fracture treatment. Hopefully the production of higher level evidence is not too far off in the future with regards to the treatment of mandibular fractures.

References

1. Champy, M., & Lodde, J. P. (1977). Study of stresses in the fractured mandible in man. Theoretical measurement and verification by extensometric gauges in situ. *Revue de Stomatologie et de Chirurgie Maxillo-Faciale, 78*(8), 545–551.
2. Schenk, R., & Willenegger, H. (1964, November). On the histology of primary bone healing. *Langenbecks Archiv für klinische Chirurgie ... vereinigt mit Deutsche Zeitschrift für Chirurgie*, *17(*308), 440–452.
3. Van Eijden, T. M. G. J., Brugman, P., Weijs, W. A., & Oosting, J. (1990). Coactivation of jaw muscles: Recruitment order and level as a function of bite force direction and magnitude. *Journal of Biomechanics, 23*, 475–485.
4. Koolstra, I. H., & Van Eijden, T. M. G. I. (1992). Application and validation of a three-dimensional mathematical model of the human masticatory system in vivo. *Journal of Biomechanics, 25*, 175–187.
5. Koolstra, I. H., & Van Eijden, T. M. G. J. (1997). The jaw open-close movements predicted by biomechanical modelling. *Journal of Biomechanics, 30*, 943–950.
6. Van Eijden, T. M. G. J., Korfage, J. A. M., & Brugman, P. (1997). Architecture of the human jaw-closing and jaw-opening. *Anatomical Record, 248*, 464–474.
7. Rubin, C. T., McLeod, K. I., & Bain, S. D. (1990). Functional strains and cortical bone adaptation: Epigenetic assurance of skeletal integrity. *Journal of Biomechanics, 23*, 43–54.

8. Arendts, F. J., & Sigolotto, C. (1990). Mechanical characteristics of the human mandible and study of in vivo behaviour of compact bone tissue, a contribution to the description of biomechanics of the mandible—Part II. *Biomedical Engineering (Berlin), 35*(6), 123–130.
9. Arendts, F. J., & Sigolotto, C. (1989). Standard measurements, elasticity values and tensile strength behaviour of the human mandible, a contribution to the biomechanics of the mandible —Part I. *Biomedical Engineering (Berlin), 34*(10), 248–255.
10. Bacon, G. E., Bacon, P. J., & Griffiths, R. K. (1980). Orientation of apatite crystals in relation to muscle attachment of the mandible. *Journal of Biomechanics, 13*(8), 725–729.
11. Van Eijden, T. M. (2000). Biomechanics of the mandible. *Critical Reviews in Oral Biology and Medicine, 11*(1), 123–136.
12. Dechow, P. C., Nail, G. A., Schwartz-Dabney, C. L., & Ashman, R. B. (1993). Elastic properties of human supraorbital bone and mandibular bone. *American Journal of Physical Anthropology, 90*(3), 291–306.
13. Schwartz-Dabney, C. L., & Dechow, P. C. (2003). Variations in cortical material properties throughout the human dentate mandible. *American Journal of Physical Anthropology, 120*(3), 252–277.
14. Gerlach, K. L., & Schwarz, A. (2002). Bite forces in patients after treatment of mandibular angle fractures with miniplate osteosynthesis according to Champy. *International Journal of Oral and Maxillofacial Surgery,* 31, 345–348.
15. Gerlach, K. L., & Schwarz, A. (2003). Load resistance of mandibular angle fractures treated with miniplate osteosynthesis. *Mund-Kiefer-Heilkunde*, 7, 241–245.
16. Champy, M., Lodde, J. P., Jaeger J. H., & Wilk A. (1976). Mandibular osteosynthesis according to the Michelet technique I. Biomechanical basis. *Revue de Stomatologie et de Chirurgie Maxillo-Faciale,* 3 569–576.
17. Sustrac, B., & Villebrun, J. P. (1976). Biomechanique des osteosyntheses par plaques vissees miniaturisees des fractures du corps de la mandibule. Etude Strasbourg: Ecole Nat. Sup. Art. Ind, 134.
18. Ewers, R., & Harle, F. (1985). Biomechanics of the midface and mandibular fractures: Is a stable fixation necessary? In E. Hjorting-Hanson (Ed.), *Oral and maxillofacial surgery* (pp. 207–211). Chicago: Quintessence.
19. Champy, M., Wilk, A., & Schnebelen, J. M. (1975). Treatment of mandibular fractures by means of osteosynthesis without intermaxillary immobilisation according to F.X. Michelet's technique. *Zahn Mund Kieferheilkd Zentralbl,* 4, 339–341.
20. Cornell, C. N., & Lane J. M. (1992). Newest factors in fracture healing. *Clinical Orthopaedics and Related Research,* 277, 197–311.
21. Michelet, F. X, Deymes, J., & Dessus, B. (1973). Osteosynthesis with miniaturized screw plates in maxillofacial surgery. *Journal of Maxillofacial Surgery,* 1, 79–84.
22. Champy, M., Lodde, J. P., Schmitt, R., Jaeger J. H., & Muster D. (1978). Mandibular osteosynthesis by miniature screwed plates via a buccal approach. *Journal of Oral Maxillofacial Surgery,* 6, 14–21.
23. Barry, C. P., & Kearns, G. J. (2007). Superior border plating technique in the management of isolated mandibular angle fractures. A retrospective study of 50 consecutive patients. *Journal of Maxillofacial Surgery,* 65, 1544–1549.
24. Scurry, W. C., Jr, Beus, K. S., McGinn, J., & Fedok, F. G. (2005). Operative time analysis of miniplate fixation of the mandible. *Facial Plastic Surgery,* 21, 176–179.
25. Ellis, E. (1997). Treatment methods for the fixation of the mandibular angle. *Journal of Cr-Maxillofac Tr*, 2, 28–36.
26. Siddiqui, A., Markose, G., Moos, K. F., McMahon, J., & Ayoub, A. F. (2007). One miniplate versus two in the management of mandibular angle fractures: A prospective randomised study. *British Journal of Oral and Maxillofacial Surgery,* 45, 223–225.
27. Ellis, E., Waler, L., & Shafer, D. (1994). Treatment of mandibular angle fractures using two noncompression miniplates. *Journal of Oral and Maxillofacial Surgery,* 52, 1032–1037.
28. Ellis, E. (1997). Treatment methods for the fixation of the mandibular angle. *Journal of Cr-Maxillofac Tr*, 2, 28–36.

29. Champy, M., & Lodde, J. P. (1977). Study of stresses in the fractured mandible in man. Theoretical measurement and verification by extensometric gauges in situ. *Revue de Stomatologie et de Chirurgie Maxillo-Faciale, 78*(8), 545–551.
30. Schenk, R., & Willenegger, H. (1964 November). On the histology of primary bone healing. *Langenbecks Archiv für klinische Chirurgie ... vereinigt mit Deutsche Zeitschrift für Chirurgie*, *17*(308), 440–452.
31. Arthur, G., & Bernado, N. (1989). A simplified technique of maxilla-mandibular fixation. *British Journal of Oral and Maxillofacial Surgery, 47*(11), 1234.
32. Coletti, D. P., Salama, A., & Caccamese, J. F., Jr. (2007 September). Application of intermaxillary fixation screws in maxillofacial trauma. *Journal of Oral and Maxillofacial Surgery,* 65(9), 1746–1750.
33. Holmes, S., & Hutchison, I. (2000). Caution in use of bicortical intermaxillary fixation screws. *British Journal of Oral and Maxillofacial Surgery, 38*(5), 574.
34. Hashemi, H. M., & Parhiz, A. (2011). Complications using intermaxillary fixation screws. *Journal of Oral and Maxillofacial Surgery, 69*(5), 1411–1414.
35. Majumdar, A. (2002). Iatrogenic injury caused by intermaxillary fixation screws. *British Journal of Oral and Maxillofacial Surgery, 40*(1), 84–88.
36. Sahoo, N. K., & Mohan, R. (2010). IMF screw: An ideal intermaxillary fixation device during open reduction of mandibular fracture. *Journal of Maxillofacial Oral Surgery, 9*(2), 170–172.
37. Key, S., & Gibbons, A. (2001). Care in the placement of bicortical intermaxillary fixation screws. *British Journal of Oral and Maxillofacial, 39*(6), 484.
38. Nasser, M., Pandis, N., Fleming, P. S., Fedorowicz, Z., Ellis, E., Ali, K. (2013, July). Interventions for the management of mandibular fractures. *Cochrane Database Systematic Review, 8*(7), CD006087.

Chapter 22
Safety and Medical Devices: The Human Factors Perspective

Morris Gordon

Abstract Whilst medical devices offer increasing fidelity and complexity that can form significant barriers to error, they open up new routes for errors and harm to occur. Much work in other industries has investigated the man machine interface and how devices can best be designed to account for such risks. This field of human factors is discussed in the context of healthcare and the state of the field reviewed.

22.1 Safety in Healthcare

For millennia health professionals have begun their careers by making a pledge that starts with a declaration of the principle to 'do no harm' [1]. These words are the culmination of a training period that has traditionally followed the time honoured practice apprenticeship, with knowledge a commodity passed directly to the learner [2]. As such, once knowledge had been digested, health professionals were essentially 'always right'. Indeed despite the starting pledge, it was often acceptable to believe that harm to patients was unavoidable and to rationalise that the majority of patients did not suffer from such events (National Health Service [NHS] Education 2013). After all, healthcare is complex and the 'doctor knows best' [3].

Attitudes to errors in health care began to change towards the later end of the twentieth century with a string of high profile incidents reported in the media [4]. The report To Err is Human: Building a Safer Health System in the USA [5: p. 39] was a game changer, making the infamous comparison of a 'Jumbo Jet of patients dying every day from medical errors'. This work was the first to use large amounts of actual patient data to estimate the national scale of the problem caused by avoidable medical error. Public awareness of these statistics since the publication of Kohn et al.'s [5] initial report led to a furore that prompted immediate action

M. Gordon (✉)
School of Medicine, University of Central Lancashire, Preston, UK
e-mail: MGordon@uclan.ac.uk

W. Ahmed and M.J. Jackson (eds.), *Surgical Tools and Medical Devices*,
DOI 10.1007/978-3-319-33489-9_22

across the globe [6]. This formed the foundation on which an industry of 'patient safety' was built. However, error continues to occur in health care with shocking frequency [7]. The need to tackle the patient safety problem globally has indeed permeated all areas of healthcare for the last 15 years. Essentially, there are three key approaches that have been taken: best practice determined by best evidence, the person approach to error, and a systems-based approach.

The first involves ensuring that the care offered is the right care that can and should be offered in the first place, essentially focussing on technical skills and delivery of health care [8]. This is characterised by clinical governance, which is now pervasive. Audit cycles, incident analysis and reporting, morbidity and mortality monitoring and protocol design have all become commonplace [9, 10]. Studies to enhance patient outcomes that focus on ensuring dissemination of and adherence to already established or recently changed principles of practice are the focus for much published research. These are often underpinned by more systematic approaches to establish what indeed constitutes best practice, such as evidence synthesis. This approach involves recognition of problems and key to this in the context of medical devices is error reporting.

The second approach is aligned to the more traditional view of error in complex organisations. The person approach advocates identifying the culpable party as the cause of an error (Reason 1998). Historically, this health care error investigation process focuses on the 'who did it' instead of the 'why did it happen' [5, 11, 12]. Reason [12] discusses this person approach to error that focuses on the unsafe acts of people at the sharp end and highlights how this is an ineffective approach to error reduction, but muses that it is preferred because 'blaming individuals is emotionally more satisfying than targeting institutions' [12: p. 70]. This views unsafe acts as arising primarily from aberrant mental processes such as forgetfulness, inattention, poor motivation, carelessness, negligence, and recklessness. Approaches to tackling specific aberrant behaviour within the NHS target include: poster campaigns [13, 14], writing another procedure or adding to existing ones ([15]; British Medical Association [BMA] 2002), threat of litigation (Quick 2012), retraining [16], naming (NHS Choices 2013), blaming and shaming (DH 2001). This wider ranging body of work is inherently flawed (Baker and Norton 2001; Berwick and Leape 1999). They focus on the individual committing error [1, 12] and as such the specific remediation actions taken, as outlined above, often do not have impact on the wider department, organisation or health service [17]. Adopting the person approach to error management can lead to a culture of fear and lead to reduced reporting of such behaviours [18]. In the majority of cases for health professionals such errors can and will go unnoticed and bear no consequences (Rosenthal 1994). It is well recognised that from a psychological perspective, this lack of consequences for the individual can further enforce the aberrant behaviour [19, 20] and exacerbate the problem. The alternative viewpoint to the person-centred view of error is the system-based approach to error.

This third systems-based approach to error was endorsed and encouraged by the NHS response to the Kohn et al. report [5], Organisation with a Memory

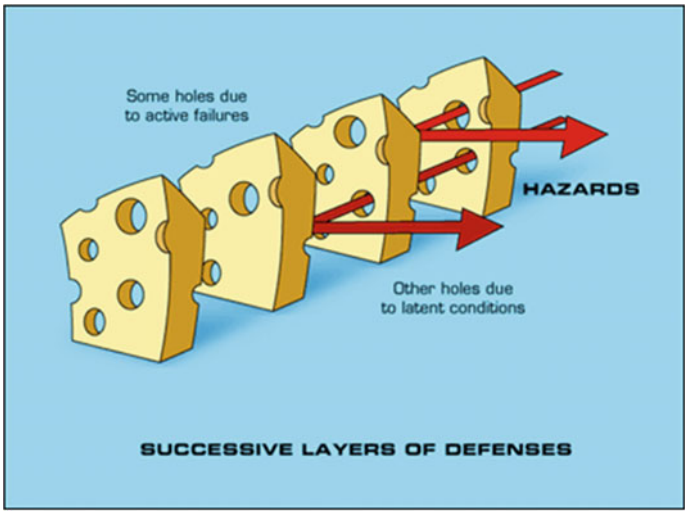

Fig. 22.1 The Swiss cheese model of error [12]. Reproduced with permission from http://patientsafetyed.duhs.duke.edu/module_e/swiss_cheese.html

(DOH 2001). This report theoretically aligned itself with the now ubiquitous Swiss cheese model of accident causation [21]. Reason hypothesises that most accidents can be traced to one or more of four levels of failure: Organisational influences, unsafe supervision, preconditions for unsafe acts, and the unsafe acts themselves. In the Swiss cheese model, an organisation's defences against failure are modelled as a series of barriers, represented as slices of Swiss cheese (Fig. 22.1). The holes in the cheese slices represent individual weaknesses in individual parts of the system, and are continually varying in size and position in all slices. The system as a whole produces failures when all of the holes in each of the slices momentarily align so that a hazard passes through all of the holes in all of the defences, leading to a failure [12].

The interplay of these three elements can be considered in the context of an example of clinical error concerning the incorrect administration of antibiotics instead of saline by a neonatal nurse to a baby. In considering this error, it was highlighted that a potential for confusion between two similar bags of fluid existed. However, this case highlights that all three methods to address error could be applied. Firstly, the knowledge and skills of the professionals could be considered, as clearer the checking process may have been incorrect. Secondly, person-centred view of error would seek to punish, publicise or retrain the individuals involve. Finally, the systems-based approach would seek to change the storage, appearance or use of the fluid to put barriers in place to prevent a similar incident. This final systems-based approach is the primary focus of human factors ergonomics (Carayon et al. 2013).

22.1.1 Human Factors

Human factors ergonomics is a recognised scientific discipline concerned with 'the understanding of interactions among humans and other elements of a system, and the profession that applies theory, principles, data and methods to design in order to optimise human well-being and overall system performance' [22, 23] although there is no consensus on a definition for this field with a number of proposals in existence [24].

Human factors is a term many involved in healthcare delivery are now familiar with and has led to increasing acknowledgement of the value of human-centred systems thinking in healthcare, even though a decade ago most had never heard of the concept [25]. There are a number of examples of how expertise within the field has been used to enhance safety in healthcare, by changing systems, environments or technology (Carayon et al. 2013). However, it is becoming clear that the term is being increasingly misappropriated in the literature ([26]; Cahan et al. 2011; Ross et al. 2009; Turner 2012). Russ et al. [27: p. 1] points out that a common misconception is that researchers refer to human factors, yet they detail the underlying cause as being human errors, a stance that clearly opposes human factor ergonomics as described above. Indeed, the term itself is not helpful as ironically human factors are essentially not interested in humans, but designing resilient systems around them (Scanlon and Karsh 2010). The subset of human factors that focusses on human behaviour as a focus for change is known as non-technical skills, with the rest of the field instead focussed on everything but the humans themselves and engineering systems in which they operate.

This conceptual dichotomy is problematic as often human factors are described as a focus for training in healthcare ([28]; Merseyside and Cheshire Health, Innovation and Education Cluster 2013), which clearly is a non-sequitur. Human factors approaches by their very nature try to avoid using training to compensate for poor system design and instead change the systems itself (Salvendy and Karwowski 2006). In his seminal piece on these issues, Catchpole articulates that transposition of industry-based approaches to enhancing human factors are flawed. Healthcare is completely different to aviation; transport, defence and nuclear power industries which are technology mediated, and have largely been engineered in the last 150 years to achieve specific goals [25].

An example often cited is the B17 bomber in the 1940s [29]. The development of a checklist to stop crashes is often cited as an example of how powerful such human factor approaches are, but the deeper understanding Catchpole [25] asks for demonstrates that it was actually a design change to the human device interface that stopped most accidents. The flap and gear levers were the same size and shape and were right next to each other, so it was easy to mistake one for the other, with disastrous consequences. A redesign the size, shape and location addressed most of the problem, with the checklist there as a final safety barrier, in line with the Swiss cheese model [12].

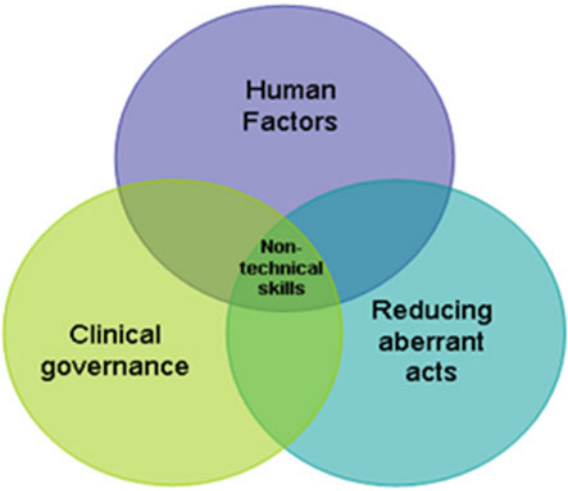

Fig. 22.2 Interplay of factors mitigating errors in healthcare

This is an important illustration of the problems within the human factors field in healthcare. Human factors ergonomics must seek to engineer the clinical environment from the ground up. This interplay of various factors is illustrated in Fig. 22.2. This demonstrates that clinical governance strategies to identify and ensure good practice, associated with punitive and monitoring processes to reduce errors are equal contributors with human factors engineering strategies to redesign systems. Of note, non-technical skills exist at the centre of this model. This exemplifiers there small but important role as a set of skills enhancing safety that are grounded human factors, can reduce errors and enhance good practice. Whilst this simple model exemplifiers this massive concepts, most specific contexts will largely be impacted from a safety perspective by governance strategies. Given the huge logistical barriers in engineering systems from the ground up in a human factors fluent manner, this is rarely achieved. Medical devices are a unique context in modern healthcare in which human factors engineering to enhance safety is truly possible.

22.2 Man–Device Interface

Humans and machines interact and affect one another. Compared to communication between humans, which can be innately adaptive, machines are limited to information displays and software that are exhibited through these visual windows. From a human factors standpoint, complex communication between humans and machines is limited by the inability to have a shared situational awareness that can be used to interpret situations according to the context. This situational awareness is absent in most machines and very restricted in even the most advanced and is key in

a human factors view of error reduction. In general, software does not allow machines to adapt to unforeseen conditions, so computers are limited in their actions and cannot adapt in this way. Nonetheless, humans often expect the machine to communicate in the same way as they do and get frustrated or angry when it does not [30]. Instead, understanding and using machines as a tool to inform human situational awareness is needed.

When considering the nature of this communication and interaction, humans offer input through physical means, such as control sticks, buttons, touch screens, keyboards or a mouse. Machines offer information and output visually, acoustically or physically. Technologies are often presented as solutions to improve patient safety and prevent medical errors [5, 31], but when considered from this conceptual standpoint of input and output of data and instructions, it becomes immediately far more complex. If technologies are to lead to patient safety improvements, they must be designed, implemented and used according to human factors engineering principles (Sage and Rouse 1999; Salvendy 2006).

22.3 Design

There are several human factors informed strategies to ensure that devices and technologies fit human behaviour and are functional. Usability evaluation and testing methods are increasingly used by manufacturers and vendors of healthcare technologies. There is much work describing medical device errors and how poor interface design of technologies can lead to direct harm to patients (NPSA 2012). As awareness of human factors ergonomics has increased, hospitals and wider healthcare establishments increasingly require information about the usability of technologies they purchase. Previous works have looked to provide practical information about usability evaluation and testing at the stage of technology design.

22.4 Transfer to Practice

There is detailed published evidence on technological and wider establishment integration that identifies principles to guide technology implementation. A review of literature by Karsh [32] highlights the following principles for technology implementation to promote patient safety:

- top management commitment to the change
- responsibility and accountability structure for the change
- structured approach to the change
- training
- pilot testing
- communication

- feedback
- simulation
- end user participation

Even after a technology has been implemented, it is important to continue monitor its use in the 'real' context and to identify potential problems and work-arounds. About 2–3 years after the implementation of bar coding medication administration (BCMA) technology in a large academic medical centre, a study of nurses' use of the technology shows a range of work-arounds (Carayon et al. 2007). In this case, nurses found work-arounds to be able to administer medications to patients in isolation rooms: it was very difficult for nurses to use the BCMA handheld device wrapped in a plastic bag; therefore, often the medication was scanned and documented as administered before the nurse would enter the patient room and administer the medication. This type of work-around results from a lack of fit between the context (i.e. patient in isolation room), the technology (i.e. BCMA handheld device) and the nurses' task (i.e. medication administration). Some of these interactions may not be anticipated at the stage of designing the technology and may be 'visible' only after the technology is in use in the real context. This emphasises the need to adopt a 'continuous' technology change approach that identifies problems associated with the technology's use (Carayon 2006; Weick and Quinn 1999).

22.5 State of the Field

The evidence base in this area is becoming well established, with the principles laid out well studied and reported. However, the field is rapidly progressing. Presented below is a digest of the current cutting edge and state of the field of ongoing research that investigate different ways to interface with and construct medical devices to support safety from a human factors perspective.

22.5.1 Cognitive Load Theory

Cognitive load theory (CLT) was developed by cognitive psychologists and assumes that the human cognitive system has a limited working memory that can hold no more than nine elements, and can actively process no more than four elements simultaneously [33]. This theory emphasises that these limitations only apply to novel information, not old knowledge. Therefore, a senior medic recognises a child with septicaemia caused by meningococcus at a single glance. By contrast, for a medical student, a patient with meningococcal septicaemia may appear to have a rash, fever and poor appetite [34].

This theory has been used to guide and enhance learning materials within medical education, but more recently employed to optimise human–machine interface design to minimise the mental load. According to human natural instincts and acquired knowledge, an expected ideal design with minimised thinking loads was devised drawing on experience from car design [35].

22.5.2 Audio to Reduce Visual Distraction

Experience within the car industry with devices such as navigation displays and media players found they were part of a distraction problem has led to the formulation of guidelines advocating various means for minimising the visual distraction from such interfaces. Recent work has investigated the role of different forms of audio to reduce such visual distraction. Spearcons (time-compressed speech sounds) and earcons (musical sounds) were investigated, but it was found that added spearcon sounds significantly reduced total glance time as well as number of glances while retaining task time [36]. Such work has implications for medical devices which often use sound, as well as visual ques.

22.5.3 Tactile Language Communication

Improvements in autonomous systems technology and a growing demand within military operations are spurring interest in communication via vibrotactile displays. A recent set of studies have investigated the use of directional, dynamic, and static tactons. Whilst performance was poor initially, with appropriate training participants were able to interpret two-tacton phrases, even when multitasking [37]. It is suggested that this may be a viable form of human device interface in the future.

22.5.4 Generic Non-technical Skills Training

As highlighted previously, non-technical skills are a unique area of safety behaviours within medicine [38, 39]. They are grounded within a human factors understanding of healthcare systems, are grounded in error wisdom and integrate with wider governance systems. The air industry have pioneered training within this area, with what is commonly termed crew resource management training a mandatory requirement by many civil aviation authorities. Problems have been encountered when transposing these courses from the relatively controlled environment of a

Table 22.1 Framework for non-technical skills training in healthcare [38]

Social factors
Communication • Clear language used • Information organised • Ensures receiver of information has understood • Confirms understanding when receiving information
Team working and Interprofessional skills *All* • Exchanges relevant information within the team • Focuses on the patient and their care when conflict arises • Values team input *Leaders* • Seeks and takes responsibility when appropriate • Identifies when colleagues are struggling and acts appropriately • Monitors and reviews task progress within the team • Coordinates activities and tasks with colleagues • Assesses capabilities of individuals within the team • Demonstrates shared plans with team
Cognitive factors
Personal behaviours • Displays personal attributes of compassion, integrity and honesty • Applies critical self-appraisal • Welcomes updates on performance • Identifies when stress may pose a risk • Recognises fatigue and considers appropriate actions to negate risk
Analytical skills *All* • Gathers and analyses information to support awareness of risk of errors • Changes trajectory when significant risk is encountered • Identifies viable options • Re-evaluates based on situational awareness *Leaders* • Encourages active dialogue within the team regarding risk • Anticipates potential future risks for the team

commercial jet to the complex healthcare environment. As such, recent works have sought to build a framework for educational outcomes grounded in health [38]. This framework is presented in Table 22.1 and can be employed by those seeking to develop medical device safety education to ensure wider non-technical skills are successfully employed.

22.6 Summary

Human errors when using medical devices do occur and will always occur (DH 2000; [12]). Human factors ergonomics is a psychology discipline that has underpinned much safety work in other industries for many years [22], focusing not on humans, but the systems and environments in which they work to stop inevitable errors from causing harm [12].

Work to apply human factors in healthcare to enhance systems and environments has shown the potential to enhance safety (Carayon et al. 2013). Human factors engineering is key to guide the design, introduction and safe use of medical devices within healthcare. Continuing research within technology and device deployment in other industries investigating human factors concepts can guide future developments in this key area. Education on the use of medical devices within healthcare should be completed in a manner the promotes non-technical skill development to ensure safe use.

References[1]

1. Donaldson, L. (2005). Patient safety: Do no harm. *Perspectives in Health—Pan American Health Organization, 10*, 1.
2. Drabkin, I. (1957). Medical education in ancient Greece and Rome. *Academic Medicine, 32*, 286–296.
3. Hartwell, M. (2005). Medical negligence: Can doctors and nurses still rely on the doctrine that they know best? *Legal Medicine (Tokyo), 7*, 293–298.
4. Department of Health (DOH). (2000). *An organisation with a memory*. Available online at http://www.dh.gov.uk/prod_consum_dh/groups/dh_digitalassets/@dh/@en/documents/digitalasset/dh_4065086.pdf. Accessed January 23, 2013.
5. Kohn, L. T., Corrigan, J. M., & Donaldson, M. S. (Eds.). (2000). *To err is human: Building a safer health system* (Vol. 627). Washington, DC: National Academies Press.
6. Watcher, B. (2011). *A game changing statistic 1 in 250*. Available online at http://community.the-hospitalist.org/2011/02/11/a-game-changing-statistic-1-in-250/. Accessed January 23, 2013.
7. National Patient Safety Agency (NPSA). (2012). *Quarterly summaries*. Available online at http://www.nrls.npsa.nhs.uk/resources/collections/quarterly-data-summaries/
8. Wong, B. M., Etchells, E. E., Kuper, A., Levinson, W., & Shojania, K. G. (2010). Teaching quality improvement and patient safety to trainees: a systematic review. *Academic Medicine, 85*, 1425–1439.
9. Philibert, I. (2009). Physicians: Practical implications organisations to the patient hand-off by resident use of strategies from high-reliability. *Quality and Safety in Health Care, 18*, 261–266.
10. Temple, J. (2010). Doctors' training and the European working time directive. *Lancet, 375* (9732), 2121.

[1]Sections of this text have been adapted from the authors previous thesis works.

11. Rasmussen, J. (1999). The concept of human error: Is it useful for the design of safe systems in health care? In C. Vincent & B. de Moll (Eds.), *Risk and safety in medicine* (pp. 31–47). London: Elsevier.
12. Reason, J. (2000). Human error: Models and management. *BMJ, 320*, 768–770.
13. NHS Kidney Care. (2012). *Evaluation of the 'hydration matters' poster campaign in acute hospital trusts*. Available at http://www.hydrationmatters.nhs.uk/assets/6/Evaluation%20of%20HM%20poster-%20FINAL.pdf. Accessed on September 9, 2013.
14. NHS Midland and East. (2012). *I trust you to care*. Available at https://www.eoe.nhs.uk/page.php?page_id=2176. Accessed on September 9, 2013.
15. Royal College of Nursing. (2010). *Guidance on safe nurse staffing levels in the UK*. Available at http://www.rcn.org.uk/__data/assets/pdf_file/0005/353237/003860.pdf. Accessed on September 9, 2013.
16. World Health Organisation. (2008). *Patient safety workshop: Learning from error*. Available at http://www.who.int/patientsafety/activities/technical/vincristine_learning-from-error.pdf. Accessed on September 9, 2013.
17. Bates, D. W., & Gawande, A. A. (2000). Error in medicine: What have we learned? *Annals of Internal Medicine, 132*(9), 763–767.
18. Cohen, M. R. (2000). Why error reporting systems should be voluntary: They provide better information for reducing errors. *BMJ, 320*(7237), 728.
19. Hammond, K. R. (1996). *Human judgement and social policy: Irreducible uncertainty, inevitable error, unavoidable injustice*. Oxford: Oxford University Press.
20. Kruger, D. J., Wang, X. T., & Wilke, A. (2007). Towards the development of an evolutionarily valid domain-specific risk-taking scale. *Evolutionary Psychology, 5*(3), 555–568.
21. Reason, J. (1990). *Human error*. New York: Cambridge University Press.
22. International Ergonomics Association. (2012). *Definition of human factors*. Available at http://www.iea.cc/. Accesses on July 25, 2013.
23. Carayon, P., & Wood, K. E. (2010). Patient safety: The role of human factors and systems engineering. *Study of Health Technology and Information, 153*, 23–46.
24. Clinical Human Factors Group. (2011). *Towards a definition of human factors*. Available online at http://www.chfg.org/news-blog/towards-a-working-definition-of-human-factors-in-healthcare. Accessed January 23, 2013.
25. Catchpole, K. (2013). Spreading human factors expertise in healthcare: Untangling the knots in people and systems. *BMJ Quality and Safety,*. doi:10.1136/bmjqs-2013-002036.
26. Bleetman, A., Sanusi, S., Dale, T., & Bruce, S. (2012). Human factors and error prevention in emergency medicine. *Emergency Medicine Journal, 29*, 389–393.
27. Russ, A., Fairbanks, R. J., & Karsh, B. T. (2013). The science of human factors: Separating fact from fiction. *BMJ Quality and Safety,*. doi:10.1136/bmjqs-2012-001450.
28. NHS Institute for Innovation and Improvement. (2006). *Safer care improving patient safety*. Available online at http://www.institute.nhs.uk/safer_care/general/human_factors.html. Accessed September 11, 2013.
29. Carroll, J. J. (1997). *Physiological problems of bomber crews in the eighth air force during WWII*. A research paper presented to air command and staff college, Maxwell, AL, USA. Available at http://www.dtic.mil/cgi-bin/GetTRDoc?Location=U2&doc=GetTRDoc.pdf&AD=ADA398044. Accessed September 11, 2013.
30. Dahm, M. (2006). *Grundlagen der Mensch-Computer-Interaktion*. München: Pearson Studium.
31. Flaspöler, E. (2009). Literature review. The human machine interface as an emerging risk. *European Agency for Safety and Health at Work*. doi:10.2802/21813.
32. Karsh, B. T. (2004, Oct). Beyond usability: Designing effective technology implementation systems to promote patient safety. *Quality and Safety in Health Care*, *13*(5), 388–394.
33. Van Merriënboer, J. G., & Sweller, J. (2010). Cognitive load theory in health professional education: Design principles and strategies. *Medical Education, 44*, 85–93.

34. Gordon, M., Chandratilake, M., & Baker, P. (2013). Low fidelity, high quality: A model for e-learning. *The Clinical Teacher, 10*, 258–263. doi:10.1111/tct.12008.
35. Huang, Y., Li, X., & Zhang, J. (2015, August 5). Optimal design method to minimize user's thinking mapping load in human–machine interactions. *Work*. Epub ahead of print.
36. Larsson, P., & Niemand, M. (2015). Using sound to reduce visual distraction from in-vehicle human–machine interfaces. *Traffic Injury Prevention, 16*(Suppl 1), S25–S30. doi:10.1080/15389588.2015.1020111.
37. Barber, D. J., Reinerman-Jones, L. E., & Matthews, G. (2015, May). Toward a tactile language for human–robot interaction: Two studies of tacton learning and performance. *Human Factors*, *57*(3), 471–490. doi:10.1177/0018720814548063. Epub, August 28, 2014.
38. Gordon, M., Baker, P., Catchpole, K., Darbyshire, D., & Schocken, D. (2015). Devising a consensus definition and framework for non-technical skills in healthcare to support educational design: A modified Delphi study. *Medical Teacher, 37*(6), 572–577.
39. Gordon, M. (2014). *Developing healthcare non-technical skills training through educational innovation and synthesis of educational research*. Ph.D. Thesis, University of Salford. Available at http://usir.salford.ac.uk/30826/

Chapter 23
Synthesis of Nanostructured Material and Its Applications as Surgical Tools and Devices for Monitoring Cellular Activities

Taimur Athar

Small particle-Smart properties—Better understanding—Reliable applications-good health.

Abstract Since the beginning of twenty-first century assembling of nanobricks with innovation and creativity lead to functional structural framework in order to fabricate a reliable–reproducible result-oriented nanodevice remains a synthetic challenge to the researchers and technologist. The use of nanomaterials as diagnostic tools is relatively a new area in medical research. The soft chemical approach help for synthesis of nanoparticle with distinctive physical, chemical, and electronic properties for various biosciences–clinical applications, opens new possibilities with controlled size particle and its distribution, surface chemistry, and agglomeration, which has attracted a remarkable interest in recent years precisely to label and to track abnormalities in vivo administration. Many contrast cell labeling and tracking strategies were used based on metal oxide nanopowder with high biocompatible to give a better contrast due to their Lewis-acid behavior of metal ions. With fast research in nano-biotechnology, demands for new synthetic approach for clinical functional materials have attracted interest for scientists. In coming times, it will revolutionize clinical studies both in vitro and vivo imaging with desired chemical composition, crystal phase, and surface morphology by better understanding biological barriers to target the drug at the malfunctional sites.

Theme:

Synthesis ⟶ Devices ⟶ Diagnostic ⟶ Treatment

T. Athar (✉)
OBC, CSIR-Indian Institute of Chemical Technology, Hyderabad 500007
Andhra Pradesh, India
e-mail: taimurathar2001@gmail.com

W. Ahmed and M.J. Jackson (eds.), *Surgical Tools and Medical Devices*,
DOI 10.1007/978-3-319-33489-9_23

23.1 Nanotechnology and Its Applications

Nanotechnology and nanoscale inorganic materials have been in use since human civilization. Nature has designed laboratory with new desired functional properties which can gives an answer to many scientific and technological problems needful for day-to-day life. Many curious questions related toward the synthesis of new functional smart materials with high performance to answers remains a difficult task for researchers. Since the beginning of twenty-first century, self assembling of nanobricks were cemented together for potential application with formation of primary nuclei and its growth, which lead to innovate creativity with an excellent functional structural framework remains a synthetic challenge. To fabricate a reliable–reproducible result-oriented nanodevice depends on crystal size, defects and its surface area by controlling interface properties by keeping stoichiometric ratio intact. Colloidal and monodispersable metal oxide nanopowder have attracted more attention for its unique multifunctional properties to understand the electronic, magnetic, and optical properties. With the help of soft chemical approach, it is easy to convert molecular precursors into their corresponding metal oxide nanomaterials with homogenous size and shape; it is evenly distribution and phase purity by controlling the rate of nucleation growth, aggregation to give unique morphological features, affect both physical and chemical properties. Aggregation was controlled by better understanding the kinetic–thermodynamic parameters by incorporating metal ions into molecular species with surface chemistry for its applications in near future. The functional properties in nanomaterials can be tailored in-depth knowledge for understanding material chemistry at the nanoscale, which depend on synthetic conditions, chemical used followed by treatment with deionized water help to improve a functional properties based on structural and surface morphology by understanding nucleation and its growth process. The fundamental chemistry involved during synthesis via chimie-douce approach help in studying innovative surface–charge morphology in smart colloidal and monodispersable materials using smart single source molecular precursors for processing to restrict intrinsic–extrinsic strain within molecular framework. Nanoparticle plays a crucial role in drug delivery system. However, the drug with target system and limited therapeutic index remains a challenge. Recent developments in nanotechnology have enabled the fabrication of materials and structures with nanosize features for biological applications to improve human health. Nanostructured materials with high surface features having a particle size less than 100 nm exhibit biological responses as compared to the micrometer-size surfaces as shown in Fig. 23.1. Metal ion plays a crucial role in coordination behavior to control a chemical functional behavior, the nucleation, growth, orientation, and to transform into nanostructure framework with high performance by tuning surface–morphology at low conductivity. The effect of metal oxide nanopowder in biological system depends on charge present on the surface which depends on electronegativity, electron affinity, as well as ionization potential of metal ions. To transform the process from micro to nanoscale needs a better understanding about the mechanism for self–assembling of nanoblock then to

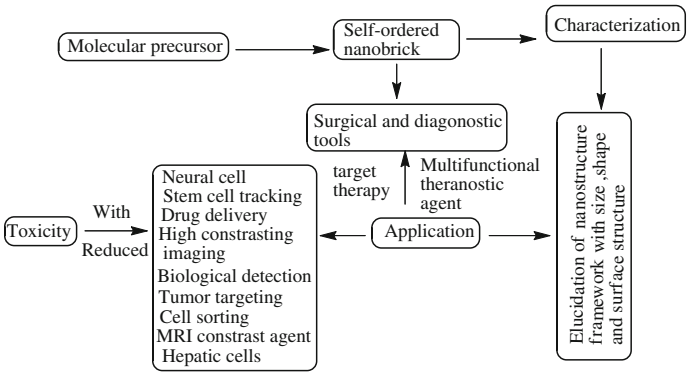

Fig. 23.1 Nanotechnology creates tools which help to diagnose and cure the disease

integrate in functional structure which is useful to integrate nanodevices via optimizing the rate of hydrolysis and kinetic parameters remain a synthetic challenge. Health care is very important in present era because many diseases take place with change in life style under constant stress–strain factors in biochemical functions. So it is important to innovate a cost-effective, patient friendly nanodevice with an enhanced lifetime and biocompatibility which will reduce human suffering. Metal oxide nanopowder has potential application in medicines and biology, which can be used in preclinical experiment for imaging contrast, MRI, immunoassays, cell tracking, tissues repair, magnetic hyperthermia, and drug delivery. Metal oxide nanopowder for clinical applications depend on physicochemical properties, toxicity, and fictionalization. Due to quantum-size effect exhibits strong surface plasmon resonance bands in the visible wavelength, SPR frequencies depend on an interparticle distance which changes into absorption spectra [1–3].

Design of nanodevices requires a strict control to correlate various aspect of nanochemistry within vivo behavior, which includes a stability, stereochemistry, charge, and lipophilicity in nanomaterials. The target organs or tissues will dictate the desired characteristics. In last 5 years, nanopowders with clinical properties have been studied to design a cost-effective bio-nanodevice. A wide range of nanoparticles along with their biomedical applications continue to expand, safety concerns with its use in vivo toxicity, hazards, and biodistributions remains unexplained. It is difficult to correlate from one type of particles from other type of particle due to intrinsic differences in physical properties (particle size, shape, etc.) and chemical properties (surface chemistry, hydrophobicity, etc.), mode of preparation and their efficiency toward a biological targets (cells, tissues, organs, animals). More emphasis is placed toward a systematic categorization of findings in vivo studies with different types of particle, sizes, shapes, surface functionalization, animal models and type of organs, toxicity assays, and distribution in different organs will be the main theme of this chapter as illustrated in Fig. 23.4. An integrated approach using a different metal ion at the molecular level helps to study a biological interaction with their long-term stability at biological pH and having desired biocompatibility and biofunctionality to control

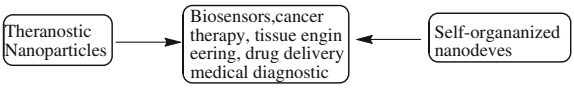

Fig. 23.2 Synergistic relationships between nanoparticles and its nanodevices

cytotoxicity criteria. Care with detailed studies in vivo help to avoid nonspecific interaction in plasma protein (opsonisation) with an uptake by reticuloendothelial systems to reach target site to give precision results in biocellular systems. Stereochemistry plays a crucial role in target materials with specific receptors having desired kinetic–thermodynamic stability. The binding of nanoparticles to biological molecules is expanding rapidly for innovation research in technological field to design a cost-effective device for clinical applications. Figure 23.2 shows the use of theranostic nanomaterials in biomedical applications to make healthy life for chronic patients [4–6].

Early diagnosis plays an important role for successful prevention and efficient treatment of diseases with significant recovering rate. However, a nanoparticle-based diagnostic tools lies with their high sensitivity and selectivity as compared to their classical applications based on nanotopography of surface area of particle. Metal oxide nanoparticles have attracted great interest because of their unique physical and chemical properties with their quantum-size effects for its novel applications. Ultra-pure nanoparticles could pass into blood stream like robust missiles to enter, recognizing a malignant tumor and which can scan the status of cancerous growth for its treatment and other abnormal cell behavior along with its defective metabolism chemistry. The surface chemistry of nanosized metal oxide particles plays a crucial role in designing diagnostic tool to differentiate the normal and defective cells behavior by studying the surface morphology of cellular behavior with high reliability and able to give reproducible results with precision. Immune system acts as a protective shield which can safeguard from biological invader. So it is necessary to design cost-effective and patient friendly devices which can be used within immune systems by applying lock–key mechanism. This chapter aims to help create a high performance and multifunctional materials by precisely controlling the well-ordered structure of pure materials in nanoscale, and also to understand the relationship between nanostructure and its functional properties for application as device for surgical applications. The ability of nanostructures to elicit altered cell behaviors, including cell adhesion, proliferation, orientation, mobility, integrin expression, cytoskeletal organization, and modulation with intracellular signaling, has increased more interest for various biomedical applications, such as orthopedic repair and regeneration. Studies have demonstrated that nanofibrous structures can favorably modulate osteoblast, osteoclast, and fibroblast activities toward implant and/or scaffold materials. Designing of surgical tools based on cellular interaction helps to analyze the toxicity of denatured cell with time. In general, the defective cell loses its cellular coordination network due to enzymes/hormone imbalances which leads to aggregations of particle in organelles due to endocytosis and hydrostatic forces [1–6]. The application of biofunctional nanoparticles in the biological system depends as

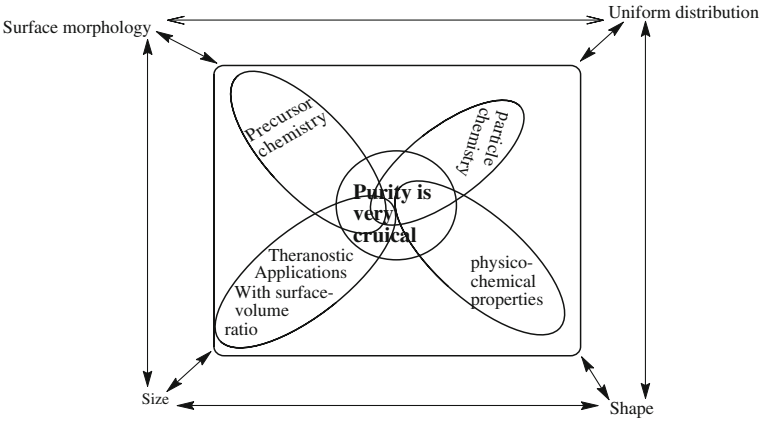

Fig. 23.3 Synergic relationship for diagnostic tool

illustrated in Fig. 23.3. Monodisperse size is very important which depends on dimension for improving applications by studying the surface chemistry in vivo. The synthesis of monodisperse metal oxide nanoparticles with compositions and tuneable sizes has made substantial progress, especially over last 20 years. Controlled synthesis along with mechanistic approach for understanding of nucleation and growth during particle formation remains unanswered. The innovative synthetic method gives a refined control in solid-state structure at the atomic level for an efficient integration of building block with well-defined stoichiometries at low temperature and finally kinetically controlled metastable structure. Aqueous synthetic approaches offers a powerful tool towards the broad aspects of rational synthesis has increased a demand for new innovative nanomaterial along with their higher reactivity of metal alkoxide as starting precursors and with water or ionic solvent to act as solvent and as well as ligand. The slightest change of reaction conditions leads to different particle morphologies, and therefore complicates the synthesis routes toward industrial production. The properties depend on surface structure and or interface which highlight a significant fraction of the total volume. The growth of metal oxide depends on experimental parameters such as precursor solution as well as on concentration of solvent, reaction time, and pH of the reaction.

The synthetic approach plays a crucial role with functional parameters as shown in Fig. 23.4.

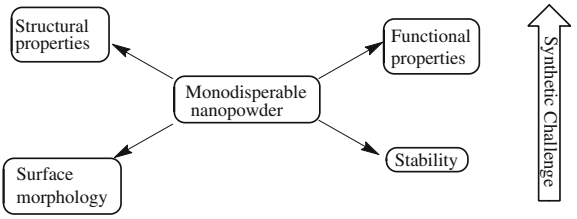

Fig. 23.4 Synthetic challenge for functional-ultra-pure nanomaterials

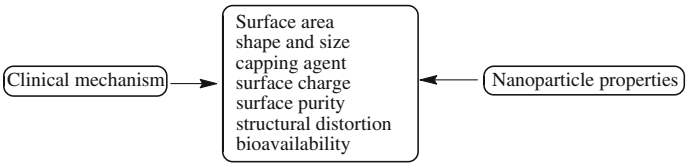

Fig. 23.5 A correlation between clinical mechanism and nanoparticle properties

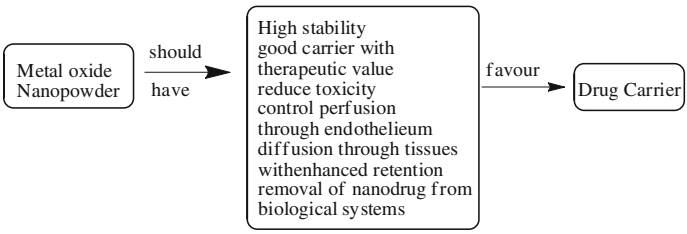

Fig. 23.6 A correlation between metal oxide nanopowder with drug carrier

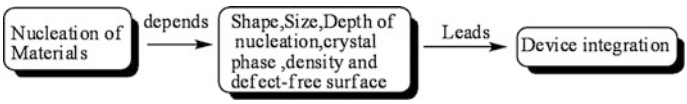

Fig. 23.7 Nucleation of nanopowder with functional properties leads to device integration

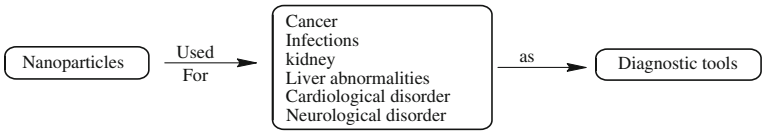

Fig. 23.8 Use of nanoparticles as diagnostic tools for detecting cellular abnormalities

The successful use of nanomaterials depends as given in Figs. 23.5 and 23.6.

The successful use of nanodevice leads to an integration which depends with nucleation as shown in Fig. 23.7.

Ultra-pure, homogenous, and colloidal nanoparticles used as diagnostic tools for various applications as illustrated in Fig. 23.8 by understanding the surface morphology for tuning desired functional properties.

The biocompatibility and biofunctional materials play a key role in applications as shown in Fig. 23.9.

Use of nanoparticles for clinical application depends on better understanding the fundamental and technical physiochemical properties in nanomaterials, which can be controlled with the help of kinetic and thermodynamic studies which finally help

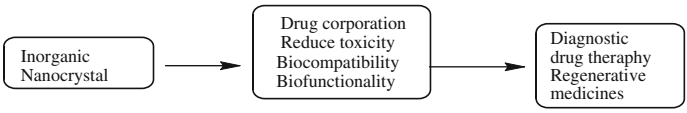

Fig. 23.9 Use of nanoparticles as diagnostic tools for nanomedicines

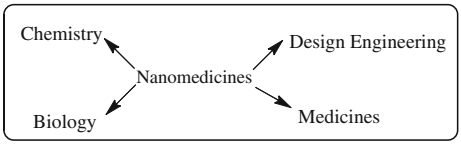

Fig. 23.10 An interdisciplinary science at the interfaces of four subjects

to overcome physiological barriers in human body. Nanoparticles used as drug help to eliminate pathogens by understanding the biological–chemical systems. How the biological systems lead to illness along with curing remains a challenge to the researchers in the present era [7–16]. We have to focus four interface subjects for its successful use of nanomedicines as depicted in Fig. 23.10.

Due to malfunctional behavior of enzymes/hormones leads to weakness in our immune systems which help to detect abnormal cell chemistry with biological fluorescent signals to enhance the functional properties in nanomaterials. The signal intensity increases with purity and due to the surface to volume ratio. The signal frequency in biological system depends on ionization potential as well as electronegativity of metal ion. It is very important to control soft and hard forces during synthesis and its treatment to cure and understand clinical chemistry by preventing agglomeration by restricting soft and hard particle forces. Agglomerated particles are difficult to remove from the body, because kidney losses its filter tendency due to blocking of nephrons, which leads to toxicity. Prominent fluorescent signals help to better understand the illness chemistry for its treatment. It is regarded that biological–chemical imbalance gives rise to illness. Using chemical interaction in the body with metal oxide nanopowder gives signal at the cell surface receptor or proteins and enzymes to give transmitter substance. How to cure illness in the biological systems with the help of nanomedicines is another challenge for clinical scientists in the present era. Curing of illness depends on the strength of cell surface along with interaction of proteins and enzymes to overcome the imbalance between biological and chemical system in between normal and defective cell in cellular systems has to be established at the cellular scale as shown in Fig. 23.11 [1–6].

Fig. 23.11 Potential use of nanoparticles for clinical applications

23.2 Desired Parameters for the Fabrication of Nanodevices for Detecting Abnormal Cellular Activities

1. Synthesis of cost-effective homogenous colloidal nanopowder with purity.
2. The large surface volume ratio with desired shape and size.
3. Tuning of surface morphology with electronic charge for design of biological devices.
4. The functional properties in nanopowder was controlled by thermodynamic–kinetic parameter during nucleation and its growth process.
5. Capable to design patient friendly nanodevices to give reproducible result with minimum time.
6. Control of inter/intraforces to prevent agglomeration for its high performance.
7. To give a high contrast with maximum absorption to study a enhanced permeability and retention.
8. Removal of unreacted nanopowder from the body without any toxic effect and without the of behavior affecting normal cell.

23.3 The Chemical Concept of Functional Metal Oxide Nanoparticles

Nanotechnology can provide a new pathway for innovation a clinical material with noblefunctional properties due to their light weight and flexible behavior along with their characteristic sensibility and multifunctional properties with wide theranostic regime. According to the theory proposed by Gleiter state [17], the surface atoms in the particle have a lower density with low coordination number with high reactivity. A large interatomic distance is able to control a low symmetry. Soft chemical approach gives large variety of metal oxide with novel functional properties with high crystallinity and uniform particle morphologies at moderate temperature. Coordination chemistry provides a new synthetic approach to design a highly organized molecular framework for "nanostructured active support materials" (NASM) with topological architectures. Ultra-pure and colloidal monodispersable syntheses take place with the help of soft chemical approach; a synthesized particle is free from agglomeration with predesigned morphology still remains a synthetic challenge. Novel synthetic approach helps to understand a synthesis of nanostructured materials from precursor, then finally to integrate into devices with the help of controlled surface morphologies. The physical properties changes with electronic, structure, and surface to volume ratio help to control the particle size, shape, and disparity at the nanoscale by controlling the nucleation and its growth process via better understanding the surface morphology during synthesis. With favorable size and shape highlight functional properties due to its quantum confinement of electron within particle regime. The particle in the nanometer range has a strong tendency to agglomerate due to hydrostatic forces as well as Van der Waals interactions and the

thermal energy by considering Boltzmann's thermal energy. With Ostwald ripening process, the small particle due to high surface energy gives a large particles with well-oriented aggregation [18–25], which has to be controlled by better understanding particle–particle intra- and interaction.

The large surface area of nanoparticles can be enhanced with dissolution of water soluble drugs. However, the relationship between surface area and drug solubility can be calculated by the Noyes Whitney equation:

$$\text{Dissolution rate} = \text{A.D.}\,(C_s - C_b)/h$$

where A = Surface area, D = Diffusivity, h = boundary layer thickness, C_s = saturation solubility, and C_b = bulk concentration.

Parameters of metal oxide nanopowder for use in drug delivery systems should have following properties [26]: Stable in blood, nontoxic, nonthrombogenic, non immunogenic, noninflammatory, no activation of neutrophils, biodegerative, and avoidance of the reticuloendothelial systems applicable to various molecules, scalable and with cost-effective synthesis.

23.4 Synthesis of Theranostic Nanoparticles

Metal oxides thermostic nanopowder can be are prepared with desired composition from soft molecular precursors that contain the metal ions as building blocks with the help of bottom-up soft chemical approach with an adjustable particle size, shape and then favorable intra and interparticle space which depends on local environment within the nano-molecular structured framework. In general theranostic homogenous and colloidal nanoparticles with ultra-purity can be synthesized via soft chemical approach with controlled functional properties having a desired shape and surface morphology by understanding the ionization potential, electronegativity, and coordination behavior of central metal ion. For synthesis of nanostructured materials, it is necessary to have sufficient stability to exist within biological environment with the help of inter-related parameters based on kinetic–thermodynamic stability, which help to understand pharmacokinetic behavior at the physiological pH as shown in Figs. 23.12, 23.13 and Tables 23.1, 23.2 [23–29].

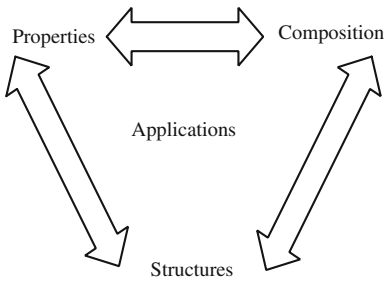

Fig. 23.12 Use of inter-related parameters—a key for success

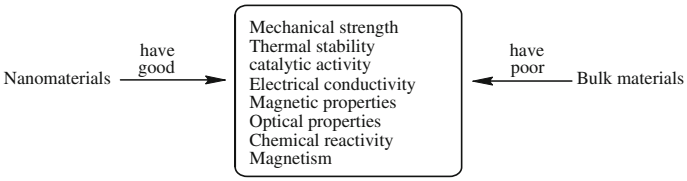

Fig. 23.13 Differences in the functional properties between nano and bulk materials

Table 23.1 Advantages of the soft chemical approach with chemical approach

Soft chemical approach	Chemical approach
Well-defined and uniform crystal morphologies	Less control over crystallite size and shape
Narrow size distribution	Broad size distribution
Ultra-purity with high homogeneity and stoichiometry	Limited purity with homogeneity and stoichiometry
Low agglomeration takes place due to control in nucleation and nuclei growth	Agglomeration not restricted due to heterogeneous nucleation and nuclei growth
Reproducible yield	Sometime reproducible yield
Large-scale production possible	Large-scale production limited
At low temperature	At moderate temperature
Kinetic and thermodynamic	Kinetic and thermodynamic stability under control

Table 23.2 Synthetic methods based on wet chemical approach [24–28]

Methods	Advantages	Disadvantages
Sol-gel	(a) Large scale-up area (b) precise control on composition (c) Low temperature is required (d) High homogeneity with desired Surface properties (e) Simple process treatment	(a) Sensitive towards atmospheric condition (b) Raw material expensive (c) Sometime toxic solvent are used (d) Limited to bench level
Hydrothermal synthesis	(a) No heat treatment is required (b) Less energy consumption (c) No milling process with less impurities (d) Complex chemical composition is obtained (e) Controlled particle size and shape (f) Cheap raw material (g) Environmental benign (h) Large scale industrial production	(a) Aggregation Rate is high (b) Chemical contamination occurs due to combustion (c) High cost equipment (d) Stringent safety precaution are required
Solvothermal synthesis	(a) Narrow particle sized distribution (b) Monolayer ligand coating required (c) Absence of aggregation in polymer matrix (d) Crystallization rate is very high	(a) Difficult for mass production (b) High cost (c) Complicated processing treatment

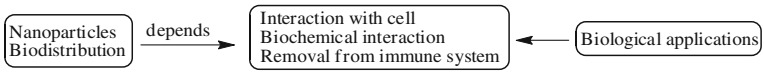

Fig. 23.14 Biodistribution depends on the properties for successful use in biological applications

With the use of Metal oxide nanopowder and good MRI contrast, maximum duration for detecting signal with the help of phagocyte properties remains another challenge to the synthetic chemists and clinical researchers for understanding the cell labeling, cell tracking and MRI contrast in vivo, which help to study thoroughly for its potential applications. Nanoparticles represents an innovative tool in research–therapies with required shape, size, thermodynamic–kinetic stability, biocompatibility, tumor targeting with encapsulation and drug delivery with large contact surface area between cell and nanomaterials remains a challenge in basic biochemical research as illustrated in Fig. 23.14 [1–26, 30].

Chemical synthesis is a key for making useful materials at the molecular level. Within this framework, a simple approach was undertaken for fabrication of nanostructured framework with controlled structure in polymeric matrix. The presence of M–O bond and π–π interactions increase a bond polarity which can be exploited for the synthesis of nanostructured materials by controlling the properties in chelating ligands. Molecular template helps to improve the crystal growth and microstructure behavior at low temperature with less processing time. New synthetic strategies based on novel molecular precursors help to improve physico-chemical properties [7–32].

Novel materials The synthesis of new high-tech and ultra-pure materials will be carried out to understand the change taking place from molecular precursor at the micro-level with tailored properties to design a multifunctional inorganic material at the nanoscale with stoichiometric ratio-structural unit under control.

Analytical tools for its characterizations Sophisticated analytical techniques will be used for its characterizations in term of structural properties and stability. It will also help to better understand the structural-surface–morphology for improving the functional properties.

23.5 State of the Art

1. Synthesis of molecular precursor for design of ultra-pure nanosized functional materials at moderate temperature by retaining compositional uniformity intact.
2. To prepare nanomaterials with tuning of chemical and microstructural properties from micro to nanoscale, which help for better understanding “Design Rule” to enhance the performance based on structural-reactivity properties relationship.

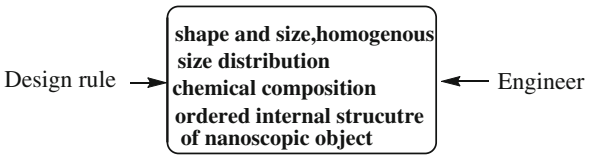

3. To improve an environmental compatibility with the help of green synthetic approach, which depends on reaction time, temperature, and the polarity of the solvents.

The interaction between single source inorganic precursor and the organic template is the key factor to design nano-hybrid materials with desired functional properties for their future use in nanotechnologies has to be clearly studied.

Rational soft chemical reactions with high crystalline and well-defined uniform particle morphologies help following scientific domains:

- The synthesis of novel materials with specific structure and properties helps to better understand the reaction pathways at a molecular level towards nanoscale.
- Large-scale synthesis of ultra-pure smart functional materials with controlled size, morphology, tuneable composition, and crystal structure—key for successful use in biological applications.
- Defect-free crystal growth with low density on the surface will have to be studied for clinical use.

The chemical parameter in the precursor plays a key role to design technological grade nanomaterials at low cost with high reliability and accurate sensitivity.

To design a nanodevice, it is necessary the following parameters have to be followed as illustrated in Fig. 23.15 for designing a nanodevice.

Synthesis and physicochemical properties of molecular precursors will be carried out to design a cost-effective monodispersable crystalline material with specific surface area by controlling surface functional properties with correct phase, size along with its shape at nanoscale as illustrated in Figs. 23.16 and 23.17.

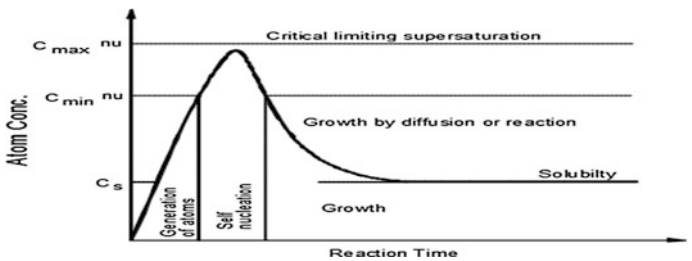

Fig. 23.15 A profile for growth with atomic concentration Vs time Methodology

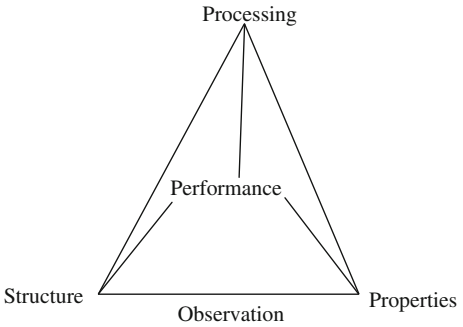

Fig. 23.16 The nanopowder parameters for functional performance

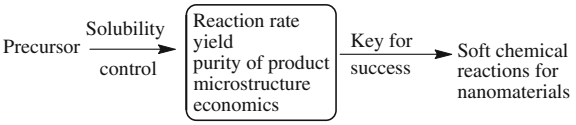

Fig. 23.17 Change in chemistry from precursors to nanomaterials

23.6 Fabrication of Functional Metal Oxide Nanopowder Depends on Following Points for Improving Process Efficiency

1. Particle size and its shape under control along with a uniform distribution.
2. Correct morphology with required phase selection.
3. Strict control between the colloidal electronic forces is required to restrict the degree of agglomeration for better understanding the surface chemistry.
4. Enhancing the physical properties based on geometric and electronic structural properties at the template–nanomaterials interface to control crystalline phenomena with the help of Ostwald ripening process.
5. Multifunctional organic ligands in molecular structure help in stability of nanomaterial by controlling the surface reactivity.

23.7 Synthesis of Biocompatible Metal Oxide Nanopowder

1. Synthesis and characterization of divalent-based metal oxide.

$$MCl_2 + 2KOR \longrightarrow M(OR)_2 + 2KCl \downarrow$$

$$M(OR)_2 + MCl_2 \longrightarrow M_2O_2 + 2RCl \uparrow$$

M = Mg, Sr, Ni, Zn.

2. Synthesis and characterization of trivalent-based metal oxide.

$$MCl_3 + 3KOR \longrightarrow M(OR)_3 + 3KCl \downarrow$$

$$M(OR)_3 + MCl_3 \longrightarrow M_2O_3 + 3RCl \uparrow$$

M = Eu, Tb, Dy, Yb, Ga, Fe

3. Synthesis and characterization of tetravalent-based metal oxide.

$$MCl_4 + 4KOR \longrightarrow M(OR)_4 + 4KCl \downarrow$$

$$M(OR)_4 + MCl_4 \longrightarrow M_2O_4 + 4RCl \uparrow$$

M = Ti, Zr, Hf, Si, Ge, Sn.

Chemical synthesis is a key for making useful materials at the molecular level. The change in chemistry from molecular precursor toward the synthesis of nanomaterial with new physical–chemical–mechanical properties largely depends on change in coordination behavior of central metal ion and also on quantum confinement of electron in nanometer sized structure. The chapter incorporates for flexible synthesis and its characterization which help to design a new nanomaterial with better understanding the particle morphology and kinetic–thermodynamic stability.

1. The synthesis and characterization of metal alkoxides and its conversion into corresponding nanomaterials for improving the efficiency based on structural-reactivity-functional properties.

(a)

$$MCl_2 + 2KM'(OR)_3 \longrightarrow 2KCl \downarrow + [M\{M'(OR)_3\}_2]$$

$$[M\{M'(OR)_3\}_2] + 3M''Cl_2 \xrightarrow[OR]{} [M\{M_2'M_3''O_6\}] + 6RCl \uparrow$$

$$[M'\{M(OR)_3\}_2] + 6H_2O \longrightarrow [M'\{M_2O_6\}] + 6\,ROH + 3\,H_2$$

M = Mg, Ca, Sr, Ba M' = $Ni^{(II)}$, Zn M'' = Ge, Sn, Ba, Sr, Ca
R = CH_3, C_2H_5, $C_3H_7^{n,i}$, $C_4H_9^{n,t}$.

(b)

$$MCl_2 + 3KOR \longrightarrow KM(OR)_3 + 2KCl$$

$$3\,KM(OR)_3 + M'Cl_3 \longrightarrow [M'\{M(OR)_3\}_3] + 3KCl$$

$$2\,[M'\{M(OR)_3\}_3] + 18H_2O \longrightarrow 2[M'\{M_3O_9\}] + 18\,ROH + 9H_2$$

M = Mg, Ca, Sr, Ba, M'= Ce, Eu, Er, Yb, Ga, Al, In, R = CH_3, C_2H_5, $C_3H_7^{n,i}$, $C_4H_9^{n,t}$

(c) $MCl_2 + 3KOR \longrightarrow KM(OR)_3 + 2KCl$

$4\,KM(OR)_3 + M'Cl_4 \longrightarrow [M'\{M(OR)_3\}_4] + 4KCl$

$[M'\{M(OR)_3\}_4] + 12\,H_2O \longrightarrow [M'\{M_4O_{12}\}] + 12\,ROH + 6H_2$

M = Be, Mg, Ca, Sr, Ba, M' = Ti, Zr, Sn, Ge, R = CH_3, C_2H_5, $C_3H_7^{n,\,i}$, $C_4H_9^{n,\,t}$.

(d) $MCl_3 + 3KM'(OR)_4 \longrightarrow 3KCl\downarrow + [M\{M'(OR)_4\}_3]$

$[M\{M'(OR)_4\}_3] + 3M''Cl_2 \longrightarrow 6RCl\uparrow + [M\{M'M''(OR)_2O_2\}_3]$

$[M\{M'(OR)_4\}_3] + 6M''Cl_2 \longrightarrow 12RCl\uparrow + [M\{M'M''_2O_4\}_3]$

$[M\{M'(OR)_4\}_3] + 12H_2O \longrightarrow [M\{M'_3O_{12}\}] + 12ROH + 6H_2$

M = Ce, Eu, Er, Yb, M' = In, Tl, Bi, Al, Ga, M'' =Co, Ni, Zn,
R = CH_3, C_2H_5, $C_3H_7^{n,\,i}$, $C_4H_9^{n,\,t}$.

(e) $MCl_2 + 2KM'(OR)_4 \longrightarrow [M\{M'(OR)_4\}_2] + 2KCl\downarrow$

$[M\{M'(OR)_4\}_2] + 2M''Cl_2 \longrightarrow 4RCl\uparrow + [M\{M'M''(OR)_2O_2\}_2]$

$[M\{M'(OR)_4\}_2] + 4M''Cl_2 \longrightarrow 8RCl\uparrow + [M\{M'M''_2O_4\}_2]$

$[M\{M'(OR)_4\}_2] + 8H_2O \longrightarrow [M\{M'_2O_8\}] + 8ROH + 4H_2$

M = Ni, Zn, M' = Ce, Er, Yb, M'' = Ge, Sn, Sr, Ba, Ca
R = CH_3, C_2H_5, $C_3H_7^{n,\,i}$, $C_4H_9^{n,\,t}$.

(f) $MCl_3 + 4KOR \longrightarrow KM(OR)_4 + 3KCl\downarrow$

$3KM(OR)_4 + M'Cl_3 \longrightarrow [M'\{M(OR)_4\}_3] + 3KCl\downarrow$

$[M'\{M(OR)_4\}_3] + 3M''Cl_4 \longrightarrow [M'\{M''MO_4\}_3] + 12RCl\uparrow$

$[M'\{M(OR)_4\}_3] + 12H_2O \longrightarrow [M'\{M_3O_{12}\}] + 12ROH + 6H_2\uparrow$

M = Ce, Eu, Tb, Er, Yb.
M' = As, Sb, Ga, In, Fe, Al.
M'' = Ge, Sn, Ti, Zr, Hf.

(g) Designed of metallic organic-inorganic hybrid materials.

Hybrid materials can be designed with the coordination of functional groups present (terminal and side chain) in polymer setup having divalent and trivalent metal ions and then characterized in terms of its structure, properties, and stability. The synthesis of hybrid materials will be carried out based on electronic properties of conjugated polymers by controlling surfactants as templates at the molecular level for their potential use. The use of metal oxide nanoparticle plays a key role in controlling the pore size by understanding and adopting the structure properties relationship at micro to nanoscale (Fig. 23.18 and Tables 23.3, 23.4).

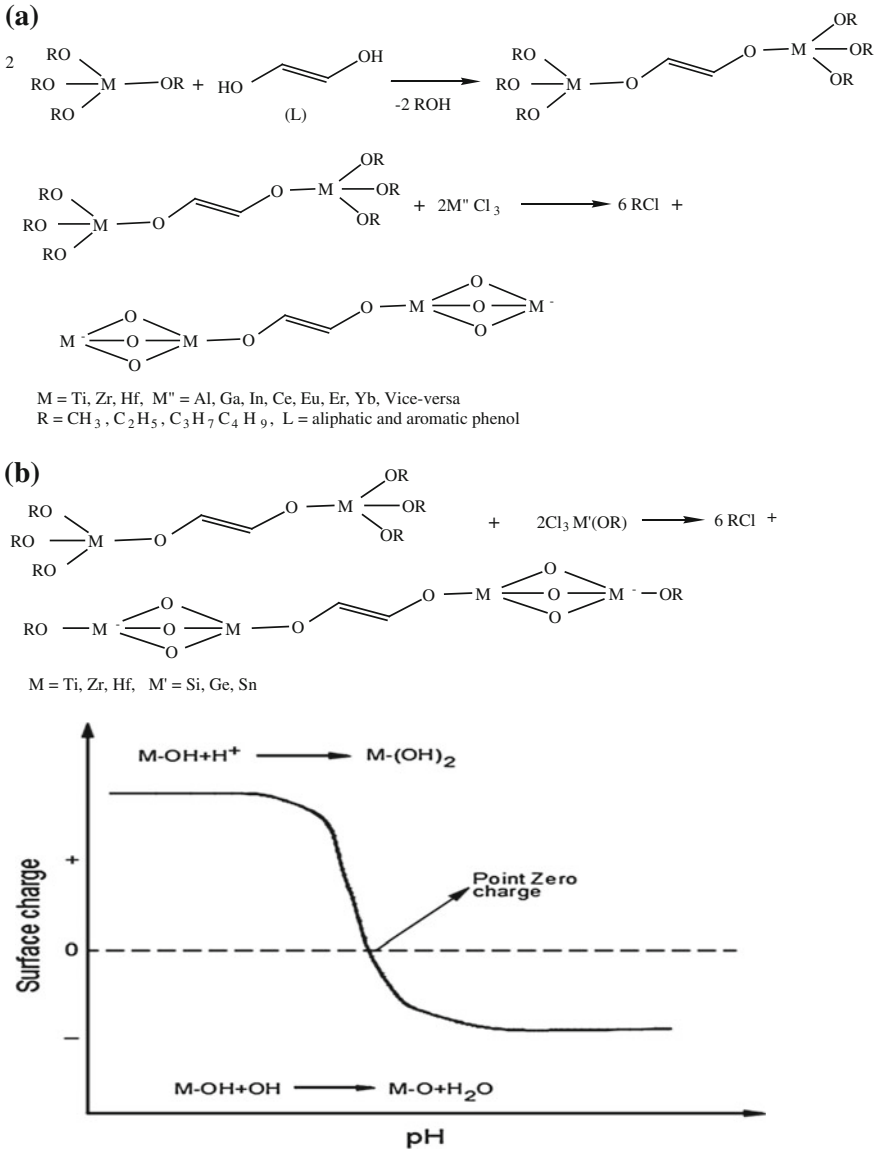

Fig. 23.18 A profile of sol-gel process in acidic and basic conditions

Table 23.3 Synthesis approach with variable parameters

Synthesis	Cost	Crystalline	Phase purity	Size distribution	Size	Stoichiometric ratio	Reaction temperature (°C)	Reproducible yields
Solid state	Fair	Very good	Fair	Wide	Micron	Non-stoichiometric	1000–1400	No
Mechanochemical	Fair	Very good	Fair	Wide	Nano	Non-stoichiometric	Moderate	Random
Precipitation	Fair	Fair	Variable	Variable	Nano	Non-stoichiometric	Moderate	Yes
Hydrolysis	Good	Variable	Good	Variable	Variable	Stoichiometric	Below 100	Yes
Sol-gel	Variable	Fair	Variable	Narrow	Nano	Variable	Below 100	Yes
Hydrothermal	Good	Very good	Good	Wide	Nano or micron	Stoichiometric	100–500	Yes
Emulsion	Good	Fair	Variable	Narrow	Nano	Non-stoichiometric	Moderate	Yes
Sonochemical	Fair	Variable	Good	Narrow	Nano	Variable	Moderate	Yes
Pyrolysis	Fair	Good	Variable	Nano-micron	Variable	Stoichiometric	500–1000	No
Combustion	Fair	Variable	Good	Variable	Variable	Variable	100–600	No

Table 23.4 Use of Metal oxide nanopowder for various applications

Catalytic	Good catalytic efficiency with high surface to volume ratio
Electrical	Good electric conductivity and magnetic properties
Magnetic	Increase in magnetic coercively up to grain size and super paramagnetic properties
Mechanical	Improved hardness and toughness and superplasticity
Optical	Spectral shift in optical absorption and fluorescence properties, increased quantum efficiency of semiconductor crystal
Sterical	Increased selectivity, hollow sphere for specific drug transportation and with controlled release
Biological	Increased permeability through biological barrier, improved biocompatibility

23.8 Characterization Techniques [33–49]

The characterization depends on the state-of-the-art instrumental and manipulates the nanostructure for design an innovative devices. Soft chemical process helps to synthesize a metal oxide nanopowder with high crystalline structure at the low temperature by controlling the reaction parameters without the use of any surfactants. Size, shape, and physicochemical properties of mondisperable nanoparticles are correlated with their chemical transformations based on synthetic parameters. Many analytical approaches were studied for structural properties at the nanoscale along with their structural-surface uniformity as well as for bulk production, which are as follows:

- Ionization takes place by photons and electrons followed by mass spectra for their analysis by means of quadrupole and time-of-flight mass spectrometers.
- Atomization and selection of neutral clusters takes place with respect to their masses.
- Transmission and scanning electron microscopes helps to predict an information regarding size/shape of the particles along with their distribution and topology at the nanoscale.
- Electron diffraction helps to study size and phase's structure along with their bond lengths.
- STM helps to determine the morphological properties along with their surface area.
- Adsorption of gases takes place by particle to give information about their surface area.
- Photoelectron spectroscopy helps to determine the electronic structure of particle.
- Conductivity measurement gives information about the conduction band, percolation, and topology in nanomaterials (Table 23.5).

Table 23.5 Techniques used for characterizations for functional nanomaterials

Method	Properties to be analyzed [33–49]
FTIR	Vibrational stretching frequency of Metal–oxygen bond known as molecular fingerprint
UV-VIS spectra	UV absorption of amorphous gels and crystalline samples were heated at different temperatures. The molecules were promoted from the ground state to an excited state. Each electron vibrates and rotates to each other
Thermal analysis	Weight loss and thermal effects occurs during their conversion from precursors into their final metal oxides nanopowder
Raman spectra	Photons scattering and interaction with other molecule to induce transitions with different energy levels
Mass spectroscopy	It is used to identify unknown sample to elucidate structure and chemical properties of fragmented entity. Separating the ionized species with respects to their mass
XRD	To study an extent of crystallization with shape and size in the sample
BET	Accessible surface area within particle
Synchrotron radiation	The storage ring when charged particle circulate at a speed close to the speed of light
SEM/TEM	To study particle shape, size, surface morphology along with extent of agglomeration
Light scattering method	Particle size distribution
Atomic force microscopy	To study the surface morphology in three dimension for topographic map along with their surface properties
DLS	To characterize dilute and transparent dispersion
Photoluminescence spectroscopy	Characterization, investigation and detection of defects point for measuring the band gap in nanomaterials
Scanning tunneling microscopy	It gives information of surface atomic information by monitoring the current at the tip position along with surface to form image
Vibrating sample magnetometer (VSM)	Magnetic properties of nanomaterials can be measured
NMR spectroscopy	It is used to determine the purity and molecular structure of sample
X-ray crystallography	To see the arrangement of atoms in three dimensional space for sample

23.9 Use of Functionalized Nanoparticles

Nanoscience and nanotechnology have become a multidisciplinary field for research which leads to cost-effective applications. The early stage of clinical diagnosis with precision results remains an important challenge in modern clinical research. Functionalization of nanomaterials with chemical or biological molecules exhibits novel clinical properties to focus track surface modification in nanomaterials to prohibit the spontaneous aggregation and which leads to an elucidating the

interface relationship between nanomaterials and biosystem. The metal oxide nanopowder passes through intravenous administration which depends on their size, morphology, charge and surface chemistry. The physicochemical properties of nanoparticles affect the pharmokinetics and biodistribution intravenously leading toward a general systemic distribution within biochemical system. The biocompatibility of nanomaterials at the subcellular and molecular detection within diagnostic spectrum with ability to monitor malfunctioned biosystem remains a challenge. Metal oxide nanopowder can be tuned with right composition, shape, size, and surface chemistries for its wide applications in biological science at the cellular level both in vitro and in vivo has to be understood in details. Analytical devices help to measure and manipulate interaction within biological moieties and cellular system to determine physical–chemical relationship between cellular components and its ability to understand mechanical and chemical forces within biological pathways, which can be used to study in detail the disease injuries and cure within a clinical parameters. In general, the change in cellular behavior helps in regulation and metabolic pathway at molecular level which is not well understood to overcome clinical barriers. Reliable and reproducible with the precision result depends on purity of nanomaterials can used be as biomarkers. Metal oxide nanopowder attach to biological molecules to exhibit high affinity with selectivity to amplify the signal for detection and molecular imaging.

Functionalization of nanoparticles helps to better understand and optimize the detection of biorelevant molecules within a biological system. Improved material properties enhance the transport properties and pharmacokinetic profiles in vivo after administration as illustrated in Fig. 23.19. Functionalized delivery systems as therapeutic level within clinical time help to overcome physiological and biochemical barrier still remains a challenge. Functionalization of nanoparticles with biocompatible chemical moieties based on structure–function relationship to enhances the clinical efficacy with minimum toxicity [50–53].

The intensive toxicity studies with time reduction can be efficiently applied with the help of through studies of quantitative structure activity–nanostructure relationship (QSANR). Cost-effective synthesis of metal oxide nanopowder has unique structural and functional properties which play an important role in biomedical applications (Figs. 23.20, 23.21 and 23.22).

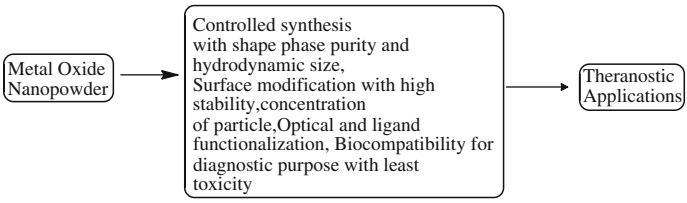

Fig. 23.19 Synergistic relationships between nanoparticles with medical applications

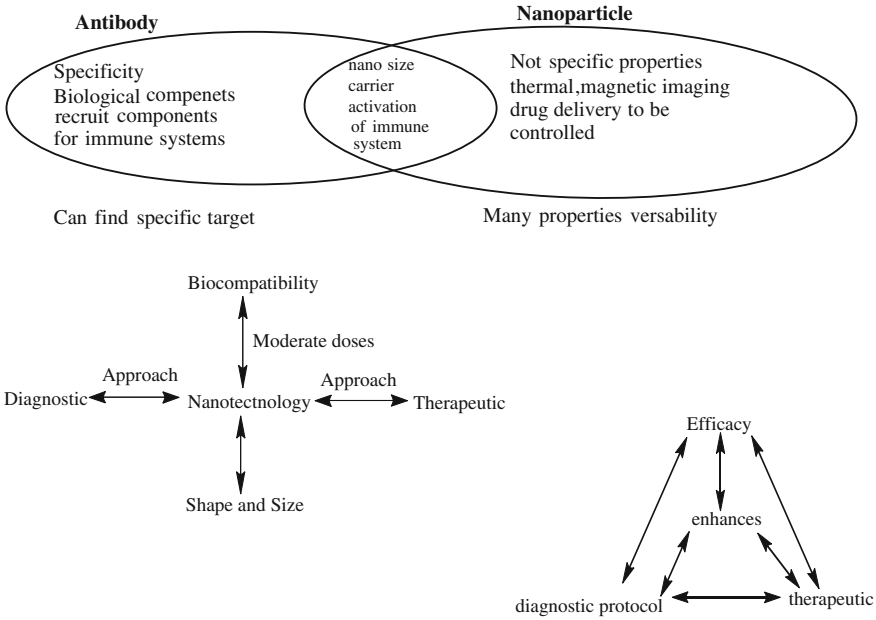

Fig. 23.20 Synergistic relationships with metal oxide nanopowder towards their applications

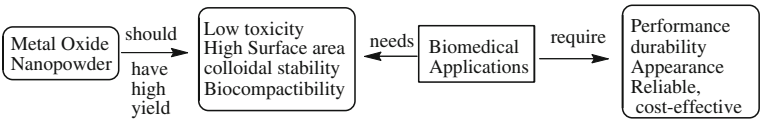

Fig. 23.21 The correlation with number of parameters on the surface with applications

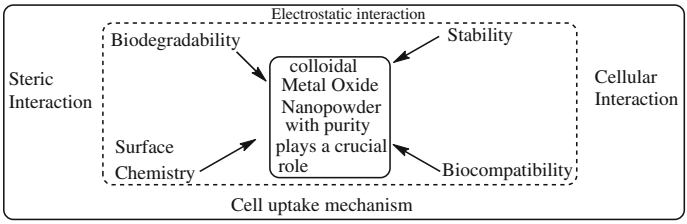

Fig. 23.22 Parameters for intracellular network in macromolecules

23.10 Magnetic Resonance Imaging

MRI is very important diagnostic tool in reporting an internal mapping for biological studies between normal and abnormal cell behavior inside the muscular machine. In general d/f-block elements are used to enhance image quality due to spin shift of 10/14 electrons. In general, dendrimers-based f-elements are used at low concentration for better imaging at different place in the human body. SPOIN nanoparticles give a good signal for liver imaging for cell tracking studies. Nanodelivery devices when implanted in body help to carry out and release of therapeutic drug, can be used in vivo imaging. Magnetic nanoparticles follow Coulomb forces and which can be aimed during tumor excision and minimizing the destruction of normal cell which help to improve the survival rate and quality of life after surgery still remains a challenge. Staining of tumor cell using fluorophores or visible dyes is used for brain tumor surgery. However, many drawbacks exists such as special lighting and fast diminishing of fluorophores/dyes as well as poor visual contrast and target specificity. Attempts have been made to synthesize well-dispersed, monodispersable, and ultra-pure clinical friendly fluorescent nanoparticle with favorable physicochemical properties via soft chemical approach. Fluorescent nanoparticle have many advantages such as selective tumor targeting, tumor–specific targeting moiety, high loading profile with high quality contrast and it zero-level toxicity. However, the selection of metal oxide nanopowder should be able to exhibit conjugation with biocompatible polymer that have a tendency to inhibit brain tumor cell proliferation and invasion to show a fluorescence that can able to cross blood-barrier to reach a target site for change into bulk particles through agglomeration with the help of hard and soft forces in the cellular systems. The polyethylene glycol-based synthetic process was synthesized to enhance biocompatible, stability at the physiological pH, nontoxic and ability to cross other biological barrier. These properties depend on monodispersity, ultra-purity with favorable surface energy, and uniform distribution based on shape and size [50–59].

23.11 Nanoprobes/Chips Array Technology

A nanomaterial gives good result when it is used as bioprobes in vitro. The bioprobes are sensitive to small targets and other defective tissues due to their enhanced volume to surface ratio, surface tailor ability with multifunctional, and intrinsic optical properties to detect and monitor signal variation in the biological system. Large surface area gives high linkages to target-specific molecules for ultrasensitive detection and with an improved sensitivity at the molecular or single cell level help for screening.

Quantum dots have nanoscale crystal with metal core which shows size-dependent optical properties. UV to near-IR region with long fluorescence is a life time help for studying biological parameters in vitro/vivo. The quantum dots

have effective link with acceptors and to amplify target signal via enhanced energy-transfer efficiency. Quantum dots with optical probes are used in signal transduction with their better fluorescence resonance energy-transfer properties which help to detect denatured proteins, peptides, as well as other defective small bioactive molecules.

23.12 Nanoparticles Use as Therapeutic Medicines

Nanoparticles with favorable shape and size can be used as nanomedicines because it has a tendency to overtake biological barrier which help to localize the specific sites in the tissue system. Metal oxide nanopowder enters in cell and then circulates through the body by overcoming blood brain barrier. The nanoparticles can be used as a vector/active carrier that to be used as drug itself. The site for target tissues can be either passive or active site for which can be localized for the release of payload. Further, nanoformulation can release drug release profile for 24 h. On the basis of diagnostic profile improve the patient conditions with the help of molecular reorganization of detective sites [4, 54].

23.13 Use of Cancer Drug Based as Nanocarrier

Treatment of cancer needs a better understanding of tumor biochemical studies with the help of diagnostic systems for its treatment modalities. In general, chemotherapy is used for the treatment of cancer; however chemotherapy have significant systemic side effects due to nonspecific action of drug during treatment either passive or active target cancer cell. Chemotherapy affects both cancerous and non-cancerous cells, thereby normal cell loses its efficacies due to toxicity. The treatment gives only 40 % success for controlling the cancerous cell, simultaneously 60 % normal cell losses its functionality, thereby patient becomes weak with nausea and drastic body loss. Due to non-coordinated behavior of cancerous cell with abnormal morphology in cellular structure and with high uncontrolled physiological behavior effect cell efficiency: (1) Undisciplined and irregular arrangement of blood vessels, (2) cancer blood vessels have an excess anionic phospholipids and proteoglycans, and (3) vascular network with increased permeability in macromolecules. Specific size nanoparticles have the ability to extravasate and accumulate into cancerous tissues due its weak cell wall increase the permeability and retention effects for an effective treatment with reduced drug toxicity. Liposomes have spherical self-closed structure with concentric lipid bilayers having inner aqueous compartment acts as a biological membranes with the help of lipids then, solubility of hydrophobic chemo drug can be increased and finally trap the drug molecule with high potency and increase a prolonged plasma half-life due to exposure of PEG surface which finally form a protective layer around liposome,

which help to reduce clearance by macrophage in reticuloendothelial system to inhibit tumor growth with reduced toxicity [1, 2, 50–59].

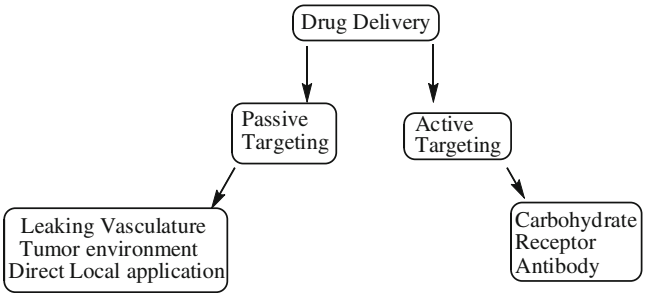

Dendrimers show good delivery system to carry out the anticancer drug. Dendrimer is also used for gene delivery for treatment of neuroblastoma and effectively modulate immune response as shown in Fig. 23.23.

23.14 Use of Nanoparticles for Vaccines/Gene Delivery

In general vaccines consists of polynucleotide, DNA vaccines and plasmid vaccines for efficient delivery to the target cell population at a localized sites in the nucleus, thereby ensuring the integrity of poly nucleotides at the target size which help to maximize the biological efficiency with continuous production of specific antibody for curing. It can be used for treatment of cardiovascular, neurological, infectious disease, wound healing and cancer [60–67].

23.15 Metallic Nanoparticles Without Any Protective Layer

Metallic nanoparticles can be used for antibacterial and antiinflammatory action leads to fast healing of wounds [60–65].

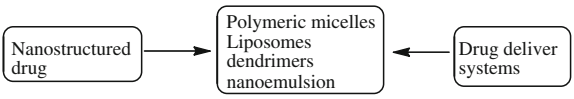

Fig. 23.23 Drug can be delivered with the use of nanocarriers as drug delivery system

23.16 Nano-Surgery

Advance research leads to a new concept which is termed as nanoscale surgery. Cellular structure can be modified at the nanoscale level using femtosecond laser pulse. From femto-laser pulse can selectively cut single strand from single cell or even organelles within a cell and which can be easily removed from the body without disturbing nearby cell. The principle for nano-cryosurgery provides a specific loading of nanoparticles around the cancerous cell. Due to rapid cooling, the loading of nanoparticles ables to freeze in the cell later on helps to induce apoptosis and for its curative efficiency. The cure of cancer can be predicted with cyrotechniques in near future [60–67].

23.17 Use of Nanoparticles in Regenerative Medicines

The damaged tissues or organs can be used for regeneration of tissues or bone with the help of biocompatible nanoparticles. In general the nanoparticle was used for skin or bone curing. Nanoparticles work as a powerhouse in regenerative applications due to its high surface energy which heals to restore bio mechanical functions by enhancing keratocyst proliferation in the epithelization to form myo-fibroblast for wound contraction due to elastic forces present in the nanostructure framework. The nano-based collagen-hydroxyapatite scaffold can be used in bone matrix for stem cell in order to enhance osteoblasts process without any toxic effects [1–6, 61–64].

23.18 Nanoparticles for Orthopedic Applications

Nanostructured surface exhibits strong influence for protein adsorption and cell adhesion morphology with differentiation as well as for production and secretion of matrix at the extracellular molecules. The synthesis of nanostructured powder depends on structure of bone with composite and hydroxyapatite crystals and collagen fibrils gives reliable results with minimum toxicity [62–74].

23.19 Renal Clearance

Renal clearance from the body is based on physical filtration the toxic, denatured protein other waste materials are passed through urine with minimal side effects. Renal clearance of size-dependent, surface charge and surface chemistry of

nanoparticles is a passive process which involves glomerular filtration and tubular secretion. However, with surface charge is another factor which absorbs serum protein elutes material through hydrodynamic process [67–74].

23.20 Conclusions

When functional nanoparticles with structure–function relationship are used as efficiently nanomedicines, they will help to enhance the diagnostic and therapeutic applications in clinical use with reduced side effect. In future with the help of better understanding biochemical reactions with nanoparticles can serve as an effective result-oriented nanotool for better health-care system. The chapter aims at "Molecular recognition" for the synthesis of functional surface morphology in nanomaterial with controlled self-assembly which can be used for its potential use in different technologies via better understanding the process involved at micro to nanoscale structural information in the molecular precursor. The synthetic proof-of-concept gives an innovative approach to enhance the surface–volume properties relationship, with the role of metal ion, the purity of the precursor along with its chemical composition. To control uniform active sites with high selectivity-activity-sensitivity remains a synthetic challenge in nanomaterials. It is concluded that Metal oxide nanopowder are very useful for clinical diagnosis as curing therapy based on for better understanding their performance with surface engineering extended toward the circulation time and to overcome biological barriers in organ, tissue, at the cellular levels with its clinical applications in the near future with favorable physicochemical properties, toxicity and rejection from the body. Toxicity is highly dependent on physical, chemical, and structural properties as well as dose intended for use as metal oxide nanopowder in diagnostic tools (Figs. 23.24 and 23.25).

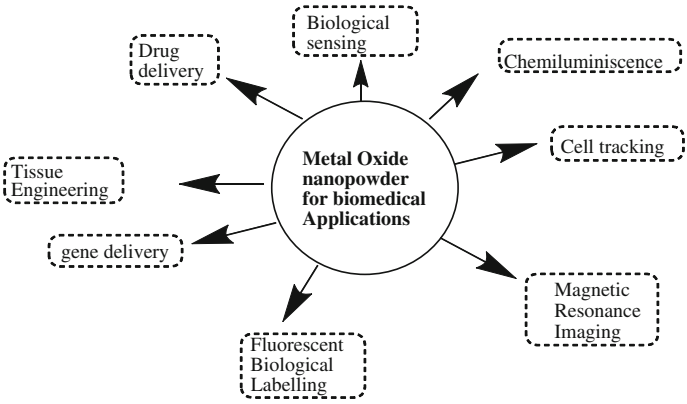

Fig. 23.24 Biomedical applications of metal oxide nanopowders

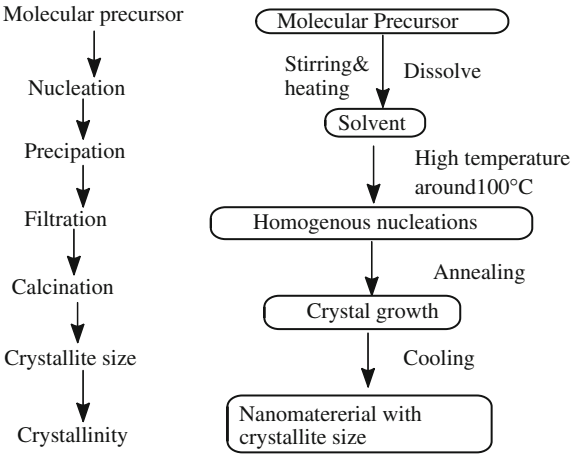

Fig. 23.25 A graphical stretch for the synthesis of nanomaterials

References

1. Talha, J. E., Nadia, M. Z., Abdelhamid, E. S., & Nasir, M. A. (2014). Handbook of soft nanoparticles for biomedical applications. In J. Callejas-Fernández & J. Estelrich (Eds.), *RSC Nanoscience and Nanotechnology* (pp. 312–341). ISBN 978-1-84973-811-8.
2. West, A. R. (1984). *Solid state chemistry and its applications* (p. 488). Hoboken: Wiley. ISBN 978-1-119-94294-8.
3. Jain, K. K. (2008). Nanomedicines: Application of nanobiotechnology in medical practice. *Medical Principles and Practice, 17*(2), 89–101.
4. Solomon, M. D., & Sourza, G. G. (2011). Recent progress in the therapeutic applications of nanotechnology. *Current Opinion in Pediatrics, 23*(2), 215–220.
5. Zhang, L., Gu, F. X., Chan, J. M., Wang, A. Z., Langer, R. S., & Farokhzad, O. C. (2008). Nanoparticles in medicines, therapeutic applications and developments. *Clinical Pharmacology and Therapeutics, 83*(5), 761–769.
6. Azzazy, H. M., Mansour, M. M., & Kazmierczak, S. C. (2006). Nanodiagnostic: A new frontier for clinical laboratory medicines. *Clinical Chemistry, 52*(7), 1238–1246.
7. Fendler, J. H. (Ed.) (1998). *Nanoparticles and nanostructured films*. Weinheim: Wiley. doi:10.1002/9783527612079
8. Jolivet, J. P. (2000). *Metal oxide chemistry and synthesis, from solution to solid state*. Chichester: Wiley. ISBN 978-0-471-97056-9.
9. Koch, C. C. (2002). *Nanostructured materials*. New York: William Andrew Publishing. ISBN 10:0-8155-1354-0-08154.
10. Yang, P. (2003). *The chemistry of nanostructured materials*. World Scientific. ISBN 130-978-981-4313-06-3.
11. Fedlheim, D. L., & Foss, C. A. (2001). *Metal nanoparticles*. CRC Press. ISBN 9780824706043.
12. Cao, G. (2004). *Nanostructures and nanomaterials*. Imperial College Press. ISBN 13:978-1860944802.
13. Vollath, D. (2008). *Nanomaterials*. Wiley. ISBN 978-3-527-33379-0.
14. Lalena, J. N., & Cleary, D. A. (2010). *Principles of inorganic materials design*. New York: Wiley. ISBN 978-0-470-40403-4.
15. Bandyopadhyay, A. K. (2007). *Nanomaterials*. New Age International. ISBN 978-81-224-2009-8.

16. Marzan, L. M., & Kamat, P. V. (2003). *Nanoscale materials*. Springer. ISBN 978-0-306-48108-6.
17. Keblinski, P., Wolf, O., Cleri, F., Phillpot, S. R., & Gleiter, H. (1998). *MRS Bulletin* 23(9), 36–41.
18. Mathur, S., Shen, H., & Nalwa, H. S. (2004). Inorganic nanomaterials from molecular templates. *Encyclopedia of Nanoscience and Nanotechnology 4*, 131–191. ISBN 1-58883-159-0.
19. Wells, F. (1975). *Structural inorganic chemistry*. Oxford: Clarendon Press. ISBN 9780198553700.
20. Klabunde, K. J., & Richards, R. M. (2012). *Nanoscale materials in chemistry* (2nd ed.). New York: Wiley. ISBN 978-0-470-22270-6.
21. Muller, A., Cheetham, A. K., & Rao, C. N. R. (2007). *Nanomaterials chemistry: Recent developments and new directions.* Wiley. doi:10.1002/352760247X
22. Fierro, J. L. G. (2005). *Metal oxide: Chemistry and applications*. Taylor & Francis. ISBN 9780824723712.
23. Schubert, U., & Hüsing, N. (2000). *Synthesis of Inorganic materials*. Weinheim: Wiley. ISBN 3-527- 29550-X.
24. Rodriguez, J. A., & Garcia, M. F. (2007). *Synthesis, properties and application of oxide nanomaterials*. Hoboken: Wiley. ISBN 978-0-471-72405-6.
25. Athar, T. (2008). Metal oxide nanopowder. In W. Ahmad & M. Jackson (Eds.), *Emerging nanotechnologies for manufacturing* (Vol. 13, pp. 13818). Eaton Avenue, Norwich, NY: William Andrews Inc. ISBN 978-0-8155-1583-8.
26. Kohli, P., & Martin, C. (2005) *Res. Curr. Pharm. Biotechnol*. *6*(1), 35–47. doi:10.2174113892010536721l
27. Mackenzie, J. D., & Bescher, E. P. (2007). Chemical routes in the synthesis of nanomaterials using the sol–gel process. *Accounts of Chemical Research 40*(9), 810–818. doi:10.1021/ar7000149.
28. Edler, K. J. (2004). *Sol-gel processing*. London: Kluwer. ISBN 1-4020-7969-9.
29. Klein, L. C. (1988). *Sol-gel technology for thin film, fibres, performs, electronic, and speciality shape*. Mill Road, Park Ridge, New Jersey,USA: Noyes Publications. ISBN 0-8155-1154-X.
30. Sapra, P., & Sarma, D. D. (2004) *The chemistry of nanomaterials: Synthesis properties and application*. In C. N. R. Rao, A. Muller & A. K. Cheetham (Eds.), Weenheem: Wiley. doi:10.1002/352760247X.ch11
31. Sakka, S. (Ed.) (2004). *Hand book of sol-gel science and technology: Processing, characterization and applications*. Norwell, USA: Kluwer Academic Publishers. ISBN 1-4020-7966-4.
32. Brinker, C. J., & Scherer, G. W. (1990). *Sol-gel science: The physics and chemistry of sol-gel processing* (p. 108). San Diego: Academic Press. ISBN 0-12-134970-5.
33. Pavia, D. L. G. L., Kriz, G. S., & Vyvyan, J. R. (2009). *Introduction to spectroscopy* (4th ed.). USA: Brooks/cole Cengage Learning. ISBN 13:978-0-495-11478-9.
34. Skoog, D. A., Holler, F. J., & Crouch, S. R. (2007). *Principles of instrumental analysis* (6th ed., p. 169). Belmont, CA: Thomson Brooks/Cole. ISBN 0495012017.
35. Stuart, H. B. (2004). *Infrared spectroscopy fundamentals and applications*. Chichester: Wiley. ISBN 978-0-470-85428-0.
36. Atkins, P., & Paula, J. (2006). *Physical chemistry* (8th ed.). New York: Oxford University Press.
37. Nakamoto, K. (2008). *Infrared and Raman spectra of inorganic and coordination compounds* (6th ed.). Wiley-Interscience. ISBN 978-0-471-74493-1.
38. Davydov, A. A. (1990). *Infrared spectroscopy of absorbed species on the surface of transition metal oxides*. Wiley. ISBN 047191813X.
39. Soacrates, G. (2001). *Infrared and Raman characteristic group frequencies: Tables and charts*. Wiley. ISBN 10 0-470-09307-2.
40. Mitra, S. (2003). *Sample preparation techniques in analytical chemistry*. New Jersey: Wiley. ISBN 0-471-32845-6.

41. Lakowicz, J. R. (2006). *Principle of fluorescence spectroscopy* (3rd ed.). Baltimore: Springer. ISBN 978-0-387-46312-4.
42. Cullity, B. D. (1978). *Elements of X-ray diffraction*. London: Addison-Wesley Publishing Company Inc. ISBN 1178511421, 9781178511420.
43. Guinier, A. (1994). *X-ray diffraction in crystals, imperfect crystals and amorphous bodies*. New York: Dover Publications. ISBN 0486680118, 9780486680118.
44. Klug, M. P., & Alexander, L. E. (1974). *X-ray diffraction procedure for polycrystalline and amorphous materials*. New York: Wiley. ISBN 978-0-471-49369-3.
45. Powder Diffraction Files. (2015–16). JCPDS. (Ed:International Center for Diffraction Data, Pasadena, CA). http://www.icdd.com/
46. Watt, I. M. (1997). *The principles and practice of electron microscopy* (2nd ed.). Cambridge: Cambridge University Press. ISBN 978-0521435918.
47. Gabbott, P. (2007). *Principles and applications of thermal analysis*. USA: Wiley-Blackwell Publishing. ISBN 978-1-4051-3171-1.
48. Niasaria, M. S., Mir, N., & Davar, F. (2009). Synthesis and characterization of NiO nanoclusters via thermal decomposition. *Polyhedron 28*(6), 1111–1114. doi:10.1066/j.poly.2009.01.026
49. Gelb, L. D., & Gubbins, K. E. (1998). Pore size distributions in porous glasses. *Langmuir 14* (8), 2097–2111. doi:10.1021/la9808418
50. Bae, K. H., Chung, H. J., & Park, T. G. (2011). Nanomaterials for cancer therapy and imaging. *Molecules and Cells 31*(4), 295–302.
51. Barreto, J. A., Malley, W. O., & Kubeil, M. (2011). Nanomaterials: Applications in cancer imaging and therapy. *Advanced Materials, 23*(12), H18–H40.
52. Jain, K. K. (2010) Advances in the field of nanooncology. *BMC Med 8*(83).
53. Ranganathan, R., Madanmohan, S., & Kesavan, A (2012). Nanomedicines: Towards development of patient-friendly drug-delivery systems for oncological applications. *International Journal of Nanomedicines 7*, 1043–1060.
54. Bhattacharya, R., & Mukherjee, P. (2008). Biological properties of Naked metal nanoparticles. *Advanced Drug Delivery Reviews, 60*(11), 1289–1306.
55. Veiseh, O., Sun, C., & Fang, C. (2009). Specific targeting of brain tumors with an optical/magnetic resonance imaging nanoprobes across the blood-brain barrier. *Cancer Research, 69*(15), 6200–6207.
56. John, R., & Boppart, S. A. (2011). Magnetomotive molecular nanoprobles. *Current Medicinal Chemistry, 18*(14), 2103–2114.
57. Orringer, D. A., Koo, Y. E., Chen, T., Kopelman, R., Sagher, O., & Philbert, M. A. (2009). Small solution for big problems: The application of nanoparticles to brain tumor diagnosis and therapy. *Clinical Pharmacology and Therapeutics, 85*(5), 531–534.
58. Mahmoudi, M., Sant, S., Wang, B., Laurent, S., & Sen, T. (2011). Superaparamagnetic Iron oxide nanoparticles (SPIONS): Development surface modification and applications in Chemotherapy. *Advanced Drug Delivery Review, 63*(1–2), 24–26.
59. Pan, Y., Du, X., Zhao, F., & Xu, B. (2012). Magnetic nanoparticles for manipulation of proteins and cells. *Chemical Society Review, 41*, 2912–2929.
60. Kuntz, E. H., & Kuntz, H. D. (2006). *Hand book of hepatology: Principles and practice: History, morphology, biochemistry, diagnostics, clinic, therapy* (2nd ed., p. 3). Heidelberg: Springer. ISBN 978-3-540-28977-7.
61. Modi, G., Pillay, V., & Choonara, Y. E. (2012). Nanotechnological applications for the treatment of neurodegenerative disorders. *Progress in Neurobiology, 88*(4), 272–285.
62. Streiecher, R. M., Schmidt, M., & Fiorito, S. (2007). Nanosurfaces and nanostructures for artificial implants. *Nanomedicines, 2*(6), 861–874.
63. Chun, Y. W., & Webster, T. J. (2007). The role of nanomedicines in growing tissues. *Annals of Biomedical Engineering, 37*(10), 2034–2047.
64. Laurencein, C. T., Kumbar, S. G., & Nukavarapu, S. P. (2007). Nanotechnology and orthopedics: A personal perspective. *Wiley Interdisciplinary Reviews: Nanomedicine and Nanobiotechnology, 1*, 6–10.

65. Hirst, S. M., Karakoti, A. S., & Tyler, R. D. (2009). Anti-inflammatory properties of CeO_2 nanoparticles. *Small (Weinheim an der Bergstrasse, Germany), 5*(24), 2848–2856.
66. Koo, O. M., Rubinstein, I., & Onyuksel, H. (2005). Role of nanotechnology in targeted drug delivery and imaging: A concise review. *Nanomedicine: Nanotechnology, Biology and Medicine*, 1193–212.
67. Wagner, V., Dullaart, A., Bock, A. K., & Zweck, A. (2007). The emerging nanomedicine landscape. *Nature and Biotechnology, 24*, 1211–1217.
68. Chakraborty, M., Jain, S., & Rani, V. (2011). Nanotechnology: Emerging tool for diagnostics and therapeutics. *Applied Biochemistry and Biotechnology, 165*(5–6), 51178–51687.
69. Riehemann, K., Schneider, S. W., Luger, T. A., Godin, B., Ferrari, M., & Fuchs, H. (2009). Nanomedicine—challenge and perspectives. *Angewandte Chemie, 48*(5), 872–897.
70. Petros, A., & DeSimone, J. M. (2010). Strategies in the design of nanoparticles for therapeutic applications. *Nature Reviews Drug Discovery, 9*, 615–627.
71. Praveen, S., Misra, R., & Sahoo, S. K. (2012). Nanoparticles: A boon to drug delivery, therapeutics, diagnostics and imaging. *Nanomedicines, 8*, 147–166.
72. Cui, Y., Wei, Q., Park, H., & Lieber, C. M. (2001). Nanowire nanosensor for highly sensitive and biological and chemical species. *Science, 293*, 1289–1293.
73. Albanese, A., Tang, P. S., & Khan, W. C. (2012). The effect of nanoparticles size, shape and surface chemistry on biological systems. *Annual Review of Biomedical Engineering, 14*, 1016.
74. Sapsford, E., Algar, W. R., Berti, L., Gemmill, K. B., Casey, B. J., Oh, E., et al. (2013). "Functionalizing nanoparticles with biological molecules: Developing chemistries that facilitate nanotechnology. *Chemical Reviews, 113*(3), 1904–2074.

Correction to: Applications of Carbon Nanotubes in Bio-Nanotechnology

T. Okpalugo, W. Ahmed and M. J. Jackson

Correction to:
Chapter 12 in: W. Ahmed and M.J. Jackson (eds.),
***Surgical Tools and Medical Devices*,**
https://doi.org/10.1007/978-3-319-33489-9_12

The published version of the book contained an author in Chap. 12 (J. A. Byrne) who did not contribute to the chapter. We have removed him as a chapter author in the revised chapter.

The updated version of this chapter can be found at
https://doi.org/10.1007/978-3-319-33489-9_12

W. Ahmed and M. J. Jackson (eds.), *Surgical Tools and Medical Devices*,
https://doi.org/10.1007/978-3-319-33489-9_24

Editors' Vitae

Prof. Mark J. Jackson
Professor of Engineering,
School of Aviation and Interdisciplinary Studies,
Kansas State University,
United States of America.

C. Eng., Engineering Council of London, U.K., 1998
M. A. Status, Natural Sciences, University of Cambridge, U.K., 1998
Ph.D., Mechanical Engineering, Liverpool, U.K., 1995
M. Eng., Mechanical & Manufacturing Engineering, Liverpool, U.K., 1991
O.N.D., Mechanical Engineering, Halton College, U.K., 1986
O.N.C. Part I, Mechanical Engineering, Halton College, U.K., 1984.

Dr. Jackson began his engineering career in 1983 when he studied for his O.N.C. part I examinations and his first-year apprenticeship training course in mechanical engineering. After gaining his Ordinary National Diploma in Engineering with distinctions and I.C.I. prize for achievement, he read for a degree in mechanical and manufacturing engineering at Liverpool Polytechnic and spent periods in industry working for I.C.I. Pharmaceuticals, Unilever Industries, and Anglo Blackwells. After graduating with a Master of Engineering (M. Eng.) degree with Distinction under the supervision of Prof. Jack Schofield, M.B.E., Dr. Jackson subsequently read for a Doctor of Philosophy (Ph.D.) degree at Liverpool in the field of materials engineering focusing primarily on microstructure–property relationships in vitreous-bonded abrasive materials under the supervision of Prof. Benjamin Mills. He was subsequently employed by Unicorn Abrasives' Central Research & Development Laboratory (Saint-Gobain Abrasives' Group) as materials technologist, then technical manager, responsible for product and new business development in Europe, and university liaison projects concerned with abrasive process development. Dr. Jackson then became a research fellow at the Cavendish Laboratory, University of Cambridge, working with Prof. John Field, O.B.E., F.R.S., on impact

W. Ahmed and M.J. Jackson (eds.), *Surgical Tools and Medical Devices*,
DOI 10.1007/978-3-319-33489-9

fracture and friction of diamond before becoming a lecturer in engineering at the University of Liverpool in 1998. At Liverpool, Dr. Jackson established research in the field of micromachining using mechanical tools, laser beams, and abrasive particles. At Liverpool, he attracted a number of research grants concerned with developing innovative manufacturing processes for which he was jointly awarded an Innovative Manufacturing Technology Center from the Engineering and Physical Sciences Research Council in November 2001. In 2002, he became associate professor of mechanical engineering and faculty associate in the Center for Manufacturing Research, and Center for Electric Power at Tennessee Technological University (an associated university of Oak Ridge National Laboratory), and a faculty associate at Oak Ridge National Laboratory. Dr. Jackson was the academic adviser to the Formula SAE Team at Tennessee Technological University. In 2004 he moved to Purdue University as Professor of Mechanical Engineering, and to the School of Aviation and Interdisciplinary Studies at Kansas State University in 2013 where he is developing programs in the area of unmanned aerial systems, bulk solids, and innovative manufacturing.

Dr. Jackson is active in research work concerned with understanding the properties of materials in the field of microscale metal cutting, micro- and nanoabrasive machining, and laser micromachining. Dr. Jackson has directed, co-directed, and managed research grants funded by the Medical Research Council, Engineering and Physical Sciences Research Council, The Royal Society of London, The Royal Academy of Engineering (London), European Union, Ministry of Defense (London), Atomic Weapons Research Establishment, National Science Foundation, N.A.S.A., U.S. Department of Energy (through Oak Ridge National Laboratory), Y12 National Security Complex at Oak Ridge, Tennessee, and Industrial Companies, which has generated research income in excess of $15 million. Dr. Jackson has organized many conferences and served as General Chair of the International Surface Engineering Congress and as Deputy President of the World Academy of Materials and Manufacturing Engineering. He has authored and co-authored over 200 publications in archived journals and refereed conference proceedings, has written a book on "microfabrication and nanomanufacturing," and is guest editor to a number of refereed journals.

Prof. Waqar Ahmed
School of Medicine,
Professor of Nanotechnology,
University of Central Lancashire,
United Kingdom.

Ph.D., Chemistry, University of Salford, U.K., 1985
B.Sc. (Hons.), Chemistry and Biochemistry, University of Salford, U.K., 1982.

Waqar Ahmed is currently Chair of Nanotechnology in the School of Medicine at the University of Central Lancashire. He obtained his B.Sc. in Science and Ph.D.

in Physical Chemistry from Salford University. His research involved "Low Pressure Chemical Vapor Deposition of In-situ Doped Polycrystalline Silicon for Microelectronic Devices" sponsored by G.E.C. Research. Along with his supervisor, Prof. Hitchman, he developed kinetic models for obtaining a better fundamental understanding of in-situ doped LPCVD process employed in semiconductor industry. The modeling work was coupled experimental work involved in-situ analysis of the gas-phase species involved in the CVD process. He spent his early career in the semiconductor industry working for GEC Hirst Research Center, Wembley, U.K., Ferranti Electronics, and INMOS, working on practical applications of CVD, ion implantation, oxidation, and diffusion processes for device manufacturers in high-pressure production environments. At G.E.C. he developed Ultra High Vacuum CVD Processes for deposition of large grained polysilicon and doped polysilicon for liquid crystal displays working primarily on developing an understanding of the kinetics of these processes and developing industrial solutions to within-wafer uniformity problems associated with in-situ doping processes. This was followed by a spell at VSW Scientific Instruments as Product Manager of the Molecular Beam Division developing novel molecular beam scattering systems for leading academics in the field such as Prof. Sir David King (Cambridge), Prof. Neville Richardson (Liverpool IRC in Surface Science), Prof. H. Reider (Berlin) and Professor John Foord (Oxford). He then set up the Surface Engineering Division with Prof. David Armour and Prof. Derek Arnell at Salford University as Operations Manager in order commercialize the surface engineering activity within the University and co-ordinated the North West Surface Engineering Initiative involving leading research centers around the North West Region including IRC in Surface Science, Liverpool; Daresbury Research Laboratories, Advanced Manufacturing Research Institute, Manchester Corrosion Protection Center, and PREST funded by the DTI. He has acted as a consultant to Daresbury Laboratory for commercialization of some of its research activity. In 2010, he founded the multidisciplinary Institute of Nanotechnology and Bioengineering involving staff and facilities several schools at UCLAN with Professor David Phoenix (now Vice Chancellor London South Bank University). His current interest involves exploring the science and applications of nanotechnology in medicine and dentistry.

He has published over 500 peer reviewed papers and authored/edited 25 books. He, and his co-workers, has also contributed to the wider industrial adoption of surface coating solutions, through research into modeling of gas phase processes in CVD and studies of tribological behavior. His move to Ulster University at the end of 2005 involved a widening of his group's research, to include the development of nanoparticles, nanocomposite coatings, laser assisted processes, and functional thin films and devices. He has been active in the international vacuum coating scene for many years, including involvement in organizing EU—Two Stroke Engine Workshops, the International Surface Engineering Congress 2004, 2005 and 2006, NanoMATS 2005 in Aveiro, Portugal, International Surface Engineering Conference in Newcastle 1995, and Thin Films 2006 in Singapore. He has acted as a Proceedings Co-Editor and Program Chair for ISEC 2005 and 2006.

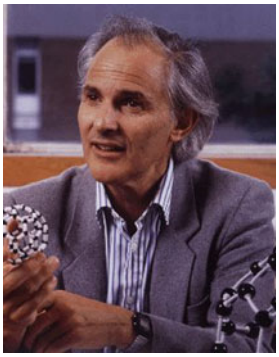

Professor Sir Harold Kroto, FRS, was born in 1939 in Wisbech, Cambridgeshire, and brought up in Bolton, Lancashire. He graduated in Chemistry at the University of Sheffield in 1961 and in 1964 received his Ph.D. there for research with R.N. Dixon on high-resolution electronic spectra of free radicals produced by flash photolysis. After 2 years of postdoctoral research in electronic and microwave spectroscopy at the National Research Council in Ottawa, Canada, he spent one year at Bell Laboratories, New Jersey, studying liquid phase interactions by Raman spectroscopy and he also carried out studies in Quantum Chemistry. He started his academic career at the University of Sussex (Brighton) in 1967, where he became a professor in 1985 and in 1991 he was made a Royal Society Research Professor. The research program at Sussex has covered several interdisciplinary areas. One area focused on the creation and spectroscopic characterization of new molecules, in particular, unstable species and reaction intermediates which contained labile multiple bonds. During a project that explored the possible source of these carbon chains in space, laboratory experiments that simulated the chemical reactions in the shells of red giant carbon stars were carried out which serendipitously uncovered the existence of C_{60} Buckminsterfullerene. In follow-up investigations of this original discovery the molecule was isolated independently at Sussex and structurally characterized. The presently active research program derives directly from the earlier work on C_{60} and focuses on the implications of the discovery for several areas of fundamental chemistry as well as the way in which it has revolutionized our perspective on carbon-based materials. The research encompasses the basic chemistry of the fullerenes, fundamental studies of carbon and metal clusters as well as carbon microparticles and nanotubes. Work on various aspects of interstellar and circumstellar molecules and dust is also in progress. Some parts of the research have been successful due to their interdisciplinary nature and this has been the result of synergistic collaborations involving primarily: colleagues J.F. Nixon, R. Taylor and D.R.M. Walton at Sussex, T. Oka at NRC (Canada), and R.F. Curl and R.E. Smalley at Rice University (Texas). Since 1990 he has been chairman of the editorial board of the Chemical Society Reviews. Sir Harold has received the following awards in the course of his career: 1981–82, Tildon Lecturer (Royal Society of Chemistry); 1990, Elected Fellow of the Royal Society; 1991, Royal Society Research Fellowship; 1992, International Prize for New Materials (American Physical Society), Italgas Prize for Innovation in Chemistry, Université Libre de Bruxelles (Doctor Honoris Causa), University of Stockholm (Doctor Honoris Causa), Longstaff Medal of the Royal Society of Chemistry, Academia Europea (Member); 1993, University of Limburg (Doctor Honoris Causa); 1994, Hewlett Packard Europhysics Prize, Moet

Hennessy and Louis Vuitton Science Pour l'Art Prize; 1995, University of Sheffield (Honorary Degree), University of Kingston (Honorary Degree); and 1996, Knighthood for services to chemistry and the Nobel Prize for Chemistry. Prof. Sir Harold W. Kroto, FRS, is currently at Florida State University, Tallahassee, Florida, USA.

Index

W. Ahmed and M.J. Jackson (eds.), *Surgical Tools and Medical Devices*,
DOI 10.1007/978-3-319-33489-9